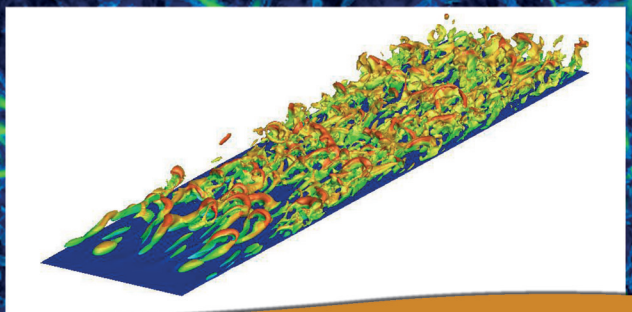
Turbulence Colloquium Marseille TCM2011

FUNDAMENTAL PROBLEMS OF TURBULENCE: 50 YEARS AFTER THE TURBULENCE COLLOQUIUM MARSEILLE OF 1961

26-30 September 2011,

Centre International de Rencontres Mathématiques, Marseille



Edited by
Marie Farge, Keith Moffatt, Kai Schneider

Turbulence Colloquium Marseille 2011

Fundamental Problems of Turbulence,

50 years after the Turbulence Colloquium Marseille 1961

Edited by
Marie Farge, Keith Moffatt and Kai Schneider

edp sciences

17 avenue du Hoggar
Parc d'activité de Courtabœuf, BP 112
91944 Les Ulis Cedex A, France

Printed in France

ISBN: 978-2-7598-1145-8

Cover: Julien Fournigault, Pôle Communication de l'École Normale Supérieure Paris, 2011.

Eight review articles and eight research papers (pp. 6–435) have been published electronically in the 'Journal of Turbulence' and are reproduced with the permission of Taylor&Francis Ltd (www.tandfonline.com).

This work is subject to copyright. All rights are reserved, whether the whole or part of the material is concerned, specifically the rights of translation, reprinting, re-use of illustrations, recitation, broad-casting, reproduction on microfilms or in other ways, and storage in data bank. Duplication of this publication or parts thereof is only permitted under the provisions of the French Copyright law of March 11, 1957. Violations fall under the prosecution act of the French Copyright law.

© EDP Sciences 2014

Contents

Foreword 1

Acknowledgements 5

Review articles

Homogeneous turbulence: an introductory review 6
by H. Keith Moffatt

Turbulent shear layers and wakes 17
by Garry Brown and Anatol Roshko

Progress in pipe and channel flow turbulence, 1961–2011 49
by John Kim

Highlights from 50 years of turbulent boundary layer research 68
by James Wallace

Turbulence before Marseille 1961 138
by Michael Eckert

Mathematics and turbulence: where do we stand? 163
by Claude Bardos and Edriss Titi

Cumulus clouds and convective boundary layers: a tropical perspective on two turbulent shear flows 198
by Roddam Narasimha

A review of relaxation and structure in some turbulent plasmas: magnetohydrodynamics and related models 223
by William Matthaeus, David Montgomery, Minping Wan and Sergia Servidio

Research articles

Lagrangian Markovianized field approximation for turbulence 260
by Wouter Bos and Jean Pierre Bertoglio

Third-order statistics and the dynamics of strongly anisotropic turbulent flows 282
by C. Cambon, L. Danaila, F.S. Godeferd and J.F. Scott

The role of directionality on the structure and dynamics of strongly anisotropic turbulent flows 322
by C. Cambon, and B.-J. Gréa

On helical multiscale characterization of homogeneous turbulence 344
by Frank G. Jacobitz, Kai Schneider, Wouter J.T. Bos, and Marie Farge

Studying Lagrangian dynamics of turbulence using on-demand fluid particle tracking in a public turbulence database 360
by Huidan Yu, Kalin Kanov, Eric Perlman, Jason Graham, Edo Frederix, Randal Burns, Alexander Szalay, Gregory Eyink and Charles Meneveau

Statistical symmetries and its impact on new decay modes and integral invariants of decaying turbulence 389
by Martin Oberlack and Andreas Zieleniewicz

Gradient trajectory analysis in a Jet flow for turbulent combustion Modelling 408
by M. Gampert, P. Schaefer, V. Narayanaswamy and N. Peters

Statistical theories versus statistical mechanics of homogeneous isotropic turbulence 426
by Tomomasa Tatsumi

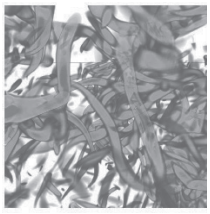
A Lie-group derivation of a multi-layer mixing length formula for turbulent channel and pipe flows 436
by Zhen-Su She, Xi Chen and Fazle Hussain

Reconsidering the `Local Equilibrium' Hypothesis for Small Scale Turbulence 456
by William K. George

Report of the final session 478

Photos and conference life..... 488

List of participants 501

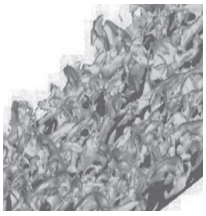


Turbulence Colloquium Marseille 2011

Fundamental Problems of Turbulence,

50 years after the Turbulence Colloquium Marseille 1961

CIRM, Marseille, 26-30 September 2011



Foreword: Turbulence Colloquium Marseille 2011:

Fundamental Problems of Turbulence, 50 years after the Marseille 1961 Conference,
Centre International de Rencontres Mathématiques (CIRM),
Marseille 26-30 September 2011, organized by
Marie Farge[1], H. Keith Moffatt[2] and Kai Schneider[3]

[1]*Ecole Normale Supérieure, Paris, France*
[2]*Trinity College, University of Cambridge, United Kingdom*
[3]*Aix-Marseille Université, Marseille, France*

1. Objective and scientific interest

Turbulence remains one of the oldest and most challenging research problems in both pure and applied science; recognition of the phenomenon can be traced back to Leonardo da Vinci who introduced the word '*Turbolenza*'. Turbulence characterises the flow of a fluid (gas, liquid or plasma) dominated by nonlinear interactions that make its description and the prediction of its evolution exceptionally difficult. Turbulence has been studied for several centuries by mathematicians as well as by physicists and engineers. It is still an open problem since no satisfactory theory is yet available, from either mathematical or physical viewpoint. Moreover, the turbulent regime may not be as universal as commonly supposed.

In 1961, Alexandre Favre organised one of the earliest international colloquia dedicated to turbulence on the occasion of the inauguration of the '*Institut de Mécanique Statistique de la Turbulence (IMST)*' that he founded in Marseille. The impact of this Colloquium was crucial and continues to play an important role 50 years later. It was attended by outstanding luminaries of the subject: Kolmogorov, Yaglom, von Karman, G.I. Taylor, Liepmann, Laufer, Corrsin, Batchelor, Kovasznay, Kraichnan, and many others. Key problems were identified and presented during review lectures given by several invited speakers, followed by extended open discussions [1]. This Colloquium led to the development of research areas that are still very much alive to this day.

2. Short description of the meeting

The Turbulence Colloquium Marseille 2011 (TCM2011) '*Fundamental Problems of Turbulence*' was organized in order to mark the 50th anniversary of this seminal meeting. It therefore

[1] 'Mécanique de la Turbulence' Proceedings of the International Colloquium held in Marseille, August 28th-September 2nd 1961, Colloques Internationaux du CNRS, 108, 1962.

followed the same pattern and adopted a similar long-term perspective. Its goal was to assess the achievements of the last 50 years of turbulence research and to identify future challenges that still remain. There were seven sessions, each devoted to a generic type of turbulent flow, together with three special sessions: a recollection of 'The Turbulence Colloquium Marseille 1961 (TCM 1961)', a presentation of mathematical ideas that arise through the study of turbulence and a final session to discuss new ideas and perspectives.

Just as for TCM1961, nine speakers were invited to present review lectures describing the state of the art in turbulence research; each session began with one of these review lectures, followed by posters and short oral presentations, and concluded with a one-hour open discussion led by the session president and recorded by a scientific secretary. More than 80 invited participants from 14 countries attended the colloquium.

TCM 2011 was chaired by four honorary presidents: Michel Coantic, Edward Spiegel, Tomomasa Tatsumi and Bryan Taylor. The review lecturers, presidents and scientific secretaries of the various sessions were as follows:

Homogeneous turbulence and flow structure

Review lecturer: H. Keith Moffatt
Presidents: Toshiyuki Gotoh and Fazle Hussain
Scientific secretaries: Wouter Bos and Michael Wilczek

Shear and wake flow turbulence

Review lecturers: Garry Brown and Anatol Roshko
Presidents: Robert Antonia and Charles Williamson
Scientific secretaries: Dmitry Kolomenskiy and Paulo Luzzatto-Fegiz

Pipe and channel flow turbulence

Review lecturer: John Kim
Presidents: Bruno Eckhardt and Zhen-Su She
Scientific secretaries: Xi Chen and Paulo Luzzatto-Fegiz

Boundary Layer Turbulence

Review lecturer: James Wallace
Presidents: Javier Jimenez and Beverley McKeon
Scientific secretaries: Sedat Tardu and Michael Wilczek

Historical session: *TCM1961*

Review lecturer: Michael Eckert
Presidents: Fabien Anselmet, Patrick Bontoux and Jean-Paul Dussauge
Scientific secretaries: Philip Schäfer and Antoine Venaille

Turbulent stirring and mixing

Review lecturer: Katepalli Sreenivasan
Presidents: Rahul Pandit and Norbert Peters
Scientific secretaries: Samriddhi Ray and Philip Schäfer

Mathematical session: ***mathematics for turbulence***

Review lecturer: Claude Bardos
Presidents: Charles Doering and Edriss Titi
Scientific secretaries: Dmitry Kolomenskiy and Romain Nguyen van yen

Geophysical turbulence

Review lecturer: Roddam Narasimha
Presidents: Herman Clercx and Joel Sommeria
Scientific secretaries: Antoine Venaille and Samriddhi Ray

Magneto-hydro-dynamic turbulence

Review lecturers: Bill Matthaeus and David Montgomery
Presidents: Bérengère Dubrulle and Shigeo Kida
Scientific secretaries: Wouter Bos and Nobu Yokoi

Final session: ***new ideas and perspectives***

3. Presidents: Eberhard Bodenschatz, Charles Meneveau and Parviz Moin
   Scientific secretaries: Lionel Larchevêque and Romain Nguyen van yen

The review lectures and the posters, together with papers, ideas and videos, can be downloaded from the colloquium's website: *http://www.turbulence.ens.fr*
The proceedings of TCM 1961 [1] have been digitalised and can also be found on the above address.

3. A guided tour through the book

Here is an outline of contributions made during *TCM2011* that are presented in this volume. Most of them have been published in the special issue of *Journal of Turbulence*.

There are eight review papers:

- H. Keith Moffatt reviews how our present understanding of homogeneous turbulence developed over the last 50 years, discussing the theory Kolmogorov presented at *TCM1961*, intermittency, the finite-time singularity problem, the skewness factor paradox, Kraichnan's direct interaction approximation, helicity and the turbulent dynamo, two-dimensional turbulence, rapid distortion theory, and problems related to passive and active scalar transport.
- Garry Brown and Anatol Roshko describe how turbulent shear layers and wakes are studied, with a particular emphasis on the experimental observation of large-scale vortical structures (coherent structures), and why they seem to play an essential role in understanding the turbulent regime.
- John Kim gives an overview of the progress made since *TCM1961* in understanding turbulent flows in pipes and channels, and addresses the unresolved issues that require further research.

- James Wallace presents a detailed survey of experimental and theoretical achievements made since *TCM1961* in the study of turbulent boundary layers.
- Michael Eckert shows how turbulence research developed up to *TCM1961*, detailing the circumstances and the environment in which new concepts emerged.
- Claude Bardos and Edriss Titi review the main theorems related to the Euler, Navier-Stokes and Prandtl equations relevant for studying turbulent flows.
- Roddam Narasimha covers recent developments in our understanding of turbulent atmospheric flows encountered in tropical clouds and in the low-wind convective regime of the atmospheric boundary layer.
- William Matthaeus, David Montgomery, Minping Wan and Sergia Servidio review the magnetohydrodynamics of several turbulent regimes encountered in plasma flows, in particular, for the electron fluid plasma that is closely related to two-dimensional hydrodynamics, and for the solar wind where three-dimensional effects become important.

This volume also includes ten research papers by participants of *TCM2011*, out of which eight have been published in the *Journal of Turbulence*. These ten papers do not cover all topics presented at the colloquium and mainly focus on: advances in statistical theory of homogeneous isotropic turbulence, helical multi-scale characterization of homogeneous turbulence, local equilibrium hypothesis, multi-layer mixing length formulae for turbulent channel and pipe flows, self-consistent closure, strongly anisotropic turbulence, statistical symmetries, turbulent combustion modelling and Lagrangian dynamics of turbulence.

The volume is concluded by the report of the final session, where the different presentations were summarized, and several open questions were proposed by the participants for future researches. Readers will also find the list of participants of *TCM2011*, together with the text of the 'final exam' they had to pass, and a selection of photos taken during the colloquium.

We thank all the participants for making *TCM2011* a successful event and we are grateful to the authors for contributing to this proceedings volume. We acknowledge *Taylor & Francis* for giving us the permission to reprint the papers of the *TCM2011* special issue published in the *Journal of Turbulence* and *EDP sciences* for publishing the book.

Bonne lecture!
Marie Farge, H. Keith Moffatt and Kai Schneider
(Paris, Cambridge and Marseille)

The organisers of *TCM2011* thankfully acknowledge the financial support from the following organisations:

- Centre International de Rencontres Mathématiques (CIRM).
- Université de la Méditerranée, Marseille.
- Total Company.
- Institut de Recherche sur la Fusion par confinement Magnétique (IRFM).
- Commissariat à l'Énergie Atomique et aux Énergies Alternatives (CEA).
- Center for Turbulence Research (CTR), Stanford University and NASA-Ames.
- Office of Naval Research Global.
- Groupement de Recherche Européen CNRS, Mécanique des Fluides Numériques.
- Institut National des Sciences de l'Univers (INSU), Centre National de la Recherche Scientifique (CNRS).
- Institut National des Sciences de l'Ingénierie et des Systèmes (INSIS), Centre National de la Recherche Scientifique (CNRS).
- Ecole Centrale de Marseille (ECM).
- European Research Community On Flow, Turbulence And Combustion (ERCOFTAC).
- Association Française de Mécanique (AFM).
- Conseil Général des Bouches du Rhône.
- Ville de Marseille.
- Ecole Normale Supérieure Paris.
- Région Provence-Alpes-Côte d'Azur (PACA).

Journal of Turbulence
Vol. 13, No. 39, 2012, 1–11

Taylor & Francis
Taylor & Francis Group

Homogeneous turbulence: an introductory review

H.K. Moffatt*

Department of Applied Mathematics and Theoretical Physics, University of Cambridge, Cambridge, UK

(*Received 3 July 2012; final version received 11 August 2012*)

A brief review of developments in the theory of homogeneous turbulence over the last 50 years is given, many of these developments stemming from lectures and discussions at the 1961 Marseille Colloquium *Mécanique de la Turbulence*. The following topics are discussed: Kolmogorov's 1961 lecture, intermittency and the finite-time singularity problem, the skewness factor paradox, Kraichnan's direct interaction approximation, helicity and the dynamo problem, two-dimensional turbulence, rapid distortion theory and the passive and active scalar problems.

Keywords: Kolmogorov; intermittency; skewness; helicity; rapid distortion

1. Marseille 1961

My credentials for presenting this opening review[1] are slender, relying as they do on the simple fact that I am one of the handful of surviving participants of the now legendary 1961 Marseille Colloque International du CNRS, Mécanique de la Turbulence (hereafter Marseille '61), which this present Colloquium seeks, if not to emulate, at least to commemorate. Allow me first to recall some features of that 1961 Colloquium that made it so special. I draw on the Proceedings [1] as a jog to my memory: a large red volume, perhaps less well-known hitherto than it should have been, but now scanned and accessible on the website <http://turbulence.ens.fr> of this present meeting.

The Colloquium was organised, and the Proceedings edited, by the late Alexandre Favre, Membre de l'Académie des Sciences, who deserves great credit for the memorable character of the event! The Scientific Committee consisted of G.K. Batchelor (my mentor and research supervisor at the time), J. Kampé de Fériet (the 'éminence grise' of French mechanics), L. Kovasznay (USA), H. Schlichting (Germany) and L. Sedov (USSR). In the event, Schlichting and Sedov were not present at the Colloquium, and Kampé de Fériet played a figurehead role, so the burden of scientific organisation fell on Batchelor, Kovasznay and Favre; they invited S. Corrsin, R.W. Stewart and H. Liepmann to act as Chairmen of various sessions – all eminent figures in the subsequent history of turbulence. But particularly memorable was the fact that three great father-figures were also present, namely Theodore von Kármán, G.I. (Sir Geoffrey) Taylor and A.N. Kolmogorov (who was accompanied by three colleagues from the Soviet Union, M.D. Millionschikov, A.M. Obukhov and A.M. Yaglom). This was a unique encounter, during that cold-war epoch, of great scientists from East and West, something that Batchelor had been particularly keen to engineer in

*Corresponding author. E-mail: hkm2@cam.ac.uk

ISSN: 1468-5248 online only
© 2012 Taylor & Francis
http://dx.doi.org/10.1080/14685248.2012.721559
http://www.tandfonline.com

difficult political circumstances. [The cold war was at its height: the Berlin blockade was in force from July to November that year, when the infamous Berlin Wall was constructed; the Soviet Union resumed nuclear testing on 1st September 1961, during the very week of Marseille'61, in response to a series of four atmospheric nuclear tests carried out by France in the Algerian Sahara between January 1960 and May 1961; and France itself was still, under General de Gaulle, in a state of political turmoil over the Algerian War of independence.]

It is noteworthy that neither Taylor nor von Kármán gave talks at the Colloquium, but they of course contributed to the discussions, and their presence lent great authority to the deliberations. Neither did Favre lecture, but his coordinating role as host was crucial. As for Millionschikov, he later rose to high office in the Soviet bureaucracy (a USSR postage stamp bearing his image was issued in 1974!), and his presence was sufficient to ensure that no member of the KGB was needed to 'keep an eye' on the Soviet delegation.

The second session of Marseille '61 was devoted to *Energy Transfer in Homogeneous Turbulence*, and it is on aspects of homogeneous turbulence that I focus in this review. Homogeneous turbulence, i.e. turbulence whose statistical properties are invariant under translations of the frame of reference, is of course a fiction: no field of turbulence is strictly homogeneous, since the presence of fluid boundaries inevitably introduces a degree of inhomogeneity. Nevertheless, 'homogeneity' is a useful idealisation that can be approximately realised in wind tunnel 'grid-generated' turbulence, widely studied in the belief that this provides a legitimate description of at least the smaller scales of turbulence far from fluid boundaries. For turbulence that is strictly homogeneous, the abstract concept of the 'ensemble average' may be conveniently replaced by the more accessible concept of the 'space average'; ergodic theory tells us that these two averages are, under the condition of homogeneity, equivalent.

Turbulence that is homogeneous may also be 'isotropic', i.e. its statistical properties may be invariant under rotations, as well as translations, of the frame of reference. In such a field of turbulence, there is no 'preferred direction': all directions are statistically equivalent. It should be noted however that isotropic turbulence need not be invariant also under mirror reflexions, a distinction that becomes crucially important when magnetohydrodynamic effects are under consideration (see §6 below).

Homogeneous turbulence may be forced or unforced. Forcing can be achieved in numerical simulations, though not in laboratory experiments, by inclusion of a random body force $\mathbf{f}(\mathbf{x}, \mathbf{t})$, itself statistically homogeneous, in the Navier–Stokes equation governing the flow. If this body force is also statistically stationary in time, a statistically steady homogeneous turbulent state can result; in this case, the ensemble average is equivalent to a time average, which is both conceptually clear and computationally convenient.

Unforced homogeneous turbulence, on the other hand, necessarily decays in time, as a result of the non-linear cascade of energy to the very small scales of motion at which viscous dissipation of kinetic energy sets in. It is an essential tenet of Kolmogorov's [2] theory that the mean rate of cascade (and subsequent decay) of energy ϵ is independent of kinematic viscosity ν in the limit $\nu \to 0$.

2. K41 and Kolmogorov's 1961 lecture

This 1941 theory of Kolmogorov (K41) was then, as still even now, a central pillar of understanding of the mechanics of turbulence, and so it was particularly fitting that he should be present at Marseille '61. In fact, a highlight of the meeting, alluded to only in a footnote to the paper by T.H. Ellison (p. 115 of the Proceedings), was the display of slides by Stewart from the observations later published in *JFM* [3] of turbulent spectra in a tidal

channel at Reynolds number (based on depth and mean velocity) up to 3×10^8. These experiments provided what Ellison described as 'by far the most convincing demonstration of the correctness of the Kolmogorov theory that has yet been made'. This was of exceptional importance for two reasons: first, because huge effort had been expended, particularly by Batchelor (and references therein) [4] in promoting the Kolmogorov theory, and much of the current understanding relied on the Kolmogorovian concept of the 'energy cascade' and the $k^{-5/3}$ energy spectrum to which this gave rise; and second, because this picture was being currently challenged by the alternative 'direct-interaction' theory of Kraichnan (1959) [5] which led to a significantly different ($k^{-3/2}$) spectrum. The tidal-channel observations reported by Stewart gave unambiguous support for the Kolmogorov scenario.

So far, so good! But then Kolmogorov was invited to give his lecture with the title 'Précisions sur la structure locale de la turbulence dans un fluide visqueux aux nombres de Reynolds élevés'. The paper is reproduced in both French and Russian in the Proceedings, and in English translation in *JFM* [6]. Kolmogorov delivered his lecture in French, and his only visual aid was the blackboard. What was so startling was that (following reference to parallel work of Obukhov and to comments that he attributed to Landau) Kolmogorov proceeded to point out fundamental inconsistencies in his own (1941) theory, in that this theory failed to take account of the spatial fluctuations in the rate of turbulent dissipation of energy ϵ, the key parameter of the theory. Kolmogorov offered arguments supporting a log-normal probability distribution for this quantity, and showed that the exponent in the energy spectrum would be slightly modified through this 'intermittency' effect. (Later work on the behaviour of higher-order structure functions of the form $S_n(r) = <(u(\mathbf{x}+\mathbf{r}) - u(\mathbf{x}))^n>$, for $n = 2, 3, 4, \ldots$, where u is, say, the velocity component parallel to the direction of the separation vector $\mathbf{r}$, has revealed that Kolmogorov's log-normal assumption itself is untenable ([7, 8]).)

This lecture, Kolmogorov's final contribution to turbulence, was, to put it mildly, a bit of a bombshell! There had been hints previously that all was not well with the Kolmogorov picture; in particular, as described in Batchelor's [4] monograph, the dimensionless flatness factor of the velocity derivative

$$F = \frac{\left\langle (\partial u/\partial x)^4 \right\rangle}{\left\langle (\partial u/\partial x)^2 \right\rangle^2}\,, \tag{1}$$

which, on the Kolmogorov theory should be a universal constant in the limit of large Reynolds number Re, in fact showed a worrying experimental increase with increasing Re, with no tendency to settle down to a limiting constant value. The implication was that, as Re increases, the vorticity of the turbulence tends to become more and more concentrated in 'fine structures' (vortex tubes and/or sheets being the most natural candidates), a picture that was hard to reconcile with the idea of an energy cascade from the energy-containing scale l_0 through a geometric sequence of length scales like $2^{-n} l_0$. Kolmogorov's revised theory, taking account of the intermittency of $\epsilon(\mathbf{x}, t)$, was however potentially capable of explaining the increase of F with Re, and even more so, of the behaviour of higher-order statistical properties of the small-scale features of the turbulence (including in particular the vorticity field).

3. Intermittency and the finite-time singularity problem

Kolmogorov's paper marked the onset of a widespread effort in the turbulence research community to understand the phenomenon of intermittency, for which many competing

models have been proposed. This has been much stimulated on the one hand by the detection of concentrated vortices within a field of turbulence [9] and on the other by direct numerical simulations (DNS), which display turbulence as a random superposition of concentrations of vortex tubes on all scales from the Taylor microscale $\sim l_0 Re^{-1/2}$ down to the Kolmogorov scale $\sim l_0 Re^{-3/4}$ (e.g. [10,11]). The cascade picture has now given way to a picture in which the progressive degradation of energy from large to small scales is simply a consequence of vortex tube stretching, each vortex tube being locally stretched (with associated decrease of cross-section, i.e. decrease of scale) by the straining flow induced by all the other vortices of the field of turbulence.

This revised picture has in turn re-stimulated interest in the fundamental problems of regularity associated with the Euler equations and the Navier–Stokes equations at very high Re as first addressed by Leray [12]: given smooth initial conditions for the vorticity field, does this field in general remain smooth for all time, or alternatively, does there exist any smooth initial condition of finite energy from which a singularity of vorticity emerges within a finite time? The question is of course fascinating in its own right, and quite independently of the general problem of turbulence. The natural initial condition to consider is a vortex-tube tangle, each tube containing axial vorticity of Gaussian cross-section. Is it not amazing that we still do not know whether such tangles can lead to a singularity or not! DNS is as yet inconclusive, in no small part because numerical techniques inevitably break down as a singularity is approached. If a singularity can indeed form, then some kind of self-similar structure (or structure within a structure) of scale decreasing to zero at the singularity time is to be expected, but such description remains elusive.

The problem is important for turbulence, because it has an obvious bearing on the structure of turbulence at the smallest scales. Considering for the moment the inviscid limit $\nu \to 0$, the Kolmogorov spectrum extends to wavenumber $k = \infty$ (i.e. zero length-scale). The time-scale for energy transfer from scale k^{-1} to scale zero, as determined dimensionally from ϵ and k, is then $t_k = \epsilon^{-1/3} k^{-2/3}$. This suggests that in the Euler limit, singularities must develop at finite time. Of course, a divergent enstrophy spectrum $\sim k^{1/3}$ suggests the same. But no explicit solution of the Euler equations has as yet revealed the singular asymptotic structure of the vorticity field that such arguments might suggest.

DNS has played an increasingly prominent role in turbulence research ever since the pioneering work of Orszag and Patterson [13] (see, for example, the recent review by Ishihara et al. [14]), and its importance cannot be over-estimated. It remains fair to say however that advances in understanding require a symbiotic interaction between DNS and theoretical analysis: each activity feeds on, and at the same time provides guidance for, the other; now only in this way can further real progress be made.

4. The paradox of the skewness factor

A related puzzle concerns the skewness factor of the velocity derivative

$$S = \frac{\left\langle (\partial u/\partial x)^3 \right\rangle}{\left\langle (\partial u/\partial x)^2 \right\rangle^{3/2}}\,, \tag{2}$$

which again, on K41 theory, should be a universal constant in the limit $Re \to \infty$. Batchelor said in his Marseille '61 lecture that 'the available measurements ... suggest that it is still decreasing (in magnitude) at the highest Reynolds numbers of the measurements, and we cannot yet be sure that the asymptotic value is non-zero'. This remains a crucial issue,

because in 3D isotropic turbulence the vorticity $\boldsymbol{\omega}$ satisfies

$$\left\langle |\boldsymbol{\omega}|^3 \right\rangle \sim |S| \left\langle \boldsymbol{\omega}^2 \right\rangle^{3/2} , \tag{3}$$

and the enstrophy equation takes the form

$$\frac{\partial \left\langle \boldsymbol{\omega}^2 \right\rangle}{\partial t} = C \left\langle \boldsymbol{\omega}^2 \right\rangle^{3/2} - 2\nu \left\langle (\nabla \times \boldsymbol{\omega})^{\mathbf{2}} \right\rangle , \tag{4}$$

where C is a dimensionless positive constant proportional to $|S|$. In the formal limit $\nu = 0$, this equation implies blow-up of enstrophy in a finite time, and again, this would appear to imply the appearance of singularities in the vorticity distribution, at least in the Euler limit. So, what is the latest information on the skewness factor in the high Re limit? I do not know that we are any nearer to a definite answer to this central question than we were in 1961.

5. Kraichnan's direct interaction approximation

Bob Kraichnan also gave a memorable lecture at Marseille '61 in which he compared various approaches to the closure problem of turbulence, including the quasi-normal (or zero-fourth-cumulants) approximation of Millionschikov [15] and his own direct-interaction approximation published two years earlier [5]. Kraichnan simply stood at the microphone and spoke for 40 minutes with extraordinary lucidity, and without the help of a single visual aid, even chalk on blackboard! His lecture was followed by a critique of 'Kraichnan's theory of turbulence' by Ian Proudman, a younger colleague of Batchelor, who had published an extensive treatment of the quasi-normal theory with W.H. (Bill) Reid some years earlier ([16]; see also [17])[2]. Proudman's critique was savage by any standard, his conclusion being: 'I do not hold out much hope for useful results from the theory [of Kraichnan]'. Kraichnan was understandably perturbed by this unfavourable assessment.

In some respects, Proudman's pessimism was justified. As mentioned earlier, the experimental evidence did not support a $k^{-3/2}$ energy spectrum, which was a key prediction of the theory. However, in his response (published as an Appendix to his own paper in the Proceedings), Kraichnan pointed out a key 'realisability' property of his theory, namely that it guaranteed that the energy spectrum would remain positive for all time. He referred to the paper by Ogura (presented at the IUGG-IUTAM Symposium that followed immediately on Marseille '61, and later published as Ogura [19]), which provided numerical evidence that the quasi-normal closure (which incidentally leads to an enstrophy equation of the form (4)) leads to the inadmissible development of a negative energy spectrum in the energy-containing range of wave-numbers. In this respect therefore, the direct interaction approximation was clearly superior (and this because it was an exact closure for a physically realisable dynamical system, although unfortunately not the Navier–Stokes system).

Kraichnan was subsequently able to modify his theory in such a way as to yield a $k^{-5/3}$ spectrum (his Lagrangian-History Direct Interaction Approximation, or LHDIA). I spent four months in Stan Corrsin's group at Johns Hopkins University (September–December 1965), and I recall that we met for a weekly sandwich-lunch discussion session, to work our way through this theory, but such was its complexity that we were not much the wiser by the end of the term. The theory [20] takes account of the 'sweeping' of small eddies by large eddies, in a mixed Lagrangian–Eulerian framework. In effect, this forces the energy transfer to be local in wave-number space, and this in turn leads on dimensional grounds

to the Kolmogorov spectrum $E(k) = C\epsilon^{2/3}k^{-5/3}$. The reward for all the hard work is that the universal constant C is determined by the theory; the downside is that, although $k^{-5/3}$ appears fairly robust, the 'constant' C varies by about $\pm 30\%$ in different experimental contexts (Monin and Yaglom [21], Chap. 8).

6. Helicity and the dynamo problem

One important aspect of homogeneous turbulence is the manner in which it acts upon a convected scalar field (like temperature) or vector field (like magnetic field), in conjunction with the effects of molecular diffusion. The passive scalar problem is to be covered in another section of this meeting, so I shall say no more here (except to recall that Philip Saffman gave a remarkable lecture at Marseille '61 on the counter-intuitive interaction of molecular and turbulent diffusion of a scalar released from a fixed point in a turbulent flow – Saffman [22]). But I would like to comment on the vector field problem, because many of the advances in our understanding of the dynamics of turbulence have come from parallel considerations concerning MHD turbulence.

The emphasis in 1961 was on the increasing degradation of energy in going from large to small scales, i.e. the production of chaos (the small-scale turbulence) from order (the large-scale shearing or straining motion). A dramatic change came from an unexpected quarter in the paper of Steenbeck et al. [23][3]. These authors recognised that a large-scale well-ordered magnetic field could arise more or less spontaneously as a result of coherent interaction of small-scale random motion and the small-scale random field fluctuations to which this motion gives rise; in other words, order could arise out of chaos. I see this now as the most far-reaching and important discovery in the context of turbulence of this last half-century; but I have to admit to a certain degree of prejudice, because I came into this topic myself quite independently from a different direction three years later. I had been intrigued by the paper of Woltjer [26] who had shown that under certain circumstances, the quantity

$$H_M = \int \mathbf{A} \cdot \mathbf{B}\, dV \tag{5}$$

(where $\mathbf{A}$ is a vector potential for $\mathbf{B}$) is an invariant in a perfectly conducting fluid. The key was to recognise that the reason for this invariance is simply that the lines of force are transported with the fluid, and their topology is therefore conserved. It was a small step to realise that the same type of invariant must exist for the vorticity field in an ideal fluid in which vortex lines are 'frozen' in the flow. This 'inviscid invariant' is the helicity

$$H = \int \mathbf{u} \cdot \boldsymbol{\omega}\, dV, \tag{6}$$

since $\mathbf{u}$ is, in effect, a vector potential for $\boldsymbol{\omega}$. This new invariant [27], [28] is a consequence of Kelvin's [29] theorem on the conservation of circulation; but it had lain undiscovered for close on 100 years since then!

It might be thought that helicity conservation, in conjunction with energy conservation, should have a profound effect on the cascade process through the inertial range (where viscous effects are negligible). Indeed, if we think of this energy cascade in terms of vortex tube stretching, then conservation of helicity does enter the picture, implying as it does, that vortex tube topology is conserved. The effect is less obvious in spectral terms; the fact

that the helicity spectrum is not positive-definite means that one cannot argue for a simple cascade of helicity from large to small scales: helicity can be created at large scales at the expense of the creation of equal and opposite helicity at small scales!

The presence of non-zero helicity does however have a profound effect on the generation of a large-scale magnetic field (the dynamo effect) as Steenbeck et al. had predicted. Even at low magnetic Reynolds number Re_m, magnetic field will grow under the effect of homogeneous turbulence provided only that the helicity is non-zero (providing an 'alpha effect'), and the space available for the growth of the field is large enough. This space requirement is easily satisfied in planetary and astrophysical contexts! There is also an enhanced diffusivity due to the turbulence (the 'beta effect'), but the alpha effect dominates on a large enough scale [30].

In his Marseille '61 lecture, 'Turbulence in compressible and electrically conductive media', Kovasznay anticipated this turbulent diffusivity effect. He also emphasised the need for a 'clear, simple and meaningful experiment' in order 'to obtain educated guesses about relative importance of different approaches'. Such an experiment has been brilliantly conceived and realised by the French team working at Paris (ENS and Saclay), Lyon and Cadarache (Monchaux [31]) have demonstrated dynamo action in a 'washing machine' in which liquid sodium is stirred into strongly helical turbulent motion by counter-rotating propellers. Both mean flow and turbulent dynamo effects are present in this experiment, which has for the first time demonstrated that the process responsible for generation of the Earth's magnetic field can indeed be simulated in the laboratory.

7. Two-dimensional turbulence

Two-dimensional turbulence was briefly discussed by Batchelor in the closing sections of his 1953 monograph, where he pointed out an important consequence of (inviscid) enstrophy conservation: the inevitability of an inverse energy cascade (although he did not use this terminology). I believe his interest in this problem was rekindled through discussions with Kraichnan at Marseille '61. At any rate, soon after, he put his research student Roger Bray to work on a numerical simulation of 2D turbulence [32]. More or less simultaneously, Kraichnan developed his ideas on the subject. Kraichnan [33] and Batchelor [34] gave his version of the enstrophy cascade, with reference to Bray's numerical results. The inverse energy cascade can also be regarded as a manifestation of the emergence of 'order out of chaos' as later clarified by McWilliams [35] in his paper 'The emergence of isolated coherent vortices in turbulent flow'. The importance of nearly 2D turbulence in the context of atmospheric dynamics has led to intense activity in this field. Density stratification, strong rotation with associated Coriolis effects, and strong 'applied' magnetic field can all (separately or possibly in conjunction) lead to 'two-dimensionalisation' of a field of turbulence, although the residual effect of weak three-dimensionality can remain of crucial importance. Such turbulence is strongly anisotropic, but nevertheless can remain homogeneous; it is a subject of continuing research interest in which real progress may be anticipated.

8. Rapid distortion theory

Homogeneous turbulence that is subjected to uniform strain, whether rotational or irrotational, remains homogeneous, although increasingly anisotropic as the effect of the strain progresses. If this straining is sufficiently rapid, then its effect on the turbulence may be treated in at least a first approximation by a linearised analysis in which nonlinear interaction

of the turbulence with itself is neglected. This is what is known as rapid distortion theory (or RDT). Like so many aspects of turbulence, RDT goes back to a paper of G.I.Taylor [36] who analysed the damping of turbulent fluctuations in flow through a contraction in a wind tunnel.

In his 1956 book, *The Structure of Turbulent Shear Flow* [37], Alan Townsend had used a version of RDT to determine the structure of what he described as the 'big eddies' in free turbulent flows. He assumed that only the irrotational part of the strain was relevant and allowed this strain to progress only until a degree of anisotropy consistent with experimental measurements was attained. In his Marseille '61 lecture on 'Free turbulent flows', Hans Liepmann made passing reference to this approach, but regarded the resulting models of eddy structure as but 'a groping for an eventual representation of a stochastic rotational field'.

I could not understand Townsend's reason for focusing on just the irrotational ingredient of the strain field, and in a later investigation I found that the effect of plane shear on turbulence was indeed quite different [38]: as is now well recognised, plane shearing is the mechanism by which streamwise vortices become prominent in the flow. S.J. Kline discovered the related 'streaks' in a turbulent boundary layer at about the same time [39]. 'Coherent structures' became a growth industry during the 1970s, a period that marked a return towards mechanistic approaches based on vortex interactions in **x**-space, in parallel with the purely statistical approach that found its most natural expression in **k**-space.

In the second edition of his book (1976, §3.12 *et seq.*), Townsend adopted the plane-shear (as opposed to the irrotational-strain) description in his approach to the energy-containing eddies, and concluded: 'Generally, the measurements of the behaviour of turbulent fluid under either irrotational distortion or plane shearing flow show that the larger eddies, possessing most but not all of the energy, are persistent and coherent structures which interact with the mean flow in the "rapid-distortion" manner, and which lose energy and interact with the smaller eddies by processes that can be modelled by an effective viscosity'. The fact that linearised RDT is more successful than we have any right to expect provides one ray of light in the continuing search for a complete theoretical description of turbulence.

Additional effects such as uniform density stratification, Coriolis forces due to rotation, and Lorentz forces due to an applied uniform magnetic field can all act in conjunction with uniform distortion to induce anisotropy in a homogeneous field of turbulence, without inducing inhomogeneity. Much work in this area has been described in the book *Homogeneous Turbulence Dynamics* by Sagaut and Cambon [40], which testifies to the continuing vitality of RDT, particularly in geo- and astro-physical contexts.

9. The active scalar field problem

If weak variations of a scalar contaminant are present in a field of turbulence, then this scalar field is subject to convection and molecular diffusion, but does not react back dynamically upon the convecting velocity field; this constitutes the 'passive scalar field problem'.

There are many circumstances however in which the contaminant *may* react back upon the velocity field. For example, if the 'contaminant' is temperature $\theta(\mathbf{x}, t)$, then buoyancy forces come into play, and the velocity field $\mathbf{u}(\mathbf{x}, t)$ is itself influenced to a greater or lesser extent by the θ-field.

In an extreme situation, we may suppose that $\mathbf{u}$ is actually 'driven' by the θ-field. This was the situation considered by Batchelor et al. [41], in their paper *Homogeneous buoyancy-generated turbulence* (Batchelor's last significant contribution to turbulence). The non-linearity $\mathbf{u} \cdot \nabla\theta$ associated with convection of θ is now just as important as the nonlinear contribution $\mathbf{u} \cdot \nabla\mathbf{u}$ to the Navier–Stokes equations.

If we consider turbulence in a rotating system at small Rossby number (i.e. dominant Coriolis effect, as in the Earth's liquid core), then the non-linear acceleration $\mathbf{u} \cdot \nabla \mathbf{u}$ is negligible, and we have a form of turbulence driven by buoyancy forces in which the sole nonlinearity is represented by the convective term $\mathbf{u} \cdot \nabla \theta$ in the advection–diffusion equation, a state of affairs that may be described as 'geostrophic turbulence'. If a linearised Lorentz force is also present, then we have 'magnetostrophic turbulence' which again (starting from a very weak field) is potentially capable of dynamo action [42]. If the statistics of the θ-distribution are assumed known, then the statistics of the velocity and magnetic fields can be deduced by linearised analysis similar to RDT. The essential problem that remains is to determine the statistical evolution of the θ-field, given the source of temperature variations, a problem whose regularity properties have recently been investigated by Friedlander [43]. This type of turbulence problem is far removed from conventional laboratory turbulence; but it contains the same essential ingredients: non-linear spreading of energy in $\mathbf{k}$-space, and dissipation by molecular diffusivity at the smallest scales. Such problems continue to present a challenge for the future.

10. Conclusion

The Marseille 1961 Turbulence Colloquium was remarkably wide-ranging in the issues that it explored, and the discussions at the Colloquium sowed the seeds for a number of important later research developments. Computers were still at a relatively primitive stage of development, but even then the numerical work of Ogura [19] that demonstrated a fundamental flaw of the quasi-normal approximation gave a hint of the central role that computation was to play in the future. The search for a fundamental theory of turbulence was very much alive then; it is still alive today, though perhaps in a slightly battered state, since so many approaches have been tried and discarded along the way. The fact that order can emerge from chaos in MHD turbulence (through the spontaneous growth of a large-scale magnetic field) is, in my view, one of the most striking discoveries of the last 50 years, as is the identification of concentrated vortices as perhaps the key element of turbulent flow. The interaction of these vortices remains a pressing problem, both for theory and numerics, and the underlying problem of regularity of the Navier–Stokes equations (otherwise known as the finite-time singularity problem) remains a central challenge for mathematically oriented fluid dynamicists, in essential partnership with experts in scientific computing. Let us hope the next 50 years will reveal the answer to this problem, one way or another!

Notes

1. Lecture delivered at the Turbulence Colloquium, Marseille 2011, commemorating Mécanique de la Turbulence, Marseille 1961.
2. A new 'cross-independence' closure theory has recently been proposed by Tatsumi [18], 54 years after the same author's first paper on the decay of isotropic turbulence, a remarkable span of sustained investigation!
3. This paper and subsequent papers by the same authors were published in German, and were not very well known in the West until translated into English by Roberts and Stix [24], and subsequent publication of the book of Krause and Rädler [25].

References

[1] A. Favre, *Proc. Int. Coll. 'Mécanique de la Turbulence', Marseille 1961*, CNRS Publisher, France. 1962 p. 108.

[2] A.N. Kolmogorov, *The local structure of turbulence in incompressible viscous fluid for very large Reynolds number*, Dokl. Akad. Nauk SSSR 30 (1941), pp. 9–13.
[3] H.L. Grant, R.W. Stewart, and A. Moilliet, *Turbulence spectra from a tidal channel*, J. Fluid Mech. 12 (1962), pp. 241–268.
[4] G.K. Batchelor, *The Theory of Homogeneous Turbulence*, Cambridge University Press, Cambridge, UK, 1953.
[5] R.H. Kraichnan, *The structure of isotropic turbulence at very high Reynolds numbers*, J. Fluid Mech. 5 (1959), pp. 497–543.
[6] A.N. Kolmogorov, *A refinement of previous hypotheses concerning the local structure of turbulence in a viscous incompressible fluid at high Reynolds number*, J. Fluid Mech. 13 (1962), pp. 82–85.
[7] F. Anselmet, Y. Gagne, E.J. Hopfinger, and R.A. Antonia, *High-order velocity structure functions in turbulent shear flows*, J. Fluid Mech. 140 (1984), pp. 63–89.
[8] U. Frisch, *From global scaling, à la Kolmogorov, to local multifractal scaling in developed turbulence*, Proc. Roy. Soc. A 434 (1991), pp. 89–99.
[9] S. Douady, Y. Couder, and M.E. Brachet, *Direct observation of the intermittency of intense vorticity filaments in turbulence*, Phys. Rev. Lett. 67 (1991), pp. 983–986.
[10] A. Vincent and M. Meneguzzi, *The dynamics of vorticity tubes in homogeneous turbulence*, J. Fluid Mech. 225 (1991), pp. 1–20.
[11] M. Yokokawa, K. Itakura, A. Uno, T. Ishihara, and Y. Kaneda, *16.4-TFlops direct numerical simulation of turbulence by a Fourier spectral method on the Earth Simulator*, 2002. Available at http://www.sc-2002.org/paperpdfs/pap.pap273.pdf.
[12] J. Leray, *Sur le mouvement d'un liquide visqueux emplissant l'espace*, Acta Math. 63 (1934), pp. 193–248.
[13] S.A. Orszag and G.S. Patterson, *Numerical simulation of three-dimensional homogeneous isotropic turbulence*, Phys. Rev. Lett. 28 (1972), pp. 76–79.
[14] T. Ishihara, T. Gotoh, and Y. Kaneda, *Study of high-Reynolds number isotropic turbulence by direct numerical simulation*, Ann. Rev. Fluid Mech. 41 (2009), pp. 165–180.
[15] M.D. Millionschikov, *On the uniform isotropic turbulent theory*, Proc. USSR Acad. Sci. Geogr. Ser. 4–5 (1941), p. 433.
[16] I. Proudman and W.H. Reid, *On the decay of a normally distributed and homogeneous turbulent velocity field*, Phil. Trans. R. Soc. 247 (1954), pp. 163–189.
[17] T. Tatsumi, *The theory of decay process of incompressible isotropic turbulence*, Proc. Roy. Soc. Lond. A 239 (1957), pp. 16–45.
[18] T. Tatsumi, *Cross-independence closure for statistical mechanics of fluid turbulence*, J. Fluid Mech. 670 (2011), pp. 365–403.
[19] Y. Ogura, *A consequence of the zero-fourth-cumulants approximation in the decay of isotropic turbulence*, J. Fluid Mech. 16 (1963), pp. 33–40.
[20] R.H. Kraichnan, *Lagrangian-history closure approximation for turbulence*, Phys. Fluids 8 (1965), pp. 575–598.
[21] A.S. Monin and A.M. Yaglom, *Statistical Fluid Mechanics: Mechanics of Turbulence*, Vol. 2, J.L. Lumley, ed., MIT Press. Cambridge, MA, 1975.
[22] P.G. Saffman, *On the effect of the molecular diffusivity in turbulent diffusion*, J. Fluid Mech. 8 (1960), pp. 273–283.
[23] M. Steenbeck, F. Krause, and K.-H. Rädler, *Berechnung der mittleren Lorentz-Feldstärke* $< \mathbf{v} \times \mathbf{B} >$ *fur ein elektrisch leitendes Medium in turbulenter, durch Coriolis-Kräfte beinfluster Bewegung*, Z. Naturforsch. 21a (1966), pp. 369–376.
[24] P. H. Roberts and M. Stix, *The turbulent dynamo. A translation of a series of papers by F.Krause, K.-H.Rädler & M.Steenbeck*, NCAR, USA, Tech. Note. 1971, p. 60.
[25] F. Krause and K.-H. Rädler, *Mean-field Magnetohydrodynamics and Dynamo Theory*, Pergamon Press, Oxford, UK, 1980.
[26] M. Woltjer, *A theorem on force-free magnetic fields*, Proc. Natl. Acad. Sci. 44 (1958), pp. 76–79.
[27] J.J. Moreau, *Constants d'un îlot tourbillonnaire en fluide parfait barotrope*, C.T.hebd. Séanc. Acad. Sci. Paris 252 (1961), pp. 2810–2812.
[28] H.K. Moffatt, *The degree of knottedness of tangled vortex lines*, J. Fluid Mech. 35 (1969), pp. 117–129.
[29] Kelvin, Lord (W. Thomson), *On vortex motion*, Trans. R. Soc. Edin. 25 (1868), pp. 217–260.

[30] H.K. Moffatt, *Magnetic Field Generation in Electrically Conducting Fluids*, Cambridge University Press, Cambridge, UK, 1978.
[31] R. Monchaux, *Generation of magnetic field by dynamo action in a turbulent flow of liquid sodium*, Phys. Rev. Lett. 98 (2007), 044502.
[32] R.W. Bray, *A study of turbulence and convection using Fourier and numerical analysis*, Ph.D. thesis, University of Cambridge, Cambridge, UK, 1966.
[33] R.H. Kraichnan, *Inertial ranges in two-dimensional turbulence*, Phys. Fluids 10 (1967), pp. 1417–1423.
[34] G.K. Batchelor, *Computation of the energy spectrum in homogeneous two-dimensional turbulence*, Phys. Fluids Suppl. II 12 (1953), pp. 233–239.
[35] J.C. McWilliams, *The emergence of isolated coherent vortices in turbulent flow*, J. Fluid Mech. 146 (1984), pp. 21–43.
[36] G.I. Taylor, *Turbulence in a contracting stream*, Z. Angew. Math. Mech. 15 (1935), pp. 91–96.
[37] A.A. Townsend, *The Structure of Turbulent Shear Flow*, 2nd ed.: 1976, Cambridge University Press, Cambridge, UK, 1956.
[38] H.K. Moffatt, *Interaction of turbulence with strong wind shear*, (A.M. Yaglom and V.I. Tatarski, eds.), Nauka, Moscow, USSR, 1967, pp. 139–156.
[39] S.J. Kline, W.C. Reynolds, F.A. Schraub, and P.W. Rundstadler, *The structure of turbulent boundary layers*, J. Fluid Mech. 30 (1967), pp. 741–773.
[40] P. Sagaut and C. Cambon, *Homogeneous Turbulence Dynamics*, Cambridge University Press, Cambridge, UK, 2008.
[41] G.K. Batchelor, V.M. Canuto, and J.R. Chasnov, *Homogeneous buoyancy-generated turbulence*, J. Fluid Mech. 235 (1992), pp. 349–378.
[42] H.K. Moffatt, *Magnetostrophic turbulence and the geodynamo*, in *Proceedings of the IUTAM Symposium on Computational Physics and New Perspectives in Turbulence*, Y. Kaneda, ed., Springer, 2007, pp. 339–346.
[43] S. Friedlander, *On the ill/well-posedness and nonlinear instability of the magnetogeostrophic equations*, Nonlinearity 24 (2011), pp. 3019–3042.

Journal of Turbulence
Vol. 13, No. 51, 2012, 1–32

Taylor & Francis
Taylor & Francis Group

Turbulent shear layers and wakes

Garry L. Brown[a*] and Anatol Roshko[b]

[a]*Department of Mechanical and Aerospace Engineering, Princeton University, Princeton, New Jersey, USA;* [b]*Division of Engineering and Applied Science, California Institute of Technology, Pasadena, California, USA*

(*Received 10 April 2012; final version received 1 August 2012*)

This paper considers the lectures on turbulent shear layers and wakes presented and discussed at the Marseille meeting in 1961 and provides our perspective on progress in understanding the mechanics of these flows since that time. The initial discussion is based on the understanding in 1961 gained from prior work. Particular emphasis is then placed on the subsequent experimental revelation of the large-scale vortical structure (coherent structure) found to be essential to understanding the mechanics of the turbulent shear layer. Critical insight into the mechanics that determines the growth rate (the shear stress), for example, is provided by the Biot–Savart relationship. Conclusions are drawn from the experiments and some unresolved questions posed. This is followed by a discussion of plane wakes. Four regions of the plane wake are identified and experimental results on the large-scale structure are discussed. Again emphasis is placed on the vorticity and the vorticity fluxes that contribute directly to the derivative of the principal Reynolds stress. Results from numerical calculations offer new insights into the mechanics, especially through the vorticity and vorticity fluxes that could not previously be measured. For this case too, conclusions are drawn and outstanding questions posed.

Keywords: turbulent shear flows

1. Introduction

The subject for this session of the 2011 meeting, turbulent shear layers and wakes, can be considered as a subset of free turbulent shear flows. It was covered in Marseille in 1961 in a session that had only two lectures, one by Liepmann [1] and the other by Coles [2]. Liepmann, in his summary, refers to the discovery by flow visualization of a sharp interface separating the multiscale, vorticity field of the 'turbulent' flow from the outer, irrotational, flow (Figure 1), as the 'single most important experimental finding in turbulent shear flows'. It was observed by Corrsin [3] and its features were further recognized by Townsend [4]. Corrsin and Kistler [5], especially, considered the properties of this interface to be important for the entrainment of irrotational fluid into the turbulent region.

Liepmann described the fluid that has small-scale rotational motions and in which the large-scale motion develops, as a 'turbular fluid', whereas earlier Townsend [6] had made the same identification but he called it the 'turbulent fluid', apparently assigning to it the principal role in the development of the mean flow. He postulated a 'typical' large-scale

*Corresponding author. Email: glb1873@msn.com

ISSN: 1468-5248 online only
© 2012 Taylor & Francis
http://dx.doi.org/10.1080/14685248.2012.723805
http://www.tandfonline.com

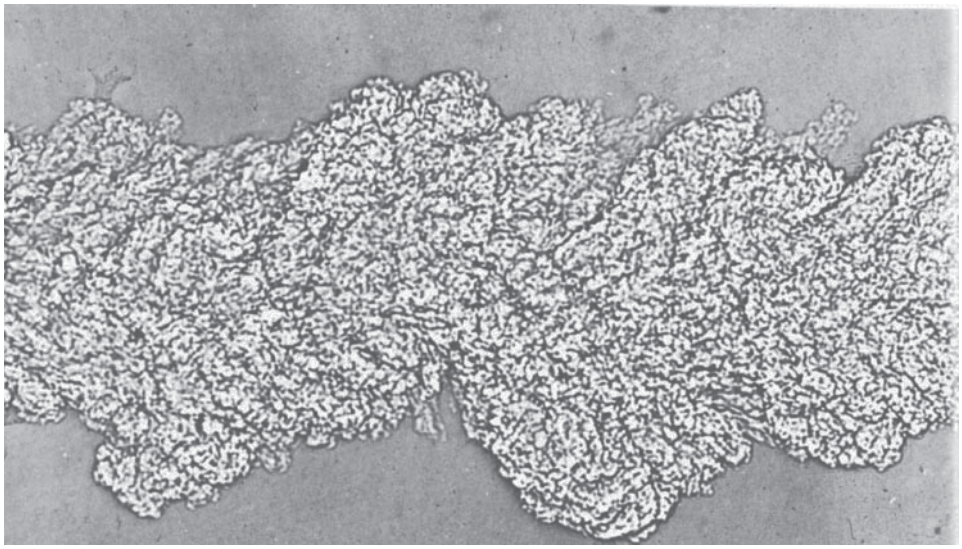


Figure 1. The wake of a bullet [Ballistic Research Laboratory (BRL), Aberdeen Proving Ground [5]).

eddy and sought to understand how the mean strain field in free shear flows interacted with large eddies within the 'turbulent' (i.e. 'turbular') fluid to provide energy to these large eddies. This large-scale motion was postulated to be associated with an eddy which was oriented *not* in the spanwise direction (the direction of the mean vorticity in plane flow) but in a plane *normal* to the spanwise direction. He had put forward an energy equilibrium hypothesis for the relationship between the large eddies and the 'main turbulence'.

By 1976, however, in the preface to his second edition, Townsend [7] commented: 'Although my current views have been developed from those I held in 1956 they have undergone considerable change. Perhaps I should thank especially Dr. H.L. Grant who, as my research student, began the process by demolishing a complete chapter before the ink was wholly dry'. He was referring to his chapter 6 in the 1956 edition 'Free turbulence: Motion of the large eddies'.

Correlation measurements within a turbulent wake by Grant [8] had resulted in a depiction of a *mean* large-eddy structure in the far wake ($x/D = 533$, $Re = 1300$), shown in Figure 2(a). Subsequently, Payne and Lumley [9] applied proper orthogonal decomposition to the measurements of Grant and arrived at the mean structure shown in Figure 2(b).

There was no discussion of these early measurements of structure at the 1961 Colloquium. An *instantaneous* structure with its vorticity in the y direction and across the whole wake has not been observed directly. With various advances in experimental methods and the advent of modern signal processing, however, there have been measurements made (e.g. [10]) to help understand what *instantaneous* large structures could account for the *mean* structure, which emerged from these early measurements as a double roller (Figures 2(a) and 2(b)) with axes *normal* to the plane of the wake.

Later, Townsend [11] explored another idea, in which the turbular fluid was considered to behave like a *viscoelastic fluid*. Further investigations of the effects of strain on homogeneous turbulence were made by Lumley in his paper 'Toward a turbulent constitutive relation' [12].

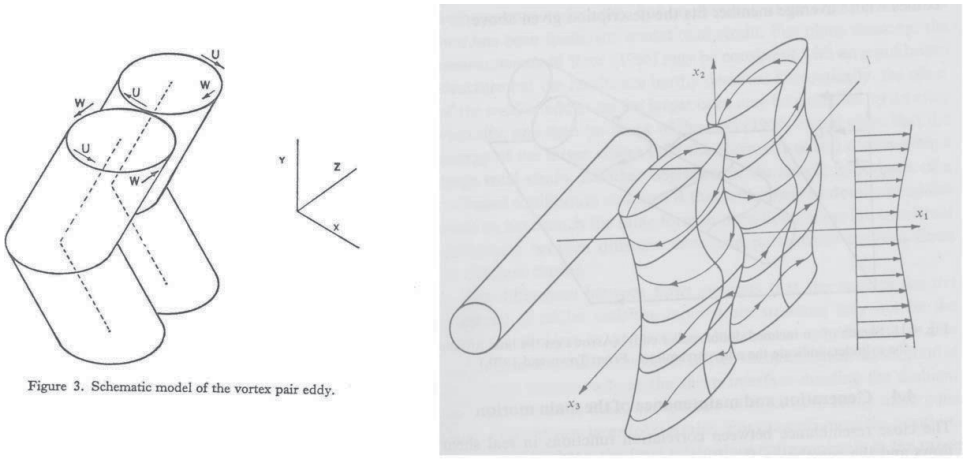


Figure 2. The depiction of a mean large-eddy structure in a circular cylinder wake obtained from velocity correlation measurements by (a) Grant [8] and obtained by proper orthogonal decomposition applied to the measurements of Grant by (b) Payne and Lumley [9]. (Both reproduced with permission).

Liepmann's view of the relation of turbular fluid to large structure had been influenced by a then-recent observation [13] of well-organized vortex shedding in the near wake of a circular cylinder at a Reynolds number of 10^7. This indicated a similarity between the vortex-shedding instability at much lower values of *Re* (of order 100) in viscous fluid and the one at high *Re*, presumably in turbular fluid. It also suggested that the large structure far downstream in a turbulent wake might be related to large-scale instability of the turbular fluid within the boundaries of the wake. In his lecture, he discussed at some length a numerical simulation of a *temporal* wake (Figure 3) by Abernathy and Kronauer (subsequently published in 1962) [14], in which two parallel vortex sheets, modeled by point vortices and separated by a 'thickness' *h*, represent the initial wake.

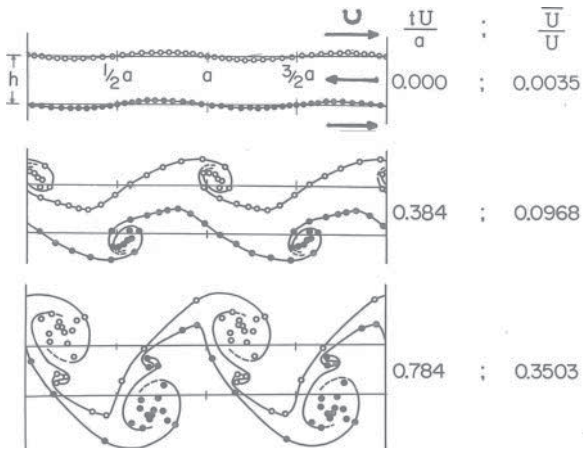


Figure 3. Evolution of two displaced vortex sheets (of opposite sign) modeled by point vortices ([14], reproduced with permission).

The unstable response to a perturbation of scale $\lambda > \delta$ leads to both large and small structures. Liepmann noted particularly that in addition to the expected large organized structure related to λ, there were also small vortical structures: 'Remembering that two-dimensional vortex motion is so much simpler than general vortex motion, one gets here a fascinating glimpse into the rapid randomization by vortex interactions and a demonstration of the statistical character of turbulence *proper*' (our italics).

In the following paper, 'Interfaces and intermittency in turbulent shear flows', Coles [2] included jets and wakes (Figure 1) as well as examples from wall-bounded flows, namely 'turbulent spots' in boundary layers, 'slugs' in pipe flow and spiral bands in circular Couette flow, which occur in *transition* regions of *wall-bounded* flows. The interface phenomenon on which Liepmann concentrated occurs in fully developed, *free* turbulent flows, as in Figure 1.

In his closing comments on free turbulence, Liepmann reiterated the experimental observation that 'free turbulent flows consist of regions of nearly homogeneous turbulence and irrotational regions. The dividing boundary is sharp and its location a stochastic function of time with scales one order of magnitude larger than the scales of the homogeneous turbulence'. Problems requiring further attention included the following items (abstracted from his longer statements):

1. the effect of strain on homogeneous turbulence,
2. the structure of turbulent interfaces,
3. the instability of turbulent flow and
4. the heuristic model of non-Newtonian fluid ... to describe the *instabilities and transport properties* in free turbulent flows (our italics).

The suggestion in item (4) that a 'turbular' fluid might be represented by some kind of *local* constitutive relationship reflected a more general theme in which the action of turbulence in diffusing the momentum had been sought through an eddy viscosity and *local* mean strain, for example, by Prandtl [15] and Taylor [16]. The concept of homogeneous, isotropic turbulence introduced by Taylor [17] provided a conceptual basis, as in Townsend (section 6.3 [6]), for a 'turbular' fluid. It also marked something of a divide in research interests. Dispersion of a scalar and the response of homogeneous turbulence to a pure strain, for example, were pursued on one path while well-defined free turbulent shear flows, where dimensional analysis and similarity arguments for the mean equations of motion are powerful tools, were pursued experimentally on the other. The latter led to a number of 'canonical' free turbulent shear flows which are 'similarity flows' ('self-preserving' or 'equilibrium' flows which no longer depend on their initial development) and for which there is only one local velocity scale, one local length scale and some global constraint (e.g. the drag for wakes or the thrust for jets). Empirical constants in such canonical shear flows essentially guided the development of practical, *local*, constitutive relationships in turbulence models but the 1961 Colloquium did not have any discussion of modeling for applications nor does the present one. The reason is partly because this 'local' concept is well known to be an important practical tool but a misleading representation of the mechanics, especially for free turbulent shear flows. The mechanics by which the self-similar state at one scale becomes self-similar at a larger scale, for example, is hidden in the empirical constants.

It was approximately a decade after the 1961 Colloquium that the picture that would have been drawn at the time of the Marseille meeting for the free shear layer (mixing layer) radically changed. The flow pictures and movies that we and others obtained [18] revealed

the essential role of the large-scale, predominantly two-dimensional (2D) *spanwise* vorticity and *the essential role of the Biot–Savart* interaction in the 'amalgamation' or 'clumping' of this vorticity to larger and larger scales. In their experiments at a 'moderate Reynolds number' (45–850) (i.e. below the mixing transition), Winant and Browand [19] described the evolution of the initial instability waves in a shear layer as a 'roll-up' into discrete vortical structures followed by a 'pairing process in which a single vortical structure, with approximately twice the spacing of the former vortices, is formed'. They observed that 'this pairing process' occurred repeatedly, 'controlling the growth of the mixing layer'. Figure 4(a) is a sequence from our movie at a considerably higher Reynolds number (3.3×10^4 at halfway along the layer). The flow is at uniform density but the two sides consist of different gas mixtures to provide a refractive index difference. The process at higher Reynolds number, evident from the movie, is more of a 'merging' or 'amalgamation' of vortical structures than a strict 'pairing' process. Figure 4(b) is a simultaneous plan view and side view at half the Reynolds number of that in Figure 4(a) and taken by Konrad [20] in the same experimental facility [18].

This picture of 'coherent structure' and the implied mechanics in a high Reynolds number turbulent shear flow were quite different from Townsend's [6] large-eddy hypothesis. The latter was influenced by tentative energy considerations that are not invoked at all, for example, in a 2D Biot–Savart interpretation of the large structure. Similarly, from Figure 4(b), the three dimensionality in the flow appears 'to ride on' and be reinforced by the 2D large-scale vortical structure and any supposed constitutive relationship for this small-scale motion is at best weakly connected to the primary Biot–Savart mechanics of the large-scale motion. The plan view shows the effect of the primary strain (especially in the 'braids' between the large-scale vortical motion) in amplifying streamwise vorticity, but it is evidently important to the production of *small scales* rather than to the *large scales* that control the growth rate and shear stress.

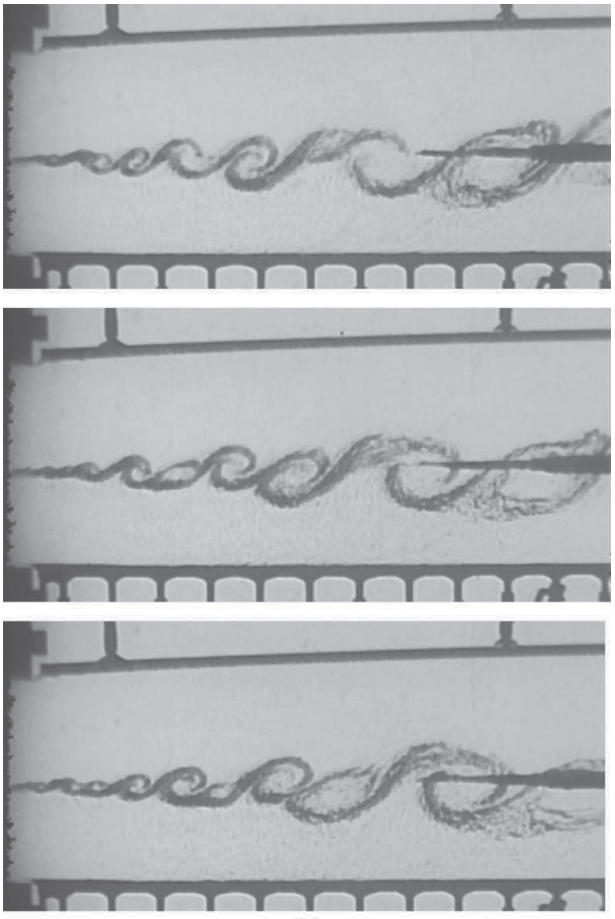
A few years earlier, the *near-wall structure* in the turbulent boundary layer, revealed in the hydrogen-bubble flow visualizations of Kline et al. [21], provided an important departure from previous understandings.

That it was a major change, 'which caught the imagination of fluid dynamicists' ([22], 'Whither Turbulence?' meeting) is evident from the premise and proceedings of that meeting. In his review of the role of coherent structures, Cantwell [23] drew attention to insights that this structure provided and in particular to the future possibilities for simulation, for new opportunities to develop explanations of underlying physical mechanisms and for control.

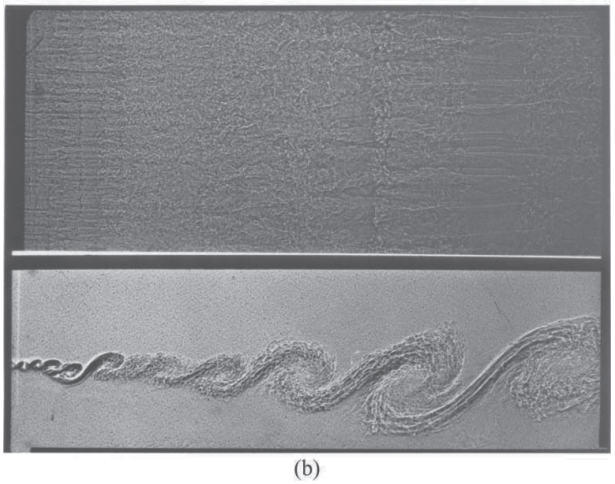
From this point of view, what has seemed increasingly necessary is to connect a 'structure' view to the underlying mechanics, which is best revealed for the rotational motion of turbulence through the vorticity equation with the necessary connection to the velocity field (viscous or inviscid flow) through the Biot–Savart relationship. Notwithstanding Taylor's vorticity transport theory [16,24] and Küchemann's subsequent view [25] that 'vortices are the muscle and sinews of fluid motion', there was mainly a passing mention of vorticity in the papers presented and in the recorded discussion of the 1961 Colloquium.

That a vorticity view has not had more experimental emphasis, despite the more recent focus on 'coherent structure', is because of the difficulty in measuring the vorticity. For computations of the Navier–Stokes equations, however, there is no such constraint. It is this view that seems particularly appropriate for this meeting and we shall emphasize it in the context of free shear layers and wakes.

One of the immediate consequences of the results shown in Figures 4(a) and 4(b) was an expectation that, for this case, a 2D flow driven by a Biot–Savart interaction between



(a)



(b)

Figure 4. (a) Turbulent mixing layer, constant density, 8 atm, $U_2/U_1 = 0.38$. A sequence of three shadowgraphs from a high-speed movie [18] each separated by a fixed time interval (time increasing from top to bottom). (The same experimental facility was used for the results in Figure 6). (b) Mixing layer, constant density, 4 atm, $U_2/U_1 = 0.38$. Side and plan view [20].

'clumps' of vorticity of the same sign may account for the principal mechanics. Early attempts were made to simulate this mechanics using distributions of point vortices to simulate a vortex sheet and its response to initial disturbance (e.g. [26,27], for spatial and temporal cases). The growth rates were determined from mean velocity profiles as was the Reynolds stress profile. Recently, results from much more extensive and more accurate calculations for both the temporal and the spatial case, using this 2D 'vortex gas' approach [28], have been obtained (Section 3). Similarly, a computational study of a spatial, 2D (high Reynolds number but viscous) mixing layer has been completed (Section 3). Some comparisons with the three-dimensional (3D) experimental results are mentioned in Section 3 along with the experimental observations on the development of three dimensionality and the central contribution it makes to 'mixing' and its weak contribution to Reynolds stress.

2. Reynolds stress and the vorticity flux

It is the spatial *derivatives* of the Reynolds stresses that enter the mean momentum equation and for incompressible flow, these are directly connected with the vorticity flux (as given in more detail in Appendix 1). In particular, for plane turbulent shear flow, the principal derivative of the Reynolds stress is

$$\frac{\partial\overline{(-u'v')}}{\partial y} = \overline{\omega_z' v'} - \overline{\omega_y' w'} - \frac{\partial}{\partial x}\left(\frac{1}{2}(\overline{u'^2} + \overline{v'^2} + \overline{w'^2})\right) + \frac{\partial\overline{u'^2}}{\partial x}, \tag{1}$$

Replacing the derivatives of Reynolds stress by these vorticity–velocity correlations was a starting point for Taylor's vorticity transport theory ([16] and [24]).

For temporal turbulent shear layers (and channel flow or Couette flow), the x derivative is identically zero and it is typically a higher-order term for spatially growing shear flows (within the 'boundary layer' approximation). In this case, the Reynolds stress gradient is obtained directly from the flux of vorticity.

Note, in passing, that for strictly 2D models of a temporal rotational flow, such as a 2D instability, the Reynolds stress *gradient* is obtained directly from $\overline{\omega_z' v'}$ (sometimes interpreted as a 'vortex force'). That is, the only contribution is from the *rotational* fluid. The spatially averaged Reynolds stress in the flow, which accounts for the rate of change of momentum on a particular plane, is obtained from the integration of $\overline{\omega_z' v'}$ from infinity. If, instead, this Reynolds stress were obtained directly from the spatial average of $\overline{u'v'}$, there may be a substantial contribution from the *irrotational* fluid if on any plane there are local regions of rotational and irrotational fluid! This is a subtlety not always appreciated.

The vorticity equation, which is derived from the Navier–Stokes equations, is

$$\frac{\partial\boldsymbol{\omega}}{\partial t} + \boldsymbol{u}\cdot\nabla\boldsymbol{\omega} = \boldsymbol{\omega}\cdot\nabla\boldsymbol{u} + \nu\nabla^2\boldsymbol{\omega}, \tag{2}$$

and the Biot–Savart relationship determines the velocity field that is necessarily associated with the vorticity field.

$$\boldsymbol{u}_\omega(x, y, z) = \iiint \frac{\boldsymbol{\omega}(\xi, \eta, \zeta)\times\boldsymbol{s}}{4\pi s^3} d\xi d\eta d\zeta, \tag{3}$$

where $\boldsymbol{s} = (x-\xi)\boldsymbol{i} + (y-\eta)\boldsymbol{j} + (x-\varsigma)\boldsymbol{k}$ and $s = |\boldsymbol{s}|$.

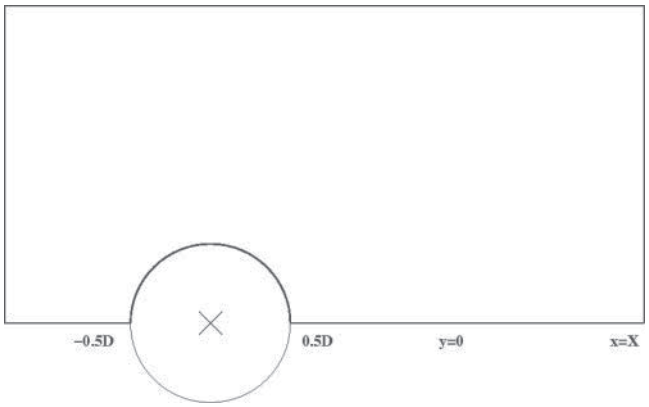


Figure 5. A control volume for a flow around a circular cylinder and for the application of Equation (6).

In terms of the vorticity, the corresponding velocity field is evidently a *global* quantity found by integrating over the whole vorticity field, so a velocity–vorticity correlation cannot be thought of as determined solely from the local velocity or vorticity.

An alternative form of Equation (2) written in conservation form is

$$\frac{\partial \omega_i}{\partial t} + \frac{\partial}{\partial x_k}\left(u_k\omega_i - \omega_k u_i - \nu\frac{\partial \omega_i}{\partial x_k}\right) = 0, \tag{4}$$

and when integrated over a volume fixed in space, it gives (Gauss's theorem)

$$\frac{d}{dt}\iiint \omega_i dV + \iint\left(u_k\omega_i - \omega_k u_i - \nu\frac{\partial \omega_i}{\partial x_k}\right) n_k dS = 0. \tag{5}$$

For a turbulent flow that is *steady* in a time mean sense, this equation is

$$\iint\left(U_k\Omega_i - \Omega_k U_i + \overline{u'_k\omega'_i} - \overline{\omega'_k u'}_i - \nu\frac{\partial \Omega_i}{\partial x_k}\right) n_k dS = 0, \tag{6}$$

where $U_k(x, y, z)$ is the time mean of $u_k(x, y, z, t)$ and similarly for the vorticity.

For a 2D flow around a symmetrical body (e.g. a circular cylinder), the mechanics is illuminated by this equation. If the fixed volume (control volume as shown in Figure 5) includes the upper surface of the body and the upper half plane, it is clear from Equation (6) that the source of spanwise vorticity is on that part of the boundary which is a solid surface (the cylinder surface, where the velocity is zero). Downstream there is a flux out of the volume on a plane perpendicular to the flow at $x = X$, which is less than that which is supplied upstream from the surface of the body and that is entirely because of the net flux of vorticity out of the volume across the plane $y = 0$, namely

$$\int_{D/2}^{X}\left[-\left(\overline{v'\omega'_z} - \overline{\omega'_y w'}\right) + \nu\frac{\partial \Omega}{\partial y}\right] dx, \tag{7}$$

since, by symmetry, $V = 0$ on this plane.

The mechanics by which the mean vorticity is 'lost' ('canceled') across $y = 0$ in the near wake is not well known but it is accessible today through direct numerical simulation (DNS) and large-eddy simulation (LES) calculations. Within approximately one diameter from the base of the cylinder, the flux of vorticity across the plane normal to the plane of symmetry is less than one half of that supplied from the surface of the body (a fact that was known to early experimenters from direct measurements of mean velocity profiles). Similarly, in the far wake, a question that arises is: To what extent does a 'large-scale' motion, which is dependent, for example, on the 'clumping' of vorticity to larger scales due to a 2D and/or 3D instability, contribute to the all-important turbulent flux $(\overline{v'\omega'_z} - \overline{\omega'_y w'})$? These are the points to which we return in Section 4.

3. Some further results, conclusions and questions on the free shear layer

3.1 *Coherent structure and Biot–Savart considerations*

The quasi '2D structure' observed in the photographs was in direct conflict with the anticipated structure (e.g. the Townsend model) and many attempts were made to examine its robustness to perturbation and its persistence to even higher Reynolds numbers, etc. Figure 8(b) [29], for example, shows the result of very substantial 3D perturbations at the splitter plate and the recovery, not far downstream, of the dominant spanwise structure.

The global constraints on the asymptotic mixing layer require linear growth and allow self-similarity, which is demonstrated by the mean velocity profile measurements shown in Figure 6. It follows that the growth of the coherent structures cannot proceed continuously and that their merging must occur randomly. Such large-scale interactions will contribute to the low wave number components of the energy spectrum.

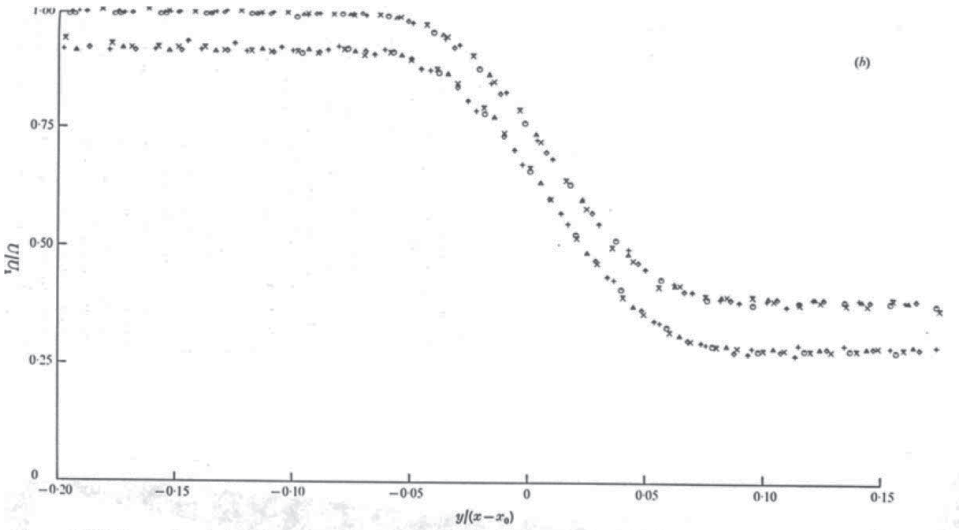


FIGURE 9. Velocity profiles of mixing layers in air, obtained from simultaneous traverse of Pitot tube and hot-wire probe. (Hot-wire profile is displaced downward for clarity.) (*a*) $U_1 = 1000\,\mathrm{cm\,s^{-1}}$, $U_2 = 143\,\mathrm{cm\,s^{-1}}$, pressure = 7 atm. $x_0 = -0{\cdot}25$ in. (*b*) $U_1 = 1000\,\mathrm{cm\,s^{-1}}$, $U_2 = 382\,\mathrm{cm\,s^{-1}}$, pressure = 7 atm. $x_0 = -0{\cdot}38$ in. x (in.): ⊙, △, 0·5; ×, 0·75; ↑, ⊠, 1·00; +, 1·50; ◇, 2·00; Z, 2·50; Y, 3·00; ⊠, 3·50.

Figure 6. Similarity in the mean velocity profile for $U_2/U_1 = 0.382$ obtained from redundant hot-wire and pitot-static measurements at seven streamwise locations, as noted in part (b) of the caption ([18], reproduced with permission).

In terms of the vorticity thickness, $\delta_\omega = (U_1 - U_2)/(\partial U/\partial y)_{\max}$, the Reynolds number, $(U_1 - U_2)\,\delta_\omega/\nu$, of the mixing layer at the stations measured in Figure 6 increases by a factor of 5 from 0.6×10^4 to 2.9×10^4, suggesting that the growth rate is independent of Reynolds number. This growth rate is $d\delta_\omega/dx = \delta'_\omega = 0.088$. It is close to the value 0.088 obtained by S. Suryanarayanan and R. Narasimha [28] in a (so-far unpublished) *2D* numerical simulation at the same value of U_2/U_1. The 'vortex gas' method used in the simulation implies independence of viscosity. The comparison is striking, particularly in the close agreement with the 'real' 3D flow, which is shown in Figure 4(b). In a 2D Navier–Stokes simulation by Carton de Wiart et al. [30], also not yet published, of a mixing layer at $U_2/U_1 = 0.38$, values of the growth rate varied from 0.082 to 0.087 with Reynolds number from 0.7×10^5 to 2.5×10^5. It is clear that there remains some uncertainty in establishing a definitive value for the growth rates in 2D and 3D shear layers.

Nevertheless, these comparisons between the 2D calculations and the 3D data lend support to the assertion that the Biot–Savart interaction between 'clumps' of vorticity (whose spanwise component is in the same direction) over scales of the order of the thickness of the layer plays a dominant role in determining the Reynolds stress; the more local contributions from 3D motions are much less important.

3.2 *Entrainment, mixing and the mixing transition*

At the time of the Marseille meeting, a boundary between the 'turbular' fluid and the potential flow was considered as an 'active' boundary. Townsend [6], for example, noted (section 3.9) that the 'boundary region between *a semi-infinite field of homogeneous turbulence and the adjacent undisturbed fluid*' (our emphasis) is 'the simple entrainment by turbulent fluid of adjacent nonturbulent fluid, which is the basic process in the spread of wakes, jets . . .'. This hypothesis was found not to be the basic mechanism for the mixing layer. Figure 4(a) suggests instead that an important mechanism that leads to the regions of 'engulfed' but unmixed fluid comes from the velocity field of the irrotational fluid, which is induced by the 'large-scale' spanwise vorticity. The irrotational fluid is engulfed as the coherent structures evolve and merge to form larger structures and the 3D 'small-scale' mixing occurs *without* a strong influence on the larger-scale motion. Thus, in a purely 2D temporal shear layer, fluid from both free streams would be found in the regions between the layers of vorticity, which form the 'coherent structures' of such a flow. If in addition to the large-scale motion there is a smaller-scale 3D motion, this engulfed fluid would be mixed more uniformly. Correspondingly, in the 3D case, there need be no change in the mean Reynolds stress but a considerable increase in the area of the interface between the two separate fluids.

Concentration measurements with a relatively high-resolution probe (but not to the scale of molecular diffusion) in gases by Konrad [20] (Figure 7) and later the direct measurements of reactant product in water by Breidenthal [31,32] identified a 'mixing-transition' Reynolds number for the mixing layer ($\frac{\Delta U \delta_\omega}{\nu} \approx 2 \times 10^3 - 8 \times 10^3$), over which there is a substantial increase in small-scale 'mixing' and, more precisely, 'mixedness' at diffusive scales [33]. Photographs by Bernal [34] showed the role of the smaller-scale streamwise vorticity in this mixing and the reinforcement of this vorticity by the straining motion between large structures (also evident in Figure 4(b)).

Similarly, photographs obtained at higher Reynolds number ($\frac{\Delta U \delta_\omega}{\nu} \approx 10^5$) and also at very high Schmidt number (in water) [37] showed local reactants in the irrotational flow on each side of the mixing layer being entrained (engulfed) by the velocity induced by the

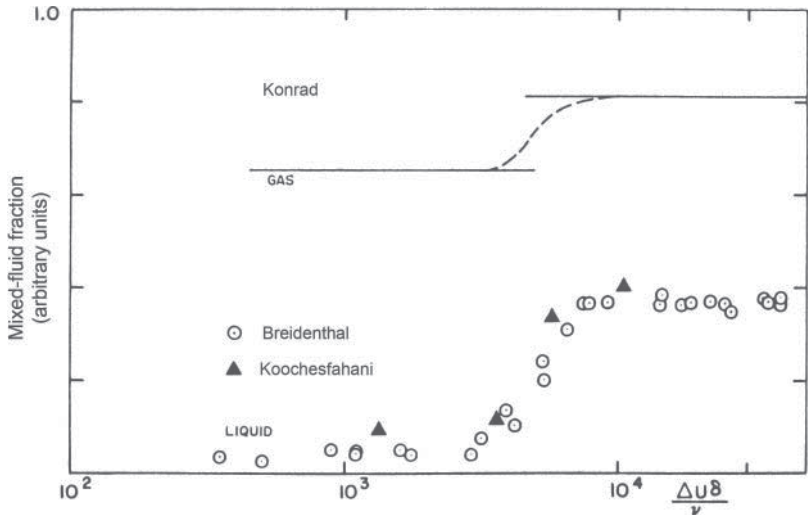


Figure 7. The 'mixing transition' in a free shear layer [20,32,35,36]. (Reproduced with permission).

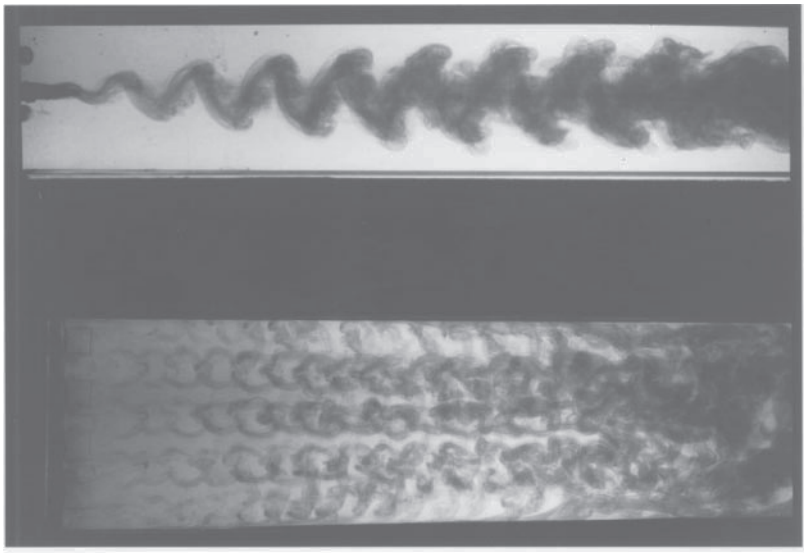
large-scale vorticity and then being rapidly mixed *to the molecular scale* within the large structure.

3.3 *Forcing and control*

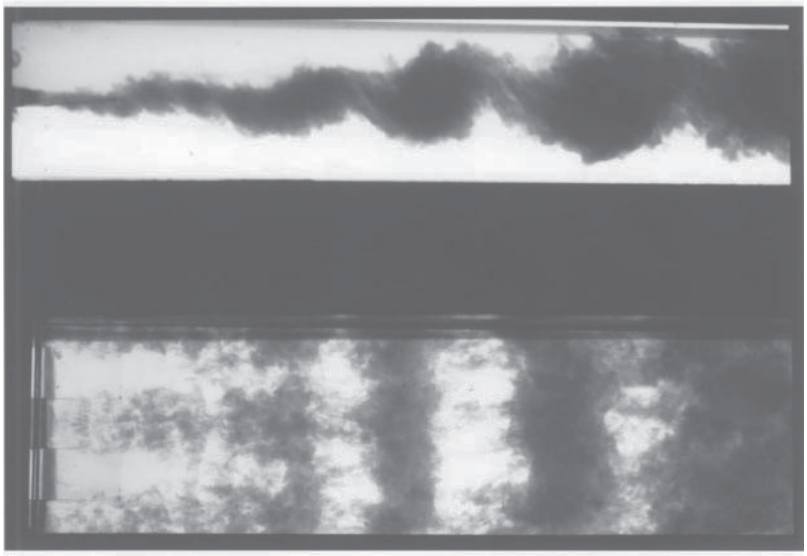
The existence of the large-scale coherent vorticity suggested ways in which this structure might be influenced or perturbed in order to gain some control over the flow. The experiments of Oster and Wygnanski [38], for example, in which the trailing edge of a shear layer was oscillated, showed that pure tone forcing could have a substantial effect. The results could be interpreted as a coupling between the forcing and a mode of the turbulent shear layer which, as it amplifies, 'wraps up shed vorticity' into clumps of a particular scale and spacing (dependent on the frequency). These structures, closely similar in strength and spacing, might be described as in a 'meta-stable' state for a period during which the Reynolds stress and the growth rate of the mean shear layer are very small, until random disturbances and Biot–Savart interactions again lead to merging and the formation of larger-scale structures. Such behavior is easily understood once the underlying coherent structure and mechanics that occurs without forcing are recognized. Attempts to 'control' turbulent flows (e.g. the base pressure behind bluff bodies or the wall friction through the Thom's effect) are not new but attempts to influence coherent structure to control the flow received a new emphasis.

3.4 *Some conclusions*

- Unlike the early emphasis on the mean velocity profile, the growth rate of the mixing layer thickness (and the corresponding Reynolds stress) is the key defining parameter.
- *Instability/Biot–Savart* is the dominant mechanics for the emergence of the large-scale structures in mixing layers and their coalescence to structures of increasing size.



(a)



(b)

Figure 8. (a) A plane wake (marked by chemical reaction between free streams) from a strongly 3D trailing edge ([29], reproduced with permission). (b) A free shear layer (marked by chemical reaction between the free streams) perturbed by a strongly 3D trailing edge ([29], reproduced with permission).

- There is *randomness* in the distribution of these structures, which leads to a linear growth rate only when many instantaneous realizations are averaged.
- If instability/Biot–Savart is the dominant mechanics, it should account for the *Reynolds stress* that is then *not local* in an eddy viscosity sense.

- The three dimensionality rides on the large-scale, approximately 2D structure.
- *Streamwise vorticity tends to persist* through the coalescence of the large structures (reinforced by regions of high strain rate between structures).
- There is a *mixing transition* at a local Reynolds number of approximately 2×10^3, due to a rapid increase in small-scale three dimensionality, which has at best a weak effect on the Reynolds stress and the growth rate.

3.5 *Some questions*

- Is there a precise asymptotic growth rate? How much does it differ in 2D and 3D shear layers? The asymptotic growth rate as a function of velocity ratio is still not known accurately (better than say 5%), probably because the flow is more sensitive to upstream and downstream boundary conditions than has been fully recognized.
- The vorticity equation with the velocity obtained from Biot–Savart is nonlinear. Is there self-forcing of larger and larger wavelengths? For a 2D *inviscid*, *temporal* case what initial conditions are sufficient for the continual coalescence to larger structures?
- *Is there universality in all turbulent shear flows of a* reverse *cascade with coalescence of vorticity to larger structures through Biot–Savart?*
- For the velocity field, which is an integral of the vorticity, how much detail in the vorticity field must be kept to predict the Reynolds stress in free shear flows (which do not have new sources of vorticity at walls or a baroclinic torque)?

4. The plane wake

Similar to the mixing layer, other 'self-preserving' or 'equilibrium' canonical-free shear flows have received particular attention with the hope of providing benchmark data, under well-defined conditions, and insight into the basic mechanics of these flows. Since the time of the 1961 Marseille meeting, various aspects of the plane wake have been clarified but numerous questions remain even for the far wake.

4.1 *The near, mid and far wakes and the asymptotic wake*

It is useful to think of four basic regions of the plane wake and, based on the results for a circular cylinder, these are as follows:

Near wake ($0 \leq x/d \leq 4$; depending on Re): There is a direct interaction between the flow and the cylinder in this region (evident, for example, from measurements of base pressure when a splitter plate is placed in this region and moved toward the base).

Mid wake ($4 \leq x/d \leq 50$): In this region, the presence of vortices shed from the cylinder is detectable but changes to this region through a splitter plate, for example, have no direct effect on the flow adjacent to the cylinder.

Far wake ($50 \leq x/d \leq 1000$): In this region, there is approximately self-similar behavior of the mean flow. The growth constants, however, are particular for the geometry of the body, which is the source of the wake even if expressed in terms of the drag on the body. The downstream limit in the inequality, in particular, is very approximate and variable and is dependent on the source of the wake.

Asymptotic wake ($x/d \geq 1000$): The growth constants in terms of the drag of the body are universal for all 2D bodies. Again the lower 'boundary' depends on the source of the wake.

4.2 *The plane far wake and asymptotic wake distinction*

The approximate similarity and growth rate of the far wake and the distinction between the far wake and the asymptotic wake (and the data which supports it) provide a comparison with the mixing layer and raise questions about the development and evolution of the structure in the flow. A summary, based on Townsend [6] and Narasimha and Prabhu [39], on which a distinction is made is given in Appendix 2.

There remain questions about how rapidly the far wake approaches the asymptotic wake. For example, the results from Wygnanski et al. [40] for wakes from different bodies with more or less intense vortex shedding showed similarity in the velocity profiles and the characteristic dependence of $\bar{u}_0$ and δ on $x - x_0$ as in the far wake (Appendix 2), but even where $\bar{u}_0/U_1$ is small ($\bar{u}_0/U_1 = 0.04$), in some cases the equivalent local value of x_0/x is still approximately 0.25 (assuming they are approaching the asymptotic state). Behind this issue are basic questions about structure and its potential evolution toward some asymptotic structure that becomes independent of initial conditions. Put simply, the questions of whether there are 'characteristic' large-scale structures for an asymptotic plane wake (characterized by the local wake thickness and the centerline velocity deficit) and, if so, what role they play are not settled.

4.3 *Structure in the plane wake*

A fundamental difference between the plane wake and the mixing layer is that the wake contains vorticity of *both signs* 'in equal amounts', so to speak. More precisely, the integrals of mean vorticity and mean vorticity flux over the layer are zero:

$$\gamma(x) = d\Gamma/dx = \int_{-\infty}^{\infty} \omega dy = 0 \quad \text{and} \quad \int_{-\infty}^{\infty} U\omega dy = 0. \tag{8}$$

A more useful statement for the mean vorticity flux is that

$$\frac{d}{dx}\int_{-\infty}^{0} U\omega dy = -\frac{d}{dx}\int_{0}^{\infty} U\omega dy,$$

i.e. the fluxes of vorticity above and below the centerline ($y = 0$) are finite but of opposite sign and they are *decreasing* (in absolute value) as the wake grows. In either laminar or turbulent wakes, vorticity is canceled by opposite-signed vorticity that has been transported across $y = 0$, respectively, by either molecular diffusion or turbulent transport (as in Equation 7). In laminar flow, the cancelation is by molecular mixing, but in turbulent flow, large regions of different sign may exist side by side and 'cancelation' occurs in the *averaged* values.

For the mixing layer, a single row of one-sign vortices is representative of the basic flow and suggestive of the primary, Kelvin–Helmholtz instability that leads to the structures discussed in the preceding sections. For the wake, the corresponding representation is two rows, one of each sign, forming 'vortex streets' with various spacing. In his classic study, von Karman found that streets of point vortices are unstable except for the asymmetric (staggered) arrangement at spacing ratio $h/\ell = 0.281$, where it is neutrally stable (ℓ is the streamwise spacing between vortices of the same sign and h is the distance between the two rows). The evolution of two vortex sheets approximated by point vortices from a *finite* perturbation was computed by Abernathy and Kronauer in the numerical simulation noted earlier. While 2D representations have been quite successful for the mixing layer, there is

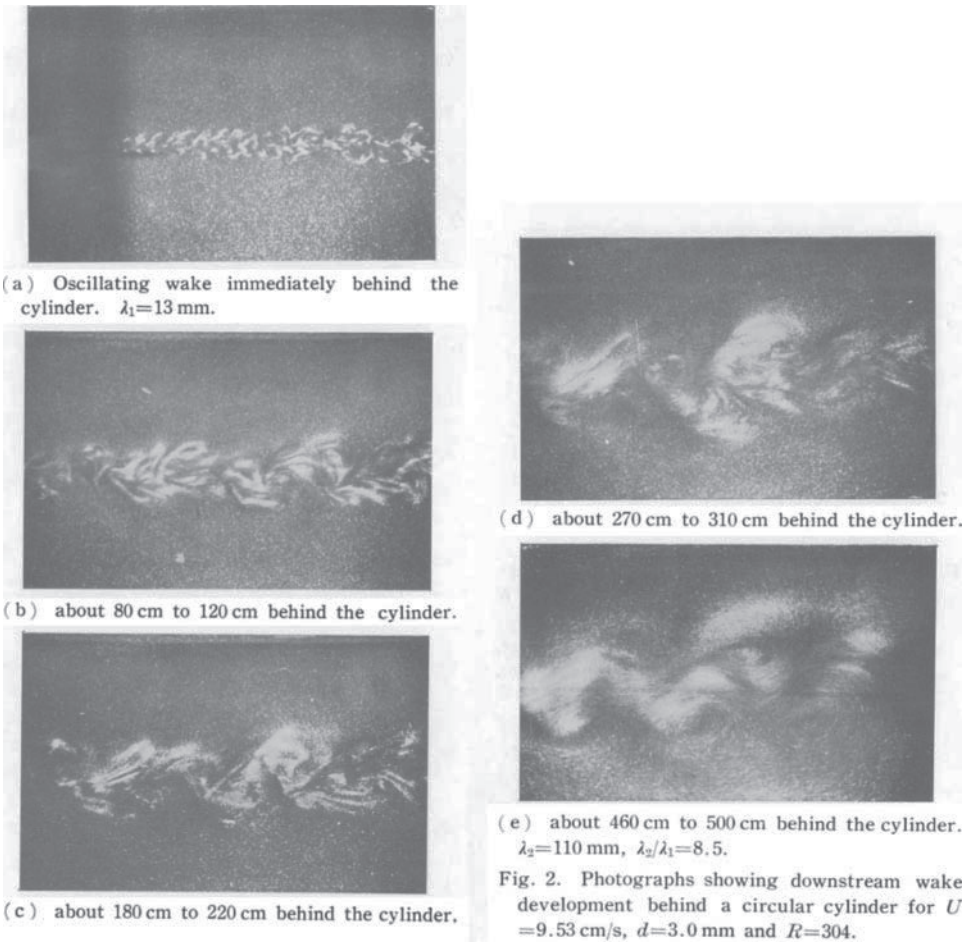
no assurance that this is the case for the wake. In fact, the double-roller structure inferred by Grant from correlation measurements implies that the primary instability structure is *3D*. But how it might be connected to instantaneous coherent structures passing through the correlation space has been a difficult question. A clue is provided by the instability investigation of Robinson and Saffman [41] on streets of vortices with finite cores. In addition to the classical perturbation of each row in the 2D plane, they added a *spanwise* perturbation to every vortex. They found that for some combinations of spacing ratio, h/ℓ, and spanwise wave length, λ/h, the spanwise amplification rate was comparable to the in-plane rate. The resulting spanwise sinuous structure of each vortex would now have the necessary components of vorticity *normal* to the plane of the wake (plus and minus) to explain the prominent components in Grant's averaged structure. What actually evolves is not yet quite clear but the pictures of Breidenthal ([29], Figure 8(a)) and the numerical simulations of Meiburg and Lasheras [42] indicate that the primary 'coherent' structures are loops that connect the opposite-signed vorticity on the opposite sides of the layer. A good discussion is given by Breidenthal. His flow pictures (Figure 8) demonstrate the strong tendency for loop structure to persist in a wake ($U_2 = U_1$, Figure 8(a)), whereas for a mixing layer ($U_2 = 0.4U_1$, Figure 8(b)), the imposed 3D structure gives way to the spanwise-organized vortices. (The seeming two dimensionality seen in the elevation view in Figure 8(a) conceals the very strong three dimensionality evident in the plan view, which was generated by the periodic disturbance at the trailing edge.)

Assuming that 'loop-like' large structure is the primary coherent structure downstream of the near wake, how does it participate in the growth of the wake? Part of it will be due to growth of the loops. This is evident in Breidenthal's photograph (Figure 8 (a)) in which the structures are seen to be growing at fixed spacing and not coalescing. Terms in the momentum equation contributing to the growth would include $\overline{v'\omega'_z}$ and $-\overline{w'\omega'_y}$ (see Section 2). Such growth would be followed by rescaling of the structure as the increased thickness becomes receptive to instability at lower wave number (larger spacing). The details of this analog of the mixing-layer 'merging' process are not yet completely clear but the following gives some useful insights.

Attention to it was first drawn by Taneda [43] who obtained edge-view visualizations (Figure 9), similar to those in Figure 8(a), of a wake at $Re = 300$ at various locations up to $x/d \simeq 1600$, where it had been rescaled by a factor of approximately 8.5, after several stages (three rescalings would give approximately 2^3).

Taneda described the phenomenon as a series of 'rearranged' (we would say *rescaled* and *reformed*) 'Karman vortex streets'. In edge view, the asymmetric far-wake pattern looks like the edge of a 'street' because the loops are aligned spanwise. The indication is that the rescaling instability drives the 3D flow toward a particular 'street' spacing (not the Karman neutrally stable value for point vortices of 0.281) in the reformed 'coherent' structure. It is difficult to define h and ℓ in these flow pictures but the spacing ratio h/ℓ appears to be in the range 0.4–0.6, significantly larger than 0.281. 'Movies' of the phenomenon are not available, as far as we know, but there are indications that a given stage (two or higher) will not be replicated in exactly the same form or in the same x interval. Thus, as in the mixing layer, it will have a statistical character in any time series measured at a given value of x.

Taneda's pictures motivated an investigation by Cimbala [44] at higher Reynolds numbers using smoke wires for visualization and hot-wire anemometry for mean and fluctuating velocity measurements. Flow patterns similar to Taneda's pictures were observed at these much higher Reynolds numbers (Figure 10(a)). Additional insight was obtained from experiments on the wake of a porous flat plate, broadside to the flow. With solidity ratio $\sigma = 29\%$, the plate does not shed vortices; smoke lines in the near wake indicate nearly



(a) Oscillating wake immediately behind the cylinder. λ_1=13 mm.

(b) about 80 cm to 120 cm behind the cylinder.

(c) about 180 cm to 220 cm behind the cylinder.

(d) about 270 cm to 310 cm behind the cylinder.

(e) about 460 cm to 500 cm behind the cylinder. λ_2=110 mm, λ_2/λ_1=8.5.

Fig. 2. Photographs showing downstream wake development behind a circular cylinder for U =9.53 cm/s, d=3.0 mm and R=304.

Figure 9. Wake rescaling at $Re = 300$ ([43], reproduced with permission).

parallel flow (Figure 10(b)). This flow develops a wake instability, which, by $x/d = 30$, has grown into a 'street' with a spacing ratio $h/\ell \simeq 1$, considerably larger than the Karman stable value. This is followed by a rescaled stage 2 with spacing ratio $h/\ell \simeq 0.5$.

Results for a body with higher solidity ($\sigma = 47\%$), shown in Figure 10 (c), still display no vortex shedding. Small structure in the near wake is followed by organized wake-instability growth and decay, followed by rescaling to stage 2, with $h/\ell \simeq 0.5$. This suggests that rescaling in the wake, similar to rescaling in the mixing layer, displays the growth and decay of an instability wave at a particular wave number α (i.e. a fixed streamwise spacing). With increasing wake thickness $\delta(x)$, the value of $\alpha\delta$ increases and amplification rate $(-\alpha_i)$ decreases, from an earlier maximum value. When $(-\alpha_i)$ reaches zero, the amplitude is at its maximum value, thereafter decaying and setting the stage for rescaling. Some confirmation of such development was obtained from statistical measurements by Cimbala from hot-wire measurements of velocity fluctuation spectra at values of Re up to 500. In particular, maximum amplitude $A(x)$ tended to occur nearer to the neutral (zero) value of $\alpha\delta$ (predicted by linear stability theory for mean wake profiles) than to the value for

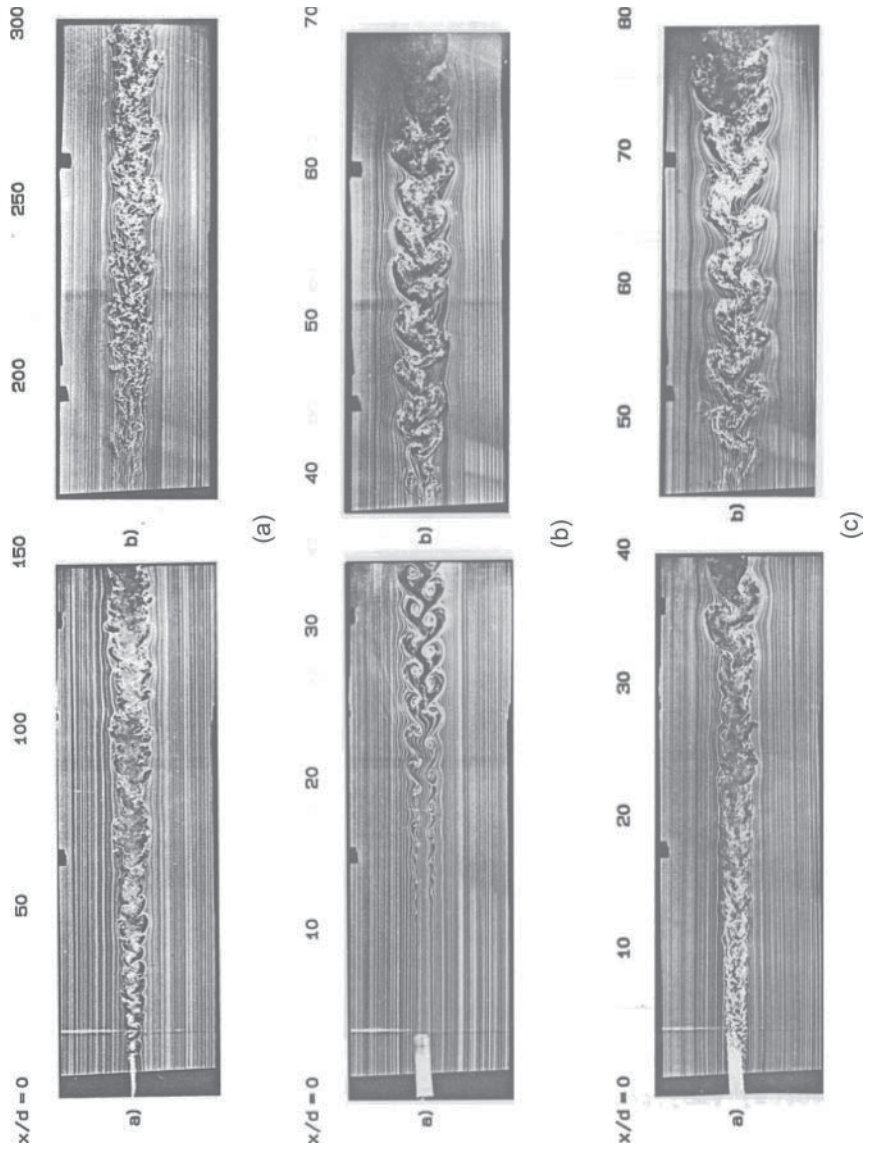


Figure 10. Smoke-wire photographs in plane wakes ([44], reproduced with permission). (a) Circular cylinder at $Re = 2200$, smoke wire at (a) $x/d = 1$ and (b) $x/d = 180$. (b) Porous flat plate at $Re = 6800$, $\sigma = 29\%$, smoke wire at (a) $x/d = 0$ and (b) $x/d = 38$. (c) Porous flat plate at $Re = 6000$, $\sigma = 47\%$, smoke wire at (a) $x/d = 0$ and (b) $x/d = 44$.

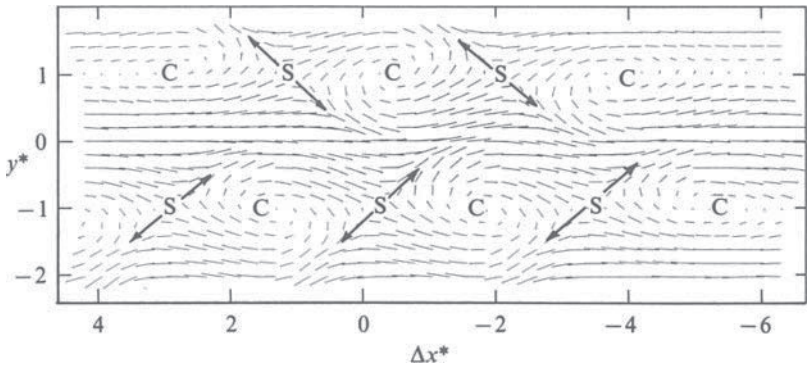


Figure 11. Conditionally sampled velocity vectors. Plane wake ($Re = 1200$, $x/d = 420$) ([10], reproduced with permission).

maximum amplification rate. This is similar to results from probability distributions of vortex frequency in mixing layers.

The flow pictures from various sources, all at low Reynolds numbers, indicate that the rescaled stages of the 'street' have a spacing ratio $h/\ell \simeq 0.5$. Even at low Reynolds number, it is difficult to make a more precise measurement but it was accomplished by Antonia et al. [10] in the wake of a circular cylinder at $Re = 1200$ and $x/d = 420$. From digital time series of conditionally measured velocities and temperature markers, they were able to reconstruct various maps of the velocity field, vorticity, etc. Figure 11 shows the velocity vectors in a coordinate system moving in the x-direction with a suitable convection speed U_C, i.e. one that produces a nearly stationary pattern of centers and saddle points. The spacing ratio $h/\ell = 0.60$. Since $\ell \simeq 15d \simeq 3\ell_1$, we suppose that this is a stage 2 structure, but *not* doubled from stage 1.

4.4 *2D Inviscid Instability and Nonlinearity*

The results of Abernathy and Kronauer [14] were obtained from a Biot–Savart calculation with two rows of vortices and with 21 vortices per wavelength for the two rows used to approximate the wake. The authors refer to the 'clouds' of vorticity that emerged and Liepmann comments that 'the similarity of the pattern to shadowgraphs of turbulent wakes is also quite obvious'. With modern computing power, a far more realistic representation of the mean velocity profile by rows of vortices of varying strength and fixed spacing is possible. Recently, Suryanarayanan and Brown [45] modeled a $\cosh^{-2}(y/\delta)$ velocity profile with 71 rows each of 58 vortices and the circulation of each vortex chosen to represent the local mean vorticity distribution for this mean velocity profile. This number of vortices per row and arrangement of rows correspond with the wavelength for the most unstable mode obtained from linear stability theory. The advantage of the Biot–Savart formulation of the inviscid stability problem is that it allows a seamless progression to nonlinearity, a straightforward calculation of the mean Reynolds stress in the linear and nonlinear regimes (as described in Section 2) and an opportunity to see a possible rescaling to longer wavelength instability. By 'experimentally' varying the initial spacing of the vortices in each row to match a vorticity eigenmode that develops (grows exponentially), exponential growth is obtained from $t = 0$ for very small initial displacement amplitude. The result of this initial growth is an exponentially growing mode, which has almost exactly

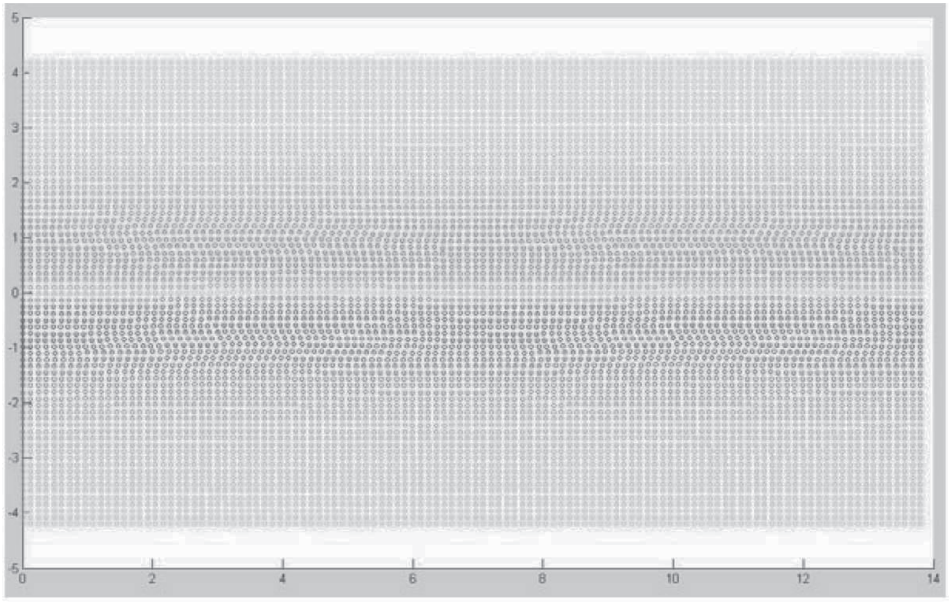
the theoretical growth rate. To explore the nonlinear development, the domain was then doubled in the x-direction to two wavelengths; there were 78 rows of 116 vortices per row (58 per wavelength). The results for increasing nondimensional time (scaled by the initial velocity deficit and the width δ) are shown in Figure 12 (where each point vortex is shown and its strength is represented by a color with maximum positive circulation being red and negative being blue). The way in which the vorticity 'clumps' and the velocity field becomes dominated by this accumulation of vorticity is very evident. Entrainment occurs by the engulfment of fluid due to the large-scale accumulated vorticity and a 'nibbling' of an active 'superlayer' is not at all representative of the mechanics in this 2D case.

The initial modal growth shows a peak Reynolds stress near the time at which the amplitude of the fundamental is a maximum. There is then a subsequent decay of this mode, the transport of vorticity of opposite sign across the layer, followed by growth in the mean velocity profile and the emergence of larger wavelength instability, even though it was initially *not* directly imposed. As with the results 50 years ago, what is interesting is the nonlinear evolution of this 'simple' 2D flow and the extent to which it may illuminate an underlying tendency for vorticity to clump to large scales through Biot–Savart creating a velocity field that 'accounts for' the vorticity transport and the entrainment of irrotational fluid.

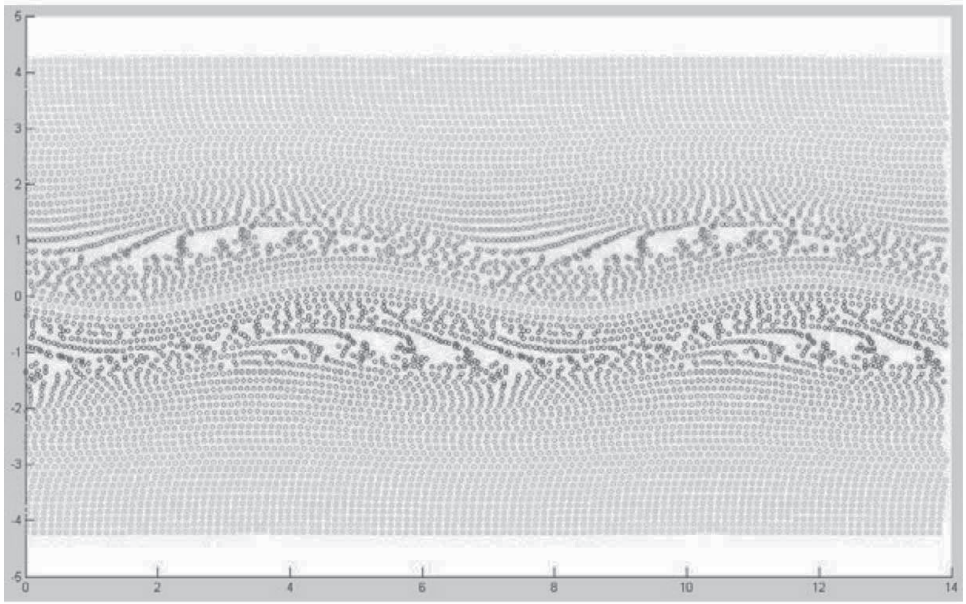
4.5 *Vorticity flux in the plane wake*

There is a wide range of experimental measurements of the near wake of a circular cylinder at $Re = 10{,}000$ but a detailed resolution of the vorticity field and the measurement of vorticity fluxes has not been possible. That this Reynolds number is now accessible, with a limited spanwise domain of approximately three diameters, to an LES calculation [46] provides a new opportunity to explore directly aspects of the vorticity transport. The LES results give a Strouhal number of 0.193 and a base pressure coefficient of -1.35, which should be compared with the experimental values of 0.20 and -1.15, respectively. The base pressure is still somewhat sensitive to shear layer transition at this Reynolds number but the discrepancy between the experimental and the calculated base pressure does raise questions about the absolute accuracy of such an LES calculation (perhaps especially for the separating boundary layer). Nevertheless, the calculation provides a special opportunity to 'see' the vorticity field and it illustrates various aspects of the vorticity flux. The database from the calculation has been provided by Ali Mani and Parviz Moin. (Mark Lohry has worked with one of us (G.L.B.) to manipulate it.) Figures 13(a) and 13(b) show, respectively, at the same time, an instantaneous picture of the spanwise vorticity and the spanwise averaged vorticity (averaged over the full span πD of the calculation). What is striking is how much of the shed vorticity is widely distributed into the near wake as a result of the Kelvin–Helmholtz instability in the separating shear layers, the three dimensionality of this shed vorticity and the large-scale velocity field imposed by the shed vortices. The result is a large flux of vorticity, as given by Equation (7), across $y = 0$ in the near wake.

The contributions to this mean flux, as functions of x/D, are shown in Figure 14(a) (where the averages were taken over only two shedding periods). For this particular figure, $V(x, y, t)$ is the *spanwise-averaged* (over the span πD of the calculation) normal component of the velocity, at time t, and $\Omega(x, y, t)$ is the spanwise-averaged, spanwise vorticity at the same time. ($v'(x, y, z, t) = v(x, y, z, t) - V(x, y, t)$, $\omega_z'(x, y, z, t)$ is similarly defined and $\overline{v'\omega_z'}$ was found from the spanwise average of the product of the fluctuations on $y = 0$



$t = 0$



$t = 20$

Figure 12. A point vortex simulation of a 2D wake instability, $t = 0$, 20, 40, 60, 120, 170 [45].

followed by the temporal average over two periods.) Interestingly, the *largest* contribution to the flux is clearly the time-averaged $\overline{V\Omega}$. This implies a large-scale, global character for the corresponding Reynolds stress field. As discussed in Section 2, since the source of vorticity on the upper half of the cylinder (Figure 5) is equal to the net flux out of a control

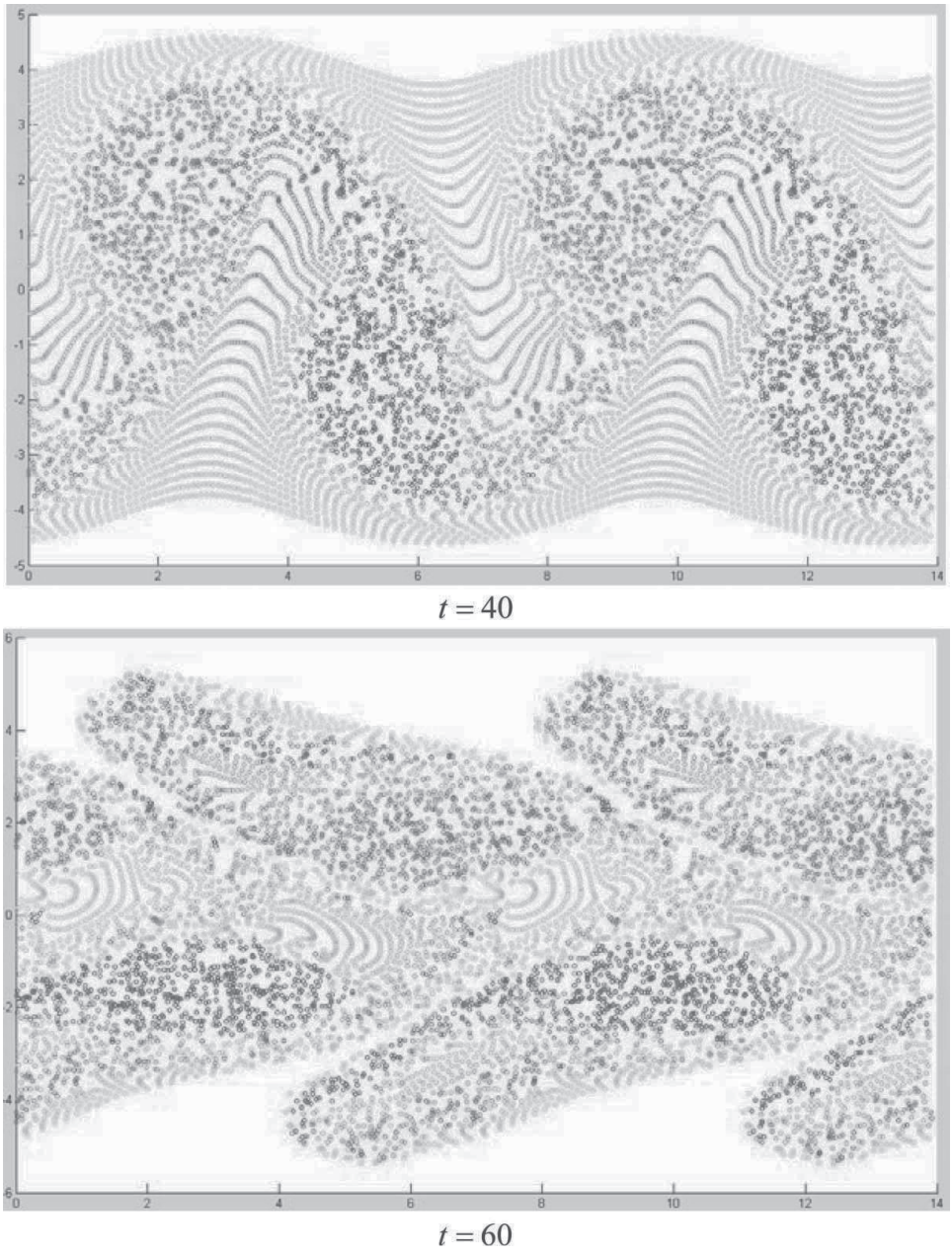
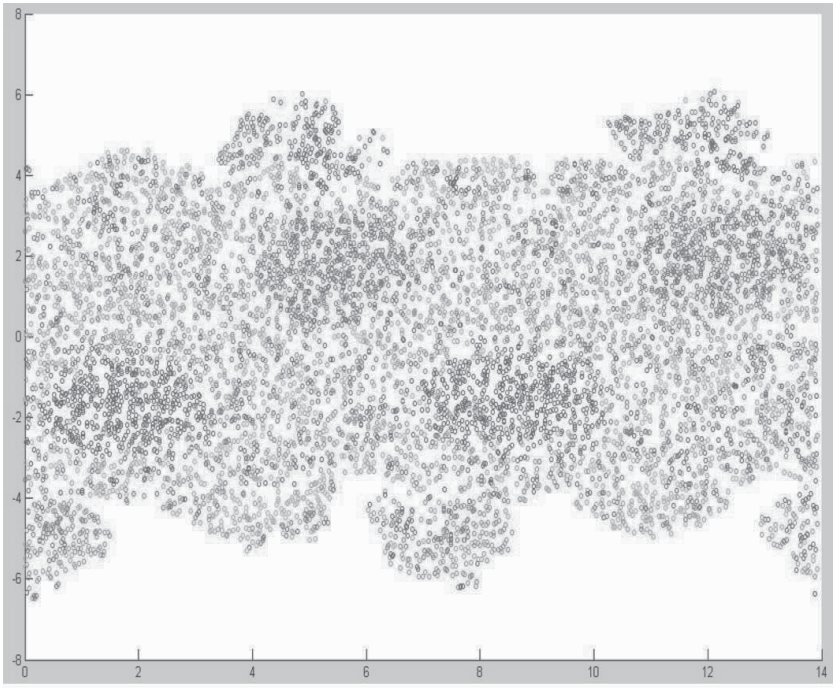
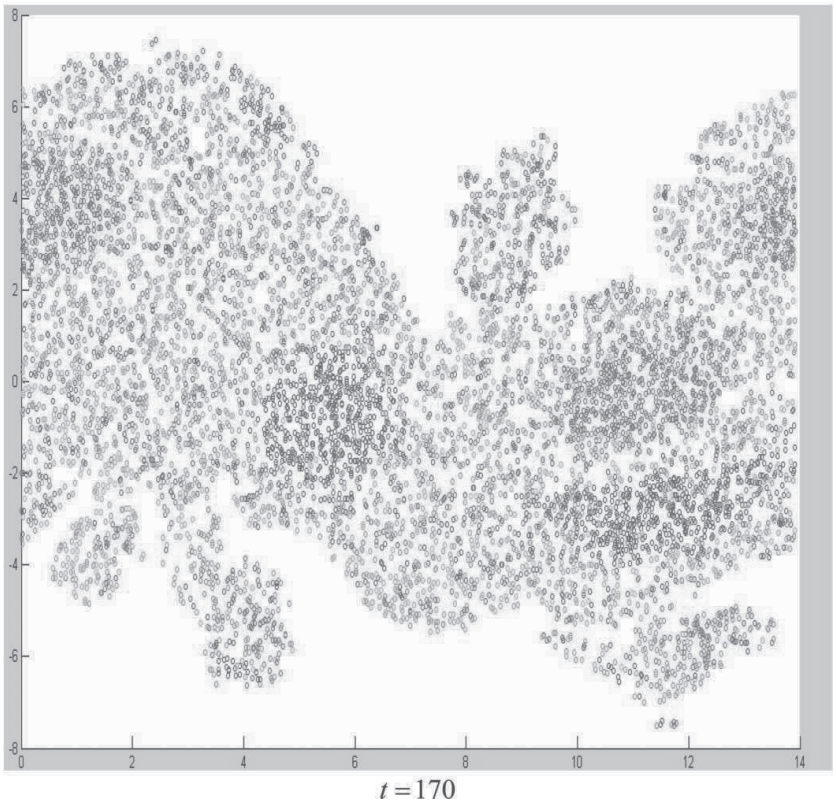


Figure 12. (Continued)

volume (shown in Figure 5 and formed by the plane $y = 0$ from the base of the cylinder and the plane $x = X$), then the integration of the vorticity flux from the base at $x = 0.5D$ to $x = X$ on $y = 0$ (as in Equation 7) will show how much of the shed vorticity has been 'lost' or 'canceled' (the remainder being a flux across the plane $x = X$). As discussed below, since the nondimensional mean flux of vorticity supplied at the wall is approximately 2.35



$t = 120$



$t = 170$

Figure 12. (Continued)

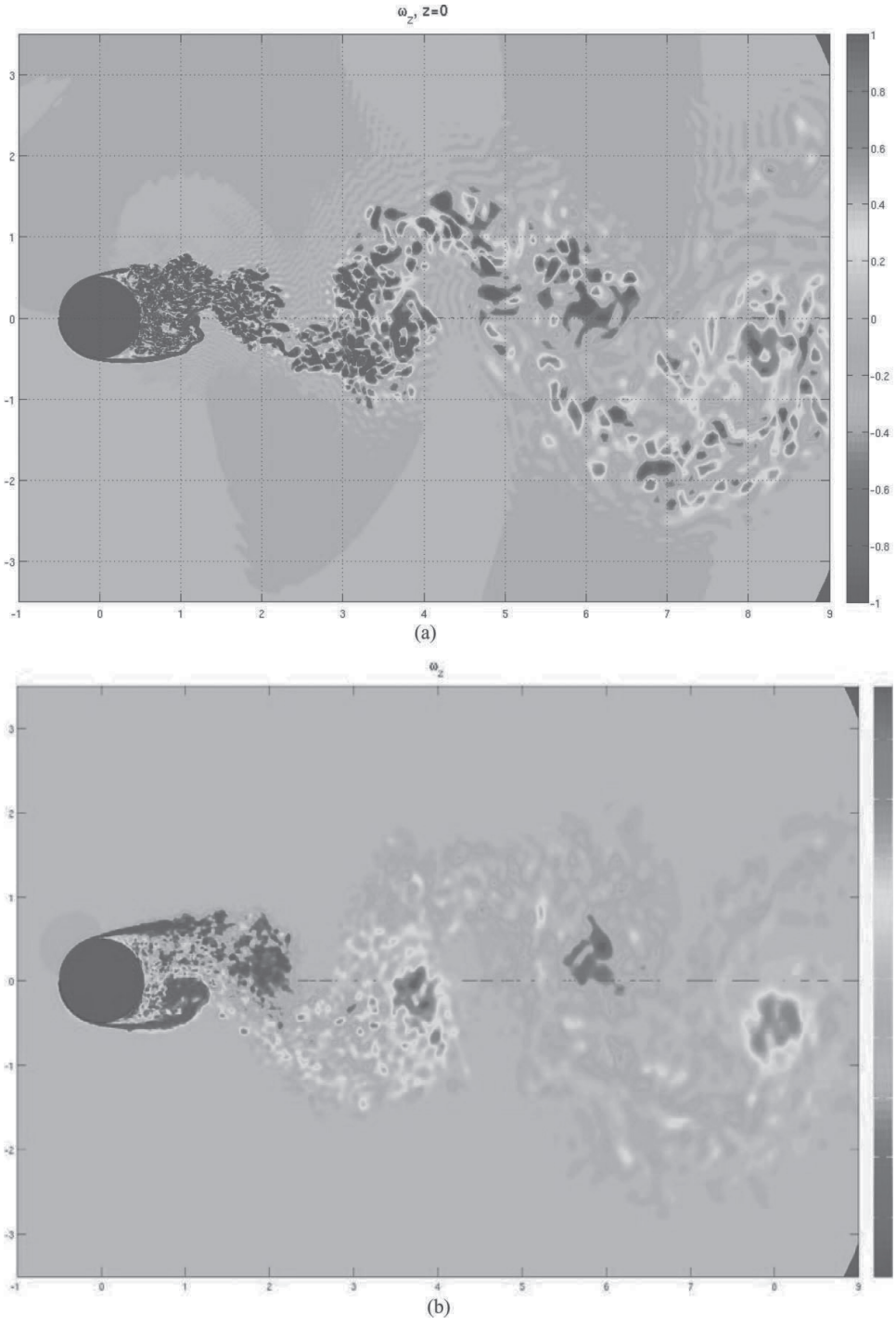


Figure 13. (a) Distribution of spanwise vorticity at a particular time on $z/D = 0$. (b) Spanwise-averaged distribution of spanwise vorticity obtained at the same time as in (a) (these figures are derived from an LES calculation of Mani et al. [46]).

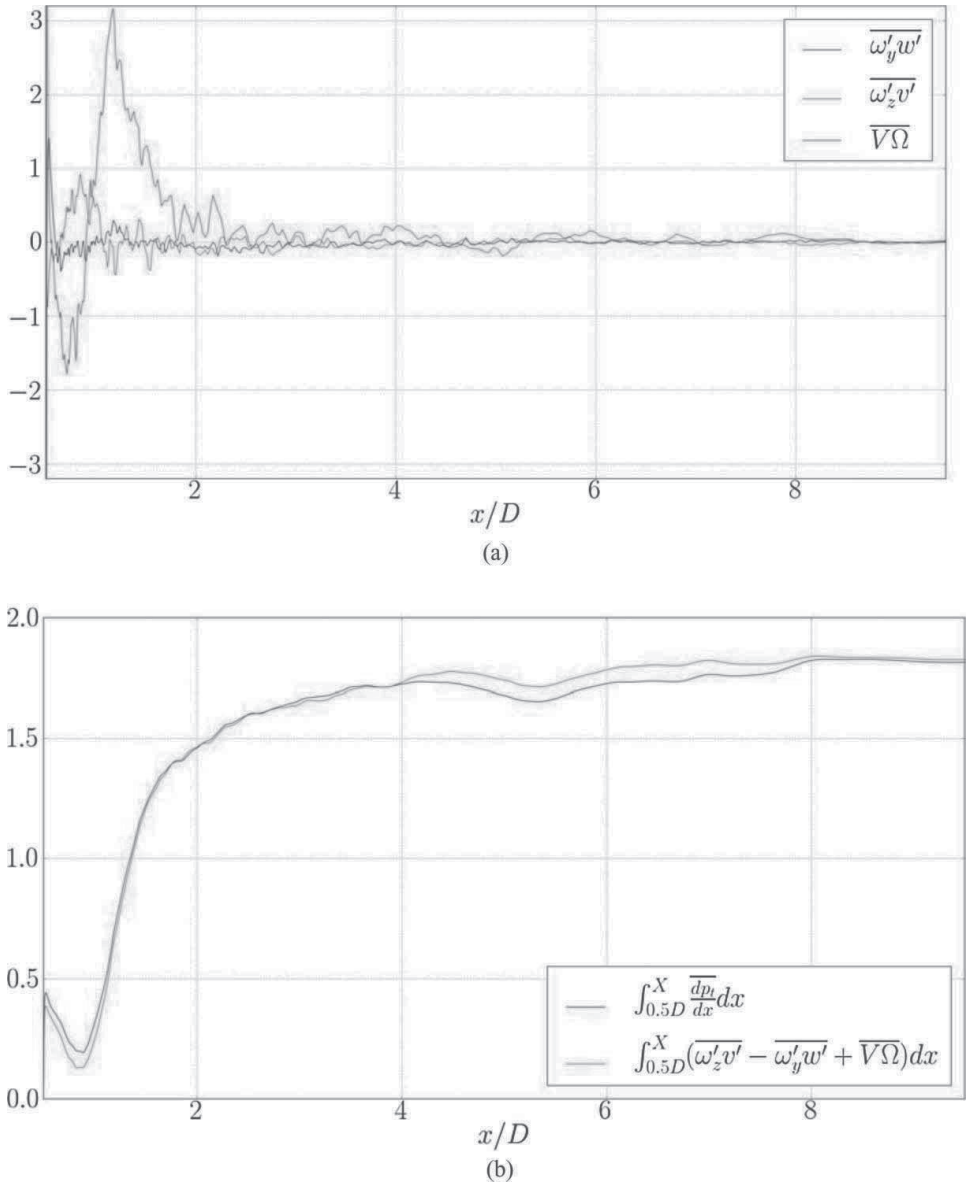


Figure 14. (a) Three contributing components of the mean vorticity flux on $y = 0$. (b) The integral of the vorticity flux on $y = 0$ and the integral of the total pressure (see Equation 11) (these figures are derived from an LES calculation of Mani et al. [46]).

for this calculation, the integration of the vorticity flux from the base, Figure 14(b), shows that one half of the vorticity supplied from the upper surface of the cylinder is canceled within one diameter from the base.

Importantly, this flux across $y = 0$ is also directly connected to the base pressure. This can be seen as follows. Using the identity $\nabla \times (\nabla \times \boldsymbol{u}) = \nabla(\nabla \cdot \boldsymbol{u}) - \nabla^2 \boldsymbol{u}$, the momentum

equation is

$$\frac{\partial \boldsymbol{u}}{\partial t} + \nabla\left(\frac{1}{2}\boldsymbol{u}\cdot\boldsymbol{u}\right) + \boldsymbol{\omega}\times\boldsymbol{u} = -\frac{1}{\rho}\nabla p + \nu\nabla^2\boldsymbol{u} = -\frac{1}{\rho}\nabla p - \nu\nabla\times\boldsymbol{\omega}. \tag{9}$$

Thus, on the surface of the cylinder, $\int_1^2 \frac{1}{\rho}\nabla p\cdot d\boldsymbol{s} = \frac{1}{\rho}(p_2 - p_1) = -\nu\int_1^2 \nabla\times\boldsymbol{\omega}\cdot d\boldsymbol{s}$ and a line integral from the forward stagnation point to the base relates the drop in pressure to the mean flux of vorticity from the surface (since $\nabla\times\boldsymbol{\omega}\cdot d\boldsymbol{s} = -\frac{\partial\omega_z}{\partial n}ds$). That is,

$$\frac{p_T - p_B}{1/2\rho U_\infty^2} = 1 - C_{pB} = \frac{1}{Re}\int_0^\pi \left|\frac{\partial\omega_z}{\partial r}\right|_{r=0.5} d\theta,$$

where velocities are scaled by U_∞ and lengths by the cylinder diameter. Thus, the magnitude of the nondimensional vorticity flux from the surface is 2.35 since $C_{pB} = -1.35$.

For a steady, high Reynolds number, free turbulent flow in which the mean viscous stresses can be neglected (and where $\boldsymbol{U}$ and $\boldsymbol{\Omega}$ are time means), the contribution to a line integral of Equation (9) between two fixed points in the fluid $d\boldsymbol{r}$ apart gives the important result that

$$\nabla\left(\frac{\overline{p}}{\rho} + \frac{1}{2}\boldsymbol{U}\cdot\boldsymbol{U} + \frac{1}{2}\overline{\boldsymbol{u}'\cdot\boldsymbol{u}'}\right)\cdot d\boldsymbol{r} = d\left(\frac{\overline{p}_T}{\rho}\right) = \left(\boldsymbol{U}\times\boldsymbol{\Omega} + \overline{\boldsymbol{u}'\times\boldsymbol{\omega}'}\right)\cdot d\boldsymbol{r}, \tag{10}$$

where the mean total pressure at a point includes here the kinetic energy of the mean flow and the mean turbulence kinetic energy.

Thus, integrating Equation (10) on $y = 0$ between the base (where the velocity is zero) and $x = X$ gives

$$\frac{\overline{p}_T(X)}{\rho} - \frac{\overline{p}_B}{\rho} = \int_{D/2}^{X}\left(\overline{v'\omega_z'} - \overline{w'\omega_y'}\right)dx. \tag{11}$$

The left-hand side and the right-hand side of Equation (11) have been plotted in Figure 14(b) (lengths, velocities and pressures scaled using the cylinder diameter and the free stream velocity). From the figure, by $x/D = 9.6$, the integral of the nondimensional flux is approximately 1.8 and the remaining flux is therefore approximately 0.55 (total approximately 2.35). That is, as $X\to\infty$, the velocity on the centerline will approach the free stream value and all of the vorticity from one side will have canceled all of the vorticity of opposite sign from the other and the total vorticity flux from the upper cylinder surface will be equal to the integrated flux across $y = 0$, as required by Equation (6). Of course, these LES calculations include a Smagorinsky diffusion model for the small scales not computed and this (small) contribution has not been included. Nevertheless, such calculations and, of course, DNS calculations offer new possibilities in understanding the mechanics of the vorticity, which generates through Biot–Savart, the velocity field and which in turn gives rise to the vorticity transport and the transport of momentum in high Reynolds-number-free turbulent shear flows.

4.6 *Some conclusions*

- Even though the turbulent wake is a highly 3D flow, there is considerable evidence that there is rescaling of a vortex-street-like structure that is characterized by groups

of 'spanwise vorticity' localized in the streamwise and spanwise directions with values for h/ℓ nearer to 0.5–0.6 than the classical, neutrally stable value for point vortices of 0.281.

- In particular, the conditional sampling that led to the velocity field obtained by Antonia et al. [10] at a Reynolds number of 1200 and $x/d = 420$ shows a remarkable degree of organization over several streamwise wavelengths. These results give a wavelength two to three times larger than that of the vortex street formed in the near wake and provide strong evidence of an underlying rescaling mechanism. The experimental results by Cimbala [44] at even higher *Re* show this rescaling and they are consistent with a view that the basic clumping of the vorticity has its origin in instability/Biot–Savart.
- The 3D instability found at low Reynolds number and supported by various theoretical and computational studies appears to manifest itself in the form of vortex loops connecting the primary upper and lower spanwise vorticity.
- Much of the spanwise vorticity shed into the near wake is strongly affected by local instabilities in the shear layer and the large-scale velocity field imposed by Biot–Savart from the accumulation of this vorticity in the shed vortices. In particular, the large net flux across the $y = 0$ plane in the immediate near wake substantially reduces the circulation of the shed vortices and also provides a different insight into the base pressure and near-wake structure.

4.7 *Some questions*

- Does the structure rescaling continue for wakes at much higher Reynolds numbers?
- Is there an asymptotic, high Reynolds number wake characterized only by the drag of the body (momentum thickness) and the distance from the body? This implies a universal structure that seems likely to require a large number of rescalings from the first-formed vortex street.
- How much does the growth rate of a 2D wake differ from the 3D one?

5. Concluding remarks

- At the time of the Marseille meeting in 1961, a goal for free turbulent shear flows was to find a constitutive relation for the turbulent or 'turbular' fluid and to take into account the relatively sharp interface (at high Reynolds numbers) between the irrotational and the rotational fluid. In some respects, it was an extension of an earlier goal to seek an eddy viscosity formulation that would enable the mean velocity profile to be predicted.
- In the last 50 years, considerable progress has been made in illuminating the mechanics of the mixing layer. There is now recognition of the central role played by instability and the Biot–Savart relationship that leads to the merging of the one-sided vorticity to form organized clumps of increasing scale. The 'mixing transition' that was found accounts for the rapid mixing to molecular scales in a high Reynolds number mixing layer. Similarly, the presence of the 'coherent structure' and an appreciation of the underlying mechanics have accounted for the response at some frequencies to external forcing and also for the dependence of entrainment ratio of the two free streams on their density ratio (though we have not discussed it here).

- Much less is known about the underlying coherent structure in the plane wake and other free shear flows in which the mean vorticity distribution is not one sided. The experimental and numerical results presented and results for other free shear flows suggest that the vorticity field also tends to form organized clumps, basically through the well-known mechanics of linear instability or more generally (i.e. including nonlinearity) through the Biot–Savart interaction. Results at relatively low Reynolds number suggest that the coherent structure in plane wakes, although 3D, is organized by spanwise vorticity, as in mixing layers.
- An understanding of the mechanics is most likely to be obtained from the vorticity. The subject stands at the beginning of a new era in which both LES and DNS calculations can provide details of the vorticity field and the fluxes of vorticity (vortex force). In this respect, there is a new opportunity to treat numerical computations much like experiments and to use them to seek not only simulations but also an understanding of the essential mechanics.
- Figure 15 is a photograph of the last launch of the Shuttle. The Reynolds number of the far-field, coflowing jet is estimated to be of the order of 10^9–10^{10}. An underlying 'coherent structure' resulting from the clumping of the vorticity seems self-evident. Will LES predict it and show the underlying mechanics and momentum transport? That could be a challenge that might be met in Marseille in 2061.



Figure 15. The last launch of the Shuttle, 8 July 2011. (NBC News – The Week of Pictures: 7–14 July. Reproduced with permission).

Acknowledgements

We gratefully acknowledge discussions during the preparation of this review with Professor Roddam Narasimha. We also thank Professors Parviz Moin and Ali Mani who made available the LES data from the simulation of the flow around a circular cylinder at $Re = 10{,}000$. Mark Lohry who manipulated the large data files and Saikishan Suryanarayanan who provided the unpublished point vortex simulations of the wake instability are very gratefully thanked. Discussions with Professor Gregoire Winckelmans, who provided unpublished results, and with Professor Tony Leonard are also gratefully acknowledged.

References

[1] H.W. Liepmann, *Free turbulent flows*, Proceedings of the First Colloquium on Mecanique de la Turbulence, Marseille, France, Centre National de la Recherche Scientifique (CNRS), Paris, 1961.

[2] D.E. Coles, *Interfaces and intermittency in turbulent shear flows*, Proceedings of the First Colloquium on Mecanique de la Turbulence, Marseille, France, Centre National de la Recherche Scientifique (CNRS), Paris, 1961.

[3] S. Corrsin *Investigation of flow in an axially symmetrical heated jet of air*, NASA Tech. Rep. NACA WR W-94, NASA Center for AeroSpace Information, Hanover, MD, 1943.

[4] A.A. Townsend, *Local isotropy in the turbulent wake of a cylinder*, Aust. J. Sci. Res. A 1(2) (1948), pp. 161–174.

[5] S. Corrsin and A.L. Kistler, *Free-stream boundaries of turbulent flows*, NASA Tech. Rep. NACA-TR-1244 (supersedes NACA Technical Note 3133), NASA Center for AeroSpace Information, Hanover, MD, 1955.

[6] A.A. Townsend, *The Structure of Turbulent Shear Flow*, Cambridge University Press, Cambridge, 1956.

[7] A.A. Townsend, *The Structure of Turbulent Shear Flow,* 2nd ed., Cambridge University Press, Cambridge, 1976.

[8] H.L. Grant, *The large eddies of turbulent motion*, J. Fluid Mech. 4 (1958), pp. 149–190.

[9] F.R. Payne and J.L. Lumley, *Large eddy structure of the turbulent wake behind a circular cylinder*, Phys. Fluids 10 (1967), pp. 1063–1065.

[10] R.A. Antonia, L.W.B. Browne, and D.K. Bisset, *A description of the organized motion in the turbulent far wake of a cylinder at low Reynolds number*, J. Fluid Mech. 184 (1987), pp. 423–444.

[11] A.A. Townsend, *The mechanism of entrainment free turbulent flows*, J. Fluid Mech. 26 (1966), pp. 689–715.

[12] J.L. Lumley, *Toward a turbulent constitutive relation*, J. Fluid Mech. 41 (1970), pp. 413–439.

[13] A. Roshko, *Experiments on the flow past a circular cylinder at very high Reynolds number*, J. Fluid Mech. 10 (1961), pp. 345–356.

[14] F.H. Abernathy and R.E. Kronauer, *The formation of vortex streets*, J. Fluid Mech. 13 (1962), pp. 1–20.

[15] L. Prandtl, *Uber die augebildete turbulenz*, ZAMM 5 (1925), pp. 136–139; Proceedings of the 2nd International Congress for Applied Mechanics, Zurich, 1926.

[16] G.I. Taylor, *Eddy motion in the atmosphere*, Phil. Trans. A 215 (1915), pp. 1–26.

[17] G.I. Taylor, *Statistical theory of turbulence*, Proc. Roy. Soc. Lond. A 151 (1935), pp. 421–454.

[18] G.L. Brown and A. Roshko, *On density effects and large structure in turbulent mixing layers*, J. Fluid Mech. 64 (1974), pp. 775–816.

[19] C.D. Winant and F.K. Browand, *Vortex pairing: The mechanism of turbulent mixing-layer growth at moderate Reynolds number*, J. Fluid Mech. 63 (1974), pp. 237–255.

[20] J.H. Konrad, *An experimental investigation of mixing in two-dimensional mixing layers*, Ph.D. thesis, California Institute of Technology, 1976.

[21] S.J. Kline, W.C. Reynolds, F.A. Schraub, and P.W. Runstadtler, *The structure of turbulent boundary layers*, J. Fluid Mech. 30 (1967), pp. 741–773.

[22] R. Narasimha, *The utility and drawbacks of conventional approaches*, in *Whither Turbulence? Turbulence at the Crossroads: Proceedings of a Workshop Held at Cornell University, Ithaca, NY, March 22–24, 1989*, J.L. Lumley, ed., Springer-Verlag, New York, 1990, pp. 13–48.

[23] B. Cantwell, *Future directions in turbulence research and the role of organized motion*, in *Whither Turbulence? Turbulence at the Crossroads: Proceedings of a Workshop Held at Cornell*

University, Ithaca, NY, March 22–24, 1989, J.L. Lumley, ed., Springer-Verlag, New York, 1990, pp. 97–131.

[24] G.I. Taylor, *The transport of vorticity and heat through fluids in turbulent motion*, Proc. Roy. Soc. Lond. A 135 (1932), pp. 685–700.

[25] D. Küchemann, *Report on the IUTAM Symposium on concentrated vortex motions in fluids*, J. Fluid Mech. 21 (1965), pp. 1–20.

[26] W.T. Ashurst, *Numerical simulation of turbulent mixing layers via vortex dynamics*, Tech. Rep. SAND-77-8613, Sandia Labs., Livermore, CA, 1977.

[27] H. Aref and E.D. Siggia, *Vortex dynamics of the two-dimensional turbulent mixing layer*, J. Fluid Mech. 100 (1980), pp. 705–737; also H. Aref, Ph.D. thesis, Cornell University, 1980.

[28] S. Suryanarayanan and R. Narasimha, *Is the growth rate of a turbulent mixing layer universal*? Abstract LE.00004, Bulletin of the American Physical Society, 63rd Annual Meeting of the APS Division of Fluid Dynamics Volume 55, Number 16, and Private Communication, 2010.

[29] R. Breidenthal, *Response of plane shear layers and wakes to strong three-dimensional disturbances*, Phys. Fluids 23 (1980), pp. 1929–1934.

[30] C. Carton de Wiart, G. Winckelmans, C. Bailly, P. Chatelan, F. Thirifay, and A. Roshko, *Similarity in 2-D spatially developing and long shear layers*, Abstract LE.00005, Bulletin of the American Psysical Society, 63rd Annual Meeting of the APS Division of Fluid Dynamics Volume 55, Number 16, and Private Communication, 2010.

[31] R.E. Breidenthal, *Structure in turbulent mixing layers and wakes using a chemical reaction*, J. Fluid Mech. 108 (1981), pp. 1–23.

[32] R.E. Breidenthal, *A chemically reacting turbulent shear layer*, Ph.D. thesis, California Institute of Technology, 1978.

[33] L.P. Bernal, R.E. Breidenthal, G.L. Brown, J.H. Konrad, and A. Roshko, *On the development of three-dimensional small scales in turbulent mixing layers*, in *Turbulent Shear Flows II (Selected Papers from Second International Symposium on Turbulent Shear Flows, Imperial College, London, July 1979)*, Springer-Verlag, New York, 1980, pp. 305–313.

[34] L.P. Bernal and A. Roshko, *Streamwise vortex structures in plane mixing layers*, J. Fluid Mech. 170 (1986), pp. 499–425; also L.P. Bernal, Ph.D. thesis, California Institute of Technology, 1981.

[35] M.M. Koochesfahani and P.E. Dimotakis, *Mixing and chemical reaction in a turbulent liquid mixing layer*, J. Fluid Mech. 170 (1986), pp. 113–126.

[36] M.M. Koochesfahani, *Experiments on turbulent mixing and chemical reaction in a liquid mixing layer*, Ph.D. thesis, California Institute of Technology, 1984.

[37] P.E. Dimotakis and G.L. Brown, *The mixing layer at high Reynolds number: Large structure dynamics and entrainment*, J. Fluid Mech. 78 (1976), pp. 535–560.

[38] D. Oster and I. Wygnanski, *The forced mixing layer between parallel streams*, J. Fluid Mech. 123 (1982), pp. 91–130.

[39] R. Narasimha and A. Prabhu, *Equilibrium and relaxation in turbulent wakes*, J. Fluid Mech. 54 (1972), pp. 1–17.

[40] I. Wygnanski, F.H. Champagne, and B. Marasli, *On the large scale structures in two dimensional, small deficit, turbulent wakes*, J. Fluid Mech. 168 (1986), pp. 31–71.

[41] A.C. Robinson and P.G. Saffman, *Three-dimensional stability of vortex arrays*, J. Fluid Mech. 125 (1982), pp. 411–428.

[42] E. Meiburg and J.C. Lasheras, *Experimental and numerical investigation of the three-dimensional transition in plane wakes*, J. Fluid Mech. 190 (1988), pp. 1–28.

[43] S. Taneda, *Downstream development of the wakes behind cylinders*, J. Phys. Soc. Jpn. 14 (1959), pp. 843–848.

[44] J.M. Cimbala, H. Nagib, and A. Roshko, *Large structure in the far wakes of two dimensional bluff bodies*, J. Fluid Mech. 190 (1988), pp. 265–298; also J.M. Cimbala, Ph.D. thesis, California Institute of Technology, 1984.

[45] S. Suryanarayanan and G.L. Brown, *Linear and non-linear stability via Biot–Savart computations*, Proceedings of the IUTAM Symposium on Bluff Body Flows, Kanpur, India, 2011.

[46] A. Mani, P. Moin, and M. Wang, *Computational study of optical distortions by separated shear layers and turbulent wakes*, J. Fluid Mech. 625 (2009), pp. 273–298.

[47] K.R. Sreenivasan and R. Narasimha, *Equilibrium parameters for turbulent wakes*, J. Fluids Eng. 104 (1982), pp. 167–170.

Appendix 1. Reynolds stress and the vorticity flux

The familiar vector identity (for $\nabla \cdot \boldsymbol{u} = 0$)

$$\boldsymbol{u} \cdot \nabla \boldsymbol{u} = \boldsymbol{\omega} \times \boldsymbol{u} + \nabla \left(\frac{1}{2} \boldsymbol{u} \cdot \boldsymbol{u} \right), \tag{A1}$$

written in summation notation, using $\frac{\partial u_k}{\partial x_k} = 0$, is

$$\frac{\partial u_i u_k}{\partial x_k} = \varepsilon_{ijk} \omega_j u_k + \frac{\partial}{\partial x_i} \left(\frac{1}{2} u_k^2 \right). \tag{A2}$$

Since $\nabla \cdot \boldsymbol{u} = 0$ for the instantaneous as well as the mean velocity, and therefore also for the fluctuating components of the velocity, the identity (A2) applies also to the fluctuating components of the velocity u_i' and it follows that

$$\frac{\partial u_i' u_k'}{\partial x_k} = \varepsilon_{ijk} \omega_j' u_k' + \frac{\partial}{\partial x_i} \left(\frac{1}{2} u_k'^2 \right). \tag{A3}$$

When Equation (A3) is averaged over time, the spatial derivatives of Reynolds stresses may be written in terms of the mean correlation in the corresponding vorticity and velocity fluctuations, together with the corresponding spatial derivative of the mean turbulence kinetic energy.

Appendix 2. The plane far wake and the asymptotic wake

For the plane wake, if the mean velocity defect is $\bar{u}(x, y) = U_1 - U(x, y)$, then if the normal Reynolds stresses, which give small departures in the static pressure and streamwise momentum flux, are neglected the drag is

$$\text{Drag} = \rho \int_{-\infty}^{+\infty} U(U_1 - U) dy = \rho \int (U_1 - \bar{u}) \bar{u} dy \equiv \rho U_1^2 \theta, \tag{A4}$$

where θ is the momentum thickness of the wake. For a body with characteristic dimension d and drag coefficient C_D, we have $\theta = C_D d/2$. Thus, to this approximation, momentum conservation requires that the length θ is independent of x for a body with a given drag.

If, at high Reynolds number, the effect of viscosity on the mean flow in the wake can be ignored and if $\bar{u}_0$ is the mean velocity deficit on the centerline and δ is the half width of the wake (where the mean velocity is $U_1 - {}^1\!/_2 \bar{u}_0$), dimensional analysis gives (for a 2D body whose shape is defined by n dimensions, d_n)

$$\frac{\bar{u}(x, y)}{U_1} = f_1 \left(\frac{x}{\theta}, \frac{y}{\theta}, \frac{d_n}{\theta} \right) \quad \text{and} \quad \frac{-\overline{u'v'}(x, y)}{U_1^2} = f_2 \left(\frac{x}{\theta}, \frac{y}{\theta}, \frac{d_n}{\theta} \right)$$

so that

$$\frac{\bar{u}_0}{U_1} = f_3 \left(\frac{x}{\theta}, \frac{d_n}{\theta} \right) \quad \text{and} \quad \frac{\delta}{\theta} = f_4 \left(\frac{x}{\theta}, \frac{d_n}{\theta} \right),$$

and therefore

$$\frac{\bar{u}(x, y)}{\bar{u}_0} = f_5 \left(\frac{y}{\delta}, \frac{\theta}{x}, \frac{d_n}{\theta} \right) \quad \text{and} \quad \frac{-\overline{u'v'}(x, y)}{\bar{u}_0^2} = f_6 \left(\frac{y}{\delta(x)}, \frac{\theta}{x}, \frac{d_n}{\theta} \right) \tag{A5}$$

(using $\frac{y}{\theta} = \frac{y}{\delta} \cdot \frac{\delta}{\theta}$, etc). If $\theta/x \to 0$, the wake defect velocity $\bar{u}$ exhibits similarity for a given body since $\frac{\bar{u}(x,y)}{\bar{u}_0(x)} = f_5(\frac{y}{\delta(x)}, 0, \frac{d_n}{\theta})$. It has been well established that for the far wake, the *shape* of the velocity profiles becomes independent of the body shape expressed by d_n/θ so that

$$\frac{\bar{u}(x, y)}{\bar{u}_0(x)} = f_7\left(\frac{y}{\delta(x)}\right). \tag{A6}$$

This equation for $\bar{u}$ applied now in the conservation of momentum Equation (A4) leads to the expression

$$\frac{\theta}{I_1\delta} = \frac{\bar{u}_0}{U_1}\left(1 - \frac{I_2}{I_1}\frac{\bar{u}_0}{U_1}\right), \tag{A7}$$

where, following [6], $I_1 = \int_{-\infty}^{\infty} f_7(\frac{y}{\delta})d(\frac{y}{\delta})$ and $I_2 = \int_{-\infty}^{\infty} f_7^2(\frac{y}{\delta})d(\frac{y}{\delta})$. The first term alone, on the right-hand side of Equation (A7), corresponds with the neglect of terms (including the anticipated normal Reynolds stress terms) in Equation (A4) of order $\bar{u}_0^2/U_1^2$ compared with $\bar{u}_0/U_1$. (Thus, for the far wake, where $\bar{u}_0/U_1$ is small, the product $\bar{u}_0\delta \to$ const, since $\frac{U_1\theta}{\bar{u}_0\delta} = I_1 - I_2\frac{\bar{u}_0}{U_1} \to I_1$.)

Similarly for $\theta/x \to 0$, the Reynolds stress from Equation (A5) will exhibit similarity for a given body. In addition to satisfying the continuity equation, similarity expressed by Equation (A6) requires the reduction of the momentum equation to an ordinary differential equation in which the coefficients are independent of x. If $\bar{u}_0/U_1 \to 0$ and all viscous and normal stresses are neglected, the x momentum equation is approximated by $-U_1\frac{\partial\bar{u}}{\partial x} = \frac{\partial(-u'v')}{\partial y}$. It then follows that to this lowest order, the Reynolds stress $-u'v'$ from Equation (A5) must exhibit similarity

$$-u'v'(x, y) = \bar{u}_0^2 f_8\left(\frac{y}{\delta(x)}\right),$$

and the x momentum equation reduces to (where $\eta = y/\delta(x)$)

$$-\left[U_1\frac{\bar{u}_0\delta}{\bar{u}_0^3}\frac{d\bar{u}_0}{dx}\right]\frac{d}{d\eta}(\eta f_7) = f_8', \tag{A8}$$

since, to this approximation, from Equation (A7), $\bar{u}_0\delta = U_1\theta/I_1$. Similarity requires the term in the square brackets to be constant and if it is put equal to k, then

$$\frac{1}{2}\frac{d}{dx}\left(\frac{U_1^2}{\bar{u}_0^2}\right) = \frac{kI_1}{\theta}. \tag{A9}$$

Integration gives an asymptotic solution for $\bar{u}_0/U_1 \to 0$,

$$\frac{\bar{u}_0^2 x}{U_1^2\theta} = \frac{1}{2kI_1}, \tag{A10}$$

and from Equation (A7)

$$\frac{\delta^2}{\theta x} = \frac{2k}{I_1}. \tag{A11}$$

In the experiments of Narasimha and Prahbu [39] and further by Sreenivasan and Narasimha [47], the values $I_1 = 2.06$, $\frac{\delta^2}{\theta x} = 0.090$ and $\frac{\bar{u}_0^2 x}{U_1^2\theta} = 2.63$ were found.

If the higher-order terms are kept in the momentum integral, as in Equation (A7), and also the higher-order terms in the x momentum equation (i.e. the same order as $V\frac{\partial U}{\partial y}$) and similarity arguments

made for the coefficients to be independent of x, then Townsend [6] and Narasimha and Prabhu [39] found that Equations (A10) and (A11) give, respectively, the leading term in asymptotic expansions and that

$$\frac{\tilde{u}_0^2 x}{U_1^2 \theta} = \frac{1}{2kI}\left(1 + O\left(\frac{\theta}{x}\right)^{\frac{1}{2}}\right), \tag{A12}$$

$$\frac{\delta^2}{\theta x} = \frac{2k}{I}\left(1 + O\left(\frac{\theta}{x}\right)^{\frac{1}{2}}\right), \tag{A13}$$

as $\theta/x \to 0$. For finite θ/x, Equations (A12) and (A13) could be separately approximated by $\frac{\tilde{u}_0}{U_1} \propto (\frac{(x-x_0)}{\theta})^{-\frac{1}{2}}$ and $\frac{\delta}{\theta} \propto (\frac{(x-x_0)}{\theta})^{\frac{1}{2}}$ over some range of θ/x. As is widely accepted, we identify the far wake as one for which $\theta/x \ll 1$ and, correspondingly, $\frac{\tilde{u}_0}{U_1} \propto (\frac{(x-x_0)}{\theta})^{-\frac{1}{2}}$ and $\frac{\delta}{\theta} \propto (\frac{(x-x_0)}{\theta})^{\frac{1}{2}}$, and define the asymptotic wake as the region where $x_0/x \to 0$ and for which Equations (A10) and (A11) would apply.

Journal of Turbulence
Vol. 13, No. 45, 2012, 1–19

Taylor & Francis
Taylor & Francis Group

Progress in pipe and channel flow turbulence, 1961–2011[†]

John Kim*

Department of Mechanical and Aerospace Engineering, University of California, Los Angeles, Los Angeles, CA 90095, USA

(*Received 3 July 2012; final version received 26 August 2012*)

Although much progress has been made in pipe and channel flow turbulence over the past 50 years since the Turbulence Colloquium Marseille 1961 (TCM 1961), these simple wall-bounded turbulent flows have continuously baffled us, refusing to reveal their true and complete nature. In a broader sense, almost everything we thought we knew about wall-bounded turbulent flows, including the scaling laws that appear in textbooks, has been the subject of further scrutiny. An overview of the progress that has been made since TCM 1961 is presented, followed by discussions on unresolved issues that would require further investigations.

Keywords: pipe; channel; wall-bounded turbulent flows; scaling laws; turbulence structures

1. Introduction

Advancements in both experimental and computational techniques have made it possible to investigate the fundamental physics of wall-bounded turbulent flows in detail. High-order turbulence statistics that were not available at TCM 1961 have become available, thanks in large part to advancements in numerical simulation of turbulent flows. The analysis of detailed turbulence statistics and instantaneous flow fields has led to an improved understanding of turbulent flows in pipes and channels at low Reynolds numbers. However, accurate numerical simulation of turbulent flows is still limited to low Reynolds numbers, and laboratory experiments continue to play an essential role even for these geometrically simple turbulent flows at high Reynolds numbers. Accurate experimental data at high Reynolds numbers have led to re-examinations of the fundamental scaling laws, but many yet remain to be resolved. For example, there is still no clear consensus as to whether the log-law mean velocity profile in the overlap region is universal (i.e., independent of Reynolds number) or even valid for large, but finite, Reynolds numbers. A proper velocity scale for turbulence statistics in the wall region has also been a subject of debate. The peak root-mean-square (rms) value of streamwise-velocity fluctuations normalized by the wall-shear velocity, u_τ, for example, continues to grow as the Reynolds number increases. This observation has led to alternative suggestions, which include an outer velocity scale

*Email: jkim@seas.ucla.edu

[†]This is a written version of the author's presentation at Turbulence Colloquium Marseille, which was held in Marseille, France, during 26–30 September 2011 (hereinafter, TCM 2011). It served as an introduction to follow-up discussions on pipe and channel flow turbulence research, past, present, and future.

ISSN: 1468-5248 online only
© 2012 Taylor & Francis
http://dx.doi.org/10.1080/14685248.2012.726358
http://www.tandfonline.com

in order to account for the Reynolds-number dependence. The identification of the second peak (or a shoulder, as asserted by some) in the outer layer at high Reynolds numbers has also led to various discussions as to the origin of the peak and the proper scaling law.

In spite of reliable experimental data at high Reynolds numbers that have become available recently, and accurate and detailed numerical data at low to moderate Reynolds numbers, many fundamental issues for these simple turbulent flows still remain to be resolved. Some issues and challenges for future research are listed below for further discussions. Naturally, many of the issues discussed in this paper also apply to turbulent boundary layers. To what extent these two canonical flows are similar in the wall region, in spite of apparent differences in the outer layer, is also of significant interest. One advantage in analyzing the internal flows over the external turbulent boundary layers is the ability to accurately determine the wall-shear stress through the pressure gradient. This point is important, since many issues under scrutiny involve very subtle differences, some of which may lie within the experimental uncertainty associated with the measurement of wall-shear stress. Internal flows, especially fully-developed pipe flows, have an additional simplification in that the streamwise direction is homogeneous.[1] Boundary layers, on the other hand, continuously grow downstream and the streamwise direction is not homogeneous, although it can be considered approximately homogeneous. This difference, however subtle it may be, may bear a significant consequence for theoretical analysis, the point of which has been advocated by George [2] who asserts, among other things, a log law for pipe and channel flows and a power law for boundary layers.

In the present paper, u, v, w denote the velocity fluctuations in the streamwise (x), wall-normal (y), and spanwise (z) directions, respectively, U represents the streamwise mean velocity, and Re and Re_τ, respectively, represent the Reynolds number based on the centerline velocity and wall-shear velocity. The superscript $^+$ denotes a quantity normalized by the wall-shear velocity, u_τ and the kinematic viscosity, ν.

2. The state-of-the-art–1961

Hinze [3] presented the state-of-the-art in turbulent pipe flow at TCM 1961. Much of the discussion was focused on the mean-velocity profile and the behavior in the wall region (e.g., the law of the wall, etc.). Although all measurements showed rough agreement with the log law, he observed noticeable variations in the values of the constants appearing in the log law, thus raising the question of universality:

> The law of the wall and the velocity-defect law might be only of approximate value, and the von Karman constant might not be a constant and Reynolds number similarity might not exist or at the most at much higher Reynolds numbers than assumed hitherto.

He also reported that the rms values of turbulence fluctuations normalized by u_τ were a function of Re. So it is apparent that some currently debated issues (see Section 4) were already recognized in 1961. Hinze's discussions also included the effects of surface roughness on the mean velocity, and concluded that a single roughness parameter, k, was insufficient to describe the roughness effect, which has recently received much attention [1].

It is worth mentioning in passing that Hinze also presented Laufer's measurements on the turbulence-kinetic energy budget [4], some parts of which, the dissipation rate in the wall region in particular, were not accurate compared with now generally accepted numerical data [5], in large part due to the then-limited capability of turbulence measurements. The production term, including the peak value and its location, on the other hand, was

accurately measured, thus indicating that the measurements of the mean velocity (including its gradient) and Reynolds shear stress were already quite accurate.

3. Progress since TCM 1961

Some progress achieved since TCM 1961 is highlighted in this section. This is by no means a complete list, and only those pertinent to issues to be discussed in Section 4 are mentioned here. For a more exhaustive list of references, the reader is referred to two recent review papers by Marusic et al. [1] and by Smits et al. [6], and the references therein.

3.1. *Experiments*

First extensive turbulence statistics were measured by Comte-Bellot [7], covering $Re =$ 57,000–230,000. Eckelmann [8] used an oil channel to measure detailed turbulence statistics and turbulence structures in the wall region for $Re = 2800$ ($Re_\tau = 143$) and 4100 ($Re_\tau = 209$). (Incidentally, Kim et al. [9] used a comparable Reynolds number for comparison, and their Reynolds number, $Re_\tau = 180$, has become the standard for many numerical simulations to follow.) Hussain and Reynolds [10] used an extremely long and high-aspect ratio channel for $Re =$ 13,800–33,300. Johansson and Alfredsson [11] measured detailed turbulence statistics for $Re = 6900 - 24{,}450$. Accurate measurements for high Re flows became available much later. Zagarola and Smits [12] reported the first Superpipe data for $Re = 31 \times 10^3 - 35 \times 10^6$ in 1998, followed by further data and analysis later [13]. Zanoun et al. [14] reported turbulence measurements in a channel for Reynolds numbers up to $Re_\tau = 5000$ ($Re = 1.2 \times 10^5$). Monty et al. [15] examined similarities and differences in pipe, channel, and boundary layer flows.

Talamelli et al. [16] discussed limitations of existing facilities and reported a plan to build a new community facility to be operated under the Center for International Cooperation in Long Pipe Experiments (CICLoPE). This would become a rather unique facility for high Reynolds number turbulence flow research, and it is worth noting a few key features of the facility. The pipe is 115 m long with 0.9 m diameter, and it is being built with the following goals:

- At least a decade of the log region, which is assumed to start at $y^+ = 200$, resulting in y^+ up to 2000.
- The log region extends up to 0.15 R^+, where R is the radius of the pipe, so R^+ should be at least 13,300.
- A sufficient range of Re to be able to study scaling behavior, estimated by them to be at least a factor of three, thus resulting in up to $R^+ = 40{,}000$.
- The smallest viscous length scale, ℓ^+, should be larger than 10 μm, considering a hotwire with a diameter of 0.6 μm, and a length of 120 μm.

Figure 1 shows the range of R^+, and the viscous length scale, ℓ, for the proposed pipe in comparison with Princeton's Superpipe. This pipe-flow facility will prove to be a useful community resource in addressing many issues, if not all, that are discussed in the present paper.

3.2. *Numerical simulations*

Direct numerical simulation (DNS) and large-eddy simulation (LES) have matured to become a powerful tool in studying turbulent flows. Its limitation to low Re notwithstanding,

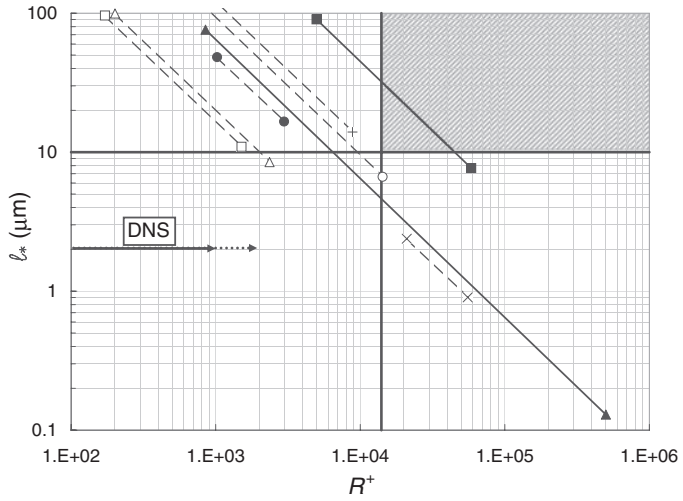


Figure 1. Range of R^+ and viscous length scale: CICLoPE (■), Superpipe (▲), Monty (•), Wygnanski & Champagne (□), Univ. of Cottbus under construction (○), Nikuradse (×), Laufer (+). See [16] for further details on the legends. Reprinted with permission from [16].

especially for DNS, it has played an essential role by providing accurate and detailed information, which are not readily available from experimental results.

Deardorff [17] was the first to perform a large-eddy simulation (LES) of a turbulent channel flow, using a very modest number of grid points, 6720, while Schumann [18, 19] followed with 65,536 grid points. Both Deardorff and Schumann could use the modest number of grid points because they used a wall-layer model in their LES. Moin and Kim [20] carried out the first LES without modeling the wall layer, using up to 516,096 grid points for $Re = 13,800$ ($Re_\tau = 640$), matching the Reynolds number used by Hussain and Reynolds [10]. Kim et al. [9] performed the first DNS of a turbulent channel flow at $Re = 3300$ ($Re_\tau = 180$), using up to 3,962,880 grid points. As mentioned earlier, the Reynolds number was chosen to closely match that of Eckelmann's [8]. It was their flow visualization, which mimicked the hydrogen bubble visualization in laboratory experiments, not detailed turbulence statistics, that convinced the experimental community that direct numerical simulation was capable to reproduce realistic turbulent flows. Eggels et al. [21] performed DNS of a turbulent pipe flow at $Re_\tau = 360$. Others followed with higher Reynolds numbers: DNS of turbulent channel flows up to $Re_\tau = 590$ [22], $Re_\tau = 934$ [23], $Re_\tau = 2003$ using 1.8×10^{10} grid points [24], DNS of pipe flows up to $Re_\tau = 1,142$ using 6.3×10^8 grid points [25]. The rather slow increase in the maximum Reynolds number reflects the fact that the ratio of the large scale (energy containing eddies) over the smallest scale (Kolmogorov scale) increases proportional to $Re_T^{3/4}$, where Re_T is the Reynolds number based on turbulent velocity and length scale, thus requiring the total number of grid points in a three-dimensional simulation to increase proportional to $Re_T^{9/4}$.

There are some other noteworthy numerical simulations: the minimal flow unit with constrained spanwise scales [26]; the autonomous cycle without the outer layer [27]; the role of the dominant linear mechanism [28]; true compressibility vs. variable-property effect for high Mach number flows [29]. These simulations were unique in that further insights into turbulence physics were gained through approaches possible only in numerical simulations

(i.e., they were fictitious flows manufactured by solving modified governing equations or boundary conditions), thus further demonstrating the power of numerical simulations.

3.3. *Theoretical considerations*

In contrast to a large body of experimental and numerical works, through which our understanding of wall-bounded turbulent flows has been advanced significantly, there have been relatively few theoretical works. One particular theoretical consideration has generated much discussion on the mean velocity profile [30–32]. This has led to the "power-law vs. log-law" debate (see, for example, [2, 33–37]), and some proposed a modified log law [38]. Arguments for the power law and pursuing debates are discussed in Section 4.1. A few other noteworthy theoretical works include: Lie group symmetry [39], scaling of the energy spectra [23], and asymptotic scaling [40].

4. Issues for further discussions

In this section, I list many unresolved issues that are currently being investigated. Once again, the reader is reminded that this is by no means a complete list, but was used as an introduction to further discussions.

4.1. *Mean velocity*

It has been commonly accepted—and we all have been taught and still teach in our classes—that for high Reynolds wall-bounded flows, there are distinctive regions: inner, outer, and overlap regions. A dimensional analysis leads to

$$U^+ = f(y^+), \tag{1}$$

for the inner (or wall) region, and

$$\frac{U_{\max} - U}{u_\tau} = g\left(\frac{y}{R}\right) \tag{2}$$

for the outer region, where R is the radius (channel half-height) of a pipe (channel). For large Re, there would be a region $\nu/u_\tau \ll y \ll R$, and in this overlap region

$$U^+ = A \log y^+ + B, \tag{3}$$

and it was believed that the above log profile is universal, i.e., A and B are independent of Re, although they may be different for different wall-bounded flows.

Barenblatt [30] claimed that a power law

$$U^+ = C(y^+)^\alpha, \tag{4}$$

where C and α depend on Re since they depend on viscosity due to incomplete similarity, would be more appropriate. After examining existing experimental data, he proposed

$$U^+ = \left(\frac{1}{\sqrt{3}} \ln Re + \frac{5}{2}\right)(y^+)^{\frac{3}{2 \ln Re}}. \tag{5}$$

Barenblatt's power law arguments can be summarized as follows:

- Both the power law and the log law have equally rigorous theoretical foundations, i.e., they are not merely convenient representations of empirical data.
- Due to incomplete similarity for large but finite Re, the dependence of the velocity gradient on the molecular viscosity does not disappear, hence leading to a power law.
- The power law applies to $40\ \nu/u_\tau \leq y \leq 0.9\ R$ (note that the power law extends much beyond the log region).
- A universal log law is related to the envelope of a family of power-law curves, each corresponding to a fixed Re (see Figure 2, bottom).

Barenblatt used, among others, Princeton's Superpipe data (Figure 2, top) to validate the power law. However, Zagarola et al. [33], after analyzing the same data, concluded that a power law and a log law co-exist: their analysis showed that for high Re pipe flows, a power law would fit better in $50 \leq y^+ \leq 500$, followed by a log law in $500 \leq y^+ \leq 0.1\ R^+$. Barenblatt and Chorin [34] argued that the Superpipe data for high Re might have been affected by surface roughness, while Smits and Zagarola [35] assured that the effect of roughness on their data was negligible. Wosnik et al. [38], on the other hand, proposed a modified law by introducing a mesolayer,

$$U^+ = \frac{1}{\kappa} \ln (y^+ + a^+) + B, \tag{6}$$

where all constants, κ, a, B, depend on Re.

It is not clear which of the two laws would prevail in the end. It is unlikely that more accurate experimental data can resolve the controversy, since the difference can be quite subtle. George [41] illustrates this point well: If a measured mean velocity gradient shows $1/y$ behavior, it would lead to a log law, but if it shows $1/y^{1-\epsilon}$, it would lead to a power law even for very small ϵ. Therefore, experimental data alone cannot settle the issue due to experimental uncertainties. Numerical data would suffer from the same problem, let alone their limitation to Re flows. Hopefully, other theoretical considerations will shed new light on this fundamental issue.

Issues regarding mean velocity profile that need to be addressed include:

- Is there a log law? If so, is it universal such that the parameters that appear in the log law are indeed constants (i.e., independent of Re)? Are they flow dependent?
- What is the minimum Re above which the log region exists unambiguously?
  - Where does the log region start and end (a general rule of thumb has been $100\ \nu/u_\tau \leq y \leq 0.15\ R$)?
  - Does it depend on Re?
  - Does it depend on boundary conditions (i.e., boundary layer vs. pipe or channel)?
- Is a power law with Re-dependent coefficients a better scaling law for high but finite Re? It is worth drawing attention to the notion that both laws have theoretical foundations—the log-law is based on the assumption of self-similarity while the power law is based on the assumption of incomplete similarity.
- What is the proper velocity scale for the defect law for the mean velocity in the outer region?
  - The previously accepted velocity scale, u_τ, has been challenged by many investigators, who have proposed a mixed velocity scale or a velocity scale based on outer velocity,

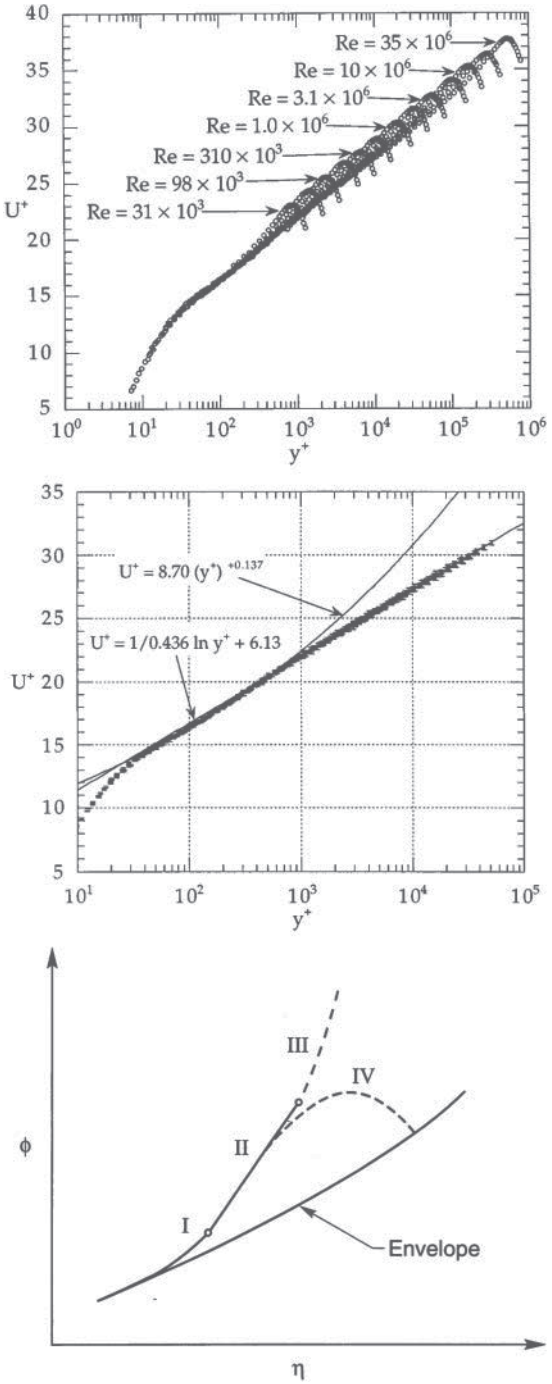


Figure 2. Mean velocity profiles for 13 different Re between 32×10^3 and 35×10^6 from Superpipe (top). Velocity profile data within 0.07 R^+ for 26 different Re [33] (middle). A family of scaling laws by Barenblatt and Chorin [32], showing slopes larger than the envelope. Top and middle figures are reprinted with permission from [33]. Copyright © Cambridge University Press 1998. Bottom figure is reprinted with permission from [32]. Copyright (1996) National Academy of Sciences, USA.

such as U_c or $U_c - U_m$, where U_c and U_m denote, respectively, the centerline velocity and mass-averaged velocity.
  - Does $U_c - U_m \to \text{const} \times u_\tau$ in the limit $Re \to \infty$, thus leading to the same velocity scale asymptotically?
- If the proper velocity scale for the outer layer is other than u_τ, is a log law still possible? Note that the usual simple matching argument would not lead to a log law unless the defect law is also scaled by u_τ, but a log law is still plausible as the leading term in a logarithmic expansion [38].
- Is the wall region, including the viscous and inertial layer in fully developed pipe flows, inherently different from that of turbulent boundary layers over a flat plate (i.e., zero pressure gradient boundary layer)?
  - Is the difference due to different outer layers?
  - Is it due to homogeneity vs. inhomogeneity?
  - Or is it simply due to the presence of the overall force balance in fully-developed internal flows (i.e., pressure gradient is balanced by the wall shear), thus rendering the wall-shear velocity to be the proper velocity scale for both inner and outer regions?

4.2. *Turbulence statistics*

It has been generally accepted that turbulence fluctuations in the wall region are scaled by u_τ (and hence independent of the outer layer, be it boundary layer, pipe or channel), streamwise velocity fluctuations and turbulent kinetic energy (TKE) peak in the buffer layer ($y^+ \approx 12$) and decay monotonically, and most of the TKE is produced in the wall region. All of these, except for the peak location, have been challenged. The location of the peak seems to be independent of Re (and also outer layer), but its value showed a Re-dependence. Some investigators have proposed to use a mixed velocity, involving u_τ and U_c. Some proposed to decompose them into contributions from small scales, which are universal in wall scaling, and those from large scales, which are Re-dependent [1]. Hultmark et al. [42], on the other hand, attributed some variations of the peak value normalized by u_τ due to an inadequate hotwire resolution, and showed no variation of the peak values when the same non-dimensional hotwire length, ℓ^+, was used for different Re (Figure 3).

The y-location, where the streamwise velocity fluctuations (and hence TKE) and the TKE production attain its maximum, appears to be independent of Re, being $y^+ \approx 12$. In a fully developed pipe or channel flow,

$$-\overline{u^+v^+} + \frac{\mathrm{d}U^+}{\mathrm{d}y^+} = 1 + \frac{1}{Re_\tau} y^+ \tag{7}$$

$$\approx 1, \quad \text{for large } Re_\tau, \tag{8}$$

and the TKE production, P^+, can be written as

$$P^+ = -\overline{u^+v^+}\frac{\mathrm{d}U^+}{\mathrm{d}y^+} \tag{9}$$

$$= \left(1 - \frac{\mathrm{d}U^+}{\mathrm{d}y^+}\right)\frac{\mathrm{d}U^+}{\mathrm{d}y^+}. \tag{10}$$

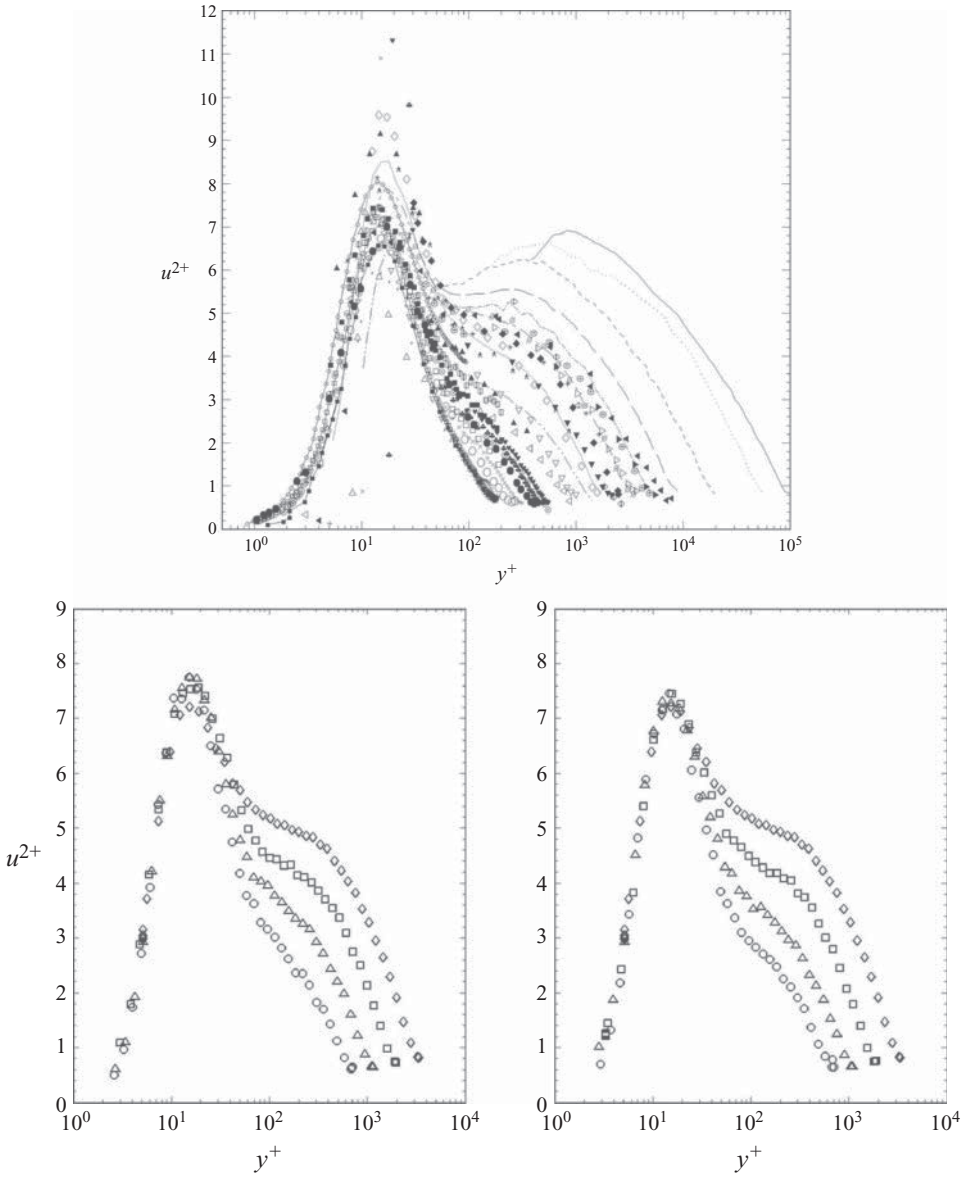


Figure 3. The effect of hotwire length on measured streamwise velocity fluctuations: various sources at $Re_D = 5.3 \times 10^3 - 5.7 \times 10^6$ (top), where Re_D denotes the Reynolds number based on the pipe diameter; with fixed ℓ (bottom left), fixed ℓ^+ (bottom right) at $Re_D = 24{,}000 - 145{,}000$. Reprinted with permission from [42]. Copyright © Cambridge University Press 2010.

Thus, P^+ achieves its maximum value 0.25, where $\mathrm{d}U^+/\mathrm{d}y^+ = 0.5$. If the mean velocity profile in the inner layer is universal, this location would be independent of Re. Note that $\mathrm{d}U^+/\mathrm{d}y^+ = 1$ at the wall and decreases monotonically as y^+ increases. Apparently $\mathrm{d}U^+/\mathrm{d}y^+ = 0.5$ around $y^+ \approx 12$ somewhere in the buffer layer.

Although the TKE production peaks in the buffer layer independent of Re, and the major contributions to the total production come from the wall region for low Re, they

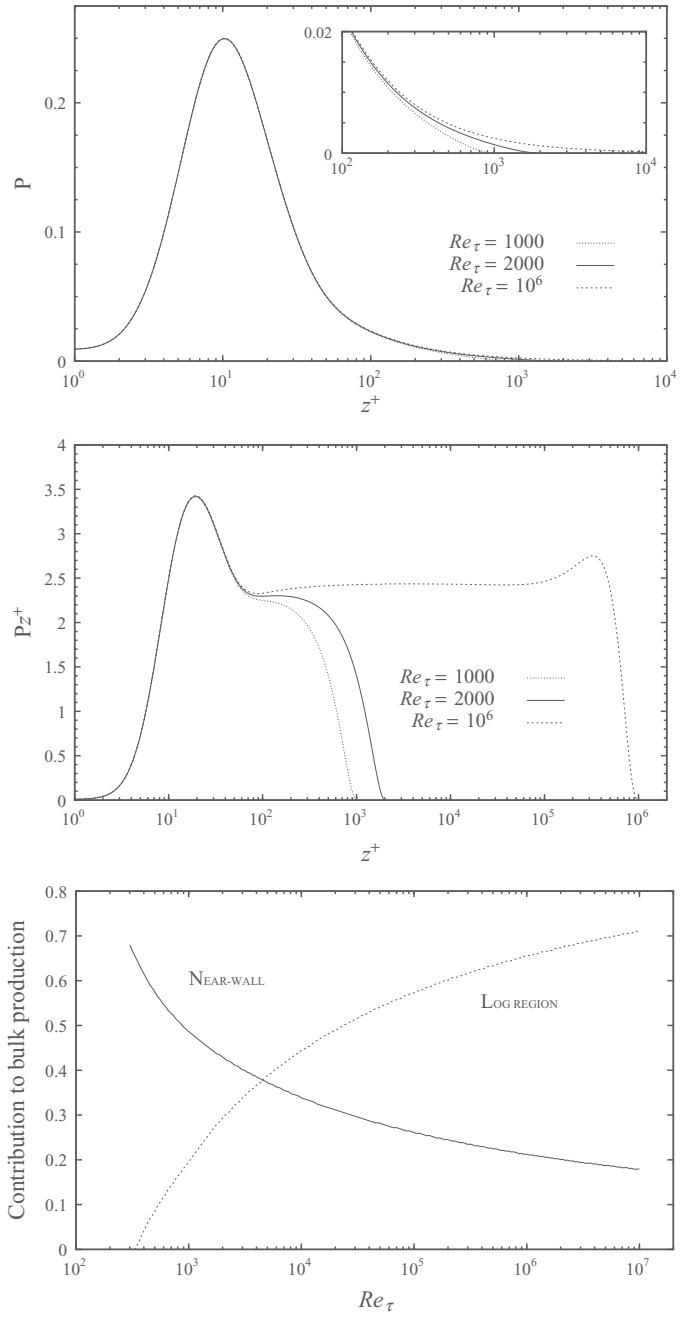


Figure 4. TKE production: typical semi-log representation (top), pre-multiplied version (middle), the ratio of TKE production to total production (bottom). Reprinted with permission from [43].

come from the log region for high Re [43]. Figure 4 shows that the change occurs at around $Re_\tau = 4200$. (Note that the data shown in the figure are actually from boundary-layer measurements, but it is assumed that a similar trend would apply to pipe and channel flows.) Whether this change signals fundamental changes in the way turbulence is produced

and maintained for high Re flows, and its implications for flow control, are of significant interest, and need to be addressed in future research.

Issues regarding the scaling of turbulence statistics include:

- What is the proper velocity scale for turbulence statistics in the wall region? The peak rms value of streamwise-velocity fluctuations when scaled by u_τ increases with Re, thus suggesting an effect of outer-scale motions.
- What is the peak rms value in the limit $Re \to \infty$?
- Is the failure of the inner-layer scaling (i.e., scaling by u_τ) due to Re-dependent attached eddies (*à la* Townsend) [44–46]?
- Although the peak rms value scaled by u_τ increases with Re, the location of the peak appears to be independent of Re, $y^+ \approx 12$, which is also the location where the production peaks independent of Re. Why?
- Is the second peak of the streamwise-velocity fluctuations real? Or should it be a shoulder (instead of a peak), and are the peaks observed in some experiments actually due to a probe-resolution problem?
- The second peak appears only at high Re. Does this suggest a significant change in turbulence characteristics beyond a certain Re?
- Should streamwise and spanwise components be scaled differently from the wall-normal component? Is this simply due to the fact that the wall affects the wall-normal component differently?
- The location of the maximum Reynolds shear stress normalized by the inner variables increases with Re, but that of the maximum production seems to be independent of Re, $y^+ \approx 12$. Why?
- Should Reynolds stresses in the wall region in internal flows be different from those in turbulent boundary layers, since they are influenced by different large scale motions (LSMs) and very large scale motions (VLSMs) in the outer layer?
- The fraction of TKE in the wall region, where the first peak is located, decreases as Re increases. Does this mean that the wall region becomes less important at high Re, to the extent that the wall region is driven by the outer region (see discussion below regarding the bottom-up vs. top-down process in Section 4.3)?

4.3. *Turbulence structures*

The existence and role of organized turbulence structures in wall-bounded turbulent flows have been well documented. (Wallace [47] in this special issue provides an overview of the literature.) The effects of these organized turbulence structures on turbulence statistics, modeling, and their implications for flow control are topics of ongoing research. For example, Kim [48] considered interfering with the regeneration mechanism of near-wall turbulence structures in an attempt to achieve skin-friction drag reduction in channel flow. In addition to the organized near-wall turbulence structures, which had attracted much attention during the 1970s and 1980s, the recent observation of large-scale motions (LSMs) and very large-scale motions (VLSMs) have led to intense research activities [49–53]. LSMs are on the order of pipe diameter or channel width, and they are believed to be formed when hairpin vortices align coherently in packets [49] (Figure 5). VLSMs are on the order of several pipe diameters or channel heights, and they are a consequence of large-scale motions associated with packets of hairpin vortices aligning coherently so that the low momentum flow from the lower half of one is passed up to the next, and so on, over a span of many LSMs

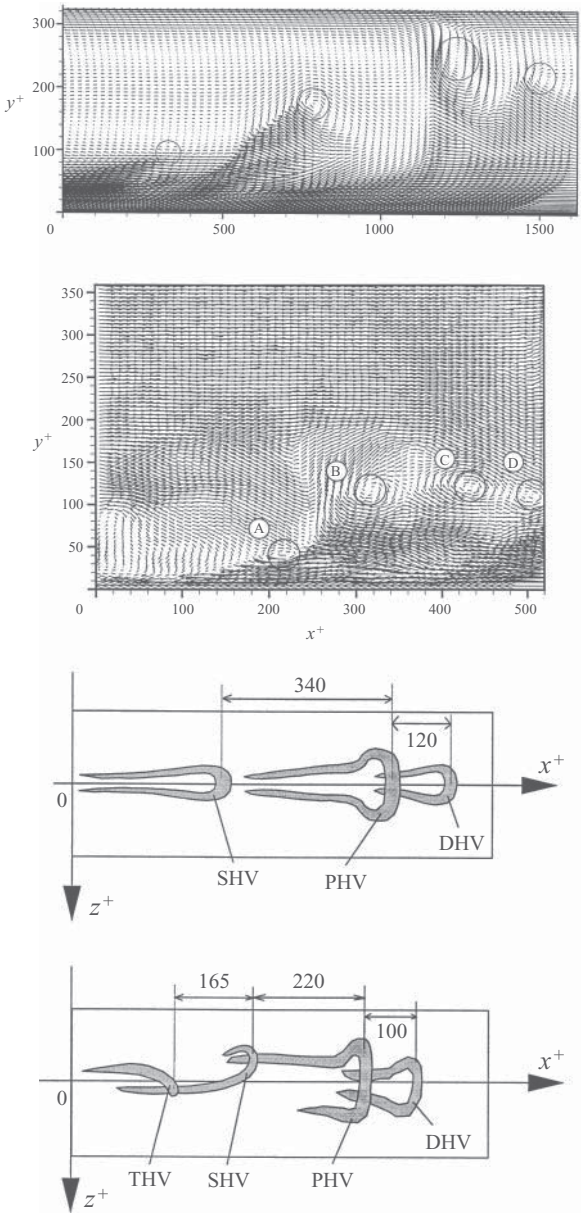


Figure 5. A packet of hairpin vortices: numerical (top), experiment (middle), a schematic of LSM (bottom two). Reprinted with permission from [49]. Copyright © Cambridge University Press 1999.

(Figure 6). The discovery of these large-scale motions have also led to intense research activities, both numerical and experimental.

It has been reported that a large fraction of turbulent kinetic energy (TKE) resides in these large-scale motions, and they influence (or leave footprints) near-wall turbulence much more than previously thought, especially at high Re [52, 53]. The influence of such large-scale motions, which are presumably flow dependent (i.e., internal flows vs. external

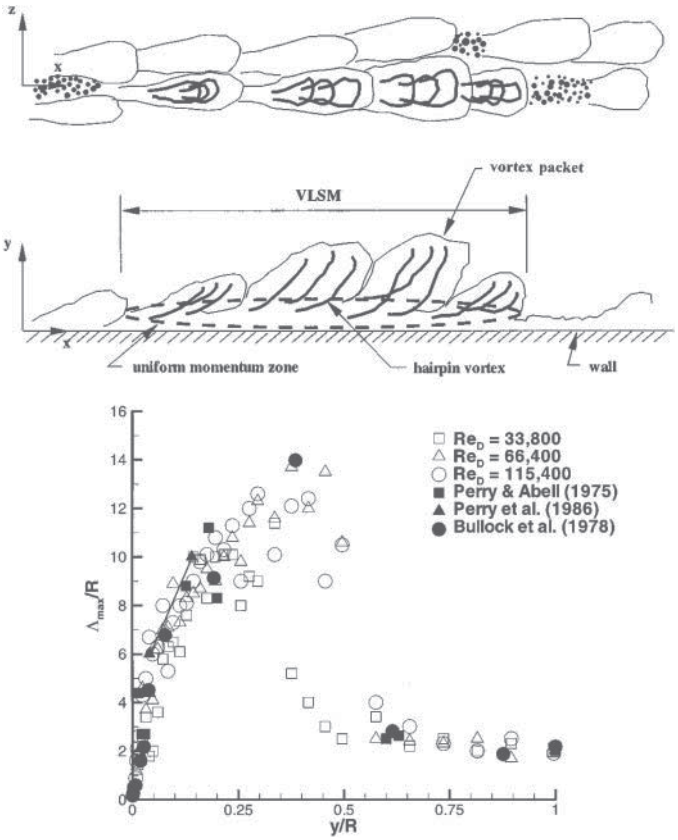


Figure 6. A schematic of VLSM, forming from packets of hairpin vortices (top), and the streamwise length scale (bottom). Reprinted with permission from [50]. Copyright 1999, American Institute of Physics.

flows), on near-wall turbulence, also raises a question as to whether near-wall turbulence, the self-sustaining mechanism in particular [54, 55], is universal, and what would be the proper scaling law for turbulence statistics in the wall region. If the effects of outer large scale motions on near-wall turbulence are significant, any control strategy for viscous drag reduction, for example, must account for such effects.

Issues regarding turbulence structures that need to be addressed include:

- Are turbulence structures close to wall–streaks, streamwise vortices, and their regeneration mechanism–universal in the sense that they are, at least in the first order, independent of outer flow?
  - In spite of the recent observation of the organized large-scale motions and their strong influence on near-wall turbulence [43], spanwise spacing of the wall-layer streaks normalized by wall variables appears to be independent of Re and flows [1]. Is this true, and why?
- Recent observations suggest that LSMs and VLSMs interact (or modulate) with near-wall turbulence [43, 56]. This seems to contradict the classical notion (*à la* Townsend)

that these large-scale outer motions are "inactive" motions, i.e., they do not contribute to the Reynolds shear stress.

- It has been shown that LSMs and VLSMs are different for internal and external flows [15]. If these different structures influence (or modulate) turbulence across the whole width (or boundary layer), different wall-layer dynamics are expected, but they appear to be very similar to each other. Why?
- Are VLSMs real, or an experimental or numerical artifact?
  - It is worth mentioning that the detection of VLSMs are mostly based on Taylor's hypothesis, the applicability of which (to large scale motions) is subject to a critical examination.
- Is the self-sustaining mechanism of near-wall turbulence universal, independent of Re and the outer flow?
- Some investigators (e.g., Julian Hunt, private communication) contend that the role of LSMs and VLSMs would become more significant as Re increases, to the extent that the bottom-up process prevalent at low Re would be replaced by a top-down process. What evidence do we have to support this notion?
  - What are the implications for flow control at high Re?
  - How do we reconcile the success of a flight test, in which a riblet surface designed to control near-wall structures achieved drag reduction even at high Re [57]?

4.4. *Effects of roughness*

Surface roughness is a defining feature of many of the high Re flows found in engineering. Understanding the effects of surface roughness attracted researchers' interest early on (e.g., Hinze's discussion at TCM 1961 [3]), and has attracted more attention recently as our interest for high Re flows grows. The interested reader is referred to a review paper by Jimenez [58]. In addition to the effect of surface roughness on skin-friction drag, which has been the primary focus, the extent to which the surface roughness affect turbulence outside the wall region has also attracted much attention [59–61].

Issues regarding the effects of surface roughness include:

- The commonly used Colebrook's formula (via the Moody chart, for example) predicts a monotonic effect of surface roughness on the drag in transitional to turbulent regime. However, new experimental data show a different trend in the transitional regime, which is consistent with Nikuradse's data (see Figure 7) and a phenomenological model of Gioia and Chakraborty [62].
- Is the notion of a hydrodynamically smooth surface for, say, $k_s^+ < 4$, valid?
- Can the roughness function (à la Hama function), ΔU^+, be determined uniquely for a given k_s^+?
- Some data suggest that the effects of surface roughness in internal flows are different from those in external flows. If so, why?
- The classical notion (à la Townsend's hypothesis) that the influence of surface roughness is confined to the wall region and that the outer flow is independent of surface roughness seems to have survived recent debates.
- There have been some anomalies, but it is now generally accepted, perhaps except for two-dimensional roughness, which seem to affect the flow further beyond the wall region compared to three-dimensional roughness, that the outer flow is unaffected by surface roughness provided that the roughness height (usually measured in terms of the

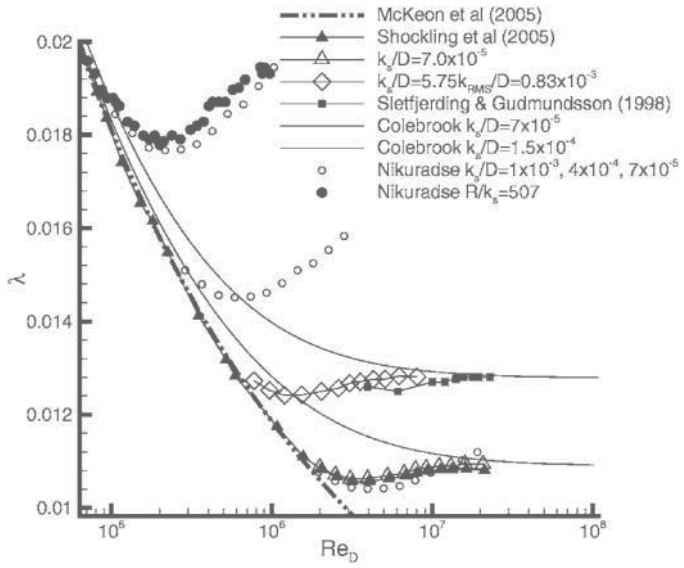


Figure 7. The friction factor for honed surfaces and most roughness types. Reprinted with permission from [63]. Copyright 2005, American Institute of Physics.

equivalent sand-grain roughness) is small compared to the pipe diameter (or channel height, or boundary layer thickness for external flows).

- The above conclusion is based primarily on mean velocity profile and rms turbulence fluctuations. It has not yet been demonstrated whether the same holds for higher-order statistics.
- How far does the roughness-affected layer extend?
- If Townsend's hypothesis holds for turbulence structures as well, how do we reconcile the recent recognition that interactions between outer flow large-scale motions and inner flow turbulence are much stronger than previously understood?
  - Does this mean that the interactions are one-way, i.e., only the outer flow can influence the inner flow, but not the other way around?

4.5. *Other miscellaneous questions*

A few unrelated questions that may be worthy of further discussions include:

- What is the required probe resolution for turbulence measurements?
  - Is the generally accepted value, $\ell^+ < 10$, sufficient?
  - In a similar vein, what is the required spatial (and temporal) resolution for numerical simulations?
    * Is the numerical grid of several wall units, which is typical for most direct numerical simulations, sufficient?
    * The usual justification that most dissipations should be captured may or may not be sufficient in addressing certain subtle issues raised above (e.g., the second peak in the rms fluctuations), in part because this justification was based on average dissipations (i.e., Kolmogorov scale) while much smaller scales may be present locally and instantaneously.

- Is there any link between LSMs/VLSMs and the exact but unstable traveling wave solutions, aka "exact coherent structures" (Eckhardt et al. [64])?
  - Although these exact traveling wave solutions have been observed only at low Re flows, there is no reason why these solutions cease to exist at higher Re.
- Fully developed pipe flows and channel flows are generally considered to be the same for all purposes, and yet their linear stability is the opposite, the former being linearly stable for all Re while the latter has a critical Re beyond which the flow is linearly unstable. Are there any differences even in fully developed turbulent flows as a consequence of different linear stability?

5. Concluding remarks

Much progress has been achieved over the past half century, owing to more accurate experimental data that have become available, and accurate and detailed numerical simulation results made possible with the advancement of efficient numerical algorithms and powerful computers. Nonetheless, this simple pipe or channel flow turbulence has been elusive, refusing to reveal its true nature. In summary:

- In spite of reliable experimental data at high Re and detailed numerical data at low to moderate Re, many fundamental issues still remain to be resolved.
- It will take a large-scale collaborative experimental effort in order to address many unresolved issues. The CiCLoPE is a step forward toward this goal.
- In spite of the remarkable advancement of modern supercomputers, the required computing power for simulation of turbulent flows at high Re flows is much beyond the capability of presently available computers, and perhaps those feasible in the near future.
- It would take a concerted effort by the whole community—theoreticians, experimentalists, computational fluid dynamicists—to improve our understanding of the true nature of turbulent flows, and to enhance our ability to manipulate them into a state with desired properties.

If there is going to be another turbulence colloquium in 50 years, say TCM 2061, their discussions may include (some pun intended, and in spite of a reminder that prediction about the future is a fool's exercise):

- How high Re is high enough? The highest Re simulation ($Re = 10^{?}$) would not be large enough.
- Extremely large scale motions (ELSMs), and a pipe or channel will never be long enough, and a computational domain will never be large enough.
- A new unified law instead of a log or power law.
- In the same way that numerical simulation and LDV/PIV have changed the way we study turbulent flows since TCM 1961, the next generation's research tools—perhaps, a three-dimensional holography virtual wind tunnel, high-level language to solve the Navier-Stokes equations, etc.,—would have made many remarkable contributions by TCM 2061.
- But, still trying to achieve turbulent pipe flows with a laminar-like drag.
- And so forth $\cdots$

Acknowledgements

I am grateful to the organizing committee of TCM 2011 (Marie Farge, Keith Moffatt, Kai Schneider) for giving me the opportunity to present this review in spite of the fact that I have not been an active player for many topics discussed in the present paper. Discussions with Bill George, who seems to know all anecdotal histories, have been enlightening and entertaining.

Note

1. Strictly speaking, the streamwise direction in a fully-developed channel flow in all laboratory experiments is not homogeneous due to the side-wall boundary layers, whereas that in numerical simulations is treated as homogeneous. In this regard, the notion that future experiments and simulations should be focused on fully-developed pipe flows warrants special attention [1].

References

[1] I. Marusic, B.J. McKeon, P.A. Monkewitz, H. Nagib, A.J. Smits, and K.R. Sreenivasan, *Wall-bounded turbulent flows at high Reynolds numbers: Recent advances and key issues*, Phys. Fluids 22 (2010), 065103.

[2] W.K. George, *Is there a universal log law for turbulent wall-bounded flows?* Phil. Trans. R. Soc. A 365 (2011), pp. 789–806.

[3] J.O. Hinze, *Turbulent pipe flow*, in *Proceedings of 1961 Mechanics of Turbulence, Steady Fully Developed Turbulence*, Marseille, France, 1961, pp. 129–165.

[4] J. Laufer, *The structure of turbulence in fully developed pipe flow*, Tech. Report, No. 1174, NACA, Washington D.C., 1954. Also available from http://ntrs.nasa.gov/archive/nasa/casi.ntrs.nasa.gov/19930092199_1993092199.pdf.

[5] N.N. Mansour, J. Kim, and P. Moin, *Reynolds-stress and dissipation-rate budgets in a turbulent channel flow*, J. Fluid Mech. 194 (1988), pp. 15–44.

[6] A.J. Smits, B.J. McKeon, and I. Marusic, *High-Reynolds number wall turbulence*, Annu. Rev. Fluid Mech. 43 (2011), pp. 353–375.

[7] G. Comte-Bellot, *Contribution à l'étude de la turbulence de conduite* [Contribution to the study of turbulence in a duct], Doctoral thesis, University of Grenoble, 1963.

[8] H. Eckelmann, *The structure of the viscous sublayer and the adjacent wall region in a turbulent channel flow*, J. Fluid Mech. 65 (1974), pp. 439–459.

[9] J. Kim, P. Moin, and R.D. Moser, *Turbulence statistics in fully developed channel flow at low Reynolds number*, J. Fluid Mech. 177 (1987), pp. 133–166.

[10] A.K.M.F. Hussain and W.C. Reynolds, *Measurements in fully developed turbulent channel flow*, J. Fluid Engrg. 97 (1975), pp. 568–578.

[11] A.V. Johansson and P.H. Alfredsson, *On the structure of turbulent channel flow*, J. Fluid Mech. 122 (1982), pp. 295–314.

[12] M.V. Zagarola and A.J. Smits, *Mean flow scaling of turbulent pipe flow*, J. Fluid Mech. 373 (1998), pp. 33–79.

[13] B.J. McKeon, J. Li, W. Jiang, J.F. Morrison, and A.J. Smits, *Further observations on the mean velocity distribution in fully-developed turbulent pipe flow*, J. Fluid Mech. 501 (2004), pp. 135–147.

[14] E.S. Zanoun, F. Durst, and H. Nagib, *Evaluating the law of the wall in two-dimensional fully developed turbulent channel flows*, Phys. Fluids 15 (2003), pp. 3079–3089.

[15] J.P. Monty, N. Hutchins, H.C.H. Ng, I. Marusic, and M.S. Chong, *A comparison of turbulent pipe, channel and boundary layer flows*, J. Fluid Mech. 632 (2009), pp. 431–442.

[16] A. Talamelli, F. Persiani, J.H.M. Fransson, P.H. Alfredsson, A.V. Johansson, H.M. Nagib, and J.-D. Rüedi, K.R. Sreenivasan, and P.A. Monkewitz, *CICLoPE–a response to the need for high Reynolds number experiments*, Fluid Dyn. Res. 41 (2009), pp. 1–21.

[17] J.W. Deardorff, *A numerical study of three-dimensional turbulent channel flow at large Reynolds numbers*, J. Fluid Mech. 41 (1970), pp. 453–480.

[18] U. Schumann, *Ein Verfahren zur direkten numerischen simulation turbulenter Strömungen in Platten- und Ringspaltkanälen und über seine Anwendung zur Untersuchung von Turbulenzmodellen* [A procedure for the direct numerical simulation of turbulent flows in plane channels and annuli and its application in the development of turbulence models], Dissertation–Universität Karlsruhe (TH), 1973.

[19] U. Schumann, *Subgrid scale model for finite difference simulations of turbulent flows in plane channel and annuli*, J. Comp. Phys. 18 (1975), pp. 376–404.
[20] P. Moin and J. Kim, *Numerical investigation of turbulent channel flow*, J. Fluid Mech. 118 (1982), pp. 342–377.
[21] J.M. Eggels, F. Unger, M.H. Weiss, J. Westerweel, J. Adrian, R. Friedrich, and F.T.M. Nieuwstadt, *Fully developed turbulent pipe flow: a comparison between direct numerical simulation and experiment*, J. Fluid Mech. 268 (1994), pp. 175–209.
[22] R.D. Moser, J. Kim, and N.N. Mansour, *Direct numerical simulation of turbulent channel flow up to* $Re_\tau = 590$, Phys. Fluids 11 (1999), pp. 8943–8945.
[23] J.C. del Alamo, J. Jimenez, P. Zandonade, and R.D. Moser, *Scaling of the energy spectra of turbulent channels*, J. Fluid Mech. 500 (2004), pp. 135–144.
[24] S. Hoyas and J. Jimenez, *Scaling of the velocity fluctuations in turbulent channels up to* $Re_\tau = 2003$, Phys. Fluids 18 (2006), 011702.
[25] X. Wu and P. Moin, *A direct numerical simulation study on the mean velocity characteristics in turbulent pipe flow*, J. Fluid Mech. 608 (2008), pp. 81–112.
[26] J. Jimenez and P. Moin, *The minimal flow unit in near wall turbulence*, J. Fluid Mech. 225 (1991), pp. 213–240.
[27] J. Jimenez and A. Pinelli, *The autonomous cycle of near-wall turbulence*, J. Fluid Mech. 389 (1999), pp. 333–359.
[28] J. Kim and J. Lim, *A linear process in wall-bounded turbulent shear flows*, Phys. Fluids 12 (2000), pp. 1885–1883.
[29] G.N. Coleman, J. Kim, and R.D. Moser, *A numerical study of turbulent supersonic isothermal-wall channel flow*, J. Fluid Mech. 305 (1995), pp. 159–183.
[30] G.I. Barenblatt, *Scaling laws for fully developed shear flow. Part 1. Basic hypothesis and analysis*, J. Fluid Mech. 248 (1993), pp. 513–520.
[31] G.I. Barenblatt and V.M. Prostokishin, *Scaling laws for fully developed shear flow. Part 2. Processing of experimental data*, J. Fluid Mech. 248 (1993), pp. 521–529.
[32] G.I. Barenblatt and A.J. Chorin, *Small viscosity asymptotics for the inertial range of local structure and for the wall region of wall-bounded turbulent shear flow*, Proc. Natl. Acad. Sci. USA 93 (1996), pp. 6749–6752.
[33] M.V. Zagarola, A.E. Perry, and A.J. Smits, *Log laws or power laws: The scaling in the overlap region*, Phys. Fluids 9 (1997), pp. 2094–2100.
[34] G.I. Barenblatt and A.J. Chorin, *Scaling of the intermediate region in wall-bounded turbulence: The power law*, Phys. Fluids 10 (1998), pp. 1043–1044.
[35] A.J. Smits and M.V. Zagarola, *Response to "Scaling of the intermediate region in wall-bounded turbulence: The power law"* , Phys. Fluids 10 (1998), pp. 1045–1046.
[36] R.L. Panton, *Composite asymptotic expansions and scaling wall turbulence*, Phil. Trans. R. Soc. A 365 (2007), pp. 733–754.
[37] H. Nagib and K.A. Chauhan, *Variations of von Kármán coefficient in canonical flows*, Phys. Fluids 20 (2008), 101518.
[38] M. Wosnik, L. Castillo, and W.K. George, *A theory for turbulent pipe and channel flows*, J. Fluid Mech. 421 (2000), pp. 115–145.
[39] M. Oberlack, *Unified approach for symmetries in plane parallel shear flows*, J. Fluid Mech. 427 (2001), pp. 229–238.
[40] B.J. McKeon and J.F. Morrison, *Asymptotic scaling in turbulent pipe flow*, Phil. Trans. R. Soc. A 365 (2007), pp. 771–787.
[41] W.K. George, *Recent advancements toward the understanding of turbulent boundary layers*, AIAA J. 44 (2006), pp. 2435–2449.
[42] M. Hultmark, S.C.C. Bailey, and A.J. Smits, *Scaling of near-wall turbulence in pipe flow*, J. Fluid Mech. 649 (2010), pp. 103–113.
[43] I. Marusic, R. Mathis, and N. Hutchins, *High Reynolds number effects in wall turbulence*, Int. J. Heat Fluid Flow 31 (2010), pp. 418–428.
[44] A.A. Townsend, *The Structure of Turbulent Shear Flows.* Cambrige University Press, New York, 1976.
[45] I. Marusic, M. Uddin, and A.E. Perry, *Similarity law for the streamwise turbulence intensity in zero-pressure gradient turbulent boundary layers*, Phys. Fluids 12 (1997), pp. 3718–3726.
[46] I. Marusic and G.J. Kunkel, *Streamwise turbulence intensity formulation for flat-plate boundary layers*, Phys. Fluids 15 (2003), pp. 2461–2464.

[47] J.W. Wallace, *Highlights of fifty years of turbulent boundary layers research*, J. Turbulence, accepted for publication, 2012.
[48] J. Kim, *Physics and control of wall turbulence for drag reduction*, Phil. Trans. R. Soc. A 369 (2011), pp. 1396–1411.
[49] J. Zhou, R.J. Adrian, S. Balachandar, and T.M. Kendall, *Mechanisms for generating coherent packets of hairpin vortices in channel flows*, J. Fluid Mech. 387 (1999), pp. 353–396.
[50] K.C. Kim and R.J. Adrian, *Very large-scale motion in the outer layer*, Phys. Fluids 11 (1999), pp. 417–422.
[51] N. Hutchins and I. Marusic, *Evidence of very long meandering features in the logarithmic region of turbulent boundary layers*, J. Fluid Mech. 541 (2007), pp. 21–54.
[52] N. Hutchins and I. Marusic, *Large-scale influences in near-wall turbulence*, Phil. Trans. R. Soc. A 365 (2007), pp. 647–664.
[53] R. Mathis, J.P. Monty, N. Hutchins, and I. Marusic, *Comparison of large-scale amplitude modulation in turbulent boundary layers, pipes, and channel flows*, Phys. Fluids 21 (2009), 111703.
[54] J.M. Hamilton, J. Kim, and F. Waleffe, *Regeneration mechanisms of near-wall turbulence structures*, J. Fluid Mech. 287 (1995), pp. 317–348.
[55] W. Schoppa and F. Hussain, *Coherent structure generation in near-wall turbulence*, J. Fluid Mech. 453 (2002), pp. 57–108.
[56] I. Marusic and W. Heuer, *Reynolds number invariance of the structure inclination angle in wall turbulence*, Phys. Rev. Lett. 99 (2007), 114504.
[57] J.D. McLean, D.N. George-Falvy, and P.P. Sullivan, *Flight-test of turbulent skin friction reduction by riblets*, Proceedings of International Conference on Turbulent Drag Reduction by Passive Means, Section 16, Royal Aeronautical Society, London, 1987, pp. 1–17.
[58] J. Jimenez, *Turbulent flows over rough walls*, Annu. Rev. Fluid Mech. 36 (2004), pp. 173–196.
[59] P. Krogstad and R.A. Antonia, *Surface roughness effects in turbulent boundary layers*, Expts. Fluids 27 (2001), pp. 450–460.
[60] K. Bhaganagar, J. Kim, and G.N. Coleman, *Effect of roughness on wall-bounded turbulence*, Flow Turbul. Combust. 72 (2004), pp. 463–492.
[61] K.A. Flack, M.P. Schultz, and T.A. Shapiro, *Experimental support for Townsend's Reynolds number similarity hypothesis on rough walls*, Phys. Fluids 17 (2005), 035102.
[62] G. Gioia and P. Chakraborty, *Turbulent friction in rough pipes and the energy spectrum of the phenomenological theory*, Phys. Rev. Lett. 96 (2006), 044502.
[63] J.J. Allen, M.A. Shockling, and A.J. Smits, *Evaluation of a universal transitional resistance diagram for pipes with honed surfaces*, Phys. Fluids 17 (2005), 121702.
[64] B. Eckhardt, T.M. Schneider, B. Hof, and J. Westerweel, *Turbulence transition in pipe flow*. Annu. Rev. Fluid Mech. 39 (2007), pp. 447–468.

Journal of Turbulence
Vol. 13, No. 53, 2013, 1–70

Taylor & Francis
Taylor & Francis Group

Highlights from 50 years of turbulent boundary layer research

James M. Wallace*

Department of Mechanical Engineering and Burgers Program for Fluid Dynamics, University of Maryland, College Park, MD 20742, USA

(*Received 3 July 2012; final version received 1 October 2012*)

This paper grew out of a survey lecture on highlights from the history of turbulent boundary layer research since the Turbulence Colloquium held in Marseille in 1961, the proceedings of which were published the next year. The highlights chosen, of course, reflect my own interests, experience and knowledge of the field. Necessarily, much important work is not mentioned, but I hope the references in the work cited will lead readers deeply into the many branches this research field has developed over these five decades. It is a rich field, and the progress in understanding this technically and scientifically important flow has been dramatic, but there is still much to learn.

Keywords: turbulence; boundary layers; wall layers

1. Introduction

Since the landmark paper of Prandtl [1], over a century ago, in which he formulated the governing boundary layer equations as simplifications of the general equations of fluid motion for flows near bounding solid surfaces, such flows have been extensively studied. Not coincidentally, Prandtl's paper appeared just after the first powered flight of an airplane by the Wright brothers. Boundary layers are of great scientific, engineering and even medical importance. They occur in a large number of natural and technological settings, e.g. the earth's atmosphere, on the surfaces of land, sea and air vehicles, and in the human body's conduits, among many others. Such flows transition from a laminar to a turbulent state when the Reynolds number is sufficiently large. The transition routes to turbulence can vary and depend on several factors. Regardless of the route however, eventually small patches of turbulence develop which grow, as they convect downstream, until they merge into one another and the whole boundary layer becomes completely turbulent.

1.1. *Reviews and monographs*

Numerous reviews of various aspects of turbulent boundary layers have been published, beginning with its treatment in the festschrift for Prandtl on the 50th anniversary of his theory by Görtler and Tollmein [2] published only six years before the 1961 Marseille Colloquium, the first international meeting devoted exclusively to turbulence. A year later, Townsend [3] published the first edition of his monograph, "On the structure of turbulent shear flow," in which the organization of bounded turbulent flows was extensively examined. Following

*Email: wallace@umd.edu

ISSN: 1468-5248 online only
© 2013 Taylor & Francis
http://dx.doi.org/10.1080/14685248.2012.738907
http://www.tandfonline.com

the Marseille Colloquium at which Rotta [4] reviewed the then state of knowledge, general reviews about turbulent boundary layers [5,6] appeared. Part four of the most recent edition of Schlichting's classic book on boundary layers [7], the first edition of which appeared in 1951, also summarizes what is generally known about their turbulent state. Furthermore, other reviews have been published that focused on the structure of turbulent boundary layers and the self-sustaining mechanism to maintain them [8–11], the multiscale processes in the logarithmic layer and their interactions with the inner layer [12], Reynolds-number effects [13–15], the effect of surface roughness on them [16], the pressure field below them on the wall [17], their control [18] and Mach number effects [19].

2. Notable developments prior to the 1961 Marseille Colloquium

Some notable developments in the half century prior to the 1961 Marseille Colloquium include the paper by King [20] that described the convective heat transfer of an infinitely long cylinder in a turbulent air stream and that prepared the way for practical measurements of turbulence with hot-wire anemometry. Measurements of the mean velocity profile in a turbulent boundary layer, agreeing with the 1/7th power law distribution, were first made in the early 1920s in the laboratory of Johannes Burgers in Delft by doctoral student van der Hegge Zijnen using very small diameter wires and reaching as close as 0.05 mm from the wall (see Eckert [21]). Burgers [22] presented these measurements at the first International Congress for Applied Mechanics held in Delft in 1924. Later in that decade, at the National Bureau of Standards (NBS) in the United States, hot-wire measurements in a wind tunnel were carried out by the group led by Hugh Dryden that laid the groundwork for later definitive turbulent boundary layer measurements in this laboratory. Figure 1 shows the NBS hot-wire anemometry equipment and wind tunnel of that period [23].

Fage and Townend [24], in a remarkable early visualization experiment using an "ultramicroscope" under intense illumination, observed the turbulent trajectories of minute particles present in ordinary tap water flowing in transparent round and square pipes. They were able to determine the distribution of the mean velocity as well as the distributions of the maximum values of all three turbulent velocity fluctuation components across the square pipe. Furthermore, they observed that the flow extremely close to the wall, in what for many more decades would continue to be called the laminar sublayer, was "sinuous",

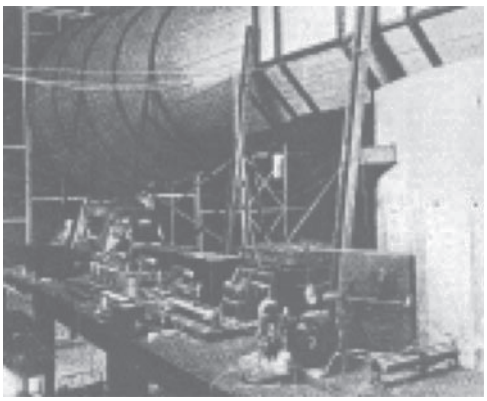


Figure 1. National Bureau of Standards wind tunnel and hot-wire anemometry instrumentation circa 1929.

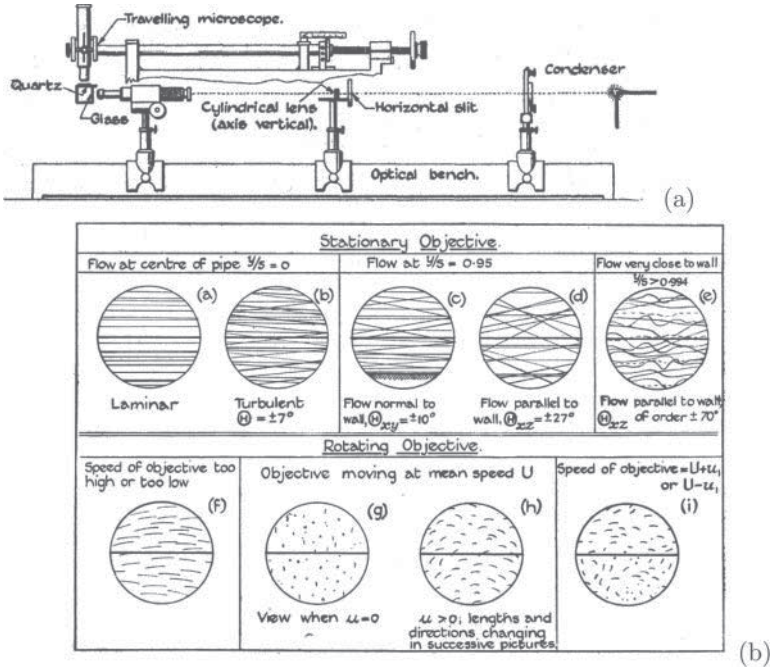


Figure 2. Sketch of (a) the "ultramicroscope" of Fage and Towend [24] and (b) particle trajectories in a round turbulent pipe flow. From Fage and Townend [24] with permission of the Royal Society of London.

i.e. not parallel to the wall. Figure 2 shows a sketch of their experimental apparatus and particle trajectories in the round pipe.

By the late 1930s at the Fifth International Congress for Applied Mechanics, Millikan [25] proposed a similarity law of logarithmic form for the mean velocity distribution in the "overlap" of the wall and outer flow regions for the case of two-dimensional, in the mean, incompressible flow. This is known as the "law of the wall" given by

$$\frac{\overline{U}}{u_\tau} = \frac{1}{\kappa} \ln\left(\frac{y u_\tau}{\nu}\right) + C, \tag{1}$$

where $\overline{U}$ is the mean streamwise velocity, y is the distance normal to the wall, u_τ is the friction velocity, ν is the the kinematic viscosity, and κ and C are both constants to be determined from experimental data. Coles [26] plotted a collection of data available at the time to demonstrate the validity of this logarithmic law in the overlap region, as shown in Figure 3(a). Coles [26] went on to develop what he called the "law of the wake" to describe the mean velocity distribution in the wake-like outer flow region of the turbulent boundary layer where the turbulence is intermittent. He expressed the mean velocity distribution as

$$\frac{\overline{U}}{u_\tau} = f\left(\frac{y u_\tau}{\nu}\right) + \frac{\Pi}{\kappa} w\left(\frac{y}{\delta}\right), \tag{2}$$

where Π is a parameter of the flow and $w(y/\delta)$ is the function he assumed common to all two-dimensional flows and subject to the condition that $w(0) = 0$, $w(1) = 2$ and

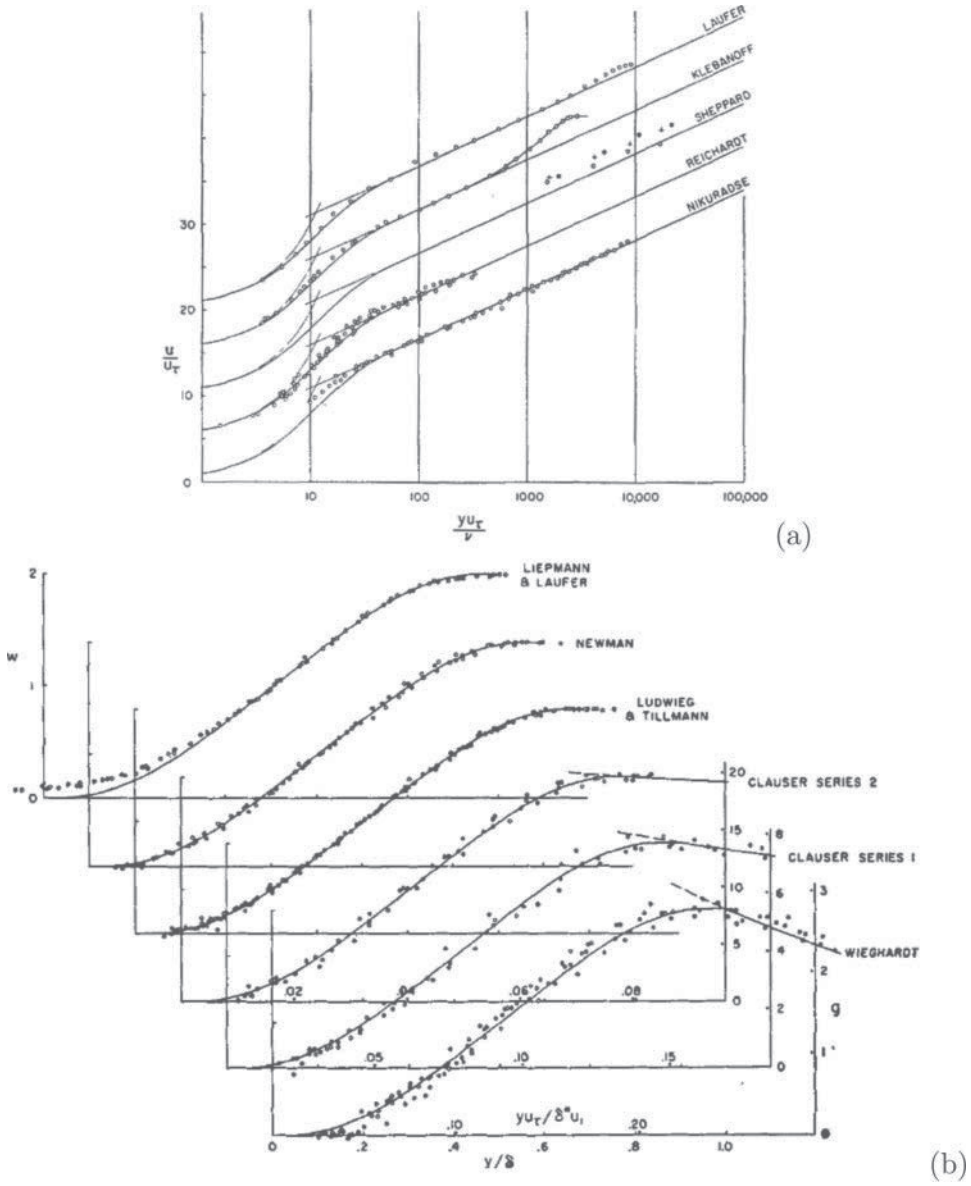


Figure 3. (a) Law of the wall and (b) law of the wake from Coles [26], copyright ©1956 Cambridge University Press.

$\int_0^2 (y/\delta) dw = 1$. Here, δ is the boundary layer thickness. Figure 3(b) shows experimental data plotted by Coles in this manner to demonstrate the law of the wake.

During the period that Coles was further developing similarity laws for the mean velocity distribution in turbulent boundary layers, hot-wire measurements of the intensities of the turbulent fluctuating velocity components and the turbulent kinetic energy (TKE) budget were carried out by Townsend [27] in Cambridge. The dissipation term in the TKE budget was only very approximately estimated from the isotropic form, and the pressure term

was obtained by difference. These results are shown in Figure 4(a) and (b). A few years later, Klebanoff [28] made similar measurements at NBS which became the benchmark for several decades. Townsend [27] also proposed a simple model of the eddy structure of the turbulent boundary layer which is shown in Figure 4(c).

In this same period of the mid-1950s, Corrsin and Kistler [29] made an extensive study of the interface, which they called the "laminar superlayer", between the outer edge of the turbulent boundary layer and the irrotational potential flow above it. They measured the intermittency function, γ, defined as the fraction of the time that the flow is turbulent, as a function of y/δ, and their plot is shown in Figure 5(a) along with a sketch of the superlayer

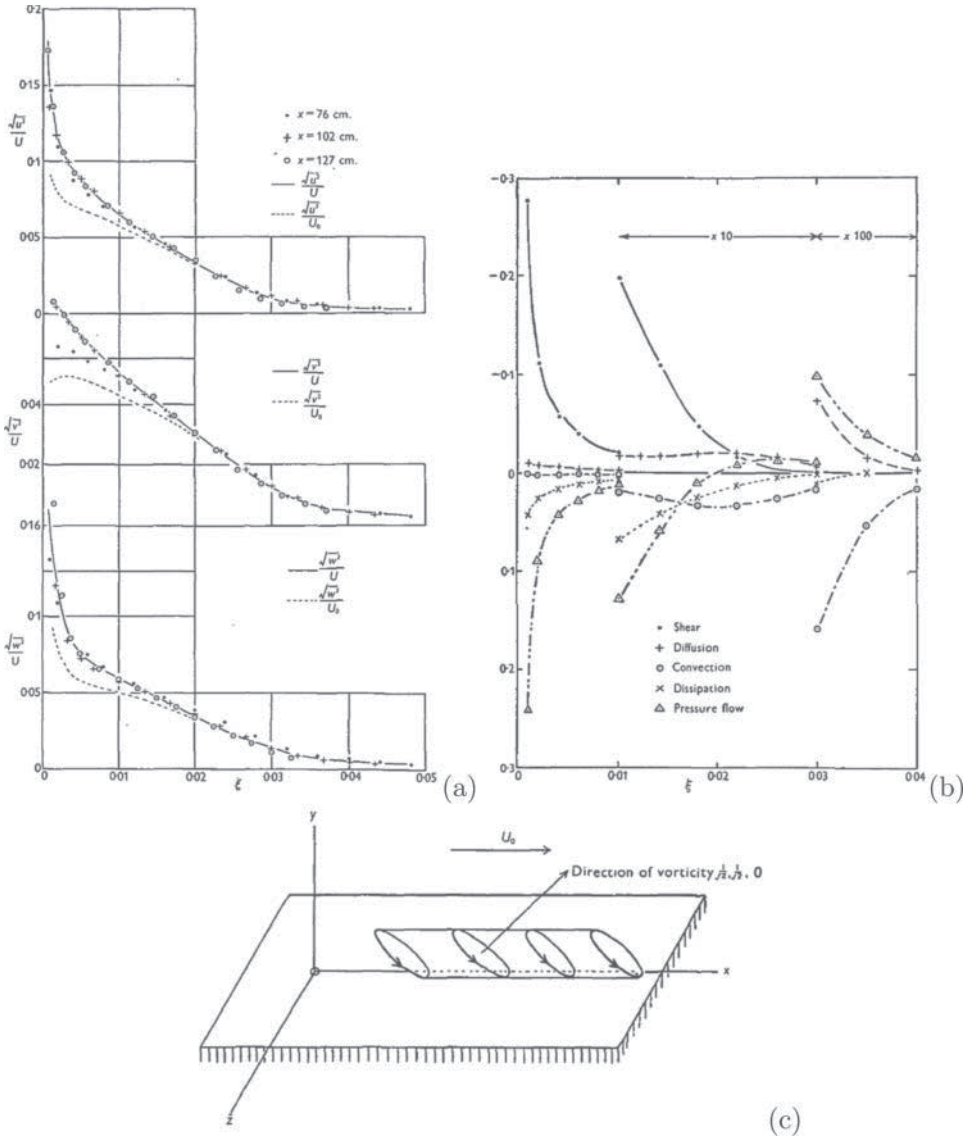


Figure 4. (a) Distribution of turbulent fluctuating component intensities, (b) estimate of the turbulent kinetic energy budget and (c) sketch of conceptual model of the eddy structure of the turbulent boundary layer. From Townsend [27], copyright ©1951 Cambridge University Press.

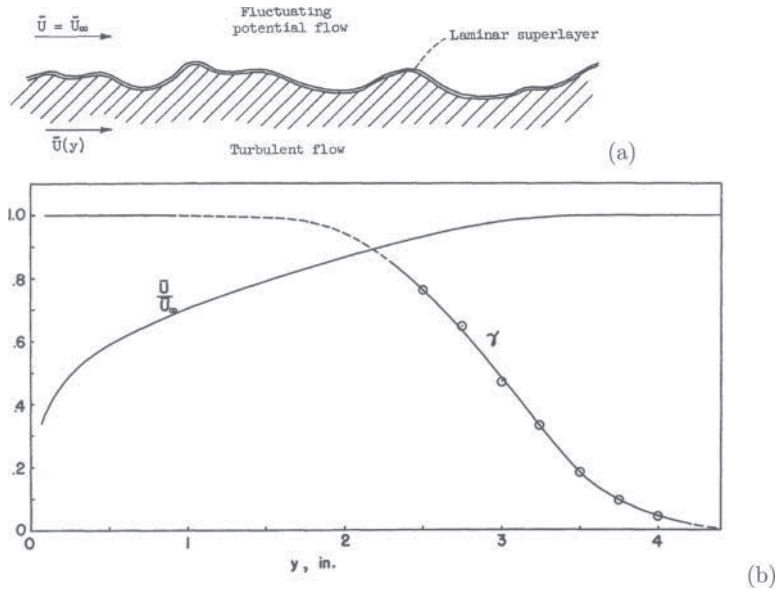


Figure 5. (a) Sketch of the "laminar superlayer" and (b) the intermittency function, γ, across the turbulent boundary layer. From Corrsin and Kistler [29] with permission of NASA.

in (b). They also developed theoretical ideas about how mean and fluctuating vorticity from within the turbulent flow propagate into the surrounding irrotational flow by viscous diffusion.

With little supporting experimental evidence to go on, Theodorsen [30] hypothesized that the underlying structure of wall-bounded and other turbulent flows was made up of vortex loops at various scales, in the form of "horseshoes". A sketch of his conceptual model of a single horseshoe in a bounded flow is shown in Figure 6, where his ideas about how momentum is transported by the action of the vortex were prescient.

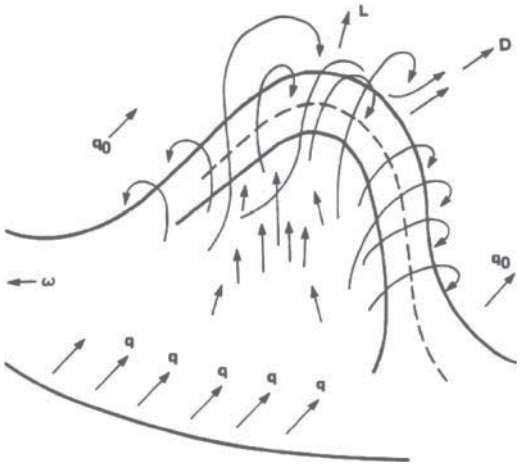


Figure 6. Sketch of "horseshoe" vortex proposed as the fundamental structural feature of bounded turbulent flows by Theodorsen [30].

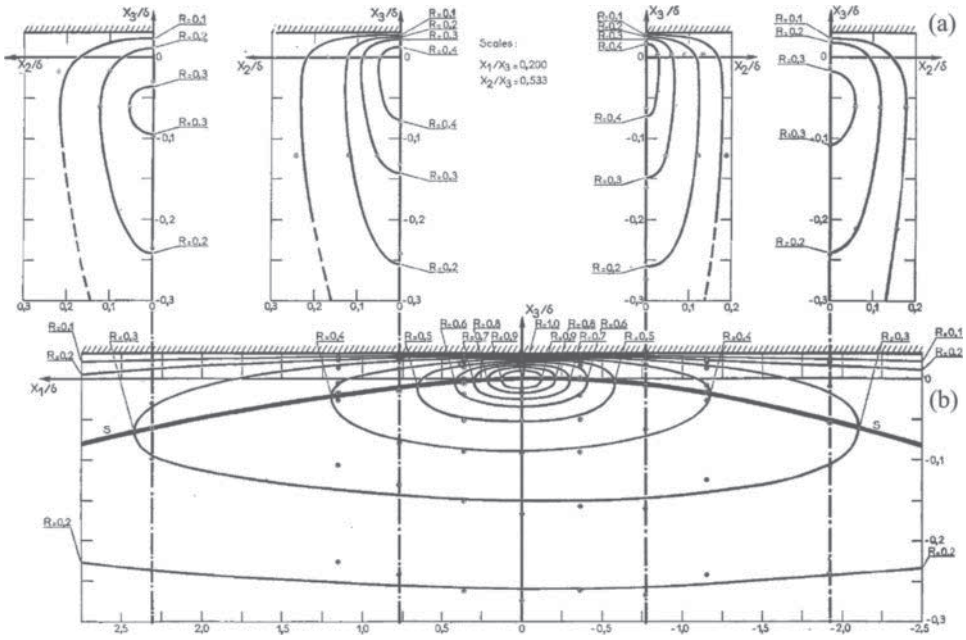


Figure 7. Space–time iso-correlation contours in the (a) cross-stream and (b) streamwise planes with optimal time delay. From Favre et al. [31], copyright ©1958 Cambridge University Press.

In the late 1950s, two noteworthy papers were published using correlation techniques. Favre et al. [31] made two-point hot-wire correlation measurements in a turbulent boundary layer, with time shifts achieved with an analog tape recorder because laboratory computers were not yet available during this period. The space–time correlation maps they produced in the two-dimensional streamwise (x–y) and cross-stream (y–z) planes with optimal time delay are shown in Figure 7. In the streamwise plane, the contours are elongated in the streamwise direction, and the locus of maximum correlation is inclined to the wall. In the cross-stream plane, the contours are elongated in the wall-normal direction and narrower in the spanwise direction.

Grant [32] made hot-wire measurements in a turbulent boundary layer of the trace terms in the correlation tensor, $R_{ij} = \overline{u_i(\mathbf{x})u_j(\mathbf{x}+\mathbf{r})}$ for $i = j$, $\mathbf{x} = (x_1, x_2, x_3)$ and $\mathbf{r} = (r_1, r_2, r_3)$. The two-point correlation coefficients of the three fluctuating velocity components, u_1, u_2 and u_3, are shown in Figure 8 as functions of spatial separations in the three coordinate directions and several locations of the fixed probe. From the shapes of these correlations, Grant attempted to construct a picture of the average eddy structure that gives rise to them.

Rotta [4], in his review at the 1961 Marseille Colloquium, emphasized the then perceived two-layer structure of the two-dimensional turbulent boundary layer, with its near wall and outer regions, and the problem of predicting the development of the flow under arbitrary pressure gradient conditions. He discussed a wide variety of experimental results available at the time for two-dimensional, incompressible, turbulent boundary layers with impermeable walls, and highlighted what he thought were pressing open questions.

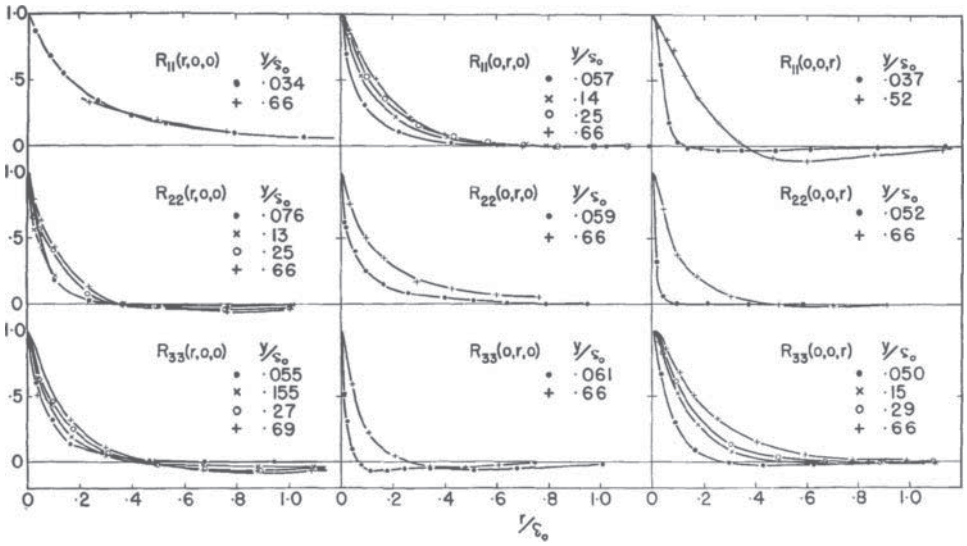


Figure 8. Two-point correlation coefficients of the three fluctuating velocity components, u_1, u_2 and u_3. From Grant [32], copyright ©1958 Cambridge University Press.

3. Research periods after the 1961 Marseille Colloquium

In the remainder of this survey, the discussion will be limited primarily to the canonical case of the smooth flat-plate, zero pressure gradient (SFP-ZPG) turbulent boundary layer. However, many papers that investigated fully developed turbulent channel flow and several for fully developed turbulent pipe flow will also be included because their near-wall statistics and structural features are similar, albeit not identical, to those of SFP-ZPG boundary layers. A much fuller discussion of open questions remaining for channel and pipe flows is provided by Kim [33] in a companion article in this special volume devoted to the 2011 Marseille Turbulence Colloquium. The important technological effects of adverse and favorable pressure gradients and roughness will not be included. There are large separate literatures on these effects which are subjects unto themselves.

The organization of the material is, for the most part, chronological. In a few cases, some of the work on a particular subject by one or more research groups will be discussed in one place, breaking the chronology somewhat. The sections of the paper indicate periods when particular types of research, described in the titles given to these sections, were the prominent, but not exclusive, activities during the periods. Within these sections, dates and topic headings in italics are used to indicate when a particularly notable development appeared for the first time and/or was first widely discussed. These are not subsections of the paper; rather they are used to highlight these notable developments in the history of this subject.

3.1. *Measurements and visualizations: 1961–1970*

3.1.1. *1962 – wall pressure correlation*

The year following the Marseille Colloquium, Willmarth and Woolridge [34] published the first of several papers from their group at the University of Michigan describing measurements of the wall pressure at two locations beneath turbulent boundary layers. Figure 9

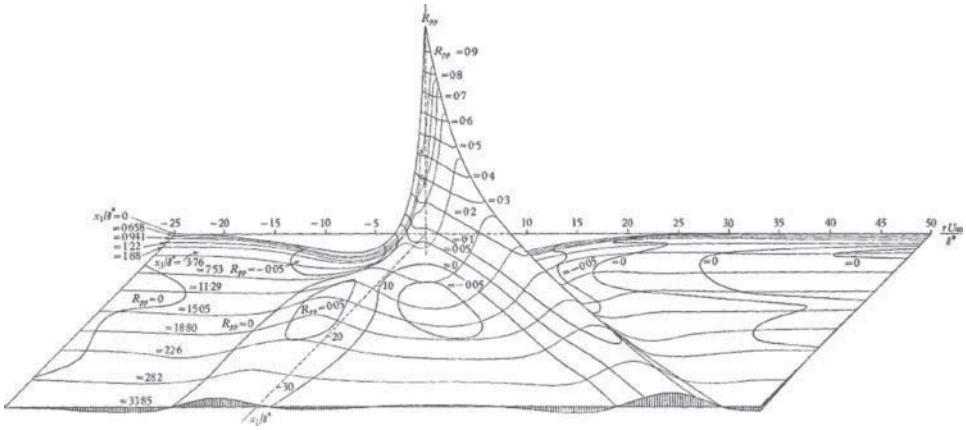


Figure 9. Wall pressure space–time correlation map beneath a turbulent boundary layer. From Willmarth and Woolridge [34], copyright ©1962 Cambridge University Press.

shows the two-point space–time correlation map constructed from these measurements in which the two horizontal axes are normalized time and the streamwise spatial displacement of the downstream pressure transducer. The vertical axis is the correlation coefficient. The striking feature of this map is the correlation ridge flowing out from the origin to the front right of the figure showing the cumulative effect of eddies of different scale with increasing time and downstream distance. The decay of this ridge is interpreted as the diminishing effect on the correlation of smaller scale eddies.

In this same decade, Bakewell and Lumley [35] made measurements in a pipe flow of glycerin in which the near-wall region could be investigated. They obtained streamlines in the radial plane using proper-orthogonal decomposition that showed the counter-rotating eddy structure in Figure 10(a) and the sketch in (b).

3.1.2. *1965 – visualized coherent structures*

Also, during this decade, two visualization experiments were completed and published, both of which excited the turbulence research community. Kline et al. [36] observed, using small hydrogen bubbles as markers, that the flow near the wall of a boundary layer is organized into

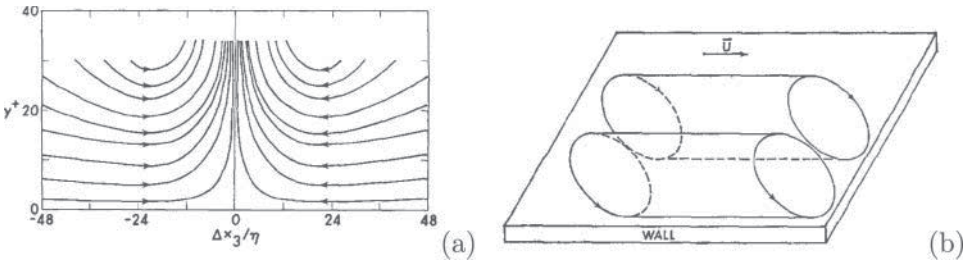


Figure 10. (a) Streamlines obtained with proper-orthogonal decomposition of hot-film measurements in a pipe flow of glycerin and (b) eddy structure sketch suggested by these measurements. Reprinted with permission from Bakewell and Lumley [35]. Copyright ©1967 American Institute of Physics.

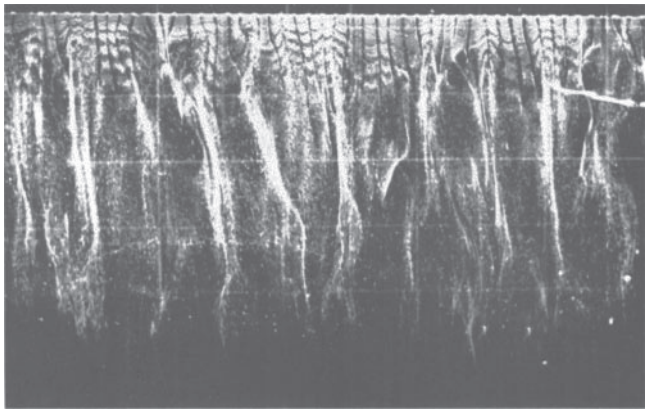


Figure 11. Hydrogen bubble marked low-speed streaks near the wall in the viscous sublayer of a turbulent boundary layer. From Kline et al. [36], copyright ©1967 Cambridge University Press.

narrow streaks of high- and low-momentum fluid, elongated in the streamwise direction. The low-momentum streaks were seen to erupt away from the wall in a seemingly chaotic manner, a process they called "bursting". These eruptions give rise to considerable Reynolds shear stress and the production of turbulent kinetic energy. A photograph of the bubble-marked streaks in the viscous sublayer is shown in Figure 11. This streaky wall-layer structure had previously been observed by Ferrell et al. [37] (see also Richardson and Beatty [38]) in a turbulent pipe flow, and by Hama (described by Corrsin [39]) in a boundary layer, but it was only with the publication of this paper by Kline et al. that the research community took much note of it.

About this same time, Corino and Brodkey [40], at Ohio State University, carried out a remarkable pipe flow experiment. Their experimental setup is shown in Figure 12. Trichloroethylene flowed in a glass pipe at turbulent Reynolds numbers, and the pipe itself was submerged in a rectangular trough filled with the stationary trichloroethylene. This fluid has almost identically the same refractive index as glass, so the motion of the fine

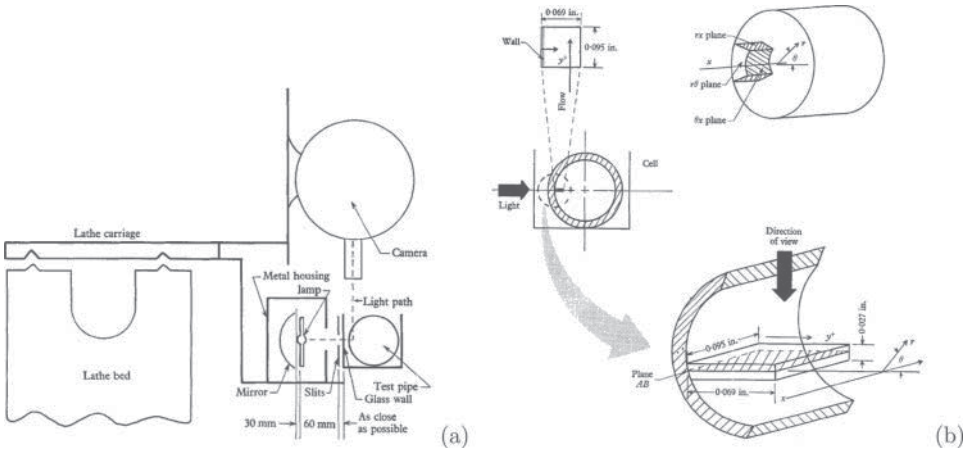


Figure 12. Pipe flow visualization experimental arrangement (a) and field of view (b). From Corino and Brodkey [40], copyright ©1969 Cambridge University Press.

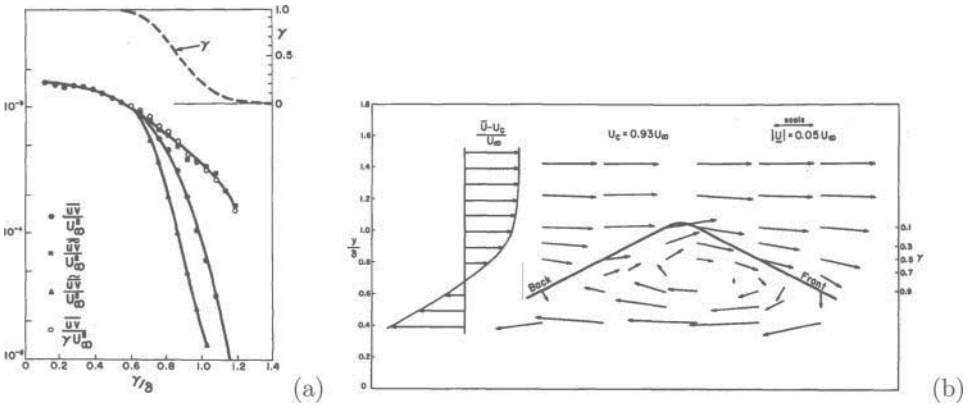


Figure 13. (a) Zone averages of Reynolds shear stress inside and outside of boundary layer "bulges" and (b) a composite sketch of the bulges. Reprinted with permission from Blackwelder and Kovasznay [42]. Copyright ©1972 American Institute of Physics.

magnesium oxide particles that were used to mark the flow in the pipe could be observed without refraction. A high-speed camera with a microscope lens was mounted on a lathe bed so that it could be translated at a speed matching the mean velocity of the flow close to the wall. The flow and the marker particles were floodlit. The microscope lens permitted a field of view that extended from the wall to only $y^+ = 45$ at $Re_d = 20 \times 10^3$. The video seen with this link (http://www.tandfonline.com/doi/suppl/10.1080/14685248.2012.738907/suppl_file/tjot_a_738907_sup_30908725.mov and also via the supplemental tab) is typical of the observations Corino and Brodkey made. The motion of the particles appears to be quite organized. A significant region of the field of view appears to slow down relative to the camera's translational speed, and then several particles in the low momentum region erupt outward from the wall in what the authors called an "ejection" event. This is followed by coordinated motion of particles toward the wall of higher momentum fluid which they called a "sweep" event. The video suggests that this particle motion toward and away from the wall is driven by a vortex, principally oriented in the streamwise direction. They found that these ejections occurred only about 18% of the time at $Re_d = 20 \times 10^3$, but they accounted for about 70% of the Reynolds shear stress.

3.2. *Conditional processing of measurements and further visualizations: 1970–1986*

In the early 1970s, experimentalists began using conditional sampling and processing to analyze turbulence measurements. This coincided with the availability of laboratory computers which made this type of analysis much easier and, for certain types of analyses, even feasible. One of the first of these types of studies was that of Kovasznay et al. [41] in which they looked at the conditional properties of the large-scale "bulges" at the upper surface of the turbulent boundary layer. In a follow-up study, Blackwelder and Kovasznay [42] measured the zone averages of the Reynolds shear stress inside and outside the turbulent bulges at fixed distances from the wall and intermittency. These zone averages are shown in Figure 13(a) along with (b) a composite sketch of bulges that they constructed.

1972 – quadrant analysis – Based on the flow visualization of the important shear stress creating ejection and sweep events by Corino and Brodkey, Wallace et al. [43] conceived of and implemented, with analog circuits, a "quadrant analysis" of the velocity fluctuations in a turbulent oil channel flow with a thick viscous sublayer. This was the simple idea

of classifying the combinations of the streamwise and wall-normal velocity fluctuations according to their signs, i.e. Q1 (+u, +v), Q2 (–u, +v), Q3 (–u, –v) and Q4 (+u, –v), which exploits the information contained in the signs of the fluctuations. This information tells whether the local flow is moving with an excess or deficit of momentum with respect to the local mean velocity and whether its motion is toward or away from the wall. The Q2 and Q4 quadrant categories have a rough correspondence to the visualized ejection and sweep motions of Corino and Brodkey [40]. Figure 14 shows the distribution across the channel of the fractional contribution to the Reynolds shear stress from each of the quadrants. In the sublayer and lower part of the buffer layer ($y^+ < 12$), Q4 sweep-type motions make the largest contribution. Further from the wall, Q2 ejection-type motions dominate. The Q2 and Q4 categories are of the mean gradient type. They are somewhat counteracted by the Q1 and Q3 counter-gradient type motions.

Willmarth and Lu [44] learned about quadrant analysis from Wallace et al. [43] and calculated the Reynolds shear stress quadrant contributions for one position in the boundary layer at $y^+ = 30$. They also expanded the idea to determine the fractional contributions of intense Reynolds shear stress motions that lie outside of what they called the "Hole", i.e. $|uv| = H$, where H is a constant. Figure 15 shows the contributions of each of the four quadrants to the Reynolds shear stress in a turbulent boundary layer at $y^+ = 30$ as a function of H. Also plotted in the figure is the percentage of the time that the uv product signal resides within the Hole. Among other things, the figure shows that, for $H = 5$, the uv product signal is outside of the Hole less than 10% of the time, but intense Q2 motions contribute about 50% of the Reynolds shear stress during this short time. In a paper a year later [45], they showed the quadrant distributions across this boundary layer and as a function of the hole size for several locations.

Brodkey et al. [46] determined other properties of the quadrants for bounded flows such as the average duration of and fraction of time spent within the quadrant events, and Wallace and Brodkey [47] related the quadrant results to the joint probability density distribution,

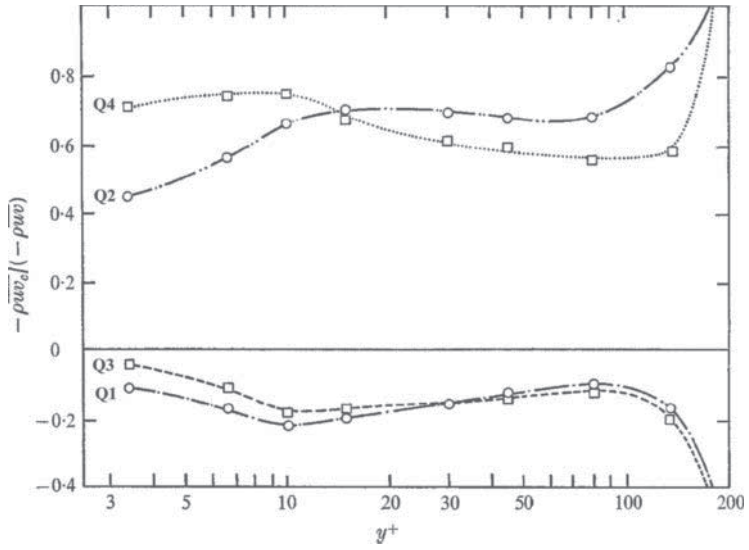


Figure 14. Fractional contributions to the Reynolds shear stress across a turbulent channel flow by velocity fluctuation quadrants. From Wallace et al. [43], copyright ©1972 Cambridge University Press.

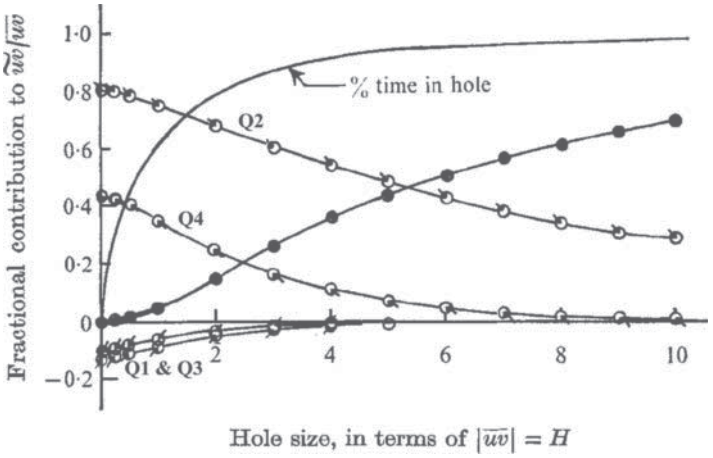


Figure 15. Fractional contributions to the Reynolds shear stress from intense events in a turbulent boundary layer at $y^+ = 30$ as a function of "Hole" size. From Willmarth and Lu [44], copyright ©1972 Cambridge University Press.

$P(u, v)$, and its covariance integrand, $uvP(u, v)$. The covariance integrand is plotted in Figure 16 for different positions normal to the wall. It is evident that the Q2 and Q4 quadrants dominate these plots over most of the channel flow. Because $\overline{uv} = \int uv(P(u, v)dudv$, the integral of each of the quadrants of the covariance integrand plots is just the contribution of that quadrant to the integral of the whole space, which is the Reynolds shear stress.

A remarkable turbulent boundary layer wall pressure experiment was designed and carried out by Emmerling [48]. The work was later extended and published by Dinkelacker et al. [49]. Emmerling mounted, flush at the wall beneath the flow, an insert with several

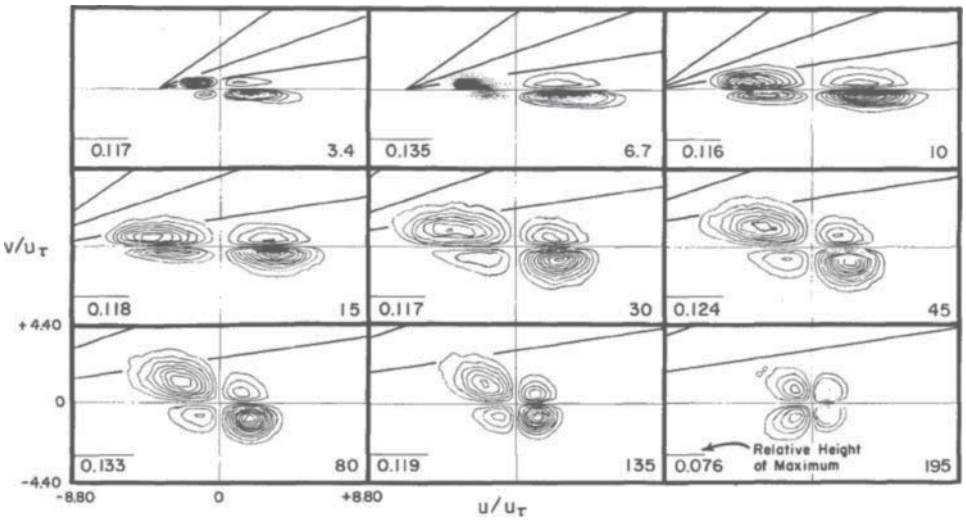


Figure 16. Contours of constant covariance integrand $uvP(u, v)$ by quadrant as a function of the y^+ distance from the wall (indicated by the number in the lower right corner of each plot). Reprinted with permission from Wallace and Brodkey [47]. Copyright ©1977 American Institute of Physics.

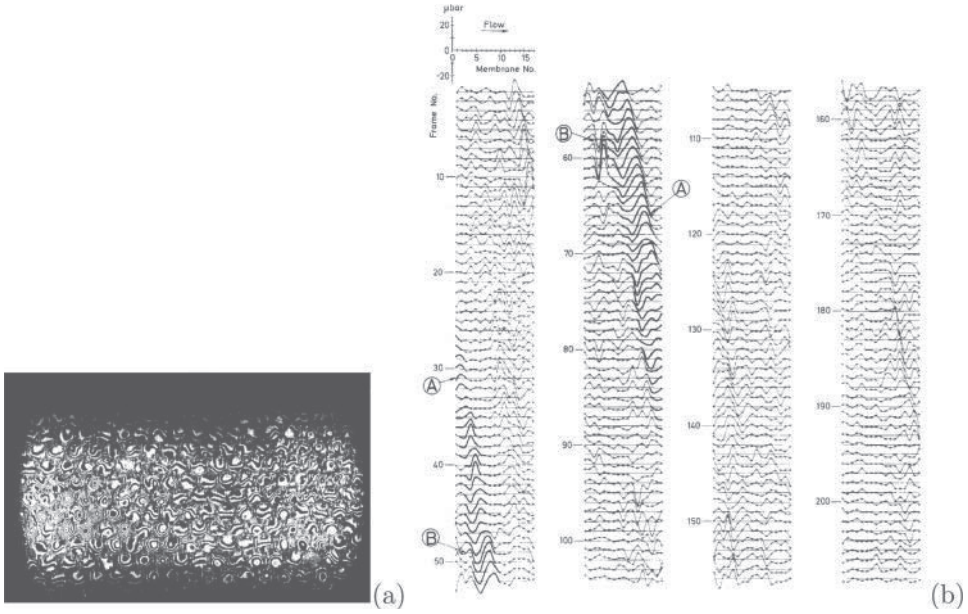


Figure 17. (a) Photograph of insert with several hundred of holes covered with a mirrored silicone foil showing interference fringes under a turbulent boundary layer and (b) time evolution of pressure pulses over a row of 17 holes. Reprinted with permission from Dinkelacker et al. [49]. Copyright ©1977 American Institute of Physics.

hundred holes covered by a mirrored silicone rubber foil. The interference fringes generated on these moving mirrored surfaces could be calibrated against a known and systematically varied surface pressure. When subjected to the turbulent boundary layer and photographed with a high-speed camera, patterns of convecting wall pressure were revealed. Figure 17(a) shows a photograph of the insert and the interference fringe pattern from one frame of the film. In (b), the pressure pulses over one row of transducers are shown as they develop in time. At the time these experiments were carried out, these data were laboriously analyzed manually. The authors concluded from their analysis that: (1) large-scale pressure patterns occur that convect downstream with a velocity up to $0.9U_\infty$ and have streamwise lengths of the order of the boundary layer thickness and spanwise widths that are even greater; (2) small-scale pressure patterns occur with sizes as small as the resolution limits of the transducers (57 viscous lengths) and which convect downstream as far as 1.6δ ($1100\ \Delta x^+$) with convection velocities as small as $0.2U_\infty$.

3.2.1. *1976 – VITA analysis*

Blackwelder and Kaplan [50] used what they called the variable integral time average (VITA) to try to detect turbulent "bursts" in a boundary layer flow. The detection condition they employed was obtained by applying VITA to the square of the local streamwise velocity fluctuations and to the local mean velocity. The difference between these quantities had to be larger than some chosen threshold, this being a measure of locally energetic events. It turned out that this criterion detected flow events for which du/dt was instantaneously large. An example of their detection scheme is shown in Figure 18(a) where their detection function, D, has values of unity when an event is identified, and zero otherwise. In (b) a

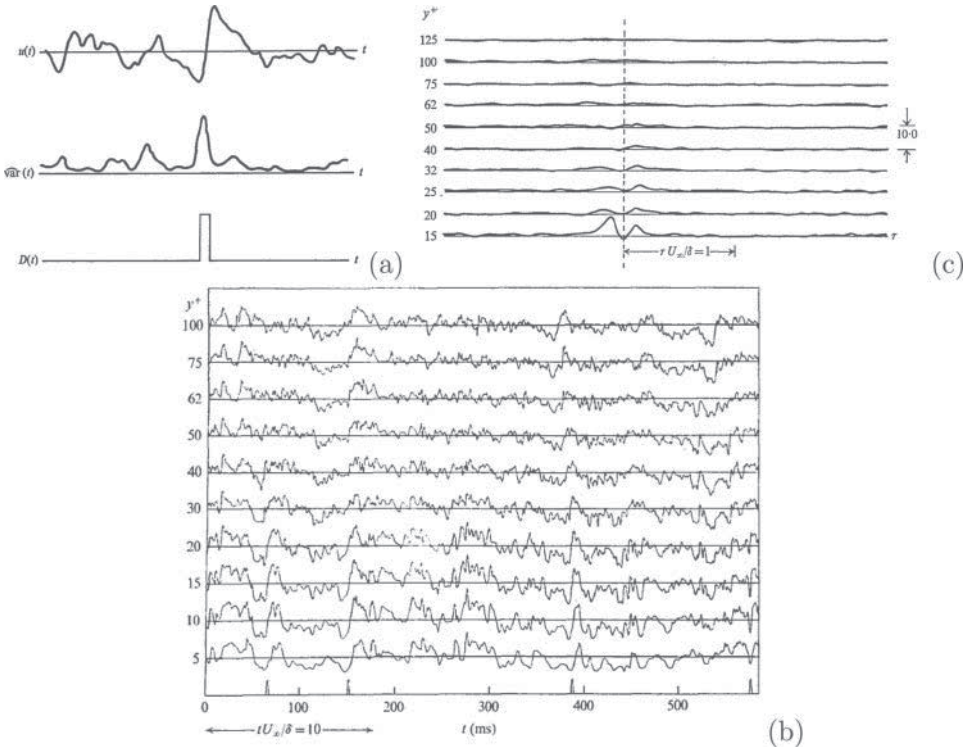


Figure 18. (a) Schematic example of VITA event detection. (b) Time series of instantaneous streamwise velocities from a rake of hot-wires with detected events at $y^+ = 15$ marked along the abscissa. (c) Conditional averages of the Reynolds shear stress signal. From Blackwelder and Kaplan [50], copyright ©1976 Cambridge University Press.

time series is shown of instantaneous streamwise velocities obtained with a rake of hot-wires located at the y^+ positions indicated. The detected events at $y^+ = 15$ are marked along the abscissa. The vertical coherence of these events at positions throughout the measurement region is striking. In (c), conditional averages of the uv product Reynolds shear stress signal, conditioned on the detection function, display coherence as the event convects downstream. The double-peaked structure was later shown to be related to the Q2 and Q4 quadrant events. Just before detection, the conditionally averaged Reynolds shear stress is nine times the local long-time average at $y^+ = 15$ and is a Q2 event.

Shortly after this investigation, Chen and Blackwelder [51] conducted a boundary layer experiment in which they heated the wall just enough so that temperature could be treated as a passive marker in the flow. Signals from a rake of temperature sensors, oriented normal to the wall, as shown in Figure 19(a), revealed ramps where the temperature suddenly dropped, and these ramps extended all the way across the boundary layer. The ramps were detected with the VITA method as in the study of Blackwelder and Kaplan. The upper temperature time series is at $0.63\,\delta$, i.e. in the intermittency region of the flow characterized by the outer interface bulges, while the lower one is just at the top of the buffer layer at $y^+ = 35$. A probe that measured the u, v and θ (temperature) fluctuations was used to investigate the velocity field around these ramp-like temperature fronts. Part (b) of the figure shows the conditionally averaged result where the vectors are constructed from the

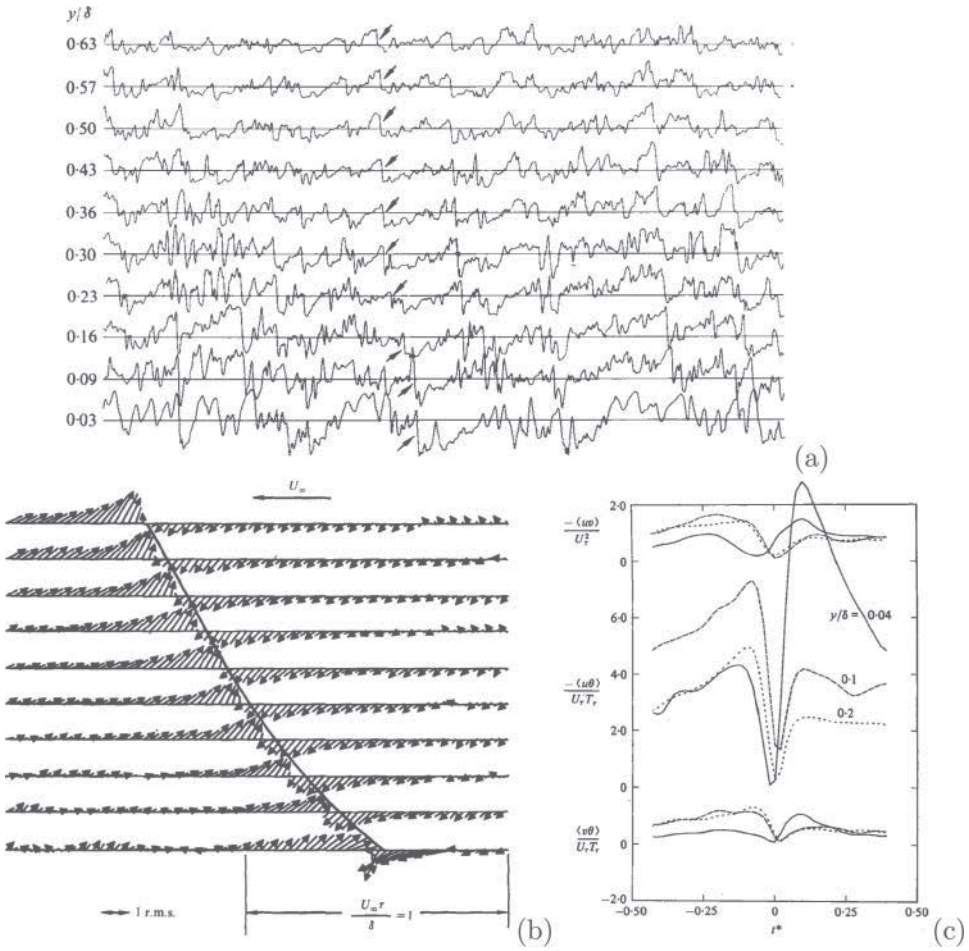


Figure 19. (a) Time series of temperature signals showing coherent ramp-like events across the flow and (b) conditionally average temperature front with velocity vector field across it. From Chen and Blackwelder [51], copyright ©1982 Cambridge University Press. (c) Conditionally averaged momentum and heat fluxes conditioned on the occurrence of a temperature front. From Antonia et al. [52], copyright ©1982 Cambridge University Press.

u and v velocity fluctuations at each y^+. Upstream of the front, all across the boundary layer and in some locations near the wall just past the mean frontline, the flow is toward the wall bringing colder fluid downward with a momentum excess. Conversely, downstream of the front, the motion is away from the wall bringing warmer fluid upward with a deficit of momentum. The front is inclined downstream with increasing distance from the wall, and, in the outer part of the boundary layer, it is associated with the "backs" of the turbulent/non-turbulent interface "bulges". A similar experiment with temperature as a passive scalar and using VITA temperature front detection was carried out by Antonia et al. [52]. Their conditionally averaged momentum and heat flux profiles across the front are shown in (c). Over the Reynolds-number range they studied, these distributions showed little variation in shape.

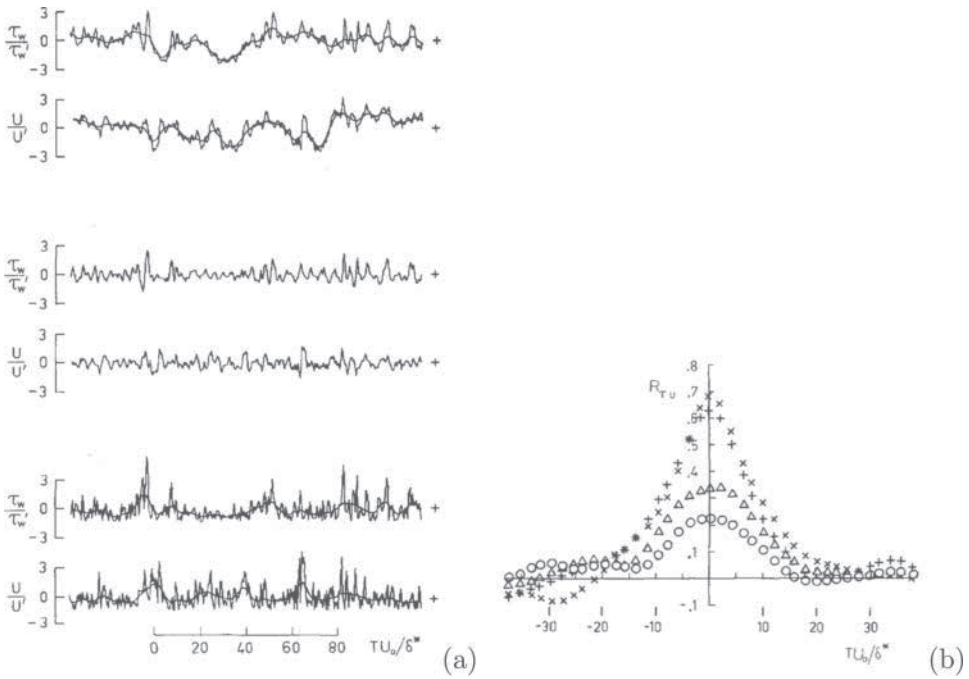


Figure 20. (a) Upper pairs: simultaneous unfiltered time series wall shear stress and streamwise velocity fluctuation signals at $y/\delta = 0.25$ and low-pass filtered signal for each variable; middle pairs: filtered subtracted from unfiltered signals leaving high-frequency residuals; lower pairs: high-frequency residuals rectified and themselves filtered. (b) Correlation coefficients with time delay between the filtered velocity and wall shear stress signals from the lower pairs with velocity probe locations: $\times$, $y/\delta = 0.05$, +, 0.25, $\triangle$, 0.5 and $\bigcirc$, 0.75. Reprinted with permission from Brown and Thomas [53]. Copyright ©1977 American Institute of Physics.

3.2.2. *1977 – inner-outer flow coupling*

About the same time as these experiments, Brown and Thomas [53] used an array of hot-wire probes in a boundary layer with $R_\theta = 1016$ and mounted above hot-film shear stress sensors embedded in the wall. Figure 20(a) shows time series signals of the wall shear stress and streamwise velocity fluctuations at $y/\delta = 0.25$. The upper pair are the unfiltered and low-pass filtered signals superimposed for each variable. The middle pair are the differences, for each variable, obtained by subtracting the filtered signals from the unfiltered ones leaving the high-frequency components remaining. Finally, these two high-frequency signals were rectified and themselves filtered, and these filtered time series plotted over the unfiltered high frequency ones, as seen from the lower pairs. These latter unfiltered signals are clearly correlated with their rectified filtered ones. The authors observe that there is a phase relationship between the slowly varying part of the wall shear stress and its high amplitude, high-frequency component. Furthermore, the filtered bottom pair of signals are also correlated with each other, and their correlation coefficient is plotted as a function of time delay in (b) for different distances from the wall of the velocity probe ranging from $y/\delta = 0.05 - 0.75$. Even when the velocity probe is far from the wall, the correlation coefficient is still a substantial 0.2.

During this period, another flow visualization experiment that strongly influenced views about the structure of turbulent boundary layer was published by Head and Bandyopadhyay

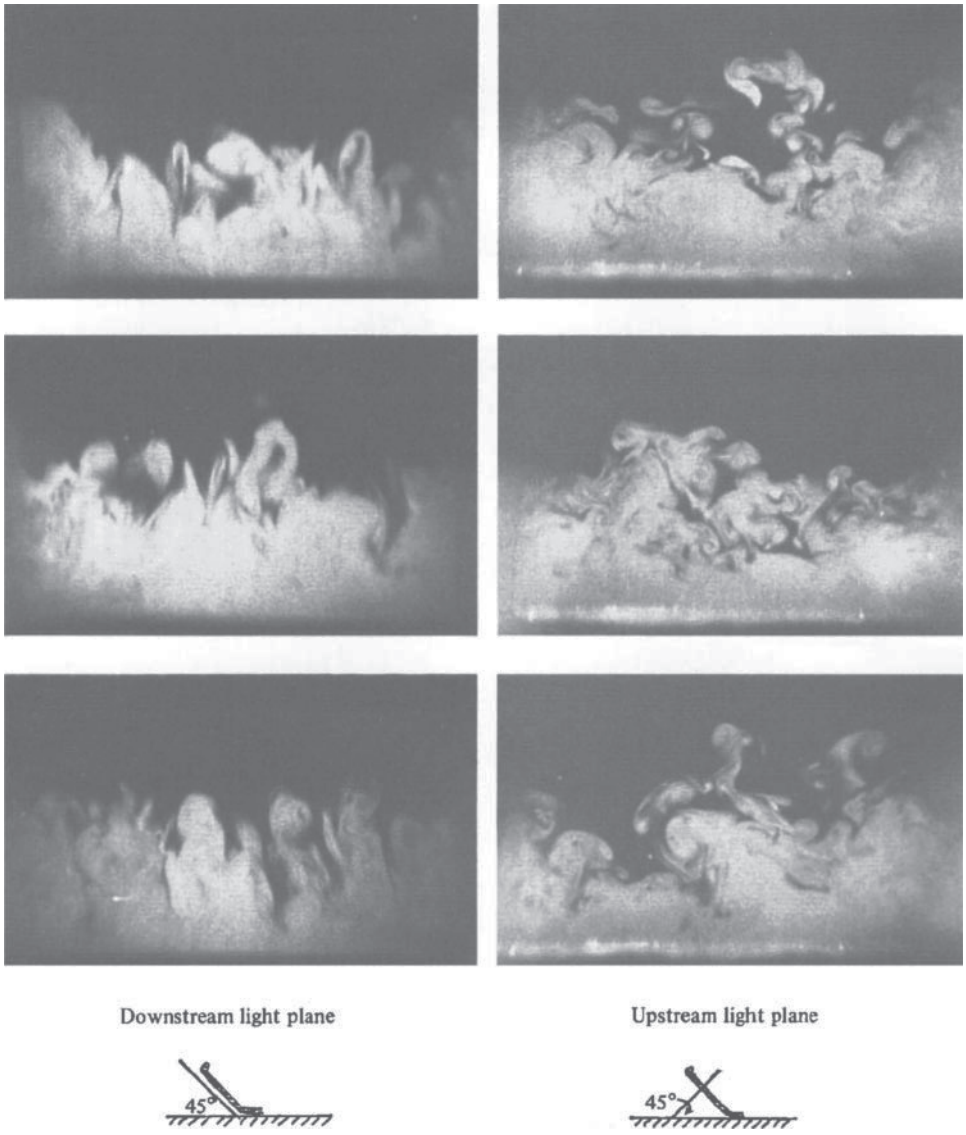


Figure 21. Smoke-marked turbulent boundary layer structures illuminated with inclined laser light sheets. From Head and Bandyopadhyay [54], copyright ©1981 Cambridge University Press.

[54]. Using smoke to mark the flow and illuminating it with light sheets inclined at 45° upstream and downstream, they observed shapes that had the appearance of vortices inclined downstream, often with hairpin-like shapes as shown in Figure 21.

Inspired by this work, Wallace et al. [55] replicated this study with some additions. Besides filling the entire boundary layer with smoke, they introduced smoke through a slot in the wall slightly upstream of the field of view and also far upstream in the free-stream potential flow at a level where it would just intersect the turbulent bulges within the field of view at the outer interface of the boundary layer. A photo of the streamwise (x–y) plane of this flow with the latter type of visualization is seen in Figure 22. Several striking features

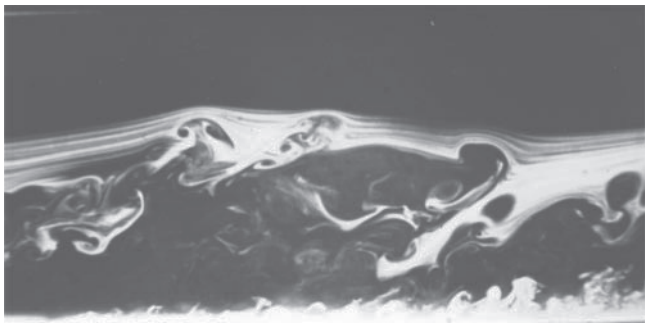


Figure 22. Turbulent boundary layer structures marked by smoke released at the lower left through a slot in the wall and far upstream in the freestream potiential flow. From Wallace et al. [55] with permission of the American Society of Civil Engineers.

are evident. "Mushroom"-shaped eddies penetrate the smoke-marked potential flow, which itself penetrates deep into the otherwise turbulent flow. Also, near-wall ejections of fluid, marked by the smoke emerging from the slot on the wall at the lower left of the image, grow in scale as they lift upward with downstream distance. The universality of the Head and Bandyopadhyay "hairpin" images was questioned at the time because they used a rather large sawtooth-shaped trip to initiate turbulence in the boundary layer. Therefore Wallace et al. [55] repeated their visualizations with no trip as well as with trips from sandpaper, a small diameter rod and a sawtooth bar, and they concluded that no essential features of the observations were affected by the type of tripping.

3.2.3. *1981 – attached hairpin eddy modeling*

Five years earlier, in the second edition of his classic book, Townsend [3] had proposed his "attached eddy" hypothesis for the structure of boundary layers. Building on this idea and the visualization study of Head and Bandyopadhyay [54], Perry and Chong [56] proposed a physical model of the boundary layer structure which they viewed as arising out of the sheets of spanwise vorticity just above the wall, the vorticity lines in which are locally perturbed upward and stretched downstream. A sketch of this idea is shown in Figure 23(a). They imagined the wall layer as a forest of "hairpin" or "horseshoe" vortices to be modeled with simplified Λ-shapes in a hierarchy of scales above the wall, but all attached to it. The sketch of these Λ-vortices in (b) is taken from a follow-up paper of Perry et al. [57] in which they extended this model to apply to the whole boundary layer. Their formulation of the model and its quantitative properties attempts to account for characteristics of the mean velocity profile, the distributions of the turbulence intensities and the form of the turbulence spectra. In (c), for example, Perry and Chong's conception of how the model accounts for the various parts of the mean velocity profile is shown.

3.3. *DNS and multi-sensor hot-wire and PIV measurements: 1986–2012*

The second half of the period since the Marseille Colloquium in 1961 that we are surveying saw the advent of (1) fully resolved and three-dimensional direct numerical simulations (DNS) of bounded turbulent flows, (2) multi-sensor hot-wire probes capable of estimating the full velocity gradient tensor, and thus enstrophy and dissipation rate, with reasonable

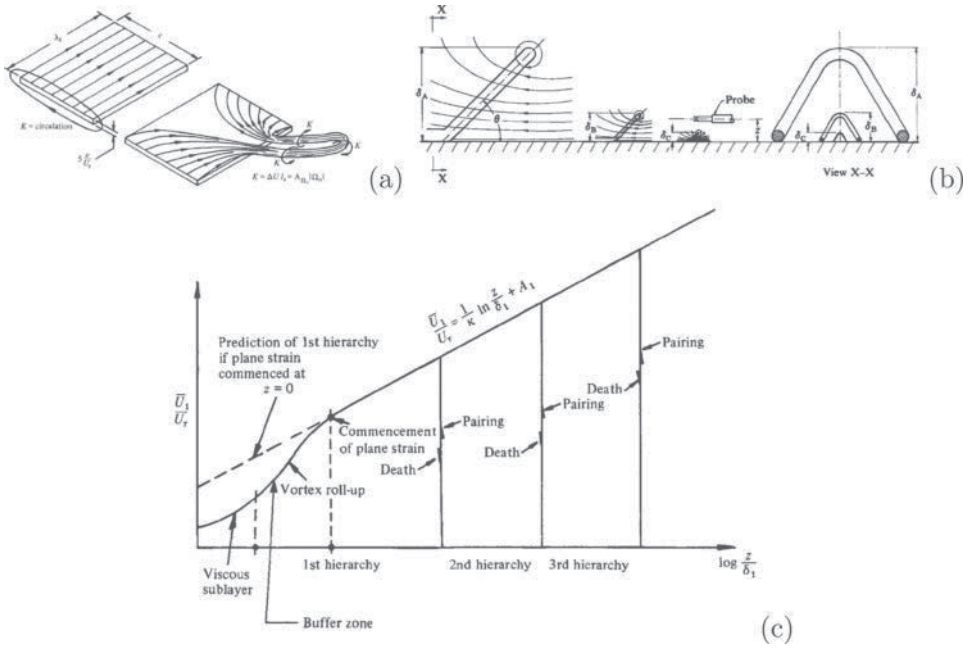


Figure 23. (a) Vortex sheet at the wall perturbed upward and stretched downstream to form a hairpin vortex, from Perry and Chong [56], copyright ©1982 Cambridge University Press, and (b) the hierarchy of Λ-shaped vortices that are used in a structural model of the turbulent boundary layer from Perry et al. [57], copyright ©1986 Cambridge University Press. (c) Mean velocity profile accounted for by the model.

resolution and accuracy, and (3) full planar field PIV and other optical experimental methods, eventually extending even to providing three-dimensional velocity vector fields.

3.3.1. *1986 – channel flow DNS*

The first DNS study that provided insight into the structure of bounded shear flows appeared in the Appendix of a turbulent channel flow study by Kim and Moin [58] that otherwise was a large-eddy simulation (LES) investigation of the vorticity field. This DNS was, in fact, the same one from which extensive flow statistics, to be discussed later, were published a year later in the celebrated paper by Kim et al. [59]. To verify that the ensemble-averaged results obtained from the LES fields would also be represented in the resolved DNS instantaneous fields, they applied the same vortex identification method that was used for the LES, viz. plotting vorticity lines in the vicinity of ejection-type (Q2) Reynolds shear stress events. Figure 24(a) shows a bundle of vorticity lines in various views that have the general shape of a horseshoe vortex, although the right-hand leg is much more elongated than the left. In (b), projections of the velocity vectors on the cross-stream (y–z) plane cutting through the right-hand leg are shown to demonstrate that, indeed, the flow there is rotating. Other instantaneous snapshots from this DNS showed that such horseshoe vortices in later stages develop Ω shapes and can eventually pinch off to form ring vortices. They also found that the vorticity line bundles plotted in the vicinity of sweep-type (Q4) events have inverted horseshoe shapes. When ensemble conditionally averaged, the Q2-initiated vorticity lines have a form very much like that obtained from the LES. The ensemble-averaged field is shown in (c), where it is also evident, as in the instantaneous fields, that the horseshoe-shaped

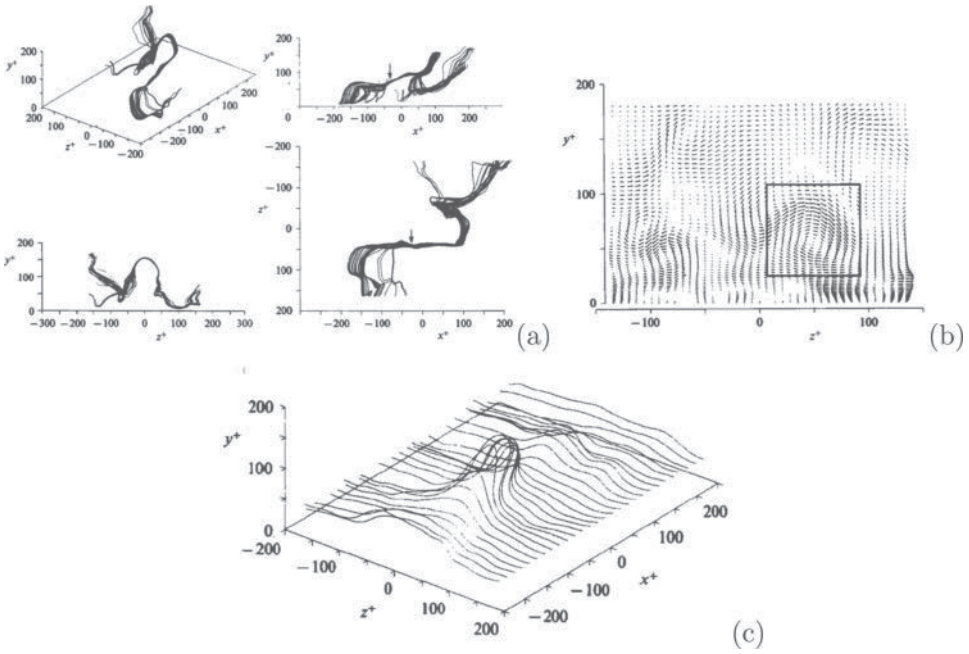


Figure 24. (a) Views of a bundle of instantaneous vorticity lines in the vicinity of an ejection-type (Q2) Reynolds shear stress event. (b) Projections of velocity vectors on the cross-stream (y–z) plane cutting through the right-hand leg of the horseshoe-shape vortex in (a). (c) Ensemble-averaged vorticity lines occurring in the vicinity of the Q2 ejection events. From Kim and Moin [58], copyright ©1986 Cambridge University Press.

vorticity lines appear to be lifted up and stretched downstream from a sheet of spanwise vorticity very close to the wall. As noted earlier, this was an underlying assumption in the vortex model of Perry and Chong [56].

Kim et al. [59] used this same DNS to obtain extensive statistics of the velocity and vorticity vector fields for this simulated turbulent channel flow at $R_\tau = 180$. In addition to the generally good agreement of this DNS study with experiments for a wide range of statistical properties, including the average spacing of low-speed streaks, what most convinced experimentalists that this virtual flow had all the characteristics of physical flows was the authors' use of flow visualization. The virtual flow markers in Figure 25 that mimic the effect of hydrogen bubbles in the physical flow are shown, and the low-speed streaks are easily identified.

3.3.2. *1987 – vorticity vector and dissipation rate hot-wire measurements*

That same year, Balint et al. [60] presented and published results from their simultaneous measurements of the three vorticity vector field components obtained in a turbulent boundary layer with the nine-sensor probe shown in Figure 26(a). In (b), their distributions of the rms values of the vorticity components are compared to their own later measurements [62] and the distributions from the channel flow DNS of Kim et al. [59] and the boundary layer DNS of Spalart [63]. Balint et al. [62] also compared the distributions of the dissipation rate for the experimental and DNS flows as shown in (c). Near the wall, when the inhomogeneous terms in the full dissipation rate expression are neglected, the estimated values

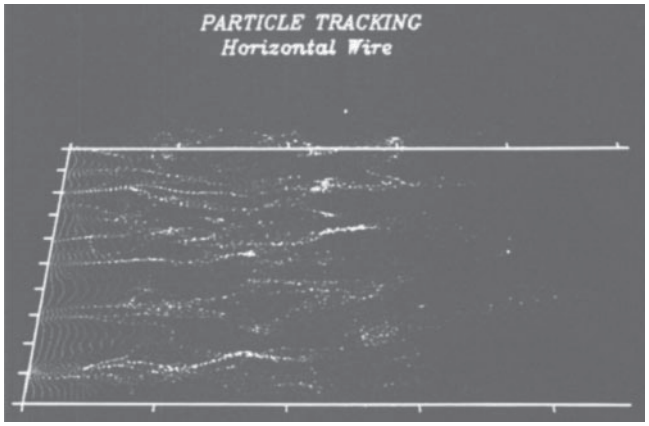


Figure 25. Virtual flow markers in a turbulent channel flow DNS near the wall indicating low-speed streaks. From Kim et al. [59], copyright ©1987 Cambridge University Press.

are considerably reduced, and this reduction in the values is much greater when isotropy is assumed to estimate the dissipation rate.

3.3.3. *1988 – boundary layer DNS*

Spalart [63] used transformed coordinates and variables for his turbulent boundary layer DNS to account for the inhomogeneity in the streamwise direction which allowed periodic boundary conditions to be used in that direction. He visualized this DNS boundary layer by plotting contours of constant vorticity in the streamwise (x–y) plane and in the same 45° inclined planes used by Head and Bandyopadhyay [54]. These contours are shown in Figure 27 which display many of the same features as the smoke visualizations.

3.3.4. *1988 – application of dynamical systems ideas*

The latter half of the 1980s was also a period in which application of ideas from dynamical systems theory were attempted with turbulent flows. Aubry et al. [64] expanded the wall region using proper orthogonal decomposition (POD) in the wall-normal direction and Fourier modes in the streamwise and spanwise directions. They then truncated this representation to obtain low-dimensional sets of ordinary differential equations from the Navier–Stokes equations via Galerkin projection. The method requires the full three-dimensional autocorrelation tensor, and the experimental turbulent pipe flow data taken in a glycerin facility by Herzog [65] was used. Among other observations, their low-order model equations produce streaks, counter-rotating vortices near the wall and intermittent high-amplitude "burst" in the Reynolds shear stress.

In the new decade of the 1990s, great interest in the structure of bounded turbulent shear flows continued, and new techniques to analyze experimental and DNS data emerged. Antonia et al. [66] used a rake of eight X-array hot-wire probes to examine the flow topology and Reynolds number effects in the streamwise (x–y) plane of a boundary layer. Sectional streamlines, drawn in a convecting frame of reference, revealed a complex pattern of vortices and stagnation points (foci and saddles in the terminology of the critical-point concepts, to be discussed later, of Perry and Chong [67]) at all Reynolds numbers. Conditional averages, conditioned on large accelerations for the streamwise velocities all across the flow, revealed

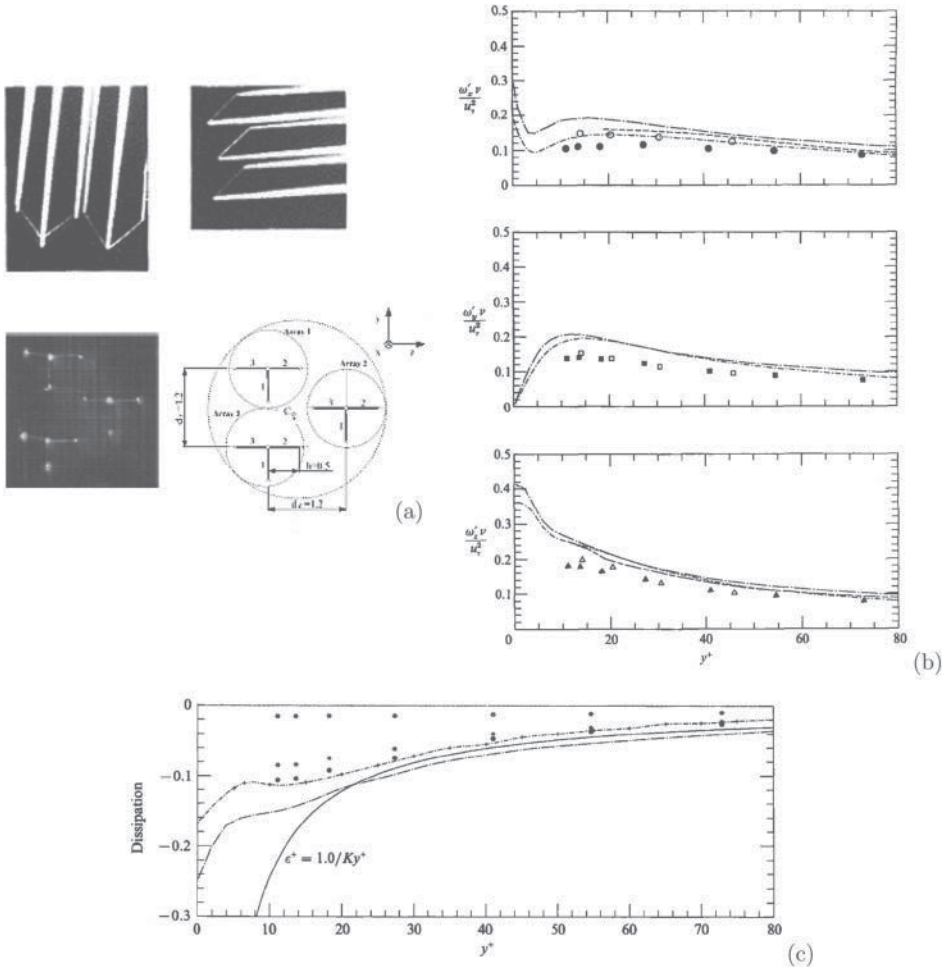


Figure 26. (a) Photos of a nine-sensor probe to measure the vorticity vector from Vukoslavĉvić et al. [61], copyright ©1991 Cambridge University Press. (b) Distribution of the vorticity component rms values from the boundary layer experiments of Balint et al. [60, 62], open and closed symbols, respectively, the channel flow DNS of Kim et al. [59], short dash–dot line, and the boundary layer DNS of Spalart [63], long dash–dot line. (c) Distribution of the dissipation rate, with the same type symbols and lines for the experiment and DNS results except the star symbols are reduced estimates of the experimental values (see text). From Balint et al. [62], copyright ©1991 Cambridge University Press.

large-scale average spanwise-oriented vortices and stagnation points, both within and at the outer edge of the boundary layer and also at all the Reynolds numbers examined.

3.3.5. *1990 – Lagrangrian analysis of Reynolds shear stress*

Bernard and Handler [68] conceived of an analytically exact method of decomposing the Reynolds stress into terms they called displacement and acceleration transport. Their analysis is based on the idea of tracking the Lagrangian paths of fluid particles, each of which passed through one of a set of random upstream positions at times $t - \tau$. These

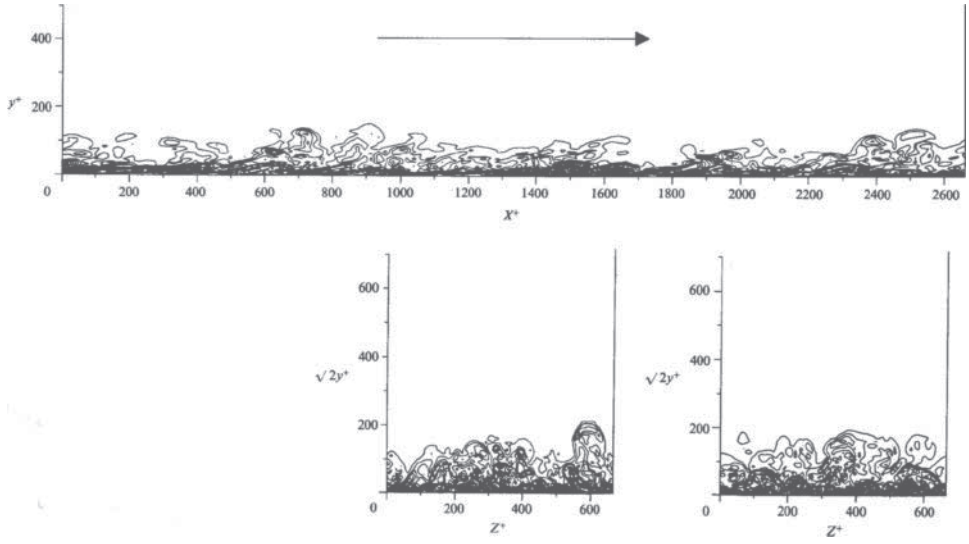


Figure 27. Contours of constant vorticity in the streamwise (x–y) plane and planes inclined downstream (left lower) and upstream (lower right) at 45°. From Spalart [63], copyright ©1988 Cambridge University Press.

particles subsequently all pass through an Eulerian downstream position at times t and create Reynolds shear stress there. Figure 28 illustrates these Lagrangian particle paths between the set of random upstream locations $\mathbf{X} = \mathbf{b}$ and any downstream Eulerian fixed location $\mathbf{X} = \mathbf{a}$. Their analysis is based on the identity

$$\overline{u_a v_a} = \overline{u_a v_b} + \overline{v_a(\overline{U}_b - \overline{U}_a)} + \overline{v_a(U_a - U_b)}. \tag{3}$$

For values of τ large enough, the correlation expressed by the first term on the right-hand-side of Equation (3) vanishes. The second term on the right-hand-side is a correlation between the fluctuating component v_a at the downstream Eulerian location and the mean velocity component differences of $\overline{U}$ between location a and locations b for an ensemble of times t. This mean velocity difference $\overline{U}_b - \overline{U}_a$ is itself a random variable because the locations b are themselves random. This term represents contributions to the Reynolds shear stress by motions of the particles along the Lagrangian paths through the Eulerian mean velocity field. Bernard and Handler [68] called this contribution displacement transport. The last term on the right-hand-side in Equation (3) is the correlation between v_a and the differences in the instantaneous velocity component U between location a and locations b for the ensemble of times t. These differences in the instantaneous velocity component represent net accelerations and decelerations of the fluid particle in the coordinate direction of U in the instantaneous field, so the authors called this correlation acceleration transport.

Figure 29(a) shows the values of the asymptotic conditions of these terms for sufficiently large τ obtained from a turbulent channel flow DNS at $R_\tau = 125$. As expected, the correlation $\overline{u_a v_b}$, denoted as term (1) in the figure, nearly vanishes at all y^+ locations. The displacement transport term $\overline{v_a(\overline{U}_b - \overline{U}_a)}$, denoted as Equation (2), is everywhere negative and makes up most of the Reynolds shear stress, denoted as term (4). The acceleration transport term $\overline{v_a(U_a - U_b)}$, denoted as term (3), is positive near the wall and becomes negative

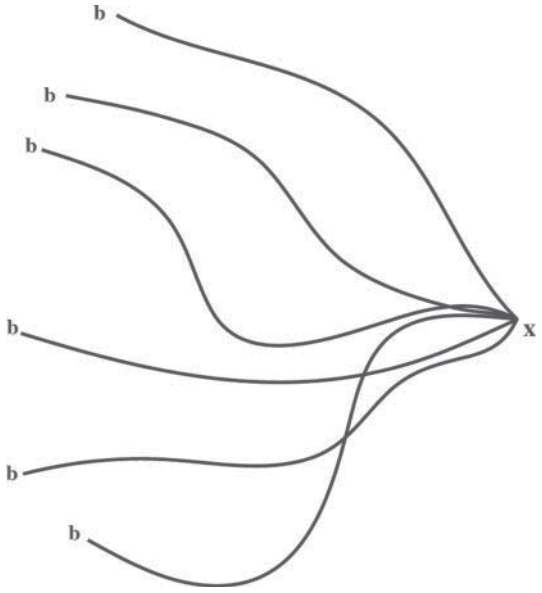


Figure 28. Lagrangrian particle paths all passing through the Eulerian position $\mathbf{X} = \mathbf{a}$ at times t, having previously been at random upstream positions $\mathbf{X} = \mathbf{b}$ at times $t - \tau$. From Bernard and Wallace [69], copyright ©2002 John Wiley & Sons.

at about $y^+ = 12$. In part (b) of the figure, the distributions of the quadrant contributions (indicated by quadrant numbers 1–4) to the dominant displacement transport term (curve (5) in the figure) are plotted, where, as expected, the ejection (Q2) and sweep (Q4) contributions are largest, with their importance changing with distance with respect to the wall.

Bernard et al. [70] developed a vortex identification method to recognize vortices in this channel flow DNS. The axes of the vortices were found to be oriented principally in the streamwise direction. Figure 30(a) shows a set of identified vortices in the computational

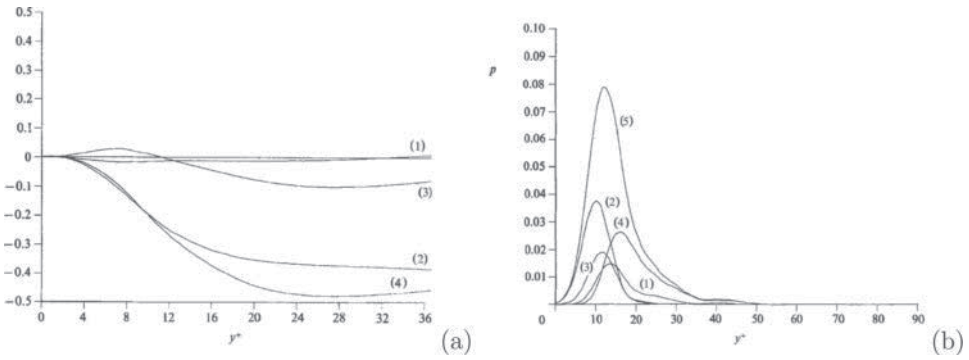


Figure 29. (a) Distributions of contributions to the Reynolds shear stress correlation coefficient: (1) from $\overline{u_a v_b}$, (2) the displacement transport term $\overline{v_a(\overline{U}_b - \overline{U}_a)}$, (3) the acceleration transport term $\overline{v_a(U_a - U_b)}$ and (4) the Reynolds shear stress itself $\overline{u_a v_a}$ at Eulerian location a. (b) Distribution of the quadrant contributions 1–4 to the displacement transport term (curve (5) in the figure) in Equation (3). From Bernard and Handler [68], copyright ©1990 Cambridge University Press.

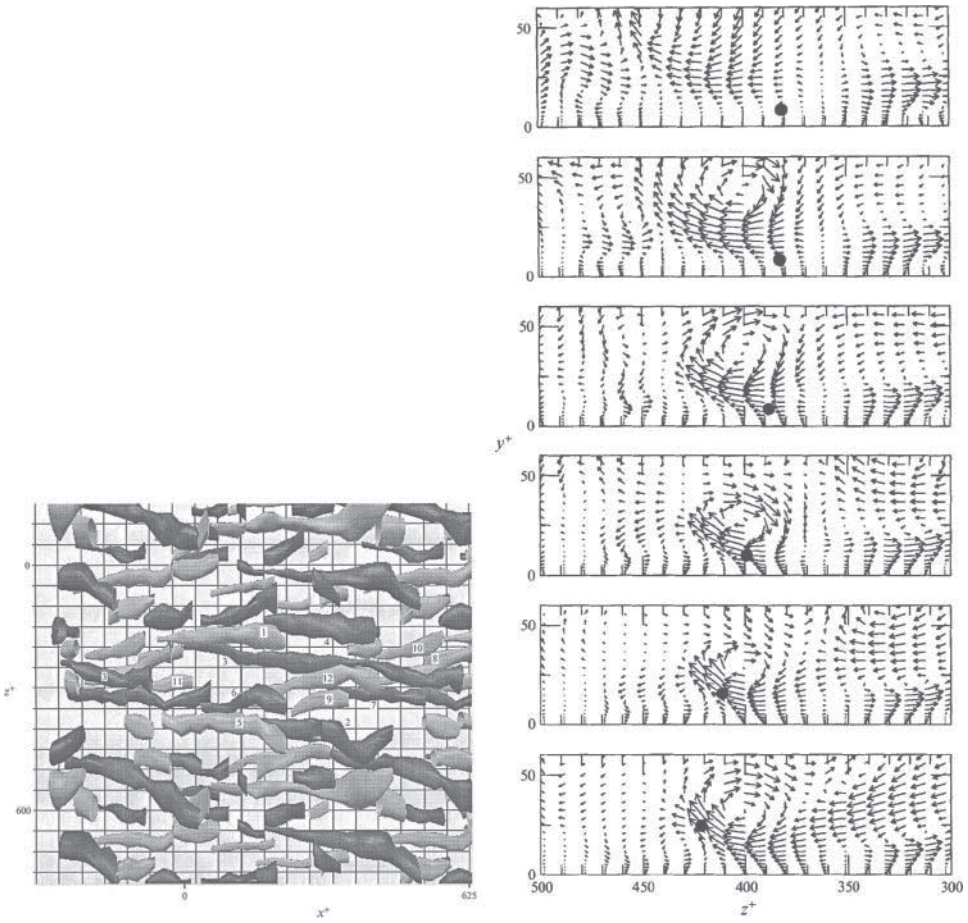


Figure 30. (a) Quasi-streamwise vortices of positive and negative signs (lighter or darker shades of grey) identified in a turbulent channel flow DNS. (b) Particle caught in the upwelling motion of a vortex and significantly contributing to the Reynolds shear stress. From Bernard et al. [70], copyright ©1993 Cambridge University Press.

domain, some with a positive and others with a negative sense of rotation. In (b), a cross-stream (y–z) plane cut through one of these vortices is shown in a series of images as time evolves. Superimposed on the velocity vector field projection on this plane are dots indicating a fluid particle whose ejection-type motion significantly contributes to the Reynolds shear stress. The authors conclude that most of the Reynolds stress is generated by particle motions associated with vortices, and these motions are an important part of both displacement and acceleration transport. Furthermore, they assert that the net stress results from the motions of only a relatively few particles that are transported across the flow by the vortices.

Wark and Nagib [71] investigated the three-dimensional velocity field in a turbulent boundary layer at $R_\theta = 4650$ conditioned on strong Q2 and Q4 Reynolds stress events at $y^+ = 35$. At this location, they found that the spatial extent of the vortices associated with the Q4 (sweep) events was larger than for the Q2 (ejection) events. For Q4, these vortices extend several boundary layer thicknesses δ in the streamwise direction and about 0.5δ

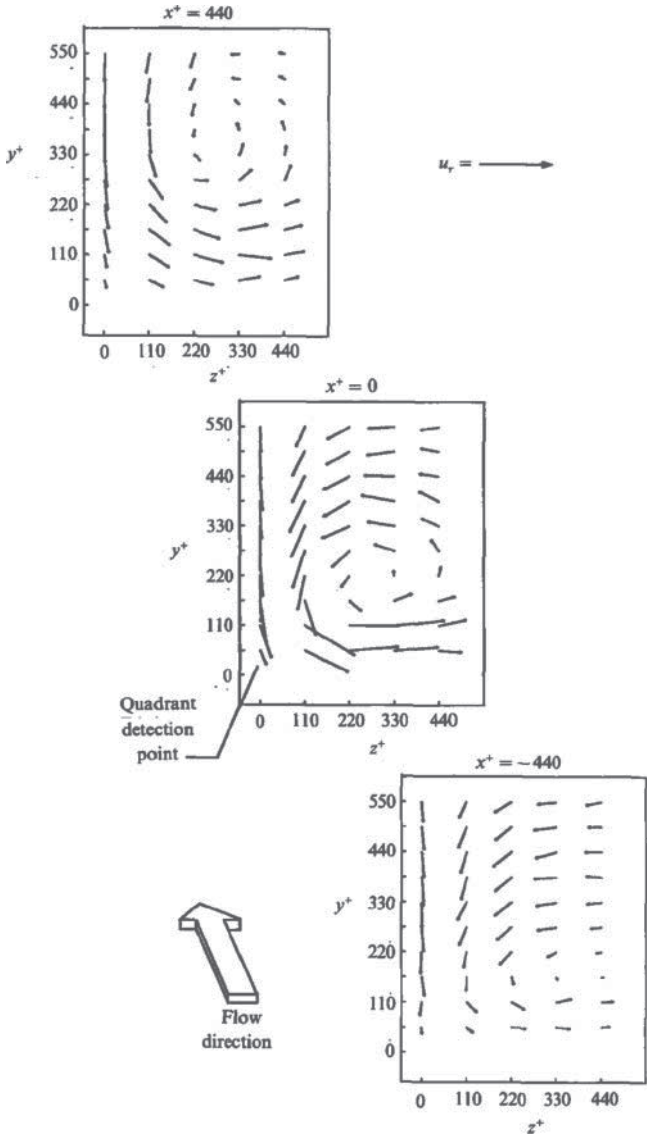


Figure 31. Velocity fluctuation vector maps conditioned on Q4 Reynolds shear stress detection at $y^+ = 35$ and $z^+ = 0$. From Wark and Nagib [71], copyright ©1991 Cambridge University Press.

in both the spanwise and wall-normal directions. Figure 31 shows the conditional vector field surrounding the detection location at $x^+ = 0$, $y^+ = 35$ and $z^+ = 0$. For the vector plane at $x^+ = -440$ upstream of the detection location, the center of the conditional vortex is at about $y^+ = 165$ and $z^+ = 275$. Downstream of this x^+ location ($x^+ = 0$ and 440), the vortex center is progressively further from the wall. These are obviously larger scale vortices than those previously observed in the wall layer by others. They also noted that when a Q4 event was detected, simultaneously a weaker Q2 event was seen in the same cross-stream plane and at the same $y^+ = 35$ distance from the wall but at $z^+ > 350$, and vice versa.

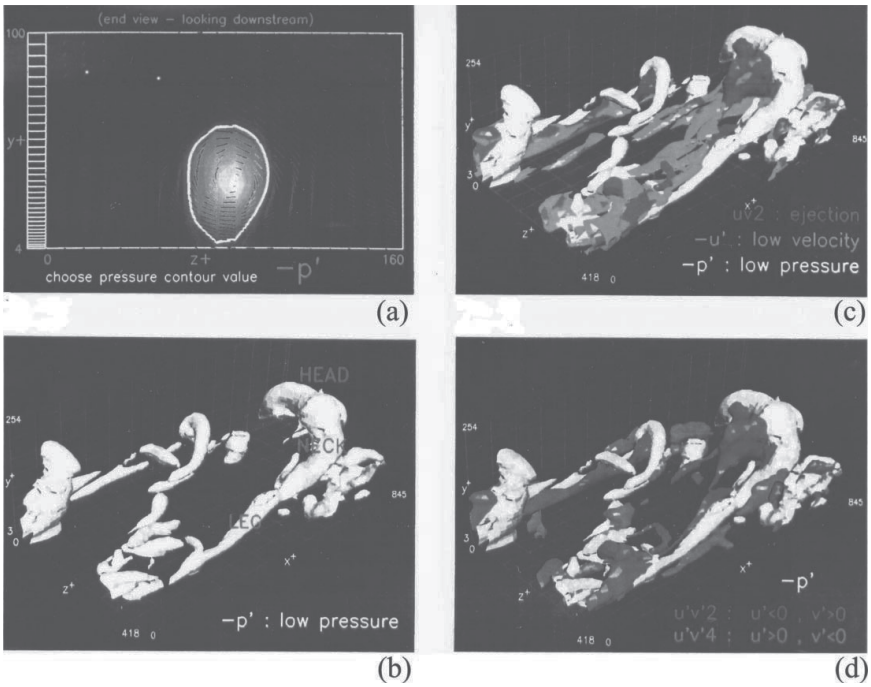


Figure 32. (a) Projections of the velocity vectors on the cross-stream (y–z) plane of a turbulent boundary layer with contours of low pressure superimposed, (b) contours of constant low pressure revealing partial (cane) hairpin vortices, (c) low-speed streak regions and (d) Q2 and Q4 Reynolds shear stress in spatial relationship to the vortices. From Robinson [72] with permission of NASA.

Robinson [72] used the turbulent boundary layer DNS databases of Spalart [63] to study the flow structure and its relationship to important transport properties of the flow. Using low pressure, below a chosen threshold with respect to the local mean pressure, as an identifier of vortex cores, as illustrated in Figure 32(a), he detected vortices in the boundary layer that often took on an incomplete horseshoe or "cane"-shaped appearance. The image in (b) is a good example; the white structures are isosurfaces of low pressure. In (c), the orange regions are of low streamwise velocity (low-speed streaks) with Q2 Reynolds shear stress (colored red) emerging out of them. Part (d) of the figure shows the spatial relationship of the Q2 (red) and Q4 (blue) Reynolds stress with respect to the inboard and outboard sides of the vortex "legs" and upstream of their heads. In his dissertation [72], and later in his review article [10], Robinson proposed a physical model of the flow structures made up of quasi-streamwise vortices and arches or horseshoes that are not necessarily spatially connected. A sketch of his model is shown in Figure 33(a). In (b), a sketch demonstrates how Robinson believed hairpin vorticity line bundles could be due simply to the action of a single quasi-streamwise vortex.

3.3.6. *1991 – power law for the overlap region*

In a series of papers beginning this year with an analysis for turbulent pipe flow [73] and later generalized and summarized in Barenblatt et al. [74], he and his co-workers challenged the long-established logarithmic law of the wall (see Section 2) for the mean

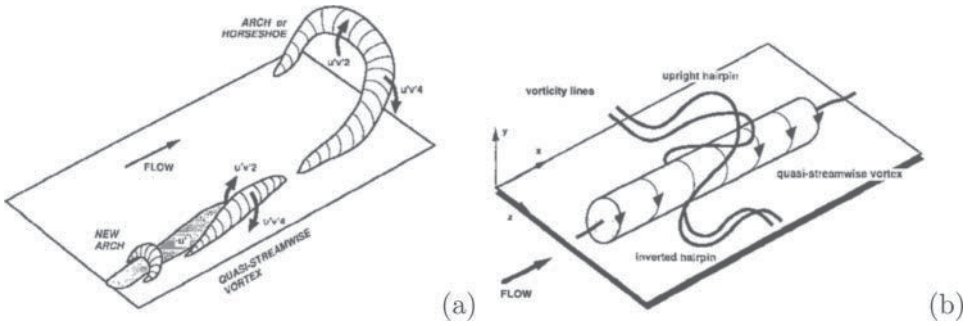


Figure 33. Sketches of (a) quasi-streamwise vortices and arch or hairpin vortices, and (b) of how hairpin vorticity lines can arise from the presence of a single quasi-streamwise vortex. From Robinson [10], reprinted with permission of Annual Reviews (www.annualreviews.org).

velocity distribution in bounded flows. They proposed a Reynolds number-dependent power law alternative given by

$$\phi = \frac{\overline{U}}{u_\tau} = \left(\frac{1}{\sqrt{3}} \ln Re + \frac{5}{2} \right) \eta^{(3/2lnRe)}, \tag{4}$$

where $\eta = u_\tau y/\nu$. This scaling law can be reduced to the form

$$\psi = \frac{1}{\alpha} \ln \left(\frac{2\alpha\phi}{\sqrt{3} + 5\alpha} \right) = \ln \eta, \tag{5}$$

where $\alpha = 3/2 \ln Re$. This alternative to the logarithmic law provoked a great deal of controversy within the turbulence research community with various research groups using assemblages of data to support each side of the argument. Figure 34 shows many different turbulent boundary layer data sets used by Barenblatt et al. [74] to support their theory.

A number of other investigators have also contributed to the debate about the proper law to describe the mean velocity profile in bounded turbulent flows. Zagarola, Smits and their coworkers took up this issue with a series of mean velocity measurements in an innovative pipe flow facility that used compressed air as the working fluid, known as the "superpipe", to achieve a Reynolds-range (based on the centerline velocity and pipe diameter) of $Re_d = 3.1 \times 10^4 - 3.5 \times 10^7$ with a surface roughness of less than three viscous lengths. In the first of these studies by Zagarola and Smits [75], they found two overlap regions, one described by a power law for $50 < y^+ < 500$ and the other by a logarithmic law for $500 < y^+ < 0.1r^+$, where r is the pipe radius. The logarithmic law only appeared for $Re_d > 3 \times 10^5$. They explain the existence of these two regions at sufficiently high Reynolds numbers as resulting from incomplete similarity in the power law region and full similarity in the logarithmic law region. Their mean velocity profiles over this wide Reynolds-number range are shown in the paper by Kim [33] on turbulent pipe and channel flows in this special volume, where he provides a fuller discussion of these issues.

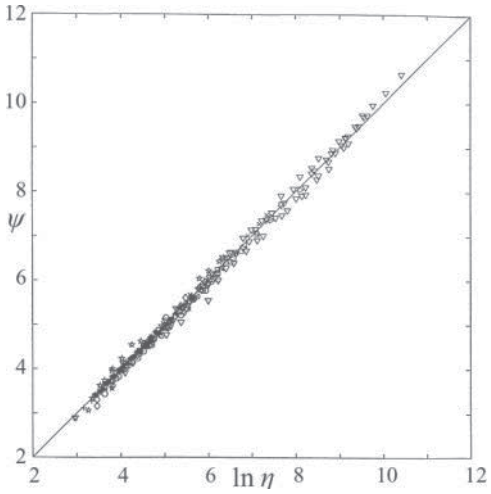


Figure 34. Comparison of power law for the mean velocity distribution with many experimental data sets. From Barenblatt et al. [74], copyright ©2000 Cambridge University Press.

3.3.7. *1991 – supersonic boundary layer structures*

Another new development in the first half of the 1990s was the use of some of the ideas discussed earlier for the investigation of supersonic boundary layers. An example of this is the experiment of Spina et al. [76] carried out in a turbulent boundary layer with $R_\theta = 81 \times 10^3$ and a Mach number of 2.9. Using a pair of parallel hot-wires separated by fixed distances varying between 0.1 and 0.6δ in both the streamwise and wall-normal directions, they detected large-scale structures that extended almost all the way across the boundary layer at angles of inclination between 45 and 60°, being shallower near the wall and steeper further away from it. They used the VITA technique to detect a sharp mass flux gradient on the backs of these large-scale structures. The authors sorted the most frequent occurrences of the quadrant motions, upstream and downstream of this interface.

Tsinober et al. [77] was the second experimental group to develop a multi-sensor hot-wire probe to measure the velocity gradient tensor in turbulent flows, extending the techniques they acquired in an earlier collaboration with the University of Maryland group [78]. Figure 35(a) shows a sketch and photograph of the 12-sensor probe they developed. With this probe, they determined the PDFs of the cosine of the angle between the vorticity vector and the eigenvectors of the rate of strain tensor for grid flow and at a location in a boundary layer. As had been previously shown for DNS data for homogeneous turbulent shear flow, the intermediate eigenvector is most aligned with the vorticity vector as seen in (b), a fact that now appears to be universally true of all turbulent flows. However, this was the first experimental evidence showing this to be the case.

Although there is a vast literature describing attempts to develop predictive methods applied to bounded turbulent flows, discussion here is limited to only one paper – that of Durbin [79]. Very little of the knowledge gained about the structure of these flows and the vortex dynamics that drive momentum and scalar transport within them has been incorporated in these modeling attempts. Even though this is also true of Durbin's efforts, it has the considerable virtues of (1) being formulated as a coordinate-system-invariant set of equations for the Reynolds stress tensor, (2) being solved for a set of boundary conditions applied at the bounding surface and thus requiring no ad hoc damping or wall functions,

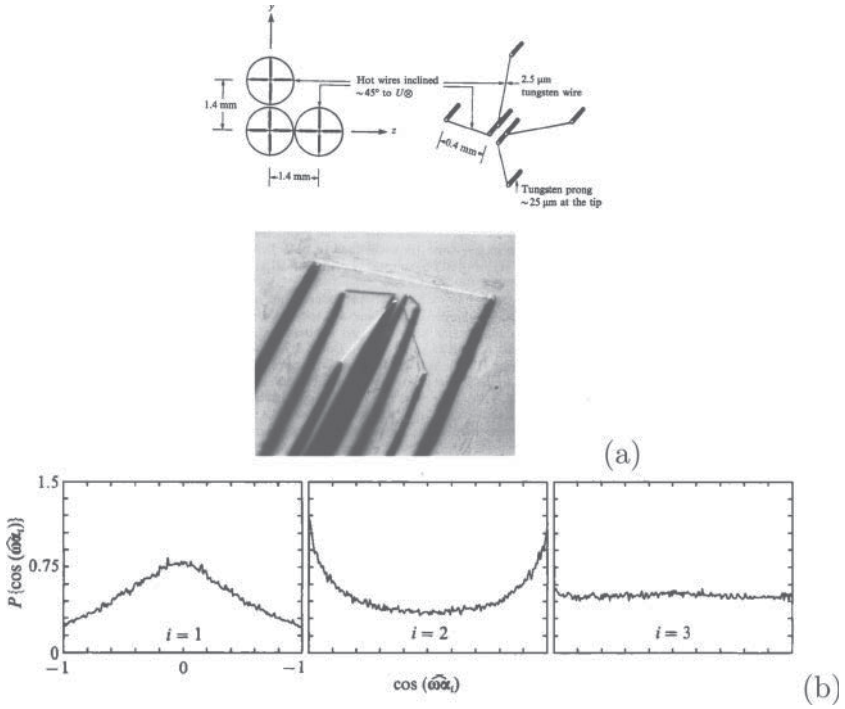


Figure 35. (a) Sketch and photograph of the 12-sensor hot-wire probe and (b) PDFs of the cosine of the angle between the vorticity vector and the eigenvectors of the rate of strain tensor in a boundary layer at $y/\delta = 0.2$. From Tsinober et al. [77], copyright ©1992 Cambridge University Press.

(3) accounting for strong inhomogeneity and anisotropy near the wall, (4) accounting in the governing equations for Reynolds-number dependence through the exact viscous terms and (5) using a relatively small number of empirical constraints obtained from experimental and DNS data. Durbin [79] has applied his model equations with considerable success, not only to zero-pressure gradient channel and boundary layer flows, but also to these flows with large adverse pressure gradients and to a boundary layer flowing around a surface with a constant radius 90° bend. Figure 36 shows Durbin's model predictions of Reynolds stress intensities compared to data from the turbulent channel flow DNS of Moser et al. [80] at $R_\tau = 395$.

Similar to the status of research to develop predictive methods, a large literature exists describing efforts to advantageously control bounded flow turbulence. Here, only one such paper will be briefly discussed, i.e. that of Choi et al. [81]. It clearly attempts to use information about the physical processes known to occur in these flows in order to implement active control manipulations. The base flow utilized was the $R_\tau = 180$ turbulent channel flow DNS of Kim et al. [59]. All the conditions of the manipulated flows were the same as the base flow except that the boundary conditions were changed to implement the control strategies. These strategies were: (1) imposition of streamwise, wall-normal and spanwise wall velocities, (2) control with selective wall-normal velocities and (3) control with sensors limited to the wall. An example of how much different control scenarios affect the flow is shown in Figure 37, where the distributions across the channel of the rms values of the vorticity components are shown. Here, v- and w-control denotes the local wall

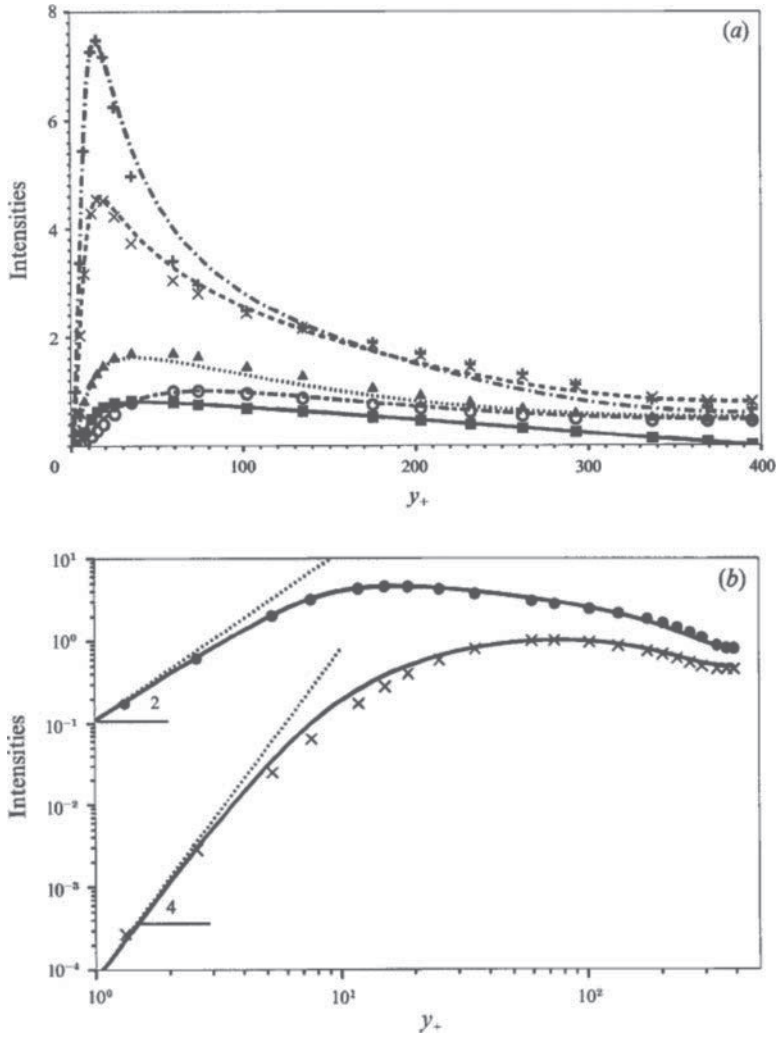


Figure 36. (a) Reynolds stress intensities computed from model predictions (lines) compared to data from the channel flow DNS (symbols) at $R_\tau = 395$ of Moser et al. [80]: + $\overline{u^2}$, × turbulent kinetic energy k, filled triangles $\overline{w^2}$, open circles $\overline{v^2}$, filled squares $-\overline{uv}$. (b) Near-wall behavior, k (upper) and $\overline{v^2}$ (lower) showing y^2 and y^4 asymptotic limits. From Durbin [79], copyright ©1993 Cambridge University Press.

boundary condition motion set to be out-of-phase, either in the wall-normal or spanwise direction, with the corresponding velocity component motion in the flow near the wall as detected by a sensor. Both of these control strategies resulted in large drag reduction.

3.3.8. *1994 – boundary layer local isotropy*

A fundamental assumption underlying most turbulent modeling and LES is that turbulence at small scales is isotropic for large enough Reynolds numbers, a prediction of Kolmogorov's universal equilibrium theory [82]. A highly regarded experimental test of

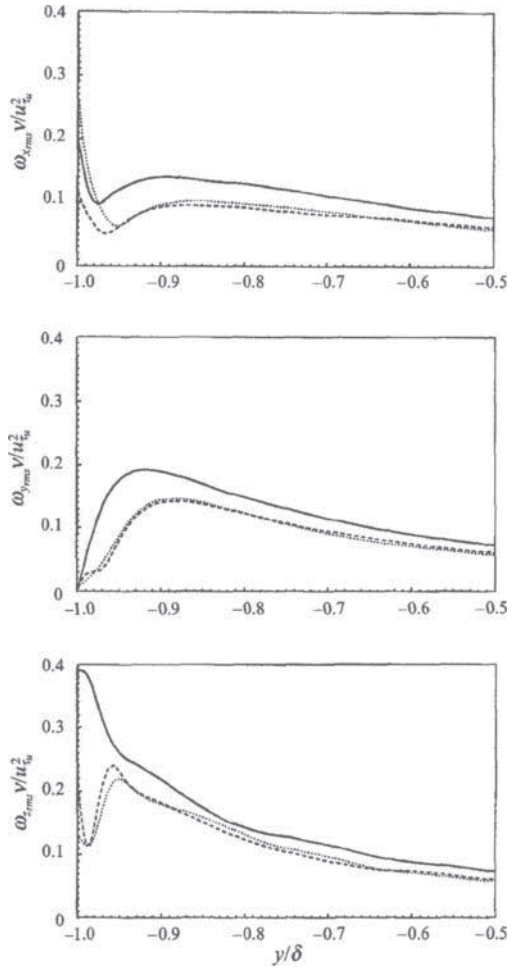


Figure 37. Distributions of the rms values of vorticity components across a turbulent channel flow for: no control (solid); v-control (dashed); w-control (dotted). $y/\delta = -1$ corresponds to the lower wall. From Choi et al. [81], copyright ©1994 Cambridge University Press.

this "local isotropy" idea for turbulent boundary layers was carried out by Saddoughi and Veeravalli [83]. They measured streamwise and cross-stream velocity fluctuations in the relatively high Reynolds-number boundary layer on the test section rough wall of the huge NASA Ames wind tunnel shown in Figure 38(a), and they applied several local isotropy tests to the data. In (b), for example, compensated frequency spectra (transformed with Taylor's hypothesis to k_1 wavenumber spectra) are plotted. Over much of the inertial subrange, the curves display the predicted plateau at the level of the Kolmogorov constant, particularly for the streamwise velocity component. In (c), the compensated second-order structure functions for these velocity fluctuation components are shown. Similarly, here, the plateaus in the inertial subrange are at the level predicted by assuming local isotropy.

During part of the period that Saddoughi and Veeravalli's [83] experiments were carried out, Wallace and Ong [84] made simultaneous measurements of the velocity vector and the velocity gradient tensor in the same wind tunnel with the 12-sensor probe shown in

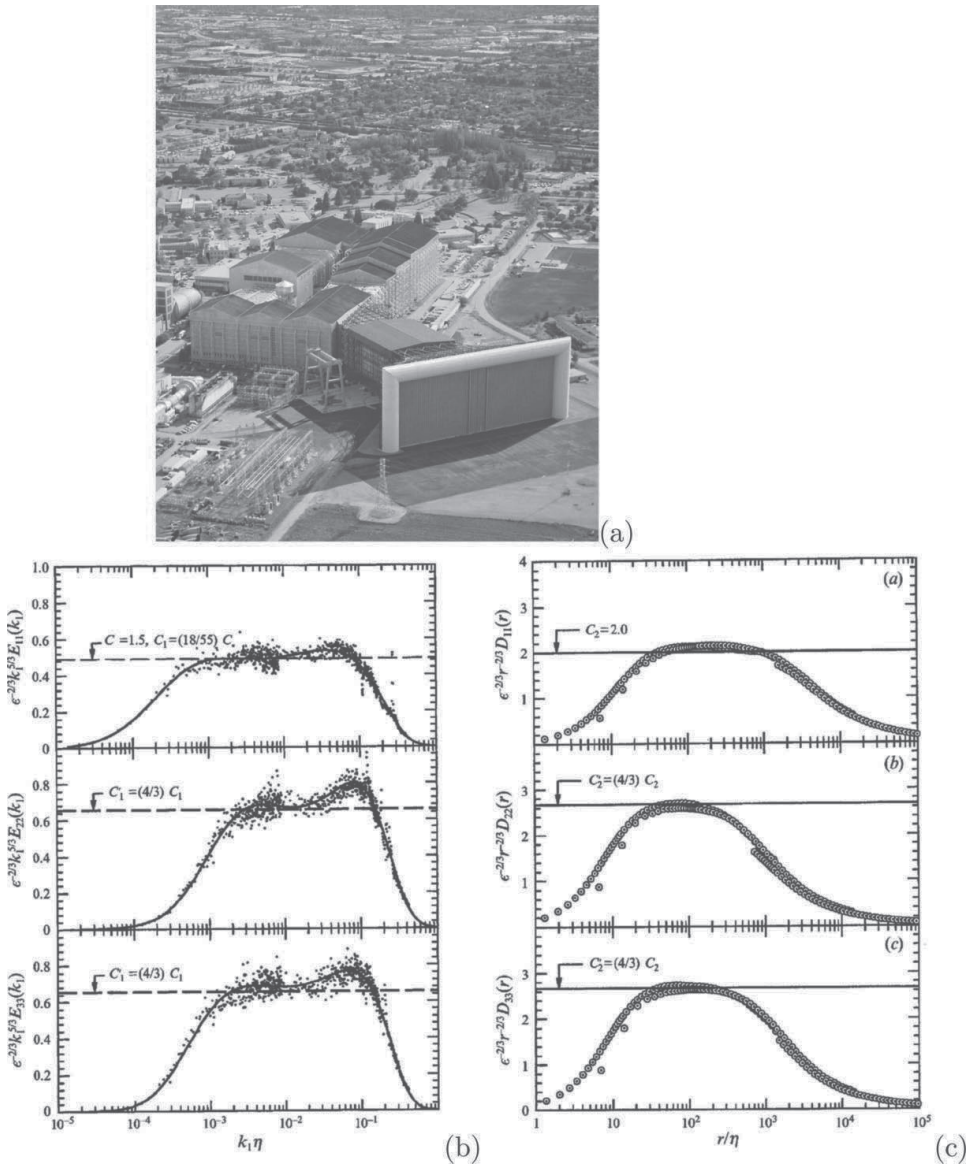


Figure 38. (a) NASA Ames windtunnel with 80′ × 120′ test section, (b) compensated velocity component wavenumber spectra and (c) compensated second-order structure functions. From Saddoughi and Veeravalli [83], copyright ©1994 Cambridge University Press.

Figure 39(a). In their paper, published much later, they tested the implications of the local isotropy hypothesis for the vorticity field. Shown in (b) are the ratios of the spectral densities of the cross-stream vorticity components to their measured values, $E^{\text{calc}}_{\omega_y}/E^{\text{meas}}_{\omega_y}$ and $E^{\text{calc}}_{\omega_z}/E^{\text{meas}}_{\omega_z}$, each calculated assuming isotropy, from the spectral density of the streamwise component, E_{ω_x}. In the inertial subrange, these ratios are approximately unity, thus satisfying the local isotropy assumption. At higher wave numbers the noise in the experimental data distorts the values of the ratios.

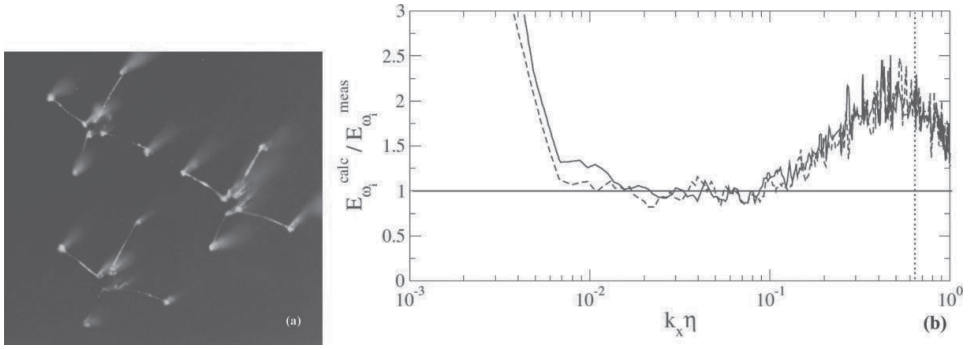


Figure 39. (a) Twelve-sensor probe used to simultaneously measure the velocity vector and the velocity gradient tensor, and (b) ratios of spectral densities of the cross-stream vorticity components calculated from the spectral density of the streamwise component, assuming isotropy, to their measured values. Solid line, ω_y; dashed line, ω_z. From Wallace and Ong [84], copyright ©2008 American Institute of Physics.

Nagano and Tagawa [85] utilized an interesting trajectory analysis technique (TRAT) of experimental hot- and cold-wire measurements of velocity components and temperature in a turbulent pipe flow to elucidate the heat transfer processes driven by coherent motions near the wall. At a location in the buffer layer, they tracked the evolution of the Reynolds shear stress signal from quadrant to quadrant in the uv hodograph plane. Four dominant patterns, with distinct phase characteristics, were identified: Q2–Q1–Q4, Q2–Q3–Q4, Q4–Q1–Q2 and Q4–Q3–Q2. Ensemble averages of time series representing these patterns are shown in Figure 40. They also found that the Q3–Q2–Q3 pattern was significant for heat transfer, and they developed an autoregressive predictive model to mimic all of these patterns.

3.3.9. *1995 – very high-Reynolds number atmospheric surface layer measurements*

Even the largest conventional wind tunnels, with the longest test sections, have rather restricted Reynolds-number ranges. A central pressing question for the research community has long been how the knowledge about the properties and structure of turbulent boundary layers gained at relatively low-Reynolds numbers from laboratory experiments and DNS apply to the high-Reynolds-number flows of many practical engineering applications. Fortuitously, the surface layer of the atmospheric boundary layer goes through neutral stability conditions around sunrise and sunset. Under those conditions, this naturally occurring, extremely high-Reynolds-number flow has characteristics that are similar to those of laboratory and computational turbulent boundary layers. Klewicki and co-workers developed the field site southwest of Salt Lake City, Utah, shown in Figure 41(a), for these types of experiments and made it available to numerous research groups. During the early summer, the surface, which varies in elevation only a few meters over a 70 mile fetch, is only slightly rough at the measurement site with a local variation of about 1–3 mm. Klewick et al. [86] released a sheet of fog just above the surface to observed low-speed streaks. Their average normalized spacing for this very high-Reynolds-number flow is almost exactly that measured by Smith and Metzler [87] in a laboratory boundary layer at low-Reynolds number, as seen in (b) of the figure. In (c), the compilation by Metzger and Klewicki [88] of high- and low-Reynolds-number data for the maxima of the distributions of the rms streamwise velocity fluctuations, scaled by inner variables, are shown. The Reynolds-number trend to

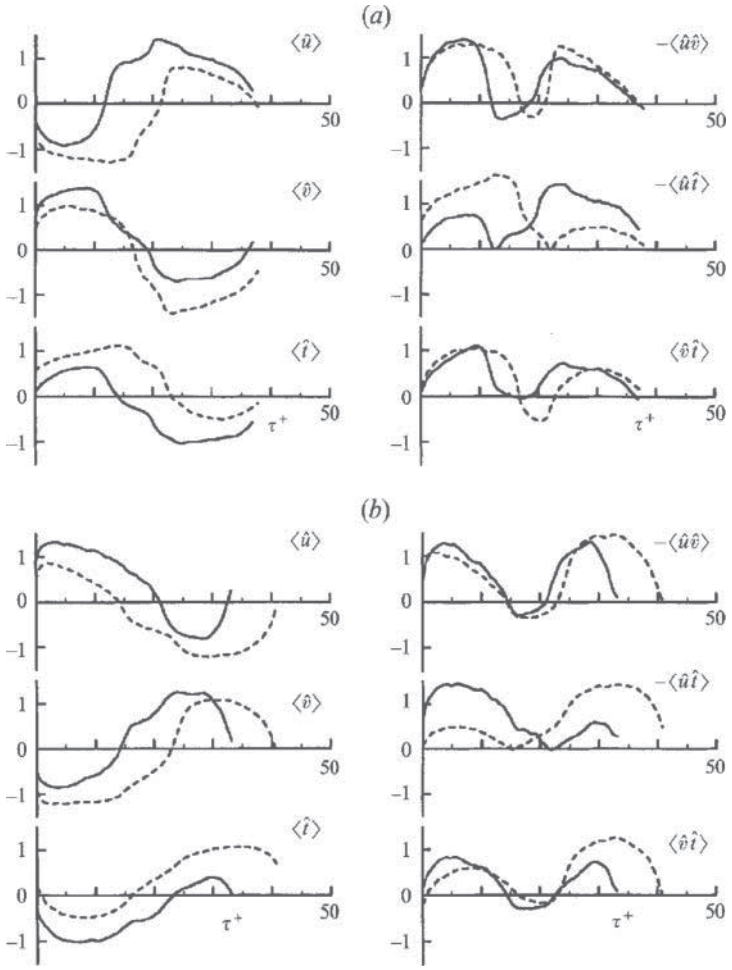


Figure 40. Ensemble-averaged characteristics of turbulence quantities in velocity and temperature fields obtained with TRAT at $y^+ = 18.5$. (a) Accelerative patterns: Q2–Q1–Q4 (solid); Q2–Q3–Q4 (dashed); (b) decelerative patterns: Q4–Q1–Q2 (solid) ; Q4–Q3–Q2 (dashed). From Nagano and Tagawa [85], copyright ©1994 Cambridge University Press.

higher values at high-Reynolds number is obvious. In (d), space–time correlations of the streamwise velocity components, from their study, are compared for the low-Reynolds-number laboratory experiment and the high-Reynolds field experiment. The fixed probe was located in the viscous sublayer in both cases. For $y^+ < 10$, the angles of inclination of the locus of maximum correlation is about 60°, independent of Reynolds number. Above that location, this angle of inclination increases a bit for the high-Reynolds-number flow.

Folz and Wallace [89] made measurements with their 12-sensor probe at this same field site. In their paper, published recently and years after the experiments were carried out, among other properties of the surface layer they compare measurements of the rms vorticity components at $y^+ = 45$ to measurements of Priyadarshana et al. [90], also taken in the surface layer, and to those of Balint et al. [62] taken in the laboratory at low-Reynolds number. These are shown in (e), where the values, as a function of location, of the high- and low-Reynolds number rms vorticity component data are similar. Note that the

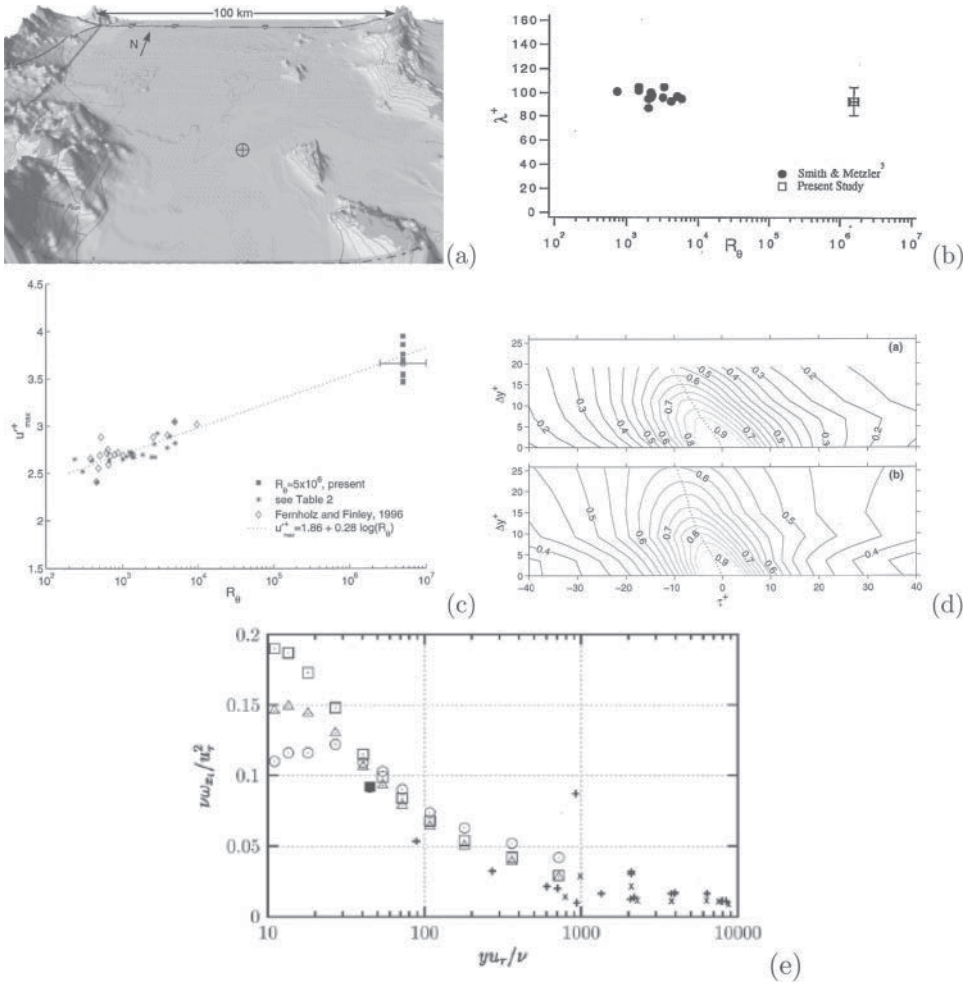


Figure 41. (a) Aerial view of the atmospheric surface layer field site southwest of Salt-Lake City, Utah. (b) Averaged normalized low-speed streak spacing for high- and low-Reynolds-number experiments, reprinted with permission from Klewicki et al. [86]. Copyright ©1995 American Institute of Physics. (c) Maxima of the distributions of rms streamwise velocity fluctuations and (d) space–time correlation function contours at low (upper plot) and high (lower plot) Reynolds number, both reprinted with permission from Metzger and Klewicki [88]. Copyright ©2001 American Institute of Physics. (e) Distributions of the rms vorticity components compared at high (filled symbols, + and ×) and low (open symbols) Reynolds numbers. Reprinted from Folz and Wallace [89] with permission from Elsevier.

values of all three components of the Folz and Wallace data (filled squares) fall virtually on top of one another.

Another atmospheric surface layer field experiment, carried out at a different site with a multi-sensor probe, and designed primarily to measure velocity derivatives, was that of Kholmyansky et al. [91]. They used a 20-sensor probe mounted at 10 m above a grass-covered flat terrain with an approximately 4 km upstream fetch. The flow conditions were nearly neutral but slightly unstable. Figure 42 shows a joint PDF-like scatter plot of the dominant enstrophy production term, $\omega_i \omega_k s_{ik}$, and the mean square strain term, $-4/3 s_{ij} s_{jk} s_{ki}$.

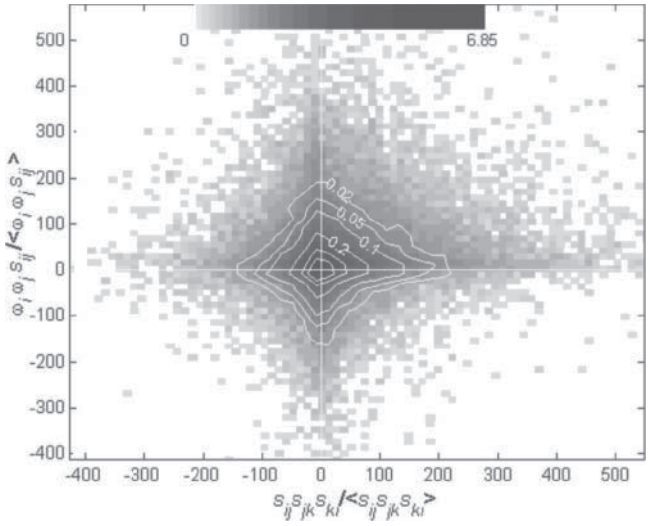


Figure 42. Scatter plot of dominant enstrophy production, $\omega_i\omega_k s_{ik}$, and mean square strain, $-4/3 s_{ij}s_{jk}s_{ki}$. Reprinted with permission from Kholmyansky et al. [91], copyright ©2001 American Institute of Physics.

The authors point out that, although the individual PDFs of these terms have similar shapes, they are only weakly correlated, as seen from the shape of the scatter plot figure.

3.3.10. *1997 – quasi-streamwise vortices and the stability of buffer layer streaks*

Jeong et al. [92] detected vortices in the turbulent channel flow simulation of Kim et al. [59] using a criterion of negative λ_2, the intermediate eigenvalue of the tensor $S_{ik}S_{kj} + R_{ik}R_{kj}$, where $S_{ij} = \frac{1}{2}(\partial U_i/\partial x_j + \partial U_j/\partial x_i)$ is the strain rate and $R_{ij} = \frac{1}{2}(\partial U_i/\partial x_j - \partial U_j/\partial x_i)$ is the rotation rate. This criterion indicates dominance of rotation over strain in a specified plane. Their investigation revealed quasi-streamwise vortices, as seen in Figure 43(a), that are not in the form of hairpins. These vortices, slightly inclined to the wall and skewed when viewed in x–z planes, occur in staggered, overlapping, opposite sign pairs as sketched in (b). They also found that a phase difference in space of the streamwise and wall-normal velocity fluctuations, caused by the advecting vortices, accounts for nearly all of the Q2 and Q4 Reynolds shear stress as well as for the counter-gradient Q1 and Q3 stress contributions. Phase differences in time had previously been found two decades earlier to account for these quadrant contributions by Wallace et al. [93] with their pattern recognition technique. From the later study of Schoppa and Hussain [94], the locations of these quadrant events, relative to a positive quasi-streamwise vortex (hashed region labeled SP) and to a low-speed streak (bold dashed line), is shown in (c) for the instantaneous field. The latter authors proposed a transient growth mechanism to describe the stability of buffer layer streaks. They argue from their analysis that vortex generation does not arise from the rollup of spanwise vortex sheets at the wall. Rather, they believe that these quasi-streamwise vortices are created by spanwise perturbations of the streaks which lead to near-wall sheets of *streamwise* vorticity and sinuous waviness of the streaks. This results in high levels of $\partial u/\partial x$ which, in turn, leads to the collapse of the ω_x sheets into streamwise vortices.

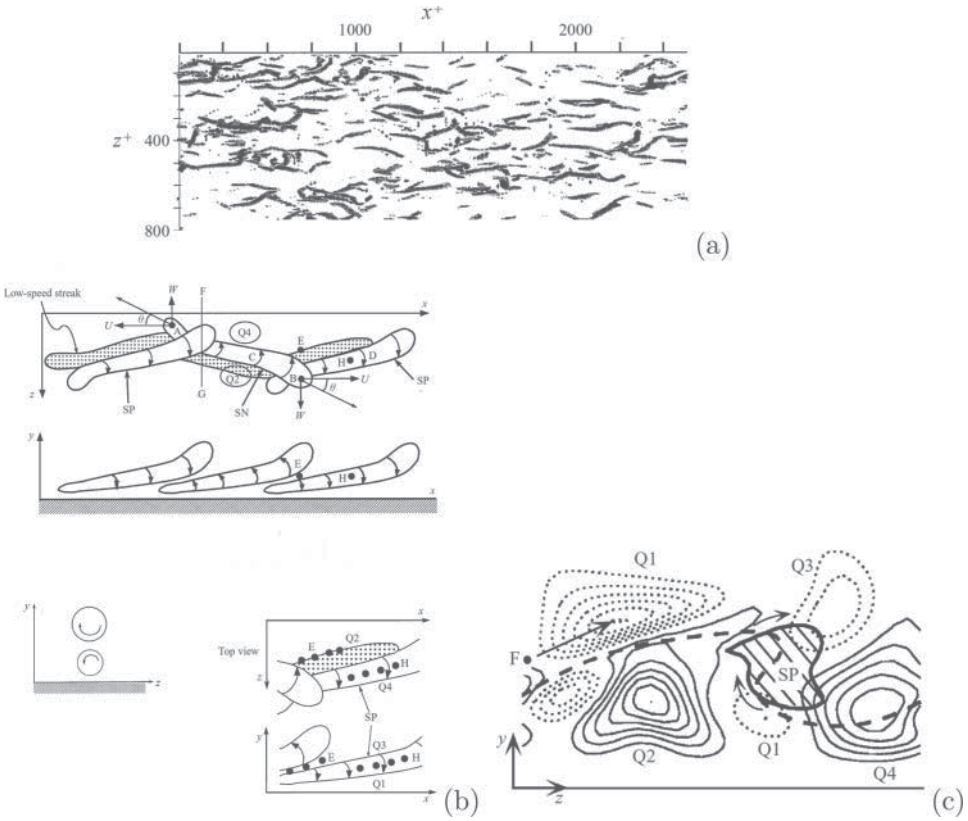


Figure 43. (a) View looking down on the turbulent channel flow showing surfaces of constant λ_2 and (b) sketches showing quasi-streamwise staggered vortices of opposite sign (SP denotes positive rotation and SN negative rotation), from Jeong et al. [92], copyright ©1997 Cambridge University Press. (c) The spatial relationship of quadrant Reynolds shear stress events with respect to a quasi-streamwise vortex (hashed and labeled SP) and low-speed streak (bold dashed line). From Schoppa and Hussain [94], copyright ©2002 Cambridge University Press.

Honkan and Andreopolus [95] was the third experimental team to develop a multi-sensor hot-wire probe to simultaneously measure the velocity vector and the velocity gradient tensor. A photograph and sketch of their probe is shown in Figure 44(a). With this 12-sensor probe, they measured the angular orientation of the projection of the vorticity vector, near the wall of a turbulent boundary layer at $y^+ = 12.5$, on to wall-normal and wall-parallel planes. In (b), the orientation angles, θ_v and ϕ_v, are indicated for the x_1–x_2 and x_1–x_3 planes, respectively. The PDFs of these angles, conditioned on the magnitudes of the vorticity components being greater than a chosen threshold, are shown in (c). For the conditioning threshold set at unity rms level, the θ_v PDFs displayed are narrow, with sharp primary peaks at 35° and -140° and secondary peaks at -35° and 140°. The PDFs for ϕ_v show peaks at -135° and -45°. The primary peak values of the PDF, conditioned so as to remove weaker levels of vorticity, are consistent with hairpin-like vorticity lines.

Ong and Wallace [96] also studied the orientation of vorticity lines in a turbulent boundary layer using the joint probability density (JPDF) and covariance integrand

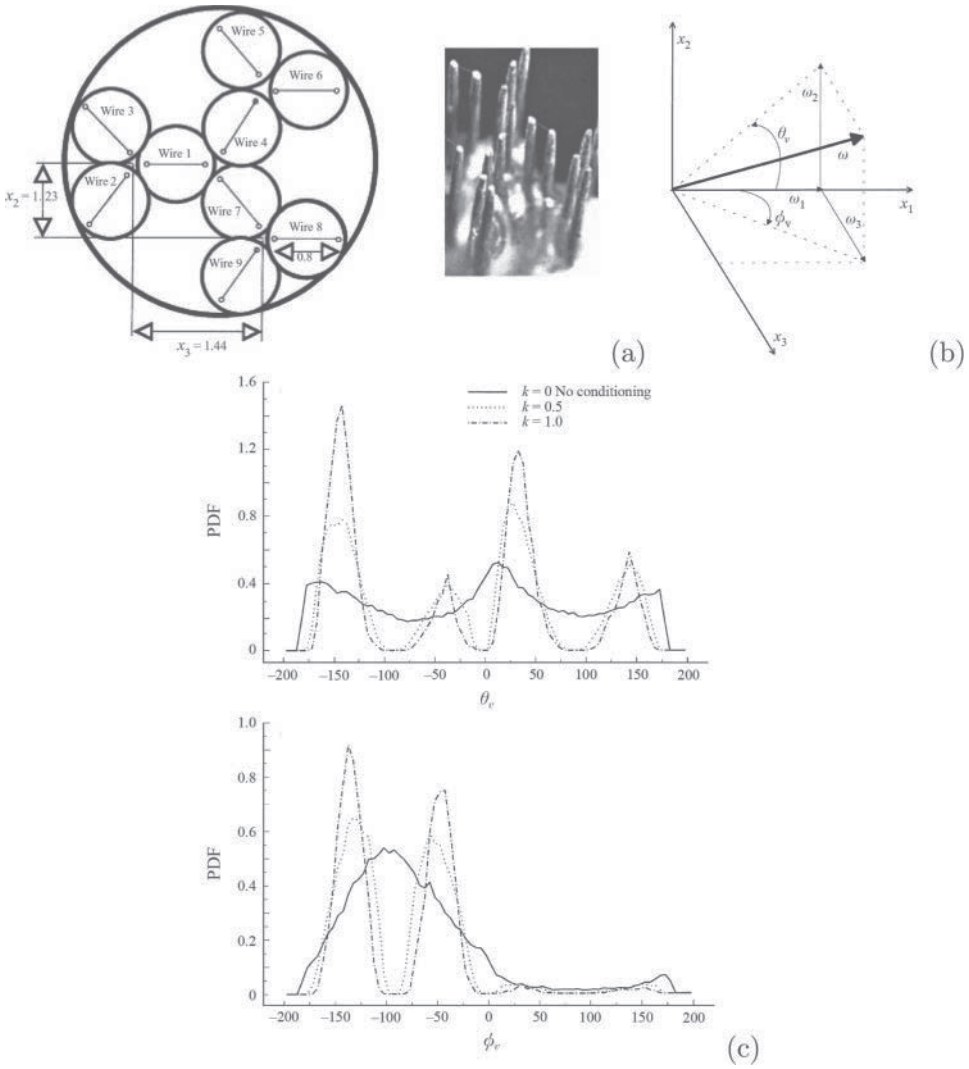


Figure 44. (a) Photograph and sketch of 12-sensor probe, (b) sketch defining angles of orientation of the vorticity vector projected on the x_1–x_2 and x_1–x_3 planes and (c) PDFs of these angles in a boundary layer at $y^+ = 12.5$. From Honkan and Andreopoulos [95], copyright ©1997 Cambridge University Press.

distributions of the three pairs of vorticity components measured with the nine-sensor probe of Balint et al. [62]. The distributions for the $P(\Omega_x, \Omega_y)$ JPDF and the $\Omega_x, \Omega_y P(\Omega_x, \Omega_y)$ covariance integrand are shown in Figure 45(a) at a location in the buffer layer and at two locations in the logarithmic layer. The JPDF is rotated toward the Q1 and Q3 quadrants, i.e. the quadrants with like sign Ω_x and Ω_y, consistent with the idea of hairpin or horseshoe vortices inclined downstream to the wall. This is even more evident for the Q1 and Q3 covariance integrand quadrants, i.e the two that contribute most to the covariance $\overline{\Omega_x \Omega_y} = \int \Omega_x, \Omega_y P(\Omega_x, \Omega_y) d\Omega_x d\Omega_y$. From the peak values of the contours in the Q1 and Q3 quadrants for all three vorticity component covariance integrand plots at each location,

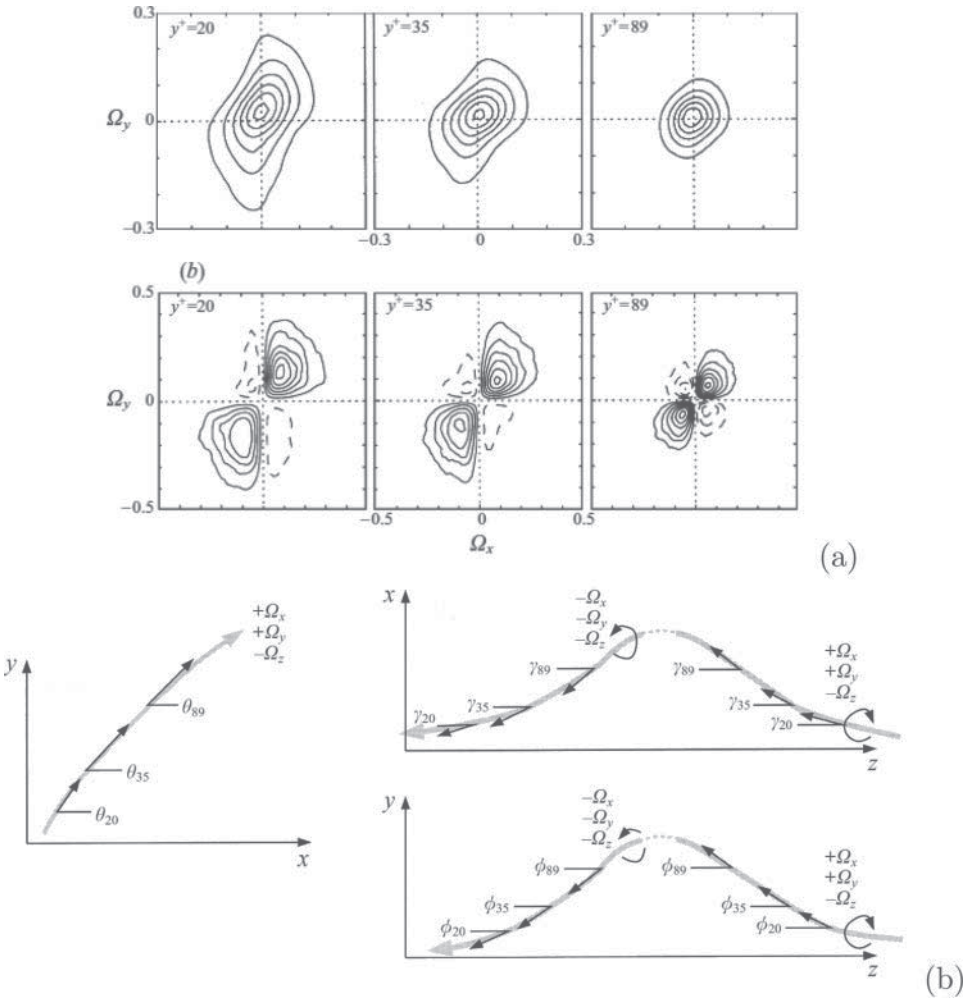


Figure 45. (a) JPDFs and covariance integrand contours from a turbulent boundary layer and (b) a sketch of the orientation of the vorticity filaments that most contribute to the covariance $\overline{\Omega_x \Omega_y}$. From Ong and Wallace [96], copyright ©1998 Cambridge University Press.

the orientations, in each coordinate plane, of the vorticity filaments making the greatest contribution to these covariances can easily be determined. These are sketched in (b) of the figure.

3.3.11. *2000 – supersonic boundary layer DNS*

A significant development at the beginning of this decade was the boundary layer DNS of Guarini et al. [97] for supersonic Mach 2.5 conditions. They presented results for adiabatic wall conditions with $Re_\theta = 1577$, and they employed Spalart's [63] method of transforming the coordinate system and rescaling the flow so as to use homogeneous boundary conditions in both the spanwise and streamwise directions. When appropriately scaled, many of the statistical properties of this compressible simulation are very similar to those found from

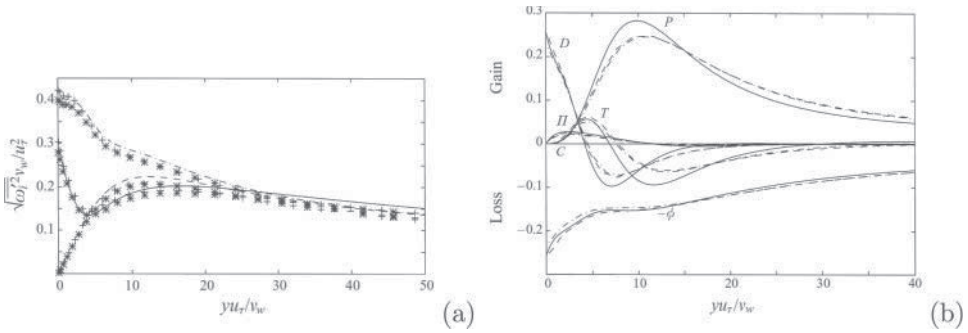


Figure 46. Comparison of (a) distribution of rms vorticity fluctuations, Guarini et al. [97], lines; Spalart [63], symbols: + $Re_\theta = 1410$ and $*$ 670). (b) Turbulent kinetic energy budgets, Guarini et al., solid lines; Spalart, dashed lines for $Re_\theta = 1410$, dashed-dotted lines for 670, copyright ©2000 Cambridge University Press.

experiments and incompressible simulations. For example, Figure 46(a) compares the distributions of the rms vorticity fluctuation components with Spalart's incompressible DNS results. In (b), the turbulent kinetic energy budgets are compared. In both cases, there is little apparent effect of compressibility. However, the authors do find some difference in the correlations between the velocity and temperature fields when their DNS results are compared to previous experimental ones.

3.3.12. *2000 – planar PIV boundary layer measurements*

Development of planar particle image velocimetry (PIV) in the 1980s produced a new experimental tool to investigate turbulent flows, including bounded flows. Adrian [98] and his coworkers have been central to this development, and they used PIV in a number of studies that revealed hitherto unknown aspects of boundary layers. Figure 47(a) is a sketch of a typical PIV field of view and its image on film from Adrian et al. [99]. In (b), they compare the distribution of the rms values of the spanwise vorticity fluctuations to previous results from DNS and hot-wire measurements. In (c), large-scale zones of constant streamwise momentum, labeled I, II and III, are evident, and in (d) high shear in ramps inclined to the wall and vortices that are interpreted as the "heads" of hairpins are highlighted. These hairpins, as had been often previously observed, account for much of the Q2 and Q4 Reynolds shear stress and can also account for the VITA event signature. Their conceptual model of these types of hairpin vortices is shown in (e), and their observation that these hairpins occur in "packets" and in a hierarchy of scales provided experimental support for the vortex auto-generation processes proposed by Zhou et al. [100, 101], as well as for some of the aspects of the Perry and Chong [56] structural model. Such a packet of vortices is highlighted in the velocity vector field shown in (f), where the grey scale indicates swirl strength. In (g), all these findings are combined in a composite sketch of their conception of the structure of the turbulent boundary layer. Adrian [102] has summarized this and other work of his and other groups in his comprehensive review marshalling the evidence for this view of the turbulent boundary layer structure.

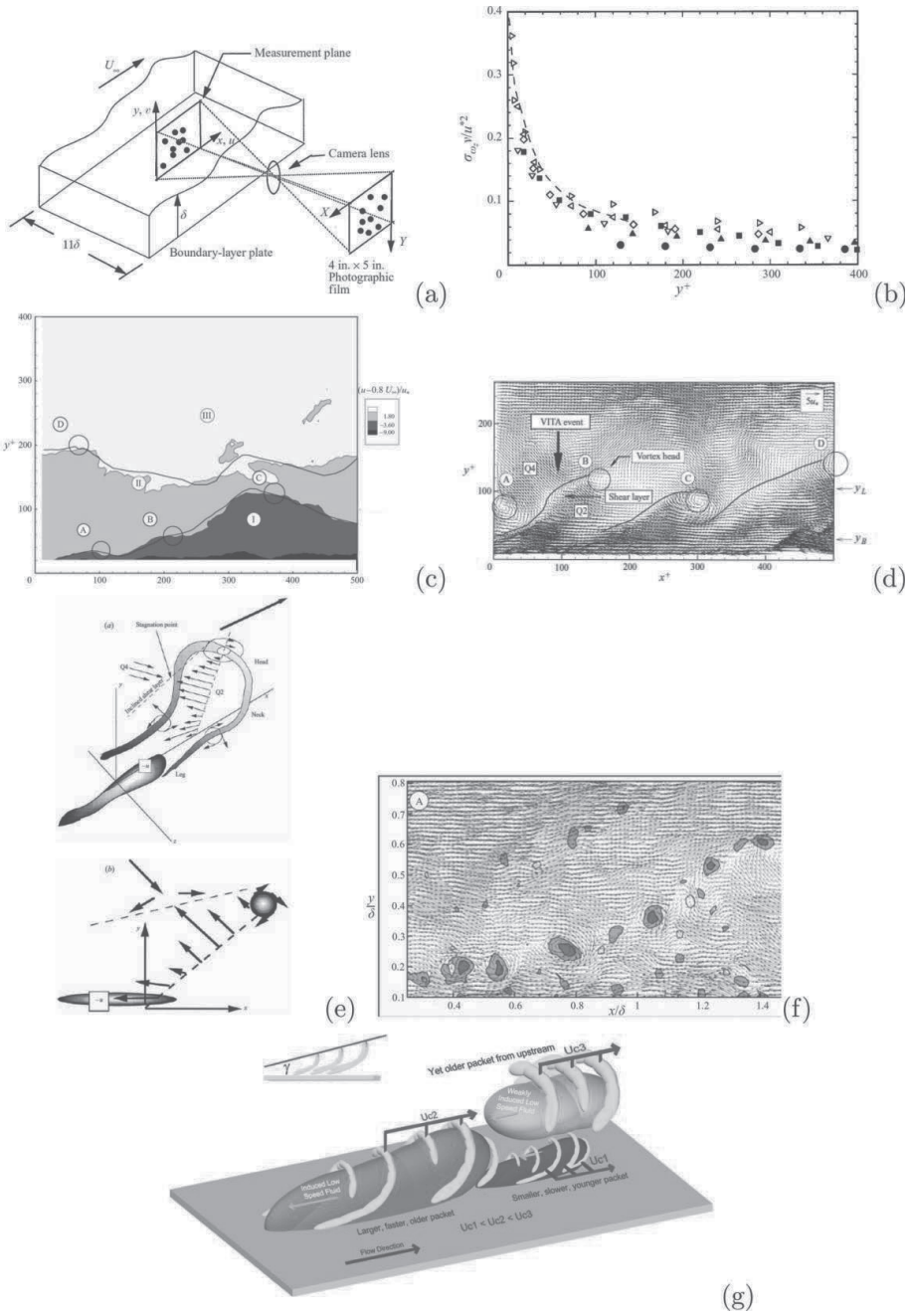


Figure 47. (a) Sketch of PIV field of view in the boundary layer and its image on film. (b) Comparison of the rms spanwise vorticity distribution from PIV measurements (filled symbols) in a turbulent boundary layer at three Reynolds numbers, with the DNS values of Spalart [63] (dashed–dotted line), experimental measured values of Klewicki [103] (horizontal triangles) and of Balint et al. [62] (inverted triangles). (c) Contours of constant streamwise momentum. (d) High shear in ramps inclined to the wall and with vortices interpreted as hairpin heads indicated by circles. (e) Conceptual model of hairpin vortices. (f) A packet of hairpin vortex heads highlighted on the convecting velocity vector field. (g) A composite sketch of the structure of the turbulent boundary layer. From Adrian et al. [99], copyright ©2000 Cambridge University Press.

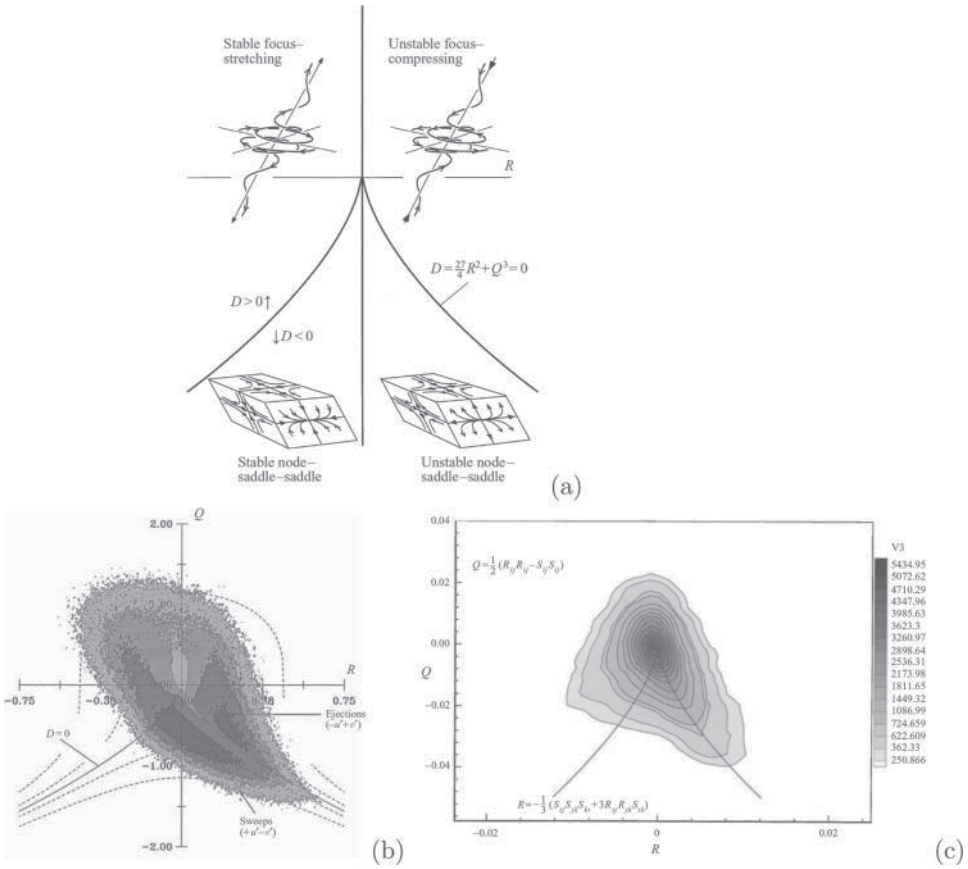


Figure 48. (a) Flow patterns in relationship to the zero discriminant of the velocity gradient tensor that emerge from critical point theory. (b) JPDF of Q and R invariants of the characteristic equation of the velocity gradient tensor with contours of time-averaged Reynolds stress corresponding to each location in the plane superimposed. Data taken from the entire turbulent boundary layer DNS of Spalart [63]. From Chacin and Cantwell [104], copyright ©2000 Cambridge University Press. (c) Q–R JPDF obtained experimentally at $y^+ = 12$ in a turbulent boundary layer with a 12-sensor hot-wire probe. From Andreopolous and Honkan [105], copyright ©2001 Cambridge University Press.

3.3.13. *2000 – analysis using critical point theory*

Chacin and Cantwell [104] used critical point theory, primarily developed by Perry and Chong [67], to analyze the Spalart [63] turbulent boundary layer DNS. For incompressible flow, the cubic discriminant of the velocity gradient tensor, A_{ij}, is $D = \frac{27}{4}R^2 + Q^3$, where $A_{ij} \equiv \partial U_i/\partial x_j \equiv S_{ij} + R_{ij}$. The characteristic equation of A_{ij} is $\lambda^3 + P\lambda^2 + Q\lambda + R = 0$, where the invariants of the tensor are: $P = -S_{ii} = 0$ for incompressible flow, $Q = \frac{1}{2}(-S_{ij}S_{ij} + R_{ij}R_{ij})$ and $R = -\frac{1}{3}(S_{ij}S_{jk}S_{ki} + 3R_{ij}R_{jk}S_{ki})$. Figure 48(a) indicates the flow patterns that emerge from critical point theory and their relationship to the zero discriminant line. Note that the patterns in the positive discriminant region are rotative patterns that are either being stretched or compressed. In (b), the "tear drop" shape JPDF of Q and R is shown for data from the entire boundary layer computational domain. This shape for the JPDF has been shown to be characteristic of all turbulent flows. The zero discriminant Villefosse line also is shown separating the rotational and saddle flow patterns. Superimposed on this

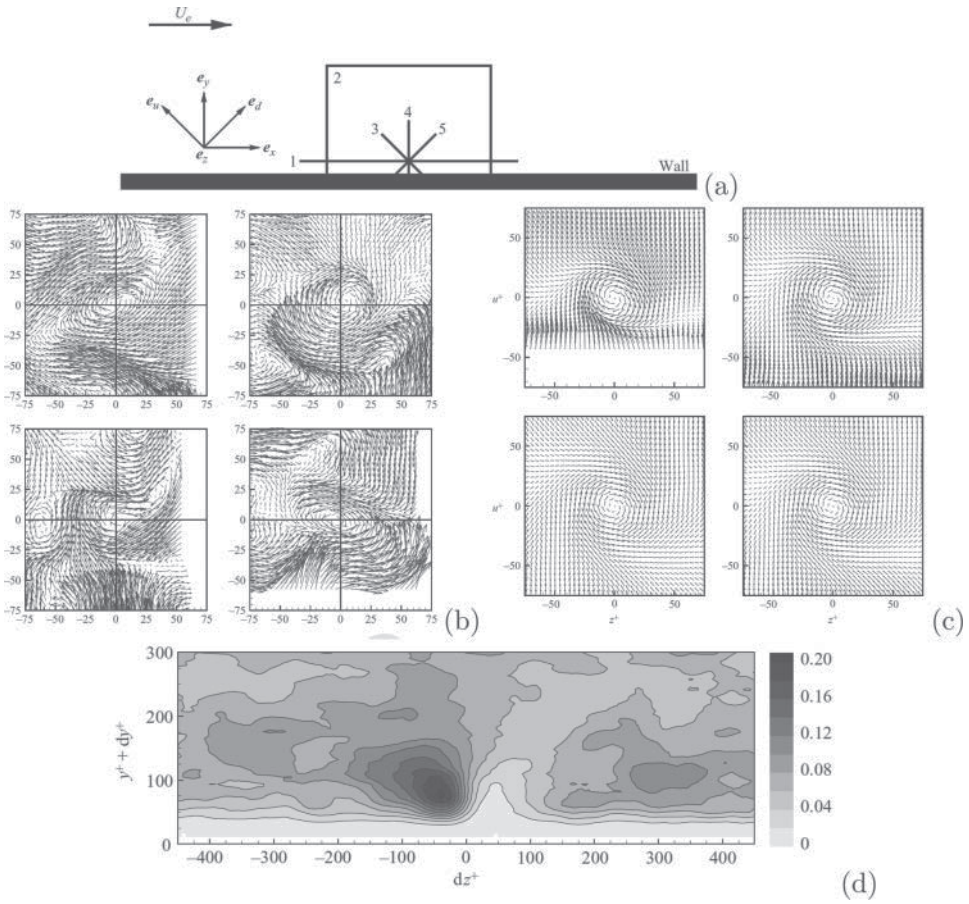


Figure 49. (a) Sketch indicating the planes in which the velocity vector field projections were obtained; (b) examples of instantaneous eddy structures that were educed from the (e_z, e_u)-plane; (c) average of educed vortices for four locations relative to the wall (clockwise from top left $y_0^+ = 50$, 75, 100 and 125) and (d) probability contours for the location of vortices with positive rotation with respect to the location of Q2 ejection events at $dz^+ = 0$ and $y^+ = 50$. From Carlier and Stanislas [106], copyright ©2005 Cambridge University Press.

figure is the time-averaged Reynolds shear stress associated with each location on the Q–R plane. There are two peaks, one located in the $D > 0$ region, which is predominantly due to Q2 ejection motions, and the other located in the $D < 0$ region, which is predominantly due to Q4 sweep motions. This tear drop-shaped JPDF of Q and R was confirmed by Andreopolous and Honkan [105] with measurements taken with their 12-sensor probe at $y^+ = 12$, as seen in (c).

Another extensive study of the turbulent boundary layer structure using planar PIV was carried out by Carlier and Stanislas [106]. They obtained the velocity vector fields in several planes including cross-stream planes tilted upstream and downstream at 45° following what had been done in the flow visualization study of Head and Bandyopadhay [54]. They used a pattern recognition technique that involved convolving a model vortex with the two-dimensional measured flow field to educe the vortices from it, and they studied Q2 and Q4 Reynolds stress events in spatial relationship to these vortices. Figure 49(a) is a sketch

indicating the planes in which the velocity vector field projections were obtained. In (b), examples of instantaneous eddy structures that were educed from the (e_z, e_u)-plane by this convolution procedure are shown. This is the cross-stream plane tilted upstream cutting through the downstream-inclined vortices. In (c), the average of these educed vortices is shown for four locations relative to the wall. In (d), probability contours are plotted for the location of vortices with positive rotation with respect to the location of Q2 ejection events that are detected at the origin of the plot at $y^+ = 50$. The scales of the regions of high probability are representative of the scale of the vortices. Viewed with the corresponding probability plot for Q4 sweep events, these figures demonstrate that the ejection and sweep events occur on opposite sides of the detected vortices. The authors concluded that the eddy structures they detected were elongated downstream and inclined to the wall at roughly 45°, and that they have a "cane"-shape with a smaller diameter and greater vorticity near the wall in the legs and a greater diameter and smaller vorticity in the heads, while maintaining almost constant circulation. The magnitude of vorticity in the detected vortices is much larger than the local rms spanwise vorticity. For the Reynolds-number range they studied, $R_\theta \leq 19 \times 10^3$, the vortices appear to scale universally in wall units with radii, r_0, of roughly 10–50 viscous units. They also appear to originate in the upper part of the buffer layer.

About the same time, Hambleton et al. [107] carried out simultaneous orthogonal plane PIV measurements in a turbulent boundary layer employing polarization of the light sheets in the two planes and polarized filters to eliminate the imaging of out-of-plane particles. The orientation of the planes were vertical (x–z) and horizontal (x–y). Here, z is the wall-normal direction, and y is spanwise. The data were processed using linear stochastic estimation (LSE) with positive and negative signed swirl (the imaginary part of the eigenvalue of, in this experiment, the two-dimensional velocity gradient tensor) as the conditioning vectors. The LSE required calculating the two-point correlation field of the conditioning swirl vector and the velocity components. Figure 50 shows the LSE field in (a) the vertical and (b) horizontal planes. The conditioning vector for this case was positive swirl at $z_{\mathrm{ref}}/\delta = 0.19$ indicated by the + in the vector field of (a). The vectors are all of unity length, so they only indicate direction. In the vertical plane, a spanwise-oriented vortex is clearly evident that is part of a ramp-like shear layer across the flow, similar to that shown in Figure 19. In the horizontal plane, two counter-rotating vortices are located just upstream of the conditioning location with an elongated region of low momentum between them that is terminated by an upstream saddle point just upstream of the dashed line. These features are consistent with a hairpin vortex structure of this LSE-constructed flow.

3.3.14. *2007 – Lagrangian structures*

Green et al. [108] have used an innovative analysis method from dynamical systems theory to detect Lagrangian structures in bounded flows. The method employs what are called direct or finite-time Lyapunov exponents (denoted as DLE or FTLE in the literature) to identify and characterize the structures. Although computationally intensive, requiring the full three-dimensional velocity field, this method has the considerable advantages of not requiring knowledge of velocity gradients, of being frame-rotational invariant and of not depending on arbitrarily chosen thresholds, in contrast to velocity gradient tensor-based methods. At every point in space, the DLE field is a scalar that characterizes, over a finite-time interval the degree of stretching of the flow about each location. The DLE scalar is a function of space and time, but is an integrated rather than instantaneous field. The authors compare structures from the DNS of a turbulent channel flow identified with the

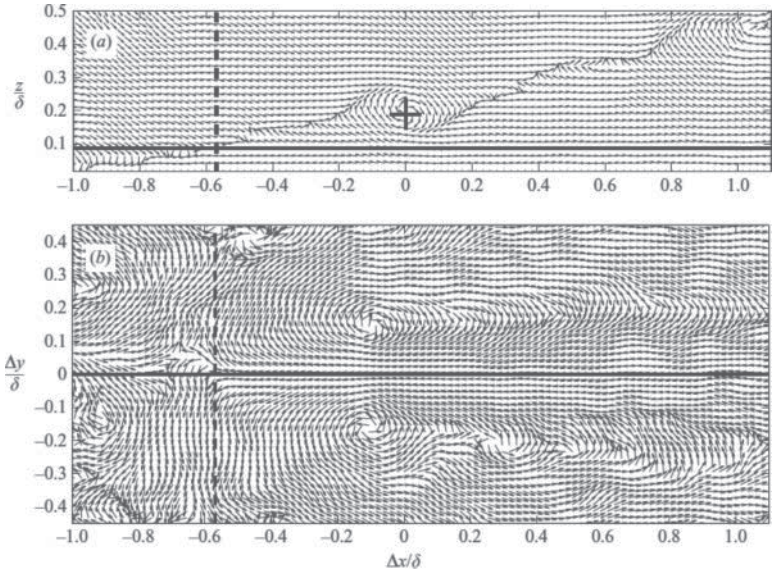


Figure 50. LSE field in (a) the vertical and (b) horizontal planes conditioned on positive swirl vector at $z_{\mathrm{ref}}/\delta = 0.19$ indicated by the $+$ in (a). The solid lines indicate the positions of the orthogonal light sheets. From Hambleton et al. [107], copyright ©2006 Cambridge University Press.

second invariant of the characteristic equation of the velocity gradient tensor (Q) criterion to those identified using the DLE method. These are shown in Figure 51 for a cross-stream (y–z) plane of a turbulent channel flow, where the correspondence is strikingly good.

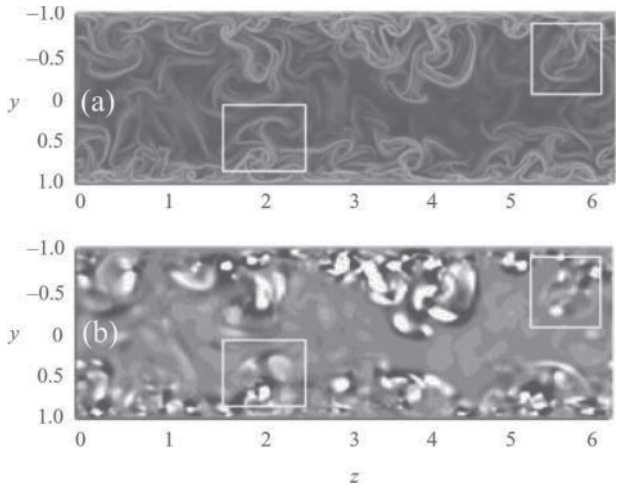


Figure 51. Comparison of structures in the boxes identified with (a) the direct Lyapunov exponent Lagrangian structure detection method to those identified with (b) the Q criterion in the cross-stream (y–z) plane of a turbulent channel flow DNS. From Green et al. [108], copyright ©2007 Cambridge University Press.

3.3.15. *2007 – very large-scale motions (VLSMs)*

A significant relatively recent discovery for all types of bounded shear flows is what are called VLSMs. Kim and Adrian [109] had observed VLSMs in a turbulent pipe flow almost a decade earlier, but they began to be more widely noted and studied about this time. Kim and Adrian had found that these coherent regions are largest in the logarithmic region, reaching scales 12–14 times longer than the pipe radius in the $0.25R < y < 0.45R$ part of the flow. Their observation was based on the pre-multiplied one-dimensional spectrum of the streamwise velocity fluctuations measured by hot-film anemometry. They conjectured that hairpin vortices align coherently in groups to form packets, and the packets themselves also align to form the VLSMs. Their sketch of this idea is shown in the companion overview paper by Kim [33] on turbulent pipe and channel flows in this special volume, so it will not be duplicated here.

Hutchins and Marusic [110] studied these VLSMs using a rake of hot-wires in two flows that extended over a decade in R_τ. They observed very long, up to 20δ, meandering stripes of positive and negative streamwise velocity fluctuations in the logarithmic and lower wake regions of the boundary layer which they compared to previous observations from PIV and DNS investigations. Notably, they concluded that the contribution to the streamwise velocity fluctuation intensities from these VLSMs increase with Reynolds number. In Figure 52(a), their one-dimensional pre-multiplied spectra of the streamwise velocity fluctuations at four Reynolds numbers illustrate this fact. They also concluded that these "superstructures" have an imprint on the near-wall region and seem to modulate it. In (b), their rake probe signals are shown for an orientation in a plane parallel to and at 0.15δ from the wall. The shading, that highlights negative streamwise fluctuations, clearly displays a VLSM for a laboratory boundary layer with $R_\tau = 14{,}380$. They also made measurements of the streamwise velocity fluctuations with an array of sonic anemometers, shown in (c), at the Utah field site at a height with respect to the surface of 0.037δ. The shading in (d) also is of negative streamwise fluctuations and also shows evidence of VLSMs for $R_\tau = 66 \times 10^4$ from these field measurements. These same authors analyzed the turbulent channel flow DNS of Del Álamo et al. [111] and observed VLSMs in this virtual flow. In the top two images of Figure 53, views of spanwise (x–y) planes at $z^+ = 15$ and 150 (here, y is spanwise and z is wall-normal) show grey scale shadings of the streamwise velocity fluctuations. The long, narrow VLSM structures are clearly visible, albeit at different scale for each location. However, in the lower two images, these planes of data have been low-pass filtered revealing the high degree of correlation between the two regions of the flow. The imprint of the logarithmic layer VLSM on the large-scale part of the buffer layer signal is clearly evident.

Mathis et al. [112] examined this imprint of the very large-scale structures in the logarithmic layer on the buffer and viscous layers, an effect previously observed by Metzger and Klewicki [88]. They showed that the imprint is on the amplitudes of the near-wall flow large scales, which, in turn, modulate the small-scale fluctuations there. A similar observation also had been made much earlier by Brown and Thomas [53], as described in 3.2.2 above, between the streamwise velocity fluctuations in the flow and the instantaneous shear stress at the wall. Mathis et al. [112] conclude, from the analysis of their data over three decades of Reynolds number, that this modulation becomes increasingly strong with increasing Reynolds number.

Ringuette et al. [113] investigated supersonic turbulent boundary layer structure using a DNS at Mach 3 and $R_\theta = 2600$. From contour plots of mass flux they also observed VLSMs, and these extended over as much as 100δ in the logarithmic layer. Furthermore,

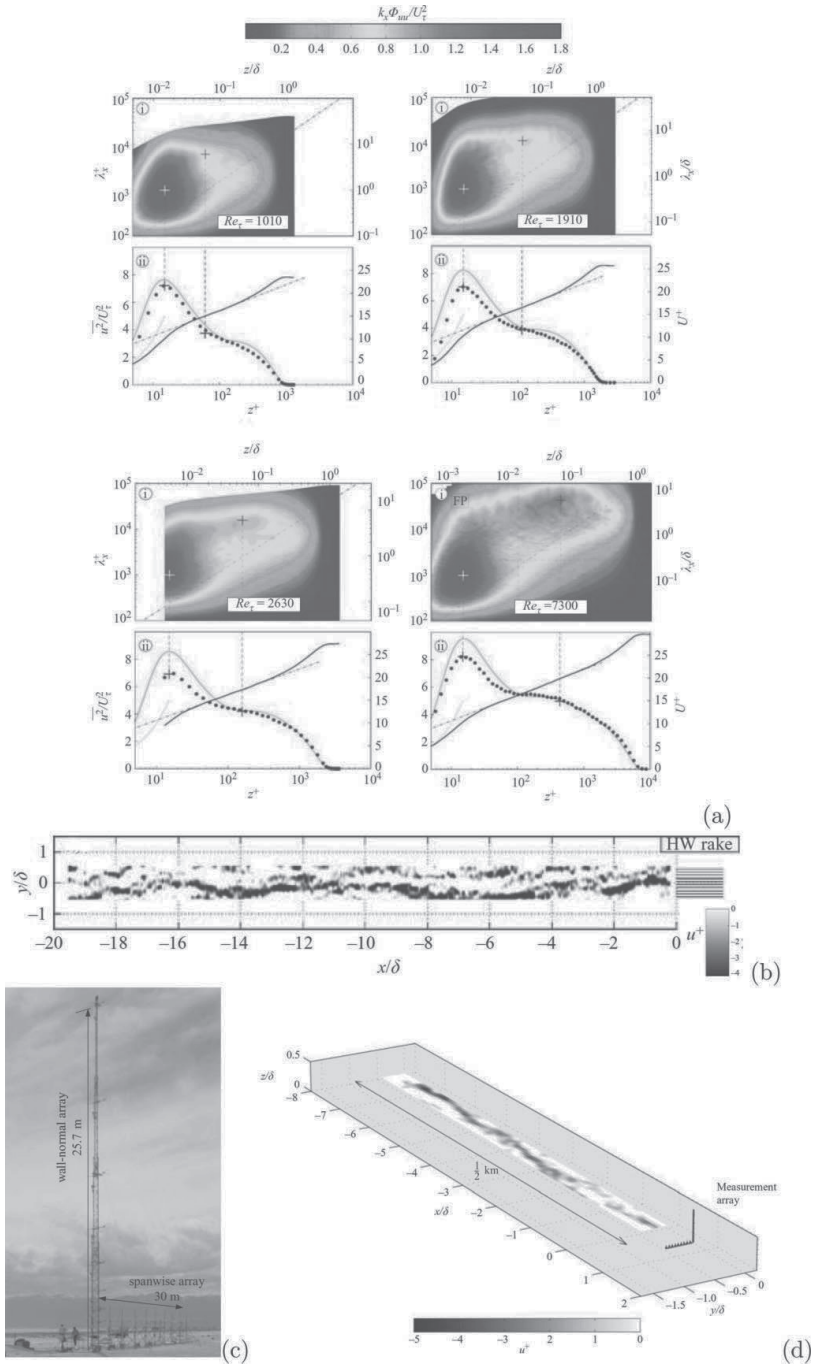


Figure 52. (a) One-dimensional pre-multiplied spectra of the streamwwise velocity fluctuations at two Reynolds numbers. (b) Streamwise velocity fluctuations from a rake of hot-wire probes oriented in a plane parallel to and at 0.15δ from the wall, with shading highlighting negative fluctuations. (c) Photograph of sonic anemometer array and tower at Utah field site. (d) Streamwise velocity fluctuations from a sonic anemometer located at 0.037δ above the ground, with shading highlighting negative fluctuations. From Hutchins and Marusic [110], copyright ©2007 Cambridge University Press.

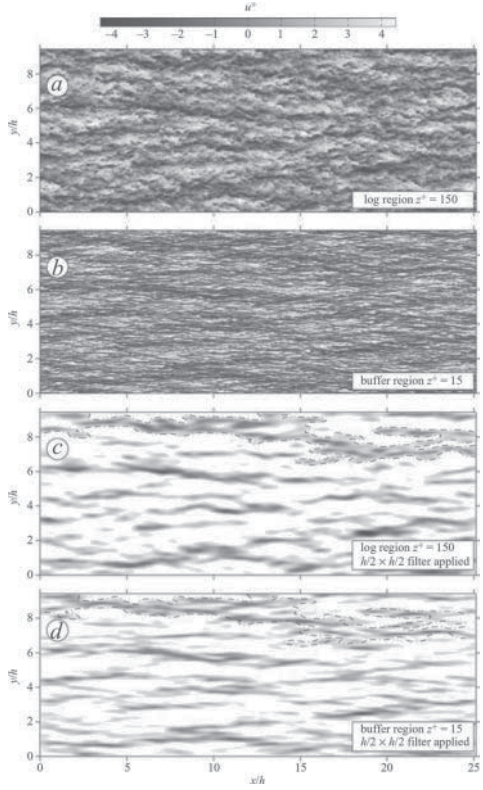


Figure 53. e) Views of spanwise (x–y) planes at $z^+ = 15$ and 150 with (upper) grey scale shadings of streamwise velocity fluctuations, and (lower) the data in these planes low-pass filtered and revealing the high degree of correlation between the two regions of the flow. From Hutchins and Marusic [110], copyright ©2007 Cambridge University Press.

they observed that hairpin packets appear to be primarily located above the long, meandering zones of low-momentum fluid, as previously suggested by Kim and Adrian [109]. Figure 54 shows color contours of low-momentum fluid at the top of the buffer layer viewed from above. The tick marks on the two horizontal black lines show locations of hairpin vortices detected by an algorithm they designed. The upper black line, with many more tick marks than the lower one, intersects the low-momentum regions much more than the higher momentum regions.

3.3.16. *2011 – hypersonic boundary layer DNS*

Duan et al. [114], of this same computational group, extended this DNS study of boundary layers to the hypersonic range. Their computations spanned nominal free-stream Mach numbers from $M = 0.3$–12 and Reynolds number ranging from $R_\theta = 1515$–11,356. The main goal of their work was to test the weak compressibility hypothesis over this range of conditions, and they found that it holds except for some increase in thermodynamic fluctuations. Figure 55(a) shows the turbulent kinetic energy budget, where it is evident that the distributions are relatively insensitive to this large variation of conditions when normalized with "semi-local units" (where, for the definitions of the friction velocity and

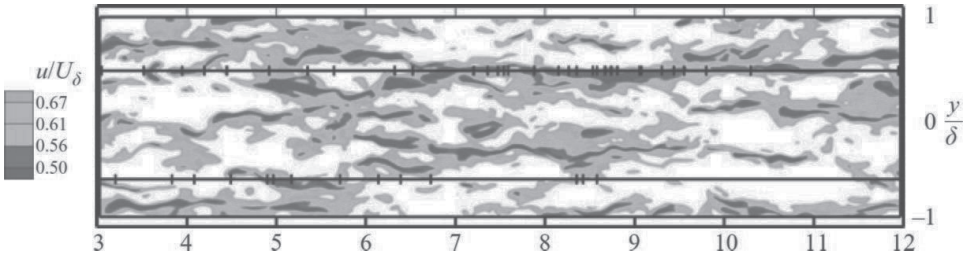


Figure 54. Contours of low-momentum fluid in a spanwise (horizontal) plane at the top of the buffer layer. Tick marks indicate locations of hairpin vortices in the streamwise (vertical) planes indicated by the black lines. From Ringuette et al. [113], copyright ©2011 Cambridge University Press.

the wall-normal location in viscous units, the wall value of the average fluid density is replaced with the local value of the average). In (b), wall-parallel planes of the boundary layer at the top of the viscous sublayer are shown, for Mach 0, 3 and 12, in which surfaces of ρu fluctuations are highlighted. Elongated low-momentum streaks are evident and are similar to each other over this Mach number range.

About the same time as the study of Ringuette et al. [113], Pirozzoli et al. [115] also completed an extensive DNS study to characterize coherent vortical structures in a spatially developing turbulent boundary layer at Mach 2 and $R_\theta = 1350$. They found that this compressible boundary layer had many similarities with incompressible ones, including an inner layer dominated by quasi-streamwise vortices and an outer layer with, among other structures, hairpins and hairpin packets. For the outer layer, they conclude that the statistically most representative structure is a vortex ring, of about 27–35 Kolmogorov lengths, η, in overall size with a core radius of 5–6η, and that is inclined at about 20° to the wall plane. It is illustrated in the sketch in Figure 56(a). This structure is similar to the "typical eddies" of Falco [116] and like that postulated by Klewicki and Falco [117] based on observations of both positive and negative spanwise vorticity events in this region. Using the same supersonic DNS, Pirozzoli et al. [118] performed a further study in which they devised

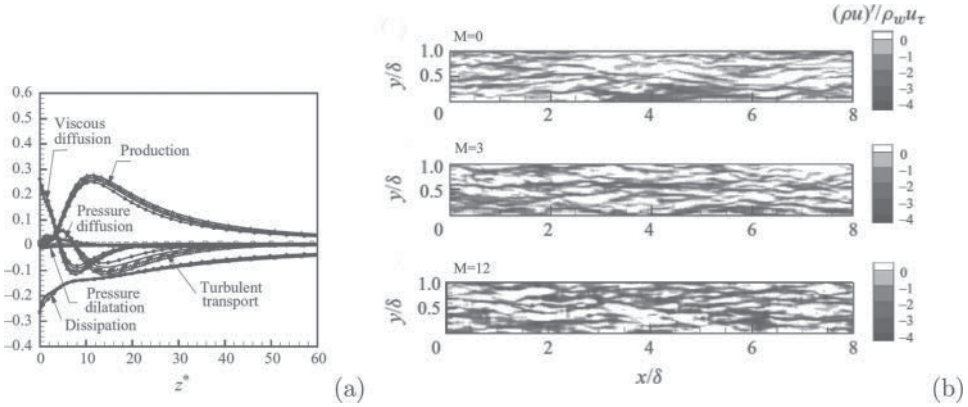


Figure 55. (a) Turbulent kinetic energy budget for $M = 0.3$–12, $R_\theta = 1515$–11, 356 and (b) elongated low-momentum regions at Mach 0, 3 and 12. From Duan et al. [114], copyright ©2011 Cambridge University Press.

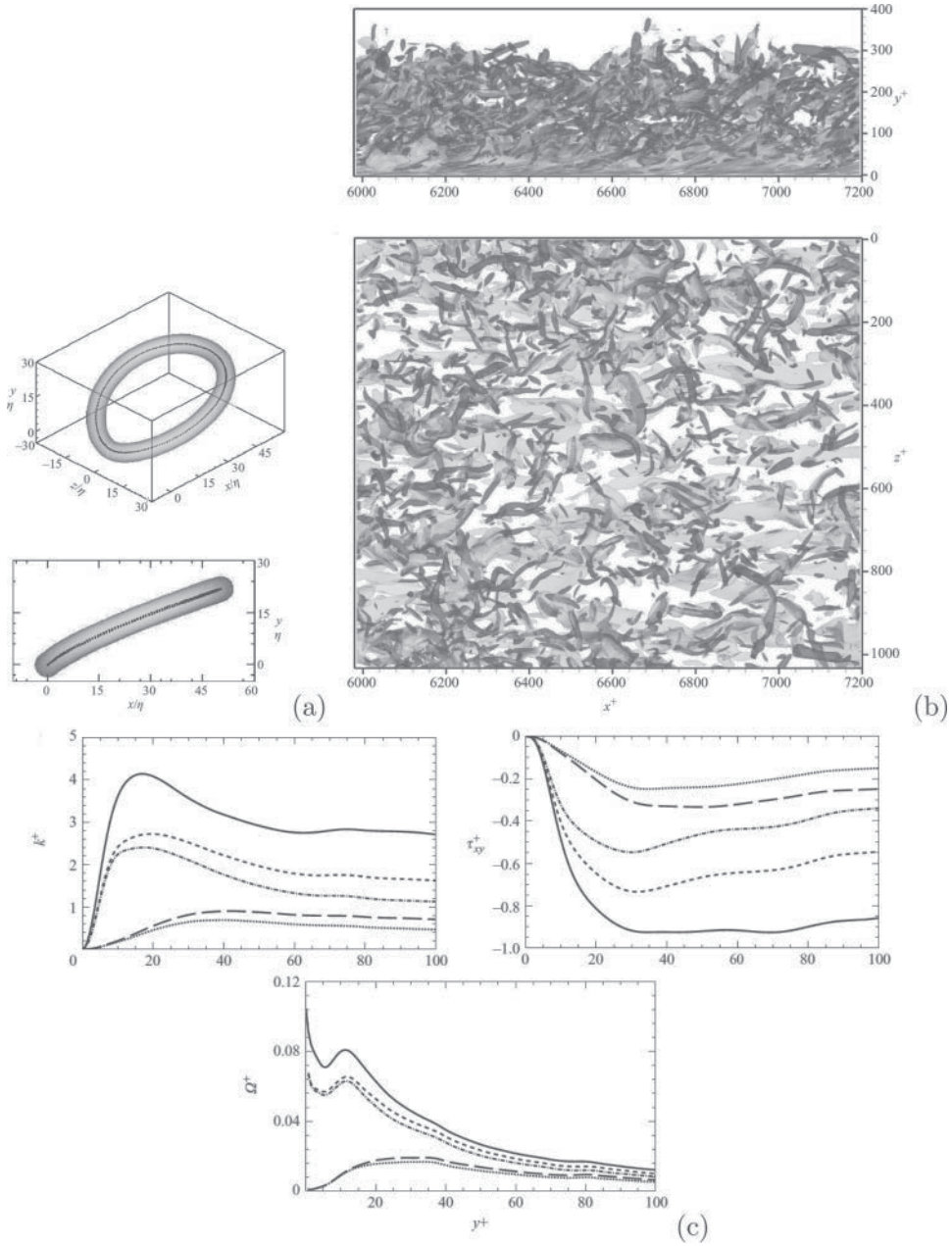


Figure 56. (a) Sketch of a statistically representative vortex ring structure in the outer region of a supersonic turbulent boundary layer. From Pirozzoli et al. [115], copyright ©2008 Cambridge University Press. (b) Streamwise (upper) and spanwise (lower) planes showing isosurfaces of tube (darker grey) and sheet (lighter grey) structures. (c) Contributions to turbulent kinetic energy, Reynolds shear stress and enstrophy from full DNS (solid line), vortex sheets (dash–dot) and vortex tubes (long dashes), as well as from two other event categories. Both from Pirozzoli et al. [118], copyright ©2010 Cambridge University Press.

an algorithm to separate vortex tube structures from vortex sheet structures, a division dating back at least to the work of She et al. [119] for a homogeneous isotropic turbulence DNS, and probably much further. Such tube (darker grey) and sheet (lighter grey) structures are shown in (b) for streamwise (x–y) and spanwise (x–z) planes. In the streamwise plane, it is evident that near the wall the sheet-type structures are much more prevalent, with the tube-type structures becoming increasingly prevalent further from the wall. From the spanwise plane view, the authors conclude that both cane-like and hairpin-like tubes are present. In (c), they plot the contributions to the turbulent kinetic energy, the Reynolds shear stress and the enstrophy from vortex sheets, vortex tubes, "strong vorticity events"and "roll-up events". For the purposes considered here, it is important only to note that the contributions to all three properties from the vortex sheet-type structures are considerably greater than that from the vortex tube-type structures. The authors conclude that vortex sheet structures have a dynamically more important cumulative effect in turbulent boundary layers than vortex tubes.

In a recent pair of papers, Lagha et al. [120, 121] also carried out supersonic and hypersonic DNS of zero pressure gradient boundary layers for a Mach number range of 2.5–20 and R_τ between 300 and 345. Turbulence statistics of both the velocity and vorticity fields were found to be very similar to those for incompressible boundary layers when the variable density was taken into account. Even low-speed streak spacings were about 100 viscous lengths at the low and high Mach numbers of 2.5 and 20, as seen in Figure 57(a) which shows contours of constant streamwise velocity fluctuations. By examining in detail the $M = 2.5$ case in the second paper, they demonstrated that the turbulence in the near-wall region is locally self-sustaining without fluctuations in the free-stream. They split the wall-normal velocity component into a coherent part, associated with vortices that fill the near-wall region, and an incoherent background part. When the latter part was dampened, the flow was little changed demonstrating the predominance of the coherent structures in determining the flow dynamics. The flow in this region is dominated by crescent-shaped vortices associated with Q2 and Q4 Reynolds shear stress at $y^+ = 15$, as seen in (b).

3.3.17. *2009 – spatially developing boundary layer DNS*

Near the end of this decade, Wu and Moin [122] carried out a DNS of a turbulent boundary layer that developed spatially from an initial Blasius profile, through by-pass transition, to a developed turbulent state, albeit at the low-Reynolds number of $R_\theta \approx 900$ at the downstream end of the computational domain. The free-stream flow above the boundary layer was perturbed by the passage of periodic patches of turbulence. The two images in Figure 58 show isosurfaces of Q in the instantaneous field (a) upstream in the transitional state within two turbulent spots, and (b) in the developed flow downstream. The color variation indicates local values of the streamwise velocity, with red indicating higher values (generally at positions further from the wall). In both the turbulent transitional spots and in the developed turbulence downstream, the images are filled with hairpin-like loops. These observations created quite a stir in the turbulence research community because such readily apparent hairpins had not been observed in experiments or DNS since the visualizations of Head and Bandyopadhyay [54]. It was questioned whether or not such pristine hairpins would continue to be apparent further downstream at higher Reynolds numbers. Wu and Moin [123] extended this DNS to $R_\theta \approx 1950$ and added constant passive heating of the wall. At higher Reynolds numbers, the vortical structure of the flow becomes visually more complex.

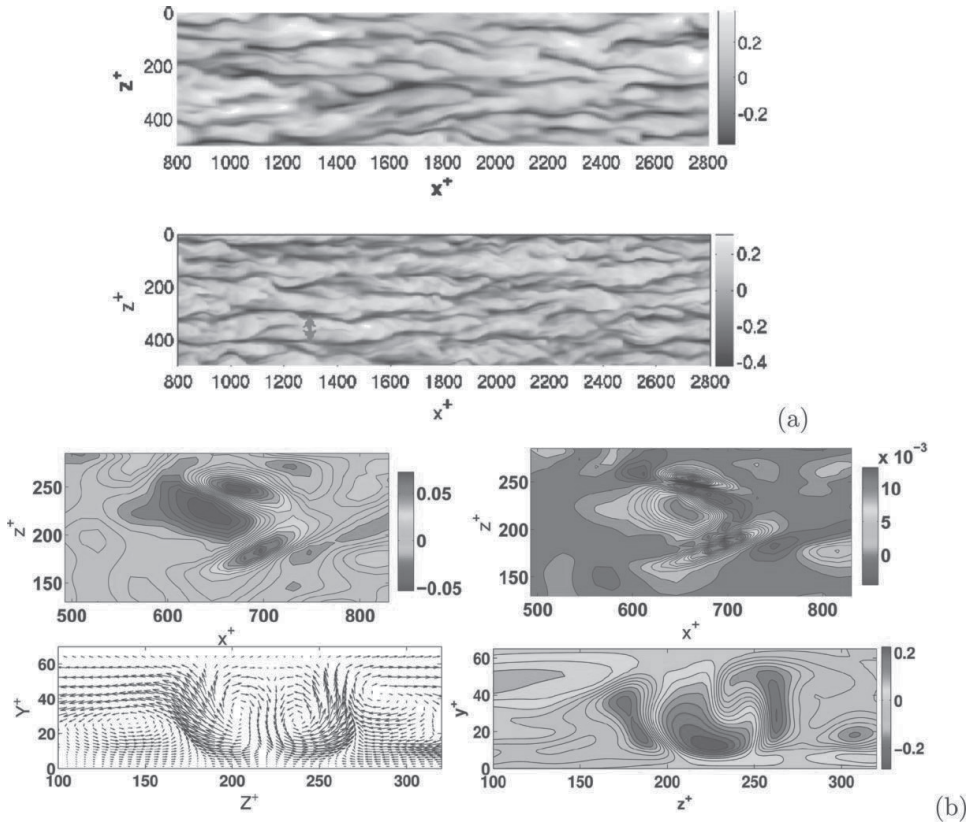


Figure 57. (a) Streamwise velocity perturbations at $y^+ = 15$ in the x–z plane for $M = 2.5$ (upper) and $M = 20$ (lower) and reprinted with permission from Lagha et al. [120]. Copyright ©2011 American Institute of Physics. Red arrows indicate 100 viscous lengths. (b) Top row from left to right: wall normal velocity and $-uv$ Reynolds shear stress at $y^+ = 15$ in the x–z plane for $M = 2.5$. Bottom row from left to right: projection of fluctuation velocity vectors on cross-stream (y–z) plane and contours of streamwise velocity fluctuation levels in this plane. Reprinted with permission from Lagha et al. [121]. Copyright ©2011 American Institute of Physics.

Park et al. [124] used the DNS of Wu and Moin [123] to compare flow statistics, including those based on the velocity gradient tensor, from isolated turbulent spots in transition to those for the developed turbulence at $R_\theta \approx 1840$. Figure 59(a) shows the evolution of the coefficient of friction, C_f, in the boundary layer as a function of Reynolds number from the Wu and Moin [123] paper. Also shown in (a) are C_f values for transitional flow at $R_\theta \approx 300$ and 500 which were extracted conditionally from the spots, excluding any non-turbulent data. The conditional transition values clearly comport with the values in the developed turbulence regime. In (b), distributions of enstrophy and dissipation rate are compared for the two transition states to the developed state. The enstrophy and dissipation rate distributions are similar to each other, and they do not change much between the transitional and developed states. Park et al. [124] also did an octant analysis based on the eight combinations of signs of the u, v and θ (temperature) fluctuations, and the distributions of the momentum and heat fluxes are shown in (c) for the transitional and developed Reynolds numbers. Octants 2 and 8, that comport with mean

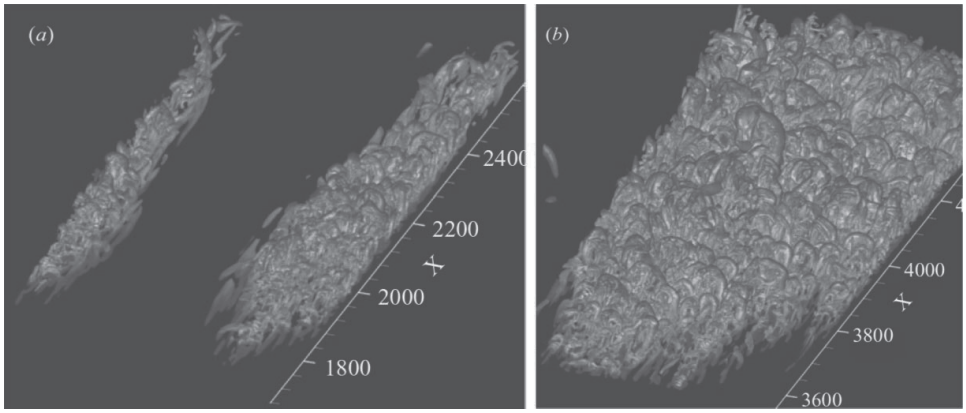


Figure 58. Isosurfaces of Q within (a) two turbulent spots and (b) at $R_\theta \approx 900$ in developed turbulence. From Wu and Moin [122], copyright ©2009 Cambridge University Press.

gradient-type transport, dominate across the wall layer. Furthermore, this pattern is maintained for both the transitional and developed turbulence states. The authors concluded that these comparisons provide strong evidence that the non-linear processes, operable in transition to generate and sustain turbulence when it first appears and the turbulent spots take on a definite structure, must be similar to the processes in the developed turbulence, even though the structure there is more complex.

Schlatter et al. [125] also performed a spatially developing DNS for Reynolds numbers up to $R_\theta = 4300$. In Figure 60, their (a) mean (at four Reynolds numbers and compared to their experimental data at $Re_\theta = 2541$) and (b) Reynolds normal and shear stress distributions are shown. They did not observe hairpin vortices at the highest Reynolds number of their simulated flow. In Schlatter and Örlü [126], they have carefully compared, for consistency, statistical properties from their DNS to those from other DNS studies. From Schlatter et al. [127], for this same DNS, pre-multiplied spanwise spectra of the streamwise velocity fluctuations are shown in (c). They display evidence of the VLSM contributions at high wavelength for the flow at $R_\theta = 4300$.

Jiménez et al. [128] have compared the characteristics of a spatially developing turbulent boundary layer DNS, with Reynolds numbers up to $Re_\theta = 1970$ and $\delta^+ = 692$, to those of channel flow DNS at $\delta^+ = 935$. Figure 61(a) shows a streamwise (x–y) plane of the rms vorticity fluctuation magnitude in which the deep incursion of boundary layer potential fluid is evident, just as they are in the photograph in Figure 22 at a similar Reynolds number. Their intermittency distribution is shown in (b) for $Re_\theta = 1100$, 1550 and 1970, where it is compared to earlier experimental measurements. In (c), isosurfaces of the discriminant of the velocity gradient tensor are shown, colored by distance from the wall. The figure shows features above about $y/\delta = 0.3$–0.4, where a complex structure is apparent with some hairpin-like loops appearing in the outer part of the flow, but certainly not dominating it.

In a very recent study by Lozano-Durán et al. [129], this same research group has expanded the use of quadrant analysis to identify three-dimensional quadrant structures (Qs) in the logarithmic and outer regions of turbulent channel flow. They differentiate between what they call wall-attached and wall-detached Qs. The former are larger and carry most of the Reynolds shear stress, while the latter are described as small, isotropic, background stress fluctuations that largely cancel each other out and thus contribute little

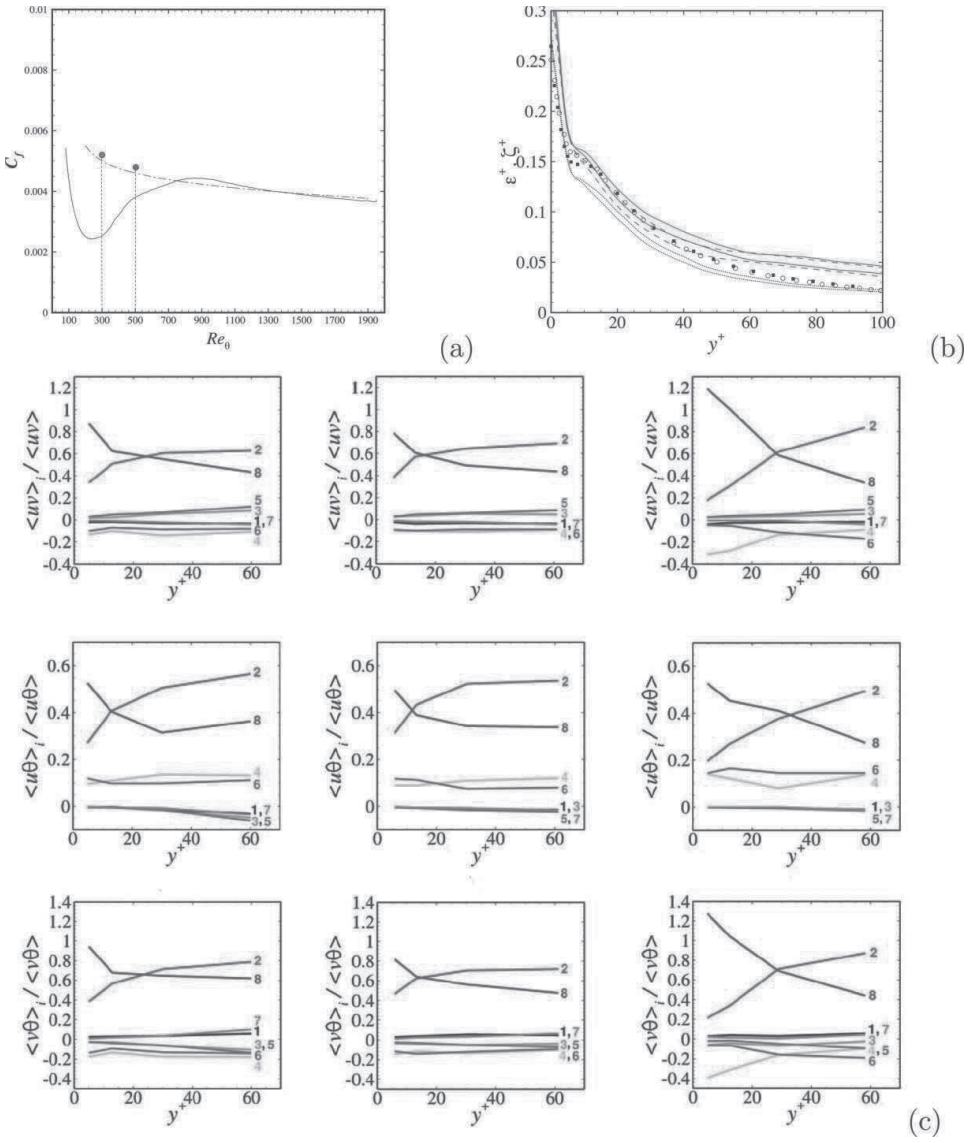


Figure 59. (a) Coefficient of friction as a function of R_θ. The two points (red and blue circles) for the transitional states were averaged only when the local flow was turbulent. (b) Distributions of enstrophy and dissipation rate for transitional and developed states and (c) distributions of the fractional contributions from octants to momentum and heat fluxes for the transitional and developed states (columns from left to right: $R_\theta = 1840$, 500 and 300. Reprinted with permission from Park et al. [124]. Copyright ©2012 American Institute of Physics.

to the mean stress. In the outer flow, the stress is mainly due to a few large Q regions. In the logarithmic layer, the predominant Qs are Q2 and Q4 regions flanking three-dimensional vortex clusters. When the DNS data are conditioned on the simultaneous occurrence of Q2 and Q4 pairs, the image in Figure 62 emerges. Here, the Q2 region (green) surrounds the vortex cluster with the Q4 region (blue) on the other side and above the cluster. The authors

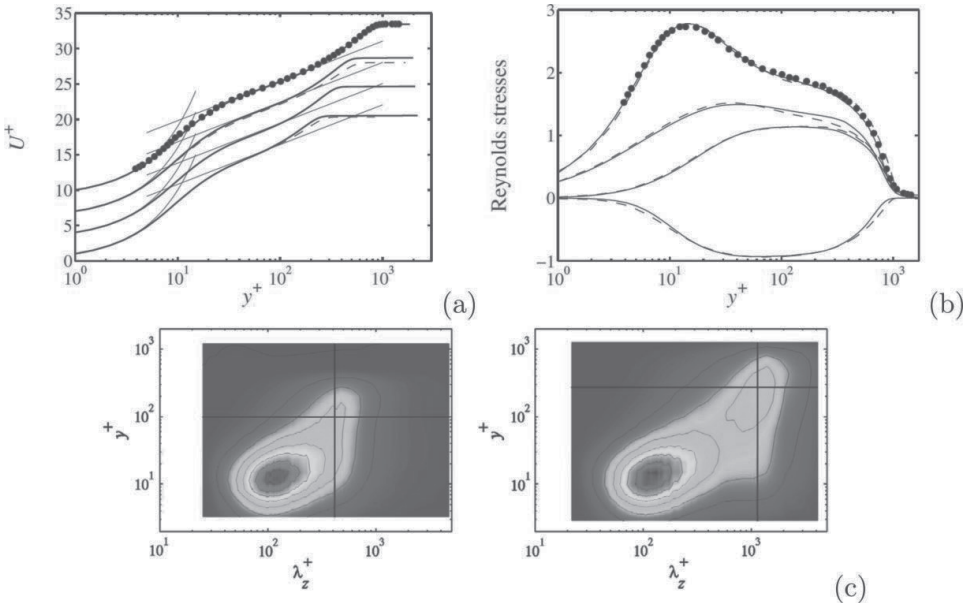


Figure 60. (a) Mean velocity profiles and (b) Reynolds normal and shear stress distributions compared to their experimental data at $Re_\theta = 2541$ and reprinted with permission from Schlatter et al. [125] Copyright ©2009. (c) Pre-multiplied one-dimensional spectra of the streamwise velocity fluctuations at $R_\theta = 1400$ (left) and 4300 (right) from Schlatter et al. [127] with permission of Elsevier.

point out that this conditionally average shape is not representative of instantaneous Qs and vortex clusters, which are more complex and are described as "sponges of flakes" and "sponges of strings", respectively.

3.3.18. *2009 – stereo, holographic and tomographic PIV and PTV*

Recently, optical methods have further developed making stereo, holographic and tomographic PIV and PTV (particle tracking velocimetry) applications for turbulent boundary layers possible. Sheng et al. [130] used digital holographic PTV to study the wall layer structure in a square duct at $Re_\tau = 1470$. Figure 63 shows their conditionally averaged vorticity lines, isosurfaces of Q and wall shear stress. The conditioning is based on the minima of wall shear stress events. The authors state that all the conditionally averaged features appear in almost all of the individual realizations that make up the conditionally sampled set. The wall shear stress minima occurs between the counter-rotating legs of the vortices where the fluid is ejected from the wall, and the maxima occur on the outboard sides of the legs where there is a downwash of sweep-type fluid.

Elsinga et al. [131] used tomographic PIV to study a Mach 2 supersonic boundary layer with $R_\theta = 34 \times 10^3$. Figure 64(a) shows an oblique view of the boundary layer from above with isosurfaces of Q indicating vortices riding over elongated VLSMs of low-speed fluid. In (b), a close-up view of the region boxed-in with red lines is shown along with the projections of the velocity vectors in a streamwise (x–y) plane cut through the box. Here, a series of arch-like vortices span the low-speed region. The authors observe that

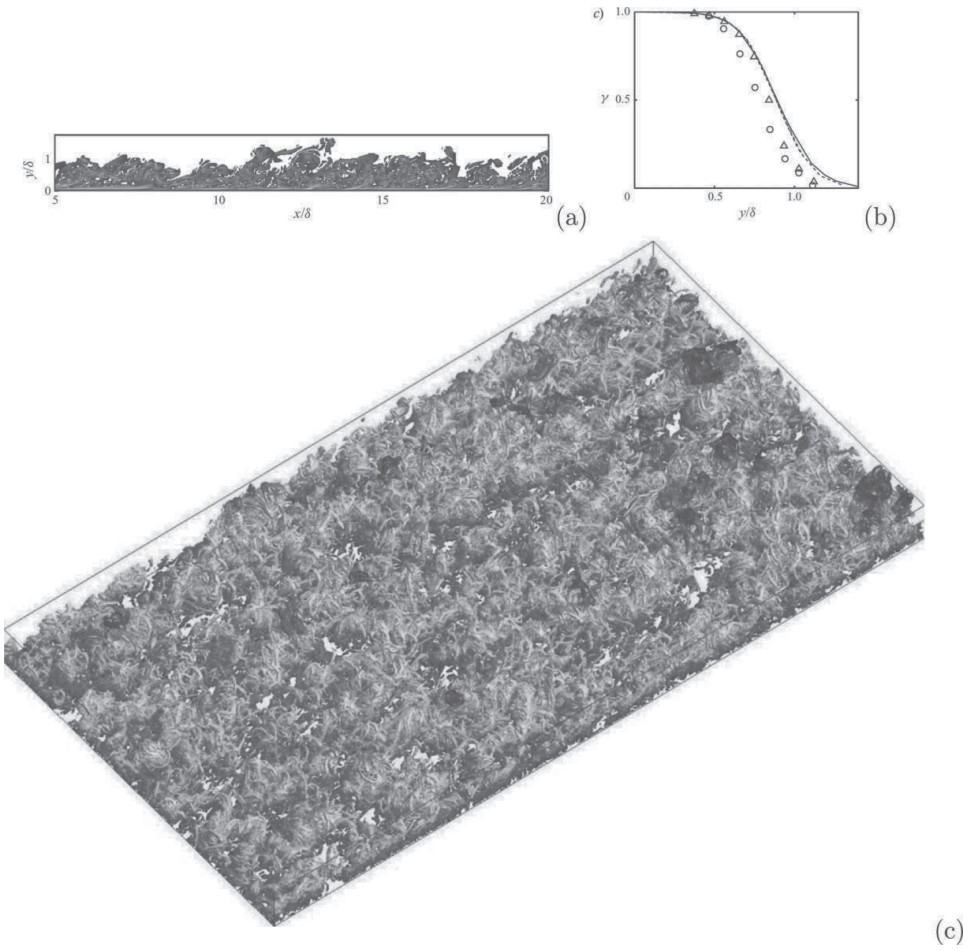


Figure 61. (a) rms vorticity fluctuation magnitude and (b) intermittency distribution for $Re_\theta = 1100$, 1550 and 1970 (lines) for boundary layer DNS compared to earlier experimental data (symbols). (c) Isosurfaces of the discriminant of the velocity gradient tensor for $Re_\theta = 1420$–1900, colored by distance from the wall ($y/\delta = 0.3 - 0.4$, deepest blue, $y \approx \delta$, brightest red). From Jiménez et al. [128], copyright ©2010 Cambridge University Press.

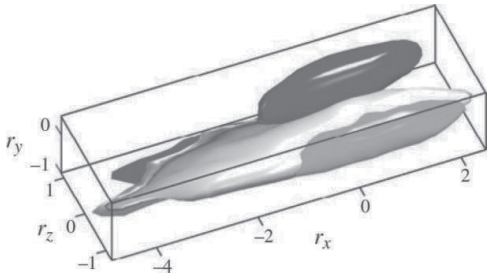


Figure 62. Conditionally averaged Q2 (green) and Q4 (blue) Reynolds shear stress regions flanking a vortex cluster region (grey). From Lozano-Durán et al. [129], copyright ©2012 Cambridge University Press.

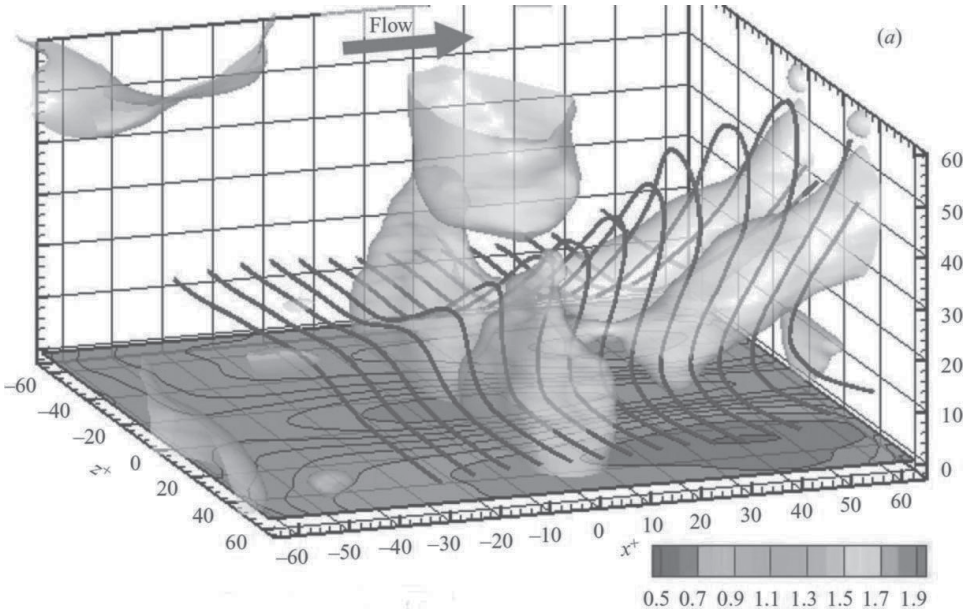


Figure 63. Conditionally averaged vorticity lines (blue), isosurfaces of the second invariant of the velocity gradient tensor, Q, (white) and wall shear stress (colored contours). From Sheng et al. [130], copyright ©2009 Cambridge University Press.

these vortices not only appear to be aligned in the streamwise direction, but also along 45° diagonals in the x–z plane.

In a study using stereo-PIV, Dennis and Nickels [132] obtained evidence for hairpin packets using conditional sampling from a turbulent boundary layer at $Re_\theta = 4700$. Vortices were identified using the swirling strength criterion of Zhou et al. [101]. In Figure 65(a), vortices (black), a long low-speed region (blue) and an adjacent high-speed region (red) are shown in a view looking down on the boundary layer. Clearly, the vortical activity is principally associated with the low-speed region. The authors state the length of the low-speed region is deceptive, because it is, as seen in other views, made up of several closely spaced low-speed regions. In (b), conditional averaged swirling fields are plotted, given spanwise swirl, from the three-dimensional data. In contrast to the asymmetric and partial hairpins from the instantaneous field in (a), the conditional averaged vortices take the form of symmetric hairpins that increase in scale with distance from the wall and are inclined at 35–40° downstream. Dennis and Nickels [132] conclude that the hairpin packet is a good "representative eddy" for a statistical model of the turbulent boundary layer structure.

Lee and Song [133] also used a boundary layer DNS, over a Reynolds number range up to $R_\theta = 2560$, to study the relationship between the VLSMs and the vortical structure of the flow. They confirmed many of the previous findings, viz. that the long, low-momentum flow regions, extending downstream up to 6δ, appear to be associated with, and even are created by, coherent, roughly streamwise aligned, hairpin-like vortices, often occurring in adjacent packets. The vortices appear to drive the momentum transport, as evidenced by concentrations of Q2 and Q4 Reynolds shear stress and their spatial relationship to the vortices. The packets increase in spanwise scale as they evolve downstream. Figure 66(a) shows a view from above the boundary layer of a spanwise (x–z) plane at $y/\delta = 0.18$ ($y^+ = 100$) that is 8δ in length. The velocity vectors are shown in a frame of reference

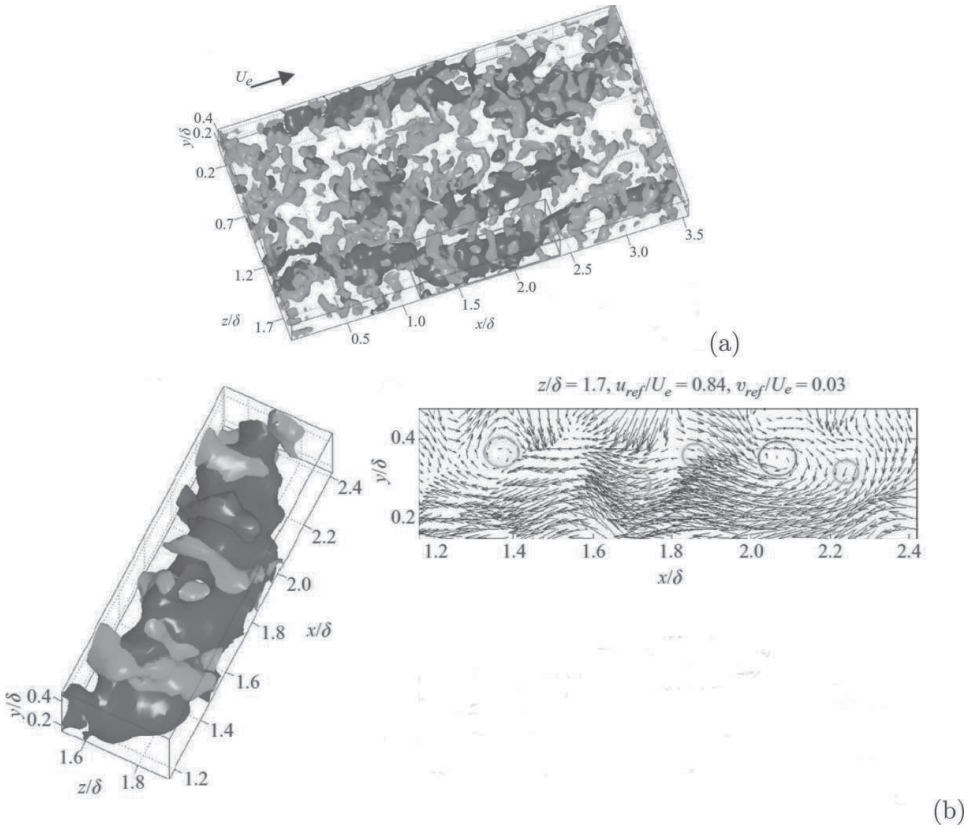


Figure 64. (a) Oblique view of a Mach 2 supersonic boundary layer from above with isosurfaces of Q (green) indicating vortices riding over elongated VLSMs of low-speed fluid (blue). (b) Zoomed in view of region in red-lined rectangular box with the projections of the velocity vectors in a streamwise $(x - y)$ plane and the vortices in this plane marked by the green and red circles. From Elsinga et al. [131], copyright ©2010 Cambridge University Press.

moving with the flow at $0.68U_\infty$. The solid lines trace the locations where the velocity fluctuations are $u^+ = -1$, and the red and blue marked regions indicate positive and negative wall-normal, two-dimensional swirl strength. It is evident from the figure that the swirling motions are roughly proximate to the VLSM regions of low momentum. In (b), isosurfaces of three-dimensional swirl strength are shown for the same domain of the flow. It is clear that many vortical structures, inclined downstream, cut through the planes that are marked A, B and C in both the (a) and (b) parts of the figure.

Guala et al. [134] used rakes of single-sensor hot-wire probes as well as a tower of sonic anemometers at the Utah field site, as shown in Figure 67(a), to study interactions between scales of turbulence from the VLSMs to the dissipative scales. They found that the signature of the VLSMS is evident throughout the wall layer affecting the energy contained in the dissipative scales in this region. In (b), low- and high-pass signals from the streamwise fluctuation measurements at distances from the surface of 20, 762, 4033, 19,296 and 40,547 viscous lengths are shown. The VLSM signatures are seen in the highly correlated low-pass filtered signals, and it is evident that, especially near the surface, at times when the low-pass filtered signal is large, the high-pass signal has greater amplitudes, and vice versa. They

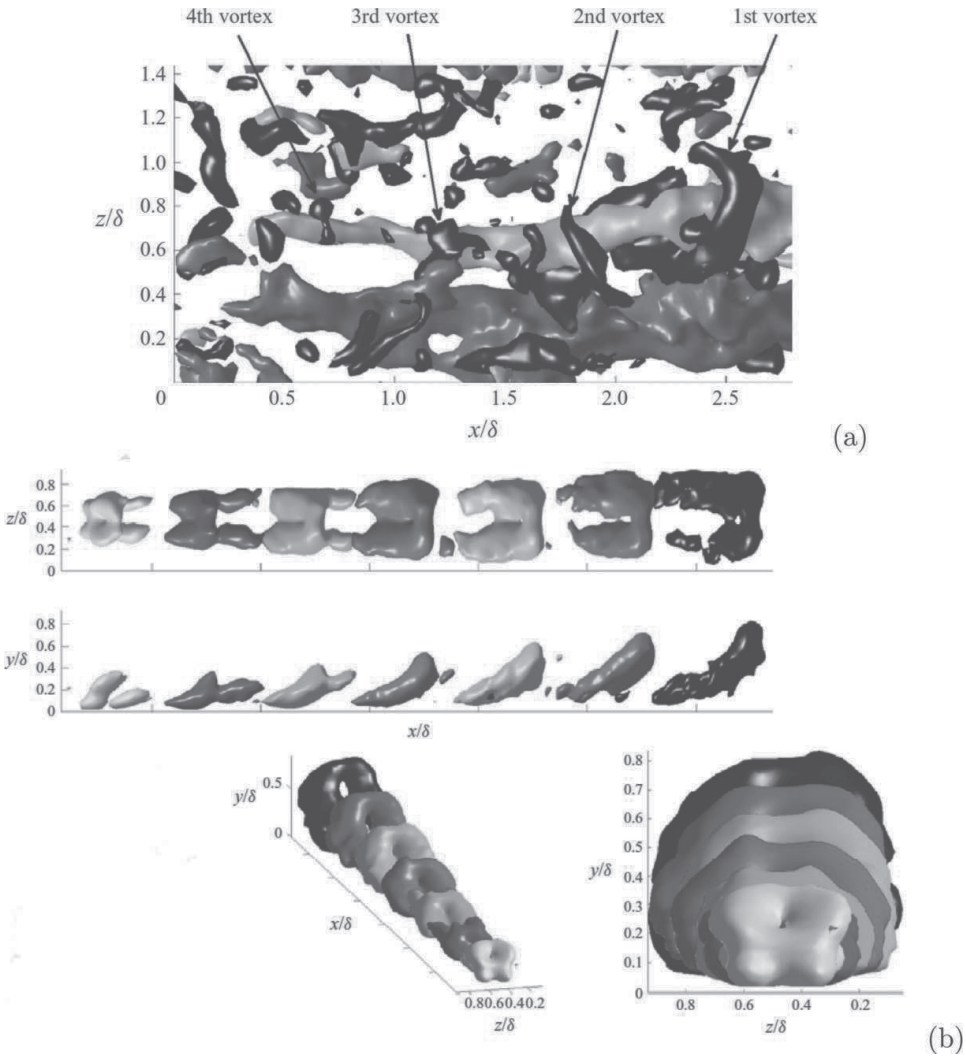


Figure 65. (a) View of the boundary layer from above with isosurfaces of swirling strength (black) indicating vortices principally riding over regions of low-speed fluid (blue) with regions of high-speed fluid (red) adjacent. (b) Conditional averaged swirling fields, given spanwise swirl, showing hairpin vortices which increase in scale with distance from the wall. From Dennis and Nickels [132], copyright ©2011 Cambridge University Press.

observed that this is also true for the isotropic estimate of the dissipation rate obtained from the time derivative of the velocity fluctuations. This modulation of the small scales by the VLSMs is consistent with the observations of Mathis et al. [112] noted earlier.

Similar to Green et al. [108], Yang and Pullin [135] compared structures in a turbulent channel flow DNS by tracking Lagrangian scalars to obtain material surfaces and also by viewing instantaneous swirling strength contours in the Eulerian field. Furthermore, they did a multi-scale and multi-directional analysis by making use of the mirror-extended curvelet transform. They defined an inclination angle in the streamwise (x–y) plane and a sweep angle in the wall parallel (x–z) plane, and found that both these angles increase with

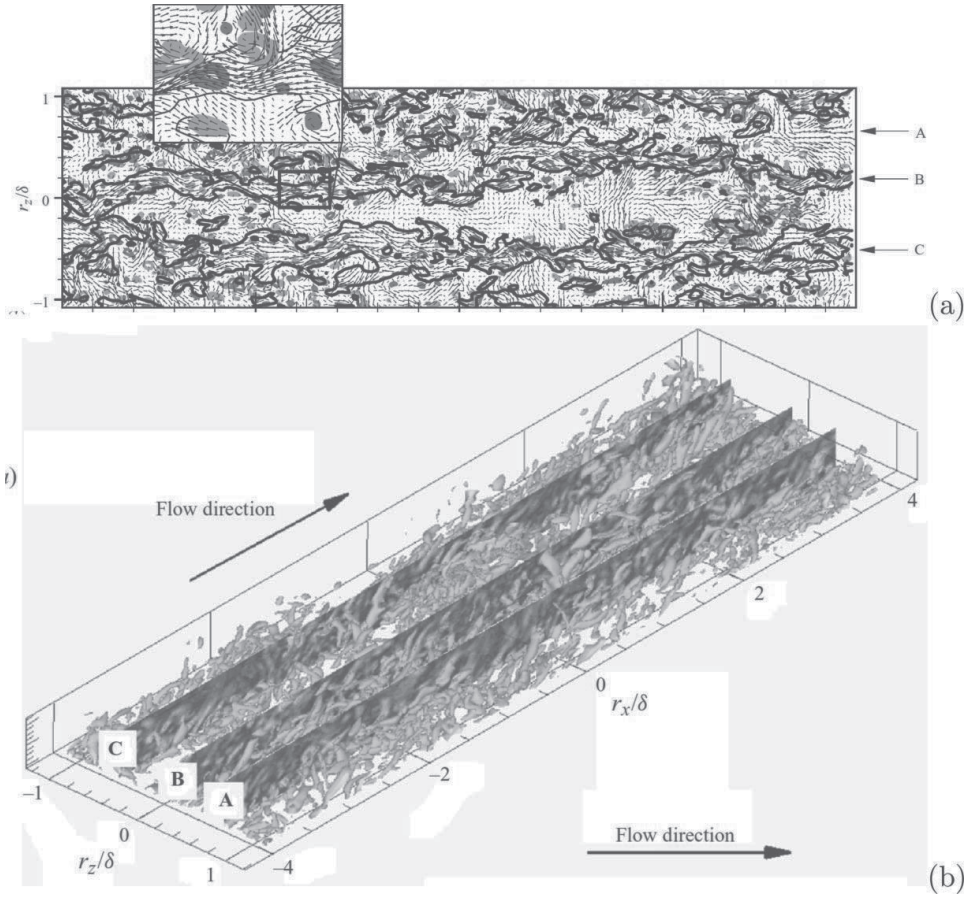


Figure 66. (a) Plan view of spanwise plane at $y/\delta = 0.18$ ($y^+ = 100$) with velocity vectors indicated in a frame of reference moving with the flow at $0.68U_\infty$. Solid lines trace the locations where the velocity fluctuations are $u^+ = -1$, and the red- and blue-marked regions indicate positive and negative wall-normal two-dimensional swirl strength. (b) Isosurfaces of three-dimensional swirl strength are shown for the same domain. From Lee and Song [133], copyright ©2011 Cambridge University Press.

time for the Lagrangian structures. The Eulerian structures near the wall have an average downstream inclination angle of 35–45° and sweep angle of 30–40° with an average scale of about 20 viscous lengths. Closer to the wall, the "legs" of these structures are less inclined and swept and are of smaller scale. They also observed that the structures occur in packets.

3.3.19. *Wavelet analysis of boundary layers*

Finally, a study, involving two of the organizers of the 2011 Marseille Colloquium, was carried out by Khujdaze et al. [136]. They used orthogonal anisotropic wavelets to analyze a turbulent boundary layer DNS at $R_\theta = 1470$ and where fringe rescaling was employed in order to exploit periodic boundary conditions in the streamwise direction. The vorticity field was decomposed into coherent and incoherent contributions by thresholding the wavelet

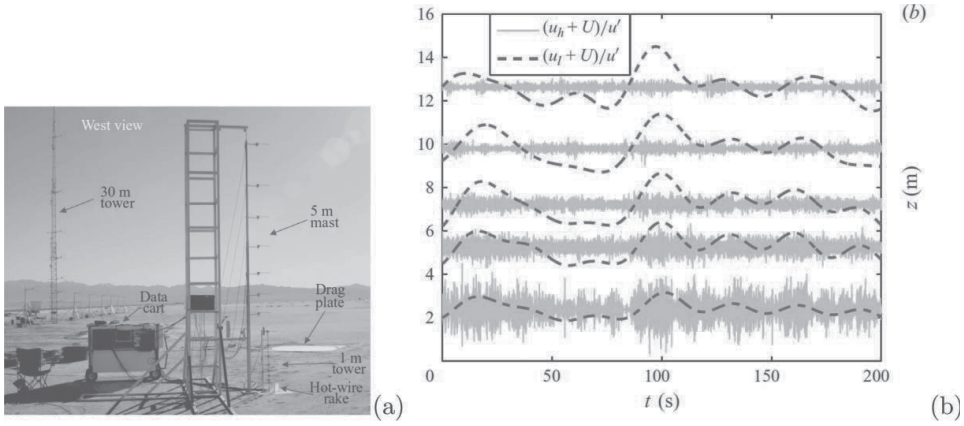


Figure 67. (a) Experimental setup at the Utah field site and (b) high- and low-pass filtered signals from a rake of hot-wire probes above the surface at (from bottom to top) 20, 762, 4033, 19,296 and 40,547 viscous lengths. From Guala et al. [134], copyright ©2011 Cambridge University Press.

coefficients. They found that less than 1% of the coefficients revealed the coherent structures in the boundary layer with the rest associated with the structureless background flow. Figure 68 displays isosurfaces of wall-normal vorticity where the coherent part is almost identical to the total field.

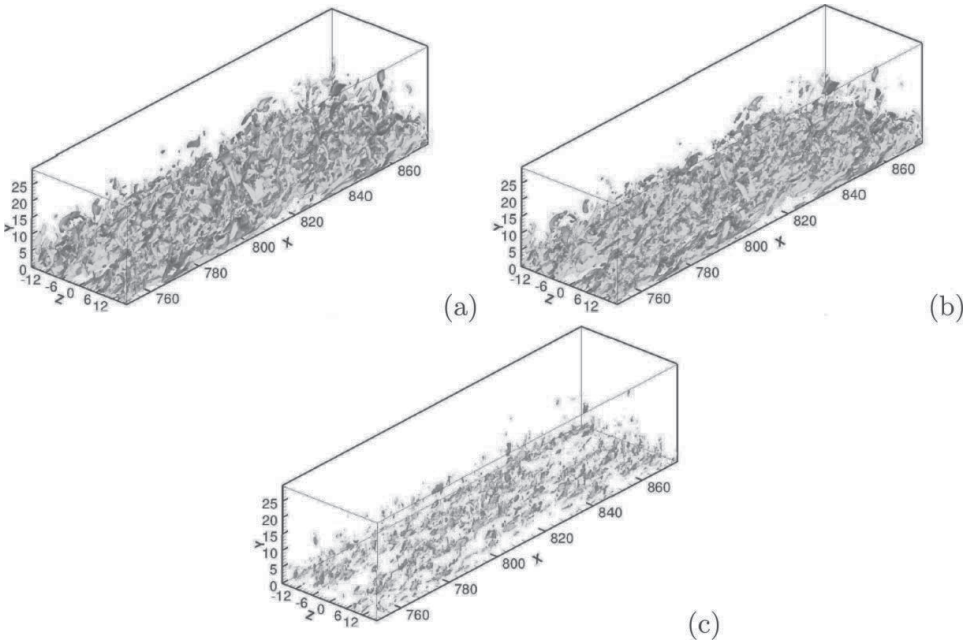


Figure 68. Oblique view of (a) total, (b) coherent and (c) incoherent isosurfaces of wall-normal vorticity decomposed with orthogonal anisotropic wavelets. From Khujdaze et al. [136] with permission of the Institute of Physics.

4. Summary and observations about future directions

- Statistical properties of the turbulent velocity fields of bounded flows have been firmly established and extended to high-Reynolds numbers and to supersonic and hypersonic conditions by means of both experiments and DNS. High-Reynolds number experiments have been done in specially designed flow facilities and at field sites. In the field, the fact that the neutrally buoyant surface layer of the atmospheric boundary layer has properties similar to laboratory flows has been exploited for experiments at very high-Reynolds numbers from which many statistical properties were seen to be rather similar to those at low-Reynolds numbers.
- Statistical properties of the turbulent velocity gradient fields and the important properties of bounded flows derived from them, such as those of the vorticity vector components and the dissipation rate, have been determined for the first time during this 50-year period by means of both experiments and DNS. The experimental methods include multi-sensor hot-wire anemometry, stereo PIV and tomography. The DNS results include those for supersonic and hypersonic Mach numbers.
- Most statistical properties of bounded turbulent flows are not strongly affected by compressibility.
- Although there is still considerable debate about the structural features of these flows, there is near consensus that vortices that are inclined downstream with respect to the wall and that have high aspect ratios, are prominent features. These vortices grow in scale with distance from the wall and are responsible for much of the momentum and scalar transport in the wall region.
- Very large-scale motions (VLSMs) have been observed in laboratory and field experiments and in DNS over a wide range of Reynolds and Mach numbers. These are coherent regions of velocity fluctuations that are very elongated in the streamwise direction and located principally in the logarithmic layer. There is quite a bit of evidence that they modulate the high-frequency fluctuations nearer the wall.
- In spite of numerous efforts to develop methods to predict essential properties of bounded turbulent flow and almost five decades of attempts to understand its structure, a marriage of these two avenues of research has not been very successful, and is one of the principal future challenges. There is renewed hope that knowledge gained about turbulence in transitioning boundary layers at low-Reynolds numbers, where the structure is much more ordered, may be helpful in this undertaking.
- Advances in understanding turbulence have been spurred by the introduction of new experimental techniques, notably novel use of multi-sensor hot-wire anemometry, various optical methods and the development of specialized flow facilities. However, the greatest advances in the second half of this 50-year period since the 1961 Marseille Turbulence Colloquium have been due to the advent and development of direct numerical simulation of turbulence. With the rapid advances in computational power and techniques, we can confidently expect continued advances in our understanding of these technically and scientifically important and fascinating flows.

Acknowledgements

The author would like to thank Marie Farge, Kai Schneider and Keith Moffatt for inviting him to give the boundary layer overview lecture at the 2011 Marseille Turbulence Colloquium on which this paper is based. The opportunity to review this subject, having been a participant in it for most of these 50 years, was a great honor and pleasure. I also want to thank the many colleagues who also have participated in the study of this subject, from whom I have learned so much and who have permitted me to use figures from their work. Interacting with them, and the many others whose work

I admire but did not cite so that this review would not become any longer than it already is, has been a professional and personal delight.

References

[1] L. Prandtl. *Über flüssigkeitbewegung bei sehr kleiner reibung*, Proceedings of the 3rd International Mathematical Congress, Heidelberg, 1904.

[2] H. Görtler and W. Tollmein (eds.), *50 Jahre Grenzschichtforschung*, Vieweg and Son, Braunschweig, 1955.

[3] A.A. Townsend, *The Structure of Turbulent Shear Flow,* 1st ed., Cambridge University Press, 1956; 2nd edition, 1976.

[4] J.C. Rotta, *Incompressible turbulent boundary layers*, Proc. Colloques Internationaux CNRS 108 (1962), pp. 255–286.

[5] L.S.G. Kovasznay, *The turbulent boundary layer*, Annu. Rev. Fluid Mech. 16 (1971), pp. 95–112.

[6] K.R. Sreenivasan, *The turbulent boundary layer*, in *Frontiers in Experimental Fluid Mechanics: Lect. Notes Engr,* Vol. 46, M. Gad-el-Hak, ed., Springer-Verlag, Berlin, 1989, pp. 189–209.

[7] H. Schlichting, *Boundary Layer Theory* (Part IV), 8th ed., (revised by K. Gersten), Springer Verlag, Berlin, 2000.

[8] W.W. Willmarth, *Structure of turbulence in boundary layers*, Adv. Appl. Mech., Academic Press, New York, N.Y., 1975, pp. 159–254.

[9] J.M. Wallace, *The vortical structure of bounded turbulent shear flow*, in *Flow of Real Fluids: Lect. Notes Physics*, Vol. 235, G. Meier and F. Obermeier, eds., Springer Verlag, Berlin, 1985, pp. 253–258.

[10] S.K. Robinson, *Coherent motions in the turbulent boundary layer*, Annu. Rev. Fluid Mech. 23 (1991), pp. 601–639.

[11] R. Panton (ed.), *Advances in Fluid Mechanics: Self-Sustaining Mechanisms of Wall Turbulence*, Computational Mechanics Publications, Southhampton, 1997.

[12] J. Jiménez, *Cascades in wall bounded turbulence*, Annu. Rev. Fluid Mech. 44 (2012), pp. 27–45.

[13] M. Gad-el-Hak and P.R. Bandyopadhyay, *Reynolds number effects in wall-bounded turbulent flows*, Appl. Mech. Rev. 47 (1994), pp. 307–365. ASME Reprint No. AMR148.

[14] I. Marusic, B.J. McKeon, P.A. Monkewitz, H.M. Nagib, A.J. Smits, and K.R. Sreenivasan, *Wall-bounded turbulent flows at high Reynolds numbers: Recent advances and key issues*, Phys. Fluids 22 (2010), 065103.

[15] A.J. Smits, B.J. McKeon, and I. Marusic, *High-Reynolds number wall turbulence*, Annu. Rev. Fluid Mech. 43 (2011), pp. 353–375.

[16] J. Jiménez, *Turbulent flows over rough walls*, Annu. Rev. Fluid Mech. 36 (2004), pp. 173–196.

[17] W.W. Willmarth, *Pressure fluctuations beneath turbulent boundary layers*. Annu. Rev. Fluid Mech. 7 (1975), pp. 13–38.

[18] D.M. Bushnell and C.B. McGinley, *Turbulence control in wall flows*, Annu. Rev. Fluid Mech. 21 (1989), pp. 1–20.

[19] E.F. Spina, A.J. Smits, and S.K. Robinson, *The physics of supersonic turbulent boundary layers*, Annu. Rev. Fluid Mech. 26 (1994), pp. 287–319.

[20] L.V. King, *On the convection of heat from a cylinder in a stream of fluid: Determination of convection constants with applications to hot-wire anemometry*, Proc. Roy. Soc. 90 (1914), pp. 563–570.

[21] M. Eckert, *The Dawn of Fluid Dynamics,* Wiley-VCH, Hoboken, N.J., 2006.

[22] J. Burgers, *The motion of fluid in the boundary layer along a plane smooth surface*, *Proc. 1st Int. Appl. Mech. Cong.* C. Biezeno and J. Burgers, eds., 1924, pp. 113–128.

[23] H. Dryden and A.M. Kuethe, *The measurement of fluctuations of air speed by the hot-wire anemometer*, NACA Rep. 320, available from NASA, Washington, D.C., 1930.

[24] A. Fage and H.C.H. Townend, *An examination of turbulent flow with an ultramicroscope*. Proc. Roy. Soc. A 135(828) (1932), pp. 656–677.

[25] C. Millikan, *A critical discussion of turbulent flows in channels and circular tubes*, Proceedings of the 5th International Congress on Applied Mechanics, Cambridge, 1938, pp. 386–392.

[26] D. Coles, *The law of the wake in the turbulent boundary layer*, J. Fluid Mech. 1 (1956), pp. 192–226.
[27] A.A. Townsend, *The structure of the turbulent boundary layer*, Math. Proc. Cambridge Phil. Soc. 47 (1951), pp. 375–395.
[28] P.S. Klebanoff, *Characteristics of turbulence in a boundary layer with zero pressure gradient*, NACA Rep. 1247, available from NASA, Washington, D.C., 1955.
[29] S. Corrsin and A.L. Kistler, *The freestream boundaries of turbulent flows*, NACA TN 3133, available from NASA, Washington, D.C., 1954.
[30] T. Theodorsen, *Mechanism of turbulence*, Proceedings of the Midwestern Conference Fluid Mechanics, 1-19, Ohio State University, Columbus, 1952.
[31] A.J. Favre, J.J. Gaviglio, and R.J. Dumas, *Further space–time correlations of velocity in a turbulent boundary layer*, J. Fluid Mech. 3 (1958), pp. 344–356.
[32] H.L. Grant, *The large eddies of turbulent motion*, J. Fluid Mech. 4 (1958), pp. 149–190.
[33] J. Kim, *Progress in pipe and channel flow turbulence, 1961–2011*, J. Turbul. 13 (2012), N45.
[34] W.W. Willmarth and C.E. Woolridge, *Measurements of fluctuating pressure at the wall beneath a thick turbulent boundary layer*, J. Fluid Mech. 14 (1962), pp. 187–219.
[35] H.P. Bakewell and J.L. Lumley, *Viscous sublayer and adjacent wall region in turbulent pipe flow*, Phys. Fluids 10 (1967), pp. 1880–1889.
[36] S.J. Kline, W.C. Reynolds, F.A. Schraub, and P.W. Runstadler, *The structure of turbulent boundary layers*, J. Fluid Mech. 30 (1967), pp. 741–773.
[37] J.K. Ferrell, F.M. Richardson, and K.O. Beatty, *Dye displacement technique for velocity distribution measurement*, Indus. Engr. Chem. 47 (1955), pp. 29–33.
[38] F.M. Richardson and K.O. Beatty, *Patterns in turbulent flow in the wall-adjacent region*, Phys. Fluids 2 (1959), pp. 718–719.
[39] S. Corrsin, *Some current problems in turbulent shear flows*, Proceedings of the 1st Symposium on Naval Hydrody, NAS-NRC Pub. No. 515, 1957, pp. 373–399.
[40] E.R. Corino and R.S. Brodkey, *A visual investigation of the wall region in turbulent flow*, J. Fluid Mech. 37 (1969), pp. 1–30.
[41] L.S.G. Kovasznay, V. Kibens, and R.F. Blackwelder, *Large-scale motion in the intermittent region of a turbulent boundary layer*, J. Fluid Mech. 41 (1970), pp. 283–325.
[42] R.F. Blackwelder and L.S.G. Kovasznay, *Time scales and correlations in a turbulent boundary layer*, Phys. Fluids 15 (1972), pp. 1545–1554.
[43] J.M. Wallace, R.S. Brodkey, and H. Eckelmann, *The wall region in turbulent shear flow*, J. Fluid Mech. 54 (1972), pp. 39–48.
[44] W.W. Willmarth and S.S. Lu, *Structure of the Reynolds stress near the wall*, J. Fluid Mech. 55 (1972), pp. 65–92.
[45] S.S. Lu and W.W. Willmarth, *Measurements of the structure of the Reynolds stress in a turbulent boundary layer*, J. Fluid Mech. 60 (1973), pp. 481–511.
[46] R.S. Brodkey, J.M. Wallace, and H. Eckelmann, *Some properties of truncated turbulence signals in bounded turbulent shear flows*, J. Fluid Mech. 63 (1974), pp. 209–224.
[47] J.M. Wallace and R.S. Brodkey, *Reynolds stress and joint probability density distribution in the u–v plane of a turbulent channel flow*, Phys. Fluids 20 (1977), pp. 351–355.
[48] R. Emmerling, *MPI für Strömungsforschung*, Bericht 9, Goettingen, 1973.
[49] A. Dinkelacker, M. Hessel, G.E.A. Meier, and G. Schewe, *Investigation of pressure fluctuations beneath a turbulent boundary layer by means of an optical method*, Phys. Fluids 20 (1977), pp. S216–S224.
[50] R.F. Blackwelder and R.E. Kaplan, *On the wall structure of the turbulent boundary layer*, J. Fluid Mech. 76 (1976), pp. 89–112.
[51] C.-H. Chen and R.F. Blackwelder, *Large-scale motion in a turbulent boundary layer: a study using temperature contamination*, J. Fluid Mech. 89 (1978), pp. 1–31.
[52] R.A. Antonia, S. Rajagopalan, C.S. Subramanian, and A.J. Chambers, *Reynolds number dependence of the structure of a turbulent boundary layer*, J. Fluid Mech. 121 (1982), pp. 123–140.
[53] G.L. Brown and A.S.W. Thomas, *Large structure in a turbulent boundary layer*, Phys. Fluids 20 (1977), pp. S243–S252.
[54] M.R. Head and P. Bandyopadhyay, *New aspects of turbulent boundary-layer structure*, J. Fluid Mech. 107 (1981), pp. 297–338.

[55] J.M. Wallace, J.-L. Balint, J.-L. Mariaux, and R. Morel, *Observations on the nature and mechanism of the structure of turbulent boundary layers*, in *Proc. 4th Engr. Mech. Div. Specialty Conf. Recent Adv. Engr. Mech Impact on Civil Engr. Pract., ASCE*, Vol. 2, W.F. Chen and A.D.M. Lewis, eds., 1983, pp. 1198–1201.
[56] A.E. Perry and M.S. Chong, *On the mechanism of wall turbulence*, J. Fluid Mech. 119 (1982), pp. 173–217.
[57] A.E. Perry, S. Henbest, and M.S. Chong, *A theoretical and experimental study of wall turbulence*, J. Fluid Mech. 165 (1986), pp. 163–199.
[58] J. Kim and P. Moin, *The structure of the vorticity field in turbulent channel flow. Part 2. Study of ensemble-averaged fields*, J. Fluid Mech. 162 (1986), pp. 339–363.
[59] J. Kim, P. Moin, and R. Moser, *Turbulence statistics in fully developed channel flow at low Reynolds number*, J. Fluid Mech. 177 (1987), pp. 133–166.
[60] J.-L. Balint, J.M. Wallace, and P. Vukoslavĉvić, *A study of the vortical structure of the turbulent boundary layer*, in *Advances in Turbulence: Proceedings of the First European Turbulence Conference*, G. Comte-Bellot and J. Mathieu, eds., Springer, Berlin, 1987, pp. 456–464.
[61] P. Vukoslavĉvić, J.M. Wallace, and J.-L. Balint, *The velocity and vorticity fields of a turbulent boundary layer. Part 1. Simultaneous measurement by hot-wire anemometry*, J. Fluid Mech. 228 (1991), pp. 25–52.
[62] J.-L. Balint, J.M. Wallace, and P. Vukoslavĉvić, *The velocity and vorticity fields of a turbulent boundary layer. Part 2. Statistical properties*, J. Fluid Mech. 228 (1991), pp. 53–86.
[63] P.R. Spalart, *Direct simulation of a turbulent boundary layer up to* $R_\theta = 1410$, J. Fluid Mech. 187 (1988), pp. 61–98.
[64] N. Aubry, P. Holmes, J.L. Lumley, and E. Stone, *The dynamics of coherent structures in the wall region of a turbulent boundary layer*, J. Fluid Mech. 192 (1988), pp. 115–173.
[65] S. Herzog, *The large scale structure in the near-wall region of turbulent pipe flow*, Ph.D. diss., Cornell University, 1986.
[66] R.A. Antonia, D.K. Bisset, and L.W.B. Browne, *Effect of Reynolds number on the topology of the organized motion in a turbulent boundary layer*, J. Fluid Mech. 213 (1990), pp. 267–286.
[67] A.E. Perry and M.S. Chong, *A description of eddying motions and flow patterns using critical-point concepts*, Annu. Rev. Fluid Mech. 19 (1987), pp. 125–155.
[68] P.S. Bernard and R.A. Handler, *Reynolds stress and the physics of turbulent momentum transport*, J. Fluid Mech. 220 (1990), pp. 99–124.
[69] P.S. Bernard and J.M. Wallace, *Turbulent Flow: Analysis, Measurement and Prediction*, John Wiley & Sons, Inc., Hoboken, NJ, 2002, p. 244.
[70] P.S. Bernard, J.M. Thomas, and R.A. Handler, *Vortex dynamics and the production of Reynolds stress*, J. Fluid Mech. 253 (1993), pp. 385–419.
[71] C.E. Wark and H.M. Nagib, *Experimental investigation of coherent structures in turbulent boundary layers*, J. Fluid Mech. 230, (1991) pp. 183–208.
[72] S.K. Robinson, *Kinematics of turbulent boundary layer structure*, Ph.D. diss., Stanford University, 1990. Also NASA TM 103859, available from NASA, Washington, D.C.
[73] G.I. Barenblatt, *On the scaling laws (incomplete self-similarity with respect to Reynolds number) in developed turbulent flow in pipes*, C. R. Acad. Sci. Paris II 313 (1991), pp. 309–312.
[74] G.I. Barenblatt, A.J. Chorin, and V.M. Prostokishin, *Self-similar intermediate structures in turbulent boundary layers at large Reynolds numbers*, J. Fluid Mech. 410 (2000), pp. 263–283.
[75] M.V. Zagarola and A.J. Smits, *Scaling of the mean velocity profile for turbulent pipe flow*, Phys. Rev. Lett. 78 (1997), pp. 239–242.
[76] E.F. Spina, J.F. Donovan, and A.J. Smits, *On the structure of high-Reynolds number supersonic turbulent boundary layers*, J. Fluid Mech. 222 (1991), pp. 293–327.
[77] A. Tsinober, E. Kit, and T. Dracos, *Experimental investigation of the field of velocity gradients in turbulent flows*, J. Fluid Mech. 242 (1992), pp. 169–192.
[78] E. Kit, A. Tsinober, J.-L. Balint, J.M. Wallace, and E. Levich, *An experimental study of helicity related properties of turbulent flow past a grid*, Phys. Fluids 30 (1987), pp. 3323–3325.
[79] P.A. Durbin, *A Reynolds stress model for near-wall turbulence*, J. Fluid Mech. 249 (1993), pp. 465–498.

[80] R.D. Moser, J. Kim, and N.N. Mansour, *Direct numerical simulation of turbulent channel flow up to* $R_\tau = 590$, Phys. Fluids 11 (1999), pp. 943–945.
[81] H. Choi, P. Moin, and J. Kim, *Active turbulence control for drag reduction in wall-bounded turbulent flows*, J. Fluid Mech. 262 (1994), pp. 75–110.
[82] A.N. Kolmogorov, *The local structure of turbulence in incompressible viscous fluid for very large Reynolds numbers*, Dokl. Akad. Nauk SSSR 30 (1941), pp. 301–305.
[83] S.G. Saddoughi and S.V. Veeravalli, *Local isotropy in turbulent boundary layers at high Reynolds numbers*, J. Fluid Mech. 268 (1994), pp. 333–372.
[84] J.M. Wallace and L. Ong, *Local isotropy of the velocity and vorticity fields in a boundary layer at high Reynolds numbers*, Phys. Fluids 20 (2008), 101506, pp. 1–7.
[85] Y. Nagano and Y. Tagawa, *Coherent motions and heat transfer in a wall turbulent shear flow*, J. Fluid Mech. 305 (1995), pp. 127–157.
[86] J.C. Klewicki, M.M. Metzger, E. Kelner, and E.M. Thurlow, *Viscous sublayer flow visualizations at* $R_\theta \approx 1{,}500{,}000$. Phys. Fluids 7 (1995), pp. 857–863.
[87] C.R. Smith and S.P. Metzler, *The characteristics of low-speed streaks in the near-wall region of a turbulent boundary layer*, J. Fluid Mech. 129 (1983), pp. 27–54.
[88] M.M. Metzger and J.C. Klewicki, *A comparative study of near wall turbulence in high and low Reynolds number boundary layers*, Phys. Fluids 13 (2001), pp. 692–701.
[89] A. Folz and J.M. Wallace, *Near-surface turbulence in the atmospheric surface layer*, Physica D 239 (2010), pp. 1305–1317.
[90] P.J.A. Priyadarshana, J.C. Klewicki, S. Treat, and J.F. Foss, *Statistical structure of turbulent-boundary-layer velocity–vorticity products at high and low Reynolds number*, J. Fluid Mech. 570 (2007), pp. 307–346.
[91] M. Kholmyansky, A. Tsinober, and S. Yorish, *Velocity derivatives in the atmospheric surface layer at* $Re_\lambda = 10^4$, Phys. Fluids 13 (2001), pp. 311–314.
[92] J. Jeong, F. Hussain, W. Schoppa, and J. Kim, *Coherent structures near the wall in a turbulent channel flow*, J. Fluid Mech. 332 (1997), pp. 185–214.
[93] J.M. Wallace, R.S. Brodkey, and H. Eckelmann, *Pattern-recognized structures in bounded turbulent shear flows*, J. Fluid Mech. 83 (1977), pp. 673–693.
[94] W. Schoppa and F. Hussain, *Coherent structure generation in near-wall turbulence*, J. Fluid Mech. 453 (2002), pp. 57–108.
[95] A. Honkan and Y. Andreopoulos, *Vorticity, strain-rate and dissipation characteristics in the near-wall region of turbulent boundary layers*, J. Fluid Mech. 350 (1997), pp. 29–96.
[96] L. Ong and J.M. Wallace, *Joint probability density analysis of the structure and dynamics of the vorticity field of a turbulent boundary layer*, J. Fluid Mech. 367 (1998), pp. 291–328.
[97] S.E. Guarini, R.D. Moser, K. Shariff, and A. Wray, *Direct numerical simulation of a supersonic turbulent boundary layer at Mach 2.5*, J. Fluid Mech. 414 (2000), pp. 1–33.
[98] R.J. Adrian, *Particle imaging techniques for experimental fluid mechanics*, Annu. Rev. Fluid Mech. 23 (1991), pp. 261–304.
[99] R.J. Adrian, C.D. Meinhart, and C.D. Tomkins, *Vortex organization in the outer region of the turbulent boundary layer*, J. Fluid Mech. 422 (2000), pp. 1–54.
[100] J. Zhou, R.J. Adrian, and S. Balachandar, *Autogeneration of near-wall vortical structures in channel flow*, Phys. Fluids 8 (1996), pp. 288–290.
[101] J. Zhou, R.J. Adrian, S. Balachandar, and T.M. Kendall, *Mechanisms for generating coherent packets of hairpin vortices in channel flow*, J. Fluid Mech. 387 (1999), pp. 353–396.
[102] R.J. Adrian, *Hairpin vortex organization in wall turbulence*, Phys. Fluids 19 (2007) 041301.
[103] J.C. Klewicki, *On the interactions of inner and outer region motions in turbulent boundary layers*, Ph.D. diss., Michigan State University, East Lansing, MI, U.S.A., 1989.
[104] J.M. Chacin and B.J. Cantwell, *Dynamics of a low Reynolds number turbulent boundary layer*, J. Fluid Mech. 404 (2000), pp. 87–115.
[105] Y. Andreopoulos and A. Honkan, *An experimental study of the dissipative and vortical motion in turbulent boundary layers*, J. Fluid Mech. 439 (2001), pp. 131–163.
[106] J. Carlier and M. Stanislas, *Experimental study of eddy structures in a turbulent boundary layer using particle image velocimetry*, J. Fluid Mech. 535 (2005), pp. 143–188.
[107] W. Hambleton, N. Hutchins, and I. Marusic, *Simultaneous orthogonal-plane particle image velocimetry measurements in a turbulent boundary layer*, J. Fluid Mech. 560 (2006), pp. 53–64.

[108] M.A. Green, C.W. Rowley, and G. Haller, *Detection of Lagrangian coherent structures in three-dimensional turbulence*, J. Fluid Mech. 572 (2007), pp. 111–120.
[109] K.C. Kim and R.J. Adrian, *Very large scale motion in the outer layer*, Phys. Fluids 11 (1999), pp. 417–422.
[110] N. Hutchins and I. Marusic, *Evidence of very long meandering features in the logarithmic region of turbulent boundary layers*, J. Fluid Mech. 579 (2007), pp. 1–28.
[111] J.C. Del Álamo, J. Jiménez, P. Zandonade, and R.D. Moser, *Scaling of the energy spectra of turbulent channel flows*, J. Fluid Mech. 500 (2004), pp. 135–144.
[112] R. Mathis, N. Hutchins, and I. Marusic, *Large-scale amplitude modulation of the small-scale structures in turbulent bounday layers*, J. Fluid Mech. 628 (2009), pp. 311–337.
[113] M.J. Ringuette, M. Wu, and M.P. Martín, *Coherent structures in direct numerical simulation of turbulent boundary layers at Mach 3*, J. Fluid Mech. 594 (2008), pp. 59–69.
[114] L. Duan, I. Beekman, and M.P. Martín, *Direct numerical simulation of hypersonic turbulent boundary layers. Part 3. Effect of Mach number*, J. Fluid Mech. 672 (2011), pp. 245–267.
[115] S. Pirozzoli, M. Bernardini, and F. Grasso, *Characterization of coherent vortical structures in a supersonic turbulent boundary layer*, J. Fluid Mech. 613 (2008), pp. 205–231.
[116] R.E. Falco, *Coherent motions in the outer region of turbulent boundary layers*, Phys. Fluids 20 (1977), pp. S124–S132.
[117] J.C. Klewicki and R.E. Falco, *On accurately measuriing statistics associated with small-scale structure in turbulent boundary layers using hot-wire probes*, J. Fluid Mech. 219 (1990), pp. 119–142.
[118] S. Pirozzoli, M. Bernardini, and F. Grasso, *On the dynamical relevance of coherent vortical structures in turbulent boundary layers*, J. Fluid Mech. 648 (2010), pp. 325–349.
[119] Z.-S. She, E. Jackson, and S.A. Orszag, *Intermittent vortex structures in homogeneous isotropic turbulence*, Nature 344 (1990), pp. 226–228.
[120] M. Lagha, J. Kim, J.D. Eldredge, and X. Zhang, *A numerical study of compressible turbulent boundary layers*, Phys. Fluids 23 (2011), 015106.
[121] M. Lagha, J. Kim, J.D. Eldredge, and X. Zhong, *Near-wall dynamics of compressible boundary layers*, Phys. Fluids 23 (2011), 065109.
[122] X. Wu and P. Moin, *Direct numerical simulation of turbulence in a nominally zero-pressure-gradient flat-plate boundary layer*, J. Fluid Mech. 630 (2009), pp. 5–41.
[123] X. Wu and P. Moin, *Transitional and turbulent boundary layers with heat transfer*, Phys. Fluids 22, (2010) 085105.
[124] G.I. Park, J.M. Wallace, P. Moin, and X. Wu, *Boundary layer turbulence in transitional and developed states*, Phys. Fluids 24 (2012), 035105.
[125] P. Schlatter, R. Örlü, Q. Li, G. Brethouwer, J.H.M. Fransson, A.V. Johansson, P.H. Alfredsson, and D.S. Henningson, *Turbulent boundary layers up to $R_\theta = 2500$ studied through simulation and experiment*, Phys. Fluids 21 (2009), 051702.
[126] P. Schlatter and R. Örlü, *Assessment of direct numerical simulation data of turbulent boundary layers*, J. Fluid Mech. 659 (2010), pp. 116–126.
[127] P. Schlatter, Q. Li, G. Brethouwer, A.V. Johansson, and D.S. Henningson, *Simulations of spatially evolving turbulent boundary layers up to $R_\theta = 4300$*, Int. J. Heat Fluid Flow 31 (2010), 251–261.
[128] J. Jiménez, S. Hoyas, M.P. Simens, and Y. Mizuno, *Turbulent boundary layers and channels at moderate Reynolds numbers*, J. Fluid Mech. 657 (2010), pp. 335–360.
[129] A. Lozano-Durán, O. Flores, and J. Jiménez, *The three-dimensional structure of momentum transfer in turbulent channels*, J. Fluid Mech. 694 (2012), pp. 100–130.
[130] J. Sheng, E. Malkiel, and J. Katz, *Buffer layer structures associated with extreme wall stress events in a smooth wall turbulent boundary layer*, J. Fluid Mech. 633 (2009), pp. 17–60.
[131] G.E. Elsinga, R.J. Adrian, B.W. Van Oudheusden, and F. Scarano, *Three-dimensional vortex organization in a high-Reynolds-number supersonic turbulent boundary layer*, J. Fluid Mech. 644 (2010), pp. 35–60.
[132] D.J.C. Dennis and T.B. Nickels, *Experimental measurement of large-scale three-dimensional structures in a turbulent boundary layer. Part 1. Vortex packets*, J. Fluid Mech. 673 (2011), pp. 180–217.
[133] J.H. Lee and H.J. Sung, *Very-large-scale motions in a turbulent boundary layer*, J. Fluid Mech. 673 (2011), pp. 80–120.

[134] M. Guala, M. Metzger, and B.J. McKeon, *Interactions within the turbulent boundary layer at high Reynolds number*, J. Fluid Mech. 666 (2011), pp. 573–604.
[135] Y. Yang and D.I. Pullin, *Geometric study of Lagrangian and Eulerian structures in turbulent channel flow*, J. Fluid Mech. 674 (2011), pp. 67–92.
[136] G. Khujadze, R. Nguyen van Yen, K. Schneider, M. Oberlack, and M. Farge, *Coherent vorticity extraction in turbulent boundary layers using orthogonal wavelets*, Eur. Turb. Conf. 13 – J. Phys. Conf. Ser. 318 (2011), 022011.

Journal of Turbulence
Vol. 13, No. 44, 2012, 1–25

Taylor & Francis
Taylor & Francis Group

Turbulence before Marseille 1961

Michael Eckert*

Deutsches Museum, Forschungsinstitut, München, Germany

(*Received 27 June 2012; final version received 28 August 2012*)

The surge of turbulence research in the first half of the twentieth century is reviewed with the focus on the institutional environment that provided an umbrella for the activities in this field. Before the Second World War, the International Congresses for Applied Mechanics served as the main stage for presenting research results on turbulence. After the War, the International Union of Theoretical and Applied Mechanics (IUTAM), organizations such as the Division of Fluid Dynamics of the American Physical Society and new journals (the *Journal of Fluid Mechanics* and *The Physics of Fluids*) added to the institutional framework for turbulence activities and publications. The development of these activities is illustrated with examples from the correspondence of some of the involved actors (such as George K. Batchelor and Francois N. Frenkiel, the editors of the new journals; both were also involved with the organization of the Marseille events in 1961).

Keywords: turbulence; history; congresses; journals

Abbreviations

AIP	American Institute of Physics
APS	American Physical Society
DFD	Division of Fluid Dynamics of the American Physical Society
DFDA	Division of Fluid Dynamics of the American Physical Society, Archives
DMV	Deutsche Mathematiker-Vereinigung
EUROMECH	European Mechanics Society
FIAT	Field Intelligence Agency, Technical
GALCIT	Guggenheim Aeronautical Laboratory at the California Institute of Technology, Caltech, Pasadena, CA (USA)
GAMM	Gesellschaft für Angewandte Mathematik und Mechanik
IAU	International Astronomical Union
ICSU	International Council of Scientific Unions
IGY	International Geophysical Year
IMST	Institut de Mécanique Statistique de La Turbulence, Marseille (France)
IUGG	International Union of Geodesy and Geophysics
IUTAM	International Union of Theoretical and Applied Mechanics
MPGA	Max-Planck-Gesellschaft, Archiv, Berlin

*Email: m.eckert@deutsches-museum.de

ISSN: 1468-5248 online only
© 2012 Taylor & Francis
http://dx.doi.org/10.1080/14685248.2012.725476
http://www.tandfonline.com

NACA	National Advisory Committee for Aeronautics
NOL	Naval Ordnance Laboratory, White Oak, MD (USA)
NSF	National Science Foundation
ONERA	Office National d'Études et de Recherches Aérospatiales, Chatillon (France)
TKC	Theodore von Kármán Collection, CalTech, Pasadena
UNESCO	United Nations Educational, Scientific and Cultural Organization, Paris (France)
ZAMM	Zeitschrift für Angewandte Mathematik und Mechanik

1. Introduction

This is not the first attempt to review many decades of turbulence research. Ten years ago, two eminent scientists of this discipline – if it may be called a discipline – reviewed "A century of turbulence" [1]. Recently, in *A Voyage Through Turbulence*, the contributions of Osborne Reynolds, Ludwig Prandtl, Andrey Nikolaevich Kolmogorov and other pioneers have been reviewed [2]. Since 1969, when the first issue of the *Annual Review of Fluid Mechanics* appeared, many subfields of turbulence have become the subject of critical survey. Furthermore, textbooks on turbulence tend to include historical surveys. Based on the citations in [3,4], the reviewers of "A century of turbulence" derived a formula for the exponential growth of the annual output of papers on turbulence since 1900 and before 1965, the year when the Russian original of this classic textbook was published [1, p. 242]. Their formula yields for the period between the end of the Second World War and the time of the Marseille events in 1961 – an annual growth from about 20 to 76 papers, and a total of 668 papers within these 16 years. The total amount of turbulence papers from the beginning of the twentieth century until 1961 is 895. Although these numbers should not be taken at face value (Lumley and Yaglom admit fluctuations of about $\pm 20\%$ near 1900 and $\pm 2.5\%$ near 1965), they hint at the order of magnitude of the quantitative output of turbulence research within the period of this review. Given the exponential growth and amount of turbulence research even before 1961 – the exponential growth agrees with the overall tendency in scientometrics in this period [5] – it is quite obvious that a survey based on the content of these research papers exceeds the space of a single review paper. Even a selection of "some key developments in turbulence research" yields more than 50 publications prior to Marseille [2, chapter 13].

In contrast to these surveys, the emphasis of the following review is on the environment in which turbulence emerged as an ever-expanding research activity. Thus, the focus is shifted from the intellectual history of turbulence to the circumstances in which turbulence became an ever-growing research effort.

2. Early traditions of scientific engineering

The history of turbulence in the nineteenth century is mainly connected with the names of Adhémar Jean Claude Barré de Saint-Venant and Joseph Boussinesq in France, and with William Thomson (Lord Kelvin), John William Strutt (Lord Rayleigh) and, in particular, Osborne Reynolds in Great Britain [6,7, chapter 6]. In France, these contributions were rooted in the tradition of scientific engineering as it emerged in the eighteenth century at the École des Ponts et Chaussées and the École Polytechnique. In Great Britain, the connection with national policy was less explicit; nevertheless, British science, too, did not flourish in isolation from practical tasks. Reynolds was praised in an obituary as Great Britain's "most distinguished scientific engineer" [8, p. 35].

In Germany, the tradition of scientific engineering was peculiar. During the first half of the nineteenth century, it was growing at newly established Polytechnic Schools following the model of the French École Polytechnique; however, by the end of the nineteenth century, when these schools were transformed into Technische Hochschulen, they were considered only secondary to the universities and had to struggle for their academic emancipation. Ludwig Prandtl, the leader of the German school of turbulence [9], began his career at the Technische Hochschulen in München and in Hannover, but rose to prominence at the University of Göttingen. At this university, there was a strong tradition of mathematics and physics (initiated by Carl Friedrich Gauss and Wilhelm Weber) to which the entrepreneurial mathematician Felix Klein added applied sciences. He called Prandtl to Göttingen as an expert of applied mechanics. Thus, by the beginning of the twentieth century, in Germany too, the tradition of scientific engineering had taken hold in an academic environment.

Scientific engineering, however, was not enough to provide a common framework for turbulence research, nor was it the only tradition. Scientists interested in problems such as flow instabilities or vortex formation did not belong to just one discipline. These problems also attracted physicists and mathematicians with no interest in engineering applications. Prandtl's boundary layer concept was first presented at the Third International Congress of Mathematicians in August 1904 in Heidelberg [10]. Four years later, Arnold Sommerfeld, professor of theoretical physics in München, introduced what became known as the Orr–Sommerfeld approach to account for the instability of flows at the Fourth International Congress of Mathematicians in 1908 in Rome [11]. William McFadden Orr, who had published his work a year earlier, also addressed this subject from the vantage point of mathematics [12]. Throughout the early decades of the twentieth century, the onset of turbulence was perceived predominantly as a challenge for theorists [13].

The lack of a common framework is also apparent from the journals in which the pertinent studies were published. There was no specialized international society on fluid mechanics, not to speak of turbulence. If a research result was not presented at a meeting such as the International Congress of Mathematicians or another mathematical conference such as the annual meetings of the Deutsche Mathematiker-Vereinigung (DMV) [14], results concerning turbulence were communicated in diverse journals such as the *Philosophical Magazine* [15] or the *Zeitschrift für Mathematik und Physik* [16]. The most frequent mode of publishing was to address an academy. In Orr's case, this was the Royal Irish Academy. Sommerfeld, in his capacity as a member of the Bavarian Academy of Science, presented some of his pupils' work in the proceedings of this academy [17–19]. Other pertinent papers on one or another aspect of turbulent flow appeared in the transactions of the academies in Amsterdam [20], Göttingen [21,22], London [23,24] or Paris [25,26].

3. The International Congresses for Applied Mechanics, 1922–1938

By the early 1920s, the situation began to change. In part, the growing awareness for "applied" specialties in science resulted from the rise of aeronautical research, where distinguished academics such as Lord Rayleigh or Prandtl assumed the role of advisors. After the First World War, applied mechanics was perceived as a discipline of its own right.

In Germany, Prandtl suggested to create a "federation of all like-minded," as he wrote to Richard von Mises in 1921. He had already discussed his plans with his former disciple Theodore von Kármán, who was now director of the Institute for Aerodynamics at the Technische Hochschule Aachen. "We suggest the foundation of an 'Association for Technical Mechanics' with the exclusive purpose to prepare and convene meetings for that specialty."[1] The audience would be the "scientific engineers." Von Mises addressed the same group as

editor of a new journal, the *Zeitschrift für Angewandte Mathematik und Mechanik (ZAMM)*. In his editorial, he had discerned turbulence among other problems as a particular challenge [27, pp. 11–12]. Prandtl and von Mises did not agree entirely about the new organization. It was founded in 1922 as Gesellschaft für Angewandte Mathematik und Mechanik (GAMM) against Prandtl's and von Kármán's emphasis on "technical" mechanics. But they shared the concern about turbulence.

Although it was hardly visible from his publications, Prandtl had a long-standing affiliation with turbulence [9]. In 1914, he had interpreted Gustave Eiffel's discovery of a sudden reduction in the drag coefficient of spheres at high flow velocities as a consequence of the transition to turbulence in the boundary layer [21]. In 1916, he had drafted a "working program for a theory of turbulence," where he discerned the onset of turbulence and fully developed turbulence as the two major problem areas for future research. In 1921, when the Deutsche Physikalische Gesellschaft, the Deutsche Gesellschaft für Technische Physik and the DMV combined their annual meetings "to bring to bear the areas of applied mathematics and mechanics to a higher degree than heretofore," as von Mises reported in his new journal [28], Prandtl used the occasion for "Remarks about the Onset of Turbulence" [29] that were intended to break the deadlock of previous studies. At the same conference, Ludwig Schiller, a physicist working temporarily in Prandtl's laboratory, surveyed the experimental investigations about the onset of turbulence [30]. These contributions served at the same time to shape the profile of the *ZAMM*. Fritz Noether reviewed the theoretical attempts concerning the onset of turbulence [31]. This paper served as a starting point for a host of further investigations of the Orr–Sommerfeld approach [13].

The initiative to form a community of applied mathematics and mechanics soon became international. In 1922, the Italian mathematician Tullio Levi-Civitá and Theodore von Kármán (by birth Hungarian) organized a gathering of like-minded mathematicians, physicists and engineers with an interest in fluid mechanics at Innsbruck in Austria [32,33]. In the following year, the momentum of these events was carried on to the Netherlands, where Johannes (Jan) Martinus Burgers and C. B. Biezeno organized the First International Congress for Applied Mechanics, held in April 1924 at Delft [34,35]. Two years later, the Second International Congresses for Applied Mechanics was held in Zürich, Switzerland. Thereafter, they were held every 4 years in another country (1930 Stockholm; 1934 Cambridge, UK; 1938 Cambridge, MA) – until the Second World War caused an interruption [36].

From the very beginning, these congresses were regarded as the preferred sites for presenting novel research on turbulence. Their importance can hardly be exaggerated. At each one of these meetings, crucial achievements were introduced and discussed. A few examples may suffice. At Innsbruck, Kármán presented his most recent theory on turbulent skin friction [37,38], and Werner Heisenberg, Sommerfeld's prodigy student, reported about some results of his early struggle with the turbulence problem that subsequently became the subject of his doctoral work [39,40]; at the Zurich Congress in 1926, Prandtl presented the mixing length concept [41]; 4 years later, Kármán chose the Stockholm Congress to introduce a similarity concept that gave rise to "Kármán's constant" and the logarithmic law for turbulent skin friction [42]. These congresses, Kármán recalled in his autobiography, served as the "playing field" for his competition with Prandtl. "The 'ball' was the search for a universal law of turbulence" [43, p. 134].

At the Fourth International Congress for Applied Mechanics held in 1934 in Cambridge, UK, the interest in turbulence was so great that the organizers of the Fifth Mechanics Congress decided to hold a special symposium on turbulence within that Congress. "Professor Prandtl kindly consented to organize this Symposium," the organizers reported

in the proceedings. They regarded this Symposium "not only the principal feature of this Congress, but perhaps the Congress activity that will materially affect the orientation of future research." Taylor's statistical theory of turbulence had been published just 3 years ago; his survey lecture [44], Hugh Dryden's communication about experimental measurements of the spectrum of turbulence at the National Bureau of Standards in Washington, DC [45] and numerous other contributions illustrated that the focus had shifted from the onset of turbulence to the statistical theory of fully developed turbulence as the major concern.

One reason for this shift was the pertinence of this theory for wind tunnel turbulence and the improvement of hot-wire anemometry. "The desire to make some direct measurement of the turbulence in wind tunnels was the incentive for the work here described," Dryden and a collaborator of his department at the National Bureau of Standards had argued in 1929 in a technical report of the National Advisory Committee for Aeronautics (NACA). They were optimistic that the method also advanced the statistical theory of fully developed turbulence, because the "great need at the present time in the further development of the theory of turbulence is more experiments on the actual fluctuations to supplement the data already available on the distribution of mean velocity" [46, p. 361]. In a subsequent report, they concluded "that turbulence is a variable of some importance at all times and that the careful experimenter will desire to measure and state its value in order that his experiments may be capable of interpretation" [47, p. 166].

The rise of the statistical theory of turbulence, therefore, was closely related to the concern about wind tunnel turbulence. At the same time, the onset of turbulence in the boundary layer of a model in a wind tunnel was found to depend critically on the degree of turbulence in the airstream. In 1938, Taylor elaborated this view in more details at the turbulence symposium of the Fifth International Congress for Applied Mechanics in Cambridge, MA. He could even present a formula that expressed the critical Reynolds number for the transition to turbulence in the boundary layer of a sphere exposed to the turbulent fluctuations caused by the grid in a wind tunnel [48, pp. 151–152]. With the obvious role of external disturbances as a cause for the transition to turbulence, the Orr–Sommerfeld approach appeared unlikely to explain the onset of turbulence. Taylor argued that "it is not proved that the boundary layer is unstable" and that "the experimental evidence is against the instability theory" [44, p. 308].

While the stability theory lost ground at this International Congress of Mechanics in 1938, it was not entirely abandoned. John L. Synge, the head of the Department of Applied Mathematics at the University of Toronto, chose this theme in the same year for a review lecture on the occasion of the 50th birthday of the American Mathematical Society. "It presents mathematical problems of no small difficulty: triumphs are few and disappointments many," he alluded to the long history of this problem. However, he also made clear that it was not *the* turbulence problem: "It is concerned with the initial stage of turbulence – its generation from steady flow – but not with turbulent motion, once established" [49, p. 227].

Thus, the two paths of turbulence research that had been discerned early in the twentieth century, the onset and fully developed turbulence, had matured by the late 1930s into well-distinct avenues. The former developed a life of its own with the focus on the Orr–Sommerfeld approach. The latter fell into the realm of statistical theory [50,51]. Shortly after 1938, a breakthrough in the statistical theory of turbulence was accomplished in Russia. It was connected mainly with the names of Andrey Nikolaevich Kolmogorov and Alexander Mikhailovich Obukhov [52]. It was published in 1941 and is known today as K41 or KO41 [53–55]. However, it remained unknown to the world outside Russia until

after the war. Its impact on the international community and its role for shaping the future course of turbulence research, therefore, belong to the post-war history of turbulence.

4. Second World War: jets, laminar wings and other wartime research on turbulence

The bulk of turbulence research during the Second World War was performed in the context of one or another aeronautical war project. One of these concerned the investigation of turbulence in jets. It was performed under contract with the NACA at the Guggenheim Aeronautical Laboratory of the California Institute of Technology (GALCIT) and carried out by von Kármán's disciple Stanley Corrsin, who completed his aeronautical engineering master's thesis in 1942 with Hans Liepmann as advisor on the "Decay of turbulence behind three similar grids" and his PhD thesis in 1947 on "Extended applications of the hot-wire anemometer", still under the guidance of Hans Liepmann. Other disciples of von Kármán involved in turbulence research were Hans Liepmann, Francis Clauser and Chia Chiao Lin. In this environment, many aspects of turbulent flows, theoretical and experimental, were investigated. In his jet study, for example, Corrsin employed a novel hot-wire measuring set. The results were published in confidential NACA Wartime Reports under the title "Investigation of flow in an axially symmetrical heated jet of air" and "Investigation of the behavior of parallel two-dimensional air jets." Thus began the outstanding career of a new American leader of turbulence research [56].

Another NACA programme was concerned with laminar flow wings and low-turbulence wind tunnels. By 1938, Eastman Jacobs, the head of the Variable-Density-Tunnel team at NACA's Langley laboratory, had elaborated by trial and error a wing profile shape that offered the prospect to keep the boundary layer for most of the upper part of the wing in the laminar state. In order to investigate such profiles a novel "two-dimensional low-turbulence pressure tunnel" was developed. In its annual report for 1939, published in 1940, the NACA announced that "a new principle in airplane-wing design" had been discovered, which reduced the drag of the wing "by approximately two-thirds" [57, pp. 109–116]. In the same year, the new principle was made available to the American aircraft industry. Attached to a fighter plane, the North American P-51 Mustang, low-drag wings became a major asset of NACA's contribution to the war effort [58, Vol. 2, p. 549].

Low-turbulence wind tunnels and low-drag wings came along with new fundamental research on the transition from laminar to turbulent flow in the boundary layer. The NACA issued research contracts to Dryden's Aerodynamics Division of the National Bureau of Standards in Washington, DC, as well as to Kármán at the GALCIT in Pasadena, CA.[2] In the course of these investigations, performed in special low-turbulence tunnels with sophisticated hot-wire equipment, both groups discovered the boundary layer instability predicted by Walter Tollmien and Hermann Schlichting at Göttingen. The results were communicated in NACA wartime reports [59–61]. With the experimental corroboration of the long-disputed Orr–Sommerfeld approach, von Kármán regarded a revision of the stability theory expedient. He suggested it to Chia-Chiao Lin as the subject of a doctoral dissertation. Lin was at that time not yet naturalized as a US citizen and thus not cleared for confidential war research. Therefore, he could not perform his PhD work in official collaboration with related NACA-sponsored research such as Liepmann's experimental investigation. The title of Lin's thesis, "On the development of turbulence," evoked no association with wartime research. In the abstract, Lin characterized his work as "based upon a study of the equation of Orr and Sommerfeld along the lines initiated by Heisenberg." Lin's work, therefore, appeared more as a fundamental contribution to an old riddle of

theoretical physics rather than as a study motivated by wartime research on low-drag wings [62].

In Germany, the Tollmien–Schlichting theory had been further pursued during the war with the goal to determine the onset of turbulence in the boundary layer along curved surfaces. Important results, such as the instability along concave walls ("Görtler instability"), were even published in the open literature [63–65]. The effort, however, was mostly theoretical. When Schlichting surveyed the state of stability theory in a wartime review lecture in 1941, he could not offer other experimental evidence than images from a water channel published in 1933, where the formation of vortices along the wall indicated some instability [66, p. 39]. The prospects of laminar profiles for practical application were regarded with more soberness than in America. The advantage of low drag involved disadvantages for other aerodynamic profile properties, as Schlichting concluded in his survey. But the German aerodynamicists closely observed the low-drag research in other countries. For example, Schlichting included in his lecture measurements from a Japanese laminar profile [66, p. 30]. Numerous tests of more or less laminar wing profiles were undertaken and communicated in wartime reports (see [67–71]). Without low-turbulence wind tunnels, however, such tests remained inconclusive. Although the Germans built such tunnels, they did not become operative for laminar wing tests before the end of the war [72].

A good deal of wartime research on turbulence in Germany addressed fully developed turbulent flows along smooth and rough walls, in pipe and channel flows, jets and layered streams. The results were circulated in dozens of wartime reports, most of them authored by Prandtl's disciples (besides Tollmien and Schlichting, in particular, Hans Reichardt, Karl Wieghardt and Fritz Schultz-Grunow; see the post-war reviews on turbulence [73,74]).

Although these are just glimpses into the wartime research in the United States and Germany, we may safely assume that comparable efforts were made also in other countries such as France, Great Britain, Japan and Russia, where the same issues will have appeared on the agenda of aeronautical research establishments.

5. 1946 – a year of revelations

The first post-war International Congress for Applied Mechanics, held from 22–29 September 1946 in Paris, was a remarkable event in the history of turbulence. Like in the preceding 1938 Congress, a special symposium on turbulence was organized. Dryden lectured at this symposium about "some recent contributions to the study of transition and turbulent boundary layers" – revealing the wartime work of his group at the National Bureau of Standards that resulted in the discovery of Tollmien–Schlichting waves [75]. Another speaker at this symposium was George K. Batchelor from Cambridge, UK, who reported about a "remarkable series of coincidences" concerning the theory of homogeneous isotropic turbulence. Batchelor informed the attendees about Kolmogorov's 1941 papers [53,54] and the theories elaborated independently from another in 1945 by Lars Onsager [76] in the United States and by Carl Friedrich von Weizsäcker and Werner Heisenberg in England during their detention at Farm Hall near Cambridge [77].

There are fascinating first-hand accounts of how Batchelor had become aware of Kolmogorov's now famous papers in the English language editions of the 1941 issues of the proceedings of the Russian Academy of Sciences, and how he became involved himself in turbulence research in 1945 [78,79]. Onsager's motivation and approach has also been analysed in great detail in [80]. It only remains to add a few remarks about the circumstances in which von Weizsäcker and Heisenberg began to work on turbulence in summer 1945.

In order to make good use of the time of their arrest, the 10 detainees started a series of colloquia in which they reviewed their mutual fields of interest. On Friday, 25 May 1945, one of them (Erich Bagge) entered in his diary: "This day was dedicated to a colloquium on turbulence." The speaker was von Weizsäcker. "A very nice idea resulted from the discussion," the entry reveals about the outcome of this colloquium [81, pp. 48–53]. Von Weizsäcker's motivation to put turbulence on the agenda of the colloquia was due to his recent work on the origin of the planetary system, in which turbulence was supposed to play a crucial role within the circumsolar gas disk from which the sun and the planets would form [82]. At Farm Hall, he derived from dimensional considerations the scaling laws of the K41 theory. Heisenberg felt challenged by von Weizsäcker's results and explored the theory in more detail. According to Batchelor, they also discussed about their work with G.I. Taylor [78, pp. 171–172] who informed them that their results were identical with those of Kolmogorov and Onsager. Back in Germany, von Weizsäcker and Heisenberg elaborated their theory and submitted their papers by December 1946 to the *Zeitschrift für Physik*, where they appeared with a time lag of almost 2 years in 1948 [83,84].

Batchelor would have been surprised to learn that Prandtl, too, had arrived independently at these results. During the last months of the war, Prandtl derived from a cascade model the same results that Kolmogorov had obtained about the dissipation length scale [9]. Prandtl's effort began in autumn 1944 and was pursued until summer 1945. His notes remained unpublished. Nevertheless, they add to the "remarkable series of coincidences" about which Batchelor had reported at the Paris Congress. From a paper that Prandtl co-authored with his disciple Karl Wieghardt and that was published in 1945 [85], it is obvious that this was his favourite subject of research during the last months of the war. Furthermore, Prandtl hinted at an unpublished paper "on the role of viscosity in the mechanism of developed turbulence" in a report to the Field Intelligence Agency, Technical, (FIAT), which reviewed German achievements in science during the war period [74, p. 77]. On a timeline of the K41 theory, Prandtl's contribution has to be placed after the pioneering Russian work and before the contributions of Onsager, Weizsäcker and Heisenberg. A first analysis is presented in [9], but the accomplishment is worth more scrutiny. From an historical perspective, it belongs to the category of multiple simultaneous discoveries [86], such as the discovery of energy conservation in the nineteenth century that has been analysed by Thomas S. Kuhn in a classic study [87].

Batchelor's and Dryden's reports at the Paris Mechanics Congress on the K41 accomplishments and the experimental verification of the Tollmien–Schlichting instability were not the only revelations that made this meeting so remarkable. In his four-page report for *Science*, Dryden singled out several other contributions to the turbulence symposium: J.O. Hinze's on the mechanism of disintegration of high-speed liquid jets; J. Kampé de Fériet's critique of the Reynolds averaging; Alexandre Favre's description of an apparatus for the measurement of time correlations in turbulent flow; C.C. Lin's revision of the Orr–Sommerfeld approach on hydrodynamic stability; and Francois Naftali Frenkiel's turbulence measurements conducted in his doctoral work under the supervision of Kampé de Fériet [75]. Unfortunately, the proceedings of this congress have never been published. But its very large international attendance (according to Dryden there were "about 100 Englishmen, 100 Frenchmen; 52 Americans; large delegations from Belgium, Holland, Italy, Switzerland, Roumania and Czechoslovakia; many from Sweden, Turkey and Poland; 3 from Russia; and 2 from China") suggests that the international research on turbulence was fairly well represented in Paris – except the work of the Germans who were not yet admitted. Those singled out in Dryden's report would present their work on turbulence again 15 years later at Marseille. If there is a single event that opened the route to

Marseille 1961, this is the turbulence symposium of the Paris Congress for Applied Mechanics in 1946.

6. A new forum – the International Union of Theoretical and Applied Mechanics (IUTAM)

However, there are rarely unique single causes for major events in the history of science. We have to take into account the international post-war reconstructions on a larger scale. Although the International Congresses for Applied Mechanics were organized by international congress committees, there was no institutional host in the form of an official international organization. In 1946, Burgers suggested to found such an organization in order to lay down a more permanent international basis. He envisioned a Union of Applied Mechanics as part of the International Council of Scientific Unions (ICSU), which had already served before the war as a forum of several disciplines [88].

Once more, the advocates of international science, von Kármán and Burgers, whose initiative had given birth to the tradition of international mechanics congresses in the early 1920s, were the key figures behind this plan.[3] Burgers further discussed the plan with the general secretary of the ICSU. He also succeeded to persuade sceptics such as G.I. Taylor. Fluid dynamics had ramifications into many disciplines, so Burgers regarded cross-fertilization as an attractive prospect: "It is taken in view, e.g., to form a joint international committee on viscosity and related matter, out of delegates nominated by the Union of Physics, the Union of Chemistry, the Union of Biology and, if it exists, the Union of Applied Mechanics." But Taylor was still hesitant: "I dare say," he responded, "it is the right thing but I think the matter should be discussed well. If I see Kármán, I will ask him what he thinks" [89, pp. 42–43].

The Paris Congress in September 1946 offered an opportunity for further discussions. Still it took a while to persuade the sceptics. The British members of the congress committee feared a loss of flexibility. Others seemed to share this concern. Only when Burgers drafted the statutes of the Union in such a way that these concerns were met, the plan materialized. On 26 December 1946, the International Union of Theoretical and Applied Mechanics (IUTAM) was officially constituted; in April 1947, its statutes were approved, and in September 1947, a provisional bureau was set up, with Richard Vynne Southwell as the acting president, Dryden as the acting treasurer and Burgers as the acting secretary [89, p. 47]. With regard to politics and funding, IUTAM, as part of the ICSU, was closely related to the United Nations Educational, Scientific and Cultural Organization (UNESCO), another newly established framework for international collaboration after the Second World War [88].

Among IUTAM's first activities was the organization of the Seventh International Mechanics Congress scheduled to take place in September 1948 in London – 2 years earlier than according to the accustomed 4-year interval because otherwise it would have interfered with the International Congress of Mathematicians scheduled for 1950. Chaired by Southwell as IUTAM's president, the congress confirmed the great interest in renewing the prewar tradition. Similar to the Paris Congress in 1946, it did not yet represent a truly international community. Among the 882 participants, the only Germans were those who had emigrated to other countries before the war. However, the absence of Prandtl and his pupils did not result in a distorted representation of specialties. The London congress made visible to what extent the field had grown since the 1920s. The proceedings comprised four volumes. Similar to 2 years before at the Paris Congress, turbulence was an outstanding theme. Batchelor presented the general lecture on "Recent developments

in turbulence research". Other remarkable presentations on turbulence were those on the decay of turbulence by Frenkiel ("Comparison between theoretical and experimental results of the decay of turbulence") and Lin ("On the law of decay and the spectrum of isotropic turbulence") or Townsend's report on turbulent diffusion ("Diffusion in the turbulent wake of a cylinder"). A number of those who had presented papers on turbulence at Paris were again performing at London, such as Batchelor, Dryden, Favre and Hinze. Although it would be premature to speak of a distinct international community of turbulence research, the London Congress has to be mentioned among the events that gave rise to its formation [90]. The subsequent quadrennial Congresses in Istanbul (1952), Brussels (1956) and Stresa (1960) – to name only those before Marseille 1961 – confirmed IUTAM's importance in this regard.

But Burgers had broader ambitions than offering a new forum for the mechanics congresses. He regarded it dissatisfactory that IUTAM would organize merely these 4-year events and remain inactive in the interim period. His primary motive for the foundation of IUTAM was to enable cross-fertilization by cooperation with other unions of the ICSU. However, there seemed to be "no great desire for joint work in this domain," he complained in a letter to Kármán in February 1948. In order to encourage such cooperation, Burgers proposed to organize international symposia between the congresses. A first step in this direction was the establishment of a committee whose task was to plan a joint symposium with the International Astronomical Union (IAU). Other committees were established for other tasks, such as promoting "computing laboratories." It was left to each committee "to co-opt members from ex-enemy countries and to admit scientists from such countries to meetings arranged by them" [89, p. 48]. While these committees consisted of individual members, IUTAM was formed by national scientific organizations as members. In 1948, IUTAM consisted of only two "adhering organisations," the Royal Society of London and the Hungarian Academy of Sciences. Over the years, however, IUTAM grew into an international organization of broad scope, encompassing a very heterogeneous mix of different national research cultures [91, p. 16]. Germany was officially invited to join the ICSU in 1950. In the same year, GAMM became a member of IUTAM.

The year 1950 may be regarded as a watershed for the reception of German science in the international arena after the Second World War. In the same year, German mathematicians were invited to participate in the International Congress of Mathematicians held in September 1950 in Cambridge, MA. Before this congress was opened, the International Union of Mathematics was founded in New York. German mathematicians, represented by the DMV, were invited to participate in its inauguration. "We will be able to perform in America completely on an equal footing with the international family of mathematicians", the chairman of the DMV informed the German participants of the Cambridge congress. However, he alerted his colleagues that the atmosphere would not be entirely relaxed: "We cannot expect that we will be greeted friendly by every participant."[4] In addition, German scientists faced visa problems. With the rise of McCarthyism, further obstacles were put in the way of a revival of international scientific relations of American scientists with colleagues from other countries. In 1954, the chairman of the Federation of American Scientists reported that foreign colleagues who were invited to America were "deeply disappointed by the increasing narrow-mindedness of U.S. authorities and by the raising of a new paper curtain between America and the rest of the world" [92].

Nevertheless, German scientists were eager to seize any opportunity to participate in conferences and accepted invitations to the United States for guest lectures even if this involved hostile reactions. IUTAM was welcomed by the German fluid dynamicists as a new international umbrella. Apart from its internationality, IUTAM also embodied a diversity

of fields where fluid dynamics would find new applications. This is illustrated by the IUTAM symposia organized with other unions. A new territory between fluid mechanics and astrophysics, for example, was opened by common symposia with the IAU. The theme of these conferences was "cosmical gas dynamics." In the course of these meetings, turbulence became firmly established as a research field of utmost pertinence for astronomers. At the first symposium held in August 1949 in Paris on "Problems of cosmical aerodynamics," Burgers emphasized in his introduction how important the "present-day developments in hydro- and aerodynamics" were for astronomers. "In particular, the problems of turbulence and those of expansion phenomena and of shock waves immediately come to the foreground." With regard to turbulence, this was illustrated by the lectures of von Weizsäcker on "Turbulence in interstellar matter" and Batchelor on "Magnetic fields and turbulence in a fluid of high conductivity" [95]. The second symposium of this series was held in July 1953 at Cambridge, UK, and displayed turbulence as a subject of growing concern [96].

Other IUTAM symposia explored common grounds with geophysicists, such as a symposium at Cornell on "Fluid mechanics in the ionosphere" in 1959 and on "Fundamental problems in turbulence and their relation to geophysics" in 1961 in Marseille [91, appendix 18]. Before I turn to the latter in more detail, however, it is expedient to add more context about the post-war reconstructions, particularly in the United States.

7. How American physics appropriated fluid dynamics

With regard to the development of radar and the atomic bomb, the Second World War was called "A physicists' war" [97, chapter 20]. Research on turbulence as was done in Dryden's and von Kármán's institutes, the physics of shock waves and other investigations from one or another branch of fluid dynamics were part and parcel of the scientific wartime effort. This legacy motivated representatives of the American Physical Society (APS) to consider fluid dynamics as a sub-discipline of physics in a new Division of Fluid Dynamics (DFD). Its foundation illustrates how specialties that had been considered mainly from the vantage point of engineering became embraced under the realm of physics. Fluid dynamics in general, and turbulence in particular, would benefit from this trend.

The history of the DFD began in June 1946, when Edward Condon, the president of the APS, appointed von Kármán, Dryden, Howard W. Emmons, John von Neumann and Raymond J. Seeger as members of a new Committee on Fluid Dynamics. Each one of them had a record of pertinent war work. Seeger, the head of the Aeroballistic Research Department at the Naval Ordnance Laboratory (NOL) at White Oak, MD, was chosen as the chairman. In August 1946, after returning from the Bikini Atoll where he was involved with atomic bomb tests, Seeger organized, as a first step at the forthcoming annual physics conference of the APS in January 1947 in New York, a symposium on "Recent trends in fluid dynamics" with von Kármán and Hans Bethe as invited lecturers. He suggested furthermore "to consider the means of continuing the advancement and diffusion of knowledge on Fluid Dynamics" at the APS business meeting during this conference.[5] In a letter to Bethe, Seeger explained the goals of his committee: "Many of us feel that Fluid Dynamics is a subject of considerable physical interest which has been neglected by physicists in the past and revived only during the war. We are eager, therefore, to continue this interest, perhaps by having a permanent committee or even a division of the American Physical Society."[6]

The New York meeting of the APS in January 1947 brought to the fore that fluid dynamics deserved indeed more attention on the part of the physics community. Dryden's collaborators, Skramstadt and Schubauer, for example, introduced the American physicists

at this meeting to their wartime discovery of boundary layer instability. The forthcoming Washington meeting of the APS in May 1947 provided another occasion to demonstrate that there was a continuous and growing interest in fluid dynamics. Seeger ascertained the interest of the editor of the *Journal of Applied Physics* and announced a growing number of papers on fluid dynamics, which were likely to be submitted to this journal in the future. "In general," he explained the scope of these papers, "the physics of fluid dynamics is understood to include aerodynamics, hydrodynamics, ballistics, water entry, and explosion phenomena."[7] The journal editor was "quite enthusiastic" and pleased to learn "that the Committee on Fluid Dynamics is considering the Journal of Applied Physics as its official outlet."[8]

Shortly after the Washington meeting, Seeger officially proposed to the Council of the APS the establishment of a DFD. The Council gave the green light at a meeting in Montreal on 20 June 1947. Subsequently, by-laws had to be formulated. The recently established Division of Solid State Physics of the APS served as a role model. In August 1947, Seeger submitted a first draft of by-laws and a circular to the secretary of the APS.[9] In October 1947, the secretary of the APS announced that the DFD has been authorized by the Council; he described its object as "the advancement and diffusion of knowledge of the physics of fluids including aerodynamics and hydrodynamics, phenomena of rarefied gases and explosions, plasticity, et al." and opened the new division for enrollment.[10] The Division's major activity was to organize meetings at least once a year "at such time and place as shall be ordered by the Executive Committee." The meetings should be organized together with the annual APS conferences. At each meeting, a Programme Committee was in charge of the organization. Official announcements should be published in the *Journal of Applied Physics*, designated for the time being as the official organ of the DFD.[11] By January 1948, the by-laws were approved.[12]

With the organizational problems settled, the focus shifted to topics suitable for sessions at forthcoming Division meetings. Among other subjects, turbulence was chosen as a topic for the joint meeting with the Aeronautical Society at the forthcoming APS conference, held in January 1949 in New York. As it turned out, the interest in turbulence was so strong that it became split in a two-session symposium of 2 days during the week of the New York meeting.[13]

In June 1949, the APS held its Semi-Centennial Meeting in Cambridge, MA. Dryden, the acting chairman of the DFD of this year, used the opportunity for a review. He praised Seeger, "a physicist who had become interested in fluid dynamics as a result of his wartime work," as the "leading spirit" behind the formation of the DFD and hoped that it resulted in a "permanent consideration of fluid dynamics by physicists." He discerned some problems "which should receive greater attention from the most capable physicists," first and foremost "that of the turbulent motion of fluids." Heisenberg's recent contribution served him as an example how a physicist whose reputation was due to his achievements in quantum physics could do pioneering work in this field as well. Alluding to Heisenberg's internment at Farm Hall, he mused that Heisenberg was "fortunately for turbulence research forcibly diverted from nuclear research and compelled to seek new interests."[14]

8. The emergence of a turbulence community

Events such as the 1949 Paris congress on "Problems of cosmical aerodynamics" organized under the umbrella of IUTAM and IAU, the Turbulence Symposium organized by the DFD the same year at the APS meeting in New York, and similar gatherings signalled the rise of turbulence as a concern for a scientific community with quite different roots – but a

common goal. A major actor in this effort was Francis Clauser whom the DFD charged with the organization of the New York Symposium.

Clauser, a student of von Kármán, was called after the war to Johns Hopkins University in order to build up a new Department of Aeronautics. Next to supersonics, he regarded turbulence as a most important field of research. In order to firmly establish turbulence on the agenda of his Department, Clauser hired in 1947 Stanley Corrsin as an assistant professor.[15] Clauser was also very eager to make his institute part of the network of military research establishments in the vicinity of Johns Hopkins, such as Seeger's Aeroballistic Department at the NOL in White Oak, MD, with whom he established a "joint venture" in turbulence research. "I believe that some kind of mutual arrangement could and should be worked out," Seeger agreed with Clauser's suggestion. "In that connection, I still have hopes that we will be able to avail ourselves of the part-time services of Corrsin. It turns out that we are becoming interested now with turbulence."[16]

With regard to the forthcoming Turbulence Symposium in New York, Clauser began in autumn 1948 to look for suitable speakers. "I have received acceptances from Chandrasekhar, Liepmann and Kovasznay to give papers," Clauser informed the chairman of the DFD by November.[17] Liepmann, from the GALCIT in Pasadena, CA, was an old acquaintance of Clauser from common years at Kármán's institute. Leslie S.G. Kovasznay had recently moved to Johns Hopkins University and Clauser had just hired him at his department "to handle a research project on the measurement of turbulence in high speed air streams by means of a hot wire anemometer," as he explained in the yearly report of his department. "Dr. Kovasznay is a graduate of the Royal Hungarian University at Budapest where he was a member of the faculty. Afterwards he was engaged in research work for one year at Cambridge, UK, before coming to this country."[18] The Indian astrophysicist Subrahmanyan Chandrasekhar had already come to America before the war to work at the Yerkes Observatory in Williams Bay, WI, run by the University of Chicago [98, chapter 9]. Another invited speaker to the New York Turbulence Symposia was the Princeton astrophysicist Martin Schwarzschild. Both, Schwarzschild and Chandrasekhar, had just begun to correspond extensively about turbulence as a subject of major concern for astrophysics.[19]

Besides astrophysicists and aeronautical scientists whose affiliation with turbulence was taken for granted, Clauser also invited the mathematician Mark Kac and the physicist George Uhlenbeck to the New York Turbulence Symposium, although they had little prior expertise on this problem. Kac responded that he knew "next to nothing about turbulence," but nevertheless accepted to deliver an invited lecture because Clauser regarded Kac's specialty of random noise as most pertinent.[20] Uhlenbeck was invited for his knowledge in statistical mechanics: "At present there is an effort to carry over into turbulence many of the concepts that have been developed in statistical mechanics," Clauser explained, "I believe that many of the people interested in turbulence would be eager to hear a discussion of the conceptual difficulties that now exist in the statistical mechanics and that would continue to be troublesome when application is made to turbulence."[21]

Although Chandrasekhar and Uhlenbeck finally could not attend, the invitations reveal the intention to look for physicists with quite different orientations. The lecturers at the New York Turbulence Symposium were Corrsin ("Some measurements in a round turbulent jet"), Kac ("Statistical analysis of random functions"), von Kármán and Lin ("Statistical theory of isotropic turbulence"), Kovasznay ("Optical methods of measuring turbulence"), Schwarzschild ("Turbulence in the atmosphere of stars") and G.C. Williams ("Combustion-generated turbulence in relation to flame propagation") [99, p. 1282]. The DFD regarded the event to be so successful that turbulence entered the agenda of future meetings as a subject of special sessions. In summer 1949, for example, at the inauguration of new

facilities of Seeger's Department on Aeroballistics, the DFD convened a 2-day conference at NOL with another special session on turbulence chaired by Burgers. The invited speakers were Kampé de Fériet ("Spectral tensor of a homogeneous turbulence"), Batchelor ("The nature of turbulent motion at large wave-numbers"), Chandrasekhar ("Development of Heisenberg's theory of the decay of isotropic turbulence"), H.B. Squire (Investigation of the turbulence characteristics of an experimental low-turbulence wind tunnel") and Frenkiel ("Some remarks on turbulent diffusion").[22] Batchelor used this occasion to promote K41 in the United States. "You will have seen previously from the programme of the dedication ceremonies that Dr. Batchelor is speaking in the turbulence symposium, on the Cambridge work in extending Kolmogoroff's theory", an NOL scientist wrote to Clauser. "He has asked me to arrange, if possible, for some lectures during his stay in the USA."[23]

The role of Batchelor's promotion of Kolmogorov's theory can hardly be exaggerated. "When you are in Cambridge, you should try to see Batchelor, he is an awfully good man and very sound contrary to the other Cambridge luminaries in astrophysics," Chandrasekhar advised Schwarzschild in May 1950 when Schwarzschild went on a trip to Europe.[24] When G.I. Taylor asked Chandrasekhar in September 1951 for a report on Batchelor concerning Batchelor's application for a fellowship at Trinity College, Chandrasekhar was again full of praise: "I am very well acquainted with Dr. Batchelor's work on the theory of turbulence. Indeed, when about two years ago I started seminar classes on 'The theory of turbulence', I found that the most satisfactory way to go about learning the subject was to read and discuss the various papers of Dr. Batchelor, one by one."[25] Batchelor's book on *The Theory of Homogenous Turbulence*, first published in 1953, "is substantial and it merits the recognition it received," Chandrasekhar still wrote 15 years later in another report; by that time, however, he expressed his opinion with the hindsight of the subsequent development. He claimed that he had become "disillusioned very rapidly by the sterility of his approach to scientific problems."[26]

Chandrasekhar's disillusionment may well have been the result of some rivalry, because Batchelor's book rendered Chandrasekhar's plan for a similar monograph obsolete. "I have in mind a book on 'The Statistical Theory of Turbulence'. At the moment there exists no monograph on the subject from which one may learn the newer developments of the past 15 years," Chandrasekhar had confessed to Neville Mott in August 1950. The plan matured into a book proposal to the Oxford publisher Clarendon Press, but when Batchelor's monograph appeared in 1953, the need for another monograph vanished. In December 1956, Chandrasekhar admitted: "I have since changed my mind and would rather write my book on stability first."[27] Chandrasekhar's *Hydrodynamic and Hydromagnetic Stability* appeared at Clarendon Press in 1961 and became a classic. The planned book on turbulence never appeared. In an interview, he remarked many years later about his work on turbulence in the early 1950s: "I did publish a few papers in the subject for two or three years; but I found that I was not making much progress. Moreover, the area was becoming controversial. I therefore left the subject and went on to problems in hydrodynamic and hydromagnetic stability which occupied me all during the fifties."[28]

It would exceed the scope of this review to report about all events that focused on turbulence in this period. John von Neumann visited in August 1949 several European centres of research and addressed a remarkable report (published only in 1963) to the Office of Naval Research [101]. Tollmien presented several reviews: in 1951 at a GAMM conference, in 1952 at the IUTAM Congress in Istanbul and in 1954 at the occasion of the 50th birthday of Prandtl's boundary layer concept [102–104]. Theodore von Kármán and Kampé de Fériet presented reviews at other occasions [105,106]. Dryden reviewed in May 1950 "The turbulence problem today" [107] at the Midwestern Conference on Fluid

Dynamics, held at the University of Illinois, Urbana, IL, in a joint meeting with the DFD, and "Fifty years of boundary-layer theory and experiment" in a banquet speech at a DFD meeting in November 1954 at Fort Monroe, VA.[29] He even presented some statistics about publications: "The turbulent incompressible boundary layer receives considerable attention with about 45 papers," he concluded. With regard to the turbulent compressible boundary layer, he counted 35 papers. "Stability and transition form the principal topic of about 70 papers," he reported about what was regarded in the 1920 as *the* turbulence problem. Dryden concluded his survey by stating: "The current total rate of production of papers is about 10 papers per month, nearly 9 times the rate immediately preceding World War II" [108]. Two years later, IUTAM chose the same theme as the subject of a special symposium held in Freiburg, Germany [109].

9. New journals

In terms of journals ready to accept research papers on turbulence, the situation by the mid-1950s was the same as before the war. When the DFD of the APS was founded in 1947, they had chosen the *Journal for Applied Physics* as their publication outlet. But this situation was regarded as unsatisfactory. According to the minutes of a DFD meeting in January 1949, there was "a feeling among a considerable number of members of the Fluid Dynamics Division that there was a real need for a new journal in this field."[30] However, it took another couple of years until this feeling was turned into action. The initiative was launched by a survey of the American Institute of Physics (AIP) to determine how the American physicists used the present journals and what needs they expressed for the future. Based on this survey, the AIP envisioned "a new pattern of journal publications."[31] The DFD seized the opportunity and revealed their plan of a *Journal of Fluid Physics*, as the secretary of the DFD wrote to the chairman of the AIP's Governing Board. "We would wish to see included in the proposed journal basic research papers in magnetohydrodynamics, shock wave phenomena, compressible and high temperature fluid flows, plastic flow, turbulence, liquid state physics, ionized fluid and plasma flows, as well as certain basic aspects of fluid physics bordering geophysics and astrophysics."[32]

Frenkiel became the major actor for the foundation of the planned journal. He had actively contributed to turbulence and presented papers at preceding IUTAM Congresses and numerous other occasions. His career mirrored the turbulent historical events of the preceding decades [110]. After his doctoral work with Kampé de Fériet and the German invasion of France in 1940, he had moved with his mentor to the Aeronautical Research Station in Toulouse. When the German occupation was extended to southern France, he was imprisoned and spent the remaining 2 years of the war in concentration camps. His wife and their unborn child were killed by the Nazis. After the war, Frenkiel emigrated to the United States, where he was employed for short periods at the Department of Aeronautical Engineering of Cornell University and at the NOL. In 1950, he joined the Applied Physics Laboratory of Johns Hopkins University at Silver Spring, MD, which had close ties with Clauser's Department of Aeronautics. The latter move was once more caused by the political events of the Cold War. In the course of Project "Paperclip," the NOL employed German aerodynamicists who had participated in the V-2 project at Peenemünde. One of them (Hermann H. Kurzweg) became Frenkiel's chief – a situation that he was unwilling to tolerate. "And five years have not wiped out from my memory Buchenwald and Auschwitz," Frenkiel wrote to Kármán shortly before quitting the NOL.[33]

As Secretary of the DFD, Frenkiel made the plan for the new journal his mission. Together with geophysicist Walter M. Elsasser, he drafted a memorandum as a first step.

"There is at present no journal in the United States in which fundamental contributions to the field of fluid physics can be published with a view of circulation among those interested in the physics rather than the engineering aspects", as they explained. The list of subject matters to be covered was as broad as in the earlier outline, except that they now specified "statistical theory of turbulence" as an additional item. "Emphasis should not be on applied mathematics but on that combination of experiment, conceptual models, and formal analysis that is thought of as characterizing good physics."[34]

By the same time, in May 1956, they learned "that Batchelor in Cambridge is about to start a new journal on Fluid Mechanics," as Elsasser informed Frenkiel. "I presume that it would be a good idea to inquire with Batchelor about his programme, but since you are nearer to the centre of things, this perhaps could better be done by you than by me."[35] Batchelor spent a week in September 1956 in Washington, DC, where he attended a symposium on naval hydrodynamics. On this occasion, he informed Schubauer "that the Journal of Fluid Mechanics is intended to be Anglo-American in character" with two associate editors from the Universities of Princeton (W.C. Griffith) and Harvard (George Carrier). "Dr. Batchelor took the view that it might be wise to wait and see whether the Journal of Fluid Mechanics could meet the needs in this field before setting up another journal."[36] Batchelor also informed Frenkiel directly about the background and tendencies of his journal.[37]

But the "wait-and-see" attitude did not fit well with the AIP intentions, which concerned the need for new journals in other physical sub-disciplines also, nor pleased it Frenkiel. "The Executive Committee of the Governing Board of the American Institute of Physics looked with very strong favor upon the idea of starting a new journal of the general scope of that on fluid physics," Frenkiel wrote 2 weeks later to Seeger, who had by this time assumed science-policy responsibilities at the National Science Foundation. "The Chairman of the Governing Board and the Director of the Institute informed me that the whole matter is expected to be brought to a climax at the time of the next meeting of the Governing Board and that there is a likelihood that the journal could be started during 1957."[38] He also circulated a questionnaire to the members of the DFD concerning the planned scope and title of the new journal.

Batchelor was "dismayed and disturbed" about this move and appealed to Frenkiel as a representative of their common field of research. "Do you not think that the Fluid Dynamics Division would be doing science a service by strengthening an international Journal rather than by setting up another national journal?"[39] But Frenkiel was already carrying the initiative a step further. He formed a committee with the task to present the Governing Board of the AIP with a more definite proposal about the new journal. At the first meeting of this committee in February 1957, Batchelor's concerns were dismissed. There was "unanimous agreement" that the proposed AIP journal and the *Journal of Fluid Mechanics* could both flourish.[40] Three weeks later, the Governing Board of the AIP authorized the establishment of the new journal, entitled "The Physics of Fluids"; the first issue was due to appear in January 1958.[41]

Batchelor was frustrated. "In these circumstances," he wrote to Frenkiel, "it is perhaps not necessary to go on talking about the pros and cons of the new journal." In an effort to cut his losses, he proposed a division of labour, along the lines suggested earlier by Raymond Emrich, that the *Journal of Fluid Mechanics* would focus "on the mechanical aspects of fluid motion" and the new AIP Journal "on the more physical aspects." Although he admitted that such a discrimination was problematic, he hoped that this would reserve most of the papers on fluid mechanics proper, such as "hydrodynamics, dynamics of compressible fluids, boundary layer and turbulent phenomena," for his own journal. "It

seems to me that these particular topics are essentially mechanical, and might well be left to JFM."[42]

If such a division of labour had been adopted, Batchelor's *Journal of Fluid Mechanics* would have become the main Anglo-American publication outlet for turbulence research. However, Frenkiel responded that he had "no authority to commit the future editorial policy of the journal" and expressed his confidence that the competition between both journals would be "of a constructive nature."[43] The next day he drafted a memo about the editorial organization of *The Physics of Fluids*. With regard to the scope of the journal, he resumed what he had drafted earlier together with Elsasser and what had been authorized with a little modification by the planning committee: "The scope of these fields of physics includes: hydrodynamics, dynamics of compressible fluids, shock and detonation wave phenomena, hypersonic physics, rarefied gases and upper atmosphere phenomena, transport phenomena, hydromagnetics, ionized fluid and plasma physics, liquid state physics, superfluidity, boundary layer and turbulence phenomena, as well as certain basic aspects of physics of fluids bordering geophysics, astrophysics, biophysics and other fields of science. Emphasis will not be on applied mathematics, but on that combination of experiment, conceptual models, and formal analysis that is thought of as characterizing good physics."[44]

On 1 July 1957, Frenkiel formally announced that the editorial board of the *The Physics of Fluids* became operative.[45] By that time, Batchelor's *Journal of Fluid Mechanics* was already in operation for more than a year; the first issue of volume 2 would appear in August 1957. Both journals flourished and had to enlarge their volume in the following years and decades. From *The Physics of Fluids* emerged *Physics of Fluids B* in 1989 and *Physics of Plasmas* in 1994. The editors of both the journals, Batchelor and Frenkiel, had contributed to turbulence research themselves with pioneering work. Turbulence ranked high on the list of topics in both the journals. Among the first papers submitted to *The Physics of Fluids*, for example, was Corrsin's paper "Statistical behavior of a reacting mixture in isotropic turbulence." In the 4 years from 1958 to 1961, both journals published 76 papers concerned with turbulence (35 in *The Physics of Fluids*, while 41 in the *Journal of Fluid Mechanics*). As Frenkiel had predicted, there was no dearth of papers [111,112].

10. Conclusion

By the time of the Marseille events in 1961, turbulence had become an active research field. Besides a host of journal papers and conference contributions, there were monographs [113–115] which provided an introduction to the field for a new generation of researchers. Yet it is difficult to assess turbulence in terms of one or another discipline. By their institutional affiliation, turbulence researchers belonged to aeronautical engineering, applied mathematics, physics, mechanics or some other discipline. As illustrated by the formation of the DFD of the APS, fluid dynamics was recognized only after the Second World War as a sub-discipline of physics. It remains to study whether this was unique for the United States or whether it reflects in general the neglect of classical fields of physics due to the rise of atomic physics during the early decades of the twentieth century. Despite the surge of turbulence research during the 1950s, turbulence was not yet a specialty of its own right. The foundation of a journal dedicated exclusively to turbulence, and the establishment of a specialized series of conferences such as the Turbulence Conferences organized by the European Mechanics Society (EUROMECH), was still decades in the future.

Turbulence came of age not only because it was perceived as a particular challenge for mathematicians and theoretical physicists from the same mould of Kolmogorov or Heisenberg, but also because of its pertinence for several other disciplines. Transdisciplinarity was

(and still is) a characteristic feature of fluid dynamics at large. This became apparent, as we have seen, in 1949 with the joint venture of IUTAM and IAU at the Paris Symposium on "Problems of cosmical aerodynamics." Besides astronomy, the disciplines with a genuine interest in fluid dynamics were meteorology, oceanography and other geophysical disciplines. In the Russian school of turbulence, for example, fundamental research on turbulence was advanced with a strong focus on geophysical applications [52]. With the proclamation of 1957 as the International Geophysical Year (IGY), fluid dynamics became internationally engaged in joint ventures with geophysics. "It may be significant that the active operation of our Editorial Board happens to start on the first day of the International Geophysical Year," Frenkiel remarked in his editorial announcement about his journal on the same day. "The scope of The Physics of Fluids includes several fields of fundamental importance to theoretical and experimental geophysics and it should be expected that our journal will contribute in some measure to the scientific interpretation and to the understanding of the numerous data obtained during IGY."[46]

The Marseille events – the colloquium held at the Institute for the Statistical Mechanics of Turbulence (IMST) from 28 August to 2 September 1961 and the symposium organized by the International Union of Geodesy and Geophysics (IUGG) and IUTAM from 4 to 9 September 1961 – also reflect this transdisciplinarity. The initiative for the latter was launched by the International Association of Meteorology and Atmospheric Physics, a sub-organization of IUGG, with a plan for a common IUTAM-IUGG symposium "on basic problems of turbulence and their relation to geophysics." In August and September 1960, the General Assembly of the IUGG and IUTAM approved this plan at their meetings in Helsinki and Stresa, respectively. A scientific committee, chaired by Frenkiel with Batchelor, Kenneth F. Bowden, Graham Sutten, Alexander M. Obukov, J. Peres and J.C. Schönfeld as members, was charged with the execution of this plan [116]. Once more, Frenkiel and Batchelor found themselves involved in a challenging organizatorial effort – this time however not as rivals but as members of the same committee. With Alexandre Favre, the director of the IMST, another promotor of turbulence research enters the stage whose activities deserve closer historical scrutiny – especially with regard to his international relations. Favre had visited Clauser's Department at Johns Hopkins University in May 1954 and subsequently spent 2 months at the California Institute of Technology in Pasadena, CA. "We had a very pleasant visit here from Professor Favre from Marseille," wrote Liepmann in July 1954 about Favre's residence at the GALCIT. "He has made some really nice space-time correlation measurements and his equipment for these measurements seems very good and at present pretty unique. Favre told me that ONERA wants him to go into high speed work on turbulence . . . ."[47]

Such haphazard remarks hint at the overall link between turbulence research and Cold War programmes during the 1950s. The work of Kovasznay, Liepmann and others in the United States should be regarded in the same context. Although the Cold War is rarely mentioned as a major factor that motivated research on turbulence, this is obvious when we consider institutions such as the NOL, where the DFD had organized a Turbulence Symposium, or the Applied Physics Laboratory (then mainly concerned with research for guided missiles) as the home of Frenkiel's Editorial Office for *The Physics of Fluids*.

These contexts should be analysed in more detail in future work on the history of turbulence. The often proclaimed riddles of turbulent flow [117] are not less fascinating from the vantage point of the historian than from the perspective of the scientist who attempts to solve them. Both have to face the transdisciplinary nature of fluid mechanics. Similar to engineers and scientists from this or that discipline, historians of science, on the one side, and historians of technology, on the other, tend to approach their subject from their

respective disciplinary grounds. Turbulence, however, does not belong to a single discipline. G.I. Taylor's statistical theory of turbulence in the 1930s, for example, was closely related to wind tunnel turbulence in aeronautical engineering. The interplay of theory and practice (hydraulics, aeronautics, ballistics, naval architecture, etc.) is a persistent trait of fluid mechanics throughout its history [118].

Yet this trait hardly shows up in models of scientific change such as Kuhn's theory of scientific revolutions [119]. The rise and fall of theories of turbulence could serve as a suitable proving ground for this model. What are the "paradigm changes" that separate different phases of "normal science" in the history of turbulence? Was Marseille 1961 such an event?

Acknowledgements

This work benefitted from a previous project on "Physik zwischen naturwissenschaftlich und technologisch orientierter Forschung: Das Beispiel der Strömungsforschung," supported by the Deutsche Forschungsgemeinschaft (FOR 393/2-1 and 393/2-2). I am particularly grateful to the staff of the archives and libraries cited in the footnotes for their help to find the pertinent source material, and to my colleagues at the Deutsches Museum where I found the appropriate environment for a work of this nature. My thanks go also to the organizers of the International Colloquium on "Fundamental problems of turbulence: 50 years after the Turbulence Colloquium Marseille 1961" for inviting me to present this historical review.

Notes

1. Prandtl to von Mises, 2 August 1921, MPGA, III, 61, Nr. 1078.
2. Material on this research is preserved in the Dryden Papers, Special Collections, The Milton S. Eisenhower Library, Johns Hopkins University, here in Subject-Files, Box 43, and Correspondence-Files ("1935-59, Misc. Dryden-Von Kármán Correspondence"); see also Dryden's correspondence with von Kármán in the Theodore von Kármán Collection at the California Institute of Technology, Pasadena, CA, Box 7, Folder 26 (TKC, 7-26).
3. Karman to Burgers, 3 June 1946, TKC, 4-25.
4. Kamke to Heisenberg, 19 July 1950, MPGA, Heisenberg Papers, Correspondence Folder 1950. Heisenberg used this opportunity to review his doctoral dissertation on turbulence, which subsequently appeared in English translation as a NACA Technical Memorandum [93,94].
5. Seeger to Darrow, 28 August 1946, APS DFD Archives, SC MS 0002, Special Collections, Lehigh University, Bethlehem, PA (henceforth abbreviated as DFDA), 4-1.
6. Seeger to Bethe, 28 August 1946. DFDA, 4-2.
7. Seeger to Hutchisson, 3 April 1947, DFDA, 4-2.
8. Hutchisson to Seeger, 15 April 1947, DFDA, 4-2.
9. Correspondence between Seeger and Darrow, June to August 1947, DFDA, 4-2 and 4-3.
10. Circular on the "Formation of a Division of Fluid Dynamics in the American Physical Society," 6 October 1947, DFDA, 4-3.
11. By-laws, undated (probably 1947), DFDA, 2-8.
12. Seeger to Darrow, 14 January 1948, DFDA, 4-4.
13. Emmons to the members of the Executive Committee, 17 August 1948 and 27 December 1948, DFDA, 4-5 and 4-6.
14. Draft of speech, 17 June 1949, Dryden Papers, Special Collections, The Milton S. Eisenhower Library, Johns Hopkins University, Pubs-files, 1949, Box 11, folder "Div of Fluid Mechanics – Amer. Physical Soc. – Cambridge 1949".
15. Clauser to Kouwenhoven, 26 May 1947, Ferdinand Hamburger Archives, Sheridan Libraries, Johns Hopkins University. Record Group 06.080, Department of Aeronautics, Subgroup 2, Series 1 (Professional Papers of Francis H. Clauser, 1946–1961, henceforth abbreviated as Clauser Papers), Folder: Kouwenhoven, William B., 1947–1953. On Corrsin's career and work on turbulence, see [56].

16. Seeger to Clauser, 26 September 1947, Clauser Papers, Folder: National Science Foundation, 1952–1961.
17. Clauser to Emmons, 2 November 1948, Clauser Papers, Folder: Turbulence Symposium, 1948–1949.
18. Clauser Papers, Folder: Isaiah Bowman, Report to, 1948–1949.
19. This correspondence is preserved in the Special Collections Research Center, University of Chicago Library, Subrahmanyan Chandrasekhar Papers 1928–1995 (henceforth abbreviated as Chandrasekhar Papers), Box 28, Folder 13.
20. Kac to Clauser, 19 November 1948, Clauser Papers, Folder: Turbulence Symposium, 1948–1949.
21. Clauser to Uhlenbeck, 16 November 1948, Clauser Papers, Folder: Turbulence Symposium 1948–1949.
22. DFDA, 1-3 and 4-7.
23. Smelt to Clauser, 13 April 1949, Clauser Papers, Folder: Smelt, Ronald, 1949.
24. Chandrasekhar to Schwarzschild, 1 May 1950, Chandrasekhar Papers, Box 28, Folder 12.
25. Chandrasekhar to Taylor, 24 September 1951, Chandrasekhar Papers, Box 31, Folder 3.
26. Chandrasekhar to O.J. Eggen, 13 September 1968, Chandrasekhar Papers, Box 11, Folder 11.
27. Chandrasekhar to Clarendon Press, 10 December 1956, Chandrasekhar Papers, Box 68, Folder 8.
28. Interview with Chandrasekhar by Spencer Weart, 31 October 1977, available at http://www.aip.org/history/ohilist/4551_3.html. The author of an obituary remarked that "Chandra perhaps wisely limited his work in this field and instead concentrated on linear stability problems" [100, p. 88].
29. DFDA, 1-3.
30. G.H. Shortley to the Members of the Committee on Publications in Fluid Dynamics, 4 April 1949, Physics of Fluids Records, 1956–1981, American Institute of Physics, Niels Bohr Library & Archives, College Park, MD (henceforth abbreviated: Physics of Fluids Records). Folder: Correspondence prior to 2 January 1958.
31. Memo by J.H. McMillen, 20 March 1956, Physics of Fluids Records, Folder: Correspondence prior to 2 January 1958.
32. Frenkiel to F. Seitz, 27 April 1956, Physics of Fluids Records, Folder: Correspondence prior to 2 January 1958.
33. Frenkiel to von Kármán, 17 February 1950, TKC, 94-12.
34. Proposal for a *Journal of Fluid Physics*, 10 May 1956, Physics of Fluids Records, Folder: Correspondence prior to 2 January 1958.
35. Elsasser to Frenkiel, 17 May 1956, Physics of Fluids Records, Folder: Correspondence prior to 2 January 1958.
36. Schubauer to Frenkiel, 26 September 1956, Physics of Fluids Records, Folder: Correspondence prior to 2 January 1958.
37. Batchelor to Frenkiel, 4 December 1956, Physics of Fluids Records, Folder: Correspondence prior to 2 January 1958.
38. Frenkiel to Seeger, 18 December 1956, Physics of Fluids Records, Folder: Correspondence prior to 2 January 1958.
39. Batchelor to Frenkiel, 7 February 1957, Physics of Fluids Records, Folder: Correspondence prior to 2 January 1958.
40. Minutes of the Meeting of the AIP Planning Committee, 21 February 1957, Physics of Fluids Records, Folder: Correspondence prior to 2 January 1958.
41. Frenkiel to Uhlenbeck and others, 5 April 1957, Physics of Fluids Records, Folder: Correspondence prior to 2 January 1958.
42. Batchelor to Frenkiel, 3 May 1957, Physics of Fluids Records, Folder: Correspondence prior to 2 January 1958.
43. Frenkiel to Batchelor, 13 May 1957, Physics of Fluids Records, Folder: Correspondence prior to 2 January 1958.
44. Draft, 14 May 1957, Physics of Fluids Records, Folder: Memorabilia for *The Physics of Fluids*.
45. Announcement, 1 July 1957, Physics of Fluids Records, Folder: Board of Editors.
46. Announcement, 1 July 1957, Physics of Fluids Records, Folder: Board of Editors.
47. Liepmann to Kármán, 15 July 1954, TKC, 18-20. See also Clauser to Martin 24 May 1954, Johns Hopkins University, Box 5: Folder: Maryland, University of, 1952–1954.

References

[1] J.L. Lumley and A.M. Yaglom, *A century of turbulence*, Flow Turbul. Combust. 66 (2001), pp. 241–286.

[2] P.A. Davidson, Y. Kaneda, K. Moffatt, and K.R. Sreenivasan (eds.), *A Voyage Through Turbulence*, Cambridge University Press, Cambridge, UK, 2011.

[3] A.S. Monin and A.M. Yaglom, *Statistical Fluid Mechanics. Mechanics of Turbulence*, Vol. 1, MIT Press, Cambridge, MA, 1971. (Original work in Russian 1965)

[4] A.S. Monin and A.M. Yaglom, *Statistical Fluid Mechanics. Mechanics of Turbulence*, Vol. 2, MIT Press, Cambridge, MA, 1975. (Original work in Russian 1965)

[5] D.J. De Solla Price, *Little Science, Big Science*, Columbia University Press, New York, 1963.

[6] O. Darrigol, *Turbulence in 19th century hydrodynamics*, Hist. Stud. Phys. Sci. 32(2) (2002), pp. 207–262.

[7] O. Darrigol, *Worlds of Flow*, Oxford University Press, Oxford, 2005.

[8] B. Launder and D. Jackson, *Osborne Reynolds: A turbulent life*, in *A Voyage Through Turbulence*, P.A. Davidson, Y. Kaneda, K. Moffatt, and K.R. Sreenivasan, eds., Cambridge University Press, Cambridge, UK, 2011, pp. 1–39.

[9] E. Bodenschatz and M. Eckert, *Prandtl and the Göttingen school*, in *A Voyage Through Turbulence*, P.A. Davidson, Y. Kaneda, K. Moffatt, and K.R. Sreenivasan, eds., Cambridge University Press, Cambridge, UK, 2011, pp. 40–100.

[10] L. Prandtl, *Über Flüssigkeitsbewegung bei sehr kleiner Reibung*, Verhandlungen des dritten Internationalen Mathematiker- Kongresses in Heidelberg vom 8. bis 13. August 1904, 1905, pp. 484–491. Available at http://www.mathunion.org/ICM.

[11] A. Sommerfeld, *Ein Beitrag zur hydrodynamischen Erklärung der turbulenten Flüssigkeitsbewegung*, Atti del IV Congresso Internazionale dei Matematici (Roma, 6–11 Aprile 1908), 3 (1909), pp. 116–124. Available at http://www.mathunion.org/ICM.

[12] W.M.F. Orr, *The stability or instability of the steady motions of a perfect liquid and a viscous liquid*, Proc. R. Ir. Acad. A 27 (1907), pp. 9–138.

[13] M. Eckert, *The troublesome birth of hydrodynamic stability theory: Sommerfeld and the turbulence problem*, Eur. Phys. J. His. 35(1) (2010), pp. 29–51.

[14] R. von Mises, *Kleine Schwingungen und Turbulenz*, Jahresbericht der Deutschen Mathematiker-Vereinigung 21 (1912), pp. 241–248.

[15] L. Rayleigh (J.W. Strutt), *On the question of stability of the flow of fluids*, Philos. Mag. 34 (1892), pp. 59–70.

[16] H. Hahn, G. Herglotz, and K. Schwarzschild, *Über das Strömen des Wassers in Röhren und Kanälen*, Zeitschrift für Mathematik und Physik 51 (1904), pp. 411–426.

[17] O. Haupt, *Über die Entwicklung einer willkürlichen Funktion nach den Eigenfunktionen des Turbulenzproblems*, Sitzungsberichte der mathematisch-physikalischen Klasse der K. Bayerischen Akademie der Wissenschaften, 1912, pp. 289–301.

[18] O. Blumenthal, *Zum Turbulenzproblem*, Sitzungsberichte der mathematisch-physikalischen Klasse der K. Bayerischen Akademie der Wissenschaften, 1913, pp. 563–595.

[19] F. Noether, *Über die Entstehung einer turbulenten Flüssigkeitsbewegung*, Sitzungsberichte der mathematisch-physikalischen Klasse der K. Bayerischen Akademie der Wissenschaften, 1913, pp. 309–329.

[20] H.A. Lorentz, *Over den weerstand dien een vloeistofstroom in eene cilindrische buis ondervindt*, Versl. K. Akad. Wet. Amsterdam 6 (1897), pp. 28–49.

[21] L. Prandtl, *Der Luftwiderstand von Kugeln*, Nachrichten der Gesellschaft der Wissenschaften zu Göttingen, Mathematisch-physikalische Klasse, 1914, pp. 177–190.

[22] F. Noether, *Zur Theorie der Turbulenz*, Nachrichten von der Gesellschaft der Wissenschaften zu Göttingen, Mathematisch-Physikalische Klasse, 1917, pp. 199–212.

[23] O. Reynolds, *An experimental investigation of the circumstances which determine whether the motion of water in parallel channels shall be direct or sinuous and of the law of resistance in parallel channels*, Philos. Trans. R. Soc. 174 (1883), pp. 935–982.

[24] O. Reynolds, *On the dynamical theory of incompressible viscous fluids and the determination of the criterion*, Philos. Trans. R. Soc. 186A (1895), pp. 123–164.

[25] A.B.J.C. de Saint-Venant, *Mémoire sur des formulaes nouvelles pour la solution des problèmes relatifs aux eaux courantes*, Comptes Rendues de l'Académie des Sciences, Paris 31 (1850), pp. 283–286.

[26] J. Boussinesq, *Essai théorique sur les lois trouvées expérimentalement par M. Bazin pour l'écoulement uniforme de l'eau dans les tuyaux découverts*, Comptes Rendues de l'Académie des Sciences, Paris 71 (1870), pp. 389–393.
[27] R. von Mises, *Zur Einführung. Über die Aufgaben und Ziele der angewandten Mathematik*, Z. Angew. Math. Mech. (ZAMM) 1 (1921), pp. 1–15.
[28] R. von Mises, *Zur Versammlung der Mathematiker und Physiker in Jena*, Z. Angew. Math. Mech. (ZAMM) 1 (1921), pp. 341–342.
[29] L. Prandtl, *Bemerkungen über die Entstehung der Turbulenz*, Z. Angew. Math. Mech. (ZAMM) 1 (1921), pp. 431–436.
[30] L. Schiller, *Experimentelle Untersuchungen zum Turbulenzproblem*, Z. Angew. Math. Mech. (ZAMM) 1 (1921), pp. 436–444.
[31] F. Noether, *Das Turbulenzproblem*, Z. Angew. Math. Mech. (ZAMM) 1 (1921), pp. 125–138, 218–219.
[32] G. Battimelli, "*Senza alcun vincolo ufficiale*": *Tullio Levi-Civitá a i Congressi Internazionali di Meccanica Applicata*, Riv. Stor. Sci. 4(1) (1996), pp. 51–80.
[33] T. von Kármán and T. Levi-Civitá, *Vorträge aus dem Gebiete der Hydro- und Aerodynamik (Innsbruck 1922)*, Springer, Berlin, 1924.
[34] F. Alkemade, *Biography*, in *Selected Papers of J.M. Burgers*, F.T.M. Nieuwstadt and J.A. Steketee, eds., Kluwer, Dordrecht, The Netherlands, 1995, pp. xi–cix.
[35] G. Battimelli, *The early international congresses of applied mechanics*, in *IUTAM. A Short History*, S. Juhasz, ed., Springer, Berlin, 1988, pp. 9–13.
[36] R.E. Doel, D. Hoffmann, and N. Krementsov, *National states and international science: A comparative history of international science congresses in Hitler's Germany, Stalin's Russia, and Cold War United States*, in *Politics and Science in Wartime: Comparative International Perspectives on the Kaiser Wilhelm Institute* (Osiris, 2nd Series), Vol. 20, 2005, pp. 46–76.
[37] T. von Kármán, *Über laminare und turbulente Reibung*, Z. Angew. Math. Mech. (ZAMM) 1 (1921), pp. 233–252.
[38] T. von Kármán, *Über die Oberflächenreibung von Flüssigkeiten*, in *Vorträge aus dem Gebiete der Hydro- und Aerodynamik (Innsbruck 1922)*, T. von Kármán und T. Leci-Civita, hrsg., Springer, Berlin, 1922, pp. 146–167.
[39] W. Heisenberg, *Nichtlineare Lösungen der Differentialgleichungen für reibende Flüssigkeiten*, in *Vorträge aus dem Gebiete der Hydro- und Aerodynamik (Innsbruck 1922)*, T. von Kármán und T. Leci-Civita, hrsg., Springer, Berlin (1924), 1922, pp. 139–142.
[40] W. Heisenberg, *Über Stabilität und Turbulenz von Flüssigkeitsströmen*, Annalen der Physik 74 (1924), pp. 577–627.
[41] L. Prandtl, *Über die ausgebildete Turbulenz*, Verhandlungen des II. Internationalen Kongresses für Technische Mechanik, Zürich: Füßli, 1927, pp. 62–75.
[42] T. von Kármán, *Mechanische Ähnlichkeit und Turbulenz*, Proceedings of the Third International Congress of Applied Mechanics, Stockholm, 1930.
[43] T. von Kármán (with L. Edson), *The Wind and Beyond*, Little, Brown and Company, Boston/Toronto, 1967.
[44] G.I. Taylor, *Some recent developments in the study of turbulence*, in *Proceedings of the Fifth International Congress on Applied Mechanics, Cambridge, MA,* J.P. Den Hartog and H. Peters, eds., John Wiley, New York, 1938, pp. 294–310.
[45] H.L. Dryden, *Turbulence investigations at the National Bureau of Standards*, in *Proceedings of the Fifth International Congress on Applied Mechanics, Cambridge, MA,* J.P. Den Hartog and H. Peters, eds., Wiley, New York, 1938, pp. 362–368.
[46] H.L. Dryden and A.M. Kuethe, *The measurement of fluctuations of air speed by the hot-wire anemometer*, NASA Tech. Rep. NACA-TR-320, NASA Center for AeroSpace Information, Hanover, MD, 1929.
[47] H.L. Dryden and A. M. Kuethe, *Effect of turbulence in wind tunnels measurements*, NASA Tech. Rep. NACA-TR-342, NASA Center for AeroSpace Information, Hanover, MD, 1929.
[48] K.R. Sreenivasan and G.I. Taylor, *The inspiration behind the Cambridge school*, in *A Voyage Through Turbulence*, P.A. Davidson, Y. Kaneda, K. Moffatt, and K.R. Sreenivasan, eds., Cambridge University Press, Cambridge, UK, 2011, pp. 127–186.
[49] J.L. Synge, *Hydrodynamic Stability*, Semicentennial Addresses of the American Mathematical Society 2 (1938), pp. 227–269.
[50] G. Battimelli, *The mathematician and the engineer: Statistical theories of turbulence in the 20's*, Riv. Stor. Sci. 1 (1984), pp. 73–94.

[51] G. Battimelli, *On the history of statistical theories of turbulence*, Rev. Mex. Fis. (Suplemento) 32(S1) (1986), pp. 3–48.
[52] G. Falkovich, *The Russian school*, in *A Voyage Through Turbulence*, P.A. Davidson, Y. Kaneda, K. Moffatt, and K.R. Sreenivasan, eds., Cambridge University Press, Cambridge, UK, 2011, pp. 209–237.
[53] A.N. Kolmogorov, *The local structure of turbulence in incompressible viscous fluid for very large Reynolds numbers*, Dokl. Akad. Nauk. SSSR 30(4) (1941), pp. 299–303. (Reprinted in *Proc. R. Soc. Lond. A* 434 (1991), pp. 9–13)
[54] A.N. Kolmogorov, *Dissipation of energy in isotropic turbulence*, Dokl. Akad. Nauk. SSSR 32(1) (1941), pp. 16–18. (Reprinted in *Proc. R. Soc. Lond. A* 434 (1941), pp. 15–17)
[55] A.M. Obukhov, *On the spectral energy distribution in a turbulent flow*, Akad. Nauk SSSR. Geogr. Geofiz. 5 (1941), pp. 453–466.
[56] C. Meneveau and J.J. Riley, *Stanley Corrsin*, in *A Voyage Through Turbulence*, P.A. Davidson, Y. Kaneda, K. Moffatt, and K.R. Sreenivasan, eds., Cambridge University Press, Cambridge, 2011, UK, pp. 238–275.
[57] J.R. Hansen, *Engineer in Charge. A History of the Langley Aeronautical Laboratory, 1917–1958*, NASA, Washington, DC, 1987. Available at http://history.nasa.gov/SP-4305/sp4305.htm.
[58] A. Roland, *Model Research: The National Advisory Committee for Aeronautics, 1915–1958*, Vols. 1–2, NASA, Washington, DC, 1985. Available at http://history.nasa.gov/SP-4103/sp4103.htm.
[59] G.B. Schubauer and H.K. Skramstad, *Laminar-Boundary-Layer Oscillations and Transition on a Flat Plate*, NACA, Washington, DC, 1943; NACA ACR, April 1943. (published again as NACA TR 909, 1948)
[60] H. Liepmann, *Investigations on laminar boundary layer stability and transition on curved boundaries*, NACA Wartime Report ACR, NACA, Washington, DC, 1943.
[61] H. Liepmann, *Investigations on laminar boundary layer stability and transition on concave walls*, NACA Wartime Report ACR, NACA, Washington, DC, 1945.
[62] C.-C. Lin, *On the development of turbulence*, Ph.D thesis, California Institute of Technology, Pasadena, CA, 1944. Available at http://resolver.caltech.edu/CaltechETD: etd-06232004-140148.
[63] H. Görtler, *Über den Einfluß der Wandkrümmung auf die Entstehung der Turbulenz*, Z. Angew. Math. Mech. (ZAMM) 20 (1940), pp. 138–147.
[64] H. Görtler, *Über eine dreidimensionale Instabilität laminarer Grenzschichten an konkaven Wänden*, Nachrichten der Gesellschaft der Wissenschaften zu Göttingen, Mathematisch-physikalische Klasse, Neue Folge, 1940, pp. 1–26.
[65] H. Görtler, *Instabilität laminarer Grenzschichten an konkaven Wänden gegenüber gewissen dreidimensionalen Störungen*, Z. Angew. Math. Mech. (ZAMM) 21 (1941), pp. 250–252, 384.
[66] H. Schlichting, *Der Umschlag laminar/turbulent und das Widerstandsproblem des Tragflügels*, Deutsche Luftfahrtforschung, Forschungsbericht Nr. 1410, Nach einem Vortrag im Seminar der Luftfahrtforschungsanstalt Hermann Göring, 20 April 1941.
[67] H. Schlichting and K. Bußmann, *Messungen an Laminarprofilen*, Bericht der Lilienthalgesellschaft 149 (1942), pp. 17–20.
[68] Breford and Müller, *Messungen am Originalflügel des Baumusters P-51 "Mustang"*, Forschungsberichte (FB) der Aerodynamischen Versuchsanstalt, 1724:2, 1943.
[69] Kopfermann and Breford, *Umschlagpunktmessungen am Originalflügel des Baumusters P-51 "Mustang"*, Deutsche Luftfahrtforschung, Untersuchungen und Mitteilungen (UM), 2035, 1943.
[70] F. Riegels and J. Liese, *Russische Laminarprofile. Teil II. Untersuchungen und Mitteilungen der deutschen Luftfahrtforschung*, 3056, 1943.
[71] K.H. Doetsch, *Versuche am Mustang-Profil über den Einfluss des Hinterkantenwinkels auf die Profileigenschaften*. *Untersuchungen und Mitteilungen der deutschen Luftfahrtforschung (UM)*, 1488, Zentrale für wissenschaftliches Berichtswesen der Luftfahrtforschung des Generalluftzeugmeisters (ZWB), Berlin-Adlershof, 1944.
[72] H. Holstein, *The large AVA-tunnel of low turbulence*, Reports and Translations, 83, 1946.
[73] H. Görtler, *Turbulenz*, in *Angewandte Mathematik*, A. Walther, ed. (Naturforschung und Medizin in Deutschland 1939–1946. Für Deutschland bestimmte Ausgabe der FIAT Review of German Science, Band 5, Teil III), 1953, pp. 75–99.

[74] L. Prandtl, *Turbulenz*, Hydro- und Aerodynamik. Herausgegeben von A. Betz. (Naturforschung und Medizin in Deutschland 1939-1946. Für Deutschland bestimmte Ausgabe der FIAT Review of German Science, Band 11), 1953, pp. 55–77.
[75] H.L. Dryden, *The international congress for applied mechanics*, Science 105 (2720) (1947), pp. 167–169.
[76] L. Onsager, *The distribution of energy in turbulence*, Phys. Rev. 68 (1945), p. 268.
[77] G.K. Batchelor, *Double velocity correlation function in turbulent motion*, Nature 158 (4024) (1946), pp. 883–884.
[78] G.K. Batchelor, *The Life and Legacy of G. I. Taylor*, Cambridge University Press, Cambridge, UK, 1996.
[79] K. Moffatt *George Batchelor: The post-war renaissance of research in turbulence*, in *A Voyage Through Turbulence*, P.A. Davidson, Y. Kaneda, K. Moffatt, and K.R. Sreenivasan, eds., Cambridge University Press, Cambridge, UK, 2011, pp. 276–304.
[80] G.L. Eyink and K.R. Sreenivasan, *Onsager and the theory of hydrodynamic turbulence*, Rev. Mod. Phys. 78(1) (2006), pp. 87–135.
[81] E. Bagge, K. Diebner, and K. Jay, *Von der Uranspaltung bis Calder Hall*, Rowohlt, Hamburg, 1957.
[82] C.F. von Weizsäcker, *Über die Entstehung des Planetensystems*, Z. Astrophys. 22 (1943), pp. 319–355.
[83] C.F. von Weizsäcker, *Das Spektrum der Turbulenz bei großen Reynoldsschen Zahlen*, Z. Phys. 124 (1948), pp. 614–627.
[84] W. Heisenberg, *Zur statistischen Theorie der Turbulenz*, Z. Phys. 124, (1948), pp. 628–657.
[85] L. Prandtl and K. Wieghardt, *Über ein neues Formelsystem für die ausgebildete Turbulenz*, Nachrichten der Gesellschaft der Wissenschaften zu Göttingen, Mathematisch-physikalische Klasse, 1945, pp. 6–19.
[86] G. Battimelli and A. Vulpiani, *Kolmogorov, Heisenberg, von Weizsäcker, Onsager: un caso di scoperta simultanea*, Atti del Terzo Congresso Nazionale di Storia della Fisica, Palermo, 1982, pp. 169–175.
[87] T.S. Kuhn, *Conservation of energy as an example of simultaneous discovery*, in *Critical Problems in the History of Science*, M. Clagett, ed., University of Wisconsin Press, Madison, 1959, pp. 321–356.
[88] F. Greenaway, *Science International: A History of the International Council of Scientific Unions*, Cambridge University Press, Cambridge, UK, 1996.
[89] W. Schiehlen and L. van Wijngaarden (eds.), *Mechanics at the Turn of the Century*, Shaker Verlag, Aachen, 2000.
[90] Proceedings of the Seventh International Congress for Applied Mechanics, 5–11 September 1948, published by the Organizing Committee (Introduction, Vol. I, Vol. II, Parts 1 and 2, Vol. III, Vol. IV), 1948.
[91] S. Juhasz (ed.), *IUTAM. A Short History*, Springer, Berlin, 1988.
[92] V.F. Weisskopf, *Visas for foreign scientists*, Bull. At. Sci. 10 (1954), pp. 68–80.
[93] W. Heisenberg, *On the stability of laminar flow*, Proceedings of the International Congress of Mathematicians. Vol. II, American Mathematical Society, Providence, RI, 1950, pp. 292–296.
[94] W. Heisenberg, *On stability and turbulence of fluid flows*, Technical Memorandum NACA TM 1291, NACA, Washington, DC, 1951. (Translated from Annalen der Physik, 74, 1924, 577–627)
[95] IUTAM and IAU (eds.), *Problems of cosmical aerodynamics*, Proceedings of the Symposium on the Motion of Gaseous Masses of Cosmical Dimensions held at Paris, August 16–19, Dayton, OH, International Union of Theoretical and Applied Mechanics and International Astronomical Union, Central Air Documents Office (Army-Navy-Air Force), 1949.
[96] IUTAM and IAU (eds.), *Gas Dynamics of Cosmic Clouds: A Symposium held at Cambridge, England, July 6–11, 1953*, International Union of Theoretical and Applied Mechanics and International Astronomical Union, Symposium Series, Symposium No. 2, 1955.
[97] D.J. Kevles, *The Physicists: The History of a Scientific Community in Modern America*, Alfred E. Knopf, New York, 1978.
[98] K.C. Wali, *Chandra: A Biography of S. Chandrasekhar*, University of Chicago Press, Chicago, IL, 1991.
[99] Proceedings of the American Physical Society, *Minutes of the 1948 Annual Meeting at New York, January 26–29, 1949*, Phys. Rev. 75 (1949), pp. 1279–1336.

[100] Tayler, R.J., *Subrahmanyan Chandrasekhar. 19 October 1910–1921 August 1995*, Biographical Memoirs of the Fellows of the Royal Society 42 (1996), pp. 80–94.
[101] J. von Neumann, *Recent Theories of Turbulence*, *John von Neumann Collected Works. Volume VI: Theory of Games, Astrophysics, Hydrodynamics and Meteorology*, Pergamon Press, New York, 1963, pp. 437–472. (Editor's note: This report to the Office of Naval Research, written by von Neumann in 1949, was not considered by the author as suitable for publication [. . .] However, it is considered by a number of workers in the field to be one of the most illuminating discussions of turbulence extant.)
[102] W. Tollmien, *Über Schwingungen in laminaren Strömungen und die Theorie der Turbulenz*, Proceedings of the 8th International Congress for Theoretical and Applied Mechanics, Istanbul (Turkey), 20–28 August 1952, pp. 23–47.
[103] W. Tollmien, *Fortschritte der Turbulenzforschung*, Z. Angew. Math. Mech. (ZAMM), 33 (1953), pp. 200–211.
[104] W. Tollmien, *50 Jahre Grenzschichtforschung, ihre Entwicklung und Problematik*, in *50 Jahre Grenzschichtforschung*, G. Henry and W. Tollmien, eds., F. Vieweg, Braunschweig, 1955, pp. 1–12.
[105] T. von Kármán, *Progress in the statistical theory of turbulence*, Proc. Natl. Acad. Sci. 34 (1948), pp. 530–539.
[106] K. de Fériet, *La notion de moyenne dans la théorie de la turbulence*, Milan J. Math. 27(1) (1957), pp. 167–207.
[107] H.L. Dryden, *The turbulence problem today*, Proceedings of the Midwestern Conference on Fluid Dynamics, first conference, May 12–13, 1950, University of Illinois, Urbana, 1951, pp. 1–20.
[108] H.L. Dryden, *Fifty years of boundary-layer theory and experiment*, Science 121(3142) (1955), pp. 375–380.
[109] H. Görtler (ed.), *Boundary Layer Research. Symposium Freiburg/Br. August 26–29, 1957*, Springer, Berlin, 1958.
[110] R. Emrich, P.S. Klebanoff, W.M. Elsasser, and H. Polachek, *Obituaries: Francois N. Frenkiel*, Phys. Today 40 (1987), pp. 123–124.
[111] J.T. Scott, *Fifty years of physics of fluids*, Phys. Fluids, 20(1) (2008), 011301–011301–4.
[112] S.H. Davis and T.J. Pedley, *Editorial: JFM at 50*, J. Fluid Mech. 554 (2006), pp. 1–4.
[113] G.K. Batchelor, *The Theory of Homogeneous Turbulence*, Cambridge University Press, Cambridge, UK, 1953.
[114] A.A. Townsend, *The Structure of Turbulent Shear Flow*, Cambridge University Press, Cambridge, UK, 1956.
[115] J.O. Hinze, *Turbulence. An Introduction to Its Mechanism and Theory*, McGraw-Hill Company, New York, 1959.
[116] F.N. Frenkiel, *Introduction to the proceedings of a symposium on fundamental problems in turbulence and their relation to geophysics, organized by the International Union of Geodesy and Geophysics and the International Union of Theoretical and Applied Mechanics held in Aix-Marseilles, September 4–9, 1961*, J. Geophys. Res. 67(8) (1962), pp. 3007–3010.
[117] M. Eckert, *Turbulenz-ein problemhistorischer Abriss*, NTM Z. Geschichte der Wissenschaften, Tech. Med. 16 (2008), pp. 39–71.
[118] M. Eckert, *Theory from wind tunnels: Empirical roots of twentieth century fluid dynamics*, Centaurus 50 (2008), pp. 233–253.
[119] T.S. Kuhn, *The Structure of Scientific Revolutions*, University of Chicago Press, Chicago, IL, 1962.

Journal of Turbulence, 2013
Vol. 14, No. 3, 42–76, http://dx.doi.org/10.1080/14685248.2013.771838

Mathematics and turbulence: where do we stand?

Claude W. Bardos[a*] and Edriss S. Titi[b,c]

[a]*Université Denis Diderot and Laboratoire J.-L. Lions, Université Pierre et Marie Curie, Paris, France;* [b]*Department of Computer Science and Applied Mathematics, Weizmann Institute of Science, Rehovot 76100, Israel;* [c]*Department of Mathematics and Department of Mechanical and Aerospace Engineering, University of California, Irvine, CA 92697-3875, USA*

(*Received 7 December 2012; final version received 24 January 2013*)

This contribution covers the topics presented by the authors at the *"Fundamental Problems of Turbulence, 50 Years after the Marseille Conference 1961"* meeting that took place in Marseille in 2011. It focuses on some of the mathematical approaches to fluid dynamics and turbulence. This contribution does not pretend to cover or answer, as the reader may discover, the fundamental questions in turbulence, however, it aims toward presenting some of the most recent advances in attacking these questions using rigorous mathematical tools. Moreover, we consider that the proofs of the mathematical statements (concerning, for instance, finite time regularity, weak solutions and vanishing viscosity) may contain information as relevant, to the understanding of the underlying problem, as the statements themselves.

Keywords: Euler equations; Navier–Stokes equations; turbulence; viscosity limit

1. Introduction

One of the main goals of this contribution is to underline the relationships between, on the one hand, standard mathematical questions and, on the other hand, classical issues in turbulence theory. However, it is important to emphasize that there are many different mathematical approaches aiming toward understanding the complex phenomenon of turbulence, and that only some of these aspects are stressed in this contribution (see also the other contributions in this special issue; and for a general user-friendly (for mathematicians and engineers) introduction the book of Frisch [1]).

A nice survey of the dynamical systems approach to turbulence and statistical solutions of Navier–Stokes equations is presented in the monographs [2], [3] and [4]. Moreover, rigorous conditions for the main tenets of the Batchelor–Kraichnan–Leith theory of 2D turbulence, namely the energy power law, enstrophy cascade and dissipation law can be found in [5–7] and references therein. Furthermore, recent interesting surveys concerning analytical studies of Euler equations can be found in [8–11] and references therein (see also [11–13] and references therein for recent surveys concerning computational studies of Euler equations).

Starting from the macroscopic Navier–Stokes–Fourier system for compressible fluid flows, we will recall the derivation of the equations of motion for incompressible fluid flows, by taking the small Mach number limit. Then by another new scaling argument, which relies on the introduction of the Reynolds number, we will introduce the Euler

*Corresponding author. Email: claude.bardos@gmail.com

© 2013 Taylor & Francis

equations as the formal zero viscosity limit of the Navier–Stokes equations. Historically, the Euler equations for ideal fluids were the first to be derived (Euler 1757), viscous effects being added only later to give the Navier–Stokes equations. These viscous effects are, as it will be stressed in the paper, essential for understanding the interaction between solid bodies and fluid flows. Moreover, recent mathematical results indicate that a more profound understanding of Euler equations seems to be essential for making any significant progress in this field. Therefore, Section 3 is devoted to the mathematical theory of Euler equations with, on the one hand, emphasis on the classical local well-posedness of the problem in the class of smooth solutions and, on the other hand, on the more recent notions of weak solutions. We will then return, in Section 4, to the Navier–Stokes equations, mostly to consider the boundary value problems and the behavior of the solutions, in particular boundary effects, when the viscosity tends to zero.

2. Preliminaries

Our approach follows three threads. First, the notion of the *Cauchy problem* for an underlying evolution equation, which means the study of the corresponding solutions of this equation, for $t > t_0$, given their state at time $t = t_0$ (often t_0 is taken equal to 0). Here the relevant issues are: the stability or instability of the solutions, their qualitative long-time behavior, and eventually the reliability of this equation for modeling the underlying phenomena at the relevant scales and under the appropriate conditions.

The second thread is the notion of *weak solutions*. This idea preexisted in mechanics and physics in the context of, for instance, calculus of variations; however, in the previous century it became systematically used with the development of functional analysis and the introduction, by Gelfand, Schwartz and Sobolev, of the notion of distributions (which are also called, by some people, generalized functions). In a nut shell, consider for example, the finite linear system of ordinary differential equations:

$$\frac{d}{dt}u + A(t)u = f \quad u(0) = u_0, \tag{1}$$

where u is an unknown vector of $n$components and $A(t)$ is a given $n \times n$ matrix with bounded entries. In case $A(t)$ is not continuous one does not expect u to be differentiable in the classical sense. Nonetheless, one would still like to make sense of the above initial value problem. To this end, one takes the Euclidean inner product, that we denote by $\langle \cdot, \cdot \rangle$, of Equation (1) with any vector field $\phi(t)$, member of a family of conveniently smooth "test functions" that are identically equal to zero when t becomes large. Then formally (because no regularity on u is assumed) integrating by parts one can consider instead the equation

$$\int_0^\infty \left[-\left\langle u(t), \frac{d}{dt}\phi(t) \right\rangle + \langle u(t), A^*(t)\phi(t) \rangle \right] dt = \langle u(0), \phi(0) \rangle. \tag{2}$$

A function $u(t)$ is said to be a weak solution of (1) if it satisfies Equation (2) for every test function $\phi \in C^\infty([0, \infty))$, identically zero identically zero for t large enough. Notice that in order for u to satisfy (2) it does not need to be a differentiable function.

In fact, without the refinement of functional analysis, this idea already goes back to Euler and Lagrange in the context of deriving the Euler–Lagrange equation in the calculus of variations. Similarly, in the context of gas dynamics there is a good reason to introduce

such a notion because compressible fluids, *even when starting from smooth initial data*, may develop shock waves which are discontinuous, and therefore have no derivative in the classical sense. Since Leray did not know much about the regularity of the solutions of the Navier–Stokes equations it was crucial in his seminal work [14] to introduce weak solutions. Of course, this weak formulation leads to a loss of information which, for instance, may prevent the analysis of stability, or the proof of uniqueness.

Weak solutions are defined as elements of some spaces of functions, which will be used below with no further introduction.

With these prerequisites, a final and third thread will be the consideration of *the equations of macroscopic perfect fluids and the relationship between them.*

We will start with the evolution of density, velocity and temperature (ρ, u, θ) given by the compressible Navier–Stokes–Fourier system of equations (cf. [15] and [16]):

$$\begin{aligned}
&\partial_t \rho + \nabla \cdot (\rho u) = 0\\
&\rho\big(\partial_t + u \cdot \nabla\big)u + \nabla p = \epsilon \nabla \cdot [\nu \sigma(u)],\\
&\frac{3}{2}\rho\big(\partial_t + u \cdot \nabla\big)\theta + \rho\theta \nabla \cdot u = \frac{1}{2}\epsilon\nu(\sigma(u) : \sigma(u)) + \epsilon\nabla[\kappa\nabla\theta],
\end{aligned}$$

with the state equations for the pressure, $p = \rho\theta$, and the stress tensor:

$$\sigma(u) = \big(\nabla_x u + (\nabla_x u)^T\big) - \frac{2}{3}(\nabla_x \cdot u)I.$$

In these equations, for any vector $u \in \mathbf{R}^3$ and any (scalar or vector valued function) v, the term $(u \cdot \nabla)v$ denotes the expression

$$(u \cdot \nabla)v = \sum_{1 \le j \le d} u_j \frac{\partial v}{\partial x_j},$$

while ν and κ denote the kinematic viscosity and the thermal diffusivity of the gas, respectively. These quantities depend on the nature of the molecular interaction, while ϵ denotes the dimensionless Knudsen number (proportional, up to a fudge constant, to the mean free path) which depends on the degree of rarefaction of the gas. A simplified system is then obtained (see, e.g., section 1.1 in [16]) for the fluctuations of order ϵ of density, velocity and temperature about a constant background state, $(\overline{\rho}, 0, \overline{\theta})$, namely,

$$\rho = \overline{\rho} + \epsilon\tilde{\rho}, \quad \theta = \overline{\theta} + \epsilon\tilde{\theta}, \quad u = \epsilon\tilde{u}. \tag{3}$$

In order to observe the cumulative effect of the small velocity, one has to consider the system for a time scale long enough (of the order of ϵ^{-1}), and hence by rescaling the time, by a factor of ϵ^{-1}, and following, for instance, the analysis presented in section 1.1 in [16], one obtains the following system:

$$\begin{aligned}
&\nabla \cdot \tilde{u} = 0, \quad \nabla(\overline{\theta}\tilde{\rho} + \overline{\rho}\tilde{\theta}) = 0,\\
&\overline{\rho}(\partial_t \tilde{u} + (\tilde{u} \cdot \nabla)\tilde{u}) + \nabla\pi = \nu\Delta\tilde{u},\\
&\frac{3}{2}\overline{\rho}(\partial_t \tilde{\theta} + (\tilde{u} \cdot \nabla)\tilde{\theta}) = \kappa\Delta\tilde{\theta},
\end{aligned}$$

where π is the unknown pressure. This system is often referred to as the incompressible Navier–Stokes–Fourier system of equations. Observe that the equations for the velocity are independent of the temperature, while the advection term, $(\tilde{u} \cdot \nabla)\tilde{\theta}$, in the temperature equation depends on the velocity. The term incompressible comes from the $\nabla \cdot \tilde{u} = 0$ condition, which implies that the Lagrangian flow map defined by

$$x \mapsto \phi(x, t), \quad \phi(x, 0) = x, \quad \dot{\phi}(x, t) = \tilde{u}(\phi(x, t), t),$$

is volume preserving. The equation $\nabla(\overline{\theta}\tilde{\rho} + \overline{\rho}\tilde{\theta}) = 0$ is known as the Bernoulli relation. Together with the equation for the temperature they describe how the flow, at this approximation level, propagates the initial fluctuations of density and temperature. In particular, if $\tilde{\rho} = \tilde{\theta} = 0$ the system reduces (hereafter the tilde will be omitted, $\overline{\rho}$ will be taken equal to 1, and following the tradition in this field we will replace the notation for the pressure π by p) to the standard incompressible Navier–Stokes equations:

$$\partial_t u + (u \cdot \nabla)u - \nu \Delta u + \nabla p = 0, \quad \nabla \cdot u = 0. \tag{4}$$

In a typical engineering or physical situation characteristic length, velocity and time scales, L, U and T, respectively, are introduced. After rescaling the relevant quantities in (4), retaining the same notation for the rescaled dimensionless velocity, spatial and temporal variables, one obtains the undimensionlized Navier–Stokes equations

$$\partial_t u + (u \cdot \nabla)u - \frac{1}{Re}\Delta u + \nabla p = 0, \quad \nabla \cdot u = 0, \tag{5}$$

where

$$Re = \frac{UL}{\nu}$$

is the dimensionless Reynolds number, which measures the ratio between a typical strength of the nonlinear advection term and a typical linear viscous dissipation in the Navier–Stokes equations. Since Equations (4) and (5) look the same (symbolically), we will abuse, hereafter, the notation and let ν represent the inverse of the Reynolds number.

In most practical applications the Reynolds number is very large (for instance, the Reynolds number is about 10^6 for the air around a moving bicycle, about 10^7 for a moving car, and is of the order of 10^{12} in meteorological applications). This naturally suggests to investigate and compare the behavior of the Navier–Stokes Equations (5), for large values of the Reynolds numbers, to that of Euler equations, which are obtained formally by substituting $Re = \infty$ in (5):

$$\partial_t u + (u \cdot \nabla)u + \nabla p = 0, \ \nabla \cdot u = 0. \tag{6}$$

Thus, the third thread in our approach would be to compare the behavior of the solutions of (5) to those of (6), as the Reynolds number $Re \to \infty$. However, as it will be developed below, the relationship between these two systems is far from being simple.

Since the above equations are derived for physical systems they are expected to respect certain global conservation laws which indeed can be deduced by simple computations, *but*

only, assuming that the solutions are smooth enough to legitimize these computations. In particular, for sufficiently smooth solutions of the incompressible Navier–Stokes equations, say subject to periodic boundary conditions in a periodic box Ω, by using the relation:

$$\int_\Omega ((u\cdot\nabla)u)\cdot u\,dx = \int_\Omega \sum_{ij} \partial_{x_j}\left(u_j\frac{u_i^2}{2}\right)dx = 0,$$

one obtains the formal energy balance:

$$\frac{d}{dt}\int_\Omega \frac{|u(x,t)|^2}{2}dx + \nu\int_\Omega |\nabla u(x,t)|^2 dx = 0. \tag{7}$$

In the incompressible Euler and Navier–Stokes equations the incompressibility condition, $\nabla\cdot u = 0$, appears as a constraint on the dynamics of the fluid particles that are governed by the equation (Newton's second law):

$$\frac{d^2x(t)}{dt^2} = \frac{d}{dt}u(x(t),t) = \nu\Delta u(x(t),t) - \nabla p(x(t),t), \tag{8}$$

with the pressure, p, being the *Lagrange multiplier* corresponding to this constraint. As such it can be eliminated by applying the Leray projection, P_σ, to the equations (see, e.g., [17] for details concerning the Leray projection and other mathematical aspects of Navier–Stokes equations). For a domain without physical boundaries (i.e., the whole space or periodic box) P_σ is the orthogonal projection from L^2 onto the subspace of divergence-free vector fields. That is, for any given $w\in L^2$, $P_\sigma w$ is defined by solving the linear system:

$$P_\sigma w = w + \nabla p \quad \text{and} \quad -\Delta p = \nabla\cdot w, \tag{9}$$

subject to period boundary conditions. In the presence of physical boundaries the Leray projection P_σ is the orthogonal projection from L^2 onto the subspace of divergence-free vector fields that are tangent to the boundary, hence P_σ is defined by solving system (9), subject to the Neumann boundary condition

$$\frac{\partial p}{\partial\vec{n}} = 0. \tag{10}$$

Eventually, due to the fact that our mathematical understanding of these problems and of their relations to turbulent flows is far from being complete, the use of explicit examples is important. Such an illuminating example is the shear flow solution of Euler equations, which is defined in $\Omega = \mathbf{R}^3$ or in a periodic box $\Omega = (\mathbf{R}/\mathbf{Z})^3$ by the formula:

$$u(x_1,x_2,x_3,t) = (u_1(x_2),0,u_3(x_1 - tu_1(x_2),x_2).$$

Indeed, u is a solenoidal vector field that solves Euler equations with the pressure $p = 0$.

Other illustrative examples are the stationary solutions of Euler equations. Observe that, with $q = p + \frac{|u|^2}{2}$, Euler equations can also be written as

$$\partial_t u + (\nabla\wedge u)\wedge u + \nabla q = 0, \quad \nabla\cdot u = 0.$$

Hence, stationary solutions are characterized by the relation $(\nabla \wedge u) \wedge u + \nabla q = 0$. In particular, any vector field that satisfies $\nabla \wedge u = \lambda(x)u$ is a stationary solution with $q = 0$ (such solutions are called Beltrami flows). In particular, any vector field that satisfies $\nabla \wedge u = 0$ forms a stationary solution. In simply connected domains this relation implies that u is a potential flow, i.e., $u = \nabla\phi$, which is divergence-free, hence ϕ is a harmonic potential $-\Delta\phi = 0$.

Finally, and for convenience we will denote by $(\cdot, \cdot)$ the L^2 inner product in the relevant domain.

3. The incompressible Euler equations

In fact, as indicated by its name, this system of equations (one of the first systems of partial differential equations for fluid mechanics to be introduced) was derived by Euler in 1757, assuming the incompressibility of the fluid. It has a very rich mathematical history with a very interesting recent important progress. The Euler equations in a domain Ω (with or without physical boundaries) are given by

$$\partial_t u + (u \cdot \nabla)u + \nabla p = 0, \ \nabla \cdot u = 0, \ \text{in } \Omega. \tag{11}$$

If Ω has physical boundaries then the system (11) is supplemented with the no-normal flow boundary condition:

$$u \cdot \vec{n} = 0 \quad \text{on} \quad \partial\Omega. \tag{12}$$

Observe that the system (11) corresponds to the limit case when the viscosity $\nu = 0$ in (4), or the Reynolds number is ∞ in (5).

In the absence of viscosity (i.e., $\nu = 0$) any *regular enough solution* to the Euler system (11) conserves the kinetic energy (compare with (7) for $\nu = 0$).

It turns out that the vorticity $\omega = \nabla \wedge u$ is "the basic quantity" both from the physical and the mathematical analysis points of view. The system (11)–(12) can be rewritten in an equivalent form in terms of the vorticity to give

$$\partial_t \omega + u \cdot \nabla\omega = \omega \cdot \nabla u, \tag{13}$$

$$\nabla \cdot u = 0, \nabla \wedge u = \omega, u \cdot \vec{n} = 0 \ \text{on } \partial\Omega. \tag{14}$$

The elliptic system given in Equation (14) fully determines u in term of ω (see, e.g., [18] and references therein), which makes the full system (13)–(14) "closed". More precisely, the operator $K : \omega \mapsto u$, defined by the unique solution to the elliptic system (14), is a linear continuous map from $C^\alpha(\Omega)$ with values in $C^{1,\alpha}(\Omega)$ (with $\alpha > 0$), and from the Sobolev $H^s(\Omega)$ with values in $H^{s+1}(\Omega)$.

Furthermore, for $2d$ flows the vorticity is perpendicular to the plane of motion and therefore Equation (13) is reduced (this can also be checked directly) to the advection equation

$$\partial_t \omega + u \cdot \nabla\omega = 0. \tag{15}$$

The quadratic nonlinearity in (13) has the following consequences, *which we describe below, providing only the essential arguments, but omitting the details of the proofs.*

3.1. *General analytical results for the 3d Euler equations*

The short time existence and uniqueness of classical solutions to the $3d$ incompressible Euler equations, with smooth enough initial data, was established (to the best of our knowledge) by Lichtenstein in 1925 [19] (see also [20, 21] and references therein for other proofs).

Theorem 3.1. *Let $u_0 \in C^{1,\alpha}(\Omega)$, with $\nabla \cdot u_0 = 0$ and $u_0 \cdot \vec{n}|_{\partial\Omega} = 0$. Then there exists a time $T_* > 0$, that depends on u_0, and functions $u \in C^0([-T_*, T_*], C^{1,\alpha}(\Omega)) \bigcap C^1([-T_*, T_*], C^{0,\alpha}(\Omega))$, and $p \in C^0([-T_*, T_*], C^{1,\alpha}(\Omega))$, such that the pair u, p solves Euler equations (11)–(12), with the initial data u_0.*

In the proof of the above theorem, the "limit" on the lifespan of the solution is a result of the following nonlinear Grönwall estimate, that controls a certain norm, $y(t)$, of the solution:

$$y' \leq C y^{\frac{3}{2}} \Rightarrow y(t) \leq \frac{y(0)}{(1 - 2tCy^{\frac{1}{2}}(0))^2}. \tag{16}$$

Consequently, for a finite time, which depends on the size of the initial data $y(0)$, the quantity $y(t)$ is finite. To validate (16) and the above argument the initial data have to be chosen in the appropriate space of regular enough functions. In particular, if we consider the solution in the Sobolev space H^s, with $s > \frac{5}{2}$, then by taking the scalar product, in H^s, of the solution with the Euler equations (11), and using the relevant Sobolev estimates one obtains:

$$\begin{aligned} \frac{1}{2}\frac{d\|u\|_{H^s}^2}{dt} &= -((u \cdot \nabla)u, u)_{H^s} = -(\nabla \cdot (u \otimes u), u)_{H^s} \\ &= ((u \otimes u) : \nabla u)_{H^s} \leq C_s \|u\|_{H^s}^2 \|\nabla u\|_{L^\infty} \leq C\|u\|_{H^s}^3, \end{aligned} \tag{17}$$

which leads to (16) and the local in time existence of a smooth solution. Observe that since $\nabla \cdot u = 0$ we have used above the fact that $(u \cdot \nabla)u = \nabla \cdot (u \otimes u)$, where $(u \otimes u)$ is the tensor (matrix) with entries $a_{ij} = u_i u_j$, for $i, j = 1, \ldots, d$.

This notion of threshold of regularity for the initial data is well illustrated with the shear flow

$$u(x, t) = (u_1(x_2), 0, u_3(x_1 - tu_1(x_2), x_2),$$

which is a well-defined solution of Euler equations with pressure $p = 0$. Computing the derivative of u_3 with respect to x_2 yields:

$$t\partial_{x_2} u_1(x_2)\partial_{x_1} u_3(x_1 - tu_1(x_2), x_2).$$

By investigating this term one observes that the initial data which is in $C^{1,\alpha}$ generate solutions that will remain in $C^{1,\alpha}$, for $t \geq 0$, and this is in full agreement with Theorem 3.1 of Lichtenstein. However, less regular initial data, say in $C^{0,\alpha}$, may, in some cases, generate

solutions that will not remain in this space, for $t > 0$, but only in C^{0,α^2} (cf. [22]). This counter-example shows that the Euler equations are ill-posed in $C^{0,\alpha}$, i.e., that Theorem 3.1 of Lichtenstein cannot be extended to $C^{0,\alpha}$ initial data.

As it is often the situation in many nonlinear evolution problems, local regularity means: local existence, uniqueness and local stability (i.e., continuous dependence on initial data). Moreover, one may exhibit a threshold for this existence, uniqueness and propagation of regularity of the initial data (including analyticity Bardos and Benachour [23], see also Kukavica and Vicol [24] and references therein). One of the simplest criteria for the regularity, up to the time T, is that the stress tensor ∇u remains bounded in $L^1(0, T; L^\infty)$. To see that we observe that this bound implies the integrability of the Lipschitz constant of the vector field u, and hence the solutions of the ordinary differential equation $\frac{dx}{dt} = u(x, t)$ will never intersect and remains smooth within the interval $[0, T]$. Consequently, and by virtue of (13), the vorticity is transported, along the particles' paths, and it is stretched by ∇u, and the latter is controlled by its $L^1(0, T; L^\infty)$ norm. However, to underline that it is the dynamics of vorticity which may induce singularities, a more sophisticated version of this criterion was established by Beale, Kato and Majda [25], to only retain the anti-symmetric part of the stress tensor $\left(\nabla u - (\nabla u)^T\right)$ (equivalent to the vorticity vector ω).

Theorem 3.2. Beale–Kato–Majda *[25] Let $u(t) \in C([0, T), H^s) \bigcap C^1([0, T), H^{s-1})$, for $s > \frac{5}{2}$, be a regular solution of the 3d incompressible Euler equations in the interval $[0, T)$. Assume that*

$$\int_0^T \|\nabla \wedge u(., t)\|_{L^\infty} dt < \infty, \tag{18}$$

then $u(t)$ can be uniquely extended to the interval $[0, T + \delta]$, for some $\delta > 0$, as a regular solution of the Euler equations.

While a companion result of Constantin, Fefferman and Majda [26] to Theorem 3.2 states that it is mostly the variations in the direction of the vorticity that may produce singularities.

Theorem 3.3. *[26] Let u be a smooth solution of the 3d Euler equations, which is defined in $Q = \Omega \times [0, T)$. Introduce the following quantities (which are well defined for every $t \in [0, T)$):*

$$k_1(t) = \sup_{x \in \Omega} |u(x, t)|, \tag{19}$$

which measures the size of the velocity, and

$$k_2(t) = \sup_{x, y \in \Omega,\, x \neq y} \frac{|\xi(x, t) - \xi(y, t)|}{|x - y|}, \tag{20}$$

which measures the Lipschitz regularity of the direction

$$\xi(x, t) = \frac{\omega(x, t)}{|\omega(x, t)|}$$

of the vorticity vector. Then under the hypotheses:

$$\int_0^T (k_1(t) + k_2(t))dt < \infty \text{ and } \int_0^T k_1(t)k_2(t)dt < \infty \tag{21}$$

the solution of the 3*d Euler equations exists, and is as smooth as the initial data, on the interval* $[0, T + \delta]$*, for some* $\delta > 0$.

It is worth mentioning that a similar criterion to Theorem 3.2, involving the symmetric part of the stress tensor $S(u) = \frac{1}{2}(\nabla u + (\nabla u)^T)$, was introduced later by Ponce [27]. See also [28] for other related blow-up criteria for the 3*d* Euler equations. Moreover, see [11] and references therein for a recent survey of the blow-up problem.

3.1.1. *About the two-dimensional Euler equations*

In the 2*d* case, the vorticity $\omega = \nabla \wedge u$ obeys the evolution equation

$$\partial_t \omega + u \cdot \nabla \omega = 0. \tag{22}$$

This transport evolution equation enforces the conservation of any L^p norm ($1 \leq p \leq \infty$) of the vorticity vector. Taking advantage of this observation in 1963 Youdovitch proved in his remarkable paper [29] the global existence and uniqueness for all solutions with initial vorticity in L^∞. If the vorticity is only in L^p for $1 < p < \infty$ one can prove the global existence (without uniqueness) of weak solutions. The same result holds also for $p = 1$, and also for the case when the vorticity is a finite Radon measure with definite sign (cf. Delort [30]) or "simple" changes of sign (cf. [31] and [32]; see also [33]). It is worth mentioning that the proof is more delicate in these limit cases when $p = 1$ or when ω is a bounded Radon measure.

3.2. *Weak solutions of Euler equations*

Definition 3.1. *A weak solution, in the time interval* $[0, T]$*, of the Cauchy problem for the Euler Equation (11), with divergence-free initial data* $u(x, 0) \in (L^2(\mathbf{R}^d))^d$*, is a divergence-free vector field*

$$u(x, t) \in L^2(0, T; R^d)^d \bigcap C([0, T]; \left(L^2(R^d)\right)_w^d)^{\,1}$$

and a distribution p *which, for any smooth test function* $\phi(x, t)$ *vanishing for* t *near* T*, satisfies the Euler equations (11) (or (6)) in the distribution sense, that is*

$$\int_0^T \int_{\mathbf{R}^d} [\, u(x, t) \cdot \partial_t \phi(x, t) + (u(x, t) \otimes u(x, t)) : \nabla_x \phi(x, t)\,]\, dx\, dt + \langle p, \nabla_x \phi \rangle$$
$$= -\int_{\mathbf{R}^d} u(x, 0) \cdot \phi(x, 0)\, dx, \tag{23}$$

where $\langle \cdot, \cdot \rangle$ *denotes the distributional action.*

It is important to observe that the hypothesis $u(x,t) \in L^2(0,T;R^d)^d$ is sufficient to insure that the matrix $u \otimes u$ is well defined as a distribution (i.e., no need for any additional hypotheses on the partial derivatives of u).

Moreover, equality (23) is equivalent to the following:

$$\int_0^T \int_{\mathbf{R}^d} [\, u(x,t) \cdot \partial_t \phi(x,t) + (P_\sigma(u(x,t) \otimes u(x,t)) : \nabla_x \phi(x,t)) \,]\, dx\, dt$$
$$= -\int_{\mathbf{R}^d} u(x,0) \cdot \phi(x,0) dx, \tag{24}$$

with P_σ denoting the Leray projection given in (9). Eventually, this is also equivalent to assuming that the relation

$$\int_0^T \int_{\mathbf{R}^d} [\, u(x,t) \cdot \partial_t \phi(x,t)) + (u(x,t) \otimes u(x,t)) : \nabla_x \phi(x,t) \,]\, dx\, dt$$
$$= -\int_{\mathbf{R}^d} u(x,0) \cdot \phi(x,0)\, dx \tag{25}$$

holds for every divergence-free test functions ϕ.

Moreover, there are other variants of the notion of weak solutions. One of the most efficient, introduced by DiPerna and Lions [16], is the notion of *dissipative solution*. It is defined in terms of the stability with respect to any smooth divergence-free vector field w (which may not be a solution of the Euler equations). Such a smooth vector field w evidently satisfies the relation:

$$\partial_t w + P_\sigma((w \cdot \nabla) w) = E, \tag{26}$$

where $E(w)$ is the residual, satisfying $P_\sigma E = E$. Notice that $E \equiv 0$ if and only if w is a smooth solution of the Euler equations (6). Next, observe that if u is a smooth divergence-free vector field then by integration by parts, with respect to the spatial variable, one obtains:

$$\int_\Omega [((u \cdot \nabla) u - (w \cdot \nabla) w) \cdot (u - w)]\, dx = \int_\Omega (u - w) S(w) (u - w)\, dx,$$

with

$$S(w) = \frac{1}{2}(\nabla w + (\nabla w)^T).$$

If in addition we assume that u is a smooth solution of the Euler equations then from (26), (6) and the relevant boundary conditions (e.g., periodic boundary conditions or (12)) we conclude

$$\frac{1}{2}\frac{d}{dt}\int_\Omega |u - w|^2\, dx = \int_\Omega (u - w) S(w) (u - w)\, dx$$
$$+ \int_\Omega E(w(x,t)) \cdot (u(x,t) - w(x,t))\, dx,$$

which, upon integration with respect to time, gives

$$\int_\Omega |u(x,t)-w(x,t)|^2 \le 2\int_0^t\int_\Omega |E(w(x,s))\cdot(u(x,s)-w(x,s))|\,dx\,ds$$
$$+\,2\int_0^t\int_\Omega |(u(x,s)-w(x,s))S(w)(u(x,s)-w(x,s))|\,dx\,ds$$
$$+\int_\Omega |u(x,0)-w(x,0)|^2\,dx\,;$$

and by virtue of Grönwall inequality yields

$$\int_\Omega |u(x,t)-w(x,t)|^2\,dx \le \Big(\int_\Omega |u(x,0)-w(x,0)|^2\,dx\Big)e^{2\int_0^t \|S(w)\|_\infty(s)ds}$$
$$+2\int_0^t \Big(\int_\Omega |E(w(x,s))\cdot(u(x,s)-w(x,s))|\,dx\Big)e^{2\int_s^t \|S(w)\|_\infty(\tau)d\tau}\,ds. \qquad (27)$$

Inspired by the above we introduce the following definition of dissipative solution for Euler Equation (6):

Definition 3.2. *A dissipative solution of Euler Equations (6) is a divergence-free vector field u which together with any smooth divergence-free vector field w (which need not be a solution of Euler equations) they satisfy the inequality:*

$$\int_\Omega |u(x,t)-w(x,t)|^2\,dx \le \Big(\int_\Omega |u(x,0)-w(x,0)|^2\,dx\Big)\,e^{2\int_0^t \|S(w)\|_\infty(s)ds}$$
$$+2\int_0^t |(\partial_t w(s)+P_\sigma((w(s)\cdot\nabla)w(s)),u(s)-w(s))|\,e^{2\int_s^t \|S(w)\|_\infty(\tau)d\tau}\,ds. \qquad (28)$$

Remark 3.1. *With the above definition one should keep in mind the following facts.*
1. Inequality (28) makes sense with no other regularity conditions on u other than the fact that it belongs to $(L^2([0,T;(L^2(\Omega))^d))^d$ ($d=2$ or $d=3$).
2. If w is a genuine smooth solution to Euler equations (6) then one has $E(w)\equiv 0$ and inequality (28) reduces to

$$\int_\Omega |u(x,t)-w(x,t)|^2\,dx \le \Big(\int_\Omega |u(x,0)-w(x,0)|^2\,dx\Big)\,e^{2\int_0^t \|S(w)\|_\infty(s)ds}, \qquad (29)$$

which implies both uniqueness of dissipative solutions, within the class of smooth solutions, and stability of dissipative solutions with respect to smooth solutions.

Below it will be observed that weak solutions of Euler equations (6) may not conserve energy. Therefore, the connection between weak and dissipative solutions of (6) requires some additional information on the control of energy. Following [34] we introduce the following:

Definition 3.3. *A divergence-free vector field $u \in L^2(0,T;R^d)^d$ is called an admissible weak solution if it is a weak solution and if it satisfies the additional hypothesis:*

$$\int_\Omega |u(x,t)|^2\,dx \le \int_\Omega |u(x,0)|^2\,dx, \qquad \textit{for all} \quad t \in [0,T]. \tag{30}$$

As a result of the above definitions we have:

Proposition 3.1. *Let u be an admissible weak solution of Euler equations (6), in $\Omega = \mathbf{R}^d$ or in a periodic domain $\Omega = (\mathbf{R}/\mathbf{Z})^d$, then u is a dissipative solution.*

Proof. Below, we only present the main idea of the proof. Let w be any smooth divergence-free vector field. The point is to compare

$$\frac{1}{2}\int_\Omega |u(x,t)-w(x,t)|^2 dx = \frac{1}{2}\int_\Omega |u(x,t)|^2 dx + \frac{1}{2}\int_\Omega |w(x,t)|^2 dx - \int_\Omega (u(x,t)\cdot w(x,t))dx$$

and

$$\frac{1}{2}\int_\Omega |u(x,0)-w(x,0)|^2 dx = \frac{1}{2}\int_\Omega |u(x,0)|^2 dx + \frac{1}{2}\int_\Omega |w(x,0)|^2 dx - \int_\Omega (u(x,0)\cdot w(x,0))dx$$

With hypothesis (30) it is then enough to show that:

$$\begin{aligned}
&\frac{1}{2}\int |w(x,t)|^2 - \int (u(x,t)\cdot w(x,t))\,dx = \frac{1}{2}\int |w(x,0)|^2 - \int (u(x,0)\cdot w(x,0))\,dx \\
&\quad + \int_0^t \frac{d}{ds}\left(\frac{1}{2}\int |w(x,s)|^2 - \int (u(x,s)\cdot w(x,s))\,dx\right) ds \\
&\quad \le \frac{1}{2}\int |w(x,0)|^2 - \int (u(x,0)\cdot w(x,0))\,dx \\
&\quad + \int_0^t \int_\Omega (u-w)S(w)(u-w)\,dx\,ds \\
&\quad + \int_0^t \int_\Omega E(w(x,s))\cdot(u(x,s)-w(x,s))\,dx\,ds,
\end{aligned}$$

or that

$$\begin{aligned}
&\frac{d}{ds}\left(\frac{1}{2}\int |w(x,s)|^2 - \int (u(x,s)\cdot w(x,s))dx\right) \le \int_\Omega (u-w)S(w)(u-w)\,dx \\
&\quad + \int_\Omega E(w(x,s))\cdot(u(x,s)-w(x,s))\,dx.
\end{aligned}$$

Here, the most nontrivial step that needs further justification is the one involving the term $\int_\Omega (\partial_s u(x,s)\cdot w(x,s))\,dx$. But since w is a smooth vector field the notion of a weak solution can be invoked.

However, for Euler equations the introduction of weak solutions corresponds to an important loss of information illustrated by the following theorems of De Lellis, Székelyhidi and Wiedemann.

Theorem 3.4. *1. Let $\Omega \subset \mathbf{R}^d$, for $d = 2, 3$, be any bounded open set, and let $T > 0$. Then for any $e(x,t) > 0$, continuous function defined on $Q = \overline{\Omega} \times [0,T] \subset \mathbf{R}^d \times \mathbf{R}_t$, there exists an infinite set of weak solutions of Euler equations in $\mathbf{R}^d$ which satisfy:*

$$\frac{|u(x,t)|^2}{2} = e(x,t), \text{ for all } t > 0 \text{ and a.e. } x \in \Omega, \quad \text{and } |u(x,t)| = 0, \text{ for all } (x,t) \notin Q.$$

2. There is an infinite set of initial data $u_0 \in L^2(\mathbf{R}^d)$ for which there exist admissible solutions (hence they are dissipative).
3. For any initial data $u_0 \in L^2(\mathbf{R}^d)$ there exists infinitely many weak solutions $u(x,t) \in C(\mathbf{R}_t; L^2(\mathbf{R}^d)_w)$, such that $u(x,0) = u_0$.

The first two statements in Theorem 3.4 are due to De Lellis and Székelyhidi, and the last one is due to Wiedemann following their approach. A complete proof of the above theorem is out of the scope of this contribution, but in the following subsection we give some comments which might be appropriate.

Comments on Theorem 3.4 The first two statements of Theorem 3.4 have, in fact, a long history over the second half of the previous century. In 1993 Scheffer [35] was the first person to observe the existence of weak solutions of Euler equations with compact support in time. Later, in 1997, Shnirelman [36] refined Scheffer's proof. The basic method was to construct approximate highly oscillating (in space and time) divergence-free vector fields u_k (with compact support in space and time), that would converge strongly in $L^2(\mathbf{R}^d \times \mathbf{R}_t)$ (in order to be able to pass to the limit in the nonlinear term $u_k \otimes u_k$), while by Equation (26) the sequence of residuals:

$$E_k := \partial_t u_k + P_\sigma((\nabla \cdot (u_k \otimes u_k)),$$

would converge weakly to zero.

Of course, such weak solutions, for which De Lellis and Székelyhidi coined the name "wild", are not physical at all. They describe a fluid flow which starting from rest and without any external force applied to it, begins to move and then goes back to rest. If this situation could be applied to "real world fluid flows" that would solve the energy crisis!

To establish their proof, De Lellis and Székelyhidi realized a striking analogy between "wild solutions" of Euler equations and the classical problem of isometric imbedding.

The simplest example of such an imbedding problem goes as follows:

Let $S^1 = \{x \in \mathbf{R}^2 : |x| = 1\} \subset \mathbf{R}^2$ be the unit circle, and, for any $r > 0$, $B^2(r) = \{x \in \mathbf{R}^2 : |x| \leq r\} \subset \mathbf{R}^2$ be the closed disc of radius r. The question is: what is the best regularity (in term of the Hölder exponent β) that is independent of r, and for which there exists a map $\phi_r \in C^\beta(S^1; B^2(r))$ (dubbed isometric imbedding) which enjoys the following property: $\phi_r(S^1)$ is, for the Riemannian metric induced by $\mathbf{R}^2$, a manifold isometric to S^1?

Now if one requires $\phi_r \in C^2$, the curvature of $\phi_r(S^1)$ should be bounded from above and below, independent of r. While to place the curve $\phi_r(S^1)$ in a ball of arbitrarily small

radius, one should expect its curvature to go to infinity, as $r \to 0$. This is an obstruction which was realized by Gauss under the name of "egregious theorem". Hence, to realize the isometric imbedding, one has to relax the regularity of the mapping ϕ_r from being C^2. What was proven (cf. [37] and the reference therein) is the existence of a small enough Hölder exponent $\alpha \in (0, 1)$, which is r independent, such that for any $r > 0$ there exists an isometric imbedding $\phi_r \in C^{1,\alpha}$ of S^1 into $\phi_r(S^1) \subset B^2(r)$. The main idea of the proof is to show first the existence of a mapping ψ_r that reduces the distance, on the Riemannian manifold $\psi_r(S^1)$, and then accumulate (add) small oscillations (wiggles of the curve) to reach the equality of the lengths; and thus prove that the isometric imbedding can be realized with the limit function of this process, $\phi_r \in C^{1,\alpha}$.

In the same way one can rewrite Euler equations as a linear system with a nonlinear constraint, namely, it is equivalent to the system:

$$\partial_t u + \nabla_x \cdot M + \nabla q = 0, \quad u(x, 0) = u_0(x), \nabla \cdot u = 0, \tag{31}$$

with the constraint

$$M = u \otimes u - \frac{|u|^2}{d} I, \tag{32}$$

where M is a traceless self-adjoint matrix, and I is the identity matrix. To solve the above system one considers, instead, the following more relaxed problem. Let Q and e be as in Theorem 3.4. Let Λ be the closed hull (in some convenient topology) of the set of all triples (u, q, M), where u is a vector field, q is a scalar, and M is a self-adjoint traceless matrix, which satisfy system (31), and the following relaxed constraint:

$$(u \otimes u) - M \leq \frac{2e(x,t)}{d} I, \text{ for almost every } (x,t) \in Q, \text{ and } |u(x,t)| = 0, \text{ for all } (x,t) \notin Q.$$

The elements of Λ are called sub-solutions of (31)–(32). Then the proof of Theorem 3.4 goes as follows. First, one should show that the set of continuous sub solutions, Λ, is not empty. Then, to conclude the proof, one constructs a sequence $(u_k, q_k, M_k) \in \Lambda$, which is constructed by adding, more and more, spatial and temporal oscillations of small amplitudes and high frequencies, and which converges strongly, in L^2, such that:

$$\lim_{k\to\infty} \left[(u_k \otimes u_k) - M_k - \frac{|u_k|^2}{d} I \right] = 0. \tag{33}$$

Remark 3.2. *1. Uniqueness among dissipative solutions, whenever one of them is regular, implies that the wild solutions stated in point 3 of Theorem 3.4 (for every initial data $u_0 \in L^2$) cannot be admissible whenever the initial data are regular. Indeed, as Wiedemann observes in [38] his construction of sub-solutions requires a jump in energy at time 0^+.*

2. Similarly the initial data giving rise in point 2 of Theorem 3.4 to admissible solutions cannot be regular; otherwise, the solutions being admissible would coincide with the unique dissipative solution. On the other hand, since the proof involves the Baire category theorem, the construction of these initial data is, in general, far from being explicit. However, for the case of Kelvin-Helmholtz type initial data:

$$u_0(x_1, x_2) = (-sign(x_2), 0), \tag{34}$$

in a periodic domain, explicit sub-solutions, and then infinitely many solutions, have been provided in [39]. In $3d$*, and for initial data of the form* $(-sign(x_2), 0, w(x_1, x_3))$*, the construction presented in [39] gives rise to an infinite set of admissible solutions, cf. [40].*

3. Eventually, with a better adapted choice of the high-frequency corrections to the sub-solutions, one can improve the spatial and temporal regularity of the wild solutions obtained at the limit. Along these lines, using Beltrami flows as building blocks for the high-frequency corrections in [41], one proves, for every fixed α *in* $(0, 1/10)$*, the existence of admissible wild solutions which belong to* $C^{0,\alpha}$*, and which exhibit strict energy decay.*

3.3. *Energy decay and turbulence*

For the Euler equations then the only natural estimate is the energy estimate which, as mentioned above, gives for smooth solution the relation:

$$\frac{1}{2}\int |u(x,t)|^2 dx = \frac{1}{2}\int |u(x,0)|^2 dx. \tag{35}$$

From this relation one deduces that any ϵ dependent family u_ϵ of smooth solutions is uniformly bounded according to the formula:

$$\forall t, \epsilon \quad |u_\epsilon(t)|_{L^2} \leq \sup_\epsilon |u_\epsilon(0)|_{L^2} < \infty. \tag{36}$$

Variants of this energy estimate (with inequality instead of equality) can be obtained and are valid in most of the physical situations (including Navier–Stokes with weakly converging initial data and viscosity going to 0 together with boundary effects) .

This implies the existence of subsequences, still denoted by u_ϵ, which are weakly converging to a limit $(\lim_{\epsilon\to 0} u_\epsilon)(x,t) \in L^\infty(\mathbf{R}_t; L^2)$. However, at this level of generality it is not possible to conclude that this limit remains a solution of Euler equations. The problem is that the weak limit of the tensor product may not be the product of the weak limits:

$$\lim_{\epsilon\to}(u_\epsilon \otimes u_\epsilon) \neq (\lim_{\epsilon\to 0} u_\epsilon) \otimes (\lim_{\epsilon\to 0} u_\epsilon) \tag{37}$$

and therefore the weak limit $\overline{u} = \lim_{\epsilon\to 0} u_\epsilon$ is solution of the equation:

$$\begin{aligned} &\nabla\cdot\overline{u} = 0, \quad \partial_t\overline{u} + \nabla(\overline{u}\otimes\overline{u}) + RT + \nabla\overline{p} = 0,\\ &\text{with} \quad RT = \lim(u_\epsilon - \overline{u}) \otimes \lim(u_\epsilon - \overline{u}). \end{aligned} \tag{38}$$

One simple example (which is due to DiPerna and Majda [42]) can be constructed with the shear flow:

$$u_\epsilon(x,t) = \left(\sin\left(\frac{x_2}{\epsilon}\right)\right), 0, w\left(x_1 - t\sin\left(\frac{x_2}{\epsilon}\right)\right)$$

which is uniformly bounded and which weakly converges to

$$\overline{u} = \left(0, 0, \int_0^1 w(x_1 - t\sin s)ds\right).$$

Obviously this is not a solution of the Euler equations, by direct inspection and also because the term $u_\epsilon^1 \partial_{x_1} w_\epsilon$ does not go to zero!

Weak limits can be interpreted in term of "coarse graining", as the deterministic counterpart of the Reynolds stress tensor for small fluctuations in the statistical theory of turbulence. In this setting one could consider, as turbulent flows which are not solutions of the Euler equations due to the appearance of the extra term RT in (38). Now the formula

$$\text{for almost every } t \quad \lim_{\epsilon\to 0} |\overline{u}(t) - u_\epsilon(t)|^2 = \lim_{\epsilon\to 0} |u_\epsilon(t)|^2 - |\overline{u}(t)|^2, \tag{39}$$

implies that the conservation of energy would give $RT = 0$ and therefore no turbulence. Hence, this implies the conjecture that turbulence would be related to anomalous energy dissipation.

Indeed, the issue of the conservation of energy for weak solutions was already raised by Onsager [43] when he formally wrote:

$$0 = \int [\nabla \cdot (u \otimes u)] \cdot u dx \simeq \int (\nabla^{\frac{1}{3}} u \cdot \nabla^{\frac{1}{3}} u \cdot \nabla^{\frac{1}{3}} u) \simeq \int |\nabla^{\frac{1}{3}} u|^3 dx. \tag{40}$$

He conjectured that any weak solution that would be more regular than $C^{0,\frac{1}{3}}$ would preserve energy. A rigorous proof of this result, inspired by the naive formula (40), was given by Constantin, E and Titi [44]. Of course this does not mean that the conservation of energy implies the regularity of the solution; simple examples of singular weak solutions which preserve energy can be constructed with the shear flow [22] or, as noticed above following ([37]), as "wild" solutions. Eventually to complete this picture it would be interesting to exhibit weak solutions less regular than $C^{0,\frac{1}{3}}$ for which energy would decay.

The first step was the construction of continuous (in space and time) solutions with decaying energy (cf. [45] for the spatially three-dimensional case, and [46] for the spatially two-dimensional case.) One of the basic ingredients in the spatially three-dimensional case was the introduction of the Beltrami flows in the construction. Then a refinement of the above method gave the existence of energy decaying weak solutions which belong to $C^{0,\alpha}$, with $\alpha < \frac{1}{10}$ (cf. [41] for the spatially three-dimensioanl case, and [47] for the spatially two-dimensional case). The most recent improvement, due to Isett [48], extend the Hölder regularity of these energy decaying solutions to $\alpha < \frac{1}{5}$, in a preprint of 171 pages!

4. Navier–Stokes equations without and with boundary effects

4.1. *Why in some cases Navier–Stokes rather than Euler*

In Section 2 the Euler equations were presented as a formal limit, as $Re \to \infty$, of Navier–Stokes equations. However, we have also added the relation between these two equations "is far from being simple". The Euler equations were derived first, and it took about 45 years to obtain Navier–Stokes equations as an "improved" model (cf. Navier [49] and Stokes [50]), taking into account the viscosity effects which are better adapted to the real fluids. Of course, at that time this was not motivated by the arguments of De Lellis and Skzékelyhidi

on wild solutions, but by the need for a mathematical description of the fluid's viscosity. Moreover, the introduction of the viscous term $-\nu\Delta u$, with the corresponding boundary conditions, is essential to describe the interaction of a fluid flow with physical obstacles. In general, this physically observed interaction cannot be described only by means of Euler equations, subject to the impermeability (no-normal flow) boundary conditions, as it will be illustrated by the following proposition:

Proposition 4.1. *Consider an obstacle $K \subset \mathbf{R}^3$, with a smooth boundary which is topologically isomorphic to a closed ball. Let u be the velocity field of a stationary solution of Euler equations in $\Omega = \mathbf{R}^3 \backslash K$, that is constant at infinity, i.e., $\lim_{|x|\to\infty} u(x) = u_\infty$, and which is satisfying the impermeability (no-normal flow) boundary condition, $u \cdot \vec{n} = 0$ on $\partial\Omega$. Then the total force exerted by the fluid flow on the obstacle K is 0.*

Proof. (cf. [51] or [21] for details) Since the fluid flow is stationary and constant at infinity it is also irrotational and therefore one has the Bernoulli theorem:

$$\nabla\left(\frac{|u|^2}{2} + p\right) = 0. \tag{41}$$

Moreover, since the obstacle K is homeomorphic to a ball in $\mathbf{R}^3$ the domain $\Omega = \mathbf{R}^3 \backslash K$ is simply connected; therefore the velocity field u fluid is both "potential" and solenoidal. Hence, it can be described by the system:

$$u = -\nabla\phi, \quad -\Delta\phi = 0. \tag{42}$$

Thus, with the asymptotic behavior, at infinity, of the Green function of the Laplacian in $\mathbf{R}^3$ (behaving like $(4\pi)^{-1}|x|^{-1}$) one has

$$u(x) = u_\infty + O(|x|^{-3}) \text{ and } p(x) = p_\infty + O(|x|^{-3}), \tag{43}$$

where the above asymptotic behavior of the pressure follows from (41). Now, to compute the force exerted by the fluid one introduces the ball $B_R = \{x \in \mathbf{R}^3, |x| < R\}$. For R large enough one has $K \subset B_R$. Therefore, thanks to the impermeability boundary condition, $u \cdot \vec{n} = 0$, one can compute, $\vec{F}$, the force exerted on K, as follows:

$$\begin{aligned}
\vec{F} &= -\int_{\partial\Omega} p\vec{n}d\sigma = -\int_{\partial\Omega}\left((u\cdot\vec{n})u + p\vec{n}\right)d\sigma \\
&\quad + \int_{|x|=R}\left((u\cdot\frac{x}{R})u + p\frac{x}{R}\right)d\sigma - \int_{|x|=R}\left((u\cdot\frac{x}{R})u + p\frac{x}{R}\right)d\sigma \\
&= -\int_{\Omega\cap B_R}\left((u\cdot\nabla)u + \nabla p\right)dx - \int_{|x|=R}\left((u\cdot\frac{x}{R})u + p\frac{x}{R}\right)d\sigma \\
&= -\int_{|x|=R}\left((u\cdot\frac{x}{R})u + p\frac{x}{R}\right)d\sigma,
\end{aligned} \tag{44}$$

where the last equality is due to (41). Finally, by virtue of (43) the relation (44) implies:

$$\vec{F} = -\int_{\partial\Omega} p\vec{n}d\sigma = -\lim_{R\to\infty}\int_{|x|=R}\left((u\cdot\frac{x}{R})u + p\frac{x}{R}\right)d\sigma = 0\,! \tag{45}$$

Remark 4.1. *The above computation was already known by d'Alembert, for this reason it is called the d'Alembert paradox. A similar computation can be performed in two dimensions, but in this case the domain* $\Omega = \mathbf{R}^2\backslash K$*, where* K *is isomorphic to a disc in* $\mathbf{R}^2$ *is not simply connected. Therefore, irrotational vector fields need not to be potential. In addition, the Green function in two dimensions behaves like* $\frac{1}{2\pi}\log\frac{1}{|x|}$*, and it produces a nonzero contribution (lift) called the Kutta-Joukowski relation.*

In conclusion, we observe that the introduction of the viscosity, and of the corresponding boundary condition associated with the Laplacian, may lead to effects that cannot be described by Euler equations (which correspond to the singular limit $\nu = 0$), and that these effects might become important for "very small" values of ν, where $\nu > 0$.

For example, the $2d$ Navier–Stokes equations in the half-plane, $x_2 > 0$, subject to Dirichlet boundary condition, is a well-posed problem; and its vorticity, ω, evolves according to the equation

$$\partial_t\omega_\nu - \nu\Delta\omega_\nu + u_\nu\cdot\nabla\omega_\nu = 0. \tag{46}$$

In the inviscid case, $\nu = 0$, the vorticity, ω, evolves according to:

$$\partial_t\omega + (u\cdot\nabla)\omega = 0, \tag{47}$$

which does not indicate any interaction of the vorticity inside the domain with the boundary $\mathbf{R}\times\{x_2 = 0\}$. However, for the viscous case, $\nu > 0$, the values of the vorticity at the boundary, $\mathbf{R}\times\{x_2 = 0\}$, will depend in a nontrivial way on the pressure. To see that, we compute the normal derivative of the vorticity at $\mathbf{R}\times\{x_2 = 0\}$, and use the incompressibility condition, $\nabla\cdot u_\nu = 0$, and the Dirichlet boundary condition, $u_\nu = 0$ at $\mathbf{R}\times\{x_2 = 0\}$, to obtain

$$\partial_{x_2}\omega_\nu = \partial_{x_2}(\partial_{x_1}u^2_\nu - \partial_{x_2}u^1_\nu) = \partial_{x_1}(\partial_{x_2}u^2_\nu) - \partial^2_{x_2}u^1_\nu = -\partial^2_{x_1}u^1_\nu - \partial^2_{x_2}u^1_\nu = -\partial^2_{x_2}u^1_\nu.$$

Next, use the evolution equation for the first component of the velocity, u^1_ν, in the Navier–Stokes equations at the boundary, $\mathbf{R}\times\{x_2 = 0\}$, to get

$$\nu\partial^2_{x_2}u_1 = \partial_{x_1}p.$$

Combining the above yields the so called Lighthill equation:

$$-\nu\partial_{x_2}\omega_\nu = \partial_{x_1}p, \text{ at } \mathbf{R}\times\{x_2 = 0\}. \tag{48}$$

The above relation, (48), implies that the variation of pressure at the boundary generates the vorticity there or vice versa. Notice that the quantities involved in (48) may be very large,

for small values of $\nu > 0$, leading (cf. Section 4.4) to important effects and interaction with the boundary.

To measure such effects, in particular in comparison with the Reynolds number, it is convenient to consider a slightly more general class of boundary conditions. Therefore, in an open smooth domain $\Omega \subset \mathbf{R}^d$, with $d = 2$ or $d = 3$, one supplements the Navier–Stokes equations

$$\partial_t u_\nu + (u_\nu \cdot \nabla)u_\nu - \nu \Delta u_\nu + \nabla p_\nu = 0, \text{ in } \Omega \tag{49}$$

with the boundary conditions

$$u_\nu \cdot \vec{n} = 0, \quad \nu(\partial_{\vec{n}} u_\nu + C(x)u_\nu)_\tau + \lambda u_\nu = 0 \text{ on } \partial\Omega, \tag{50}$$

$$\text{with} \quad \lambda(\nu, x) \geq 0, \ C(x) \in C(\mathbf{R}^n; \mathbf{R}^n), \tag{51}$$

where $\vec{n}$ is denoting the outward normal to $\partial\Omega$, and $\vec{a}_\tau = \vec{a} - (\vec{a} \cdot \vec{n})\vec{n}$ is the tangential component of the vector $\vec{a}$ at the boundary $\partial\Omega$. Of course, when the problem is considered in the whole space, or in a periodic box, these boundary conditions are omitted. In (50) there are two statements which represent, on one hand, the impermeability condition $u_\nu \cdot \vec{n} = 0$, which is in some sense universal (independent of the fluid, and in particular of whether it is viscous or inviscid) and, on the other hand, a condition which models the friction between the fluid flow and the boundary, and which may exhibit some nontrivial behavior in terms of the Reynolds number. With $\lambda(\nu) = \infty$, the second statement corresponds to the Dirichlet boundary condition: the component of the velocity on the plane tangent to $\partial\Omega$ being also zero and, therefore, it is called the "no-slip" boundary condition.

In the more general case, $C(x)$ is a linear bounded operator acting on the space of tangent vectors to $\partial\Omega$ with the $L^2(\partial\Omega)-$norm. With a convenient choice of $C(x)$ this statement includes the following conditions:

$$(S(u_\nu) \cdot \vec{n})_\tau = (\partial_{\vec{n}} u_\nu)_\tau - (\nabla^t \vec{n} \cdot u_\nu)_\tau \Rightarrow \nu(S(u_\nu) \cdot \vec{n})_\tau + \lambda u_\nu = 0 \tag{52}$$

and

$$(\nabla \wedge u_\nu) \wedge \vec{n} = (\partial_{\vec{n}} u_\nu)_\tau + (\nabla^t \vec{n} \cdot u_\nu)_\tau \Rightarrow \nu(\nabla \wedge u_\nu) \wedge \vec{n} + \lambda u_\nu = 0. \tag{53}$$

Condition (52) is the standard Fourier law, which can be either derived by phenomenological arguments, or deduced from a boundary condition for the Boltzmann equations, due to the atomic structure of the wall (cf. [52, 53] and [54]). Condition (53) emphasizes the role of the vorticity.

Integrating by parts after multiplying Equation (49) by u_ν, and using some standard trace estimates one obtains the:

Proposition 4.2. *Any smooth solution of the Navier–Stokes equations, (49), with the boundary conditions (50), satisfies the relation (energy balance):*

$$\frac{1}{2}\frac{d}{dt}\int_\Omega |u_\nu(x,t)|^2 dx + \nu \int_\Omega |\nabla u_\nu|^2 dx + \int_{\partial\Omega} \lambda(x)|u_\nu(x,t)|^2 d\sigma = \nu \int_{\partial\Omega} C(u_\nu)_\tau u_\nu d\sigma \, ; \tag{54}$$

and the ν-uniform estimate:

$$\frac{d}{dt}\int_\Omega \frac{|u_\nu(x,t)|^2}{2}dx + \nu\int_\Omega |\nabla u_\nu|^2 dx + \int_{\partial\Omega}\lambda(x)|u_\nu(x,t)|^2 d\sigma = o(\nu). \qquad (55)$$

4.2. *Basic mathematical results for the Navier–Stokes equations*

From the estimate (54) one deduces, and this was the original contribution of Leray [14], that for any initial data $u_0 \in L^2$ there exists (globally in time) a weak solution to the Cauchy problem. However, there are several important differences between the $2d$ and $3d$ cases. In the $2d$ case one can prove that for any $u_0 \in L^2$ the solutions are unique and that the formal energy equality (54) is exact and can be justified rigorously. In the $3d$ case the situation (which is an object of the present Clay prize) is more complex. With no restriction on the size of the viscosity, ν, when it is compared inversely to the spatial oscillation in the initial data (even very smooth initial data), the only result available is the (global in time) existence of a weak solution which satisfies the energy inequality, i.e., instead of the equality sign $=$ in (54) one has the inequality sign $\leq$. Such weak solutions that satisfy the energy inequality in (54) are called Leray–Hopf solutions. It is worth mentioning that all the known existence proofs of weak solutions to the Navier–Stokes equations lead at the end to Leray–Hopf solutions. The uniqueness of weak solutions, or Leray–Hopf weak solutions, and the propagation of regularity, for any time, of the initial data are still open problems.

There is a long history of questions of global regularity and of blow-up criteria of smooth solutions of the $3d$ Navier–Stokes equations, taking a full advantage of the regularizing effect of the Laplacian. As observed in Theorem 3.2 the absence of blow-up for the solutions of the $3d$ Euler equations is enforced by the Beale–Kato–Majda condition, which concerns the vorticity. For the Navier–Stokes equations it is enough to assume that the velocity remains bounded to ensure the regularity.[2] This condition can be widely improved starting from the pioneer works of Prodi [55] and Serrin [56], involving the $L^p((0,T), L^q(\Omega))$ norms of the velocity field, with $\frac{1}{p}+\frac{1}{q}=1$ (for more details see, for example, the survey articles [57–59] and references therein). Most recently, there have also been some criteria for global regularity of the $3d$ Navier–Stokes equations involving the pressure (cf. [60] and references therein). In addition, some other sufficient regularity conditions were recently established in terms of only one component of the stress tensor ∇u (cf. [61] and references therein). Furthermore, in the presence of certain spatial symmetries, such as axisymmetric [62] or helical [63] flows, the Navier–Stokes equations are known to be globally well-posed, but such results are still out of reach for Euler equations (see, e.g., [64] and references therein for some related results concerning helical Euler equations). It is worth mentioning that the vorticity stretching term, which is the main characteristic of $3d$ flows verses $2d$ flows, is nontrivial for axisymmetric and helical flows.

Eventually, the two following sharp results (even, if once someone proves that weak solutions of Navier–Stokes equations are always smooth) have a genuine interest by the detail and the physical interpretation of their proofs.

- Caffarelli, Kohn and Nirenberg [65]:

For any initial data $u_0 \in L^2$ there is a weak solution (called a suitable solution) for which the support of its singularity set, in space-time, is contained in a set whose one-dimensional Hausdorff measure is zero. This means that the singularity set, in space-time, is "less" than one-dimensional.

- Seregin and Sverak [66]:

Smooth solutions of the $3d$ Navier–Stokes equations remain smooth for as long as either the pressure is bounded from below, or the Bernoulli pressure $\frac{|v|^2}{2} + p$ is bounded from above.

For instance what [65] says is that the velocity of the fluid cannot be too big, say $|u| > M$, except in regions which are small with respect to M. The result of [66] can also be interpreted by saying that for as long as there are no cavities in the flow the solution can be uniformly controlled. Of course, the minute cavities are formed the Navier–Stokes equations are no longer valid as a physical model.

4.3. *Zero viscosity limit of solutions of Navier–Stokes in the absence of boundary*

As mentioned in the previous section, the introduction of the viscous term, i.e., the Navier–Stokes equations, is essential in order to take into account boundary effects. Conversely, in the absence of physical boundaries, one has the following proposition: the behavior, as the viscosity $\nu \to 0$, of Leray–Hopf weak solutions of the Navier–Stokes equations is related to the behavior of the solutions of the Euler equations according to

Proposition 4.3. *1. For given initial data, $u_0 \in L^2(\mathbf{R}^d)$, Leray–Hopf weak solutions of the Navier–Stokes equations are bounded (uniformly with respect to ν) in $L^\infty(\mathbf{R}_t; L^2(\mathbf{R}^d_x))$.*
2. Any weak limit, $\overline{u}$, as $\nu \to 0$, of such a family of Leray–Hopf weak solutions of Navier–Stokes equations is a dissipative solution of Euler equations.
3. Assume that, with u_0 as initial data, Euler equations have a smooth solution $u(t)$, in the time interval $[0, T]$. Then $\overline{u}(t) = u(t)$, for all $t \in [0, T]$.

Remark 4.2. *The issue in the above proposition is that, in the absence of boundary effects (with boundary the situation is completely different, see section 4.4, below), any weak limit of solutions to the Navier–Stokes equations is a dissipative solution to the Euler equation. Then the next issue does not concern Navier–Stokes equations but the dissipative solution of the Euler equations. In the presence of a smooth solution (with the same initial data) of Euler equations point 2 of Poposition 3.1 implies that this weak limit is the smooth solution of the Euler equations. Hence, it is unique and nothing spectacular happens as described with more details in Remark 4.3.*

Proof of the Proposition 4.3: By definition, a Leray–Hopf weak solutions $u_\nu(x, t)$ to Navier–Stokes equations satisfies the energy inequality (here without boundary terms, since there is no physical boundary):

$$\frac{1}{2}\int_{\mathbf{R}^d} |u_\nu(x,t)|^2 dx + \nu \int_0^t \int_{\mathbf{R}^d} |\nabla u_\nu(x,s)|^2 dx ds \leq \frac{1}{2}\int_{\mathbf{R}^d} |u_0(x)|^2 dx. \tag{56}$$

Therefore, u_ν is uniformly bounded in $L^\infty(\mathbf{R}_t; L^2(\mathbf{R}^d_x))$ and, modulo extraction of a subsequence, converges weak$-*$ in this space to a limit $\overline{u}$. Proceeding as in Section 3.2 (for rigorous justification of all the steps below one can follow the arguments introduced in [67]),

for any divergence-free smooth test function $w(x,t)$ satisfying

$$\partial_t w + P_\sigma((w\cdot\nabla)w) = E(w), \tag{57}$$

one obtains the estimate:

$$\begin{aligned}
&\int_{\mathbf{R}^d} |u_\nu(x,t)-w(x,t)|^2 dx + 2\nu\int_0^t\int_{\mathbf{R}^d} |\nabla u_\nu(x,s)|^2 dxds\\
&\quad\le 2\int_0^t\int_{\mathbf{R}^d} |(E(w(x,s))\cdot(u(x,s)-w(x,s)))|dxds\\
&\quad+2\nu\int_0^t\int_{\mathbf{R}^d} (\nabla u_\nu(x,s)\cdot\nabla w(x,s))dxds\\
&\quad+2\int_0^t\int_{\mathbf{R}^d} |(u_\nu(x,s)-w(x,s)S(w)(u_\nu(x,s)-w(x,s))|dxds\\
&\quad+\int_{\mathbf{R}^d} |u_0(x)-w(x,0)|^2 dx.
\end{aligned}\tag{58}$$

Thanks to Grönwall Lemma one has:

$$\begin{aligned}
\int_{\mathbf{R}^d} |u_\nu(x,t)-w(x,t)|^2 &\le \left(\int_{\mathbf{R}^d} |u_0(x)-w(x,0)|^2 dx\right) e^{2\int_0^t \|S(w)\|_\infty(s)ds}\\
&+2\int_0^t\left[\int_{\mathbf{R}^d} |(E(w(x,s))\cdot(u_\nu(x,s)-w(x,s)))|e^{2\int_s^t\|S(w)\|_\infty(\tau)d\tau}dx\right]ds\\
&+2\nu\int_0^t\left[\int_{\mathbf{R}^d}(\nabla u_\nu(x,s)\cdot\nabla w(x,s))dx e^{2\int_s^t\|S(w)\|_\infty(\tau)d\tau}\right]ds.
\end{aligned}\tag{59}$$

Thus, by virtue of the energy estimate,

$$2\nu\int_0^T\int_{\mathbf{R}^d}|\nabla u_\nu(x,s)|^2 dxds \le \int_{\mathbf{R}^d}|u_0(x)|^2dx,$$

there exists a subsequence of u_ν, which will also be labeled u_ν, such that $\sqrt{\nu}\nabla u_\nu$ converges weakly in $L^2([0,T];L^2(\mathbf{R}^d_x))$. As a result one has

$$\lim_{\nu\to 0} 2\nu\int_0^t\left[\int_{\mathbf{R}^d}(\nabla u_\nu(x,s)\cdot\nabla w(x,s))dx\, e^{2\int_s^t\|S(w)\|_\infty(\tau)d\tau}\right]ds = 0.$$

Moreover, as noticed above, the weak convergence gives

$$\int_{R^d} |\overline{u}(x,t) - w(x,t)|^2 \leq \liminf_{\nu\to 0} \int_\Omega |u_\nu(x,t) - w(x,t)|^2$$

and

$$\int_0^t \left[\int_{\mathbf{R}^d} |(E(w(x,s)) \cdot (\overline{u}(x,s) - w(x,s)))|\, e^{2\int_s^t \|S(w)\|_\infty(\tau)d\tau} dx \right] ds$$

$$= \lim_{\nu\to 0} \int_0^t \left[\int_{\mathbf{R}^d} |(E(w(x,s)) \cdot (u_\nu(x,s) - w(x,s)))| dx\, e^{2\int_s^t \|S(w)\|_\infty(\tau)d\tau} \right] ds.$$

Consequently, one has:

$$\int |\overline{u}(x,t) - w(x,t)|^2 \leq \left(\int |u_0(x) - w(x,0)|^2 dx \right) e^{2\int_0^t \|S(w)\|_\infty(s)ds}$$

$$+ 2\int_0^t \left[\int_{\mathbf{R}^d} |(E(w(x,s)) \cdot (\overline{u}(x,s) - w(x,s)))dx| e^{2\int_s^t \|S(w)\|_\infty(\tau)d\tau} \right] ds. \quad (60)$$

Remark 4.3. *1. The most important remark following this proof is the fact that in the presence of a smooth solution of Euler equations any weak limit will coincide with this smooth solution and since the smooth solution conserves energy one has*

$$\lim_{\nu\to 0} \left(\nu \int_0^t \int_{\mathbf{R}^d} |\nabla u_\nu(x,s)| dx ds \right)$$

$$\leq \frac{1}{2} \int_{\mathbf{R}^d} |u_0(x)|^2 dx - \lim_{\nu\to 0} \frac{1}{2} \int_{\mathbf{R}^d} |u_\nu(x,t)|^2 dx$$

$$\leq \frac{1}{2} \int_{\mathbf{R}^d} |u_0(x)|^2 dx - \frac{1}{2} \int_{\mathbf{R}^d} |u(x,t)|^2 dx = 0 \quad (61)$$

and therefore there is no anomalous dissipation of energy (the energy dissipation rate which appears in Kolmogorov theory of turbulence is 0.)

2. In fact, as said above, regularity is known to propagate for smooth solution of the 2d Euler equations, therefore, in 2d with smooth initial data, the energy will always be conserved and there will be no anomalous dissipation of energy (or enstrophy). The appearance of singularities, after some (long?) time, for the 3d Euler equations with smooth initial data is still a challenging open problem. Therefore, it may happen (even with smooth initial data) that, after some long time, anomalous dissipation of energy appears in the limit, as $\nu \to 0$. Thus, anomalous dissipation would be a criterion for blow-up of the solutions of 3d Euler equations.

3. Moreover, returning to the contributions of De Lellis and Székelyhidi, one should keep in mind that there exists in 2d or 3d an infinite set of initial data, $u_0 \in L^2$, such that for each u_0 there is an infinite set of corresponding dissipative solutions for Euler equations. In this situation the above consideration does not apply. For such initial data there may be anomalous dissipation of energy. In this case, since the fact of being dissipative does not

imply the uniqueness of the solution, one should consider other types of uniqueness criteria, or selection mechanism for uniqueness. A natural candidate for unique solution of Euler equations would be a viscosity limit solution, namely the limit solution, $\bar{u}$, of a family of solutions, u_ν, of Navier–Stokes equations, when the viscosity $\nu \to 0$. This assertion is not proven with full generality, but some examples built with the shear flow, cf. [40], indicate that this should be the case.

Remark 4.4. *Extension of the Proposition 4.3, assuming more regularity in the initial data, can be found in [68] (see also [17]). Assuming that the Euler equations have a smooth solution in the time interval* $[0, T]$*, it is shown that the same is true for the solution of Navier–Stokes equations with the same initial data on the same time interval for* ν *small enough. Moreover, the rates of convergence in higher norms are estimated (see also [69] for similar results concerning the Euler−*α *regularization model.)*

4.4. *Viscosity limit with boundary effects*

Unlike the previous section the emphasis here is put on the viscosity limit, in both the $2d$ and the $3d$ cases, in the presence of physical boundaries. In fact, in as far as our understanding of this problem goes, there is not much difference between the $2d$ and the $3d$ cases. Thus, it will be assumed that the solution of Euler equations (with given fixed and smooth initial data u_0) is smooth for $t \in [0, T]$. In the $2d$ case the global regularity of Euler equations, i.e. for all $T > 0$, was proven by Wolibner in 1933 [70], and it will be assumed in the present discussion for the $3d$ case as well. As said above, the introduction of Navier–Stokes equations allows to take into account additional boundary effects (in particular the production and shedding of vorticity near the boundary). One may link these effects with anomalous dissipation of energy, as $\nu \to 0$, and conclude that turbulent regimes which are observed in the fluid flow, even far from the boundary, where one could talk of *homogenous and isotropic turbulence,* is not a smooth solution of Euler equations.

In fact, the number of boundary conditions required for Navier–Stokes equations is 3, and this number is reduced to one in the case of Euler equations, i.e., $u \cdot \vec{n} = 0$, generating a boundary layer near the boundary. However, since the problem is nonlinear, this boundary layer may not be confined to the boundary and instead it may propagate, by means of the nonlinear advection term, inside the bulk of the flow.

Here also dissipative solutions to the Euler equations will be used; but an important modification will be introduced in their definition. In the present case, smooth solutions of Euler equations may have nonzero tangential component at the physical boundary, thus comparing them to test functions that have compact support in the domain (i.e., without interaction with the boundary) is not enough to characterize the limit of Navier–Stokes solutions, as the viscosity $\nu \to 0$. The modified definition of dissipative solutions for the Euler equations is:

Definition 4.1. *Consider the Euler equations in a domain* Ω*, with nonempty boundary* $\partial\Omega \neq \emptyset$*. A vector field* u *is called a dissipative solution up to the boundary, for the Euler equations, if for every smooth divergence-free test vector field,* w*, which is tangent to the boundary* $\partial\Omega$ *(i.e.,* $w \cdot \vec{n} = 0$ *on* $\partial\Omega$*), and which has bounded support in* Ω*, one has the*

estimate:

$$\frac{1}{2}\int_\Omega |u(x,t)-w(x,t)|^2 \le \int_0^t \int_\Omega |(E(w(x,s)), u(x,s)-w(x,s))|dxds$$
$$+\int_0^t \int_\Omega |(u(x,s)-w(x,s)S(w)u(x,s)-w(x,s))|dxds$$
$$+\frac{1}{2}\int_\Omega |u(x,0)-w(x,0)|^2 dx, \tag{62}$$

where $E(w)$ is the residual as in Equation (26).

This is the same criterion as in (27), but with a larger class of test functions, w. In particular, if there exists a smooth solution $u(x,t)$ with initial data $u_0(x)$, any dissipative solution up to the boundary with the same initial data does coincide with this smooth solution. Such a result would not be valid if only test functions with compact support in Ω were used in the criterion (27).

Theorem 4.1. *In dimensions 2 or 3, for any ν dependent family of Leray–Hopf weak solutions, on the time interval $[0,T]$, of the Navier–Stokes equations*

$$\partial_t u_\nu + u_\nu \cdot \nabla u_\nu - \nu \Delta u_\nu + \nabla p_\nu = 0,$$

in a domain Ω, with boundary conditions

$$u_\nu \cdot \vec{n} = 0,\ \nu(\partial_{\vec{n}} u_\nu + C(x)u_\nu)_\tau + \lambda(\nu,x)u_\nu = 0 \ \text{on}\ \partial\Omega, \tag{63}$$
$$\text{and}\ \lambda(\nu,x) \ge 0,\ \ C(x) \in C(\mathbf{R}^n;\mathbf{R}^n)\,; \tag{64}$$

and with fixed initial data u_0, one has the following assertions:

1. If u_ν converges weak$-*$, in $L^\infty((0,T);L^2(\Omega))$, to a function $u(x,t)$, which is, for all $t \in (0,T)$, a smooth solution of the Euler equations, then u_ν converges strongly to u, and it does not dissipate energy in the limit as $\nu \to 0$; namely,

$$\epsilon(\nu,T) = \lim_{\nu\to 0}\int_0^T (\nu\int_\Omega |\nabla u_\nu|^2 dx + \int_{\partial\Omega}\lambda(\nu)|u_\nu(x,t)|^2 d\sigma)dt = 0. \tag{65}$$

2. If $(\nu\frac{\partial u_\nu}{\partial \vec{n}})_\tau \to 0$, as $\nu \to 0$, even in a very weak sense (for instance, in the sense of distribution in $\mathcal{D}'(\partial\Omega\times(0,T))$), then any weak limit, $\overline{u}$, of the sequence u_ν is a dissipative solution up to the boundary of the Euler equations.

3. (Kato criterion) If the sequence u_ν satisfies the estimate:

$$\lim_{\nu\to 0}\int_0^T \nu \int_{\{d(x,\partial\Omega)<c\nu\}\bigcap\Omega} |\nabla u_\nu(x,t)|^2 dxdt = 0, \tag{66}$$

then the hypothesis of the point 2 above is satisfied, and therefore any weak limit of the sequence u_ν is a dissipative solution up to the boundary of Euler equations.

Proof. Below, we will sketch some of the main ideas of the proof.

Equation (65) represents the dissipation of energy over the time $[0, T]$, the term $\int_0^T(\nu \int_\Omega |\nabla u_\nu|^2 dx)dt$ represents the dissipation of energy due to the fluid viscosity, and $\int_0^T(\int_{\partial\Omega} \lambda(\nu)|u_\nu(x,t)|^2 d\sigma)dt$ represents the dissipation of energy due to the friction of the fluid flow with the boundary. In the special case of the Dirichlet boundary condition for the Navier–Stokes equations this second term does not appear because the velocity field, u_ν, is zero on the boundary.

Point 1 follows from the energy estimate

$$\frac{1}{2}\int_\Omega |u_\nu(x,t)|^2 dx + \nu \int_0^T \int_\Omega |\nabla u_\nu|^2 dx + \int_{\partial\Omega} \lambda(x)|u_\nu(x,t)|^2 d\sigma \leq \int_\Omega |u_0|^2 dx + o(1),$$

where $o(1)$ stands for a term that tends to zero, as $\nu \to 0$. The above energy inequality is obtained in a similar way as for the Leray–Hopf weak solutions of the Navier–Stokes system; however, this time using the boundary conditions (63)–(64). For this reason we also call weak solutions of Navier–Stokes equations that satisfy the above energy inequality Leray–Hopf weak solutions.

Observe, thanks to the weak$-*$ convergence in $L^\infty((0,T); L^2(\Omega))$ of u_ν to a smooth solution u of Euler equations, that one has

$$\frac{1}{2}\int_\Omega |u_0(x))|^2 dx = \frac{1}{2}\int_\Omega |u(x,t)|^2 dx = \frac{1}{2}\int_\Omega |u(x,t)|^2 dx \leq \lim_{\nu\to 0} \frac{1}{2}\int_\Omega |u_\nu(x,t)|^2 dx. \tag{67}$$

Concerning point 2, the main difference between the problem without physical boundary and the current problem with boundary comes from the, only uncontrolled, extra term in the computation of

$$-\nu \int_0^T \int_\Omega (\Delta u_\nu \cdot (u_\nu - w))dx dt,$$

which, thanks to the boundary conditions $w \cdot \vec{n} = 0$ and (63)–(64), gives a boundary term of the form

$$\nu \int_0^T \int_{\partial\Omega} ((\frac{\partial u_\nu}{\partial \vec{n}})_\tau \cdot w_\tau)d\sigma dt. \tag{68}$$

Thus to establish point 2 one needs to show that the above term goes to zero, as $\nu \to 0$. By virtue of the density of the set of smooth test functions, w, in Definition 4.1 (see estimate (62)), it is enough to consider in the criterion stated in point 2, and to test it for, C^∞ test functions.

Next, we show point 3. For any smooth $w(x,t)$ tangent to $\partial\Omega$ for all $t \in (0,T]$, one constructs (following Kato [71]) a family $w_\nu(s,\tau,t)$ (here τ and s are the local tangential and normal coordinates at $\partial\Omega$, respectively), for small $\nu > 0$, of smooth divergence-free test functions, which are tangent to the boundary, $\partial\Omega$, and which also satisfy the following

properties: For every $\nu > 0$, w_ν coincides with w on $\partial\Omega \times (0, T)$, and its support is contained in

$$\Omega_\nu \times (0, T) = \{x \in \Omega : d(x, \partial\Omega) < \nu\} \times (0, T).$$

Moreover, w_ν satisfied the estimates

$$|\partial_t w_\nu|_{L^\infty} \leq C, \quad |\nabla_\tau w_\nu|_{L^\infty} \leq C, \quad |\partial_s w_\nu|_{L^\infty} \leq \frac{C}{\nu}. \tag{69}$$

Next, we show that (66) implies $\lim_{\nu\to 0}((\nu\frac{\partial u_\nu}{\partial\vec{n}})_\tau, w_\tau)_{L^2(\partial\Omega\times(0,T))} = 0$. Observe that $((\nu\frac{\partial u_\nu}{\partial\vec{n}})_\tau, w_\tau)_{L^2(\partial\Omega\times(0,T))} = ((\nu\frac{\partial u_\nu}{\partial\vec{n}})_\tau, (w_\nu)_\tau)_{L^2(\partial\Omega\times(0,T))}$, and hence this expression can be deduced from Navier–Stokes equations, subject to the boundary conditions (63)–(64), according to the formula

$$\begin{aligned} 0 &= \int_0^T (0, w_\nu)dt = \int_0^T ((\partial_t u_\nu + \nabla\cdot(u_\nu \otimes u_\nu) - \nu\Delta u_\nu + \nabla p_\nu), w_\nu)dt \\ &= -\int_0^T (u_\nu, \partial_t w_\nu)dt - \int_0^T ((u_\nu\cdot\nabla)w_\nu, u_\nu)dt \\ &\quad + \nu\int_0^T (\nabla u_\nu, \nabla w_\nu)dt - (\nu\partial_{\vec{n}} u_\nu, w_\nu)_{L^2(\partial\Omega\times(0,T))}, \end{aligned} \tag{70}$$

which implies the estimate:

$$\left|(\nu\partial_{\vec{n}} u_\nu, w_\nu)_{L^2(\partial\Omega\times(0,T))}\right| = \left|\int_0^T ((u_\nu\cdot\nabla)w_\nu, u_\nu)dt\right| + o(1). \tag{71}$$

Eventually, using (69), the control of the energy and the Poincaré inequality, one obtains

$$\left|\int_0^T ((u_\nu\cdot\nabla)w_\nu, u_\nu)dt\right| \leq C\int_0^T\int_{\Omega_\nu} \nu|\nabla u_\nu|^2 dxdt. \tag{72}$$

Therefore, thanks to (66), (71) and (72) one concludes

$$\lim_{\nu\to 0}((\nu\frac{\partial u_\nu}{\partial\vec{n}})_\tau, w_\tau)_{L^2(\partial\Omega\times(0,T))} = 0.$$

This completes the proof of point 3.

Remark 4.5. *The boundary conditions (63)–(64) together with the hypothesis* $\lim_{\nu\to 0}\lambda(\nu) = 0$ *imply that any weak limit of the family* u_ν*, of Leray–Hopf weak solutions of the Navier–Stokes equations, is a dissipative solution up to the boundary of Euler equations. The hypothesis of point 2 involves only* ν *times the tangential component of the normal derivative of the velocity. This point of view can be combined with the hypothesis of point 3, and this was done by Wang [72]. The condition proposed by Wang (which at the end of the day will be equivalent to all the others) involves only the tangential component of the normal derivative of the velocity, but in a layer slightly thicker than the Kato layer,*

which is the well-known thickness of viscous sublayer as predicted by von Karman (1930) logarithmic profile. In a situation where the convergence to the regular solution of Euler equations is insured it is possible to give many details of the rate of this convergence, the nature of the boundary layer and so on. There is a huge literature along these lines, to cite a few see, for example, [73–75] and references therein.

Remark 4.6. *When $\lambda(\nu)$ does not go to zero, in particular, in the most extreme case (the Dirichlet boundary conditions) when $\lambda(\nu) = \infty$, there is no information on the nature of the limit, at this level of generality.*

However, one can underline the interpretation of the above theorem by stating that any of the following facts:

•There is no production of vorticity at the boundary.

•There is no anomalous dissipation of energy in a layer of size ν, at the boundary, and, of course, no anomalous dissipation of energy in the whole fluid flow domain.

•There is conservation of energy as $\nu \to 0$,

implies that the zero viscosity limit does not exhibit any turbulent behavior. This is meant in the sense that the limit solution of Navier–Stokes equations, as $\nu \to 0$, is as smooth as the corresponding solution of Euler equations, and that no nontrivial Reynolds stresses tensor (in the sense of coarse graining) appears at the limit.

On the other hand, if one of the above statements is not true, due to boundary effects, one cannot say that the limit is a dissipative solution up to the boundary of Euler equations in contrast with the case without boundaries.

Nontrivial Reynolds stresses tensor (in the sense of coarse graining) may occur either when the weak limit, $\overline{u}$, as $\nu \to 0$, is not a weak solution of Euler equations, or when $\overline{u}$ is a weak solution of Euler equations that is obtained as the limit of Navier–Stokes equations with energy decay, i.e., $\overline{u}$ is a weak admissible solution of Euler equations. However, even so, some concentration of oscillations (turbulence) near the boundary may prevent it to be a dissipative solution up to the boundary of Euler equations. This pathologic type of weak solutions of Euler equations can in fact be constructed. For instance one can consider the restriction to the domain $x_2 > 0$ of the wild solutions given by [39].

4.5. *More about boundary effects and Prandtl equations*

In this section we follow very closely our presentation (cf. [8]) concerning the Prandtl equations. What essentially prevents the existence of more definite results, in the general case, is that what would be a boundary layer, in the zero viscosity limit, may not remain near the boundary and will actually detach from the boundary due to its rolling up into vortices which will, by the advection term, penetrate the bulk of the fluid flow forming the wake of the solid body.

However, this fact does not prevent more specific theoretical or practical studies. If one assumes, as a hypothesis, that the variation of the tangential component, and the size of the normal component, of the velocity of the fluid, near the boundary, are of the order of ϵ^{-1} and ϵ, respectively, (with $\epsilon = \sqrt{\nu}$), then by a change of scale near this boundary one may use the Prandtl equations (cf. [76] and for more recent discussion concerning the relation between the issue of 0 viscosity limit and the Prandlt equations [77]). We recall below the planar Prandtl equations for the case of a flat boundary: start from the Navier–Stokes equations in the half-plane, $\{(x_1, x_2) \in \mathbf{R}^2 : x_2 > 0\}$, with the no slip boundary condition,

$u_\nu(x_1, 0, t) \equiv 0$,

$$\partial_t u_1^\nu - \nu \Delta u_1^\nu + u_1^\nu \partial_{x_1} u_1^\nu + u_2^\nu \partial_{x_2} u_1^\nu + \partial_{x_1} p^\nu = 0, \tag{73}$$

$$\partial_t u_2^\nu - \nu \Delta u_2^\nu + u_1^\nu \partial_{x_1} u_2^\nu + u_2^\nu \partial_{x_2} u_2^\nu + \partial_{x_2} p^\nu = 0, \tag{74}$$

$$\partial_{x_1} u_1^\nu + \partial_{x_2} u_2^\nu = 0, \tag{75}$$

$$u_1^\nu(x_1, 0) = u_2^\nu(x_1, 0) = 0 \text{ for } x_1 \in \mathbf{R}, \tag{76}$$

then introduce the scale $\epsilon = \sqrt{\nu}$ and the change of variable which corresponds to a boundary layer in a parabolic problem, taking into account that the normal component of the velocity on the boundary, u_2, remains 0:

$$X_1 = x_1, X_2 = \frac{x_2}{\epsilon}, \tag{77}$$

$$\tilde{u}_1(x_1, X_2) = u_1(x_1, x_2), \tilde{u}_2(x_1, X_2) = \epsilon u_2(x_1, x_2). \tag{78}$$

Going back to the original notation (x_1, x_2) and letting ϵ go to zero, one obtains formally the system:

$$\tilde{u}_1(x_1, 0, t) - U_1(x_1, t) = 0, \tag{79}$$

$$\partial_{x_2} \tilde{p}(x_1, x_2) = 0 \Rightarrow \tilde{p}(x_1, x_2, t) = \tilde{P}(x_1, t) \tag{80}$$

$$\partial_t \tilde{u}_1 - \partial_{x_2}^2 \tilde{u}_1 + \tilde{u}_1 \partial_{x_1} \tilde{u}_1 + \tilde{u}_2 \partial_{x_2} \tilde{u}_1 = -\partial_{x_1} \tilde{P}(x_1, t), \tag{81}$$

$$\partial_{x_1} \tilde{u}_1 + \partial_{x_2} \tilde{u}_2 = 0, \tag{82}$$

$$\tilde{u}_1(x_1, 0, t) = \tilde{u}_2(x_1, 0, t) = 0 \text{ for } x_1 \in \mathbf{R}, \tag{83}$$

$$\lim_{x_2 \to \infty} \tilde{u}_1(x_1, x_2) = 0. \tag{84}$$

Equations (79) and (80) describe the fact that the boundary layer solution will match a solution of incompressible Euler equations. $U_1(x_1, t)$ and $\tilde{P}(x_1, t)$ are the tangential velocity and the pressure, respectively, on the boundary, $x_2 = 0$, of the solution to the Euler equations with the same initial data. Finally, the solution is written as a sum of regular functions: the boundary layer term, as computed above, and the solution of Euler equations, denoted $u_{\text{int}}(x_1, x_2, t)$

$$\begin{pmatrix} u_1^\nu(x_1, x_2, t) \\ u_2^\nu(x_1, x_2, t) \end{pmatrix} = \begin{pmatrix} \tilde{u}_1^\nu(x_1, \frac{x_2}{\sqrt{\nu}}, t) \\ \sqrt{\nu} \tilde{u}_2^\nu(x_1, \frac{x_2}{\sqrt{\nu}}, t) \end{pmatrix} + u_{\text{int}}(x_1, x_2, t). \tag{85}$$

Remark 4.7. *The validity of the Prandtl approximation is consistent with Kato's criterion (point 3 of Theorem 4.1) because with (85) one has*

$$\nu \int_0^T \int_{\Omega \cap \{d(x, \partial\Omega) \le c\nu\}} |\nabla \wedge u_\nu(x, s)|^2 dx ds \le C\sqrt{\nu}. \tag{86}$$

Remark 4.8. *At least one example showing that the Prandtl expansion cannot be always valid has been constructed by Grenier [78]. Solutions are considered in the domain*

$$\mathbf{R}_{x_1}/\mathbf{Z} \times \mathbf{R}^+_{x_2}.$$

Grenier starts with a solution u^ν_{ref} of the pressure-less Navier–Stokes equations given by

$$u^\nu_{ref} = (u_{ref}(t, \frac{y}{\sqrt{\nu}}), 0), \tag{87}$$

$$\partial_t u_{ref} - \partial^2_Y u_{ref} = 0, \tag{88}$$

where $Y = \frac{y}{\sqrt{\nu}}$. Using a convenient and explicit choice of the function u_{ref}, with some sharp results on instabilities, a solution of Euler equations of the form

$$\tilde{u} = u_{ref} + \delta v + O(\delta^2 e^{2\lambda t}) \quad \text{for} \quad 0 < t < \frac{1}{\lambda |\log \delta|} \tag{89}$$

is constructed. It is then shown that the vorticity generated at the boundary, by the solution of Navier–Stokes equations (with the same initial data), is too strong to allow the convergence of the Prandtl expansion. One should observe that, once again, this is an example with infinite energy. It would be interesting to see if such an example could be modified to enter the class of finite energy solutions and analyze how it would violate Kato's criterion (66).

It is important to observe that the mathematical properties of Prandtl equations exhibit the pathology of a situation based on the hypothesis that the boundary layer does not detach. First, one can prove the following.

Proposition 4.4. *Let $T > 0$ a finite positive time, and let $(U(x,t), P(x,t)) \in C^{2+\alpha}(\mathbf{R}_t \times (\mathbf{R}_{x_1} \times \mathbf{R}^+_{x_2}))$ be a smooth solution of the 2d Euler equation satisfying for $t = 0$ the compatibility condition $U_1(x_1, 0, t) = U_2(x_1, 0, t) = 0$ (only the boundary condition $U_2(x_1, 0, t) = 0$ is preserved by Euler's dynamics). Then the following facts are equivalent:*

1. With initial data $\tilde{u} = 0$, the boundary condition $\tilde{u}_1(x_1, 0, t) = U_1(x_1, 0, t)$ in (79) and the right-hand side in (80) given by $\tilde{P}(x_1, t) = P(x_1, 0, t)$, Prandtl equations have a smooth solution for $0 < t < T$.

2. The solution $u_\nu(x,t)$, with initial data $u_\nu(x,0) = U(x,0)$ and with no-slip boundary condition, at the boundary $x_1 = 0$, converges in $C^{2+\alpha}$ to the solution of Euler equations, as $\nu \to 0$.

The fact that the hypotheses 1 (and 2), above, may be violated for some t is related to the appearance of a detachment zone and the generation of vorticity at the boundary (which may eventually generate turbulence in the bulk of the fluid flow). This is well illustrated in

the analysis of Prandtl equations written in the following simplified form:

$$\partial_t \tilde{u}_1 - \partial^2_{x_2} \tilde{u}_1 + \tilde{u}_1 \partial_{x_1} \tilde{u}_1 + \tilde{u}_2 \partial_{x_2} \tilde{u}_1 = 0 \, \partial_{x_1} \tilde{u}_1 + \partial_{x_2} \tilde{u}_2 = 0, \tag{90}$$

$$\tilde{u}_1(x_1, 0) = \tilde{u}_2(x_1, 0) = 0 \text{ for } x_1 \in \mathbf{R}, \tag{91}$$

$$\lim_{x_2 \to \infty} \tilde{u}_1(x_1, x_2) = 0, \tag{92}$$

$$\tilde{u}_1(x_1, x_2, 0) = \tilde{u}_0(x_1, x_2). \tag{93}$$

Regularity in the absence of detachment corresponds to a theorem of Oleinik [79]. She proved that global smooth solution does exist if the initial profile is monotonic, i.e.,

$$\tilde{u}(x, 0) = (\tilde{u}_1(x_1, x_2), 0), \, \partial_{x_2} \tilde{u}_1(x_1, x_2) \neq 0. \tag{94}$$

On the other hand, initial conditions with "recirculation properties" leading to a finite time blow-up have been constructed by E and Enquist [80]. An interesting aspect of these examples is that the blow-up generally does not occur exactly on the boundary, but inside the domain supporting the hypothesis that this blow-up is due to the roll-up of the boundary layer which increases the velocity gradients.

The above pathology appears in the fact that the Prandtl equations are highly unstable. This comes from the determination $\tilde{u}_2$ in term of $\tilde{u}_1$ by the equation:

$$\partial_{x_1} \tilde{u}_1 + \partial_{x_2} \tilde{u}_2 = 0. \tag{95}$$

With this observation more recent and systematic studies of these instabilities can be found in [81] and [82].

Therefore it is only with analytic initial data (in fact analyticity with respect to the tangential variable is enough) that one can obtain (using an abstract version of the Cauchy-Kowalewsky theorem) the existence of a smooth solution of Prandtl equations for a finite time and the convergence to the solution of Euler equation during the same time (cf. Asano, Caflisch-Sammartino and Cannone-Lombardo-Sammartino [83–85], and more recently with the less stringent hypothesis on the x_2 asymptotic behavior in [86].)

5. Conclusion

This contribution is organized around the issues of the Cauchy problem, and the relevant boundary effects, in equations of motion of incompressible fluids. It presents some mathematical tools and results (theorems) that have been developed over the last, and the present, century for investigating certain basic properties of solutions of equations of fluid flows. There are many different mathematical approaches, that complement each other, to address these challenging problems; however, we chose to focus, in this contribution, only on certain mathematical aspects that are concerned with:

- The relation between the different equations of fluid motion in terms of well identified scaling parameters.
- The existing results (far from being complete at the time of this writing) about classical solutions of these equations.
- The notion of weak solutions (as used by Leray in his thesis or in the sense of distributions, as introduced by Gelfand and Schwartz). In particular, we recall that the notion of weak solutions (even with conservation or decay of energy) is not precise enough

to characterize the convenient (physically relevant) solutions of the Cauchy problem for Euler equations. This is in spite the fact that the relation between the regularity of solutions of Euler equations and the non conservation of energy is related to the Onsager conjecture in turbulence theory.

- The analysis of the zero viscosity limit for solutions of Navier–Stokes equations, with or without boundary effects. In the absence of boundary effects this convergence is a direct consequence of the existence (or nonexistence) of smooth solutions, with the same initial data, for the Euler equations; while in the presence of boundary effects the situation is completely different and the non-convergence (following a theorem of T. Kato) is related to the anomalous dissipation of energy, in the limit as $\nu \to 0$. This anomalous dissipation of energy corresponds, in the Kolmogorov theory of turbulence, to the non-vanishing limit of the positive mean rate of dissipation of energy, ϵ, as $\nu \to 0$.
- Lastly, the Prandtl equations are shortly discussed. We recall that these equations are in general ill-posed and that in the case when they are well-posed, which is the "laminar regime", the Kato criterion (of the above mentioned Kato theorem) is obviously satisfied, and as a result there is no anomalous dissipation of energy. Beside their importance (in situations where they are valid) for engineering sciences applications, the Prandtl equations became basic models for a systematic mathematical analysis of boundary layer in many other situations.

Acknowledgements

We wish to thank Marie Farge and Kai Schneider for the invitation to the conference "Fundamental Problems of Turbulence, 50 Years after the Marseille Conference 1961" from which this contribution has originated. Many thanks also to Marie Farge for her careful reading and hence scientific contribution to the present manuscript. The work of E.S.T. is supported in part by the NSF grants DMS-1009950, DMS-1109640 and DMS-1109645. E.S.T. also acknowledges the support of the Minerva Stiftung/Foundation.

Notes

1. The subscript w refers to the weak continuity. In the present setting this means that for any $\phi \in L^2(R^d)$ the function$t \mapsto (u(t), \phi(t))$ is continuous. Moreover such property follows from relation (23).
2. The appearance of unbounded, or very large velocity, is not inconsistent with the physical derivation of the equations. This is because, as it has been mentioned in Section 2, the incompressible Navier–Stoke equations can be deduced as a small Mach number approximation. In this case the velocity u_ϵ is replaced by $\epsilon\tilde{u}_\epsilon$, and the fact that u_ϵ is bounded does not imply that $\tilde{u}_\epsilon$, the solution of the "incompressible" equations, needs to be also uniformly bounded.

References

[1] U. Frisch, *Turbulence*, Cambridge University Press, Cambridge, 1995.
[2] P. Constantin, C. Foias, and R. Temam, *Attractor, Representing Turbulent Flows*, Memoir A.M.S., 53, 1985, pp. 314.
[3] C. Foias, O. Manley, R. Rosa, and R. Temam, *Navier–Stokes Equations and Turbulence*, Cambridge University Press, Cambridge, 2001.
[4] C. Foias, *What do the Navier–Stokes equations tell us about turbulence?*, in *Contemporary Mathematics, Vol. 208, Harmonic analysis and Nonlinear Differential Equations*, Amer. Math. Soc., Providence, RI, M. L. Lapidus, L. H. Harper and A. J. Rumbos, eds., 1997, pp. 151–180.
[5] N. Balci, C. Foias, M.S. Jolly, and R. Rosa, R. *On universal relations in 2-D turbulence*, Discrete & Contin. Dynamical Systems A 27 (2010), pp. 1327–1351.

[6] R. Dascaliuc, C. Foias, and M. Jolly, *Some specific mathematical constraints on 2D turbulence*, Physica D 237 (2008), pp. 3020–3029.
[7] C. Foias, M.S. Jolly, O.P. Manley, and R. Rosa, *Statistical estimates for the Navier–Stokes equations and the Kraichnan theory of 2-D fully developed turbulence*, J. Statist. Phys. 108 (2002), pp. 591–645
[8] C. Bardos and E.S. Titi, *Euler equations of incompressible ideal fluids*, Uspekhi Mat. Nauk 62(3) (375) (2007), pp. 5–46. Also in Russian Math. Surveys 62(3) (2007), pp. 409–451.
[9] P. Constantin, *Euler equations, Navier–Stokes equations and turbulence*, in *Mathematical Foundation of Turbulent Viscous Flows*, in Springer Lecture Notes in Mathematics, Vol. 1871, Lectures given at the C.I.M.E. Summer School, Martina Franca, Italy, M. Cannone and T. Miyakawa, eds., Springer, Berlin, 2006, pp. 1–43.
[10] P. Constantin, *On the Euler equations of incompressible fluids*, Bull. Amer. Math. Soc. 44 (2007), pp. 603–621.
[11] J.D. Gibbon, *The 3D Euler equations: Where do we stand?*, Physica D 237 (2008), pp. 1894–1904.
[12] M.D. Bustamente and R.M. Kerr, *3D Euler in a 2D symmetry plane*, Physica D 237 (2008), pp. 1912–1920.
[13] T.Y. Hou, *Blow-up or no blow-up? The interplay between theory & numerics*, Physica D 237 (2008), pp. 1937–1944.
[14] J. Leray, *Sur le mouvement d'un liquide visqueux emplissant l'espace*, (French) Acta Math. 63(1) (1934), pp. 193–248.
[15] L.D. Landau and E.M. Lifshitz, *Fluid Mechanics*, Pergamon Press, New York, 1959.
[16] P.L. Lions, *Mathematical Topics in Fluid Mechanics*, Vol. 1, Incompressible Models, Oxford Lecture Series in Mathematics and its Applications, Oxford, 1996.
[17] P. Constantin and C. Foias, *Navier–Stokes Equations*, Chicago Lectures in Mathematics, University of Chicago Press, Chicago, IL, 1988.
[18] A. Ferrari, *On the blow-up of solutions of the 3-D Euler equations in a bounded domain*, Commun. Math. Phys. 155 (1993), pp. 277–294.
[19] L. Lichtenstein, *Über einige Existenzproblem der Hydrodynamik homogener unzusammendrückbarer, reibunglosser Flüssikeiten und die Helmholtzschen Wirbelsalitze*, Mat. Zeit. Phys. 23 (1925), pp. 89–154; 26 (1927), pp. 193–323; 32 (1930), pp. 608.
[20] A.J. Majda and A.L. Bertozzi, *Vorticity and Incompressible Flow*, Cambridge Texts in Applied Mathematics, Vol. 27, Cambridge University Press, Cambridge, 2002.
[21] C. Marchioro and M. Pulvirenti, *Mathematical Theory of Incompressible Nonviscous Fluids*, Applied Mathematical Sciences, Vol. 96, Springer-Verlag, New York, 1994.
[22] C. Bardos and E.S. Titi, *Loss of smoothness and energy conserving rough weak solutions for the 3d Euler equations*, Discrete Contin. Dyn. Syst. Ser. S 3(2) (2010), pp. 185–197.
[23] C. Bardos and S. Benachour, *Domaine d'analyticité des solutions de l'équation d'Euler dans un ouvert de* $\mathbf{R}^n$, Annal. Sc. Normale Sup. di Pisa, Volume dédié à Jean Leray (1978), pp. 507–547.
[24] I. Kukavica and V. Vicol, *On the analyticity and Gevrey-class regularity up to the boundary for the Euler equations*, Nonlinearity 24(3) (2011), pp. 765–796.
[25] J.T. Beale, T. Kato, and A. Majda, *Remarks on the breakdown of smooth solutions for the 3D Euler equations*, Commun. Math. Phys. 94 (1984), pp. 61–66.
[26] P. Constantin, C. Fefferman, and A. Madja, *Geometric constraints on potential singular solutions for the* $3-D$ *Euler equation*, Commun. Partial Diff. Equations 21 (1996), pp. 559–571.
[27] G. Ponce, *Remarks on a paper by J.T. Beale, T. Kato, and A. Majda*, Commun. Math. Phys. 98 (1985), pp. 349–353.
[28] J. Deng, T.Y. Hou, and X. Yu, *Geometric properties and nonblowup of 3D incompressible Euler Flow*, Commun. Partial Diff. Equations 30 (2005), pp. 225–243.
[29] V.I. Yudovich, *Non stationary flow of an ideal incompressible liquid*, Zh. Vych. Mat. 3 (1963), pp. 1032–1066.
[30] J.-M. Delort, *Existence de nappes de tourbillon en dimension deux*, J. Amer. Math. Soc. 4 (1991), pp. 553–586.
[31] M.C. Lopes Filho, H.J. Nussenzveig Lopes, and Z. Xin, *Existence of vortex sheets with reflection symmetry in two space dimensions*, Arch. Ration. Mech. Anal. 158(3) (2001), pp. 235–257.
[32] A. Majda, *Remarks on weak solutions for vortex sheets with a distinguished sign*, Indiana Univ. Math. J. 42 (1993), pp. 921–939.

[33] C. Bardos, J. Linshiz, and E.S. Titi, *Global regularity and convergence of a Birkhoff-Rott−α approximation of the dynamics of vortex sheets of the 2D Euler equations*, Commun. Pure Appl. Math. 63(6) (2010), pp. 697–746.
[34] C. De Lellis and L. Székelyhidi, Jr., *On admissibility criteria for weak solutions of the Euler equations*, Arch. Ration. Mech. Anal. 195(1) (2010), pp. 225–260.
[35] V. Scheffer, *An inviscid flow with compact support in space-time*, J. Geom. Anal. 3 (1993), pp. 343–401.
[36] A. Shnirelman, *On the nonuniqueness of weak solutions of the Euler equations*, Commun. Pure Appl. Math. 50 (1997), pp. 1261–1286.
[37] C. De Lellis and L. Székelyhidi, Jr., *The h-principle and the equations of fluid dynamics*, Bull. Amer. Math. Soc. (N.S.) 49(3) (2012), pp. 347–375.
[38] E. Wiedemann, *Existence of weak solutions for the incompressible Euler equations*, Ann. Inst. H. Poincaré Anal. Non Linaire 28(5) (2011), pp. 727–730.
[39] L. Székelyhidi, *Weak solutions to the incompressible Euler equations with vortex sheet initial data*, C.R. Math. Acad. Sci. Paris, 349(19–20) (2011), pp. 1063–1066.
[40] C. Bardos, E.S. Titi, and E. Wiedemann, *Vanishing viscosity as a selection principle for the Euler equations: The case of 3D shear flow*, C.R. Acad. Sci. Paris 350(15–16) (2012), pp. 757–760.
[41] C. De Lellis and L. Székelyhidi, Jr., *Dissipative Euler Flows and Onsager's Conjecture* arXiv:1205.3626v1 [math.AP] 16 May 2012.
[42] R. DiPerna and A. Majda, *Oscillations and concentrations in weak solutions of the incompressible fluid equations*, Commun. Math. Phys. 108(4) (1987), pp. 667–689.
[43] L. Onsager, *Statistical hydrodynamics*, Nuovo Cimento 6(2) (1949), pp. 279–287.
[44] P. Constantin, W. E, and E.S. Titi, *Onsager's conjecture on the energy conservation for solutions of Euler's equation*, Commun. Math. Phys. 165 (1994), pp. 207–209.
[45] C. De Lellis and L. Székelyhidi, Jr., *Dissipative Continuous Euler flows*, arXiv:1202.1751v1 [math.AP], 8 April 2012.
[46] A. Choffrut, C. De Lellis, and L. Székelyhidi, Jr., *Dissipative Continuous Euler Flows in Two and Three Dimensions*, arXiv:1205.1226v1 [math.AP].
[47] A. Choffrut, *h-Principles for the Incompressible Euler equations*, arXiv:1209.5964v1 [math.AP], 26 September 2012.
[48] P. Isett, *Hölder Continuous Euler Flows in Three Dimensions with Compact Support in Time*, arXiv:1211.4065v1 [math.AP].
[49] C. Navier, *Mémoire sur les lois du mouvement des fluides*, Mém. Acad. Sci. Inst. France 6 (1822), pp. 389–440.
[50] G. Stokes, *On the theories of the internal friction of fluids in motion*, Trans. Cambridge Philos. Soc. 8, 287 (1845).
[51] A. Chorin and J. Marsden, *A Mathematical Introduction for Fluid Mechanics*, 3rd ed., Springer, New York, 1997.
[52] K. Aoki, T. Inamuro, and Y. Onishi, *Slightly rarefied gas flow over a body with small accommodation coefficient*, J. Phys. Soc. Japan 47 (1979), pp. 663—–671.
[53] C. Bardos, F. Golse, and L. Paillard, *The incompressible limit of the Boltzmann equation with accommodation boundary condition*, Commun. Math. Sci. 10(1) (2012), pp. 159–190.
[54] N. Masmoudi and L. Saint-Raymond, *From the Boltzmann equation to the Stokes-Fourier system in a bounded domain*, Commun. Pure Appl. Math. 56 (2003), pp. 1263–1293.
[55] G. Prodi, *Un teorema di unicità per le equazioni di Navier–Stokes*, Ann. Mat. Pura Appl. 48 (1959), pp. 173–182.
[56] J. Serrin, *On the interior regularity of weak solutions of the Navier–Stokes equations*, Arch. Rational Mech. Anal. 9 (1962), pp. 187–191.
[57] P. Germain, *Multipliers, paramultipliers, and weak-strong uniqueness for the Navier–Stokes equations*, J. Diff. Equations 226 (2006), pp. 373–428.
[58] O.A. Ladyzhenskaya, *The sixth millennium problem: Navier–Stokes equations, existence and smoothness*, (Russian) Uspekhi Mat. Nauk. 58(2) (2003), pp. 45–78; translation in Russian Math. Surveys 58(2) (2003), pp. 251–286.
[59] R. Temam, *Some developments on Navier–Stokes equations in the second half of the 20th century*, Development of Mathematics 1950–2000, Birkhauser, Basel, 2000, pp. 1049–1106.
[60] C. Cao and E.S. Titi, *Regularity criteria for the three-dimensional Navier–Stokes equations*, Indiana Univ. Math. J. 57 (2008), pp. 2643–2662.

[61] C. Cao and E.S. Titi, *Global regularity criterion for the* 3*D Navier–Stokes equations involving one entry of the velocity gradient tensor*, Arch. Rational Mech. Anal. 202 (2011), pp. 919–932.
[62] O.A. Ladyzhenskaya, *On unique solvability of three-dimensional Cauchy problem for the Navier–Stokes equations under the axial symmetry.* Zap. Nauchn. Sem. LOMI 7 (1968), pp. 155–177. (In Russian)
[63] A. Mahalov, E.S. Titi, and S. Leibovich, *Invariant helical subspaces for the Navier–Stokes equations*, Arch. Rat. Mech. Anal. 112 (1990), pp. 193–222.
[64] B. Ettinger and E.S. Titi, *Global existence and uniqueness of weak solutions of 3-D Euler equations with helical symmetry in the absence of vorticity stretching*, SIAM J. Math. Anal. 41(1) (2009), pp. 269–296.
[65] L. Caffarelli, R. Kohn, and L. Nirenberg, *Partial regularity of suitable weak solutions of the Navier–Stokes equations*, Commun. Pure Appl. Math. 35 (1982), pp. 771–831.
[66] G. Seregin and V. Sverák, *Navier–Stokes equations with lower bounds on the pressure*, Arch. Rational Mech. Anal. 163 (2002), pp. 65–86.
[67] J. Serrin, *The initial value problem for the Navier–Stokes equations,* in *Nonlinear Problems (Proc. Symp., Madison, WI)*, University of Wisconsin Press, Madison, WI, 1963, pp. 69–98.
[68] N. Masmoudi, *Remarks about the inviscid limit of the Navier–Stokes system*, Commun. Math. Phys. 270 (2007), pp. 777–788.
[69] J. Linshiz and E.S. Titi, *On the convergence rate of the Euler-α, inviscid second-grade fluid, model to the Euler equations*, J. Stat. Phys. 138(1) (2010), pp. 305–332.
[70] W. Wolibner, *Un théorème sur l'existence du mouvement plan d'un fluide parfait homogène incompressible, pendant un temps infiniment long*, Math. Z. 37(1) (1933), pp. 698–726.
[71] T. Kato, *Remarks on Zero Viscosity Limit for Nonstationary Navier–Stokes Flows With Boundary*, Seminar on Nonlinear Partial Differential Equations (Berkeley, Calif., 1983), Math. Sci. Res. Inst. Publ., Vol. 2, Springer, New York, 1984, pp. 85–98.
[72] X. Wang, *A Kato type theorem on zero viscosity limit of Navier–Stokes flows*, Indiana Univ. Math. J. 50 (2001), pp. 223–241.
[73] H. Beirão da Veiga and F. Crispo, *The 3-D inviscid limit result under slip boundary conditions. A negative answer*, J. Math. Fluid Mech. 14(1) (2012), pp. 55–59.
[74] H. Beirão da Veiga and F. Crispo, *A missed persistence property for the Euler equations and its effect on inviscid limits*, Nonlinearity 25 (2012), pp. 1661–1669.
[75] L. Wang, Lizhen, Z. Xin, and A. Zang, *Vanishing viscous limits for 3D Navier–Stokes equations with a Navier-slip boundary condition*, J. Math. Fluid Mech. 14(4) (2012), pp. 791–825.
[76] L. Prandtl, *Uber flussigkeits-bewegung bei sehr kleiner reibung*. In Actes du 3me Congrès international des Mathematiciens, Heidelberg, Teubner, Leipzig, 1904, pp. 484–491.
[77] X. Wang, *Examples of boundary layers associated with the incompressible Navier–Stokes equations*, Chin. Ann. Math. Ser. B 31(5) (2010), pp. 781–792.
[78] E. Grenier, *On the nonlinear instability of Euler and Prandtlequations*, Commun. Pure Appl. Math. 53(9) (2000), pp. 1067–1109.
[79] O. Oleinik, *On the mathematical theory of boundary layer for an unsteady flow of incompressible fluid*, J. Appl. Math. Mech. 30(5) (1966), pp. 952–974.
[80] W. E and B. Engquist, *Blowup of solutions of the unsteady Prandtl's equation*, Commun. Pure Appl. Math. 50(12) (1997), pp. 1287–1293.
[81] D. Gérard-Varet and E. Dormy, *On the ill-posedness of the Prandtl equation*, J. Amer. Math. Soc. 23 (2010), pp. 591–609.
[82] D. Gérard-Varet and T. Nguyen, *Remarks on the ill-posedeness of the Prandtl equation*, Asymptot. Anal. 77(1-2) (2012), pp. 71–88.
[83] A. Asano, *Zero-viscosity Limit of the Incompressible Navier–Stokes Equations*, Conference at the IVth Workshop on Mathematical Aspects of Fluid and Plasma dynamics, Kyoto, 1991.
[84] M. Sammartino and R. Caflisch, *Zero viscosity limit for analytic solutions, of the Navier–Stokes equation on a half-space. I-II*, Commun. Math. Phys. 192(2) (1998), pp. 433–461.
[85] M. Lombardo, M. Cannone, and M. Sammartino, *M. Well-posedness of the boundary layer equations*, SIAM J. Math. Anal. 35(4) (2003), pp. 987–1004.
[86] I. Kukavica and V. Vicol, *On the local existence of analytic solutions to the Prandtl boundary layer equations*, Commun. Math. Sci. 11(1) (2013), pp. 269–292.

Journal of Turbulence
Vol. 13, No. 47, 2012, 1–25

Taylor & Francis
Taylor & Francis Group

Cumulus clouds and convective boundary layers: a tropical perspective on two turbulent shear flows

Roddam Narasimha*

Jawaharlal Nehru Centre for Advanced Scientific Research, Bangalore, India

(*Received 22 June 2012; final version received 1 August 2012*)

This paper is a review prepared for the second Marseille Colloquium on the mechanics of turbulence, held in 2011, 50 years after the first. The review covers recent developments in our understanding of the large-scale dynamics of cumulus cloud flows and of the atmospheric boundary layer in the low-wind convective regime that is often encountered in the tropics. It has recently been shown that a variety of cumulus cloud forms and life cycles can be experimentally realized in the laboratory, with the transient diabatic plume taken as the flow model for a cumulus cloud. The plume is subjected to diabatic heating scaled to be dynamically similar to heat release from phase changes in clouds. The experiments are complemented by exact numerical solutions of the Navier–Stokes–Boussinesq equations for plumes with scaled off-source heating. The results show that the Taylor entrainment coefficient first increases with heating, reaches a positive maximum and then drops rapidly to zero or even negative values. This reduction in entrainment is a consequence of structural changes in the flow, smoothing out the convoluted boundaries in the non-diabatic plume, including the tongues engulfing the ambient flow. This is accompanied by a greater degree of mixedness in the core flow because of lower dilution by the ambient fluid. The cloud forms generated depend strongly on the history of the diabatic heating profile in the vertical direction. The striking effects of heating on the flow are attributable to the operation of the baroclinic torque due to the temperature field. The mean baroclinic torque is shown to peak around a quasi-cylindrical sheet situated midway between the axis of the flow and the edges. This torque is shear-enhancing and folds down the engulfment tongues. The increase in mixedness can be traced to an explosive growth in the enstrophy, triggered by a strong fluctuating baroclinic torque that acts as a source, especially at the higher wave numbers, thus enhancing the mixedness. In convective boundary layers field measurements show that, under conditions prevailing in the tropics, the eddy fluxes of momentum and energy do not follow the Monin–Obukhov similarity. Instead, the eddy momentum flux is found to be linear in the wind speed at low winds; and the eddy heat flux is, to a first approximation, governed by free convection laws, with wind acting as a small perturbation on a regime of free convection. A new boundary layer code, based on heat flux scaling rather than wall-stress scaling, shows promising improvements in predictive skills of a general circulation model.

Keywords: cloud fluid dynamics; laboratory simulation of cumulus clouds; transient non-diabatic plume; entrainment; baroclinic torque; low-wind convective boundary layers

*Email: roddam@caos.iisc.ernet.in

ISSN: 1468-5248 online only
© 2012 Taylor & Francis
http://dx.doi.org/10.1080/14685248.2012.718782
http://www.tandfonline.com

1. Introduction

This paper is based on a review presented at the 50th anniversary of a landmark event in the history of turbulence research: namely the organization of an international colloquium on the 'Mechanics of Turbulence' held during August/September 1961 at Marseille, France. A week later (4–9 September 1961), a second international symposium was also held at Marseille, this time on 'Fundamental Problems in Turbulence and their Relation to Geophysics'. The proceedings of the Mechanics symposium are available in book form [1], and of the Geophysics symposium as a special issue of the *Journal of Geophysical Research* (JGR) [2]. In 2011, there was no separate meeting on turbulence in geophysics; instead, one session in the Mechanics meeting was devoted to the subject. Incidentally, such a session was most appropriate, because some of the pioneering studies in turbulence were often inspired by the atmosphere and the oceans. There is, for example, the celebrated paper by G.I. Taylor on eddy motions in the atmosphere [3], which explored for the first time fundamental mechanistic ideas about the structure of turbulent shear flows, such as the relation between the vorticity flux and Reynolds stresses in 2D flow. L.F. Richardson's famous jingle describing the cascade process appears in his prescient book on numerical weather prediction [4]. His well-known 4/3 power law for the relation between the effective diffusivity in particle dispersion and inter-particle separation [5] was the first such general assertion in turbulence, and perhaps an intuitive precursor of Kolmogorov-type arguments. Richardson was also responsible for the number named after him, an indispensable parameter in stratified turbulent shear flows.

In his editorial introduction to the JGR issue, François Frenkiel noted that the 'outstanding feature of atmospheric turbulence appears to be its control by the vertical gradient of density', and listed the major problems as turbulence in stratified flows, the effect of the earth's rotation, interaction between turbulence and wave motion, and turbulent transport. During the last 50 years, extensive studies have been made on these problems. This review will however be on a subject that attracted only two papers in the 1962 JGR special issue, namely what was then called 'thermal turbulence'. This field has grown enormously in the last few decades, especially if we expand it to include convection and clouds. Part of the reason for the growth is the recognition of the key role that clouds play in climate change science and in tropical circulations. According to one estimate [6], a 5% increase in short-wave cloud forcing would be enough to compensate for the increase in greenhouse gases during the entire 250-year period between 1750 and 2000. The 2007 Assessment Report of IPCC [7] declared that cloud processes remained among the greatest uncertainties in climate modelling. But, of course, beyond all this, clouds have fascinated and enchanted man for millennia. The desire to understand and interpret the free display of messages painted on the sky for public gaze by moist air has held an irresistible attraction to many scientists as much as to poets and painters for a long time; what is new is that those messages have taken on great urgency.

2. The tropics

Is the title of the paper justified in claiming to present a 'tropical perspective'? The tropics are so named because of the Tropics of Cancer and Capricorn, at $\pm 23.5^\circ$ latitude. A definition based on features specific to tropical climatology suggests meandering boundaries in the belt $\pm$ 20°–30° straddling the equator [8]. Within these boundaries is an area that covers about half the global land surface, receives about two-thirds of global precipitation and is home to about 45% of the world's population. Net radiation (solar – terrestrial) received

at the top of the atmosphere shows an excess of 60–70 W/m^2 (incoming – outgoing) near the equator, and a deficit of order 100 W/m^2 near the poles [8, 9]. This tropical surplus is exported poleward by the atmospheric and (to a lesser extent) oceanic circulations: without this energy transport, which is part of the machinery of the atmosphere–ocean heat engine, the equator–pole temperature difference would have risen to 100°C from the current 40°C [10]. So atmosphere–ocean circulations in the tropics or originating therefrom are of global significance from many points of view.

The most important dynamical difference between the tropics and the higher latitudes is the dominant role of convection in the tropics. The normal component of the Coriolis force, which is such a major player at higher latitudes, vanishes at the equator, but this, of course, does not mean that it is not important in the tropics, because the tropics cover a latitude band that is nearly a third of the total.

There are other factors that distinguish the tropics, apart from convection-dominated dynamics; thus, wind speeds are relatively low, many regional atmospheric circulations switch during the year, and summers are wet and winters dry in the northern hemisphere (and vice versa in the southern hemisphere); within the wet season, there are quasi-cyclic fluctuations with periods of the order of 30–40 days (conspicuous as propagating cloud bands in the Indian monsoons, [11]). As Charney and Shukla suggested long ago [12], these and other considerations suggest that predictability should be inherently higher in the tropics. But it has not been possible to translate that potential predictability into an actual improvement in predictive skill, and empirical prediction methods, with all their flaws, are to this day at least competitive with dynamical ones [13]. Clearly, there are deep fundamental problems with current general circulation models, moist convection being one of the most significant ones.

Our purpose here is to present a review of two basic problems that underlie these special characteristics of the tropical atmosphere. The first is cumulus cloud flow, which is the basic ‘molecule’ of moist convection in the tropics. The second is low-wind convective boundary layers, with particular reference to some new scaling arguments. Both are considered chiefly from a fluid dynamics rather than a meteorological point of view.

3. Cumulus clouds

> Shall we compare you to a laminar flow?
> You are more lovely and more sinuous.
> Rough winter winds shake branches free of snow,
> And summer’s plumes churn up in cumulus.
>
> (Stanley Corrsin 1984, on Hans Liepmann’s 70th birthday)

3.1. *Introduction*

No two clouds are identical, but it is possible to classify all clouds into a finite number of characteristic forms, following a binary system of Latin words devised by Luke Howard in 1802. For example, the familiar genus called cumulus is defined as ‘detached clouds, generally dense and with sharp outlines, developing vertically in the form of rising mounds, domes or towers, of which the bulging upper parts often resemble a cauliflower . . .’ [14]. There are four cumulus species: cu. humilis, cu. mediocris, cu. congestus and cu. fractus. During its life cycle, the genus or species of a cloud may change: we shall see an example later. In the tropical convective regimes that play a key role in climate change and monsoon circulations, the cumulus cloud is a major actor. It can rise all the way to the tropopause

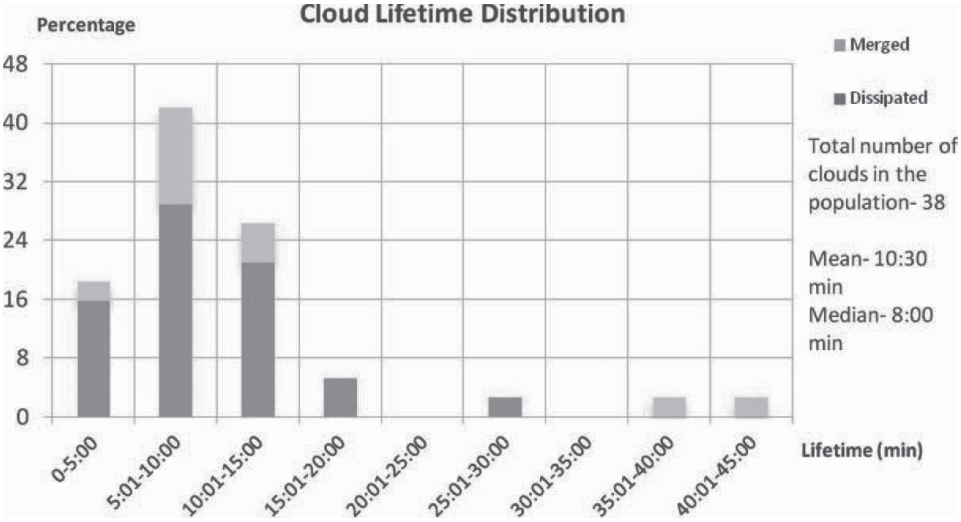


Figure 1. Distribution of cloud life times, as estimated from the time-lapse cloud movies on the Arizona State University website [16].

(about 15 km over the equator) and even beyond: images from the joint US–Japanese satellite TRMM show cloud towers touching 20 km or more in Hurricane Katrina, which hit the Gulf of Mexico and the regions around it in 2005. Such towers are efficient conveyors of heat over the whole vertical extent of the atmosphere. At the other end of the height range are short fluffy piles or heaps of fleece. Among all the numerous cloud types that are described in the World Meterological Organization *International Cloud Atlas* (WMO 1995 [14]), the cumulus cloud is a *flow* cloud par excellence (vertical velocities can be of order 1–5 m/s). With slight modification of a regal metaphor proposed by Herbert Riehl [15], we can call the cumulus cloud the queen of the tropical sky.

In general, cumulus clouds evolve on time scales of the order of minutes to an hour (although large-scale convective systems could have a life of the order of a day). Figure 1 shows the distribution of life time of cumulus clouds from time-lapse movies taken during the morning hours in Arizona [16]: the median is of order 10 min. A typical eddy turnover time for clouds with effective diameter 10^2–10^3 m would be in the range of tens of seconds to tens of minutes; time of ascent in a rising cloud would be an order of magnitude larger, say O (10^2–10^3 s). Clearly, therefore, a typical cumulus cloud is rarely in a steady state, and is best seen as a transient flow.

Research in cloud flows has been hampered because it has had to depend till now almost exclusively on field studies (often using various types of radar and aircraft) and modelling. As each cloud is unique, it is difficult to obtain enough field data to define robust statistics. Furthermore, clouds occur sporadically in space and intermittently in time, making systematic field studies difficult and expensive. No effective laboratory studies have been possible either, because there is no technique or apparatus yet that can handle all the major complexities of a cloud [17] – from the microphysics of condensation to what we shall call the macrodynamics of the large-scale turbulence structure of cloud flows. A collection of studies in a recent survey [18, 19] contains a table (Lohmann and Schwartz [19], pp. 531–555) that is chastening: of 15 entries in the list of problem areas in clouds, scientific understanding is rated ‘very low’ in as many as 12. The fact is that cumulus clouds are

complex, multi-phase, phase-transitioning free turbulent shear flows, often interacting with radiation also in complex ways, and remain to this day a great fluid dynamics challenge (greater than that of turbulence, according to Emanuel [20]).

Of these problems, a major one concerns the entrainment characteristics of a cumulus cloud, because these determine its interaction with the rest of the atmosphere: we can think of entrainment as having the same central scientific position in cloud fluid dynamics that, for example, the skin friction does in the study of turbulent boundary layers.

3.2. *Early models*

The history of cloud dynamics studies has been marked by much debate and controversy, especially on the issue of entrainment. The issue was first raised by Stommel in 1947 [21], with his proposal that an ascending current in the cloud entrains dry air laterally from its surroundings. Over the years, several investigations seemed to support this proposal, but beginning with Warner [22] there was the alternative proposal that it was entrainment from the cloud top that was important – not from the sides. The different observational data and the inferences drawn from them have been summarized in a brief historical review by Reuter [23]. In parallel, there were various proposals for the fluid-dynamical model that best describes cloud flow. Among the first of these was one by Scorer and Ludlam [24], according to which a cumulus cloud resembles a thermal or a bubble, that is, the flow due to an instantaneous point source of buoyancy. Turner [25, 26] made various investigations and proposed different models ranging from the thermal just mentioned and a Hill's spherical vortex, through vertical jets mixing laterally with the surroundings, to (finally) a starting plume. For a steady self-similar plume (as it is called in the meteorological literature; equivalent to 'self-preserving' in Townsend's terminology [27], often also called 'equilibrium' in the fluid dynamics literature), certain general ideas in turbulent shear flows suggest a lateral entrainment velocity proportional to a characteristic velocity (e.g. the centerline value) of the plume. This idea, an extension of a hypothesis used by G.I. Taylor in 1945 [28] (at that time investigating nuclear explosions), was proposed by Morton et al. [29]. But in the end, none of these proposals has given satisfactory results, and in fact, the similarity plume idea was abandoned in the 1970s because of contradictions with observations. Fluid-dynamical investigations have till recently been unable to identify what may be called a canonical cumulus flow, that is, one which retains only the most essential physics that gives the problem its distinguishing character, and maximally idealizes the rest.

The first attempts to simulate clouds were basically thermostatic in nature: there was no flow, but adiabatic cooling of moist air produced liquid water droplets constituting the cloud. A more recent account of such efforts is the cloud box or fog chamber of Mossop [30]. Early work on possible models for cloud *flows* was pioneered by Scorer, Turner and others. These have been reviewed by Simpson [31] and Houze [32]. In an interesting experiment in which chemical reactions were used to produce a large number of small gas bubbles whose total volume increases with time (thus enhancing buoyancy), Turner [33] studied the flow resulting from an instantaneous point source of buoyancy. However, his experiments revealed an accelerating cloud whose width (like that of the self-preserving plume) grew linearly with height – something that is rare in a cumulus cloud for which the normal shapes are either piles or towers. Shy and Breidenthal [34] studied the stability of strato-cumulus clouds by simulating evaporative cooling. Johari [35] presented interesting flow visualizations relevant to break-away clouds. None of these however was close enough to natural cumulus clouds.

3.3. *The transient diabatic plume as a canonical cumulus flow*

At Jawaharlal Nehru Centre (JNC) and Indian Institute of Science (IISc) at Bangalore, India, we have since the 1990s been pursuing the idea that a cumulus cloud flow should be seen as belonging to a new class of turbulent free shear flows. It is instructive to ask ourselves first in what way a cloud flow will be different from the free turbulent flows that Liepmann [36] reviewed at Marseille 50 years ago. He starts with the thought that 'an inviscid incompressible fluid, initially irrotational and in a field of conservative forces, will remain irrotational except for surfaces of concentrated vorticity'. Now, the simplest approximation applicable to a cloud flow is perhaps the Boussinesq assumption. This postulates (1) density differences in the fluid so small that div **u** nearly vanishes and the inertial terms retain the constant-density form and (2) buoyancy body force is comparable to inertia force, because fluid accelerations are small compared with the acceleration due to gravity. It turns out that while the buoyancy force is conservative in this case because it is gravitational, a substantial baroclinic torque can be exerted on the flow because of appreciable horizontal gradients in density coupled with a nearly vertical pressure gradient. We may therefore expect a baroclinic source of vorticity in a Boussinesq cloud flow.

To make these considerations more concrete, let us consider plumes briefly, as some special kind of plume seems like a natural choice for a fluid dynamical model of cloud flow. Turner [26] defines a plume as a convective free shear flow 'produced under gravity by a density contrast between the source fluid and its environment', 'the velocity and density fields [being] interdependent'. With respect to clouds, the source fluid would be the same as the ambient, rising convectively over a warm patch of some finite size on an impenetrable surface (solid or fluid). It may be generated in the laboratory in many different ways: for example, by using fluids of different densities, by introducing or creating a suitable hot patch on the surface or by allowing warmed fluid of lower density below the impermeable surface to ooze up into cooler fluid through an orifice in the surface.

We consider a round turbulent plume rising along the vertical z-axis in a surrounding medium of constant density ρ_o. Its (kinematic) buoyancy flux is defined as

$$F = 2\pi \int_0^\infty wg[(\rho - \rho_o)/\rho_o]r\,dr, \tag{1}$$

where w is the velocity along the z-axis, ρ the density in the plume, ρ_o a reference density in the ambient, g the acceleration due to gravity and r the radial distance from the centre of the plume at the source.

The quantity $\rho_o F$ is the weight deficiency flux of the plume (unit: force/time) and is invariant in z. If ν is the kinematic viscosity of the fluid (assumed constant), the flow has an intrinsic length scale $F_0^{2/5} g^{-3/5}$ and time scale $F_0^{1/5} g^{-4/5}$. Hence, the plume has an 'intrinsic' Reynolds number:

$$\mathrm{Re}^* = F_0^{1/5} g^{-2/5} \nu^{-1}. \tag{2}$$

For a plume of cloud-like dimensions (w = O [1 m/s], diameter $\sim 10^2$–10^3m), $\rho_o F \sim 10^5$–10^6 N/s and R^* is of order 10^7–10^8. In laboratory experiments of the kind we have been conducting with water as working fluid, with a diameter of order 10 cm and velocities of order 10 cm/s, $\rho_o F \sim 10^3$–10^4 N/s, $Re^* = \mathrm{O}(10^2$–$10^3)$ – still far from a natural cloud. (However, a tripling of the linear dimension of the water tank we have built will generate

plumes whose force rate would be comparable to that of a small cloud.) If Reynolds numbers are sufficiently large, the viscosity is anyway asymptotically irrelevant in large-scale flow development; and this principle leads to a far-field self-preserving solution depending only on F_0,

$$b(z) \sim z,\ w_c(z) \sim F_0^{1/3} z^{-1/3}, \tag{3}$$

respectively for the width and the centreline velocity of the plume.

Under conditions described above, the flow may be assumed to be governed by the Boussinesq equation. (In the natural cloud of moist air, this is a useful impressionistic model for a single-phase cloud fluid in a neutrally stratified medium, as will be argued elsewhere [37].) We shall write the governing equations for the simulation – whether in the laboratory or on the computer – assuming the Boussinesq approximations to be valid, but with a prescribed heat release function (Basu and Narasimha [38], BaN henceforth). The resulting 'diabatic Boussinesq' model is

$$\nabla.\mathbf{u} = 0, \quad \text{(mass)}, \tag{4}$$

$$\frac{\partial \mathbf{u}}{\partial t} + (\mathbf{u}.\nabla)\mathbf{u} = \frac{1}{\rho_o}\nabla p + \nu\nabla^2\mathbf{u} - \mathbf{g}\beta T \quad \text{(momentum)}, \tag{5}$$

$$\frac{\partial T}{\partial t} + (\mathbf{u}.\nabla)T = \kappa\nabla^2 T + \frac{J}{\rho_0 c_p} \quad \text{(energy)}, \tag{6}$$

where $\mathbf{u}$ is fluid velocity, p is pressure, T the excess temperature over the ambient reference T_o, β the coefficient of thermal expansion (defined by $\rho - \rho_\mathrm{o} = -\rho_\mathrm{o}\beta\ T$), J the amount of heat released into the flow per unit volume (in general a function of both space and time) and κ the thermal diffusivity. If the above equations are used for describing the situation in the atmosphere, ρ and T would have to be taken as potential density and temperature, respectively; some other conditions will also apply (see Turner [26] for a discussion).

By taking the curl of (5), we have the vorticity equation:

$$\frac{\partial \boldsymbol{\omega}}{\partial t} + (\mathbf{u}.\nabla\boldsymbol{\omega}) - (\boldsymbol{\omega}.\nabla)\mathbf{u} - \nu\nabla^2\boldsymbol{\omega} = \beta\mathbf{g} \times \nabla T \quad \text{(vorticity)}. \tag{7}$$

These considerations have become particularly relevant because it has recently been shown (Narasimha et al. 2011 [39], N++ henceforth) that it is possible to create lab-scale flows that reproduce a variety of naturally occurring cumulus cloud forms, and even track their complete life cycles. The flow model underlying these simulations is a transient plume with volumetric diabatic heating scaled dynamically to simulate latent heat release from phase changes in clouds. The apparatus used for this purpose is based on earlier studies (Bhat & Narasimha [40], BhN henceforth) on steady jet and plume flows with injection of volumetric heating. The principle of the technique is to use a jet or plume of electrically conducting ('active') fluid that issues vertically upward in a tank, of size 1 m square $\times$ 1.5 m height, containing an ambient fluid that is highly resistive deionized water. A set of electrodes placed at different heights across the flow permits application of voltages on the electrically conducting fluid as it rises through the electrodes, the distribution of heating in the vertical being obtained by solving an appropriate fluid-electrical circuit using Kirchoff's

laws. It was found that the flow is governed by a non-dimensional bulk heat release number

$$G = \frac{Q}{b_b U_b^3} \frac{g\beta}{\rho_o C_p}, \tag{8}$$

where C_p is specific heat at constant pressure, Q the total off-source volumetric heat put into the flow, and b_b and U_b are, respectively, characteristic length and velocity scales, for example, at condensation level in the cloud or the beginning of heat generation in the apparatus. In the atmospheric cloud Q is O (1 W/m^3) [41] and $G = 0.1$–2 [42]. The same range of values of G can be obtained in water subjected to a heating rate of order 4 MW/m^3, which over a volume of order 250 cm^3 is a manageable 1–2 kW.

A new version of this apparatus has now been built at JNC with additional capabilities that include: (1) temporal variation of the total heating as well as its profile in the vertical through manual active control, (2) introduction of lower- and upper-level stratifications to simulate inversions capping the atmospheric boundary layer and/or occurring near the tropopause, (3) controlling plume/jet flow history in time and (4) continuous monitoring and recording of flow development in time. The initial jet velocity is only controlled in an on/off mode. Flow Reynolds number can be varied over the range 1×10^3 to 3×10^3.

Using these new capabilities, it is possible to investigate unsteady or transient flows, and demonstrate thereby how a variety of observed natural cumulus cloud genera and species (in the WMO 1995 [14] terminology) can be reproduced. These include: cu. congestus, cu. mediocris and cu. fractus, alto-/strato-cumulus cumulogenitus, and break-away clouds. Furthermore, the *evolution* of cumulus cloud flows can be tracked in time. Examples are shown in Figure 2 (more will be found in [39]). The remarkable similarity between natural clouds and simulated cloud flows suggests that a strong candidate for the canonical cumulus flow is what we have called a *transient diabatic plume*. The convective plume that seems a natural model for cloud flow has to be in addition *transient* (see Figure 1) and *diabatic* in the sense that heat is released into the flow above a certain height that corresponds to the condensation level in a natural cloud. The distribution of heat injected along the vertical and its variation in time have a strong influence on the evolution of the cloud flow, and determine the nature and type of cloud flow generated. These appear to be the essential elements that govern cumulus macrodynamics.

3.4. *Steady diabatic plumes and jets*

While waiting for accurate measurements in transient flows (Vybhav et al. 2012 [43] presents some preliminary results), it is of value to examine the experimental and computational data that have already been acquired on steady diabatic plumes and jets, because they can offer some unique insights into entrainment in diabatic flows, including cumulus clouds. The first set of such experiments [40, 42], respectively on steady jets and plumes subjected to off-source heating have been followed by two other studies, respectively in Delaware (Agarwal and Prasad [44] and Agarwal et al. [45]) and Florida (Venkatakrishnan et al. [46]). In all these experiments, the entrainment has been directly measured using laser Doppler or particle imaging velocimetry.

The major results from the experiments are collected in Figure 3. It first shows a PLIF (planar laser-induced fluorescence) image of a steady diabatic plume [47]. It will be seen that the effect of heat release on the internal structure of the turbulent flow is dramatic. The classical (nondiabatic) plume below the heat release zone (HRZ) shows the usual ‘tongues’ that protrude *from* the core flow, as well as the deep incursions of ambient fluid *into* it (in fact,

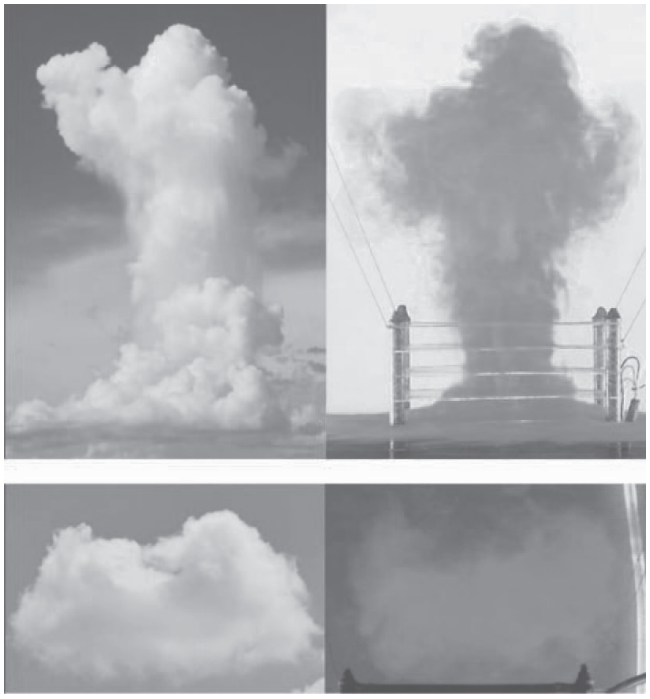


Figure 2. Two matched pairs of natural clouds (left) and laboratory simulations (right). Top: convective tower capped by a bulbous cloud top of the cumulus congestus type. (Natural cloud from http://img.photobucket.com/albums/v493/scubastza/Blog%20Stuff/cloud.jpg). (Image of natural cloud from NOAA Research, courtesy of Jim W Lee, National Weather Service) Lower panel: Natural cloud and a laboratory simulation of a cumulus mediocris, possibly changing into a cumulus fractus with frayed edges.

one can even see a rare 'hole' of ambient fluid across this flow). However, the diabatic flow in and beyond HRZ takes on a different character: its boundaries are no longer as convoluted as in the non-diabatic flow, and there are few or no patches of ambient fluid within the core flow. Figure 3a shows the variation of the reciprocal of the centreline velocity with height. In the self-preserving non-diabatic jet, this increases linearly with downstream distance, as confirmed by data for the unheated jet in the figure. Except in a short region just above the lowest level at which heat is released, heating reduces the decay rate in the centreline velocity; as G increases, the decay is first arrested and then even reversed: the centreline velocity eventually increases with height, that is, the flow accelerates. Concurrently, as Figure 3b shows, the jet width that increases linearly with height in non-diabatic flow tends to remain constant or even thin down as more heat is released. (Preceding this trend, in the 'exceptional' region mentioned above, there is a slight increase in jet width just above the first station of heat release.) The extent of this reduction ($\triangle b$) increases with the amount of heat release; interestingly, the fractional change in jet width is proportional to the square root of G, as shown in Figure 3c. This confirms the important role that the parameter G plays in determining flow development.

Figures 3d and 3e show the effect of heating on the longitudinal turbulent intensity (root mean square [rms] value) $\hat{u}_c$ at the centreline. (Note: There is a change in notation at this point, as the velocity component along the main flow is denoted by u in this section

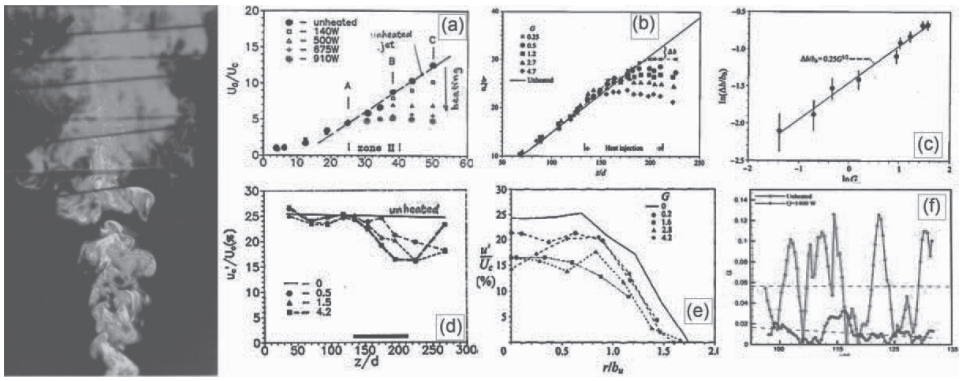


Figure 3. A collage of diagrams summarizing the most striking features of steady diabatic plumes and jets. (Photograph on left) PLIF image of diabatic plume [47], showing the dramatic change in the turbulent structure of the plume almost immediately after the beginning of the heat release slightly above the halfway mark in the photograph. Note the hole in the non-diabatic plume a little below the halfway mark. The picture suggests a 'mixedness transition' due to volumetric heat release. (a) Variation of the reciprocal of the centerline velocity with height at different amounts of heat release (BhN). (b) Streamwise variation of scalar jet width at different values of the heat release parameter G (BhN). (c) The reduction in width shown in (b), as a function of G, increasing like $G^{1/2}$ (BhN). (d) Normalized value of the streamwise turbulence intensity at the centerline (BhN). (e) Radial variation of the normalized streamwise turbulence intensity at $z/d = 225$ at different values of G (BhN). (f) Spatial variation of the entrainment coefficient with and without diabatic heating [46]. Left: Reproduced with permission from [47]. (a)-(e): Reproduced with permission from [40]. (f): Reproduced with permission from [46].

henceforth, instead of w as in previous sections.) Towards the top of HRZ, the normalized intensity $\hat{u}_c/U_c$ at the centreline decreases from about 25% at the beginning to about 17% towards the end of HRZ. There is some evidence that $\hat{u}_c/U_c$ is relaxing towards its value in the unheated jet beyond the end of HRZ. Figure 3e shows the radial distribution of the normalized turbulent intensity at $z/d = 225$ just above the end of HRZ. The variation along the centreline is consistent with the data in Figure 3d; in all cases, the turbulent zone is narrower than in the unheated flow. Interestingly, it appears as if the maximum intensity at the highest value of G ($= 4.2$) occurs at a radius of around 0.75 times the velocity thickness b_u of the jet, defined as the radius to $e^{-1}U_c$.

It is interesting that some of these changes are qualitatively similar to those observed in a boundary layer subjected to a highly favourable pressure gradient. In relaminarizing flow, for example, we know that the boundary layer thins down with streamwise distance and normalized turbulent intensity falls [48]. The flow changes in Figure 3a are comparable to those in the studies of Falco on accelerating turbulent boundary layers (see Van Dyke [49], p. 96). The analogy to accelerating flows was noted by BhN, and the effect of acceleration on the flow dynamics has been discussed by Breidenthal [50].

Finally, we look at entrainment. Now, many different definitions of entrainment rate have been reported in the cloud dynamics literature [29, 51, 52]. For our purposes, the most relevant is the 'entrainment coefficient' α_E, introduced through the following equation [29]:

$$(dm/dz) = \alpha_E(2\pi\rho_o b U_c), \tag{9}$$

where $m(z)$ is the total vertical mass flow rate at z.

Figure 3f shows the measured entrainment coefficient in the experiments of Venkatakrishnan et al. [46]. The measurements were confined to the region above HRZ and, following an implied proposal of Turner [25], α_{E} in (9) was evaluated as the product of the (inward) normal velocity V at radius b and the circumference $2\pi b$, taking b as the radius, where $u = U_{\mathrm{c}}/e$. Although this procedure can be questioned, the results are striking, and two things stand out in the data. First, there are large fluctuations in the local values of the entrainment coefficient over downstream distance. This is consistent with entrainment being associated with coherent structures or (in the presence of heat release) their remnants. An average line drawn through these large fluctuations is however in good agreement with the equilibrium value quoted for α_{E} by Turner [25]. In the diabatic jet, however, both the mean value and the fluctuations are dramatically lower, showing that there are large departures from the equilibrium values associated with jet flow. In both cases, the fluctuations in α_{E} are comparable to the respective mean values (so one should be cautious in estimating α_{E} from short-time or -distance measurements).

Figure 4, replotted with a different orientation from a summary diagram in N++ (2011) [39], shows the vertical variation of α_{E} measured in three different laboratories [40, 44, 46, 53], all using apparatus similar to that originally developed by BhN. A detailed comparative analysis of the results from the different experiments is presented by Diwan et al. [54]. Four [40, 46, 53] of the five datasets shown are in broad agreement with each other. They show a mild increasing trend above the cloud-base level (z_b) and reach a maximum; this is followed by a relatively steep decline, often to nearly zero, in the upper HRZ and/or beyond. Observations in natural clouds [55–57] show a broadly similar behaviour. The fifth dataset [44] shows α_{E} rising first to a very high value in the lower HRZ, later falling to zero or even negative values in the middle, and rising once again towards the end. The precise

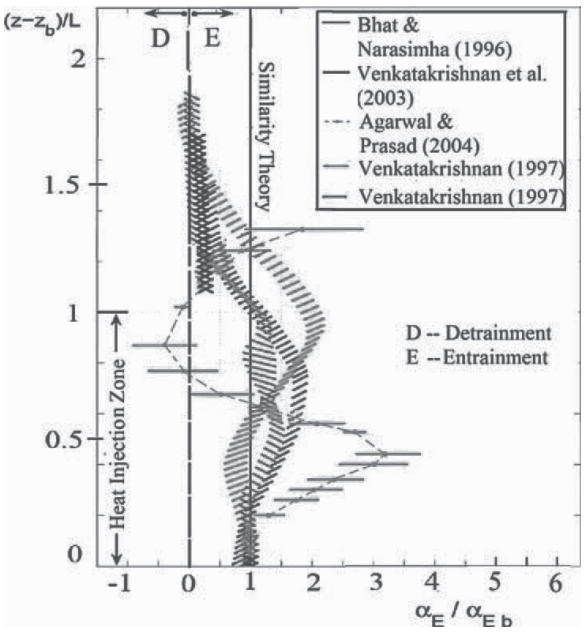


Figure 4. Experimental data available to date on a normalized entrainment coefficient in diabatic jets and plumes. *Sources*: Bhat and Narasimha [40], Venkatakrishnan et al. [46], Agarwal and Prasad [44] and Venkatakrishnan [53]. Based on [39].

reasons for this behaviour are not known, but Diwan et al. point out that they may lie in the excessive turbulence levels found at the base of HRZ in these experiments, and a much shorter HRZ than in the other experiments, with only one or two coherent structures in the zone, leading to large fluctuations in local values of α_E [54, 58].

The early rise in α_E is perhaps not unexpected, but the following decline to little or no entrainment appears counter-intuitive. The evidence from both laboratory and computer simulations however do suggest a plausible explanation in terms of the dynamics of coherent structures (BhN, BaN). Coherent structures have been shown [59, 60] to be responsible for inducing the motion of ambient fluid into the flow through an engulfment process. This is followed by a stirring or mingling phase where fluid is drawn into the core of the flow in a way that results in large increases in the interface area between ambient fluid and core fluid. These two processes culminate in mixing at the molecular level. If the coherent structures are distorted or disrupted, as the evidence suggests they are in diabatic flows, the very first engulfment stage is weakened or suppressed, and the entrainment decreases. Furthermore, a 'protected core' of undiluted fluid develops in the flow as a consequence of the significant drop in entrainment [61–63]. The same mechanism can account for the occurrence of tall, nearly cylindrical towers in tropical convection [15].

The diabatic plume model thus suggests plausible scenarios for the many puzzling phenomena that are exhibited by cumulus cloud growth and evolution.

Steady-flow simulations, of the kind described above, may be directly relevant to certain types of relatively more long-lived tropical deep convection, such as those that occur with large-scale convective systems. Numerical solutions of a fully compressible cloud-resolving large-eddy simulation (LES) model for steady-state moist convection have recently been reported by Romps and Kuang [64]. A major output of this work is a dilution-related variable termed 'purity', computed as an average over a statistically steady, homogeneous state attained during an integration over a 25 km $\times$ 25 km area for a duration of 24 h. Purity is estimated by tracking tagged passive 'purity' tracers released at cloud base and computing their concentration at any level in suitably thresholded 'cloudy parcels'. A measure of purity is then defined as a flux-weighted time average in such a way that it has a value of unity at cloud base and declines due to mixing with ambient as fluid rises through the cloud. Although this 'purity' index has not been directly measured yet in the laboratory, a related entrainment-dependent measure defined as 'diabatic purity' (N++ 2011), [39] may be estimated. Comparisons between laboratory results and the computer simulations show that they are very similar, provided the height at which condensation is complete in the atmosphere, as indicated by the presence of a knee in the computed purity curve, is replaced in the laboratory simulations by the height at the top end of HRZ; experiment and simulation are then in surprisingly good agreement (N++ 2011), [39]. This suggests that the purity computed by Romps and Kuang is fairly directly related to the entrainment of ambient fluid into the cloud flow.

3.5. *Computer simulations*

The situation studied in the laboratory, with heat injection from an external source acting as a proxy for latent heat release, has been simulated on the computer using the Boussinesq assumptions by BaN. They solved a temporal analogue of the spatial problem investigated in the laboratory, and presented results on the time evolution of a cylindrical mixing layer in a computational box periodic in all three directions. In the temporal simulation, heat is added over a certain duration that corresponds to the length of the heat injection zone in the experiments.

Computer simulations of spatially developing flows have been reported by Agarwal et al. [44]. They introduced an additional equation governing a scalar concentration C (e.g. of the acid in the active fluid of the experiment). The coupled system is then solved to obtain flow variables. The flow parameters in these experiments have a bulk Richardson number of 12, which is about 40 times higher than in their own or the other experiments. Furthermore, the Prandtl and Schmidt numbers are different in the simulation and experiments, so a direct comparison is difficult [54, 58].

An interesting simulation of conditionally unstable moist convection has recently been reported by Pauluis and Schumacher [65]. They investigate the Rayleigh-Bènard problem with a simple thermodynamics model for phase transitions. In contrast to the solutions of the classical problem, the convection they obtain is highly asymmetric with respect to the vertical direction. The simulations are carried out at a moist convection Rayleigh number of 3.73×10^5. Solutions presented are those of the Navier–Stokes–Boussinesq equations. The results show that self-sustained conditionally unstable convection is possible and exhibit a self-aggragation into clouds. This constitutes an important first step in handling moist convection instability.

We focus here on the BaN results, for this is still the only source yet for any data on the vorticity fields. In these simulations, the heat release takes place over $t = 25$–32 (in flow units based on velocity and diameter at $t = 0$.) The results are summarized in Figure 5. Figure 5a shows the jet in the periodic box; as Equation 7 shows the baroclinic torque is given by $\beta\ \mathbf{g} \times \text{grad}\ T$, which depends only on the horizontal gradient of the temperature since the direction of $\mathbf{g}$ is vertical. Furthermore, because of the axisymmetry in the mean flow, $\partial\overline{T}/\partial\varphi = 0$ and the mean torque has only an azimuthal component proportional to $\partial\overline{T}/\partial r$, which acts in the direction shown in Figure 5a for a warm flow into a cooler ambient (BaN): the torque is seen to be shear-enhancing. To the extent that the temperature has a fluctuating component T', the baroclinic torque will also experience similar fluctuations, proportional to $\nabla T'$.

As the other diagrams in Figure 5 show, the effect of the baroclinic torque can be dramatic. In Figure 5, the contours of the azimuthal vorticity in the heated and unheated cases are compared. In the unheated case (Figure 5b), a coherent structure can be clearly seen: it is approximately conical over a toroidal ring at the bottom, with the vorticity more or less concentrated in a conical sheath above the ring. There is little vorticity in the middle of the structure. In the heated case (Figure 5c), the vorticity levels are huge compared with those in the unheated case. The neat structure of Figure 5b has been replaced by a much more disordered distribution: one may barely discern here a distorted version of a structure penetrating into the next similarly distorted structure that is its downstream neighbour. Vorticity of both signs (red and blue) can now be seen, with the blue predominating in the middle. The spread of vorticity laterally does not show either the large axial variation in width or the convoluted boundaries that are characteristic of the unheated jet. The azimuthal vorticity distributions are accompanied by similar distributions of vorticity in the radial and axial directions as well (not explicitly shown here).

Figure 5d shows the distribution of axial vorticity in diametral planes across the flow – unheated in the upper row and heated in the lower row. The images in each row correspond to the narrowest and broadest sections of the instantaneous flow in the computational domain. Interestingly, the vorticity in the heated case is once again intense, but what is more occurs in streamwise pairs or loops that are such that the induced velocities are often expulsive. Srinivas et al. [66] proposed that such streamwise vorticity may arise from the vortex rings that form in the various stages of flow development, through the Widnall instability that introduces an axial component into the vorticity field sustained by counter-rotating pairs.

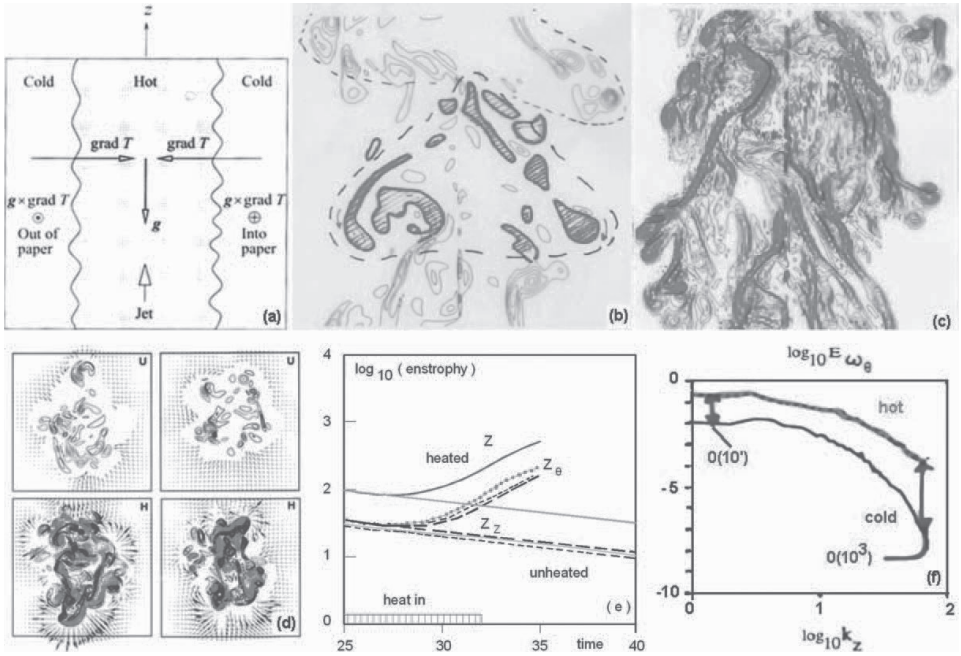


Figure 5. A collage of diagrams summarizing the most striking features of direct numerical solutions of the Navier–Stokes–Boussinesq equations. All data used in the diagrams are from the solutions carried out for BaN [38], but parts of (b), (c) and (d) were not published in [38]. Flow parameters: Re = 1600, Prandtl number Pr = 7, heat release number $G^* = 0.04$. (For definition of G^*, see BaN38, p. 203.) Solutions at $t = 35$, heat injection from $t = 25$ to 32. Vorticity contours at intervals of 0.5; dashed lines negative, solid lines positive. (a) Schematic of temporal flow problem solved, showing directions of gravity, mean temperature gradient and the mean baroclinic torque acting in the azimuthal direction. (b) Azimuthal vorticity contours in an axial section of the non-diabatic jet, showing a coherent structure (situated within the dashed closed curve). Contours start from –0.5. (c) Axial section through a diabatic jet with all other parameters being the same as in (b). (d) Diametral cross-sections showing streamwise vorticity in unheated (top row) and heated (bottom row) jets. (Left) Narrowest cross-section; (right) widest cross-section of flow. (e) Comparison of the evolution of enstrophy in heated (bold lines) and unheated (light lines) jets. (f) Computed spectra of the azimuthal component of the enstrophy for unheated (full line) and heated (dashed line) jets. (a), (e), (f): Reproduced with permission from [38]; (b), (c), (d): Based on work done and reported in [38].

(A similar instability was first noted in wavelet transforms of PLIF imagery by Narasimha et al. [67].) The existence of such counter-rotating vortex pairs has recently been confirmed in the direct numerical simulation (DNS) results of Sau [68]. (Streamwise vorticity has also been observed in the early stages of flow development by Liepmann and Gharib [69].) From the BaN results, it would appear that such streamwise vortex pairs can work both ways: drawing ambient fluid into the core flow or (more often) expelling core fluid into the ambient.

Figure 5e shows the three components of the enstrophy (corresponding to each of the three components of the vorticity), comparable to each other in magnitude – in fact, so close that in terms of rms values, the vorticity field is nearly isotropic. By $t = 35$ units, enstrophy in the heated flow is higher by an order of magnitude. The spectrum of the circumferential component of the vorticity (Figure 5f) is about an order of magnitude higher over the lower wave numbers, and some three orders of magnitude higher at very high wave numbers.

The DNS results show good qualitative agreement with available experimental data on spatially growing jets. Diabatic heating accelerates the flow, arrests jet growth and enhances the mean vorticity. The turbulence levels within the flow go up, but relative to the changes in mean velocity they drop, as in the experiments.

There are no experimental results yet on the vorticity fields, and we now consider how the results of the numerical simulation might be explained.

3.6. *The baroclinic torque as key player?*

To understand the structural changes that occur in cloud-like diabatic flows, it is useful to begin with an analysis of the vorticity results of Figure 5 and Section 3.5. At the present stage, there are not enough data yet to quantify the connections between the different flow variables, but the *nature* of the connections is reasonably clear.

First, vorticity can be decomposed into mean and fluctuating components $\mathbf{\Omega}$ and $\boldsymbol{\omega}'$, respectively, exactly as in the Reynolds decomposition of velocity into $\mathbf{U} + \mathbf{u}'$; similarly for the temperature, $\overline{T} + T'$. From (7), specializing now to the temporal problem handled in BaN, we can write an equation for $\partial\mathbf{\Omega}/\partial t$, which in the non-diabatic case will include the usual terms representing the stretching and tilting of $\mathbf{\Omega}$ and $\boldsymbol{\omega}'$, respectively, by the mean and fluctuating strains, the divergence of the mean advection of ω' by $\mathbf{u}'$, that is, div $(\mathbf{u}'.\nabla)\boldsymbol{\omega}'^{1}$ (see [70]) and, finally, viscous diffusion. In the diabatic case, there is in addition the mean baroclinic torque with only an azimuthal component given by $-\beta g(\partial\overline{T}/\partial r)$, as in Figure 5a. Now the temperature gradient $\partial\overline{T}/\partial r$ is zero at the centreline as well as towards the edge of the flow and, at any given height, is likely to have a ring-like maximum somewhere midway in the flow cross-section where $\partial\overline{T}/\partial r$ is a maximum. (In early stages of development, experiments [44] suggest that the temperature distribution might be bimodal, in which case there is a smaller inner ring of maximum torque opposite in sign to the outer ring.) Hence, the baroclinic torque is highest along a tubular region well *within* the flow.

The sign of the torque and its circumferential orientation are such as to increase the velocity in the core of the flow and depress it towards and beyond the edges – which simultaneously slows lateral growth and centreline velocity decay and enhances mean vorticity. The downward velocity induced at the edges by the baroclinic torque 'folds' the tongues down and squashes the in-between spaces through which irrotational ambient fluid is drawn in to the main flow, thus affecting the engulfment process (as in Figure 5c). The relative acceleration of the core fluid is probably responsible for a degree of resemblance to some of the effects of acceleration on turbulent boundary layers (BhN [50]) and wakes [71]. Thus, the rather unintrusive, diffuse edges noticed in the top half of Figure 3a, relative to what in the classical nondiabatic plume in the bottom half of the same figure is a sharp but highly convoluted boundary, are similar to what is seen in a turbulent boundary layer in a highly favourable pressure gradient (e.g. Falco's flow visualizations in Van Dyke [49], p. 96). However, the BhN experiments show that the effects of heating become gradually more pronounced as the value of the heat release number goes up: when the heating is still modest (say G less than about 2), the decay in the centreline velocity of the jet becomes progressively milder as G increases, changing to true acceleration only at higher values of G ($\sim$4) and the baroclinic torque. Thus, it seems plausible that the effect of acceleration is not an independent cause but is instead one consequence of the operation of the baroclinic torque as it becomes more dominant.

When we turn to the structure of turbulence, the quantity that is most interesting to study is the turbulence enstrophy, $(1/2)\ |\omega'|^2 = (1/2)\ |\omega'_i\omega'_i|$, whose governing equation

can be derived from the dynamics Equation (7) for $\boldsymbol{\omega}$. It is first of all important to note that $\hat{\omega}$ (the rms value) is of order $\hat{u}_c/\lambda$ or U_c/λ (noting that $\hat{u}_c = \mathrm{O}(U_c)$), where λ is the Taylor microscale, so $\hat{\omega}$ tends to be larger than Ω, which is $\mathrm{O}(U_c/b)$, by a factor $b/\lambda = \mathrm{O}\,(U_c b/\nu)^{1/2}$. The same argument applies to the mean flow and turbulent strain tensors S_{ij} and s_{ij}, respectively. By making order-of-magnitude estimates for each of the 8(!) terms in the enstrophy equation, it quickly emerges that the dominant term in the non-diabatic flow represents turbulence straining turbulence; it is the only term that is a triple product of the larger velocity derivatives of order $\hat{u}_c/\lambda$, namely $\overline{\omega_i'\omega_j's_{ij}}$, and consequently also the largest; this could be balanced by the viscous dissipation [70].

In the diabatic flow, the baroclinic source in the equation for $\boldsymbol{\omega}'$ is just $\beta\mathbf{g} \times \nabla T'$, which again acts in the horizontal plane but is not any longer limited to the azimuthal component. The source for enstrophy is

$$\overline{\beta\boldsymbol{\omega}'.(\mathbf{g} \times \nabla T')} \equiv \beta\mathbf{g}.(\overline{\boldsymbol{\omega}' \times \nabla T'}). \tag{10}$$

Noting that $\beta\nabla T' = -(\nabla\rho')/\rho_o$, and taking $\nabla\rho'$ as of order $\hat{\rho}_c/\lambda_\rho$, where $\hat{\rho}_c$ is (say) the centreline rms of value ρ', and introducing λ_ρ as the Taylor microscale for the density field (although no measurements of λ_ρ are known to the author), the enstrophy source is of order

$$\frac{\mathbf{g}}{\rho_o}\frac{U_c}{\lambda}\frac{\hat{\rho}_c}{\lambda_\rho}, \tag{11}$$

where $\hat{\rho}$ will be determined by the heat release. This term seems to be responsible for the explosive increase in enstrophy found in the BaN simulations, particularly in the spectrum at high wave numbers (see Figure 5f).

It is tempting to speculate that this source of enstrophy may be responsible for the small-scale structure that characterizes the fluffy dome or cauliflower cumulus. In any case, the enormous increase in the small-scale activity in the vorticity field appears to correlate with the similarly dramatic change seen in the PLIF image on Figure 3a, where almost immediately above the beginning of heat release, the structure of the flow is visibly altered. In particular, the convoluted boundaries seen in the non-diabatic plume, including the 'tongues' engulfing the ambient fluid, are no longer prominent. Within the core flow, dye concentration is much more uniformly distributed, with hardly any ambient fluid not only near the centreline but even at a radius of about the velocity width for the flow. This incidentally provides a plausible explanation for the 'protected core' that has often been observed in natural cumuli [61] and in laboratory experiments on diabatic plumes [46, 54]. All of this indicates a much greater degree of 'mixedness' in a core flow and is consistent with a drastically *reduced* engulfing entrainment and an equally drastically *enhanced* molecular mixing in the core. The latter can plausibly be attributed to the enormous increase in small-scale enstrophy, leading to a corresponding increase in the interface area between partially diluted active fluid and whatever ambient fluid is being or has been entrained. In fact, the changes noticed following heat release into the flow recall the 'mixing' transition in free shear flows discussed by Roshko [72]. Roshko's emphasis on the role of small-scale turbulence and his suggestion that the phenomenon should be more appropriately called the 'mixedness transition' seem particularly relevant for understanding the changes seen in Figures 3a and 5c: diabatic heating appears to trigger a mixedness transition in the flow.

In summary then, based on an analysis of the data from the physical and numerical experiments that have been carried out to date, the following brief explanation can be offered for the apparently strange behaviour of round jets and plumes subjected to cloud-like off-source heating. The heating generates a mean baroclinic torque that peaks around a quasi-cylindrical sheet (ring in cross-section) situated roughly midway between the axis of the flow and the edges. The sign of the torque is such that it leads to a differential acceleration across the flow: positive near the axis and negative near and beyond the edges. This enhances the shear and thins down the flow. It also smoothes out the bulginess and folds down the engulfment tongues that characterize the flow, leading to a reduction in entrainment at the engulfment stage. This lower entrainment is however accompanied by greater mixedness in the core. The latter can be traced to an explosive growth in the turbulent enstrophy, triggered by a strong fluctuating baroclinic torque that overwhelms both the other two dominant mechanisms that determine enstrophy, namely turbulence straining turbulence and viscous dissipation. The turbulent enstrophy strengthens the small-scale structure in the flow, which increases interface area and hence also the mixedness. Perhaps, it is also responsible for the fluffy edges of cumulus tops.

4. The Convective Atmospheric Boundary Layer

4.1. *Introduction*

In the last 50 years, a great deal of work has been done in atmospheric boundary layers in general and in convective boundary layers in particular. Recent surveys are available in Wyngaard [73]. However, tropical convective boundary layers do present a special problem, and we shall discuss it briefly here.

The standard approach to the atmospheric surface layer is provided by the Monin–Obukhov (M-O) similarity theory, which has been widely studied and applied. This theory adopts as velocity scale the friction velocity U_*, as in neutrally stable turbulent boundary layers, but an additional scale is introduced into the problem in the form of the Obukhov length L, involving U_* and the sensible heat flux $\rho_0 C_p \overline{w'T'}$, where w' is the surface-normal fluctuating velocity and T' the turbulent temperature fluctuation. The properties of the boundary layer are then taken as functions of z/L. This theory has generally been very successful, but not in the tropics, where the winds are generally relatively low (typically less than a few metres per second at 10-m height). Atmospheric scientists attempting to simulate tropical circulations such as the monsoons have found that the predictions improve if the eddy fluxes are (empirically) enhanced beyond those given by the standard M-O theory at low winds [74]. Various prescriptions (including some that are rather empirical) have therefore been often proposed prescribing higher fluxes at low winds to get more realistic results [75–78]. It has also been explicitly shown [79] that eddy flux measurements in the atmosphere do not agree with the M-O theory at low winds.

4.2. *The atmospheric boundary layer in the tropics and heat flux scaling*

A major field campaign carried out in India, called MONTBLEX-90 (for the Monsoon Trough Boundary Layer Experiment 1990), provided flux data at four stations spanning the breadth of the country from Jodhpur (26°18′N, 73°04′E) on the eastern edge of the Thar desert to Kharagpur near the head of the Bay of Bengal (references [80] and [81] give a comprehensive account). The fluxes were all directly measured by the eddy correlation technique using sonic anemometers on 30-m masts. Useful supplementary data turned out to be available in the boundary layer field experiment BLX83 [78], carried out in May–June 1983 at Chickasha, OK (35°02′N, 97°51′E). Here, the mixed-layer depth (defined as the

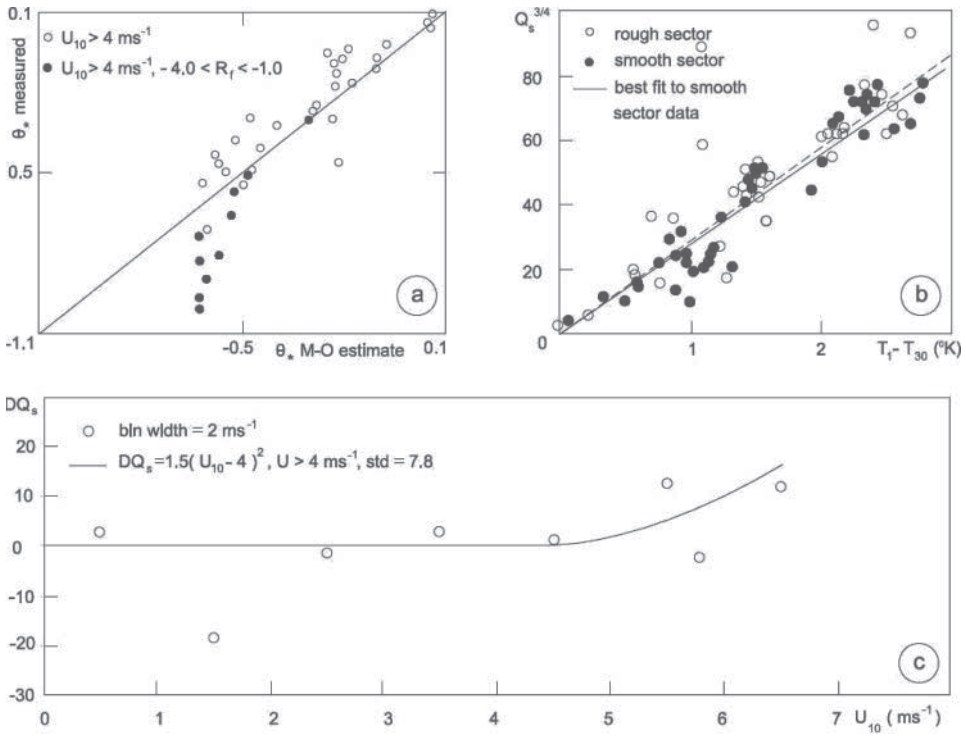


Figure 6. Heat flux in weakly forced atmospheric convection [82]. (a) Comparison of friction temperature θ_* as estimated from direct measurements of sensible heat flux and from the Monin–Obukhov theory. (b) Plot of $Q_s^{4/3}$ against a temperature differential across the mast; data from MONTBLEX-90. Open symbols: rough sector, filled symbols: smooth sector; full line: all sectors, dashed line: smooth sector (specially added for the present work). (c) Deviation of measured Q_s from the best straight-line fit to the data in (b), as a function of wind speed at 10-m height. Reproduced with permission from [82].

height at which there was a 50:50 mixture of free-atmosphere and mixed-layer air) was also measured, and 24 out of 28 datasets had mixed-layer wind-speeds of less than 10 m/s. Both these datasets have been analyzed by Rao and Narasimha [82] in detail, and a summary of the main conclusions is provided in Figures 6–8.

Figure 6a compares measured values of the friction temperature θ_* with estimates from the M-O theory [82] (θ_* being defined by the relation $\theta_* = -\overline{w'\theta_v'}/U_*$, where θ_v' is the virtual potential temperature). It is seen that the M-O theory satisfactorily predicts the heat flow when $U_{10} > 4$ m/s (U_{10} being the wind speed 10 m above ground), but not under convectively unstable conditions at lower winds. Figure 6b shows measured eddy sensible heat flux Q_s (derived from $\overline{w'T'}$) against a characteristic temperature differential ΔT, taken in the present case across the height of the mast. The linear dependence of $Q_s^{4/3}$ on ΔT is what is expected in free convection (e.g. [27]). It is seen that in the smooth sector, that is, in the range of wind direction where the air was flowing over appreciably smoother terrain, free convection theory predicts the heat flux well. A more detailed analysis [79] shows that there is, in fact, a weak dependence on U_{10}, but for $U_{10} < 4$ m/s, the heat flux is independent of wind speed and depends solely on the temperature differential (Figure 6c). The BLX83 data show broadly similar behaviour for $U_{ML} < 8$ m/s, where U_{ML} is wind speed at mixed-layer height.

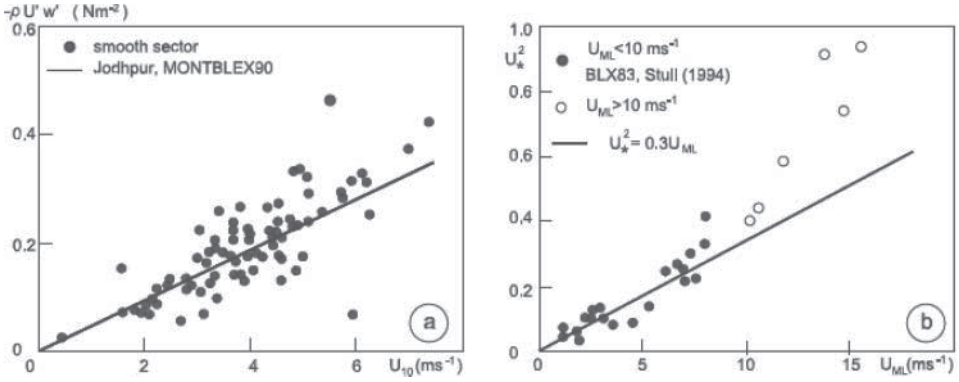


Figure 7. Momentum flux in weakly forced atmospheric convection [82]. (a) Measured momentum flux at 4 m above surface. (b) Momentum flux as measured using the direct correlation techniques from a low-flying aircraft in BLX-83. Reproduced with permission from [82].

Turning now to the momentum flux, Figures 7a and 7b show its variation with the same reference wind speeds, U_{10} and U_{ML}, respectively. The surprising result here is that the fluxes are *linear* in the wind speed – up to $U_{10} \sim 6$ m/s at Jodhpur, $U_{\mathrm{ML}} \sim 10$ m/s in BLX83. Incidentally, it is seen that at Jodhpur, the wind speeds are generally below 5 m/s,

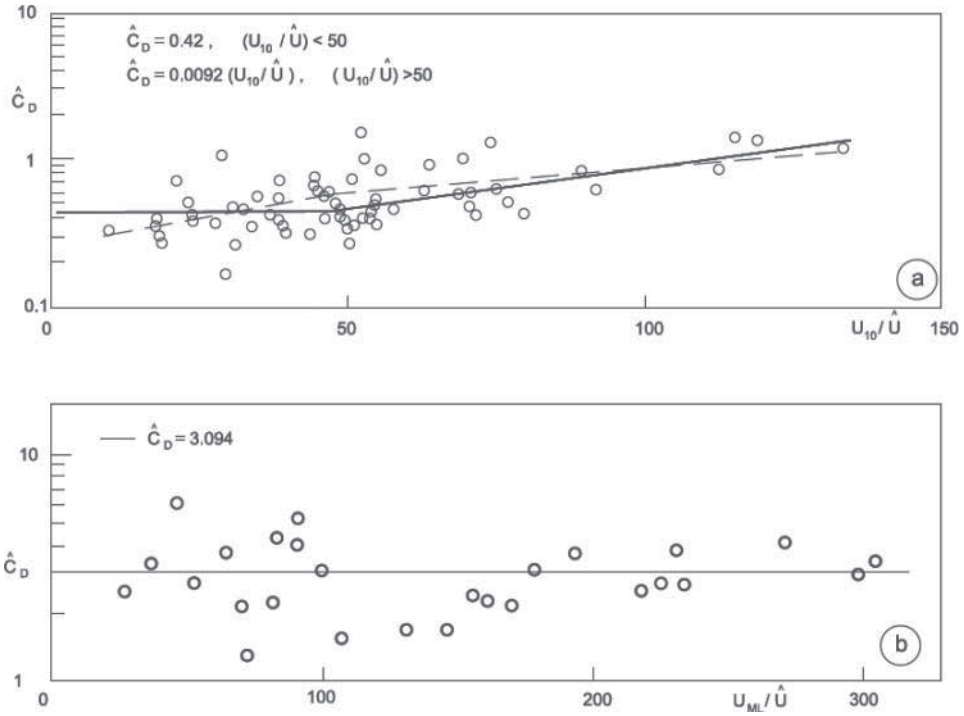


Figure 8. Variation of the newly defined drag coefficient with wind speed (see text for the definition). Dashed line in the upper diagram is a revised fit made for the present work. Redrawn with permission based on [82].

only rarely touching 7 m/s – confirming how (even during the monsoon months) wind speeds are low in the tropics. The BLX83 data are interesting because the wind speeds here are often higher, and so serve to confirm the existence of a distinct low-wind regime below $U_{\mathrm{ML}} = 10$ m/s. The linear dependence in a convectively turbulent flow cannot, of course, have anything to do with the well-known Stokes flow linear dependence of drag on flow velocity. Instead, these results are best seen as identifying a sub-regime in mixed convection, called 'weakly forced' by Rao and Narasimha [79]. In pure free convection (i.e. no cross-wind), the surface stress induced by convective motion in the neighbourhood of a rising axisymmetric (in-the-mean) column of air will, in general, have a vanishing spatial average $\langle U_* \rangle$ from symmetry considerations (as the friction due to air moving radially in at any azimuthal angle will be cancelled out by that moving in the opposite direction). (Even when there is no symmetry, U_* will anyway be small.) A weak cross-wind is then only a small perturbation on natural convection and produces a stress that is linear in wind speed. An appropriate perturbation procedure for the problem has been defined by Rao and Narasimha [79], but a full analysis has not yet been made.

There is a related investigation in a paper by Grachev [83], who examined laboratory experiments on convection between parallel plates carried out by Ingersoll [84] and others, using the Prandtl–Kolmogorov *K-L* model. He considered that momentum flux between air and ocean does not provide a good test because of strong directional irregularity in mean wind – we certainly do not find that to be the case with respect to our analysis of data from Jodhpur.

Rao and Narasimha [79] proceeded to consider various candidates for a new velocity scale that is related to surface heat flux rather than the wall stress, including the one implicit in Grachev's work. One particularly simple and appropriate velocity scale under weakly forced convection is defined by the relation

$$\hat{U} = \frac{Q_s}{\rho_o C_p \Delta\theta},$$

where Q_s is the surface heat flux, C_p the specific heat at constant pressure, ρ_o the surface density and $\Delta\theta$ a characteristic difference in the potential temperature between the surface layer and the mixed layer. A drag coefficient using heat flux scaling would then be defined by

$$\hat{C}_D = \frac{D}{\rho_o \hat{U} U_o}.$$

Figure 8 shows that this drag coefficient hardly varies with wind speed at low winds.

Raju and Narasimha [85] made a detailed study of the engineering literature on convective heat transfer and found independent evidence for the existence of the weakly forced convection regime. For example, below a densimetric Froude number of 1.65, the heat flux from a circular cylinder in cross-flow is unaffected by the cross-flow velocity.

The atmospheric general circulation model Varsha, written at the National Aerospace Laboratories, Bangalore, by Sinha et al. [86], incorporates the above ideas through a new boundary layer module and reports appreciable improvement over an M-O code in prediction of rainfall as well as cyclone tracks [87, 88].

5. Concluding remarks

Studies of cumulus clouds are now being pursued in many different directions. Very broadly, they can be divided into two groups : (1) those concerning microphysics, dealing with such

issues as the effect of condensation nuclei, water droplet and ice particle size distributions, multiple-phase fluid dynamics in high wave number (Kolmogorov scale) turbulence, interactions with radiation and allied subjects [89, 90]; and (2) large-scale structure of clouds and cloud flows, entrainment and 'purity', effects of stratification, collective behaviour of cloud and other convective systems and related issues. It is now being increasingly realized that the two areas, which we will for convenience call microphysics and macrodynamics, strongly influence each other. The work described in this paper is very largely concerned with the latter, but it can be noted that the problem is not closed because the approach here has been to consider the diabatic heating as given, or at least as a parameter under the experimenter's control. In the natural cloud, this of course is not the case (except possibly in weather modification experiments), and closure would have to be obtained by linking macrodynamics with microphysics and thermodynamics. Similarly, the microphysics studies need information about high wave number turbulence, but this is strongly affected (also as we have seen here) by macrodynamics. Thus, micro and macro are strongly coupled, and finding suitable models for this coupling remains a major challenge in cloud dynamics. If the proposal that the transient diabatic plume is an appropriate fluid dynamics model for cumulus flow is correct, it identifies the single most important parameter in macrodynamics. The challenge then is to see if microphysics can help in closing the system through effective predictions of expected heat release associated with phase transitions. Correspondingly, the major flow parameters that dominate microphysics may need to be identified, possibly going beyond the high wave number characteristics of turbulent cumulus flow.

If the transient diabatic plume is a useful model, we should ask what the major challenges are likely to be in pursuing that line of enquiry. Compared with our knowledge of various canonical free shear flows such as jets, wakes and plumes, we are still in the exploratory stage in cloud flows, and an enormous amount of work needs to be carried out before we can approach a comparable level of knowledge. At a more fundamental level, it is necessary to examine the well-known limitations of the Boussinesq equations for buoyancy-dominated flows and explore what modifications or improvements would be most important if we were to demand conclusions that might be directly applicable to natural clouds. Cloud modelling is a major need in both climate change science and tropical circulation dynamics, and it is a great challenge to see how insights from both laboratory and numerical experiments, the latter including direct solutions of the Navier–Stokes–Boussinesq equations (possibly modified or improved), can be used to develop better cloud models.

Again, in convective atmospheric boundary layers relevant for the tropics, the weakly forced convection limit needs to be studied in much greater detail, theoretically, in wind tunnel experiments and by DNS/LES simulations.

Whether such efforts will succeed is always hard to predict, but if they do, they can lead to exciting advances in tropical and global meteorology.

Acknowledgements

During the last two decades while the work reported here was being carried out, I have had the pleasure of working with many students, colleagues and post-docs. Among the first of these were G.S. Bhat, Prof V.H. Arakeri, R. Elavarasan, Amit Basu, and Prof. A. Prabhu. More recently, in rough anti-chorological order, I am grateful to Prof. K.R. Sreenivas, Prof. G.S. Bhat and Dr Sourabh S. Diwan, and to D. Subrahmanyam, G.R. Vybhav Rao, Dr L. Venkatakrishnan, Prof. A. Prabhu, Dr Kusuma G. Rao, Dr S.V. Kailas, H.V. Raju, Dr S. Rudrakumar, S. Ameenulla, S. Siddhartha, V. Saxena, and Dr U.N. Sinha. Mr Sukruth Satheesh helped in preparing Figure 1. The work has been supported at various times by the Department of Science and Technology, New Delhi; the Defence Research and Development Organization, New Delhi; US Office of Naval Research, Arlington, VA; Tata Computing Research Laboratories, Pune; and, most recently, by JNC and by Intel Technology

India Private Limited, Bangalore. I am grateful to the Centre for Atmospheric and Oceanic Sciences, Indian Institute of Science, for their continued hospitality.

Note

1. In tensor notation $(\partial^2/\partial x_j \partial x_k)\, u'_j \omega'_k$, after using div $\mathbf{u}' = 0$.

References

[1] A. Favre (ed.), *The Mechanics of Turbulence*. Proceedings of CNRS International Colloquium, Marseilles, Centre National de la Recherche Scientifique (CNRS), Paris, 1964.
[2] F.N. Frenkiel (ed.), *International symposium on fundamental problems in turbulence and their relation to geophysics*, J. Geophys. Res. 67 (1962), pp. 3005–3235.
[3] G.I. Taylor, *Eddy motion in the atmosphere*, Phil. Trans. R. Soc. A 240 (1915), pp. 1–26.
[4] L.F. Richardson, *Weather Prediction by Numerical Process*, Cambridge University Press, Cambridge, 1922.
[5] L.F. Richardson, *Atmospheric diffusion shown on a distance-neighbour graph*, Proc. R. Soc. A 110 (1926), pp. 709–737.
[6] V. Ramaswamy, O. Boucher, J. Haigh, D. Hauglustaine, J. Haywood, G. Myhre, T. Nakajima, G.Y. Shi, and S. Solomon, *Radiative forcing of climate change contents, in Climate Change 2001: The Scientific Basis. Contribution of Working Group I to the Third Assessment Report of the IPCC*, J.T. Houghton, Y. Ding, D. J. Griggs, N. Noguer, P. J. van der Linden, D. Xiaosu, K. Maskell, and C. A. Johnson, eds., Cambridge University Press, Cambridge, 2011, pp. 349–416.
[7] D.A. Randall, R.A. Wood, S. Bony, R. Colman, T. Fichefet, J. Fyfe, V. Kattsov, A. Pitman, J. Shukla, J. Srinivasan, R.J. Stouffer, A. Sumi, and K.E. Taylor. *Climate Change 2007: The Physical Science Basis. Contribution of Working Group I to the Fourth Assessment Report of the IPCC*, Cambridge University Press, Cambridge, 2007.
[8] G.R. McGregor and S. Nieuwolt, *Tropical Climatology: An Introduction to the Climates of the Low Latitudes*, 2nd ed., Wiley, Chichester, 1998.
[9] J.P. Peixoto and A. Oort, *Physics of climate*, Rev. Mod. Phys. 56 (1984), pp. 365–429.
[10] R.S. Lindzen, *Climate dynamics and global change*, Annu. Rev. Fluid Mech. 26 (1994), pp. 353–378.
[11] D.R. Sikka and S. Gadgil, *On the maximum cloud zone and ITCZ over the Indian longitudes during the southwest monsoon*, Mon. Weather Rev. 108 (1980), pp. 1122–1135.
[12] J.G. Charney and J. Shukla, *Predictability of monsoons, in Monsoon Dynamics*, M.J. Lighthill and R.P. Pierce, eds., Cambridge University Press, Cambridge, 1981, pp. 99–109.
[13] B.N. Goswami, M.C. Wheeler, C. Gottschalck, and D.E. Waliser, *Intraseasonal variability and forecasting: a review of recent research, The Global Monsoon System: Research and Forecast*, 2nd ed., in C.-P. Chang, Y.H. Ding, N.-C. Lau, R. Johnson, B. Wang, and T. Yasunari, eds., World Scientific Publishing, Singapore, 2011, pp. 389–407.
[14] WMO, *International Cloud Atlas*, Vol. 1, World Meteorological Organization (WMO), Geneva, 1975.
[15] H. Riehl, *Climate and Weather in the Tropics*, Academic Press, New York, 1979.
[16] Arizona State University (ASU), Santa Catalina Mountain Cloud Project, 16 August 2002. (2002). Available at http://prism.engineering.asu.edu/research/bg.php.
[17] F. Stratmann, O. Möhler, R.A. Shaw, and H. Wex. *Laboratory cloud simulation: Capabilities and future directions*, in *Clouds in the Perturbed Climate System: Their Relationship to Energy Balance, Atmospheric Dynamics, and Precipitation, Strüngmann Forum Reports*, J. Heintzenberg and R.J. Charlson, eds., 2009, MIT Press, Cambridge, MA, pp. 127–147.
[18] J. Heintzenberg and R.J. Charlson (ed.), *Clouds in the Perturbed Climate system, Their Relationship to Energy Balance, Atmospheric Dynamics, and Precipitation*, MIT Press, Cambridge, MA, 2009.
[19] U. Lohmann and S.E. Schwartz, *Aerosols and clouds in chemical transport models and climate models*, in *Clouds in the Perturbed Climate System: Their Relationship to Energy Balance, Atmospheric Dynamics, and Precipitation*, J. Heintzenberg and R.J. Charlson, eds., MIT Press, Cambridge, MA, 2009, pp. 531–555.
[20] K. Emanuel, *Atmospheric Convection*, Oxford University Press, Oxford, 1994.
[21] H. Stommel, *Entrainment of air into a cumulus cloud*, J. Meteorol. 4 (1947), pp. 91–94.

[22] J. Warner, *On steady-state one dimensional models of cumulus convection*. J. Atmos. Sci. 27 (1970), pp. 1035–1040.
[23] G.W. Reuter, *A historical review of cumulus entrainment studies*, Bull. Am. Meteorol. Soc. 67 (1986), pp. 151–154.
[24] F.H. Ludlam and R.S. Scorer, *Cloud Study*, John Murray, London, 1957.
[25] J.S. Turner, *Turbulent entrainment: The development of the entrainment assumption, and its application to geophysical flows*, J. Fluid Mech. 173 (1986), pp. 431–471.
[26] J.S. Turner, *Buoyancy Effects in Fluids*, Cambridge University Press, Cambridge, 1973.
[27] A.A. Townsend, *The Structure of Turbulent Shear Flow*, Cambridge University Press, Cambridge, 1956.
[28] G.I. Taylor, *Dynamics of a mass of hot gas rising in air* (Report no. MDDC 919/LADC 276), Technical Information Division, US Atomic Energy Commission, Oak Ridge, TN, 1945.
[29] B.R. Morton, G.I. Taylor, and J.S. Turner, *Turbulent gravitational convection from maintained and instantaneous sources*, Proc. R. Soc. A 234 (1956), pp. 1–23.
[30] S.C. Mossop, *Production of laboratory clouds*, Q. J. R. Meteorol. Soc. 110 (1984), pp. 275–279.
[31] J.-A. Simpson (eds.), *Cumulus clouds: Early aircraft observations and entrainment hypotheses*, in *Mesoscale Meteorology: Theories, Observations and Models*, D.K. Lilly and T. Gal-Chen, eds., 1983, D. Reidel, Dordrecht, pp. 355–445.
[32] R.A., Houze, Jr., *Cloud Dynamics*, Academic Press, San Diego, CA, 1993.
[33] J.S. Turner, *Model experiments relating to thermals with increasing buoyancy*, Q. J. Roy. Meteor. Soc. 89 (1963), pp. 62–74.
[34] S. Shy and R.E. Breidenthal, *Laboratory experiments on the cloud-top entrainment instability*, J. Fluid Mech. 214 (1990), pp. 1–15.
[35] H. Johari, *Mixing in thermals with and without buoyancy reversal*, J. Atmos. Sci. 49 (1992), pp. 1412–1426.
[36] H.W. Liepmann, *Free turbulent flows*, in *The Mechanics of Turbulence*, Proceedings of CNRS International Symposium, Marseilles, Centre National de la Recherche Scientifique (CNRS), Paris Sep. 1961, 1964, pp. 211–227.
[37] R. Narasimha, 2012 (to be published).
[38] A.J. Basu and R. Narasimha, *Direct numerical simulation of turbulent flows with cloud-like off-source heating*, J. Fluid Mech. 385 (1999), pp. 199–228.
[39] R. Narasimha, S.S. Diwan, S. Duvvuri, K.R. Sreenivas, and G.S. Bhat, *Laboratory simulations show diabatic heating drives cumulus-cloud evolution and entrainment*, Proc. Natl. Acad. Sci. USA 108 (2011), pp. 16164–16169.
[40] G.S. Bhat and R. Narasimha, *A volumetrically heated jet: Large-eddy structure and entrainment characteristics*, J. Fluid Mech. 325 (1996), pp. 303–330.
[41] D.D. Churchill and R.A. Houze, Jr., *Effects of radiation and turbulence on the diabatic heating and water budget of a stratiform region of a tropical cloud cluster*, J. Atmos. Sci. 48 (1991), pp. 903–922.
[42] L. Venkatakrishnan, G.S. Bhat, A. Prabhu, and R. Narasimha, *Experiments on a plume with off-source heating: Implications for cloud fluid dynamics*, J. Geophys. Res. 104 (1999), pp. 14271–14281.
[43] G.R. Vybhav, S.S. Diwan, K.R. Sreenivas, R. Narasimha, L. Venkatakrishnan, and P. Suriyanarayanan, *Laboratory simulation of the life-cycle of a cumulus congestus cloud*, Proceedings of the International Conference on "Opportunities and Challenges in Monsoon Prediction in a Changing Climate," (OCHAMP-2012), Pune, India, 2012.
[44] A. Agarwal and A.K. Prasad, *Evolution of a turbulent jet subjected to volumetric heating*, J. Fluid Mech. 511 (2004), pp. 95–123.
[45] A. Agarwal, K.R. Sreenivas, and A.K. Prasad, *Velocity and temperature measurements in an axisymmetric turbulent jet with cloud-like off-source heating*, Int. J. Heat Mass Transfer 47 (2004), pp. 1433–1444.
[46] L. Venkatakrishnan, R. Elavarasan, G.S. Bhat, A. Krothapalli, and L. Lourenco, *Particle image velocimetry study of a cloud-like flow*, Curr. Sci. 85 (2003), pp. 778–785.
[47] L. Venkatakrishnan, G.S. Bhat, A. Prabhu, and R. Narasimha, *Visualization studies of cloud-like flows*, Curr. Sci. 74 (1998), pp. 597–606.
[48] R. Narasimha and K.R. Sreenivasan, *Relaminarisation of fluid flows*, Adv. Appl. Mech. 19 (1979), pp. 221–301.
[49] M. Van Dyke, *An Album of Fluid Motion*, Parabolic Press, Stanford, CA, 1982.

[50] R.E. Breidenthal, *The effect of acceleration on turbulent entrainment*, Phys. Scr. T 132 (2008), 014001.
[51] D.M. Romps, *A direct measure of entrainment*, J. Atmos. Sci. 67 (2010), pp. 1908–1927.
[52] A.P. Siebesma and J.W.M. Cuijpers. *Evaluation of parametric assumptions for shallow cumulus convection*, J. Atmos. Sci. 52 (1995), pp. 650–666.
[53] L. Venkatakrishnan, *Development of a plume with off-source volumetric heating*, Ph.D. diss., Indian Institute of Science, Bangalore, 1997.
[54] S.S. Diwan, R. Narasimha, G.S. Bhat, and K.R. Sreenivas, *Laboratory studies of anomalous entrainment in cumulus cloud flows*, J. Phys.: Conf. Ser. 318 (2011), 072014.
[55] E. Hicks, C. Pontikis, and A. Rigaud, *Entrainment and mixing processes as related to droplet growth in warm midlatitude and tropical clouds*, J. Atmos. Sci. 47 (1990), pp. 1589–1618.
[56] G.R. Taylor and M.B. Baker, *Entrainment and detrainment in cumulus clouds*, J. Atmos. Sci. 48 (1991), pp. 112–121.
[57] G.W. Reuter and M.K. Yau, *Mixing mechanisms in cumulus congestus clouds. Part 1: Observations*, J. Atmos. Sci. 44 (1987), pp. 781–797.
[58] R. Narasimha and G.S. Bhat, *Recent experimental and computational studies related to the fluid dynamics of clouds*, in *Computational Physics and New Perspectives in Turbulence: Proceedings of the IUTAM Symposium Nagoya, Japan*, Y. Kaneda, ed., Springer, Dordrecht, 2008, pp. 313–320.
[59] G.L. Brown and A. Roshko, *On density effects and large structure in turbulent mixing layers*, J. Fluid Mech. 64 (1974), pp. 775–816.
[60] A. Roshko, *Structure of turbulent shear flows: A new look*, AIAA J. 14 (1976), pp. 1349–1357.
[61] H. Riehl and J. Malkus, *On the heat balance in the equatorial trough zone*, Geophysica 6 (1958), pp. 503–538.
[62] A.M. Blyth, *Entrainment in cumulus clouds*, J. Appl. Meteorol. 32 (1993), pp. 626–641.
[63] P.H. Austin, M.B. Baker, A.M. Blyth, and J.B. Jensen, *Small-scale variability in warm continental cumulus clouds*, J. Atmos. Sci. 42 (1985), pp. 1123–1138.
[64] D.M. Romps and Z. Kuang, *Do undiluted convective plumes exist in the upper tropical troposphere?* J. Atmos. Sci. 67 (2010), pp. 468–484.
[65] O. Pauluis and J. Schumacher, *Self-aggregation of clouds in conditionally unstable moist convection*, Proc. Natl. Acad. Sci. USA 108 (2011), pp. 12623–12628.
[66] A. Srinivas, G.S. Bhat, and R. Narasimha, *Dynamic eduction of coherent structures in turbulent jet flow imagery by wavelet techniques: Part I*, J. Turbulence 8 (2007), pp. 1–14.
[67] R. Narasimha, V. Saxena, and S.V. Kailas, *Coherent structures in plumes with and without off source heating using wavelet analysis of flow imagery*, Exp. Fluids 33 (2002), pp. 196–201.
[68] A. Sau, *Role of streamwise dynamics in spreading and mixing of flows through a rectangular sudden expansion*, Phys. Fluids 23 (2011), 083602.
[69] D. Liepmann and M. Gharib, *The role of streamwise vorticity in the near-field entrainment of round jets*, J. Fluid Mech. 245 (1992), p. 643.
[70] H. Tennekes and J.L. Lumley, *A First Course in Turbulence*, MIT Press, Cambridge, MA, 1972.
[71] A. Prabhu and R. Narasimha, *Turbulent non-equilibrium wakes*, J. Fluid Mech. 54 (1972), pp. 19–38.
[72] A. Roshko, *The mixing transition in free shear flows*, in *The Global Geometry of Turbulence*, J. Jimenez, ed., Plenum Press, New York, NY, 1991, pp. 3–11.
[73] J.C. Wyngaard, *Turbulence in the Atmosphere*, Cambridge University Press, Cambridge, 2010.
[74] M.J. Miller, A.C.M. Beljaars, and T. Palmer, *The sensitivity of the ECMWF model to the parametrization of evaporation from the tropical oceans*, J. Clim. 5 (1992), pp. 418–434.
[75] J.J. Hack, B.A. Boville, B.P. Briegleb, J.T. Kiehl, P.J. Rasch, and D.L. Williamson, *Description of the NCAR Community Climate Model (CCM2)*. NCAR Technical Note NCAR/TN-382+STR, NTIS PB93-221802/AS. Climate and Global Dynamics Division, National Center for Atmospheric Research, Boulder, CO, 1993.
[76] J.S. Godfrey and A.C.M. Beljaars, *On the turbulent fluxes of buoyancy, heat and moisture at the air-sea interface at low wind speeds*, J. Geophys. Res. 96 (1991), pp. 22043–22048.
[77] A.C.M. Beljaars, *The parameterization of surface fluxes in large-scale models under free convection*, Q. J. R. Meteorol. Soc. 121 (1994), pp. 255–270.
[78] R.B. Stull, *A convective transport theory for surface fluxes*, J. Atmos. Sci. 51 (1994), pp. 3–22.
[79] K.G. Rao and R. Narasimha, *Heat- flux scaling for weakly forced turbulent convection in the atmosphere*, J. Fluid Mech. 547 (2006), pp. 115–135.

[80] M. Goel and H.N. Srivastava, *Monsoon trough boundary layer experiment (MONTBLEX)*, Bull. Am. Meteorol. Soc. 71 (1990), pp. 1594–1600.
[81] R. Narasimha, D.R. Sikka, and A. Prabhu (eds.), *The Monsoon Trough Boundary Layer*, Indian Academy of Sciences, Bangalore, 1997.
[82] K.G. Rao and R. Narasimha, *Estimation of drag coefficient at low wind speeds over the monsoon trough land region during MONTBLEX-90*, Geophys. Res. Lett. 23 (1996), pp. 2617–2620.
[83] A.A. Grachev, *Temperature profile and heat transfer in free turbulent convection along a horizontal surface*, Izv. Atmos. Ocean. Phys. 25 (1989), pp. 132–140.
[84] A.P. Ingersoll, *Thermal convection with shear at high Rayleigh number*, J. Fluid Mech. 25 (1966), pp. 209–228.
[85] H.V. Raju and R. Narasimha, *Limiting cross-flow velocity below which heat flux is determined by natural convection*, Int. J. Heat Mass Transfer 46 (2003), pp. 4975–4978.
[86] U.N. Sinha, T.N. Venkatesh, V.R. Sarasamma, S. Rajalakshmy, K. Bhagyalakshmi, A.K. Verma, C.K. Sreelekha, and K.L. Resmi, *NMITLI GCM code: Varsha 1.0, PD FS 0516*, National Aerospace Laboratories, Bangalore, 2005.
[87] T.N. Venkatesh, V. Mudkavi, S. Rajalakshmy, V.R. Sarasamma, U.N. Sinha, and R. Narasimha, *Preliminary results on the simulation of the 1999 Orissa super cyclone using GCM with a new boundary layer code*, Mausam 57 (2006),pp. 119–128.
[88] G. Mrudula and K. Vijayakumari, *Effect of the new boundary layer scheme on Varsha rainfall forecasts – A case study*, Project Document PDFS 1206, National Aerospace Laboratories, Bangalore, 2012.
[89] Z. Warhaft, *Laboratory studies of droplets in turbulence towards understanding the formation of clouds*, Fluid Dyn. Res. 41 (2009), 011201.
[90] R.A. Shaw, *Particle-turbulence interactions in atmospheric clouds*, Ann. Rev. Fluid Mech. 35 (2003), pp. 183–227.

Journal of Turbulence
Vol. 13, No. 37, 2012, 1–37

Taylor & Francis
Taylor & Francis Group

A review of relaxation and structure in some turbulent plasmas: magnetohydrodynamics and related models

William H. Matthaeus[a*], David C. Montgomery[b], Minping Wan[a] and Sergio Servidio[c]

[a]*Department of Physics and Astronomy & Bartol Research Institute, University of Delaware, Newark, DE 19716, USA;* [b]*Department of Physics and Astronomy, Dartmouth College, Hanover, NH 03755, USA;* [c]*Dipartimento di Fisica, Universita della Calabria, Rende, Italia*

(*Received 16 April 2012; final version received 13 June 2012*)

A brief overview is provided as an introduction to hydrodynamic-like turbulence that characterizes the dynamics of plasmas in several parameter regimes. This includes magnetohydrodynamics (MHD), the electron fluid plasma, which is closely related to two-dimensional hydrodynamics, and the solar wind, which is usually viewed as a laboratory for three-dimensional MHD, with more involved plasma physics at the dissipative scales. An emphasis is placed on energy decay, spectra, relaxation processes, coherent structures, and higher statistics with selected applications in solar wind and laboratory plasmas.

Keywords: magnetohydrodynamics; solar wind; turbulence theory; intermittency; relaxation; plasma physics

1. Introduction

The scope of turbulence theory has broadened remarkably in the recent era. Technological advances have broadened the study of turbulence to a variety of systems while also motivating and enabling various applications. This breadth offers a great challenge in responding to the charge "to assess the achievements of the last 50 years of turbulence research and to identify future challenges that still remain" given to this Colloquium. The challenge is daunting even in the relatively limited context of the present review. Here, some topics are reviewed in magnetohydrodynamic (MHD) turbulence, and its close relatives in plasma physics, such as Guiding Center Fluid or two-fluid (Hall) MHD. Experimental techniques, computing technology, remote sensing methods, and *in situ* spacecraft observations have allowed ideas of MHD turbulence theory to deeply penetrate space physics, solar physics, astrophysics, cosmology laboratory plasma and fusion physics, geophysics and planetology, and numerous materials science and engineering applications. Recognizing the futility of engaging all of these subjects here, this review will focus on some advances that relate these new subjects to classical turbulence ideas, while touching on associated applications, mainly in the solar wind, the corona, and laboratory electron plasmas. In the conclusions section, a brief and incomplete attempt will be made to point toward some important subjects that are entirely neglected here.

*Corresponding author. Email: whm@udel.edu

ISSN: 1468-5248 online only
© 2012 Taylor & Francis
http://dx.doi.org/10.1080/14685248.2012.704378
http://www.tandfonline.com

2. Models and physical quantities of interest

A plasma, described here as an electrically conducting gas or fluid, evolves in response to both mechanical and electromagnetic forces. To describe its dynamics in a simple way, one can begin with the momentum equation for hydrodynamics, and add a Lorentz force on the fluid elements. This depends on the low-frequency magnetic field and the electric current density. The magnetic field can then be advanced in time through Faraday's law, with a closure based on Ohm's law. For simplicity, as in hydrodynamic turbulence, the focus is often on the constant density incompressible model, which provides an adequate context for the issues of MHD turbulence that are of primary concern here (see [18]). Ignoring compressible effects necessarily discards at the onset important and detailed features of the plasmas that MHD is intended to approximate. Nevertheless, this is a quick way to arrive at the study of the nonlinear scale-to-scale couplings that are at the core of the turbulence problem. The problem of compressible plasma turbulence is much larger and is entirely outside the current scope apart from a few remarks below and in the conclusions.

The incompressible MHD model, in terms of the fluid velocity $\mathbf{u}$ and the magnetic field $\mathbf{B}$, involves the momentum equation

$$\frac{\partial \mathbf{u}}{\partial t} + \mathbf{u} \cdot \nabla \mathbf{u} = -\frac{1}{\rho}\nabla p + \frac{1}{4\pi\rho}(\nabla \times \mathbf{B}) \times \mathbf{B} + \nu \nabla^2 \mathbf{u} \tag{1}$$

and the magnetic induction equation

$$\frac{\partial \mathbf{B}}{\partial t} = \nabla \times (\mathbf{u} \times \mathbf{B}) + \mu \nabla^2 \mathbf{B}. \tag{2}$$

The plasma density ρ, the kinematic viscosity ν, and the magnetic diffusivity μ, are assumed to be uniform constants. Therefore, both the velocity and magnetic field are solenoidal, $\nabla \cdot \mathbf{u} = \nabla \cdot \mathbf{B} = 0$. The pressure p, as in incompressible hydro, provides a constraint that maintains incompressibility, and is determined by taking the divergence of Equation (1). The dimensionless Reynolds number $R = uL/\nu$ (where u is a typical velocity and L a typical length scale) and magnetic Reynolds number $R_m = uL/\mu$ are measures of the relative strength of the non-linear terms and linear (dissipative) terms in the dynamical equations. Highly turbulent MHD occurs at high values of R and R_m.

We recall that MHD is frequently applied to space and astrophysical plasmas for which the derivation of the model is not so clear as one would like. This contrasts the more firm conceptual basis hydrodynamics or gas dynamics, which rests either on macroscopic or perturbative (such as Chapman Enskog expansion) approaches given in standard texts on statistical mechanics. For plasmas with low collisionality, the basic structure of MHD emerges from conservation of mass, momentum, and energy, along with the Maxwell–Ampere and Faraday laws, upon ignoring displacement current and adopting a suitable form of Ohm's law. However, in some applications, there may not be a clear path to closing the system with a single isotropic pressure field, or a convincing calculation of viscosity, resistivity, and other transport coefficients such as thermal conductivity. The study of the origin of dissipation in space and astrophysical plasmas leads to problems of great importance and difficulty, as does the investigation of the physics of the pressure tensor. Many topics relating to the kinetic physics of the solar wind have been studied extensively (see, e.g., [88]). Equally difficult and important problems arise in connection with boundary conditions that might need to be imposed, as the number and type of imposed conditions will differ in plasma and fluid models.

A customary approach in numerical work is to employ scalar dissipation coefficients, with values based on numerical limitations of spatial resolution rather than on physical realism. For turbulent MHD, this is justified in part by assuming that the non-linear cascade is mainly from large to small scales, and the kinetic dissipation mechanisms act to absorb whatever energy arrives at small scales through spectral transfer. This is only partially satisfactory, and a more comprehensive theoretical understanding of the nature of dissipation in low-collisionality MHD applications is desirable, though it may be neither simple in nature nor of universal form. On the optimistic side, when observations are available, e.g., for the solar wind [29], one sees a broad inertial range that separates energy-containing and dissipation ranges [77]. One can infer an effective Reynolds number for the solar wind in this way. Ignoring the difference between viscous and resistive dissipation, one might employ the hydrodynamic estimate of the dissipation wavenumber $k_d = (\epsilon/\nu^3)^{1/4}$. Using the Taylor–von Karman estimate of the decay rate $\epsilon = u^3/\lambda$, this can be cast in the form $k_d\lambda = R^{3/4}$, or $R = (k_d\lambda)^{4/3}$, where R is the Reynolds number. The quantity $k_d\lambda$ is approximately the bandwidth of the inertial range. Therefore, for a three to four decades inertial range (e.g., the solar wind, approximately), one has $R \approx 10^5$ (see, e.g., [169]). For the lower solar corona, a five to six decades inertial range is estimated, so $R \approx 10^8$. For such high Reynolds numbers, the MHD approximation becomes progressively better at the larger scales.

The energy is a quantity that garners much attention in hydro and in MHD, because the non-linear couplings in the fluid equations do not change their value, and therefore it is meaningful to speak of a "cascade" that exchanges energy among scales without changing the total amount present. In the high-Reynolds-number cascade, there are many couplings that drive larger scale structures, and many that drive smaller scale structures. When there is a source of energy at large scales, and either dissipation (or for some other reason a deficit) of energy at small scales, then the latter class is dominant, sometimes by only a modest margin. This effect leads to a net transfer of energy from large to small scales. We will say more about this later. For now we call attention to a feature of MHD that distinguishes it from simple hydrodynamics – namely the potential presence of more than one cascade. This is caused by the fact that there is more than one quadratic quantity that is preserved by MHD nonlinear couplings.

For homogeneous (periodic) incompressible MHD with zero mean magnetic field, there are three (known) ideal quadratic invariants: energy, $E = \langle |\mathbf{v}|^2 + |\mathbf{b}|^2 \rangle$, cross-helicity $H_c = \langle \mathbf{v} \cdot \mathbf{b} \rangle$, and magnetic helicity $\langle \mathbf{b} \cdot \mathbf{a} \rangle$. Here, $\mathbf{b} = \nabla \times \mathbf{a}$ and $\mathbf{a}$ is the magnetic vector potential. There is a lot more that can be said about the role of these additional invariants, and more will follow in later sections, but for now we note that the presence of as many as three conserved quadratic fluxes in an "inertial range" restricts the dynamics in important ways and gives rise to interesting effects such as inverse cascade, enhancement of nonlocal couplings, and special properties of solutions such as $1/f$ noise. (In hydrodynamics, there are two invariants – energy and kinetic helicity – but the latter is often viewed as of less importance than the additional ideal invariants of MHD. See [70].

The magnetic field may contain a uniform part $\mathbf{B_0}$ (below, the "DC magnetic field") or a smoothly varying part (which we identify as a local mean magnetic field) plus small-scale fluctuations $\mathbf{b}$, that is, $\mathbf{B} = \mathbf{B_0} + \mathbf{b}$. The large-scale magnetic field supports propagation of hydromagnetic waves; here, for the incompressible case, we call these Alfvén waves [6, 7, 106, 125]. These waves are fluctuations transverse to the mean magnetic field, propagating along the mean magnetic field direction at the Alfvén speed $V_A = B_0/\sqrt{4\pi\rho}$.

Even the simplest MHD case, assuming incompressibility, isotropy, stationarity, and homogeneity, is more complex than hydrodynamics. There are two distinct fields to deal

with, the magnetic and velocity field, and additional complexity due to Alfvén wave propagation effects. There are at least two classes of timescales involved, the non-linear time and the Alfvén crossing time. Moreover, the large-scale magnetic field introduces a preferred direction and anisotropic effects on the fluctuations are present.

Here, we arrive at a major difference between fluid and MHD turbulence. Unlike fluid turbulence, the nonlocal effect of large scales upon the small scales, described earlier as "sweeping," is an important issue for MHD turbulence. Beginning with the work of Iroshnikov [65] and Kraichnan [71], it has been argued that such effects play a significant role in MHD turbulence, even in the case of absent DC magnetic fields. If there is a strong, large-scale magnetic field, the small-scale fluctuations are subject to a sweeping-like effect due to Alfvén wave propagation. To discuss this, it is useful to write MHD in a more symmetric form, in terms of the so-called Elsässer fields, $\mathbf{z}_+ = \mathbf{u} + \mathbf{b}/\sqrt{4\pi\rho}$ and $\mathbf{z}_- = \mathbf{u} - \mathbf{b}/\sqrt{4\pi\rho}$

$$\frac{\partial \mathbf{z}_\pm}{\partial t} \mp \mathbf{V_A} \cdot \nabla \mathbf{z}_\pm = -\mathbf{z}_\mp \cdot \nabla \mathbf{z}_\pm - \frac{1}{\rho}\nabla P + \mu \nabla^2 \mathbf{z}_\pm, \tag{3}$$

where we have explicitly separated a term involving the large-scale magnetic field (written here in terms of the Alfvén velocity $\mathbf{V_A}$). For simplicity, we assumed $\nu = \mu$. The total pressure $P = p + B^2/8\pi$ acts to enforce the constraints $\nabla \cdot \mathbf{z}_\pm = 0$.

Either $\mathbf{z}_+ = 0$ or $\mathbf{z}_- = 0$ provides exact solutions of the ideal MHD equations. The nonzero field is often said to correspond to *wave packets* that propagate along the mean field direction. This description can be misleading because the "packets" may not be localized, and also may not propagate. Nonpropagating fluctuations with wavevectors strictly perpendicular to the mean magnetic field have zero phase speed. In any case, one sees from the MHD equations that both type of fluctuations $\mathbf{z}_\pm$ are needed for the non-linear terms to be nonzero and sustain turbulence [42, 71].

Kraichnan [70] noted that the mean magnetic field sweeps the small-scale structures which interact and during that time non-linear transfer of energy between length scales occurs (in the Kraichnan picture the "wave packets" suffer brief "collisions" during which energy transfer occurs). One can see then that the mean magnetic field induces an inhibition of the nonlinear energy cascade [35].

For high-Reynolds-number MHD turbulent flows in astrophysical and space environments, there is scale separation to distinct physical processes at large and small scales. Specifically, one divides the dynamics into a small-scale part that contains "small–small" and "large–small" couplings, and a large-scale part (see [1, 176]), reminiscent of k-epsilon and other hydrodynamic turbulence modeling approaches [82]. This type of "turbulence transport theory" generalizes WKB theory for MHD and plasma waves [7, 60], and has proven useful in mapping turbulence amplitudes across large distances within the corona and heliosphere [23, 175]. Adaptations of transport theory can apparently help explain both the origin of the solar wind [38, 166] and the highly nonadiabatic profile of temperature throughout the interplanetary medium [24, 39]. Due to space and time limitations, we will not review transport theory further, but concentrate on theories of homogeneous and/or local processes in MHD turbulence and its related aspects.

3. Energy decay

A central result of turbulence theory is the similarity decay of energy (per unit mass) for the free decay problem [66]. For moderate to high Reynolds numbers, the rate of decay of

energy becomes independent of viscosity, and is governed by the action of the large-scale eddies. The basic physical content of this simplest turbulence phenomenology is captured in the equations for decay of energy per unit mass U^2 and the similarity length scale L, namely

$$\frac{dU^2}{dt} = -\alpha \frac{U^3}{L}; \qquad \frac{dL}{dt} = \beta L. \tag{4}$$

During similarity decay of isotropic turbulence, the correlation functions are stretched and recalled according to

$$R(r) = U^2(t)\hat{R}(r/L(t)). \tag{5}$$

For MHD, the analogous development proceeds by forming the two-point correlation functions of the Elsässer fluctuations, and examining the conditions for a similarity solution [168]. For globally isotropic MHD turbulence (lacking an imposed DC magnetic field), the consistency conditions for a similarity solution, in terms of Elsässer energies Z_+^2 and Z_-^2 and associated length scales L_+ and L_-, are

$$\frac{dZ_+^2}{dt} = -\alpha_+ \frac{Z_+^2 Z_-}{L_+}; \quad \frac{dZ_-^2}{dt} = -\alpha_- \frac{Z_+ Z_-^2}{L_-}, \tag{6}$$

$$\frac{dL_+}{dt} = \beta_+ Z_-; \quad \frac{dL_-}{dt} = \beta_- L_+, \tag{7}$$

where $\alpha_\pm$, $\beta_\pm$ are constants. Note that these equations require two distinct length scales $L_+ \neq L_-$ whenever the cross-helicity is nonzero and $Z_+ \neq Z_-$.

Variations of the basic phenomenology of MHD decay include consideration of the influence of very large-scale eddies on similarity decay of energy [52], and heuristic treatments of anisotropy [13] and cross-helicity [89]. These suggested variations of the theory make assumptions that show clearly how properties of the spectral distributions can directly influence energy decay.

When a DC magnetic field is present and the fluctuations are assumed to be axisymmetric about this direction, one allows in principle at least four characteristic lengths L parallel $\parallel$ and perpendicular $\perp$ for both $+$ and $-$ fluctuations. One finds that additional restriction needs to be imposed to find a similarity solution. One solution is that the parallel and perpendicular length scales remain in constant proportion to one another for all relevant time scales, that is, $L_+^\parallel / L_+^\perp = q_+$, and $L_-^\parallel / L_-^\perp = q_-$, for constants $q_\pm$.

These requirements for similarity decay hint at nonuniversal properties of MHD turbulence because ratios such as L_+/L_- and $q_\pm$ can apparently take on any value. This leads in principle to many types of MHD turbulence. More discussion on this will appear later. Note that even if there is not a universal decay law, there still may be interesting families of similarity decay. It's just that having more than one cascaded quantity complicates the picture. Similarity decay in three-dimensional (3D) MHD has been examined in simulations [18, 63], but usually employing only one length scale. The impact of multiple dimensionless parameters, and multiple cascades, complicates MHD and can provoke us to question whether "universality" remains a useful concept (see [168]), but this remains an open and hotly discussed issue.

On the narrower question of existence of similarity decay laws, it is interesting to note that an analogous situation occurs in two-dimensional (2D) hydrodynamics, where energy $E = \frac{1}{2}\langle u^2 \rangle$ and enstrophy $\Omega = \frac{1}{2}\langle |\nabla \times \mathbf{u}|^2 \rangle$ are both inviscid quadratic invariants, and both a direct and inverse cascade are possible [74]. This leads to interest in self-organized behavior in the long time limit of decay, which will be discussed further below in Section 6. Here, we show some evidence that this type of system can engage in a similarity decay of the direct cascaded quantity – in this case, enstrophy Ω. The system in question is a Penning trap containing a pure nonneutral electron plasma, operating in a parameter range in which the cyclotron frequency is much larger than the plasma frequency. In this regime, the equation of motion for the coarse-grained number density of electrons is identical to the vorticity equation in 2D hydrodynamics. Meanwhile, since the $E \times B$ drift velocity is divergenceless, and the electric potential due to the electron charges obeys a Poisson equation, there is an almost complete analogy between the fluid-scale electron motions in the Trap, and the equations for a 2D incompressible fluid in a circular container. See [43].

To a reasonable degree of approximation, the electron density $n(r, \theta, t)$ follows 2D, z-averaged, $\mathbf{E} \times \mathbf{B}$ drift motion [43], where

$$\mathbf{v}_D = -\frac{c\nabla\phi \times \hat{\mathbf{z}}}{B}, \qquad \nabla^2\phi = -4\pi|e|n, \tag{8}$$

where ϕ is the electrostatic potential and $\mathbf{E} = -\nabla\phi$. For this system, $\mathbf{v}_D$ is equivalent to the 2D fluid velocity $\mathbf{v}$, with the vorticity ω proportional to electron number density n, and stream function ψ proportional to $-\phi$ the potential. Because of this analogy, the evolution of the system is governed by the 2D NS equation for one-sign vorticity,

$$\frac{\partial\omega}{\partial t} + (\mathbf{v}\cdot\nabla)\omega = \nu\nabla^2\omega, \tag{9}$$

where $\mathbf{v} = \nabla\psi \times \hat{\mathbf{z}}$ and $\nabla^2\psi = -\omega$. The term involving viscosity ν is familiar in hydrodynamics but not well-motivated in the guiding center plasma case, as the dissipation mechanisms may differ significantly in NS and Penning trap cases [76].

The three-dimensionality of the real experiment must be neglected, and differences between the nonideal effects in the electron plasma and 2D hydro must be neglected. Interestingly, [140] good agreement is found in comparing 2D hydrosimulations and Penning Trap data (see Figure 1) when the boundary conditions in the simulation are chosen to be free-slip, even though there is viscous diffusion in the interior. This boundary condition corresponds to a perfect conductor, having constant potential.

Figure 1 shows important features of 2D hydro that are also analogous to features of MHD in both 2D and 3D. In particular, one sees the simultaneous formation of large-scale

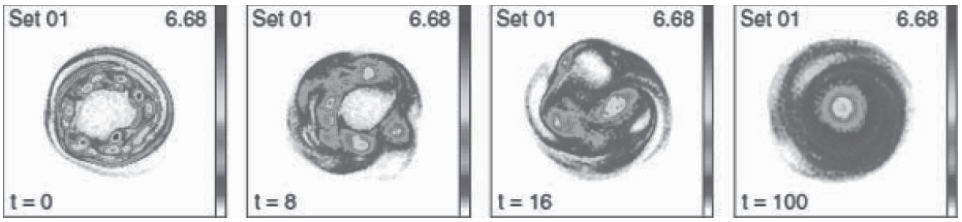


Figure 1. Vorticity images showing evolution of Penning trap data [140]. Reproduced with permission from Rodgers et al., Phys. Rev. Lett., 2010, copyright (2010) by the American Physical Society.

coherent structures that persist for long times, and the small-scale features of the cascade including small-scale (presumably) dissipative structures. In 2D hydro, the observed transfer to large scales is an inverse transfer of energy. The direct transfer to small scale is an *enstrophy cascade*. In 2D MHD, the inverse transfer is that of mean square magnetic potential [48–50, 101] and the direct cascade is an energy cascade. In 3D MHD, the direct cascade is again of energy, and when magnetic helicity if present there can be an inverse cascade. The behavior of cross-helicity is intermediate (see [158]).

If we assume a similarity decay for 2D hydrodynamics or for the Penning trap system, then it is possible to state a modified decay law that turns out to work reasonably well. The needed modification is based on the recognition that much of the vorticity distribution is somehow "destined" to be locked up in the long-lived metastable state that is eventually achieved in Penning trap relaxation (see the following section). Suppose this metastable state has an enstrophy Ω_{ms}. If one removes Ω_{ms} from the budget of enstrophy that has an impact on the direct cascade, then a similarity law can be written for the remaining "free enstrophy" Ω^{F}or excess above this long-term value [141]. To continue, assume that the global enstrophy decay timescale τ depends only on Ω^{F} and a characteristic length scale l. The only dimensionally consistent choice is $\tau = 1/\sqrt{\Omega^{\mathrm{F}}}$. This is analogous to $\tau = l/\sqrt{E}$ in 3D, where l is a correlation length. Then, free enstrophy changes in time according to $d\Omega^{\mathrm{F}}/dt = -a\,\Omega^{\mathrm{F}\frac{3}{2}}$, for which the solution is

$$\frac{\Omega^{\mathrm{F}}}{\Omega_0^{\mathrm{F}}} = \left(1 + 2\,a\,\sqrt{\Omega_0^{\mathrm{F}}}(t - t_0)\right)^{-2}. \tag{10}$$

Here, $\Omega_0^{\mathrm{F}} = \Omega^{\mathrm{F}}(t_0)$ is the initial free enstrophy. For an initially disordered fluid with large Ω_0^{F}, Equation (10) gives $\Omega^{\mathrm{F}} \sim t^{-2}$ for $a\sqrt{\Omega_0^{\mathrm{F}}}t \gg 1$, as in the isotropic case predicted by Batchelor [8]. The conditions for turbulence to be of sufficient strength to justify a similarity law such as Equation (10) are not entirely clear, although large $\Omega_0^{\mathrm{F}}/\Omega_{ms}^{\mathrm{F}}$ would seem favorable.

Figure 2 shows a test of the proposed similarity decay of free enstrophy, employing data from the University of Delaware Penning trap [105]. The final metastable state enstrophies for each experimental run were used to compute Ω_{ms}, in terms of which the free enstrophy was computed. A variety of different experimental initial conditions were used in the comparison. It is apparent that the similarity decay of free enstrophy is a reasonable hypothesis for these datasets. This is encouraging with regard to extending the von Karman–Howarth analysis to more complex systems involving more than one cascaded quantity, such as MHD in 2D and helical MHD in 3D.

4. Spectra and variability

Probably the most famous result from classical hydrodynamic turbulence theory is the inertial range spectrum in which the omnidirectional energy is distributed across a wide range of (inertial range) wavenumbers k with a power-law spectrum varying as $k^{-5/3}$. For hydrodynamic turbulence in the inertial range, the only important timescale is the local non-linear time $\tau_{nl} = (ku_k)^{-1}$ for wavenumber k and u_k the contribution to the speed from excitations near k. Then, the energy decay rate can be written $\epsilon \sim u_k^2/\tau_{sp}$, for spectral transfer time τ_{sp}. However, here the only choice is $\tau_{sp} = \tau_{nl}$, so using $u_k^2 = k\mathcal{E}(k)$ for omnidirectional energy spectrum $\mathcal{E}$, one finds the Kolmogorov spectrum $\mathcal{E}(k) = C\epsilon^{2/3}k^{-5/3}$.

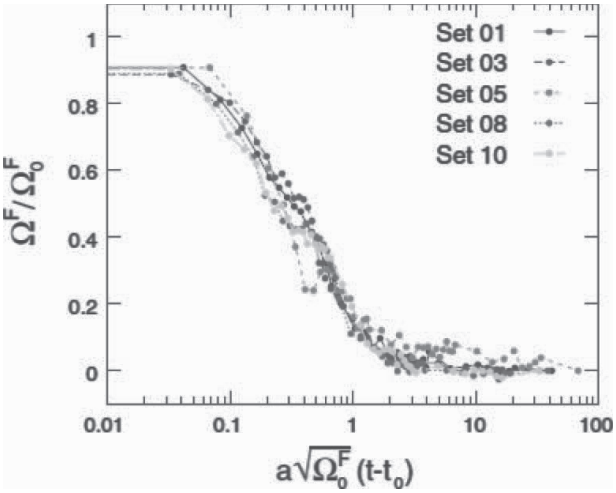


Figure 2. Scaled free enstrophy versus adjusted nonlinear time [140]. Reproduced with permission from Rodgers et al., Phys. Rev. Lett., 2010, copyright (2010) by the American Physical Society.

For MHD, the situation is complicated by the multiplicity of available time scales, thus rendering ambiguous the spectral transfer time, which could, for example, depend on both non-linear time and Alfvén time. For zero cross-helicity, let us designate the amplitude at k as $Z_k = Z_{k+} = Z_{k-}$, and write the large-scale magnetic field as B_0. This may be either externally applied, or $B_0 \sim Z$ if it is due to the large-scale fluctuations themselves. Then, for the Kolmogorov-like theory of isotropic MHD, one chooses $\tau_{sp} = \tau_{nl}$ as in the hydro case, and the Kolmogorov spectrum is reproduced with $\mathcal{E}(k) = C\epsilon^{2/3}k^{-5/3}$ being the omnidirectional spectrum of the total incompressible energy. The theory of Kraichnan [71] supposes that the k-independent transfer of energy ϵ must be in direct proportion to the triple lifetime. Then, $\epsilon = \tau_3(k)[\mathcal{E}(k)]^2k^4 = \tau_3(k)Z_k^2/\tau_{nl}^2(k)$. One notices here that the spectral transfer time in principle differs from the non-linear time, and must involve the lifetime of the triple correlations. Kraichnan chooses the triple lifetime to be the Alfvén time $\tau_3(k) = \tau_A(k)$. From this, it transpires that the energy spectrum is $\mathcal{E}(k) = C_{Kr}\epsilon^{1/2}B_0^{1/2}k^{-3/2}$. Pouquet et al. [133] made the important observation that the Alfvén time may be due to a uniform large-scale field or else the large-scale magnetic fluctuations, which have a similar influence on much smaller scale inertial range fluctuations.

For finite cross-helicity, $Z_k^+ \neq Z_k^-$. For this case and assuming a Kolmogorov-like spectral theory, the development only involves the local non-linear times scales $\tau_{nl}^{\pm}(k)$. Then (see [71, 177]), one finds that $\epsilon^{\pm} = C^{\pm}(Z_k^{\pm})^2/\tau_{nl}^{\pm} = C^{\pm}k(Z_k^{\pm})^2Z_k^{\mp} = C^{\pm}k^{5/2}E^{\pm}(k)\sqrt{E^{\mp}(k)}$. From these two relations, we conclude that the steady Kolmogorov-like high-Reynolds-number MHD energy spectra are $E^{\pm}(k) = C_{\pm}\epsilon_{\pm}^{2/3}[\epsilon_{\pm}/\epsilon_{\mp}]^{1/3}k^{-5/3}$. Thus, the non-linear time scales in the steady inertial range, can be written as $\tau_{nl}(k) \sim [C_{\pm}^{1/2}\epsilon_{\pm}^{1/3}[\epsilon_{\pm}/\epsilon_{\mp}]^{1/6}k^{2/3}]^{-1}$. We note that the Elsässer energy spectra shown in Figure 3 admit a range of wavenumbers in which the spectral form roughly varies in accord with a $k^{-5/3}$ behavior. Such wavenumber spectra are consistent with local scale-to-scale transfer dominated by nonlinearity and strain. However, the physics of time decorrelation is distinct and may still depend on other effects and therefore other available MHD time scales.

One example is the advection (or sweeping) characteristic time at scale $1/k$, which may be expressed as $\tau_{sw}(k) \sim (ku_{\rm rms})^{-1}$. Here, the root-mean-square turbulent velocity

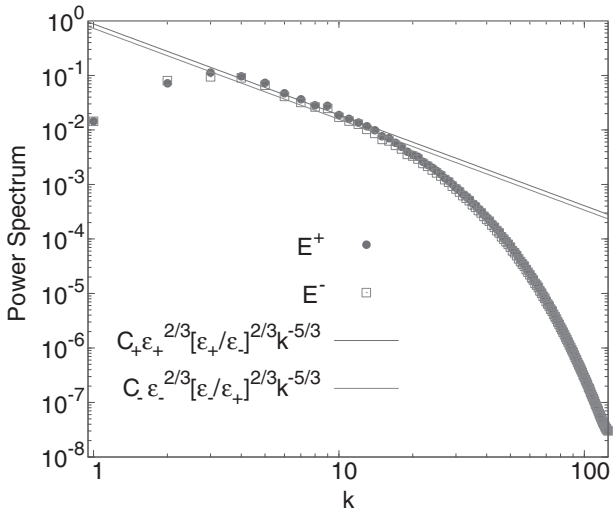


Figure 3. Elsässer energy spectral densities E^+ (blue bullets) and E^- (red open squares) as a function of the wavenumber k. The dashed lines represent (see text) $E^{\pm} = C_{\pm}\epsilon_{\pm}^{2/3}[\epsilon_{\pm}/\epsilon_{\mp}]^{2/3}k^{-5/3}$, for $C_{\pm} = 2$, $\epsilon_+ = 0.26$, and $\epsilon_- = 0.24$ [147]. Reproduced with permission from Servidio et al., Europhys. Lett., 2011, copyright (2011) by the European Physical Society.

$u_{\rm rms} = \langle |\mathbf{u}|^2 \rangle$ is a global quantity that is typically dominated by contributions from the large scales. Analogously, a characteristic Alfvèn time (averaged over direction, see [71]) can be defined as $\tau_A(k) \sim (kb_{\rm rms})^{-1}$.[1] The root-mean-square magnetic field $b_{\rm rms}$ could, in principle, include contributions from both the fluctuations as well as a mean (uniform or very large-scale) magnetic field. For the simulation employed here, $b_{\rm rms}$ is due only to fluctuations, which are assumed to have an isotropic distribution. It is worthy of note that the sweeping and Alfvénic propagation time scales both vary as $\sim k$. Finally, the viscous dissipation time is defined as $\tau_d \sim (\nu k^2)^{-1}$. In the inertial region, for reasonably small values of ν, both sweeping- and eddy-turnover times are much smaller than the diffusive time. The wavenumber λ_d at which the dissipation and nonlinear times are equal, $\tau_{nl}(1/\lambda_d) = \tau_d(1/\lambda_d)$, denotes the termination of the inertial range, and serves to define the Kolmogorov dissipation scale λ_d. Generally speaking, in high-Reynolds-number turbulence, and for wavenumbers k in the inertial range, we expect an ordering such that $\tau_{nl}(k) > \tau_{nl}^{\pm}(k) > \tau_{sw}(k) \simeq \tau_A(k) > \tau_d(k)$. Indeed, such ordering allows among other things, the possibility of quasi-equilibrium properties within the inertial range.

The topic of the "correct" inertial range power-law index for MHD turbulence is another perennially discussed hot topic. The ambiguity between Kolmogorov $-5/3$ and Kraichnan $-3/2$ scaling is often debated, and to some extent the dichotomy can be resolved simply by allowing the lifetime of the triple correlations to be a composite of several effects [133], so that

$$\frac{1}{\tau_3(k)} = \frac{1}{\tau_{nl}(k)} + \frac{1}{\tau_A(k)} + \ldots . \tag{11}$$

Indeed, using just the Alfvén and non-linear time contributions to τ_3 one can find a "spectral law" that interpolates neatly between $-5/3$ and $-3/2$ as the ratio of these two effects varies.

In the discussion of energy spectra, it is traditional to appeal to examples. As we will presently see, this is not necessarily reliable. Nevertheless, at this point, it is worthwhile to

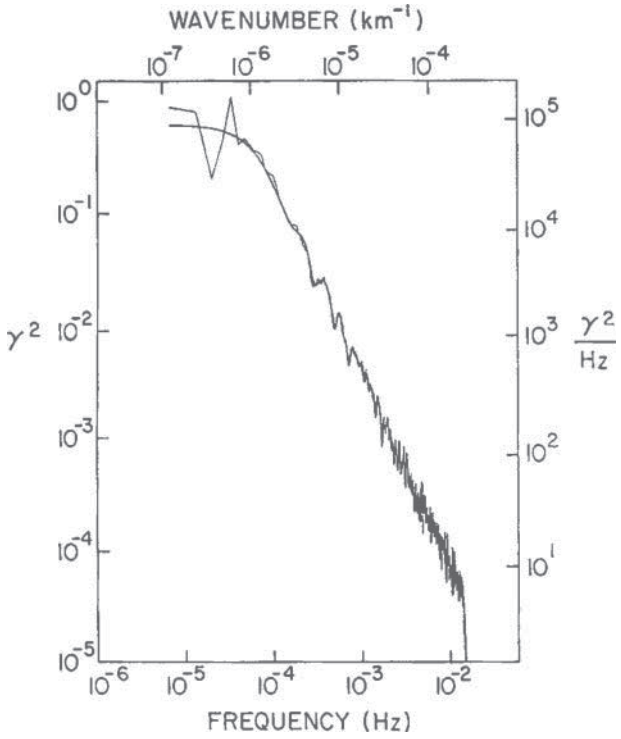


Figure 4. Magnetic energy spectrum from Voyager 2 data, taken from Matthaeus and Goldstein [90]. The spectral slope is very close to $-5/3$. Reproduced with permission from Matthaeus & Goldstein, J. Geophys. Res., 1982, copyright (1982) by the AGU.

illustrate that the observed wavenumber spectrum of magnetic fluctuations in the solar wind sometimes presents a very nice picture. Figure 4 shows an example of the one-dimensional trace magnetic field spectrum computed from an interval Voyager 2 data [91]. It is probably fair to say that this spectrum is "somewhat typical" and lies close to the $5/3$ prediction. The velocity field spectrum is often a little different [128], which is implied by the nonconstant Alfvén ratio $E_v(k)/E_b(k)$ [91]. Of course, the steady spectral prediction, assuming local transfer and ignoring intermittency (see [142]), pertains only to the ideally conserved flux of *total energy*, $u^2 + b^2$, so this disparity is not of essential concern. Furthermore, the exchange of energy between velocity and magnetic field is known to be highly nonlocal [1].

Unfortunately, the solar wind is not so cooperative in presenting a single picture that one can claim evidences universality of one theoretical formulation. For example, Vasquez et al. [163] computed wavenumber spectra using Taylor hypothesis from 960 intervals of single-spacecraft magnetic field data measured by the ACE spacecraft. The apparent inertial range spectra were fitted with a power-law $\sim f^{-q}$ in the (spacecraft frame) frequency range of 8 mHz to 0.1 Hz. The interval length used is one to several hours. The typical correlation scale, confirmed by multi-point spacecraft observation [5, 95] is about 10^6 km, which corresponds to about 40 min using a 400 km/s typical solar wind speed. Therefore, the intervals used in the Vasquez et al. study are a few correlation lengths in duration and should be long enough to obtain good estimates of the spectral index, with some spread due to finite sample size. The distribution of spectral indices q so obtained are shown in a histogram, reproduced here in Figure 5. One see that the distribution is not only approximately centered on the Kolmogorov value of 1.67, but also substantially overlaps

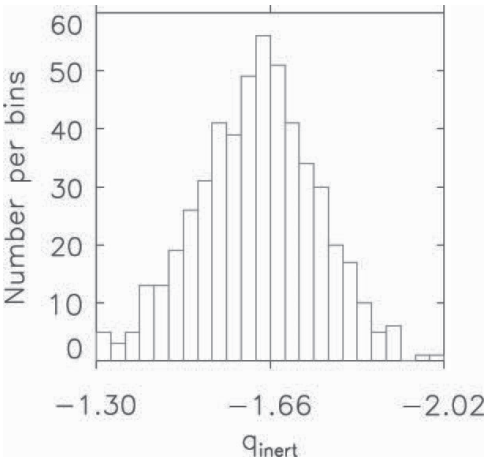


Figure 5. Histogram of the slope of the energy spectrum from solar wind data at 1 AU [162]. Reproduced with permission from Vasquez et al., J. Geophys. Res., 2007, copyright (2007) by the AGU.

with the 1.5 Kraichnan–Iroshnikov value. and has a half-width that includes values from about 1.4 to 1.8.

Of course, the solar wind is not a controlled experiment, so some of this observed variation of spectral index may be from transient events, variations and nonsteady conditions, or even non-MHD effects. Another possibility, that variation of q is due to anisotropy, is discussed later in the following section.

In contrast to the solar wind observations, computer simulations provide controlled experiments. Nevertheless, the conditions imposed in simulations can differ in subtle ways according to variations in approach, including diverse forcing functions, boundary conditions, initial conditions, ratios of length scales, etc. Another major factor is the presence and strength of an applied uniform magnetic field. All of these can influence results on the spectral distributions and inertial range spectral indices obtained in simulation. This point was emphasized in a striking way in a recent paper by Lee et al. [81]. In this study, three simulation results in 3D MHD are contrasted, each starting from approximately the same global energy, cross-helicity, and magnetic helicity, and having the same Reynolds numbers. Even the energy spectra are very similar, each initial condition being an MHD generalization of the Taylor Green vortex. When the simulations are analyzed at the time of peak dissipation, the results (see Figure 6) show very different spectra, k-dependence of Alfvén ratio, and other parameters such as the ratio of Alfvén to nonlinear times. The compensated total energy spectra are shown for these three runs, reproduced from the Lee et al. paper [81].

The kind of variability seen in the aforementioned solar wind and simulation results suggest that MHD turbulence may be rather more variable than hydrodynamic turbulence. The problem with variability runs even deeper for "inverse cascade systems" such as 2D hydro, 2D MHD, 3D MHD, the Penning trap electron plasma, and similar systems. This is because such systems have a strong tendency to accumulate excitations in a only a few of its degrees of freedom, thus setting up a system that through enhancements of nonlocal interactions, can generate low-frequency $1/f$ noise [40]. This type of scale-invariant noise is particularly frustrating to practical attempts to uncover typical or average behavior. Systems with $1/f$ noise have long time tails on temporal correlation functions that thwart attempts to invoke the classical ergodic theorem in estimating ensemble averages though time integration. Interestingly, this feature seems to be absent in homogeneous hydrodynamic turbulence, but

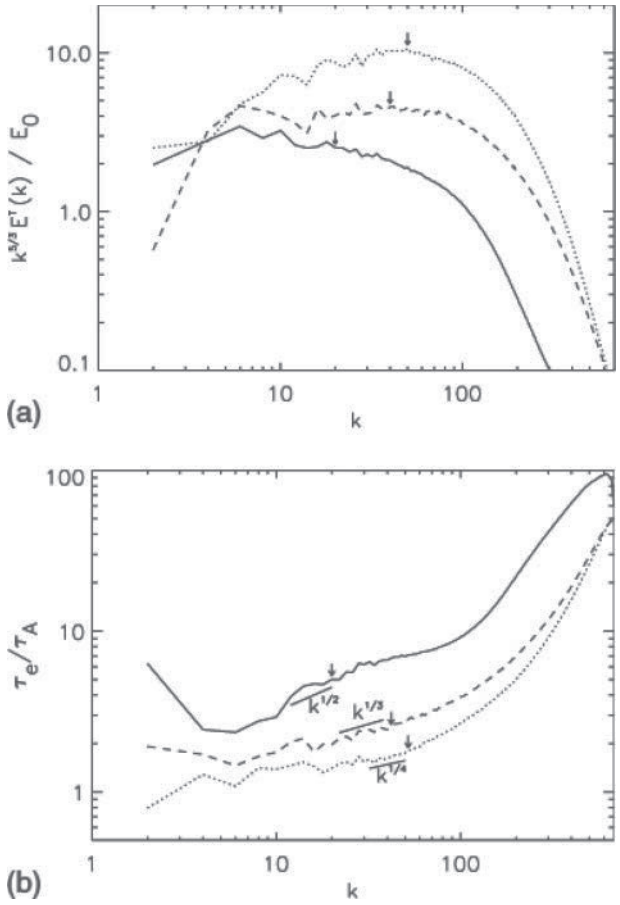


Figure 6. Total energy spectra (a) compensated by $k^{5/3}$ and averaged over $\delta t = 0.5$ (1.52 turnover times) about the maximum of dissipation and ratio of nonlinear to Alfvén time scales as a function of wave number (b) for three runs from different initial fields but with the same initial energy spectra. Slopes are given only as a reference. The three arrows indicate the magnetic Taylor scale. Note that the three spectra follow noticeably different spectral laws and possibly different scale dependence for their time scales as well [80]. Reproduced with permission from Lee et al., Phys. Rev. E., 2010, copyright (2010) by the American Physical Society.

is present in systems that admit quasi-invariants, thus emulating temporarily the properties of systems that are strictly multiple ideal invariant inverse cascade systems [41, 104]. It is of interest that $1/f$ noise is observed in dynamo experiments and in the solar wind [96, 132].

5. Anisotropy

As mentioned in the Introduction, the mean magnetic field imposes a preferred direction on MHD turbulence that cannot be removed by a Galilean transformation [71]. One of the associated effects, recognized long ago in laboratory plasma devices [139, 178] is the generation of fluctuations that maintain stronger correlation along the magnetic field than perpendicular to it. This effect was simulated first in 2D MHD [149], and later in 3D [124]. These studies showed that spectral transfer is unimpeded in the perpendicular direction in k-space, but is suppressed in the parallel direction. Non-linear couplings that pump energy

to smaller scales having larger perpendicular gradients are relatively unaffected by wave propagation effects. On the other hand, couplings that produce stronger parallel gradients are suppressed by Alfvén-wave-like couplings that become ever stronger as the mean field strength is increased. This reasoning led to a rederivation of the equations of Reduced MHD (RMHD) [156] using an expansion in a small parameter that is in effect $\epsilon = b/B_0$ [111] for r.m.s. fluctuation strength b. Order-one nonlinear couplings are found to occur for values of parallel wavenumber satisfying $k_\parallel < \epsilon k_\perp$. Thus, strong RMHD couplings occur when the large-scale perpendicular Alfvén time $1/(bk_\perp)$ is less than the parallel Alfvén time $\tau_A(k_\parallel)$, or $bk_\perp > B_0 k_\parallel$ [173]. Later, Goldreich and Sridhar [54] in effect refined this condition by employing the local non-linear time $\tau_{nl}(k) = 1/(b_k k_\perp)$ instead of the transverse Alfvén time $1/(bk_\perp)$, and assuming steady state turbulence. The marginal condition for RMHD then becomes $b_k k_\perp \sim B_0 k_\parallel$, which is known as "critical balance."

Independent of details, all of the above experimental, theoretical, and simulation results point toward the preference of MHD turbulence to excite more strongly those fluctuations that have stronger perpendicular, rather than parallel, gradients.

Evidence has also been accumulating that the solar wind contains a strong admixture of fluctuations that are in the above sense, quasi-two-dimensional [58]. There are a number of ways by which solar wind anisotropy can be measured. One approach [93] is to measure a large number of two-point correlation functions (employing the Taylor hypothesis) at 1AU, with the radial direction, along which the observations are made, varying from interval-to-interval relative to the mean magnetic field direction. After accumulating the estimates, assuming axisymmetry about the mean field, and averaging, the result is the so-called Maltese cross-correlation, shown in Figure 7. This observation led to use of a "two-component model" for solar wind fluctuations that no only proved useful in scattering theory and observations [14,148] but also led to direct observational tests of anisotropy [15] which confirmed that this parameterization of anisotropy corresponds reasonably well to observed solar wind properties. It is also interesting that considerations of the low-Mach-number approach to incompressibility in MHD at low to moderate plasma beta (thermal pressure over magnetic pressure) gives rise in a natural way to geometrical restrictions that correspond directly to the two-component model [174].

6. Global relaxation

It has been recognized for quite some time that the magnetic field plays a special role in electrodynamics, leading the possibility of global relaxation processes that favor special final states (e.g., [34,170,179]). This approach gained favor in the 1970s when Taylor [159,160] offered a physically motivated explanation for relaxation to force-free states in Reversed Field Pinch experiments, often regarded, along with spheromaks [26] as the canonical laboratory devices for observation of MHD activity. This revival of relaxation theory occurred almost simultaneously with the description of inverse cascade in 3D MHD, driven by finite magnetic helicity [46]. The inverse cascade phenomenon in driven MHD is associated with the requirement that the nonlinear couplings must simultaneous conserve two ideal invariants, the energy E and magnetic helicity H_m. In analogy to its 2D hydrodynamic antecedent [72], the transfer of turbulent excitation to higher wavenumber is accompanied by a concomitant transfer to lower wavenumbers, in order to simultaneously respect both conservation laws.

It is possible to establish the possibility of inverse cascade in a system such as 3D MHD by appeal to the absolute equilibrium Gibbs ensemble for an ideal Fourier Galerkin representation of the system, having a finite number of degrees of freedom, and exact set of quadratic conservation laws, and a Liouville theorem for maintenance of the canonical

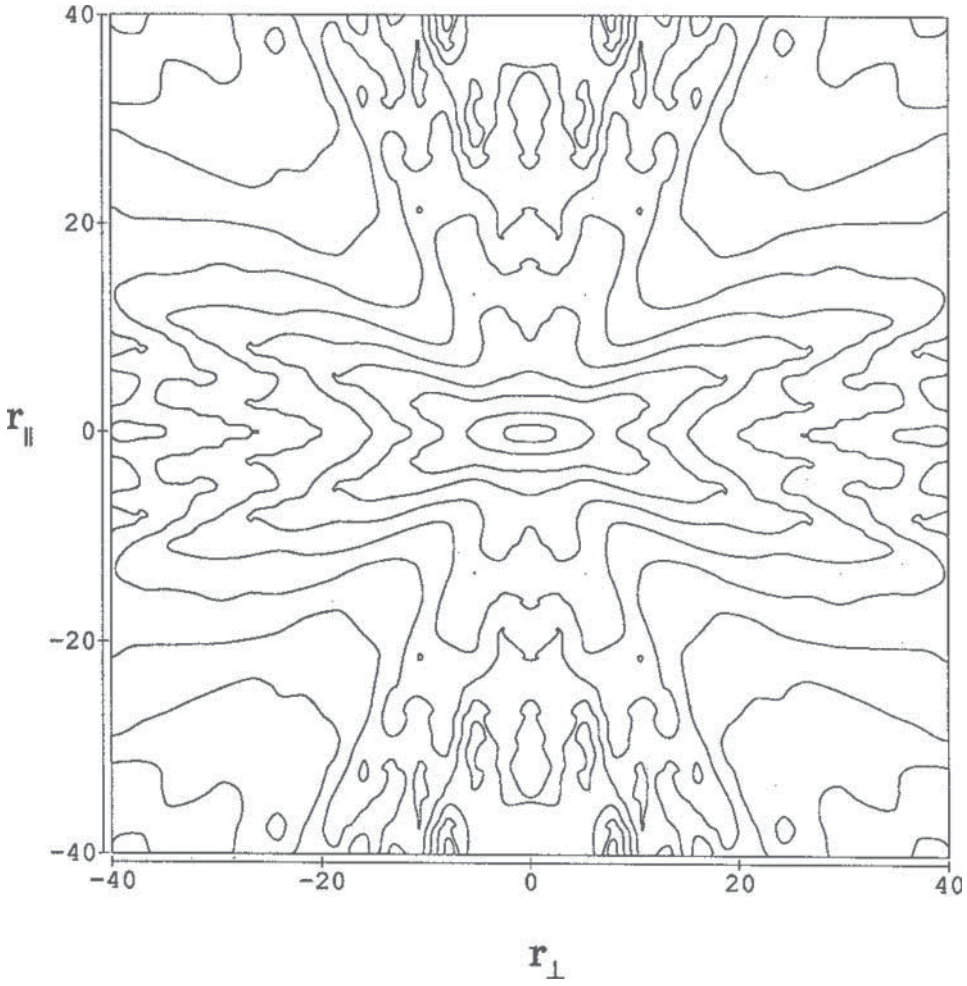


Figure 7. Two-point autocorrelation of the magnetic field $\mathbf{b} \cdot \mathbf{b}'$ as a function of coordinates parallel, and perpendicular, the mean magnetic field (axisymmetry assumed) in the solar wind at 1AU from $\approx$ 600 days of ISEE-3 data. (From [93]). Reproduced with permission from Matthaeus et al., J. Geophys. Res., 1990, copyright (1990) by the AGU.

Gibbsian distribution [46, 72, 80, 145, 157]. When "Bose condensation" of a quantity into the longest allowed wavelength modes occurs for the Galerkin system as its number of included modes tends toward infinity, this is taken to be indicative of an inverse cascade for the corresponding driven dissipative system. This activity has led to identification of inverse cascades in 2D hydro, 3D MHD, 2D MHD, 3D Hall MHD, drift wave turbulence, and other systems.

Adaptation of the same physical reasoning to the case of decaying turbulence, leads to a set of *selective decay* principles [19, 90, 109, 110] that describe potential relaxed states of an MHD turbulent system. Schematically, if A is an inverse cascaded quantity and E a direct cascade quantity, then the selective decay principle predicts that spectral transfer leads to minimization of the ratio E/A, subject possibly to auxiliary constraints, and often limited by allowed eigenmode structure (i.e., geometry). Selective decay is a broad dynamical

relaxation principle that accounts for behavior such as Taylor relaxation and the tendency for 2D MHD and hydro to evolve toward states characterized by long-lived large-scale structures.

Searching for numerical evidence in MHD in support of selective decay led to the realization that there can be competing relaxation processes in MHD turbulence. Selective decay involves the energy and the magnetic invariant, but what about the third invariant, the cross-helicity H_c?

It has long been known that minimizing energy subject to constant H_c leads to what are sometimes called large-amplitude Alfvén waves, or "Alfvénic states" [6, 7, 106, 125]. Note that here familiar Alfvénic units are used. For incompressible MHD, these states are described by $\mathbf{v} = \mathbf{b}$ at all points in space, or $\mathbf{v} = -\mathbf{b}$ at all points. These states (if permitted by boundary conditions) persist for all time in the absence of dissipation, as they lead to a full cancellation of the non-linear terms. The same solutions survive if a uniform mean magnetic field $\mathbf{B}_0$) is added to the fluctuation $\mathbf{b}$; for that case, the solutions propagate either along $\mathbf{v} = \mathbf{b}$ the $\mathbf{B}_0$ direction, or antiparallel to it ($\mathbf{v} = -\mathbf{b}$).

Large-amplitude Alfvénic states are in fact one of the defining characteristics of observed solar wind turbulence and are frequently observed [9–12, 27, 29], especially in the inner heliosphere. A classic example of Alfvénic turbulence in the solar wind from the Belcher and Davis paper is shown in Figure 8.

Based on the special position occupied by Alfvénic solutions, and their observation in space, Dobrowolney et al. [42] predicted that these states should emerge dynamically from MHD turbulence. This was verified in closure theory [55], and subsequently seen to emerge from turbulence evolution in 3D simulations [134] and in 2D simulations [92] (see Figure 9). It is interesting to note that Alfvénic states appear to emerge from a *dynamic*

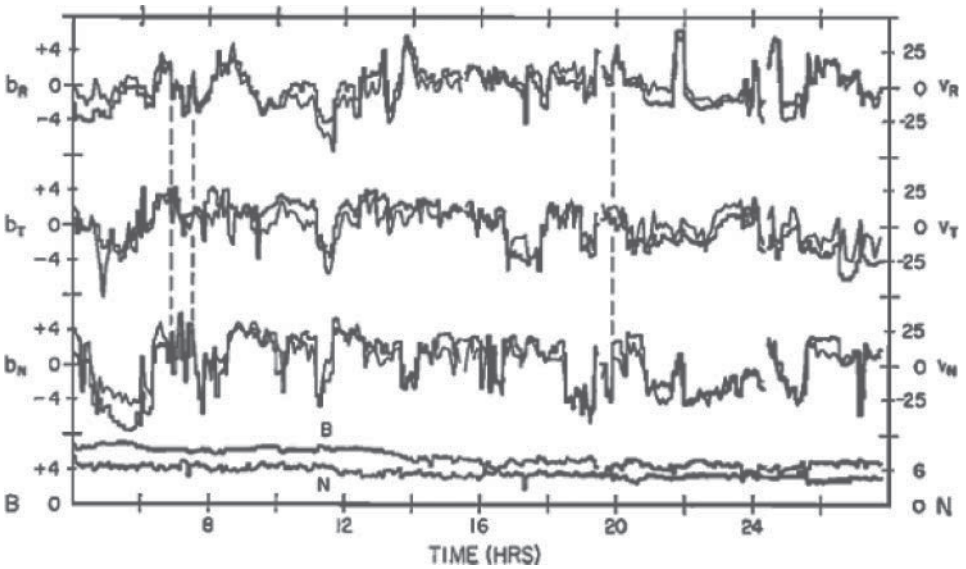


Figure 8. Twenty-four hours of magnetic field and plasma data demonstrating the presence of nearly pure Alfvén waves. The upper six curves are 5.04-min bulk velocity components in km/s (diagonal lines) and magnetic field components averaged over the plasma probe sampling period, in gammas (horizontal and vertical lines). The lower two curves are magnetic field strength and proton number density [12]. Reproduced with permission from Belcher & Davis, J. Geophys. Res., 1971, copyright (1971) by the AGU.

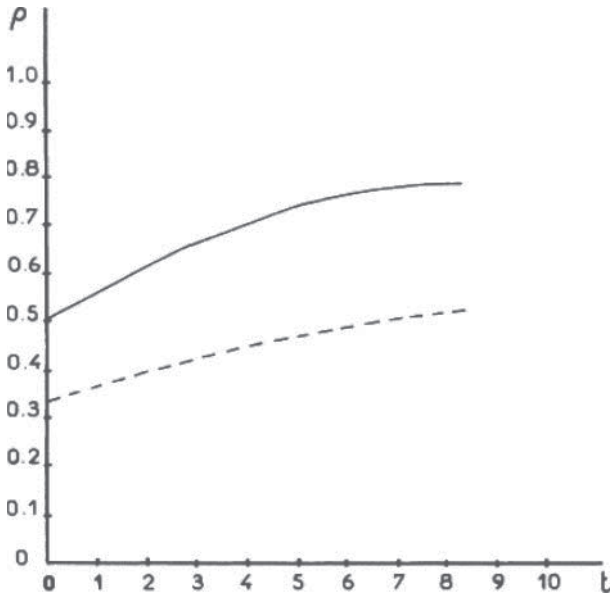


Figure 9. Evolution of the normalized cross-helicity ρ. Dashed line, random initial conditions; solid line, Orszag–Tang vortex [133]. Reproduced with permission from Pouquet et al., Phys. Rev. A., 1986, copyright (1986) by the American Physical Society.

alignment process that can be globally described by minimizing E for a specified H_c, or minimizing $\langle \mathbf{u}^2 + \mathbf{b}^2 \rangle / \langle \mathbf{u} \cdot \mathbf{b} \rangle$.

In the 1980s, with evidence emerging in simulations and experiments that magnetic-invariant-driven relaxation such as selective decay indeed occurs, while also the solar wind and other simulation results supporting dynamic alignment, the natural question to ask was whether both can be realized. Unfortunately, the answer is immediately seen to be negative, as can easily be demonstrated. 3D MHD selective decay (or Taylor relaxation) requires minimizing $E/H_m = (E_v + E_b)/H_m$. This clearly requires that $E_v = (1/2)\langle u^2 \rangle \to 0$. Therefore, one cannot also require that $\mathbf{u} = \pm \mathbf{b}$ unless both fields vanish.

How close can one get to states that compromise between the two principles? Ting et al. [161] examined this issue in 2D MHD using simulations and developed an explanation for observed final states based on minimizing energy subject to conservation of both the magnetic invariant A and the cross-helicity H_c. The three-dimensional version of this study was later carried out [158], using the same approach as employed by Ting et al. for 2D. The constrained minimum energy states [119, 158, 161], incorporating constraints from both selective decay and dynamic alignment principles, are determined from the variational problem

$$\delta \int [(|\boldsymbol{v}|^2 + |\boldsymbol{b}|^2) - \alpha_1 \boldsymbol{v} \cdot \boldsymbol{b} - \alpha_2 \boldsymbol{a} \cdot \boldsymbol{b}] d^3x = 0, \tag{12}$$

where α_i are Lagrange multipliers. The aforementioned Euler–Lagrange equation implies that in the relaxed (long-time) state, equilibrium is characterized by long-wavelength states that have the properties that

$$A_1 \boldsymbol{v} = A_2 \boldsymbol{b} = A_3 \boldsymbol{j} = A_4 \boldsymbol{\omega}, \tag{13}$$

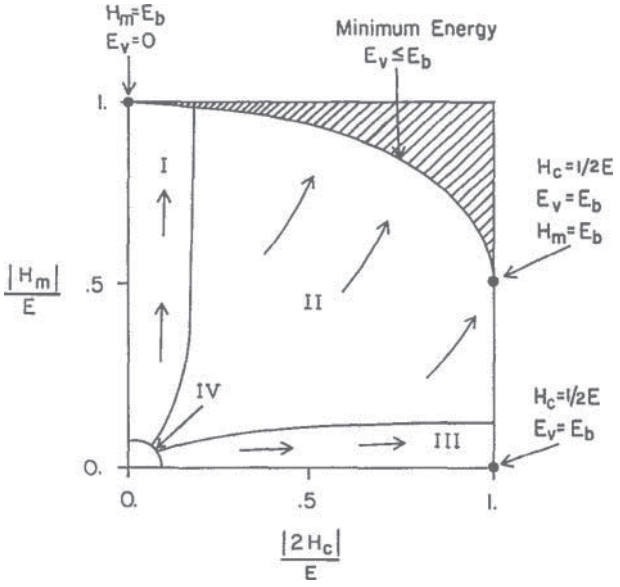


Figure 10. Parameter space for evolution of 3D MHD spanned by axes that measure the ratios H_m/E (indicative of selective decay) and H_c/E (indicative of dynamic alignment). Evolution of a large number of simulations (a few are shown) demonstrates that most cases evolve toward the extremal curve that is analytically computed by minimizing energy subject to constancy of both H_m and H_c [158]. Reproduced with permission from Striling & Matthaeus, Phys. Fluids B, 1991, copyright (1991) by the American Institute of Physics.

where A_1, A_2, A_3, and A_4 are constants related to the Lagrange multipliers, and $\boldsymbol{a}$ is the potential vector ($\boldsymbol{b} = \nabla \times \boldsymbol{a}$), $\boldsymbol{j} = \nabla \times \boldsymbol{b}$ is the current density, and $\boldsymbol{\omega} = \nabla \times \boldsymbol{v}$ is the vorticity. It is noteworthy that this principle predicts the parameter space curve (as illustrated in Figure 10) toward which most numerically computed solutions eventually evolve.

The empirical demonstration that many simulation cases evolve toward the constrained minimum energy curve is rather interesting, but falls short of being a predictive theory in a few ways. First, there is no definitive way to determine precisely the position on the minimum energy curve to which a particular simulation will evolve. Second, some simulations do not evolve toward the curve, but rather get "lost" in the middle of the space, exhausting their energy before they can evolve to a boundary. Others evolve toward the small region near the origin labeled "IV" in Figure 10 which is characterized by a vanishing magnetic field. This "hydrodynamic region" of behavior seems to be attained by turbulence with large-scale, strong velocity shears. If sufficiently dominant, the strong velocity field might drive zero cross-helicity fluctuations into the inertial range, thus destroying eventually the initial H_c. If the magnetic helicity is insufficient to produce a strong selective decay effect, this high shear turbulence can evolve toward a "hydrodynamic-like" state. It is interesting that the highly Alfvénic states observed in the inner heliosphere [12] eventually evolve toward *lower* cross-helicity as observed at 1AU and beyond [137]. One explanation offered for this [138] is that the shear associated with high-speed–low-speed stream interfaces destroys the cross-helicity, as in the aforementioned Region IV behavior. This addresses why the solar wind apparently does not dynamically align.

It is apparent that selective decay and dynamic alignment are powerful but imperfect (or at least incomplete) principle for understanding relaxation in MHD. Efforts to describe

turbulent relaxation as precisely as possible some time ago once again turned attention to the related field of 2D incompressible. Very long simulation runs in 2D periodic geometry showed that the system approached the selective decay state with regard to some metrics, but slowly [94] in part due to the tendency of isolated vortices to form [20, 98]. As vortices merge, with bursts of turbulent activity, the system ever more slowly approaches the target state of selective decay. Further quantitative study revealed [112, 113] that another principle, i.e., that of *maximum entropy*, is an even better descriptor of the relaxation. In this, one postulates an entropy of the form

$$S = -\int \omega_+ \log \omega_+ \, d^2x - \int \omega_- \log \omega_- \, d^2x, \tag{14}$$

where $\omega = \omega_+ - \omega_-$, while $\omega_+ \geq 0$ and $\omega_- \geq 0$. This allows for addition of the same arbitrary constant to both $\omega_\pm$, but for a "minimalist" prescription with $\omega_+\omega_- = 0$ everywhere initially. At that moment, the aforementioned definition reduces to $S = -\int |\omega| \log |\omega| \mathrm{d}^2x$, while the full prescription in Equation (14) is appropriate for the time-dependent problem [112]. Upon employing standard variational methods, it is possible to derive an equation for the maximum entropy subject to the constraint of constant energy and signed flux (see [112]). The "sinh-Poisson" equation that describes this relaxed state had been derived earlier using a discrete line vortex representation [108], and the applicability of that approach to decaying viscous continuum 2D turbulence was revived following these computations (see, e.g., [21, 22, 135, 136]). It is noteworthy that the correlation coefficient of the time-dependent computed solution with the selective decay state in these kinds of numerical experiments eventually exceeds 90 or 95%, but the correlation with the maximum entropy state has been measured to be as high as 0.995. By now, this experiment has been repeated numerous times.

One may of course wonder how robust this result is for various 2D hydro systems, parameters, and initial conditions, and in view of prior experience with relaxation in 2D MHD this would seem prudent. In fact, Huang and Driscoll [64] reported an experimental observation that selective decay is more accurate than maximum entropy as a predictor of an observed metastable state in the 2D hydro-like Penning trap electron fluid. Rodgers et al. [140] reexamined this conclusion using a series of initial conditions for the electron trap experiments that varied in their initial complexity and turbulence level. An example of one such initial condition is shown in the left panel of Figure 1. The conclusion was given that, for these particular experiments, the maximum entropy description worked at least as well as selective decay, the two descriptions being about equivalent at low levels of initial turbulence. For smaller scale more complex initial data, the maximum entropy description became progressively more favored. There is the additional element of complex plasma physics involved in these electron experiments, so the results may be considered interesting, but not conclusive in the realm of fluid theory. However, it is noteworthy that in both MHD and in 2D hydro, there is evidence that the distinct relaxation processes may be operative and may compete, sometimes with one only slightly favored in the evolution. Furthermore, initial data appear to be a significant factor in guiding the eventual relaxation.

The fact that a maximum entropy theory is a slightly better predictor of the final state than is selective decay in 2D hydro is noteworthy in itself and may be viewed as ample motivation to find suitable maximum entropy theories and predictions for 2D MHD and 3D MHD. However, in spite of some beginnings toward this type of theory (e.g., [110]), there has not yet been to our knowledge a convincing demonstration of maximum entropy in MHD turbulence.

The aforementioned lack of clarity regarding relaxation and maximum entropy has persisted for several decades in spite of heavy mathematical methods that have been brought to bear on the subject of fluid entropies (e.g., [51]). The latter reference demonstrated in a rather abstract mathematical way that solutions of the Navier–Stokes equations with a single signed vorticity after long times, approach an Oseen vortex solution that is related to a maximum entropy functional such as that given earlier. A recent publication clarified this conclusion in a way perhaps more accessible to physicists [115]. Temporarily adopting the notation of that paper, we can consider solutions of the Navier–Stokes equation in infinite 2D space without boundaries and initially a single sign of vorticity. Suppose then that the entropy Equation (14) is maximized subject to conservation of integrated vorticity

$$\Omega \equiv \int \omega \, d^2x = \text{const} \tag{15}$$

and the relation

$$\Gamma \equiv \int \frac{\omega r^2}{t} d^2x = 4\nu\Omega + \frac{1}{t}\int r^2\omega_0 \, d^2x, \tag{16}$$

which from the equation of motion, is independent of time. It is possible then to show that constrained maximum entropy solutions are of the form

$$\omega = \frac{\Omega^2}{\pi\Gamma t} \exp\left[-\Omega r^2/\Gamma t\right]. \tag{17}$$

Then, as t becomes large, $\Gamma \to 4\nu\Omega$, and one finds

$$\omega \underset{t\to\infty}{\Rightarrow} \frac{\Omega}{4\pi\nu t} \exp\left[\frac{-r^2}{4\nu t}\right], \tag{18}$$

which has the form of the standard Oseen vortex solution of the Navier–Stokes equation. This calculation shows that at least for this one simple case, a maximum entropy solution will emerge at long times. It may be the only case for which a unique solution to the turbulent relaxation question is known.

At this point, it may be worthwhile to remark upon boundary conditions and how they might affect the evolution of turbulence, particularly in computations. It has become an almost unquestioned article of faith that the important features of turbulence can be recovered by imposing rectangular periodic boundary conditions of sufficiently high resolution. This has been true even though some investigators were aware that periodicity imposed some undesirable limitations: for example, they prohibit the existence of any net flux of vorticity or electric current to pass through the computational volume, and have other drawbacks [114]. In recent years, there have been some decaying 2D turbulence computations that have revealed strong differences in their late time evolution that are different for differing boundary conditions. In addition to the unbounded, relaxing Oseen vortex calculation just described, there have been 2D decaying turbulent computations that have shown widely different results for no-slip circular boundaries [83, 84], no-slip rectangular boundaries [36, 59], free-slip circular boundaries [140], and stress-free circular boundaries [84]. All these have been for Navier–Stokes situations, and MHD analogs are only beginning to be explored. It seems clear that there are vast regimes in turbulence situations

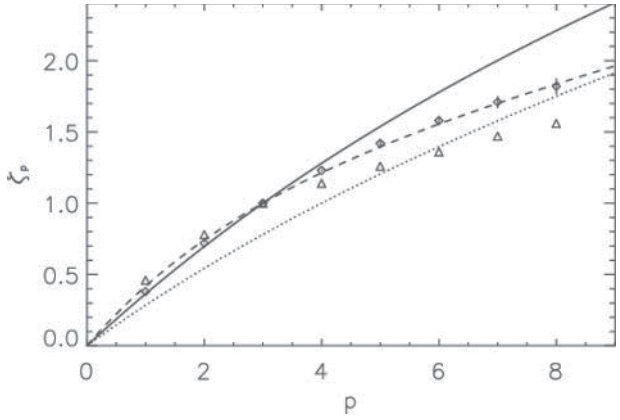


Figure 11. Scaling exponents ζ_p for 3D MHD turbulence (diamonds) and relative exponents ζ_p/ζ_3 for 2D MHD turbulence (triangles). The continuous curve is the She–Leveque model, the dashed curve the modified model for MHD, and the dotted line the IK model. (Muller & Biskamp, PRL, 2000) Reproduced with permission from Biskamp & Muller, Phys. Plasmas, 2000, copyright (2000) by the American Institute of Physics.

where boundary condition effects strongly affect the evolution of the turbulent field in ways that cannot be captured with rectangular periodic assumptions and theories that assume homogeneity and isotropy. It may be expected to be inevitable that less emphasis will be placed on Fourier spectra and dimensional analysis for bounded problems.

7. Intermittency, discontinuities and magnetic structures

Simulations of magnetohydrodynamic (MHD) turbulence [17, 131] and solar wind observations [32, 61, 87, 153] each show evidence for intermittency in the form of characteristic small-scale structures. A familiar, theoretically motivated approach to characterizing

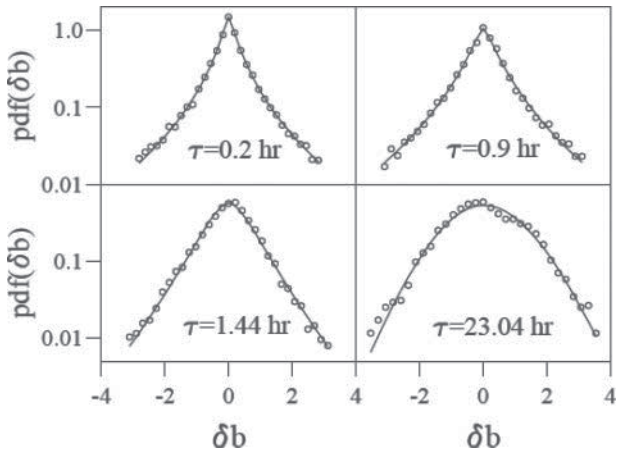


Figure 12. The scaling behavior of the PdF for δb as calculated from the experimental data (white symbols) in the fast streams. The full lines represent the fit obtained through a model [152]. Reproduced with permission from Sorriso-Valvo et al., Geophs. Res. Lett., 1999, copyright (1999) by the AGU.

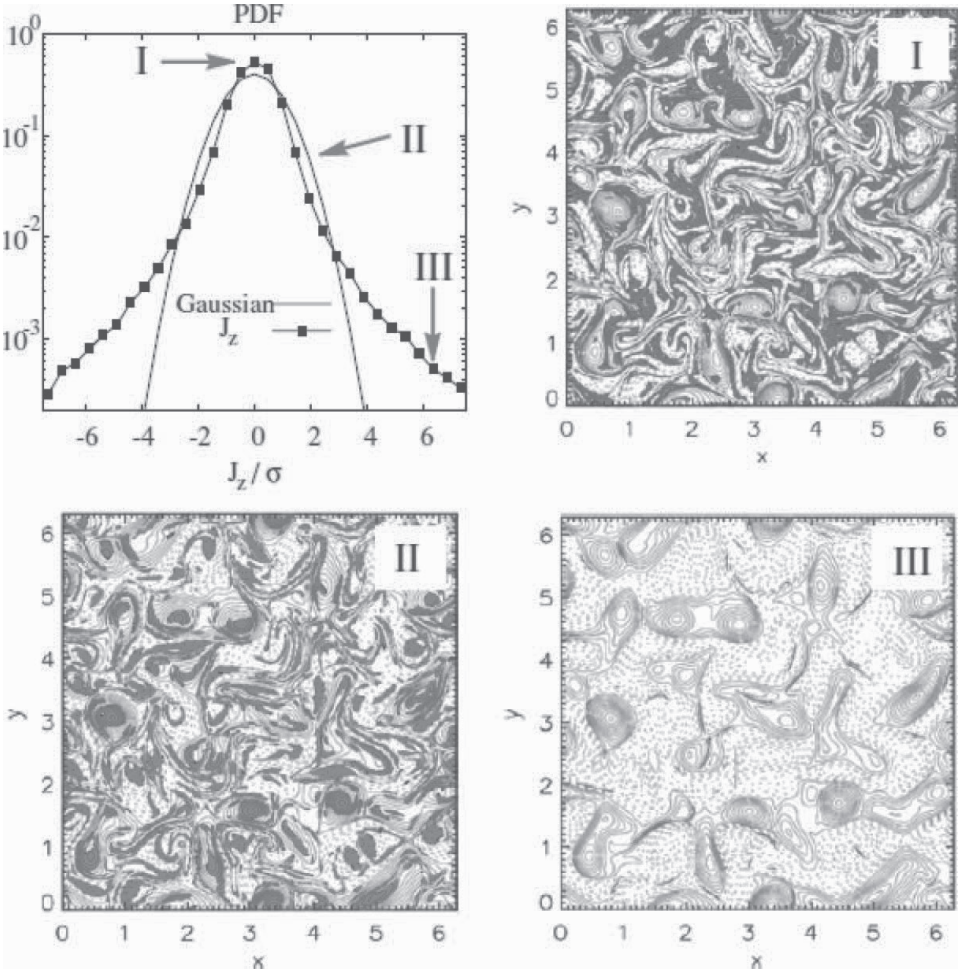


Figure 13. PDF of the out-of-plane electric current density J_z from the 2D simulation, compared to a reference Gaussian (standard deviation σ). For each region I, II, and III, magnetic field lines (contours of constant magnetic potential A_z: >0 solid, <0 dashed) are shown; the colored (red) regions are places where the selected band (I, II, or III) contributes [56]. Reproduced with permission from Greco et al., Astrophys. J., 2009, copyright (2009) by the AAS.

intermittency is to examine the scaling of the exponents of the higher order structure functions. Examples are shown here from MHD simulation, in Figure 11, and from solar wind observations, in Figure 12. These scalings can be studied on their own, but, as our hydrodynamics colleagues remind us [154], the significance of these scalings is that they correspond in some way to *structure* and *enhanced dissipation.* For 2D MHD, it is fairly easy to visualize this association. The highly dissipative coherent structures can be identified as current sheets that form dynamically between interacting magnetic islands [16, 33, 90, 129, 164]. Figure 13 demonstrates how the non-Gaussian tails of the current distribution in a 2D MHD simulation correspond to strong current sheets of this type. This is less easy to demonstrate in 3D and in the solar wind.

To pursue understanding intermittency in MHD and in the solar wind, a reasonable hypothesis is that the well-known frequent appearance of structures traditionally identified as magnetic discontinuities [30, 162] are related to intermittency of turbulence. As a

preliminary step, a recent simulation study [56] showed intermittency- and discontinuity-identification methods, and concluded that a substantial fraction of the observed discontinuities may be related to flux tube boundaries and intermittent structures that appear spontaneously in MHD turbulence [33, 90, 129, 144, 163, 164].

A well-known feature of solar wind observations is, in fact, the appearance of sudden changes in the magnetic field vector, defined as directional discontinuities (DDs), which are detected throughout the heliosphere [28, 30, 116, 117, 153, 162]. These changes are often seen at time scales of 3–5 min, although similar discontinuities are seen at smaller time scales [163]. One interpretation of magnetic discontinuities is that they are the walls between filamentary structures of a discontinuous solar wind plasma [28, 31]. An alternative possibility is that the observed discontinuities are the current sheets that form as a consequence of the MHD turbulent cascade [90, 165]. Recent studies on magnetic discontinuities show that their statistical properties are very similar to distributions obtained from simulations of MHD turbulence [56, 57]. This line of reasoning argues that thin current sheets are characteristic coherent structures expected in active intermittent 2D and 3D MHD turbulence [102], and which are therefore integral to the dynamical couplings across scales.

In order to establish a link between solar wind discontinuities and spatial patches of strong current sheets, we illustrate here a comparison between solar wind datasets and direct numerical simulations of MHD. Regarding the simulations, we focus on properties of discontinuities that are recorded by magnetic field measurements at a single spacecraft in interplanetary space. We adopt a spacecraft-like sampling through the simulation domain (see Greco et al. [56]), interpolating the magnetic field data along the one-dimensional path s, so we can identify discontinuities (TDs) with the following procedure:

(1) First, to describe rapid changes in the magnetic field, we look at the increments

$$\Delta \boldsymbol{b}(s, \Delta s) = \boldsymbol{b}(s + \Delta s) - \boldsymbol{b}(s), \tag{19}$$

where Δs the spatial separation or lag. For this simulation, we choose a small-scale lag, $\Delta s \simeq 0.67\lambda_{diss}$, which is comparable to the turbulence dissipation scales (see previous sections).

(2) Second, employing only the sequence of magnetic increments, we compute the normalized magnitude

$$\Im(\Delta s, \ell, s) = \frac{|\Delta \boldsymbol{b}(s, \Delta s)|}{\sqrt{\langle |\Delta \boldsymbol{b}(s, \Delta s)|^2 \rangle_\ell}}, \tag{20}$$

where $\langle \bullet \rangle_\ell = (1/\ell) \int_\ell \bullet \, ds$ denotes a spatial average over an interval of length ℓ, and Δs is the spatial lag in Equation (19). The square of the above quantity has been called the *Partial Variance of Increments* (PVI) [56] and the method abbreviated as the PVI method. For the numerical analysis performed here, $\ell \simeq 535\lambda_C$, where $\lambda_C = 0.18$ is the turbulence correlation length – a natural scale for computing averages.

The PVI time series, evaluated using Equations (19) and (20), is reported in Figure 14. The illustration spans more than 500 correlation lengths. This spatial signal has been compared to a time signal measured by the ACE solar wind spacecraft [150], near 1 AU, over a period of about 20 days (lower panel of the figure). In order to facilitate the

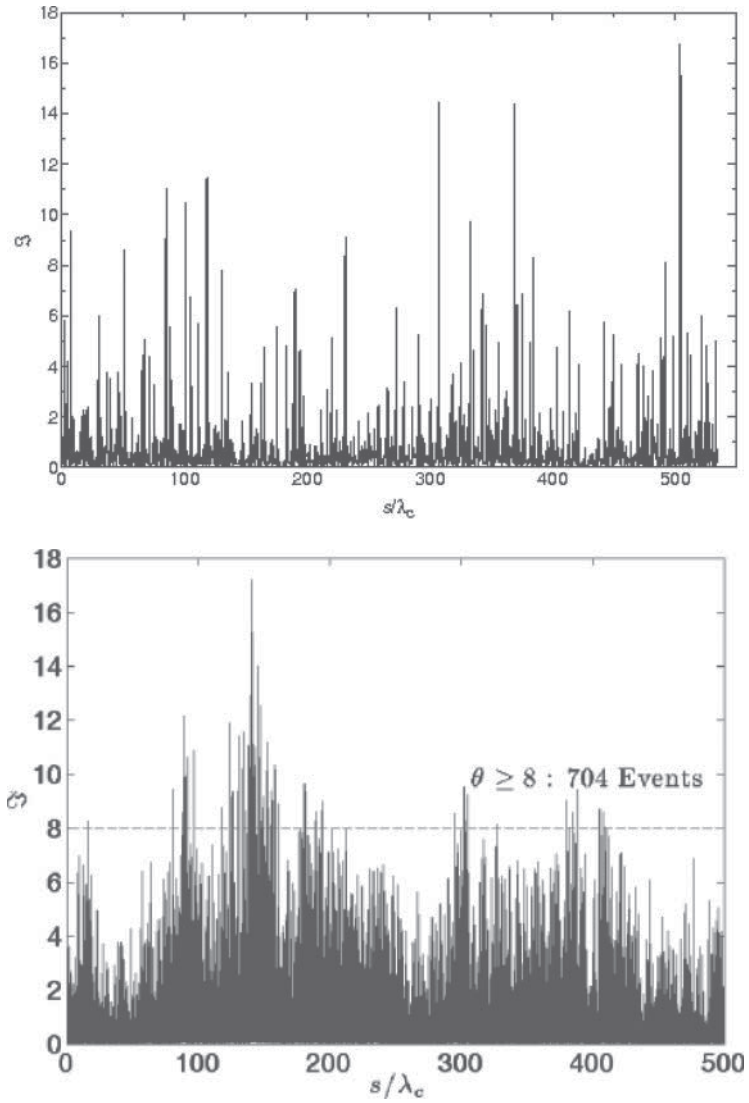


Figure 14. Top: Spatial signal $\Im(\Delta s, \ell, s)$ (PVI) obtained from the simulation by sampling along the trajectory s in the simulation box, with $\Delta s \simeq 0.67\lambda_d$ and $\ell \simeq 535\lambda_C$. Bottom: Same quantity obtained from solar wind data, with $\Delta s = 20$ s and $\ell \simeq 500\lambda_C$.

comparison, we converted the time signal to a spatial signal, using the average velocity of the flow, and then normalized to a solar wind magnetic correlation length of 1.2×10^6 km.

The PVI increment time series is bursty, suggesting the presence of sharp gradients and localized coherent structures in the magnetic field that represent the spatial intermittency of turbulence. These events may correspond to what are qualitatively called "tangential discontinuities" and, possibly, sites of enhanced dissipation and magnetic reconnection.

Imposing a threshold θ on Equation (20), a collection of stronger discontinuities along the path s can be identified. That is, we select portions of the trajectory in which the

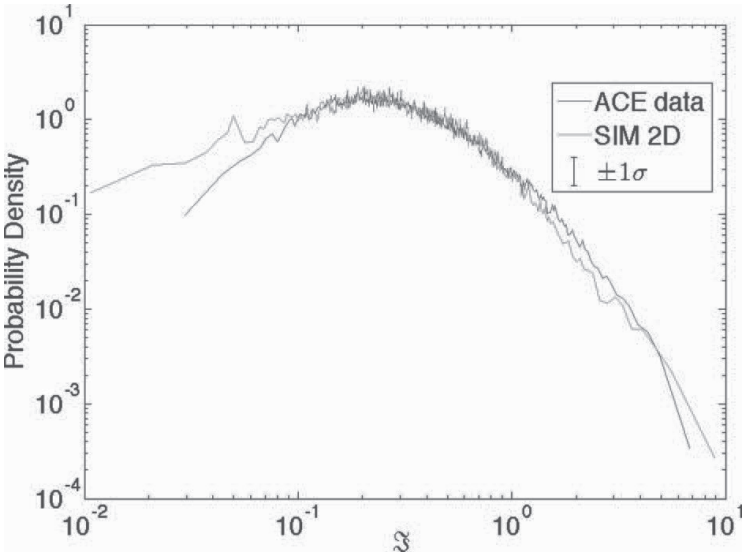


Figure 15. Probability density function of the spatial signal $\Im$ (PVI) obtained from ACE measurements (blue line) and simulation (red line). The error bar $\pm\sigma$ is displayed in the legend and the value of σ is the expected fractional error in the PDF due to counting statistics.

condition

$$\Im(\Delta s, \ell, s) > \theta \tag{21}$$

is satisfied, and we will employ this condition to identify candidate coherent structures and potential reconnection sites. To understand the physical meaning of the threshold θ, we recall from [56, 57] that the probability distribution of the PVI statistic derived from a non-Gaussian turbulent signal is empirically found to strongly deviate from the pdf of PVI computed from a Gaussian signal, for values of PVI greater than about 3. As PVI increases to values of 4 or more, the recorded "events" are extremely likely to be associated with coherent structures and therefore inconsistent with a signal having random phases. Thus, as θ is increased, stronger and more rare events are identified, associated with highly non-Gaussian coherent structures.

Finally, in Figure 15, we show the probability distribution functions of the PVI signal for both the observational and simulation data. The comparison tells us that there is a great similarity within the errors [121].

8. Local relaxation and nongaussianity

The two central features of MHD turbulence discussed in the last two sections are generally studied independently: intermittency of inertial range fluctuations, and MHD relaxation processes. The first manifests through the appearance of high kurtosis of vorticity and current, multifractal scaling of moments, and inhomogeneous dissipation of energy (in space). The second is characterized by distinctive states such as Taylor relaxation, selective decay, global dynamic alignment, and helical dynamo action [90, 100, 119, 158, 159, 161]. As described earlier, relaxation has most often been viewed as a consequence of multiple

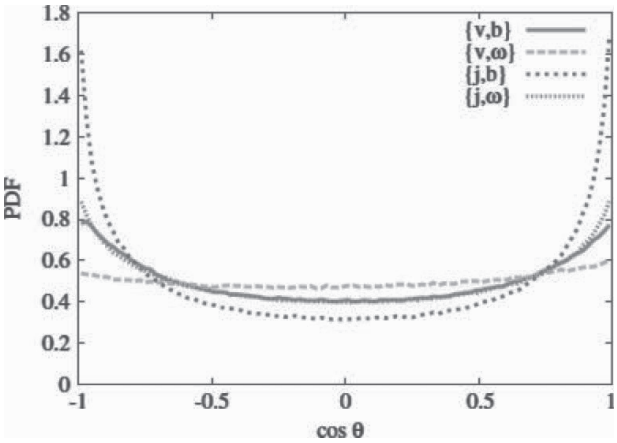


Figure 16. PDFs of the cosine of the angle for the sets of field. (Servidio et al., PRL, 2008) The sets of fields are: $\{\boldsymbol{v}, \boldsymbol{b}\}$ (red), $\{\boldsymbol{v}, \boldsymbol{\omega}\}$ (green), $\{\boldsymbol{j}, \boldsymbol{b}\}$ (blue), $\{\boldsymbol{j}, \boldsymbol{\omega}\}$ (pink). Reproduced with permission from Servidio et al., Phys. Rev. Lett., 2008, copyright (2008) by the American Physical Society.

global ideal conservation principles, characterized by dynamical times much longer than the characteristic times of intermittency.

Recently [144], it has been demonstrated that undriven MHD turbulence spontaneously generates coherent spatial correlations of several types, associated with local Beltrami fields, local Alfvénic correlations, i.e., directional alignment of velocity and magnetic fields, local force-free states, and anti-alignment of magnetic and fluid acceleration components. These correlations suppress nonlinearity to levels lower than what is obtained from Gaussian fields, and occur in spatial patches. These are not true quasi-equilibria, as the non-linearity is only very rarely fully suppressed, but the systematic occurrence of these correlations indicates that the turbulence adjusts to the presence of large forces through a rapid dynamical response to reduce these stresses. These rapid relaxation processes are necessarily local, simultaneously occurring in various locations without regard to global compatibility other than the global conservation laws. Intuitively, this picture gives rise to a cellularization of the turbulence, which is in fact observed in simulations [97,144] and in the solar wind [122].

To demonstrate the rapid local relaxation of MHD turbulence, we illustrate the distributions (PDFs) of the angle [75, 126]

$$\cos\theta = \frac{\mathbf{f}\cdot\mathbf{g}}{|\mathbf{f}||\mathbf{g}|}, \tag{22}$$

where $\{\mathbf{f}, \mathbf{g}\}$ represents one of $\{\boldsymbol{v}, \boldsymbol{b}\}$, $\{\boldsymbol{v}, \boldsymbol{\omega}\}$, $\{\boldsymbol{j}, \boldsymbol{b}\}$, and $\{\boldsymbol{j}, \boldsymbol{\omega}\}$. In Figure 16, these four PDFs are shown. The initial Gaussian distribution with null (net) helicities corresponds to imposing a flat initial distribution of Equation (22). Quickly, as the nonlinearity develops, strong alignments appear. These aligned (anti-aligned) fields correspond to a Beltramization of the magnetofluid, similar to the Navier–Stokes (NS) case. Even though global helicities remain small, the magnetofluid locally self-organizes into patches which contain several types of correlations.

Since the conclusions bear a close resemblance to the properties of 3D MHD global relaxation, it is tempting to extend the original interpretations. Global long-time relaxation gives rise to the same Beltrami properties as suggested in Figure 16, for both velocity $\boldsymbol{v}$ and magnetic $\boldsymbol{b}$ fields. These emerge from variational principles [90, 109, 161] in which

minimum energy states [119,158,161] are solutions to Equation (12). The associated Euler–Lagrange equations imply that the relaxed states are described by: $\boldsymbol{v} \propto \boldsymbol{b} \propto \boldsymbol{j} \propto \boldsymbol{\omega}$, where $\boldsymbol{a}$ is the potential vector ($\boldsymbol{b} = \nabla \times \boldsymbol{a}$), $\boldsymbol{j} = \nabla \times \boldsymbol{b}$ is the current density, and $\boldsymbol{\omega} = \nabla \times \boldsymbol{v}$ is the vorticity. In global relaxation, these conditions are applied to the entire system and at large times, with the coefficients of proportionality implied in Equation (13) taken to be uniform constants. However, the observation of local patches of enhanced Beltrami, force-free, and Alfvénic correlations at short times suggests another interpretation in which the coefficients of proportionality defining the generalized Beltrami states are viewed as piecewise constant and time-varying. It remains for further work to show if this description can adequately account for the cellular structure of MHD turbulence, in which patches of correlation are bounded by near-discontinuous slowly evolving coherent structures that separate the relaxed regions.

There are numerous quantitative implications of the aforegiven picture of rapid relaxation, only some of which have been examined so far. One consequence of the increased probability of occurrence of the Beltrami correlations ($\cos\theta = \pm 1$) is the emergence of regions in which the non-linear term has become suppressed and the energy cascade has become inhibited [67]. From a simple look at the MHD equations, the alignment observed in Figure 16 suggests that the strength of the nonlinear term is "suppressed" [144]. Indeed, quantitative examination of simulations data has shown that the turbulent accelerations ($|\frac{\partial \boldsymbol{v}}{\partial t}|$, $|\frac{\partial \boldsymbol{b}}{\partial t}|$) are much weaker than if they were computed with a Gaussian (random) field [144].

While the rapid alignment processes occur, suppressing the strength of the nonlinear terms, it was also shown that enhancement of the kurtosis occurs, thus supporting the interpretation as the development of "cells." The kurtosis is an elementary measure of the degree of the intermittency of the system. Therefore, if the suppression is driven by nonlinear relaxation, then one would expect to see signatures of coherent structure formation even in ideal flows. Indeed, it was suggested years ago [47] that current sheets form exponentially fast in ideal MHD. Recent analysis of both dissipative and ideal 2D MHD simulations demonstrated that spectral transfer, beginning from band-limited Gaussian initial conditions, gives rise to high kurtosis excitations at the higher wavenumbers [167], even at very early times.

The overall picture, in which it may be possible to understand the close linkages between cascade and intermittency, between rapid local relaxation and suppression of nonlinearity, between coherent structures and cellular boundaries, and ultimately between slow global relaxation and fast local relaxation, remains far from complete. The connections reviewed earlier have been established in both 2D and 3D MHD studies, but the picture in 3D is of course less clear, due to both physical complexity and numerical limitations. Much more work will be needed to complete this picture, and to establish a firmer analytical understanding beyond the sketchy suggestions implied earlier.

It does appear however that a general view is emerging that the non-linear dynamics of decaying 3D incompressible MHD leads spontaneously to several rapid, local relaxation processes, favoring states having strong aligned or anti-aligned fields, namely those that suppress the strength of nonlinearities. The production of spatial patches of these correlations requires that the statistical distribution of velocity and magnetic field become non-Gaussian, as can be seen by formulating the correlations of (at least) fourth order, such as $\langle(\mathbf{v} \cdot \mathbf{b})^2\rangle$ that must grow to form Alfvénic patches Our conclusion is that this multifaceted rapid relaxation is intimately related to the formation of spatial intermittent structures. A simple real space picture emerges: when patches of suppression of non-linearity are formed, the fourth-order statistics become non-Gaussian, as the gradients become concentrated along

boundaries of the patches. For example, two regions can become approximately force-free, but the boundary between them will not be force-free [25]. This would concentrate nonlinear activity near cellular boundaries of turbulence. Magnetic reconnection is one example of the type activity that can occur at these boundaries [146].

9. Third-order law in MHD

A well known Kolmogorov–Yaglom law relates the third-order structure function to the energy dissipation rate [45, 68, 107]. Usually, it is stated with the assumptions of isotropy, homogeneity, and time stationarity of the statistics of velocity increments $\delta\boldsymbol{u} = \boldsymbol{u}(\boldsymbol{x}+\boldsymbol{r}) - \boldsymbol{u}(\boldsymbol{x})$ [velocity $\boldsymbol{u}$, spatial positions $\boldsymbol{x}+\boldsymbol{r}$ and $\boldsymbol{x}$]. It also apparently requires adoption of the von Kármán hypothesis [66] that the rate of energy dissipation ϵ approaches a constant nonzero value as Reynolds number tends to infinity. Without the need for assuming isotropy, one finds

$$\frac{\partial}{\partial r_i}\langle \delta u_i \, |\delta\boldsymbol{u}|^2 \rangle = -4\epsilon, \tag{23}$$

where $\langle \cdots \rangle$ indicates an ensemble average and a sum on repeated indices is implied. If isotropy is further assumed then,

$$\langle \delta u_L \, |\delta\boldsymbol{u}|^2 \rangle = -\frac{4}{d}\epsilon \, |\boldsymbol{r}| \,, \tag{24}$$

where d is the number of spatial dimensions and $\delta u_L = \hat{\boldsymbol{r}} \cdot \delta\boldsymbol{u}$ is the increment component measured in the direction of the unit vector $\hat{\boldsymbol{r}}$ parallel to the relative separation $\boldsymbol{r}$.

Extension of the third-order law to the case of incompressible MHD was reported by [130], who remained close to the approximations made in the hydrodynamic case. Without assuming isotropy, they found

$$\frac{\partial}{\partial r_i}\left\langle \delta z_i^{\mp} \left|\delta \boldsymbol{z}^{\pm}\right|^2 \right\rangle = -4\epsilon^{\pm}, \tag{25}$$

which, after adoption of isotropy, reduces to,

$$\left\langle \delta z_L^{\mp} \left|\delta \boldsymbol{z}^{\pm}\right|^2 \right\rangle = -\frac{4}{d}\epsilon^{\pm} r, \tag{26}$$

where $\delta\boldsymbol{z}^{\pm} = \boldsymbol{z}^{\pm}(\boldsymbol{x}+\boldsymbol{r}) - \boldsymbol{z}^{\pm}(\boldsymbol{x})$ are the increments of the Elsässer variables and $\delta z_L^{\pm} = \hat{\boldsymbol{r}} \cdot \delta\boldsymbol{z}^{\pm}$. The constants $\epsilon^{\pm}$ are the mean energy dissipation rates of the corresponding variables $\boldsymbol{z}^{\pm} = \boldsymbol{u} \pm \boldsymbol{b}$, where $\boldsymbol{b}$ is the magnetic field fluctuation in Alfvén speed units.

There has been a flurry of activity in the past few years, geared toward measurement of the cascade rate in the solar wind using various forms of the isotropic third-order law [85, 86, 152, 155], including the anisotropic form [123]. Many of these estimates arrive at heating rates around 10^4 JKg^{-1}s^{-1}, which agrees well with estimates from temperature gradients [163]. (See also [37]). Another approach to study of the third-order law begins with an exact law and then imposes symmetries to find possible special solutions (e.g., [53, 127]. It is not known if these solutions are realizable.

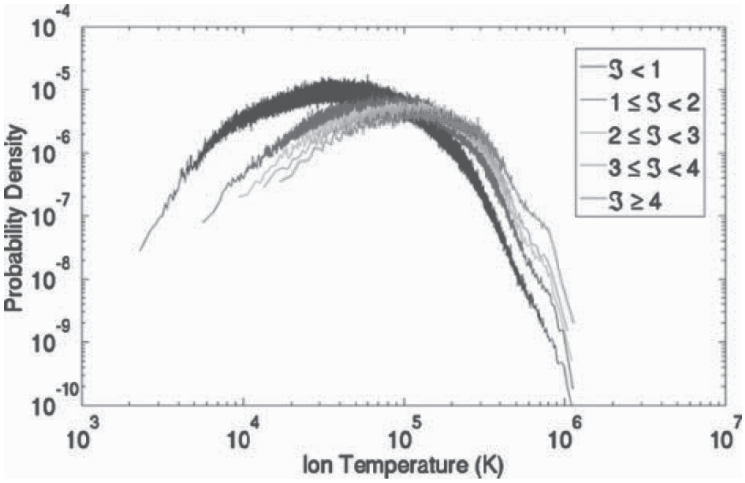


Figure 17. PDFs of the ion temperature, where each PDF corresponds to a different range of PVI values $\Im$, where $\Im(\Delta s, \ell, s) = |\Delta \boldsymbol{b}(s, \Delta s)| / \left\langle |\Delta \boldsymbol{b}(s, \Delta s)|^2 \right\rangle_\ell^{1/2}$. As the PVI values increase, the probability density decreases at lower temperatures and increases at higher temperatures. Also, the mean ion temperature increases with increasing PVI. The corresponding PDFs for electron heat flux magnitude, electron temperature, and local dissipation behave in a similar manner [120]. Reproduced with permission from Osman et al., Astrophys. J., 2011, copyright (2011) by the AAS.

10. Extension to KRSH and intermittency of dissipation

The Kolmogorov-Refined Similarity Hypothesis (KRSH) [69] is the unproven but extraordinarily useful theoretical construct that connects the probability distributions of inertial range increments and averages of the dissipation function [118,154]. The extension to MHD is not completely straightforward, for the usual reasons that there is more than one cascaded field, and ambiguities arise. For a useful starting place, see [99]. It is noteworthy that the KRSH might be formally viewed as the motivation for scaling studies of higher order structure functions, yet, as described earlier, this activity has proceeded [17, 61, 87, 131, 153], in spite of the absence of a clear statement of the correct form of the hypothesis. (This may be an oxymoron of sorts, since the KRSH is a working hypothesis.)

Apart from complications associated with MHD Theory, application of KRSH extensions to low-density solar wind and astrophysical plasmas must confront another great problem – we do not know the correct functional form of the dissipation function, or even the complete roster of appropriate physical processes to include in it. The problem of examining possible dissipation processes in the solar wind and interstellar medium is a very active one at present, and a complete review would be well outside the present scope. For a few starting points, see [3, 4, 77–79, 143, 151]. A fuller understanding of this problem is a great challenge for the coming years.

As a final remark on this point, we note that for a low-density space plasma one might expect to find relationships of the form (schematically)

$$\frac{\delta Z_s^3}{s} \sim \epsilon_s \to T_s, \tag{27}$$

where δZ_s is a measure of the (possibly mixed) magnitude of vector increments at separation s, ϵ_s is the average of the dissipation function over scale s, and T_s is a measure of the similarly averaged temperature, or perhaps the local temperature excess. The first relationship in

Equation (27) is akin to the KRSH, although the precise form of the increment might be a fruitful topic of conversation (see [99]). The second relationship is even less clear, although intuitively it seems that if one deposits a large amount of heat locally, the temperature very well might increase. The first relationship cannot be examined in the solar wind because we do not know ϵ. The second relationship cannot be examined in most simulations because they are incompressible, and in any case we do not know the correct form of the heat conduction for a plasma such as the solar wind. But what we can do is assume the second relationship and then compare increments to temperature averages in the solar wind. This was done recently by Osman et al. [121]. The approach was to employ the PVI statistic discussed in an earlier section to find locations of near-discontinuous magnetic structure. The higher values of PVI indicate more rare and stronger discontinuities. Then, the proton temperature (and other diagnostics) were conditionally sampled for increasing PVI. One such result is reproduced here in Figure 17. It is readily apparent that the samples with large PVI are hotter on average and have hotter tails. This is completely consistent with the idea that the dissipation function, whatever it is in the solar wind, is more active within and near the coherent structures. Evidently the solar wind plasma, even though it is not hydrodynamics nor even precisely an MHD medium, shares with classical turbulence the ideas that the dissipative structures are localized, providing a meaning to the ideas of intermittency for this plasma that is similar to what Kolmogorov's ideas mean for hydrodynamics.

11. Conclusions and omissions

MHD turbulence and its applications to real physical systems remains a fascinating, complex, and rapidly developing field of physics. Naturally, many of its features remain close to their hydrodynamic antecedents, but numerous new complications arise. Here, we aimed to provide a quick sampling of some MHD results for homogeneous plasmas, for related systems in 2D hydro and electron plasmas, and for a major field of application in the solar wind. The subject is big enough that a complete review of even these special topics has not been possible, and we apologize for what have doubtless been numerous and egregious oversights on the discussion and references.

We have made essentially no attempt to cover very important fields such as laboratory plasmas, astrophysics, magnetic reconnection, planetary, stellar, and laboratory dynamo theory, MHD power generation and other industrial applications, as well as deeper connections with plasma physics through multispecies fluid models and other variants of the MHD plasma. The omission of discussion of relaxation in laboratory reversed field pinch, spheromak, and tokamak plasmas is particularly egregious due to the close relationship those studies have to those that are included here. For excellent reviews and introductory material in these areas, see [25, 26, 62, 160].

On the theoretical side, an important class of questions exists regarding the issue of *nonlocal* contributions to spectral transfer [103], which we have alluded to several times earlier, but not discussed in any detail. It is intriguing to note that MHD couplings are decidedly more nonlocal [1] than their hydrodynamic counterparts. In part, this is due to interactions with large-scale shear or with a large-scale or DC magnetic field [2, 71, 133], but in any case scale nonlocality introduces challenging features into the subject that may not be anticipated by strict reliance on the standard Kolmogorov–Obukhov reasoning that has dominated the subject.

Another major deficiency here is the lack of discussion of closures [55, 73, 120, 133]. These provide capable even if complex tools that are potentially useful in addressing future

questions about MHD and plasma turbulence both of a theoretical and practical nature. One high-powered example is the two-scale direct interaction approximation that has been applied to development of tractable MHD closures (e.g., [172]). These indeed have the potential to make progress in problems of current interest [171]; however, as with other interesting subjects, there has not been an opportunity to delve into that interesting subject here.

We hope that, within the limited context of the sample provided here, there may be adequate connections afforded by the references for an interested reader to get a foothold in a few interesting problems relating to turbulence in magnetized fluids, and in the physics of the solar wind.

Acknowledgments

This research has been supported by the NSF SHINE program ATM-0752135, the Solar Terrestrial program AGS-1063439, and by NASA through the MMS mission NNX08AT76G, the Solar Probe Mission (ISIS subcontract, and the Heliophysics Theory program. W.H. Matthaeus is grateful for the hospitality of the University of Calabria, the assistance of Lorenzo Servidio, and the support for collaborators from the EU TURBOPLASMA program.

Note

1. The unaveraged Alfvén timescale is $(\mathbf{k} \cdot \mathbf{B}_0)^{-1}$, where $\mathbf{B}_0$ is the mean magnetic field. This induces anisotropy [149] and the possibility of important additional time-scale effects. Here, we deal only with the isotropic case.

References

[1] A. Alexakis, P.D. Mininni, and A. Pouquet, *Shell-to-shell energy transfer in magnetohydrodynamics. I. Steady state turbulence*, Phys. Rev. E 72 (2005), 046301.

[2] A. Alexakis, B. Bigot, H. Politano, and S. Galtier, *Anisotropic fluxes and nonlocal interactions in magnetohydrodynamic turbulence*, Phys. Rev. E 76 (2007), 056313.

[3] O. Alexandrova, J. Saur, C. Lacombe, A. Mangeney, J. Mitchell, S.J. Schwartz, and P. Robert, *Universality of solar-wind turbulent spectrum from MHD to electron scales*, Phys. Rev. Lett. 103 (2009), 165003.

[4] S.D. Bale, J.C. Kasper, G.G. Howes, E. Quataert, C. Salem, and D. Sundkvist, *Magnetic fluctuation power near proton temperature anisotropy instability thresholds in the solar wind*, Phys. Rev. Lett. 103 (2009), 211101.

[5] A. Balogh, C.M. Carr, M.H. Acuña, M.W. Dunlop, T.J. Beek, P. Brown, K.-H. Fornacon, E. Georgescu, K.-H. Glassmeier, J. Harris, G. Musmann, T. Oddy, and K. Schwingenschuh, *The Cluster magnetic field investigation: overview of in-flight performance and initial results*, Ann. Geophys. 19 (2001), p. 1207.

[6] A. Barnes, *Collisionless heating of the solar-wind plasma, 1. Theory of the heating of collisionless plasma by hydromagnetic waves*, Astrophys. J. 154 (1968), p. 751.

[7] A. Barnes, *Hydromagnetic waves and turbulence in the solar wind*, in *Solar System Plasma Physics*, Vol. 1, E.N. Parker, C.F. Kennel, and L.J. Lanzerotti, eds., Elsevier Science, Amsterdam, North-Holland, 1979, p. 251.

[8] G.K. Batchelor, *Computation of the energy spectrum in homogeneous two-dimensional turbulence*, Phys. Fluids 12 (1968), p. II-233.

[9] B. Bavassano, M. Dobrowolny, F. Mariani, and N.F. Ness, *Radial evolution of power spectra of interplanetary Alfvénic turbulence*, J. Geophys. Res. 87 (1982), p. 3617.

[10] B. Bavassano, M. Dobrowolny, G. Fanfoni, F. Mariani, and N.F. Ness, *Statistical properties of MHD fluctuations associated with high-speed streams from Helios-2 observations*, Sol. Phys. 78 (1982), p. 373.

[11] B. Bavassano and E.J. Smith, *Radial variation of interplanetary alfvénic fluctuations: Pioneer 10 and 11 observations between 1 and 5 AU*, J. Geophys. Res. 91 (1986), p. 1706.
[12] J.W. Belcher and L. Davis, Jr., *Large-amplitude Alfvén waves in the interplanetary medium, 2*, J. Geophys. Res. 76 (1971), p. 3534.
[13] A. Beresnyak and A. Lazarian, *Structure of stationary strong imbalanced turbulence*, Astrophys. J. 702 (2009), p. 460.
[14] J.W. Bieber, W.H. Matthaeus, C.W. Smith, W. Wanner, M. Kallenrode, and G. Wibberenz, *Proton and electron mean free paths: The Palmer consensus revisited*, Astrophys. J. 420 (1994), p. 294.
[15] J.W. Bieber, W. Wanner, and W.H. Matthaeus, *Dominant two-dimensional solar wind turbulence with implications for cosmic ray transport*, J. Geophys. Res. 101 (1996), p. 2511.
[16] D. Biskamp and H. Welter, *Dynamics of decaying two-dimensional magnetohydrodynamic turbulence*, Phys. Fluids B 1 (1989), p. 1964.
[17] D. Biskamp and W.-C. Muller, *Scaling properties of three-dimensional isotropic magnetohydrodynamic turbulence*, Phys. Plasmas 7 (2000), p. 4889.
[18] D. Biskamp, *Magnetohydrodynamic Turbulence*, Cambridge University Press, Cambridge, 2003.
[19] A. Bondeson, G. Marklin, Z.G. An, H.H. Chen, Y.C. Lee, and C.S. Liu, *Tilting instability of a cylindrical spheromak* , Phys Fluids 24 (1981), p. 1682.
[20] M. Brachet, M. Meneguzzi, H. Politano, and P.-L. Sulem, *The dynamics of freely decaying two-dimensional turbulence*, J. Fluid Mech. 194 (1988), p. 333.
[21] H. Brands, J. Stulemeyer, R.A. Pasmanter, and T.J. Schep, *A mean field prediction of the asymptotic state of decaying 2D turbulence*, Phys. Fluids 9 (1997), p. 2815.
[22] H. Brands, P.H. Chavanis, R. Pasmanter, and J. Sommeria, *Maximum entropy verses minimum enstrophy vortices*, Phys. Plasmas 11 (1999), p. 3465.
[23] B. Breech, W.H. Matthaeus, J. Minnie, J.W. Bieber, S. Oughton, C.W. Smith, and P.A. Isenberg, *Turbulence transport throughout the heliosphere*, J. Geophys. Res. 113 (2008), A08105.
[24] B. Breech, W.H. Matthaeus, S.R. Cranmer, J.C. Kasper, and S. Oughton, *Electron and proton heating by solar wind turbulence*, J. Greophys. Res. 114 (2009), A09103.
[25] M.R. Brown, *Experimental evidence of rapid relaxation to large scale structures in turbulent fluids: Selective decay and maximal entropy*, J. Plasma Phys. 57 (1996), p. 203.
[26] M.R. Brown, *Experimental studies of magnetic reconnection*, Phys. Plasmas 6 (1999), p. 1717.
[27] R. Bruno, B. Bavassano, and U. Villante, *Evidence for long period Alfvén waves in the inner solar system*, J. Geophys. Res. 90 (1985), p. 4373.
[28] R. Bruno, V. Carbone, P. Veltri, E. Pietropaolo, and B. Bavassano, *Identifying intermittency events in the solar wind*, Planet. Space Sci. 49 (2001), p. 1201.
[29] R. Bruno and V. Carbone, *The solar wind as a turbulence laboratory*, Living Rev. Sol. Phys. 2 (2005), p. 4. Available at http://www.livingreviews.org/lrsp-2005-4.
[30] L.F. Burlaga, *Micro-scale structures in the interplanetary medium*, Sol. Phys. 4 (1968), p. 67.
[31] L.F. Burlaga, *Directional discontinuities in the interplanetary magnetic field*, Sol. Phys., 7 (1969), p. 54.
[32] L.F. Burlaga, *Intermittent turbulence in the solar wind*, J. Geophys. Res. 96 (1991), p. 5847.
[33] V. Carbone, P. Veltri, and A. Mangeney, *Coherent structure formation and magnetic field line reconnection in magnetohydrodynamic turbulence*, Phys. Fluids A 2 (1990), p. 1487.
[34] S. Chandrasekhar and L. Woltjer, *On force-free magnetic fields*, Proc. Natl. Acad. Sci. USA 44 (1958), p. 285.
[35] S. Chen and R.H. Kraichnan, *Inhibition of turbulent cascade by sweep*, J. Plasma Phys. 57 (1997), p. 187.
[36] H.J.H. Clercx, S.R. Maassen, and G.J.F. van Heijst, *Spontaneous spin-up during the decay of of 2D turbulence in a square container with rigid boundaries*, Phys. Rev. Lett. 80 (1998), p. 5129.
[37] P.J. Coleman, *Turbulence, viscosity, and dissipation in the solar-wind plasma*, Astrophys. J. 153 (1968), p. 371.
[38] S.R. Cranmer, *Coronal holes*, Living Rev. Sol. Phys. 6 (2009).
[39] S.R. Cranmer, W.H. Matthaeus, B.A. Breech, and J.C. Kasper, *Empirical constraints on proton and electron heating in the fast solar wind*, Astrophys. J. 702 (2009), p. 1604.
[40] P. Dmitruk and W.H. Matthaeus, *Low-frequency 1/f fluctuations in hydrodynamic and magnetohydrodynamic turbulence*, Phys. Rev. E 76 (2007), 036305.

[41] P. Dmitruk, P.D. Mininni, A. Pouquet, S. Servidio, and W.H. Matthaeus, *Emergence of very long time fluctuations and 1/f noise in ideal flows*, Phys. Rev. E 83 (2011), 066318.
[42] M. Dobrowolny, A. Mangeney, and P. Veltri, *Fully developed anisotropic hydromagnetic turbulence in interplanetary space*, Phys. Rev. Lett. 45 (1980), p. 144.
[43] C.F. Driscoll and K.S. Fine, *Experiments on vortex dynamics in pure electron plasmas*, Phys. Fluids B 2 (1990), p. 1359.
[44] W.M. Elsasser, *The hydromagnetic equations*, Phys. Rev. 79 (1950), p. 183.
[45] U. Frisch, *Turbulence*, Cambridge University Press, Cambridge, 1995.
[46] U. Frisch, A. Pouquet, J. Léorat, and A. Mazure, *Possibility of an inverse cascade of magnetic helicity in magnetohydrodynamic turbulence*, J. Fluid Mech. 68 (1975), p. 769.
[47] U.Frisch, A.Pouquet, P.-L.Sulem, and M. Meneguzzi, *The dynamics of two-dimensional ideal MHD*, J. Mech. Theor. Appl. 2 (1983), p. 191.
[48] D. Fyfe and D. Montgomery, *High beta turbulence in two-dimensional magnetohydrodynamics*, J. Plasma Phys. 16 (1976), pp. 181–191.
[49] D. Fyfe, G. Joyce, and D. Montgomery, *Magnetic dynamo action in two-dimensional turbulent magneto-hydrodynamics*, J. Plasma Phys. 17 (1977), p. 317.
[50] D. Fyfe, D. Montgomery, and G. Joyce, *Dissipative, forced turbulence in two-dimensional magnetohydrodynamics*, J. Plasma Phys. 17 (1977), p. 369.
[51] T. Gallay and C.E. Wayne, *Global stability of vortex solutions of the twodimensional navier-stokes equation*, Commun. Math. Phys. 255 (2005), p. 97.
[52] S. Galtier, H. Politano, and A. Pouquet, *Self-similar energy decay in magnetohydrodynamic turbulence*, Phys. Rev. Lett. 79 (1997), p. 2807.
[53] S. Galtier, *Exact vectorial law for axisymmetric magnetohydrodynamics turbulence*, Astrophys. J. 704 (2009), p. 1371.
[54] P. Goldreich and S. Sridhar, *Toward a theory of interstellar turbulence: II. Strong Alfvénic turbulence*, Astrophys. J. 438 (1995), p. 763.
[55] R. Grappin, U. Frisch, J. Léorat, and A. Pouquet, *Alfvénic fluctuations as asymptotic states of MHD turbulence*, Astron. Astrophys. 105 (1982), p. 6.
[56] A. Greco, P. Chuychai, W.H. Matthaeus, S. Servidio, and P. Dmitruk, *Intermittent MHD structures and classical discontinuities*, Geophys. Res. Lett. 35 (2008), L19111.
[57] A. Greco, W.H. Matthaeus, S. Servidio, P. Chuychai, and P. Dmitruk, *Statistical analysis of discontinuities in solar wind ACE data and comparison with intermittent MHD turbulence*, Astrophys. J. 691 (2009), L111.
[58] K. Hamilton, C.W. Smith, B.J. Vasquez, and R.J. Leamon, *Anisotropies and helicities in the solar wind inertial and dissipation ranges at 1 AU*, J. Geophys. Res. 113 (2008), A01106.
[59] G.J.F. van Heijst, H.J.H. Clercx, and D. Molenaar, *The effects of solid boundaries on confined two-dimensional turbulence*, J. Fluid Mech. 554 (2006), p. 411.
[60] J.V. Hollweg, *Alfvén waves in the solar wind: Wave pressure, Poynting flux, and angular momentum*, J. Geophys. Res. 78 (1973), p. 3643.
[61] T.A. Horbury, A. Balogh, R.J. Forsyth, and E.J. Smith, *Ulysses observations of intermittent heliospheric turbulence*, Adv. Space Phys. 19 (1997), p. 847.
[62] W. Horton, *Drift waves and transport*, Rev. Mod. Phys. 71 (1999), p. 735.
[63] M. Hossain, P.C. Gray, D.H. Pontius, Jr., W.H. Matthaeus, and S. Oughton, *Phenomenology for the decay of energy-containing eddies in homogeneous MHD turbulence*, Phys. Fluids 7 (1995), p. 2886.
[64] X.-P. Huang and C.F. Driscoll, *Relaxation of 2D turbulence to a metaequilibrium near the minimum enstrophy state*, Phys. Rev. Lett. 72 (1994), p. 2187.
[65] P.S. Iroshnikov, *Turbulence of a conducting fluid in a strong magnetic field*, Sov. Astron. 7 (1964), p. 566.
[66] T. de Kármán and L. Howarth, *On the statistical theory of isotropic turbulence*, Proc. R. Soc. Lond. A 164 (1938), p. 192.
[67] R.M. Kerr, *Histograms of helicity and strain in numerical turbulence*, Phys. Rev. Lett. 59 (1987), p. 783.
[68] A.N. Kolmogorov, *Dissipation of energy in the locally isotropic turbulence*, C. R. Acad. Sci. U.R.S.S. 32 (1941), p. 16. [Reprinted in Proc. R. Soc. London, Ser. A 434 (1991), p. 15].
[69] A.N. Kolmogorov, *A refinement of previous hypotheses concerning the local structure of turbulence in a viscous incompressible fluid at high Reynolds number*, J. Fluid Mech. 12 (1962), p. 82.

[70] R.H. Kraichnan, *Helical turbulence and absolute equilibrium*, J. Fluid Mech. 59 (1973), p. 745.
[71] R.H. Kraichnan, *Inertial-range spectrum of hydromagnetic turbulence*, Phys. Fluids 8 (1965), p. 1385.
[72] R.H. Kraichnan, *Inertial ranges in two-dimensional turbulence*, Phys. Fluids 10 (1967), p. 1417.
[73] R.H. Kraichnan and S. Nagarajan, *Growth of turbulent magnetic fields*, Phys. Fluids 10 (1967), p. 859.
[74] R.H. Kraichnan, *Statistical dynamics of two-dimensional flow*, J. Fluid Mech. 67 (1975), p. 155.
[75] R.H. Kraichnan and R. Panda, *Depression of nonlinearity in decaying isotropic turbulence*, Phys. Fluids 31 (1988), p. 2395.
[76] J.M. Kriesel and C.F. Driscoll, *Measurements of viscosity in pure-electron plasmas*, Phys. Rev. Lett. 87 (2001), 135003.
[77] R.J. Leamon, C.W. Smith, N.F. Ness, W.H. Matthaeus, and H.K. Wong, *Observational constraints on the dynamics of the interplanetary magnetic field dissipation range*, J. Geophys. Res. 103 (1998), p. 4775.
[78] R.J. Leamon, C.W. Smith, N.F. Ness, and H.K. Wong, *Dissipation range dynamics: Kinetic Alfvén waves and the importance of β_e*, J. Geophys. Res. 104 (1999), 22331.
[79] R.J. Leamon, W.H. Matthaeus, C.W. Smith, G.P. Zank, D.J. Mullan, and S. Oughton, *MHD-driven kinetic dissipation in the solar wind and corona*, Astrophys. J. 537 (2000), p. 1054.
[80] T.D. Lee, *On some statistical properties of hydrodynamical and magneto-hydrodynamical fields*, Q. Appl. Math. 10 (1952), p. 69.
[81] E. Lee, M.E. Brachet, A. Pouquet, P.D. Mininni, and D. Rosenberg, *Lack of universality in decaying magnetohydrodynamic turbulence*, Phys. Rev. E 81 (2010), 016318.
[82] M. Lesieur, *Turbulence in Fluids*, 2nd ed., Kluwer, Dordrecht, The Netherlands, 1990.
[83] S. Li and D.C. Montgomery, *Decaying two-dimensional turbulence with rigid walls*, Phys. Lett. A 218 (1996), p. 281; and A222, 461 (1996) (erratum).
[84] S. Li, D.C. Montgomery, and W.B.Jones, *Two dimensional turbulence with rigid, circular walls*, Theor. Comput. Fluid Dyn. 9 (1997), p. 167.
[85] B.T. MacBride, M.A. Forman, and C.W. Smith, *Turbulence and third moment of fluctuations: Kolmogorov's 4/5 law and its MHD analogues in the solar wind*, in *Proceedings Solar Wind 11: Connecting Sun and Heliosphere*, B. Fleck and T.H. Zurbuchen, eds., (ESASP-592), EuropeanSpaceAgency, TheNetherlands, 2005, p. 613.
[86] B.T. MacBride, C.W. Smith, and M.A. Forman, *The turbulent cascade at 1 AU: Energy transfer and the third-order scaling for MHD*, Astrophys. J. 679 (2008), p. 1644.
[87] E. Marsch and C.-Y. Tu, *Non-Gaussian probability distributions of solar wind fluctuations*, Ann. Geophys. 12 (1994), p. 1127.
[88] E. Marsch, *Kinetic physics of the solar corona and solar wind*, Living Rev. Solar Phys. 3 (2006), p. 1. Available at http://www.livingreviews.org/lrsp-2006-1.
[89] J. Mason, F. Cattaneo, and S. Boldyrev, *Dynamic alignment in driven magnetohydrodynamic turbulence*, Phys. Rev. Lett. 97 (2006), 255002.
[90] W.H. Matthaeus and D. Montgomery, *Selective decay hypothesis at high mechanical and magnetic reynolds numbers*, Ann. New York Acad. Sci. 357 (1980), p. 203.
[91] W.H. Matthaeus and M.L. Goldstein, *Measurement of the rugged invariants of magnetohydrodynamic turbulence*, J. Geophys. Res. 87 (1982), p. 6011.
[92] W.H. Matthaeus and D. Montgomery, *Dynamic alignment and selective decay in MHD*, in *Statistical Physics and Chaos in Fusion Plasmas*, C.W. Horton, Jr. and L.E. Reichl, eds., Wiley, New York, 1984, pp. 285–291.
[93] W.H. Matthaeus, M.L. Goldstein, and D.A. Roberts, *Evidence for the presence of quasi-two-dimensional nearly incompressible fluctuations in the solar wind*, J. Geophys. Res. 95 (1990), 20673.
[94] W.H. Matthaeus, W.T. Stribling, D. Martínez, S. Oughton, and D. Montgomery, *Selective decay and coherent vortices in two-dimensional incompressible turbulence*, Phys. Rev. Lett. 66 (1991), p. 2731.
[95] W.H. Matthaeus, S. Dasso, J.M. Weygand, L.J. Milano, C.W. Smith, and M.G. Kivelson, *Spatial correlation of solar-wind turbulence from two-point measurements*, Phys. Rev. Lett. 95 (2005), 231101.

[96] W.H. Matthaeus, B. Breech, P. Dmitruk, A. Bemporad, G. Poletto, M. Velli, and M. Romoli, *Density and magnetic field signatures of interplanetary 1/f noise*, Astrophys. J. 657 (2007), L121.
[97] W.H. Matthaeus, A. Pouquet, P.D. Mininni, P. Dmitruk, and B. Breech, *Rapid alignment of velocity and magnetic field in magnetohydrodynamic turbulence*, Phys. Rev. Lett. 100 (2008), 085003.
[98] J.C. McWilliams, *Emergence of isolated coherent vortices in turbulent flow*, J. Fluid Mech. 146 (1984), p. 21.
[99] J.A. Merrifield, W.-C. Müller, S.C. Chapman, and R.O. Dendy, *The scaling properties of dissipation in incompressible isotropic three-dimensional magnetohydrodynamic turbulence*, Phys. Plasmas 12 (2005), 022301.
[100] P.D. Mininni, D.O. Gómez, and S.M. Mahajan, *Dynamo action in hall magnetohydrodynamics*, Astrophys. J. 567 (2002), L81.
[101] P.D. Mininni, D. Montgomery, and A. Pouquet, *A numerical study of the alpha model for two-dimensional magnetohydrodynamic turbulent flows*, Phys. Fluids 17 (2005), 035112.
[102] P.D. Mininni and A. Pouquet, *Finite dissipation and intermittency in magnetohydrodynamics*, Phys. Rev. E 80 (2009), 025401.
[103] P. Mininni, *Scale interactions in magnetohydrodynamic turbulence*, Ann. Rev. Fluid Mech. 43 (2011), p. 377.
[104] P.D. Mininni, P. Dmitruk, W.H. Matthaeus, and A. Pouquet, *Large-scale behavior and statistical equilibria in rotating flows*, Phys. Rev. E 83 (2011), 016309.
[105] T.B. Mitchell, X.J. Wang, and L.F. Rossi, *Stability of elliptical electron vortices*, in *Non-Neutral Plasma Physics VI,* Vol. 862 of American Institute of Physics Conference Series, M. Drewsen, U. Uggerhoj, and H. Knudsen, eds., October 2006, pp. 29–38.
[106] H.K. Moffatt, *Magnetic Field Generation in Electrically Conducting Fluids*, CUP, New York, 1978.
[107] A.S. Monin and A.M. Yaglom, *Statistical Fluid Mechanics*, Vols. 1 and 2, MIT Press, Cambridge, MA, 1971 and 1975.
[108] G. Joyce and D. Montgomery, *Negative temperature states for the two-dimensional guiding-centre plasma*, J. Plasma Phys. 10 (1973), p. 107.
[109] D. Montgomery, L. Turner, and G. Vahala, *Three-dimensional magnetohydrodynamic turbulence in cylindrical geometry*, Phys. Fluids 21 (1978), p. 757.
[110] D. Montgomery, L. Turner, and G. Vahala, *Most probable states in magnetohydrodynamics*, J. Plasma Phys. 21 (1979), p. 239.
[111] D.C. Montgomery, *Major disruptions, inverse cascades, and the strauss equations*, Phys. Scr. T2 (1982), p. 83.
[112] D.C. Montgomery, X. Shan, and W.H. Matthaeus, *Navier-stokes relaxation to sinh-poisson states at finite reynolds numbers*, Phys. Fluids A 5 (1993), p. 2207.
[113] D. Montgomery, W.H. Matthaeus, W.T. Stribling, D. Martinez, and S. Oughton, *Relaxation in two dimensions and the sinh-poisson equation*, Phys. Fluids A 4 (1992), p. 3.
[114] D.C. Montgomery and J.W. Bates, *The geometry and symmetries of magnetohydrodynamic turbulence: Anomalies of spatial periodicity*, Phys. Plasmas 6 (1999), p. 2727.
[115] D.C. Montgomery and W.H. Matthaeus, *Oseen vortex as a maximum entropy state of a two dimensional fluid*, Phys. Fluids 23 (2011), 075104.
[116] N.F. Ness and L.F. Burlaga, *Spacecraft studies of the interplanetary magnetic field*, J. Geophys. Res. 106 (2001), 15803.
[117] M. Neugebauer, *Comment on the abundances of rotational and tangential discontinuities in the solar wind*, J. Geophys. Res. 111 (2006), A04103.
[118] M. Nelkin, *Universality and scaling in fully developed turbulence*, Adv. Phys. 43 (1994), p. 143.
[119] S. Ohsaki and Z. Yoshida, *Variational principle with singular perturbation of hall magneto-hydrodynamics*, Phys. Plasmas 12 (2005), 064505.
[120] S.A. Orszag, *Analytical theories of turbulence*, J. Fluid Mech. 41 (1970), p. 363.
[121] K.T. Osman, W.H. Matthaeus, A. Greco, and S. Servidio, *Evidence for inhomogeneous heating in the solar wind*, Astrophys. J. 727 (2011), L11.
[122] K.T. Osman, M. Wan, W.H. Matthaeus, B. Breech, and S. Oughton, *Directional alignment and non-gaussian statistics in solar wind turbulence*, Astrophys. J 741 (2011), p. 75.

[123] K.T. Osman, M. Wan, W.H. Matthaeus, J.M. Weygand, and S. Dasso, *Anisotropic third-moment estimates of the energy cascade in solar wind turbulence using multi-spacecraft data*, Phys. Rev. Lett. 107 (2011), 165001.
[124] S. Oughton, E.R. Priest, and W.H. Matthaeus, *The influence of a mean magnetic field on three dimensional magnetohydrodynamic turbulence*, J. Fluid Mech. 280 (1994), p. 95.
[125] E.N. Parker, *Cosmical Magnetic Fields: Their Origin and Activity*, Oxford University Press, Oxford, UK, 1979.
[126] R.B. Pelz, V. Yakhot, S.A. Orszag, L. Shtilman, and E. Levich, *Velocity-vorticity patterns in turbulent flow*, Phys. Rev. Lett. 54 (1985), p. 2505.
[127] J. Podesta, M.A. Forman, and C.W. Smith, *Anisotropic form of third-order moments and relationship to the cascade rate in axisymmetric*, Phys. Plasmas 14 (2007), 092305.
[128] J.J. Podesta, *Dependence of solar-wind power spectra on the direction of the local mean magnetic field*, Astrophys. J. 698 (2009), p. 986.
[129] H. Politano, A. Pouquet, and P.-L. Sulem, *Inertial ranges and resistive instabilities in two-dimensional magnetohydrodynamic turbulence*, Phys. Fluids B 1 (1989), p. 2990.
[130] H. Politano and A. Pouquet, *Dynamical length scales for turbulent magnetized flows*, Geophys. Res. Lett. 25 (1998), p. 273.
[131] H. Politano, A. Pouquet, and V. Carbone, *Determination of anomalous exponents of structure functions in two-dimensional magnetohydrodynamic turbulence*, Europhys. Lett. 43 (1998), p. 516.
[132] Y. Ponty, H. Politano, and J.-F. Pinton, *Simulation of induction at low magnetic prandtl number*, Phys. Rev. Lett. 92 (2004), 144503.
[133] A. Pouquet, U. Frisch, and J.Léorat, *Strong MHD helical turbulence and the nonlinear dynamo effect*, J. Fluid Mech. 77 (1976), p. 321.
[134] A. Pouquet, M. Meneguzzi, and U. Frisch. *Growth of correlations in magnetohydrodynamic turbulence*, Phys. Rev. A 33 (1986), p. 4266.
[135] R. Robert and J. Sommeria, *Statistical equilibrium states for two-dimensional flows*, J. Fluid Mech. 229 (1991), p. 291.
[136] R. Robert and J. Sommeria, *Relaxation towards a statistical equilibrium state in two-dimensional perfect fluid dynamics*, Phys. Rev. Lett. 69 (1992), p. 2776.
[137] D.A. Roberts, L.W. Klein, M.L. Goldstein, and W.H. Matthaeus, *The nature and evolution of magnetohydrodynamic fluctuations in the solar wind: Voyager observations*, J. Geophys. Res. 92 (1987), 11021.
[138] D.A. Roberts, M.A. Goldstein, W.H. Matthaeus, and S. Ghosh, *Velocity sheer generation of soler wind turbulence*, J. Geophys. Res. 97 (1992), 17115.
[139] D.C. Robinson and M.G. Rusbridge, *Structure of turbulence in the zeta plasma*, Phys. Fluids 14 (1971), p. 2499.
[140] D.J. Rodgers, S. Servidio, W.H. Matthaeus, D.C. Montgomery, T.B. Mitchell, and T. Aziz, *Hydrodynamic relaxation of an electron plasma to a near-maximum entropy state*, Phys. Rev. Lett. 102 (2009), 244501.
[141] D.J. Rodgers, W.H. Matthaeus, T.B. Mitchell, and D.C. Montgomery, *Similarity decay of enstrophy in an electron fluid*, Phys. Rev. Lett. 105 (2010), 234501.
[142] A.A. Ruzmaikin, D.D. Sokoloff, and A.M. Shukurov, *The dynamo origin of magnetic fields in galaxy clusters*, Mon. Not. R. Astron. Soc. 241 (1989), p. 1.
[143] F. Sahraoui, M.L. Goldstein, P. Robert, and Y.V. Khotyaintsev, *Evidence of a cascade and dissipation of solar-wind turbulence at the electron gyroscale*, Phys. Rev. Lett. 102 (2009), 231102.
[144] S. Servidio, W.H. Matthaeus, and P. Dmitruk, *Depression of nonlinearity in decaying isotropic MHD turbulence*, Phys. Rev. Lett. 100 (2008), 095005.
[145] S. Servidio, W.H. Matthaeus, and V. Carbone, *Statistical properties of ideal three-dimensional hall magnetohydrodynamics: The spectral structure of the equilibrium ensemble*, Phys. Plasmas 15 (2008), 042314.
[146] S. Servidio, W.H. Matthaeus, M.A. Shay, P.A. Cassak, and P. Dmitruk, *Magnetic reconnection in two-dimensional magnetohydrodynamic turbulence*, Phys. Rev. Lett. 102 (2009), 115003.
[147] S. Servidio, W.H. Matthaeus, P. Dmitruk, and V. Carbone, *Time decorrelation in isotropic magnetohydrodynamic turbulence*, Europhys. Lett. 96 (2011), 55003.
[148] A. Schalchi, *Nonlinear Cosmic Ray Diffusion Theories, Astrophysics Space Science Library*, Vol. 362, Springer, Berlin, 2009.

[149] J.V. Shebalin, W.H. Matthaeus, and D. Montgomery, *Anisotropy in MHD turbulence due to a mean magnetic field*, J. Plasma Phys. 29 (1983), p. 525.
[150] C.W. Smith, J. L'Heureux, N.F. Ness, M.H. Acuna, L.F. Burlaga, and J. Scheifele, *The ACE magnetic fields experiment*, Space Sci. Rev. 86 (1998), p. 611.
[151] C.W. Smith, K. Hamilton, B.J. Vasquez, and R.J. Leamon, *Dependence of the dissipation range spectrum of interplanetary magnetic fluctuationson the rate of energy cascade*, Astrophys. J. 645 (2006), L85.
[152] L. Sorriso-Valvo, R. Marino, V. Carbone, A. Noullez, F. Lepreti, P. Veltri, R. Bruno, B. Bavassano, and E. Pietropaolo, *Observation of inertial energy cascade in interplanetary space plasma*, Phys. Rev. Lett. 99 (2007), 115001.
[153] L. Sorriso-Valvo, V. Carbone, P. Veltri, G. Consolini, and R. Bruno, *Intermittency in the solar wind turbulence through probability distribution functions of fluctuations*, Geoph. Res. Lett. 26 (1999), p. 1801.
[154] K.R. Sreenivasan, and R.A. Antonia, *The phenomenon of small-scale turbulence*, Annu. Rev. Fluid Mech. 29 (1997), p. 435.
[155] J.E. Stawarz, C.W. Smith, B.J. Vasquez, M.A. Forman, and B.T. MacBride, *The turbulent cascade and proton heating in the solar wind at 1 au*, Astrophys. J. 697 (2009), p. 1119.
[156] H.R. Strauss, *Nonlinear, three-dimensional magnetohydrodynamics of noncircular tokamaks*, Phys. Fluids 19 (1976), 134.
[157] T. Stribling and W.H. Matthaeus, *Statistical properties of ideal three-dimensional magnetohydrodynamics*, Phys. Fluids B 2 (1990), p. 1979.
[158] T. Stribling and W.H. Matthaeus, *Relaxation processes in a low-order three-dimensional magnetohydrodynamics model*, Phys. Fluids B 3 (1991), p. 1848.
[159] J.B. Taylor, *Relaxation of toroidal plasma and generation of reverse magnetic fields*, Phys. Rev. Lett. 33 (1974), p. 1139.
[160] J.B. Taylor, *Relaxation and magnetic reconnection in plasmas*, Rev. Mod. Phys. 58 (1986), p. 741.
[161] A.C. Ting, W.H. Matthaeus, and D. Montgomery, *Turbulent relaxation processes in magnetohydrodynamics*, Phys. Fluids 29 (1986), p. 3261.
[162] B.T. Tsurutani and E.J. Smith, *Interplanetary discontinuities - Temporal variations and the radial gradient from 1 to 8.5 AU*, J. Geophys. Res. 84 (1979), p. 2773.
[163] B.J. Vasquez, C.W. Smith, K. Hamilton, B.T. MacBride, and R.J. Leamon, *Evaluation of the turbulent energy cascade rates from the upper inertial range in the solar wind at 1 AU*, J. Geophys. Res. 112 (2007), A07101.
[164] P. Veltri and A. Mangeney, *Scaling laws and intermittent structures in solar wind MHD turbulence*, Solar Wind IX, AIP Conference Proceedings 471, Nantucket, MA, (1999), p. 543.
[165] P. Veltri, *MHD turbulence in the solar wind: Self-similarity, intermittency and coherent structures*, Plasma Phys. Control. Fusion 41 (1999), A787.
[166] A. Verdini, M. Velli, W.H. Matthaeus, S. Oughton, and P. Dmitruk, *A turbulence-driven model for heating and acceleration of the fast wind in coronal holes*, Astrophys. J. Lett. 708 (2010), L116.
[167] M. Wan, S. Oughton, S. Servidio, and W.H. Matthaeus, *Generation of non-Gaussian statistics and coherent structures in ideal magnetohydrodynamics*, Phys. Plasmas 16 (2009), 080703.
[168] M. Wan, S. Oughton, S. Servidio, and W.H. Matthaeus, *von Karman self-preservation hypothesis for MHD turbulence and its consequences for universality*, J. Fluid Mech. 697 (2012), p. 296.
[169] J.M. Weygand, W.H. Matthaeus, M. El-Alaoui, S. Dasso, and M.G. Kivelson, *Anisotropy of the taylor scale and the correlation scale in plasma sheet magnetic field fluctuations as a function of auroral electrojet activity*, J. Geophys. Res. 115 (2010), A12250.
[170] L. Woltjer, *A theorem on force-free magnetic fields*, Proc. Natl. Acad. Sci. USA 44 (1958), p. 489.
[171] N. Yokoi, R. Rubenstein, F. Hamba, and A. Yoshizawa, *A turbulence model for magnetohydrodynamic plasmas*, J. Turb. 9 (2008), p. 1.
[172] A. Yoshizawa, *Three equation modeling of inhomogeneous compressible turbulence based on a two-scale direct-interaction approximations*, Phys. Fluids A 2 (1990), p. 838.
[173] G.P. Zank and W.H. Matthaeus, *The equations of reduced magnetohydrodynamics*, J. Plasma Phys. 48 (1992), p. 85.

[174] G.P. Zank, S. Oughton, F.M. Neubauer, and G.M. Webb, *Properties of mass-loading shocks 2. Magnetohydrodynamics*, J. Geophys. Res. 97 (1992), 17051.
[175] G.P. Zank, W.H. Matthaeus, and C.W. Smith, *Evolution of turbulent magnetic fluctuation power with heliocentric distance*, J. Geophys. Res. 101 (1996), 17093.
[176] Y. Zhou and W.H. Matthaeus, *Transport and turbulence modeling of solar wind fluctuations*, J. Geophys. Res. 95 (1990), 10291.
[177] Y. Zhou, W.H. Matthaeus, and P. Dmitruk, *Magnetohydrodynamic turbulence and time scales in astrophysical and space plasmas*, Rev. Mod. Phys. 76 (2004), p. 1015.
[178] S.J. Zweben and R.J. Taylor, *Phenomenological comparison of magnetic and electrostatic fluctuations in the Macrotor tokamak*, Nucl. Fusion 21 (1981), p. 193.
[179] D.R. Wells, *Dynamic stability of closed plasma configurations*, J. Plasma Phys. 4 (1970), p. 645.

Journal of Turbulence, 2013
Vol. 14, No. 1, 99–120, http://dx.doi.org/10.1080/14685248.2012.758422

Taylor & Francis
Taylor & Francis Group

Lagrangian Markovianized field approximation for turbulence

Wouter J.T. Bos* and Jean-Pierre Bertoglio

LMFA-CNRS, Ecole Centrale de Lyon, Université de Lyon, Ecully, France

(*Received 4 July 2012; final version received 9 December 2012*)

In a previous communication (W.J.T. Bos and J.-P. Bertoglio 2006, Phys. Fluids , 18, 031706), a self-consistent Markovian triadic closure was presented. The detailed derivation of this closure is given here, relating it to the Direct Interaction Approximation and Quasi-Normal types of closure. The time-scale needed to obtain a self-consistent closure for both the energy spectrum and the scalar variance spectrum is determined by evaluating the correlation between the velocity and an advected displacement vector-field. The relation between this latter correlation and the velocity–scalar correlation is stressed, suggesting a simplified model of the latter. The resulting closed equations are numerically integrated and results for the energy spectrum, scalar fluctuation spectrum and velocity–displacement correlation spectrum are presented for low, unity and high values of the Schmidt number.

Keywords: triadic closure; turbulence; passive scalar; velocity–scalar cross-correlation

1. Introduction

The stochastic nature of turbulence introduces the necessity of a statistical description. Typical statistical descriptors are the mean velocity and the moments of the turbulent fluctuations. In isotropic turbulence the mean velocity is zero and the velocity fluctuations reduce to their geometrically simplest form. Still the interaction of a large number of lengthscales renders the description difficult. A phenomenological description of isotropic turbulence was proposed by Kolmogorov [1], leading to a prediction of the distribution of energy over different lengthscales in a turbulent flow assuming that high Reynolds number turbulence is locally isotropic and that mode interactions are local in scale-space. Experiments [2], presented at the famous Marseille Conference in 1961, confirmed the predicted energy distribution, proportional to $k^{-5/3}$, with k the wavenumber. Deriving this description from first principles, i.e. starting from the Navier–Stokes equations, is a formidable task. Indeed phenomenological models (e.g. [3,4]) reproduced the correct wavenumber dependence of the energy distribution, but the models did not have any direct relation to the Navier–Stokes equations.

A first attempt to build a model for the multi-scale dynamics of a turbulent flow could start from the observation that the single-point velocity statistics seem close to Gaussian. If is assumed that all velocity moments behave in a Gaussian manner, one is directly led to the erroneous conclusion that all different lengthscales are independently decaying under the influence of viscosity since the interaction between modes is governed by triple correlations which are zero in a Gaussian field. Indeed, in a Gaussian field modes are statistically independent and this precludes energy transfer among scales. It is thus clear

*Corresponding author. Email: wouter.bos@ec-lyon.fr

© 2013 Taylor & Francis

that at the level of third order moments, cumulants, defined as the differences of quantities with respect to their Gaussian values, cannot be neglected.

A logical attempt to obtain a correct description of turbulence would then consist in closing the hierarchy of moments by an assumption of Gaussianity at the first level which does allow the triple correlations to be non-zero, in other words, at the level of quadruple correlations. This quasi-normal assumption [5–7] is well documented in the textbook by Monin and Yaglom [8]. Unfortunately, this approach leads to non-physical results, since the energy-spectrum predicted by the quasi-normal model becomes negative at long-times [9], as was carefully suggested previously by Kraichnan [10].

A great breakthrough in the theory of turbulence was the introduction of the Direct Interaction Approximation (DIA) [11]. The great difference with the foregoing attempts is that it is a two-time theory, introducing a new quantity, the response function, corresponding to the response of a turbulent flow on an infinitesimal perturbation. The big difference with the quasi-normal approximation is that cumulants of all orders are allowed to be non-zero and quadruple moments are not assumed to be Gaussian. This issue was at the heart of the discussion between Ian Proudman and Robert Kraichnan at the conference in Marseille [12,13] (see also [14]). Later works showed how these higher order cumulants can be determined within the DIA framework [15,16]. The DIA theory suffered, however, from both a theoretical and a practical weakness.

The theoretical weakness consists in the fact that DIA does not predict the correct inertial range behavior (i.e. in agreement with Kolmogorov's prediction). This was traced back to the fact that its dynamical behavior is not invariant to Galilean transformations [17] and the defect was corrected for by reformulating the theory in a Lagrangian coordinate system [18]. This yielded a description, called the Lagrangian History DIA which gives correct asymptotic behavior for the energy spectrum. However, the formulation becomes extremely complicated in this new set of coordinates. A simplified, or abridged, version was proposed in the same work and an even simpler description of the same type is the Lagrangian Renormalized Approximation (LRA) [19,20].

The practical weakness of these theories, both DIA and the Lagrangian versions, is the two-time character which precludes a computation of long-time statistics, unless the time-history is truncated at some time difference. To obtain a practical statistical model for the dynamics of turbulence, one needs a procedure called Markovianization. This procedure is based on the assumption that the statistical two-time behavior of the turbulent quantities is known, so that the theories can be simplified to a dynamical description which only depends on the current time. Kraichnan proposed such a procedure and applied it to DIA, yielding an approximation known as the Test Field Model [21]. The two-time quantities are in this approach assumed to be exponentially decaying with a typical time-scale which is determined by comparing the decorrelation of a fully compressible field, the test field, with the decorrelation of the advecting velocity field. A simplified version of the Test Field Model is the Eddy-Damped Quasi-Normal Markovian model [22], in which this time-scale is heuristically modeled by a phenomenological straining time-scale of the Heisenberg type [4].

In a previous work [23], we proposed a method to determine this time-scale self-consistently in the framework of the EDQNM theory, using the observation that this time-scale in Lagrangian History DIA is the correlation-time of a fluid particle along a trajectory. In the present article, we will show how our theory is related to the DIA. This will in particular show why a certain number of terms which appeared in the original formulation have to be taken equal to zero for consistency with DIA. We will also apply the approach to the problem of the diffusion of a passive scalar. In the framework of the EDQNM theory, we will propose a model for the scalar flux spectrum, which significantly

simplifies the level of complexity with respect to the models proposed in previous works [24–27].

2. Lagrangian dynamics, Markovianization and determination of the correlation time-scale

Let us introduce the spectral tensor, which is the key quantity in the statistical description of a turbulent flow.

$$\Phi_{ij}(\boldsymbol{k}, t, s) = \mathcal{F}_{(\boldsymbol{r})}\left\{\overline{u_i(\boldsymbol{x}, t)u_j(\boldsymbol{x}+\boldsymbol{r}, s)}\right\} \tag{1}$$

$$= \overline{u_i(\boldsymbol{k}, t)u_j^*(\boldsymbol{k}, s)}, \tag{2}$$

with $\mathcal{F}_{(\boldsymbol{r})}$ a Fourier transform with respect to $\boldsymbol{r}$, $u_i(\boldsymbol{k}, t)$ the Fourier transform of the velocity and the overline denoting an ensemble average. The conjugate $u_j^*(\boldsymbol{k}, s) = u_j(-\boldsymbol{k}, s)$ since the velocity is a real quantity in physical space. In incompressible, mirror-symmetric, isotropic turbulence this quantity is entirely determined by a scalar function, $E(k, t, s)$, the energy spectrum, by the relation

$$\Phi_{ij}(\boldsymbol{k}, t, s) = \frac{E(k, t, s)}{4\pi k^2} P_{ij}(\boldsymbol{k}), \tag{3}$$

with

$$P_{ij}(\boldsymbol{k}) = \delta_{ij} - \frac{k_i k_j}{k^2}. \tag{4}$$

The goal of the present work is to obtain a statistical model for the dynamics of $E(k, t, t) \equiv E(k, t)$. The original DIA theory was based on the above quantities, or representatives, yielding a $k^{-3/2}$ inertial range scaling. This behavior was related to the fact that an Eulerian description does not distinguish between the decorrelation of the velocity modes by the effects of pressure and viscosity on one hand and the sweeping of the small scales by the large scales on the other hand. Sweeping does not contribute to the energy transfer among scales which is the physical mechanism behind the $k^{-5/3}$ prediction. Indeed an Eulerian observer would have no way to see if the decorrelation is due to sweeping or not. To correctly capture the dynamics one needs a Lagrangian description. In other words, one needs to change the representative from (1) to a Lagrangian formulation. Kraichnan reformulated his theory in Lagrangian coordinates [18]. Hereto he introduced the generalized velocity, $u_i(\boldsymbol{x}, t|s)$, defined as the velocity measured at time s on the trajectory which passes at t through $\boldsymbol{x}$. The first time argument is called the labeling time, and the second, the measuring time. This velocity is illustrated in Figure 1. We can associate the Lagrangian position function to this velocity, $x_i(\boldsymbol{x}, t|s)$, defined as the position of the fluid particle at time s on the trajectory which passes through $\boldsymbol{x}$ at time t. These quantities are related to the Eulerian velocity and coordinate system by

$$\boldsymbol{u}(\boldsymbol{x}, t|t) = \boldsymbol{u}(\boldsymbol{x}, t), \tag{5}$$

$$\boldsymbol{x}(\boldsymbol{x}, t|t) = \boldsymbol{x}. \tag{6}$$

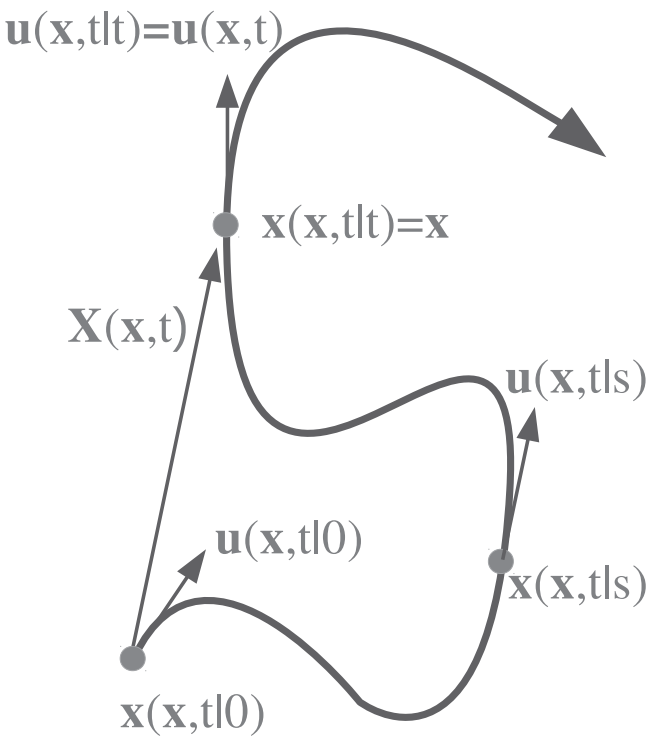


Figure 1. Illustration of the generalized velocity, Lagrangian position vector and displacement vector.

The key quantity that we will use in the following is the Eulerian displacement field $\boldsymbol{X}$ related to the generalized velocity field through the relation

$$X_i(\boldsymbol{x}, t) = \int_0^t u_i(\boldsymbol{x}, t|s)ds = x_i(\boldsymbol{x}, t|t) - x_i(\boldsymbol{x}, t|0). \tag{7}$$

The displacement field is an Eulerian field, which measures at each point $\boldsymbol{x}$ in a fixed, Eulerian, coordinate system the displacement with respect to its original position (at $t = 0$) of the particle which is at point $\boldsymbol{x}$ at time t (see, for example, the discussion in [28]). The displacement vector is also illustrated in Figure 1. Its evolution is given by

$$\frac{\partial X_i(\boldsymbol{x}, t)}{\partial t} + u_j(\boldsymbol{x}, t)\frac{\partial}{\partial x_j}X_i(\boldsymbol{x}, t) = u_i(\boldsymbol{x}, t). \tag{8}$$

Note that since the displacement field is a quantity measured in an Eulerian coordinate system, the evolution equation contains a convective derivative.

Using the generalized velocity, the spectral velocity-tensor now contains four time-arguments

$$\Phi_{ij}(\boldsymbol{k}, t|s; t'|s') = \overline{u_i(\boldsymbol{k}, t|s)u_j^*(\boldsymbol{k}, t'|s')}. \tag{9}$$

However, in the LRA [19] or in the Abridged Lagrangian History DIA [18], the resulting model equations only contain quantities of the form

$$\Phi_{ij}(\boldsymbol{k}, t|t; t|s) = \overline{u_i(\boldsymbol{k}, t|t) u_j^*(\boldsymbol{k}, t|s)}, \tag{10}$$

i.e. one of the velocities is evaluated at a fixed point, since the labeling and measuring time coincide, and the other is moving along its Lagrangian trajectory. The resulting model thus only contains two-time quantities, like the Eulerian DIA, but the time-difference is evaluated along a particle trajectory. The difference between LRA and the Abridged Lagrangian History DIA is that in the former, time derivatives are taken with respect to the measuring time, whereas in the latter these derivatives are taken with respect to the labeling time.

We note that the Lagrangian velocity is not solenoidal. The Eulerian velocity is incompressible so that $\Phi_{ij}(\boldsymbol{k}, t|t; t|s)$ is solenoidal in its first index i. Isotropy and mirror-symmetry imply then that the tensor $\Phi_{ij}(\boldsymbol{k}, t|t; t|s)$ is proportional to $P_{ij}(\boldsymbol{k})$. We can, therefore, define the spectrum

$$\Phi_{ij}(\boldsymbol{k}, t|t; t|s) = \frac{E(k, t|t; t|s)}{4\pi k^2} P_{ij}(\boldsymbol{k}), \tag{11}$$

but this relation is not valid for $\Phi_{ij}(\boldsymbol{k}, t|s; t'|s')$. Since only two-time quantities are used in the following, the spectral tensors and spectra will not be denoted by the four time-arguments, but will be denoted by their short-hand notation

$$\Phi_{ij}(\boldsymbol{k}, t|s) \equiv \Phi_{ij}(\boldsymbol{k}, t|t; t|s) \tag{12}$$

$$E(k, t|s) \equiv E(k, t|t; t|s). \tag{13}$$

This notation should not introduce confusion, because we will only consider spectra in which three of the time-arguments are evaluated at t. Note that the Lagrangian and Eulerian representative coincide when $s = t$

$$E(k, t|t) = E(k, t, t) = E(k, t). \tag{14}$$

The Abridged Lagrangian History DIA constitutes a closed set of equations, yielding a $k^{-5/3}$ inertial range behavior. The equation governing the evolution of $E(k, t)$ is

$$\left[\frac{\partial}{\partial t} + 2\nu k^2\right] E(k, t) = \int\!\!\int_{\Delta}\int_0^t [xy + z^3] p E(q, t|s) \left[k^2 G(k, t|s) E(p, t|s) - p^2 G(p, t|s) E(k, t|s)\right] ds \frac{dpdq}{pq}, \tag{15}$$

in which $G(k, t|s)$ is the response function measured along a trajectory. The symbol Δ indicates the domain in the pq-plane in which k, p, q can form a triangle (in other words $|p - q| \leq k \leq |p + q|$) and x, y, z are given by

$$\begin{aligned} x &= -p_i q_i/(pq) \\ y &= k_i q_i/(kq) \\ z &= k_i p_i/(kp). \end{aligned} \tag{16}$$

The LRA equations differ from (15) in that the right-hand side (RHS) contains quantities of the form $G(k, s|t)$ and $E(k, s|t)$ instead of quantities of the form $G(k, t|s)$ and $E(k, t|s)$. In other words, the labeling and measuring times are inverted in the two-time quantities. We will not consider the LRA in the following. In the Abridged Lagrangian History DIA, Equation (15) is part of a system of three equations, the other two giving the evolution for $E(k, t|s)$ and $G(k, t|s)$, respectively. The equations, although simpler than the original Lagrangian History DIA equations, remain rather complicated and depend on the entire time-history of the flow. Our goal is to simplify the description to obtain a model that does not depend on the entire time-history of the flow, while retaining as much as possible from the original description. We will now explain how we obtain such a model.

We introduce the correlation function $R(k, t|s)$ as

$$R(k, t|s) = \frac{E(k, t|s)}{E(k, t, t)}, \tag{17}$$

which allows to rewrite (15) as

$$\left[\frac{\partial}{\partial t} + 2\nu k^2\right] E(k, t) = \iint_{\Delta} [xy + z^3] pE(q, t)[\hat{\Theta}(kpq)k^2 E(p, t) - \hat{\Theta}(pkq)p^2 G(p, t)E(k, t)]\frac{dpdq}{pq}, \tag{18}$$

with

$$\hat{\Theta}(kpq) = \int_0^t G(k, t|s)R(p, t|s)R(q, t|s)ds. \tag{19}$$

At this point we have not introduced any assumptions with respect to the Abridged Lagrangian DIA. A first assumption that we make is

$$R(k, t|s) = G(k, t|s) \text{ for } t > s, \tag{20}$$

which is a fluctuation–dissipation hypothesis, which leads to

$$\left[\frac{\partial}{\partial t} + 2\nu k^2\right] E(k) = \iint_{\Delta} \Theta(kpq)[xy + z^3] pE(q)\left[k^2 E(p) - p^2 E(k)\right]\frac{dpdq}{pq}, \tag{21}$$

with

$$\Theta(kpq) = \int_0^t G(k, t|s)G(p, t|s)G(q, t|s)ds. \tag{22}$$

The fluctuation–dissipation theorem can be proven to hold rigorously in equilibrium thermodynamics, but in turbulence, corresponding to an out-of-equilibrium dissipative system, this is not the case [29]. It is observed in [30] that in the Abridged Lagrangian History DIA, the fluctuation–dissipation relation is violated. In the LRA, however, which is different from Lagrangian History DIA with respect to the choice of the representative, the fluctuation–dissipation relation holds surprisingly [19,20]. The precise form of the relation

between G and R is, therefore, not uniquely determined and can have important consequences for the Markovian models which result from the assumption, in particular when wave-like phenomena are considered [31].

In the above description, only the *triad time-scale* $\Theta(kpq)$ depends on the time-history of the flow, through the temporal dependence of the response function $G(k,t|s)$. Therefore, by modeling the time-dependence of $G(k,t|s)$, or equivalently $R(k,t|s)$, a single-time description can be obtained. It is at this point that we will proceed in simplifying the description, by introducing specific assumptions on the time-dependence of $R(k,t|s)$. A plausible assumption is that two-time correlations decay exponentially with the time-difference. This cannot be correct for very small times since the time-dependence should be differentiable at zero time difference and such a discontinuity can influence the results in the case of compressible turbulence [32]. A Gaussian time-dependence could be assumed to get correct behavior around zero. It was, however, shown that in the incompressible case the results are relatively insensitive to the exact choice [33], since only the integrals over the exponential are required and the exact form of the time-correlation does not appear in the final expressions. For convenience we will assume, therefore, an exponential time-dependence here

$$R(k,t|s) = \exp\left[-\frac{|t-s|}{\tau(k,t)}\right]. \tag{23}$$

Note that also the choice that τ is here a function of t (and not of s) is a nontrivial assumption. We can integrate both sides of this expression with respect to s to obtain an expression for $\tau(k,t)$

$$\tau(k,t) = \int_{t_0}^{t} R(k,t|s)ds \left(1 - \exp\left[-\frac{|t-t_0|}{\tau(k,t)}\right]\right)^{-1}. \tag{24}$$

For the sake of simplicity, we will consider here the case in which the turbulence has been created a time long before we evaluate it, by taking the limit of t_0 tending towards $-\infty$. This gives the expression

$$\tau(k,t) = \int_{-\infty}^{t} R(k,t|s)ds = \int_{-\infty}^{t} \frac{E(k,t|s)}{E(k,t|t)}ds. \tag{25}$$

The essential step to get a closed model expression for $\tau(k,t)$, which was proposed in [23], was the explicit integration of $E(k,t|s)$ with respect to s. Using relation (7), we can evaluate the integral (25)

$$\begin{aligned}\int_{-\infty}^{t} E(k,t|s)ds &= 2\pi k^2 \mathcal{F}_{(r)}\left\{\int_{-\infty}^{t} \overline{u_i(\boldsymbol{x},t|t)u_i(\boldsymbol{x}+\boldsymbol{r},t|s)}ds\right\} \\ &= 2\pi k^2 \mathcal{F}_{(r)}\left\{\overline{u_i(\boldsymbol{x},t|t)X_i(\boldsymbol{x}+\boldsymbol{r},t)}\right\} \\ &= F(k,t,t),\end{aligned} \tag{26}$$

in which we introduced a new quantity, the velocity–displacement cross-correlation spectrum $F(k,t,s)$

$$\overline{u_i(\boldsymbol{k},t)X_j(-\boldsymbol{k},s)} = \frac{F(k,t,s)}{4\pi k^2}P_{ij}(\boldsymbol{k}), \tag{27}$$

and we will write

$$F(k,t,t) = F(k,t). \tag{28}$$

At this point we have obtained an Eulerian single-time expression for the Lagrangian time-scale

$$\tau(k,t) = \frac{F(k,t)}{E(k,t)}. \tag{29}$$

If the equation for $E(k,t)$ is completed by an equation for $F(k,t)$, we obtain a closed set of equations, if the equation for $F(k,t)$ does not introduce other unknown quantities. In [23] this was accomplished within the framework of the EDQNM closure. In the next section we will obtain similar expressions, using the DIA formalism which will clarify uncertainties in the original derivation. It was observed by Kraichnan [18] that the evolution of $E(k,t|t)$ in the Abridged Lagrangian History DIA is given by the same equation as $E(k,t)$ in the Eulerian DIA. The only difference is that the two-time quantities are now evaluated along particle trajectories. We will use this as an *ansatz* in the following and we will derive the Eulerian DIA expression for $F(k,t)$, in which we will evaluate the two-time correlations using Kraichnan's generalized Lagrangian description. In Section 6 the resulting equations will be numerically integrated and results will be presented for both the dynamics of the kinetic energy spectrum and the dynamics of a passive scalar advected by turbulent flow.

3. Derivation of the evolution equation for the velocity–displacement cross-correlation

We will focus in this section on the derivation of the evolution equation for the wavenumber spectrum of the correlation between the velocity u_i and the displacement vector X_i of a fluid particle. The DIA formalism will be used to evaluate the triple correlations which appear in this equation. A Markovianization procedure is applied to the resulting expressions to obtain a single-time expression. We will try to give a self-contained description of all the operations used in this derivation. However, for a justification of the assumptions in the DIA we refer to the original work [11] or to later works that discuss the justification of the Lagrangian variants of the DIA [19,34–36]. The statistically isotropic and mirror-symmetric case will be considered but in principal this derivation could also be performed for the anisotropic case.

The starting point are the equations for u_i and X_i

$$\begin{aligned}
&\frac{\partial u_i(\boldsymbol{x},t)}{\partial t} + u_j(\boldsymbol{x},t)\frac{\partial}{\partial x_j}u_i(\boldsymbol{x},t) = -\frac{\partial p(\boldsymbol{x},t)}{\partial x_i} + \nu\frac{\partial^2}{\partial x_j^2}u_i(\boldsymbol{x},t)\\
&\frac{dX_i(\boldsymbol{x},t)}{dt} \equiv \frac{\partial X_i(\boldsymbol{x},t)}{\partial t} + u_j(\boldsymbol{x},t)\frac{\partial}{\partial x_j}X_i(\boldsymbol{x},t) = u_i(\boldsymbol{x},t),
\end{aligned} \tag{30}$$

which in Fourier space are written as

$$\Big[\frac{\partial}{\partial t}+\nu k^2\Big]u_i(\boldsymbol{k},t)=-\frac{i}{2}P_{ijm}(\boldsymbol{k})\iint\delta_{\boldsymbol{k}-\boldsymbol{p}-\boldsymbol{q}}u_j(\boldsymbol{p},t)u_m(\boldsymbol{q},t)d\,\boldsymbol{p}d\boldsymbol{q}$$
$$\frac{\partial X_i(-\boldsymbol{k},t)}{\partial t}=i\boldsymbol{k}_j\iint\delta_{\boldsymbol{k}-\boldsymbol{p}-\boldsymbol{q}}u_j(-\boldsymbol{p},t)X_i(-\boldsymbol{q},t)d\,\boldsymbol{p}d\boldsymbol{q}+u_i(-\boldsymbol{k},t), \tag{31}$$

with

$$P_{ijm}(\boldsymbol{k})=k_jP_{im}(\boldsymbol{k})+k_mP_{ij}(\boldsymbol{k}). \tag{32}$$

Multiplying the first equation by $X_i(-\boldsymbol{k},t)$, the second by $u_i(\boldsymbol{k},t)$, summing and ensemble averaging gives

$$\Big[\frac{\partial}{\partial t}+\nu k^2\Big]F(k,t,t)=T^u(k,t)+T^X(k,t)+E(k,t,t), \tag{33}$$

with

$$T^u(k,t)=-i\pi k^2P_{ijm}(\boldsymbol{k})\iint\delta_{\boldsymbol{k}-\boldsymbol{p}-\boldsymbol{q}}\overline{u_j(\boldsymbol{p},t)u_m(\boldsymbol{q},t)X_i(-\boldsymbol{k},t)}d\,\boldsymbol{p}d\boldsymbol{q}$$
$$T^X(k,t)=2i\pi k^2\boldsymbol{k}_j\iint\delta_{\boldsymbol{k}-\boldsymbol{p}-\boldsymbol{q}}\overline{u_i(\boldsymbol{k},t)u_j(-\boldsymbol{p},t)X_i(-\boldsymbol{q},t)}d\,\boldsymbol{p}d\boldsymbol{q}. \tag{34}$$

The DIA is a perturbation method in which the small parameter is the influence of a single triad interaction on the velocity field, compared to the velocity field obtained by the interaction of all other triad interactions. In practice, DIA expressions are obtained by replacing, in the correlations that one is interested in, the velocity field by

$$u_i\to u_i^{(0)}+u_i^{(1)}, \tag{35}$$

and using a similar expression for the displacement vector X_i. The part $u_i^{(0)}$ is the velocity field that would exist if all triad interactions are retained, except for one that we will call $(\boldsymbol{k},\boldsymbol{p},\boldsymbol{q})$. Since in a homogeneous flow an infinite number of triads interact, $u_i^{(0)}$ is supposed to be close to the actual velocity field. The contribution $u_i^{(1)}$ corresponds to the velocity field induced by the interaction $(\boldsymbol{k},\boldsymbol{p},\boldsymbol{q})$ only. The justification of this approach can be interpreted in terms of the coupling strength between the different modes that should be sufficiently small. If this coupling is weak enough and the number of modes tends to infinity, the DIA procedure should give good results. This was tested in [37] on a toy-model in which both the coupling strength and the number of modes could be varied.

After replacing all u's and X's in T^u by (35) and developing, we find that

$$T^u(\boldsymbol{k})=-i\pi k^2P_{ijm}(\boldsymbol{k})\iint\delta_{\boldsymbol{k}-\boldsymbol{p}-\boldsymbol{q}}\Big[\underbrace{\overline{u_j^{(0)}(\boldsymbol{p})u_m^{(0)}(\boldsymbol{q})X_i^{(0)}(-\boldsymbol{k})}}_{\text{zeroth order}}$$
$$+\underbrace{\overline{u_j^{(1)}(\boldsymbol{p})u_m^{(0)}(\boldsymbol{q})X_i^{(0)}(-\boldsymbol{k})}+\overline{u_j^{(0)}(\boldsymbol{p})u_m^{(1)}(\boldsymbol{q})X_i^{(0)}(-\boldsymbol{k})}+\overline{u_j^{(0)}(\boldsymbol{p})u_m^{(0)}(\boldsymbol{q})X_i^{(1)}(-\boldsymbol{k})}}_{\text{first order}}$$
$$+\text{ second and higher order}\Big]\,d\,\boldsymbol{p}d\boldsymbol{q}, \tag{36}$$

in which time-arguments were omitted to shorten the expression. A similar expression is obtained for T^X. In the DIA only the first non-vanishing order is retained in addition to the zeroth order contribution. Higher order contributions should contribute insignificantly if the contribution of a single triad is indeed infinitesimally small. For the triple correlations considered here, the zeroth order contribution (first term on the RHS) in the above expression is equal to zero. The first non-vanishing contribution is the first-order contribution. The Direct Interaction contributions can be written for, for example $u_j(\boldsymbol{p}, t)$ and $X_i(\boldsymbol{k}, t)$, as

$$\begin{aligned} u_j^{(1)}(\boldsymbol{p}, t) &= -i P_{jab}(\boldsymbol{p}) \int_0^t G(\boldsymbol{p}, t, s)\big[u_a^{(0)}(\boldsymbol{k}, s)u_b^{(0)}(-\boldsymbol{q}, s)\big]ds \\ X_i^{(1)}(-\boldsymbol{k}, t) &= ik_a \int_0^t G^X(\boldsymbol{k}, t, s)\big[u_a^{(0)}(-\boldsymbol{p}, s)X_i^{(0)}(-\boldsymbol{q}, s) + u_a^{(0)}(-\boldsymbol{q}, s)X_i^{(0)}(-\boldsymbol{p}, s)\big]ds, \end{aligned} \tag{37}$$

in which $G(\boldsymbol{k}, t, s)$ and $G^X(\boldsymbol{k}, t, s)$ are the response function of the velocity and displacement field, respectively. These are unknown quantities at this point.

These direct interaction contributions are substituted into expression (36). To illustrate the derivation of the final expression we take the first term on the second line of expression (36), which we will denote $T_1(k)$, and we will work out the final expression for this term. Upon substituting (37) in this term we obtain

$$\begin{aligned} T_1(k) = -\pi k^2 \int_0^t \iint \delta_{\boldsymbol{k}-\boldsymbol{p}-\boldsymbol{q}} G(\boldsymbol{p}, t, s) P_{ijm}(\boldsymbol{k}) P_{jab}(\boldsymbol{p}) \\ \times \overline{u_a^{(0)}(\boldsymbol{k}, s)u_b^{(0)}(-\boldsymbol{q}, s)u_m^{(0)}(\boldsymbol{q}, t)X_i^{(0)}(-\boldsymbol{k}, t)} d\boldsymbol{p}d\boldsymbol{q}ds. \end{aligned} \tag{38}$$

This expression is exactly what would be obtained using the quasi-normal approach, for a particular choice of G, the viscous Green-function. However, DIA does not only take into account viscous decorrelation, but also non-linear decorrelation and the DIA expression for G will, therefore, differ from the viscous Green-function. In the limit, which we will consider, in which the flow is constituted of a very large number of modes, we can write the correlation in (38) as a product of double correlations (note that this is no assumption of Gaussianity of the velocity modes, as for example discussed in [37])

$$\overline{u_a^{(0)}(\boldsymbol{k}, s)u_b^{(0)}(-\boldsymbol{q}, s)u_m^{(0)}(\boldsymbol{q}, t)X_i^{(0)}(-\boldsymbol{k}, t)} = P_{bm}(\boldsymbol{q}) \frac{E(q, t, s)}{4\pi q^2} P_{ai}(\boldsymbol{k}) \frac{F(k, s, t)}{4\pi k^2}, \tag{39}$$

in which we used the isotropic expressions for the velocity and velocity–displacement tensors. Introducing this in the above expression we find

$$\begin{aligned} T_1(k) = -\pi k^2 \int_0^t \iint \delta_{\boldsymbol{k}-\boldsymbol{p}-\boldsymbol{q}} G(\boldsymbol{p}, t, s) P_{ijm}(\boldsymbol{k}) P_{jab}(\boldsymbol{p}) P_{bm}(\boldsymbol{q}) P_{ai}(\boldsymbol{k}) \\ \times \frac{E(q, t, s)}{4\pi q^2} \frac{F(k, s, t)}{4\pi k^2} d\boldsymbol{p}d\boldsymbol{q}ds, \end{aligned} \tag{40}$$

which can be written as

$$T_1(k) = -\pi k^2 \iint \delta_{\boldsymbol{k}-\boldsymbol{p}-\boldsymbol{q}} \int_0^t ds\ G(p,t,s)kp\ f_1(k,p,q) \times E(q,t,s)F(k,s,t)(16\pi^2 k^2 q^2)^{-1} d\boldsymbol{p}d\boldsymbol{q}, \tag{41}$$

with $f_1(kpq) = (kp)^{-1} P_{ajm}(\boldsymbol{k}) P_{jab}(\boldsymbol{p}) P_{bm}(\boldsymbol{q})$ in which we used that $P_{ijm}(\boldsymbol{k}) P_{ai}(\boldsymbol{k}) = P_{ajm}(\boldsymbol{k})$. The convolution integral can be rewritten as a function of the wavenumber only. The details of this simplification are given in the appendix of the book by Leslie [38]. The resulting expression is

$$\iint \delta_{\boldsymbol{k}-\boldsymbol{p}-\boldsymbol{q}} d\boldsymbol{p}d\boldsymbol{q} \to \iint_\Delta 2\pi pqk^{-1} dpdq, \tag{42}$$

in which Δ indicates the domain in the pq-plane in which k, p, q can form a triangle (in other words $|p-q| \le k \le |p+q|$). This yields

$$T_1(k) = -\frac{1}{8} \int_\Delta \int_0^t ds\ G(p,t,s) f_1(k,p,q) p^3 E(q,t,s) F(k,s,t) \frac{dp}{p} \frac{dq}{q}. \tag{43}$$

We see that the unknown quantities in this description are the 2-time quantities $E(k,t,s)$, $F(k,s,t)$, $G(k,t,s)$. It is here that we replace these quantities by their analogues defined on Lagrangian trajectories

$$\begin{aligned} E(k,t,s) &\to E(k,t|s) \\ G(k,t,s) &\to G(k,t|s) \\ F(k,t,s) &\to F'(k,t|s) \\ F(k,s,t) &\to F''(k,t|s), \end{aligned} \tag{44}$$

with

$$\begin{aligned} F'(k,t|s) &= 2\pi k^2 \overline{u_i(\boldsymbol{k},t) X_i(-\boldsymbol{k},t|s)} \\ F''(k,t|s) &= 2\pi k^2 \overline{u_i(\boldsymbol{k},t|s) X_i(-\boldsymbol{k},t)}, \end{aligned} \tag{45}$$

in which the difference between F' and F'' arises due to the asymmetric character of the velocity–scalar displacement correlation. As in Section 2, expression (23), we will use the assumption that the two-time quantities decay exponentially in time by posing

$$G(k,t|s) = H(t-s) \exp[-(t-s)\eta(k)] \tag{46}$$

$$G^X(k,t|s) = H(t-s) \exp[-(t-s)\eta^X(k)] \tag{47}$$

$$E(k,t|s) = E(k,t)[G(k,t|s) + G(k,s|t)] \tag{48}$$

$$F'(k,t|s) = F(k,t)[G(k,s|t) + G(k,t|s)] \tag{49}$$

$$F''(k,t|s) = F(k,t)[G^X(k,s|t) + G^X(k,t|s)]. \tag{50}$$

The Heaviside functions $H(t)$ appear since the response functions correspond to the response at time s to a perturbation applied at time t. There is obviously no response before the perturbation is applied. Note further that (48), (49) and (50), which link the response functions to the velocity time-correlations, are, like expression (20), a specific form of the fluctuation–dissipation theorem. Using the above expressions, the time-integral will, in the long-time limit, yield

$$\int_{-\infty}^{t} ds\; G(p,t|s)E(q,t|s)F''(k,t|s) = \Theta^F(kpq)E(q,t)F(k,t), \tag{51}$$

with

$$\Theta^F(kpq) = \frac{1}{\eta^X(k)+\eta(p)+\eta(q)}. \tag{52}$$

We repeat the foregoing analysis for the remaining two terms in T^u_{ip} and the three terms of T^X_{ip}. The Direct Interaction contribution stemming from the X_i in each term yields two contributions, whereas every u_i yields only one contribution (c.f. the symmetry used in expression (40)). The total number of terms is then eight. In the following all quantities are evaluated at time t so that we will omit the time arguments. The resulting equation is

$$\left[\frac{\partial}{\partial t}+\nu k^2\right]F(k) = \sum_{i=1}^{8} T_i(k) + E(k), \tag{53}$$

with

$$T_1(k) = -\frac{1}{8}\int_\Delta \Theta^F(kpq)f_1(k,p,q)p^3E(q)F(k)\frac{dp}{p}\frac{dq}{q} \tag{54}$$

$$T_2(k) = -\frac{1}{8}\int_\Delta \Theta^F(kpq)f_2(k,p,q)q^3E(p)F(k)\frac{dp}{p}\frac{dq}{q} \tag{55}$$

$$T_3(k) = +\frac{1}{8}\int_\Delta \Theta^F(kpq)f_3(k,p,q)k^3E(p)F(q)\frac{dp}{p}\frac{dq}{q} \tag{56}$$

$$T_4(k) = +\frac{1}{8}\int_\Delta \Theta^F(kpq)f_4(k,p,q)k^3E(q)F(p)\frac{dp}{p}\frac{dq}{q} \tag{57}$$

$$T_5(k) = -\frac{1}{4}\int_\Delta \Theta^F(qpk)f_5(k,p,q)p^3E(k)F(q)\frac{dp}{p}\frac{dq}{q} \tag{58}$$

$$T_6(k) = +\frac{1}{4}\int_\Delta \Theta^F(qpk)f_6(k,p,q)k^3E(p)F(q)\frac{dp}{p}\frac{dq}{q} \tag{59}$$

$$T_7(k) = -\frac{1}{4}\int_\Delta \Theta^F(qpk)f_7(k,p,q)q^3E(k)F(p)\frac{dp}{p}\frac{dq}{q} \tag{60}$$

$$T_8(k) = -\frac{1}{4}\int_\Delta \Theta^F(qpk)f_8(k,p,q)q^3E(p)F(k)\frac{dp}{p}\frac{dq}{q}. \tag{61}$$

Symmetries allow to show that $T_1(k) = T_2(k)$ and $T_3(k) = T_4(k)$, which reduces the number of terms to six. The geometrical functions $f_1, .., f_8$ can be expressed as a function of the cosines x, y, z, defined in expressions (16). This yields

$$f_1 = (kp)^{-1} P_{123}(\boldsymbol{k}) P_{214}(\boldsymbol{p}) P_{34}(\boldsymbol{q}) = 2(xy + z^3) \tag{62}$$

$$f_2 = (kq)^{-1} P_{123}(\boldsymbol{k}) P_{24}(\boldsymbol{p}) P_{314}(\boldsymbol{q}) = 2(xz + y^3) \tag{63}$$

$$f_3 = (k)^{-2} k_1 P_{234}(\boldsymbol{k}) P_{13}(\boldsymbol{p}) P_{24}(\boldsymbol{q}) = 1 - xyz - 2y^2 z^2 + y^2 - z^2 \tag{64}$$

$$f_4 = (k)^{-2} k_1 P_{234}(\boldsymbol{k}) P_{23}(\boldsymbol{p}) P_{14}(\boldsymbol{q}) = 1 - xyz - 2y^2 z^2 - y^2 + z^2 \tag{65}$$

$$f_5 = (kp)^{-1} k_1 P_{23}(\boldsymbol{k}) P_{124}(\boldsymbol{p}) P_{34}(\boldsymbol{q}) = xy + z^3 - z + zx^2 \tag{66}$$

$$f_6 = (k)^{-2} k_1 P_{234}(\boldsymbol{k}) P_{13}(\boldsymbol{p}) P_{24}(\boldsymbol{q}) = f_3 \tag{67}$$

$$f_7 = (kq)^{-1} k_1 P_{23}(\boldsymbol{k}) P_{13}(\boldsymbol{p}) q_2 = z(x + yz) \tag{68}$$

$$f_8 = 2(kq)^{-1} k_1 P_{12}(\boldsymbol{p}) q_2 = 2(y + xz). \tag{69}$$

Note that f_4 and f_2 are not needed when symmetry is used to show that $T_1(k) = T_2(k)$ and $T_3(k) = T_4(k)$. Since $f_6 = f_3$, we eventually only need five different factors.

The last step in obtaining closure is the determination of $\eta(k)$ and $\eta^X(k)$. Comparison of Equation (48) with (23) shows that within the framework of our assumptions

$$\eta(k) = \tau(k)^{-1} = E(k,t)/F(k,t). \tag{70}$$

Note that the current model, as it was presented in [23] defined $\eta(k)$ as

$$\eta(k) = E(k,t)/F(k,t) + \nu k^2. \tag{71}$$

Indeed it is now clear that within the framework of the assumptions introduced in the derivation of the current model, the viscous frequency should not be added. It is implicitly contained in the expression for $F(k)$.

We have obtained a closed expression, if the unknown quantity $\eta^X(k)$ is specified. We note here that the displacement is a quantity which will not diffuse along a trajectory, neither by pressure, nor by molecular effects. This suggests the choice

$$\eta^X(k) = 0, \tag{72}$$

in analogy with Lagrangian History DIA arguments for the passive scalar. There is, however, a difference between the equation of the displacement vector and the passive scalar. Indeed, the equation of the displacement vector (30) contains on the RHS the velocity. This forcing is correlated with the displacement. Some analogy exists between this case and the linearly forced Burgers equation. In the latter case the triad relaxation time is directly determined by the correlation-time of the velocity, as was shown by applying the LHDIA technique to Burgers' equation [39]. In order to test the influence of this time-scale on the results, we will also perform simulations in which

$$\eta^X(k) = \mathcal{T}^{-1}, \tag{73}$$

in which $\mathcal{T}$ is the integral time-scale of the velocity field. It will be shown that this choice does not significantly change the results.

4. Equations for the evolution of the energy spectrum and the scalar variance spectrum

Using the above method, equations can be derived for the evolutions of the energy spectrum and of the scalar variance spectrum. The latter is defined by

$$E_\theta(k,t,s) = 2\pi k^2 \overline{\theta(\boldsymbol{k},t)\theta(-\boldsymbol{k},s)}. \tag{74}$$

The resulting equations are identical to the ones given by the EDQNM approach or the test-field model. The only difference is the specification of the time-scale. The equations are

$$\left[\frac{\partial}{\partial t} + 2\nu k^2\right] E(k) = \iint_\Delta \Theta(kpq)[xy + z^3] p E(q) \left[k^2 E(p) - p^2 E(k)\right] \frac{dpdq}{pq}, \tag{75}$$

$$\left[\frac{\partial}{\partial t} + 2\alpha k^2\right] E_\theta(k) = \iint_\Delta \Theta^\theta(kpq)[1 - z^2] p E_\theta(q) \left[k^2 E(p) - p^2 E(k)\right] \frac{dpdq}{pq}. \tag{76}$$

The time-scales which appear in these expressions are

$$\Theta(kpq) = \frac{1}{\eta(k) + \eta(p) + \eta(q)}, \qquad \Theta^\theta(kpq) = \frac{1}{\eta^\theta(k) + \eta'(p) + \eta^\theta(q)}. \tag{77}$$

Using the arguments from the last section, the time-scale $\eta(k)^{-1}$ is given by expression (29). The time-scale associated to the decorrelation of a passive scalar on a Lagrangian trajectory can be inferred from the equation for the scalar

$$\frac{d\theta}{dt} = \alpha \Delta \theta, \tag{78}$$

which suggests that the scalar decorrelation is given by

$$\eta^\theta(k) = \alpha k^2, \tag{79}$$

since on a Lagrangian trajectory the scalar only decorrelates under the action of diffusion. We note that this choice for the scalar is inherent to the choice of the representative [40–42]. For example, the decorrelation time-scale for the velocity is modified if the DIA is applied to the strain-rate instead of to the velocity. However, we will use the above choice, expression (79).

For comparison, it is perhaps useful here to recall the expressions for the time-scales which are used in the EDQNM model [22]. These are

$$\eta(k) = \lambda \sqrt{\int_0^k s^2 E(s) ds} + \nu k^2, \qquad \eta'(k) = \lambda' \sqrt{\int_0^k s^2 E(s) ds} + \nu k^2,$$

$$\eta^\theta(k) = \lambda_\theta \sqrt{\int_0^k s^2 E(s) ds} + \alpha k^2. \tag{80}$$

The value of λ was determined and given the value 0.36 by comparison with the test-field model, the latter being calibrated by comparison with the DIA in a case in which DIA was assumed to give correct results. The value for λ_θ was given the value 0 in [43], using similar arguments as above regarding the Lagrangian decorrelation of a scalar fluctuation. In the same work λ' was given a value different from λ. The parameter λ' appearing in $\Theta^\theta(kpq)$ was determined by comparison with experimental results for the turbulent Prandtl number and was given the value unity. The different values for λ and λ' in the two different time-scales are in contradiction with the outcome of DIA. However, a certain flexibility is allowed if one drops the fluctuation–dissipation theorem. Even more freedom is obtained if one changes the representative used in the analysis. From a practical point of view one might argue that the appearance of adjustable constants in a model allows the user to choose them in comparison with observation rather than by using physical arguments and assumptions.

These expressions for the time-scales used in the EDQNM closure were only recalled here for comparison. They will not be used in the remainder of this work.

5. EDQNM expression for the spectrum of the velocity–scalar cross-correlation

It is at this point that we want to point out a possible simplification of the EDQNM model as proposed and derived in [24–27]. In these works the EDQNM expression was derived for the spectrum of the velocity–scalar correlation spectrum. The resulting expressions contained a time-scale of the form (80). However, in the light of the present derivation it seems that the level of sophistication of that model was higher than the standard EDQNM model. Indeed, the considerations in the present work suggest a much simpler expression to model the scalar flux spectrum. Using the analogy between a passive scalar generated by a mean-scalar gradient and the displacement-vector, expression (29) suggests the following model for the scalar flux spectrum $F_{u\theta}(k)$:

$$\begin{aligned} F_{u\theta}(k) &= \Gamma E(k)/\eta_F(k) \\ &= \Gamma E(k)\left[\lambda_F\sqrt{\int_0^k s^2E(s)ds} + (\nu+\alpha)k^2\right]^{-1}, \end{aligned} \tag{81}$$

with Γ the strength of the mean scalar gradient and λ_F a model constant. This modeling would be of the level of approximation of the EDQNM model and would avoid having to program the lengthy evolution equations which appear in the previous works.

6. Numerical results

In this section we numerically integrate Equations (53), (75) and (76). In these expressions we will insert for $\eta(k)$ and $\eta^\theta(k)$

$$\eta(k) = E(k,t)/F(k,t); \quad \eta^X(k) = 0; \quad \eta^\theta(k) = \alpha k^2. \tag{82}$$

We will first consider decaying turbulence, starting from an initial distribution

$$E(k) = Bk^4\, e^{-2(k/k_L)^2}, \tag{83}$$

with B chosen to normalize the energy to unity. $k_L = 10$ and the first wavenumber of the domain is $k_0 = 1$. Wavenumber space is discretized using a geometrical discretization $k_i = k_0 r^{i-1}$. This possibility in two-point closures to use a geometrical discretization allows to attain much higher Reynolds numbers than in direct numerical simulations for a much lower cost. The discretization in the present computations is approximately 15 wavenumbers per decade. The viscosity is equal to $\nu = 8 \cdot 10^{-8}$. From the initial condition we let the turbulence decay until it reaches a self-similar state in which $e/\epsilon \sim t$, with the kinetic energy and viscous dissipation, respectively determined by

$$e = \int E(k)dk, \qquad \epsilon = 2\nu \int k^2 E(k)dk. \tag{84}$$

All results are evaluated in this phase and the Reynolds number, defined as

$$R_\lambda = \sqrt{\frac{20}{3}\frac{e^2}{\nu\epsilon}} \tag{85}$$

is at the time of evaluation 5000. The scalar spectra are initialized to have the same shape as the kinetic energy. Mixing at three different Schmidt numbers, $Sc = \nu/\alpha$, is evaluated, $Sc = 0.01, 1, 20$. For the computations at $Sc = 0.01$ and $Sc = 20$, in order to clearly produce scaling behavior, both the velocity and the scalar field are forced at the lowest wavenumbers, $k \leq 2$. For the case in which $Sc = 20$, the Reynolds number is taken equal to $R_\lambda = 100$ and the discretization is refined to 50 wavenumbers per decade to more accurately capture nonlocal interactions which play an essential role in the physics of the Batchelor range.

6.1. *Results for the velocity field for high Reynolds number decaying turbulence*

Results for decaying isotropic turbulence at $R_\lambda = 5000$ are shown in Figure 2. We observe that the Kolmogorov constant is of order 1.7. It is observed that in the present model the bottleneck effect, that is, the increasing value of the compensated plot in the beginning of the dissipation range, is absent. Note that this bottleneck is far more pronounced in the EDQNM

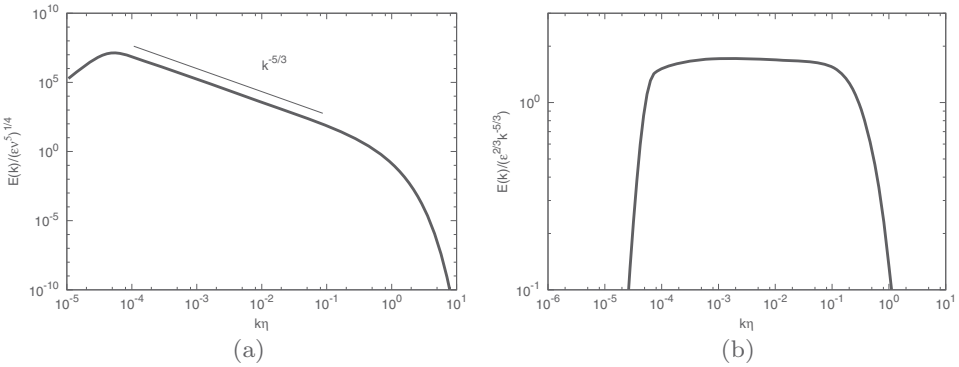


Figure 2. Energy spectrum (a) and in compensated form (b) for decaying isotropic turbulence, modeled by the present closure approach.

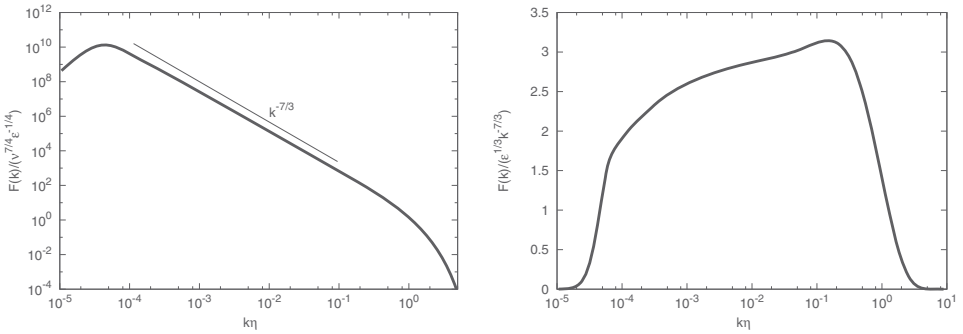


Figure 3. Velocity–displacement cross-correlation spectrum (a) and in compensated form (b) for decaying isotropic turbulence, modeled by the present closure approach.

model [44]. Indeed, the bottleneck is generated by the fact that nonlocal interactions are cut off in the dissipation range, thereby decreasing the transfer of energy so that it piles up [43]. This effect is very sensitive to the relative value of the viscous time-scale compared to the local (in k-space) turbulent time-scale. For example, the bottleneck can be increased by decreasing the value of λ in the EDQNM model.

The constant in

$$F(k) = C_F \epsilon^{1/3} k^{-7/3} \tag{86}$$

is order $C_F \approx 2.5$ as shown in Figure 3. The energy transfer spectrum is shown in Figure 4(a). In Figure 4(b) we see that if we compare the $\eta(k)$ given by our model to $\lambda\sqrt{\int_0^k s^2 E(s)ds}$, there is a short range in which the two are approximately proportional, with a value of $\lambda \approx 0.5$.

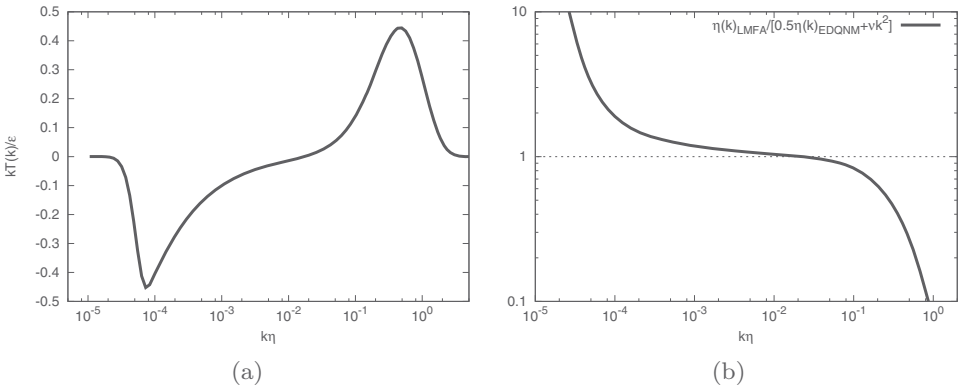
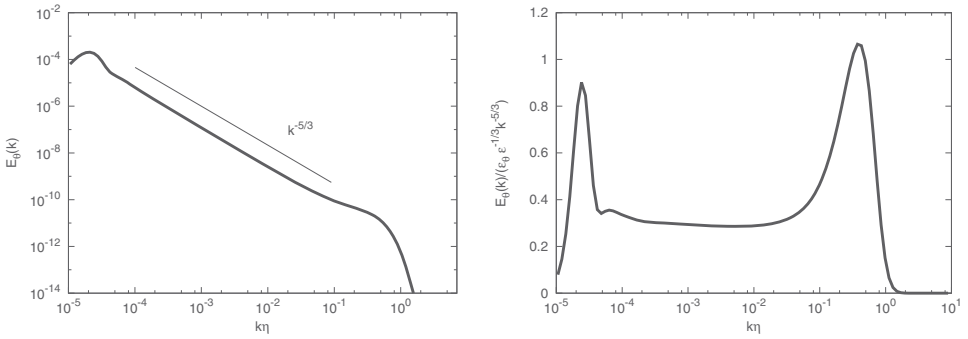


Figure 4. Energy transfer (a) and spectrum of the typical (eddy-damping) time-scale compared to a Heisenberg type time-scale, usually employed in the EDQNM model (b).



(a) (b)

Figure 5. (a) Passive scalar variance spectrum corresponding to a decaying passive scalar at unity Schmidt number. The velocity field is characterized in Figure 2. (b) Compensated form.

6.2. *Results for the mixing of an isotropic passive scalar*

In Figure 5 we show the spectrum of a passive scalar which is freely decaying. The initial spectrum is equal to the spectrum of the velocity field and the spectra are computed at the same time-instant as in Figure 2. A clear inertial-convective range is observed in which the scalar variance distribution is proportional to $k^{-5/3}$, in agreement with classical arguments [45,46]. In the compensated representation it is observed that the dimensionless constant in

$$E_\theta(k) = C_\theta \epsilon_\theta \epsilon^{-1/3} k^{-5/3} \tag{87}$$

is around 0.3 according to our closure. This is about one half of the generally observed value in experiments and numerical simulations [47]. This underprediction is a well-known deficiency of Lagrangian History DIA and its relatives. It can be cured for by changing the representative on which the closure is based [40–42]. This would constitute an interesting perspective, but is not tried in the present work. We note that EDQNM predicts a more realistic value for C_θ [43]. We stress, however, that this value is directly related to the parameter λ'. If this value was chosen equal to λ in the cited reference, then the value for C_θ would be of the same order as the one predicted by our theory. We further observe that a large bottleneck is observed in all these results.

6.3. *Mixing of an isotropic passive scalar at small and large Schmidt number*

We also carried out computations for small and large Schmidt number and the results are shown in Figure 6. It is observed in Figures 6(a) and (b) that the closure manages to reproduce the inertial diffusive range [48]

$$E_\theta(k) = \frac{1}{3} C_k \epsilon_\theta \epsilon^{2/3} \alpha^{-3} k^{-17/3}. \tag{88}$$

In Figures 6(c) and (d), we observe also that the viscous-convective range is reproduced [49]

$$E_\theta(k) = C'_\theta \epsilon_\theta \nu^{1/2} \epsilon^{-1/2} k^{-1}. \tag{89}$$

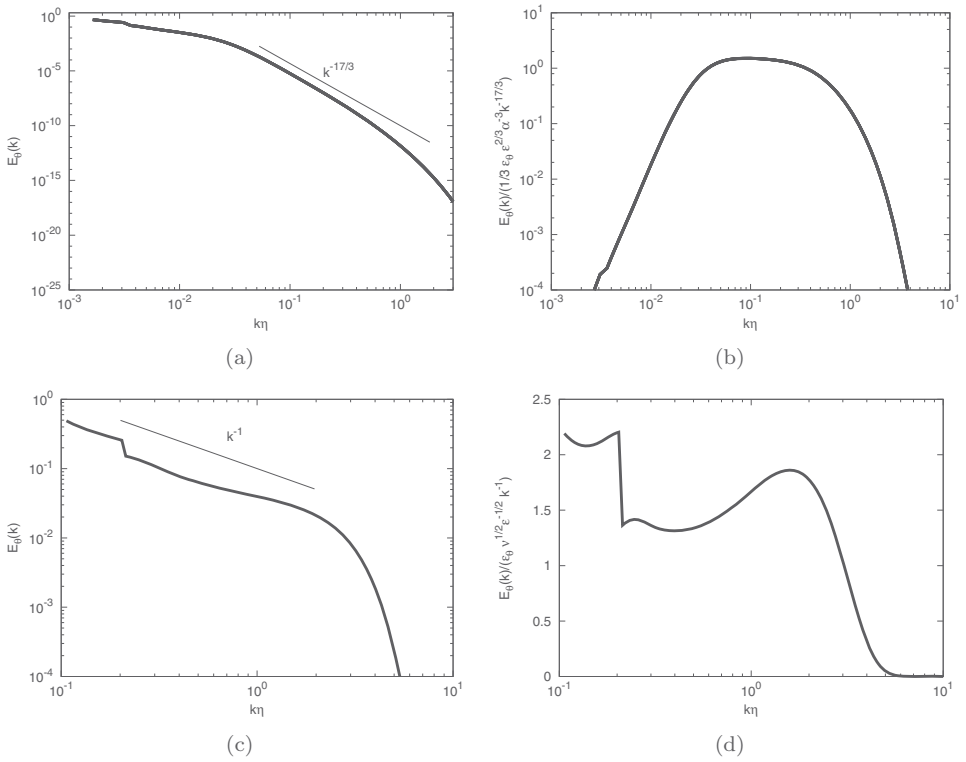


Figure 6. Passive scalar variance spectrum corresponding to a stationary passive scalar, injected in the large scales at small and high Schmidt numbers. Scalar spectrum at $Sc = 0.01$ (a) and in compensated form (b). $Sc = 20$ (c) and in compensated form (d).

6.4. *Influence of the correlation time-scale of the displacement vector*

To test the influence of the correlation time-scale of the displacement vector on the results, we performed a simulation, in which we changed the time-scale of the displacement vector

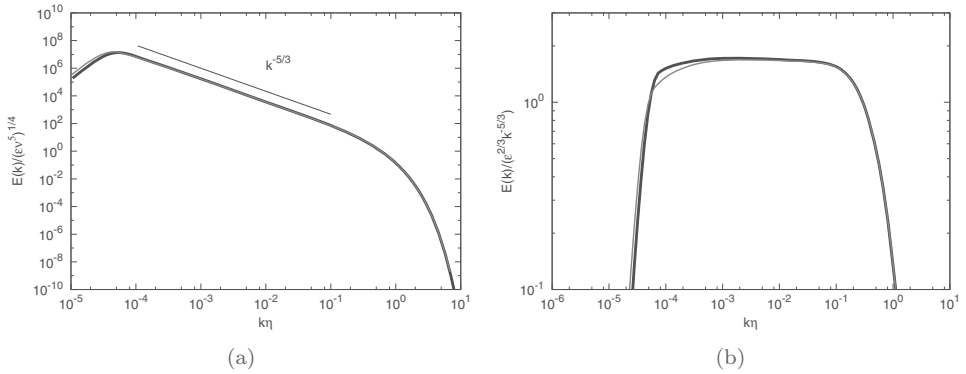


Figure 7. Influence of the correlation time-scale of the displacement vector on the energy spectrum. Energy spectrum (a). Black corresponds to $\eta^X(k) = 0$. The red graph corresponds to $\eta^X(k) = \mathcal{T}^{-1}$. Compensated spectrum (b).

from zero ($\eta^X(k) = 0$) to the integral time-scale ($\eta^X(k) = \mathcal{T}^{-1}$), as described in the last paragraph of Section 3. The results are shown in Figure 7. Clearly, the influence of this change in correlation time is not dramatic in the current application. Only in the large scales of the energy spectrum a small influence is observed. In the inertial and dissipation range the change in time-scale does not seem to influence the results. The reason for this is that in $\Theta^F(kpq)$, only one of the three wave-vectors, $\boldsymbol{k}$ is influenced by this change. The $\eta(p)$ and $\eta(q)$ rapidly dominate over the $\eta^X(k)$, since $\eta(k)$ is an increasing function of k in the inertial range.

7. Concluding remarks

In the present work, we derived a self-consistent Markovian closure starting from the DIA formalism and using the fluctuation–dissipation assumption. Closure was obtained by relating the turbulence time-scale to the spectrum of the cross-correlation of fluid-particle-displacement and velocity, $F(k, t)$. The general idea was announced in a letter [23], but the details of the idea were not given there. In the present work, we show how the present closure is related to the Abridged Lagrangian History DIA, and how the introduction of the displacement vector allows to measure the Lagrangian decorrelation in an Eulerian reference frame. We want to stress that such a single-time closure could perhaps also be obtained applying a similar procedure to the two-time correlations in the LRA, which was not tried here.

The closure was numerically integrated at large Reynolds number ($R_\lambda = 5000$). Results were presented for the energy spectrum and transfer spectrum. Results for the mixing of an isotropic passive scalar were shown for Schmidt numbers 0.01, 1 and 20, respectively and classical scaling was reproduced.

In starting from DIA it becomes clear why a certain number of terms should be neglected in previous works. These terms were present in work on the velocity–scalar cross-correlation spectrum [24–27] and correspond in these studies to non-linear transfer terms which were linearly dependent on the mean-scalar gradient. They should be removed if consistency is required with first-order renormalized perturbation theories such as DIA. They appear as terms which are second order in the formal expansion parameter in the DIA approximation.

Furthermore, a simplified model for the scalar flux spectrum was proposed (81), with a level of complexity comparable to the standard EDQNM model for the energy spectrum.

Let us finish by noting the following: during the Marseille congress 50 years ago, Kraichnan presented his DIA [13] to the scientific community. Many things have changed since then: computational power has increased enormously, making possible the direct numerical simulation of laboratory experiments, advanced experimental techniques allow to visualize almost every feature of a turbulent flow. However, the theoretical description of turbulence, derived from the Navier–Stokes equations, has still not advanced enormously beyond DIA-related approaches. The physical insights obtained from these triadic closures are still an indispensable building block of our description of turbulent flows.

Acknowledgements

Robert Rubinstein is acknowledged for many discussions on DIA and related issues. The authors are thankful to the organizers of the Turbulence Colloquium Marseille 2011, Marie Farge, Keith Moffatt and Kai Schneider for having organized a very stimulating scientific meeting. Two referees have significantly contributed to the improvement of the present work through their comments and suggestions.

References

[1] A. Kolmogorov, *The local structure of turbulence in incompressible viscous fluid for very large Reynolds numbers*, Dokl. Akad. Nauk SSSR 30 (1941), p. 301.

[2] H.L. Grant, R.W. Stewart, and A. Moilliet, *Turbulence spectra from a tidal channel*, J. Fluid Mech. 12 (1962), p. 241.

[3] C. Leith, *Diffusion approximation to inertial energy transfer in isotropic turbulence*, Phys. Fluids 10 (1967), pp. 435–472.

[4] W. Heisenberg, *Zur statistischen Theorie der Turbulenz*, Z. Physik 124 (1948), p. 628.

[5] M. Millionschikov, *On theory of homogeneous isotropic turbulence*, Dokl. Akad. Nauk SSSR 32 (1941), p. 615.

[6] T. Tatsumi, *The theory of decay process of incompressible isotropic turbulence*, Proc. R. Soc. Lond. A 239 (1957), p. 16.

[7] I. Proudman and W. Reid, *On the decay of a normally distributed and homogeneous turbulent velocity field*, Phil. Trans. R. Soc. Lond. A 247 (1954), pp. 163–189.

[8] A. Monin and A. Yaglom, *Statistical Fluid Mechanics II*, MIT Press, Cambridge, MA, 1975.

[9] Y. Ogura, *A consequence of the zero-fourth-cumulant approximation in the decay of isotropic turbulence*, J. Fluid Mech. 16 (1963), pp. 33–40.

[10] R.H. Kraichnan, *Relation of fourth-order to second-order moments in stationary isotropic turbulence*, Phys. Rev. 107 (1957), p. 1485.

[11] R. Kraichnan, *The structure of isotropic turbulence at very high Reynolds numbers*, J. Fluid Mech. 5 (1959), pp. 497–543.

[12] I. Proudman, *On Kraichnan's theory of turbulence*, in *Mecanique de la Turbulence, Coll. Internationale du CNRS a Marseille,* CNRS, Paris, 1962, pp. 107–112.

[13] R. Kraichnan, *Relations among some deductive theories of turbulence*, in *Mecanique de la Turbulence, Coll. Internationale du CNRS a Marseille,* CNRS, Paris, 1962, pp. 99–106.

[14] R. Rubinstein and W. Bos, *Cumulant corrections in turbulence: Quasi-normal approximation, direct interaction approximation, and non-Gaussian properties of turbulence*, in *Progress in Turbulence and Wind Energy IV, Springer Proceedings in Physics,* M. Oberlack, J. Peinke, A. Talamelli, L. Castillo, and M. Hölling, eds., Vol. 141, Springer, Heidelberg, 2012, pp. 25–30.

[15] H. Chen, J. Herring, R. Kerr, and R. Kraichnan, *Non-Gaussian statistics in isotropic turbulence*, Phys. Fluids A 1 (1989), p. 1844.

[16] W. Bos, R. Rubinstein, and L. Fang, *Reduction of mean-square advection in turbulent passive scalar mixing*, Phys. Fluids 24 (2012), 075104.

[17] R. Kraichnan, *Kolmogorov's hypotheses and Eulerian turbulence theory*, Phys. Fluids 7 (1964), p. 1723.

[18] R. Kraichnan, *Lagrangian-history closure approximation for turbulence*, Phys. Fluids 8 (1965), p. 575.

[19] Y. Kaneda, *Renormalized expansions in the theory of turbulence with the use of the Lagrangian position function*, J. Fluid Mech. 107 (1981), pp. 131–145.

[20] Y. Kaneda, *Inertial range structure of turbulent velocity and scalar fields in a Lagrangian renormalized approximation*, Phys. Fluids 29 (1986), pp. 701–708.

[21] R. Kraichnan, *An almost-Markovian Galilean-invariant turbulence model*, J. Fluid Mech. 47 (1971), p. 513.

[22] S. Orszag, *Analytical theories of turbulence*, J. Fluid Mech. 41 (1970), p. 363.

[23] W. Bos and J.P. Bertoglio, *A single-time two-point closure based on fluid particle displacements*, Phys. Fluids 18 (2006), 031706.

[24] S. Herr, L. Wang, and L. Collins, *EDQNM model of a passive scalar with a uniform mean gradient*, Phys. Fluids 8 (1996), p. 1588.

[25] M. Ulitsky and L. Collins, *On constructing realizable, conservative mixed scalar equations using the eddy-damped quasi-normal Markovian theory*, J. Fluid Mech. 412 (2000), pp. 303–329.

[26] W. Bos, H. Touil, and J.P. Bertoglio, *Reynolds number dependency of the scalar flux spectrum in isotropic turbulence with a uniform scalar gradient*, Phys. Fluids 17 (2005), 125108.

[27] W. Bos and J.P. Bertoglio, *Inertial range scaling of scalar flux spectra in uniformly sheared turbulence*, Phys. Fluids 19 (2006), 025104.

[28] S. Corrsin, *Theories of turbulent dispersion*, in *Mecanique de la Turbulence, Coll. Internationale du CNRS a Marseille*, CNRS, Paris, 1962, pp. 27–52.

[29] R.H. Kraichnan, *Deviations from fluctuation-relaxation relations*, Phys. A 279 (2000), p. 30.
[30] R. Kraichnan, *Isotropic turbulence and inertial range structure*, Phys. Fluids 9 (1966), pp. 1728–1752.
[31] J. Bowman, J.A. Krommes, and M. Ottaviani, *The realizable Markovian closure. I. General theory, with application to three-wave dynamics*, Phys. Fluids B 5 (1993), p. 3558.
[32] G. Fauchet and J.P. Bertoglio, *Un modèle en deux points pour la turbulence compressible*, C. R. Acad. Sci. Paris, Série IIb 327 (1999), p. 665.
[33] R. Kraichnan, *Inertial-range transfer in two- and three-dimensional turbulence*, J. Fluid Mech. 47 (1971), p. 525.
[34] R. Kraichnan, *Eulerian and Lagrangian renormalization in turbulence theory*, J. Fluid Mech. 83 (1977), p. 349.
[35] S. Kida and S. Goto, *A Lagrangian direct-interaction approximation for homogeneous isotropic turbulence*, J. Fluid Mech. 345 (1997), p. 307.
[36] Y. Kaneda, *Lagrangian renormalized approximation of turbulence*, Fluid Dyn. Res. 39 (2007), p. 526.
[37] S. Goto and S. Kida, *Sparseness of nonlinear coupling: Importance in sparse direct-interaction perturbation*, Nonlinearity 15 (2002), p. 1499.
[38] D. Leslie, *Developments in the Theory of Turbulence*, Oxford University Press, Oxford, 1973.
[39] R. Kraichnan, *Lagrangian-history statistical theory for Burgers' equation*, Phys. Fluids 11 (1968), p. 265.
[40] R. Kraichnan and J. Herring, *A strain-based Lagrangian-history turbulence theory*, J. Fluid Mech. 88 (1978), pp. 355–367.
[41] J. Herring and R. Kraichnan, *A numerical comparison of velocity-based and strain-based Lagrangian-history turbulence approximations*, J. Fluid Mech. 91 (1979), pp. 581–597.
[42] T. Gotoh, J. Nagaki, and Y. Kaneda, *Passive scalar spectrum in the viscous-convective range in two-dimensional steady turbulence*, Phys. Fluids 12 (2000), pp. 155–168.
[43] J. Herring, D. Schertzer, M. Lesieur, G. Newman, J. Chollet, and M. Larcheveque, *A comparative assessment of spectral closures as applied to passive scalar diffusion*, J. Fluid Mech. 124 (1982), p. 411.
[44] J. André and M. Lesieur, *Influence of helicity on the evolution of isotropic turbulence at high Reynolds number*, J. Fluid Mech. 81 (1977), p. 187.
[45] S. Corrsin, *On the spectrum of isotropic temperature fluctuations in an isotropic turbulence*, J. Appl. Phys. 22 (1951), p. 469.
[46] A. Obukhov, *Structure of the temperature field in turbulent flows*, Isv. Geogr. Geophys. Ser. 13 (1949), p. 58.
[47] K. Sreenivasan, *The passive scalar spectrum and the Obukhov-Corrsin constant*, Phys. Fluids 8 (1996), pp. 189–196.
[48] G. Batchelor, I.D. Howells, and A.A. Townsend, *Small-scale variation of convected quantities like temperature in turbulent fluid. Part 2. case of large conductivity*, J. Fluid Mech. 5 (1959), p. 134.
[49] G. Batchelor, *Small-scale variation of convected quantities like temperature in turbulent fluid. Part 1. small conductivity*, J. Fluid Mech. 5 (1959), p. 113.

Journal of Turbulence, 2013
Vol. 14, No. 3, 121–160, http://dx.doi.org/10.1080/14685248.2013.780128

Taylor & Francis
Taylor & Francis Group

Third-order statistics and the dynamics of strongly anisotropic turbulent flows

C. Cambon[a], L. Danaila[b], F.S. Godeferd[a*] and J.F. Scott[a]

[a]*LMFA, Université de Lyon, École centrale de Lyon, France;* [b]*CORIA, Université de Rouen, France*

(*Received 18 September 2012; final version received 20 February 2013*)

Anisotropy is induced by body forces and/or mean large-scale gradients in turbulent flows. For flows without energy production, the dynamics of second-order velocity or second-order vorticity statistics are essentially governed by triple correlations, which are at the origin of the anisotropy that penetrates towards the inertial range, deeply altering the cascade and the eventual dissipation process, with a series of consequences on the evolution of homogeneous turbulence statistics: in the case of rotating turbulence, the anisotropic spectral transfer slaves the multiscale anisotropic energy distribution; *nonlinear* dynamics are responsible for the *linear* growth in terms of Ωt of axial integral length-scales; third-order structure functions, derived from velocity triple correlations, exhibit a significant departure from the $4/5$ Kolmogorov law. We describe all these implications in detail, starting from the dynamical equations of velocity statistics in Fourier space, which yield third-order correlations at three points (triads) and allow the explicit removal of pressure fluctuations. We first extend the formalism to anisotropic rotating turbulence with 'production', in the presence of mean velocity gradients in the rotating frame. Second, we compare the spectral approach at three points to the two-point approach directly performed in physical space, in which we consider the transport of the scalar second-order structure function $\langle(\delta q)^2\rangle$. This calls into play componental third-order correlations $\langle(\delta q)^2\delta\mathbf{u}\rangle(\mathbf{r})$ in axisymmetric turbulence. This permits to discuss inhomogeneous anisotropic effects from spatial decay, shear, or production, as in the central region of a rotating round jet. We show that the above-mentioned important statistical quantities can be estimated from experimental planar particle image velocimetry, and that explicit passage relations systematically exist between one- and two-point statistics in physical and spectral space for second-order tensors, but also sometimes for third-order tensors that are involved in the dynamics.

Keywords: turbulence; anisotropy; third-order statistics

1. Introduction

Anisotropy is induced by body forces, such as Coriolis, buoyancy, Lorentz forces, and/or by large-scale (mean) gradients of velocity, density, or external magnetic field, in turbulent flows, buoyant or not, electrically conducting or not. It is often considered that anisotropy only affects the largest scales of the turbulent flow, so that the cascade of anisotropy only mildly penetrates towards the scales in the inertial range, with eventually no direct impact on the dissipative range, according to the view inherited from [1]. In this scheme, large-scale anisotropy induced by body forces and/or mean gradients is just considered as a particular modality of 'forcing' the largest scales. This viewpoint is radically questioned for flows in which the body force responsible for anisotropy is energy conserving. The simplest

*Corresponding author. Email: fabien.godeferd@ec-lyon.fr

© 2013 World Bank

example is turbulence in a rotating fluid in the absence of artificial forcing. In that case, the Coriolis force can profoundly modify the dynamics of the cascade, not by direct action on second-order velocity correlations, but via the third-order moments. Indeed, it is well known that there is no linear effect of rotation on the second-order, single-time moments of homogeneous turbulence (see e.g. [2]), a result which was recently rediscovered by [3] using a linearized direct numerical simulation (DNS).

If the turbulence is initially Gaussian, it will remain so according to linear theory. Since all statistics of a Gaussian field are determined by its second-order moments, if these are time-independent (as for rotating, homogeneous turbulence according to inviscid linear theory), the velocity field will have exactly the same single-time statistical properties (including higher order moments) at all times. This precludes the suggestion by some authors (see [4] and our later discussion) that linear theory can provide an explanation of observed anisotropy in rotating, homogeneous turbulence, at least in the Gaussian case.

Nonlinearity produces energy transfer between different spatial scales, as in classical Kolmogorov theory, but the transfer may be significantly modified in the anisotropic case. This leads us to consider third-order moments of velocity because, whenever equations for the second-order (energy-containing) moments are formulated, third-order moments appear as the origin of energy transfer (and indeed of more subtle correlations). Thus, a clear understanding of third-order statistics is essential.

Some idea of the effect of rotation can be obtained using linear theory to calculate the third-order moments. Of course, this only gives interesting answers if the initial flow is non-Gaussian; otherwise, the third-order moments are zero and there is no spectral evolution. Starting from an initial, non-Gaussian, isotropic flow, isotropy is broken and many of the qualitative effects of the Coriolis force are recovered: global inhibition of the energy transfer, yielding a reduction of the dissipation rate, creation of increasing anisotropy by transfer of energy towards the zero-frequency plane in wave-vector space (see figure 6 in [2]). The same approach has been used by [5] (at first order in time) and [6] (general linear solution for three-point third-order moments in its appendix) to study the creation of triple vertical vorticity correlations, with results showing the observed preference for cyclonic vorticity. Although this approach yields interesting results concerning anisotropy, the effects are only transient because phase-mixing is expected to suppress all third-order moments at moderately large Ωt, and probably damp any other statistics reflecting departure from Gaussianity. Nonlinear effects of the dynamics of the third-order moments, absent in the above theory, need to be included.

Wave turbulence theory, surveyed by [7], provides a relatively recent and rigorous framework for studying the limit of weak nonlinearity in systems for which the linear dynamics consist of dispersive waves. It shows that any strong initial departure from Gaussian statistics in weakly nonlinear, homogeneous turbulence is essentially erased during a transient phase of the order of the wave periods. Once this is achieved, there remains small departure from Gaussianity (and indeed weakly non-Gaussian statistics appear spontaneously if the flow is initially Gaussian). Small third-order moments are maintained by nonlinear forcing from fourth-order moments. The third-order moments in turn control the second-order ones. This is as in quasi-normal spectral closure and provides a firm basis for such closures in the weakly nonlinear limit. Nonlinear transfer is strongly inhibited by the requirement of resonance of the wave-vector triads responsible for such transfer. For rotating turbulence, weak nonlinearity corresponds to a small Rossby number, R_o, a case for which [8] give analytical details (see also [9]), numerical results and a discussion of the relationship between quasi-normal closure and wave turbulence. Resonant inhibition of nonlinear transfer leads to spectral evolution on a time-scale R_o^{-1} larger than the large

eddy turnover time. Anisotropy develops from isotropic initial conditions due to nonlinear energy transfer towards the plane of zero frequency in wave-vector space. However, two-dimensionalization does not occur: the fraction of energy at or near the zero-frequency plane remains small at all times. The cascade to small scales is strongly anisotropic, producing angle-dependent spectra which become more and more (not less) anisotropic, the smaller the scale considered.

In order to overcome the asymptotic limitation of wave turbulence theory, and to incorporate transient linear effects on third-order moments, we will use a fully nonlinear closure model, called EDQNM3 (eddy-damped quasi-normal Markovian), capable of matching both small-time and very large time effects. This model offers significant improvements with respect to the EDQNM2 version used by [2] and [10], in terms of consistency and realizability, but with very little differences in numerical results in the practical domain – for experiments and DNS – of moderate Rossy number and moderate elapsed time.

Before rediscussing the related formalism, it is perhaps useful to clarify a possible misunderstanding about what is 'linear' and 'nonlinear' dynamics. Faced with the lack of answer of linear theory [so-called rapid distortion theory (RDT)] for predicting second-order statistics in rotating turbulence, [11] suggested that the formation of anisotropic structures cannot be studied in classical homogeneous turbulence, and they propose either to look at the purely linear evolution from compact vorticity sources or to define integral length-scales not from second-order velocity (or vorticity) correlations but from quartic correlations (see [3,4]), invoking a loss of phase coherence in homogeneous turbulence. It is important to notice that the above-mentioned 'drawbacks' of homogeneous turbulence are only for linear prediction of single-time second-order correlations. In our general approach, the linear Coriolis effect is generated, before application to any statistics, by Green's function of inertial waves, or

$$\widehat{G}_{ij}(\boldsymbol{k}, t, t') = \Re\left(N_i(-\boldsymbol{k})N_j(\boldsymbol{k})\exp(\mathrm{i}\sigma_k(t-t'))\right), \tag{1}$$

in which $\boldsymbol{N}(\boldsymbol{k})$ is the eigenmode of inertial waves, and

$$\sigma_k = 2\Omega\frac{k_\parallel}{k} \tag{2}$$

is the *anisotropic* dispersion law frequency of inertial waves.

The 'overhat' denotes a Fourier transform, and, if necessary, it is extended in the sense of distributions if applied to a non-smooth variable, such as a random realization of the velocity field $\boldsymbol{u}$. The linear solution may thus be expressed locally in Fourier space as $\hat{u}_i(\boldsymbol{k}, t) = \widehat{G}_{ij}(\boldsymbol{k}, t, t')\hat{u}_j(\boldsymbol{k}, t')$, or as a convolution integral in physical space as $u_i(\boldsymbol{x}, t) = \iiint G_{ij}(\boldsymbol{x}-\boldsymbol{x}', t, t')u_j(\boldsymbol{x}', t')\mathrm{d}^3\boldsymbol{x}'$.

When applied to a particular non-Gaussian realization of an initial velocity field, this anisotropic operator can produce anisotropic patterns due to the differential propagation of inertial waves over various orientations, depending on their frequency. On the one hand, if used only for RDT prediction of second-order statistics, the operator gives no significant effect of rotation. This is not because the second-order spectral tensor defined by

$$\langle\hat{u}_i^*(\boldsymbol{p}, t)\hat{u}_j(\boldsymbol{k}, t)\rangle = \hat{R}_{ij}(\boldsymbol{k}, t)\delta^3(\boldsymbol{k}-\boldsymbol{p}) \tag{3}$$

is not affected by a phase correction, or $\hat{\boldsymbol{u}}(\boldsymbol{k}) \rightarrow \hat{\boldsymbol{u}}(\boldsymbol{k}) \exp(\mathrm{i}\alpha_k)$: the linear solution generated by Green's function (1) involves two terms, one with $\mathrm{e}^{\mathrm{i}\sigma_k t}$ and the other with $\mathrm{e}^{-\mathrm{i}\sigma_k t}$, and thus does not reduce to a single multiplicative phase term. The reason for the lack of answer of a linear solution for spectral energy is simply the Coriolis force produces no energy. The same result about the lack of linear effect of the Coriolis force can be obtained from the Kármán–Howarth equation in physical space, or the equation governing the trace of $R_{ij}(\boldsymbol{r}, t)$,

$$R_{ij}(\boldsymbol{r}, t) = \langle u_i(\boldsymbol{x}, t) u_j(\boldsymbol{x} + \boldsymbol{r}, t) \rangle, \tag{4}$$

as well, when discarding the contribution of third-order statistics. On the other hand, a dedicated phase operator, generated by the three-fold product of Green's functions in Equation (1),

$$\exp\left(\mathrm{i}(\sigma_k \pm \sigma_p \pm \sigma_q)(t - t')\right), \quad \boldsymbol{q} = -\boldsymbol{k} - \boldsymbol{p}, \tag{5}$$

does affect the third-order spectral tensor $\boldsymbol{S}$ defined by

$$\langle \hat{u}_n(\boldsymbol{p}, t) \hat{u}_m(\boldsymbol{q}, t) \hat{u}_i(\boldsymbol{k}, t) \rangle = S_{nmi}(\boldsymbol{k}, \boldsymbol{p}, t) \delta^3(\boldsymbol{k} + \boldsymbol{p} + \boldsymbol{q}). \tag{6}$$

More generally, the exponential multiplier in Equation (5) is present from the very beginning in the nonlinear part of the equations for wave-amplitude (47), derived from basic Navier–Stokes equations in a rotating frame, before applying any statistical treatment or any assumption, as recalled and revisited in Section 4.1.

This is the underlying dynamical support for 'cubic RDT', asymptotic wave turbulence theory, and EDQNM matching them, discussed above. On the one hand, the dominant underlying Coriolis effect which can be understood in homogeneous anisotropic turbulence *at small time* is a *linear effect applied to cubic correlations.* If linear theory gives no answer for double correlations, we do not need to drop the context of homogeneous turbulence, but to look at RDT for the further order, whence to cubic correlations. Using an example in a much more complex context – but perhaps more popular for physicists – if wave-turbulence theory does not work with three-wave interactions, one does not need to drop wave-turbulence theory, but to move to four-wave interactions, and so on. On the other hand, in the typical equations that govern second-order statistics, or $\hat{\mathsf{R}}$ here, the cubic term, or $\mathsf{S}(\boldsymbol{k}, \boldsymbol{p}, t)$ here, is called into play because of the *quadratic nonlinearity* of Navier–Stokes equations: in this sense, our approach, generalized to any time and to any initial Rossby number, is nonlinear, and the dynamics of second-order statistics – in the absence of energy production – *are slaved to third-order statistics.*

We close this long preamble by an example supported by an experimental approach to homogeneous anisotropic rotating turbulence. Typical integral length-scales along the axial direction were first calculated by [2] and first measured by [12], as $L_{\perp}^{(\parallel)}$, for transverse velocity fluctuations, and $L_{\parallel}^{(\parallel)}$ for axial velocity fluctuations. The main result was to show a dynamical 'decoupling' of these two correlation length-scales, with $L_{\parallel}^{(\parallel)}$ poorly affected by rotation and $L_{\perp}^{(\parallel)}$ having a linear growth in time (Ωt) after a transitional macro Rossby number close to 1. The later *linear growth rate* in time does not result from the sole *linear dynamics*, and is recovered only by looking at the impact of the Coriolis force on nonlinear transfer terms mediated by cubic correlations, as found in previous studies using anisotropic EDQNM and a fully nonlinear DNS [2,10,13,14].

We hope to make definitely clear these aspects of rotating turbulence dynamics in this paper using new more explicit equations and new numerics.

A second aim of this article is to bridge statistics and dynamics for homogeneous, possibly strongly anisotropic, turbulence in both physical space and Fourier space. Our preamble has emphasized the interest of triple velocity at three points [or $\mathbf{S}(\boldsymbol{k}, \boldsymbol{p}, t)$ in terms of triads] for dynamics. This carries more information than the classical third-order structure function – at two-point only – but only the latter is easy to measure. Accordingly, dynamical equations will be first studied in Fourier space, but statistical quantities will be extracted also in physical space, for both second-order and third-order correlations.

Our special interest for the dynamics of triple correlations at three points, or the equation which governs $\mathbf{S}(\boldsymbol{k}, \boldsymbol{p}, t)$, calls into play the classical closures from Kraichnan's and Orszag's legacy. Their conventional name of 'two-point closures' being misleading – two-point closures do exist for third-order two-point correlations present in Kármán–Howarth type equations – we will refer to them as 'triadic' closures. Sometimes their role can be restricted to generating information not available – too noisy, too cumbersome – from physical and numerical experiments. For instance, RDT for triple-vorticity correlations was shown to be nontrivial and informative by [5] – to first order in time – [47] and especially by [6]. It can be exactly expressed as an integral of an initial value of $\mathbf{S}(\boldsymbol{k}, \boldsymbol{p}, t)$, weighted by the time-dependent operator in Equation (5). Accordingly, we need to know the initial distribution of triple velocity, or vorticity, at three points, or for every triad, have information which is very difficult to generate directly in physical space, even for isotropic turbulence – assuming initial isotropy as in [5,6] – but this can be systematically done in terms of the sole initial energy spectrum using basic EDQNM, from [15].

Other cases with no production and involving waves, not revisited here, can be addressed with the same approach. The first one is stably-stratified, rotating or not, turbulence, in which there is an additional term of buoyancy fluctuation with its own transport equation, and in which there is no production of toroidal (or quasi-geostrophic with rotation) energy as well as no production of total – kinetic + potential – wave energy [16,17]. The other case of Alfvénic turbulence has similar aspects: an additional induction equation for the fluctuating magnetic field and no production of total – kinetic + magnetic – energy.

In addition, we will consider turbulent flows with 'production', but restricted to the velocity field only (no coupled fields for the sake of simplicity). In this case, RDT for predicting second-order statistics is already relevant and perhaps less attention has to be paid to the proper dynamics of third-order statistics. Nevertheless, all the tools used in the cases without production will be generalized to a rotating shear flow in Section 2, including triadic closures altered by linear distorting operators. In order to have a parallel two-point approach directly performed in physical space, we consider the flow with production in this context. This approach cannot give new results on the dynamics of cubic correlations, but it has the merit to partially relax the assumption of homogeneity, assuming only local homogeneity, and to exhibit what are the relevant two-point cubic correlations to measure and to investigate in a scale-by-scale budget.

This article consists of six parts. The anisotropic description is addressed in Section 2, in both physical space and spectral space, in general cases with mean-shear-production effects. A brief reminder of the isotropic case is given in Section 3, with emphasis on third-order statistics and a recap for the isotropic turbulence formulae in Table 1. In Section 4, emphasis is placed on rotating turbulence as a case of flow 'without production', in which the dynamics mediated by triple correlations are essential. The case of quasi-static magnetohydrodynamics (QS-MHD) is given as a toy model for explaining a complete transition from three-dimensional structure to two-dimensional one, in contrast to the more complex case of rotating turbulence. The technical aspects of derivation of statistics for anisotropic

Table 1. Recap of the relationships between second- and third-order statistics in physical and spectral space for isotropic turbulence.

Physical-space quantity	Relationship
Second-order statistics in terms of the energy spectrum $E(k)$	
Longitudinal correlation $f_L(r)$	$u'^2 f_L(r) = 2\int_0^\infty g_3(kr)E(k)\mathrm{d}k$ with $g_3(kr) = \dfrac{\sin kr - kr\cos kr}{k^3r^3}$
Two-point correlation tensor $R_{ii}(r)$	$R_{ii}(r) = 2\int_0^\infty \dfrac{\sin kr}{kr}E(k)\mathrm{d}k$
Second-order structure function $\langle(\delta q)^2\rangle$	$\langle(\delta q)^2\rangle = 2\int_0^\infty \left(1-\dfrac{\sin kr}{kr}\right)E(k)\mathrm{d}k$
Third-order statistics in terms of the energy transfer spectrum $T(k)$	
Two-point correlation tensor $Q_{ilm}(\boldsymbol{r}) = \langle u_i(\boldsymbol{x})u_l(\boldsymbol{x})u_m(\boldsymbol{x}+\boldsymbol{r})\rangle$	$Q_{lmi}(\boldsymbol{r}) = u'^3\left[\dfrac{1}{2}\left(K - r\dfrac{\partial K}{\partial r}\right)\dfrac{r_l r_m r_i}{r^3} + \dfrac{1}{4}\left(2\dfrac{K}{r}+\dfrac{\partial K}{\partial r}\right)(r_i\delta_{lm}+r_m\delta_{il}) - \dfrac{1}{2}K\dfrac{r_l}{r}\delta_{im}\right]$ with $u'^3K(r) = 2r\int_0^\infty g_5(kr)T(k)\mathrm{d}k$ and $g_5(kr) = \dfrac{3(\sin kr - kr\cos kr) - (kr)^2\sin kr}{(kr)^5}$
Longitudinal two-point third-order correlation $R_{LL,L}(t)$	$R_{LL,L}(r,t) = r\int_0^\infty g_3(kr)T(k,t)\mathrm{d}k$
Third-order structure function $\langle\delta u_L\,(\delta q)^2\rangle$	$\langle\delta u_L\,(\delta q)^2\rangle = 4r\int_0^\infty g_3(kr)T(k)\mathrm{d}k$

flows, both in Fourier space and in physical space, are contrasted and partly reconciled in Section 5. Section 6 is devoted to a conclusion.

2. Sheared homogeneous turbulence in a rotating frame

In the presence of a mean velocity gradient, the Navier–Stokes equation includes additional advection and deformation terms linked to the mean – or large-scale – velocity field U_i:

$$\left(\frac{\partial}{\partial t} + u_j\frac{\partial}{\partial x_j}\right)u_i + \underbrace{2\epsilon_{inj}\Omega_n u_j}_{\text{Coriolis force}} + \underbrace{U_j\frac{\partial u_i}{\partial x_j} + \frac{\partial U_i}{\partial x_j}u_j}_{\text{additional convection-production terms}} = -\frac{\partial p}{\partial x_i} + \nu\nabla^2 u_i. \quad (7)$$

In view of the importance of rotating flows, we also consider an additional Coriolis force with angular velocity $\boldsymbol{\Omega}$. Of course, solid-body rotation corresponds to a pure antisymmetric mean velocity gradient, and could be addressed as such in a Galilean frame of reference; it is, however, easier to treat it as a Coriolis force in the comoving rotating frame of reference. Accordingly, the antisymmetric part of $\partial U_i/\partial x_j$, or $\boldsymbol{W} = \epsilon_{ijn}U_{n,j}$, and the system vorticity $2\boldsymbol{\Omega}$ yield different terms in Equation (7). In addition, in Equation (7), p is the pressure divided by a reference density, and can incorporate the centrifugal force in a rotating frame. In general, the mean flow gradient with a non-zero symmetric part is not consistent with axisymmetry for the fluctuations, except near the centerline of axisymmetric convergent or divergent ducts.

2.1. *From Craya's equations to generalized Lin equations*

In the presence of a mean flow with space-uniform gradients $A_{ij}(t) = \partial U_i/\partial x_j$, consistent with homogeneity for the fluctuations, in a frame rotating or not, spectral equations are easily generalized, including transport and 'production' from Equation (7). The counterpart of Equation (7) in Fourier space with additional mean flow terms is

$$\dot{\hat{u}}_i + M_{ij}\hat{u}_i + \mathrm{i}P_{imn}(\boldsymbol{k})\widehat{u_m u_n} = 0, \tag{8}$$

with

$$M_{ij} = \left(\delta_{in} - 2\frac{k_i k_n}{k^2}\right) A_{nj} + 2P_{in}\epsilon_{nmj}\Omega_n. \tag{9}$$

The $\dot{}$ corresponds to $\partial/\partial t + A_{ij}x_j\partial/\partial x_j$, mean flow advection in physical space, and to $\partial/\partial t - A_{ji}k_j\partial/\partial k_j$ in Fourier space. It is generally solved following a system of characteristic lines defined by

$$x_i = F_{ij}(t, t_0)X_j;\ k_i = F^{-1}_{ji}(t, t_0)K_j, \tag{10}$$

which is consistent with 'shear wave' (astrophysics), 'Kelvin mode' (linear stability), or 'Rogallo space' (engineering), depending on the community (see [18,19], for details.) The first equation in (10) is the mean flow trajectory, $\boldsymbol{X}$ being the position at time t_0, or the Lagrangian coordinate for the mean. The matrix $\mathbf{F}$ is the gradient of displacements, or 'Cauchy matrix', obtained from the mean velocity gradient A_{ij} by $\dot{F}_{ij} = A_{im}F_{mj}$. The quadratic nonlinearity corrected by fluctuating pressure involves Kraichnan's projector

$$P_{inm}(\boldsymbol{k}) = \frac{1}{2}\left(k_m\left(\delta_{in} - \frac{k_i k_n}{k^2}\right) + k_n\left(\delta_{im} - \frac{k_i k_m}{k^2}\right)\right). \tag{11}$$

From Equation (8), one derives the equation for $\hat{\mathbf{R}}$ as

$$\dot{\hat{R}}_{ij} + 2\nu k^2\hat{R}_{ij} + M_{in}\hat{R}_{nj} + M_{jn}\hat{R}_{in} = T_{ij}, \tag{12}$$

in which the right-hand side calls into play contributions from two-point, third-order correlations, as an integral of the third-order *triadic* spectral tensor, namely

$$T_{ij}(\boldsymbol{k}) = \mathrm{i}P_{inm}(\boldsymbol{k})\iiint S_{nmj}(\boldsymbol{k}, \boldsymbol{p}, t)\mathrm{d}^3\boldsymbol{p} + \mathrm{i}P_{jnm}(\boldsymbol{k})\iiint S^*_{nmi}(\boldsymbol{k}, \boldsymbol{p}, t)\mathrm{d}^3\boldsymbol{p}. \tag{13}$$

2.1.1. *Using the general $e, Z, \mathcal{H}$ decomposition*

The most general decomposition, for arbitrary anisotropy, of the spectrum of the two-point correlation tensor $\hat{\mathbf{R}}$ is [2]

$$\hat{R}_{ij}(\boldsymbol{k}, t) = e(\boldsymbol{k}, t)P_{ij} + \Re[Z(\boldsymbol{k}, t)N_i(\boldsymbol{k})N_j(\boldsymbol{k})] + \mathrm{i}\epsilon_{ijn}\frac{k_n}{k}\mathcal{H}(\boldsymbol{k}, t), \tag{14}$$

with details in [18]. This amounts to prescribing the following set of second-order spectral terms: kinetic energy density $e(\boldsymbol{k})$ (real-valued), polarization $Z(\boldsymbol{k})$ (complex-valued),

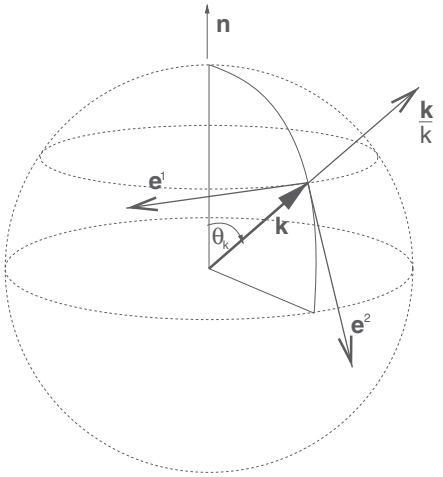


Figure 1. Craya–Herring frame of reference, also a polar-spherical frame with polar angle along **n**.

helicity $\mathcal{H}(\boldsymbol{k})$ (real-valued), with their angle-dependent distribution in Fourier space, in contrast with the use of the unique spectrum of kinetic energy $E(k)$, which is only the spherical integral of $e(\boldsymbol{k})$. This decomposition involves the classical projection operator $P_{ij} = \delta_{ij} - k_i k_j/k^2$, as well as the helical mode $\boldsymbol{N}(\boldsymbol{k})$, defined below. It is consistent with the two-component 'solenoidal' decomposition

$$\hat{\boldsymbol{u}}(\boldsymbol{k}, t) = u^{(1)}(\boldsymbol{k}, t)\boldsymbol{e}^{(1)}(\boldsymbol{k}) + u^{(2)}(\boldsymbol{k}, t)\boldsymbol{e}^{(2)}(\boldsymbol{k}), \tag{15}$$

or equivalently

$$\hat{\boldsymbol{u}}(\boldsymbol{k}, t) = \xi_+(\boldsymbol{k}, t)\boldsymbol{N}(\boldsymbol{k}) + \xi_-(\boldsymbol{k}, t)\boldsymbol{N}^*(\boldsymbol{k})\,, \tag{16}$$

with

$$\boldsymbol{N}(\boldsymbol{k}) = \boldsymbol{e}^{(2)}(\boldsymbol{k}) - \mathrm{i}\boldsymbol{e}^{(1)}(\boldsymbol{k}), \tag{17}$$

in which $(\boldsymbol{e}^{(1)}, \boldsymbol{e}^{(2)}, \boldsymbol{e}^{(3)} = \boldsymbol{k}/k)$ is an orthonormal right-handed frame of reference, often referred to as the Craya–Herring frame (see Figure 1). According to the figure, it is clear that this local frame of reference coincides with a basic ($\boldsymbol{e}^{(1)} =$ zonal, $\boldsymbol{e}^{(2)} =$ meridional, $\boldsymbol{e}^{(3)} =$ radial) frame for $\boldsymbol{k}$ in a polar-spherical frame of reference, with a given polar axis $\boldsymbol{n}$, say. Even if it is particularly suited for axisymmetric turbulence, around the same polar axis, this decomposition is not restricted to that case and can be used for arbitrary anisotropy: in the presence of a mean plane shear flow, for instance, there is no axisymmetry, and the choice of $\boldsymbol{n}$ along the vertical direction of the mean plane shear yields the simplest formulation ([18, chap. 6])

This $(e, Z, \mathcal{H})$ decomposition results as well from a conventional decomposition of $\hat{\mathbf{R}}$ in terms of trace and deviator, but restricted to the spectral plane normal to $\boldsymbol{k}$, or

$$\hat{R}_{ij} = \frac{1}{2}\hat{R}_{nn}P_{ij} + \underbrace{\Re\left(\hat{R}_{ij} - \frac{1}{2}\hat{R}_{nn}P_{ij}\right)}_{\text{polarization}} + \underbrace{\Im\left(\hat{R}_{ij} - \frac{1}{2}\hat{R}_{nn}P_{ij}\right)}_{\text{helicity}}.$$

In the above equation and in the current paragraph, for simplicity, we drop the explicit $\boldsymbol{k}$ dependence. It is clear that the polarization part is only generated by the Z-term, whereas the helicity part is only generated by the $\mathcal{H}$-term, with inverse relationships given below. Equation (14) can be derived from the decomposition of $\hat{\boldsymbol{u}}$ in terms of $\boldsymbol{N}$ and $\boldsymbol{N}^*$ in (15), using $N_i^* N_j = P_{ij} + \mathrm{i}\epsilon_{ijn}k_n/k$, with $e_i^{(1)}e_j^{(1)} + e_i^{(2)}e_j^{(2)} + k_i k_j/k^2 = \delta_{ij}$ and $\mathrm{i}(e_i^{(1)}e_j^{(2)} - e_j^{(1)}e_i^{(2)}) = \mathrm{i}\epsilon_{ijn}k_n/k$, because the frame of reference ($\boldsymbol{e}^{(1)}$, $\boldsymbol{e}^{(2)}$, $\boldsymbol{e}^{(3)} = \boldsymbol{k}/k$) is orthonormal and right-handed. Accordingly, the real part of $N_i^* N_j$ generates the 'energy' part, its imaginary part yields the 'helicity' part, and the terms $N_i N_j$ and $N_i^* N_j^*$ generate the 'polarization' part. Conversely, the basic scalar spectra are derived from any arbitrarily anisotropic spectral tensor – here $\hat{\mathbf{R}}$ – as follows:

$$e = (1/2)\hat{R}_{ii}; \quad Z = (1/2)\hat{R}_{ij}N_i^* N_j^*; \quad k\mathcal{H} = (1/2)\mathrm{i}k_m\epsilon_{imj}\hat{R}_{ij}. \tag{18}$$

The most general and the simplest realizability condition, or condition for the Hermitian covariance matrix $\hat{\mathbf{R}}(\boldsymbol{k}, t)$ to be definite-positive in agreement with the definition (3), can be written as

$$\mid Z(\boldsymbol{k}) \mid \leq \sqrt{(e(\boldsymbol{k}))^2 - (\mathcal{H}(\boldsymbol{k}))^2} \quad \forall \boldsymbol{k}.$$

(see e.g. [10]).

2.1.2. *Generalized Lin equations*

Equation (12) is equivalent to a set of three equations, in terms of $(e, Z, \mathcal{H})$, so that Lin's equation in isotropic turbulence is generalized as

$$\dot{e} + 2\nu k^2 e + \underbrace{\frac{\dot{k}}{k}e + \Re\left(Z\left[\boldsymbol{N}\cdot\mathbf{S}\cdot\boldsymbol{N}\right]\right)}_{\text{explicit RDT part for } e} = T^{(e)}(\boldsymbol{k}, t) \tag{19}$$

$$\dot{Z} + 2\nu k^2 Z + \underbrace{\frac{\dot{k}}{k}Z + e\left[\boldsymbol{N}^*\cdot\mathbf{S}\cdot\boldsymbol{N}^*\right] + +2\mathrm{i}Z\left((2\boldsymbol{\Omega} + \boldsymbol{W}/2)\cdot\boldsymbol{e}^{(3)} - \Omega^E\right)}_{\text{explicit RDT part for } Z} = T^{(Z)}(\boldsymbol{k}, t) \tag{20}$$

$$\dot{\mathcal{H}} + 2\nu k^2 \mathcal{H}(\boldsymbol{k}, t) = T^{(\mathcal{H})}(\boldsymbol{k}, t). \tag{21}$$

In addition to classical dissipation terms and time-derivative terms, other exact linear terms in these equations display coefficients proportional to $\frac{\dot{k}}{k} = -\left[\boldsymbol{e}^{(3)}\cdot\mathbf{S}\cdot\boldsymbol{e}^{(3)}\right]$, $\boldsymbol{N}\cdot\mathbf{S}\cdot\boldsymbol{N}$ and $\boldsymbol{N}^*\cdot\mathbf{S}\cdot\boldsymbol{N}^*$ expressed in terms of only the symmetric part $\mathbf{S}$ of the mean velocity gradient matrix and the orientation of the wave vector. [In this paragraph only, $\mathbf{S}$ does *not* designate the previously encountered third-order spectral tensor $\mathbf{S}(\boldsymbol{k}, \boldsymbol{p}, t)$.]

Only the purely imaginary coefficient in the Z-equation displays the antisymmetric, vortical, part of the mean velocity gradient matrix, via the tilting vorticity $2\boldsymbol{\Omega} + \boldsymbol{W}/2$ and the rotation vector component Ω^E, which expresses the solid-body motion of the local Craya frame with respect to a fixed frame of reference, following characteristic lines. Details of the algebra are given in Appendix.

Considering nonlinear contributions, the transfer terms are displayed on the right-hand side of these equations, in agreement with

$$T^{(e)} = \frac{1}{2} T_{ii}; \quad T^{(Z)} = \frac{1}{2} T_{ij} N_i^* N_j^*; \quad kT^{(\mathcal{H})} = \frac{1}{2} \mathrm{i} k_m \epsilon_{imj} T_{ij}. \tag{22}$$

As in isotropic turbulence, more information on the generalized third-order transfer tensor T_{ij} is obtained from the third-order spectral tensor, defined in Equation (6), via Equation (13). Its dynamics are obtained via

$$\left(\frac{\partial}{\partial t} + \nu(k^2 + p^2 + q^2) \right) S_{ijn}(\boldsymbol{k}, \boldsymbol{p}, t) + M_{im}(\boldsymbol{q}) S_{mjn} + M_{mj}(\boldsymbol{k}) S_{imn} + M_{mn}(\boldsymbol{p}) S_{ijm} = \mathcal{T}_{ijn}(\boldsymbol{k}, \boldsymbol{p}, t). \tag{23}$$

In both equations for second- and third-order spectral tensors, pressure effects connected to the solenoidal property of the velocity field are exactly accounted for, absorbed in M_{ij} for the linear part, as well as in the right-hand side term resulting from nonlinearity.

All these equations are exact and can be used to generate all second-order statistics, single-point as well as two-point, and third-order statistics, from single-point to three-point. If, in addition, triadic closures are needed, we propose to start from the following EDQN approximation:

$$\mathcal{T}_{ijn} = \mathcal{T}_{ijn}^{QN} - (\eta(k,t) + \eta(p,t) + \eta(q,t))\, S_{ijn}, \tag{24}$$

in which the difference of the triadic cubic term from its quasi-normal expression [superscript (QN) here] is modelled as an extra-diffusion, via an eddy-damping (ED) term, specified in the next section. Applications of this general EDQN closure, with three tractable Markovian versions (EDQNM – 1,2,3) in which the intrinsic memory of triple correlations is truncated, were proposed in the simple axisymmetric case of rotating turbulence and QS-MHD turbulence, with new results given in Section 4.

2.1.3. *Relevant time-scales in anisotropic EDQNM*

In the conventional approach to anisotropic flows, a simple parameter comparing 'linear' and 'nonlinear' time-scales appears in the evolution equation for turbulent kinetic energy. One can also use inverse time-scales, or frequencies, for convenience. The nonlinear time-scale can of course be the eddy turnover time computed as $\mathcal{K}/\varepsilon$.

For instance, considering a pure shear flow with mean shear rate $\mathcal{S}$, in the single-point counterpart of Equation (19), the ratio of the linear inverse time-scale $\mathcal{S}$ to the non-linear one is $\mathcal{S}\mathcal{K}/\varepsilon$, and is often referred to as *shear rapidity*. In rotating flows, the inverse of the Rossby number plays a similar role, changing $\mathcal{S}$ into 2Ω. However, this dimensional analysis does not account for the fact that $\mathcal{S}$ and 2Ω appear in linear operators of different mathematical nature: $\mathcal{S}$ and 2Ω are modulated by a different angle-dependent spectral coefficient in $\mathbf{M}\hat{\boldsymbol{u}}$ in Equation (8): $\mathcal{S}k_1k_2/k^2$ for a pure shear flow and $\sigma_k = 2\Omega k_3/k$ for a rotating flow. In terms of physical phenomenon, the linear mechanism amounts to vortex stretching and tilting in shear flows, with the net production scaling with $\mathcal{S}$ in the energy equation. The analogous term vanishes in the rotating flow case, since inertial waves, although dispersive, are energy-conserving.

In such a flow without production, the quantitative comparison between 'linear' and 'non-linear' frequencies must be shifted to the level of third-order correlations. We therefore discard the generalized Lin equations or single-point counterparts, and consider Equations (23) and (24), which are at the core of the triadic closure. The relevant 'linear' frequency is $T_L^{-1} = \sigma_k \pm \sigma_p \pm \sigma_q$ on the left-hand side of Equation (23), and the 'nonlinear' one T_{NL}^{-1} is the ED term [second term on the right-hand side of Equation (24)]. $T_{NL}^{-1} \gg T_L^{-1}$ in the case of strong turbulence marginally altered by rotation, and $T_{NL}^{-1} \ll T_L^{-1}$ in the case of strong rotation. The quasi-normal part $\mathcal{T}_{ijn}^{QN}$ can be expressed exactly in terms of $(e,Z,\mathcal{H})$ as a sum of products, and must be considered as the dominant source term in Equation (24) combined with Equation (23) in all cases.

Finally, in order to span the widest possible range of Rossby numbers up to infinity, one needs to discuss the scaling of the crucial time-scale $\eta(k,t)$ in isotropic EDQNM. At a high Reynolds number, there is a direct link between the inertial scaling of the energy spectrum $E(k)$ and the exponent of the ED frequency $\eta(k)$ (see e.g. [18, pp. 423–425]). The Kolmogorov-type scaling $\eta \sim \epsilon^{1/3}k^{2/3}$, initially proposed by Orszag [15], yields $k^{-5/3}$, whereas a sweeping-type scaling $\eta \sim ku'$ yields $k^{-3/2}$. In all the EDQNM models we used, η is evaluated as Corrsin's or Batchelor's frequency

$$\eta(k) = A\sqrt{\int_0^k p^2 E(p)\mathrm{d}p}, \tag{25}$$

as proposed by [20,21]. This choice is consistent with the straining-type Kolmogorov time-scale at a high Reynolds number, but does not explicitly prescribe a given spectral slope. This last model is therefore a good candidate for exploring finite Reynolds number effects [22,23], the effect of dimensionality in two-dimensional isotropic or three-dimensional isotropic turbulence, and, more generally, anisotropic situations in which the time-scale in the RDT terms on the left-hand side of Equation (23) competes with η. Additional discussion is offered in [24,25] in the MHD context, for fluids and plasmas.

2.2. *Approach to generalized Kármán–Howarth equations in physical space*

It is possible to derive an equation for $R_{ij}(\boldsymbol{r},t)$ from Equation (7), as done by Craya, and more recently by [26].

In physical space, only the trace of this equation is commonly considered, often under the form of Kármán–Howarth (K–H) equations, with some variants given by [27], especially in terms of velocity increments for structure functions. In anisotropic turbulence, pressure–velocity correlation terms rear their ugly head for the deviatoric part of **R**-equation, and this appears as a difficult point even in single-point Reynolds-stress models. In a two-point **R**-equation, it would be almost intractable to manage a componental K–H type equation by solving exactly all terms related to pressure–velocity correlations in terms of velocity only, even if the integro-differential form resulting from solving a Poisson equation can formally be written. In counterpart, large-scale effects such as inhomogeneity and anisotropy of the flow can be evaluated when investigating the kinetic energy at a given scale $\langle \delta u_i \delta u_i \rangle \equiv \langle (\delta q)^2 \rangle$. We recall that the velocity increment is

$$\delta u_i = u_i(\boldsymbol{x}+\boldsymbol{r},t) - u_i(\boldsymbol{x},t), \tag{26}$$

used in the following for studying the transport equation for $\langle(\delta q)^2\rangle$ and the role of related cubic structure functions. From e.g. [28],

$$-\langle \delta u_1 (\delta q)^2 \rangle + 2\nu \frac{\mathrm{d}}{\mathrm{d}r} \langle (\delta q)^2 \rangle = \frac{4}{3} \langle \epsilon \rangle r \tag{27}$$

is another version of the 4/5 Kolmogorov law, with an explicit viscous term, for a flow with a privileged mean flow direction x_1. For an inhomogeneous shear flow, $\boldsymbol{u}$ ought to be replaced by the total velocity $\boldsymbol{u} + \boldsymbol{U}$. For very small scales, Equation (27) complies with another form of $\langle \epsilon \rangle$, viz. [29]

$$\langle \epsilon \rangle_q = 3\nu \left\langle \frac{\partial u_i}{\partial x_1} \frac{\partial u_i}{\partial x_1} \right\rangle. \tag{28}$$

Following from (28), another definition of the Taylor microscale is $\lambda = \left(5\nu \langle u_i u_i \rangle / \langle \epsilon \rangle_q\right)^{1/2}$, from which the Reynolds number $R_\lambda \equiv (\langle u_i u_i \rangle /3)^{1/2} \lambda/\nu$ can be built. These forms will be used in the following.

The focus here is to derive a scale-by-scale energy budget equation for the total kinetic energy $(\delta q)^2$ in the anisotropic context, and further adapt it to the region surrounding a round jet axis. (The case of a round jet is chosen as an instance of weakly inhomogeneous axisymmetric flow, although other flows with similar properties could be investigated, such as an axisymmetric wake.)

Following the same mathematical development as presented in [30], [31], [29], and [27], we write the incompressible Navier–Stokes equations at the two points $\boldsymbol{x}$ and $\boldsymbol{x}^+$, which are separated by the increment $\boldsymbol{r} = \boldsymbol{x}^+ - \boldsymbol{x}$. Under these conditions, by decomposing the total velocity field in a mean and a fluctuating component, and by considering that frames at points $\boldsymbol{x}$ and $\boldsymbol{x}^+ = \boldsymbol{x} + \boldsymbol{r}$ are independent, the equation for the velocity increment $\delta u_i = u_i^+ - u_i$ becomes

$$\begin{aligned} &\frac{\partial}{\partial t}(\delta u_i) + \delta\left(U_\alpha \frac{\partial u_i}{\partial x_\alpha}\right) + \delta\left(u_\alpha \frac{\partial U_i}{\partial x_\alpha}\right) + 2\epsilon_{inj}\Omega_n \delta u_j + u_\alpha^+ \frac{\partial}{\partial x_\alpha^+}(\delta u_i) + u_\alpha \frac{\partial}{\partial x_\alpha}(\delta u_i) \\ &\quad = -\left(\frac{\partial}{\partial x_i} + \frac{\partial}{\partial x_i^+}\right)\frac{(\delta p)}{\rho} + \nu\left(\frac{\partial^2}{\partial x_\alpha^2} + \frac{\partial^2}{\partial x_\alpha^{+2}}\right)(\delta u_i). \end{aligned} \tag{29}$$

By subtracting and adding $u_\alpha \partial(\delta u_i)/\partial x_\alpha^+$ to the left-hand side of (29), we obtain

$$\begin{aligned} &\frac{\partial}{\partial t}(\delta u_i) + \delta\left(U_\alpha \frac{\partial u_i}{\partial x_\alpha}\right) + \delta\left(u_\alpha \frac{\partial U_i}{\partial x_\alpha}\right) + \delta(u_\alpha)\frac{\partial}{\partial x_\alpha^+}(\delta u_i) + 2\epsilon_{inj}\Omega_n \delta u_j u_\alpha \frac{\partial}{\partial x_\alpha^+}(\delta u_i) \\ &\qquad + u_\alpha \frac{\partial}{\partial x_\alpha}(\delta u_i) = -\left(\frac{\partial}{\partial x_i} + \frac{\partial}{\partial x_i^+}\right)\frac{(\delta p)}{\rho} + \nu\left(\frac{\partial^2}{\partial x_\alpha^2} + \frac{\partial^2}{\partial x_\alpha^{+2}}\right)(\delta u_i). \end{aligned} \tag{30}$$

Following the approach suggested by [31], we also consider the gradient with respect to the midpoint

$$\boldsymbol{X} = \frac{1}{2}\left(\boldsymbol{x} + \boldsymbol{x}^+\right). \tag{31}$$

Thus,

$$\frac{\partial}{\partial x_\alpha^+} \equiv \frac{\partial}{\partial r_\alpha} + \frac{1}{2}\frac{\partial}{\partial X_\alpha} \qquad \text{and} \qquad \frac{\partial}{\partial x_\alpha} \equiv -\frac{\partial}{\partial r_\alpha} + \frac{1}{2}\frac{\partial}{\partial X_\alpha}, \tag{32}$$

resulting in $\partial/\partial X_\alpha = \partial/\partial x_\alpha + \partial/\partial x_\alpha^+$.

By taking into account (32), multiplying Equation (30) by $2\delta u_i$, and averaging, we finally obtain

$$\begin{aligned}
&\frac{\partial}{\partial t}\langle(\delta q)^2\rangle(\boldsymbol{r}) + 2\langle\delta\left(U_\alpha\frac{\partial u_i}{\partial x_\alpha}\right)\delta u_i\rangle(\boldsymbol{r}) + 2\langle\delta\left(u_\alpha\frac{\partial U_i}{\partial x_\alpha}\right)\delta u_i\rangle(\boldsymbol{r}) \\
&\qquad + \frac{1}{2}\left\langle\left[\frac{\partial}{\partial x_\alpha} + \frac{\partial}{\partial x_\alpha^+}\right]\left[u_\alpha + u_\alpha^+\right](\delta q)^2\right\rangle \\
&\qquad + \frac{\partial}{\partial r_\alpha}\langle\delta u_\alpha(\delta q)^2\rangle(\boldsymbol{r}) = -2\left(\frac{\partial}{\partial x_i} + \frac{\partial}{\partial x_i^+}\right)\langle\delta p\delta u_i\rangle(\boldsymbol{r}) \\
&\qquad + 2\nu\frac{\partial^2}{\partial {r_\alpha}^2}\langle(\delta q)^2\rangle(\boldsymbol{r}) - 2\left(\langle\epsilon\rangle + \langle\epsilon\rangle^+\right).
\end{aligned} \tag{33}$$

In Equation (33), each term depends on the spatial vector $\boldsymbol{r}$. Equation (33) is a very general form of the scale-by-scale kinetic energy budget at a scale $\boldsymbol{r}$, in which all the large-scale effects are present: unsteadiness, advection by mean velocity, shear, turbulent diffusion, pressure-diffusion; as well as 'traditional' terms: advection by the turbulent field, molecular diffusion and dissipation.

In manipulating Equation (33), the disadvantage is that too many terms are present, among which one is the pressure–velocity correlation term. This term cannot be properly inferred from experimental data and therefore further hypotheses are necessary. Conditions under which such a term can be discarded are: local homogeneity, open flows where the mean velocity and mean pressure variations are negligible.

To discuss more and to contrast the last equation and its Fourier counterpart, or e-Equation (19) the fact that R_{ii} is replaced by an incremental form $\langle(\delta q)^2\rangle$ merits more attention – replacing e by a mixing of e and single-point turbulent kinetic energy – but is not essential, anyway.

3. Purely isotropic or 'isotropized' case

An important goal of our article, which is to establish a Fourier physical 'dictionary', is already well advanced for isotropic turbulence. Only new salient results will be given here. In addition, from the previous general setting with shear and rotation, presented in Section 2, it is possible to spherically average equations for anisotropic turbulence, so that an 'isotropized' formalism can be valid for an anisotropic flow. In so doing, one may distinguish two cases: (a) 'weakly anisotropic' turbulence, corresponding to anisotropic turbulence in which the classical scalings of Kolmogorov theory would still apply for the isotropized statistics, both spectral and physical; (b) strongly anisotropic turbulence in which the isotropized statistics would exhibit a strong departure from classical scalings, and would require an explicitly anisotropic analysis, as done in this article.

For instance, the spherical averaging of e-equation yields an equation for the radial energy spectrum:

$$\frac{\partial E(k,t)}{\partial t} + T^L(k,t) + P(k,t) + 2\nu k^2 E(k,t) = T(k,t), \tag{34}$$

with additional terms of 'linear spectral transfer', $T^{(L)}(k,t)$ and 'production' $P(k,t)$, easily derived from Equation (19), with respect to the basic Lin equation. In the case of rotating turbulence, discussed at length in the Introduction, the latter Equation (34) is the same with and without rotation, with and without anisotropy, but $T(k,t)$ could be radically different, concentrating the Coriolis effect in the anisotropic case with rotation.

We do not discuss the relationship for second-order statistics in the isotropic case. All correlations in physical space, longitudinal and transverse correlation functions, related second-order structure functions, *etc.*, can be expressed in terms of the sole 'radial' energy spectrum by exact quadratures, and inverse formulae exist as well (see Table 1).

Analytical equations linking quantities in physical space to the spectral ones are less known at the third order. Derivation of a third-order structure function from the spectral transfer term $T(k)$ was done by [32], with an interesting approach to the $4/5$ law from closures for $T(k)$, and detailed algebra can be found in some lecture notes by Brachet & Frisch, so that the details are not given here. This formalism was recently used by [22] for revisiting the finite Reynolds effect on the $4/5$ Kolmogorov law.

The general tensor $Q_{ilm}(\boldsymbol{r}) = \langle u_i(\boldsymbol{x})u_l(\boldsymbol{x})u_m(\boldsymbol{x}+\boldsymbol{r})\rangle$ can be expressed in terms of $u'^3K(r) = r^{-3}Q_{ilm}r_ir_lr_m$ only as

$$Q_{lmi}(\boldsymbol{r}) = u'^3\left[\frac{1}{2}\left(K - r\frac{\partial K}{\partial r}\right)\frac{r_lr_mr_i}{r^3} + \frac{1}{4}\left(2\frac{K}{r} + \frac{\partial K}{\partial r}\right)(r_i\delta_{lm} + r_m\delta_{il}) - \frac{1}{2}K\frac{r_l}{r}\delta_{im}\right]. \tag{35}$$

(See equation (6.141) in [33] in which $\boldsymbol{x}-\boldsymbol{r}$ and $\boldsymbol{x}$ are used, whereas our convention is to use $\boldsymbol{x}$ and $\boldsymbol{x}+\boldsymbol{r}$ following [34].)

The third-order tensor Q_{ijm} can be expressed in terms of spectral quantities as

$$Q_{ijm}(\boldsymbol{r}) = \iiint\left(\iiint S_{ijm}(\boldsymbol{k},\,\boldsymbol{p})\mathrm{d}^3\boldsymbol{p}\right)\exp(\mathrm{i}\boldsymbol{k}\cdot\boldsymbol{r})\mathrm{d}^3\boldsymbol{k}, \tag{36}$$

with S_{ijm} given by (6). It therefore appears that the spectral tensor related to $Q_{ilm}(\boldsymbol{r})$ is exactly

$$T_{ilm}(\boldsymbol{k}) = \iiint S_{ilm}(\boldsymbol{k},\,\boldsymbol{p})\mathrm{d}^3\boldsymbol{p}, \tag{37}$$

illustrating a simple rule of contraction of information: setting to zero the vector separating two points in physical space amounts to integrating over the related wave vector in Fourier space. As in Equation (35), it is possible to express $T_{ilm}(\boldsymbol{k})$ in terms of a single scalar function. The best candidate is the energy transfer term $T(k)$ which is involved in Lin's equation and is given by $T(k) = 2\pi k^2 T_{ii}(\boldsymbol{k})$, or

$$T(k) = 4\pi k^2 \mathrm{i}k_i T_{ijj}(\boldsymbol{k}), \tag{38}$$

from Equation (13).

As in (35) in physical space, a unique form of $T_{ilm}(\boldsymbol{k})$ is found by 'isotropic expansion', *i.e.* expressing the most general third-order tensor that may be generated by a single scalar. Thus, one obtains

$$T_{ijm}(\boldsymbol{k}) = -\mathrm{i}\frac{T(k)}{8\pi k^3}\left[\frac{k_i}{k}\left(\delta_{jm} - \frac{k_j k_m}{k^2}\right) + \frac{k_j}{k}\left(\delta_{im} - \frac{k_i k_m}{k^2}\right)\right], \tag{39}$$

using (38) along with $k_m T_{ijm} = 0$ and $T_{ijm} = T_{jim}$. Incidentally, one finds immediately that $T_{ijm} = -(T(k)/(4\pi k^4))P_{ijm}$ from (11), so that $T_{iim} = 0$, a property that can be extended to (35) which ensures $Q_{lii} = 0$.

For instance, $u'^3 K(r)$ is expressed as

$$u'^3 K(r) = 2r\int_0^\infty g_5(kr)T(k)\mathrm{d}k, \tag{40}$$

in which the weighting function in terms of kr,

$$g_5(kr) = \frac{3(\sin kr - kr\cos kr) - (kr)^2 \sin kr}{(kr)^5}, \tag{41}$$

is found as in [32]. (The same integrals arise when deriving any other third-order correlation from spectra, with fractional functions different from g_5.)

Finally, going back to dynamics, one just recalls that the K–H equation

$$\frac{\partial}{\partial t}(u'^2 f_L) = \left(\frac{\partial}{\partial r} + \frac{4}{r}\right)\left(R_{LL,L}(r,t) + 2\nu\frac{\partial}{\partial r}\left(u'^2 f_L\right)\right) \tag{42}$$

with

$$R_{LL,L}(r,t) = \langle u_i(\boldsymbol{x},t)u_m(\boldsymbol{x},t)u_i(\boldsymbol{x}+\boldsymbol{r},t)\rangle\frac{r_m}{r} \tag{43}$$

is the counterpart of Lin's equation that governs the energy spectrum $E(k)$.

Note that the function $R_{LL,L}(r,t)$ can be expressed in terms of $u'^3 K(r)$ and thus in terms of $T(k)$ as well using (40), so that

$$R_{LL,L}(r,t) = r\int_0^\infty g_3(kr)T(k,t)\mathrm{d}k, \tag{44}$$

with $g_3(kr)$ given in Table 1. The inverse equation, expressing $T(k)$ in terms of $R_{LL,L}$, can be found in [34] and [33] [equations (6.150) and (6.151) in the latter book].

The third-order structure function readily derives from (40) using

$$\langle(\delta u_L)^3\rangle(r) = 6u'^3 K(r) \tag{45}$$

so that it involves the same weighting function $g_5(kr)$ as given by (41). It is clear that the $4/5$ Kolmogorov law can be recovered at very high Reynolds number from the properties of the energy transfer $T(k)$. This implies that the negative loop of $T(k)$ at small k and its positive loop at higher k are significantly separated by a plateau of almost zero transfer,

with a zero crossing at k_I, say. In this limit, one finds

$$T(k,t) \sim 2\nu k^2 E(k,t) \qquad \text{if } k > k_I$$

and

$$\frac{\partial E}{\partial t} \sim T(k,t) \qquad \text{if } k < k_I \ ,$$

with $\int_0^{k_I} T(k,t)\mathrm{d}k \to -\varepsilon$ and $\int_{k_I}^{\infty} T(k,t)\mathrm{d}k \to \int_0^{\infty} 2\nu k^2 E(k,t)\mathrm{d}k = \varepsilon$.

At moderate Reynolds number, $\int_{k_I}^{\infty} T(k)\mathrm{d}k$ is far below ε so that the normalized third-order structure function $-\langle(\delta u_L)^3\rangle(r)/r/\varepsilon$ is far below its asymptotic $4/5$ limit.

In addition, according to the exact equivalence of the general formulae (35) and (39), all second-order triple-velocity correlations, for any component, using increments or not, should scale as r at sufficiently high Reynolds number, and not only the third-order structure function.

4. Typical flow cases: rotating turbulence, QS-MHD, jet

4.1. *Rotating turbulence. New insight into an altered* $4/5$ *law.*

Helical modes generate a complete basis for expanding any solenoidal velocity field. For the flow subjected to a Coriolis force in the rotating frame, the decomposition

$$\hat{\boldsymbol{u}}(\boldsymbol{k},t) = \sum_{s=\pm 1} a_s(\boldsymbol{k},t) e^{s\mathrm{i}\sigma_k t} \boldsymbol{N}(s\boldsymbol{k}) \tag{46}$$

is completely general, with σ_k in Equation (2), and can be seen as defining a new set of two variables, a_+ and a_-, which can be substituted to the velocity Fourier modes in Cartesian coordinates. Of course, *constant* $a_\pm$ correspond to the linear regime of inertial waves, whereas *slowly evolving* amplitudes $a_\pm(\boldsymbol{k}, \epsilon t)$, with ϵ a small parameter, can be the starting point of the weakly nonlinear inertial wave turbulence theory. If nothing is said about the time-dependency of $a_\pm$, one can at least derive their exact equation by injecting Equation (46) in the Navier–Stokes Equation (8), yielding

$$\left(\frac{\partial}{\partial t} + \nu k^2\right) a_s(\boldsymbol{k},t) = \sum_{s',s''=\pm 1} \iiint_{k=p+q} M_{ss's''}(\boldsymbol{k},\boldsymbol{p}) \mathrm{e}^{-\mathrm{i}(s\sigma_k + s'\sigma_p + s''\sigma_q)t} a^*_{s'}(\boldsymbol{p},t) a^*_{s''}(\boldsymbol{q},t) \mathrm{d}^3\boldsymbol{p}, \tag{47}$$

with an exact geometric factor $M_{ss's''}$, proportional to a $(\boldsymbol{p},\boldsymbol{q})$ symmetrized part of $N_n(-s\boldsymbol{k})N_n(-s'\boldsymbol{p})k_m N_m(-s''\boldsymbol{q})$. One recovers the principal role of the time-depending and rotation-depending operator in Equation (5), in that it modulates and alters basic nonlinearity, at any time and at any Rossby number.

Going back to statistics, exact Lin equations are found in Fourier space by discarding the 'RDT-like' terms in Equations (19) and (20), related to the mean irrotational strain, and by replacing the tilting vorticity by the system vorticity, with $\Omega^E = 0$ in Equation (20).

With respect to the system of Equations (19) and (20), only the polarization anisotropy is affected by an explicit rotation-dependent phase term as $4\mathrm{i}\Omega(k_\parallel/k)Z$, which involves twice the dispersion law of inertial waves (2), since Z is quadratic. The dynamics of energy and helicity, with their whole anisotropic distribution, are themselves completely slaved to cubic transfer terms mediated by nonlinear interactions through the dynamical equation

$$\left(\frac{\partial}{\partial t}+2\nu k^2\right)(e,\mathcal{H})=T^{(e,\mathcal{H})}(\boldsymbol{k},t).$$

In this case, $e, Z, \mathcal{H}$ variables are directly linked to the amplitudes defined in Equation (46), with $a_+a_+^*+a_-a_-^*$ generating the energy spectrum e, $a_+a_+^*-a_-a_-^*$ generating the helicity spectrum, and a_+a_- generating the 'slow' part $Z\mathrm{e}^{2\mathrm{i}\sigma_k t}$ of the polarization spectrum.

As an additional simplification, the simplest statistical case consistent with exact dynamical equations is axisymmetry without mirror-symmetry (or semi-axisymmetry, rediscussed in Section 5), with a zero-helicity spectrum. Accordingly, the anisotropic distribution of e and Z in wave space is reduced to a two-component dependency in terms of $k_\parallel$, $k_\perp$ using cylindrical coordinates, or in terms of k, $\cos\theta_k=k_\parallel/k$ using polar-spherical coordinates.

Of course, implicit nonlinear effects of rotation are essential, for they are shown to alter the nonlinear transfer terms T^e and T^Z [right-hand sides of Equations (19) and (20) from which all RDT-generated terms are removed], with a refined anisotropic picture consistent throughout the results of wave-turbulence theory, EDQNM axisymmetric closure and DNS/LES ([8,10,18, chap. 4]).

Some recent studies reconsider the problem of rotating turbulence, not from the angle of its anisotropic structure and related modified cascade, but from the angle of a modified *internal* intermittency, in line with a post-Kolmogorov *vulgate* supported by a very large amount of publications devoted to scaling and intermittency. An emerging conjecture is that the classical K41 scaling for structure functions of arbitrary order p, $\langle(\delta u)^p\rangle(r)\sim r^{p/3}$, ought to be replaced by r^{ζ_p} with a scaling law of the so-called 'anomalous exponents' ζ_p close to $p/2$.

This conjecture was proposed by [35], but from an experimental facility of rotating turbulence far from homogeneity. Note also that a former experimental result in a flow produced between corrotating disks (PhD of Catherine Simand [36], also reported in [18, p. 159]) foreshadowed it, as shown in Figure 5.

Our ambition in this article is restricted to the statistics of order 2 and 3 only, but with a deeper investigation of their dynamics and to answer the question about what one can say about second- and third-order structure functions.

Very crude assumptions and explanations exist to support the $p/2$ relationship. For instance, the purely isotropic (or isotropized) law proposed by [37] is

$$E(k)=\sqrt{\Omega\varepsilon}\,k^{-2},$$

from dimensional analysis. This scaling is consistent with a law in r for the isotropic (or isotropized) second-order structure function, using well-known isotropic formulae reported in Table 1. We believe this may be the first evidence that the $p/2$ 'conjecture' is checked for $p=2$. Results from experiment [38] and DNS (see [6,39,40], among others) are not so simple. Seiwert *et al.* [38] found $\zeta_2=1.4$, and not 1, in rough agreement with a spectrum in $k^{-2.4}$, and not k^{-2}. The value of ζ_2 is measured from a longitudinal structure function,

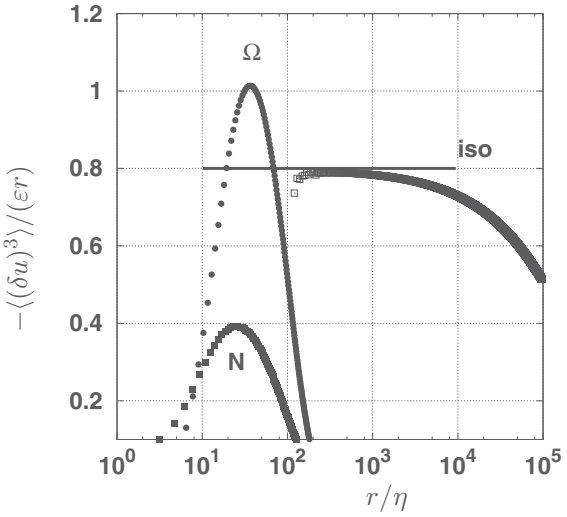


Figure 2. Normalized third-order structure function for isotropic turbulence, rotating (label Ω) and stably-stratified turbulence (label N). The results from the isotropic EDQNM model are obtained at $Re \simeq 3 \times 10^7$, whereas the more complex anisotropic EDQNM(3) model reaches $Re = 1000$ and 7000 for the stratified and rotating cases, respectively. (Taken from [43]). (The permission has been obtained from Physica D).

with $r = r_\perp$ separated in the direction normal to the axis of rotation, whereas the energy spectrum is measured from fast Fourier transform of transverse velocity signals.

In other works (see e.g. [39]), a kind of rescaling dubbed extended self-similarity is used for plotting ζ_p/ζ_2, in order to support the $p/2$ conjecture. It is somewhat difficult to envisage rational support for a modified $4/5$ Kolmogorov law, on the grounds of a new $r^{3/2}$ law for the third-order structure function, in agreement with the $p/2$ 'conjecture'.

This problem is delicate to address by DNS, which mixes possible finite-Reynolds effects with intermittency, with few studies addressing explicitly the anisotropy of the flow ([41] among a few others). Recent experimental results are available at higher Reynolds number, but they are affected by inhomogeneity and all relevant statistics are not measurable, as reported by [42].

In this context, the anisotropic EDQNM(3) model is useful, which matches the asymptotic limit of wave turbulence and compares well with DNS. A first attempt by [43] shows a perfect recovery of the $4/5$ law in isotropic turbulence without rotation, in line with our analysis of Section 3, and a significant alteration of its counterpart in both rotating and stably-stratified turbulence (Figure 2). Under rotation, the normalized ratio $-\langle(\delta u_L)^3\rangle/r/\varepsilon$ can be much larger than $4/5$, reaching a maximum of about 1, but there is no evidence for a plateau at the corresponding values of the Reynolds numbers.

The EDQNM(3) results for rotating turbulence have also been used to compute the different terms appearing in Equation (19), among which is the spectral transfer term $T^{(e)}(\mathbf{k})$. The latter is also the Fourier transform of the third-order term appearing in the Kármán–Howarth–Monin equation

$$-\frac{1}{4}\boldsymbol{\nabla}\cdot\langle(\delta q)^2\,\delta\mathbf{u}\rangle = \frac{\partial}{\partial_t}R_{ii} - 2\nu\nabla^2 R_{ii}.$$

Since the spectrum of $T^{(e)}(\mathbf{k})$ depends on k and μ_k, the distribution of $-\frac{1}{4}\nabla \cdot \langle (\delta q)^2 \, \delta \mathbf{u} \rangle$ is not expected to be isotropic, and depends on the separation r_x and r_z along the horizontal and the vertical axes. This representation was used by [44] for rotating turbulence without shear, using experimental data, in order to characterize the anisotropic distribution of the nonlinear transfer. Our result of Figure 4 exhibits a departure from isotropy, although not as clearly as the spectral representation does when plotting the spectrum of $T^{(e)}(\mathbf{k})$. It also shows the negative transfer from the intermediate scales to the smaller ones, and a small negative transfer from the largest scales.

4.2. *QS-MHD*

This case is given here as an illustration of a simplified model in which production terms are present. A two-stage scenario of two-dimensionalization, rediscussed below, was proposed long ago in rotating turbulence by [45]. This scenario was shown to be irrelevant in deep rotating flows, in the absence of explicit vertical confinement, although it may apply to shallow-water rotating flows. This scenario was confirmed by [46] in the case of QS-MHD, in the purely homogeneous case. Accordingly, further insight into rotating turbulence is gained by contrasting the equations and results for both the rotating and the QS-MHD cases.

We consider MHD at low magnetic Reynolds number and very high kinetic Reynolds number, which is permitted by a very low – 10^{-5} to 10^{-7} – magnetic Prandtl number, as for a liquid metal. We subject the flow to a strong external magnetic field in the axial direction. For these parameters, it is possible to get rid of the explicit induction equation for the fluctuating magnetic field, which is replaced by an instantaneous term in the Navier–Stokes equation. This term is the Lorentz force, which amounts to a simple anisotropic Ohmic dissipation term

$$F_i = -M_0^2 (\Delta)^{-1} \frac{\partial^2 u_i}{\partial x_\parallel}.$$

M_0^2 is an inverse time-scale, proportional to the imposed magnetic field, and the Δ^{-1} operator holds for the inverse of the Laplacian operator. In three-dimensional Fourier space, the latter force is simply

$$\hat{F}(\boldsymbol{k}, t) = -M_0^2 \cos^2 \theta_k \hat{u}_i. \tag{48}$$

Accordingly, the relevant Lin-type equations for the energy and polarization spectra are

$$\left(\frac{\partial}{\partial t} + 2\nu k^2 + 2M_0^2 \cos^2 \theta_k \right) e(\boldsymbol{k}, t) = T^{(e)}(\boldsymbol{k}, t), \tag{49}$$

$$\left(\frac{\partial}{\partial t} + 2\nu k^2 + 2M_0^2 \cos^2 \theta_k \right) Z(\boldsymbol{k}, t) = T^{(Z)}(\boldsymbol{k}, t). \tag{50}$$

The reader is referred to [47] for a detailed comparison between DNS and EDQNM2 results, demonstrating the complete transition from three-dimensional to two-dimensional. A complementary discussion for simple modelling issues is offered by [48], and Figure 6 (from [47]) illustrates the role of directionality in kinetic energy spectra of QS-MHD turbulence.

4.3. *Definition and discussion of key anisotropy indicators, from three-dimensional to two-dimensional structure*

We focus in the following two sections on describing how third-order statistical quantities, *viz.* the transfer terms in Lin-type equations, pilot the dynamics of one-point first-order statistics, and of two-point second-order statistics. We choose to illustrate the anisotropy of the Reynolds stress tensor, and the directional integral scales of two-point correlations, which clearly demonstrate the added value of the e–Z spectral decomposition.

4.3.1. *Reynolds stress tensor anisotropy*

In homogeneous, arbitrarily anisotropic, turbulence, it is possible to relate all two-point and single-point second-order statistics in physical space to the basic spectral scalars e, Z, $\mathcal{H}$ via quadratures. A very simple example is given by the second-order structure function $\langle(\delta q)^2\rangle$, which can be written as

$$\langle(\delta q)^2\rangle(\boldsymbol{r}) = 2\iiint (1-\exp(\mathrm{i}\boldsymbol{k}\cdot\boldsymbol{r}))\, e(\boldsymbol{k})\mathrm{d}^3\boldsymbol{k}. \tag{51}$$

Further simplification due to axisymmetry, with $e(\boldsymbol{k}) = e(k_\perp, k_\parallel)$ or $e(\boldsymbol{k}) = e(k, \mu_k)$, with $\mu_k = \cos\theta_k$, is possible.

Although several equations can be given for second-order correlators, two-point as well as single-point, we illustrate here the case of the Reynolds stress tensor and integral length-scales. From the decomposition (14), the following three-fold splitting is obtained for the Reynolds stress tensor:

$$\langle u_i u_j\rangle = \iiint \hat{R}_{ij}(\boldsymbol{k},t)\mathrm{d}^3\boldsymbol{k} = q^2\left(\frac{\delta_{ij}}{3} + \underbrace{b_{ij}^{(e)} + b_{ij}^{(Z)}}_{b_{ij}}\right), \tag{52}$$

where the two contributions to the deviatoric part bij of the Reynolds stress tensor are given by

$$q^2 b_{ij}^{(e)} = \iiint \left(e - \frac{E}{4\pi k^2}\right) P_{ij}(\boldsymbol{k})\mathrm{d}^3\boldsymbol{k}, \quad q^2 b_{ij}^{(Z)} = \iiint \Re\left(Z N_i N_j\right)\mathrm{d}^3\boldsymbol{k}. \tag{53}$$

Similar decompositions can be found for the dedicated tensors addressed in the structure-based modelling approach of [49] in physical space, an approach which can be related to our fully anisotropic description (see [10,18] for details on the derivation of 'dimensionality', 'circulicity' and 'stropholysis' terms). In addition, any statistical quantity defined by replacing the velocity fluctuation by the vorticity fluctuation is obtained by substituting $k^2 e$ and $-k^2 Z$ to e and Z, respectively.

The relationship in (53) shows that the anisotropy tensor b_{ij} is the sum of two distinct contributions: $b_{ij}^{(e)}$ from which the directional (or dimensionality) anisotropy originates and $b_{ij}^{(Z)}$ which accounts for polarization anisotropy. This decomposition explains unexpected RDT results in rotating flows with *anisotropic* initial data, since only $b_{ij}^{(e)}$ concentrates the information on the nonlinear impact of the Coriolis force on the lessening of dimensionality.

In axisymmetric turbulence, with or without mirror symmetry, only the single-axial component $b_\parallel = b_{ij}n_i n_j$ is needed for representing the complete single-point deviatoric tensor, because

$$b_{ij} = -\frac{3}{2}\underbrace{b_{ij}n_i n_j}_{b_\parallel}\left(\frac{1}{3}\delta_{ij} - n_i n_j\right), \tag{54}$$

so that the e–Z splitting can be analyzed only on this axial component:

$$b_\parallel = b_\parallel^{(e)} + b_\parallel^{(Z)}. \tag{55}$$

Unlike the Reynolds stress tensor anisotropy, which cannot characterize dimensionality, $b_\parallel^{(e)}$ is an indicator of two-dimensionality in the sense of Taylor–Proudman, or invariance of velocity with respect to the axial direction. Upon introduction of an angle β, which characterizes the conical structure of the energy spectral distribution in (53), as proposed by [50] in QS-MHD, one finds

$$b_\parallel = \frac{1}{6} - \frac{1}{2}\cos^2\beta. \tag{56}$$

This angle provides the first significant harmonic of the angular dependence of the spectral energy distribution $e(\boldsymbol{k})$. The Shebalin angle, introduced later by [51], is rather relative to the angular shape of the spectral vorticity distribution $k^2 e(\boldsymbol{k})$. In three-dimensional isotropic turbulence, $\cos^2\beta = 1/3$ and $b_\parallel^{(e)} = 0$, whereas in two-dimensional turbulence, $\cos^2\beta = 0$ and $b_\parallel^{(e)} = 1/6$. Depending on the polarization, which is only significant near the two-dimensional manifold, $k_\parallel = 0$ for both rotating turbulence and QS-MHD turbulence (for different reasons, rediscussed further in Section 4.3.2), two cases can be distinguished, depending on the *dimensionality* and *componentality* dimensions of the flow:

1. *The two dimensional-three component (2D–3C) case in which the axial variability is completely suppressed, with* $\partial/\partial x_\parallel = 0$. Equivalently, the energy spectrum is only non-zero at $k_\parallel = 0$, but with the same amount of spectral energy in the horizontal and vertical components. In this case, elongated structures in the axial direction, or quasi-Taylor columns, include both vortices and jets. This case is characterized by $b_\parallel^{(e)} = 1/6$, $b_\parallel^{(Z)} = 0$. It exactly corresponds to the asymptotic state resulting from RDT in QS-MHD, or in discarding the right-hand sides of Equations (49) and (50). Examining the Reynolds stress tensor, one recovers the counter-intuitive fact that the axial component is exactly twice its transverse counterpart, or $\langle u_\parallel^2\rangle/\langle u_\perp^2\rangle = 2$.
2. *The 2D-2C case in which the axial variability and the vertical velocity are completely suppressed.* Elongated structures in the axial directions are only vortices. This case is characterized again by $b_\parallel^{(e)} = 1/6$, but with $b_\parallel^{(Z)} = -1/2$ yielding $b_\parallel = -1/3$. The intuitive result of $\langle u_\parallel^2\rangle/\langle u_\perp^2\rangle = 0$ is recovered.

Although partial two-dimensionalization is induced by rotation, none of these extreme values is obtained in homogeneous rotating turbulence started with initial conditions of three-dimensional isotropy. A maximum value $b_\parallel^{(e)} \sim 0.08$, much lower than the two-dimensional limit $1/6$, is found in different numerical and theoretical studies [8,10,14].

The 2D–3C case with transition to 2D–2C is only approached in the case of QS-MHD turbulence studied by [46] and [47]. The linear Ohmic dissipation operator acts directly on the energy spectrum to concentrate energy towards the two-dimensional manifold, whereas nonlinear terms mainly result in a polarization of this energy. Polarization in the quasi-two-dimensional manifold – the neighborhood of the two-dimensional manifold in spectral space – was shown to be induced by different cascade processes: a classical two-dimensional cascade for the (vortical) horizontal velocity mode and a direct cascade for the vertical (jetal) velocity mode, as for a passive scalar transported by two-dimensional turbulence.

These studies have shown that $b_{\parallel}^{(e)}$ is a relevant parameter of two-dimensionalization, but not an accurate one in its own: the parameter $b_{\parallel}^{(e)}$ only appears as the first angular harmonic of the angular dependence of the energy spectrum, with averaged k-modulus dependency. It is hardly available from measurements in physical experiments, and can only be computed from models or data of numerical simulations. This drawback is absent when considering the integral length-scales presented in the following section.

4.3.2. *Directional two-point correlation scales*

For three-dimensional axisymmetric turbulent flows, in which trends towards two-dimensional structure are important, two different integral length-scales with axial separation are of particular interest: they were measured by [12] in rotating turbulence, and accurately predicted by DNS/LES and anisotropic EDQNM in [10], and by [17] in stably stratified turbulence. From the definitions in physical space

$$\langle u_{\parallel}^2 \rangle L_{\parallel}^{(\parallel)} = \int_0^{\infty} R_{33}(r\boldsymbol{e}_3)\mathrm{d}r\,, \tag{57}$$

$$\langle u_{\perp}^2 \rangle L_{\perp}^{(\parallel)} = \langle u_1^2 \rangle L_{11}^{(3)} = \langle u_2^2 \rangle L_{22}^{(3)} = \frac{1}{2}\int_0^{\infty} \left(R_{11}(r\boldsymbol{e}_3) + R_{22}(r\boldsymbol{e}_3)\right)\mathrm{d}r, \tag{58}$$

one derives

$$\langle u_{\parallel}^2 \rangle L_{\parallel}^{(\parallel)} = 2\pi^2 \int_0^{\infty} \left(e(k_{\perp}, k_{\parallel} = 0) + Z(k_{\perp}, k_{\parallel} = 0)\right) k_{\perp}\mathrm{d}k_{\perp} \tag{59}$$

and

$$\langle u_{\perp}^2 \rangle L_{\perp}^{(\parallel)} = \pi^2 \int_0^{\infty} \left(e(k_{\perp}, k_{\parallel} = 0) - Z(k_{\perp}, k_{\parallel} = 0)\right) k_{\perp}\mathrm{d}k_{\perp}, \tag{60}$$

using axisymmetry and either a fixed or a cylindrical system of coordinates. In these definitions, the integral length-scales $L_{ii}^{(j)}$ related to the velocity component (no summation over the subscript i in this section) and separated along the (superscript j) axial direction are multiplied by the related Reynolds stress components. We retain these multiplying coefficients in order to emphasize the role of the two-dimensional manifold $k_{\parallel} = 0$, defined in spectral space but influential on physical space statistics. Moreover, this also demonstrates the need for computing the polarization Z in this manifold, since it is the one that differentiates between $L_{\perp}^{(\parallel)}$ and $L_{\parallel}^{(\parallel)}$ in Equations (60) and (59).

The salient feature of physical and numerical experiments in rotating turbulence is a kind of 'decoupling' of $L_{\parallel}^{(\parallel)}$ and $L_{\perp}^{(\parallel)}$: $L_{\perp}^{(\parallel)}$ grows linearly in time under the effect of

rotation, whereas $L_{\parallel}^{(\parallel)}$ is weakly affected by rotation, as evidenced experimentally by [12] and confirmed by later studies, discussed below. Because $\langle u_i^2\rangle L_{ii}^{(3)}$ are inviscid invariants in the linear regime, the nonlinear polarization transfer is required to explain this behaviour. The inviscid nonlinear equations are

$$\frac{\mathrm{d}}{\mathrm{d}t}(\langle u_{\parallel}^2\rangle L_{\parallel}^{(\parallel)}) = 2\pi^2 \int_0^{\infty} \left(T^{(e)}(k_\perp, k_\parallel = 0, t) + T^{(Z)}(k_\perp, k_\parallel = 0, t)\right) k_\perp \mathrm{d}k_\perp\,, \quad (61)$$

$$\frac{\mathrm{d}}{\mathrm{d}t}(\langle u_{\perp}^2\rangle L_{\perp}^{(\parallel)}) = \pi^2 \int_0^{\infty} \left(T^{(e)}(k_\perp, k_\parallel = 0) - T^{(Z)}(k_\perp, k_\parallel = 0)\right) k_\perp \mathrm{d}k_\perp. \quad (62)$$

These equations are the same in rotating and QS-MHD turbulence, because the M_0^2 term vanishes at $k_\parallel = 0$, illustrating again a case of second-order statistics slaved to cubic statistics. The dynamical role of the polarization transfer $T^{(Z)}$ in the two-dimensional manifold $k_\parallel = 0$ is exactly reflected by $\frac{\mathrm{d}}{\mathrm{d}t}(\langle u_{\parallel}^2\rangle L_{\parallel}^{(\parallel)} - 2\langle u_{\perp}^2\rangle L_{\perp}^{(\parallel)})$.

The growth of polarization in the two-dimensional manifold is observed in QS-MHD turbulence, and explains its two-dimensionalization. This argument cannot be invoked for freely decaying rotating turbulence. The reason is that the two-dimensionalization of rotating turbulence is only partial at the time the integral length-scale decoupling appears. This threshold corresponds to a unit macro Rossby number. The linear growth rate of $L_{\perp}^{(\parallel)}$ observed in recent experimental studies [4] can therefore not uniquely be explained by examining only the linear effect of rotation on two-point correlations.

Typical length-scales can also be defined for smaller scales, upon replacing the velocity by the vorticity [3,4]. In that case, the relevant equations in this section are readily derived by changing e into $k^2 e$ and Z into $-k^2 Z$.

4.3.3. *Time-scales of the evolution of large turbulent structures*

Useful scalings for Reynolds stress components, integral length-scales, and 'two-dimensional energy components' mixing them can be proposed as follows.

Following [13], one of the simplest way to obtain the scalings in rotating turbulence was to consider first the invariance of an 'infrared' range, or the following asymptotic series expansion of the spherically averaged energy spectrum near $k = 0$:

$$E(k) = 2\pi k^2 \left(B_0 + B_2 k^2 + \cdots\right).$$

Only the cases of invariant B_0 (Saffman invariant) and quasi-invariant B_2 (Loitsanski integral) were considered. In the non-rotating case, well-known energy decay laws are recovered as

$$\langle u^2\rangle \propto B_0^{2/5} t^{-6/5}, \quad k^2 \text{ spectrum}, \quad (63)$$

and

$$\langle u^2\rangle \propto B_2^{2/7} t^{-10/7}, \quad k^4 \text{ spectrum}\,.$$

The effect of rotation was accounted for by multiplying the above scaling laws by a $(\Omega t)^x$ factor, with an unspecified exponent. The exponent was eventually fixed by a scaling in

$1/\Omega$ of the nonlinear transfer, yielding

$$\frac{\mathrm{d}\langle u^2\rangle}{\mathrm{d}t} = \frac{1}{\Omega} B_0^{-2/3} \langle u^2\rangle^{8/3}, \tag{64}$$

and a similar relationship for the k^4 spectrum. Integration of the latter equation yielded

$$\langle u^2\rangle \propto B_0^{2/5} \Omega^{3/5} t^{-3/5}. \tag{65}$$

Considering the already remarkable agreement of the decay exponent predicted with the k^2 infrared spectrum with EDQNM, DNS, wave turbulence and even experiments [6,8,42], we will restrict our attention to this case only. The fact that the decay exponent in rotating turbulence is very close to half its value in isotropic non-rotating turbulence is recovered from all the above-mentioned studies, and is remarkable. Looking at the anisotropy, there is no reason to consider different scalings for $\langle u_\parallel^2\rangle$ and $\langle u_\perp^2\rangle$, with 'rapid' phase mixing tending to damp $b_\parallel^Z$ and two-dimensionalization weakly affecting $b_\parallel^{(e)}$. A value weakly larger than 1 is expected for the ratio $\langle u_\parallel^2\rangle/\langle u_\perp^2\rangle$, consistent with $b_\parallel^{(e)} \sim 0.08$ and $b_\parallel^{(Z)} \sim 0$, but often this ratio is found smaller than 1 in DNS because of finite-box effects, yielding an artificial negative value of $b_\parallel^{(Z)}$.

We can now move to the related scaling of integral length-scales. The scaling method by [13] can be applied to any integral length-scale $L_{ii}^{(j)}$ (no summation on i), but two of them present a particular interest:

$$L_\parallel^\parallel \propto B_0^{1/5} \Omega^{-3/20} t^{1/4}\,, \tag{66}$$

$$L_\perp^{(\parallel)} \propto B_0^{1/5} \Omega^{3/5} t = B_0^{1/5} \Omega^{-2/5} (\Omega t). \tag{67}$$

Once again, the remarkable result of the linear growth in time of the latter integral length-scale, with a much slower growth of the other one, cannot be considered as fortuitous. Regarding the related 'two-dimensional energy components', one finds

$$\langle u_\perp^2\rangle L_\perp^{(\parallel)} \propto B_0^{3/5} \Omega^{6/5} t^{2/5}, \quad \langle u_\parallel^2\rangle L_\parallel^{(\parallel)} \propto B_0^{3/5} \Omega^{9/20} t^{-7/20}.$$

These scalings were roughly recovered in DNS/LES by [13], using the DNS database by [10]. They are tested here against results of anisotropic EDQNM(3) simulations using larger Reynolds numbers and better angular discretization, presented in Figure 3.

The results are obtained from the EDQNM(3) model for $T^{(e)}$ and $T^{(z)}$ (detailed equation in [10,18]) in solving the generalized Lin equations for e and Z. Axisymmetry is assumed, so that spectral space is discretized in polar coordinates (k,θ_k) in an azimuthal plane, with 61 wavenumbers logarithmically spaced, and 83 angles spaced with a sine distribution, thus providing an excellent resolution around the slow manifold ($\theta_k \simeq \pi/2$). Time marching uses a classical second-order scheme, explicit for the integral transfer term, and implicit for viscosity.

Initial data are purely isotropic without helicity; if initialized to zero, the helicity spectrum remains zero. There is no forcing, and the rotation is introduced from the very beginning of the computation. The resulting growth of the most rotation amplified integral length-scale $L_{11}^{(3)}$ is plotted in the same Figure 3 for different k^2 and k^4 initial spectra at small k, the rest of the initial spectrum being narrow-banded with an exponential decay

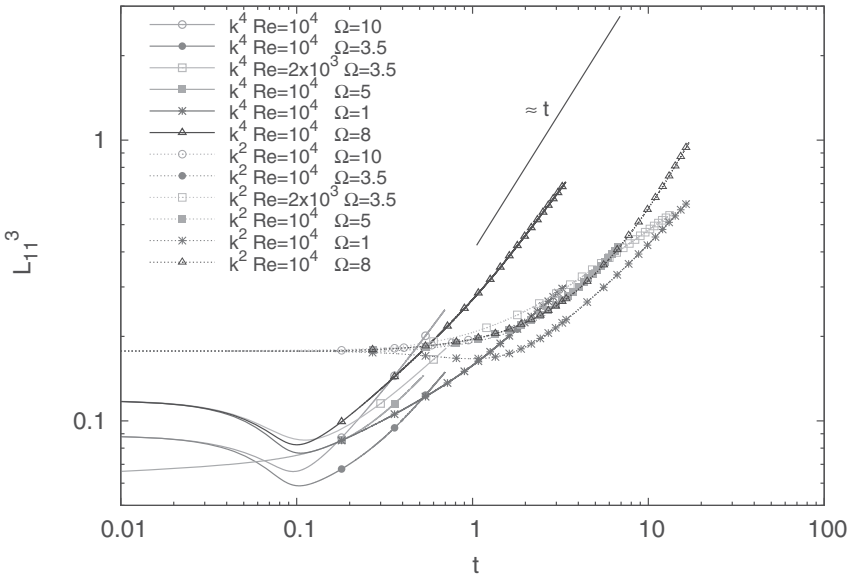


Figure 3. Evolution of the integral scale L_{11}^3 from EDQNM computations at different values of the Reynolds and rotation numbers, and for two infrared scalings of the kinetic energy spectrum, in k^2 or in k^4. The power-law t^1 is also shown.

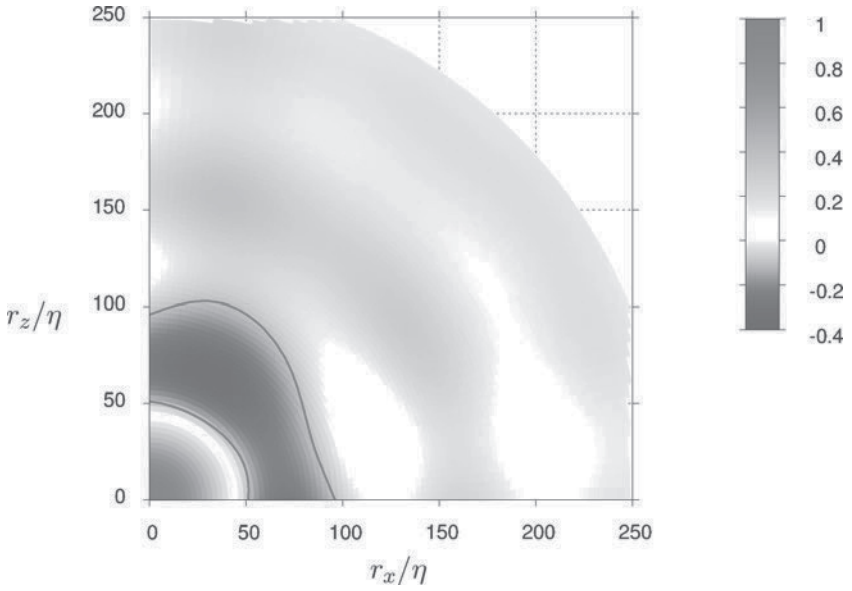


Figure 4. Spatial distribution of $-\frac{1}{4}\boldsymbol{\nabla}\cdot\langle(\delta q)^2\,\delta\mathbf{u}\rangle$ normalized by the value at $(r_x,r_z)=(0,0)$, as a function of the horizontal and vertical separations, r_x and r_z, normalized by the Kolmogorov scale. The two isolines indicate the negative value -0.05 to highlight the negative transfer zone.

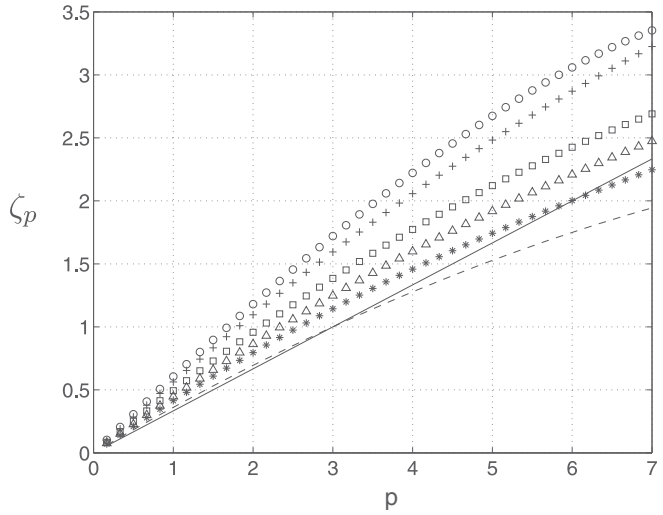


Figure 5. ζ_p exponents for pth-order structure functions as a function of p, at positions closer and closer (symbols, from the bottom to top) to the core of an intense vortex ('French washing machine' with corrotative disks at a rotation rate 30 Hz, see [36]). The solid line corresponds to $\zeta_p = p/3$ (Kolmogorov 1941 scaling). (Reproduced from [18], with permission of the Cambridge University Press.)

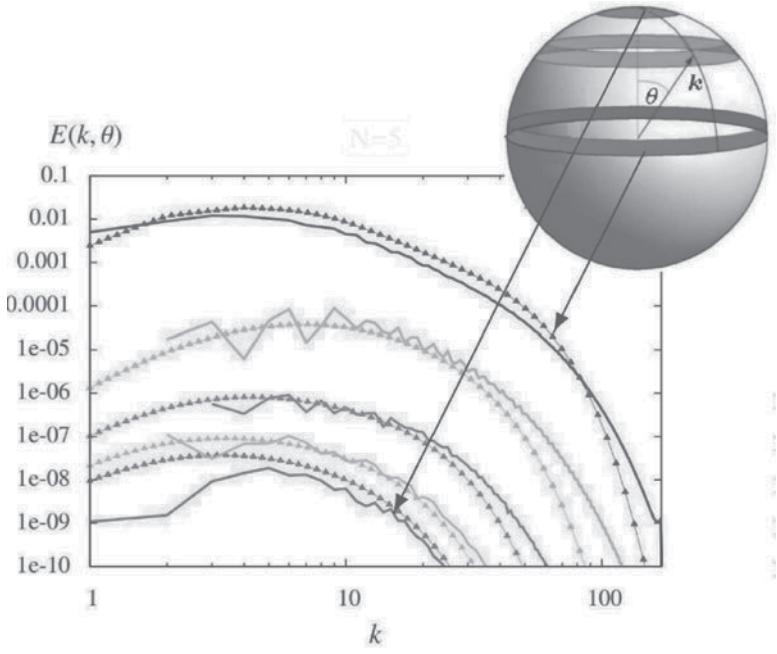


Figure 6. Angle-dependent energy spectra in QS-MHD turbulence at interaction parameter $N = 5$: DNS (full lines) and anisotropic EDQNM (dots). Five angular sectors in Fourier space, centered on θ_k, are chosen between $\theta = 0$ (pole) and $\theta = \pi/2$ ('equator', two-dimensional manifold), with a constant step $\Delta\theta = \pi/10$. (From [47].) (Permission obtained from JFM)

in the small scales. Therefore, after an initial transient, in which the dynamics of rotating turbulence adjust to develop the inertial cascade down to the dissipative scales, a self-similar spectral evolution is observed. After this transient, the figure shows the power-law increase of the $L_\perp^{(\parallel)} = L_{11}^3$ integral length-scale. Again, we present results for spectra with two different scalings in the large scales: k^2 or k^4, and for five different rotation numbers, spanning an order of magnitude variation in the rotation rates, and two different Reynolds numbers. In the k^4 case, $L^{(\parallel)}$ exhibits a power-law behavior with an exponent close to unity, and a multiplicating factor dependent on the value of the Rossby and Reynolds numbers. Figure 3 also shows the result for the k^2 case, with a slight variation of the time power-law dependence of $L^{(\parallel)}$, from unity to 1.5. In all cases, the multiplicating factor proposed by [13] is not recovered, by far. Upon decreasing the Reynolds number from 10^4 to 2×10^3, the effect of viscosity is felt in the evolution after a few eddy turnover times, when kinetic energy has decreased enough for the dissipation to play a more important role in the dynamics.

For QS-MHD, scalings for $\langle u_\parallel^2 \rangle$, $\langle u_\perp^2 \rangle$ and integral length-scales result from pure linear dynamics, but their nonlinear scaling is not completely obvious from DNS and EDQNM by [47]. Useful scaling laws for these quantities, and especially for $\ell^\parallel = L_\perp^\parallel$, are offered by [52], but ignoring the dynamical decoupling between $L_\perp^\parallel$ and $L_\parallel^\parallel$.

4.4. *Cubic correlations in physical and Fourier spaces*

Looking at third-order statistics, things are more complicated. In contrast with the isotropic case, the general two-point third-order spectral tensor T_{imj} cannot be expressed in terms of the generalized transfer tensor $T_{ij}(\boldsymbol{k})$.

Some third-order correlators in physical space can be exactly expressed in terms of triple integrals of $T^{(e)}$, $T^{(Z)}$, $T^{(\mathcal{H})}$ defined in (22), weighted by specific functions, generalizing isotropic relationship. Other ones require to inspect closely the triadic structure in (13) and of the tensor $S_{ijm}(\boldsymbol{k}, \boldsymbol{p})$ underlying the $T^{e,Z,\mathcal{H}}(\boldsymbol{k})$ terms. For instance, for triple-vorticity correlations, both two-point and single-point, one may need to know beforehand the underlying triadic structure of the initial vorticity distribution [6]. Overall, spectral closures ranging from wave-turbulence theory to anisotropic EDQNM are still well suited for the purpose of closing any third-order triadic term in terms of second-order ones (e, Z, $\mathcal{H}$ in the anisotropic context).

The case of the correlations $\langle \delta u_\parallel (\delta q)^2 \rangle(\boldsymbol{r})$ and $\langle \delta u_\perp (\delta q)^2 \rangle(\boldsymbol{r})$ is particularly interesting, given their importance for modelling the jet flow in the next section. For instance, by time derivation of Equation (51), one can equate

$$-\frac{\partial}{\partial r_i} \langle \delta u_i (\delta q)^2 \rangle(\boldsymbol{r}, t) \tag{68}$$

to

$$2 \iiint \exp(\mathrm{i}\boldsymbol{k}\cdot\boldsymbol{r}) T^{(e)}(\boldsymbol{k}, t) \mathrm{d}^3\boldsymbol{k} \tag{69}$$

in (33).

A term-by-term comparison can be done as well for the e-Equation (19) and the $\langle (\delta q)^2 \rangle$-Equation (33) in Section 2, using the integral transform (51).

4.5. *Towards a jet in physical space*

We choose here, without loss of generality, to pursue our study in Section 2.2 in the particular case of a central region of a round jet, for which the flow is statistically stationary at a given position, so that time derivatives of any time-averaged statistics are zero. The first term of Equation (33) is therefore equal to zero. In addition, in this region, pressure-containing terms as well as turbulent diffusion terms are neglected. Under these conditions, Equation (33) becomes

$$2\langle\delta\left(U_\alpha\frac{\partial u_i}{\partial x_\alpha}\right)\delta u_i\rangle(\boldsymbol{r})+2\langle\delta\left(u_\alpha\frac{\partial U_i}{\partial x_\alpha}\right)\delta u_i\rangle(\boldsymbol{r})+\frac{\partial}{\partial r_\alpha}\langle\delta u_\alpha(\delta q)^2\rangle(\boldsymbol{r})$$
$$=+2\nu\frac{\partial^2}{\partial {r_\alpha}^2}\langle(\delta q)^2\rangle(\boldsymbol{r})-2\left(\langle\epsilon\rangle+\langle\epsilon\rangle^+\right). \tag{70}$$

The first term on the left-hand side of (70) is a spatial decay term D and the second one is a production term P. The last one is the third-order term, corresponding in physical space to the third-order correlation, or transfer, terms presented previously in spectral space. All the others are classical terms. (Note that in the absence of large-scale and molecular terms, Equation (70) reduces to $\frac{\partial}{\partial r_\alpha}\langle\delta u_\alpha(\delta q)^2\rangle(\boldsymbol{r})=-2\left(\langle\epsilon\rangle+\langle\epsilon\rangle^+\right)$, which has also been discussed by [53].) Therefore, Equation (70) formally writes

$$D(\boldsymbol{r})+P(\boldsymbol{r})+\frac{\partial}{\partial r_\alpha}\langle\delta u_\alpha(\delta q)^2\rangle(\boldsymbol{r})=\ 2\nu\frac{\partial^2}{\partial {r_\alpha}^2}\langle(\delta q)^2\rangle(\boldsymbol{r})-2\left(\langle\epsilon\rangle+\langle\epsilon\rangle^+\right). \tag{71}$$

An anisotropic axisymmetric treatment is to be further applied to Equation (71), in which each term depends on the spatial vector $\boldsymbol{r}$. Note also that this is a scalar equation, representing the scale-by-scale kinetic energy. Let us assume that the flow is axisymmetric about a direction specified by $\boldsymbol{n}$. The statistical correlations of the flow properties will then be invariant for rotations in planes normal to $\boldsymbol{n}$ and symmetries with respect to planes containing $\boldsymbol{n}$. We note

$$r^2=\boldsymbol{r}\cdot\boldsymbol{r}\qquad\text{and}\qquad\mu_r\equiv\boldsymbol{r}\cdot\boldsymbol{n}/r. \tag{72}$$

In this context, each term of the equations depends on two variables: r and μ_r. Large-scale inhomogeneous variations might be observed along the axisymmetry (decay) direction $\boldsymbol{n}$. We consider that statistics are homogeneous in planes perpendicular to $\boldsymbol{n}$.

Let us write the expressions of each of the four terms in Equation (71):

1. The decay term, for which we consider that the mean velocity has a main component along the axisymmetric decay direction $\boldsymbol{n}$,

$$D(r,\mu_r)\simeq U_n\frac{\partial}{\partial n}\langle(\delta q^2)(r,\mu_r)\rangle. \tag{73}$$

2. The production term $P(r,\mu_r)$, after considering a uniform shear in the considered region, is

$$P(r,\mu_r)=2\left[\langle(\delta u_\perp)^2\rangle-\langle(\delta u_\parallel)^2\rangle\right]\frac{\partial U_n}{\partial n}, \tag{74}$$

where $\perp$ indicates any direction perpendicular to the axisymmetry axis $\boldsymbol{n}$ and $\parallel$ designates the direction of $\boldsymbol{n}$.

3. The advection term $\frac{\partial}{\partial r_\alpha}\langle \delta u_\alpha (\delta q)^2\rangle(\boldsymbol{r})$ is written in a manner similar to [54] and [55]:

$$\langle \delta u_\alpha (\delta q)^2\rangle(\boldsymbol{r}) = M_a(r,\mu_r) r_\alpha + N_a(r,\mu_r) n_\alpha, \tag{75}$$

where only two scalars M_a and N_a appear (the subscript a stands for the 'advection' term in the kinetic energy budget equation). The scalars $M_a(r,\mu_r)$ and $N_a(r,\mu_r)$ can be determined from planar experiments inferring the three velocity components (2D–3C). The measurement plane must include the axisymmetry vector $\boldsymbol{n}$, for example, particle image velocimetry measurements in planes including $\boldsymbol{n}$ and in one plane perpendicular to the axis, via the measurable $\langle \delta u_\parallel (\delta q)^2\rangle$ and $\langle \delta u_\perp (\delta q)^2\rangle$ using

$$\begin{aligned}
\langle \delta u_\perp (\delta q)^2\rangle(r,\mu_r) &= M_a(r,\mu_r) r\sqrt{1-\mu_r^2} + 0\,,\\
\langle \delta u_\parallel (\delta q)^2\rangle(r,\mu_r) &= M_a(r,\mu_r) r\mu_r + N_a(r,\mu_r).
\end{aligned} \tag{76}$$

This leads to the experimentally determinable scalars:

$$\begin{aligned}
M_a(r,\mu_r) &= \frac{\langle \delta u_\perp (\delta q)^2\rangle(r,\mu_r)}{r\sqrt{(1-\mu_r^2)}}\,,\\
N_a(r,\mu_r) &= \langle \delta u_\parallel (\delta q)^2\rangle(r,\mu_r) - \langle \delta u_\perp (\delta q)^2\rangle(r,\mu_r)\frac{\mu_r}{\sqrt{1-\mu_r^2}}.
\end{aligned} \tag{77}$$

(Note the singularity that arises for either $r=0$ or $\mu_r = 1$, *i.e.* around the axisymmetry axis $\boldsymbol{n}$ or for very small scales.)

Therefore, for the axisymmetric case, $\frac{\partial}{\partial r_\alpha}\langle \delta u_\alpha (\delta q)^2\rangle(\boldsymbol{r})$ becomes

$$\frac{\partial}{\partial r_\alpha}\langle \delta u_\alpha (\delta q)^2\rangle(\boldsymbol{r}) \equiv \left(r\frac{\partial}{\partial r} + 3\right) M_a(r,\mu_r) + \left(\mu_r\frac{\partial}{\partial r} + \frac{1-\mu_r^2}{r}\frac{\partial}{\partial \mu_r}\right) N_a(r,\mu_r). \tag{78}$$

4. The dissipative term $\mathrm{Diss}(r,\mu_r)$ is to be further explicited as

$$\begin{aligned}
\mathrm{Diss}(r,\mu_r) &= 2\nu\frac{\partial^2}{\partial r_\alpha^2}\langle (\delta q)^2\rangle = 2\nu\left[\frac{\partial^2}{\partial r^2} + \frac{2}{r}\frac{\partial}{\partial r} - \frac{2\mu_r}{r^2}\frac{\partial}{\partial \mu_r} + \frac{1-\mu_r^2}{r^2}\frac{\partial^2}{\partial \mu_r^2}\right]\langle (\delta q)^2\rangle\\
&= 2\nu\Delta_{r,\mu_r}\langle (\delta q)^2\rangle,
\end{aligned} \tag{79}$$

where the Laplacian operator is $\Delta_{r,\mu_r} = \frac{\partial^2}{\partial r^2} + \frac{2}{r}\frac{\partial}{\partial r} - \frac{2\mu_r}{r^2}\frac{\partial}{\partial \mu_r} + \frac{1-\mu_r^2}{r^2}\frac{\partial^2}{\partial \mu_r^2}$.

To sum up, Equation (71) can therefore be written as

$$\begin{aligned}
&D(r,\mu_r) + P(r,\mu_r) + \left(r\frac{\partial}{\partial r} + 3\right) M_a(r,\mu_r) + \left(\mu_r\frac{\partial}{\partial r} + \frac{1-\mu_r^2}{r}\frac{\partial}{\partial \mu_r}\right) N_a(r,\mu_r)\\
&\quad = 2\nu\Delta_{r,\mu_r}\langle (\delta q)^2\rangle(r,\mu_r) - 2\left[\langle \epsilon\rangle + \langle \epsilon\rangle^+\right].
\end{aligned} \tag{80}$$

Finally, in order to simplify the mathematical form of this equation, we introduce V such that

$$N_a(r,\mu_r)=\left[2+r\frac{\partial}{\partial r}\right]V=\frac{1}{r}\frac{\partial}{\partial r}\left[r^2V\right]; \tag{81}$$

the scalar $V(r,\mu_r)$ can be determined experimentally

$$V=\frac{1}{r^2}\int_0^r sN_a(s,\mu_r)\mathrm{d}s, \tag{82}$$

where s is a dummy variable. We further define

$$\mathcal{N}_a=\left(\mu_r\frac{\partial}{\partial r}+\frac{1-\mu_r^2}{r}\frac{\partial}{\partial\mu_r}\right)V, \tag{83}$$

which is determinable from experiments, and by using the identity [55]:

$$\left(\mu_r\frac{\partial}{\partial r}+\frac{1-\mu_r^2}{r}\frac{\partial}{\partial\mu_r}\right)\left(r\frac{\partial}{\partial r}+2\right)=\left(r\frac{\partial}{\partial r}+3\right)\left(\mu_r\frac{\partial}{\partial r}+\frac{1-\mu_r^2}{r}\frac{\partial}{\partial\mu_r}\right). \tag{84}$$

Equation (80) becomes

$$\begin{aligned}&D(r,\mu_r)+P(r,\mu_r)+\left(r\frac{\partial}{\partial r}+3\right)\left(M_a(r,\mu_r)+\mathcal{N}_a(r,\mu_r)\right)\\&\quad=2\nu\Delta_{r,\mu_r}\langle(\delta q)^2\rangle(r,\mu_r)-2\left[\langle\epsilon\rangle+\langle\epsilon\rangle^+\right].\end{aligned} \tag{85}$$

With $G=M_a(r,\mu_r)+\mathcal{N}_a(r,\mu_r)$ and $\left(r\frac{\partial}{\partial r}+3\right)=\frac{1}{r^2}\frac{\partial}{\partial r}\left(r^3\right)$, and after integration with respect to r, the final axisymmetric form of the scale-by-scale energy budget equation is

$$\begin{aligned}G(r,\mu_r)=&-\frac{2}{3}\left[\langle\epsilon\rangle+\langle\epsilon\rangle^+\right]+2\nu\frac{1}{r^3}\int_0^r s^2\Delta_{r,\mu_r}\langle(\delta q)^2\rangle\mathrm{d}s\\&-\frac{1}{r^3}\int_0^r s^2\left(D(r,\mu_r)+P(r,\mu_r)\right)\mathrm{d}s.\end{aligned} \tag{86}$$

Note the importance of (86) with respect to the known classical equations:

- It obviously reduces to the isotropic '4/3' law. The term G has the physical signification of the energy transferred by turbulence, at a scale r and at a spatial position r,μ_r. It is the equivalent of the term $\langle\delta u(\delta q)^2\rangle$ in axisymmetric turbulence.
- It contains large-scale terms (decay and production) which are very important in the context of the validation against experimental data.
- It contains an explicit variation of the mean kinetic energy dissipation rate $\langle\epsilon\rangle$ with the space point, and so with the flow inhomogeneity and anisotropy.

Equation (86) is very general and involves terms depending on both r and μ_r. A decomposition of each term in a more explicit dependence on r and μ_r is possible by using, *e.g.* spherical harmonics discussed in the following Section 5.1. We also note that the addition

of a Coriolis term for rotating turbulence in Equation (86) would lack to affect the double correlation terms, and would leave a trace only in the triple correlation ones.

5. Technical aspects of the anisotropic description in both physical space and Fourier space

5.1. *Exact correspondence between frame-invariant, scalar, quantities*

If attention is restricted to two-point statistics, any frame-invariant statistical quantity can be expanded in terms of scalar spherical harmonics (SSH) in a similar way in both spaces. It is possible to consider expansion of tensors using a set of scalars that need to be 'true' scalars. 'True' in the sense that each may be built as the trace of some tensor, so that it is invariant under any change of the right-handed orthonormal frame of reference. True scalars can be directly expanded in a series of SSH. For instance, the trace of correlation tensors, in both spectral and physical spaces, is given by

$$\hat{R}_{ii}(\boldsymbol{k}) = \sum_{n=0}^{N} \sum_{m=-2n}^{2n} \varphi_{2n}^{m}(k) Y_{2n}^{m}(\theta_k, \phi_k) \tag{87}$$

and

$$R_{ii}(\boldsymbol{r}) = \sum_{n=0}^{N} \sum_{m=-n}^{n} r_{2n}^{m}(r) Y_{2n}^{m}(\theta_r, \phi_r). \tag{88}$$

In the expansions above, (k, θ_k, ϕ_k) denotes the coordinates of the vector $\boldsymbol{k}$ in a system of polar-spherical coordinates, whereas r, θ_r, ϕ_r are their counterparts for the vector $\boldsymbol{r}$. Although the expansion uses a given polar-spherical system of coordinates, which is relevant in the axisymmetrical case but not restricted to it, the maximum degree N of the expansion is frame-indifferent. The *degree*, denoted by $2n$, is only even, due to Hermitian properties of the spectral tensor, whereas the *order*, denoted by m, takes any integer value such that $0 \leq \mid m \mid \leq 2n$ at fixed n. SSH modes are defined by

$$Y_n^m(\theta, \phi) = P_n^m(\theta) \mathrm{e}^{\mathrm{i}m\phi}, \tag{89}$$

in terms of generalized Legendre polynomials P_n^m. Only the 'basic' Legendre polynomials $P_n^0(\cos\theta)$ are used for expanding axisymmetric 'true' scalar functions, when the polar axis of the system of reference coincides with the axis of symmetry. Exact relationships between scalar coefficients in both spaces are found, term to term, under a single integral. Details of calculations for analytically calculating angle-dependent integrals can be found following [56] (in French and without details) and [57]. They can be obtained from the authors upon request.

$$\varphi_n^m(k) = \frac{1}{(2\pi)^2} \int_0^\infty r^2 \mathcal{F}_n(kr) r_n^m(r) \mathrm{d}r, \tag{90}$$

where the weighting coefficients

$$\mathcal{F}_n(kr) = \int_{-1}^{1} P_n^0(x) \mathrm{e}^{-\mathrm{i}krx} \mathrm{d}x \tag{91}$$

can be tabulated (PhD of Claude Teissèdre, 1984, in French). The functions $\varphi_n^m(k)$ amount to first type, half-integer order, Bessel functions. Of course, this equation generalizes the order 0 in which $\mathcal{F}_0(kr) = 2(\sin kr)/(kr)$ [see also $R_{ii}(r)$ in terms of $E(k)$ in Table 1].

Conversely, the inverse formula can be written as

$$r_n^m(r) = 2\pi \int_0^\infty k^2 \mathcal{F}_n^*(kr)\varphi_n^m(k)\mathrm{d}k, \tag{92}$$

using the same method.

5.2. *Importance of tensorial developments. Differences in both spaces*

The isometric properties of the Fourier transform are illustrated in the previous section. Furthermore, all the tensorial developments can be carried out in the same way in both spaces, accounting for some statistical symmetry, such as isotropy and axisymmetry. The flow will be implicitly supposed homogeneous, unless otherwise stated. In physical space, arbitrary anisotropy cannot be afforded as in Fourier space, and a restricted group of symmetries is involved. ([58] mention a huge number of terms, attributed to [59], but this huge expansion is not practically tractable.) Usually, isotropy, semi-isotropy, axisymmetry and semi-axisymmetry are successively addressed in an order of increasing complexity. The prefix 'semi' refers to rotational symmetry, but does not require mirror symmetry. The group of rotations gathers orthogonal transformations $\mathbf{Q}$ with $\det \mathbf{Q} = 1$ and the semi-group of mirror symmetries gathers orthogonal transformations with $\det \mathbf{Q} = -1$. Further analysis is required in the axisymmetric case, for mirror symmetries with respect to a plane containing the polar symmetry axis $\boldsymbol{n}$ and for mirror symmetries with respect to the plane normal to $\boldsymbol{n}$. The complete group includes the inversion symmetry, or invariance by changing $\boldsymbol{r}$ into $-\boldsymbol{r}$.

Expansions of increasing complexity are found by forming sums of terms within the following tensorial bases:

- Isotropy: only δ_{ij} and r_n are needed for generating statistical correlations via tensorial products weighted by scalar functions of the variable $r = \sqrt{r_n r_n}$.
- Semi-isotropy: the tensorial basis consists of the previous terms, plus $\epsilon_{ijn} r_n / r$. Interesting applications can be found in the MHD context [60,61].
- Axisymmetry: with respect to isotropy, the additional vector term is n_i, the fixed axial vector.
- Semi-axisymmetry: the tensorial basis includes, in addition to the preceding case, $\epsilon_{ijn} r_n / r$, $\epsilon_{ijn} n_n$.

In the isotropic case [retaining only the first two terms in equation (93) below] and in the semi-isotropic case, the tensorial expression of R_{ij}, for instance, involves 'basic scalars' only depending on r. In the axisymmetric and semi-axisymmetric cases, they depend on r and on $\mu_r = (\boldsymbol{r}/r)\cdot\boldsymbol{n}$.

The case of full axisymmetry with mirror symmetry was studied by several authors, among whom were Chandrasekhar and Batchelor. The expansion of $R_{ij}(\boldsymbol{r})$ in terms of four 'scalars'

$$R_{ij}(\boldsymbol{r}) = A(r, \mu_r)\delta_{ij} + B(r, \mu_r)\frac{r_i r_j}{r^2} + C(r, \mu_r)\left(n_i \frac{r_j}{r} + n_j \frac{r_i}{r}\right) + D(r, \mu_r) n_i n_j \tag{93}$$

can be rewritten in terms of only two functions, with the implicit use of a vector potential proposed by Chandrasekhar, since $\partial R_{ij}(\boldsymbol{r})/\partial r_j = 0$.

In the more general case of semi-axisymmetry, therefore possibly without mirror symmetry, [62] obtained a more convenient arrangement of the tensorial terms, favoring the components of fluctuating velocity in a local frame attached to $\boldsymbol{r}$, which is a classical frame of reference in cylindrical coordinates with fixed axis $\boldsymbol{n}$:

$$\boldsymbol{e}^{(1)}(\boldsymbol{r}) = \frac{\boldsymbol{r}\times\boldsymbol{n}}{\mid \boldsymbol{r}\times\boldsymbol{n} \mid}; \quad \boldsymbol{e}^{'(2)}(\boldsymbol{r}) = \boldsymbol{n}\times\boldsymbol{e}^{(1)}(\boldsymbol{r}). \tag{94}$$

The fact that $(\boldsymbol{e}^{(1)}, \boldsymbol{e}^{'(2)}, \boldsymbol{n})$ form an orthonormal right-handed frame of reference yields some simplifications and easier extraction of the 'basic scalars' from tensorial equations, and identification to measured quantities. It is also possible to take advantage of relations such as $\partial e_i^{(1)}/\partial r_j = -e_j^{(1)} e_i^{'(2)}/ \mid \boldsymbol{r}\times\boldsymbol{n} \mid$ to account for incompressibility. In the following, we will also introduce $\boldsymbol{e}^{(1)}$ and $\boldsymbol{e}^{(2)}$ ($\boldsymbol{e}^{(2)} \neq \boldsymbol{e}^{'(2)}$) as the unit vectors which are attached to a polar-spherical system of coordinates with the polar axis $\boldsymbol{n}$, so that $\boldsymbol{e}^{(1)}(\boldsymbol{r})$, $\boldsymbol{e}^{(2)}(\boldsymbol{r})$, $\boldsymbol{r}/r$ is orthonormal and right-handed, with $\boldsymbol{e}^{(1)} \perp \boldsymbol{n}$.

In view of application to structure functions, it is interesting to project the velocity increment on the two above-mentioned frames of reference for $\boldsymbol{r}$. Using the cylindrical frame, in line with [62] and [53], one finds

$$\delta\boldsymbol{u} = \underbrace{(\delta u)_r \boldsymbol{e}^{(1)}(\boldsymbol{r}) + (\delta u)_\theta \boldsymbol{e}^{'(2)}(\boldsymbol{r})}_{\delta u_\perp} + \delta u_\parallel \boldsymbol{n}. \tag{95}$$

Of course, $\delta\boldsymbol{u} = \boldsymbol{u}(\boldsymbol{x}+\boldsymbol{r}) - \boldsymbol{u}(\boldsymbol{x})$ depends also on the position vector $\boldsymbol{x}$, but this dependence disappears in any averaged quantity by statistical homogeneity. Using the polar-spherical frame related to $\boldsymbol{r}$ with polar axis $\boldsymbol{n}$,

$$\delta\boldsymbol{u} = \underbrace{(\delta u)_r \boldsymbol{e}^{(1)}(\boldsymbol{r}) + (\delta u)_v \boldsymbol{e}^{(2)}(\boldsymbol{r})}_{\delta u_T} + \delta u_L \frac{\boldsymbol{r}}{r}, \tag{96}$$

in which the subscripts 'L' and 'T' stand for 'longitudinal' and 'transverse', respectively.

On the one hand, a vector such as $\boldsymbol{e}^{(1)}$ is 'semi-axisymmetric', since its definition exhibits a tensorial function in terms of $\boldsymbol{r}$, $\boldsymbol{n}$ and ϵ_{ijm}. On the other hand, $\boldsymbol{e}^{'(2)}$ and $\boldsymbol{e}^{(2)}$ display only 'axisymmetric' functions.

The same frame of reference is even more useful in $\boldsymbol{k}$ space, where it corresponds to the Craya–Herring frame (Figure 1).

In addition, a possible generalization of the Kármán–Howarth equation to this axisymmetric case was discussed by [62], as well as the structure of some mixed pressure–velocity correlations and of some spectra, although the tensorial formalism was not general, with an inappropriate use of the terminology 'dyadic' for tensors.

Because of the symmetry-preserving properties of the Fourier transform, any tensorial decomposition of $R_{ij}(\boldsymbol{r})$ has an exact counterpart in terms of $\hat{R}_{ij}(\boldsymbol{k})$. Besides, the incompressibility constraint yields a dramatic simplification, with algebraic relationships between the basic scalars available in Fourier space only, so that only four scalars are needed to describe arbitrary anisotropy. We recall that the basic scalars in Fourier space depend only on k in isotropic and semi-isotropic cases and on k and $\mu_k = (\boldsymbol{k}/k)\cdot\boldsymbol{n}$ in

axisymmetric and semi-axisymmetric cases. These properties in Fourier space are not mentioned by [58,62,63].

The generalization of the analysis can be made at any order, as shown in [18, end of chap. 2]. Because the velocity field in Fourier space is actually two-component, thanks to the exact incompressibility condition, using either the Craya–Herring frame or the helical frame, Nth-order velocity correlations at N points are generated by $N + 2$ basic scalars. More common statistics such as Nth-order correlations at P points (with $P < N$, and $P = 2$ for structure functions) are obtained by integrating in Fourier space. The reader is also referred to the triangle diagram (see [18, fig. 2.6], for the most general survey of P-point, Nth-order correlations and the related closure problem.)

6. Conclusion

The focus of this article is the role of cubic correlations, either connected to a nonlinear energy transfer in Fourier space or to third-order structure functions in physical space. In some anisotropic flows without production, there is no linear operator, like the advection and distortion by a mean shear, directly acting on the energy or energy distribution, so that the entire dynamics are slaved to the above-mentioned cubic correlations. In one of the simplest case of anisotropic flow without production, rotating turbulence, the Coriolis force produces no energy but deeply alters the cubic correlations which govern its dynamics, as it modulates and alters by a triadic inertial wave operator [*e.g.* Equations (5) and (47)] the whole nonlinearity in Navier–Stokes equations. These facts were not discussed in recent articles about rotating turbulence [3,4], so that a clarification was needed. In addition, new results about structure functions are derived from the analysis first performed in Fourier space, for technical reasons. One finds a radical change in the third-order structure function under significant rotation, with no recovery of the conventional $4/5$ Kolmogorov law. Another point is to question classical scalings for the time evolution of typical second-order statistics. In sheared turbulence, for instance, with a mean shear rate S, an evolution-law scaling as St is routinely attributed to linear terms, as in the so-called RDT for predicting second-order statistics, whereas nonlinear evolution is expected to scale with a nonlinear time-scale, e.g. t/τ_{NL} with $\tau_{\mathrm{NL}} \sim \ell/u'$. Our best counter-example in rotating turbulence is the linear (in Ωt) growth of the typical integral length-scale $L_{\perp}^{(\parallel)}$, that is, the most rotation-amplified componental integral length-scale, whose evolution is slaved to the transfer term evaluated at the two-dimensional manifold $k_{\parallel} = 0$, $T^{(e)} - T^{(Z)}$, whereas this quantity is invariant in conventional inviscid RDT [2,3]. Very simple scalings proposed by [13] for kinetic energy and all componental integral length-scales are revisited on this occasion. On the one hand, the relevance of a dynamical Equation (64), in addition to a priori scalings, is confirmed for the decay law of kinetic energy, yielding, in the rotating case, half the decay exponent found in the isotropic, non-rotating, case. On the other hand, such an equation is too simple for studying the decay of integral length-scales, or of the related two-dimensional energy components. Accordingly, the complete scalings of [13] are not confirmed: the linear (in time) law for the evolution of the most amplified componental integral length-scale appears to be robust, and not dependent on the initial slope of the energy spectrum, either in k^2 or in k^4. More dynamical insight into this behaviour can be investigated using exact Equations (61) and (62), and related equations for cubic transfer terms $T^{(e,Z)}$.

In order to extend the domain of dynamical analysis in three-dimensional Fourier space, the case of a shear flow in a rotating frame is addressed, with generalization of Lin equations for the set energy spectrum/polarization deviator/helicity spectrum, as done for the case of pure rotation, which generates the most general anisotropic second-order spectral

tensor. Although we do not propose here quantitative results yet, this formalism offers new perspectives to analyze DNS, beyond the classical comparison of linear dynamics, or conventional RDT for second-order statistics, and fully nonlinear results, as in e.g. [64]. In parallel, a complementary approach to sheared turbulence is performed directly in physical space, looking at a modified Kármán–Howarth equation for the second-order structure function of kinetic energy. Although the two-point approach cannot provide such in-depth analysis of cubic terms, with their anisotropic proper dynamics, as the three-point approach (or triadic in Fourier space), the direct approach in physical space is more flexible, allows to relax the strict constraints of statistical homogeneity – local homogeneity becoming a reasonable assumption – and helps to identify which componental third-order structure functions are relevant and measurable.

Finally, a very systematic comparison of statistics is given in the last section in three-dimensional Fourier space and in physical space. Exact term-to-term relationships are given for frame-invariant quantities expanded in terms of SSH, generalizing an isotropic relationship recalled in Table 1. Limitations of approaches to componental quantities, using an orthonormal frame of reference for the $\boldsymbol{r}$ vector, in line with [53,62], in physical space, are clearly demonstrated. In addition, the use of a similar frame of reference for $\boldsymbol{k}$ (as in Figure 1) to that for $\boldsymbol{r}$ can completely solve the problem of deriving the minimal number of components for generating correlations of any order, as for a rank-2 velocity field in terms of solenoidal modes.

Acknowledgements

This work is supported by the French National Research Agency (ANR) under contract number 08-BLAN-0076 'ANISO'.

References

[1] A.N. Kolmogorov, *The local structure of turbulence in incompressible viscous fluid for very large Reynolds numbers*, Dokl. Akad. Nauk. SSSR 30 (1941), pp. 299–303.
[2] C. Cambon and L. Jacquin, *Spectral approach to non-isotropic turbulence subjected to rotation*, J. Fluid Mech. 202 (1989), pp. 295–317.
[3] K. Yoshimatsu, M. Midorikawa, and Y. Kaneda, *Columnar eddy formation in freely decaying homogeneous rotating turbulence*, J. Fluid Mech. 677 (2011), pp. 154–178.
[4] P.J. Staplehurst, P.A. Davidson, and S.B. Dalziel, *Structure formation in homogeneous, freely decaying, rotating turbulence*, J. Fluid Mech. 598 (2008), pp. 81–103.
[5] J.N. Gence and C. Frick, *Birth of the triple correlations of vorticity in an homogeneous turbulence submitted to a solid body rotation*, C. R. Acad. Sci. Paris, Série IIB 329(4) (2001), pp. 351–356.
[6] L.J.A. van Bokhoven, C. Cambon, L. Liechtenstein, F.S. Godeferd, and H.J.H. Clecx, *Refined vorticity statistics of decaying rotating three-dimensional turbulence*, J. Turb. 9 (2008), (N6).
[7] A.C. Newell and B. Rumpf, *Wave turbulence*, Ann. Rev. Fluid Mech. 43 (2011), pp. 59–78.
[8] F. Bellet, F.S. Godeferd, J.F. Scott, and C. Cambon, *Wave turbulence in rapidly rotating flows*, J. Fluid Mech. 562 (2006), p. 83.
[9] S. Galtier, *Weak inertial-wave turbulence theory*, Phys. Rev. E 68 (2003), 015301.
[10] C. Cambon, N.N. Mansour, and F.S. Godeferd, *Energy transfer in rotating turbulence*, J. Fluid Mech. 337 (1997), pp. 303–332.
[11] P.A. Davidson, P.J. Staplehurst, and S.B. Dalziel, *On the evolution of eddies in a rapidly rotating system*, J. Fluid Mech. 557 (2006), pp. 135–144.
[12] L. Jacquin, O. Leuchter, C. Cambon, and J. Mathieu, *Homogeneous turbulence in the presence of rotation*, J. Fluid Mech. 220 (1990), pp. 1–52.
[13] K.D. Squires, J.R. Chasnov, N.N. Mansour, and C. Cambon, *The asymptotic state of rotating homogeneous turbulence at high reynolds numbers*, in *Application of Direct and large Eddy Simulation to Transition and Turbulence*, AGARD Conference proceedings 551, (1994), Neuilly-sur-Seine, France, pp. 4-1 to 4-9, ISBN 10:9283600061.

[14] Y. Morinishi, K. Nakabayashi, and S.Q. Ren, *Dynamics of anisotropy on decaying homogeneous turbulence subjected to system rotation*, Phys. Fluids 13(10) (2001), p. 2912.
[15] S.A. Orszag, *Analytical theories of turbulence*, J. Fluid Mech. 41 (1970), pp. 363–386.
[16] F.S. Godeferd and C. Cambon, *Detailed investigation of energy transfers in homogeneous stratified turbulence*, Phys. Fluids 6(6) (1994), p. 2084.
[17] F.S. Godeferd and C. Staquet, *Statistical modelling and direct numerical simulation of decaying stably-stratified turbulence. part 2, large-scale and small-scale anisotropy*, J. Fluid Mech. 486 (2003), pp. 115–159.
[18] P. Sagaut and C. Cambon, *Homogeneous Turbulence Synamics*, Cambridge University Press, New York, USA, 2008.
[19] A. Salhi and C. Cambon, *Stability of rotating stratified shear flow: An analytical study*, Phys. Rev. E 81 (2010). 026302.
[20] A. Pouquet, M. Lesieur, A. André, and C. Basdevant, *Evolution of high Reynolds number two-dimensional turbulence*, J. Fluid Mech. 75 (1975), pp. 305–319.
[21] J.C. André and M. Lesieur, *Influence of helicity on the evolution of isotropic turbulence at high reynolds number*, J. Fluid Mech. 81 (1977), pp. 187–207.
[22] J. Tchoufag, P. Sagaut, and C. Cambon, *Spectral approach to finite reynolds number effects on Kolmogorov's 4/5 law in isotropic turbulence*, Phys. Fluids, 24 (2012), 015107.
[23] L. Danaila and R.A. Antonia, *Spectrum of a passive scalar in moderate reynolds number homogeneous isotropic turbulence*, Phys. Fluids 21(11) (2009), pp. 111702–111706.
[24] Y. Zhou, W.H. Matthaeus, and P. Dmitruk, *Colloquium: Magnetohydrodynamic turbulence and time scales in astrophysical and space plasmas*, Rev. Mod. Phys. 76 (2004), p. 1015.
[25] Y. Zhou, *Renormalization group theory for fluid and plasma turbulence*, Phys. Rep. 488 (2010), pp. 1–49.
[26] M. Oberlack, *Non-isotropic dissipation in non-homogeneous turbulence*, J. Fluid Mech. 350 (1997), pp. 351–374.
[27] A.S. Monin and A.M. Yaglom, *Statistical Fluid Mechanics*, volume 2. MIT Press, Cambridge, MA, 1975.
[28] R.A. Antonia, M. Ould-Rouis, F. Anselmet, and Y. Zhu, *Analogy between predictions of Kolmogorov and Yaglom*, J. Fluid Mech. 332 (1997), p. 395.
[29] L. Danaila, F. Anselmet, T. Zhou, and R.A. Antonia. *Turbulent energy scale-budget equations in a fully developed channel flow*, J. Fluid Mech. 430 (2001), p. 87.
[30] P. Burattini, R.A. Antonia, and L. Danaila, *Similarity in the far field of a turbulent round jet*, Phys. Fluids 17 (2005), 025101.
[31] R.J. Hill, *Applicability of Kolmogorov's and Monin's equations of turbulence*, J. Fluid Mech. 353 (1997), p. 67.
[32] J. Qian, *Inertial range and the finite Reynolds effect of turbulence*, Phys. Rev. E 55 (1997), pp. 337–342.
[33] J. Mathieu and J.F. Scott, *An Introduction to Turbulence Flow*, Cambridge University Press, Cambridge, 2000.
[34] G.K. Batchelor, *The Theory of Homogeneous Turbulence*, Cambridge University Press, Cambridge, 1953.
[35] C.N. Baroud, B.B. Plapp, Z.-S. She, and H.L. Swinney, *Anomalous self-similarity in a turbulent rapidly rotating fluid*, Phys. Rev. Lett. 88 (2002), 114501.
[36] C. Simand, F. Chill, and J.-F. Pinton, *Structure, dynamics and turbulence features of a confined vortex*, in *Vortex Structure and Dynamics*, volume 555 of *Lecture Notes in Physics*, A. Maurel and P. Petitjeans, eds., Springer, Berlin, Heidelberg, 2000, pp. 291–298. .
[37] Y. Zhou, *A phenomenological treatment of rotating turbulence*, Phys. Fluids 7 (1995), p. 2092.
[38] J. Seiwert, C. Morize, and F. Moisy, *On the decrease of intermittency in decaying rotating turbulence*, Phys. Fluids 20 (2008), 071702.
[39] M. Thiele and W.-C. Müller, *Structure and decay of rotating homogeneous turbulence*, J. Fluid Mech. 637 (2009), pp. 425–442.
[40] T. Teitelbaum and P.D. Mininni, *The decay of turbulence in rotating flows*, Phys. Fluids 23(6) (2011), 065105.
[41] M.A. Taylor, S. Kurien, and G.L. Eyink, *Recovering isotropic statistics in turbulence simulations: The Kolmogorov 4/5th law*. Phys. Rev. E 68 (2003), 026310.
[42] F. Moisy, C. Morize, M. Rabaud, and J. Sommeria, *Decay laws, anisotropy and cyclone-anticyclone anisotropy in decaying rotating turbulence*, J. Fluid Mech. 666 (2011), pp. 5–35.
[43] F.S. Godeferd, *Relating statistics to dynamics in axisymmetric homogeneous turbulence*, Physica D. Nonlinear Phenom. 241(7) (2012), pp. 794–802.

[44] C. Lamriben, P.-P. Cortet, and F. Moisy, *Direct measurements of anisotropic energy transfers in a rotating turbulence experiment*, Phys. Rev. Lett. 107(2) (2011), 024503.
[45] F. Waleffe, *Inertial transfers in the helical decomposition*, Phys. Fluids A 5 (1993), 026310.
[46] B. Favier, F.S. Godeferd, C. Cambon, and A. Delache, *On the two-dimensionalization of quasi-static MHD turbulence*, Phys. Fluids 22 (2010), 075104.
[47] B. Favier, F.S. Godeferd, C. Cambon, A. Delache, and W.J.T. Bos, *Quasi-static magnetohydrodynamic turbulence at high Reynolds number*, J. Fluid Mech. 681 (2011), pp. 434–461.
[48] C. Cambon and B.J. Gréa, *The role of directionality on the structure and dynamics of strongly anisotropic flows*, preprint (2013), to appear in Journal of Turbulence. 14(1) (2013), pp. 50–71.
[49] S.C. Kassinos, W.C. Reynolds, and M.M. Rogers, *One-point turbulence structure tensors*. J. Fluid Mech. 428 (2001), pp. 213–248.
[50] R. Moreau, *On Magnetohydrodynamic Turbulence*, Proceedings of the Symposium on Turbulence of Fluids and Plasmas, New York, April 16–18, 1968, pp. 359–372, Brooklyn, New York, 1970.
[51] J.V. Shebalin, W.H. Matthaeus, and D. Montgomery, *Anisotropy in MHD turbulence due to a mean magnetic field*, J. Plasma Phys. 29(03) (1983), pp. 525–547.
[52] N. Okamoto, P.A. Davidson, and Y. Kaneda, *On the decay of low-magnetic-reynolds-number turbulence in an imposed magnetic field*, J. Fluid Mech. 651 (2010), pp. 295–318.
[53] S. Galtier, *Exact vectorial law for homogeneous rotating turbulence*, Phys. Rev. E 80(4) (2009), 046301.
[54] G.K. Batchelor, *The role of big eddies in homogeneous turbulence*, Proc. Roy. Soc. 195(1043) (1949), pp. 513–532.
[55] B.K. Shivamoggi and R.A. Antonia, *Isotropic and axisymmetric turbulence of passive scalars*, Fluid Dyn. Res. 26 (2000), pp. 95–104.
[56] C. Cambon and C. Teissèdre, *Application of spherical harmonics to the representation and calculation of the kinematic parameters in homogeneous anisotropic turbulence*. Académie des Sciences, Comptes Rendus, Série II Mécanique, Physique, Chimie, Sciences de l'Univers, Sciences de la Terre 301(2) (1985), pp. 65–68.
[57] A.R. Edmonds, *Angular Momentum in Quantum Mechanics*, 3rd ed., Princeton University Press, New Jersey, 1974.
[58] M. Ould-Rouiss, *Axisymmetric form of Kármán-Howarth equation and its limiting forms*, Eur. Phys. J. B 15 (2000), pp. 339–347.
[59] G.K. Batchelor, *The theory of axisymmetric turbulence*, Proc. R. Soc. Lond. A 186(1007) (1946), pp. 480–502.
[60] Moffatt, *Magnetic Field Generation in Electrically Conducting Fluids*, 1st ed., Cambridge University Press, Cambridge, 2–3, (1978), pp. 43–164.
[61] T. Gomez, H. Politano, and A. Pouquet, *Exact relationship for third-order structure functions in helical flows*, Phys. Rev. E 61(5) (2000), pp. 5321–5325.
[62] E. Lindborg, *Kinematics of homogeneous axisymmetric turbulence*, J. Fluid Mech. 302 (1995), pp. 179–201.
[63] L. Biferale and I. Procaccia, *Anisotropy in turbulent flows and in turbulent transport*, Phys. Rep. 414(2–3) (2005), pp. 43–164.
[64] A. Salhi and C. Cambon, *An analysis of rotating shear flow using linear theory and dns and les results*, J. Fluid Mech. 347 (1997), pp. 171–195.

Appendix. Generalized Lin equations with mean flow effects

From the second-order Craya equation for the spectral tensor $\hat{\mathbf{R}}$, rewritten as Equation (12), with the eikonal equation

$$\dot{k}_i = -A_{ji}k_j, \tag{A1}$$

equations for e, Z, $\mathcal{H}$ are readily derived using the most general decomposition, valid for arbitrary anisotropy and arbitrary helicity:

$$\hat{R}_{ij} = eP_{ij} + \Re\left(ZN_iN_j\right) + \mathrm{i}\epsilon_{ijn}\frac{k_n}{k}\mathcal{H}, \tag{A2}$$

with reciprocal definitions

$$e = \frac{1}{2}\hat{R}_{mm}, \quad Z = \frac{1}{2}\hat{R}_{ij}N_i^* N_j^*, \quad \mathcal{H} = \mathrm{i}\epsilon_{inm}\frac{k_i}{k}\hat{R}_{nm}. \tag{A3}$$

Remark on helicity: The helicity spectrum in the theoretical, continuous, case is given by

$$\frac{1}{2}\langle\widehat{\boldsymbol{\omega}}_i^*(\boldsymbol{p})\hat{u}_j(\boldsymbol{k})\rangle = k\mathcal{H}(\boldsymbol{k})\delta^3(\boldsymbol{k}-\boldsymbol{p}), \tag{A4}$$

so that the single-point statistical helicity is

$$\frac{1}{2}\langle\boldsymbol{\omega}\cdot\boldsymbol{u}\rangle = \iiint k\mathcal{H}(\boldsymbol{k})\mathrm{d}^3\boldsymbol{k},$$

and a radial helicity spectrum $H(k)$ could be defined by spherically averaging $k\mathcal{H}(\boldsymbol{k})$, so that $\frac{1}{2}\langle\boldsymbol{\omega}\cdot\boldsymbol{u}\rangle = \int_0^\infty H(k)\mathrm{d}k$. One recovers the same relationship as for the kinetic energy, successively passing from $e(\boldsymbol{k})$ to $E(k)$, then to $(1/2)\langle u_i u_i\rangle$. Of course, $k\mathcal{H}(\boldsymbol{k})$ contains a lot more information than the single-point helicity correlation does, because there is a bijection between this spectral scalar and the two-point correlation scalar in physical space $\langle\boldsymbol{\omega}(\boldsymbol{x})\boldsymbol{u}(\boldsymbol{x}+\boldsymbol{r})\rangle$. Basic definitions suggest to work with $k\mathcal{H}(\boldsymbol{k})$ instead of $\mathcal{H}(\boldsymbol{k})$, and to drop the factor $1/2$ in (A4). Our choice here was used by [2] and can be justified by the simplest form of the realizability constraint

$$e(\boldsymbol{k}) \geq \sqrt{|\ Z(\boldsymbol{k})\ |^2 + \mathcal{H}^2(\boldsymbol{k})} \quad \forall\boldsymbol{k}, \tag{A5}$$

and by the fact that the Lin-type equation for $\mathcal{H}$, or $\dot{\mathcal{H}} + 2\nu k^2\mathcal{H} = T^{(H)}$, rediscussed below, is simpler than the one for $k\mathcal{H}$, which should be $k\dot{\mathcal{H}} - \frac{k}{k^2}(k\mathcal{H}) + 2\nu k^2(k\mathcal{H}) = T^{(kH)}$.

The simplest equation is the one for the three-dimensional helicity spectrum $k\mathcal{H}(\boldsymbol{k})$ which decouples from 'RDT' terms, except for the mean advection given by the overdot. From (A3) one computes

$$\dot{\mathcal{H}} = \mathrm{i}\dot{e}_i^{(3)}\epsilon_{inm}\hat{R}_{nm} + \mathrm{i}\epsilon_{inm}e_i^{(3)}\dot{\hat{R}}_{nm},$$

and it is clear that the linear 'RDT' contribution from $M_{in}\hat{R}_{nj} + M_{jn}\hat{R}_{in}$ vanishes because the helicity spectrum involves only the antisymmetric, imaginary, as well as the imaginary part of the spectral tensor. The contribution from the time-derivative of the unit vector $\boldsymbol{e}^{(3)} = \boldsymbol{k}/k$ also vanishes because $\epsilon_{inm}\hat{R}_{nm} = 2\mathrm{i}e_i^{(3)}\mathcal{H}$ and $\dot{\boldsymbol{e}}^{(3)}\cdot\boldsymbol{e}^{(3)} = 0$, so that

$$\dot{\mathcal{H}}(\boldsymbol{k}(t),t) + 2\nu k^2\mathcal{H}(\boldsymbol{k},t) = T^{(h)}(\boldsymbol{k},t). \tag{A6}$$

The e-equation is simply found by taking half the trace of (12), so that

$$\dot{e} + 2\nu k^2 e + M_{in}\left(eP_{in} + \Re\left(ZN_iN_n\right)\right) = T^{(e)}.$$

One finds

$$\dot{e} + 2\nu k^2 e + A_{nm}\left(-e\frac{k_n k_m}{k^2} + \Re\left(ZN_nN_m\right)\right) = T^{(e)}, \tag{A7}$$

in which the linear 'RDT' term is the spectrum of 'production' $A_{nm}\hat{R}_{nm}$, with $A_{nn}=0$, and without contribution from the Coriolis force. The spectral contribution from pressure-strain terms is zero as well.

Only linear RDT terms in the Z-equation can display explicit Coriolis and pressure-strain rate effects. This equation is found by calculating

$$\dot{Z}=\frac{1}{2}\left(\dot{\hat{R}}_{ij}N_i^*N_j^*+\hat{R}_{ij}\left(\dot{N}_i^*N_j^*+N_i^*\dot{N}_j\right)\right).$$

One also needs to time-derive the helical modes according to the eikonal Equation (A1). This can be done by starting from the Craya–Herring frame for which

$$\dot{\boldsymbol{e}}^{(\alpha)}\cdot\boldsymbol{e}^{\beta}=\epsilon_{\alpha\beta3}\Omega^E,\quad\text{with}\quad\Omega^E=-e_i^{(2)}A_{ij}e_j^{(1)}-k\frac{n_iA_{ij}e_j^{(1)}}{k_\perp},\quad k_\perp=\mid\boldsymbol{k}\times\boldsymbol{n}\mid,\qquad\text{(A8)}$$

where the Greek indices take the values 1 and 2 only. (The Craya–Herring frame being orthonormal, its motion with respect to the fixed frame is that of a rigid solid and thus governed by a single 'entrainment rotation vector', with the relevant component Ω^E here.) In the same way, one finds $\dot{\boldsymbol{e}}^{(3)}=-A_{ji}e_j^{(3)}+A_{nm}\frac{k_nk_m}{k^2}\boldsymbol{e}^{(3)}$. Accordingly, the entrainment terms derive from $\dot{\boldsymbol{N}}\cdot\boldsymbol{N}^*=2\mathrm{i}\Omega^E$ and $\dot{\boldsymbol{N}}\cdot\boldsymbol{e}^{(3)}=-\boldsymbol{N}\cdot\dot{\boldsymbol{e}}^{(3)}=\boldsymbol{e}^{(3)}\cdot\mathbf{A}\cdot\boldsymbol{N}$, so that

$$\dot{\boldsymbol{N}}=\left(\boldsymbol{e}^{(3)}\cdot\mathbf{A}\cdot\boldsymbol{N}\right)\boldsymbol{e}^{(3)}-\mathrm{i}\Omega^E\boldsymbol{N},\quad\dot{\boldsymbol{N}}^*=\left(\boldsymbol{e}^{(3)}\cdot\mathbf{A}\cdot\boldsymbol{N}^*\right)\boldsymbol{e}^{(3)}+\mathrm{i}\Omega^E\boldsymbol{N}^*.\qquad\text{(A9)}$$

The total entrainment term in the Z-equation finally reduces to

$$\frac{1}{2}\hat{R}_{ij}\left(\dot{N}_i^*N_j^*+N_i^*\dot{N}_j^*\right)=2\mathrm{i}\Omega^EZ,$$

and the other part can be written as

$$\frac{1}{2}\dot{\hat{R}}_{ij}N_i^*N_j^*=-2\nu k^2Z-N_i^*M_{in}\hat{R}_{nj}N_j^*,$$

with $\hat{R}_{nj}N_j^*=eN_n^*+ZN_n$ and $N_i^*M_{in}=N_i^*A_{in}+2N_i^*\epsilon_{ipn}\Omega_p$. The linear part of the Z-equation becomes

$$\dot{Z}+2\nu k^2Z=-e\left[\boldsymbol{N}^*\cdot\mathbf{A}\cdot\boldsymbol{N}^*\right]-Z\left(\left[\boldsymbol{N}^*\cdot\mathbf{A}\cdot\boldsymbol{N}\right]+2N_m^*\epsilon_{mpn}\Omega_pN_n-2\mathrm{i}\Omega^E\right).$$

Final simplifications result from

$$\boldsymbol{N}^*\cdot(\boldsymbol{\Omega}\times\boldsymbol{N})=\boldsymbol{\Omega}\cdot(\boldsymbol{N}\times\boldsymbol{N}^*)=-2\mathrm{i}\boldsymbol{\Omega}\cdot\boldsymbol{e}^{(3)},\qquad\text{(A10)}$$

and from

$$\boldsymbol{N}\cdot\mathbf{A}\cdot\boldsymbol{N}=-\boldsymbol{e}^3\cdot\mathbf{A}\cdot\boldsymbol{e}^{(3)}+\mathrm{i}\boldsymbol{W}\cdot\boldsymbol{e}^{(3)},\qquad\text{(A11)}$$

using $N_i^* N_j = P_{ij} + \mathrm{i}\epsilon_{ijp} e_j^{(3)}$ and the mean vorticity $W_i = \epsilon_{inm} A_{mn}$. This also suggests to use a splitting of $\mathbf{A}$ in terms of its symmetric part $\mathbf{S}$ and its antisymmetric part, the latter involving mean vorticity, such that

$$A_{nm} = S_{nm} + \frac{1}{2}\epsilon_{npm} W_p. \tag{A12}$$

Finally, the unexpectedly simple equation for Z is

$$\dot{Z} + 2\nu k^2 Z + e\,[\boldsymbol{N}^*\cdot\mathbf{S}\cdot\boldsymbol{N}^*] - Z\left(\left[\boldsymbol{e}^{(3)}\cdot\mathbf{S}\cdot\boldsymbol{e}^{(3)}\right] + \mathrm{i}\left(4\boldsymbol{\Omega} + \boldsymbol{W}\right)\cdot\boldsymbol{e}^{(3)}\right) - 2\Omega^E\Big) = T^{(Z)}. \tag{A13}$$

In the end, the complete set of equations is found as

$$\dot{e} + 2\nu k^2 e + \frac{\dot{k}}{k} e + \Re\left(Z\,[\boldsymbol{N}\cdot\mathbf{S}\cdot\boldsymbol{N}]\right) = T^{(e)}, \tag{A14}$$

$$\dot{Z} + 2\nu k^2 Z + \frac{\dot{k}}{k} Z + e\,[\boldsymbol{N}^*\cdot\mathbf{S}\cdot\boldsymbol{N}^*] + \mathrm{i}Z\left(\left(4\boldsymbol{\Omega} + \boldsymbol{W}\right)\cdot\boldsymbol{e}^{(3)} - 2\Omega^E\right) = T^{(Z)}, \tag{A15}$$

$$\dot{\mathcal{H}}(\boldsymbol{k}(t), t) + 2\nu k^2 \mathcal{H}(\boldsymbol{k}, t) = T^{(H)}(\boldsymbol{k}, t), \tag{A16}$$

with

$$\frac{\dot{k}}{k} = -\left[\boldsymbol{e}^{(3)}\cdot\mathbf{S}\cdot\boldsymbol{e}^{(3)}\right].$$

These equations generalize the basic Lin equation for $E(k, t)$ in isotropic turbulence. They were extensively studied by [2,8,10], in the case of purely rotating turbulence – without mean shear – in which the linear 'RDT' part exactly vanishes, to the notable exception of a rotation-dependent phase term in the Z-equation, *so that all nontrivial dynamics came from spectral transfer terms $T^{(e,Z,H)}$ mediated by cubic velocity correlations.*

In the presence of a mean flow gradient A_{nm}, and in the rotating frame, the generalized set of Lin equations is less complicated than expected, with some important properties:

- The equation for the three-dimensional helicity spectrum remains decoupled, and is only affected by the mean-flow advection term, but without any 'production'. A bit surprisingly, the equation for $\mathcal{H}$ is simpler than the one for the 'true' helicity spectrum $k\mathcal{H}$, whereas the structure of the other equations is simplified by using ke and kZ.
- The new terms in the e-equation only reflect linear 'RDT' effects of the symmetric part of the distorting mean velocity gradient. This motivates a splitting of the production spectrum in terms of e, or directional anisotropy, and Z, or polarization anisotropy.
- The equation for the polarization anisotropy term Z is rather simple. New linear 'RDT' terms only involve e and Z, and not Z^*. The phase term, which amounts to rotating the plane of polarization, is related to twice the dispersion frequency $2\boldsymbol{\Omega}\cdot\boldsymbol{e}^{(3)}$, $\boldsymbol{e}^{(3)} = \boldsymbol{k}/k$ of inertial waves for purely rotating turbulence [2]. It is replaced by a similar term, which seems to display the 'tilting vorticity' in Equation (A16), $2\boldsymbol{\Omega} + \boldsymbol{W}/2$, instead of the absolute vorticity $2\boldsymbol{\Omega} + \boldsymbol{W}$. In addition to this phase term, which incorporates all the antisymmetric, or mean vorticity, part of the distorting gradient, the other linear 'RDT' terms only involve the symmetric, pure strain, part, as for the e-equation.

Journal of Turbulence, 2013
Vol. 14, No. 1, 50–71, http://dx.doi.org/10.1080/14685248.2012.762455

The role of directionality on the structure and dynamics of strongly anisotropic turbulent flows

C. Cambon[a,*] and B.-J. Gréa[b]

[a]*LMFA, Ecole Centrale de Lyon, CNRS, INSA, UCB, F-69134 Ecully Cedex, France;* [b]*CEA, DAM, DIF, F-91297 Arpajon, France*

(*Received 15 September 2012; final version received 14 December 2012*)

Strong anisotropy in turbulent flows may be induced by body forces, Coriolis, buoyancy, Lorentz, and/or by large-scale gradients. These effects combined to the redistribution pressure terms are first identified by an angle dependence of the wave vector $\boldsymbol{k}$ in Fourier space, the *directionality*. The resulting anisotropic structure is not taken into account in classical *phenomenological* theory, using essentially 'isotropised' dimensional analysis. Besides, it is generally hidden in practical engineering models by means of tuned constants, which may vary if the flow changes of nature. In this paper, different examples of anisotropic turbulence are revisited and compared to each other in order to shed light on fundamental aspects of this specific turbulence. To begin with, flows without energy production like rotating turbulence are considered. In this case, isotropy is broken by mean of third-order correlations in the equations. These correlations quantify the interscale energy transfer, and must be investigated at three-point, or triad by triad in Fourier space. This allows to account for the role of typical anisotropic frequency $2\Omega\cos\theta_k$, with θ_k the angle of the wave vector to the axis of rotation, and to simultaneously restore the role of phase coherence. We pursue the discussion with a second flow case, with production, quasi-static magnetohydrodynamics. This illustrates turbulence forced towards two-dimensional structure by an explicit Ohmic dissipation term. Linear dynamics displays an angle (called Moreau, or Shebalin) capable of reflecting the basic anisotropy in models as simple as $\mathcal{K}-\varepsilon$. In the final phase of transition towards 2D structure, however, dynamics are essentially driven by third-order velocity correlations, and both successive linear and nonlinear phases yield counter-intuitive anisotropic results. The last case considered here is the turbulent mixing induced by a Rayleigh-Taylor instability. It is shown that anisotropy plays a central role in the dynamics of the mixing zone by means of an angular *dimensionality parameter* similar to the Moreau angle but for the density field, and appearing in a global model of buoyancy-drag equation.

Keywords: turbulence; anisotropic structure; third-order correlations; phase coherence; cascade

1. Introduction

1.1. *Context of the turbulence colloquium marseille (TCM): a missing theme?*

Many aspects of turbulent flows were surveyed and discussed during this colloquium, from homogeneous, not necessarily isotropic, turbulence in the first session. The concept of homogeneous anisotropic turbulence, however, never appeared as such, except in the first keynote lecture by Keith Moffatt [1], who mentioned Rapid Distortion Theory (RDT)

*Corresponding author. Email: claude.cambon@ec-lyon.fr

© 2013 Taylor & Francis

and Kraichnan's nonlinear closures, so that some related aspects, often marginal, were postponed to the last two sessions, devoted to Geophysical Turbulence and Magnetohydrodynamic Turbulence. Let us advocate for a specific theme *homogeneous, possibly strongly anisotropic, turbulence*, as a part of fundamental research – prior to dedicated applications –, with three examples: Rotating turbulence, Quasi-Static magnetohydrodynamics, and instable density stratification.

Rotating turbulence illustrates a flow case without explicit energy production, in which the role of anisotropy in energy transfer is essential. In contrast, anisotropy is triggered by direct linear mechanisms in the other two cases, anisotropic Ohmic dissipation in QSMHD turbulence, and anisotropic production in Rayleigh-Taylor generated turbulence. In each case, anisotropy plays a different role, but the angle-dependent quantity expressing the directionality is proposed to give a useful unifying perspective.

1.2. *Theoretical tools for investigating the theme, brief discussion*

1.2.1. *Limitations of the isotropised dimensional analysis*

A key for understanding the anisotropic structure from dynamical equations, at least in quasi-incompressible turbulence, is the solenoidal projection. In the basic Navier-Stokes equation, the quadratic nonlinear term is not divergence-free, so that the pressure gradient may exactly balance the *dilatational* contribution of the nonlinear term, preserving only its *solenoidal*, divergence-free contribution. This role of solenoidal projection yields preferred orientation in basic operators and is very simply illustrated by linearizing the nonlinear terms around a mean motion, as in the so-called Rapid Distortion Theory. For instance, the (inverse) time scales 2Ω (system vorticity) for a rotating fluid, and the Brunt-Väisälä frequency N for a stratified fluid, are eventually modulated by an orientation parameter which depends on the orientation of the wave vector $\boldsymbol{k}$ of the velocity Fourier mode under consideration with the preferential direction $\boldsymbol{n}$, say vertical, bearing the system vorticity or the gravitational acceleration. Accordingly, the basic external frequency is not 2Ω or N, but the anisotropic dispersion frequency:

$$\sigma_{rot} = \pm 2\Omega \cos\theta_k, \quad \sigma_{strat} = \pm N \sin\theta_k, \quad \text{with } \theta_k = (\boldsymbol{k}, \boldsymbol{n}). \tag{1}$$

Let us just recall that Equation (1) explains the appearance of St Andrews Cross structures when locally stirring, at fixed temporal frequency, a rotating fluid or a stably-stratified medium. In engineering modelling, essentially RANS using single-point closures, previous angle-dependent frequencies cannot be accounted for. Use of two-point formalism, essentially spectral in [2], offers possibilities for extending classical modelling – both RANS and LES – with scale-to-scale information. Nevertheless, use of spherical averaging in wave-space leads to partially isotropised models, which are not really convenient in case of strong anisotropy. Angle-dependent frequencies, however, may have an equivalent in simple models, in cases with energy production/dissipation, such as the Moreau angle or Shebalin angle, identified in MHD and, more recently, in unstable stratification for the density variance (or potential energy). Setting aside just now this distinction of flows with and without production, we will retain that the linear terms and the nonlinear ones always interact in a subtle way. Spectral Linear Theory (SLT)[1] allows us to identify the efficient angle-dependent frequency to account for, as a prerequisite before performing a fully nonlinear analysis. As a single example, the elliptical flow instability, especially at

weak eccentricity, cannot be understood if one ignores the angle-dependent coefficient in the first equation in (1), which allows parametric resonance.

This rapid survey illustrates the limitations of too simple isotropised models, in which dimensional analysis uses 2Ω, N, and even S (shear or strain rate) in a similar way, as for defining Rossby or Froude numbers with respect to nonlinear turnover time. We also show the interest of 3D Fourier space for the simplest (algebraic) solenoidal projection. Fourier space is an invaluable tool, for SLT and for triadic closures from the legacy of Kraichnan [3] and Orszag [4], not to mention Craya [5].

1.2.2. *Third-order correlations and phase coherence*

Homogeneous anisotropic turbulence deserves study, that it cannot be analysed completely by dimensional considerations that might be adequate in the isotropic case, and that even if linear theory (called SLT here) provides much more information than it does in the isotropic case, nonlinearity cannot be neglected.

Looking at the equations which govern second-order statistics, quadratic nonlinearity of basic equations result in the presence of third-order correlations. Importance of three-point cubic correlations is demonstrated in various homogeneous flow cases [6]. As our best example, phase coherence of three-point cubic velocity correlations is essential for understanding the dynamics of decaying rotating turbulence. Anisotropic third-order correlations were recently investigated experimentally in this case [7], which is theoretically addressed in Section 3. In addition, the very subtle saturated transition from 3D to 2D structure, shown in rotating turbulence, is contrasted with a complete two-dimensionalization obtained in quasi-static magnetohydrodynamics, allowing a mutual better physical understanding in both cases.

1.3. *Organization*

This paper is organized as follows. Solenoidal projection and exact separation between terms from linear and nonlinear origin is addressed in Section 2, with application to second-order and third-order statistics. Rotating and QSMHD turbulence are discussed in Section 3. The case of unstable stratification is presented in Section 4, and Section 5 is devoted to conclusions and perspectives.

2. Revisiting the structure of anisotropic homogeneous turbulence

2.1. *Separation between linear and nonlinear terms*

Our starting point is the Navier-Stokes equation for a three-dimensional incompressible velocity field $\boldsymbol{u}(\boldsymbol{x}, t)$. The role of the pressure fluctuation is to ensure the divergence-free constraint, or $\nabla \cdot \boldsymbol{u} = 0$ for the velocity field. Accordingly, the pressure gradient exactly balances the dilatational part of the nonlinear term in N-S equations, so that only its solenoidal part is kept. We do not discuss here the general Helmholtz decomposition in terms of dilatational and solenoidal contributions, nor the integro-differential formalism for extracting its solenoidal contribution from any vector field. This operation of solenoidal projection is done algebraically in 3D Fourier space, using the classical projection operator, or

$$P_{ij} = \delta_{ij} - \frac{k_i k_j}{k^2}, \tag{2}$$

so that the counterpart of N-S equations in Fourier space is

$$\left(\frac{\partial}{\partial t} + \nu k^2\right)\hat{\boldsymbol{u}}(\boldsymbol{k}, t) + \mathbf{P}(\widehat{\boldsymbol{\omega} \times \boldsymbol{u}}) = 0, \tag{3}$$

in which the relevant nonlinearity is given by the Lamb vector, with $\boldsymbol{\omega}$ the vorticity vector. The overhat denotes three-dimensional Fourier transform – specified further in Equation (9) – from now on, and ν is the kinematic viscosity.

In classical SLT, this equation is linearized around a simple incompressible mean, or base, flow, with space-uniform velocity gradients A_{ij}, with $A_{ii} = 0$, so that u_i must be replaced by $u_i + A_{ij}x_j$ in the basic equation. We consider in addition that the flow is seen in a rotating frame with angular velocity $\boldsymbol{\Omega}$. Accordingly, our basic dynamical equation is now

$$\dot{\hat{\boldsymbol{u}}} + \nu k^2 \hat{\boldsymbol{u}} + \mathbf{M}\hat{\boldsymbol{u}} + \mathbf{P}\overbrace{[(2\boldsymbol{\Omega} + \boldsymbol{\omega}) \times \boldsymbol{u}]}^{\text{Fourier T.}} = 0, \tag{4}$$

keeping the complete nonlinear contribution – which is neglected in SLT – so that linear and nonlinear contributions are exactly accounted for in a separate way. In agreement with spectral linear theory (SLT), the overdot denotes time-derivation following the characteristic lines given by the eikonal equation

$$\dot{k}_i + A_{ji}k_j = 0, \tag{5}$$

so that the wavevector is considered as time dependent. This is equivalent to follow the mean flow trajectories in physical space, given by

$$\dot{x}_i - \underbrace{A_{ij}x_i}_{\langle U_i \rangle} = 0. \tag{6}$$

As for the nonlinear term, use of a projection operator allows to account for the pressure term, which is slaved to the solenoidal constraint. Accordingly, the linear term generated by the effect of the mean flow, via $\mathbf{A}$ is exact and reduces to a matrix $\mathbf{M}$ which depends only on $\mathbf{A}$ and on the direction of the wavevector, as

$$M_{ij} = \left(\delta_{in} - 2\frac{k_i k_n}{k^2}\right) A_{nj}. \tag{7}$$

2.2. *Second-order statistics, description and dynamics*

We will now consider the most general two-point and single-point second-order statistics. All this information derives in physical space from the correlation tensor

$$R_{ij}(\boldsymbol{r}) = \langle u_i(\boldsymbol{x}) u_j(\boldsymbol{x} + \boldsymbol{r}) \rangle, \tag{8}$$

which only depends on the separation vector $\boldsymbol{r}$ assuming statistical homogeneity. The brackets mean statistical averaging over a very large number of realizations from now on.

The 3D Fourier transform of (8) gives the second-order spectral tensor

$$\hat{R}_{ij}(\boldsymbol{k}) = \frac{1}{(2\pi)^3} \iiint_{-\infty}^{\infty} R_{ij}(\boldsymbol{r}) \exp(-\imath \boldsymbol{k}\cdot\boldsymbol{r}) d^3\boldsymbol{r}. \tag{9}$$

Of course, the same information is included in $\mathbf{R}$ and $\hat{\mathbf{R}}$, but the latter presents a simpler structure due to the algebraic form of the divergence-free constraint in 3D Fourier space. Using the reduced rank of the velocity vector in Fourier space, the spectral tensor is shown to be rank-2 using

$$\langle \hat{u}_i^*(\boldsymbol{p}) \hat{u}_j(\boldsymbol{k}) \rangle = \hat{R}_{ij}(\boldsymbol{k}) \delta^3(\boldsymbol{k} - \boldsymbol{p}), \tag{10}$$

and $k_i \hat{u}_i(\boldsymbol{k}) = 0$.

From the most general definition of the spectral tensor, Hermitian definite-positive, with $k_i \hat{R}_{ij} = \hat{R}_{ij} k_j = 0$ (incompressibility from $k_i \hat{u}_i = 0$), is found its explicit rank-2 form:

$$\hat{\mathbf{R}} = \begin{pmatrix} e - \Re Z & \Im Z + \imath \mathcal{H} & 0 \\ \Im Z - \imath \mathcal{H} & e + \Re Z & 0 \\ 0 & 0 & 0 \end{pmatrix}. \tag{11}$$

This expression is found in the orthonormal Craya-Herring frame of reference $(\boldsymbol{e}^{(1)}, \boldsymbol{e}^{(2)}, \boldsymbol{e}^{(3)})$ [6,8], so that the third line and the third column correspond to the direction of $\boldsymbol{k}$, along $\boldsymbol{e}^{(3)} = \boldsymbol{k}/k$. The reduced nonzero contribution in the plane normal to $\boldsymbol{k}$ is generated by four real scalar terms, the 3D spectrum of energy $e(\boldsymbol{k}) = (1/2)\hat{R}_{ii}$, depending on the full vector $\boldsymbol{k}$ in arbitrary anisotropic flow, the 3D helicity spectrum $k\mathcal{H}(\boldsymbol{k}) = \imath k_n \epsilon_{nij} \hat{R}_{ij}$, and the polarization term $Z = (1/2)\hat{R}_{ij} N_i^* N_j^*$. This last term is complex-valued, with $\Re$ and $\Im$ denoting real and imaginary parts, and appears in a more intrinsic form using the frame of helical modes ($\boldsymbol{N} = \boldsymbol{e}^{(2)} - \imath \boldsymbol{e}^{(1)}$, $\boldsymbol{N}^* = \boldsymbol{e}^{(2)} + \imath \boldsymbol{e}^{(1)}$, $\boldsymbol{e}^{(3)}$)^2 derived from the Craya-Herring frame [6, 9, 10]. It is clear that its modulus $\mid Z \mid$ is invariant to any change of orthonormal frame of reference, as e and $\mathcal{H}$ are.

The exact splitting of the spectral tensor in terms of four contributions, a purely isotropic one (iso), a contribution from directional anisotropy (dir), a contribution from polarization anisotropy (pol), and a contribution from helicity (hel) comes from a trace-deviator decomposition but restricted to the plane normal to $\boldsymbol{k}$, so that

$$\hat{R}_{ij} = \underbrace{\frac{E(k)}{4\pi k^2} P_{ij}(\boldsymbol{k})}_{\hat{\mathbf{R}}^{(iso)}} + \underbrace{\left(e(\boldsymbol{k}) - \frac{E(k)}{4\pi k^2} \right) P_{ij}(\boldsymbol{k})}_{\hat{\mathbf{R}}^{(dir)}} + \underbrace{\Re\left(Z(\boldsymbol{k}) N_i(\boldsymbol{k}) N_j(\boldsymbol{k}) \right)}_{\hat{\mathbf{R}}^{(pol)}} + \underbrace{\imath \epsilon_{ijn} \frac{k_n}{k} \mathcal{H}(\boldsymbol{k})}_{\hat{\mathbf{R}}^{(hel)}}. \tag{12}$$

Without looking at the detail of the helical base, the decomposition is completely intrinsic with $\hat{R}_{ij}^{(iso)} + \hat{R}_{ij}^{(dir)} = (1/2)\hat{R}_{nn} P_{ij}$, $\hat{R}_{ij}^{(pol)} = \Re(\hat{R}_{ij} - (1/2)\hat{R}_{nn} P_{ij})$ and $\hat{R}_{ij}^{(hel)} = \imath \Im(\hat{R}_{ij} - (1/2)\hat{R}_{nn} P_{ij})$, using the projection operator $P_{ij} = \delta_{ij} - k_i k_j / k^2 = \Re(N_i^* N_j)$. This above decomposition is reflected in any two-point, in physical and in Fourier space, or single-point statistical descriptor.

Time dependence was not specified in the first part of this section. It is now reintroduced for looking at the dynamics. The general dynamical equation for $\hat{\mathbf{R}}$ derives from (4), using (10), as

$$\dot{\hat{R}}_{ij}(\boldsymbol{k},t) + 2\nu k^2 \hat{R}_{ij}(\boldsymbol{k},t) + M_{in}(\boldsymbol{k})\hat{R}_{nj}(\boldsymbol{k},t) + M_{jn}(\boldsymbol{k})\hat{R}_{in}(\boldsymbol{k},t) = T_{ij}(\boldsymbol{k},t). \tag{13}$$

The structure of the left-hand-side rigorously derives from SLT, linear with respect to $\hat{\mathbf{R}}$, whereas the right-hand side gathers the contribution from triple correlations mediated by nonlinearity, with implicit nonlinear redistribution terms by pressure. Details on T_{ij} are not given here (see, e.g. [9]), but its structure is discussed firstly in Section 2.4. Competition between purely linear terms and transfer terms is possible. From the reduced form of $\hat{\mathbf{R}}$ in (11), it is clear that the former equation can be replaced by a set of three equations for $(e, Z, \mathcal{H})$ without lack of information, for instance:

$$\dot{e} + 2\nu k^2 e + \underbrace{\frac{\dot{k}}{k}e + \Re\left([\boldsymbol{N}\cdot\mathbf{A}\cdot\boldsymbol{N}]\,Z\right)}_{\text{exact linear part from e and Z}} = T^{(e)} \tag{14}$$

Complete equations for the full set $(e, Z, \mathcal{H})$ are derived and discussed in [11], with exact linear terms on the left-hand-side, coming from SLT, and with third-order contributions $T^{e,Z,H}$ in the right-hand-side, as general transfer terms derived from Equation (17).

2.3. *Turbulence and interactions, additional coupled fields*

As typical examples, we first consider a fluctuating buoyancy term b in stratified turbulence, as an active scalar. In addition to the four scalar real spectra that describe the two-point second-order statistics, in (11) or in (12), the scalar spectrum of buoyancy variance must be added, together with two co-spectra related to toroidal and poloidal buoyancy fluxes [12]. In both stable and unstable stratification (the latter considered in Section 4.1), we can consider additional simplification due to axisymmetry with mirror symmetry, as the simplest symmetry consistent with dynamical equations. In this case, the toroidal- poloidal cross spectrum (or the imaginary part of Z, which generates the *stropholysis* term coined by [13]), the helicity spectrum and the spectrum of toroidal buoyancy flux identically vanish.

Another case of active vector is the fluctuating magnetic field in MHD. The set of basic spectra describing two-point second order statistics result to 10 in the most general anisotropic case, assuming only homogeneity and incompressibility [14].

2.4. *The role of cubic correlations in the dynamics of two-point second-order statistics, from isotropy to anisotropy*

In conventional isotropic turbulence, it is clear that all information for two-point and single-point second-order statistics is given by the energy spectrum $E(k)$. It is well known that very different types of velocity realizations can have the same spectrum. For instance, a realistic 'turbulent' realization, with tube-like vortex structures, e.g. [15], is turned into an unstructured one, by multiplying the individual velocity Fourier modes by uncorrelated phases, or

$$\hat{\boldsymbol{u}}(\boldsymbol{k}) \to \hat{\boldsymbol{u}}(\boldsymbol{k})e^{\imath\phi_k}. \tag{15}$$

Of course, the realistic turbulent field and the 'phase-randomized' one have the same energy spectrum, according to (10) and (12) (first term).

From a dynamical viewpoint, the role of the nonlinear spectral transfer term in creating, or restoring, phase coherence, is essential, from the basic Lin equation

$$\frac{\partial E}{\partial t} + 2\nu k^2 E = T. \tag{16}$$

$T(k,t)$ is mediated by cubic velocity correlations and reflects the cascade process ($T = (1/2)T_{ii}$ in (4).) Accordingly, the transfer term results from spherically averaging a contribution from $\langle \hat{u}_i(\boldsymbol{k})\widehat{\omega}_n(\boldsymbol{p})\hat{u}_m(\boldsymbol{q})\rangle$, with $\boldsymbol{k}+\boldsymbol{p}+\boldsymbol{q}=0$ using the expression of the Fourier transform of the Lamb vector in (3) as a convolution product. The third-order triadic tensor $S_{imn}(\boldsymbol{k},\boldsymbol{p},t)$ resulting from

$$\langle \hat{u}_i(\boldsymbol{k})\hat{u}_m(\boldsymbol{p})\hat{u}_n(\boldsymbol{q})\rangle = S_{imn}(\boldsymbol{k},\boldsymbol{p})\delta^3(\boldsymbol{k}+\boldsymbol{p}+\boldsymbol{q}), \tag{17}$$

is eventually called in to play in the integrand of $T(k)$, using the velocity Fourier modes only, via $\widehat{\boldsymbol{\omega}}(\boldsymbol{k}) = \imath\boldsymbol{k}\times\hat{\boldsymbol{u}}(\boldsymbol{k})$.

In pseudo-spectral DNS, for decaying isotropic turbulence, conventional initialization prescribes a narrow-band energy spectrum, and the initial velocity realization is not skewed, as for a Gaussian distribution, and contains no structure. A realistic velocity field with tube-like vortex structures, however, can emerge via nonlinear evolution. This evolution is consistent with creation of inertial spectrum and spectral transfer for a skewed velocity field. This behaviour is obtained by directly solving the Lin Equation (16), with $T(k,t)$ given by a robust *triadic* closure, e.g. EDQNM-type [16]. In contrast with DNS, EDQNM has no limitation in term of Reynolds number, allowing recent results on finite-Reynolds number effects [17] and prediction of two-point and single-point skewness factors.

In simple engineering modelling, however, the structure and dynamics of three-point third-order correlations do not need to be known. This is obvious in decaying isotropic turbulence, in which the basic $\mathcal{K}-\varepsilon$ model reproduces the temporal decay of kinetic energy $\mathcal{K}$ as t^{-n}. This implies that the specific closure of the dissipation ε equation does not depend of the accurate budget given by the Lin equation, or ([18])

$$\frac{d\varepsilon}{dt} = 2\nu\int_0^\infty k^2 T(k,t)dk - (2\nu)^2\int_0^\infty k^4 E(k,t)dk \sim -\frac{n+1}{n}\frac{\varepsilon^2}{\mathcal{K}}. \tag{18}$$

One should recall that the first contribution to the variation of ε is positive, with the integral giving the nonlinear vortex stretching $\langle u_{i,j}\omega_i\omega_j\rangle$ term, whereas the second is negative and corresponds to the explicit linear 'dissipation of dissipation' term. As another useful balance equation, looking at two-point correlations, the 4/5 Kolmogorov law for the third-order structure function $S_3(r)$, or

$$S_3(r) = -\frac{4}{5}\varepsilon r,$$

is asymptotically found from the Kármán-Howarth equation, or from the Lin equation, without knowing all details on $S_{imn}(\boldsymbol{k},\boldsymbol{p},t)$ in (17) generating $T(k)$.

Due to anisotropy, things are completely different in our three examples, rotating, QSMHD, and unstable stratification, as investigated in the following. Because the interplay

with linear terms – other than the purely viscous one in isotropic turbulence – and nonlinear terms is important, we will organise this investigation around the following systematic study:

- to display the key anisotropic parameter of the linear term from basic equations such as (4),
- to investigate its role using generalized Lin equations for two-point second-order statistics, as (14),
- to investigate its role in equations governing three-point third-order statistics, if needed,
- to look at consequences on simple modelling.

3. Rotation and QSMHD

3.1. *Purely rotating, homogeneous anisotropic turbulence*

Replacing $\boldsymbol{\omega}$ by the absolute vorticity $\boldsymbol{\omega} + 2\boldsymbol{\Omega}$ in Equation (3), or discarding $\boldsymbol{A}$ terms in (4), it is found that the solenoidal projection of the Coriolis force, $\mathbf{P}(2\boldsymbol{\Omega} \times \hat{\boldsymbol{u}})$, amounts to modulate the effective angular velocity by the following angular – angle-dependent in Fourier space – parameter:

$$2\boldsymbol{\Omega}\cdot\frac{\boldsymbol{k}}{k}\times\hat{\boldsymbol{u}}.$$

This modified rotation frequency is similar to the Coriolis parameter on the surface of a rotating sphere, and also gives the dispersion frequency of inertial waves Equation (1).

Looking at generalized Lin equations, it is shown that the angle dependence in $\cos\theta_k$ is not present in the e-equation, which is not explicitly altered by system rotation:

$$\left(\frac{\partial}{\partial t} + 2\nu k^2\right) e(\boldsymbol{k}, t) = T^{(e)}(\boldsymbol{k}, t). \tag{19}$$

It is only present in the Z-equation, as

$$\left(\frac{\partial}{\partial t} + 2\nu k^2 + 4t\,\Omega\cos\theta_k\right) Z(\boldsymbol{k}, t) = T^{(Z)}(\boldsymbol{k}, t), \tag{20}$$

(e.g. [9], the third equation for the helicity spectrum is not discussed here.) Spherically averaging the angle-dependent Lin Equation (19), one recovers the isotropised basic Equation (16). Accordingly, the effect of rotation cannot be explicitly found in this equation, nor in the equivalent scalar Kármán-Howarth equation for second-order two-point correlations in physical space. This only reflects that the Coriolis force produces no energy. Accordingly, the effect of rotation is hidden in the nonlinear transfer terms mediated by cubic velocity correlations, $T^{(e)}$ in the scalar Equation (19), with complementary effects in (20); the theoretical study of the effect of rotation, at least in homogeneous turbulence, ought to be started with the investigation of the dynamics of triple correlations in the rotating frame. In addition, in order to conserve the exact separation between linear and nonlinear effects due to the solenoidal projection, we ought to work with these third-order correlations at three point. This involves the third-order tensor in Equation (17), whose dynamics in a rotating frame is the base of all theoretical studies, including wave turbulence theory and triadic closures, from [9] to the most recent overview in [11].

We will not go back to this statistical approach here, but identify the main points from the sole analysis of the basic equations for the fluctuating velocity. Phase coherence is essential in rapidly rotating turbulence, which reduces to *inertial wave turbulence* at low Rossby number. Because the basis of the helical modes is convenient for both the rotating (they are eigenmodes of the linear regime) and the nonrotating case (they diagonalize the Curl operator), the velocity field in Fourier space is expressed as

$$\hat{\boldsymbol{u}}(\boldsymbol{k},t) = a_+(\boldsymbol{k},t)e^{2\imath\Omega\cos\theta_k t}\boldsymbol{N}(\boldsymbol{k}) + a_-(\boldsymbol{k},t)e^{-2\imath\Omega\cos\theta_k t}\boldsymbol{N}^*(\boldsymbol{k}), \tag{21}$$

which displays the above mentioned dispersion law of inertial waves.

The linear regime of inertial waves is immediately recovered in replacing the *slow amplitudes* a_s, $s = \pm 1$[3] by constant terms, related to initial data at $t = 0$. The regime of weak nonlinearity for wave turbulence theory corresponds to a multiscale time separation between *rapid* phases and *slow* amplitudes, leading to $a_s(\boldsymbol{k},t) \to a_s(\boldsymbol{k},\epsilon t)$ with ϵ really a small parameter of the order of the Rossby number. On the other hand, if nothing is specified on the time dependency of a_s in (21), arbitrary nonlinearity, and arbitrary Rossby number from 0 to infinite (no rotation) can be accommodated: One can define from (21) only the most convenient set of variables, a_s, $s = \pm 1$ to study rotating turbulence.

Substituting (21) into (3) (with $\boldsymbol{\omega} \to \boldsymbol{\omega} + 2\boldsymbol{\Omega}$), an exact, purely nonlinear equation for a_s is derived as

$$\left(\frac{\partial}{\partial t} + \nu k^2\right) a_s(\boldsymbol{k},t) = \sum_{s',s''=\pm 1} \iint\!\!\int_{\boldsymbol{k}+\boldsymbol{p}+\boldsymbol{q}=0} \exp\left(2\imath\Omega t\left(s\cos\theta_k + s'\cos\theta_p + s''\cos\theta_q\right)\right)$$
$$\times M_{ss's''}(\boldsymbol{k},\boldsymbol{p}) a^*_{s'}(\boldsymbol{p},t) a^*_{s''}(\boldsymbol{q},t) d^3\boldsymbol{p} \tag{22}$$

with $s = \pm 1$. Without rotation, $\Omega = 0$, the typical triadic phase term in the exponential is zero, and one recovers the alternative of basic Navier-Stokes equations using helical Fourier modes, with the purely geometric triadic factor $M_{ss's''}$ specified in [9], [10] and [6]. In the presence of rotation, the classical triadic interaction is weighted by the exponential term, often referred to as the resonance operator.

We have now all the basic formalism to discuss the role of coherent phases in homogeneous rotating turbulence, as follows.

3.1.1. *Discussion, application to modelling*

(1) *The cascade in rotating turbulence.* If the viscosity is set to zero in Equation (22), the system becomes of course energy conserving and also keeps the volume in phase space because of the Liouville's property $\sum_{s,\boldsymbol{k}} \frac{\partial \dot{a}_s(\boldsymbol{k},t)}{\partial a_s(\boldsymbol{k},t)} = 0$. These characteristics make possible the use of statistical mechanics tools and lead to the conclusion that the truncated system (keeping only wave numbers smaller than a finite limit) of Euler equations should converge towards a thermal equilibrium with equipartition of energy as first shown by [19]. This is well observed numerically in [20]. In particular, the final state should be completely isotropic despite the anisotropic phase mixing term in (22). However, the anisotropic structure of the phase term breaks the isotropy of the system if initially stated during the transient regimes. Therefore, anisotropy would persist only because of the sink of energy created by the viscous effects. Of course, the

same explanation holds for the existence of an energy cascade in HIT, without rotation, but we are faced now with an anisotropic cascade.

(2) *Nature of the cascade.* Reintroducing a finite dissipation, even weak and in the limit of vanishing ν, the first effect of rotation is to damp the nonlinearities in general, via the phase term in Equation (22). Although significant nonlinearities can survive at small Ωt, at very large Ωt they are strongly reduced by *phase-mixing*[4]. Eventually, (small) nonlinearities survive due to *the resonant triads*, those for which the phase is almost zero in the exponential term. As a consequence, the interscale energy transfer $T^{(e)}$ in (19) is diminished in average, as the triadic phase term does in (22), resulting in a reduced dissipation rate of energy (see [21] for example).
An angle-dependent energy spectrum is dynamically created, but slaved to the spectral transfer term. Anisotropic shape of the energy spectrum, $e(k, k_\parallel/k)$ or $e(k_\parallel, k_\perp)$, is consistent with axisymmetry without mirror symmetry, and compatible with an incomplete, or saturated, two-dimensionalization.

(3) How these effects can be incorporated in simple statistical modelling? Setting aside the linear term in the Z Equation (20), which can explain the purely linear alteration of initial anisotropy by rotation, the breaking of isotropy is mediated by the triadic phase term $\exp(2\imath\,\Omega t(\pm\cos\theta_k \pm \cos\theta_p \pm \cos\theta_q))$, which appears in the equation governing three-point third-order statistics – exactly as it appears in (22). Accordingly, there is little hope to account for its role, even roughly in simple models from $\mathcal{K}-\varepsilon$ to modified Kárman-Howarth equations. The effect of rotation, however, should explicitly alter the first term in Equation (18), as it dramatically alters the 4/5 Kolmogorov law [11].

In spite of a significant anisotropy consistent with a partial transition from 3D to 2D structure, complete two-dimensionalization with inverse cascade by the sole effect of the Coriolis force remains an open problem in decaying homogeneous turbulence. On the other hand, complete two-dimensionalization can be achieved in quasi-static magnetohydrodynamics (QSMHD), and new insights are found contrasting homogeneous rotating turbulence and homogeneous QSMHD.

3.2. *Quasi-static MHD : a toy model with linear forcing of two-dimensional structure*

The QSMHD case is sufficiently simple to be disconnected from the complex coupling of Navier-Stokes and induction equation for the magnetic field, present in MHD. At very small magnetic Prandtl number, e.g. in a liquid metal, under strong external magnetic field, Alfvén waves are inhibited, and the fluctuating magnetic field is slaved to the velocity field in such a way that it can be removed from consideration.

The basic equation replacing (4), and replacing the one in a rotating frame is (see [25] for its derivation)

$$\left(\frac{\partial}{\partial t}+\nu k^2\right)\hat{\boldsymbol{u}}+M_0^2\cos^2\theta_k\hat{\boldsymbol{u}}+\mathbf{P}\widehat{\boldsymbol{\omega}\times\boldsymbol{u}}=0. \tag{23}$$

Only recall that M_0 is proportional to the magnitude of an external uniform magnetic field, which give the axial (or vertical) direction. The typical linear term $M_0^2\cos^2\theta_k\hat{\boldsymbol{u}}$ results from the solenoidal projection of the simplified (QS) Lorentz force. Equation (23) will be

considered from now on as a basic Navier-Stokes equation with additional *linear term, leading to force two-dimensional structure*.

Starting from isotropic turbulence, in which all directions of the wavevector are populated with the same density of energy, the linear term will selectively damp velocity contributions with inclined wavevectors, so that it will tend to concentrate the spectral density of turbulent kinetic energy towards purely transverse wavevectors $k_\parallel \sim 0$. Of course, $k_\parallel = 0$ characterizes the two-dimensional manifold, or the contribution of modes in which the axial variability $\partial/\partial x_\parallel$ is removed by integration in physical space. The fully nonlinear equations are consistent with axisymmetry with mirror symmetry, so that all two-point second-order statistics derive from the previously mentioned energy spectrum $e(k_\parallel, k_\perp, t)$ and from its polarization term $Z(k_\parallel, k_\perp, t)$. Governing equations derive from (23) as

$$\left(\frac{\partial}{\partial t} + 2\nu k^2 + 2M_0^2 \cos^2\theta_k\right) e(\boldsymbol{k}, t) = T^{(e)}(\boldsymbol{k}, t), \tag{24}$$

and

$$\left(\frac{\partial}{\partial t} + 2\nu k^2 + 2M_0^2 \cos^2\theta_k\right) Z(\boldsymbol{k}, t) = T^{(Z)}(\boldsymbol{k}, t). \tag{25}$$

In this case, because of the mirror symmetry, the complex-valued polarization term Z is real, and e and Z are given by the sum and the difference, respectively, of the two eigenvalues, s_1^2 and s_2^2 of the spectral tensor $\hat{\mathbf{R}}$. These eigenvalues correspond also to toroidal and poloidal energy spectra, considered in Section 4.1.

Pseudo-spectral DNS were used for solving Equation (23), with axisymmetry used for evaluating directly e and Z, by averaging on sectors in Fourier space around both k and its polar angle with respect to the axial direction, or $\cos\theta_k = k_\perp/k$: This gives simultaneously the ring-to-ring and shell-to-shell spectral distribution, as shown in Figure 1. The same information was obtained by directly solving Equations (24) and (25), in which $T^{(e)}$ and $T^{(z)}$ are closed by a dedicated, fully axisymmetric, EDQNM−2 model (see also Figure 1). All statistical quantity, two-point as well as single-point, is derived from this information. Details of both approaches, with cross-fertilization, are given in [24]. In addition, the anisotropic structure, which is reflected statistically on Figure 1, is visualized in Figure 2.

3.2.1. *Inviscid SLT regime*

This regime is well known since the pioneering study of Keith Moffatt (1977) [25]. Exponentially growing anisotropic structure is found from the linear – with $T^{(e,Z)} = 0$ – solution of (24,25). All related second-order statistics are analytically derived, combining algebraic and Erf functions.

Three-dimensional isotropic initial data are given by $e = E(k, 0)/(4\pi k^2)$ and $Z = 0$. Z remains zero, whereas e concentrates towards its 2D limit, or

$$e(k_\perp, k_\parallel) = \frac{E(k, t=\infty)}{2\pi k}\delta(k_\parallel),\ Z = 0.$$

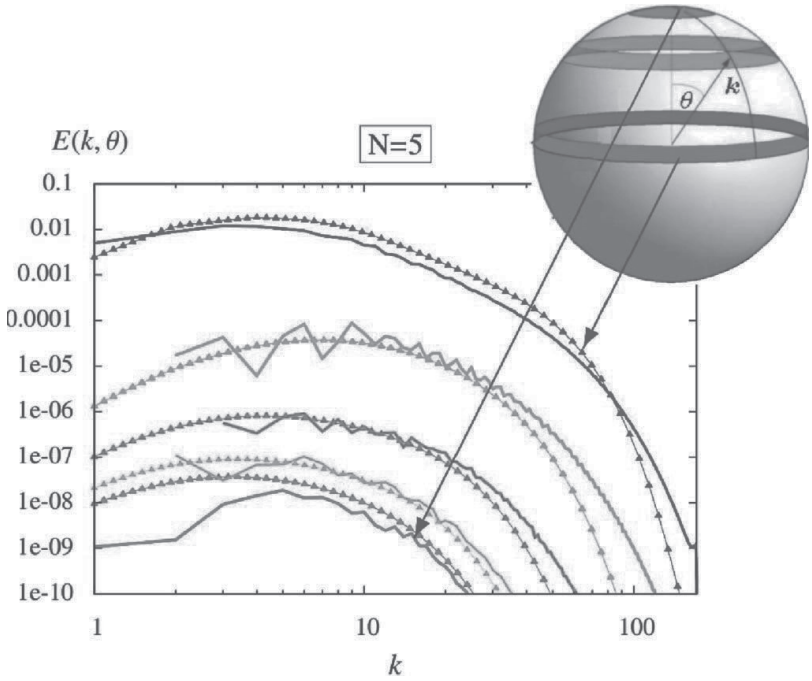


Figure 1. Angle-dependent energy spectra, DNS (full lines) and EDQNM$_2$ (dots). 5 angles θ_k in Fourier space are chosen from 0 (pole) to $\pi/2$ (equator), with a constant step ($\pi/10$.) Adapted from [24] by Alexandre Delache. Reproduced with permission (in progress) of Cambridge University Press.

Typical asymptotic anisotropic ratios are found for the Reynolds stress tensor and the vorticity tensor as

$$\frac{\langle u_\parallel^2 \rangle}{\langle u_\perp^2 \rangle} = 2, \quad \frac{\langle \omega_\parallel^2 \rangle}{\langle \omega_\perp^2 \rangle} = 2.$$

At least the first result is counter-intuitive. Initially, the Reynolds stress is spherical (3D isotropic), with $\frac{\langle u_\parallel^2 \rangle}{\langle u_\perp^2 \rangle} = 1$, and this ratio increases monotonically from 1 to 2. The explanation

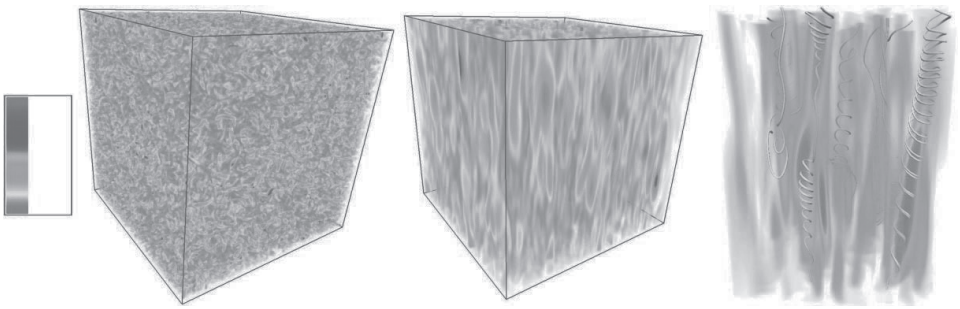


Figure 2. Volume rendering of the enstrophy using VAPOR. From left to right: Initial isotropic condition, Final state for $R_B \sim M_0^2(L/u') = 5$, zoom of the latter picture with streamlines in white. First DNS results for QSMHD, unpublished.

comes from the divergence-free constraint, which means orthogonality of the Fourier mode and the wavevector. Accordingly, a relative depletion of energy around axial wavevectors means a depletion of energy in the transverse direction. More physically, a 2D-3C (two-dimensional, three-component) state is reached, so that 2D – i.e. without axial variability – are favoured, but they consist of both vortical structures – with vertical vorticity and no vertical velocity – and 'jettal' structures, with only vertical, up-and-down, velocity (and horizontal vorticity). Accordingly, $e - Z$ at $k_\parallel = 0$ quantifies vortical 2D structures, whereas $e + Z$ at $k_\parallel = 0$ quantifies jettal 2D structures. Other statistical indicators are the integral length scales with axial separation, related to either axial velocity components $L_\parallel^{(\parallel)}$ or to transverse velocity components $L_\perp^{(\parallel)}$.

3.2.2. *The nonlinear regime in a subsequent step*

Some characteristics of the linear regime are qualitatively present, but the new element is the rise of polarization near the two-dimensional manifold, due to a very specific behaviour of $T^{(e)}$ and $T^{(z)}$ in (24,25). In short, energy is concentrated near the 2D manifold, in a first phase where the linear effect is dominant. After this first phase, the linear term becomes less and less active, because it is zero at $k_\parallel = 0$, and the nonlinear dynamics is essential. This nonlinear dynamics is very close to a 2D-2C cascade for the transverse mode $e - Z$, cascade mediated by $T^{(e)} - T^{(z)}$, with a conventional inverse cascade for energy with reduced dissipation. On the other hand, the mode $e + Z$ for 'jettal axial energy' behaves as the spectrum of a passive scalar transported by 2D-2C turbulence: Direct cascade and eventual dissipation. All our results from DNS and axisymmetric EDQNM are consistent for confirming this scenario, which is reflected on all derived statistical indicators: The RST (Reynolds Stress Tensor) ratio $\frac{\langle u_\parallel^2 \rangle}{\langle u_\perp^2 \rangle}$ begins to increase (linear phase) but eventually decreases after a maximum towards a zero value (nonlinear polarization with selected damping of 'jettal' 2D energy). Instead of the Reynolds stress tensor, the 2D energy components, $2\langle u_\perp^2 \rangle L_\perp^{(\parallel)}$ and $\langle u_\parallel^2 \rangle L_\parallel^{(\parallel)}$ are precise indicators of the polarization near the 2D manifold. Their difference is zero in the linear regime, so that its significant value means a large polarization induced by nonlinearity.

3.2.3. *Application to modelling*

The angular parameter immediately derives from (24), and yields the equation for the turbulent kinetic energy $\mathcal{K}$ as:

$$d\mathcal{K}/dt = -2M_0^2 \cos^2 \gamma_u \mathcal{K} - \varepsilon, \tag{26}$$

in which ε is the conventional dissipation rate due to kinematic viscosity, whereas the typical Ohmic dissipation term displays the *Moreau angle* [26][5] , denoted γ_u, such as

$$\cos^2 \gamma_u = \frac{\iiint \cos^2 \theta_k e(\boldsymbol{k}, t) d^3\boldsymbol{k}}{\iiint e(\boldsymbol{k}, t) d^3\boldsymbol{k}}. \tag{27}$$

This angle is also crucial for the development of the anisotropy of the Reynolds stress tensor. Considering the deviatoric part of the Reynolds stress tensor, it can be split into two

different contributions, reflecting directional anisotropy and polarization anisotropy, or

$$b_{ij} = b_{ij}^{(dir)} + b_{ij}^{(pol)},$$

according to Equation (12), and all components derive from the single one b_{33} in axisymmetric turbulence. Finally, $b_{33}^{(dir)}$ is directly linked to the Moreau angle, as well as to the significant component D_{33} of the 'dimensionality structure tensor' [13] by

$$b_{33}^{(dir)} = \frac{1}{6} - 2\cos^2\gamma_u,\ \cos^2\gamma_u = \frac{D_{33}}{2\mathcal{K}}.$$

As shown in [24], the evolution of γ_u, or equivalently of $b_{33}^{(dir)}$, is given by the linear, SLT, regime, so that DNS runs with different R_B (initial rapidity parameter, product of M_0^2 by a nonlinear turnover time) collapse well with the linear one, in terms of the 'linear' timescale $M_0^2 t$. This is not because the directional anisotropy is purely 'linear', as is the polarization anisotropy purely nonlinear: We have checked that the directional anisotropy is reduced by the nonlinearity, comparing the angular distribution in Figure 2 with the analytical one given by SLT, at the same $M_0^2 t$. Accordingly, it appears that the first nontrivial angular harmonic of the $e(\boldsymbol{k})$-distribution evolves according to SLT, but not the higher-order ones. Even if this suggests to replace $\cos^2\gamma_u$ by its *linear* analytic time-evolution in (26), there is no hope to mimic the whole evolution by a $\mathcal{K}-\varepsilon$ model. When $\cos^2\gamma_u \to 0$, the flow begins to be dominated by two-dimensional and anisotropic (vortical vs. jettal components) dynamics, which cannot be accounted for in the sole conventional ε- equation. Indeed, one can check that the classic procedure, which copies the two terms in $\frac{1}{\varepsilon}\frac{d\varepsilon}{dt}$ from the two terms in $\frac{1}{\mathcal{K}}\frac{d\mathcal{K}}{dt}$, with different tuned constants, so that

$$\frac{d\varepsilon}{dt} = -C_{\epsilon 1} M_0^2 \cos^2\gamma_u \varepsilon - C_{\epsilon 2}\frac{\varepsilon^2}{\mathcal{K}},$$

cannot reproduce a transition towards 2D structure, even in replacing the constants by more sophisticated parameters. Note that in the 2D limit, the first term in Equation (18) vanishes, radically altering the meaning of the term with $C_{\epsilon 2}$.

4. New approach to unstable density-stratification

In the case of density stratification, using Boussinesq approximation, the velocity field remains divergence-free, but a new buoyancy term is present in Equation (4), as

$$\frac{\partial \hat{\boldsymbol{u}}}{\partial t} + \nu k^2 \hat{\boldsymbol{u}} + \mathbf{P}\widehat{\boldsymbol{\omega}\times\boldsymbol{u}} = b\mathbf{P}\boldsymbol{n}. \tag{28}$$

The buoyancy scalar b is proportional to the gravitational acceleration, and to the stratifying agent, density or temperature of the mixed fluids. It is an active scalar, but it is governed by the same equation as a passively advected scalar, in the presence of a mean buoyancy gradient $\frac{d\langle B\rangle_H}{dx_3}$[6], or

$$\frac{\partial \hat{b}}{\partial t} + \nu k^2 \hat{b} + \frac{d\langle B\rangle_H}{dx_3}\hat{u}_3 = -\imath k_i \widehat{u_i b}. \tag{29}$$

The case of uniform, vertical ($\boldsymbol{n} = -\boldsymbol{g}/g, n_i = \delta_{i3}$) mean buoyancy gradient, is considered in the later equation.

4.1. *Homogeneous axisymmetric turbulence driven by a uniform, destabilising, mean density gradient*

Because there is an important buoyancy-driven production of energy, already shown by SLT, the detailed analysis of nonlinear dynamics is less important than in the stable case. Generalized Lin-type equations, however, are still useful in terms of the four spectra: The three kinds of energy density, $e^{(tor)} = e_n^{(1)} \hat{R}_{nm} e_m^{(1)}$, $e^{(pol)} = e_n^{(2)} \hat{R}_{nm} e_m^{(2)}$, $e^{(pot)}$ the spectrum of buoyancy renormalized by $\frac{1}{N^2}$ and F the poloidal buoyancy flux. The equation for the toroidal energy spectrum is the same as in the stable case, with only an implicit buoyancy-driven effect in the nonlinear toroidal energy transfer. The system of equations for the stratified case [12] is modified as

$$\left(\partial_t + 2\nu k^2\right) e^{(tor)} = T^{(tor)}, \tag{30}$$

$$\left(\partial_t + 2\nu k^2\right) e^{(pol)} + 2N \sin\theta_k F = T^{(pol)}, \tag{31}$$

$$\left(\partial_t + 2\nu k^2\right) e^{(pot)} + 2N \sin\theta_k F = T^{(pot)}, \tag{32}$$

$$\left(\partial_t + 2\nu k^2\right) F + N \sin\theta_k \left(e^{(pol)} + e^{(pot)}\right) = T^{(F)}, \tag{33}$$

with $N^2 = |\frac{d\langle B\rangle_H}{dx_3}|$.

SLT for second-order statistics is recovered in the limit of zero spectral transfer terms in the right-hand-side. In this limit, both spectra of poloidal and potential energy are affected by the same exponential growth rate $\exp(2Nt \sin\theta_k)$, so that their difference is only due to possible different initial data. This exponential growth affects the spectrum $F(k, \theta_k)$ of poloidal buoyancy flux as well.

4.2. *Towards turbulent mixing following Rayleigh-Taylor instability*

Extension of the homogeneous case in the above Section 4.1 to a buoyancy-driven mixing zone, which is unsteady and strongly inhomogeneous in one direction, vertical here, is challenging. We will consider the turbulent mixing zone (TMZ) which is initialized by Rayleigh-Taylor instability, when a heavy fluid of density ρ_1 and a lighter fluid of density ρ_2, initially superimposed, mix together by effect of gravity g. If the Atwood number defined as $\mathcal{A} = \frac{\rho_1 - \rho_2}{\rho_1 + \rho_2}$ is small, then it can be assumed that the mean velocity field equals zero. The mean buoyancy term is given by $\langle B\rangle_H = 2\mathcal{A}g\langle C\rangle_H$ where $\langle C\rangle_H$ is the mean concentration profile of light fluid. Similarly, the buoyancy fluctuating term can be expressed by the fluctuating concentration of lighter fluid as $b = 2\mathcal{A}gc$.

On the one hand, equations similar to the ones in (31–33) are relevant because after a rapid transient phase, the thickness of the mixing layer – initially zero – becomes significant, and an average frequency $N(t)$ can be defined, in agreement with a quasi-uniform mean concentration gradient across the mixing layer (justified only for small $\mathcal{A}$).[7] On the other hand, the parameter $N(t)$ cannot be controlled, and remains an internal parameter of the problem.

Following a recent work [28], the Equation (29) for the active scalar b is replaced by a similar equation for c, with the equivalent Brunt-Väisälä frequency, $N(t)$, related as follows

with the mean vertical concentration gradient:

$$N = \left(-2\mathcal{A}g \frac{d\langle C \rangle_H}{dx_3} \right)^{1/2} \text{ with } \frac{d\langle C \rangle_H}{dx_3} = -\beta / L(t). \tag{34}$$

The second part of this equation displays the crucial linkage of the mean vertical concentration gradient, evaluated at the centre of the mixing layer, to the typical thickness length $L(t)$ of the TMZ, via a shape parameter β, specified in [28].

Finally, up to a different scaling and slightly different definition of spectra, Equations (31), (32) and (33) yield an equivalent system in terms of k-averaged spectra, as $\mathcal{E}_{u_3 c}$ given below, so that they eventually depend on t and θ_k. The system of equations governing the TMZ is finally completed by an equation for the evolution of the lengthscale $L(t)$, as

$$\frac{dL}{dt} = \frac{12}{L} \int_0^\pi \mathcal{E}_{u_3 c}(\theta_k) \sin\theta_k d\theta_k, \tag{35}$$

in which $\mathcal{E}_{u_3 c}(\theta_k)$ is proportional to the vertical buoyancy flux $F(k, \theta_k, t) \sin\theta_k$ in Equation (32), integrated over k.

If the transfer terms are neglected in (31,32,33), this leads to what we called *the rapid acceleration model* in [28]. This model does not include nonlinear interactions of the fluctuating flow with itself, but, in contrast with conventional SLT for homogeneous distorted turbulence, the system of equations contains a full coupling between the mean flow (i.e. the evolving $L(t)$) and the fluctuating turbulent quantities. In that sense, this approach is similar to a weakly-non linear quasi-homogeneous method proposed in [29].)

It is possible to show that the above analysis yields to a buoyancy-drag equation under the following form:[8]

$$\ddot{L} = \underbrace{-C_d \frac{\dot{L}^2}{L}}_{\text{drag}} + \underbrace{C_b \mathcal{A} g}_{\text{buoyancy}} \quad . \tag{36}$$

Such Equations, e.g. (36), are commonly used by engineers to evaluate the growth of TMZ. The original idea may be traced back to [30] and has been followed by numerous versions. The drawback, however, is that the two constants of drag and buoyancy for this model are empirical and have to be adjusted. The analysis gives an analytical expression for these coefficients function of the turbulent quantities as follows:

$$C_b = 4 \sin^2\gamma (1 - \Theta), \text{ and } C_d = 2/C_b, \tag{37}$$

where the dimensionality parameter $\sin^2\gamma$ reflects the angle-dependent structure, or directional anisotropy, of the spectrum of concentration variance, also proportional to the spectrum of potential energy, as

$$\sin^2\gamma = \frac{\iiint \sin^2\theta_k e^{(pot)}(\boldsymbol{k}, t) d^3\boldsymbol{k}}{\iiint e^{(pot)}(\boldsymbol{k}, t) d^3\boldsymbol{k}}, \tag{38}$$

and Θ is the global molecular mixing parameter introduced by [31]:

$$\Theta = \frac{\int_{-\infty}^{+\infty} \langle C(1-C)\rangle_H dx_3}{\int_{-\infty}^{+\infty} \langle C\rangle_H (1-\langle C\rangle_H) dx_3}. \tag{39}$$

Note that this parameter is equal to 1 for a perfect mixing in which there is no fluctuation of concentration, or $C = \langle C\rangle_H$; it is equal to zero in the initial stage of the TMZ, which corresponds to a pure interface between the two fluids. In addition, the closure of the coefficient C_d (first proposed by [32]) globally accounts for dissipative effects, fed by nonlinear terms – e.g. the nonlinear transfer terms in the right-hand-sides of Equation (31)–(33) – which are neglected in the basic version of the rapid acceleration model considered above, not to mention dilution effects as the TMZ growths.

This buoyancy-drag equation has no equivalent in the stable case, in which potential and poloidal energy spectra oscillate with opposite phases in the linear regime of gravity waves, so that their sum is conservative. In Rayleigh-Taylor mixing, a fundamental coefficient is the growth rate α of the half-width of the mixing zone [33]. A classical way to define it is by the formula [34]:

$$\alpha = \frac{\dot{L}^2}{8\mathcal{A}gL}. \tag{40}$$

When g is constant, a self-similar regime establishes corresponding to α constant. In this case, the mixing zone evolves as:

$$L(t) = 2\alpha\mathcal{A}gt^2. \tag{41}$$

It is recognized now that the α parameter has non-unique values. Large discrepancies between experiments on numerical simulations has been observed and explained by the influence of initial conditions. In [28], it is shown that the growth parameter is directly linked to the global mixing parameter Θ and the dimensionality parameter $\sin^2\gamma$. Therefore, the angular dependence of the concentration spectra is of great importance as it influences directly the growth of the mixing zone.

The structure of the unsteady mixing layer is visualized on Figure 3, obtained from a high resolution DNS. The dimensionality parameter is directly associated to the large scale vertical structures observed. To confirm this, we show the evolution of α and the radial spectrum of $\sin^2\gamma$ – not integrating over the wavenumber k in Equation (38) – during this simulation on Figure 4. The radial spectrum of the dimensionality parameter is shown, with different elapsed times corresponding to the eventual stabilization of the α parameter, whose evolution from the beginning of the calculation is given at the bottom. The corresponding shape of the radial concentration spectrum is given at the top, during the same time interval.

4.3. *Analogies and differences between the QSMHD and unstably stratified flow*

Analogies and differences between the QSMHD flow case and the TMZ can be discussed as follows.

In both cases, basic SLT suggests the important angle-dependent parameter in Fourier space – hidden variable – which yields a 'Moreau angle' [26], as γ_u in Equation (27)

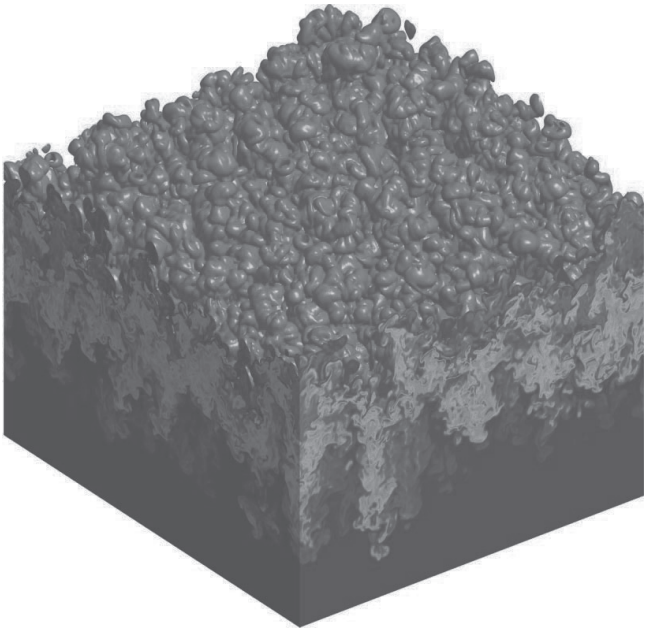


Figure 3. Visualization of the instantaneous mixing layer, by iso-concentration surfaces. DNS from the TRICLADE numerical code.

for the kinetic energy anisotropic distribution in QSMHD, and γ in Equation (27) as its counterpart γ in Equation (38) for the potential energy in TMZ. The latter term is present in the 'buoyancy-drag' Equation (36) for TMZ, and results from the angular dependence of the potential energy spectrum. On the other hand, the Moreau angle can be given by an analytical approximation (derived from SLT) in QSMHD, whereas the situation is much more complex for the TMZ because the parameter $\sin^2\gamma$ results from the whole evolution, with nonlinear coupling between the 'mean' and the 'fluctuating' flow. It is clear that there is no obvious model of time-evolution for it, and that it remains far from its two-dimensional limit ($\sin^2\gamma = 1$, similar to $\sin^2\gamma_u = 1$). Finally, the intrinsic nonlinearity mediated by cubic correlations, and mimicked by the sole parameter C_d in (36), is probably less crucial in TMZ than in QSMHD.

5. Conclusions and perspectives

5.1. *Importance of the orientation parameter(s) in simple modelling*

In spite of its complexity, the study of the TMZ offers a very good example of the importance of the orientation parameter expressing the directionality and derived from basic spectral equations, even in a simple model – buoyancy-drag equation. The analysis of analogies and difference with QSMHD is enlightening. Only the latter case can be understood in anisotropic but strictly homogeneous turbulence, and the challenge is to follow a complete transition from 3D to 2D structure. Elongated structures mainly result from a linear mechanism, with 'production' in the energy equation; this is a production by a violent instability in TMZ, tending to increase the energy and to concentrate it towards the horizontal wave vectors, and a differential smoothing by Ohmic dissipation in QSMHD, decreasing the energy of all Fourier modes with oblique wavevector except for the

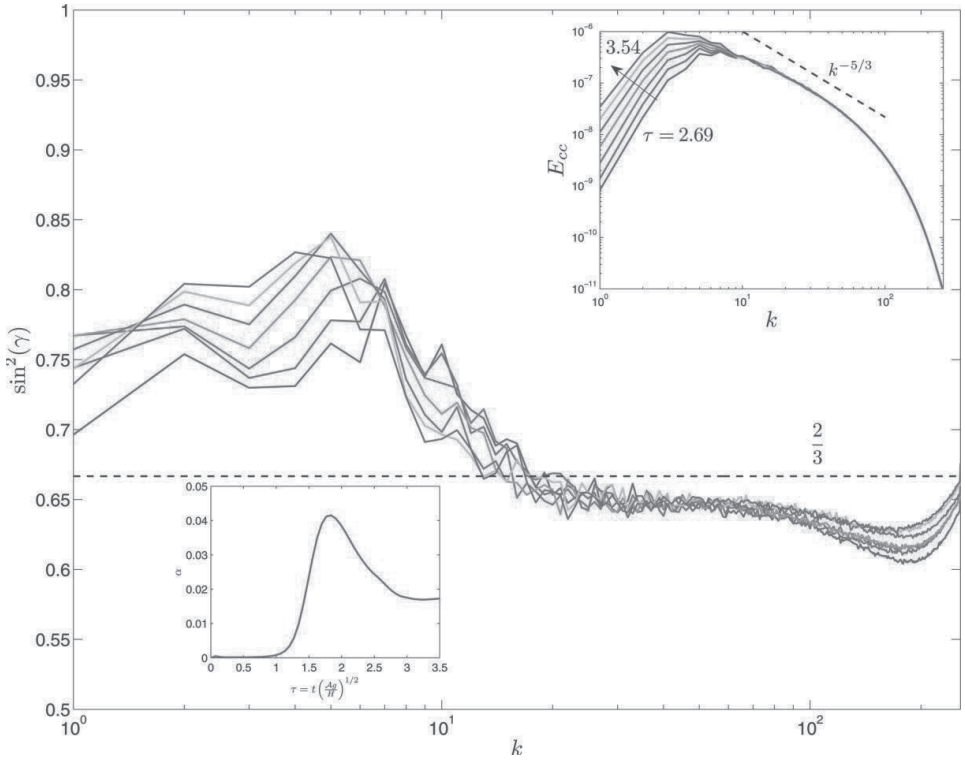


Figure 4. Radial (in k) spectrum of the dimensionality parameter $\sin^2\gamma$; top: Related development of the radial spectrum of the variance of concentration; bottom: Development of the α parameter. H is the horizontal length of the computational domain, with $2H$ in the vertical.

horizontal ones. Both Figures 2 and 3 show elongated structures in the vertical direction: They display the violent mixing of density in Figure 3, and isovorticity, or isovelocity structures, in Figure 2, but elongated structures hold for the poloidal velocity as well in TMZ. More detail on the poloidal/potential energy can be suggested by Equations (32) and (33), and are left to a subsequent study.

The intrinsic nonlinear dynamic, related to the generalized transfer terms in the right-hand-side of (31–33) is less crucial, at least in global models, in TMZ, than in QSMHD, in which the corresponding $T^{(e)}$, $T^{(z)}$ terms in (24,25) completely control the ultimate phase of two-dimensionalization, from 3-component to 2-component structure.

Dynamics completely slaved to third-order correlations is found in rotating turbulence, with a partial transition from 3D to 2D structure much more subtle than in the QSMHD case. This case offers the best example of turbulence without production.

5.2. *Dynamics of third-order correlations and phase coherence*

Phase coherence is essential in the dynamical and structural approach to turbulence. If it is partially lost looking at two-point second-order velocity correlations, but an important contribution is restored at the level of three-point third-order correlations, which quantify the interscale energy cascade. This issue remains relevant for quasi-homogeneous turbulence, working in Fourier space, especially for strongly anisotropic flow cases, such as rotating

turbulence, revisited in this article. Stably-stratified turbulence [12], with conservation of total, kinetic + potential, energy, and MHD Alfvénic turbulence [35,36], with conservation of total, kinetic + magnetic, without mean magnetic field, are other examples 'without production' which might be treated with the same approach. Dynamical creation of phase coherence in third-order three-point correlations is illustrated by sophisticated triadic closures, from isotropic EDQNM to anisotropic one matching wave-turbulence theory, and full DNS. As shown in Figure 1, anisotropic structure is consistently reproduced from DNS and EDQNM$_2$. Generalized EDQNM allows to reach very high Reynolds number and is a very good tool for investigating the inertial range, from isotropic to anisotropic turbulence. Only at largest k, EDQNM seems to systematically overdissipate with respect to DNS. On the other hand, small k are very noisy in DNS, due to the poor angular discretization in Fourier space at smallest k. When spatial averaging is used in DNS, indeed, such as azimuthal averaging in axisymmetric turbulence, one has to be aware of the poor sampling at the lowest wavenumber in classical pseudo-spectral DNS. This suggests to use triadic closures as a reliable model for the infrared range, with a support for a 'supergrid' model instead of a subgrid one.

Information on anisotropy for second and third-order statistics can be directly found in physical space, or using other modes than Fourier modes, as briefly discussed as follows. For instance, the Kármán-Howarth-Monin-type equation is routinely used for getting information on third-order structure function(s) from the equations that govern second-order one. In isotropic turbulence, this equation carries out the same information as the Lin Equation (16) does, but there is no simple equivalent in physical space of the equations governing the deviatoric part of the second-order correlation tensor, as the Z-equations used here. In these anisotropic situations, only the scalar Kármán-Howarth equation is used, which correspond to the e-equation. As a last point, only two-point correlations are investigated using structure functions, whereas triadic closures, for instance, deal with the equation governing the three-point third-order spectral tensor in (17). It seems that the advantage of Fourier space for performing algebraically the solenoidal projection largely balances its drawback of treating the nonlinearity via a convolution product. Beyond Fourier space, the interest of three-point statistics was pointed out by Lumley [37], using POD, in order to overcome the lack of some real phase information in spatial two-point second-order correlations.

Acknowledgements

This article reflects collective work and discussions with Alexandre Delache and Fabien S. Godeferd, partly supported by the French National Research Agency (ANR) under contract number 08-BLAN-0076 'ANISO'. It was improved thanks to referees, particularly one of them who helped us to focus our purpose.

Notes

1. We no longer use RDT nomenclature, for three reasons: (i) if the mean flow characteristics do not depend on space as a constant gradient of density there is no distortion, (ii) 'rapid' for 'linear' is often misleading, (iii) many recent studies based on SLT, especially in stability analysis – e.g. elliptical flows – and/or in astrophysics – e.g. shearing sheet approximation for accretion discs – do not even mention RDT.
2. the vector $\boldsymbol{N}$ should not be confused with the Brunt-Väisälä frequency N.
3. in order to simplify, we write a_s in spite of $a_{sign(s)}$.
4. Accordingly, Equations (21) and (22) help understanding the limit of inertial wave turbulence (see [22] and the recent review of wave turbulence theory by Newell [23]) but here their use is more general, for any Rossby number, and at any time.

5. A similar angle is more popular as the Shebalin angle, in [27], but it is connected to the directional dependence of the enstrophy instead of the energy, with a factor k^2 to be added in the integrand of eq. (27), for instance. We hope to stress the priority of René Moreau, involved in the first experiments of QSMHD in turbulent mercury.
6. $\langle\rangle_H$ refers to the averaging process in the physical space along the horizontal plane perpendicular to $\boldsymbol{n}$.
7. More precisely, a reasonable assumption to simplify the analysis of such flows is to suppose that the characteristic scale of variation for the mean gradient of concentration is much greater than the characteristic vertical scale for the turbulent quantities.
8. In fact, the buoyancy-drag equation appears as a reduction of the rapid acceleration model to its central manifold (see [28] for details).

References

[1] H.K. Moffatt, *Homogeneous turbulence*, in International Colloquium on Fundamental Problems of Turbulence: 50 Years after the Turbulence Colloquium Marseille 1961, CIRM, Marseille, September 26–30, 2011.
[2] R. Schiestel, *Modeling and Simulation of Turbulent Flows*, Wiley & Sons, London, 2007.
[3] R.H. Kraichnan, *The Closure Problem of Turbulence Theory*, Courant Institute of Mathematical Science, New York University, New York, 1961.
[4] S.A. Orszag, *Lectures on the statistical theory of turbulence*, in Summer School of Theoretical Physics, Les Houches, France, July 1973.
[5] A. Craya, Ph.D. diss., P.S.T. Ministere de l Air (Fr), 1958, p. 345.
[6] P. Sagaut & C. Cambon, *Homogeneous Turbulence Dynamics*, Cambridge University Press, New York, 2008.
[7] C. Lamriben, P.P. Cortet, F. Moisy, *Direct measurements of anisotropic energy transfers in a rotating turbulence experiment*, Phys. Rev. Lett. 107(2) (2011), 024503.
[8] J.R. Herring, *Approach of axisymmetric turbulence to isotropy*, Phys. Fluids 17 (1974), p. 859.
[9] C. Cambon and L. Jacquin, *Spectral approach to non-isotropic turbulence subjected to rotation*, J. Fluid Mech. 202 (1989), pp. 295–317.
[10] F. Waleffe, *Inertial transfers in the helical decomposition*, Phys. Fluids A 5 (1993), pp. 677–685.
[11] C. Cambon, L. Danaila, F.S. Godeferd, and J.F. Scott, *Third-order statistics and the dynamics of strongly anisotropic flows*, JoT, same issue, under revision.
[12] F.S. Godeferd and C. Cambon, *Detailed investigation of energy transfers in homogeneous stratified turbulence*, Phys. Fluids 6 (1994), pp. 2084–2100.
[13] S.C. Kassinos, W.C. Reynolds, and M.M. Rogers, *One-point turbulence structure tensors*, J. Fluid Mech. 428 (2001), pp. 213–248.
[14] C. Cambon, F.S. Godeferd, and B. Favier, *Incorporating linear dynamics and strong anisotropy in KS. application to diffusion in rotating, stratified, MHD turbulence, and to aeroacoustics*, in *New Approaches in Modeling Multiphase Flows and Dispersion in Turbulence, Fractal Methods and Synthetic Turbulence* (ERCOFTAC Series 18), 2012, ISBN 978-94-007-2505-8.
[15] Y. Kaneda and T. Ishihara, *Energy dissipation rate and energy spectrum in high resolution direct numerical simulations of turbulence in a periodic box*, Phys. Fluids 15, (2003), p. 21.
[16] S.A. Orszag, *Analytical theories of turbulence*, J. Fluid Mech. 41 (1970), pp. 363–386.
[17] J. Tchoufag, P. Sagaut, and C. Cambon, *Spectral approach to finite Reynolds number effects on Kolmogorov 4/5 law in isotropic turbulence*, Phys. Fluids 24 (2012), 015107.
[18] H. Tennekes and J.L. Lumley, *A First Course in Turbulence*, The MIT Press, Cambridge, MA, 1972.
[19] R. Kraichnan, *Irreversible statistical mechanics of incompressible hydromagnetic turbulence*, Phys. Rev. 109 (1958), p. 1407.
[20] Y. Yamasaki, Y. Kaneda, and R. Rubinstein, *Dynamics of inviscid truncated model of rotating turbulence*, Phys. Rev. 71 (2002), pp. 81–92.
[21] Y. Morinishi, K. Nakabayashi, and S.Q. Ren, *Dynamics of anisotropy on decaying homogeneous turbulence subjected to system rotation*, Phys. Fluids 13(10) (2001), pp. 2912–2923.
[22] F. Bellet, F.S. Godeferd, J.F. Scott, and C. Cambon, *Wave turbulence in rapidly rotating flows*, J. Fluid Mech. 562 (2006), pp. 83–121.
[23] A.C. Newell and B. Rumpf, *Wave turbulence*, Annu. Rev. Fluid Mech. 43 (2011), pp. 59–78.

[24] B. Favier, F.S. Godeferd, C. Cambon, A. Delache, and W.J.T. Bos, *Quasi-static magnetohydrodynamic turbulence at high Reynolds number*, J. Fluid Mech. 681 (2011), pp. 434–461.
[25] H.K. Moffatt, *On the suppression of turbulence by a uniform magnetic field*, J. Fluid Mech. 28 (1967), p. 571.
[26] R. Moreau, *On Magnetohydrodynamic Turbulence*, Proceedings of Symposia on Turbulence of Fluid and Plasma, Polytechnic Institute of Brooklyn, Brooklyn, NY, 1968, pp. 359–372.
[27] J.V. Shebalin, W.H. Matthaeous, and D. Montgomery, *Anisotropy in MHD turbulence due to mean magnetic field*, J. Plasma Phys. 29 (1983), p. 525.
[28] B.-J. Gréa, *The rapid acceleration model and the growth rate of a turbulent mixing zone induced by Rayleigh-Taylor instability*, Phys. Fluids. 25 (2013), to appear.
[29] J.C.R. Hunt and D.J. Carruthers, *Rapid distortion theory and the problems of turbulence*, J. Fluids. Mech, 502 (1990), pp. 233–271.
[30] R.M. Davies and G.I. Taylor, *The mechanics of large bubbles rising through extended liquids and through liquids in tubes*, Proc. R. Soc. A 200 (1950), pp. 375–390.
[31] D.L. Youngs, *Numerical simulation of mixing by Rayleigh-Taylor and Richtmeyer-Meshkov instabilities*, Laser Part. Beams 12 (1994), pp. 725–750.
[32] O. Poujade and M. Peybernes, *Growth rate of Rayleigh-Taylor turbulent mixing layers with the foliation approach*, Phys. Rev. E. 81 (2010), 016316.
[33] D.L. Youngs, *Numerical simulation of turbulent mixing by Rayleigh-Taylor instability*, Physica. D. 12 (1984), pp. 32–44.
[34] J.R. Ristorcelli and T.T. Clark, *Rayleigh-Taylor turbulence: Self-similar analysis and direct numerical simulations*, J. Fluid Mech. 507 (2004), pp. 213–253.
[35] P.S. Iroshnikov, *Turbulence in a conducting fluid in a strong magnetic field*, Sov. Astron. 7 (1964), p. 566.
[36] R. Kraichnan, *Inertial-range spectrum in hydromagnetic turbulence*, Phys. Fluids 8 (1965), p. 1385.
[37] J.L. Lumley, *The structure of inhomogeneous turbulent flows*, in *Atmospheric Turbulence and Radio Wave Propagation*, A.M. Yaglom and V.I. Tatarski, eds., Nauka, Moscow, 1967, p. 166.

Journal of Turbulence
Vol. 13, No. 35, 2012, 1–16

Taylor & Francis
Taylor & Francis Group

On helical multiscale characterization of homogeneous turbulence

Frank G. Jacobitz[a], Kai Schneider[b], Wouter J.T. Bos[c], and Marie Farge[d]

[a]*Mechanical Engineering Program, University of San Diego, San Diego, California, USA;* [b]*M2P2-CNRS & CMI, Aix-Marseille Université, Marseille Cedex 13, France;* [c]*LMFA-CNRS, Ecole Centrale de Lyon, Université de Lyon, Ecully Cedex, France;* [d]*LMD-IPSL-CNRS, Ecole Normale Supérieure, Paris Cedex 5, France*

(*Received 30 November 2011; final version received 28 June 2012*)

The helical properties of five prototypical homogeneous turbulent flows are investigated: statistically steady forced isotropic turbulence, decaying isotropic turbulence, decaying rotating turbulence, growing sheared turbulence, and growing rotating sheared turbulence with a rotation ratio $f/S = +0.5$. The five turbulent flows were originally studied using direct numerical simulations, and well-developed flow fields are chosen for this analysis. For comparison, a solenoidal uncorrelated Gaussian random field is included in the analysis as a sixth case. An orthogonal wavelet decomposition is used to study the scale-dependent properties of the cases. It is found that flows with growing turbulent kinetic energy and turbulent motion at large scales show a maximum in the relative kinetic helicity probability distribution functions (PDFs) at zero, corresponding to a trend to local two-dimensionalization of the flow with vorticity and velocity tending to be perpendicular. Flows with decaying turbulent kinetic energy and turbulent motion at small scales, however, show maxima of the relative kinetic helicity PDFs at plus and minus one, indicating a preference for helical motion with a trend to alignment or anti-alignment of vorticity and velocity. The PDFs of relative super-helicity always assume maxima at plus and minus one for all flows. The helical properties of statistically steady forced isotropic turbulence follow those of flows with decaying turbulent kinetic energy and a small asymmetry in the relative helicity PDFs is observed. Joint PDFs of relative kinetic helicity and relative super-helicity show that the quantities tend to have the same sign for all flows, including the random field, indicating that super-helicity dissipates kinetic helicity.

Keywords: helicity; homogeneous isotropic and anisotropic turbulence; scale-dependent statistics; direct numerical simulation

1. Introduction

The helicity of a solenoidal vector field is a scalar valued signed quantity defined by the scalar product of a vector with the inverse of its curl, i.e., the Biot–Savart integral. For example, the kinetic helicity is defined as $H_u = \boldsymbol{u} \cdot \boldsymbol{\omega}$, where $\boldsymbol{u}$ is the velocity and $\boldsymbol{\omega} = \nabla \times \boldsymbol{u}$ is the vorticity. The mean kinetic helicity, defined as $\langle H_u \rangle = \int H_u d^3x$, was introduced to study turbulence [1]. It was shown to provide a measure for the linkage of vortex lines and it is conserved in the inviscid limit of the Navier–Stokes equations [2–4]. Furthermore, helicity allows to quantify the effects that are due to a lack of reflectional symmetry or chirality. Geometrical and topological effects involving helicity, encountered

*Corresponding author. Email: jacobitz@sandiego.edu

ISSN: 1468-5248 online only
© 2012 Taylor & Francis
http://dx.doi.org/10.1080/14685248.2012.711476
http://www.tandfonline.com

in numerous turbulent flows with a wide spectrum of applications ranging from astro-, geo-, and plasma-physics to classical fluid- and aero-dynamics, can thus be characterized. For a review on helicity, we refer to Moffatt and Tsinober [5].

Helical structures, corresponding to swirling flow, are present in a variety of turbulent flows. In electrically conducting fluids, helical structures are responsible for the alpha effect which amplifies the magnetic field by the so-called dynamo action [6–8]. In the atmosphere, tornadoes and hurricanes are characterized by strong swirling motion. Helicity plots are used in meteorology to identify such strong storms and to forecast their genesis [9, 10]. Helicity is necessary to maintain strong localized atmospheric vortical structures [11]. Magnetic helicity plays a key role for the magnetic confinement of the plasma in thermonuclear fusion devices, such as tokamaks. Swirling motion, e.g., streamwise vortices in boundary layers, leading and trailing edge vortices shed from wings, can be frequently observed in aerodynamics [12].

Normalizing helicity by the norms of the corresponding vectors yields the relative helicity that corresponds to the cosine of the angle between both vectors. For the relative kinetic helicity, we thus have $h_u = H_u/(|\boldsymbol{u}||\boldsymbol{\omega}|)$. Helical structures are characterized by alignment or anti-alignment of velocity and vorticity vectors, which implies $h_u = \pm 1$. Prototypical examples for flows with maximal helicity are Beltrami flows, i.e., flows for which the velocity field is an eigenvector of the curl operator. Maximum helicity, the perfect alignment of velocity and vorticity, results in a local depletion of the nonlinear term in the Navier–Stokes equation [13, 14], which is known as local flow Beltramization. In this case, the Lamb vector, i.e., the vector product between velocity and vorticity vanishes, so that the whole nonlinear term, which corresponds to the solenoidal part of the Lamb vector, is locally equal to zero.

In Kerr [15], helicity and strain have been studied in forced isotropic turbulence considering histograms, while Pelz et al. [14] investigated local helicity in turbulent channel flow and turbulent Taylor–Green flow. Shell models of isotropic turbulence have been used to study helicity and its transfer [16, 17]. High-resolution direct numerical simulations of forced helical rotating turbulence have been studied in Mininni and Pouquet [18, 19]. The alignment of velocity and vorticity in various flow types, such as shear flow, channel flow, and strained flow, was examined in Rogers and Moin [20]. In their simulations, it was shown that the alignment of velocity and vorticity was significantly weaker than in the investigation of Pelz et al. [14]. They questioned the results of the latter and the role of helicity fluctuations in three-dimensional turbulence in general. The generation and destruction mechanisms of cross helicity, defined by the scalar product between the velocity and the magnetic field, in magnetohydrodynamic turbulence have been studied in Yokoi [21].

The balance equation for mean kinetic helicity has been discussed by Sanada [22] for isotropic turbulence. Sanada conjectured that the dissipation of mean kinetic helicity $\langle H_u \rangle$ is determined by mean super-helicity $\langle H_\omega \rangle = \langle \boldsymbol{\omega} \cdot (\nabla \times \boldsymbol{\omega}) \rangle$. Since the two mean helicities are signed quantities, mean super-helicity can dissipate mean kinetic helicity only if the two quantities have the same sign. Evidence supporting Sanada's conjecture was given more recently by Galanti and Tsinober [23] for isotropic turbulence with helical or non-helical forcing.

In Jacobitz et al. [24], the influence of initial mean kinetic helicity was studied for homogeneous turbulent shear flow. In order to gain insight into the evolution of the kinetic energy and kinetic helicity, an analysis of the spectral tensor, the two-point correlation of velocity in Fourier space, was performed (see also Cambon et al. [25] and Sagaut and Cambon [26]). The spectral tensor was decomposed into its mirror-symmetric part (related to kinetic energy) and its anti-symmetric part (related to kinetic helicity). This

analysis showed that the evolution equations of the two parts are only linked through the nonlinear interaction terms. Therefore, kinetic helicity only influences the evolution of kinetic energy through the nonlinear term. The influence of initial mean kinetic helicity on the flow evolution resembles the influence of mean kinetic helicity on decaying isotropic turbulence: the initial decay of the kinetic energy is weakened. This finding is in agreement with Kraichnan's prediction that energy transfer is slowed down by helical motion [27].

The helical properties of rotating sheared turbulence were investigated in Jacobitz et al. [28]. It was concluded that the growing cases are characterized by a tendency toward local two-dimensionalization, while decaying cases exhibit a preference for swirling motion. A motivation for the present study is to investigate if these findings hold for a wider class of homogeneous turbulent flows.

In the present study, the helical properties of six cases are investigated: a solenoidal uncorrelated Gaussian random field, statistically steady forced isotropic turbulence [29], decaying isotropic turbulence [30], decaying rotating turbulence [31], growing sheared turbulence, and growing rotating sheared turbulence with a rotation ratio $f/S = +0.5$ [28, 32]. The turbulent flows were studied using direct numerical simulations and details can be found in the respective publications. All cases initially do not contain mean kinetic helicity and they remain free from it. However, this does not concern the local kinetic helicity and regions with strong kinetic helicity can exist in a flow free from mean kinetic helicity.

The purpose of this study is to answer three questions: first, what are the local helical properties of the turbulent flows, and are the helical properties related to the fate, growth, or decay of the turbulence? Second, do helical properties vary with the scale of the turbulent motion? This question is addressed using a wavelet-based decomposition of the turbulent motion into different scales as proposed in Yoshimatsu et al. [33]. Third, does super-helicity act to diminish kinetic helicity?

2. Results

In this section, the helical properties of a solenoidal Gaussian random field, statistically steady forced isotropic turbulence, decaying isotropic turbulence, decaying rotating turbulence, growing sheared turbulence, and growing rotating sheared turbulence are presented first. Then, a wavelet-based scale-dependent analysis considers helicity at different scales of turbulent motion. Finally, the role of super-helicity as a dissipative mechanism for kinetic helicity is investigated.

An overview of the different flows is given in Table 1. The statistically steady forced isotropic turbulence case of Vincent and Meneguzzi [29] has a Taylor microscale Reynolds number $Re_\lambda = 150$. The decaying isotropic turbulence case of Jacobitz et al. [30] is taken at an eddy-overturning time $t^* = t\epsilon/K = 3$, where $K = \langle u_k u_k \rangle/2$ is the turbulent kinetic

Table 1. Properties of the turbulent flows considered in this study.

Case	Source	Re_λ	Fate
Gaussian white noise			
Forced isotropic turbulence	Vincent and Meneguzzi (1991)	150	Steady
Isotropic turbulence	Jacobitz et al. (2005)	27	Decay
Rotating turbulence	Liechtenstein et al. (2005)	60	Decay
Sheared turbulence	Jacobitz et al. (2008)	72	Growth
Rotating and sheared	Jacobitz et al. (2008)	100	Growth

energy, $\epsilon = \nu\langle\partial u_i/\partial x_k \partial u_i/\partial x_k\rangle$ is the dissipation rate, and ν is the kinematic viscosity. The Taylor microscale Reynolds number is $Re_\lambda = q\lambda/\nu = 27$, where $q = \sqrt{2K}$ is the magnitude of velocity and $\lambda = \sqrt{5\nu q^2/\epsilon}$ is the Taylor microscale. The decaying rotating turbulence by Liechtenstein et al. [31] is taken at an eddy-overturning time $t^* = 3$. The Taylor microscale Reynolds number is $Re_\lambda = 60$ and the Rossby number is $Ro = q/(fL) = 0.025$, where $f = 2\Omega$ is the Coriolis parameter and L is an integral length scale. The growing sheared turbulence and growing rotating sheared turbulence by Jacobitz et al. [32] are taken at a non-dimensional time $St = 5$, where S is the uniform mean shear. The Taylor microscale Reynolds numbers are $Re_\lambda = 72$ and $Re_\lambda = 100$, respectively. The shear numbers are $SK/\epsilon = 4.8$ and $SK/\epsilon = 6.0$, respectively. For the rotating sheared turbulence case, the rotation ratio is $f/S = +0.5$ and the Rossby number is $Ro = 0.166$. All flows were studied using direct numerical simulations based on a Fourier-pseudospectral method at a resolution of 256^3 grid points.

2.1. *Helical properties of the flows*

Figure 1 shows the probability distribution functions (PDFs; estimated from a histogram with 100 equidistant bins) of relative kinetic helicity h_u for the six cases considered in this study. For the case of the solenoidal Gaussian random field, a uniform distribution is obtained without a preference for any value of h_u. The two cases of statistically steady forced isotropic turbulence and decaying isotropic turbulence are characterized by maxima at $h_u = \pm 1$, corresponding to a higher probability for alignment or anti-alignment of velocity and vorticity, i.e., helical or swirling motion. The decaying rotating turbulence case shows an approximately even distribution of relative kinetic helicity with just a slight maximum at $h_u = +1$. The two cases of growing sheared turbulence and growing rotating sheared turbulence with $f/S = +0.5$, however, exhibit a maximum at $h_u = 0$, corresponding to a preference for velocity and vorticity to be perpendicular, i.e., local two-dimensionalization of the flows.

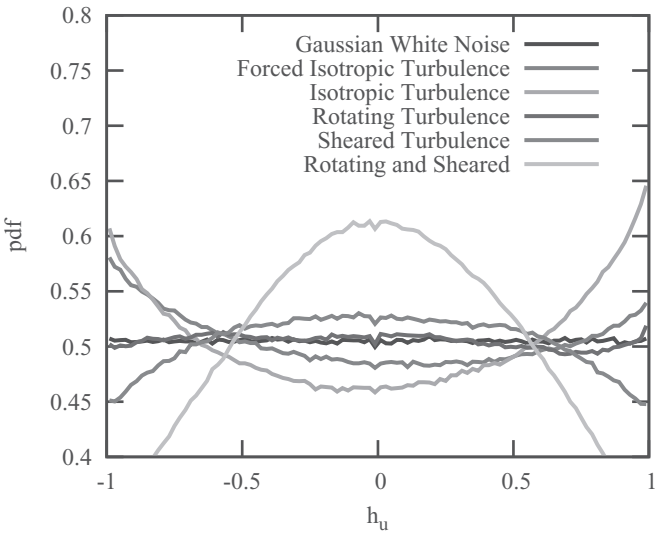


Figure 1. PDFs of relative kinetic helicity h_u for the six cases.

It is found that growing turbulence has a tendency to local two-dimensionalization of the flow, while decaying turbulence is characterized by helical motion. Statistically steady forced isotropic turbulence shows a trend similar to the results obtained for decaying turbulence. These findings are consistent with a previous study restricted to rotating sheared turbulence with different rotation ratios [28]. Growing turbulence was observed for rotation ratios $0 \leq f/S \leq 1$, which corresponds to an anti-parallel arrangement of the system rotation and the flow's mean vorticity due to shear. For these growing cases, a preference for $h_u = 0$ was observed. For all other cases, including those with a parallel arrangement of system rotation and mean vorticity, decay of the turbulence was obtained. For those decaying cases, a preference of $h_u = \pm 1$ was found in the simulations. The local two-dimensionalization observed in the cases in which the kinetic energy is growing is to a certain extent consistent with the fact that in two-dimensional flows the energy is less efficiently transferred to the small scales than in three-dimensional flows. For shear flows, these finding are consistent with a higher likelihood of vanishing kinetic helicity in regions of low-energy dissipation rate [34]. The interpretation of the helical motion for the remaining flows is not entirely clear. The local helical properties observed in the decaying or statistically steady flows indicate clearly the three-dimensional character of these flows, and in the isotropic case this is consistent with an energy cascade toward small scales, which is more efficient than for two-dimensional turbulence. However, these local helicity fluctuations do at the same time weaken the nonlinear term, so that the transfer of energy to small scales is not optimal.

The corresponding PDFs of relative super-helicity h_ω are given in Figure 2. Again, for the solenoidal Gaussian random field, a uniform distribution is obtained without a preference for any value of h_ω. In contrast to the relative kinetic helicity h_u, the relative super-helicity h_ω shows pronounced maxima at $h_\omega = \pm 1$ for all turbulent flows and it does not aid with a further classification of the fate of the flows. This result is again in agreement with the previous study of rotating sheared turbulence by Jacobitz et al. [28].

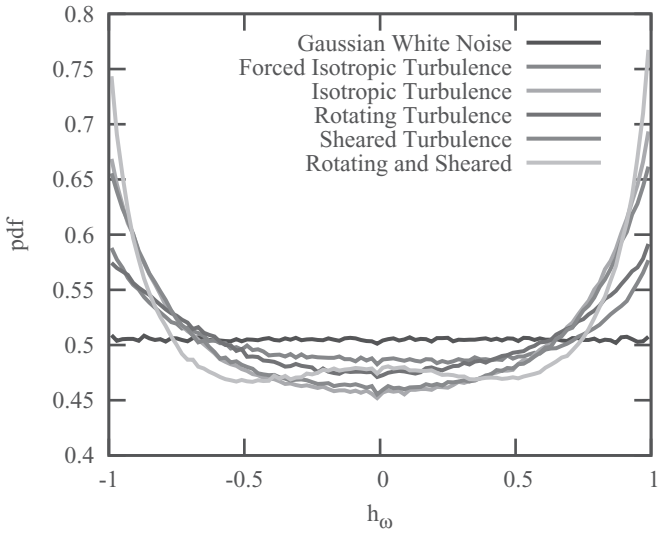


Figure 2. PDFs of relative super-helicity h_ω for the six cases.

2.2. *Scale-dependent analysis*

The wavelet representation of turbulent flows (see, for example, Farge [35] as well as Schneider and Vasilyev [36]) allows for a clear scale separation. To obtain the scale contributions of velocity $\mathbf{u}^j$ (and similarly for vorticity and its curl), the flow field $\mathbf{u} = (u_1, u_2, u_3)$, given at resolution $N = 2^{3J}$ with $J = 8$, is decomposed into an orthogonal wavelet series using Coiflet 12 wavelets:

$$\mathbf{u}(\mathbf{x}) = \sum_{\lambda} \widetilde{\mathbf{u}}_\lambda \psi_\lambda(\mathbf{x}). \tag{1}$$

The multiindex $\lambda = (j, \mathbf{i}, \mu)$ denotes scale index j (with $0 \leq j \leq J-1$), spatial position $\mathbf{i}$ (with 2^{3j} values for each j and μ), and seven spatial directions $\mu = 1, \ldots, 7$ of each wavelet ψ_λ [35]. Due to the orthogonality of the wavelets, the coefficients are given by $\widetilde{\mathbf{u}}_\lambda = \langle \mathbf{u}, \psi_\lambda \rangle$, where $\langle \cdot, \cdot \rangle$ denotes the L^2-inner product. The coefficients measure fluctuations of $\mathbf{u}$ at scale 2^{-j} and around position $\mathbf{i}/2^j$ for each of the seven possible directions. Fixing j and summing only over $\mathbf{i}$ and μ in Equation (1), the contribution $\mathbf{u}^j$ at scale j is obtained and by construction we have $\mathbf{u} = \sum_j \mathbf{u}^j$. Analogously, the contributions ω^j and $(\boldsymbol{\nabla} \times \boldsymbol{\omega})^j$ at scale 2^{-j} are obtained.

Thus, the scale-dependent kinetic helicity can be defined as follows:

$$H_{u^j} = \mathbf{u}^j \cdot \boldsymbol{\omega}^j. \tag{2}$$

Here, $\mathbf{u}^j$ and $\boldsymbol{\omega}^j$ are velocity and vorticity at scale 2^{-j}, respectively, as proposed in Yoshimatsu et al. [33] for isotropic turbulence. For $j \neq 0$, the scale-dependent kinetic helicity H_{u^j} is a Galilean invariant of the flow, though H_u itself is not. This is based on the fact that the mean velocity of $\mathbf{u}^j$ vanishes due to the vanishing moment property of the wavelets [35].

Accordingly, the scale-dependent relative kinetic helicity can be defined as

$$h_{u^j} = H_{u^j}/(|\boldsymbol{u}^j||\boldsymbol{\omega}^j|). \tag{3}$$

Analogously, the scale-dependent super-helicity $H_{\omega^j} = \boldsymbol{\omega}^j \cdot (\nabla \times \boldsymbol{\omega})^j$ and the corresponding relative quantity h_{ω^j} are obtained. These scale-dependent quantities yield further insight into the geometrical statistics at different scales of motion. In the following, we analyze the different turbulent flows.

PDFs of scale-dependent relative kinetic helicity h_{u^j} (left column) and relative super-helicity h_{ω^j} (right column) are presented in Figures 3 and 4 for the six different cases considered here. The figures show the PDFs of the total relative helicities and the PDFs of the scale-dependent helicities at scales $j = 3$ to $j = 7$. Note that largest scales $j = 1$ and $j = 2$ are not shown, since the flow contains only a small number of wavelet modes at those scales and the PDFs are consequently poorly converged.

For the solenoidal Gaussian random field (3, top), the uniform distribution for the total helicities persists at all scales as expected. For statistically steady forced isotropic turbulence (3, center), decaying isotropic turbulence (3, bottom), and decaying rotating turbulence (4, top), the smallest scales of motion show maxima at $h_{u^j} = \pm 1$. In the case of forced isotropic turbulence, the maxima at $h_{u^j} = \pm 1$ for smaller scales are the least pronounced, but a maximum at $h_{u^j} = 0$ is observed for the larger scales. For decaying isotropic turbulence and decaying rotating turbulence, the larger scales of motion do not

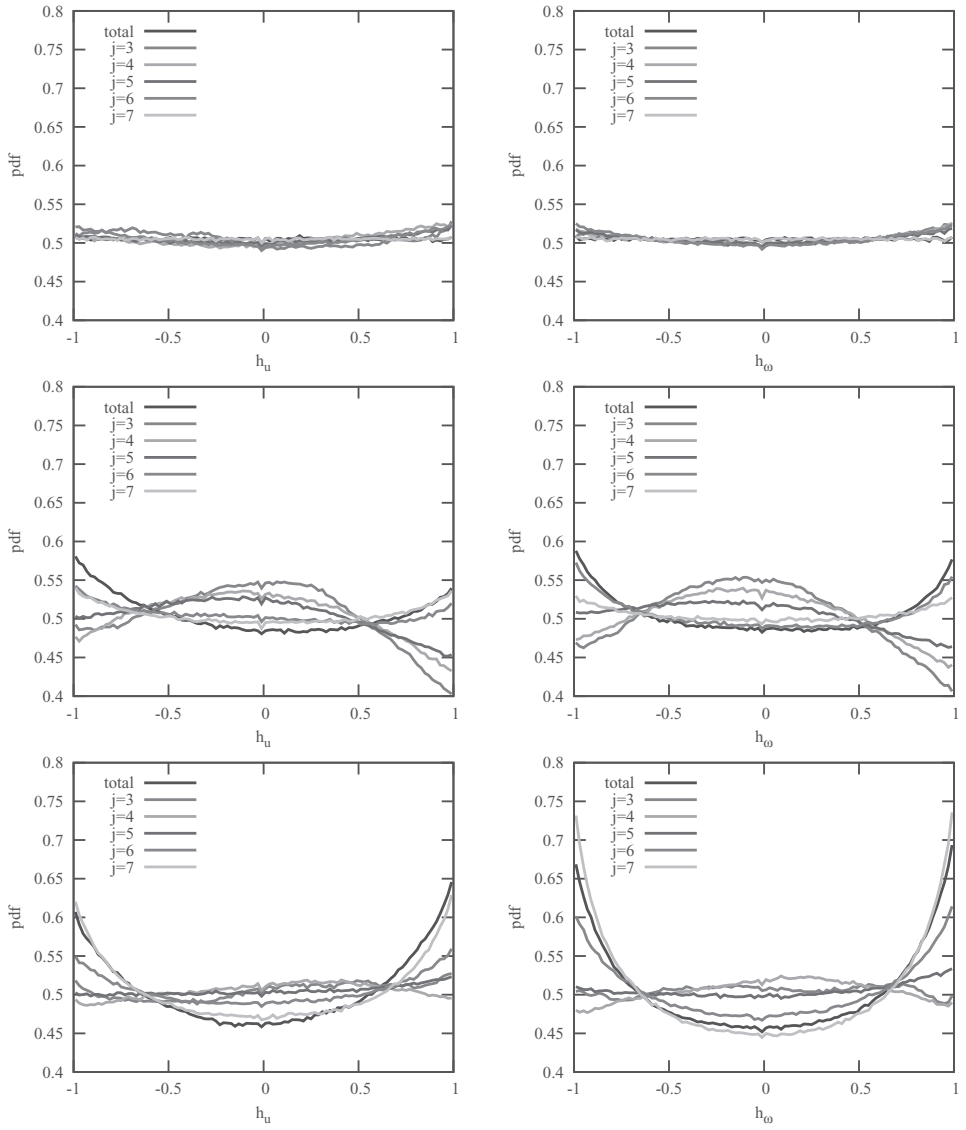


Figure 3. PDFs of scale-dependent kinetic helicity h_{u^j} (left column) and super-helicity h_{ω^j} (right column) for a Gaussian random field (top), forced isotropic turbulence (center), and decaying isotropic turbulence (bottom).

show a clearly defined maximum. For growing sheared turbulence (4, center), the PDFs of scale-dependent relative kinetic helicity of the larger scales with $j = 3, 4$, and 5 show a maximum at $h_{u^j} = 0$, corresponding to a trend to local two-dimensionalization of the flow at large scales. The smaller scales with $j = 6$ and 7 have maxima at $h_{u^j} = \pm 1$, corresponding to a trend to helical motion at small scales. For growing rotating sheared turbulence with $f/S = +0.5$ (4, bottom), a similar result as for sheared turbulence is obtained, but the probability for local two-dimensionalization at large scales and helical motion at small scales is even more pronounced.

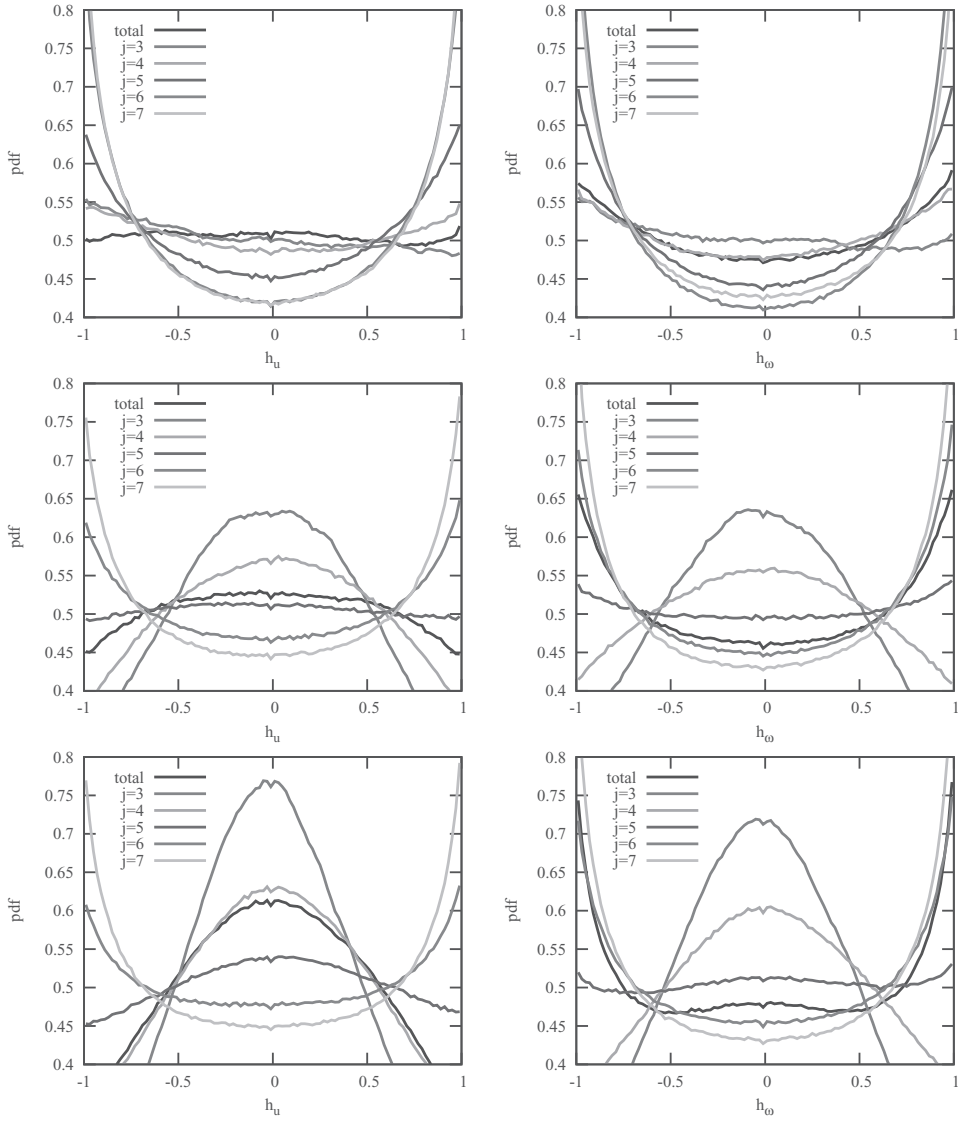


Figure 4. PDFs of scale-dependent kinetic helicity h_{u^j} (left column) and super-helicity h_{ω^j} (right column) for decaying rotating turbulence (top), growing sheared turbulence (center), and growing rotating sheared turbulence with $f/S = +0.5$ (bottom).

The PDFs of scale-dependent relative super-helicity of these three cases also yield a maximum at $h_{\omega^j} = 0$ for the larger scales with $j = 3, 4,$ and 5 and maxima at $h_{\omega^j} = \pm 1$ at the smaller scales $j = 6$ and 7. For decaying rotating turbulence and decaying rotating sheared turbulence with $f/S = +5$, the scale-dependent kinetic helicity PDFs show maxima for $h_{u^j} = \pm 1$ at all scales $j > 3$. Similarly, the scale-dependent relative super-helicity PDFs yield maxima for $h_{\omega^j} = \pm 1$ for all scales considered.

The decomposition of velocity and vorticity into scale-dependent contributions first as well as the decomposition of the kinetic helicity directly yield the same mean kinetic

helicity values for each scale 2^{-j}, i.e., the sum over j of the scalewise mean helicities results in the total mean helicity. This property is similar to the feature obtained for the helicity spectrum, i.e., the sum of the helicity spectrum over all wavenumbers yields the total mean helicity. The reason for the equivalence of both decompositions is that the wavelets are orthogonal with respect to scale index j. Thus, the velocity components u^j and the vorticity components ω^j are orthogonal, i.e., $\langle u^j, \omega^{j'} \rangle = 0$ for $j \neq j'$. However, the pointwise scale-dependent helicities differ.

In analogy to the spectrum, we prefer to use the scale decomposition of velocity and vorticity. This scale-dependent helicity could be called helicity scalogram (contributions of helicity per scale) in analogy with the energy scalogram (contribution of energy per scale), where the velocity is decomposed in scale contributions and not the energy. The scalograms can be related to Fourier spectra, using a relation between the scale index j and the wavenumber $k_j = k_\psi 2^j$, where k_ψ is the centroid wavenumber of the wavelet [35]. The scalogram corresponds to a smoothed version of the Fourier spectrum. The smoothing kernel is the square of the Fourier transform of the wavelet. As frequency increases, i.e., at small scales, the smoothing interval becomes larger, which explains why the wavelet spectrum is a well-conditioned statistical estimator.

The scale-dependent helicity introduced in Rodriguez Imazio and Mininni [37] corresponds to a low-pass-filtered helicity, considering decreasing box sizes, whereas the wavelet-based scale-dependent helicity corresponds to a band-pass-filtered helicity, considering bands of increasing wavenumber, which yields incremental information on the helicity of the flow scale by scale. The latter quantity can be compared with the Fourier helicity spectrum, which gives the helicity distribution wavenumber by wavenumber, whereas the former gives some cumulative information, since information on the helicity of the larger scale contributions of the flow is included in the helicity of the smaller scale contributions. Hence, both quantities do not yield the same values.

2.3. *Dissipation of kinetic helicity*

The evolution of mean kinetic helicity $\langle H_u \rangle$ is described by a transport equation:

$$\frac{d}{dt}\langle H_u \rangle = -2\nu \langle H_\omega \rangle + \langle F \rangle. \tag{4}$$

Here, $F = 2\boldsymbol{f} \cdot \boldsymbol{\omega}$ accounts for the forcing term $\boldsymbol{f}$ in the momentum equation and vanishes for the flows considered here due to their mirror symmetry property. The kinematic viscosity of the fluid is ν. Dissipation of mean kinetic helicity $\langle H_u \rangle$ by mean super-helicity $\langle H_\omega \rangle$ requires that both mean helicities have the same sign. Sanada [22] conjectured that the two helicities indeed have the same sign for isotropic turbulence.

Motivated by this study, further evidence to support a local dissipative mechanism of kinetic helicity by super-helicity is provided: first, the PDFs of the cosine of the angle between velocity and the curl of vorticity are considered. Second, the joint PDFs of relative kinetic helicity with relative super-helicity are determined. Third, the two relative helicities are used to color isosurfaces of vortical structures.

Using the vector identity

$$\nabla \times \nabla \times \boldsymbol{u} = -\nabla^2 \boldsymbol{u}, \tag{5}$$

it follows that

$$\boldsymbol{u} \cdot \nabla \times \nabla \times \boldsymbol{u} = \boldsymbol{\omega} \cdot \boldsymbol{\omega} - \nabla \cdot (\boldsymbol{u} \times \boldsymbol{\omega}). \tag{6}$$

Averaging over a domain with periodic boundary conditions or boundaries on which the normal component of $\boldsymbol{u} \times \boldsymbol{\omega}$ vanishes leads then to the expression

$$\langle \boldsymbol{u} \cdot \nabla \times \nabla \times \boldsymbol{u} \rangle = \langle \boldsymbol{\omega} \cdot \boldsymbol{\omega} \rangle > 0. \tag{7}$$

It can, therefore, be deduced that there is a larger probability that the vectors $\boldsymbol{u}$ and $\nabla \times \nabla \times \boldsymbol{u}$ are aligned than that they are anti-aligned. From the larger probability of alignment, it follows that there is a larger likelihood that the kinetic helicity $H_u = \boldsymbol{u} \cdot \boldsymbol{\omega}$ and the super-helicity $H_\omega = \boldsymbol{\omega} \cdot \nabla \times \boldsymbol{\omega}$ have the same sign [22]. The higher likelihood for the same sign also applies to the relative helicities h_u and h_ω [23].

Figure 5 shows the PDF of the cosine of the angle between velocity $\boldsymbol{u}$ and the curl of vorticity $\nabla \times \nabla \times \boldsymbol{u} = -\nabla^2 \boldsymbol{u}$ for the six cases. The PDFs are strongly skewed supporting a high probability for the alignment of the two vectors. The most strongly skewed PDF is observed for the solenoidal Gaussian random field, indicating that the alignment is a kinematic property of the curl operator. In contrast, the least skewed PDF is found for forced isotropic turbulence. For the four remaining cases, all directly computed from the Navier–Stokes equations, the PDFs are similar with maxima in between those found for the random field and the forced isotropic turbulence case.

The impact of forcing in isotropic turbulence simulations on the alignment is investigated in more detail in Figure 6. The figure shows decaying isotropic turbulence and results from three well-developed forced isotropic turbulence simulations by Vincent and Meneguzzi [29], Yeung et al. [38], and da Silva et al. [39]. The three forced isotropic turbulence fields are chosen at a time corresponding to the statistically steady regime. Different forcing methods are used in these studies: Vincent and Meneguzzi [29] use a deterministic

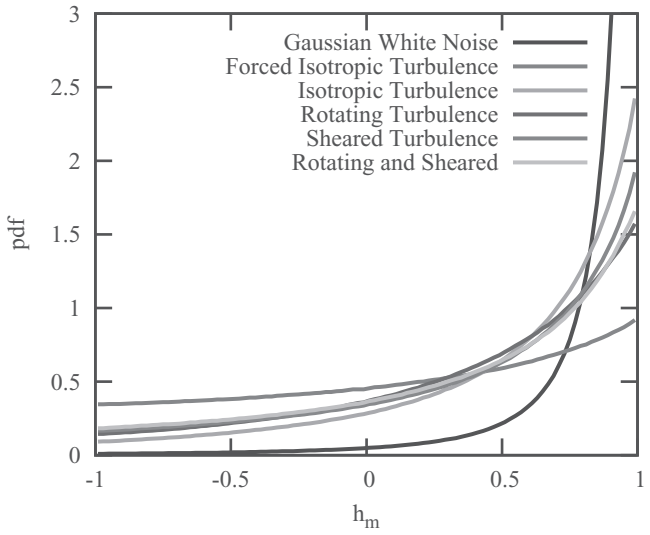


Figure 5. PDFs of the cosine of the angle between velocity u and curl of vorticity $\nabla \times \nabla \times u$ for the six cases.

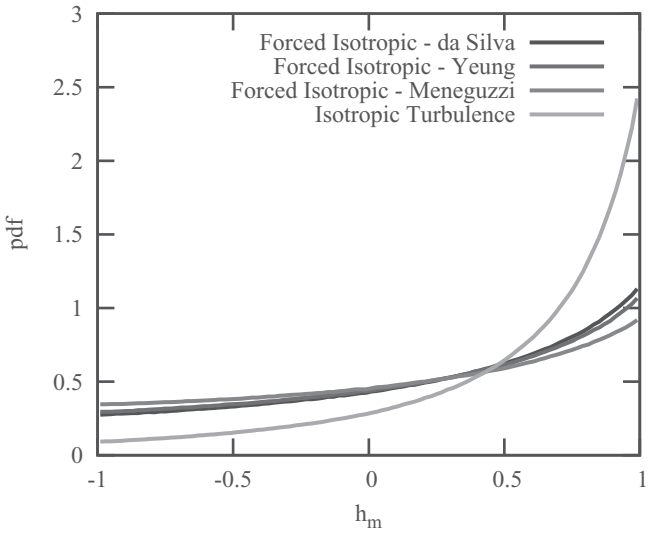


Figure 6. PDFs of the cosine of the angle between velocity u and curl of vorticity $\nabla \times \nabla \times u$ for isotropic turbulence cases.

forcing mechanism with a constant amplitude for all Fourier modes with wavenumber components equal to zero or one as described by Kerr [40]. Yeung et al. [38] use the stochastic forcing scheme by Eswaran and Pope [41]. The forcing consists of a forcing acceleration in the low wavenumber band, which is based on an Ornstein-Uhlenbeck random process (six in total). The work of da Silva et al. [39] uses the stochastic volume forcing algorithm developed by Alvelius [42]. The results suggest that the forcing mechanisms employed in the forced isotropic turbulence simulations have an impact on the alignment of velocity and the curl of vorticity. It appears that the forcing mechanisms also introduce a small amount of mean kinetic helicity and the resulting PDF of relative kinetic helicity is not symmetric around zero (see Figure 1).

To further verify that there is a high probability that the two helicities even locally have the same sign, joint PDFs of relative kinetic helicity h_u with relative super-helicity h_ω are shown in Figure 7. For all cases, a strong correlation of the signs of the two helicities is indeed observed. This sign correlation thus supports that super-helicity diminishes kinetic helicity.

Note that the one-dimensional PDFs of h_u and h_ω can be obtained by integration of the joint PDF over h_ω and h_u, respectively. Therefore, a joint PDF that is approximately symmetric along its diagonal axis will yield similarly shaped PDFs for h_u and h_ω. These features are indeed observed for cases with decaying turbulent kinetic energy, forced isotropic turbulence, and the Gaussian random field. In contrast, one possibility to obtain different shapes for the PDFs of h_u and h_ω is an asymmetric joint PDF. Hence, this symmetry is broken for the cases with growing turbulent kinetic energy.

Figure 8 shows isovorticity surfaces for three of the six cases considered here: forced isotropic turbulence (top), decaying rotating turbulence (center), and growing sheared turbulence (bottom). No preferred orientation is visible in the case of forced isotropic turbulence. Vertical columns are present in rotating turbulence, while inclined structures are observed for sheared turbulence. The isovorticity surfaces are colored with relative

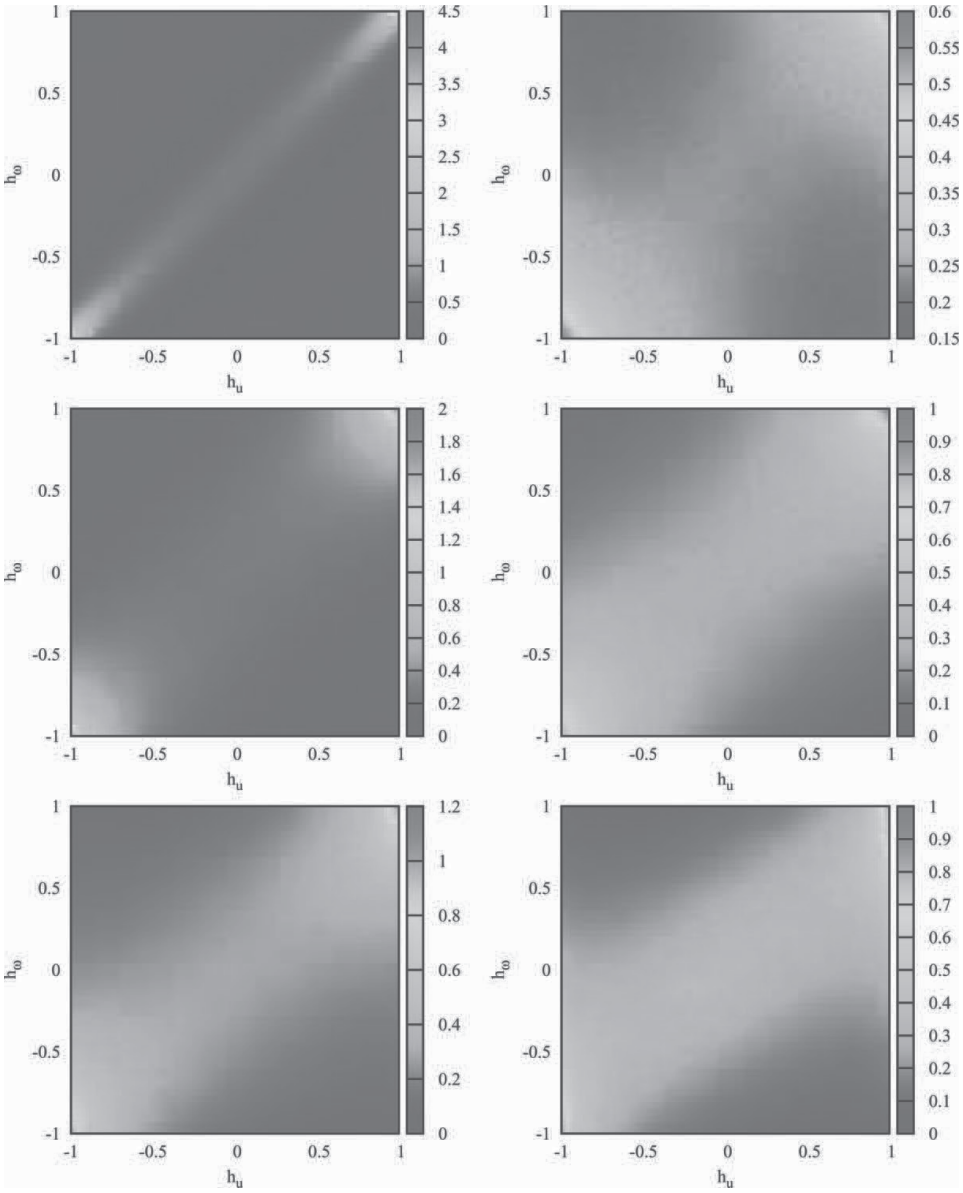


Figure 7. Joint PDFs of kinetic helicity h_u and super-helicity h_ω for a Gaussian random field (top left), forced isotropic turbulence (top right), decaying isotropic turbulence (center left), rotating turbulence (center right), sheared turbulence (bottom left), and growing rotating sheared turbulence with $f/S = +0.5$ (bottom right).

kinetic helicity h_u (left) and relative super-helicity h_ω (right). For a given flow structure, it is likely that the same sign is found. This visual observation thus indicates a high likelihood that the signs of h_u and h_ω are indeed correlated.

All indicators considered in this study suggest that super-helicity acts as a dissipative process for kinetic helicity also locally in anisotropic homogeneous turbulence.

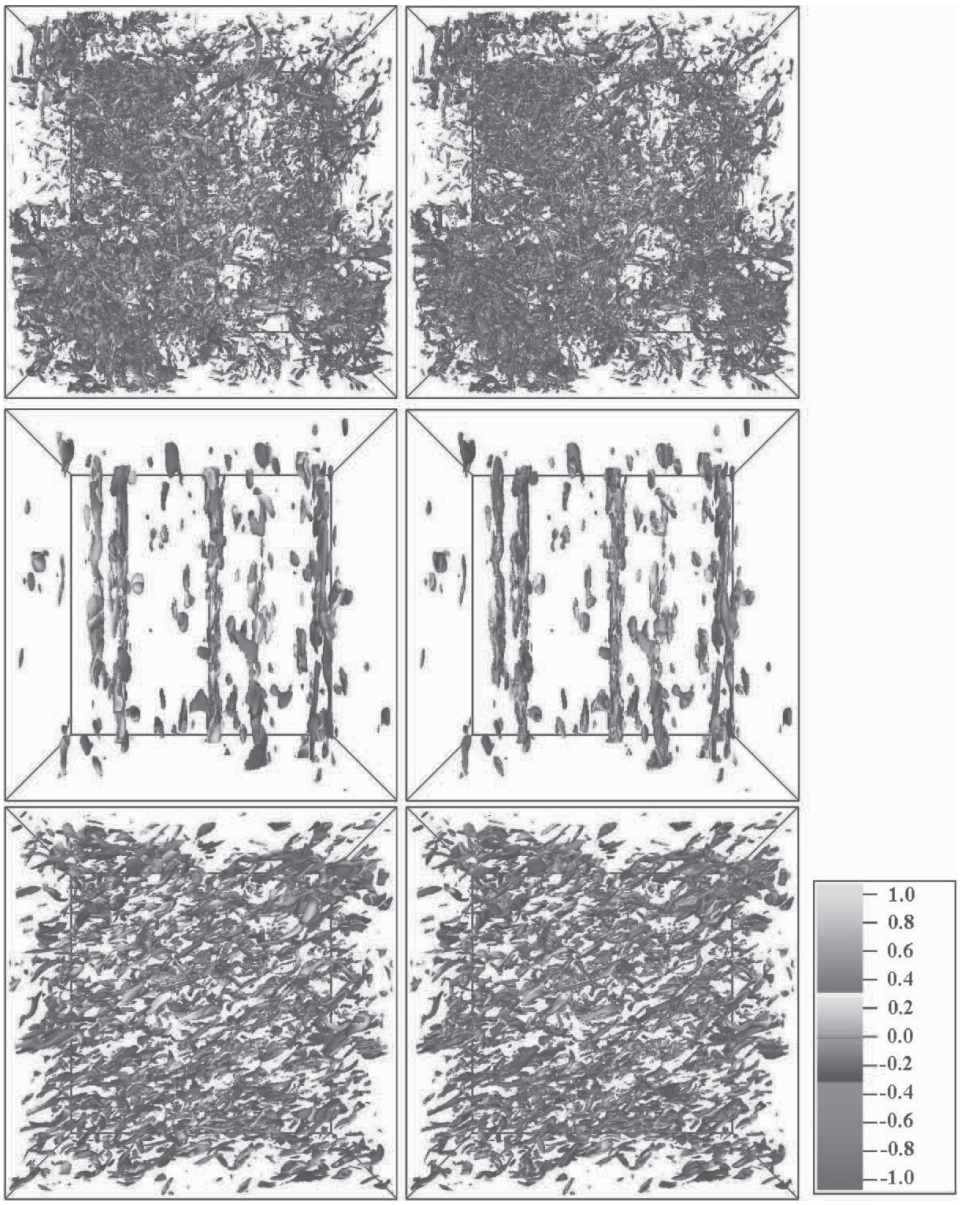


Figure 8. Isovorticity structures colored with kinetic helicity h_u (left) and super-helicity h_ω (right) for forced isotropic turbulence (top), rotating turbulence (center), and sheared turbulence (bottom).

3. Conclusions

To summarize, helical properties of five prototypical turbulent flows were investigated and compared to the helical properties of a solenoidal Gaussian random field. For the PDFs of kinetic helicity h_u, a maximum at $h_u = 0$ was observed for cases with growing turbulent kinetic energy, while a maximum at $h_u = \pm 1$ was found for decaying cases. Thus, for growing cases, the PDFs of kinetic helicity h_u indicate a larger probability that

velocity and vorticity are perpendicular, corresponding to local two-dimensionalization of the flow. This finding is consistent with the two-dimensionalization of the fluctuating strain rate for growing turbulent shear flow [43]. For decaying cases, the PDFs of kinetic helicity h_u show a preference for the alignment or anti-alignment of velocity and vorticity, corresponding to helical motion. For all cases, however, the PDFs of super-helicity h_ω always assume a maximum at $h_\omega = \pm 1$. The helical properties of the statistically steady forced isotropic turbulence case were found to follow those of flows with decaying turbulent kinetic energy.

Scale-dependent PDFs of kinetic helicity show that large scales tend to have a maximum at $h_{u^j} = 0$, corresponding to two-dimensionalization of the flows, while small scales tend to show a maximum at $h_{u^j} = \pm 1$, corresponding to helical motion. These observations hold for all types of turbulent flows considered in this study.

Consideration of the alignment of velocity with the curl of vorticity, joint PDFs of relative kinetic helicity and relative super-helicity, as well as isovorticity surfaces colored with kinetic helicity and super-helicity all indicate a high probability that h_u and h_ω have the same sign even locally. Thus, super-helicity tends to diminish kinetic helicity for the different homogeneous turbulent flows studied here.

Acknowledgements

We would like to thank Claude Cambon, Fabien Godeferd, Lukas Liechtenstein, Carlos da Silva, and P.K. Yeung for the use of their direct numerical simulation results. We are thankful for many fruitful discussions with Claude Cambon. F.G.J. acknowledges hospitality and support from the Laboratoire de Mécanique, Modélisation & Procédés Propres at Aix-Marseille Université, Marseille, France, as well as an International Opportunity Grant from the University of San Diego, San Diego, California. M.F. and K.S. acknowledge financial support from the Association CEA-Euratom and the French Research Federation for Fusion Studies within the framework of the European Fusion Development Agreement under contract V.3258.001. W.B. and K.S. acknowledge financial support from the French Research Agency (ANR), project SiCoMHD, contract ANR-11-BLAN-045.

References

[1] R. Betchov, *Semi-isotropic turbulence and helicoidal flows*, Phys. Fluids 4 (1961), pp. 925–926.
[2] M.A. Berger and G.B. Field, *The topological properties of magnetic helicity*, J. Fluid Mech. 147 (1984), pp. 133–148.
[3] H.K. Moffatt, *The degree of knottedness of tangled vortex lines*, J. Fluid Mech. 35 (1969), pp. 117–129.
[4] J.-J. Moreau, *Constants d'un ilôt tourbillonnaire en fluide parfait barotrope*, C. R. Acad. Sci., Paris 252 (1961), pp. 2810–2812.
[5] H.K. Moffatt and A. Tsinober, *Helicity in laminar and turbulent flow*, Annu. Rev. Fluid Mech. 24 (1992), pp. 281–312.
[6] E.N. Parker, *Hydromagnetic dynamo models*, Astrophys. J. 122 (1955), pp. 293–314.
[7] A. Pouquet, M. Lesieur, and J. Leorat, *Strong MHD helical turbulence and the non-linear dynamo effect*, J. Fluid Mech. 77 (1976), pp. 321–354.
[8] M. Steenbeck, F. Kause, and K.H. Rädler, *Berechnung der mittleren Lorentz-Feldstärke für ein elektrisch leitendes Medium in turbulenter, durch Coriolis-Kräfte beeinflußter Bewegung*, Zs. f. Naturforschung 21a (1966), p. 369.
[9] G.V. Levina and M.T. Montgomery, *A first examination of the helical nature of tropical cyclogenesis*, Dokl. Earth Sci. 434 (2010), pp. 1285–1289.
[10] P.M. Markowski, J.M. Straka, E.N. Rasmussen, and D.O. Blanchard, *Variability of storm-relative helicity during VORTEX*, Mon. Weather Rev. 126 (1998), pp. 2959–2971.
[11] K.K. Droegemeier, S.M. Lazarus, and R. Davies-Jones, *The influence of helicity on numerically simulated convective storms*, Mon. Weather Rev. 21 (1993), pp. 2005–2029.

[12] M. Kholmyansky, M. Shapiro-Orot, and A. Tsinober, *Experimental observations of spontaneous breaking of reflectional symmetry in turbulent flow*, Proc. R. Soc. Lond. A 457 (2001), pp. 2699–2717.
[13] E. Levich and A. Tsinober, *On the role of helical structures in three-dimensional turbulent flow*, Phys. Lett. A 93 (1983), pp. 293–297.
[14] R. Pelz, V. Yakhot, S. Orszag, L. Shtilman, and E. Levich, *Velocity-vorticity patterns in turbulent flow*, Phys. Rev. Lett. 54 (1985), pp. 2505–2508.
[15] R.M. Kerr, *Histograms of helicity and strain in numerical turbulence*, Phys. Rev. Lett. 59 (1987), pp. 783–786.
[16] R. Benzi, L. Biferale, R. Kerr, and E. Trovatore, *Helical-shell models for three dimensional turbulence*, Phys. Rev. E 53 (1996), 3541.
[17] L. Biferale, D. Pierotti, and F. Toschi, *Helicity transfer in turbulent models*, Phys. Rev. E Rap. Comm. 57 (1998), R2515.
[18] P.D. Mininni and A. Pouquet, *Rotating helical turbulence. Part I. Global evolution and spectral behavior*, Phys. Fluids 22 (2010a), 035105.
[19] P.D. Mininni and A. Pouquet, *Rotating helical turbulence. Part II. Intermittency, scale invariance, and structures*, Phys. Fluids 22 (2010b), 035106.
[20] M.M. Rogers and P. Moin, *The structure of the vorticity field in homogeneous turbulent flows*, J. Fluid Mech. 176 (1987), pp. 33–66.
[21] N. Yokoi, *Modeling the turbulent cross-helicity evolution: production, dissipation, and transport rates*, J. Turbul. 12 (2011), N27.
[22] T. Sanada, *Helicity production in the transition to chaotic flow simulated by Navier-Stokes equation*, Phys. Rev. Lett. 70 (1993), pp. 3035–3038.
[23] B. Galanti and A. Tsinober, *Physical space properties of helicity in quasi-homogeneous forced turbulence*, Phys. Lett. A 352 (2006), pp. 141–149.
[24] F.G. Jacobitz, K. Schneider, W.J.T. Bos, and M. Farge, *Influence of initial mean helicity in homogeneous turbulent shear flow*, Phys. Rev. E 84 (2011), 056319.
[25] C. Cambon, D. Jeandel, and J. Mathieu, *Spectral modelling of homogeneous non-isotropic turbulence*, J. Fluid Mech. 104 (1981), pp. 247–262.
[26] P. Sagaut and C. Cambon, *Homogeneous Turbulence Dynamics*, Cambridge University Press, Cambridge, 2008.
[27] R.H. Kraichnan, *Helical turbulence and absolute equilibrium*, J. Fluid Mech. 59 (1973), pp. 745–752.
[28] F.G. Jacobitz, K. Schneider, W.J.T. Bos, and M. Farge, *On the structure and dynamics of sheared and rotating turbulence: Anisotropy properties and geometrical scale-dependent statistics*, Phys. Fluids 22 (2010), 085101.
[29] A. Vincent and M. Meneguzzi, *The spatial structure and statistical properties of homogeneous turbulence*, J. Fluid Mech. 225 (1991), pp. 1–20.
[30] F.G. Jacobitz, M.M. Rogers, and J.H. Ferziger, *Waves in stably stratified turbulent flow*, J. Turbul. 6 (2005), N32.
[31] L. Liechtenstein, F.S. Godeferd, and C. Cambon, *Nonlinear formation of structures in rotating stratified turbulence*, J. Turbul. 4 (2005), N24.
[32] F.G. Jacobitz, L. Liechtenstein, K. Schneider, and M. Farge, *On the structure and dynamics of sheared and rotating turbulence: Direct numerical simulation and wavelet-based coherent vortex extraction*, Phys. Fluids 20 (2008), 045103.
[33] K. Yoshimatsu, N. Okamoto, K. Schneider, Y. Kaneda, and M. Farge, *Intermittency and scale-dependent statistics in fully developed turbulence*, Phys. Rev. E 79 (2009), 026303.
[34] J.M. Wallace, *Twenty years of experimental and direct numerical simulation access to the velocity gradient tensor: What have we learned about turbulence?* Phys. Fluids 21 (2009), 021301.
[35] M. Farge, *Wavelet transforms and their applications to turbulence*, Annu. Rev. Fluid Mech. 24 (1992), pp. 395–458.
[36] K. Schneider and O.V. Vasilyev, *Wavelet methods in computational fluid dynamics*, Annu. Rev. Fluid Mech. 42 (2010), pp. 473–503.
[37] P. Rodriguez Imazio and P.D. Mininni, *Cancellation exponents in helical and non-helical flows*, J. Fluid Mech. 651 (2010), pp. 241–250.
[38] P.K. Yeung, D.A. Donzis, and K.R. Sreenivasan, *High-Reynolds-number simulation of turbulent mixing*, Phys. Fluids 17 (2005), 081703.

[39] C.B. da Silva, R.J.N. dos Reis, and J.C.F. Pereira, *The intense vorticity structures near the turbulent/non-turbulent interface in a jet*, J. Fluid Mech. 685 (2011), pp. 165–190.
[40] R. Kerr, *Higher-order derivative correlations and the alignment of small-scale structures in isotropic numerical turbulence*, J. Fluid Mech. 153 (1985), pp. 31–58.
[41] V. Eswaran and S.B. Pope, *An examination of forcing in direct numerical simulations of turbulence*, Comput. Fluids 16 (1988), pp. 257–278.
[42] K. Alvelius, *Random forcing of three-dimensional homogeneous turbulence*, Phys. Fluids 11 (1999), 1880.
[43] J.G. Brasseur and W. Lin, *Kinematics and dynamics of small-scale vorticity and strain-rate structures in the transition from isotropic to shear turbulence*, Fluid Dyn. Res. 36 (2005), pp. 357–384.

Journal of Turbulence
Vol. 13, No. 12, 2012, 1–29

Taylor & Francis
Taylor & Francis Group

Studying Lagrangian dynamics of turbulence using on-demand fluid particle tracking in a public turbulence database

Huidan Yu[a†], Kalin Kanov[b], Eric Perlman[b], Jason Graham[a], Edo Frederix[a+], Randal Burns[b], Alexander Szalay[c], Gregory Eyink[d] and Charles Meneveau[a*]

[a]*Department of Mechanical Engineering;* [b]*Department of Computer Science;* [c]*Department of Physics and Astronomy;* [d]*Department of Applied Mathematics and Statistics, The Johns Hopkins University, Baltimore, MD 21218, USA*

(*Received 17 December 2011; final version received 28 February 2012*)

A recently developed public turbulence database system (http://turbulence.pha.jhu.edu) provides new ways to access large datasets generated from high-performance computer simulations of turbulent flows to perform numerical experiments. The database archives 1024^4 (spatial and time) data points obtained from a pseudo-spectral direct numerical simulation (DNS) of forced isotropic turbulence. The flow's Taylor-scale Reynolds number is $Re_\lambda = 443$, and the simulation output spans about one large-scale eddy turnover time. Besides the stored velocity and pressure fields, built-in first- and second-order space differentiation, as well as spatial and temporal interpolations are implemented on the database. The resulting 27 terabytes of data are public and can be accessed remotely through an interface based on a modern Web-services model. Users may write and execute analysis programs on their host computers, while the programs make subroutine-like calls (*getFunction*s) requesting desired variables (velocity and pressure, and their gradients) over the network. The architecture of the database and the initial built-in functionalities are described in a previous paper of *Journal of Turbulence* (Y. Li, E. Perlman, M. Wan, Y. Yang, R. Burns, C. Meneveau, R. Burns, S. Chen, A. Szalay, and G. Eyink, *A public turbulence database cluster and applications to study Lagrangian evolution of velocity increments in turbulence*, J. Turbul. 9 (2008), p. N31). In the present paper, further developments of the database system are described; mainly the newly developed *getPosition* function. Given an initial position, integration time-step, as well as an initial and end time, the *getPosition* function tracks arrays of fluid particles and returns particle locations at the end of the trajectory integration time. The *getPosition* function is tested by comparing with trajectories computed outside of the database. It is then applied to study the Lagrangian velocity structure functions as well as the tensor-based Lagrangian time correlation functions. The roles of pressure Hessian and viscous terms in the evolution of the symmetric and antisymmetric parts of the velocity gradient tensor are explored by comparing the time correlations with and without these terms. Besides the *getPosition* function, several other updates to the database are described such as a function to access the forcing term in the DNS, a new more efficient interpolation algorithm based on partial sums, and a new Matlab interface.

Keywords: forced isotropic turbulence; Lagrangian time correlation; particle tracking; turbulence database; web services

*Corresponding author. Email: meneveau@jhu.edu †Present address: Department of Mechanical Engineering, Indiana University–Purdue University, Indianapolis, IN, USA. +Permanent address: Mechanical Engineering, Eindhoven University of Technology, The Netherlands.

ISSN: 1468-5248 online only
© 2012 Taylor & Francis
http://dx.doi.org/10.1080/14685248.2012.674643
http://www.tandfonline.com

1. Introduction

Due to advances in computer hardware and algorithms, turbulence simulations supported by high-performance computing infrastructures have continued to expand. Direct Numerical Simulations (DNS) of turbulent flows using on the order of 1000^3–4000^3 grid points have been reported [1–4]. In the turbulence research community, the prevailing approach is that individual researchers perform large simulations that are analyzed during the runs and only a small subset of time-steps are stored for subsequent and by necessity more "static" analysis. A number of representative snapshots are stored, while the majority of the time evolution has to be discarded. As a result, much of the computational effort is not utilized as effectively as it could have been. In fact, often large simulations of the same process must be repeated after new questions arise that were not initially obvious. Storing the entire space-time history of a simulation, however, generates datasets that are very large and very difficult to access using prevailing approaches. Thus, the increasingly larger, top-ranked simulations run the risk of becoming less and less accessible to the wider turbulence scientific community.

As a step to develop new effective ways to translate the massive amounts of computational turbulence data into meaningful knowledge, a new "cyber fluid dynamics" paradigm has been proposed, which combines high-fidelity DNS of turbulence with modern database technology [5]. The newly created Johns Hopkins University (JHU) public turbulence database (http://turbulence.pha.jhu.edu) archives a 27-terabytes (TB) dataset from a DNS of forced isotropic turbulence consisting of 1024^4 (spatial and time) samples, spanning about one large-scale eddy turnover time. The database stores velocity and pressure fields. The domain size is in a $[0, 2\pi]^3$ domain and the Taylor-microscale Reynolds (Re) number is $Re_\lambda \simeq 433$. The spatial resolution is $dx = 2\pi/1024$ and the Kolmogorov scale is $\eta_K = 0.00287$ so that $dx/\eta_K \sim 2.1$. The turbulence integral scale is $L = 1.376$, the velocity root-mean-square (rms) value is $u' = 0.681$ and the mean dissipation rate is $\epsilon = 0.092$, in the units of the simulation. The Kolmogorov time-scale is $\tau_K = 0.045$. The stored time-steps are separated by a time-interval of 0.002 (the original DNS was performed with a time-step of 2×10^{-4} using a very conservative Courant-Friedrichs-Lewy condition (CFL) condition [5]).

One of the hallmarks of the database is a web services interface that allows users to access data in a user-friendly fashion while allowing maximum flexibility to execute desired analysis tasks. Remote users may write and execute analysis programs on their own computers, while their programs make subroutine-like calls named *getfunction*s (e.g. *getVelocityAndPressure*, *getVelocityGradient*, *getPressureLaplacian*, etc.) requesting desired variables, such as velocity, pressure, and their gradients, over the network. First- and second-order space differentiation as well as spatial and temporal interpolations are implemented on the database as pre-defined functions. Instead of being restricted to analysis on the fly during DNS, researchers may write and execute more specialized analysis programs on their host computers at any time.

The data and the initial built-in functionalities have already been described in detail in a previous publication [5]. Due to easy accessibility and flexibility, the database has attracted researchers from all over the world since its inception, and its use has resulted in various publications [6–14]. Nevertheless, current functionalities focus on extracting data at single time-steps of the turbulent field, best suited for Eulerian studies of turbulence. There is also considerable interest in the Lagrangian description of turbulence. A Lagrangian description of turbulence has advantages in studies of turbulent transport and mixing processes, as well as relating statistics with dynamical descriptions following fluid particles. An extensive database of the precomputed Lagrangian trajectories for a large number of fluid and

inertial particles, and turbulence quantities along the trajectories, has been in operation for several years [15].

The study of turbulence from the Lagrangian viewpoint has a long history, with the earliest works of Taylor [16] and Richardson [17], both pre-dating Kolmogorov [18]. It was recognized that transport issues are addressed naturally from the Lagrangian viewpoint, which has since been successfully employed in the theoretical treatment of turbulent mixing [19–23]. The Lagrangian concepts are also useful when considering entrainment processes at turbulent/laminar interfaces [24], and the Lagrangian stochastic models are widely used to model processes ranging from atmospheric pollution transport to turbulent combustion [25]. The Lagrangian dynamics of the velocity gradient tensor can be used to understand many fundamental and intrinsic properties of small-scale motions in high-Reynolds turbulence [12]. Studying the Lagrangian turbulence requires following a large number of particle trajectories in order to capture the overall space and time-scales. In spite of significant progress in recent years [22, 26, 27], experimental Lagrangian measurements remain challenging, especially for high Reynolds number turbulence. Extraction of Lagrangian data from DNS is conceptually easy, but requires the full time evolution to have been stored, such as in the JHU turbulence database, or to store the trajectories of a predefined set of particles [15]. To track fluid particles with arbitrary initial locations, or even for backward tracking over extended time periods, trajectories must be recomputed on demand. However, using currently available tools in the JHU turbulence database, users must send requests back and forth over the network for each integration time-step of the particle tracking. Improvements to this approach must follow the best practices of databases, such as "move the program to the data" [28].

As a new tool to facilitate Lagrangian analysis, we develop the *getPosition* function inside the database. It tracks arrays of particles moving with the flow and returns particle locations at the end of the trajectory integration time. The relevant algorithm and data management approach for the new *getPosition* function is described in Section 2, and the implementation is tested by comparing trajectories computed inside and outside the database. In Section 3, we study the Lagrangian velocity structure functions and compare the results from the JHU database at $R_\lambda \sim 430$ with the results from the literature at other Reynolds numbers. In Section 4, we study the Lagrangian time correlation functions of the symmetric and antisymmetric parts of the velocity gradient tensor in which the impact of various terms in the corresponding dynamical evolution equation is quantified systematically, including these terms separately. In Section 5, we use the data to examine important features of a model for the pressure Hessian tensor and how its predictions compare with the data. We summarize the results in Section 6 with a short discussion. Other recent updates to the JHU database, such as the new *getForce* function, more efficient algorithms for interpolation, as well as new Matlab interfaces, are presented and documented in Appendices A, B, and C, respectively.

2. The *getPosition* function: algorithm and data handling

Existing database built-in functionalities can retrieve velocity, pressure, as well as their derivatives at a specific location and time within the archived time history. To study the Lagrangian turbulence, one needs to perform an integration operation along fluid particle trajectories, e.g., using the Runge–Kutta method, which at present requires data transfers between a user's computer and the database at every small time-step needed in the Lagrangian integration. A more user-friendly and efficient approach would be for a user to

let the database compute the fluid trajectories by doing computations in the database. In this section we describe the algorithm used for such integration, as well as the way the computations are performed inside the various database layers. The end result is a new *getfunction* called *getPosition* that allows to track arrays of fluid particles simultaneously and returns final particle locations at the end of the specified trajectory integration time. It supports both forward and backward tracking of fluid particles.

2.1. *Fluid particle-tracking algorithm*

The *getPosition* function uses the second-order accurate Runge–Kutta integration. Given fluid particle locations $\mathbf{X}_p$ at a user-specified start time (t_{ST}), the function returns the particle locations at a user-specified end time (t_{ET}). The user also specifies a particle integration time-step (Δt_p^*). Forward tracking is accomplished by specifying $t_{ET} > t_{ST}$, whereas backward tracking is accomplished by specifying $t_{ET} < t_{ST}$. The sign of the time-step need not be specified to make distinction between forward and backward tracking, since inside the tracking algorithm it is taken to be $\Delta t_p = \text{sign}[t_{ET} - t_{ST}]|\Delta t_p^*|$.

Particle tracking is accomplished by integrating the following equation between times t_{ST} and t_{ET}

$$\frac{d\mathbf{x}_p}{dt} = \mathbf{u}(\mathbf{x}_p, t), \quad \mathbf{x}_p(t_{ST}) = \mathbf{X}_p, \tag{1}$$

where $\mathbf{x}_p(t)$ and $\mathbf{u}(\mathbf{x}_p, t)$ denote the position of the fluid particle originating (at initial time t_{ST}) from position $\mathbf{X}_p$ and the velocity field at the particle location, respectively. To advance the particle positions between two successive time instants t_m and $t_{m+1}(= t_m + \Delta t_p)$, the predictor step yields an estimate

$$\mathbf{x}_p^*(t_m) = \mathbf{x}_p(t_m) + \mathbf{u}(\mathbf{x}_p(t_m), t_m)\Delta t_p. \tag{2}$$

The corrector step then gives the particle position at t_{m+1} as

$$\mathbf{x}_p(t_{m+1}) = \mathbf{x}_p(t_m) + \Delta t_p \frac{1}{2}\left[\mathbf{u}(\mathbf{x}_p(t_m), t_m) + \mathbf{u}(\mathbf{x}_p^*(t_m), t_{m+1})\right]. \tag{3}$$

or

$$\mathbf{x}_p(t_{m+1}) = \mathbf{x}_p(t_m) + \frac{1}{2}\left[\mathbf{x}_p^*(t_m) - \mathbf{x}_p(t_m)\right] + \frac{1}{2}\Delta t_p \mathbf{u}(\mathbf{x}_p^*(t_m), t_{m+1}). \tag{4}$$

The integration proceeds until t_m reaches the user-specified t_{ET}. The last integration time-step is typically done using a smaller time-step so that the integration ends exactly at the specified t_{ET}. GetPosition then returns $\mathbf{x}_p(t_{ET})$ for all particles that were at initial locations $\mathbf{X}_p$.

For this integration scheme, the time-stepping error is of order $(\Delta t_p)^3$ over one time-step. In general, accurate spatial and time interpolations are crucial to obtain the fluid velocities while tracking particles along their trajectories. Spatial interpolation with various optional orders of accuracy can be specified by the user. Time interpolation is done by default using PHCIP [5]. To call this function, a user needs to provide t_{ST}, particle number, an array containing the positions of each particle at t_{ST}, Δt_p^*, and t_{ET}. On output, an array

containing the positions of each particle at t_{ET} is returned. As a time-step for particle tracking, in what follows we use $\Delta t_p = 0.0004$ for tests and applications (i.e. there are five particle-tracking time-steps for each database time-step), unless stated otherwise.

2.2. *Data and particle movements across servers*

Due to the movement of particles within different portions of the data volume, the implementation of the *getPosition* function on the various database layers is less straightforward than the existing functions. In general, the data sets are stored in multiple data servers, e.g. the current 27-TB DNS data are partitioned across six data servers. For the existing functions, since only one specific time is touched, all the operations associated with a particular point in space, including temporal and spatial interpolation, differentiation, etc. can be executed within one of the data servers that store the data. The upper-level web server plays a role to break down the user's batch query into pieces corresponding to each of the database servers and thus assigns each point query to a particular server, where the data retrieval and computation happens. Each of the data servers perform the requested computation for their portion of the entire batch. The retrieved variables are returned to the web server, where they are assembled and sent back to the user.

For *getPosition*, because of the movement of fluid particles, it is often the case within the desired time-integration period, that particles leave one data server and enter another data server either after the prediction semi-step (Equation (2)) or the full time-step (Equation (4)). In our current implementation, in order to alleviate the individual database servers from the burden of keeping track of each individual particle and whether it is within the boundaries of each server, we reassign all of the particles after each semi- or full-step.

Figure 1 shows the movement of data between the web server and the database servers. During the first iteration of the algorithm the predictor step is evaluated. The initial set of particle positions ($\mathbf{x}_p(t_m)$) is distributed among the database servers according to the spatial and temporal partitionings of the data. This step requires the velocity for each particle at initial positions ($\mathbf{u}(\mathbf{x}_p(t_m), t_m)$). The distribution of points across database servers ensures that the data are available locally on each database server. Each set of predictor positions ($\mathbf{x}^*_p(t_m)$) is evaluated according to Equation (2) in the computational module of

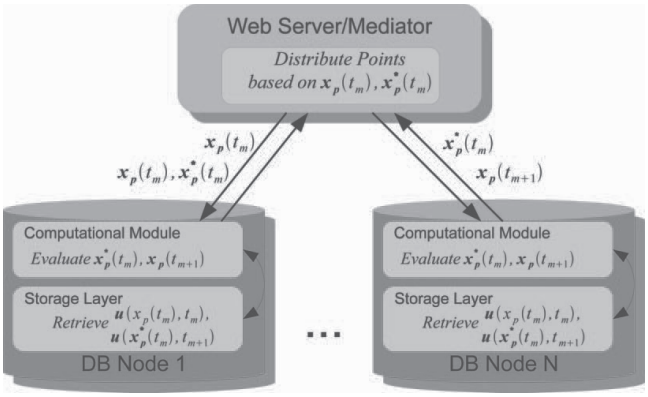


Figure 1. Interaction and data movement between the web server and database server during the execution of the *getPosition* function.

each database server. The predictor positions are then returned to the web server. Using the predictor positions, the web server reassigns the particles to the database servers, and the corrector step is evaluated using Equation (4). This step requires the retrieval of the velocity for each particle at the predictor positions ($\mathbf{u}(\mathbf{x}_p^*(t_m), t_{m+1})$) and the initial particle positions, both of which are provided by the web server. Positions $\mathbf{x}_p(t_{m+1})$ are again evaluated in the computational module of each database server and returned to the web server. This process continues until the specified t_{ET} is reached. The reassignment of particles before each step in the Runge–Kutta integration ensures that the data requested for each particle position are guaranteed to be found on the database server that is issuing the request and performing the integration.

2.3. *Accuracy tests and performance*

The accuracy of particle tracking inside the database (using *getPosition*) is tested by comparing the trajectories with those evaluated using particle tracking as coded on a local host (called "local tracking"), which involves calls to the database at each of the integration time-steps. The integration algorithm in both methods is identical, as described above. It is found that both approaches return the same trajectories, typically up to the sixth or seventh digit after the decimal point (essentially machine accuracy and chaotic behavior). The agreement is illustrated below by comparing *getPosition* and local coding for two fluid particles and tracking them from the beginning to the final time available in the database. Figure 2 shows the coordinates of two particles starting from $x = 3.02,\ y = 3.57,\ z = 5.36$ (empty symbols) and $x = 3.97,\ y = 4.96,\ z = 4.29$ (solid symbols), and moving along with the local flow. The particles are tracked in the whole-time domain until $t \approx 45\tau_K$. Solid lines denote the integration done on a "local computer", whereas symbols denote the integration done using the *getPosition* function.

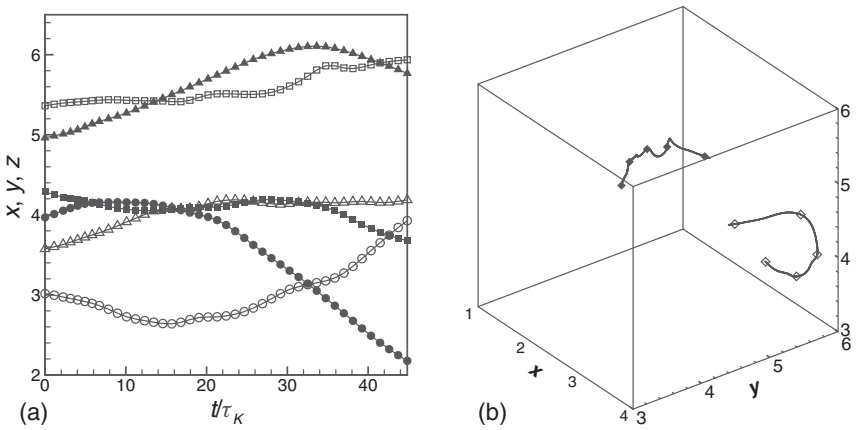


Figure 2. (a) Time evolution of two arbitrary fluid particles in *x, y, z* directions using the *getPosition* function (symbols) and local coding (lines) using the same integral algorithm. Circles: x; triangles: y, squares: z. Empty symbols: particle 1 starting from $x = 3.02,\ y = 3.57,\ z = 5.36$; solid symbols: particle 2 starting from $x = 3.97,\ y = 4.96,\ z = 4.29$. Lines denote the integration done on a "local computer", whereas symbols denote the integration done using the *getPosition* function. (b) 3D view of two particle tracks (symbols same as in part (a)).

A noticeable feature of *getPosition* compared to the Eulerian-based *getFunctions* is the time expense because of the needed small integration time-step and the need to call the *getVelocity* function twice in each integration step as described in Section 2 (Equations (1)–(4)). For large number of particles (e.g. over 100) and long integration time, the resulting calls can be very time-consuming if the particles are selected randomly in the entire domain. In practice, it is more efficient to collect particles from several randomly selected sub-cubes, e.g. consisting of 16^3 or 32^3 DNS grid-points. This is more efficient because it minimizes I/O of the data that are stored in atoms of size 72^3 [5]. Overall, more sampling particles are typically needed to achieve the same statistical convergence as compared to sampling randomly over the entire domain, but the overall efficiency is still significantly improved with such "sub-cube sampling".

When comparing the speed of the *GetPosition* function with the speed of tracking the particles on a local computer, we remark that it is difficult to obtain fully repeatable performance measures, since the performance depends greatly on typical network speeds and system load, which can vary greatly over time. Nevertheless, the relative trends as shown in Figure 3 are typically observed. The figure compares integration times when using *GetPosition* and particle tracking coded on a local computer ("local coding"), respectively, using exactly the same algorithm. To perform the comparison, we select 10 sub-cubes of size N (N grid-points on a side) at random locations, and track N^3 particles starting at each of the grid-points inside each sub-cube. We test two integration time-steps Δt_p and total tracking time $t_{ET} - t_{ST}$. The time required to finish the total integration is obtained for each of the 10 sub-cubes, and the times are averaged over 10 sub-cubes. Sub-cube sizes between $N = 2$ and $N = 49$ were used, corresponding 8 to 117,649 particles being tracked in each cube. In Figure 3, *getPosition* clearly shows the speedup against the local coding. For larger Δt_p and small $t_{ET} - t_{ST}$ in plot (a), the speedup increases suddenly as the particle number increases above ∼4000. For large particle numbers, the time expense to use the *getPosition* function can be three times less than tracking the particles on a local computer relying on data transfers at each intermediate time. For the case of smaller Δt_p and longer $t_{ET} - t_{ST}$

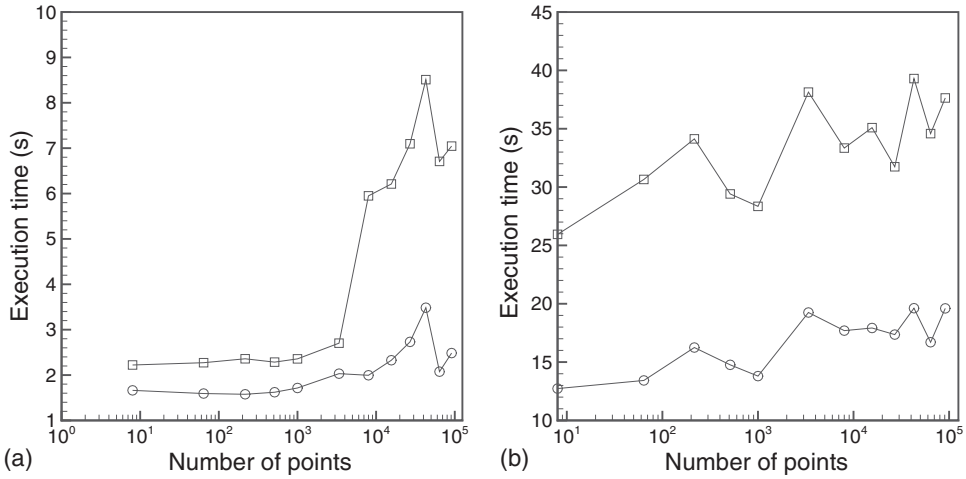


Figure 3. Performance comparison of *getPosition* (circles) vs. local coding (squares) of integration for particle tracking with integration time-step Δt_p and time $t = t_{ET} - t_{ST}$. (a) $\Delta t_p = 6.67 \times 10^{-4}$, $t_{ET} - t_{ST} = 6.0 \times 10^{-3}$; (b)$\Delta t_p = 4.0 \times 10^{-4}$, $t_{ET} - t_{ST} = 2.0 \times 10^{-2}$.

shown in plot (b), the execution time is observed to increase more gradually. The time required to finish the integration using *GetPosition* increases weakly even as the particle number increased significantly. This is because the sub-cube size (N) is always smaller than the 72^3 data-atoms. Hence, I/O needs are taxed about the same regardless of the value of N.

As mentioned before, the *getPosition* function may be used for backward tracking. An interesting test is to track particles forward in time, arrive at some final position, and then follow this operation by backward tracking for the same amount of time in order to determine how far from the original position the fluid particle has been displaced. In the absence of roundoff and discretization errors, one would expect the initial and final positions to be the same independent of time. In the presence of roundoff and discretization errors in a highly chaotic flow, one expects exponential spreading of fluid particle displacements, with the Lyapunov exponents of the order of the appropriate inverse eddy turnover time-scales. Suppose a fluid particle is located initially at $\mathbf{X}_p$. It is first tracked forward from the initial time $t_{ST} = 0$ until the time $t_{ET} = t$ using *getPosition* (with an integration time-step, $\Delta t_p = 0.0004$). The final positions are then used as initial positions for backward tracking, setting $t_{ST} = t$ and $t_{ET} = 0$ (with the same integration time-step $|\Delta t_p| = 0.0004$). We denote the return location as $\mathbf{X}'_p$. Such tracking is performed for a set of thousands of particles. For small t we track 10,000 particles, for intermediate t we use 6000 particles, and for long times ($t > 1.7$), a set of 2000 fluid particles is tracked. The difference between $\mathbf{X}_p$ and $\mathbf{X}'_p$ is quantified using the rms position-difference (denoted as $\delta x_{\rm rms}$, $\delta y_{\rm rms}$, and $\delta z_{\rm rms}$) of the three components of the position-difference vector $\mathbf{X}'_p - \mathbf{X}_p$.

The results from such forward and backward tracking tests are shown in Figure 4, where the three rms values are shown as functions of the forward–backward integration time t. At small t, the errors observed in Figure 4 are of the order of machine accuracy 10^{-7} and can thus be considered to be round-off errors. At larger t, the growth of rms displacement appears consistent with the Lyapunov exponents appropriate for different separation scales.

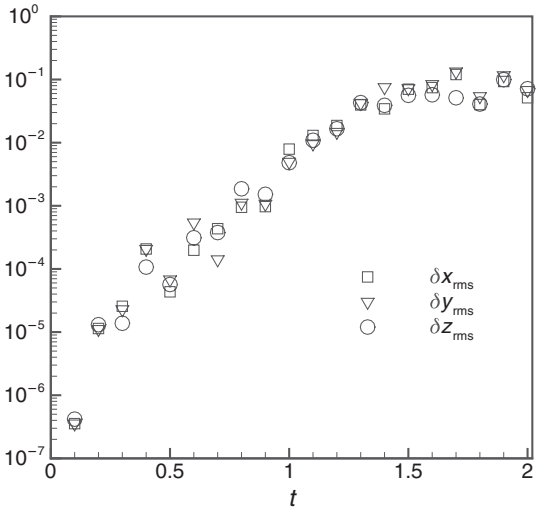


Figure 4. Root mean square of three coordinates of the position-difference vector arising from forward and backward fluid particle tracking using the *getPosition* function, plotted as function of forward–backward tracking time t.

At small t (at $t < \tau_K$), we expect that the errors will grow as $\sim \exp(t/\tau_K)$, where $\tau_K = 0.044$ is the Kolmogorov time-scale of the data. This translates into a relatively steep slope of $log_{10}(e)/0.044 \sim 10$. Up to times $t \approx 1$, the rms separation distance upon return remains smaller than one grid-spacing $dx \sim 6 \times 10^{-3}$. Once the separation distances grow to scales pertaining to the inertial range, one expects Lyapunov exponents of the order of $\epsilon^{1/3}\delta x_{\rm rms}^{-2/3}$ (where $\epsilon \approx 0.093$ is the mean dissipation rate of the data). For example, for $\delta x_{\rm rms} = 0.1$, this corresponds to a slope of $log_{10}(e) \times 0.093^{1/3} \times 0.1^{-2/3} \sim 0.9$ in the log-linear plot. The range of slopes mentioned is quite consistent with the trends observed in Figure 4.

3. Lagrangian velocity structure functions

In this section, the new *getPosition* function is used to evaluate the Lagrangian structure functions. It is well known that velocity differences across two points separated by a distance r are highly intermittent in the inertial range of scales for $\eta \ll r \ll L$ [29]. Much of the past evidence for intermittency has been obtained from Eulerian quantities, i.e. the moments of the spatial velocity increments. Among others, anomalous scaling of velocity increment moments, and the evolving shapes of their probability density functions (PDF) at different scales, are regarded as Eulerian hallmarks of intermittency [29]. Intermittency in temporal velocity statistics, which for proper Galilean invariance properties should be evaluated in the Lagrangian frame, moving with the fluid, has been studied in detail only more recently. This is due to advances in experimental techniques [22, 26, 27] and in computer simulations [30], as well as the availability of the Lagrangian time-series of turbulence (such as that from data described in [31]).

A quantity of central interest for Lagrangian studies of turbulence is the Lagrangian velocity structure function (LVSF). In analogy to the Eulerian velocity structure function, the LVSF is defined as

$$S_p(\tau) = < (\delta_\tau v)^p > = < [v(t+\tau) - v(t)]^p >, \tag{5}$$

where v denotes a single velocity component of a fluid particle. The time-lag is taken along a fluid particle trajectory. There have been detailed assessments of the scaling behavior, $S_p(\tau) = < (\delta_\tau v)^p > \sim \tau^{\xi(p)}$, with a focus on the scaling exponent $\xi(p)$ and its dependence on moment order p. Recently, Biferale et al [30] presented a detailed comparison between state-of-the-art experimental and numerical data of LVSF in turbulence. In their paper [30], the DNS data were obtained from a statistically homogeneous and isotropic turbulent flow with $Re_\lambda = 178$ and 284. The experimental data were obtained at Reynolds number ranging from $Re_\lambda = 350$ to 815 in a swirling water flow between counter-rotating baffled disks. They analyzed intermittency at both short, $\tau \approx \tau_\eta$, and intermediate, $\tau_\eta < \tau \ll T_L$, time-lags.

Here we use the DNS data ($Re_\lambda = 443$) in the JHU turbulence database to compute LVSFs. We use the *getPosition* function to track about 14, 000 fluid particle trajectories. For the sake of efficiency, when calling *getPosition* as mentioned above, we collect particle trajectories starting from sub-cubes chosen randomly from the entire domain, and then randomly select particles in each sub-cube. The particle number varies with the sub-cube size, as indicated in Table 1. The largest time-lag is about $45\tau_K$, within the database's available time range.

Figure 5 shows the compilation of the normalized second-order LSVFs at different Reynolds numbers from three datasets from DNS and four datasets from experimental measurements. The solid line is from the analysis of the data in the JHU turbulence

Table 1. Sub-cube sizes and particle numbers used for starting location of fluid particle tracking.

Sub-cube size	Number of sub-cubes	Particles per sub-cube	Total particle #
128	2	800	1600
64	20	400	8000
32	26	200	3200
16	15	100	1500

database, and symbols are reproduced from Figure 1 in Ref. [30]. Solid symbols are for two DNS results with relatively low Reynolds numbers and empty symbols are for experimental data. The second-order LVSF increases in a short time range ($\tau < \tau_K$), reaches maximum at $\tau \approx 5\tau_K$, and then decreases at large times ($\tau > 10\tau_K$). However, no extended plateau is observed in the intermediate time range, indicating that the power law regime typical of the inertial range has not yet been achieved. The trends are mostly consistent between low Reynolds DNS and high Reynolds experiments, although near the peak, the present results overshoot the experimental data by about 3%.

Based on the standard Kolmogorov scaling that assumes $S_p(\tau) \propto v_{\rm rms}^p Re_\lambda^{-p/2}(\tau/\tau_K)^{p/2}$ where the relations of $\varepsilon \propto v_{\rm rms}^3/L$ and $T_L/\tau_K \propto Re_\lambda$ have been used (see [30]), we plot the second- and fourth-order LVSF compensated using $Re_\lambda^{p/2}/v_{\rm rms}^p$ in Figure 6. Again, the solid line is from the JHU turbulence database and symbols are digitized from Figure 3 in Ref. [30]. It is seen that the solid line follows the trends of the other datasets quite well, with good collapse between various lines for different Reynolds numbers as indicated.

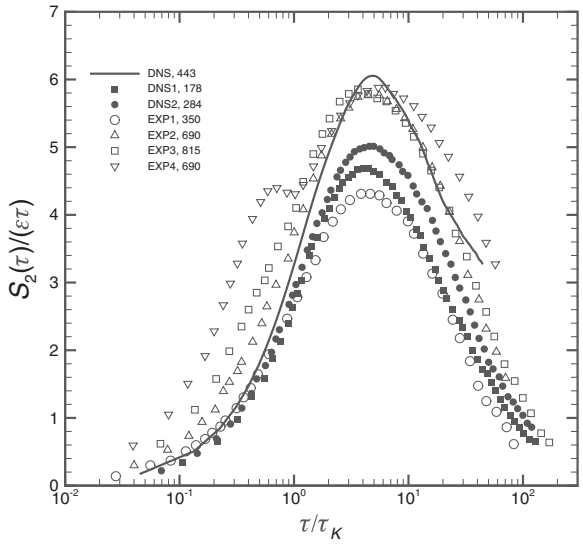


Figure 5. Time evolution of the normalized second-order Lagrangian velocity structure function (averaged over the three components), i.e. $S_2(\tau)/(\varepsilon\tau)$, at various Reynolds numbers in turbulence. The solid line is computed from the data in the JHU turbulence database ($R_\lambda = 443$), and solid symbols and empty symbols are reproduced from Figure 1 in Ref. [30].

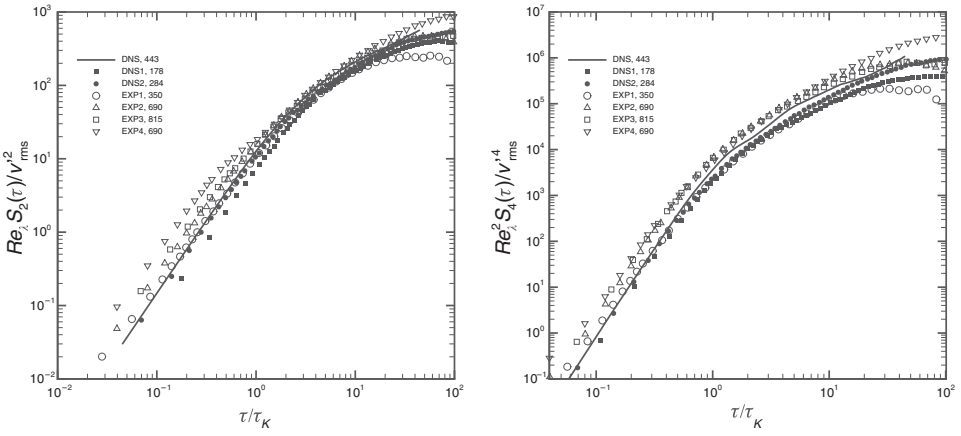


Figure 6. Log–log plots of the second- and forth-order LVSF compensated using $Re_\lambda^{p/2}/v_{\rm rms}^p$ vs. normalized time-lag. (a) $p = 2$; (b) $p = 4$. The solid line is computed from the JHU turbulence database ($R_\lambda = 443$), and solid and empty symbols are obtained from Figure 1 in Ref. [30].

It is concluded that the *getPosition* function can be used quite effectively to probe the Lagrangian statistics in turbulence. There is good agreement with prior data regarding temporal, Lagrangian structure functions.

4. Tensor-based Lagrangian time correlations of strain- and rotation-rates

The dynamics of the velocity gradient tensor A_{ij} is of significant interest [12] because it encodes rich information about turbulence through its nine components (in three dimensions). The Lagrangian autocorrelation time-scales for tensor elements themselves [7, 8, 32] are of particular interest in the construction of models and for general physical understanding. The time evolution of **A** following fluid particles can be obtained quite simply by taking the gradient of the NS equations. For incompressible flow, the resulting equation reads

$$\frac{dA_{ij}}{dt} = -A_{ik}A_{kj} - \frac{\partial^2 p}{\partial x_i \partial x_j} + \nu \frac{\partial^2 A_{ij}}{\partial x_k \partial x_k}, \tag{6}$$

where d/dt stands for the Lagrangian material derivative and p is the pressure divided by the density of the fluid. The first term on the right-hand side of Equation (6) denotes the nonlinear self-interaction of **A**, the second term is a tensor called pressure Hessian $P_{ij} \equiv \partial^2 p/\partial x_i \partial x_j$, and the third is the viscous term. The tensor **A** contains nine elements, among which eight components are independent, noticing the incompressibility condition. The elements by themselves are not coordinate system invariants. So rather than evaluating nine separate temporal autocorrelation functions for each tensor element, their characterization should be done more compactly in a frame-invariant fashion. With this in mind, as in [7] and [8], we use the tensor-based Lagrangian time correlation function of a second-rank tensor **C** defined as

$$\rho_{\mathbf{C}}(\tau) \equiv \frac{\langle C_{ij}(t_0)C_{ij}(t_0+\tau)\rangle}{\sqrt{\langle (C_{mn}(t_0))^2\rangle \cdot \langle (C_{pq}(t_0+\tau))^2\rangle}}. \tag{7}$$

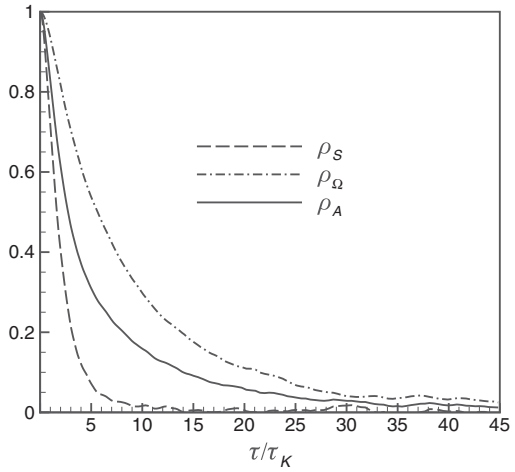


Figure 7. Lagrangian autocorrelation function of full tensor **A** (solid line), its symmetry part (dash dot line), and antisymmetric part (dash line).

The tensor **C** can be taken as **A** but the same can also be done for the strain-rate tensor $\mathbf{S} = \frac{1}{2}(\mathbf{A}+\mathbf{A}^T)$ and the rotation tensor $\mathbf{\Omega} = \frac{1}{2}(\mathbf{A}-\mathbf{A}^T)$, as well as the pressure Hessian tensor P_{ij} in Equation (6).

Measurements of $\rho_{\mathbf{C}}(\tau)$ for $C_{ij} = A_{ij}$, S_{ij}, and Ω_{ij} are performed using the JHU turbulence database, with the Lagrangian tracking done using the *getPosition* function. Over 10,000 fluid particles initially located at random positions in the whole domain are tracked over one large eddy turnover time. Tensor values are extracted along their trajectories. We show results on tensor-based Lagrangian autocorrelation functions of velocity gradient **A** and its related parts in Figure 7. Repeating the analysis already performed in [7] we also present the autocorrelation functions of **S** (dash line) and **Ω** (dash dot line). As shown in Figure 7 and discussed in [7], the rotation exhibits much more "persistence" in time than deformation rate. As can be expected, $\rho_{\mathbf{A}}$ (sold line in Figure 7) falls between $\rho_{\mathbf{S}}$ (dash line) and $\rho_{\mathbf{\Omega}}$ (dash dot line) because **A** is a linear combination of **S** and **Ω**. Quantitatively, as **S** completely loses its time memory when the time-lag is long enough ($\tau \sim 10\tau_K$), correlation functions of **A** and **Ω** display slower decay and lose most correlation after about $\tau \sim 30\tau_K$. These trends were already noted in [7]. While qualitatively this result is in good agreement with theoretical predictions [33], numerical simulations [34, 35], and experimental observations [36], here the difference between strain- and rotation-rates is much more marked than that implied by the prior studies, which focused on the scalar square-magnitudes of these variables.

A natural question to ask is, what are possible factors that cause the significant difference in decay rates between strain- and rotation-rates.

One possible factor for the slow decay of rotation-rate could be due to contributions from fluid particles that occur around and near small-scale vortical structures (worms). These structures are known to be relatively long-lived. Inside such structures, the vorticity would be relatively constant, pointing along the axis of the "worm", and thus the rotation tensor would be time-persistent in magnitude and direction. The idea then is to recompute the autocorrelation function by systematically including or excluding rotation-dominated flow regions. There are many ways to accomplish this, and we have experimented with several. In

the end, results pertaining to using the second invariant (Q-criterion) are qualitatively quite similar to those of the other criteria, so those based on the Q-criterion are presented here.

The second invariant of $\mathbf{A}$ is defined as $Q = -\frac{1}{2}Tr(\mathbf{AA}) = -\frac{1}{2}A_{ij}A_{ji} = \frac{1}{2}(\Omega_{ij}\Omega_{ij} - S_{ij}S_{ij})$ for an incompressible flow ($A_{ii} = 0$). It is often used to identify vortices as flow regions with positive Q, i.e. $Q > 0$ [37]. We undertake analysis using conditional averaging based on the Q-criterion at the initial time of the correlation function ($\tau = 0$), attempting to include ($Q(t_0) > 0$) or exclude ($Q(t_0) < 0$) initial points that are more or less likely to be part of "worms" (elongated rotation-dominated coherent structures). The conditional autocorrelations for rotation-rate $\mathbf{\Omega}$ are thus computed according to

$$\rho^{+}_{\mathbf{\Omega}}(\tau) \equiv \frac{\langle \Omega_{ij}(t_0)\Omega_{ij}(t_0+\tau)|Q(t_0) > 0\rangle}{\sqrt{\langle(\Omega_{mn}(t_0))^2|Q(t_0) > 0\rangle\langle(\Omega_{pq}(t_0+\tau))^2|Q(t_0) > 0\rangle}}, \tag{8}$$

and similarly $\rho^{-}_{\mathbf{\Omega}}(\tau)$ for $Q(t_0) < 0$.

In Figure 8, the line with filled symbols is for positive Q conditional averaging, designed to focus mostly on worms. It should be remarked that flow visualizations have shown that $Q > 0$ isolates quite successfully regions that visually correspond to elongated vortices in turbulence. Higher thresholds can also be used and the trends are qualitatively quite similar to those shown. Clearly, Figure 8 shows that the correlation decay is even slower if one focuses only on the rotation-dominated regions. But the difference with the unconditional results is not that particularly large. When conditioning on $Q < 0$, i.e. excluding entirely the rotation-dominated regions, the decay is slightly faster than the unconditional results. However, the decay is still considerably slower than the decay of $\mathbf{S}$. This demonstrates that

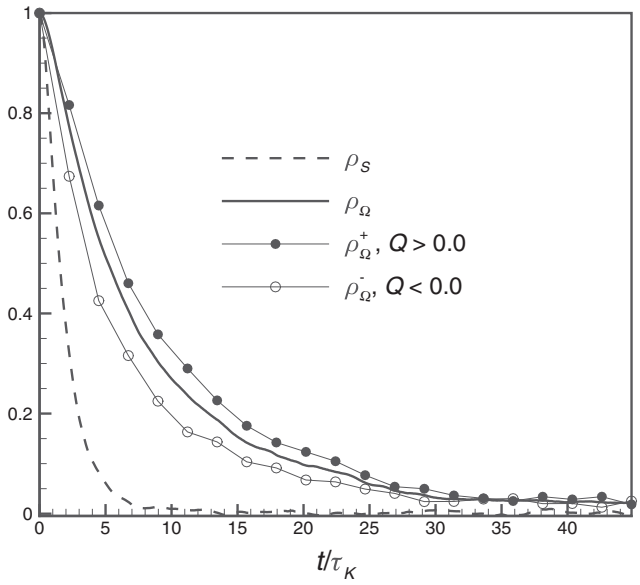


Figure 8. Conditional autocorrelations of rotation-rate tensor with different $Q(0) > 0$ and $Q(0) < 0$. Lines with filled symbols correspond to $Q(0) > 0$ (dominated by rotation, plausibly more associated to "worms") and lines with empty symbols correspond to $Q(0) < 0$ (exclusion of "worms" by focussing on strain-dominated regions). Solid and dashed lines are non-conditional autocorrelations of the rotation-rate tensor and strain-rate tensor, respectively.

the coherent structures ("worms") play a role in the slower decay rate of autocorrelation, but perhaps not a dominant role, and certainly not the only one.

Another possible cause for the rapid decay of strain-rate is the distinct role of the pressure Hessian. The coupled Equations (9) and (10) for Lagrangian evolutions of strain- and rotation-rate tensors can be easily derived from the evolution of the velocity tensor (Equation (6)) [38, 39]:

$$\frac{DS_{ij}}{Dt} = \Omega_{jk}\Omega_{ik} - S_{jk}S_{ik} - P_{ij} + \nu\nabla^2 S_{ij}, \tag{9}$$

$$\frac{D\Omega_{ij}}{Dt} = \Omega_{jk}S_{ik} - S_{jk}\Omega_{ik} + \nu\nabla^2 \Omega_{ij}. \tag{10}$$

In the equations, the symmetric pressure Hessian appears only in the evolution of strain-rate (Equation (9)), but not in the rotation-rate (Equation (10)), implying a direct effect of pressure on strain-rate but only an indirect effect on rotation-rate (through the vortex stretching and tilting by the strain-rate).

We use two ways to examine how pressure affects the dynamics of strain- and rotation-rates. First, we examine the correlation functions of terms on the right-hand side of Equation (9) with the rate-of-change of $\mathbf{S}$ respectively. Specifically, we look at the deviatoric parts of the pressure Hessian, $P^d_{ij} = -[P_{ij} - P_{kk}\delta_{ij}/3]$, and mutual interaction term, $M^d_{ij} = \Omega_{jk}\Omega_{ik} - S_{jk}S_{ik} - 1/3(\Omega_{mk}\Omega_{mk} - S_{np}S_{np})\delta_{ij}$. The correlation coefficient of the rate-of-change of $\mathbf{S}$, $\mathbf{a_S} = D\mathbf{S}/Dt$, with these terms is defined as,

$$\rho_{a_\mathbf{S}\mathbf{C}} = \frac{\langle a_{S_{ij}} C_{ij}\rangle}{\sqrt{\langle (a_{S_{mn}})^2\rangle \langle (C_{pq})^2\rangle}}, \tag{11}$$

where $\mathbf{C}$ can be $\mathbf{P}^d$ or $\mathbf{M}^d$. We find that the correlation of $\mathbf{P}^d$ with $a_\mathbf{S}$ ($\rho_{a_\mathbf{S}\mathbf{P}} \sim 0.75$) is much larger than that of $\mathbf{M}^d$ with $a_\mathbf{S}$ ($\rho_{a_\mathbf{S}\mathbf{M}} \sim 0.17$), implying that pressure Hessian (its deviatoric part) has a more dominant effect on the dynamics of strain-rate compared to the "velocity gradient self-interaction part". The pressure Hessian depends upon nonlocal flow processes that at any given position introduce additional randomness. Thus, the fact that the temporal decorrelation of strain-rate is much faster than that of rotation is to be expected if in its evolution equation the effects of pressure Hessian dominate rather than the self-stretching terms.

In order to explore the effects of various terms further, we investigate the dynamics of S_{ij} and Ω_{ij} systematically by integrating their evolution Equations (9) and (10), first including only the inviscid self-stretching terms without pressure or viscosity, then including the pressure Hessian term, and, finally, comparing the results to full DNS, which also includes viscous terms. Numerical time-integration of ODEs in Equations (9) and (10) is performed using the fourth-order Runge–Kutta algorithm in the cases with only self-stretching, and also with the pressure Hessian available in the JHU database. The values of S_{ij}, Ω_{ij}, and P_{ij} at the start time of the integration are retrieved along the trajectories. Over 10,000 fluid particle locations are tracked using the *GetPosition* function during the time evolution in order to obtain the instantaneous pressure Hessian components from the turbulence database. We compare the time correlations computed from the solutions of Equations (9) and (10) with the DNS data analysis. In Figure 9, solid symbols are for rotation rate, while empty symbols are for strain-rate. Three types of results are shown: circles (DNS analysis, i.e. including self-stretching inviscid terms, pressure Hessian, as well as viscous terms), squares (dynamics with self-stretching inviscid terms and pressure Hessian but without

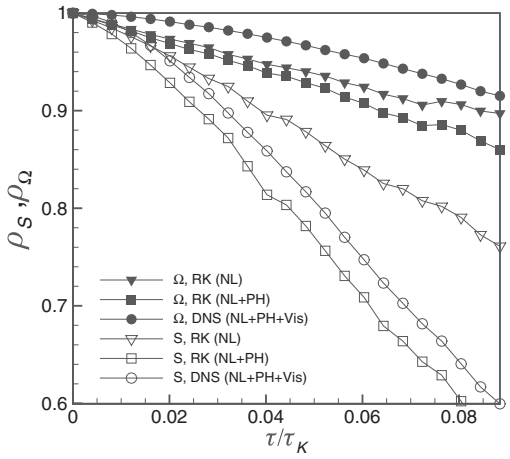


Figure 9. Lagrangian autocorrelation functions of strain- and rotation-rate tensors obtained through particle tracking in the DNS data (circles), and from the Runge–Kuta integration of strain- and rotation-rate tensors according to Equations (9) and (10), including the pressure Hessian term but without viscous terms (squares), and without the pressure Hessian term nor viscous terms (triangles). In all cases, time-integration is done following the same particle trajectories tracked in the database using the *GetPosition* function. NL: nonlinear term; PH: pressure Hessian term; Vis: viscous term.

viscous terms), and triangles (dynamics with self-stretching inviscid terms but without pressure Hessian and no viscous terms).

As can be seen in Figure 9, for the decay of the correlation function for the strain-rate, the pressure Hessian plays a dominant role in accelerating the decay-rate away from the longer time-scales it would have if only the inertial self-stretching terms were retained (triangles). Interestingly, if the pressure Hessian term is included but not the viscous term (squares), the decorrelation is even slightly faster than if the viscosity is included as in DNS. The difference is not major and we do not have any clear explanation why viscous forces would, in this case, slightly increase the memory of the strain-rate tensor evolution. Conversely, for the rotation memory, inclusion of pressure Hessian changes very little the decay of correlation. The change observed occurs because the strain-rate becomes more rapidly decorrelated with pressure effects, and this modulates the vortex stretching and tilting by the strain-rate tensor. Inclusion of viscous effects reduces correlation by a small further amount.

5. Testing the recent fluid deformation approximation to model pressure Hessian

In this subsection, we examine a recently proposed model for the anisotropic pressure Hessian term in Equation (6) that can be used in stochastic Lagrangian models for the velocity gradient tensor. As a background about the model, we recall that assuming the pressure Hessian is isotropic (i.e. neglecting $\partial^2_{ij} p - \partial^2_{kk} p\, \delta_{ij}/3$) and neglecting the viscous term in Equation (6) leads to a closed formulation for **A**, the so-called Restricted-Euler (RE) equation. The RE system is a set of nine (eight independent) ordinary differential equations for A_{ij} that has analytical solutions [40]. Remarkably, this simple system is already sufficient to explain a number of non-trivial geometrical trends found in real turbulence [40, 41]. Nevertheless, the RE system leads to nonphysical finite-time singularities because the self-stretching is not constrained by any energy exchange or loss mechanism in the system. In

the past two decades, modeling efforts have aimed at regularizing the RE system to avoid the nonphysical singularity (see [12] for a review). One of the efforts is the recent fluid deformation approximation (RFDA) as proposed in [42]. The starting point of RFDA is the Eulerian–Lagrangian change of variables,

$$\frac{\partial^2 p(\mathbf{x},t)}{\partial x_i \partial x_j} \approx \frac{\partial x_{p,m}}{\partial x_i}\frac{\partial x_{p,n}}{\partial x_j}\frac{\partial^2 p(\mathbf{x},t)}{\partial x_{p,m}\partial x_{p,n}}, \tag{12}$$

where spatial gradients of $D_{ij} = \frac{\partial x_i}{\partial x_{p,j}}$ are neglected. As mentioned above, $\mathbf{x}$ and $\mathbf{x}_p$ denote the Eulerian space location and the Lagrangian particle location, respectively. The Lagrangian pressure Hessian, $\frac{\partial^2 p(\mathbf{x},t)}{\partial x_{p,m}\partial x_{p,n}}$, is modeled as an isotropic tensor based on the assumption that as time progresses, one loses memory about relative orientations of the initial locations $\mathbf{x}_p$ as far as the present value of pressure is concerned. By introducing the Cauchy-Green tensor $\mathbf{C}$, $C_{ij} \equiv \frac{\partial x_i}{\partial x_{p,m}}\frac{\partial x_j}{\partial x_{p,n}}$, and using the Poisson equation as a constraint, the pressure Hessian becomes

$$\frac{\partial^2 p(\mathbf{x},t)}{\partial x_i \partial x_j} = -\frac{Tr(\mathbf{A}^2)}{Tr(\mathbf{C}^{-1})}C^{-1}_{ij}. \tag{13}$$

Based on the idea that any causal relationship between initial and present orientations will be lost after a characteristic Lagrangian correlation time-scale of tensor $\mathbf{A}$, the Cauchy-Green tensor $\mathbf{C}$ in Equation (13) is further replaced by a new tensor called the "recent Cauchy-Green tensor" $\mathbf{C}_{\tau_K}$ that can be expressed in terms of simple matrix exponentials, $\mathbf{C}_{\tau_K} = e^{\tau_K \mathbf{A}} e^{\tau_K \mathbf{A}^T}$.

The trace of the pressure Hessian requires no modeling, since it is equal to the trace of $-\mathbf{A}^2$, by construction in the model, and by the incompressibility condition in real turbulence. Hence, we only examine the deviatoric part of this tensor. We compare the temporal autocorrelations of the deviatoric pressure Hessian by using the tensor-based correlation function as defined in Equation (7). Particle tracks are evaluated using the *GetPosition* function using over 10,000 particles. The model uses matrix exponential evaluations [43]. The results are shown in Figure 10. The dashed line is from the RFDA-based model, and the solid line from DNS. It is seen that the autocorrelations computed from the model decay more slowly than DNS. The deviatoric pressure Hessian in DNS looses most of its memory at $\tau \approx 1.5\tau_K$, whereas the model term maintains some memory up to $\tau \approx 4\tau_K$. While the model has shown promise in predicting many features of the velocity gradient tensor in turbulence [42, 44], challenges remain in applications at high Reynolds numbers. The present observations of differing correlation times may point to possible improvements in the model.

Next, we test how the modeled pressure Hessian captures features of individual realizations and time-series of the two most relevant invariants of the velocity gradient $\mathbf{A}$, the Q and R invariants. Q has already been defined as $Q = -\frac{1}{2}A_{ij}A_{ji}$, while R is given by $R = -\frac{1}{3}A_{ij}A_{jk}A_{ki}$. Physically these invariants are interpreted as quantifying the competition of enstrophy versus dissipation, and of enstrophy production versus dissipation production, respectively. The dynamics and statistics of these two variables have attracted much interest. Their evolution equations are derived by forming appropriate products with

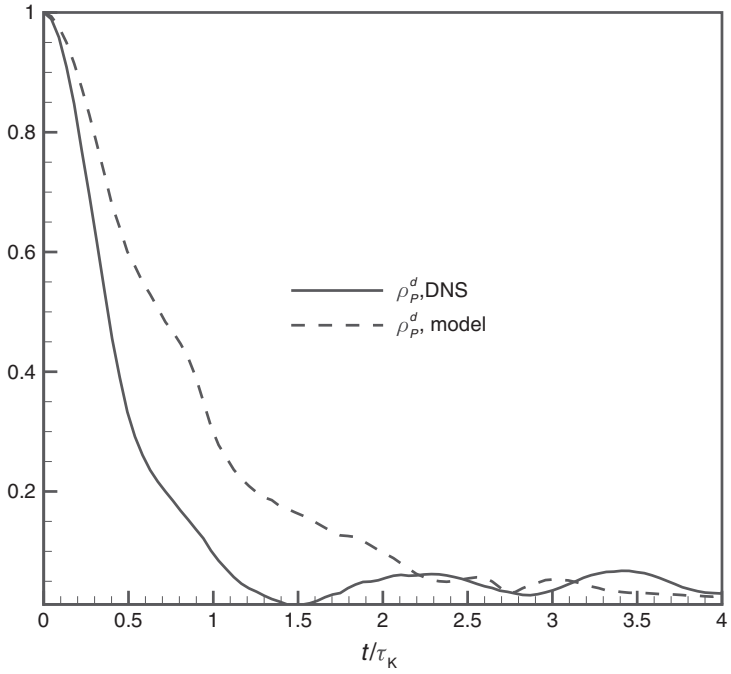


Figure 10. The Lagrangian autocorrelation function of deviatoric pressure Hessian from DNS (solid line) and modeling (dash line).

Equation (6) and taking the trace [40]:

$$\frac{dQ}{dt} = -3R - A_{ik}P_{ki} - A_{ik}V_{ki}, \tag{14}$$

$$\frac{dR}{dt} = \frac{2Q^2}{3} - A_{ij}A_{jk}P_{ki} - A_{ij}A_{jk}V_{ki}, \tag{15}$$

where $V_{ij} \equiv \nu\partial^2 A/\partial x_i \partial x_j$.

We track a single particle and record a time-series of relevant terms across the entire time range available in the database. Figure 11 shows various terms from DNS. The dashed line is the rate of change of Q and R as evaluated from their database values along the trajectory, the circles are the restricted Euler self-stretching term, the solid line comes from the pressure Hessian, and the triangles are viscous terms. The viscous term is evaluated based on taking the difference of other terms on the right-hand side to the temporal rates of change of Q and R.

As can be seen, the dynamics are highly intermittent with a sudden, rapid burst of activity near $t/\tau_K \sim 31$ for this particular fluid particle's history. It is observed that the pressure Hessian is a major contribution to the sum and it mainly opposes self-stretching, whereas the viscous term is small and contributes only marginally. Very interestingly, close examination shows that the pressure Hessian has a "phase delay" that follows rapid changes in the velocity gradient invariants. The delay appears to be of the order of $\sim \frac{1}{2}\tau_K$.

Next, the ability of the RFDA-based model in [42] for pressure Hessian to predict the effects on the invariants is shown by providing an enlarged view of time-series in

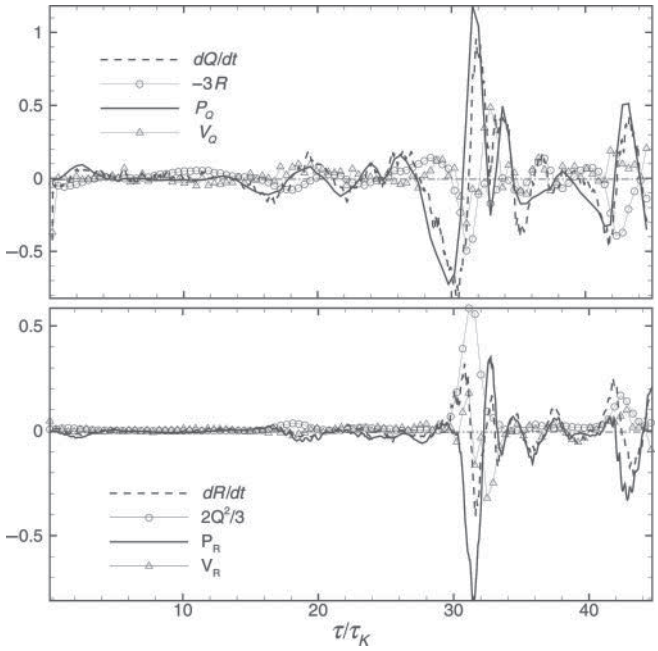


Figure 11. Sample time-series for various terms in the evolution of Q (top) and R(bottom) for some fluid particle along its trajectory during the entire time duration in the database (approximately one large-eddy turnover time).

the vicinity where the burst of activity is observed. In Figure 12 we compare the DNS pressure Hessian term with that predicted by the RFDA model, where the pressure Hessian contracted with A_{ij} and $A_{ik}A_{kj}$ is obtained from the RFDA-based model. Qualitatively, there is a general agreement of the occurrences of large peaks, and their signs. However, the model amplitudes appear to be somewhat too large, and the model does not predict some of the smaller amplitude fluctuations. It is also quite obvious that the model "predates" the real pressure Hessian by about $\sim \frac{1}{2}\tau_K$, which is not surprising, since it is based on the local velocity gradient tensor through the matrix exponential closure. Finally, the previous observations can be made more quantitative by computing the two-time cross-correlation function between the real and modeled pressure Hessian tensors. We use an expression similar to Equation (7) written as a cross-correlation between two different tensor time signals. In particular, in Equation (7) we take $C_{ij}(t_0)$ to be the modeled pressure Hessian, and $C_{ij}(t_0 + \tau)$ to be the real Hessian tensor. Figure 13 shows the resulting cross-correlation function. It confirms the prior observations: There is a peak correlation after a time delay of about $\sim \frac{1}{2}\tau_K$ so that the model predates the real pressure Hessian signal in time. The correlation peak of around 40% is quite substantial, given the many assumptions made in deriving the model. Such observations will be useful in motivating further improvements to the model.

6. Summary and discussion

This paper describes algorithms and implementation details of updates to the JHU turbulence public database system, made after the first publication [5] describing the original

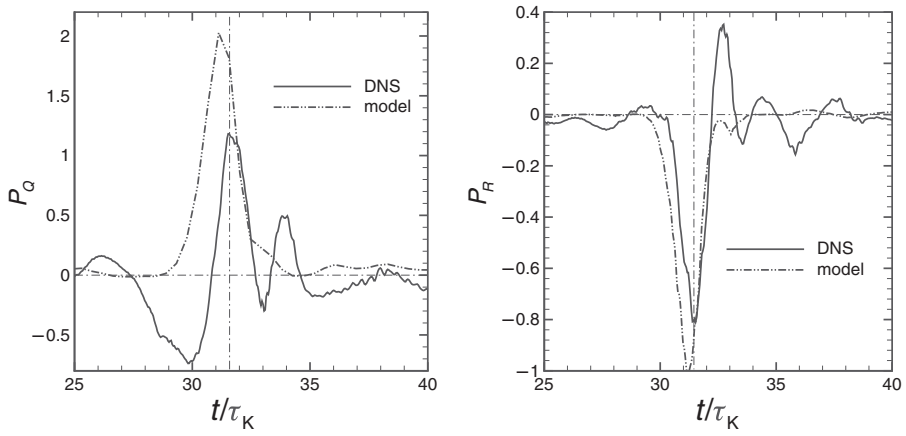


Figure 12. Contributions of pressure Hessian to the dynamics of Q (left) and R (right). DNS: solid line; model: dash line.

system. The updates include new *GetFunction*s, namely *GetPosition*, to track a number of fluid particles moving along with the simulated flow and is useful in Lagrangian studies of turbulence. Also, the *GetForce* function is developed in order to query the forcing term that was used in DNS during simulation (see Appendix A).

Table 2 lists the complete *getFunction*s available for use.

Other recent upgrades also include improved interpolation schemes (Appendix B) and a new library for Matlab access (Appendix C).

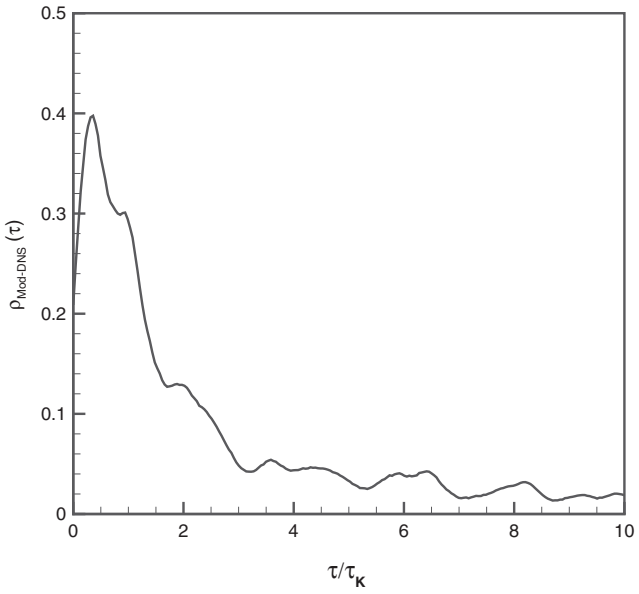


Figure 13. Two-time cross-correlation function between real and modeled pressure Hessian (its deviatoric part).

Table 2. List of *GetFunctions* for queries to the JHU turbulence public database. The entries mean the following. diff: differentiation (FD: centered finite difference, options for 4th-, 6th-, and 8th-order accuracies); int: interpolation type (NoInt: no interpolation; Lag: Lagrangian polynomial interpolation, options for 4th-, 6th-, and 8th-order accuracies); PCHIP: piecewise cubic Hermite interpolation.

Function name	Spatial diff.	Spatial int.	Temporal int.	Outputs
GetVelocity	–	NoInt, Lag 4,6,8	NoInt, PCHIP	u_i
GetVelocityAndPressure	–	NoInt, Lag 4,6,8	NoInt, PCHIP	u_i, p
GetVelocityGradient	FD 4,6,8	NoInt, Lag 4,6,8	NoInt, PCHIP	$\frac{\partial u_i}{\partial x_j}$
GetPressureGradient	FD 4,6,8	NoInt, Lag 4,6,8	NoInt, PCHIP	$\frac{\partial p}{\partial x_i}$
GetVelocityHessian	FD 4,6,8	NoInt, Lag 4,6,8	NoInt, PCHIP	$\frac{\partial^2 u_k}{\partial x_i \partial x_j}$
GetPressureHessian	FD 4,6,8	NoInt, Lag 4,6,8	NoInt, PCHIP	$\frac{\partial^2 p}{\partial x_i \partial x_j}$
GetVelocityLaplacian	FD 4,6,8	NoInt, Lag 4,6,8	NoInt, PCHIP	$\frac{\partial^2 u_i}{\partial x_j \partial x_j}$
GetForce	–	NoInt, Lag 4,6,8	NoInt, PCHIP	f_i
GetPosition	–	Lag 4,6,8	PCHIP	$x_i(t_{ET})$

The new *GetPosition* function was applied to measure various Lagrangian statistical features of turbulence. In terms of Lagrangian structure functions, we document good agreement with a variety of previously published results, both numerical and experimental. New results are obtained in characterizing the precise effects of pressure Hessian and viscous terms in the Lagrangian evolution of the strain- and rotation-rate tensors. The faster decay of autocorrelation for the strain-rate tensor is confirmed to be, clearly, related to the pressure Hessian effects. They tend to be more "stochastic" than the self-stretching terms. The viscous terms were seen to slightly enhance the memory for the strain-rate while decreasing memory for the rotation-rate (or vorticity).

The new tool was also used to examine the time evolution of pressure Hessian and to compare it with a recent model based on the local velocity gradient tensor. The comparisons were made using the Lagrangian autocorrelation function and its rate of decay, comparing DNS with the model. It was found that the model decays more slowly, showing that the true pressure Hessian has dynamics that are more short lived than the velocity gradients upon which the model is based. Some representative observations about the model were also made on hand of individual time traces along Lagrangian trajectories, comparing terms in the equations of invariants Q and R. It is observed that the pressure Hessian "lags" strong excursions in velocity gradients, consistent with a "restitution mechanism" that needs some time to build up the required response.

Further ongoing developments of the public database system include additional datasets such as magneto-hydrodynamic turbulence, and turbulent channel flow.

Acknowledgements

The authors acknowledge the valuable assistance from other members of the database team (Jan VandeBerg, Rich Ercolani, Sue Werner, and Victor Paul). This research is supported by a National

Science Foundation CDI-II grant no. CMMI-0941530. E. Frederick acknowledges international travel support from the Eindhoven University of Technology.

References

[1] P.K. Yeung, S.B. Pope, and B.L. Sawford, *Reynolds number dependence of Lagrangian statistics in large numerical simulations of isotropic turbulence*, J. Turbul. 7 (2006), N58.

[2] S. Hoyas and J. Jimenez, *Scaling of velocity fluctuations in turbulent channels up to* $Re_\tau = 2000$, Phys. Fluids 18 (2006), 011702.

[3] J. Schumacher, K.R. Sreenivasan, and V. Yakhot, *Asymptotic exponents from low-Reynolds number flows*, New J. Phys. 89 (2007), pp. 1–19.

[4] T. Ishihara, T. Gotoh, and Y. Kaneda, *Study of high Reynolds number isotropic turbulence by direct numerical simulation*, Annu. Rev. Fluid Mech. 41 (2009), pp. 4165–4180.

[5] Y. Li, E. Perlman, M. Wan, Y. Yang, R. Burns, C. Meneveau, R. Burns, S. Chen, A. Szalay, and G. Eyink, *A public turbulence database cluster and applications to study Lagrangian evolution of velocity increments in turbulence*, J. Turbul. 9 (2008), p. N31.

[6] B. Lüthi, M. Holzner, and A. Tsinober, *Expanding the Q-R space to three dimensions*, J. Fluid Mech. 641 (2009), pp. 497–501.

[7] H. Yu and C. Meneveau, *Lagrangian refined Kolmogorov similarity hypothesis for gradient time-evolution in turbulent flows*, Phys. Rev. Lett. 104 (2010), 084502.

[8] H. Yu and C. Meneveau, *Scaling of conditional Lagrangian time correlation functions of velocity and pressure gradient magnitudes in isotropic turbulence*, Flow Turbul. Combust. 85 (2010), pp. 457–472.

[9] M. Holzner, M. Guala, B. Lüthi, A. Liberzon, N. Nikitin, W. Kinzelbach, and A. Tsinober, *Viscous tilting and production of vorticity in homogeneous turbulence*, Phys. Fluids 22 (2010), 061701.

[10] A.G. Gungor and S. Menon, *A new two-scale model for large eddy simulation of wall-bounded flows*, Prog. Aero. Sci. 46 (2010), pp. 28–45.

[11] W. Liu and E. Ribeiro, *Scale and rotation invariant detection of singular patterns in vector flow fields*, SSPR & SPR Proceedings of the 2010 Joint IAPR International Conference on Structural, Syntactic, and Statistical Pattern Recognition, LNCS No. 6218, pp. 522–531.

[12] C. Meneveau, *Lagrangian dynamics and models of the velocity gradient tensor in turbulent flows*, Annu. Rev. Fluid Mech. 43 (2011), pp. 219–245.

[13] C.C. Wu and T. Chang, *Rank-ordered multifractal analysis (ROMA) of probability distributions in fluid turbulence*, Nonlinear Processes Geophys. 18 (2011), pp. 261–268.

[14] G.L. Eyink, *Stochastic flux freezing and magnetic dynamo*, Phys. Rev. E, 83 (2011), 056405.

[15] F. Toschi, *iCFDdatabase2*, available at http://mp0806.cineca.it/icfd.php (accessed December 2011).

[16] G.I. Taylor, *Diffusion by continuous movements*, Proc. London Math. Soc. 20 (1922), pp. 196–212.

[17] L.F. Richardson, *Atmospheric diffusion shown on a distance-neighbor graph*, Proc. R. Soc. London, Ser. A 110 (1926), pp. 709–737.
[18] A.N. Kolmogorov, *The local structure of turbulence in incompressible viscous fluid for very large Reynolds numbers*, Dokl. Akad. Nauk SSSR 30 (1941), pp. 301–314; also Proc. R. Soc. A 434 (1991), pp. 9–13.
[19] B.I. Shraiman and E.D. Siggia, *Scalar turbulence*, Nature 405 (2000), pp. 639–646.
[20] B. Sawford, *Turbulent relative dispersion*, Annu. Rev. Fluid Mech. 33 (2001), p. 289–317.
[21] P.K. Yeung, *Lagrangian investigations of turbulence*, Annu. Rev. Fluid Mech. 34 (2002), pp. 115–142.
[22] F. Toschi and E. Bodenschatz, *Lagrangian properties of particles in turbulence*, Annu. Rev. Fluid Mech. 41 (2009), pp. 375–404.
[23] G. Falkovich, K. Gawedzki, and M. Vergassola, *Particles and fields in fluid turbulence*, Rev. Mod. Phys. 73 (2001), pp. 913–975.
[24] M. Holzner, A. Liberzon, N. Nikitin, B. Lüthi, W. Kinzelbach, and A. Tsinober, *A Lagrangian investigation of the small-scale features of turbulent entrainment through particle tracking and direct numerical simulation*, J. Fluid Mech. 598 (2008), pp. 465–475.
[25] S.B. Pope, *Lagrangian PDF methods for turbulent flows*, Annu. Rev. Fluid Mech. 26 (1994), pp. 23–63.
[26] R. Zimmermann, H.T. Xu, Y. Gasteuil, M, Bourgoin, R. Volk, J.F. Pinton, and E. Bodenschatz, *The Lagrangian exploration module: An apparatus for the study of statistically homogeneous and isotropic turbulence*, Rev. Sci. Instrum. 81 (2010), 055112.
[27] D.H. Kelley and N.T. Ouellette, *Separating stretching from folding in fluid mixing*, Nature Phys. 7 (2011), pp. 477–480.
[28] Szalay, A., S.P.Z. Kunszt, A. Thakar, J. Gray, D. Slutz, and R.J. Brunner *Designing and mining multi-terabyte astronomy archives: The Sloan digital sky survey*, Proceedings of the ACM SIGMOD International Conference on Management of Data, Dallas, TX, 2000.
[29] U. Frisch, *Turbulence: The legacy of A. N. Kolmogorov*, Cambridge University Press, Cambridge, UK, 1995.
[30] L. Biferale, E. Bodenschatz, M. Cencini, A.S. Lanotte, N.T. Ouellette, F. Toschi, and H. Xu, *Lagrangian structure functions in turbulence: A quantitative comparison between experiment and direct numerical simulation*, Phys. Fluids 20 (2008), 065103.
[31] L. Biferale, G. Boffetta, A. Celani, A. Lanotte, and F. Toschi, *Particle trapping in three-dimensional fully developed turbulence*, Phys. Fluids 17 (2005), 021701.
[32] R. Benzi, L. Biferale, E. Calzavarini, D. Lohse, and F. Toschi, *Velocity-gradient statistics along particle trajectories in turbulent flows: The refined similarity hypothesis in the Lagrangian frame*, Phys. Rev. E 80 (2009), 066318.
[33] R.H. Kraichnan and J.R. Herring, *A strain-based Lagrangian-history turbulence theory,* J. Fluid Mech. 88 (1978), pp. 355–367.
[34] P.K. Yeung, *Lagrangian characteristics of turbulence and scalar transport in direct numerical simulations*, J. Fluid Mech. 427 (2001), pp. 241–274.
[35] P.K. Yeung, S.B. Pope, E.A. Kurth, and A.G. Lamorgese, *Lagrangian conditional statistics, acceleration and local relative motion in numerically simulated isotropic turbulence*, J. Fluid Mech. 582 (2007), pp. 399–422.

[36] M. Guala, A. Liberzon, A. Tsinober, and W. Kinzelbach, *An experimental investigation on Lagrangian correlations of small-scale turbulence at low Reynolds number*, J. Fluid Mech. 574 (2007), pp. 405–427.
[37] J.C.R. Hunt, A.A. Wray, and P. Moin, *Eddies, stream, and convergence zones in turbulent flows*, Research Rep. CTR-S88, Center for Turbulence, Stanford University Stanford, CA, pp. 193–208, 1988.
[38] K.K. Nomura and G.K. Post, *The structure and dynamics of vorticity and rate of strain in incompressible homogeneous turbulence*, J. Fluid Mech. 377 (1998), pp. 65–97.
[39] A. Tsinober, *An Informal Conceptual Introduction to Turbulence*, 2nd ed., Springer, New York, 2009.
[40] B.J. Cantwell, *Exact solution of a restricted Euler equation*, Phys. Fluids A 4 (1992), p. 782.
[41] P. Vieillefosse, *Local interaction between vorticity and shear in a perfect incompressible fluid*, J. Phys. (France) 43 (1982), p. 837.
[42] L. Chevillard and C. Meneveau, *Lagrangian dynamics and statistical geometric structure of turbulence*, Phys. Rev. Lett. 97 (2006), 174501.
[43] Y. Li, L. Chevillard, G.L. Eyink, and C. Meneveau, *Matrix exponential-based closures for the turbulent subgrid-scale stress tensor*, Phys. Rev. E, 79 (2009), 016305.
[44] L. Chevillard, L. Biferale, F. Toschi, and C. Meneveau, *Modeling the pressure Hessian and viscous Laplacian in turbulence: Comparisons with DNS and implications on velocity gradient dynamics*, Phys. Fluids 20 (2008), 101504.
[45] K. Kanov, E. Perlman, R. Burns, Y. Ahmad, and A. Szalay, *I/O streaming evaluation of batch queries for data-intensive computational turbulence*, Supercomputing 2011.
[46] R.J. Purser and L.M. Leslie, *An efficient interpolation procedure for high-order three-dimensional semi-Lagrangian models*, Mon. Weather Rev. 119 (1991), p. 2492.

Appendix A. *GetForce* function

Information about the forcing term $f_i(x, y, z, t)$ (force per unit mass, $i = x, y, z$) applied during DNS has been stored in the database and can be retrieved using the function *GetForce*.

During DNS, an effective forcing is applied in Fourier space by rescaling low-k Fourier modes (with magnitudes $0.5 \leq k \leq 2.5$, $k = \sqrt{k_x^2 + k_y^2 + k_z^2}$) to maintain their kinetic energy to prescribed values consistent with the $-5/3$ spectrum. The forcing region is divided into two shells, $0.5 \leq k \leq 1.5$ and $1.5 < k \leq 2.5$. The spectrum is held fixed at a value of 0.3 in shell $0.5 \leq k \leq 1.5$, and at a value equal to 0.13 in shell $1.5 < k \leq 2.5$ shell (these values are obtained empirically so that the simulated spectrum is close to a $k^{-5/3}$ trend at low k).

In order to represent rescaling in terms of a forcing term, we express time-advancement in terms of a first-order time-advancement and write the discretized Navier–Stokes equation (NSE) in Fourier space as follows:

$$\hat{u}_i^{n+1}(k_x, k_y, k_z) = \hat{u}_i^{n+}(k_x, k_y, k_z) + \hat{f}_i(k_x, k_y, k_z)dt, \tag{A1}$$

in which $\hat{u}_i^{n+} = \hat{u}_i^n + (\cdots)dt$ with $(\cdots)$ for terms on the right-hand side of NSE, but excluding the forcing term. Also, dt is the time-step of the DNS.

In the DNS, the rescaling induces a difference between $\hat{u}_i^{n+}$ and $\hat{u}_i^n$ in the wave-number range $0.5 \leq k \leq 2.5$ that is equivalent to a force-term defined in two shells as follows:

$$\hat{f}_i^n(k_x, k_y, k_z) = \frac{1}{dt}\left(\frac{0.55}{\sqrt{\sum_{0.5\leq k\leq 1.5}[(\hat{u}_x^{n+})^2 + (\hat{u}_y^{n+})^2 + (\hat{u}_z^{n+})^2)]/2}} - 1\right) \hat{u}_i^{n+}(k_x, k_y, k_z) \tag{A2}$$

for shell $0.5 \leq k \leq 1.5$ and

$$\hat{f}_i^n(k_x, k_y, k_z) = \frac{1}{dt}\left(\frac{0.36}{\sqrt{\sum_{1.5\leq k\leq 2.5}[(\hat{u}_x^{n+})^2 + (\hat{u}_y^{n+})^2 + (\hat{u}_z^{n+})^2)]/2}} - 1\right) \hat{u}_i^{n+}(k_x, k_y, k_z) \tag{A3}$$

for shell $1.5 < k \leq 2.5$, where $\hat{u}_x$, $\hat{u}_y$, $\hat{u}_z$ denote the three velocity components in Fourier space and $k = \sqrt{k_x^2 + k_y^2 + k_z^2}$ is the magnitude of wavenumber vector $\mathbf{k}$. In this way, the energy in these shells $E(k=1) = \sum_{0.5\leq k\leq 1.5}(\hat{u}_x^2 + \hat{u}_y^2 + \hat{u}_z^2)/2$ and $E(k=2) = \sum_{1.5<k\leq 2.5}(\hat{u}_x^2 + \hat{u}_y^2 + \hat{u}_z^2)/2$ is maintained at 0.3 and 0.13.

There exist in total 80 discrete wave-number modes in these two shells. There are 20 modes for $k_x = 0$, 30 modes for $k_x > 0$, and another 30 modes for $k_x < 0$. In the database, the complex Fourier coefficients $\hat{f}_x$, $\hat{f}_y$, $\hat{f}_z$ corresponding to $k_x \geq 0$ (50 modes) are stored, the remaining 30 modes ($k_x < 0$) are the conjugates of modes $k_x > 0$.

Using the *GetForce* function, force values at any prescribed position (x, y, z) are evaluated in the database from the forcing's Fourier coefficients using direct summation of the Fourier series according to

$$f_i(x, y, z, t_n) = \sum_{k_x,k_y,k_z} e^{i(k_x x + k_y y + k_z z)}\ \hat{f}_i^n(k_x, k_y, k_z), \tag{A4}$$

where i can be x, y, and z. Values of $f_i(x, y, z, t)$ at arbitrary times t can be obtained by specifying PCHIP temporal interpolation.

In order to document the use of this function, we examine various terms in the NSE,

$$\partial_t \mathbf{u} + \mathbf{u}\cdot\nabla\mathbf{u} = -\nabla p + \nu\nabla^2\mathbf{u} + \mathbf{f} \tag{A5}$$

that were solved during DNS (as explained above, the forcing term is implicitly included in the spectral rescaling at every time-step). We evaluate the local square error defined according to

$$\sigma_{dif}^2 = \langle[\partial_t \mathbf{u} + \mathbf{u}\cdot\nabla\mathbf{u} - (-\nabla p + \nu\nabla^2\mathbf{u} + \beta\mathbf{f})]^2\rangle. \tag{A6}$$

The goal is to compare the case where we include ($\beta = 1$) and do not include ($\beta = 0$), the forcing term. We would expect that including the forcing term should reduce the error. If we evaluate the velocity gradients occurring in the nonlinear term, the pressure gradient, and the viscous Laplacian using pseudo-spectral differentiation, and use the same time-differentiation as used in the DNS, the error should be exactly zero (to machine accuracy)

at every point in the domain. However, if we use the spatial finite differencing available in the *getFunction*s, and the first-order time derivative, some error is expected. Instead, if we box-filter each of the terms in boxes of size $\Re$, with increasing $\Re$ the error would be expected to become smaller. Especially the difference between including and not including the forcing term (which by construction only affects the largest scales of the flow) is expected to become larger as $\Re$ grows.

Thus, we also define the error associated with the coarse-grained terms according to

$$\sigma^2_{dif,\Re} = \langle([\partial_t \mathbf{u} + \mathbf{u}\cdot\nabla\mathbf{u}]_\Re - [(-\nabla p + \nu\nabla^2\mathbf{u} + \beta\mathbf{f}]_\Re))^2\rangle. \tag{A7}$$

The square brackets $[...]_\Re$ denote box-filtering in a cube of size $\Re$. In Figure A1 we show dependence of the rms error $\sigma_{dif,\Re}$ as a function of $\Re$.

The computation of σ_{dif} follows three steps: First, randomly generate N cubes with size $\Re$ in the whole domain; second, collect all the terms in Equation (A5) by calling *getVelocity*, *getVelocityGradient* for the left-hand side and *getPressureGradient, getVelocityLaplacian*, and *getForce* for the right-hand side for every point in each cube and compute the mean of each term; third, evaluate the square error. The filter size $\Re$ varies from 0.006 to 0.3, corresponding 1 to 49 grid-points. In the figure, it is seen that when the filter size is small, say $\Re < 0.02$, forcing seems not to play a role because the numerical errors introduced from differentiation and time/spatial interpolations dominate and suppress any effects of the forcing term. As filter size increases, the numerical errors fade such that the forcing term becomes more important. When the filter size is large enough, e.g. $\Re > 0.2$, the difference between left- and right-hand sides of Equation (A5) vanishes when forcing is included, while $\sigma_{\mathrm{rms},\Re}$ without forcing remains quite large, making the effects of the forcing term apparent in closing the balance in the momentum equation.

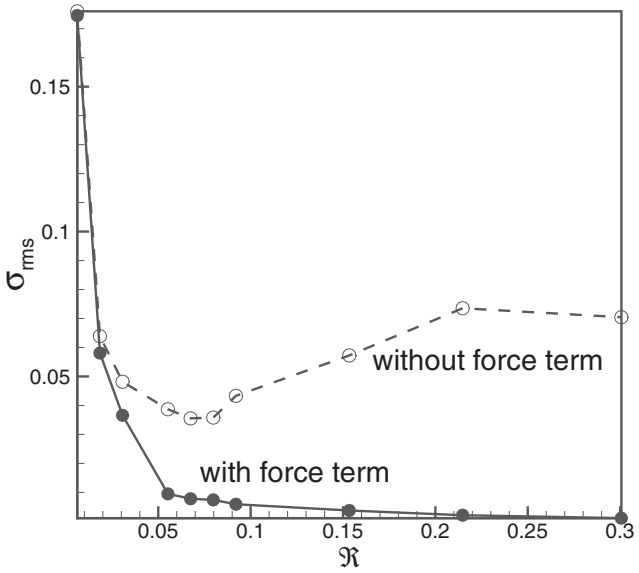


Figure A1. Magnitude of error between left- and right-hand sides of Equation (A5) and dependence on the box-filtering size $\Re$, including the force term (closed circles) and not including the force term (empty circles).

Appendix B. Partial sums evaluation for interpolations

We have implemented a new method for the evaluation of spatial interpolation used in the database routines, which we summarize below. The method is described in more detail in [45]. It is also applicable to the temporal interpolation and differentiation evaluations, but we are still in the process of implementing it for those computations.

The database routines perform the Lagrange polynomial interpolation of order specified by the user. For Nth-order Lagrange polynomial interpolation of a point $\mathbf{p}'$ in 3D space, we have

$$f(\mathbf{p}') = \sum_{k=1}^{N} l_z^{q-\frac{N}{2}+k}(z') \sum_{j=1}^{N} l_y^{p-\frac{N}{2}+j}(y') \sum_{i=1}^{N} l_x^{n-\frac{N}{2}+i}(x') \cdot f(x_{n-\frac{N}{2}+i}, y_{p-\frac{N}{2}+j}, z_{q-\frac{N}{2}+k}) \,. \tag{B1}$$

In the above equation, $\mathbf{p}' = (x', y', z')$ is the target location and the data stored in the database at location (x_i, y_j, z_k) is given by $f(x_i, y_j, z_k)$. Since data in the database are stored at the nodes of a discrete grid, the grid location (x_n, y_p, z_q) is computed as $n = int(\frac{x'}{\Delta x} + \frac{1}{2})$, $p = int(\frac{y'}{\Delta y} + \frac{1}{2})$, $q = int(\frac{z'}{\Delta z} + \frac{1}{2})$, where Δx, Δy, and Δz are the widths of the grid in the x, y and z dimensions, respectively. The Lagrange coefficients l in Equation (B1) are as follows:

$$l_\theta^i(\theta') = \frac{\prod_{j=\alpha-\frac{N}{2}+1, j\neq i}^{\alpha+\frac{N}{2}} (\theta' - \theta_j)}{\prod_{j=\alpha-\frac{N}{2}+1, j\neq i}^{\alpha+\frac{N}{2}} (\theta_i - \theta_j)} \,, \tag{B2}$$

where θ can be x, y, or z, and α can be n, p, or q, respectively.

The evaluation of the Lagrange polynomial interpolation requires data from a cube of width N around the target location. In the current version of the database, edge overlap ensures that all of the necessary data are contained within a single database atom, and hence a single database I/O is needed to perform computation. However, in general the data may be spread across multiple such database atoms or even across multiple database servers. In order to ensure the efficient processing of large batch queries submitted by our users, we evaluate the interpolation by means of partial sums.

The Lagrange polynomial interpolation as well as any other linear computation can be executed in parts by maintaining and updating a partial sum of the final result. We make use of this observation to evaluate multiple target positions at the same time and by means of a single, sequential pass over the data. We process all target positions in the user's batch and determine the entire set of database atoms that need to be read from the database in order to perform the interpolation of each target. For each database atom read from the database we increment the partial sums of all target positions whose interpolation kernel intersects the database atom. Once all such atoms are processed, the interpolation of each target position has been evaluated.

We make use of efficient procedures of Purser and Leslie [46] in the computation of Lagrange coefficients. They present efficient ways to organize the coding, eliminating redundant multiplications and making use of the fact that the values in the denominator of

Equation (B2) are constant to reduce the time complexity of the computation of coefficients to $O(N)$ from $O(N^3)$.

Appendix C. Matlab interface

The Matlab interface allows clients to interact with the turbulence database directly from a Matlab session. This interface is based on Matlab web service functions, which communicate with the database directly using the Simple Object Access Protocol (SOAP). All communication with the JHU turbulence database cluster is controlled through the TurbulenceService Matlab class. This class creates SOAP messages, queries the database, and parses the database response. For each database function a wrapper function has been created to perform data translation and retrieval. One major advantage of the Matlab interface to that of its C and Fortran counterparts is the readily available functions and tool boxes that Matlab provides. With the Matlab interface, clients can retrieve sections of spatiotemporal data from the database, view the data with Matlab's plotting tools, or perform secondary calculations on the data, all from the same Matlab session.

A standard distribution of Matlab contains a set of functions for creating (*createSoapMessage*), sending (*callSoapService*), and parsing (*parseSoapResponse*) SOAP messages. These routines use a W3C compliant Document Object Model (DOM) approach for constructing and parsing the Extensible Markup Language (XML)-formatted SOAP message. The DOM provides a generic mechanism to create XML documents. However, while being robust and dynamic, the DOM approach holds the disadvantage of being computationally inefficient for large XML documents – this inefficiency becomes a limiting factor for large database queries. To avoid this critical problem, we have developed faster replacement functions to create and send the SOAP message, and to parse the SOAP response. Therefore, by performing low-level string operations instead of employing the DOM, we can rapidly build and parse extensive XML documents leading to a $100x$ speedup over the original DOM approach. Due to this increase in efficiency, the Matlab interface possesses similar performance characteristics as those of the C and Fortran database interfaces.

The bases for the Matlab database functions are created by using the *createClassFromWsdl* utility. This utility generates the TurbulenceService Matlab class from the Web Service Definition Language (WSDL) functions of the database web service. These generated files are modified to incorporate the newly developed faster Matlab SOAP routines. The purpose of the TurbulenceService class is to accommodate a request to the database by taking data from Matlab, generating an appropriate SOAP message, sending the message to the database, and finally retrieving and parsing the database response. While providing a direct mechanism for interacting with the database, the TurbulenceService class returns data packaged in a Matlab structure array, which may not be necessarily intuitive to most Matlab users. We have therefore created wrapper functions, which translate the response structure into directly accessible Matlab vectors.

The following code snippets illustrate the complete mechanism, starting from user-generated request data and ending with a parsed database response, stored in *response*. From a Matlab script, request data will be provided to the *getVelocity* TurbulenceService wrapper function as demonstrated in Listing 1. This wrapper function calls the TurbulenceService *TS_getVelocity* function (see Listing 2), and translates its structure into a vector of velocity components. The *TS_getVelocity* function illustrated in Listing 3 assembles the data in a Matlab structure, creates the SOAP message, sends the SOAP message, and parses the

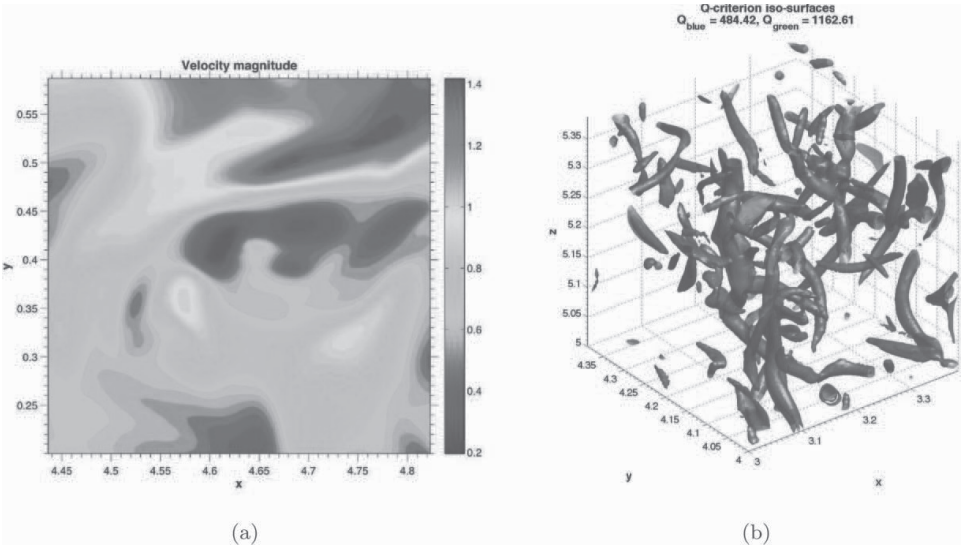


Figure C1. (a) Velocity contour plot generated using the Matlab interface as available for download. (b) Visualization of "worms" using iso-Q surfaces in a small subset of the data generated using the Matlab implementation of *getVelocityGradients* to evaluate A_{ij}, computing the invariant $Q = -\frac{1}{2}A_{ij}A_{ji}$ at every point, and using Matlab 3D plotting tools.

Listing 1. Example call to get Velocity from Matlab interface.

```
% Set client authentication key
authkey = '...';
% Set target database
dataset = 'isotropic1024coarse';
% Set temporal interpolation scheme
temporal = 'PCHIP';
% Set spatial interpolation scheme
spatial = 'Lag6';

% Create a set of (x,y,z)-coordinates to query at a randomly
% chosen time step
points(1:3,:) = ...;
time = 0.002 * randi(1024, 1);

% Call TurbulenceService wrapper to perform getVelocity request at
% specified points
response = getVelocity(authkey, dataset, time, ..., points);
```

SOAP response. (A similar TurbulenceService is implemented for the *getPosition* function, as illustrated in Listing 4).

For illustration of *getVelocity*, in Figure C1(a) is a velocity contour plot of sample data from the turbulence database. The data were retrieved using the *getVelocity* function from the Matlab interface and the contour plot was generated using Matlab standard contour plotting tools. In Figure C1(b) a visualization of "worms" is shown in a small sub-cube of the data at $t = 0$, using iso-Q surfaces generated using the Matlab implementation of *getVelocityGradients* to evaluate A_{ij}, computing the invariant $Q = -\frac{1}{2}A_{ij}A_{ji}$ at every point in Matlab, and using Matlab 3D plotting tools.

Listing 2. Sample getVelocity wrapper function.

```
function response = getVelocity(authkey, dataset, time, ..., points)

  % Create the TurbulenceService object and call TS_getVelocity
  obj = TurbulenceService;
  responseStruct = TS_getVelocity(obj, authkey, dataset, ..., points);

  % Return a vector of velocity components
  response = getVector(resultStruct.GetVelocityResult.Vector3);

end
```

Listing 3. Sample TS_getVelocity TurbulenceService class function.

```
function responseStruct = TS_getVelocity(obj, authkey, dataset, ..., points)

  % Construct a Matlab structure containing the data
  data = struct('points', struct('x', points(1,:), ...), ...);

  % Create the XML document, call the service and parse the response
  soapMessage = createSoapMessage('GetVelocity', data, ...);
  response = callSoapService(URL, soapMessage, ...);
  responseStruct = parseSoapResponse(response);

end
```

Listing 4. Example call to getPosition from Matlab interface.

```
% Set client authentication key
authkey = '...';
% Set target database
dataset = 'isotropic1024coarse';
% Set spatial interpolation scheme
spatial = 'Lag6';

% getPosition integration settings
startTime=0.364;
endTime=0.376;
lagDt=0.0004;

% Create a set of (x,y,z)-coordinates
points(1:3,:) = ...;

% Call TurbulenceService wrapper to perform getPosition request at
% specified points between startTime and endTime
response = getPosition(authkey, dataset, startTime, endTime, lagDt,... , points);
```

Journal of Turbulence, 2013
Vol. 14, No. 2, 4–22, http://dx.doi.org/10.1080/14685248.2012.759229

Taylor & Francis
Taylor & Francis Group

Statistical symmetries and its impact on new decay modes and integral invariants of decaying turbulence

Martin Oberlack[abc*] and Andreas Zieleniewicz[a]

[a]*Chair of Fluid Dynamics, Technische Universität Darmstadt, Darmstadt, Germany;* [b]*Center of Smart Interfaces, Technische Universität Darmstadt, Darmstadt, Germany;* [c]*Graduate School of Computational Engineering, Technische Universität Darmstadt, Darmstadt, Germany*

(*Received 5 September 2012; final version received 10 December 2012*)

Classical decay laws of isotropic turbulence usually derived from the von Kármán–Howarth equation are essentially based on two paradigms. First, scaling symmetries of space and time, both tracing back to the Navier–Stokes equations in the limit of large Reynolds numbers (or $r \gg \eta$), give rise to a temporal power-law decay for the turbulent kinetic energy and at the same time an algebraic growth of the integral length scale at an exponent that is uniquely coupled to the latter energy decay. Second, global invariants such as Birkhoff or Loitsianskii integrals determine the exponent of both power laws. We presently show that this class of decay laws may be considerably extended considering the entire set of multi-point correlation equations that admit a much wider class of symmetries. It was recently shown that these new symmetries are of paramount importance, e.g. in deriving the logarithmic law of the wall being an analytic solution of the multi-point equations. For the present case, it is particularly an additional scaling group, which we call statistical scaling group, that gives rise to two additional families of 'canonical' decay laws including those with an exponential characteristic for both the kinetic energy and the integral length scale. Finally, a second rather generic group admitted by all linear differential equations corresponding to the superposition principle induces an infinite set of scaling laws of rather complex form that may match rather generic initial conditions. All scaling laws are analyzed in the light of the above-mentioned integral invariants that have been further extended in the present contribution to an exponential-type invariant.

Keywords: symmetries; invariant solutions; decaying turbulence; multi-point correlation; integral invariants

1. Introduction

The idea of two- and multi-point correlation equations in turbulence was presumably first established by Keller and Friedmann [1]. In the beginning, it was assumed that all correlation equations of tensor orders higher than two may be neglected; in fact, Keller and Friedmann only wrote a shortened version of it and did not give the full hierarchy of all correlation equations.

Theoretical considerations led to the result that all higher correlations have to be taken into account. Consequently, all multi-point correlation (MPC) equations have to be considered in the symmetry analysis to follow, as only this guaranties completeness of the results and, most importantly, results and solutions for correlations of lower order will be consistent with all higher-order correlations.

*Corresponding author. Email: oberlack@fdy.tu-darmstadt.de

© 2013 Taylor & Francis

Even if only the two-point version of the full set of MPC equations is considered (see [2]), this equation alone is already a rather monstrous equation. Considering its full three-dimensional (3D) time-dependent version, it exhibits non-local behavior in the mean velocity terms, e.g. in the production terms, and thus, it does not even constitute a partial differential equation (DE) in the usual sense.

G. I. Taylor [3] had the ingenious idea to introduce the concept of homogeneous isotropic turbulence, which then von Kármán and Howarth [4] used in the context of two-point correlations. This led to an essential reduction of the full two-point correlation equation to the so-called von Kármán–Howarth equation, which is a scalar equation of diffusion type for the longitudinal velocity correlations – though still unclosed if only two points are considered.

Probably, because isotropic turbulence is the simplest turbulent flow we can think of, it initiated a landslide of new publications to date, where two key branches may be mentioned in particular. On the one hand, the von Kármán and Howarth equation was one of the starting points of Kolmogorov's theories (see [5, 6]) and directly led to the famous $4/5$th-law [6].

On the other hand, von Kármán and Howarth in ref. [4] showed that a self-similar solution may be generated, which in turn describes the decay of isotropic turbulence and further leads to a reduced ordinary DE. Hence, this may have been the starting point of generating invariant solutions for turbulent flows that we nowadays know have their origin in the admitted Lie symmetries. Only one year later, Loitsianskii [7] proposed an integral invariant that fixed the up-to-this-point unknown scaling exponent of turbulent kinetic energy of decaying turbulence. Over the following decades, other integral quantities have been proposed to be time invariant such as the Birkhoff integral [8] as the decay behavior corresponding to the Loitsianskii integral was hardly ever observed.

In more recent papers, George and coworkers [9–11] derived the decay laws in a fundamental way using the method of equilibrium analysis. Based on these works, also the influences of the integral length scale [12] and of the boundary conditions [13] on the decay law are discussed. More details are given in the following sections.

All of the above branches are still actively followed and the reader may pardon if only the classical publications are mentioned as nowadays a tremendous number of publications have appeared on isotropic turbulence.

In the present contribution, we follow the second branch of analysis of the von Kármán and Howarth equation or rather the MPC equation and the main aim is to unify the various decay laws under a common umbrella, which, as we later observe, is spanned by Lie symmetry group analysis.

In Section 2, we derive the full infinite set of MPC equations where the two-point version of it is reduced to the von Kármán and Howarth equation. In Section 3, we give a brief introduction to Lie symmetry groups and present the set of Lie symmetries admitted by the multi-point equations, including the new statistical symmetries that may not directly be taken from the Euler or Navier–Stokes equations. In Section 4, we present a complete set of classical and new possible scaling laws for decaying isotropic turbulence, all of them based on the symmetries of the correlation equations. Hence, we unify all scaling laws under the same concept and further invoke classical and new integral invariants that may determine some of the appearing scaling parameters.

2. Two- and multi-point correlation equations

In this section, we briefly review the two- and multi-point correlation equations and basic notation and further details may be taken from ref. [14]. The initial point of the entire analysis

to follow is based on the Navier–Stokes equations for an incompressible fluid under the assumption of a Newtonian material with constant density and viscosity. In Cartesian tensor notation, we have the continuity and the momentum equation, respectively,

$$\frac{\partial U_k}{\partial x_k} = 0, \qquad \frac{\partial U_i}{\partial t} + U_k \frac{\partial U_i}{\partial x_k} + \frac{\partial P}{\partial x_i} = \nu \frac{\partial^2 U_i}{\partial x_k \partial x_k} + F_i, \quad i = 1, 2, 3, \tag{1}$$

and $t \in \mathbb{R}^+$, $\boldsymbol{x} \in \mathbb{R}^3$, $\boldsymbol{U} = \boldsymbol{U}(\boldsymbol{x}, t)$ and $P = P(\boldsymbol{x}, t)$ represent time, position vector, instantaneous velocity vector and pressure in which the density has been absorbed. Later, the external sink or source term F_i is usually set to zero except when stated otherwise.

2.1. *MPC equations*

In ref. [14], two different sets of MPC equations are derived. The first is based on the instantaneous values of $\boldsymbol{U}$ and P while the second one is in accordance with the classical notation based on the decomposition between mean and fluctuating quantities – the latter denoted by $\boldsymbol{u}$ and p. Since we presently deal with homogeneous and, in fact, isotropic turbulence, the mean velocity and the mean pressure may be set to zero. Hence, instantaneous values are identical to the fluctuating quantities and, thus, in Equation (1), we set $\boldsymbol{U} = \boldsymbol{u}$ and $P = p$ to be consistent with the notation in ref. [14].

In order to write the MPC equations in a very compact form, we introduce the following notation. The multi-point velocity correlation tensor of order $n + 1$ is defined as follows:

$$R_{i_{\{n+1\}}} = R_{i_{(0)} i_{(1)} \ldots i_{(n)}} = \overline{u_{i_{(0)}}(\boldsymbol{x}_{(0)}) \ldots u_{i_{(n)}}(\boldsymbol{x}_{(n)})}, \tag{2}$$

where the first index of the $R_{i_{\{n\}}}$ tensor defines the tensor character of the term and the second index in braces denotes the order of the tensor. The curly brackets point out that not an index of a tensor but an enumeration is meant. It is important to mention that the indices start with 0, which is an advantage when introducing a new coordinate system based on the Euclidean distance of two space points. The value in curly brackets is the actual order of the tensor and takes into account that counting of the tensor index starts at zero.

In some cases, the list of indices is interrupted by one or more other indices, which is pointed out by attaching the replaced value in brackets to the index

$$R_{i_{\{n+1\}}[i_{(l)} \mapsto k_{(l)}]} = \overline{u_{i_{(0)}}(\boldsymbol{x}_{(0)}) \ldots u_{i_{(l-1)}}(\boldsymbol{x}_{(l-1)}) u_{k_{(l)}}(\boldsymbol{x}_{(l)}) u_{i_{(l+1)}}(\boldsymbol{x}_{(l+1)}) \ldots u_{i_{(n)}}(\boldsymbol{x}_{(n)})}. \tag{3}$$

This is further extended by

$$R_{i_{\{n+2\}}[i_{(n+1)} \mapsto k_{(l)}][\boldsymbol{x}_{(n+1)} \mapsto \boldsymbol{x}_{(l)}]} = \overline{u_{i_{(0)}}(\boldsymbol{x}_{(0)}) \ldots u_{i_{(n)}}(\boldsymbol{x}_{(n)}) u_{k_{(l)}}(\boldsymbol{x}_{(l)})}, \tag{4}$$

where not only the index $i_{(n+1)}$ is replaced by $k_{(l)}$, but also the independent variable $\boldsymbol{x}_{(n+1)}$ is replaced by $\boldsymbol{x}_{(l)}$. If indices are missing, e.g. between $i_{(l-1)}$ and $i_{(l+1)}$, we define

$$R_{i_{\{n\}}[i_{(l)} \mapsto \emptyset]} = \overline{u_{i_{(0)}}(\boldsymbol{x}_{(0)}) \ldots u_{i_{(l-1)}}(\boldsymbol{x}_{(l-1)}) u_{i_{(l+1)}}(\boldsymbol{x}_{(l+1)}) \ldots u_{i_{(n)}}(\boldsymbol{x}_{(n)})}. \tag{5}$$

Finally, if the pressure is involved, we get

$$P_{i_{\{n\}}[l]} = \overline{u_{i_{(0)}}(\boldsymbol{x}_{(0)}) \ldots u_{i_{(l-1)}}(\boldsymbol{x}_{(l-1)}) p(\boldsymbol{x}_{(l)}) u_{i_{(l+1)}}(\boldsymbol{x}_{(l+1)}) \ldots u_{i_{(n)}}(\boldsymbol{x}_{(n)})}, \tag{6}$$

which is, considering all the above definitions, sufficient to derive the MPC equations based on the velocity and pressure fluctuations to obtain the $\mathcal{T}$-equation:

$$\mathcal{T}_{i_{\{n+1\}}} = \frac{\partial R_{i_{\{n+1\}}}}{\partial t} + \sum_{l=0}^{n} \left[\frac{\partial R_{i_{\{n+2\}}[i_{(n+1)} \mapsto k_{(l)}]}[\boldsymbol{x}_{(n+1)} \mapsto \boldsymbol{x}_{(l)}]}{\partial x_{k_{(l)}}} + \frac{\partial P_{i_{\{n\}}[l]}}{\partial x_{i_{(l)}}} - \nu \frac{\partial^2 R_{i_{\{n+1\}}}}{\partial x_{k_{(l)}} \partial x_{k_{(l)}}} \right] = 0, \tag{7}$$

for $n = 1, \ldots, \infty$.

Loosely speaking, Equation (7) implies the full statistical information of the Navier–Stokes equations at the expense of dealing with an infinite-dimensional chain of DEs starting with order 2, i.e. $n = 1$. The rather remarkable consequence of the derivation is that Equation (7) is a linear equation which considerably simplifies the finding of Lie symmetries to be pointed out later.

From Equation (1), a continuity equation for $R_{i_{\{n+1\}}}$ and $P_{i_{\{n\}}[l]}$ can be derived:

$$\frac{\partial R_{i_{\{n+1\}}[i_{(l)} \mapsto k_{(l)}]}}{\partial x_{k_{(l)}}} = 0, \quad \frac{\partial P_{i_{\{n\}}[k][i_{(l)} \mapsto m_{(l)}]}}{\partial x_{m_{(l)}}} = 0, \quad \text{for } k, l = 0, \ldots, n \text{ and } k \neq l. \tag{8}$$

At this point, we adopt the classical notation of distance vectors. Accordingly, the coordinate transformations are

$$\boldsymbol{x} = \boldsymbol{x}_{(0)}, \qquad \boldsymbol{r}_{(l)} = \boldsymbol{x}_{(l)} - \boldsymbol{x}_{(0)} \quad \text{with} \quad l = 1, \ldots, n, \tag{9}$$

while any term with $\partial / \partial x_k$ will be omitted later because of homogeneity.

For consistency reasons, the first index $i_{(0)}$ is replaced by i. Thus, the indices of the tensor $R_{i_{\{n+1\}}}$ are $R_{i i_{(1)} i_{(2)} \ldots i_{(n)}}$. Using the rules of transformation (9), the $\mathcal{T}$-equation leads to

$$\begin{aligned} \mathcal{T}_{i_{\{n+1\}}} = {} & \frac{\partial R_{i_{\{n+1\}}}}{\partial t} \\ & - \sum_{l=1}^{n} \left[\frac{\partial R_{i_{\{n+2\}}[i_{(n+1)} \mapsto k_{(l)}]}[\boldsymbol{x}_{(n+1)} \mapsto \boldsymbol{x}]}{\partial r_{k_{(l)}}} - \frac{\partial R_{i_{\{n+2\}}[i_{(n+1)} \mapsto k_{(l)}]}[\boldsymbol{x}_{(n+1)} \mapsto \boldsymbol{r}_{(l)}]}{\partial r_{k_{(l)}}} \right] \\ & + \sum_{l=1}^{n} \left(- \frac{\partial P_{i_{\{n\}}[0]}}{\partial r_{m_{(l)}}} \bigg|_{[m_{(l)} \mapsto i]} + \frac{\partial P_{i_{\{n\}}[l]}}{\partial r_{i_{(l)}}} \right) \\ & - \nu \sum_{l=1}^{n} \left(\sum_{m=1}^{n} \frac{\partial^2 R_{i_{\{n+1\}}}}{\partial r_{k_{(m)}} \partial r_{k_{(l)}}} - \frac{\partial^2 R_{i_{\{n+1\}}}}{\partial r_{k_{(l)}} \partial r_{k_{(l)}}} \right) = 0, \\ & \text{for} \quad n = 1, \ldots, \infty, \end{aligned} \tag{10}$$

and the two continuity equations become

$$\sum_{j=1}^{n} \frac{\partial R_{i_{\{n+1\}}[i_{(0)} \mapsto k_{(j)}]}}{\partial r_{k_{(j)}}} = 0, \quad \frac{\partial R_{i_{\{n+1\}}[i_{(l)} \mapsto k_{(l)}]}}{\partial r_{k_{(l)}}} = 0, \quad \text{for} \quad l = 1, \ldots, n, \tag{11}$$

and

$$\sum_{j=1}^{n} \frac{\partial P_{i_{\{n\}}[k][i\mapsto m_{(j)}]}}{\partial r_{m_{(j)}}} = 0, \quad \text{for} \quad k = 1, \ldots, n,$$

$$\frac{\partial P_{i_{\{n\}}[k][i_{(l)}\mapsto m_{(l)}]}}{\partial r_{m_{(l)}}} = 0, \quad \text{for} \quad k = 0, \ldots, n, \quad l = 1, \ldots, n, \quad k \neq l. \tag{12}$$

2.2. *Two-point correlation tensor equations*

The first tensor equation of the infinite chain (10) propagates $R_{i_{\{2\}}}$, which has a close link to the Reynolds stress tensor

$$\lim_{x_{(k)}\to x_{(l)}} R_{i_{\{2\}}} = \lim_{x_{(k)}\to x_{(l)}} R_{i_{(0)}i_{(1)}} = \overline{u_{i_{(0)}} u_{i_{(1)}}}(\boldsymbol{x}_{(l)}), \quad \text{with} \quad k \neq l. \tag{13}$$

As a special case of Equation (10), we consider $n = 1$; thus, we derive the equation for the two-point correlation tensor. To abbreviate the notation, we introduce the following nomenclature:

$$R_{i_{\{2\}}} = R_{ii_{(1)}} = R_{ij}. \tag{14}$$

In this case, Equation (10) reduces to

$$\mathcal{T}_{i_{\{2\}}} = \frac{\partial R_{ij}}{\partial t} - \frac{\partial \overline{pu}_j}{\partial r_i} + \frac{\partial \overline{u_i p}}{\partial r_j} - 2\,\nu \frac{\partial^2 R_{ij}}{\partial r_k \partial r_k} - \frac{\partial}{\partial r_k}\left[R_{(ik)j} - R_{i(jk)}\right] = 0. \tag{15}$$

The vectors $\overline{pu}_j$ and $\overline{u_i p}$ are special cases of $P_{i_{\{n\}}[k]}$ and defined as

$$\overline{pu}_j(\boldsymbol{x}, \boldsymbol{r}, t) = \overline{p(\boldsymbol{x}_{(0)}, t)\, u_j(\boldsymbol{x}_{(1)}, t)} \quad \text{and} \quad \overline{u_i p}(\boldsymbol{x}, \boldsymbol{r}, t) = \overline{u_i(\boldsymbol{x}_{(0)}, t)\, p(\boldsymbol{x}_{(1)}, t)}. \tag{16}$$

For the two-point continuity equations, we obtain reduced forms of Equations (11) and (12), i.e.

$$\frac{\partial R_{ij}}{\partial r_j} = 0, \quad \frac{\partial \overline{pu}_j}{\partial r_j} = 0. \tag{17}$$

2.3. *von Kármán–Howarth equation*

Furthermore, employing the usual assumption of homogeneous and isotropic turbulence, the two-point tensors R_{ij}, $\overline{pu}_j$, $\overline{u_i p}$, $R_{(ik)j}$ and $R_{i(jk)}$ may be further reduced. While $\overline{pu}_j$, $\overline{u_i p}$ vanish identically [4], we have

$$R_{ij} = \mathcal{G}\delta_{ij} + (\mathcal{F} - \mathcal{G})\frac{r_i r_j}{r} \quad \text{with} \quad \mathcal{G} = \mathcal{F} + \frac{r}{2}\frac{\partial \mathcal{F}}{\partial r}, \tag{18}$$

where $\mathcal{F}$ and $\mathcal{G}$ are the longitudinal and transversal two-point correlation functions depending on $r = |\boldsymbol{r}|$ and t only and the last relation in Equation (18) emerged from the first continuity equation in (17). The triple correlation also reduces to a single scalar longitudinal two-point triple correlation function $\mathcal{K}$ and its complex tensor form may be taken from ref. [4]. Here $\mathcal{F}$, $\mathcal{G}$ and $\mathcal{K}$ are normalized as

$$\mathcal{F}(r,t) = \overline{u'^2}(t) f(r,t), \quad \mathcal{G}(r,t) = \overline{u'^2}(t) g(r,t), \quad \mathcal{K}(r,t) = \overline{u'^2}(t)^{3/2} k(r,t). \tag{19}$$

Using the above, we obtain the von Kármán–Howarth equation as

$$\frac{\partial \mathcal{F}}{\partial t} = \frac{1}{r^4}\frac{\partial}{\partial r}\left[r^4\left(\mathcal{K} + 2\nu\frac{\partial \mathcal{F}}{\partial r}\right)\right]. \tag{20}$$

From the two-point version of the continuity equation (17), we derive the two relations (see [2])

$$\int_0^\infty r g \,\mathrm{d}r = 0 \quad \text{and} \quad f = \frac{2}{r^2}\int_0^r r g \,\mathrm{d}r, \tag{21}$$

where the first one implies that g features negative values while the second one is an immediate consequence of the second relation in Equation (18) and implies

$$\lim_{r\to\infty} f r^2 = 0, \tag{22}$$

or in other words, f decays faster than r^{-2} as r tends to infinity.

Similarly, there exists an exact integral relation for the triple correlation

$$\int_0^\infty r q(r) \mathrm{d}r = 0 \tag{23}$$

in transversal direction in the q-notation as it was introduced by von Kármán and Howarth [4].

Subsequently, we observe that the latter integrals of the correlation functions possess important consequences for the convergence of the decay laws.

3. Symmetries and invariant solutions of the MPC equations

3.1. *Introduction to symmetries and invariant solutions of DEs*

For clarity, we may briefly introduce the notion of symmetry, in particular, Lie symmetry. A Lie symmetry defines a transformation

$$\boldsymbol{x}^* = \boldsymbol{f}(\boldsymbol{x}, \boldsymbol{y}; a), \quad \boldsymbol{y}^* = \boldsymbol{g}(\boldsymbol{x}, \boldsymbol{y}; a), \tag{24}$$

obeying group properties which maps a given DE

$$\mathcal{D}(\boldsymbol{x}, \boldsymbol{y}) = 0 \tag{25}$$

to itself, i.e. we observe

$$\mathcal{D}(\boldsymbol{x}, \boldsymbol{y}) = 0 \quad \Leftrightarrow \quad \mathcal{D}(\boldsymbol{x}^*, \boldsymbol{y}^*) = 0, \tag{26}$$

or in other words, Equation (24) is a form of invariant transformation of the DE (25).

The particularity of a Lie symmetry refers to the fact that Equation (24) depends on the parameter $a \in \mathbb{R}$ and at the same time observes group properties where a denotes the group parameter. This implies that the transformation (24) may be written in infinitesimal form

$$\boldsymbol{x}^* = \boldsymbol{x} + a\,\boldsymbol{\xi}(\boldsymbol{x}, \boldsymbol{y}) + O(a^2), \quad \boldsymbol{y}^* = \boldsymbol{y} + a\,\boldsymbol{\eta}(\boldsymbol{x}, \boldsymbol{y}) + O(a^2), \tag{27}$$

with the infinitesimals $\boldsymbol{\xi} = \frac{\partial \boldsymbol{f}}{\partial a}|_{a=0}$ and $\boldsymbol{\eta} = \frac{\partial \boldsymbol{f}}{\partial a}|_{a=0}$ and, most importantly, the knowledge of the infinitesimals is equivalent and sufficient to regain the global transformation (24). With this, the invariance in Equation (26) under Equation (24) may be re-written as

$$[X\,\mathcal{D}]|_{\mathcal{D}=0} = 0 \quad \text{with} \quad X = \xi_i \frac{\partial}{\partial x_i} + \eta_j \frac{\partial}{\partial y_j}. \tag{28}$$

Because of the complexity of the problem, it is absolutely imperative to compute the symmetries in infinitesimal form from the latter condition (28) (see [15]). A variety of computer algebra packages have been developed to aid this comprehensive and tedious endeavor while presently we have primarily adopted GeM (see [16]) written for Maple.

The final step to generate new solutions, in fact mostly invariant solutions, from symmetries is the idea of invariant solutions. For this, we seek for solutions of the form

$$\boldsymbol{y} = \boldsymbol{\Theta}(\boldsymbol{x}), \tag{29}$$

which remain invariant under one or several of the symmetries admitted by the equation or written in operator notation

$$X\,[\boldsymbol{y} - \boldsymbol{\Theta}(\boldsymbol{x})] = 0 \quad \text{with} \quad X = \xi_i \frac{\partial}{\partial x_i} + \eta_j \frac{\partial}{\partial y_j}. \tag{30}$$

Given the admitted infinitesimals for Equation (25) are known, i.e. have been computed from the equation under investigation, we may re-write Equation (30) as

$$\xi_i(\boldsymbol{x}, \boldsymbol{\Theta}) \frac{\partial \Theta_j}{\partial x_i} = \eta_j(\boldsymbol{x}, \boldsymbol{\Theta}), \tag{31}$$

which is a hyperbolic system with the characteristic equations

$$\begin{aligned} \frac{\mathrm{d}x_1}{\xi_1(\boldsymbol{x}, \boldsymbol{y})} = \frac{\mathrm{d}x_2}{\xi_2(\boldsymbol{x}, \boldsymbol{y})} = \cdots = \frac{\mathrm{d}x_m}{\xi_m(\boldsymbol{x}, \boldsymbol{y})} \\ = \frac{\mathrm{d}y_1}{\eta_1(\boldsymbol{x}, \boldsymbol{y})} = \frac{\mathrm{d}y_2}{\eta_2(\boldsymbol{x}, \boldsymbol{y})} = \cdots = \frac{\mathrm{d}y_n}{\eta_n(\boldsymbol{x}, \boldsymbol{y})}. \end{aligned} \tag{32}$$

In Lie group theory, the latter is often referred to as invariant surface condition. The integrants or characteristics thereof are then the invariants and, in fact, define the invariant

solutions – in fluid mechanics often denoted self-similar solutions if a scaling group is involved.

Finally, note that the symmetries in infinitesimal form of a given DE define a linear vector space, or in other words, any linear combination of infinitesimal also defines a symmetry. As will be seen later, it is this combination of several symmetries that allows for a wide range of different invariant solutions, i.e. in the turbulence community known as turbulent scaling laws.

3.2. *Symmetries of two- and multi-point equations and the condition of invariant solutions*

Subsequently, we present each symmetry on both global (24) and infinitesimal form (28), although we only display those symmetries related to the present problems of decaying turbulence. A more comprehensive set of symmetries of the MPC equations is presented in ref. [14] and the corresponding voluminous Lie algebra is given in ref. [17].

In the limit of infinite Reynolds number, classical scaling symmetries of the two- and multi-point correlation equations are immediate consequences of continuity and momentum equation (1) where scaling of space is given by

$$\begin{aligned} &t^* = t, \quad \boldsymbol{r}^* = \mathrm{e}^{a_1}\boldsymbol{r}, \quad R^*_{i_{\{n\}}} = \mathrm{e}^{na_1} R_{i_{\{n\}}}, \quad P^*_{i_{\{n\}}} = \mathrm{e}^{(n+1)a_1} P_{i_{\{n\}}}, \\ &X = r_i \frac{\partial}{\partial r_i} + 2R_{ij}\frac{\partial}{\partial R_{ij}} + 3R_{ijk}\frac{\partial}{\partial R_{ijk}} + \cdots + 3P_i\frac{\partial}{\partial P_i} + 4P_{ij}\frac{\partial}{\partial P_{ij}} + \cdots, \end{aligned} \tag{33}$$

and scaling of time yields

$$\begin{aligned} &t^* = \mathrm{e}^{a_2} t\,, \quad \boldsymbol{r}^* = \boldsymbol{r}\,, \quad R^*_{i_{\{n\}}} = \mathrm{e}^{-na_2} R_{i_{\{n\}}}\,, \quad P^*_{i_{\{n\}}} = \mathrm{e}^{-(n+1)a_2} P_{i_{\{n\}}}, \\ &X = t\frac{\partial}{\partial t} - 2R_{ij}\frac{\partial}{\partial R_{ij}} - 3R_{ijk}\frac{\partial}{\partial R_{ijk}} + \cdots - 3P_i\frac{\partial}{\partial P_i} - 4P_{ij}\frac{\partial}{\partial P_{ij}} + \cdots. \end{aligned} \tag{34}$$

In the limit of isotropic turbulence, the latter two groups, respectively, convert to

$$\begin{aligned} &t^* = t\,, \quad r^* = \mathrm{e}^{a_1} r\,, \quad \mathcal{F}^* = \mathrm{e}^{2a_1}\mathcal{F}\,, \quad \mathcal{K}^* = \mathrm{e}^{3a_1}\mathcal{K}, \\ &X = r\frac{\partial}{\partial r} + 2\mathcal{F}\frac{\partial}{\partial \mathcal{F}} + 3\mathcal{K}\frac{\partial}{\partial \mathcal{K}} \end{aligned} \tag{35}$$

and

$$\begin{aligned} &t^* = \mathrm{e}^{a_2} t\,, \quad r^* = r\,, \quad \mathcal{F}^* = \mathrm{e}^{-2a_2}\mathcal{F}\,, \quad \mathcal{K}^* = \mathrm{e}^{-3a_2}\mathcal{K}, \\ &X = r\frac{\partial}{\partial r} - 2\mathcal{F}\frac{\partial}{\partial \mathcal{F}} - 3\mathcal{K}\frac{\partial}{\partial \mathcal{K}}. \end{aligned} \tag{36}$$

Together with translation in time

$$t^* = t + a_3\,, \quad \boldsymbol{r}^* = \boldsymbol{r}\,, \quad R^*_{i_{\{n\}}} = R_{i_{\{n\}}}\,, \quad P^*_{i_{\{n\}}} = P_{i_{\{n\}}}, \quad X = \frac{\partial}{\partial t}, \tag{37}$$

which for isotropic turbulence transforms as

$$t^* = t + a_3, \quad r^* = r, \quad \mathcal{F}^* = \mathcal{F}, \quad \mathcal{K}^* = \mathcal{K}, \quad X = \frac{\partial}{\partial t}, \tag{38}$$

we have the complete set of symmetries relevant for isotropic turbulence and which originally stem from the fundamental equations of fluid mechanics (1).

For the analysis to follow, note that the latter set of symmetries is considerably enlarged for the infinite set of MPC equations (7) and (8). This was first observed in ref. [14] and further extended in ref. [17]. Hence, this is also true for the von Kármán–Howarth equation (20), which, independent of this, was first investigated with respect to its symmetries in refs. [18] and [19]. We subsequently term these symmetries as statistical symmetries. In ref. [14], it was shown that these new symmetries are crucial for the derivation and understanding of turbulent scaling laws and constitute a key ingredient, e.g. for the logarithmic law of the wall.

For the present case, we consider two new statistical symmetries. The first one is a scaling symmetry

$$\begin{aligned} &t^* = t, \quad \boldsymbol{r}^* = \boldsymbol{r}, \quad R^*_{i_{\{n\}}} = \mathrm{e}^{a_s} R_{i_{\{n\}}}, \quad P^*_{i_{\{n\}}} = \mathrm{e}^{a_s} P_{i_{\{n\}}}, \\ &X = R_{ij}\frac{\partial}{\partial R_{ij}} + R_{ijk}\frac{\partial}{\partial R_{ijk}} + \cdots + P_i\frac{\partial}{\partial P_i} + P_{ij}\frac{\partial}{\partial P_{ij}} + \cdots, \end{aligned} \tag{39}$$

which for isotropic turbulence becomes

$$t^* = t, \quad r^* = r, \quad \mathcal{F}^* = \mathrm{e}^{a_s}\mathcal{F}, \quad \mathcal{K}^* = \mathrm{e}^{a_s}\mathcal{K}, \quad X = \mathcal{F}\frac{\partial}{\partial \mathcal{F}} + \mathcal{K}\frac{\partial}{\partial \mathcal{K}}. \tag{40}$$

It is a rather obvious property that naturally arises out of linearity of the system (7) and (8) and, consequently, also of the von Kármán–Howarth equation.

The second statistical symmetry also has its origin in the linearity of the above system and essentially delineates their super-position principle. For the multi-point equations, we have

$$\begin{aligned} &t^* = t, \quad \boldsymbol{r}^* = \boldsymbol{r}, \quad R^*_{i_{\{n\}}} = R_{i_{\{n\}}} + a_z \hat{R}_{i_{\{n\}}}, \quad P^*_{i_{\{n\}}} = P_{i_{\{n\}}} + a_z \hat{P}_{i_{\{n\}}}, \\ &X = \hat{R}_{i_{\{n\}}}\frac{\partial}{\partial R_{i_{\{n\}}}} + \hat{P}_{i_{\{n\}}}\frac{\partial}{\partial P_{i_{\{n\}}}}, \end{aligned} \tag{41}$$

where $\hat{R}_{i_{\{n\}}}$ and $\hat{P}_{i_{\{n\}}}$ denote any solution of the system (7) and (8), respectively. For the von Kármán–Howarth equation, Equation (41) decreases to

$$t^* = t, \quad r^* = r, \quad \mathcal{F}^* = \mathcal{F} + a_z\hat{\mathcal{F}}, \quad \mathcal{K}^* = \mathcal{K} + a_z\hat{\mathcal{K}}, \quad X = \hat{\mathcal{F}}\frac{\partial}{\partial \mathcal{F}} + \hat{\mathcal{K}}\frac{\partial}{\partial \mathcal{K}}, \tag{42}$$

with $\hat{\mathcal{F}}$ and $\hat{\mathcal{K}}$ being any solution of Equation (20).

A third class of statistical symmetries exist (see [14]), which is absolutely crucial for shear flow. It is one of the key ingredients of the logarithmic law of the wall, and has implicitly been used in essentially all turbulence models as they are usually calibrated using the log law. For the case of decaying turbulence, these symmetries may not be invoked because of physical reasons.

As the end point of the construction of invariant solutions is the invariant surface condition (32), we may for the present problem of decaying isotropic turbulence employ a linear combination of all symmetries of the von Kármán–Howarth equation, i.e. Equations (35), (36), (38), (40) and (42) into Equation (32) to obtain

$$\frac{\mathrm{d}t}{a_2 t + a_3} = \frac{\mathrm{d}r}{a_1 r} = \frac{\mathrm{d}\mathcal{F}}{[2(a_1 - a_2) + a_s]\mathcal{F} + a_z\hat{\mathcal{F}}} = \frac{\mathrm{d}\mathcal{K}}{[3(a_1 - a_2) + a_s]\mathcal{K} + a_z\hat{\mathcal{K}}}, \tag{43}$$

which is the key equation to derive the classical and new turbulent scaling laws later.

Note that George et al. [9, 11] derived many of the results below using equilibrium similarity in the case of homogeneous turbulence. In this analysis, conditions similar to the relation (43) have implicitly been used.

4. Scaling laws of decaying turbulence and corresponding integral invariants

In the subsequent analysis, we first review the classical scaling laws of decaying turbulence in the light of those symmetries only stemming from Euler and Navier–Stokes equations and essentially revisiting and extending the work in ref. [20]. In a second step, the new statistical symmetries are invoked into the analysis and an extended set of turbulent scaling laws is generated prolonging the ideas first outlined in ref. [14]. If not stated otherwise, the large Reynolds number limit is always employed for the analysis of the von Kármán–Howarth equation in the following sections.

4.1. *Scaling laws of decaying turbulence from classical symmetries*

The starting point for this section is Equation (43) with the limitation that only the classical symmetries with the constants a_1, a_2 and a_3 are non-zero. Invoking this into Equation (43) and integrating, we find the following invariants:

$$\tilde{r} = \frac{r}{t^{\frac{2}{\sigma+3}}}, \quad \tilde{\mathcal{F}} = \frac{\mathcal{F}}{t^{-2\frac{\sigma+1}{\sigma+3}}} = \frac{\overline{u'^2} f}{t^{-2\frac{\sigma+1}{\sigma+3}}}, \quad \tilde{\mathcal{K}} = \frac{\mathcal{K}}{t^{-3\frac{\sigma+1}{\sigma+3}}} = \frac{\overline{u'^2}^{3/2} k}{t^{-3\frac{\sigma+1}{\sigma+3}}}, \tag{44}$$

and $\sigma = (2 - 3\frac{a_1}{a_2})/\frac{a_1}{a_2}$, where, in order to make an invariant solution, $\tilde{\mathcal{F}}$ and $\tilde{\mathcal{K}}$ may depend on $\tilde{r}$ as this is also an invariant. With this, we obtain the invariant solutions

$$\mathcal{F} = t^{-2\frac{\sigma+1}{\sigma+3}}\tilde{\mathcal{F}}(\tilde{r}), \quad \mathcal{K} = t^{-3\frac{\sigma+1}{\sigma+3}}\tilde{\mathcal{K}}(\tilde{r}), \tag{45}$$

which for $\mathcal{F}(r = 0)$ or $\tilde{\mathcal{F}}(\tilde{r} = 0)$ implies

$$\overline{u'^2} \sim t^{-2\frac{\sigma+1}{\sigma+3}}. \tag{46}$$

For later purposes, we further define the integral length scale and the turbulent Reynolds number as

$$\ell(t) = \int_{r=0}^{\infty} f(r, t)\mathrm{d}r \quad \text{and} \quad Re_t = \frac{\sqrt{\overline{u'^2}(t)}\ell(t)}{\nu}, \tag{47}$$

where ℓ always converges due to Equation (21). Employing $\tilde{r}$ in Equation (44) into Equation (47), we find

$$\ell(t) = t^{\frac{2}{\sigma+3}} \int_{\tilde{r}=0}^{\infty} f(\tilde{r}) \mathrm{d}\tilde{r} \sim t^{\frac{2}{\sigma+3}} \quad \text{and} \quad Re_t = \frac{\sqrt{\overline{u'^2}(t)}\ell(t)}{\nu} \sim t^{-\frac{\sigma-1}{\sigma+3}}. \tag{48}$$

4.1.1. *Loitsianskii integral:* $\sigma = 4$

In 1939, Loitsianskii [7] suggested from an integrated form of the von Kármán–Howarth equation (20) that

$$\Lambda = \overline{u'^2} \int_0^{\infty} r^4 f(r) \mathrm{d}r \tag{49}$$

is an invariant, i.e. independent of time t. Kolmogorov [21] recognized that this leads to the following temporal development:

$$\overline{u'^2} \sim t^{-10/7}, \quad \ell \sim t^{2/7}, \quad Re_t \sim t^{-3/7}, \tag{50}$$

which also corresponds to the low wave number energy spectrum $E(k) = \frac{\Lambda}{3\pi} k^4$.

4.1.2. *Birkhoff integral:* $\sigma = 2$

One and a half decades later in 1954, Birkhoff [8] suggested that

$$B = \overline{u'^2} \int_0^{\infty} r^2 \left(3f(r) + r \frac{\partial f}{\partial r} \right) \mathrm{d}r = \overline{u'^2} \lim_{r \to \infty} [r^3 f(r)] \tag{51}$$

is another invariant emerging from the volume integral of the two-point correlation function R_{ij} in r-space. Saffman [22] derived the corresponding temporal development

$$\overline{u'^2} \sim t^{-6/5}, \quad \ell \sim t^{2/5}, \quad Re_t \sim t^{-1/5}, \tag{52}$$

with the corresponding low wave number energy spectrum $E(k) = \frac{B}{\pi} k^2$.

4.1.3. *Generalized Birkhoff integral of algebraic type*

The idea of Birkhoff may be further generalized (see [23, 24]) to

$$B_m = \overline{u'^2} \int_0^{\infty} r^m \left((m+1) f(r) + r \frac{\partial f}{\partial r} \right) \mathrm{d}r = \overline{u'^2} \lim_{r \to \infty} [r^{m+1} f(r)], \tag{53}$$

which, if Equation (46) and $\tilde{r}$ in Equation (44) have been implemented into the integral, leads to $\sigma = m$ and the corresponding temporal development of the key turbulence parameters $\overline{u'^2}$, ℓ and Re_t may be taken from Equations (46) and (48) with σ replaced by m. It is apparent from the right-hand side of Equation (53) that the invariant B_m only exists if f

converges to zero as $r^{-(m+1)}$ for $r \to \infty$. From Equation (21), we find that a non-zero B_m may only exist for $m > 1$.

The form of the invariant may directly be employed into the von Kármán–Howarth equation (20) such that the entire equation is manipulated according to the operator $r^m((m+1) + r\frac{\partial}{\partial r})$ applied to f in the inner part of the integral (53). Doing so, the resulting right-hand side of the Kármán–Howarth equation appears to be a divergence expression. After integration about r in the domain $r \in (0, \infty)$, we obtain

$$\frac{\mathrm{d}B_m}{\mathrm{d}t} = \left[r^{m-3} \frac{\partial}{\partial r} \left[r^4 \left(\mathcal{K} + 2\nu \frac{\partial \mathcal{F}}{\partial r} \right) \right] \right] \Bigg|_0^\infty . \tag{54}$$

Note that B_m may only be an invariant if the right-hand side is zero and hence $\mathcal{K}$ has to converge to zero faster than r^{-m} as r tends to infinity.

In ref. [25], Vassilicos assumed a more general integral invariant that integrates both the Loitsianskii and Birkhoff integrals into one theory. The invariants we analyzed in this section are special cases of the invariants suggested by Vassilicos.

4.1.4. *Generalized Birkhoff integral of exponential type*

The generalized Birkhoff integral of algebraic type (53) will be further extended by considering the limit $m = \infty$. In this limit, r^m may be formally replaced by $\mathrm{e}^{r/a}$ including some other modifications where a is a constant length scale. In order to comprehend this, we first define the generalized Birkhoff integral of exponential type

$$B^{(a)} = \overline{u'^2} \int_0^\infty \mathrm{e}^{r/a} \left(\left(\frac{r}{a} + 1 \right) f(r) + r \frac{\partial f}{\partial r} \right) \mathrm{d}r = \overline{u'^2} \lim_{r \to \infty} [\mathrm{e}^{r/a} r f(r)]. \tag{55}$$

In order for Equation (55) to not diverge, it requires a rather stringent convergence rate for f of mixed exponential-algebraic decay to be further discussed later. With this in mind, we apply the operator $\mathrm{e}^{r/a}((\frac{r}{a} + 1) + r\frac{\partial}{\partial r})$ to the von Kármán–Howarth equation (20) and integrate over the domain $r \in (0, \infty)$ to obtain

$$\frac{\mathrm{d}B^{(a)}}{\mathrm{d}t} = \left[\frac{\mathrm{e}^{r/a}}{r^3} \frac{\partial}{\partial r} \left[r^4 \left(\mathcal{K} + 2\nu \frac{\partial \mathcal{F}}{\partial r} \right) \right] \right] \Bigg|_0^\infty . \tag{56}$$

Also here, in order to have a vanishing right-hand side, it requires a $\mathcal{K}$ that decays faster than $\mathrm{e}^{-r/a}/r$. An obvious scaling law may not be deduced from the above as the invariant solutions (46) and $\tilde{r}$ in Equation (44) do not lead to a constant $B^{(a)}$ even in the limit of a constant length scale, which corresponds to $\sigma = \infty$. This case will be discussed in the next section.

4.1.5. *Constant integral length scale*

Considering the above, we may also suggest other more commonly known physical quantities being an invariant, i.e. independent of time, such as the integral length scale

$$\ell = \int_0^\infty f(r)\mathrm{d}r = \text{const.} \tag{57}$$

As a result, we immediately obtain from Equation (44) that

$$\sigma = \infty, \tag{58}$$

and accordingly from Equation (46), we find

$$\overline{u'^2} \sim t^{-2}, \quad Re_t \sim t^{-1}. \tag{59}$$

We want to note that George and Wang [10] derived this decay law for the turbulent kinetic energy based on equilibrium similarity using the same assumption that the integral length scale remains constant in time.

Physically, the present case corresponds to high Reynolds number turbulence in a box of length L where the integral length scale has reached the box size $\ell \sim L$. This rather artificial case has been explored in an experiment by Stalp et al. [26] with liquid helium in a finite rectangular box flow, and in a numerical simulation by Borue and Orszag [27]. In both, the experiment and the numerical simulation, the t^{-2} decay law for the energy decay is observed.

The constant length scale assumption is formally in line with the integral in the invariant (55); still, the pre-factor $\overline{u'^2}$ is varying in time and thus $B^{(a)}$ is not time invariant.

This rather stringent concept of a global invariance may be further extended in the sense that the right-hand side of Equation (56) may not necessarily be assumed zero but it itself is a function of time only such that an ordinary differential in time emerges. In order to comprehend this, from Equation (56) we replace $\mathcal{K}$ according to the classical notation in Equation (19) with $\overline{u'^2}(t)^{3/2}k$ to observe assuming that k converges exactly as $\mathrm{e}^{-r/a}/r$, we have

$$\frac{\mathrm{d}\overline{u'^2}}{\mathrm{d}t} \sim \overline{u'^2}^{3/2}. \tag{60}$$

The latter, apparently, is fully consistent with the $\overline{u'^2}$ scaling in Equations (59) and (45) in the limit $\sigma = \infty$.

Physically, the above-mentioned constant box assumption requires a very fast decay of the correlation functions when approaching the box limits. Interestingly, this is fully in line with the very fast spatial exponential-algebraic decay according to Equations (55) and (56).

4.1.6. *Constant turbulent Reynolds number decay*

For this final case, it is unnecessary to invoke the large Reynolds number limit since it is the only case that allows for full similarity of all terms in the von Kármán–Howarth equation (20). Since the Reynolds number is assumed to be an invariant, i.e. independent of time, we have

$$Re_t = \text{const.} \tag{61}$$

From Equation (48), we immediately find

$$\sigma = 1 \quad \text{and} \quad \overline{u'^2} \sim t^{-1}, \quad \ell \sim t^{\frac{1}{2}}. \tag{62}$$

Although from a similarity point of view, only this case is fully consistent with all terms in Equation (20) – the decay law (62) is essentially never observed from experimental or direct numerical simulation (DNS) data. We may further note that this case does not correspond to any of the invariants above as the value $\sigma = 1$ would lead to $m = 1$. This, however, would lead to a vanishing B_1 in Equation (53) as f tends to zero faster than r^{-2}. Although, formally, an invariance reduction is achieved for all terms in the von Kármán–Howarth equation (20), there are strong physical arguments that impose strong doubts on Equation (62).

4.2. *Extended set of decaying turbulence scaling laws from statistical symmetries*

Although without having been explicitly stated, statistical symmetries of the type (40) or (42) have implicitly been used for many years, e.g. in turbulence models and more seldom for turbulent scaling laws such as the exponential decay of turbulence first suggested by George and Wang [10]. The first explicit use may have been the work by Oberlack and Rosteck [14].

4.2.1. *Extended algebraic decay laws*

In the first step for the construction of the new scaling laws, we extend the set of non-zero group parameters a_1, a_2 and a_3 by a_s. Still, in the first place, a_z remains zero. Employing this in the invariant surface condition (43) and conducting the integration, we obtain

$$\tilde{r} = \frac{r}{t^{\frac{2}{\sigma+3}}}, \quad \tilde{\mathcal{F}} = \frac{\mathcal{F}}{t^{-2\frac{\sigma+1}{\sigma+3}+\sigma_s}} = \frac{\overline{u'^2}\, f}{t^{-2\frac{\sigma+1}{\sigma+3}+\sigma_s}}, \quad \tilde{\mathcal{K}} = \frac{\mathcal{K}}{t^{-3\frac{\sigma+1}{\sigma+3}+\sigma_s}} = \frac{\overline{u'^2}^{3/2} k}{t^{-3\frac{\sigma+1}{\sigma+3}+\sigma_s}}, \tag{63}$$

with $\sigma = (2 - 3\frac{a_1}{a_2})/\frac{a_1}{a_2}$ and $\sigma_s = \frac{a_s}{a_2}$. Re-writing this in terms of an invariant solution for $\mathcal{F}$ and $\mathcal{K}$, we obtain

$$\mathcal{F} = t^{-2\frac{\sigma+1}{\sigma+3}+\sigma_s}\tilde{\mathcal{F}}(\tilde{r}), \quad \mathcal{K} = t^{-3\frac{\sigma+1}{\sigma+3}+\sigma_s}\tilde{\mathcal{K}}(\tilde{r}). \tag{64}$$

In terms of the classical turbulence parameters, we derive

$$\overline{u'^2} \sim t^{-2\frac{\sigma+1}{\sigma+3}+\sigma_s}, \quad \ell \sim t^{\frac{2}{\sigma+3}}, \quad Re_t \sim t^{-\frac{\sigma-1}{\sigma+3}+\frac{\sigma_s}{2}}. \tag{65}$$

The latter results do not affect the invariants such as Equation (49) or (51) but instead $\overline{u'^2}$ and the integral length scale ℓ are no longer closely coupled via the parameter σ. Instead, if a_s is non-zero, it induces an additional degree of freedom and hence a one-parametric set of solutions is generated. In order to derive them, we implement $\mathcal{F}$ above and $\tilde{r}$ in Equation (63) into Loitsianskii integral (49) to obtain

$$\Lambda \sim t^{\frac{2(4-\sigma)}{\sigma+3}+\sigma_s}. \tag{66}$$

As the invariant is constant in time, we immediately obtain

$$\sigma = \frac{8 + 3\sigma_s}{2 - \sigma_s}, \tag{67}$$

which apparently has the classical Loitsianskii case in the limit $\sigma_s = 0$.

Similarly, Birkhoff's results may be extended by substituting Equation (45) and $\tilde{r}$ from Equation (63) into the generalized Birkhoff integral (53) to derive

$$B_m \sim t^{\frac{2(m-\sigma)}{\sigma+3}+\sigma_s}, \tag{68}$$

which implies

$$\sigma = \frac{2m + 3\sigma_s}{2 - \sigma_s} \tag{69}$$

and reduces to the Birkhoff classical case for $m = 2$ and $\sigma_s = 0$.

We recall that the latter result relies on the fact that the generalized Birkhoff invariant B_m is an invariant, i.e. independent of time, which heavily relies on the assumption as in Equation (54) that $\mathcal{K}$ decays faster than r^{-m}.

As an alternative to the analysis above, we may put forward an argument similar to the derivation in the context of Equation (60). Therein, we have presumed that the right-hand side of the integrated von Kármán–Howarth equation does not vanish and hence no invariant exists in the usual sense. Similarly, in the present context, we assume f to decay as $r^{-(m+1)}$ and $\mathcal{K}$ tends to zero as r^{-m}. With this, the relation (54) leads to the balance

$$\frac{\mathrm{d}B_m}{\mathrm{d}t} \sim \ell^m \lim_{r=0} \mathcal{K}. \tag{70}$$

The latter may easily be verified by implementing Equations (45) and (63) into Equations (53) and (54) to verify equal powers of time on both the sides.

Finally, note that the row of scaling laws for the correlation function in Equation (64) may easily be extended to higher-order correlations that have the following form

$$R_{i_{\{n\}}} \sim t^{-n\frac{\sigma+1}{\sigma+3}+\sigma_s}. \tag{71}$$

4.2.2. *Exponential decay law – the singular limit $\sigma = -3$*

From Equation (45) or (64), it is apparent that the value $\sigma = -3$ is a singular value as the exponent diverges. From the basic definition of σ as in Equation (44), we deduce that this case traces back to the group parameter a_2 of scaling of time being zero. In this case, the latter invariant solutions are not valid any longer and we have to return to the invariant surface condition (43). We integrate the invariants under the constraint $a_2 = 0$ to obtain

$$\tilde{r} = r\mathrm{e}^{\omega t}, \quad \tilde{\mathcal{F}} = \mathcal{F}\mathrm{e}^{(2\omega+\omega_s)t} = \overline{u'^2} f \mathrm{e}^{(2\omega+\omega_s)t}, \quad \tilde{\mathcal{K}} = \mathcal{K}\mathrm{e}^{(3\omega+\omega_s)t} = \overline{u'^2}^{3/2} k \mathrm{e}^{(3\omega+\omega_s)t}, \tag{72}$$

with $\omega = -a_1/a_3$ and $\omega_s = a_s/a_3$ and both ω have dimension of the inverse of a time scale. The corresponding invariant solutions are

$$\mathcal{F} = \mathrm{e}^{-(2\omega+\omega_s)t}\tilde{\mathcal{F}}(\tilde{r}), \quad \mathcal{K} = \mathrm{e}^{-(3\omega+\omega_s)t}\tilde{\mathcal{K}}(\tilde{r}). \tag{73}$$

From this, the temporal development of the key turbulence quantities obeys the following scaling laws:

$$\overline{u'^2} \sim \mathrm{e}^{-(2\omega+\omega_s)t}, \quad \ell \sim \mathrm{e}^{-\omega t}, \quad Re_t \sim \mathrm{e}^{-(2\omega+\omega_s/2)\,t}. \tag{74}$$

At the first place, the convergence properties of the above integrals are not affected by the change from the algebraic to the exponential behavior. Exploring the new exponential scalings (73) with respect to the integrals (49), (51) and (53), we observe

$$\Lambda \sim \mathrm{e}^{-(7\omega+\omega_s)t} \tag{75}$$

for the Loitsianskii integral that yields

$$\omega = -\frac{\omega_s}{7}. \tag{76}$$

Similarly, the Birkhoff integral and its generalization (53) yield

$$B_m \sim \mathrm{e}^{-((m+3)\omega+\omega_s)t}, \tag{77}$$

which implies

$$\omega = -\frac{\omega_s}{m+3}, \tag{78}$$

with $m = 2$ as the classical Birkhoff case.

It is interesting to note that this exponential scaling law does not have any limiting case for vanishing statistical scaling group $a_s = 0$, which corresponds to $\omega_s = 0$. From the Loitsianskii integral in Equation (75), we derive that this would lead to the singular case $\omega = 0$, which is physically meaningless. On the other hand, from the Birkhoff generalized integral (77), setting $\omega_s = 0$ would lead to $m = -3$, which is singular and is essentially excluded as no non-zero invariant exists.

Again, as mentioned earlier, where B_m at two places is not interpreted as an invariant, but rather may depend on time, an analog analysis may be put forward for the present case. Therefore, we introduce Equations (73) and (72) into Equations (53) and (54) and making the same assumption for the decay of f and $\mathcal{K}$ as in the context of Equation (70), we find that the relation (70) still holds also for the present case.

From a physical and, hence, a symmetry point of view, it is important to note that the latter scaling behavior due to $a_2 = 0$ corresponds to a symmetry breaking of scaling of time. Thus, an external time scale has to be permanently imposed on the turbulent flow field while it is decaying. Two possible scenarios may be considered to achieve this. First, rotation imposes a constant global time scale on the flow. Both from experiments and DNS, an increased decay is not observed due to rotation, but instead the decay rate is considerably decreased with increasing rotation rate. More likely, an exponential decay may be accomplished by introducing a sink term into the Navier–Stokes equations (1) with a constant time scale, e.g.

$$F_i = -\frac{U_i}{\tau}, \tag{79}$$

with τ being a constant time scale at least of the same order as the largest time scale in the flow. Activating the latter in the Navier–Stokes equations and investigating the amended equations with respect to its symmetry properties immediately reveals the symmetry breaking $a_2 = 0$ or in other words, the scaling of time according to Equation (34) has disappeared. In fact, instead of a sink term, a source term of similar type with a positive sign on the right-hand side of Equation (79) may be imposed, which would lead to a change in sign for ω. No such simulations are known to the authors.

4.2.3. *Exponential decay law – the singular limit* $\sigma = \infty \ \wedge \ \sigma_s = \infty$

In Equation (58), we have used the constant length scale constraint which from Equation (48) induces $\sigma = \infty$ and in terms of the group parameters means $a_1 = 0$ as may be taken from the definition of σ as in Equation (63). If at the same time, $a_2 = 0$ is imposed, we find that $\sigma_s = \infty$, provided the only remaining scaling group a_s is non-zero. Using these limits, the invariants in Equation (63) are no longer valid and hence we need to impose the constraints $a_1 = a_2 = 0 \ \wedge \ a_s \neq 0$ into the invariant surface condition (43) to obtain

$$\tilde{r} = r, \quad \tilde{\mathcal{F}} = \mathcal{F}\,\mathrm{e}^{\omega_s t} = \overline{u'^2}\, f\,\mathrm{e}^{\omega_s t}, \quad \tilde{\mathcal{K}} = \mathcal{K}\,\mathrm{e}^{\omega_s t} = \overline{u'^2}^{3/2} k\,\mathrm{e}^{\omega_s t}, \tag{80}$$

with $\omega_s = a_s/a_3$, as for Equation (72). The corresponding invariant solutions are

$$\mathcal{F} = \mathrm{e}^{-\omega_s t}\tilde{\mathcal{F}}(\tilde{r}), \quad \mathcal{K} = \mathrm{e}^{-\omega_s t}\tilde{\mathcal{K}}(\tilde{r}). \tag{81}$$

From this, the temporal development of the key turbulence quantities obeys the following scaling laws:

$$\overline{u'^2} \sim \mathrm{e}^{-\omega_s t}, \quad \ell \sim \text{const.}, \quad Re_t \sim \mathrm{e}^{-\omega_s/2\, t}. \tag{82}$$

Note that this exponential decay was first suggested by George and Wang [10] and the first clear hint toward its existence appeared in refs. [28] and [29]. The key idea of this experiment was the generation of turbulence behind a grid with a special structure, e.g. an I-shaped element as used in the experiments mentioned before, which was iterated and scaled at the same time such that a fractal-type structure was established. Hence, the various sizes of the elements imposed multiple length scales onto the turbulent flow and, at the same time, as the fractal grid passes through at a fixed velocity, this generates a sequence of multiple time scales. As a consequence, the various length and time scales may impose a symmetry breaking of both space and time scaling with $a_1 = a_2 = 0$, as it has been used earlier. Note also that the classical group alone would not have been able to establish these new solutions (81) and (82) and only the inclusion of the additional statistical scaling group gave rise to its establishment.

None of the above integrals (49), (51), (53) or (55) constitute an invariant with respect to the invariant solutions (81). Still, as it has been discussed for various cases earlier, the integrated version of the von Kármán–Howarth equation may still be consistent with Equation (54) or (56) as long as certain spatial decaying properties are obeyed, as pointed out earlier in the context of the relation (70).

4.2.4. *Linear combinations of decay laws*

Up to this point, the rather generic symmetry group (42) has not been employed. It simply states the common super-position principle of linear DEs. Although not common in the turbulence community, all 'complete' statistical theories of turbulence, i.e. Hopf's functional approach [30], Lundgren's distribution function approach [31] and the MPC approach introduced in Section 2.1, are based on linear equations – certainly all of them possess infinite dimensions. Hence, all of them obey the related group (41) or (42), which for the present case means that any linear combination of the above-established decay laws is a valid solution of the von Kármán–Howarth equation or, if generalized to any higher-order correlation, is also a solution of the entire infinite set of MPC equations (7) with its side conditions (8).

For the present case of decaying turbulence, it has been observed by Mazellier and Vassilicos [32] that a certain decay appears to be exponential at the beginning of the decay phase, while later it changes to an algebraic behavior. It is rather apparent that this may come up due to the combination of an exponential and an algebraic decay where the power-law behavior is always the dominant one as time tends to infinity.

5. Summary and conclusions

The main achievement of the present contributions on decaying turbulence scaling laws is the derivation of new scaling laws and further, the unification of all of them under a common umbrella of Lie symmetry groups. This includes various algebraic and exponential scaling laws. Further, a rather generic group stating the super-position principle of linear equations gives rise to the unfamiliar result that any linear combination of scaling laws is also a scaling law. Although explicit formulas have mainly been derived for the isotropic correlation function appearing in the von Kármán–Howarth equation, Lie group theory guarantees that scaling laws for any higher-order correlation function can be generated. Besides the scaling laws, some extended integral invariants have been derived and put into context with the parameters appearing in the turbulent scaling laws.

Although, from a Lie symmetry point of view, the present analysis is complete for the scaling laws and its possible combinations, two main questions remain unanswered. First, it is still unknown which scaling parameter is related to a given initial condition, e.g. in a DNS or in an experiment. A discussion of this problem in some special cases is given by George [13]. Second, the spatial decay behavior in correlation space is an open question. This is intimately related to our inability to generate a complete solution to the MPC equation even for the simplest case of isotropic turbulence.

References

[1] L. Keller and A. Friedmann, *Differential gleichungen für die turbulente Bewegung einer kompressibelen Flüssigkeit*, in *Proceedings of the 1st International Congress on Applied Mechanics*, C.B. Biezeno and J.M. Burgers, eds., Delft, Netherlands, 1924, pp. 395–405, DELFT—TECHNISCHE BOEKHANDEL EN DRUKKERIJ J. WALTMAN JR.—192S.

[2] J.C. Rotta, *Turbulente Strömungen: Eine Einführung in die Theorie und ihre Anwendung*, in *Leitfäden der Angewandten Mathematik und Mechanik*, Vol. 15, B.G. Teubner Verlag, Stuttgart, 1972.

[3] G.I. Taylor, *Statistical theory of turbulence*, Proc. R. Soc. Lond. A Math. Phys. Sci. 151 (1935), pp. 421–444.

[4] T. von Kármán and L. Howarth, *On the statistical theory of isotropic turbulence*, Proc. R. Soc. Lond. A Math. Phys. Sci. 164 (1938), pp. 192–215.

[5] A.N. Kolmogorov, *The local structure of turbulence in incompressible viscous fluid for very large Reynolds numbers*, Docl. Akad. Nauk SSSR 30(4) (1941), pp. 299–303.

[6] A.N. Kolmogorov, *Dissipation of energy in the locally isotropic turbulence*, Docl. Akad. Nauk SSSR 32(1) (1941), pp. 19–21.
[7] L.G. Loitsianskii, *Some basic laws of isotropic turbulent flow*, Rep. No. 440 (Trans. NACA Tech. Memo. 1079), Central Aero Hydrodynamics Institute, Moscow, 1939.
[8] G. Birkhoff, *Fourier synthesis of homogeneous Turbulence*, Commun. Pure Appl. Math. 7 (1954), pp. 19–44.
[9] W.K. George and M.M. Gibson, *The self-preservation of homogeneous shear flow turbulence: GeorgeGibson 1992*, Exp. Fluids 13 (1992), pp. 229–238.
[10] W.K. George and H. Wang, *The exponential decay of homogeneous turbulence*, Phys. Fluids 21 (2009), 025108.
[11] W.K. George, *The decay of homogeneous isotropic turbulence*, Phys. Fluids A 4 (1992), pp. 1492–1509.
[12] H. Wang and W.K. George, *The integral scale in homogeneous isotropic turbulence*, J. Fluid Mech. 459 (2002), pp. 429–443.
[13] W.K. George, *Asymptotic effect of initial and upstream conditions on turbulence*, J. Fluids Eng. 134 (2012), 061203–1.
[14] M. Oberlack and A. Rosteck, *New statistical symmetries of the multi-point equations and its importance for turbulent scaling laws*, Discrete Continuous Dyn. Syst. Ser. S 3 (2010), pp. 451–471.
[15] G.W. Bluman, A.F. Cheviakov, and S.C. Anco (eds.), *Applications of Symmetry Methods to Partial Differential Equations*, Applied Mathematical Sciences, Vol. 168, Springer, New York, 2010.
[16] A.F. Cheviakov, *GeM software package for computation of symmetries and conservation laws of differential equations*, Comp. Phys. Comm. 176(1) (2007), pp. 48–61.
[17] A. Rosteck and M. Oberlack, *Lie algebra of the symmetries of the multi-point equations in statistical turbulence theory*, J. Nonlinear Math. Phys. 18 (2011), pp. 251–264.
[18] S.V. Khabirov and G. Ünal, *Group analysis of the von Kármán-Howarth equation. Part I. Submodels*, Commun. Nonlinear Sci. Numer. Simul. 7 (2002), pp. 3–18.
[19] S.V. Khabirov and G. Ünal, *Group analysis of the von Kármán-Howarth equation. Part II. Physical invariant solutions*, Commun. Nonlinear Sci. Numer. Simul. 7 (2002), pp. 19–30.
[20] M. Oberlack, *On the decay exponent of isotropic turbulence*, Proc. Appl. Math. Mech. 1 (2002), pp. 294–297.
[21] A.N. Kolmogorov, *Decay of isotropic turbulence in incompressible viscous fluids*, Docl. Akad. Nauk SSSR A 31 (1941), p. 538.
[22] P.G. Saffman, *The large-scale structure of homogeneous turbulence*, J. Fluid Mech. 27 (1967), pp. 581–593.
[23] M. Oberlack and N. Peters, *Closure of the two-point correlation equation in physical space as a basis for Reynolds stress models*, in *Near Wall Turbulent Flows*, R.M.C. So, C.G. Speziale, and B.E. Launder, eds., Elsevier, Amsterdam, 1993, pp. 85–94.
[24] M. Oberlack and N. Peters, *Closure of the two-point correlation equation as a basis for Reynolds stress models*, Appl. Sci. Res. 51 (1993), pp. 533–538.
[25] J.C. Vassilicos, *An infinity of possible invariants for decaying homogeneous turbulence*, Phys. Lett. A 375 (2011), pp. 1010–1013.
[26] S.R. Stalp, L. Skrbek, and R.J. Donnelly, *Decay of grid turbulence in a finite channel*, Phys. Rev. Lett. 82 (1999), pp. 4831–4834.
[27] V. Borue and S.A. Orszag, *Self-similar decay of three-dimensional homogeneous turbulence with hyperviscosity*, Phys. Rev. E 51 (1995), pp. R856–R859.
[28] D. Hurst and J.C. Vassilicos, *Scalings and decay of fractal-generated turbulence*, Phys. Fluids 19 (2007), 035103–035103–31.
[29] R.E. Seoud and J.C. Vassilicos, *Dissipation and decay of fractal-generated turbulence*, Phys. Fluids 19 (2007), 105108–105108–11.
[30] E. Hopf, *Statistical hydromechanics and functional calculus*, J. Ration. Mech. Anal. 1 (1952), pp. 87–123.
[31] T.S. Lundgren, *Distribution functions in the statistical theory of turbulence*, Phys. Fluids 10 (1967), pp. 969–975.
[32] N. Mazellier and J.C. Vassilicos, *Turbulence without Richardson-Kolmogorov cascade*, Phys. Fluids 22 (2010), 075101.

Journal of Turbulence, 2013
Vol. 14, No. 1, 147–164, http://dx.doi.org/14685248.2012.747688

Taylor & Francis
Taylor & Francis Group

Gradient trajectory analysis in a Jet flow for turbulent combustion modelling

M. Gampert*, P. Schaefer, V. Narayanaswamy and N. Peters

Institut für Technische Verbrennung, RWTH-Aachen University, Templergraben 64, Aachen, Germany

(*Received 29 August 2012; final version received 2 November 2012*)

Based on planar high-speed Rayleigh scattering measurements of the mixture fraction Z of propane discharging from a turbulent round jet into co-flowing carbon dioxide at nozzle-based Reynolds numbers Re_0 = 3000–8600, we use scalar gradient trajectories to investigate the local structure of the turbulent scalar field with a focus on the scalar turbulent/non-turbulent interface. The latter is located between the fully turbulent part of the jet and the outer flow. Using scalar gradient trajectories, we partition the turbulent scalar field into these three regions according to an approach developed by Mellado et al. (J.P. Mellado, L. Wang, and N. Peters, *Gradient trajectory analysis of a scalar field with external intermittency*, J. Fluid Mech. 626 (2009), pp. 333–365.). Based on these different regions, we investigate in a next step zonal statistics of the scalar probability density function (pdf) $P(Z)$ as well as the scalar difference along the trajectory ΔZ and its mean scalar value Z_m, where the latter two quantities are used to parameterize the scalar profile along gradient trajectories. We show that the scalar pdf $P(Z)$ can be reconstructed from zonal gradient trajectory statistics of the joint pdf $P(Z_m, \Delta Z)$. Furthermore, on the one hand we relate our results for the scalar turbulent/non-turbulent interface to the findings made in other experimental and numerical studies of the turbulent/non-turbulent interface, and on the other hand discuss them in the context of the flamelet approach and the modelling of pdfs in turbulent non-premixed combustion. Finally, we compare the zonal statistics for $P(Z)$ with the composite model of Effelsberg and Peters (E. Effelsberg and N. Peters, *A composite model for the conserved scalar pdf*, Combust. Flame 50 (1983), pp. 351–360) and observe a very good qualitative and quantitative agreement.

Keywords: jet flow; gradient trajectory; turbulent/non-turbulent interface; scalar pdf; flamelet theory

1. Introduction

Turbulent mixing is a subject of immense interest owing to its occurrence in numerous engineering applications, which involve the mixing of a scalar in a turbulent flow field. In a two-feed system, the state of mixing can be uniquely defined by a parameter called the mixture fraction Z, which is defined as the mass fraction of fuel stream in a given fuel–air mixture,

$$Z = \frac{m_f}{m_f + m_{\text{air}}}, \tag{1}$$

*Corresponding author. Email: m.gampert@itv.rwth-aachen.de

© 2013 Taylor & Francis

where the subscripts f and "air" refer to fuel stream and air, respectively. According to this definition, Z varies between $Z = 0$ and $Z = 1$. The mixture fraction and the associated scalar dissipation rate χ, which is defined as

$$\chi = 2D\left(\frac{\partial Z}{\partial x_i}\right)^2, \tag{2}$$

where D denotes the molecular diffusivity and repeated indices i imply summation over the three spatial dimensions, are very important parameters in non-premixed combustion; for instance, these describe the turbulent flame structure on the basis of the laminar flamelet theory [1, 2]. Combustion occurs when the fuel mass fraction in a fuel/oxidizer mixture reaches a particular value, called the stoichiometric mixture fraction Z_{st}. The value of Z_{st} is about 0.06 for different hydrocarbon/air mixtures; for instance, for a propane–air mixture, $Z_{st} = 0.06095$. Owing to the low values of stoichiometric mixture fraction, combustion occurs at the outer boundary of a turbulent fuel jet, which is characterized by turbulent regions adjacent to non-turbulent ones. When experimental investigations are performed, for instance, at the edge of a turbulent jet flow, the signal varies abruptly between a turbulent and a non-turbulent character for measurements of scalar quantities. Corrsin and Kistler [3] first termed the layer at the outer edge of this turbulent/non-turbulent (T/NT) interface the laminar superlayer. We are considering a scalar quantity only so that we will refer to the region in which the scalar signal changes from a turbulent to a laminar character in the following as the scalar T/NT interface to point out that all analyses are conducted in a scalar field. At the outer edge of this scalar T/NT interface a layer is present that will in the following be termed diffusive scalar sublayer in analogy to [3].

Detailed spatial analyses of this region have been carried out experimentally (e.g. [4–7]) and numerically (e.g. [8–10]), see [11] for a review of recent investigations, giving deeper insight into the vorticity dynamics close to the T/NT interface. In addition, Westerweel et al. [12] examined the temperature field of a non-isothermal jet and observed a good agreement of statistics with the ones obtained from the investigation of concentration and axial momentum [5,7,8,13,14] so that the findings presented in the following are considered to also apply to the fields of velocity and vorticity.

In a previous work, cf. [15], the contribution of the T/NT interface to the mixture fraction probability density function (pdf) *P(Z)* at various axial and radial locations has been examined, and the composite model proposed in [16] for the mixture fraction pdf in non-premixed combustion has been used. Thereby, the structure of the scalar T/NT interface in this free shear flow has been identified and it was concluded that the T/NT interface and its contributions to the mixture fraction pdf are of major importance, particularly in the early part of the jet. Then statistics such as the pdf of the location of the T/NT interface and the scalar profile across the latter were investigated and found to be in good agreement with literature data, cf. [7]. In addition, the scaling of the thickness δ of the scalar T/NT interface was analyzed at Reynolds numbers, $Re_\lambda = 60$–140, where Re_λ denotes the local Reynolds number based on the Taylor scale λ, using the mixture fraction profile in interface normal direction. It was observed that $\delta/L \propto Re_\lambda^{-1}$, where L is an integral length scale, meaning that $\delta \propto \lambda$ – a finding that is in good agreement with dimensional scaling arguments postulated by da Silva and Taveira [9].

The region of the T/NT interface was recently further analyzed by Mellado et al. [17]. In this work, the latter authors investigate the Direct Numerical Simulation (DNS) of a temporally evolving shear layer using gradient trajectories. Mellado et al. [17] applied this analysis to partition the scalar field into a fully turbulent zone, a zone containing

the T/NT interface and the outer laminar flow. Based on different regions, they examined the probability of these three zones at different locations in the shear layer and investigated the scalar pdf and the conditional scalar dissipation rate in the zones in the presence of external intermittency.

To this end, scalar gradient trajectories are calculated from each grid point in ascending and descending directions until a local extremum is reached, at which the scalar gradient vanishes and the Hessian is either positive-definite (minimum) or negative-definite (maximum). We define the local direction $\mathbf{n}$ of a gradient trajectory as

$$\mathbf{n} = \frac{\nabla Z}{\mid \nabla Z \mid}, \tag{3}$$

which is followed until the trajectory hits an extreme point. The projected velocity difference Δu_n, with

$$\Delta u_n = \mathbf{u}^+ \cdot \mathbf{n}^+ - \mathbf{u}^- \cdot \mathbf{n}^-, \tag{4}$$

along such a trajectory, where the superscripts denote the location at the maximum and minimum points, respectively, as well as between its bounding extreme points has been investigated for instance by Wang [18] and Gampert et al. [19, 20], where a linear scaling $\langle \Delta u_n \mid s \rangle \propto s \cdot a_\infty$ has been found to be universally valid, where s denotes the separation arc length along a gradient trajectory and a_∞ is the asymptotic value of the conditional mean strain rate acting on long gradient trajectories.

Peters [21] related such a gradient trajectory formulation in the mixture fraction field to the flamelet theory [1] in non-premixed combustion. The latter is a detailed multiscale approach in combustion modelling, which employs a non-equilibrium formulation in a thin layer in the vicinity of stoichiometric mixture Z_{st} as a microscale model. This microscale model, called flamelet equations, introduces the mixture fraction Z as an independent coordinate. Such flamelets often exist in the scalar T/NT interface, as the stoichiometric mixture is also frequently located here. Though the mixture fraction is a conserved scalar that represents the element mass fraction, Peters [21] shows that it may also be interpreted as a scaled coordinate along gradient trajectories,

$$\frac{\partial Z}{\partial n} = \left(\frac{\chi_Z}{2D} \right)^{1/2}, \tag{5}$$

where $\partial / \partial n = \mathbf{n} \cdot \nabla$ and χ_Z is the instantaneous, fluctuating scalar dissipation rate that is evaluated at a mixture fraction isoline. Based on this ansatz, Peters and Wang [22] derived a balance equation for the instantaneous scalar dissipation rate as a function of the mixture fraction.

The present study continues the investigation of the scalar T/NT interface in a turbulent jet flow and analyses the scalar pdf conditioned on different regions of the flow field using gradient trajectories. To this end, we perform high-frequency planar Rayleigh scattering measurements of pure propane C_3H_8 discharging from a free round jet into co-flowing pure CO_2. In this case, the local mass fraction $Y_{C_3H_8}$ of propane is equal to the mixture fraction Z,

$$Z = Y_{C_3H_8} = \frac{X_{C_3H_8} W_{C_3H_8}}{X_{C_3H_8}(W_{C_3H_8} - W_{CO_2}) + W_{CO_2}}. \tag{6}$$

In Equation (6), $X_{C_3H_8}$ is the propane mole fraction and $W_{C_3H_8}$ and W_{CO_2} are the molecular weights of propane and CO_2, respectively. In Section 2, we describe the experimental arrangement together with the calculation of scalar gradient trajectories, present the results for the zonal statistics in Section 3 and those for the composite model in Section 4 and finally conclude our paper in Section 5.

2. Experiment

The measurement technique and the post-processing data have been described and validated in companion papers, cf. [15,23] so that only a brief description is given in the following.

The experiments were performed in a co-flowing turbulent jet facility. Figure 1 shows the schematic of experimental setup. The facility consists of a center tube made of steel with an inner diameter of 12 mm. The surrounding co-flow tube had a diameter of 150 mm and a length of 450 mm, which was large enough to reduce the experimental setup to a two-stream problem. In the latter tube a honeycomb is installed in the lower third to guarantee a uniform velocity profile.

Research grade propane (99.95% pure) was fed through the center tube using a flow controller (OMEGA FMA-2600A) at various flow rates to achieve the desired Reynolds number. The co-flow gas was chosen as CO_2 owing to its larger Rayleigh cross-section, which was necessary to obtain an accurate determination of scalar gradient trajectories. For different experimental runs, the mean velocity of CO_2 was 0.05 m/s. Table 1 shows the flow configurations of all experimental runs made in this work. The Reynolds number Re_D based on jet exit conditions was varied between 3000 and 8610 and the corresponding jet exit velocity was between 1.15 m/s and 3.3 m/s. Furthermore, Re_λ $(= u_{\rm rms}\lambda_u/\nu_{\rm Cl})$ is the local Taylor-based Reynolds number on the center line. For the calculation of this quantity, $u_{\rm rms}$ has been measured using Laser Doppler Anemometry (LDA), the kinematic viscosity on the centerline $\nu_{\rm Cl}$ has been determined using the local concentration of two gases, while the Taylor length $\lambda_u (= (15\, u_{\rm rms}\nu_{\rm Cl}/\varepsilon)^{1/2})$ of the velocity field has been computed using an approximation formula to estimate ε taken from [24]. The latter has also been employed for the calculation of the Kolmogorov scale, η $(=(\nu^3/\varepsilon)^{1/4})$. Although these length scales are consequently not calculated directly from the measurements, and therefore have to be treated with caution, previous results suggest a quite accurate prediction, cf. [15,23] so that these will be used in the following to interpret the data.

The objective of the experiments was to obtain temporally and spatially highly resolved scalar field images, which were acquired using high-speed two-dimensional Rayleigh

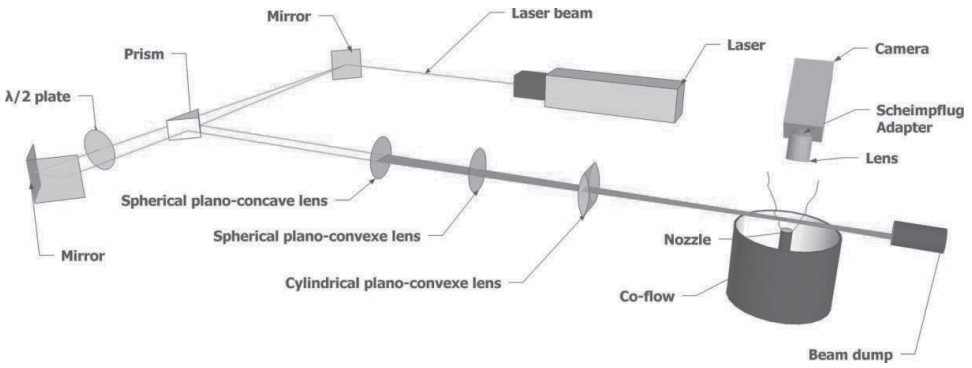


Figure 1. Experimental setup for high-speed Rayleigh scattering measurements.

Table 1. Experimental parameters.

x/d	10	15	20	30
Jet exit velocity, $\mathbf{U_0}$ **(m/s)**	1.15	1.76	1.82	3.30
Mean centerline velocity, $\mathbf{U_{Cl}}$ **(m/s)**	0.57	0.61	0.50	0.62
Mean centerline mixture fraction, $\Theta_{\mathbf{Cl}}$	0.38	0.24	0.18	0.13
Kolmogorov scale, η **(mm)**	0.18	0.20	0.26	0.24
Velocity Taylor scale, $\lambda_{\mathbf{u}}$ **(mm)**	2.30	3.32	4.26	4.61
Centerline viscosity, $\nu_{\mathbf{Cl}}$ **(mm^2/s)**	6.50	6.95	7.40	7.50
Nozzle-based Reynolds number, $\mathbf{Re_0}$	3000	4500	4750	8610
Taylor-based Reynolds number, $\mathbf{Re}_\lambda$	61	72	71	96

scattering imaging. Laser-Rayleigh scattering is used to determine the instantaneous mass fraction of the binary mixture of jet and reservoir gas in a small focal plane within the turbulent core of the jet around the center line.

For the Rayleigh scattering imaging, two frequency-doubled beams ($\lambda_f = 527$ nm) from a high-frequency dual-head Nd:YLF laser (Litron Lasers LDY303HE-PIV) were combined to deliver the energy of about 32 mJ/p at 1 kHz (32 W). To account for energy fluctuations, the signal is corrected on a shot-by-shot basis by a 12 bit energy monitor (LaVision Online Energy Monitor). The polarization of both beams was normal to the jet axis which maximized the Rayleigh scattering signals from the radial-azimuthal plane. The beams were transformed into a horizontal collimated sheet using a combination of a Galilean telescope (expansion ratio of 1.5) and a cylindrical lens. The width and the thickness (FWHM) of the resultant sheet were approximately 10 mm and 0.3 mm, respectively. Images were acquired at 1 kHz using a high-speed CMOS camera (LaVision HighSpeedStar 6) fitted with a camera lens (Nikon f.l. = 85 mm) stopped at $f/1.4$. An extension ring of 20 mm length was placed between the camera and the lens to minimize the working distance; the resulting field of view is about 60×60 mm. The signal-to noise ratio (SNR) in the pure propane region of raw images was over 40. The time interval between the successive images was 1 ms, while the in-plane resolution was 100 microns. This resolution is of the order of the Kolmogorov scale η, thus allowing a detailed investigation of gradient trajectories. The images were recorded using commercial software (LaVision 7.2) and were further processed using computer codes written in-house.

The major sources of systematic uncertainties are the departure from linearity of the camera response and the presence of noise in both propane and CO_2 streams. The departure from the linearity of the camera response is within 4%, as quoted by the manufacturer. The image noise was minimized using an optimal filter designed for the propane stream so that the scalar spectrum follows Pope's model [25]. However, there is residual noise left in the CO_2 after applying the optimal filter, which induces uncertainty in the calculation of scalar gradients. The combined uncertainty arising from these sources is estimated to be below 5%. Based on these corrected images, the signals corresponding to pure CO_2 and pure propane, respectively, are calibrated and used to convert the recorded photon counts to propane mass fraction. The impact of post-processing is illustrated in Figure 2, where (a) a sample raw image recorded at $x/d = 20$ and (b) the corresponding post-processed image are shown.

In the next step, the recorded time series of the plane at a fixed downstream location x/d is transformed into a spatial signal in streamwise direction with $\Delta x = U \cdot \Delta t$ based on Taylor's hypothesis, see [26]. Hence, we obtain a frozen three-dimensional mixture

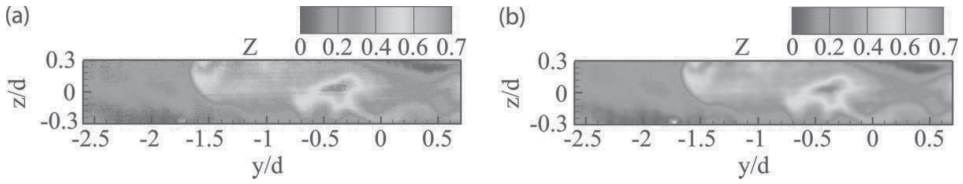


Figure 2. (a) Examplary raw and (b) post-processed images obtained at $x/d = 20$.

fraction field. Due to the importance of two-point statistics and spatial gradient quantities in turbulence, it is common to use Taylor's hypothesis to estimate spatial derivatives [27–29].

The camera resolves a plane of 1024×1024 pixels at a frequency of 1 kHz. This bounds the jet exit velocity U_0 to a value, at which the resolution in the x-direction remains at the order of the Kolmogorov scale at the various downstream positions x/d. Finally, the mean concentration Θ on the center line is given. Note that the analysis of the mixture fraction volume has been restricted in radial direction to $\tilde{r}(= r/(x - x_0)) < 0.1$, where x_0 denotes the virtual origin of the jet and has been found to be $x_0/d = -1.75$, cf. [23], and is performed at each axial location using three statistically independent sets of 5400 consecutive images.

3. Zonal statistics based on gradient trajectories

As described in Section 1, we will examine in the following the mixture fraction fields based on the procedure developed by Mellado et al. [17] using gradient trajectories. To this end, the flow is partitioned into three different regions using the statistics of scalar gradient trajectories – namely a fully turbulent zone, an outer flow region and embedded within these two the scalar T/NT interface.

In the following, gradient trajectories together with scalar minimum and maximum points are used to detect the different regions of the scalar field, see Figure 3 for an illustration: If a gradient trajectory associated with one specific grid point connects one minimum and one maximum point, this point is considered to be inside the fully turbulent zone.

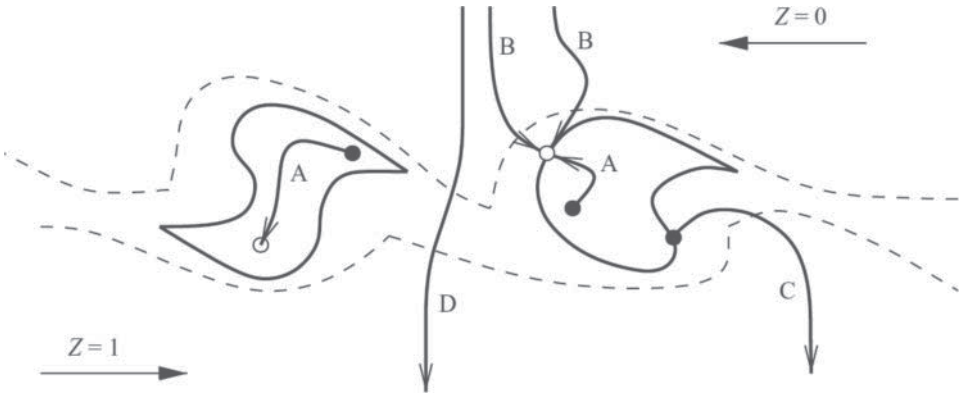


Figure 3. Flow partitioning based on gradient trajectories: A: Trajectory from minimum to maximum, fully turbulent zone; B: from upper stream to maximum, upper turbulent interface; C: from minimum to lower stream, lower turbulent interface (B and C will be called the scalar T/NT interface); D: from upper stream to lower stream, quasi-laminar diffusion layers (figure taken from [17]).

On the contrary, if the trajectory connects a maximum with the outer stream, where the mixture fraction $Z = 0$, then that point belongs to the scalar T/NT interface. In addition, the trajectory might theoretically proceed through the studied flow region without any intermediate extreme point, thus defining the so-called quasi-laminar diffusion layer. However, this effect is not observed in the present study. Finally, all points whose trajectories do not reach an extreme point are considered to be in the outer flow. The approach has already been successfully applied in [23], where it has been used to study the profiles of the zonal probability of three different regions over the non-dimensional radial coordinate $\tilde{r}$. It has been found that for $\tilde{r} < 0.08$ the scalar field is dominated by the fully turbulent region with an increasing contribution of the scalar T/NT interface, which is already present on the centerline with a zonal probability of approximately 0.05. For $\tilde{r} > 0.18$ in contrast, it is most probable to find the outer flow, whose contribution is not negligible starting at $\tilde{r} < 0.06$. In-between, however, the structure of the scalar field is mainly dominated by the scalar T/NT interface. In the present study, we will investigate in particular the zonal statistics of the scalar pdf $P(Z)$ in different regions in more detail.

Let us note that this partitioning is based on non-local information, as the grid points at a given radial distance from the centerline with a scalar value between the free-stream and the centerline value might belong to the scalar T/NT interface and the distinction is only possible by following the corresponding trajectory. Mellado et al. [17] showed that this non-local approach allows detecting engulfed regions, which is not possible if the interface definition is based on a single-valued envelope surface. However, an outer limit to the interface is also set by a threshold in the magnitude of the scalar gradient, below which the scalar is approximately a homogenous field with the outer flow value $Z = 0$. This second criterion defines the conventional intermittency function and separates the non-turbulent zones from the scalar T/NT interface.

As an example, in Figure 4 trajectories within the fully turbulent zone are shown to share a minimum point and reach eight different maximum points. Obviously, the resulting gradient trajectories are of strongly varying shape and intertwisted nature.

This differentiation between the outer non-turbulent zones and the T/NT interface has been introduced for several reasons. First, it is needed from the numerical point of view because the gradient approaches zero as one moves toward the outer homogeneous region so that below a threshold there is only noise, and the gradient direction is numerically undetermined. Second, this distinction is the conventional one used to define the intermittency factor and can be used to compare with traditional results using only this quantity. Finally, it is also useful to simplify possible models, since the pdf of the scalar field in these non-turbulent regions is just a delta function at the outer flow value $Z = 0$ and the scalar dissipation can be approximated by zero. In summary, a point at a given distance r from the centerline can be a part of the non-turbulent outer flow, belonging to the scalar T/NT interface or be located within a turbulent region.

In a first step, we calculate the extreme points in the experimentally obtained three-dimensional mixture fraction field as well as the corresponding gradient trajectories using the same numerical procedures already applied, for instance, in [19, 20, 30] so that we can afterwards define different regions in the scalar field. Figure 5 shows representative mixture fraction fields measured at $x/D = 10$. One clearly observes the following three different regions in the figure: A: the fully turbulent part of the flow, B: the scalar T/NT interface, where the value of the mixture fraction drops from the turbulent to the outer flow value ($Z = 0$) and C: the co-flow, which, by definition, corresponds to $Z = 0$ (note that in the co-flow region (C), the measured mixture fraction value fluctuates between $Z = 0$ and $Z = 0.03$, which is caused by the residual noise that is left after data-processing).

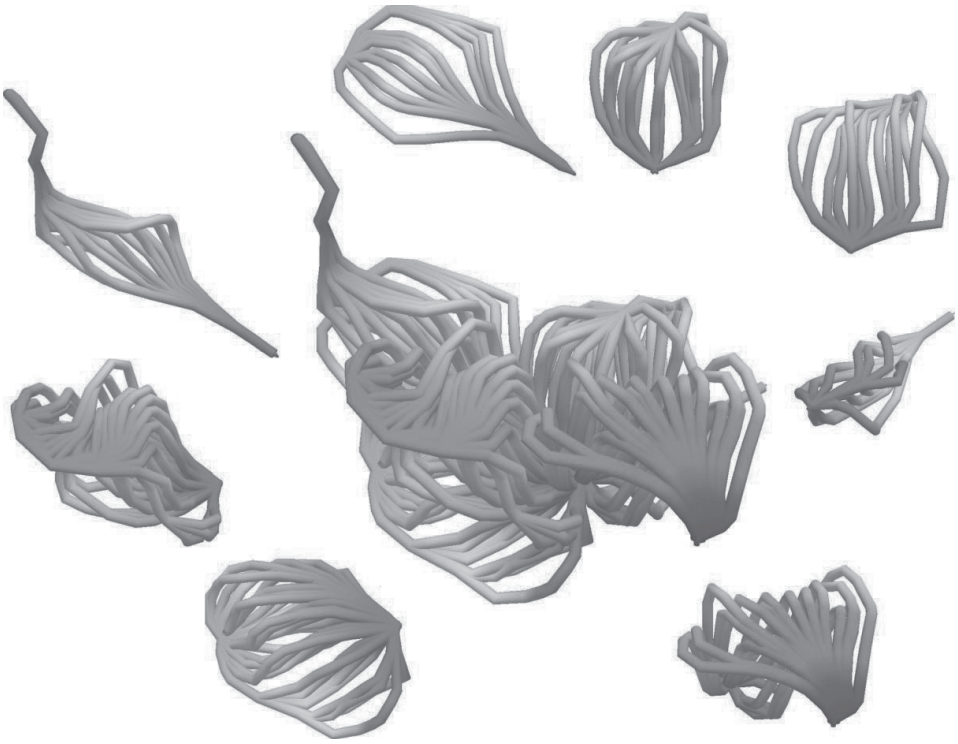


Figure 4. Example of gradient trajectories in the turbulent zone based on the mixture fraction field Z obtained at $x/d = 20$ and $Re_0 = 4750$. All trajectories share the same minimum point and connect it with eight different maximum points. The scalar value increases from minimum point (blue) to maximum point (red).

In some of the instantaneous realizations, we observe the presence of multiple T/NT interfaces due to the separation of turbulent eddies from the main flow as illustrated in Figure 5(b). These occasional patches are disconnected from the main jet body due to the breaking away of vortical eddies – a physical process that is called detrainment. However, for free shear flows detrainment is a small effect, as such patches are usually re-entrained within a few eddy time scales, cf. [31].

The parametrization of the scalar field along a gradient trajectory is necessary for statistical investigation. To this end, Peters and Trouillet [32] propose to use the arithmetic

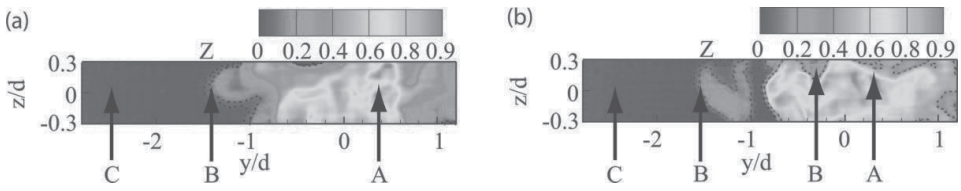


Figure 5. Sample instantaneous mixture fraction fields Z obtained at $x/d = 10$ and $Re_0 = 3000$ illustrating different regions of the flow field – A: inner turbulent flow, B: turbulent/non-turbulent interface and C: outer co-flow: (a) Instantaneous mixture fraction field with a single interface, and (b) instantaneous mixture fraction field with multiple turbulent/non-turbulent interfaces.

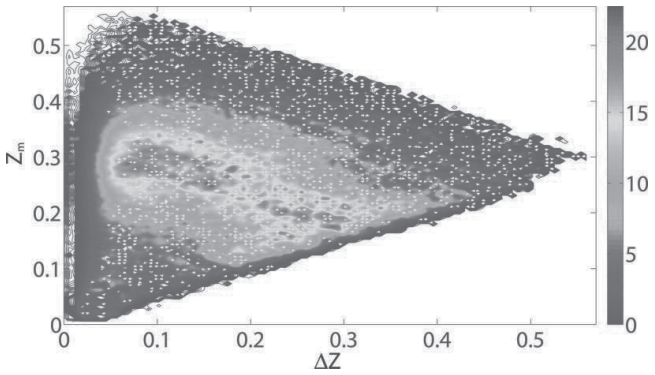


Figure 6. Isocontour lines of jpdf $P(Z_m, \Delta Z)$ for the whole domain within $\tilde{r} < 0.1$ obtained at $x/d = 15$.

mean Z_m of the minimum and maximum values of extremal points that bound the gradient trajectory,

$$Z_m = \frac{Z_{\max} + Z_{\min}}{2} \tag{7}$$

as well as the scalar difference ΔZ, where

$$\Delta Z = Z_{\max} - Z_{\min}. \tag{8}$$

Based on these quantities, the latter authors study the role of quasi-one-dimensional dissipation layers (Q1DLs) in turbulent scalar mixing. To this end, they replace the scalar Z by Z_m and ΔZ as independent variables based on which they, on the one hand, try to reconstruct the profiles of a scalar and its dissipation rate along gradient trajectories, and on the other hand formulate an equation for the joint probability distribution function (jpdf) $P(Z_m, \Delta Z)$ following the findings of O'Brien [33], who considered the pdf of a reactive–diffusive scalar. Computing for each grid point in the experimentally obtained mixture fraction field within $\tilde{r} < 0.1$ the corresponding gradient trajectories, we can in a first step calculate $P(Z_m, \Delta Z)$ for the overall domain. As shown in Figure 6, we obtain a triangular shaped jpdf, which has a distinct maximum at around $Z_m = 0.30$ and $\Delta Z = 0.15$. The theoretical boundaries of this jpdf are given by $Z_m = \Delta Z/2$ and $Z_m + \Delta Z/2 = 0.6$, as $Z = 0.6$ is the maximum mixture fraction value.

Based on the method described above, we distinguish between this jpdf the fully turbulent $P_t(Z_m, \Delta Z)$ and the interface $P_s(Z_m, \Delta Z)$ regions. The resulting jpdfs are shown in Figure 7(a) for the scalar T/NT interface and in Figure 7(b) for the turbulent region. We observe in Figure 7(a) that all values of this jpdf are concentrated around $Z_m = \Delta Z/2$, as the criterion for the interface detection is that the trajectory connects the outer flow ($Z = 0$) with a maximum point so that $Z_m = (Z_{\max} + Z_{\min})/2 = Z_{\max}/2$ and $\Delta Z = Z_{\max} - Z_{\min} = Z_{\max}$. However, though the jpdf in the T/NT interface should only be represented by a line defined by $Z_m = \Delta Z/2$, it has a thin distinct width, which is limited by the above-mentioned residual noise level after post-processing. Furthermore, it has a maximal probability at $Z_m = 0.16$ and $\Delta Z = 0.32$ from which we find a decreasing probability toward the origin and the longest trajectories for which $Z_m = 0.29$ and $\Delta Z = 0.58$. From Figure 7(b), which shows the jpdf $P_t(Z_m, \Delta Z)$ in the fully turbulent region, it is obvious that the rest of the

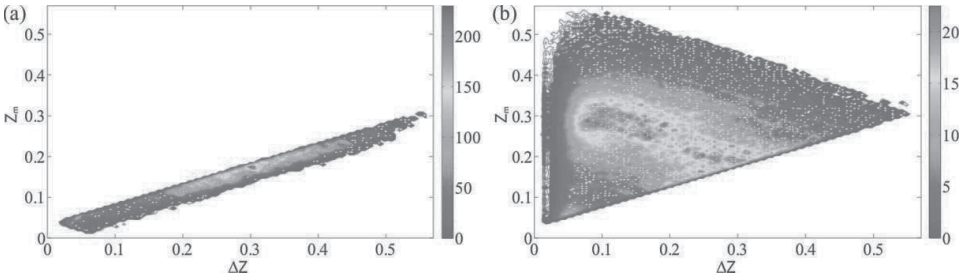


Figure 7. Isocontour lines of the jpdfs (a) $P_s(Z_m, \Delta Z)$ for the the T/NT interface region, and (b) $P_t(Z_m, \Delta Z)$ for the fully turbulent part of the domain within $\tilde{r} < 0.1$ obtained at $x/d = 15$.

total jpdf (cf. Figure 6) corresponds to the turbulent part. As a total jpdf, it has a triangular shape with a maximum at around $Z_m = 0.1 - 0.2$ and $\Delta Z = 0.30$ with a cropped off lower edge due to missing T/NT interface contributions. Naturally, the jpdf in the outer flow has a peak at $Z_m = \Delta Z = 0$.

In Figure 8, the marginal pdfs for (a) Z_m and (b) ΔZ are shown. For $P_t(Z_m)$ in the turbulent zone, we find an almost Gaussian bell-shaped pdf with a mean of approximately $Z_m = 0.25$, where also the maximum of the pdf is located. Furthermore, $P_t(Z_m)$ ranges from $Z_m = 0$ to 0.5 in contrast to $P_s(Z_m)$ in the scalar T/NT interface. The latter marginal pdf is zero for mixture fraction values larger than $Z_m = 0.28$, a finding that is expected, as in this region of the field the mixture fraction decreases from its turbulent to the outer flow value so that even theoretically only a maximal value of $Z_m = 0.5$ is possible.

We observe in Figure 8(b) that while the turbulent pdf $P_t(\Delta Z)$ starts at $\Delta Z_t = 0$ and ranges up to $\Delta Z_t = 0.31$, the pdf conditioned on the T/NT interface has its lowest value at $\Delta Z_s = 0.06$ and ranges up to $\Delta Z_s = 0.56$. This finding translates directly to the observed jump of the scalar value across the T/NT interface, cf. [7, 15]. In addition, it is evident from Figure 8(b) that the region of stoichiometric mixture is frequently located within the scalar T/NT interface – a finding that is in good qualitative agreement with the results of Mellado et al. [17]; quantitative differences of the actual values of $P(\Delta Z)$ and the range of Z-values originate in the different flow setup that is considered by the latter authors.

As the T/NT interface starts in the outer flow with $Z = 0$ and ranges up to $Z = \Delta Z_s = 0.56$, the value of the stoichiometric mixture for propane and air $Z_{st} = 0.06095$ is always located along such a gradient trajectory. Furthermore, we notice that the shape of $P_s(\Delta Z)$ in the interface qualitatively strongly resembles $P_s(Z_m)$, which is due to the definition of

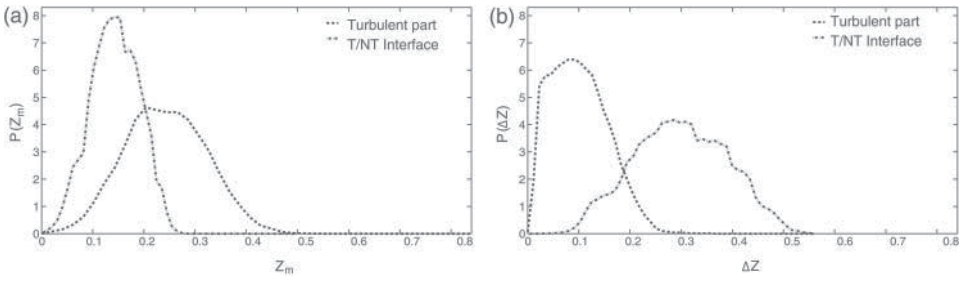


Figure 8. Marginal pdfs (a) $P(Z_m)$, and (b) $P(\Delta Z)$ for the fully turbulent part and the T/NT interface obtained at $x/d = 15$.

the T/NT interface region based on trajectories. As the latter starts in the outer flow at $Z = 0$, we obtain $\Delta Z = Z_{\max}$ and $Z_m = Z_{\max}/2$ so that we find the same shape for the pdfs of ΔZ and Z_m, which for Z_m is just shifted to smaller values and rescaled to an area of unity. In contrast, the scalar difference between the extreme points of gradient trajectories in the fully turbulent zone is much smaller with a mean of $\Delta Z = 0.1$ so that this region is characterized by many small fluctuations in the scalar field.

Based on the jpdf of these two parameters (cf. Figures 6 and 7), we will in the following investigate the scalar pdf $P(Z)$ in the different regions of the field and show that it can be reproduced from $P(Z_m, \Delta Z)$ obtained by the gradient trajectory statistics. In a first step, we therefore write the overall pdf in terms of its different contributions [15–17],

$$P(Z) = \gamma[(1 - s)P_t(Z) + sP_s(Z)] + (1 - \gamma)P_o(Z), \tag{9}$$

where γ is the intermittency factor defined as the fraction of the signal that is not due to the outer flow and s is the interface contribution, given by the fraction of the T/NT interface within the remaining part. Furthermore, $P_t(Z)$ is the scalar pdf in the fully turbulent zone, $P_s(Z)$ denotes the pdf stemming from the T/NT interface and $P_o(Z)$ is the scalar pdf in the outer flow, which by definition is a delta peak at zero. Each of these pdfs as well as the overall one can be calculated purely from the jpdf of the introduced gradient trajectory parameters by Peters and Trouillet [32],

$$P_i(Z) = \int_0^1 \int_0^{\Delta Z_{\max}} P_l(Z; Z_m, \Delta Z) P_i(Z_m, \Delta Z) d\Delta Z dZ_m. \tag{10}$$

In Equation (10), $P_i(Z_m, \Delta Z)$ is the zonal jpdf of Z_m and ΔZ, while $P_l(Z)$ is the local distribution function of Z within the gradient trajectory of length l. However, as the latter is unknown, we follow the approximation of Peters and Trouillet [32], who assume a sine

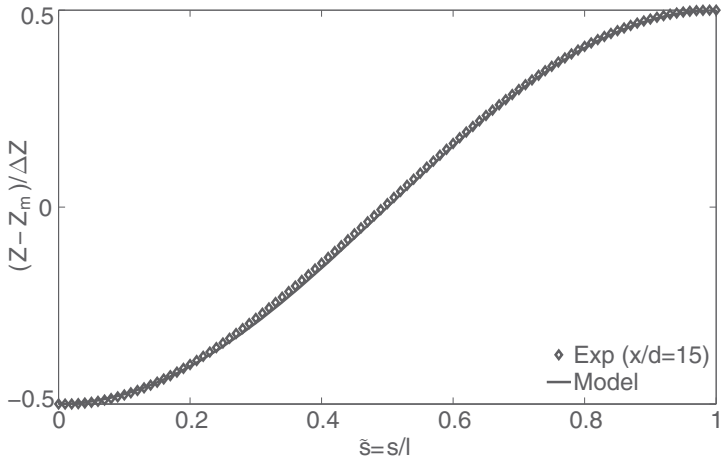


Figure 9. Comparison of the model ansatz from Equation (11) for the mean scalar profile along a gradient trajectory together with the experimental data obtained at $x/d = 15$.

function for the monotonic profile of Z, yielding

$$Z = Z_m + \frac{\Delta Z}{2} \sin(\pi \tilde{s} - \pi/2), \tag{11}$$

where $\tilde{s} = s/l$ is a normalized coordinate along the trajectory, which increases linearly from zero to one. This ansatz for the scalar profile (solid line) together with the experimental data averaged over all trajectories (diamond markers) are exemplary shown for $x/d = 15$ over the normalized coordinate $\tilde{s}$ in Figure 9. In this figure, we observe a very good agreement of the model curve with the experimental data with only marginal deviations around the inflection point.

Using such a scalar profile, we obtain [34]

$$P_l(Z; Z_m, \Delta Z) = \frac{P(s)}{\mid \partial Z/\partial s \mid} \tag{12}$$

that can be computed for each combination $(Z_m, \Delta Z)$ following [32]

$$P_l(Z; Z_m, \Delta Z) = \frac{\pi^{-1}}{\mid (Z - Z_m + \Delta Z/2)^{1/2}(Z_m + \Delta Z/2 - Z)^{1/2} \mid}. \tag{13}$$

Introducing Equation (12) in Equation (10) together with the jpdfs shown in Figures 6 and 7 allows us to reconstruct the scalar pdfs within the different zones of the scalar field; see Figure 10 calculated from the data obtained at $x/d = 15$. We observe for the experimentally obtained pdf (open circles) a bimodal shape with a maximum at $Z = 0.23$, a non-zero value at the origin of $P(Z = 0)$ close to unity and and intermittency factor $\gamma = 0.995$. In addition, the scalar pdfs computed separately for the turbulent and the interface parts are shown weighted by its respective prefactors according to Equation (9) together with the reconstructed overall pdf, which is also calculated according to Equation (9) (note that the pdf of the outer flow region P_o is not shown in Figure 10 as it is only a delta peak at the origin). Nevertheless, it is included in the total pdf to which it only

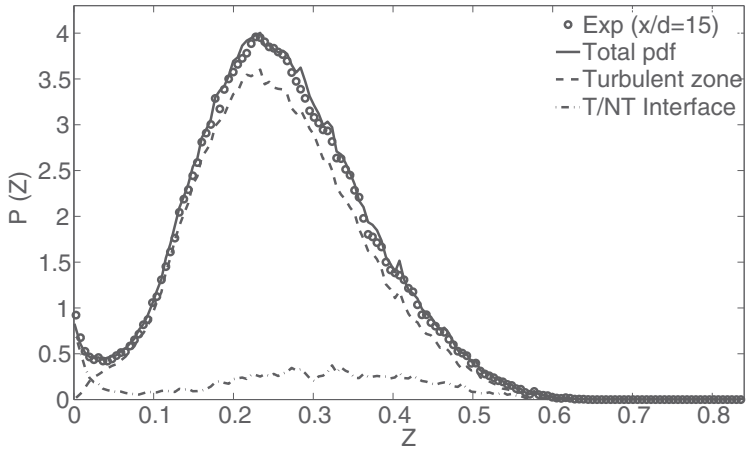


Figure 10. Comparison of the measured pdf $P(Z)$ obtained at $x/d = 15$ with the one calculated from Equation (9). In addition, the weighted zonal pdfs of the fully turbulent $\gamma[(1 - s)P_t(Z)]$ and the scalar T/NT interface $\gamma[sP_s(Z)]$ are shown.

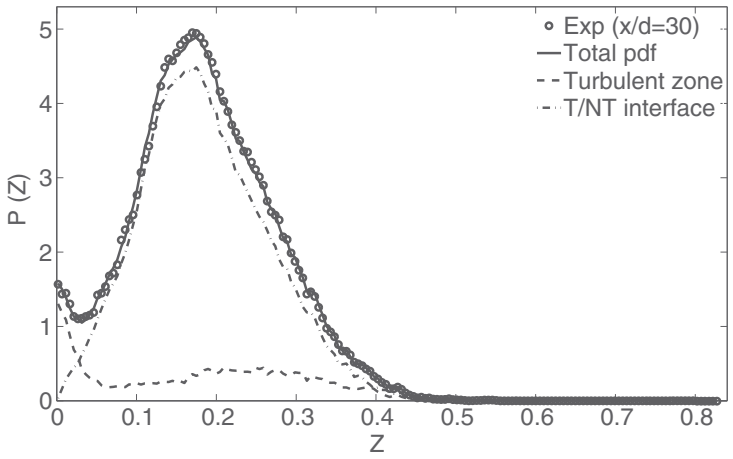


Figure 11. Comparison of the measured pdf $P(Z)$ obtained at $x/d = 30$ with the one calculated from Equation (9). In addition, the weighted zonal pdfs of the fully turbulent $\gamma[(1-s)P_t(Z)]$ and the scalar T/NT interface $\gamma[s\,P_s(Z)]$ are shown.

has a very small contribution ($1-\gamma = 0.005$). We observe a very good qualitative and quantitative agreement of the reconstructed pdf with the measured one, further validating that the ansatz (Equation (11)) is in close agreement with the real scalar profile along the tajectories. Furthermore, we can attribute specific parts of the measured pdf to different flow regions. In the fully turbulent part, the pdf is close to a Gaussian shape with a value of $P(Z=0) = 0$ at the origin and a maximum at $Z = 0.23$, the location of which coincides with the one of the total pdf. In contrast, the pdf of the T/NT interface recovers the non-zero value of the measured pdf at the origin, which is not due to contributions from the outer flow only. In addition, it has a non-zero value over the whole range of mixture fraction values with a small maximum at approximately $Z = 0.33$. This may be explained by the fact that the T/NT interface contains not only the T/NT interface itself but also the adjacent regions up to the first maximum point. Finally, its contribution s calculated from the fraction of the interface region within the non-outer flow part is $s = 0.107$.

The same trends described for Figure 10 can also be observed in Figure 11, where the scalar pdfs within the different zones of the scalar field are shown, which are computed from the data obtained at $x/d = 30$. For the experimental pdf again a bimodal shape is found that seems to stem from the interface contributions to the total pdf (see dashed line) which has a maximum at $Z = 0.17$, a non-zero value at the origin of $P(Z=0)$ and extends up to $Z = 0.46$. Further, we find $\gamma = 0.984$ and $s = 0.140$ and observe again a very good agreement between reconstructed and measured pdfs. In addition, the pdf of the fully turbulent part has the shape of a Gaussian bell-curve as in Figure 10 with a value of $P(Z=0) = 0$ at the origin and a maximum, whose location again coincides with the one of the total pdf.

4. Evaluation of a composite model for the mixture fraction pdf

The previous findings are not only of importance for the physical understanding of turbulent mixing but also for the well-established presumed pdf approach to model scalar pdfs in turbulent non-premixed combustion. One of the most widely used approaches undertaken for predictions in intermittent flow regions is to presume a β-pdf, bi-variate or

multi-variate β-distributions (see [35] and for instance [36] for a discussion and comparison of various scalar pdf models in non-premixed combustion). It should be emphasized that, similar to the β-pdf, the bi-variate and multi-variate distributions were also developed to approximate the experimentally determined pdfs $P(Z)$. Furthermore, it is vital to note that the β-pdf can assume only the values of zero or infinity at $Z = 0$; this is a clear deficiency with respect to the pdf shown in Figure 10. For highly intermittent cases, one may argue that the β-pdf's flexibility of generating a singularity at $Z = 0$ is favorable. Such an argument, however, ignores the fact that the physics of the fully turbulent region and the T/NT interface are quite different. Whereas the physics of the fully turbulent region is determined by the stochastic fluctuations, the interface is strongly influenced by molecular transport.

Effelsberg and Peters [16] showed that the mixture fraction pdf in intermittent regions can be physically explained by considering separate contributions from the fully turbulent flow, the scalar T/NT interface and the outer co-flow. As this composite model has recently been successfully validated for the mixture fraction pdf at various radial and axial locations of a jet flow, cf. [15], we compute the composite model and its zonal contributions according to [16] for the experimentally obtained pdf at $x/d = 15$ so that the results can be compared with the gradient trajectory statistics discussed in the previous chapter. To this end, we first calculate the intermittency factor (γ) for the measured pdf $P(Z)$ in the propane-CO_2 jet. Based on γ and $P(Z)$, we then calculate the composite model pdf $P_c(Z)$ following Equation (9).

To obtain the pdfs for the fully turbulent part $P_t(Z)$ and the interface part $P_s(Z)$, we compute the model parameters (s, k, α_t and γ_t) from the first four moments of the measured pdf of Z using the relations given in [16].

We use the parameters α_t, β_t and γ_t to construct a beta function that is hypothesized to model the pdf contribution from the fully turbulent part

$$P_t(Z_t) = \frac{\Gamma(\gamma_t)}{\Gamma(\alpha_t)\Gamma(\beta_t)} Z_t^{\alpha_t - 1}(1 - Z_t)^{\beta_t - 1}. \tag{14}$$

Note that α_t, β_t and γ_t in the above equation are related as $\gamma_t = \alpha_t + \beta_t$. To obtain the pdf contribution from the T/NT interface, we assume the mixture fraction profile across the scalar T/NT interface as follows:

$$Z = Z_t \left[\frac{y}{\delta}\right]^{1/(1-k)}, \tag{15}$$

where Z_t is a random variable whose distribution is given by Equation (14), which corresponds to the mixture fraction at the edge of the turbulent region and k is one of the model parameters. Using these parameters, the pdf contribution from the scalar T/NT interface is calculated as follows:

$$P_s(Z) = \frac{1 - k}{Z^k} \int_Z^1 Z_t^{k-1} P_t(Z_t) dZ_t. \tag{16}$$

For a detailed description of the derivation, refer to [16]. The resulting composite pdf together with the weighted zonal pdfs of the fully turbulent and the T/NT interface regions are shown in Figure 12. In addition, a β-pdf is included for comparison and illustration of the above deficiencies that has been calculated using the first two moments of the experimental pdf.

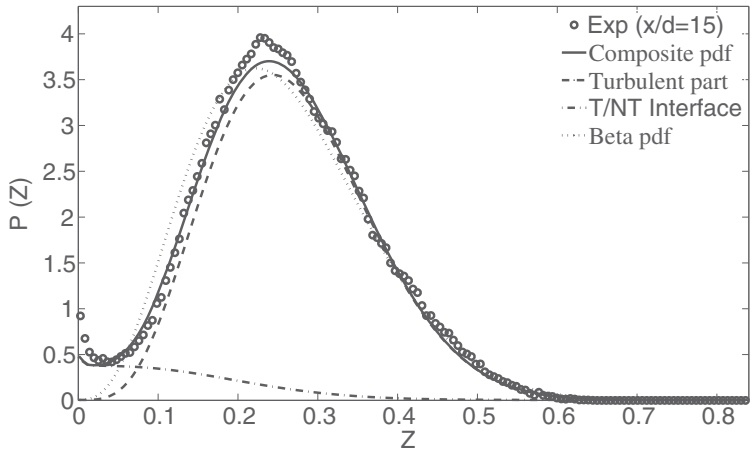


Figure 12. Comparison of the measured pdf $P(Z)$ obtained at $x/d = 15$ with the model pdf for conserved scalar quantities of Effelsberg and Peters [16]. Furthermore, the weighted zonal pdfs of the fully turbulent $\gamma[(1-s)P_t(Z)]$ and the T/NT interface regions $\gamma[sP_s(Z)]$ as calculated from the composite model are shown.

Overall, we observe a very good agreement for the composite model as compared with the measured pdf. For the calculation of the model pdf, we have solved the equations relating the first four moments of the measured pdf to the model parameters for which we have obtained $s = 0.088$, $k = 0.009$, $\alpha_t = 5.243$ and $\beta_t = 14.033$. Both location and value of the maximum lie almost on top of each other. The same is valid for the tail of the pdf, where the composite model only slightly overpredicts the values for $P(Z)$. The composite model also reproduces the bimodal shape of the pdf, although it underpredicts the region close to the origin, where it does not recover the quite steep rise that is present in the pdf that is computed from the experiment.

Regarding the contributions to the composite pdf that are modelled to be stemming from the fully turbulent part, we observe a very similar shape as for the zonal pdf shown in Figure 10. The location and the value of the maximum are in good agreement; however, behind the latter the model pdf decreases slower to zero than the zonal pdf obtained from gradient trajectory statistics. Nevertheless, the intersection with the x-axis is for both pdfs at around $Z = 0.62$. Another difference between model and experiment is present at the origin. While the measured pdf starts at $Z = 0$ and already contributed significantly to the overall pdf in the region ranging up to $Z = 0.10$, the modelled pdf only starts at $Z = 0.03$ and is smaller than the T/NT interface contributions up to $Z = 0.08$.

The same findings as for the fully turbulent zone are valid for the pdf of the scalar T/NT interface. Qualitatively, we observe a good agreement of the model pdf with the one calculated from gradient trajectories. However, while the latter starts at almost at the same value as the modelled pdf, it decreases faster to small values of $P(Z)$ but contributes to the overall pdf in the whole range of Z-values up to $Z = 0.62$. In contrast, the model pdf for the T/NT interface has a significant contribution to the composite pdf up to $Z = 0.30$ but is already zero for values larger than $Z = 0.41$. In addition, it decreases monotonically to zero. It is evident that the way the T/NT interface pdf is modelled by the composite pdf model, this enables the reproduction of the bimodal shape of the overall pdf. In addition, we note that the model predicts a value of $s = 0.088$, which is slightly smaller than the actual value of $s = 0.107$. This difference can be explained by comparing the different shapes of

the mixture fraction along a gradient trajectory and in the composite model, cf. Equations (11) and (15). While along a gradient trajectory the mixture fraction is assumed to follow a sine profile, it is modelled linearly in the limit of k approaching zero in the composite pdf. Thus, the volume fraction occupied by the T/NT interface can be expected to be larger for the analysis based on gradient trajectories, which will result in larger values for s.

In summary, we find a very good overall agreement of the composite model with that of the zonal analysis and the pdf that is computed from the measurements. In addition, the zonal mixture fraction pdf calculated from gradient trajectory statistics and the model are qualitatively close to each other, although slight quantitative differences are present. These findings further highlight, on the one hand, the impact of the scalar T/NT interface on the mixture fraction pdf in the early part and particularly at the edge of a turbulent jet flow, and on the other hand give indications on how to develop and optimize existing models that are currently employed in the computation of turbulent non-premixed combustion.

5. Conclusion

We have presented planar high-speed Rayleigh scattering measurements of the mixture fraction Z of propane discharging from a turbulent round jet into co-flowing CO_2 at nozzle-based Reynolds numbers $Re_0 = 3000$–8600, based on which we have investigated the local structure of the turbulent scalar field as well as the scalar pdf using scalar gradient trajectories.

The latter have been calculated for every grid point, and scalar profiles along the latter are parametrized by the arithmetic mean Z_m of minimum and maximum values of extremal points that bound the gradient trajectory and the scalar difference ΔZ between them. Using these parameters, we have partitioned the turbulent scalar field into three regions – a fully turbulent one, where each trajectory connects a minimum and a maximum point, the outer flow with $Z = 0$ and a meandering scalar T/NT interface, where a maximum point is connected with the outer flow via a gradient trajectory – the latter structure is embedded within the former two. In the next step, we have investigated the jpdf $P(Z_m, \Delta Z)$ as well as the marginal pdfs $P(Z_m)$ and $P(\Delta Z)$ in different zones and observe distinct characteristics for each of them: many small fluctuations together with a large mean scalar value are typical for the fully turbulent region, while the regularly observed large jump of scalar value is caught by the gradient trajectory statistics in the scalar T/NT interface. As the latter starts in the outer flow at $Z = 0$, it also directly follows from this large jump that the T/NT interface trajectories frequently contain the comparatively small value of stoichiometric mixture Z_{st}.

Then we have presented a method to reconstruct the overall scalar pdf $P(Z)$ based on gradient trajectory statistics using the jpdf $P(Z_m, \Delta Z)$ in the different zones of the scalar field. We observe a good agreement between the experimentally obtained pdf with the reconstructed one, where $P_t(Z)$ in the turbulent part has the shape of a Gaussian-bell curve, while $P_s(Z)$ in the T/NT interface has a non-zero value at the origin from which it decreases to zero.

Finally, we discuss the impact of the former results on modelling approaches for pdfs of conserved scalar quantities. To this end, we compare the measured pdf with the one obtained from the composite model of Effelsberg and Peters [16]. We observe a very good agreement of the composite model with the experimentally obtained pdf. The fully turbulent pdfs agree in shape and value for $P(Z)$, while the zonal mixture fraction pdfs calculated from gradient trajectory statistics and the model are qualitatively close to each other but exhibit slight quantitative deviations.

Acknowledgements

This work was funded by the Research School “BrenaRo” and the Cluster of Excellence “Tailor-Made Fuels from Biomass," which is funded by the Excellence Initiative of the German Federal state governments to promote science and research at German universities.

References

[1] N. Peters, *Laminar diffusion flamelet models in non-premixed turbulent combustion*, Progr. Energy Combust. Sci. 10 (1984), pp. 319–339.
[2] N. Peters, *Turbulent Combustion*, Cambridge University Press, Cambridge, UK, 2000.
[3] S. Corrsin and A.L. Kistler, *Free-stream boundaries of turbulent flows*, NACA Rep. 1244, 1955.
[4] C.F.J. Westerweel T. Hofmann, and J. Hunt, *The turbulent/non-turbulent interface at the outer boundary of a self-similar turbulent jet*, Exp. Fluids 33 (2002), pp. 873–878.
[5] M. Holzner, A. Liberzon, N. Nikitin, W. Kinzelbach, and A. Tsinober, *Small-scale aspects of flows in proximity of the turbulent/nonturbulent interface*, Phys. Fluids 19 (2007), 071702.
[6] M. Holzner, B. Luethi, A. Tsinober, and W. Kinzelbach, *Acceleration, pressure and related quantities in the proximity of the turbulent/non-turbulent interface*, J. Fluid Mech. 639 (2007), pp. 153–165.
[7] J. Westerweel, C. Fukushima, J. Pedersen, and J. Hunt, *Momentum and scalar transport at the turbulent/non-turbulent interface of a jet*, J. Fluid Mech. 631 (2009), pp. 199–230.
[8] C.B. da Silva and J.C. Pereira, *Invariants of the velocity-gradient, rate-of-strain, and rate-of-rotation tensors across the turbulent/nonturbulent interface in jets*, Phys. Fluids 20 (2008), 055101.
[9] C.B. da Silva and R.R. Taveira, *The thickness of the turbulent/nonturbulent interface is equal to the radius of the large vorticity structures near the edge of the shear layer*, Phys. Fluids 22 (2010), 121702.
[10] C.B. da Silva and J.C. Pereira, *The role of coherent vortices near the turbulent/non-turbulent interface in a planar jet*, Phil. Trans. R. Soc. A369 (2011), pp. 738–753.
[11] J. Hunt, I. Eames, C. da Silva, and J. Westerweel, *Interfaces and inhomogeneous turbulence*, Philos. Trans. R. Soc. London A 369 (2011), pp. 811–832.
[12] J. Westerweel, A. Petracci, R. Delfos, and J. Hunt, *Characteristics of the turbulent/non-turbulent interface of a non-isothermal jet*, Phil. Trans. R. Soc. A 369 (2011), pp. 723–737.
[13] J. Westerweel, C. Fukushima, J. Pedersen, and J. Hunt, *Mechanics of the turbulent nonturbulent interface of a jet*, Phys. Rev. Lett. 95 (2005), 174501.
[14] M. Holzner, A. Liberzon, N. Nikitin, B. Lthi, W. Kinzelbach, and A. Tsinober, *A Lagrangian investigation of the small-scale features of turbulent entrainment through 3D-PTV and DNS*, J. Fluid Mech. 598 (2008), pp. 465–475.
[15] M. Gampert, V. Narayanaswamy, P. Schaefer, and N. Peters, *Superlayer contributions to the mixture fraction pdf in a turbulent round jet flow*, J. Fluid. Mech. (submitted).
[16] E. Effelsberg and N. Peters, *A composite model for the conserved scalar pdf*, Combust. Flame 50 (1983), pp. 351–360.
[17] J.P. Mellado, L. Wang, and N. Peters, *Gradient trajectory analysis of a scalar field with external intermittency*, J. Fluid Mech. 626 (2009), pp. 333–365.
[18] L. Wang, *Scaling of the two-point velocity difference along scalar gradient trajectories in fluid turbulence*, Phys. Rev. E 79 (2009) 046325.
[19] M. Gampert, J.H. Goebbert, P. Schaefer, M. Gauding, N. Peters, F. Aldudak, and M. Oberlack, *Extensive strain along gradient trajectories in the turbulent kinetic energy field*, New J. Phy. 13 (2011), 043012.
[20] M. Gampert, P. Schaefer, J. Goebbert, and N. Peters, *Decomposition of the field of the turbulent kinetic energy into regions of compressive and extensive strain*, Physica Scripta T (in press).
[21] N. Peters, *Multiscale combustion and turbulence*, Proceedings of the 32nd Symposium on Combustion, Montreal, Canada, 2008; Proc. Combust. Inst. 32 (2009), pp. 1–25.
[22] N. Peters and L. Wang, *The central role of the scalar dissipation rate in non-premixed combustion*, Proceedings of the 5th US Combustion Meeting, San Diego, CA, 2007.
[23] V. Narayanaswamy, M. Gampert, J. Goebbert, and N. Peters, *Scalar gradient trajectory measurements using high-frequency cinematographic planar Rayleigh scattering*, Exp. Fluids (submitted).

[24] C.A. Friehe, C.W. Van Atta, and C.H. Gibson, *Jet turbulence dissipation rate measurements and correlations*, AGARD Conference Proceedings on Turbulent Shear Flows, CP-93 (1971), pp. 18.1–18.7.
[25] S. Pope, *Turbulent Flows*, Cambridge University Press, Cambridge, UK, 2000.
[26] G.I. Taylor, *The spectrum of turbulence*, Proc. R. Soc.London A 164 (1938), p. 476.
[27] A. Tsinober, E. Kit, and T. Dracos, *Experimental investigation of the field of velocity gradients in turbulent flows*, J. Fluid Mech. 242 (1992), pp. 169–192.
[28] M. Kholmyansky and A. Tsinober, *On an alternative explanation of anomalous scaling and how well-defined is the concept of inertial range*, Phys. Lett. A 373 (2009), pp. 2364–2367.
[29] R.A. Antonia and K.R. Sreenivasan, *Log-normality of temperature dissipation in a turbulent boundary layer*, Phys. Fluids 20 (1977), pp. 1800–1804.
[30] P. Schaefer, M. Gampert, J.H. Goebbert, L. Wang, and N. Peters, *Testing of different model equations for the mean dissipation using Kolmogorov flows*, Flow Turbul. Combust. 85 (2010), pp. 225–243.
[31] A. Hussain and A. Clark, *On the coherent structure of the axisymmetric mixing layer: A flow-visualization study*, J. Fluid Mech. 104 (1981), pp. 263–294.
[32] N. Peters and P. Trouillet, *On the role of quasi-one-dimensional dissipation layers in turbulent scalar mixing* , in *Annual Research Briefs*, Center for Turbulence Research, Stanford University, California, 2002, pp. 27–40.
[33] E.E. O'Brien, *The probability density function (pdf) approach to reacting turbulent flows*, in *Turbulent Reacting Flows*, P.A. Libby and F.A. Williams eds., Springer Berlin Heidelberg, 1980, pp. 67–75.
[34] A. Papoulis *Probability, Random Variables and Stochastic Processes*, 3rd ed., McGraw-Hill, Columbus, OH, 1991.
[35] S. Girimaji, *Assumed β-pdf model for turbulent mixing: Validation and extension to multiple scalar mixing*, Combust. Sci. Technol. 78 (1991), p. 177.
[36] G.M. Goldin and S. Menon, *A Comparison of scalar pdf turbulent combustion models*, Combust. Flame 113 (1998), pp. 442–453.

Journal of Turbulence
Vol. 13, No. 31, 2012, 1–10

Taylor & Francis
Taylor & Francis Group

Statistical theories versus statistical mechanics of homogeneous isotropic turbulence

Tomomasa Tatsumi*

Department of Physics, Faculty of Science, Kyoto University (Professor Emeritus)
26-6 Chikuzendai, Momoyama, Fushimi, Kyoto 612-8032, Japan

(*Received 3 April 2012; final version received 8 June 2012*)

The present paper is concerned with the "closure problem of turbulence," which constituted the main subject of the Session on the "Energy transfer in homogeneous turbulence" in the last Turbulence Colloquium Marseille (TCM) 1961.

It is usual in statistical theory of turbulence to express the random velocity field of turbulence in terms of the velocity correlations of various orders and deal with the set of dynamical equations governing these velocity correlations. This way is, however, associated with the difficulty of unclosedness since each equation involves two velocity correlations of different orders as unknowns according to the nonlinearity of the Navier–Stokes equation, and hence we have to introduce some relationship between the velocity correlations of different orders in order to make the set of equations closed.

Among various *closure* theories proposed so far, the *quasi-normal closure* by Proudman and Reid (Proudman and W.H. Reid, Phil. Trans. R. Soc. Lond. A 247 (1954), pp. 163–189) and Tatsumi (T. Tatsumi, Proc. Roy. Soc. Lond. A 239 (1957), p. 16.) and the *direct-interaction closure* by Kraichnan (R.H. Kraichnan, J. Fluid Mech. 5 (1959), pp. 497–543.) have been taken up in the Session and critical survey and evaluation have been made on these theories. Apart from particular merits and demerits of the theories, it has been recognized that they still remain in approximate levels with either partial or no fulfillment of Kolmogorov's nonzero inertial energy-dissipation hypothesis.

More recently, Tatsumi (T. *Tatsumi, in Geometry and Statistics of Turbulence*, T. Kambe ed., Kluwer, 2001, pp. 3–12.) formulated statistical mechanics of fluid turbulence in terms of the Lundgren–Monin equations (T.S. Lundgren, Phys. Fluids, 10 (1967), pp. 969–975; A.S. Monin, PMM J. Appl. Math. Mech. 31 (1967), pp. 1057–1068.) for the multipoint velocity distributions of turbulence and the *cross-independence closure* of these equations. It has been shown by Tatsumi (T. Tatsumi, J. Fluid Mech. 670 (2011), pp. 365–403.) that this closure provides us with exact closure of the Lundgren–Monin equations and thus exact solution to any problem concerning the mean velocity products.

Keywords: Homogeneous turbulence; statistical velocity-distribution; cross-independence closure

I. Introduction

A. Randomness and determinism of turbulence

In view of the subtitle of the present Colloquium, "*Fundamental Problems of Turbulence,*" let us consider the fundamental characters of turbulence, *randomness* and *determinism.*

*Email: tatsumi@skyblue.ocn.ne.jp

ISSN: 1468-5248 online only
© 2012 Taylor & Francis
http://dx.doi.org/10.1080/14685248.2012.702910
http://www.tandfonline.com

The high complexity of turbulent flows at large Reynolds numbers is most adequately dealt with statistically in terms of the *random motions* in space, but we should not forget that each realization of turbulent flows involves *deterministic motions* in time governed by the dynamical equation of motion. Without *randomness,* the turbulent motion reduces to a *chaotic* dynamical motion, while lacking of *determinism*, the turbulent motion becomes a *stochastic* random process. Thus, the difficulty of turbulence really arises from this coexistence of the *randomness* and the *determinism* in its character.

Speaking more specifically, turbulent motions can be statistically expressed in two ways, either in terms of the mean products of the multipoint turbulent velocities or by the joint probability distributions of these velocities. In either way, the randomness takes place only at a certain initial time, and the evolutions of the mean velocity products and the joint velocity distributions in time are determined dynamically. This standpoint of the *initial randomness* is not necessarily taken in common, but it will be maintained in the statement of this paper.

B. Statistics and dynamics of turbulence

During the last half a century, our knowledge on the *chaotic* motion and the *stochastic* process has made a big progress and now it constitutes an indispensable part of our common sense. It is our earnest wish to be able to formulate statistical mechanics of fluid turbulence having both random and deterministic characters.

II. Dynamical aspect of turbulence

A. Equations of motion

We consider homogeneous isotropic turbulence in an incompressible viscous fluid governed by the Navier–Stokes equation for the velocity $\mathbf{u}(\mathbf{x}, t)$

$$\left(\frac{\partial}{\partial t}-\nu\left|\frac{\partial}{\partial \mathbf{x}}\right|^2\right)\mathbf{u}+\left(\mathbf{u}\cdot\frac{\partial}{\partial \mathbf{x}}\right)\mathbf{u}=-\frac{\partial}{\partial \mathbf{x}}\left(\frac{p}{\rho}\right) \tag{1}$$

and the nondivergence condition

$$\frac{\partial}{\partial \mathbf{x}}\cdot\mathbf{u}=\mathbf{0}, \tag{2}$$

where $p(\mathbf{x}, t)$ denotes the pressure and ρ and ν the density and the kinetic viscosity of fluid, respectively.

B. Mean velocity products

Historically speaking, the randomness of turbulent velocity field $\mathbf{u}(\mathbf{x}, t)$ has mostly been represented by means of the *mean velocity products* at a certain number of points such as follows:

$$\begin{aligned} U^{(2)}_{ij}(\mathbf{r},t) &= \langle u_i(\mathbf{x}_1, t)\, u_j(\mathbf{x}_2, t)\rangle, \\ U^{(3)}_{ijk}(\mathbf{r}, \mathbf{r}'; t) &= \langle u_i(\mathbf{x}_1, t)\, u_j(\mathbf{x}_2, t)\, u_k(\mathbf{x}_3, t)\rangle, \\ U^{(4)}_{ijkl}(\mathbf{r}, \mathbf{r}', \mathbf{r}''; t) &= \langle u_i(\mathbf{x}_1, t)\, u_j(\mathbf{x}_2, t)\, u_k(\mathbf{x}_3, t)\, u_l(\mathbf{x}_4, t)\rangle, \end{aligned} \tag{3}$$

with $\mathbf{r} = \mathbf{x}_2 - \mathbf{x}_1$, $\mathbf{r}' = \mathbf{x}_3 - \mathbf{x}_1$, and $\mathbf{r}'' = \mathbf{x}_4 - \mathbf{x}_1$,where the brackets $\langle \quad \rangle$ denote the average with respect to the probability distribution of concern and each of suffixes i, j, k, l takes values $(1, 2, 3)$. According to the homogeneity, the mean velocity $\langle u_i(\mathbf{x}_1, t)\rangle$ can be taken to zero and the velocity products are functions of the relative distances $\mathbf{r}$, $\mathbf{r}'$, and $\mathbf{r}''$of the points.

C. Equations for mean velocity-products

The equations for the mean velocity products are obtained by using Equations (1) and (2), and the first two of them are expressed as follows:

$$\left(\frac{\partial}{\partial t} - \nu\left|\frac{\partial}{\partial \mathbf{r}}\right|^2\right) U_{ij}^{(2)}(\mathbf{r},t) = \sum_{k=1}^{3}\frac{\partial}{\partial r_k}\left\{U_{ijk}^{(3)}(\mathbf{r},\mathbf{0};t) - U_{jik}^{(3)}(-\mathbf{r},\mathbf{0};t)\right\} + \frac{\partial}{\partial r_i}P_j(\mathbf{r},t) - \frac{\partial}{\partial r_j}P_i(\mathbf{r},t), \tag{4}$$

$$\left[\frac{\partial}{\partial t} - \nu\left(\left|\frac{\partial}{\partial \mathbf{r}}\right|^2 + \left|\frac{\partial}{\partial \mathbf{r}'}\right|^2\right)\right] U_{ijk}^{(3)}(\mathbf{r},\mathbf{r}';t)$$
$$= \sum_{l=1}^{3}\left[\left(\frac{\partial}{\partial r_l} + \frac{\partial}{\partial r_l'}\right) U_{ijkl}^{(4)}(\mathbf{r},\mathbf{r}',\mathbf{0};t) - \frac{\partial}{\partial r_l}U_{jikl}^{(4)}(-\mathbf{r},\mathbf{r}'-\mathbf{r},\mathbf{0};t) - \frac{\partial}{\partial r_l'}U_{jikl}^{(4)}(-\mathbf{r}',\mathbf{r}-\mathbf{r}',\mathbf{0};t)\right] + \left(\frac{\partial}{\partial r_i} + \frac{\partial}{\partial r_i'}\right)P_{jk}(\mathbf{r},\mathbf{r}';t)$$
$$- \frac{\partial}{\partial r_j}P_{ik}(-\mathbf{r},\mathbf{r}'-\mathbf{r};t) - \frac{\partial}{\partial r_k}P_{ij}(-\mathbf{r}',\mathbf{r}-\mathbf{r}';t), \tag{5}$$

where $P_i(\mathbf{r},t) = (1/\rho)\langle p(\mathbf{x},t)\, u_i(\mathbf{x}+\mathbf{r},t)\rangle$ and $P_{ij}(\mathbf{r},\mathbf{r}';t) = (1/\rho)\left\langle p(\mathbf{x},t)\, u_i(\mathbf{x}+\mathbf{r},t)\right.$ $\left. u_j(\mathbf{x}+\mathbf{r}',t)\right\rangle$ denote the pressure–velocity products but they are eliminated later using Equation (2).

Thus, the problem of turbulence is reduced to the dynamical problem concerning the equations for the mean velocity products as dynamical variables. This formalism constitutes *dynamical approach* to turbulence and the statistical theories of turbulence developed so far mostly belong to this category.

In this context, it should be noted that Equation (4) is not solvable as itself since it includes two unknowns $U^{(2)}$ and $U^{(3)}$, so that we have to introduce some relationship between these velocity products for closing this equation. This situation does not change even if we proceed to the next stage since Equation (5) for $U^{(3)}$ includes the higher-order term $U^{(4)}$. This problem constitutes the central difficulty in the theory of turbulence which is known as the *dynamical closure problem.*

D. Fourier transform of turbulent velocity

For homogeneous turbulence, mathematical analysis is drastically simplified by taking the Fourier transform of the velocity $\mathbf{u}(\mathbf{x}, t)$ as

$$\mathbf{u}(\mathbf{x},t) = \int \widetilde{\mathbf{u}}(\mathbf{k},t)\exp(i\mathbf{k}\cdot\mathbf{x})\, d\mathbf{k}, \tag{6}$$

and working throughout in the wave-number space.

The equation for the transformed velocity $\widetilde{\mathbf{u}}(\mathbf{k}, t)$ is derived from Equations (1) and (2) as

$$\left(\frac{\partial}{\partial t} + \nu k^2\right) \widetilde{\mathbf{u}}(\mathbf{k}, t) = -i \int (\mathbf{k} \cdot \widetilde{\mathbf{u}}(\mathbf{k} - \mathbf{k}', t)) \times \left[\widetilde{\mathbf{u}}(\mathbf{k}', t) - \frac{\mathbf{k}}{k^2}(\mathbf{k} \cdot \widetilde{\mathbf{u}}(\mathbf{k}', t))\right] d\mathbf{k}', \tag{7}$$

where $k = |\mathbf{k}|$ and the pressure term has been eliminated using the orthogonal condition, and

$$\mathbf{k} \cdot \widetilde{\mathbf{u}}(\mathbf{k}, t) = 0. \tag{8}$$

The mean velocity products defined by Equation (3) are written as

$$\begin{aligned} U_{ij}^{(2)}(\mathbf{r}, t) &= \int \widetilde{U}_{ij}^{(2)}(\mathbf{k}, t) \exp(i\mathbf{k} \cdot \mathbf{x})\, d\mathbf{k}, \\ U_{ijk}^{(3)}(\mathbf{r}, \mathbf{r}'; t) &= \int\int \widetilde{U}_{ijk}^{(3)}(\mathbf{k}, \mathbf{k}'; t) \exp[i(\mathbf{k} \cdot \mathbf{r} + \mathbf{k}' \cdot \mathbf{r}')] d\mathbf{k} d\mathbf{k}', \\ U_{ijkl}^{(4)}(\mathbf{r}, \mathbf{r}', \mathbf{r}''; t) &= \int\int\int \widetilde{U}_{ijk}^{(4)}(\mathbf{k}, \mathbf{k}', \mathbf{k}''; t) \\ &\quad \times \exp[i(\mathbf{k} \cdot \mathbf{r} + \mathbf{k}' \cdot \mathbf{r}' + \mathbf{k}'' \cdot \mathbf{r}'')] d\mathbf{k} d\mathbf{k}' d\mathbf{k}'', \end{aligned} \tag{9}$$

with $\mathbf{k} + \mathbf{k}' + \mathbf{k}'' = 0$.

E. Equations for mean Fourier-transformed velocity-products

Equations (4) and (5) for the velocity products $U_{ij}^{(2)}(\mathbf{r}, t)$ and $U_{ijk}^{(3)}(\mathbf{r}, \mathbf{r}'; t)$ are expressed in terms of their Fourier transforms as follows:

$$\begin{aligned} &\left(\frac{\partial}{\partial t} + 2\nu k^2\right) \widetilde{U}_{ij}^{(2)}(\mathbf{k}, t) = -i k_k \sum_{l=1}^{3} \int \Big\{ \Delta_{il}(\mathbf{k})\, \widetilde{U}_{ljk}^{(3)}(\mathbf{k}, \mathbf{k}'; t) \\ &\qquad - \Delta_{jl}(\mathbf{k})\, \widetilde{U}_{lik}^{(3)}(-\mathbf{k}, \mathbf{k}'; t) \Big\} d\mathbf{k}', \end{aligned} \tag{10}$$

$$\begin{aligned} &\left[\frac{\partial}{\partial t} + \nu(|\mathbf{k}|^2 + |\mathbf{k}'|^2 + |\mathbf{k}''|^2)\right] \widetilde{U}_{ijk}^{(3)}(\mathbf{k}, \mathbf{k}'; t) \\ &\qquad = -i \sum_{(\mathbf{k}, \mathbf{k}', \mathbf{k}'')}^{(i,j,k)} \sum_{l,m=1}^{3} k_l'' \Delta_{im}(\mathbf{k})\, \widetilde{U}_{mjkl}^{(4)}(\mathbf{k}, \mathbf{k}', \mathbf{0}; t), \end{aligned} \tag{11}$$

$$\Delta_{ij}(\mathbf{k}) = \delta_{ij} - \frac{k_i k_j}{k^2}, \tag{12}$$

where the pressure terms have been eliminated using Equation (8), $\sum_{(\mathbf{k}, \mathbf{k}', \mathbf{k}'')}^{(i,j,k)}$ means the summation with respect to the simultaneous changes of (i, j, k) and $(\mathbf{k}, \mathbf{k}', \mathbf{k}'')$, and δ_{ij} denotes Kronecker's delta.

Just like Equations (4) and (5) for the mean velocity products $U^{(2)}$ and $U^{(3)}$, Equations (10) and (11) for the mean Fourier velocity products $\widetilde{U}^{(2)}$and $\widetilde{U}^{(3)}$are also unclosed, but the process for the closure is found to be much simpler for the latter than the former. Actually, various closure schemes, including the *quasi-normal closure* by Proudman and Reid [8] and Tatsumi (1957, [9]), have been applied to the latter set of equations.

F. Dynamical closure problem

After the early days of phenomenological research of turbulence during the first half of the last Century, the people's interest has been directed to the deductive theories of turbulence based on the equation of motion and the law of probability conservation. I myself have been looking for a fine closure scheme for the equations like Equations (10) and (11).

At that time, I have been informed through an abstract journal that a quasi-normal relationship has been proposed as the closure hypothesis by Chou Peiyuan [2] and M. Millionshchikov [5] using the zero-fourth cumulant approximation. Since, however, no concrete result has been given in the abstract, I decided to work on it myself and, after laborious manipulation of isotropic tensors, obtained the closed equation for the energy spectrum in scalar form. This result has been reported in NCTAM 1955 and sent to G.K. Batchelor asking for his help concerning its publication and it has been communicated by Sir Geoffrey Taylor to the Royal Society of London and published as Tatsumi [9]. At the same time, I have been informed that a paper on the same subject and similar results had been published by Proudman and Reid [8]. Then, I have realized that the previous works by Chou and Millionshchikov have been of the nature of proposals.

III. Turbulence Colloquium Marseille 1961

Now, looking back to the Proceedings of the last Turbulence Colloquium Marseille (1961), we find that the dynamical closure problem of turbulence has already been one of the central problems in the Session on "Energy Transfer in Homogeneous Turbulence" presided by Batchelor.

A. Introductory remarks by Batchelor

Batchelor states in his Introductory Remarks as follows (uncited parts are indicated by (– – –)):

"There is some experimental evidence [1,12] to suggest that, so far as the effect of the energy-containing eddies is concerned, the joint probability distribution of **u** at two different values of **x** is roughly normal, that is, that cumulants (– – –) beyond the second are roughly zero; a normal distribution is a plausible property of the velocity contributed by the energy-containing eddies.

On the above basis, a number of calculations [8,9] have been made concerning the decay of homogeneous turbulence. These exploratory studies have not yet yielded much new informatiion, but they have shown that the approximations employed are capable of yielding an initial distribution of the rate of energy transfer which in some respects is sensible. (– – –)

A method of estimating the effect of the nonlinear interaction between different Fourier coefficients has recently been suggested by Kraichnan [3]. (– – –) Dr. Proudman is making a critical assesment of the idea in this same session, and I shall say no more here."

B. Short lectures by Kraichnan and Proudman

The short lectures by Kraichnan and Proudman can be outlined by their summaries.

Kraichnan's summary: "A brief and qualitative discussion is given of some relationships among several deductive approaches to isotropic turbulence theory which have been advanced in the past decade. Included are (– – –) the quasi-normality approximation of Proudman and Reid and Tatsumi, and the modified perturbation expansion of Kraichnan and Wyld."

Proudman's summary: "This paper is a brief review of the kinematical and dynamical foundations of Kraichnan's theory of homogeneous turbulence. (– – –) In the dynamical part, the general connection between Kraichnan's ⟨⟨direct interaction hypothesis⟩⟩ and the zero-fourth-cumulant theories is examined. It is suggested that Kraichnan's theory has the same very general faults as the zero-fourth-cumulant theories, and that it is not likely to lead to useful results – especially for the smaller eddies to which it is conceptually most suited."

C. Tatsumi's comments

It is a great pity that I was not invited to the Colloquium and unable to join the hot discussions in this Session. Generally speaking, I have to admit that the quasi-normal approximation can exhibit serious defects due to its lack of nonzero energy dissipation at large Reynolds numbers. Nevertheless, I would like to note some minor questions for better understanding of the discussions.

First, Kraichnan refers to Ogura's calculation [7] of the energy spectrum equation due to the quasi-normal approximation. In this context, I wonder how the initial form of the energy tranfer function in this equation has been assumed. If it has been deleted for any reason, it causes large deformation of the solution at large Reynolds numbers.

Second, I remember that Kraichnan's works on the energy spectrum have been concerned with the local isotropic turbulence of Kolmogorov's sense which is stationary and including the non-zero energy dissipation as the external parameter. I wonder how it can be formulated for the decaying homogeneous isotropic turbulence of Taylor's sense.

Anyway, the difficulties concerning the quasi-normal theory of turbulence are completely resolved in the statistical approach to turbulence as described later.

IV. Statistical approach to turbulence

A. Multipoint velocity distributions

The randomness of turbulence can either be expressed in terms of the *probability distribution functions* (PDF) of the multipoint velocities of turbulence $\mathbf{u}(\mathbf{x}_n, t)$ $(n \geq 1)$ such as

$$
\begin{aligned}
&f(\mathbf{v}, \mathbf{x}, t) = \langle \delta(\mathbf{u}(\mathbf{x}, t) - \mathbf{v}) \rangle , \\
&f^{(2)}(\mathbf{v}_1, \mathbf{v}_2; \mathbf{x}_1, \mathbf{x}_2; t) = \langle \delta(\mathbf{u}(\mathbf{x}_1, t) - \mathbf{v}_1)\, \delta(\mathbf{u}(\mathbf{x}_2, t) - \mathbf{v}_2) \rangle , \\
&f^{(3)}(\mathbf{v}_1, \mathbf{v}_2; \mathbf{v}_3; \mathbf{x}_1, \mathbf{x}_2, \mathbf{x}_3; t) = \langle \delta(\mathbf{u}(\mathbf{x}_1, t) - \mathbf{v}_1)\, \delta(\mathbf{u}(\mathbf{x}_2, t) - \mathbf{v}_2)\, \delta(\mathbf{u}(\mathbf{x}_3, t) - \mathbf{v}_3) \rangle ,
\end{aligned}
\tag{13}
$$

where $\mathbf{v}_m$ $(m \geq 1)$ denote the probability variables corresponding to the velocities $\mathbf{u}_m = \mathbf{u}(\mathbf{x}_m, t)$ $(m \geq 1)$, δ the three-dimensional delta function, the brackets $\langle\ \rangle$ the probability average with respect to the distribution of concern, and the suffix $n = 1$ for the

one-point velocity distribution and its arguments have been omitted for brevity. This formalism constitutes *statistical approach* to turbulence.

B. Statistical closure problem

The equations for the velocity distributions $f^{(n)}$ $(n \geq 1)$ have been obtained by Lundgren [4] and Monin [6] in 1967 independently, but these equations are also unclosed in the sense that the equation for the distribution $f^{(n)}$ includes the distribution $f^{(n+1)}$ in its degenerate form as a new unknown. This is the same closure problem as that we have encountered in the dynamical formalism. Fortunately, however, the present closure is concerned not with nonlinear but with the linear system of the probability distributions. This is indeed the reason why this statistical closure is much easier to deal with than the dynamical closure mentioned in the last section.

C. Cross-independence closure

The simplest relation for this purpose may be the assumption of *statistical independence* between the velocities at two points,

$$f^{(2)}(\mathbf{v}_1, \mathbf{v}_2; \mathbf{x}_1, \mathbf{x}_2; t) = f(\mathbf{v}_1, \mathbf{x}_1, t)\, f(\mathbf{v}_2, \mathbf{x}_2, t), \tag{14}$$

which is generally valid for large distance $r = |\mathbf{x}_2 - \mathbf{x}_1| \to \infty$ according to the asymptotic independence of the velocities $(\mathbf{u}_1, \mathbf{u}_2)$ in this limit, but not otherwise, particularly for small distance $r \to 0$.

Likewise, if we consider the sum and difference of the velocities $(\mathbf{u}_1, \mathbf{u}_2)$ as

$$\mathbf{u}_+ = \frac{1}{2}(\mathbf{u}_1 + \mathbf{u}_2), \quad \mathbf{u}_- = \frac{1}{2}(\mathbf{u}_2 - \mathbf{u}_1), \tag{15}$$

which may be called the cross-velocities in short, and define the distributions of the cross-velocities as

$$\begin{aligned} g_+(\mathbf{v}_+, \mathbf{x}_1, \mathbf{x}_2; t) &= \langle \delta(\mathbf{u}_+(t) - \mathbf{v}_+) \rangle, \quad g_-(\mathbf{v}_-, \mathbf{x}_1, \mathbf{x}_2; t) = \langle \delta(\mathbf{u}_-(t) - \mathbf{v}_-) \rangle, \\ g^{(2)}(\mathbf{v}_+, \mathbf{v}_-; \mathbf{x}_1, \mathbf{x}_2; t) &= \langle \delta(\mathbf{u}_+(t) - \mathbf{v}_+)\, \delta(\mathbf{u}_-(t) - \mathbf{v}_-) \rangle, \end{aligned} \tag{16}$$

the independence relation between the distributions g_+ and g_- can be expressed as

$$g^{(2)}(\mathbf{v}_+, \mathbf{v}_-; \mathbf{x}_1, \mathbf{x}_2; t) = g_+(\mathbf{v}_+, \mathbf{x}_1, \mathbf{x}_2; t)\; g_-(\mathbf{v}_-, \mathbf{x}_1, \mathbf{x}_2; t). \tag{17}$$

If we consider the identity,

$$f^{(2)}(\mathbf{v}_1, \mathbf{v}_2; \mathbf{x}_1, \mathbf{x}_2; t)\, d\mathbf{v}_1 d\mathbf{v}_2 = g^{(2)}(\mathbf{v}_+, \mathbf{v}_-; \mathbf{x}_1, \mathbf{x}_2; t)\, d\mathbf{v}_+ d\mathbf{v}_-,$$

and the Jacobian, $\partial(d\mathbf{v}_+, d\mathbf{v}_-)/\partial(d\mathbf{v}_1, d\mathbf{v}_2) = 2^{-3}$, the relation (17) is written as

$$f^{(2)}(\mathbf{v}_1, \mathbf{v}_2; \mathbf{x}_1, \mathbf{x}_2; t) = 2^{-3} g_+(\mathbf{v}_+, \mathbf{x}_1, \mathbf{x}_2; t)\; g_-(\mathbf{v}_-, \mathbf{x}_1, \mathbf{x}_2; t), \tag{18}$$

which gives the *cross-independence closure relation* for the distribution $f^{(2)}$.

Unlike the relation (14), the cross-independence relation (18) is valid for both large and small distances $r \to \infty$ and $r \to 0$, but generally not in between.

D. Closed equations for velocity distributions

The closed equations for the multipoint velocity distributions can be obtained by applying the cross-independence closure hypothesis like Equation (18) to the Lundgren–Monin equations of various orders [10]. Here, we shall express the first two equations for homogeneous isotropic turbulence, and reference may be made to Tatsumi [10, 11] for more details.

One-point velocity distribution:

$$\left[\frac{\partial}{\partial t}+\alpha(t)\left|\frac{\partial}{\partial \mathbf{v}_1}\right|^2\right] f(|\mathbf{v}_1|,t)=0. \tag{19}$$

$$\begin{aligned}\alpha(t)&=\frac{2}{3}\nu\lim_{|\mathbf{r}|\to 0}\left|\frac{\partial}{\partial \mathbf{r}}\right|^2\int|\mathbf{v}_-|^2 g_-(\mathbf{v}_-,\mathbf{r},t)\,d\mathbf{v}_-\\&=\frac{1}{3}\nu\sum_{i,j=1}^{3}\left\langle\left(\frac{\partial \mathbf{u}_i(\mathbf{x}_1,t)}{\partial x_{1j}}\right)^2\right\rangle=\frac{1}{3}\varepsilon(t),\end{aligned} \tag{20}$$

with $\mathbf{r}=\mathbf{x}_2-\mathbf{x}_1$, where the distribution f is isotropic with respect to $\mathbf{v}_1$ in accordance with that of Equation (19) and ε denotes the mean *energy dissipation* rate of turbulence.

Two-point velocity distribution (energy-containing range)

$$\begin{aligned}&\left[\frac{\partial}{\partial t}+(\mathbf{v}_2-\mathbf{v}_1)\cdot\frac{\partial}{\partial \mathbf{r}}+\sum_{m=1}^{2}\left\{\nu\frac{\partial}{\partial \mathbf{v}_m}\cdot\mathbf{v}_m\left|\frac{\partial}{\partial \mathbf{r}}\right|^2+\alpha(t)\left|\frac{\partial}{\partial \mathbf{v}_m}\right|^2\right\}\right]\\&\quad\times f^{(2)}(\mathbf{v}_1,\mathbf{v}_2;\mathbf{r};t)=\sum_{m=1}^{2}\left\{(-1)^m\frac{\partial}{\partial \mathbf{v}_m}\beta(\mathbf{v}_m,t)\right\}\cdot\frac{\partial}{\partial \mathbf{r}}f^{(2)}(\mathbf{v}_1,\mathbf{v}_2;\mathbf{r};t),\end{aligned} \tag{21}$$

$$\begin{aligned}\beta(\mathbf{v}_1,t)&=\frac{1}{4\pi}\int\int|\mathbf{r}'|^{-1}\left((\mathbf{v}_1+2\mathbf{v}'_-)\cdot\frac{\partial}{\partial \mathbf{r}'}\right)\left(1+\mathbf{v}'_-\cdot\frac{\partial}{\partial \mathbf{v}_1}\right)g_-(\mathbf{v}'_-,\mathbf{r}',t)d\mathbf{v}'_-d\mathbf{r}',\\\beta(\mathbf{v}_2,t)&=\frac{1}{4\pi}\int\int|\mathbf{r}''|^{-1}\left((\mathbf{v}_2+2\mathbf{v}''_-)\cdot\frac{\partial}{\partial \mathbf{r}''}\right)\left(1+\mathbf{v}''_-\cdot\frac{\partial}{\partial \mathbf{v}_2}\right)g_-(\mathbf{v}''_-,\mathbf{r}'',t)d\mathbf{v}''_-d\mathbf{r}'',\end{aligned} \tag{22}$$

where $\mathbf{r}'=\mathbf{x}_3-\mathbf{x}_1$, $\mathbf{r}''=\mathbf{x}_3-\mathbf{x}_2$.

Two-point velocity distribution (local-similarity range)

In this range, the equations are expressed in terms of the local variables normalized by Kolmogorov's length $\eta=(\nu^3/\varepsilon_0)^{1/4}$ and velocity $\upsilon=(\nu\varepsilon_0)^{1/4}$, ε_0 being a representative value of $\varepsilon(t)$, as

$$\mathbf{x}^*=\mathbf{x}/\eta,\quad t^*=t/(\eta/\upsilon),\quad \mathbf{u}^*(\mathbf{x}^*,t^*)=\mathbf{u}(\mathbf{x},t)/\upsilon,\quad p^*(\mathbf{x}^*,t^*)=p(\mathbf{x},t)/\upsilon^2. \tag{23}$$

Then, the equations are expressed as follows:

$$\left[\frac{\partial}{\partial t^*}+\left(\mathbf{v}_2^*-\mathbf{v}_1^*\right)\cdot\frac{\partial}{\partial \mathbf{r}^*}+\left(\frac{\partial}{\partial \mathbf{v}_1^*}\cdot\mathbf{v}_1^*+\frac{\partial}{\partial \mathbf{v}_2^*}\cdot\mathbf{v}_2^*\right)\left|\frac{\partial}{\partial \mathbf{r}^*}\right|^2\right] f^{(2)*}\left(\mathbf{v}_1^*,\mathbf{v}_2^*;\mathbf{r}^*;t^*\right)$$

$$=-\left[\sum_{\pm}\alpha_{\pm}^*\left(\mathbf{r}^*,t^*\right)\left|\frac{\partial}{\partial \mathbf{v}_{\pm}^*}\right|^2+\left\{\frac{\partial}{\partial \mathbf{v}_1^*}\beta\left(\mathbf{v}_1^*,t^*\right)-\frac{\partial}{\partial \mathbf{v}_2^*}\beta\left(\mathbf{v}_2^*,t^*\right)\right\}\cdot\frac{\partial}{\partial \mathbf{r}^*}\right] \tag{24}$$

$$\times f^{(2)*}\left(\mathbf{v}_1^*,\mathbf{v}_2^*;\mathbf{r}^*;t^*\right),$$

$$\alpha_{\pm}^*\left(\mathbf{r}^*,t^*\right)=\frac{2}{3}\nu\lim_{|\mathbf{r}^{*\prime}|\to 0}\left|\frac{\partial}{\partial \mathbf{r}^{*\prime}}\right|^2\int\left|\mathbf{v}_{\pm-}^{*\prime}\right|^2 g_{\pm-}^*\left(\mathbf{v}_{\pm-}^{*\prime};\mathbf{r}^*,\mathbf{r}^{*\prime};t^*\right)d\mathbf{v}_{\pm-}^{*\prime}, \tag{25}$$

$$\beta^*\left(\mathbf{v}_1^*,t^*\right)=\frac{1}{4\pi}\int\int\left|\mathbf{r}^{*\prime}\right|^{-1}\left(\left(\mathbf{v}_1^*+2\mathbf{v}_-^{*\prime}\right)\cdot\frac{\partial}{\partial \mathbf{r}^{*\prime}}\right)\left(1+\mathbf{v}_-^{*\prime}\cdot\frac{\partial}{\partial \mathbf{v}_1^*}\right)$$

$$\times g_{\pm-}^*\left(\mathbf{v}_-^{*\prime},\mathbf{r}^{*\prime},t^*\right)d\mathbf{v}_-^{*\prime}d\mathbf{r}^{*\prime}, \tag{26}$$

$$\beta^*\left(\mathbf{v}_2^*,t^*\right)=\frac{1}{4\pi}\int\int\left|\mathbf{r}^{*\prime\prime}\right|^{-1}\left(\left(\mathbf{v}_2^*+2\mathbf{v}_-^{*\prime\prime}\right)\cdot\frac{\partial}{\partial \mathbf{r}^{*\prime\prime}}\right)\left(1+\mathbf{v}_-^{*\prime\prime}\cdot\frac{\partial}{\partial \mathbf{v}_2^*}\right) \tag{27}$$

$$\times g_{\pm-}^*\left(\mathbf{v}_-^{*\prime\prime},\mathbf{r}^{*\prime\prime},t^*\right)d\mathbf{v}_-^{*\prime\prime}d\mathbf{r}^{*\prime\prime},$$

E. Two-point statistics of homogeneous isotropic turbulence

Now, Equation (19) for the one-point velocity distribution f, Equation (21) for the two-point velocity distribution $f^{(2)}$ for the energy-containing range, and Equation (24) for the two-point velocity distribution $f^{(2)*}$ for the local-similarity range, constitute a closed deterministic set of equations which govern the evolution of these velocity distributions in time irrespective to the higher order velocity distributions. It was already proved in Tatsumi [11] that the *cross-independence closure* hypothesis which has been used for deriving these equations is an exact closure, so that, under the cross-independence hypothesis, this set of equations provides us with an exact statistical description of homogeneous isotropic turbulence so far as the two-point statistics are concerned.

V. Conclusion

We have observed in Section III several problems and difficulties of the theory of turbulence at the time of the last TCM 1961, and it is our great pleasure to be able to know that many of them have been resolved at the time of the present TCM 2011. I wish to express my hearty thanks and compliments to the devoted effort of the Organisers, Marie Farge, Keith Moffatt, and Kai Schneider.

References

[1] G.K. Batchelor, *The theory of Homogeneous turbulence*. Cambridge University Press, Cambridge, 1953.

[2] P.-Y. Chou, *On an extension of Reynolds' method of finding apparent stress and the nature of turbulence.* Chin. J. Phys. 4 (1940), pp. 1–33.

[3] R.H. Kraichnan, J. Fluid Mech. 5 (1959), pp. 497–543.

[4] T.S. Lundgren, *Distribution functions in the statistical theory of turbulence.* Phys. Fluids 10 (1967), pp. 969–975.
[5] M. Millionshchikov, *On the theory of homogeneous isotropic turbulence.* C. R. Acad. Sci. U.R.S.S. 32 (1941), p. 615.
[6] A.S. Monin, *Equations of turbulent motion.* PMM J. Appl. Math. Mech. 31 (1967), pp. 1057–1068.
[7] Y. Ogura, *A consequence of the zero-fourth-cumulant approximation in the decay of isotropic turbulence.* J. Fluid Mech. 16 (1963), pp. 38–41.
[8] I. Proudman and W.H. Reid, *On the decay of normally distributed and homogeneous turbulent velocity fields.* Phil. Trans. R. Soc. Lond. A 247 (1954), pp. 163–189.
[9] T. Tatsumi, *Theory of decay process of incompressible isotropic turbulence.* Proc. Roy. Soc. Lond. A 239 (1957), p. 16.
[10] T. Tatsumi, *Mathematical physics of turbulence.* in *Geometry and Statistics of Turbulence*, T. Kambe, T. Nakano, and T. Miyauti, eds., Kluwer, Dordrecht, 2001, pp. 3–12.
[11] T. Tatsumi, *Cross-independence closure for statistical mechanics of fiuid turbulence.* J. Fluid Mech. 670 (2011), pp. 365–403.
[12] M. Uberoi, J. Aero. Sci. 20 (1953), p. 197.
[13] H.W. Wyld, Jr., *Formulation of the theory of turbulence in an incompressible fiuid.* Ann. Phys., NY 14 (1961), p. 143.

A Lie-group derivation of a multi-layer mixing length formula for turbulent channel and pipe flows

Zhen-Su She[a*] Xi Chen[a] and Fazle Hussain[a,b]

[a] *State Key Laboratory for Turbulence and Complex Systems and Department of Mechanics and Aerospace Engineering, College of Engineering, Peking University, Beijing 100871, P.R. China*;
[b] *Department of Mechanical Engineering, Texas Tech University, Lubbock, TX 79409-1021, USA*

(*May 2013*)

A novel Lie-group analysis of the (unclosed) mean momentum equation (MME) for turbulent channel and pipe flows yields an analytic multi-layer formula for the entire mixing length profile (hence the mean velocity profile). Simple Lie-group arguments lead to three kinds of local dilation-invariant expressions of the mixing length, which we believe to be the most basic solutions of MME describing each statistically autonomous layer. The first kind - a power-law solution - is valid for viscous sublayer, buffer layer, log-layer, and a newly identified central core. Remarkably, the second - a defect power-law of form $1 - r^m$ - describes a recently found new bulk zone of channel and pipe flows. In addition, a simple ansatz describing a relation between invariants of the mixing length and its gradient, is shown to describe scaling transition between two adjacent layers. The theory thus proposes a quantification of the multi-layer structure, and identifies three kinds of physically meaningful parameters: group-invariant scaling, layer thickness and transition sharpness. Our results are validated by direct numerical simulation (DNS) of channel and pipe flows, while extensive contrast with numerous empirical data and the determination of all layers' parameters will be discussed elsewhere.

Keywords: Lie-group; multi-layer; mixing length; channel and pipe

1. Introduction

Wall-bounded turbulent flow has received considerable recent attention because of its relatively simple geometry and its relevance to a large variety of engineering applications [1]. It enables direct insight into fundamental turbulence physics, as well as direct verification by local (such as profiles of mean velocity, Reynolds stress, fluctuation intensities, etc.) and integral measurements (such as skin friction and heat transfer). The fundamental challenge is to predict the mean flow properties, including the mean velocity profile (MVP), the Reynolds stress, the kinetic energy, etc; however, a deductive theory of this kind is still missing.

A recent model by L'vov, Proccacia and Rodenko (cited hereinafter as LPR) [2] is noteworthy, as they deal with the MME and the balance equations for the kinetic energy and the Reynolds stress. Several physical arguments regarding energy cascade, dissipation and balance in the average Reynolds stress equation, enable LPR to prescribe the mixing length profile which involves two artificial functions inspired from the limited DNS data - one connecting the log-layer to the wall (e.g.

*Corresponding author. Email: she@pku.edu.cn

a wall function) and the other to the center (e.g. a bulk function). This two-layer model achieves a good accuracy in describing the data, but the asymptotic behaviors for the wall and bulk functions are not correct [3], and their extensions to describe other flows and other profiles (energy dissipation, kinetic energy, etc) are not obvious.

Recently, a SED theory [4] has been proposed to reconsider this problem of determining the mean velocity profile of canonical wall-bounded flows from first principles. It is known that the mean momentum equation is unclosed, and the determination of the mean strain requires a modeling of the Reynolds stress. Prandtl's [5] mixing length model provides a way to model the Reynolds stress. In the past, simple models for the mixing length were adopted; the most famous is the Karman's linear law of the distance to the wall, leading to a logarithmic profile for the mean velocity. The log-law has had a tremendous success in predicting the Reynolds number dependence of the friction coefficient and in calibrating the computational fluid dynamics (CFD) models of turbulent flows such as K-ϵ or $K-\omega$ [1]. Nevertheless, the validity of the logarithmic profile, even for simple wall-bounded flows, has been questioned [7–9], owing to the ad hoc nature of the arguments behind its derivation. In [4], we have extended the classical mixing length theory of Prandtl and von Karman by proposing a multi-layer formula for the entire profile of the mixing length ℓ_M^+ - hence the entire mean velocity profile - written as

$$\ell_M^+ = \rho \left(\frac{y^+}{y_{sub}^+}\right)^{\frac{3}{2}} \left(1+(\frac{y^+}{y_{sub}^+})^{p_1}\right)^{\frac{1}{2p_1}} \left(1+(\frac{y^+}{y_{buf}^+})^{p_2}\right)^{\frac{-1}{p_2}} \frac{1-r^m}{m(1-r)Z_c} \left(1+(\frac{r}{r_{core}})^{-2}\right)^{\frac{1}{4}}, \tag{1}$$

where y^+ is the coordinate normal to the wall, r is the radial distance of the pipe, y_{sub}^+, y_{buf}^+ and r_{core} are parameters specifying the thicknesses of the layers ($Z_c = (1+r_{core}^2)^{1/4}$ is a normalization factor), p_1 and p_2 are parameters describing the sharpness of the transitions between the layers, m is a parameter specifying a geometry-dependent scaling for the bulk flow (empirical study shows that $m=4$ for channel and $m=5$ for pipe [4]), and the superscript '+' denotes wall unites normalization by the wall friction velocity u_τ and viscosity. This formula (1), seemingly complex, is in fact composed of a series of simple functions, namely

$$\ell_M^+ \approx \left(\rho/y_{sub}^{+3/2}\right) y^{+\frac{3}{2}}, \qquad y^+ \ll y_{sub}^+, \quad r \to 1 \tag{2}$$

$$\approx \left(\rho/y_{sub}^{+2}\right) y^{+2}, \qquad y_{sub}^+ \ll y^+ \ll y_{buf}^+, \quad r \to 1 \tag{3}$$

$$\approx \left(\rho y_{buf}^+/y_{sub}^{+2}\right) y^+ \approx \kappa y^+, \qquad y_{buf}^+ \ll y^+, \quad r \to 1 \tag{4}$$

$$\approx \frac{\kappa(1-r^m)Re_\tau}{m}, \qquad y_{buf}^+ \ll y^+, \quad r_{core} \ll r \leq 1 \tag{5}$$

$$\approx \frac{\kappa r_{core}^{1/2} Re_\tau}{m Z_c r^{1/2}}, \qquad r \to 0 \tag{6}$$

$$\kappa = \rho y_{buf}^+/y_{sub}^{+2}. \tag{7}$$

Clearly, formula (1) is consistent with the log-law (see (4)), and at the same time describes the finite Re modification (see (5)) taking into account the effect of outer flow geometry (with the parameter m), so it naturally reconciles the log-law and power-law debate. All functional forms from (2) to (6) are analytically given, which is a definite step beyond the LPR model [2]. The purpose of this paper is to present

analytic derivation of (1), employing a novel Lie-group formalism.

The main hypothesis in this derivation is that turbulent fluctuations recover dilation symmetry (discussed below) either from the wall or from the center (for channel or pipe), which is believed to be a general feature of wall-bounded turbulent shear flows. Such dilation symmetry manifests in a power law scaling of a relevant length (order) function defined using both fluctuation and mean quantities. The introduction of the order function [4] is inspired by the observation that a real turbulent flow system (such as a turbulent pipe) differs in a fundamental way from idealized system of homogeneous isotropic turbulence or homogeneous shear turbulence by involving a series of statistically distinct states of fluctuations. For example, fluctuations near the wall in the so-called viscous sublayer in a pipe is very different from that in the bulk flow. In each layer/region, the energy dynamics display different dominant mechanisms. For instance, in viscous sublayer, pressure transport balances the viscous dissipation and diffusion, while in buffer layer, production (by the mean shear) balances viscous dissipation. As the number of terms in the energy equation is finite, the number of balance mechanisms is finite, hence the finite number of layers.

This multi-state/multi-layer feature is believed to be generic for all systems at a truly far-from-equilibrium state; wall turbulence is one of them. Any measure that quantifies the symmetry property of each state and also describes transitions between one state to another is thus named order function, in close analogy to 'order parameters' in statistical physics [6], which effectively captures the unknown effects of fluctuation structures on the mean and reveals phase transitions (which means from one macroscopic state to another) at macroscopic scales. Our order function plays exactly the same role - capturing effects of turbulent fluctuations on the mean and displaying varying scaling symmetry in the mean profile. A specific fluctuation field responsible for the vertical momentum transfer is the product of streamwise and vertical fluctuations - the Reynolds stress - which is to be described by the mixing length (order) function. Our central task here is to characterize the statistical state of each layer using the scaling of the mixing length, and then the solution of the mean momentum equation. In the future, a complete deductive theory would explain why each layer is necessary and how its quantitative property is derived.

The paper is organized as follows. In section 2, we establish a formal framework for the Lie-group analysis applied to the MME, where an extended phase space including the mixing length and its gradient is introduced. The analysis is applied in Section 3, by assuming the existence of local dilation invariant solution, to derive a specific function form of the mixing length for turbulent channel and pipe flows. In section 4, we validate the theory using DNS data. Section 5 contains a summary and discussion of future studies.

2. Lie-group analysis of the inner and outer MME

Lie-group analysis is a well-founded method of finding invariant solutions of differential equations [10]. Recently, Oberlack [11] and Lindgren *et al* [12] use it to derive local scaling laws in the mean velocity, including log-law and power-law, for unclosed Reynolds-averaged Navier-Stokes (RANS) equations. When studying multi-point statistical symmetry, Oberlack and Andreas [13] assert that there exist a large number of possibilities for defining invariant groups, due to the possible new scaling arising from the fluctuations. On the other hand, empirical data from DNS show well-behaved mean profiles, while finding new governing principles to derive it is a challenge. For a symmetry analysis, this amounts to selecting the

right invariant groups, which likely correspond to statistically restored symmetries by fully developed turbulence, postulated by Frisch [14]. Finding these right symmetries embedding true invariant solutions of the RANS equations (i.e. the MME) is an important step forward in the symmetry analysis of turbulence.

A key realization here is that although the RANS equation and its boundary conditions for a channel or pipe possess a dilation group (but not a Galilean group), the empirical mean velocity solution seem to break the dilation invariance. Even locally, the mean velocity does not have a recognized scaling invariance, except near the wall with a rather trivial linear scaling in y^+. Specifically, when the RANS equation undergoes a dilation transformation, the group invariant of the mean velocity solved by using the Lie-group method is no longer invariant, as can be easily checked with any empirical mean velocity profile. Classical Lie-group analysis seemed to meet a bottleneck, yielding very few results. This obstacle is overcome here by the introduction of additional variables, namely mixing length and its gradient (both order functions), as group invariants.

Note that in the statistical physics of phase transitions, order parameters are considered to the primary variables describing the macroscopic state; we carry out the same tradition: regarding the order functions (i.e. mixing length and its spatial gradient) as fundamental variables describing the dilation-symmetry of the underlying fluctuation field (i.e. Reynolds stress). In other words, when undergoing dilation transformation, the mixing length and its gradient display specific scaling in each layer, and a generalized symmetry relating the mixing length with its gradient describes the transitions between the layers. This Lie-group formalism thus enables us to show that there exists a dilation-group which leaves the governing equation (i.e. the RANS equation) invariant under the postulated scaling symmetry for the mixing length. While the mean velocity is itself no longer invariant under the dilation transformation, the mixing length maintains the scaling symmetry.

This unconventional use of the Lie-group analysis embodies a physical insight about the problem, namely that the mixing length and its gradient are the right variables to represent the symmetry property of the fluctuations (e.g. the Reynolds stress). As noted by Cantwell [10], group theory begins when all the science needed to deduce the solution has been established. In wall turbulence, the physics that has been overlooked so far is the existence of the dilation-group symmetry displayed by the mixing length in each of layers like sublayer, buffer, bulk and core. A general feature uncovered here is that distinct layers do possess symmetries, and there exist appropriate order functions to display them. Including order function as additional variables in the symmetry analysis of the RANS equation marks the essential difference between this work and all previous symmetry analysis of the RANS equation.

For a channel/pipe flow, the MME is [15]:

$$\frac{d^2U^+}{dy^{+2}} - \frac{d\left\langle uv\right\rangle^+}{dy^+} = -\frac{1}{Re_\tau}, \tag{8}$$

where U is the streamwise mean velocity, u and v are streamwise and normal fluctuating velocities, Re_τ is wall friction Reynolds number, and other notions are described above. Integrating along the normal direction yields

$$S^+ + W^+ = r \tag{9}$$

where $S^+ = dU^+/dy^+$, $W^+ = -\langle uv\rangle^+$ and $r = 1 - y^+/Re_\tau$). Prandtl's [5] mixing length, see Fig.1, defines a length function linking the Reynolds stress and the

mean shear stress:

$$\ell_M^+ = \frac{\sqrt{W^+}}{S^+}. \tag{10}$$

Then, the MME becomes:

$$\ell_M^{+2} S^{+2} + S^+ - r = 0. \tag{11}$$

Note that ℓ_M^+ fully determines the mean shear stress,

$$S^+(y^+; Re_\tau) = \frac{-1 + \sqrt{4r\ell_M^{+2}}}{2\ell_M^{+2}} \tag{12}$$

and then the MVP. Prandtl [5] assumed a linear,

$$\ell_M^+ = \kappa y^+ \tag{13}$$

which leads to

$$S^+ \approx \frac{1}{\ell_M^+} \approx \frac{1}{\kappa y^+} \tag{14}$$

since $W^+ \approx 1$, and therefore the logarithmic law for MVP

$$U^+ \approx \frac{1}{\kappa} \ln\left(y^+\right) + B \tag{15}$$

with Karman constant $\kappa \approx 0.41$ and $B \approx 5.2$ [15]. The logarithmic law is widely used in engineering models, albeit invalid in the near wall region and center flow because ℓ_M departs from the linear scaling (13) when the wall distance y is out of the overlap region; see in Fig.1. In fact, in the viscous sublayer, Taylor expansion [15] yields $W^+ \propto y^{+3}$, $S^+ \approx 1$, thus $\ell_M^+ \propto y^{+3/2}$. In the core region, according to the central symmetry, the mean velocity profile is parabolic, thus $S^+ \propto r$; which together with $W^+ \approx r$, gives $\ell_M \propto 1/\sqrt{r}$. Note that these two power-law scalings are sharply different from (13). Although various modifications have been made ever since, such as the damping function by van Driest [19] and the wall function in the LPR model [2], a derivation of mixing length function with correct asymptotic behaviors is not achieved yet.

The Lie-group analysis presented below is novel in the following aspect. By substituting in $W^+ = (\ell_M^+ S^+)^2$, we rewrite the governing equation (8) as:

$$\mathscr{C} = \frac{\partial^2 U^+}{\partial y^{+2}} + 2\ell_M^{+2}\left(\frac{\partial U^+}{\partial y^+}\right)\left(\frac{\partial^2 U^+}{\partial y^{+2}}\right) + 2\ell_M^+ \dot{\ell}_M^+ \left(\frac{\partial U^+}{\partial y^+}\right)^2 + \frac{1}{Re_\tau} = 0 \tag{16}$$

with wall conditions: $U^+(0) = \ell_M^+(0) = 0$. Note that (8) is an ordinary differential equation, but since we consider below a family of solutions for varying Re_τ and regard Re_τ as an independent variable, the partial differentiation is introduced in (16). This is the so-called inner MME (in wall units), and the primary variables are expanded to include the mixing length ℓ_M^+ and its spatial gradient $\dot{\ell}_M^+ = \partial \ell_M^+ / \partial y^+$.

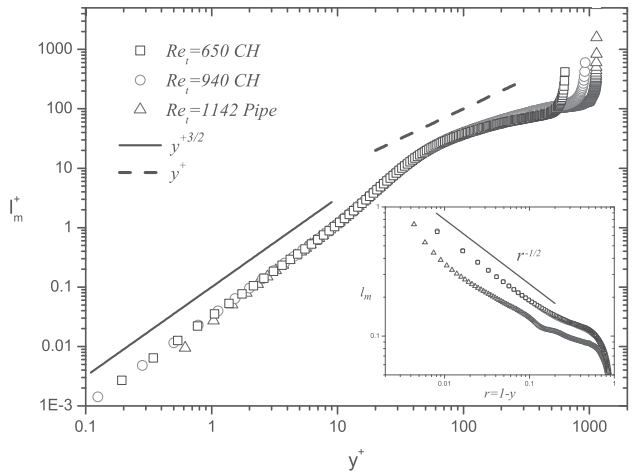


Figure 1. Profile of the mixing length as a function wall distance y^+. The solid line indicates the near wall power-law scaling with exponent 3/2, dashed line the linear scaling in the overlap region according to [5]. Inset shows the central power-law scaling with exponent $-1/2$, where $\ell_M = \ell_M^+/Re_\tau$, and $r = 1 - y$ is the distance to the center. DNS data from Iwamoto *et al.* [16] at $Re_\tau = 650$, Hoyas and Jimenez [17] at $Re_\tau = 940$, Wu and Moin [18] at $Re_\tau = 1142$.

Similarly, in central unit r, we have the outer MME ($\dot{\ell}_M = \partial \ell_M / \partial r$):

$$\mathscr{N} = \frac{-1}{Re_\tau}\frac{\partial^2 U^+}{\partial r^2} + 2\ell_M^2 \frac{\partial U^+}{\partial r}\frac{\partial^2 U^+}{\partial r^2} + 2\ell_M \dot{\ell}_M \left(\frac{\partial U^+}{\partial r}\right)^2 - 1 = 0 \qquad (17)$$

with center condition $U^+(0) = U_c^+, \ell_M(0) = \infty$ where U_c^+ is the centerline velocity. Note that in (16) and (17), in addition to independent variable y^+ (or r) and Re_τ, and dependent variable U, we now have an expanded function space including ℓ_M and $\dot{\ell}_M$. This expansion is essential, since it allows one to formulate specific assumptions about the scaling symmetry of the fluctuation fields (or of some specific measure of it, e.g. the Reynolds stress), which then allows one to specify the solution manifold. In other words, using ℓ_M and $\dot{\ell}_M$, we quantify the symmetry behavior of the Reynolds stress, and use it to derive a solution for the mean velocity. Our Lie-group analysis not only identifies simple scaling symmetries of ℓ_M, locally valid in each of layered structures, but also defines a generalized symmetry in the prolonged space of ℓ_M and $\dot{\ell}_M$, describing a universal transition between one layer to another, and then fulfills the goal of defining a complete solution for U. The generalized symmetry is a truly hidden symmetry which describes the multi-layer structure of wall-sheared turbulence. Since the multi-layer structures are generic to far-from-equilibrium systems, our treatment is of general interest for many flows.

2.1. *Symmetry transformation*

The analysis consists of the following three standard steps. *Step one* is to define the symmetry transformations. Here, the Lie group transformation S_ε can be expressed as

$$\mathbf{t}^* = \Phi(\mathbf{t}, \mathbf{x}, \varepsilon); \quad \mathbf{x}^* = \Psi(\mathbf{t}, \mathbf{x}, \varepsilon), \qquad (18)$$

where the superscript $*$ denotes transformed variables, $\mathbf{t} = (y^+, Re_\tau)$ and $\mathbf{x} = (U^+, \ell_M^+)$ are independent and dependent variables, respectively, and Φ, Ψ are analytic functions of $\mathbf{t}$, $\mathbf{x}$ and a continuous parameter ε. In this setting, the symmetry transformation of (16) satisfies

$$\mathscr{C}(\mathbf{t}, \mathbf{x}) = 0 \quad \Leftrightarrow \quad \mathscr{C}(\mathbf{t}^*, \mathbf{x}^*) = 0. \tag{19}$$

As the calculation of all of the admitted symmetry transformations is well developed using the Lie's theory [10], the basic methodology is introduced in the Appendix A. It turns out that only the dilation symmetry transformation is admitted, which can be verified by a simple procedure as below.

Note that since U^+ and y^+ appear in (16) only differentially, there is an obvious invariance under independent translations of either variable. However, due to the wall condition $U^{+^*} = \ell_m^{+^*} = 0$ at $y^{+^*} = 0$, the translation symmetry is broken. Moreover, one can also search for scaling symmetries of the form:

$$y^{+*} = e^{\epsilon} y^+, \qquad Re_\tau^* = e^{c_1 \epsilon} Re_\tau, \qquad U^{+*} = e^{c_2 \epsilon} U^+, \qquad \ell_M^{+*} = e^{\alpha \epsilon} \ell_M^+. \tag{20}$$

where ϵ varying and c_1, c_2, α being arbitrary (to be determined) constant parameters. Substituting these into (16) gives directly

$$\begin{aligned} e^{(2-c_2)\varepsilon} \frac{\partial^2 U^{+*}}{\partial y^{+*2}} + e^{(3-2c_2-2\alpha)\varepsilon} 2\ell_M^{+*2} \left(\frac{\partial U^{+*}}{\partial y^{+*}} \right) \left(\frac{\partial^2 U^{+*}}{\partial y^{+*2}} \right) \\ + e^{(3-2c_2-2\alpha)\varepsilon} 2\ell_M^{+*} \dot{\ell}_M^{+*} \left(\frac{\partial U^{+*}}{\partial y^{+*}} \right)^2 + e^{c_1 \varepsilon} \frac{1}{Re_\tau^*} = 0 \end{aligned} \tag{21}$$

Invariance requires the two conditions

$$2 - c_2 = 3 - 2c_2 - 2\alpha = c_1 \tag{22}$$

which permits two of the four scaling parameters to be eliminating, i.e.

$$c_1 = 1 + 2\alpha; \qquad c_2 = 1 - 2\alpha. \tag{23}$$

Thus, the dilation symmetry transformations including the derivation of mixing length function are

$$\begin{aligned} y^{+*} &= e^{\epsilon} y^+, & Re_\tau^* &= e^{(1+2\alpha)\epsilon} Re_\tau, \\ U^{+*} &= e^{(1-2\alpha)\epsilon} U^+, & \ell_M^{+*} &= e^{\alpha\epsilon} \ell_M^+, \qquad \dot{\ell}_M^{+*} = e^{(\alpha-1)\epsilon} \dot{\ell}_M^+. \end{aligned} \tag{24}$$

Note that it is easy to search for the dilation symmetry through the above approach. However, to decline other possible symmetries, one need a systematic procedure. Appendix A gives all of the admitted symmetry transformations, where only dilation and translation transformations are permitted.

Here, we briefly discuss the meaning of the above symmetry transformation. Consider the transformation from the state characterized by (y^+,Re_τ) to that by (y^{+*}, Re_τ^*). We call a symmetry in U^+ to denote the fact that the actual (empirical) solution of the mean velocity U^+ at the latter state equals the transformed mean velocity, namely U^{+*}. In other words, if U^{+*} does not equal the actual solution, we say that the symmetry in U^+ breaks down. Previous works [11, 12] applying the Lie-group analysis to the RANS equation were restricted to the case with

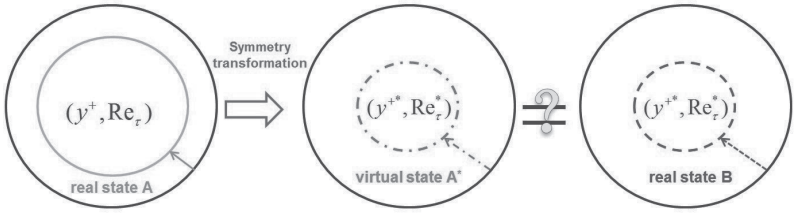


Figure 2. Sketch of the symmetry analysis for a turbulent pipe flow. A real turbulent state $A = (y^+, Re_\tau, U^+, \ell_M^+, \dot{\ell}_M^+)$ is denoted by a solid line. Consider a dilation transformation (24) to a new state $A^* = (y^{+*}, Re_\tau^*, U^{+*}, \ell_M^{+*}, \dot{\ell}_M^{+*})$. Compared the transformed state A^* (denoted by a dot-dashed line) with the real state $B = (y^{+*}, Re_\tau^*, U^{+ES}, \ell_M^{+ES}, \dot{\ell}_M^{+ES})$ (denoted by a dashed line). Here, the superscript ES denotes empirical solution provided by experimental or DNS data, which is the true solution at (y^{+*}, Re_τ^*). The symmetry analysis consists in asking: is there any similarity between A^* and B? Previous works ([11, 12]) focus on the symmetry in the mean velocity itself, namely demanding $U^{+*} = U^{+ES}$; we argue that this symmetry is broken, at least in most parts of the flow domain, that is, $U^{+*} \neq U^{+ES}$. Instead, we postulate the symmetry of the mixing length and its gradient, because they represent the restored symmetry [14] by turbulent fluctuations (e.g. effect of the Reynolds stress on the mean shear).

no symmetry-breaking of U^+. But, if one wants to derive solutions of the RANS equation from symmetry analysis, the situation of symmetry-breaking needs to be considered, since the empirical MVP from either DNS or experimental data do not seem to have a simple scaling form.

The new idea introduced here consists in recovering the statistical restored scaling symmetry by turbulent fluctuations in wall-bounded flow with extra variables, namely the mixing length and its gradient, see Fig. 2. By assuming scaling symmetry in ℓ_M^+, we assert that the transformed mixing length, ℓ_M^{+*}, is the actual solution at the latter state corresponding to the independent variables (y^{+*}, Re_τ^*). This postulated scaling symmetry leads immediately to a power-law solution of ℓ_M, which corresponds to the similarity solution of the first kind described below.

Another similarity solution (of the second kind) corresponds to a case of symmetry-breaking in ℓ_M, but a maintained scaling symmetry in $\dot{\ell}_M$, which is a solution of defect power-law. A third kind of similarity solution is derived under an assumption of a generalized symmetry relation between ℓ_M and $\dot{\ell}_M$, when the scaling symmetries of both quantities break down. These details are presented in section 2.2.

Step two is to define group-invariants, which are obtained by solving the characteristic equation: $dt_i/d\xi_i = dx_i/d\eta_i$, written as:

$$\begin{aligned} \frac{dy^+}{y^+} &= \frac{dRe_\tau}{(1+2\alpha)Re_\tau} = \frac{d\ell_M^+}{\alpha\ell_M^+} = \frac{d\dot{\ell}_M^+}{(\alpha-1)\dot{\ell}_M^+} \\ &= \frac{dU^+}{(1-2\alpha)U^+} = \frac{d\dot{U}^+}{-2\alpha\dot{U}^+} = \frac{d\ddot{U}^+}{-1-2\alpha\ddot{U}^+} \end{aligned} \tag{25}$$

The solutions to (25) define following group-invariants:

$$\begin{array}{lll} H = \mathrm{Re}_\tau/y^{+(1+2\alpha)}, & F_1 = \ell_M^+/y^{+\alpha}, & F_2 = \dot{\ell}_M^+/y^{+(\alpha-1)}, \\ G_1 = U^+/y^{+(1-2\alpha)}, & G_2 = \dot{U}^+ y^{+2\alpha}, & G_3 = \ddot{U}^+ y^{+(1+2\alpha)}. \end{array} \tag{26}$$

These group-invariants, functions of $y+$ and Re_τ, are the so-called similarity variables [10]. Note that F_1 and F_2 are equivalent to the invariant $q = y/\sqrt{x\nu/U_\infty}$ defining the similarity variable in a Blasius boundary layer.

Finally, in *step three*, we rewrite $\mathscr{C} = 0$ in terms of the group-invariants,

$$\mathscr{C} = G_3 + 2F_1^2 G_2 G_3 + 2F_1 F_2 G_2^2 + 1/H = 0 \tag{27}$$

Geometrically, $\mathscr{C} = 0$ defines an invariant-surface in the variable space of $\mathbf{t}$ and $\mathbf{x}$, which is invariant under a dilation group of transformation, and the infinitesimals are tangent vectors to the invariant-surface. The so-called invariant solution, for example, $\Theta(\mathbf{t}, \mathbf{x}) = 0$, satisfying the invariant surface condition, i.e. $X\Theta|_{\Theta=0} = 0$, must be a function of similarity variables. The present work seeks invariant solution in an extended coordinate space including the mixing length and its gradient, namely $\Theta(F_1, F_2) = 0$, (e.g. ξ_{y^+}, $\eta_{\ell_M^+}$ and $\eta_{\dot{\ell}_M^+}$).

Similarly, the transformed variables for the outer MME are

$$\begin{aligned} r^* &= e^{\epsilon} r, \qquad\qquad Re_\tau^* = e^{(1/2+\alpha)\epsilon} Re_\tau, \\ U^{+*} &= U_c^+ - e^{(3/2-\alpha)\epsilon}(U_c^+ - U^+), \quad \ell_M^* = e^{\alpha\epsilon}\ell_M, \quad \dot{\ell}_M^* = e^{(\alpha-1)\epsilon}\dot{\ell}_M. \end{aligned} \tag{28}$$

and we derive a set of group-invariants for the outer flow, by performing the above analysis to the outer MME (in center units):

$$\begin{aligned} &H = \mathrm{Re}_\tau / r^{1/2+\alpha}, && F_1 = \ell_M / r^{\alpha}, && F_2 = \dot{\ell}_M / r^{\alpha-1}, \\ &G_1 = \left(U_c^+ - U^+\right) / r^{3/2-\alpha}, && G_2 = \dot{U}^+ / r^{5/2-\alpha}, && G_3 = \ddot{U}^+ / r^{7/2-\alpha} \end{aligned} \tag{29}$$

where $\cdot$ denotes r-gradient; the outer MME in terms of group-invariants is

$$\mathscr{N} = -G_3/H + 2F_1^2 G_2 G_3 + 2F_1 F_2 G_2^2 - 1 = 0 \tag{30}$$

It is interesting to contrast (27) and (30) with similar forms of the Blasius equation for a laminar boundary layer. Following [10], the Blasius equation written in streamfunction ψ is

$$\frac{\partial \psi}{\partial y}\frac{\partial^2 \psi}{\partial x \partial y} - \frac{\partial \psi}{\partial x}\frac{\partial^2 \psi}{\partial y^2} - \nu \frac{\partial^3 \psi}{\partial y^3} = 0 \tag{31}$$

It can be verified that this equation is invariant under the following dilation symmetry transformations:

$$x^* = e^{\epsilon} x; \qquad y^* = e^{\lambda\epsilon} y; \qquad \psi^* = e^{(1-\lambda)\epsilon}\psi \tag{32}$$

The group parameter λ is determined by the free stream condition, i.e.

$$\frac{\partial \psi}{\partial y}|_{y=\infty} = U_\infty = const. = \frac{\partial \psi^*}{\partial y^*}|_{y^*=\infty} \tag{33}$$

which leads to

$$\lambda = 1 - \lambda; \qquad \lambda = 1/2, \tag{34}$$

with the following group invariants:

$$f = \frac{\psi}{\sqrt{\nu U_\infty x}}; \qquad q = \frac{y}{\sqrt{x\nu/U_\infty}} \tag{35}$$

Substituting them into (31) yields

$$\frac{d^3 f}{dq^3} + \frac{f}{2}\frac{d^2 f}{dq^2} = 0 \tag{36}$$

This equation can be re-written as

$$X_{III} + \frac{1}{2} X X_{II} = 0 \tag{37}$$

where X_i represents the ith order derivative of the invariant f.

The Blasius equation (37) are the equivalent of our equations (27) and (30), but with an important difference: (37) is a closed equation, while (27) and (30) contain two dependent variables (U and ℓ_M). The well-known closure problem of turbulence requires the introduction of closure hypothesis. In a symmetry analysis, closure hypothesis comes from symmetry assumption. In the previous attempts [11, 12], symmetry is imposed simply on the mean velocity, that is, the group invariant of U^+ is assumed to be constant, i.e.

$$G_1(y^+, Re_\tau) = G_1(y^{+*}, Re_\tau^*) = const. \tag{38}$$

As shown in ([11]), with this assumption, candidate solutions of power-law and defect power-law can be obtained for the mean velocity,

$$U^+ = G_1 y^{+\beta}, \qquad or \qquad U^+ = U_c^+ - G_1 r^\beta. \tag{39}$$

The power-law solution finds its correspondence with the linear scaling in the viscous sublayer with $\beta = 1$; the defect power law solution, $U^+ = U_c^+ - G_1 y^\beta$ in coordinate y, corresponds to flow solution near the central part of a channel, according to Oberlack [11], with fitting parameters $G_1 = 5.83$ and $\beta = 1.69$. However, it can be shown that this latter solution contradicts the central symmetry condition, $U_c^+ - U^+ \propto r^2$, hence should be regarded as non-physical. Therefore, we consider that imposing the invariance on U to derive closure solutions of the RANS equation is not successful.

With the introduction of the new dependent variables, ℓ_M and its gradient, the situation is different. First, we are given new freedom in constructing the solutions, because the symmetry associated with the fluctuations (included in ℓ_M) can be treated separately. Secondly and most importantly, we can independently verify if the assumed symmetry is true. If ℓ_M is not a good variable, we can study a variant of it, until we find the good order function. Thirdly, as shown below, we are able to derive rigorously two local solutions near the wall and around the centerline of a channel/pipe, similarly as deriving the 1/2 exponent in (34) for laminar boundary layer. Finally, this program yields a general procedure, with the concept of the order function, of performing symmetry analysis for unclosed problems involving fluctuations. Below, we show that only three kinds of symmetries are sufficient for determining the full profile of mean shear and hence mean velocity according to (12), which is highly encouraging.

2.2. *Three kinds of similarities for mixing length*

When considering the possible symmetries of ℓ_M^+ and $\dot{\ell}_M^+$, three cases naturally arise.

2.2.1. Power-law

The simplest situation is that the scaling symmetries of ℓ_M^+ and $\dot{\ell}_M^+$ are both maintained, as the group parameter ϵ continuously changes. This can be sketched by the mapping:

$$\begin{pmatrix} y^+ \\ Re_\tau \\ \ell_M^+ \\ \dot{\ell}_M^+ \end{pmatrix} \quad \Rightarrow \underbrace{\begin{pmatrix} y^{+*} \\ Re_\tau^* \\ \ell_M^{+*} \\ \dot{\ell}_M^{+*} \end{pmatrix}}_{Transformed-variables} \quad \rightarrow \underbrace{\begin{pmatrix} = y^{+*} \\ = Re_\tau^* \\ = \ell_M^{+*ES} \\ = \dot{\ell}_M^{+*ES} \end{pmatrix}}_{Empirical-solution} \tag{40}$$

where the superscript ES denotes the empirical solution. With this symmetry assumption, (26) yields constants F_1 and F_2:

$$F_1 = c_1, \quad and \quad F_2 = \alpha c_1. \tag{41}$$

Solving (26), we thus have a power-law solution for ℓ_M^+:

$$\ell_M^+ = c_1 y^{+\alpha} \tag{42}$$

Note that $F_2/F_1 = \alpha$ is a key quantity to characterize the solution. Since the scaling symmetry is postulated, the actual solution may realize only a specific value of α. Thus, the scaling symmetry assumption provides a candidate solution to be validated by empirical data. Specifically, the theory proposes to plot the empirical data in terms of a so-called diagnostic function:

$$\gamma = F_2/F_1 = \partial ln(\ell_M^+)/\partial ln(y^+), \quad or \quad \gamma = F_2/F_1 = \partial ln(\ell_M)/\partial ln(r). \tag{43}$$

If the empirical γ displays a plateau in a range of y^+ (or r), then, a local scaling symmetry of ℓ_M^+ is validated, and the value of the plateau is thus α which guarantees the dilation invariance of the RANS equation. Such tests carried out for DNS channel and pipe flow data indeed show that $\alpha = 3/2$ in the viscous sublayer, and $\alpha = -1/2$ in the central core, which can be easily obtained from the near wall asymptotic analysis. There two exponents also can be derived from physical invariants at the boundaries as (33) for the Blasius equation, see Section 3.

2.2.2. Defect Power-law

The second situation is that the scaling symmetry of ℓ_M^+ breaks down, but that of $\dot{\ell}_M^+$ is maintained. This takes place in the bulk flow (for $r = O(1)$), where the mixing length tends to a finite value of the order of the radius of the pipe (or the half width of the channel). This finite length breaks the scaling symmetry and any dilation invariance. Using the outer variable r for the outer MME, we then have the following mapping:

$$\begin{pmatrix} y^+ \\ Re_\tau \\ \ell_M \\ \dot{\ell}_M \end{pmatrix} \quad \Rightarrow \underbrace{\begin{pmatrix} y^{+*} \\ Re_\tau^* \\ \ell_M^* \\ \dot{\ell}_M^* \end{pmatrix}}_{Transformed-variables} \quad \rightarrow \underbrace{\begin{pmatrix} = y^{+*} \\ = Re_\tau^* \\ \neq \ell_M^{+*ES} \\ = \dot{\ell}_M^{+*ES} \end{pmatrix}}_{Empirical-solution} \tag{44}$$

It can be expressed as

$$F_1 \neq c_1, \quad and \quad F_2 = c_2. \tag{45}$$

This solution is postulated for describing the bulk flow. Integrating (29) once using (45), we obtain $\ell_M = c' + F_2 r^m/m$, where c' is an integration constant and m is an exponent characterizing the power-law of $\dot{\ell}_m$. Furthermore, using the boundary condition: $\ell_M \to 0$ as $r \to 1$, then $c' = -F_2/m$. Thus,

$$\ell_M = -F_2(1 - r^m)/m. \tag{46}$$

Note an interesting asymptotic behavior of (46): as $r \to 1$, $\ell_M \to -F_2(1-r) = \kappa y$; thus we obtain $\kappa = -F_2$. In other words, the classical Karman constant is a Lie-group invariant of the gradient of the mixing length which is valid not only for the overlap region, but for the whole bulk region also. Here, we call (45) the similarity of the second kind, and (46) the defect power-law.

Note that (46) is obtained by employing a prolongation in the Lie-group analysis, which deserves a further comment. Bluman and Kumei [20] proposed to describe the similarity of the first kind as displaying invariant curve, while the similarity of the second kind (with the symmetry-breaking of the original scaling variable) displaying an invariant family of curves parameterized by ϵ. In other words, the latter case is characterized by an invariant manifold composed of a family of invariant curves.

2.2.3. Composite solution

Finally, consider the situation when both symmetries in ℓ_M^+ and $\dot{\ell}_M^+$ break down, as sketched below:

$$\begin{pmatrix} y^+ \\ Re_\tau \\ \ell_M^+ \\ \dot{\ell}_M^+ \end{pmatrix} \quad \Rightarrow \quad \underbrace{\begin{pmatrix} y^{+*} \\ Re_\tau^* \\ \ell_M^{+*} \\ \dot{\ell}_M^{+*} \end{pmatrix}}_{Transformed-variables} \quad \to \quad \underbrace{\begin{pmatrix} = y^{+*} \\ = Re_\tau^* \\ \neq \ell_M^{+*ES} \\ \\ \neq \dot{\ell}_M^{+*ES} \end{pmatrix}}_{Empirical-solution} \tag{47}$$

In fact, this happens during a transition from one scaling state to another, when there exist several local scaling states in a system composed of a multi-layer structure, with exponents γ_I $(I = 1, 2, ...)$ each characterizing a layer. What would happen now? The weak-invariance-principle formulated above applies here, and suggests finding a new form which is yet left invariant under the group transformation; this would be then a generalized symmetry which describes a continuous transition from one power-law solution, $\ell_M^{+I} = F_1^I y^{+\gamma_I}$ to another, $\ell_M^{+II} = F_1^{II} y^{+\gamma_{II}}$. Let us sketch this generalized invariance law using an abstract function Θ as:

$$\Theta(\ell_M^+, \dot{\ell}_M^+) = 0 \quad \underbrace{\Rightarrow \quad \Theta(\ell_M^{+*}, \dot{\ell}_M^{+*}) = 0}_{Transformed-variables} \quad \to \quad \underbrace{\Theta^{ES}(\ell_M^{+*}, \dot{\ell}_M^{+*}) = 0}_{Empirical-solution} \tag{48}$$

A specific ansatz is proposed as follows:

$$\Theta \equiv (\gamma - \gamma_I) - (\gamma_{II} - \gamma_I)(F_1^{II}/F_1)^n \tag{49}$$

where $\gamma(y^+) = F_2/F_1$ and $F_1(y^+) = \ell_M^+(y^+)/y^{+\gamma_{II}}$ are variables, while all other symbols are constants. In particular, n is a parameter specifying the transition

sharpness. (48) implies that $\Theta = 0$ is an invariant property under the dilation group transformation; it can be shown that it satisfies the so-called invariant surface condition (see appendix). In other words, $\Theta = 0$ is a generalized symmetry - an invariant surface in the function space of $\ell_M^+, \dot{\ell}_M^+$ that is tangent to the Lie-group operator, in analogy to the simple power-law and defect power-law solutions. The postulated ansatz (49) imposes a specific invariance form, which would be constructive if (49) yields the actual empirical solution. Our subsequent studies, reported here and elsewhere, show that it is indeed the case.

One may wonder how (49) is motivated? In fact, $\Theta = 0$ can be rewritten as

$$\frac{\gamma - \gamma_I}{\gamma_{II} - \gamma_I} = \left(\frac{F_1^{II}}{F_1}\right)^n \tag{50}$$

For adjacent layers I and II, $\gamma = F_2/F_1$ as a function of y^+, must vary smoothly and monotonically from γ_I to γ_{II}. As a result, it is easy to verify that (50) has the desired asymptotic behavior: γ goes to γ_I at one end and to γ_{II} at the other end. Let $y_c^+ = \left(F_1^I/F_1^{II}\right)^{1/(\gamma_{II}-\gamma_I)}$ denote such a location in the middle of the transition that $\ell_M^{+I}(y_c^+) = \ell_M^{+II}(y_c^+)$. Then, for $y^+ \gg y_c^+$, $F_1 \to F_1^{II}$, the r.h.s. of (50) goes to 1, as expected. For $y^+ \ll y_c^+$, $F_1^{II}/F_1 \to (y^+/y_c^+)^{\gamma_{II}-\gamma_I}$, and the r.h.s. of (50) goes to zero for $p = n(\gamma_{II} - \gamma_I) \gg 1$. The latter can always be guaranteed by choosing an appropriate n (thus n specifies the sharpness of the transition between two adjacent layers). Therefore, (50) connects the two asymptotic states of power-law invariance with desired scalings.

From (50), we find an analytical expression for ℓ_M^+ valid across the two layers as:

$$\ell_M^{+(I-II)} = F_1^I y^{+\gamma_I} \mathbf{B}^{I-II}(y^+; y_c^+, p) \tag{51}$$

where the transition function $\mathbf{B}$ is defined as

$$\mathbf{B}^{I-II}(y^+; y_c^+, p) = \left(1 + \left(y^+/y_c^+\right)^p\right)^{(\gamma_{II}-\gamma_I)/p}. \tag{52}$$

It works as a blending procedure to switch between layers, which has been used as an interpolation function in many models, e.g. Batchelor [21] used it to describe the transition of the velocity structure function from the dissipative to inertial range. We derive it only by a continuity and smoothness argument on the Lie-group invariants. Here, we show that a dilation-invariant structure is behind $\mathbf{B}$; it would be intriguing to investigate why this form is so generic and what determines the transition sharpness.

3. The multi-layer description of turbulent channel and pipe flows

Now, we apply the above analysis to turbulent channel and pipe flows. The notion of the multi-layer comes from empirical observations well known in the literature [15]. For the inner region, one first meets with the so-called viscous sublayer very close to the wall; then, a buffer layer where coherent near-wall structures such as streamwise vortices dominate the dynamics [22]. Then is the overlap region between the inner solution and the outer solution. For the outer region, there is a bulk flow, with a core around the center. With the Lie-group formalism developed above, these layers can be described analytically and quantified with parameters related to local scaling, transition location and transition sharpness. Below, we derive analytical expressions of the mixing length for all of these layers.

3.1. *Inner flow*

The viscous sublayer is assumed to hold a similarity of the first kind, and is analytically described by a power-law scaling of the mixing length as:

$$\ell_M^{+sub} = F_1^{sub} y^{+3/2} \tag{53}$$

This result can be justified by a near-wall expansion in the small fluctuation amplitude: $u \sim y^+$ and $v \sim y^{+2}$ such that $W^+ \sim y^{+3}$. Since $S^+ \approx 1$ near the wall, $\ell_M^+ \sim y^{+3/2}$, consistent with (53). Note that the symmetry transformation itself does not select the exponent 3/2; only further physical consideration related to the boundary constraint is able to offer a concrete proposal. Following the argument leading to (34), a similar constraint as (33) is $S^+ = 1$ at vanishing y^+, which yields $W^+/\ell_M^{+2} = 1 = W^{+*}/(\ell_M^{+*})^2 \sim (y^{+*})^3/(\ell_M^{+*})^2$. Thus, $\alpha = 3/2$ in (24).

For large y^+ when (53) ceases to be valid, we postulate new layers with the power-law scaling of a distinct exponent, and identify them with the buffer-layer and the log-layer. The reason behind this assumption lies in the belief that the dilation-group invariance should be a robust property throughout the whole near-wall region. Indeed, an empirical study with the diagnostic function γ of the DNS channel flow data confirms our assumption with the following results:

$$\ell_M^{+buf} = F_1^{buf} y^{+2} \tag{54}$$

$$\ell_M^{+log} = F_1^{log} y^{+} = \kappa y^{+} \tag{55}$$

The exponent 2 for the buffer layer is believed to be related to coherent vortical structures, such as streamwise vortices whose core is mostly located at $y^+ \approx 25$ [22], which will be studied in details elsewhere.

Then, the generalized symmetry - ansatz (50) - yields a composite formula valid across both the sublayer and buffer layer as

$$\ell_M^{+(sub-buf)} = \ell_M^{+sub} \mathbf{B}^{s-b}(y^+; y_{sub}^+, p_1), \tag{56}$$

where $\mathbf{B}^{s-b} = (1 + (y^+/y_{sub}^+)^{p_1})^{1/2p_1}$. Similarly,

$$\ell_M^{+(buf-log)} = \ell_M^{+buf} \mathbf{B}^{b-l}(y^+; y_{buf}^+, p_2) \tag{57}$$

valid across the buffer and log layer, where $\mathbf{B}^{b-l} = (1+(y^+/y_{buf}^+)^{p_2})^{-1/p_2}$. The test of these formula is presented below.

3.2. *Outer flow*

As mentioned above, the bulk flow is characterized by the finite mixing length which leads to a dilation-symmetry-breaking. By assuming that the dilation-symmetry is still maintained in the gradient of the mixing length, we arrive at a defect power-law solution,

$$\ell_M^{bulk} = \kappa(1 - r^m)/m. \tag{58}$$

Empirical study shows that $m = 4$ for channel and $m = 5$ for pipe. We have then a similarity of the second kind. Note that (58) smoothly match the log-layer

$\ell_M^{log} = \kappa y$ independent of m. The bulk solution (58) is also a discovery of the present theory. A verification by the DNS channel flow data is presented in Fig.2, where the compensated plot of ℓ_M^+ by (58) clearly shows a plateau.

Near the centreline ($r \to 0$), we find an extra layer called core, where the mixing-length diverges as $\ell_M \propto 1/\sqrt{r}$. This is consistent with a similarity solution of the first kind:

$$\ell_M^{core} = F_1^{core} r^{-1/2} \tag{59}$$

where the exponent $\gamma_{core} = -1/2$ is derived from an invariant central condition

$$\frac{1}{r}\frac{\partial U^+}{\partial r} = \frac{1}{r^*}\frac{\partial U^{+*}}{\partial r^*} = const. \tag{60}$$

which, using (28), leads to

$$3/2 - \alpha = 2; \qquad \alpha = -1/2. \tag{61}$$

This determination is again similar to the argument used to derive (34) in the Blasius equation. It is consistent with a central symmetry argument: as $r \to 0$, $W^+ \approx r$ and $S^+ \propto r$, hence, $\ell_M \propto r^{-1/2}$. Furthermore, using (50), the Lie-group theory yields a matching from (59) to a constant mixing length in the bulk flow with scaling exponent zero, $\ell_M \to \ell_0 = \kappa/m$; and the composite solution from the bulk to the central core is thus

$$\ell_M^{bulk-core} = (\kappa/m)\mathbf{B}^{b-c}(r; r_{core}, p_3)/Z_c \tag{62}$$

where $\mathbf{B}^{b-c} = (1 + (r/r_{core})^{p_3})^{-1/2p_3}$ and $Z_c = \mathbf{B}^{b-c}(r = 1)$ is a normalization factor.

3.3. *A complete formula using multiplicative rule*

By applying similarity solutions of all three kinds, we have achieved a series of analytical expressions, valid for sub-buffer layer (56), buffer-log layer (57), bulk-core layer. Now we attempt to connect them together to form a complete formula for the mixing length profile, i.e.(1).

Following [23], the multiplicative rule, $\phi^{I-III} = \phi^{I-II}\phi^{II-III}/\phi^{Common}$, is applied to (56) and (57), yielding a matching solution for the inner flow

$$\ell_M^{+In} = \ell_M^{+sub}\mathbf{B}^{s-b}\mathbf{B}^{b-l} \tag{63}$$

where the factor for the common state ℓ_M^{+buf} cancels. Similarly, applying the multiplicative rule to (58) and (62), the outer solution is

$$\ell_M^{Out} = \ell_M^{bulk}\mathbf{B}^{b-c}/Z_c \tag{64}$$

Finally, applying the multiplication rule to (63) and (64), we obtain a matching solution for the mixing length profile valid in the entire domain:

$$\ell_M^+ = \ell_M^{+In}\ell_M^{+Out}/\ell_M^{+Common} = \ell_M^{+In}\ell_M^{+Out}/\ell_M^{+log}, \tag{65}$$

which yields (1).

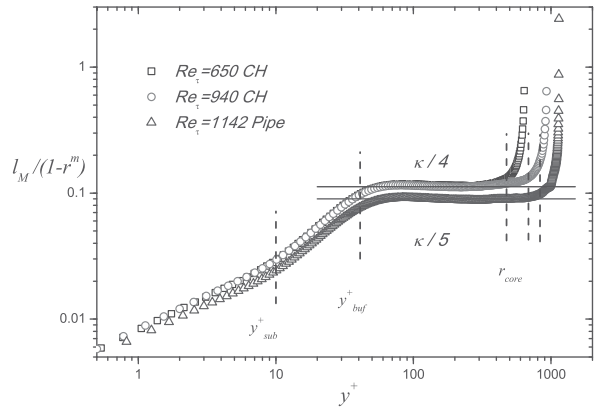


Figure 3. The mixing length function from DNS data divided by the bulk flow solution reveals a four-layer structure, i.e. viscous sublayer, buffer layer, bulk zone and core layer, separated by y^+_{sub}, y^+_{buf} and r_{core}.

Note that $\ell_M^{+Out} = Re_\tau \ell_M^{Out}$ in (65); and $\rho \equiv \kappa y^{+2}_{sub}/y^+_{buf}$ in (1). The coefficients in (1) can be measured locally and independently since they are derived layer by layer: y^+_{sub}, y^+_{buf} and r_{core} are the successive transition locations between sublayer, buffer layer and core layer, respectively; $m = 4$ for channel and 5 for pipe represents different bulk; and p_i is transition sharpness ($i = 1, ...$), less sensitive to the prediction of MVP. After all of the parameters are determined, (1) gives a highly accurate mean velocity profile over a wide range of Re (discussed elsewhere).

4. Verification by DNS data

We have outlined above a novel Lie-group analysis for determining the mixing length profile. This analysis can be subjected to a test by DNS data. In other words, the invariance property of the mixing length function postulated in the analysis can go through scrutiny against DNS data which are the true Navier-Stokes solutions. Currently, there exist several DNS datasets for channel and pipe flows for Re_τ up to thousands. We have selected two channel flows from Iwamoto *et al.* [16] at $Re_\tau = 650$ and Hoyas and Jimenez [17] at $Re_\tau = 940$, and one pipe flow of Wu and Moin [18] at $Re_\tau = 1142$, which are believed to be well-resolved. The data confirm the multi-layer similarity law for the mixing length, as below.

Fig. 3 shows a clear evidence for the newly discovered bulk flow structure, $1 - r^m$ ($m = 4$ for channel and 5 for pipe), using a compensated plot of the observed mixing length (e.g. divided by $1 - r^m$), in which each of the inner layers and the core (divergent) layer are also very visible. The existence of the central core is due to a switch of the kinetic energy generation mechanism, from mean shear (production) to turbulent transport. Close to the centreline, the mean shear approaches zero, and finite energy dissipation is balanced by turbulent transport. The thickness of each layer is an important parameter, sketched in Fig. 3 (the demarcation for the core layer is sketched by $y^+_{core} = (1 - r_{core})Re_\tau$, hence increasing with Re), whose accurate determination from DNS data will be discussed elsewhere.

5. Conclusion and Discussions

In this paper, we present a derivation of the recently proposed multi-layer formula (1) for the mixing length [4], motivated from a novel Lie-group symmetry analysis. We find that the inner and outer MMEs, expressed not only in terms of the mean velocity, but also the mixing length and its gradient - the latter representing effects of fluctuations (Reynolds stress), only admit dilation symmetry, which leads to three kinds of similarity solutions for the mixing length function soundly validated by DNS data.

The approach expresses the closure solutions in terms of three sets of parameters: scaling exponent, transition location (thickness in layered structure) and transition sharpness. These parameters are unique to the dilation-group, which are, in general, functions of Re, but at large Re, they are believed to be Re-independent. In previous works [11, 12], the Re (viscosity) effect is typically neglected by assuming a Re-independent solution of the mean velocity, which is obviously invalid because of the complex matching between the inner and outer solutions. This problem is solved here by writing down separately the inner and outer MME, and the Re-similarity is guaranteed by involving Re explicitly in the transformation. At large enough Re, the Re-similarity may be translated to Re-independence; in this case, the Lie-group invariant F_1 becomes truly invariant:

$$F_1(y^+, Re_\tau) = F_1(y^{+*}, Re_\tau^*) = F_1(y^{+*}, Re_\tau) = const. \tag{66}$$

where the first equation stems from the symmetry transformation, and the second from Re-independence, as mentioned before. Empirical study in a turbulent pipe shows that the Re independence only holds for $Re_\tau > 5000$, while a slow increase of the parameters y^+_{buf} and r_{core} is found below this critical Re. The details will be discussed elsewhere. With a model of Re-dependence of the parameters, the theory (1) predicts the mean velocity profile for all Re.

What does the symmetry analysis using the Lie-group formalism add to our understanding more than making a direct postulate of power-law or other ansatz for ℓ_M? The answer is that a Lie-group formalism guarantees that the RANS equation remains invariant under the (dilation) group of transformation, hence any ansatz used here yields a (candidate) similarity solution. In other words, the family of solutions based on power-law, defect power-law and the generalized invariance ansatz of ℓ_M form a set of invariant solutions of the RANS equation, when ℓ_M is treated as one dependent variables. Future study would clarify why ℓ_M is so special to possess this invariance; once it is done, a new avenue of solving the closure problem of turbulence would be opened.

Thus, we speculate to have formulated a general framework for turbulence closure problem: searching for group-invariant properties of relevant length order functions representative of the fluctuation structures (e.g. the mixing length and some other length order functions), and then solving for the mean velocity (which has a symmetry-breaking) from the MME. This procedure can be extended to other mean quantities by introducing relevant order functions which possess the required symmetry and guarantee the invariance of the relevant balance equations. Ultimately, whether such closure solutions are true solutions need to be verified against empirical data. If verified, the length order function (and its gradient) is indeed the right quantity, since the order function is, by definition, the quantity displaying distinct symmetry. Hence, we achieve a logically consistent framework.

Note that the Lie-group formalism is a necessary and powerful tool for the present success. Only with the present formalism, an analytical expression for the mixing

length is obtained, for the first time, wholly motivated from symmetry consideration, i.e. dilation-group invariance. While power-law form for the mixing length can be motivated from simple scaling arguments, the present formalism accomplishes two additional aspects which would be difficult otherwise: a defect-power law form for the bulk flow and a series of matched forms derived from the generalized invariance ansatz. Note that the ansatz requires only simple assumptions about the continuity and smoothness for describing the variation of the local group invariants. Finally, it is remarkable that there exist only three distinct classes of similarity solutions, associated with the dilation group of the mixing length with its prolongation.

Finally, we note that the mixing length is only one example of the order functions, specifically representing the effect of the Reynolds stress in the mean momentum transfer. The complexity of turbulent flows is that they generally encompass a hierarchy set of order functions, each displaying a specific type of turbulent transfers. One will find other order functions responsible for turbulent transfer of kinetic energy, temperature, etc. Our preliminary study has already identified several other order functions in compressible turbulent boundary layers [24], rough pipe [25], and Reyleigh-Benard convection. Thus, the concept of the order function is general, applicable to many other flow systems, and the Lie-group formalism developed in the present work is also of general interest. The present analysis opens a promising direction for modeling the mean profiles in a wide class of turbulent wall-bounded flows.

6. Acknowledgements

We thank Y. Wu, J. Chen, Y.S. Zhang, Y.Z. Wang and J.H. Xie for helpful discussions. We also thank the referees for helpful suggestions and discussions. This work is supported by National Nature Science Fund 90716008 and by MOST 973 project 2009CB724100.

References

[1] Wilcox, D.C. 2006 *Turbulence Modeling for CFD.* DCW Industries.
[2] L'vov, V.S., Procaccia, I. & Rudenco, O. 2008 Universal Model of Finite Reynolds Number Turbulent Flow in Channels and Pipes. *Phys. Rev. Let.* **100**, 050504(1-4).
[3] Wu, Y., Chen, X., She, Z.S. & Hussain, F. 2012 Incorporating boundary constraints to predict mean velocities in turbulent channel flow, *Science China - Physics, Mech. & Astro.* **55**(9): 1-5.
[4] She, Z.S. Chen, X., Wu, Y. & Hussain, F. 2010 New perspectives in statistical modeling of wall-bounded turbulence. *Acta. Mech. Sinica.* **26**, 847-861.
[5] Prandtl, L. 1925 Bericht uber die Entstehung der Turbulence. *Z. Angew. Math. Mech.* **5**, 136-139.
[6] Kadanoff, L. P. 2009 More is the same; phase transitions and mean field theories. *J. Stat. Phys.* **137**, 777-797.
[7] Barenblatt, G.I. 1993 Scaling laws for fully developed turbulent shear flows.Part 1. Basic hypotheses and analysis. *J. Fluid Mech.* **248**, 513-520.
[8] George, W.K & Castillo, L. 1997 Zero-pressure-gradient turbulent boundary layer. *Appl. Mech. Rev.* **50**,689-729.
[9] Barenblatt, G.I., Chorin, A.J. & Prostokishin, V.M. 2000 Self-similar intermediate structures in turbulent boundary layers at large Reynolds numbers. *J. Fluid. Mech.* **410**, 263-283.
[10] Cantwell, B.J. 2002 *Introduction to symmetry analysis.* Cambridge Univ. Press.
[11] Oberlack, M. 2001 A unified approach for symmetries in plane parallel turbulent shear flows. *J. Fluid Mech.* **427**, 299-328.
[12] Lindgren, B., Osterlund, J.M. & Johansson A.V. 2004 Evaluation of scaling laws derived from Lie group symmetry methods in zero-pressure-gradient turbulent boundary layers. *J. Fluid Mech.* **502**, 127-152.
[13] Oberlack, M. & Andreas R. 2010 New statistical symmetries of the multi-point equations and its importance for turbulent scaling laws. *Discr. Cont. Dynamic. Sys. S* **3**, 3.
[14] Frisch, U. 1995 *Turbulence.* Cambridge Univ. Press.
[15] Pope, S.B. 2000 *Turbulent Flows.* Cambridge Univ. Press.

[16] Iwamoto, K., Suzuki, Y. & Kasagi, N. 2002 Database of fully developed channel flow. *THTLAB Internal Report, No. ILR-0201*; see http://www.thtlab.t.utokyo. ac.jp.
[17] Hoyas, S. & Jimenez, J. 2006 Scaling of the velocity fluctuations in turbulent channels up to $Re_\tau = 2003$. *Phys. Fluids.* **18**, 011702; see http://torroja.dmt.upm.es/ftp/channels/.
[18] Wu, X.H. & Moin, P. 2009 Direct numerical simulation of turbulence in a nominally zero-pressure-gradient flat-plate boundary layer. *J. Fluid. Mech.* **630**, 5-41.
[19] Van Driest, E.R. 1956 On turbulent flow near a wall, Journel of the aeronautical sciences, Vol. 23, p. 1007.
[20] Bluman, G. W. & Kumei S. 1989 *Symmetries and differential equations* Springer-Verlag New York, Inc.
[21] Batchelor, G.K. 1951 Pressure fictuations in isotropic turbulence. *Proc. Cambridge Philos. Soc.* 47, 359.
[22] Schoppa, W. & Hussain, F. 2002 Coherent structure generation in near-wall turbulence. *J. Fluid. Mech.* **453**, 57-108.
[23] Van Dyke M., 1964 *Perturbation Methods in Fluid Mechanics* Academic, New York.
[24] Zhang Y.S., Bi W.T., Hussain F., Li X.L. & She Z.S., 2012 Mach-Number-Invariant Mean-Velocity Profile of Compressible Turbulent Boundary Layers. *Phys. Rev. Lett.* 109, 054502.
[25] She Z.S., Wu Y., Chen X. & Hussain F., 2012 A Multi-state Description of Roughness Effects in Turbulent Pipe Flow. *New J. Physics*, 14 093054.

Appendix A. Calculations of the admitted symmetries of (16)

Note that S_ε can also be expressed in an infinitesimal form:

$$\mathbf{t}^* = \mathbf{t} + \overrightarrow{\xi}(\mathbf{t},\mathbf{x})\varepsilon + O(\varepsilon^2); \quad \mathbf{x}^* = \mathbf{x} + \overrightarrow{\eta}(\mathbf{t},\mathbf{x})\varepsilon + O(\varepsilon^2), \tag{A1}$$

where $\overrightarrow{\xi} = \partial\Phi/\partial\varepsilon|_{\varepsilon=0} = (\xi_{y^+}, \xi_{Re_\tau})$ and $\overrightarrow{\eta} = \partial\Psi/\partial\varepsilon|_{\varepsilon=0} = (\eta_{U^+}, \eta_{\ell_M^+})$ are the so-called infinitesimals. Then, Taylor expansion, $\mathscr{C}(\mathbf{t}^*,\mathbf{x}^*) = \mathscr{C}(\mathbf{t},\mathbf{x}) + \varepsilon X\mathscr{C} + O(\varepsilon^2)$, yields the following equation for the infinitesimals [11]:

$$X\mathscr{C}|_{\mathscr{C}=0} = \left(\overrightarrow{\xi}\cdot\frac{\partial}{\partial\mathbf{t}} + \overrightarrow{\eta}\cdot\frac{\partial}{\partial\mathbf{x}} + X_p\right)\mathscr{C} = 0, \tag{A2}$$

where X is the so called Lie-group operator, and $X_p = \eta_{\dot{U}^+}\partial_{\dot{U}^+} + \eta_{\ddot{U}^+}\partial_{\ddot{U}^+} + \eta_{\dot{\ell}_M^+}\partial_{\dot{\ell}_M^+}$ is referred to as the 'prolongation'. The infinitesimals can be solved by the software *Maple13*, since (A2) is an set of linear homogeneous differential equations for them, and the results are:

$$\begin{aligned} \xi_{y^+} &= a_1 y^+ + b_1, & \xi_{\mathrm{Re}_\tau} &= a_2\mathrm{Re}_\tau, \\ \eta_{\ell_M^+} &= (-a_1 + a_2)\ell_M^+/2, & \eta_{U^+} &= (2a_1 - a_2)U^+ + b_2, \end{aligned} \tag{A3}$$

where coefficients a_i and b_i $(i = 1, 2)$ denote dilations and translations, respectively. Now, the no-slip wall condition, i.e. $U^{+^*} = \ell_m^{+^*} = 0$ at $y^{+^*} = 0$, leads to $b_1 = b_2 = 0$; thus, near the wall, only the dilations are permitted. Normalized by the parameter a_1, we have

$$\begin{aligned} \xi_{y^+} &= y^+, & \xi_{\mathrm{Re}_\tau} &= (1 + 2\alpha)\mathrm{Re}_\tau, \\ \eta_{\ell_M^+} &= \alpha\ell_M^+, & \eta_{U^+} &= (1 - 2\alpha)U^+, \end{aligned} \tag{A4}$$

where $\alpha = (-1 + a_2/a_1)/2$ is the only remaining parameter specifying the local scaling of the mixing length. In addition, the infinitesimals for the derivatives are $\eta_{\dot{U}^+} = -2\alpha\dot{U}^+$, $\eta_{\ddot{U}^+} = (-1 - 2\alpha)\ddot{U}^+$ and $\eta_{\dot{\ell}_M^+} = (\alpha - 1)\dot{\ell}_M^+$ using the contact condition. Integration of these infinitesimals leads to the global transformations as in (24).

Appendix B. Discussion on the generalized symmetry (49)

Note that (49) can be written as a function of similarity variables: $\Theta(F_1, F_2) = F_2/F_1 - d_1 - d_2 F_1^n = 0$, where d_1 and d_2 are both constants. Substituting $F_1 = \ell_M^+/y^{+\alpha}$, $F_2 = \dot{\ell}_M^+/y^{+(\alpha-1)}$ into it, yields:

$$\Theta(F_1, F_2) = y^+ \dot{\ell}_M^+/\ell_M^+ - d_1 - d_2(\ell_M^+/y^{+\alpha})^n. \tag{B1}$$

As the Lie-group operator in the variable space $(y^+, \ell_M^+, \dot{\ell}_M^+)$ is:

$$X = y^+ \frac{\partial}{\partial y^+} + \alpha \ell_M^+ \frac{\partial}{\partial \ell_M^+} + (\alpha - 1)\dot{\ell}_M^+ \frac{\partial}{\partial \dot{\ell}_M^+}. \tag{B2}$$

Hence,

$$\begin{aligned} &X\Theta = X(y^+ \dot{\ell}_M^+/\ell_M^+ - d_1 - d_2(\ell_M^+/y^{+\alpha})^n) \\ &= (y^+ \dot{\ell}_M^+/\ell_M^+ - \alpha y^+ \dot{\ell}_M^+/\ell_M^+ + (\alpha - 1) y^+ \dot{\ell}_M^+/\ell_M^+) - d_2(n\alpha(\ell_M^+/y^{+\alpha})^n - n\alpha(\ell_M^+/y^{+\alpha})^n) \\ &= 0. \end{aligned} \tag{B3}$$

Reconsidering the 'Local Equilibrium' Hypothesis for Small Scale Turbulence

William K George*

Department of Aeronautics, Imperial College, SW7 2AZ London, UK

(*30 August 2012*)

The assumption of the *local equilibrium* of small scale turbulence has been a principal underpinning of modern turbulence theory for more than 70 years, the so-called 'Kolmogorov' or 'K41' theory[1]. The leading examples of it are the scaling in Kolmogorov variables for small scale turbulence, the 4/5's law for the third-order structure function, the $k^{-5/3}$-range in velocity spectra, and the familiar $\varepsilon = u^3/L$ which is incorporated into most turbulence models. It is argued herein that the assumption of *local' equilibrium* is in fact *not* satisfied in general for non-stationary and inhomogeous flows, but is applicable only for flows which are in strict equilibrium (e.g., forced homogeneous turbulence). It is shown, however, that it can be satisfied approximately in at least some thin shear flows (e.g., boundary layers, jets, wakes, etc.) where energy production and dissipation are nearly in balance. Finally it is demonstrated that a $k^{-5/3}$-'law' can be recovered, albeit one in which the constant is flow-dependent.

Keywords: turbulence, local equilibrium, small scale turbulence, non-stationarity,universal equilibrium

1. The 'local equilibrium' hypothesis

The assumption of '*local equilibrium*' underlies many of the ideas we have come to accept as 'fact', or at least to have been experimentally verified. The 'classical' arguments to justify it have been summarized in Appendix I. The purpose of this section is to review the consequences of the *local equilibrium* assumption, and in particular how the results we have come to accept as true depend on it. Then it will be clear what we must give up, or at least re-justify, if 'local equilibrium' is not valid.

1.1. *Spectral equations for decaying turbulence*

For the simplest example, consider the problem originally considered by Batchelor (no doubt motivated by the concurrent grid turbulence experiments of Townsend) to build the case for 'K41' originally: namely, decaying homogenous turbulence described by the following spectral energy equation:

$$\frac{\partial E}{\partial t} = T - 2\nu k^2 E \tag{1}$$

*Corresponding author. Email: georgewilliamk@gmail.com

[1]There were many who built upon and contributed to Kolmogorov's original work to construct what we generally regard to be the theoretical framework for modern turbulence research. In the absence of a better word we refer to this framework, or paradigm, collectively herein as 'K41', with apologies to Kolmogorov for any extensions of his work he might not have approved of.

Note that *ALL* time variations in this paper refer to the temporal variation of ensemble-averaged quantities; i.e., only the *averaged* properties of fluctuating quantities are considered, no instantaneous ones. Thus $\partial/\partial t = 0$ of any averaged quantity corresponds to a stationary random process, while $\partial/\partial t \neq 0$ clearly must be non-stationary. The three-dimensional energy spectrum function, $E(k,t)$, is obtained by integrating the trace of the three-dimensional spectrum (which is itself obtained by the three-dimensional Fourier transform of the two-point velocity correlation tensor) over spherical shells of radius $k = |\vec{k}|$ (v. Monin and Yaglom [9]); i.e.,

$$E(k,t) = \frac{1}{2}\oint_{k=|\vec{k}|} FT_{\vec{k}}[\langle u_i(\vec{x},t)u_i(\vec{x}+\vec{r},t)\rangle]dS(k) \tag{2}$$

The integral of $E(k,t)$ over all wavenumbers is the energy, $\langle u_i u_i\rangle/2$, and the integral of $2\nu k^2 E(k,t)$ is the average dissipation rate (hereafter referred to as just the dissipation), $\overline{\varepsilon}$; i.e.,

$$\frac{1}{2}\langle u_i u_i\rangle = \frac{3}{2}u^2 = \int_0^\infty E(k,t)dk \tag{3}$$

$$\overline{\varepsilon} = 2\nu\langle s_{ij}s_{ij}\rangle = \int_0^\infty k^2\ E(k,t)dk \tag{4}$$

where s_{ij} is the fluctuating strain rate. *Note that in general the energy, dissipation and spectra are time-dependent since the flow is considered to be non-stationary.*

$T(k,t)$ itself is the spectral transfer of energy arising from the non-linear interactions, the net effect of which at all wavenumbers is zero. The non-linear spectral transfer is often written as a spectral flux, say $\varepsilon_k(k,t)$:

$$T(k,t) = -\frac{d\varepsilon_k}{dk} \tag{5}$$

The spectral flux, ε_k should not to be confused with the dissipation, $\overline{\varepsilon}$, although the choice of closely related symbols is made because they will be seen to have been 'believed' to be closely related.

1.2. *The universal equilibrium range*

Since Kolmogorov [1, 2] (or see Batchelor [4]), the local equilibrium hypothesis is normally used to neglect the left-hand-side of equation 1 for all wavenumbers satisfying $kL >> 1$ where L is an integral scale; i.e., for all wavenumbers well-removed from the energy-containing range we write simply:

$$0 = T - 2\nu k^2 E \tag{6}$$

$$= -\frac{d\varepsilon_k}{dk} - 2\nu k^2 E \tag{7}$$

In the second equation we have replaced the partial derivative with respect to k by an ordinary derivative since the turbulence at the highest scales is now presumed to be at equilibrium (except as reflected through the instantaneous value of $\overline{\varepsilon}$).

This time-independent equation has been generally regarded as describing all turbulence at high Reynolds number, regardless of whether the flow is homogeneous or not, at least as long as the Reynolds number is sufficiently high. Such flows are referred to as being at least *locally homogeneous* and the high wavenumber range of the spectrum to comprise a *universal equilibrium range* (a term apparently first used by Batchelor (c.f. [4]).

Equation 7 has been the starting point for many attempts to build spectral models for turbulence, from Onsager[13], Heisenberg[15] and Kovasznay[16] in the 1940's to the more recent Corrsin/Pao [17, 18] and Lin/Hill [19, 20] models. A simple Google search on 'local equilibrium' yields thousands of hits showing that equation 1 is of no less interest today.

1.3. *Kolmogorov similarity*

Integrating equation 7 with respect to k from k to infinity yields:

$$\varepsilon_k(k) = 2\nu \int_k^\infty k'^2 E(k')dk' \tag{8}$$

Clearly for wavenumbers lower than those making a significant contribution to the integral (but not so low as to be outside the equilibrium range), the integral is very nearly equal to the dissipation (see equation 4). Thus in this spectral gap *if it exists*, $\varepsilon_k = \overline{\varepsilon}$. But even if the scale separation is not great enough for a significant gap to exist, the hypothesis of local equilbrium alone is sufficient to insure that the only parameters affecting the highest wavenumbers are ν and $\overline{\varepsilon}$.

An immediate consequence of the assumed 'local equilibrium' of the small scale motions (or high wavenumbers) is that the energy spectrum in the resulting universal equilibrium range must scale only with the $\overline{\varepsilon}$ and ν, yielding the so-called 'equilbrium range' spectrum as:

$$E(k,t) = \overline{\varepsilon}^{1/4}\nu^{5/4} f_{Kol}(k^+) \tag{9}$$

where $f_{Kol}(k^+)$ is the dimensionless spectrum for the local equilibrium range, and $k^+ = k\ \eta_{Kol}$ is a dimensionless wavenumber non-dimensionalized by the so-called 'Kolmogorov microscale, η_{Kol}, defined as:

$$\eta_{Kol} = (\nu^3/\varepsilon)^{1/4}. \tag{10}$$

Further, $f_{Kol}(k^+)$ has widely been assumed to be 'universal', i.e., the same for all turbulent flows.

It is but a small step (v. Batchelor [4]) to argue that if the Reynolds number is sufficiently high, say $L/\eta_{Kol} >>>> 1$, then there must also exist a range in which the spectral dissipation term, $2\nu k^2 E$, is also negligible so that the spectral flux therein, say $\varepsilon_{k\ gap}$, must be constant and equal to the dissipation. Thus in this so-called 'inertial subrange', $\varepsilon_{k\ gap} = \overline{\varepsilon}$. By arguing on dimensional grounds alone that the spectrum in the inertial subrange should depend only on the spectral flux, ε_k, and k, this in turn leads to one of the most famous results in turbulence; namely the so-called 'Kolmogorov's $k^{-5/3}$-law':

$$E(k) = \alpha_{Kol}\ {\varepsilon_{k\ gap}}^{2/3} k^{-5/3} = \alpha_{Kol}\ \overline{\varepsilon}^{2/3} k^{-5/3} \tag{11}$$

It was in fact first derived in this spectral form by Obukov [21]. Kolmogorov [1] himself used the second-order velocity structure function, $S_2(r) = \langle u_1(x,y,z)u_1(x+r,y,z)\rangle$, to obtain a corresponding $r^{2/3}$-law. In a separate paper [2] he also examined the inertial range of the third-order structure function, $S_3(r)$, which can be shown to equal to $4\ \overline{\varepsilon} r/5$ with no adjustable constants. The latter is now known as Kolmogorov's four-fifths law (v. [8, 11]).

Monin and Yaglom [9], for example (see Appendix I), use similar arguments applied to decaying turbulence to obtain heuristically the result that if the Reynolds number is sufficiently high to have an inertial subrange so that $\varepsilon_{k\ gap} = \overline{\varepsilon}$ there, then it must also be true *on dimensional grounds alone* that:

$$\varepsilon = A\frac{u'3}{L}. \tag{12}$$

where A is a constant of order unity. This is sometimes called the '*zeroth-law*' of turbulence. A consequence, is the '*dissipation anomaly*', so-named by Onsager [13], which suggests there can be dissipation even in the limit of zero viscosity. Note that so widespread is the belief that this is correct that many actually take equation 12 with $A = 1$ to be the definition of the integral scale (see discussion in [14]).

2. Is there really a 'local equilbrium' range?

This section reconsiders whether the neglect of the left-hand-side of equation 1 is ever justified. It does so by defining quantitative measures of 'local equilbrium', then asking under what conditions they are satisified. The analysis is illustrated by the example of decaying turbulence, both because it is a non-stationary flow and because it is the flow used in the 'classical' arguments of Appendix I. Subsequent sections consider other flows.

2.1. *How should we test the 'local equilibrium' hypothesis?*

There are at least two questions we can ask to test the 'local equilibrium' hypothesis:

(1) Are the unsteady (non-stationary) terms in the two-point spectral (or correlation) equations really less unimportant at the higher wavenumbers (smaller scales) than at the lower wavenumbers (larger scales)?
(2) Are the unsteady (non-stationary) terms in the two-point spectral (or correlation) equations really ever negligible?

Both questions can be answered quantitatively by examining the behavior of the time-derivative of the spectrum, say $\partial E(k,t)/\partial t$. For question (1) we will examine the behavior of the inverse of the spectral decay time scale defined by $(1/E)\partial E/\partial t$. Of particular interest will be how it varies from low to high wavenumbers, especially when compared to the overall decay time ${u'}^2/\overline{\varepsilon}$. For question (2) we will examine what effect $\partial E/\partial t$ would have on the overall equation if not neglected.

2.2. $(1/E)\partial E/\partial t$ *in the inertial subrange*

Inertial subrange First consider only the inertial subrange. If Kolmogorov's equilibrium hypothesis is correct at all, then it must surely be correct for the spectrum derived by assuming it to be correct, namely the inertial subrange result of equation 11. Substituting equation 11 into the full spectral equation 1 and neglecting the viscous terms yields:

$$\frac{\partial E}{\partial t} = \frac{2}{3}\ \alpha_{Kol}\ \overline{\varepsilon}^{-1/3}\ k^{-5/3} \frac{d\overline{\varepsilon}}{dt} \tag{13}$$

so

$$\frac{1}{E}\frac{\partial E}{\partial t} = \frac{2}{3}\ \frac{1}{\overline{\varepsilon}} \frac{d\overline{\varepsilon}}{dt} \tag{14}$$

This can be compared to the time scale for the overall decay, u'^2/ε; thus

$$\frac{u'^2}{\varepsilon}\left(\frac{1}{E}\frac{dE}{dt}\right) = \frac{2}{3}\left(\frac{u'^2}{\overline{\varepsilon^2}}\ \frac{d\overline{\varepsilon}}{dt}\right) \tag{15}$$

If the inertial range is really in local equilibrium, this ratio should be negligible and diminish with increasing wavenumber, thereby justifying the neglect of the time derivative entirely. Clearly the ratio is not diminishing with increasing wavenumber. Moreover whether it is small or not has nothing do with any spectral property or turbulence scale, only how close the flow itself is to real statistical equilibrium (i.e., $d\overline{\varepsilon}/dt \equiv 0$).

Note that contrary to the classical argument (c.f., Batchelor [4, 9], also Appendix I), the time scale ratio of equation 15 is quite different than that obtained by the classical argument using $T_k = 1/\sqrt{k^3 E(k)}$ which yields a time scale ratio in the inertial subrange of $(1/\sqrt{\alpha_{Kol}})(kL)^{-2/3}$. T_k is indeed a correct estimate of the time scale (or turnover time) of a hypothetical turbulent velocity fluctuation associated an 'eddy' of 'size' $1/k$. *But it is not a time scale for the spectral decay with time*, which is what we need to consider to neglect the time derivative in equation 1. The result obtained here represents the actual temporal variation of the spectrum, and will be seen to lead to very different conclusions about the nature of the spectra at large wavenumbers.

Example: Power law decay of homogeneous turbulence Decaying turbulence (and arguments about it) were crucial in the early acceptance of Kolmogorov's theories (c.f., the Batchelor/Townsend experiments referenced by Monin and Yaglom and summarized in Appendix I), so we consider it first. If the turbulence is decaying as a power of t, say $u'^2/u'^2_o \propto (t/t_o)^{-n}$, then $\overline{\varepsilon} = -(3/2)\ du'^2/dt = (3/2)\ n\ (u'^2_o/t_o)\ [t/t_o]^{-n-1}$. So

$$\left(\frac{u'^2}{\overline{\varepsilon^2}}\ \frac{d\overline{\varepsilon}}{dt}\right) = -\frac{2}{3}\left[\frac{n+1}{n^2}\right] \tag{16}$$

It follows immediately that for power law decay the right-hand of equation 15 reduces to:

$$\frac{u'^2}{\varepsilon}\ \frac{1}{E}\frac{dE}{dt}\bigg|_{inertial} = -\frac{4}{9}\left[\frac{n+1}{n^2}\right] \tag{17}$$

Typically $1 \leq n \leq 5/2$ (George [25]), so the corresponding time scale ratios in the inertial subrange vary from 8/9 to 46/225. Note that these only represent limits for power law decay, since some fractal grids, for example, can produce turbulence which behaves very differently; e.g., [27, 28]. Nonetheless, for even exponentially decaying turbulence,the time-scale ratio, $(u'^2/\overline{\varepsilon}^2)d\overline{\varepsilon}/dt$, is of order unity.

Thus, even using Kolomogov's inertial subrange spectrum (which has been derived by assuming the time derivative on the left-hand-side of equation 1 to be zero), the rate of relative spectral change in the inertial subrange for this non-stationary flow is not only independent of wavenumber, it is of order one. Moreover it is constant during decay; and hence time-independent. If n depends on the initial (or upstream conditions in the case of a grid), so does this ratio. This example alone has provided the counter-example needed to disprove the local equilibrium hypothesis and the idea of a universal equilibrium range. Note, however, that this does not imply there may be other situations where local equilibrium does apply; and we shall see that there are!

2.3. *The universal equilbrium versus energy-containing ranges*

Now let's look more generally at the entire 'universal equilibrium range' and energy-containing ranges, again *assuming* them to exist. The question we wish to answer is whether one can be assumed to be in equilibrium relative to the other.

The energy-containing range For low wavenumbers, the conventional wisdom (since Batchelor 1948) has been that spectra should scale as (c.f. Tennekes and Lumley [7], Gamard and George [14]):

$$E(k,t) = u^2 L\ f_L(\tilde{k}) \tag{18}$$

where $\tilde{k} = kL$. Differentiation yields immediately:

$$\frac{1}{E}\frac{\partial E}{\partial t}\bigg|_{low} = -\left(\frac{\overline{\varepsilon}}{u^2}\right)\left\{\frac{2}{3} + \frac{u'^2}{\overline{\varepsilon}}\left(\frac{1}{L}\frac{dL}{dt}\right)\left[1 + \frac{\tilde{k}_L f'_L}{f_L}\right]\right\} \tag{19}$$

where $f'_L(\tilde{k}) = df_L/d\tilde{k}$ and k_L is any representative wavenumber in the energy-containing range. If we choose $L = u'^3/\overline{\varepsilon}$,

$$\frac{1}{L}\frac{dL}{dt} = -\frac{\overline{\varepsilon}}{u^2} - \frac{1}{\overline{\varepsilon}}\frac{d\overline{\varepsilon}}{dt} \tag{20}$$

Substituting this into equation 19 yields:

$$\frac{1}{E}\frac{\partial E}{\partial t}\bigg|_{low} = -\frac{2}{3}\left(\frac{\overline{\varepsilon}}{u^2}\right)\left\{1 + \frac{3}{2}\left[1 + \left(\frac{u'^2}{\overline{\varepsilon}^2}\frac{d\overline{\varepsilon}}{dt}\right)\right]\left[1 + \frac{\tilde{k}_L f'_L}{f_L}\right]\right\} \tag{21}$$

Note that this result reduces to equation 15 if the inertial subrange spectrum is substituted. Also note that unlike the inertial subrange result of the preceding section, this result is proportional to $u'^2/\bar{\varepsilon}$, consistent with our choice above of it as representative of the time-scale of the energetic scales. Clearly it is the erroneous choice by classical argument of the time scale $1/\sqrt{k^3E(k)}$ as representative of the spectral decay in the inertial sublayer which is incorrect.

Universal equilbrium range For high wavenumbers, the full Kolmogorov-scaled universal equilibrium range spectrum of equation 9 yields:

$$\frac{1}{E}\frac{\partial E}{\partial t}\bigg|_{high} = \frac{1}{4}\left(\frac{1}{\bar{\varepsilon}}\frac{d\bar{\varepsilon}}{dt}\right)\ \left[1\ -\ \frac{k_H^+ f'_{Kol}}{f_{Kol}}\right] \tag{22}$$

where k_H^+ is any representative number in the universal equilibrium range and since $(1/\eta_{Kol})d\eta_{Kol}/dt = -(1/4)(1/\bar{\varepsilon})d\bar{\varepsilon}/dt$. Note that for the inertial subrange this reduces to the same result as equation 15 above. And as for the inertial subrange result above, the predominate prefactor is $(1/\bar{\varepsilon})d\bar{\varepsilon}/dt$ with only a weak dependence on the spectrum itself, at least for k_H^+ of order unity or less.

The relative variation The plausibility arguments usually invoked (e.g., Batchelor [4, 7, 9] and Appendix I) claim that $(1/E)\partial E/\partial t|_{low}$ is important while $(1/E)\partial E/\partial t|_{high}$ is not. Their ratio is given by:

$$\frac{(1/E)\ \partial E/\partial t|_{high}}{(1/E)\ \partial E/\partial t|_{low}} = -\frac{3}{8}\left(\frac{u'^2}{\bar{\varepsilon}^2}\frac{d\bar{\varepsilon}}{dt}\right)\left\{\frac{\left[1\ -\ \frac{k_H^+ f'_{Kol}}{f_{Kol}}\right]}{1+\frac{3}{2}\left[1+\left(\frac{u'^2}{\bar{\varepsilon}^2}\frac{d\bar{\varepsilon}}{dt}\right)\right]\left[1+\frac{\tilde{k}_L f'_L}{f_L}\right]}\right\} \tag{23}$$

In the inertial subrange this yields unity as it should. The wavenumber dependence in the denominator can be neglected at least near the peak in the spectrum where $f'_L \approx 0$. The wavenumber dependence in the numerator depends on the shape of the spectrum itself, which is generally accepted to roll-off exponentially near $k^+ = 1$, with a $k^{+-5/3}$ prefactor. To explore this further we need to introduce a spectral model. For this case we will choose the Lin-Hill spectrum [19, 20], even though any other choice would be acceptable. But by choosing one derived from the 'equilibrium hypothesis' we ensure that we have not biased the conclusions.

Lin-Hill spectral model A useful 'K41-based' spectral model for the high wavenumber spectrum is the so-called Lin-Hill spectrum [14, 19, 20] given by:

$$f_H(k^+) = \alpha_{Kol}k^{+-5/3}\ [1+k^{+2/3}]\ exp\left\{-2\alpha[k^{+4/3}/(4/3)\ +\ k^{+2}/2]\right\} \tag{24}$$

Note that this model spectrum is in effect an infinite Reynolds number spectrum, since it varies as $k^{+-5/3}$ in the limit as $k^+ \to 0$. It can be spliced together with a von-Kàrmàn-type spectrum to form a composite spectrum for finite Reynolds numbers (e.g., [14]). But since we are primarily interested in the high wavenumber behavior we forego this additional complexity.

Differentiation yields immediately:

$$\frac{k^+ f'_H}{f_H} = -\frac{5}{3}\left\{1-\frac{2}{5}\frac{k^{+2/3}}{\left[1+k^{+2/3}\right]}\ +\ \frac{6}{5}\alpha_{Kol}\ [k^{4/3}\ +\ k^{+2}]\right\} \tag{25}$$

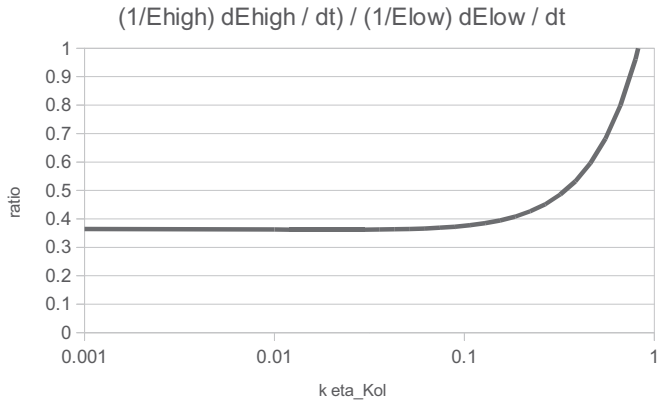


Figure 1. Ratio of high wavenumber spectral time derivative to low wavenumber spectral time derivative using equation 27 with $n = 1.25$ and $\alpha_{Kol} = 1.7$. Note that ratio is constant over the inertial subrange, and that curve bends up sharply only well beyond the peak in dissipation spectrum which is at about $k\eta_{Kol} \approx 0.2$.

Substitution into the numerator of equation 27 yields

$$\frac{(1/E)\ \partial E/\partial t|_{high}}{(1/E)\ \partial E/\partial t|_{low}} = -\frac{3}{2}\left(\frac{u'^2}{\bar{\varepsilon}^2}\frac{d\bar{\varepsilon}}{dt}\right)\left\{\frac{\left[1\ -\ \frac{1}{4}k^{+2/3}\left[1+k^{+2/3}\right]^{-1}\ +\ \frac{3}{4}\alpha_{Kol}\ \left[k^{4/3}\ +\ k^{+2}\right]\right]}{1+\frac{3}{2}\left[1+\left(\frac{u'^2}{\bar{\varepsilon}^2}\frac{d\bar{\varepsilon}}{dt}\right)\right]\left[1+\frac{\tilde{k}_L f'_L}{f_L}\right]}\right\} \tag{26}$$

The denominator can be simplified if we evaluate ${f'}_L$ at the maximum of f_L (as in the Monin/Yaglom citation in Appendix I); this reduces to approximately:

$$\frac{(1/E)\ \partial E/\partial t|_{high}}{(1/E)\ \partial E/\partial t|_{low}} \approx -\frac{3}{2}\left(\frac{u'^2}{\bar{\varepsilon}^2}\frac{d\bar{\varepsilon}}{dt}\right)\left\{\frac{\left[1\ -\ \frac{1}{4}k^{+2/3}\left[1+k^{+2/3}\right]^{-1}\ +\ \frac{3}{4}\alpha_{Kol}\ \left[k^{4/3}\ +\ k^{+2}\right]\right]}{1+\frac{3}{2}\left[1+\left(\frac{u'^2}{\bar{\varepsilon}^2}\frac{d\bar{\varepsilon}}{dt}\right)\right]}\right\} \tag{27}$$

E.g.. Power law decaying turbulence Application of equation 16 derived above yields:

$$\frac{(1/E)\ \partial E/\partial t|_{high}}{(1/E)\ \partial E/\partial t|_{low}} \approx \frac{2}{5}\left(\frac{n+1}{n^2}\right)\left\{\frac{\left[1\ -\ \frac{1}{4}k^{+2/3}\left[1+k^{+2/3}\right]^{-1}\ +\ \frac{3}{4}\alpha_{Kol}\ \left[k^{4/3}\ +\ k^{+2}\right]\right]}{1+\frac{2}{5}\left(\frac{n+1}{n^2}\right)}\right\} \tag{28}$$

Figure 2.3 shows plot of equation 28 using $n \approx 1.25$ and $\alpha_{Kol} = 1.7$. This ratio has a low wavenumber asymptote of 0.36 and increases to only 0.48 at ${k^+}_H = 0.32$, which is well past the peak in the dissipation spectrum. It begins to increase quite

rapidly beyond this wavenumber, but still has a value of only 1.25 at $k^+{}_H = 1$. Clearly this is not the order of magnitude variation that would be the minimum requirement for a universal equilibrium range and neglect of the $\partial E/\partial t$-term at high wavenumbers relative to those at low wavenumbers. At most Kolmogorov's equilibrium assumption is valid only for k^+ very close to unity or greater, and surely not over the range in which the dissipation spectrum makes its largest contribution to the dissipation integral. And not at all over the entire $k^{-5/3}$-range (the so-called inertial subrange).

A different spectral model for the high wavenumbers would only change this ratio slightly. This suggests strongly that there is very little difference between the statistical stationarity of the high wavenumbers and the low ones, *even when the high and low wavenumber spectra are evaluated based on the assumption that the high wavenumbers are in statistical equilibrium.* The relative stationarity of both are determined by the statistical stationarity of the turbulence itself as measured by $(u'^2/\overline{\varepsilon})d\overline{\varepsilon}/dt$.

2.4. *How important is $\partial E/\partial t$ relative to the other terms in the equation?*

We have seen in the analysis above, that there is no support for the local equilibrium asssumption, except when the flow itself is at statistical equilibrium or very close to k^+ of unity). But might there be other reasons for which the unsteady term in the spectral (or correlation) equation can be neglected in a non-stationary flow? This question is best addressed by substituting in the spectral energy equation for the non-linear spectral transfer using the spectral flux defined in equation 5; i.e.,

$$\frac{\partial E}{\partial t} = -\frac{\partial \varepsilon_k}{\partial k} \; - \; 2\nu k^2 E \tag{29}$$

One way to see the effect of even a residual $\partial E/\partial t$ term is to integrate equation 1. Integration with respect from k to ∞ yields immediately:

$$\begin{aligned} \varepsilon_k(k,t) &= 2\nu \int_k^\infty k'^2 E(k',t)dk' + \frac{\partial}{\partial t}\int_k^\infty E(k',t)dk' \\ &= \overline{\varepsilon} + \left\{ \frac{\partial}{\partial t}\int_k^\infty E(k',t)dk' - 2\nu \int_0^k k'^2 E(k',t)dk' \right\} \end{aligned} \tag{30}$$

In decaying turbulence, both terms in braces on the right-hand-side are negative, therefore both must be negligible over at least a small range (or gap) to have $\varepsilon_{k\ gap} \approx \overline{\varepsilon}$. But if there is never such a range, then $\overline{\varepsilon}$ can never with just ν characterize the dissipation range. Moreover, if $d\overline{\varepsilon}/dt$ is important (in addition to just $\overline{\varepsilon}$), then simply including finite Reynolds number effects by the ratio L/η_k (as in Tennekes and Lumley [7] and Gamard and George [14]) is not sufficient to account for the overlap. (Note a recent paper by Laizet et al. [30] reaches similar conclusions from a very different perspective.) Whether an approximately $k^{-5/3}$-range can still exist or not we address in Section 4 below; but if so, it will most surely not be the traditional one with presumed universal constants.

The ratio of $\partial E/\partial t$ to $T(k,t) = -\partial \varepsilon_k/\partial k$ alone is complicated by the fact that in the high Reynolds number limit, the Kolmogorov-based theories would argue that $T \equiv 0$. Thus no matter how small $\partial E/\partial t$ or $2\nu k^2 E$ are, they both remain of residual importance.

The only attempts to directly measure the spectral flux in a decaying turbulence are due to Van Atta and his co-workers (Van Atta and Chen [31], Helland et al. [32]). Those attempts made clear that even at values of R_λ of several hundred there was really no region of constant spectral flux, and in fact the non-linear transfer had maximum slope as it went though zero. In fact, they suggested that perhaps Lumley's criterion [33] of $(k/\varepsilon_k)d\varepsilon_k/dk << 1)$ for buoyancy-dominated flows might be more appropriate. Modern DNS (see George and Wang [34]) of decaying turbulence are even less supportive of the classical picture.

By contrast, the recent success of theories which include the temporal derivative term for all wavenumbers have been remarkably successful in describing a variety of experiments in non-stationary homogeneous flows. Appendix II discusses the history of these flows, and the recent progress in understanding them. All of these theories are in conflict with 'K41'; and none assume local equilibrium, but instead an equilibrium among the terms in the spectral (or structure function) equations themselves (so-called 'equilibrium similarity, [29]).

2.5. *Viscous term: the origin of 'local equilibrium'*

The purpose of this section is to show that in spite of the failure of the arguments of Townsend and Batchelor (and many since, e.g., Monin and Yaglom [9]) to justify Kolmorogov's assumed state of local equilibrium, there is as least one region where the assumption is nearly correct This is the range very close to the Kolmogorov microscale. To see this consider the ratio of the time derivative on the left-hand side in Kolmogorov variables, which is easily computed by dividing equation 22 by $2k^2E$. The result is:

$$\left(\frac{1}{2\nu k^2 E}\right)\frac{\partial E}{\partial t} = \frac{1}{4}\left(\frac{(\nu/\overline{\varepsilon})^{1/2}}{\overline{\varepsilon}}\frac{d\overline{\varepsilon}}{dt}\right)\left[\frac{1}{2k^{+2}}\right]\left[1 - \frac{k_H^+ f'_{Kol}}{f_{Kol}}\right]$$
$$= \frac{1}{4}\left(\frac{\nu}{u'L}\right)^{1/2}\left(\frac{L}{u}\right)\frac{1}{\overline{\varepsilon}}\left(\frac{d\overline{\varepsilon}}{dt}\right)\left[\frac{1}{2k^{+2}}\right]\left[1 - \frac{k_H^+ f'_{Kol}}{f_{Kol}}\right] \quad (31)$$

Near $k^+ = 1$, the inverse dependence on the square root of the Reynolds number $u'L/\nu$ pretty much overwhelms anything else so the $\partial E/\partial t$-term can be neglected. Nonetheless, because of the squared dependence on k^+, for $k^+ < 1$ the $\partial E/\partial t$ term can re-enter the balance quite rapidly with diminishing wavenumber if $(L/u)(1/\overline{\varepsilon})d\overline{\varepsilon}/dt$ is of order unity. For example, at $k^+ = 0.01$ the Reynolds number must be four orders of magnitude greater to achieve the same criterion for negligibility. Note the effect of $\partial E/\partial t$ re-entering the problem is quite different than that accounted for in an overlap analysis at finite Reynolds number (c.f., Tennekes and Lumley [7], Gamard and George [14]). The reason is that here $d\overline{\varepsilon}/dt$ enters explicity. To this point, no spectral model appears to allow for this. The equilibrium similarity analysis of George [25] (and those based on the same ideas, e.g. Seoud and Vasillicos [27], etc) do, however, account for it implicitly.

2.6. *Conclusions about equilibrium*

As should be clear from even the cursory presentation in section 1 above, the consequence on turbulence theory for the lack of validity of local equilibrium are devastating. Without it there is no universal equilibrium range, no inertial subrange, no constancy of the spectral flux, no $\overline{\varepsilon} = u'^3/L$, and hence no dissipation anomaly.

But yet we have come to believe in these things. The next section discusses why.

3. Why have the equilibrium range results appeared to be correct?

Experiments over the past 70 years (and especially until the early 1960's) have given rather mixed messages about the validity of 'K41''. This section explains why.

3.1. *Homogenous turbulence*

Obviously flows that are statistically stationary (like forced turbulence) satisfy the equilibrium hypothesis identically; i.e., $d\overline{\varepsilon}/dt \equiv 0$. Hence the 'local equilibrium' hypothesis is satisfied identically. Moreover this immediately implies a region in which the spectral flux is equal to the dissipation in the limit of infinite Reynolds number [8]. This makes understandable the recent success of large 'forced turbulence' simulations in verifying both it and its consequences (e.g., Kaneda et al. [36], Ishihara et al. [37])

By contrast, the canonical unsteady homogenous flows like decaying turbulence, homogeneous shear flow turbulence, etc. have long been problematical from the perspective of Kolmogorov theories, and have even been referred to as 'anomalous'. I will discuss these in more detail in the next section, but given the considerations of the preceding section the reason for this failure is quite obvious: $(u'^2/\overline{\varepsilon})\ [(1/\overline{\varepsilon})d\overline{\varepsilon}/dt]$ is not negligible. Hence none of the subsequent arguments and deductions relating to 'K41' from these flows can be assumed to be valid either, even at high Reynolds number, at least without new arguments for them.

3.2. *Statistically stationary inhomogeneous flows*

An important question is whether we can explain the lack of success to verify 'K41' in attempts to generate these 'homogeneous' flows as a stationary random process in a windtunnel. The $\partial/\partial t$ of any average quantity is zero. So it would seem 'local equilibrium' is also satisfied identically. But because the turbulence is convected by the mean flow we know that $D/Dt \approx U\ \partial/\partial x$ acts like $\partial/\partial t$ in such flows. In fact, what we observe depends on the flow we are looking at. For example, as noted below, we do indeed see something like $\overline{\varepsilon} \propto u^3/L$ in jets and other shear flows, even at modest Reynolds numbers; but not in most grid turbulence experiments. Why?

The answer lies in the dissipation transport equation which can be written quite succinctly as (Launder et al. [38], Tsinober [11]):

$$\frac{D\overline{\varepsilon}}{Dt} = \frac{\partial\overline{\varepsilon}}{\partial t} + U_j\frac{\partial\overline{\varepsilon}}{\partial x_j} = D_{\overline{\varepsilon}}\ +\ P_{\overline{\varepsilon}} + T_{\overline{\varepsilon}} \tag{32}$$

where $D_{\overline{\varepsilon}}$ is the dissipation of dissipation, $P_{\overline{\varepsilon}}$ is the production of dissipation, and $T_{\overline{\varepsilon}}$ can be interpreted as a turbulent transport of dissipation. If the flow is truly statistically stationary the first term on the left-hand-side is identically zero leaving only:

$$U_j\frac{\partial\overline{\varepsilon}}{\partial x_j} = D_{\overline{\varepsilon}}\ +\ P_{\overline{\varepsilon}} + T_{\overline{\varepsilon}} \tag{33}$$

Our main interest then is in the terms on the right-hand-side, $D_{\overline{\varepsilon}}$, $P_{\overline{\varepsilon}}$, and $T_{\overline{\varepsilon}}$. The last (the turbulence transport of dissipation) can often be neglected relative to the others if the flow is homogeneous in planes parallel to the direction of the mean flow.

At high Reynolds number, $D_{\overline{\varepsilon}}$ is dominated by terms not unlike the dissipation terms in the equation for the turbulence kinetic energy, except with products of fluctuating second derivatives instead of fluctuating first derivatives multiplying the kinematic viscosity. In homogeneous flows they are proportional to the fourth spectral moment; i.e.,

$$D_{\overline{\varepsilon}} = 4\nu^2 \int_0^\infty k^4 E(k,t) dk \tag{34}$$

Similarly the production of dissipation in a homogenous flow is proportional to the second spectral moment of the non-linear spectral transfer; i.e.,

$$P_{\overline{\varepsilon}} = 2\nu \int_0^\infty k^2 T(k,t) dk \tag{35}$$

The dissipation of dissipation and production of dissipation terms are pretty much important in any turbulent flow and never zero; and can in fact be related to directly to the amplification and diffusion of mean square vorticity (or entstrophy). If the local equlibrium hypothesis is invoked, these are in exactly balance, so the left hand side of equation 33 is zero. There are additional terms involving the mean flow if there are mean flow gradients, especially in the production term (v. Tennekes and Lumley [7], Tsinober [11]).

Of special interest to us here is how single-point turbulence modellers close this dissipation equation. Usually (and with very little justification[1]) the many derivative moments on the right-hand-side are modelled as simply being proportional to the energy dissipation and energy production divided by the time scale of the energetic scales; i.e.,

$$D_{\overline{\varepsilon}} = C_1 \frac{\overline{\varepsilon}}{u'^2/\overline{\varepsilon}} \tag{36}$$

and

$$P_{\overline{\varepsilon}} = C_2 \frac{P}{u'^2/\overline{\varepsilon}} \tag{37}$$

where P is the rate at which turbulence energy is produced by from the *mean* flow.

Clearly this breakdown into terms proportional to the dissipation and production of turbulence energy is not even close to being correct, since the latter includes only production from the mean flow, so the former must include the production of dissipation by the turbulence itself as well. Nonetheless these simple models work reasonably well for thin shear flows, and for an obvious reason (at least in hindsight). Even though the details and physics of the models are completely wrong, it is the imbalance locally between the production and dissipation that creates the

[1]Curiously this model equation applied to homogeneous flows turns out to be an exact consequence of the equilibrium similarity theories, e.g., George [25] and George and Gibson [50].

mean transport of dissipation on the left-hand side. And if these two are nearly in balance, *as they are in nearly every simple shear flow*, then $(u'^2/\overline{\varepsilon})\ (1/\overline{\varepsilon})U d\overline{\varepsilon}/dx$ is quite small as well.

For example, in one of the few inhomogeneous flows where the dissipation was actually measured, along the centerline of the high Reynolds number jet turbulence experiment of Hussein et al. [39], $(u'^2/\overline{\varepsilon})\ (1/\overline{\varepsilon})U d\overline{\varepsilon}/dx \approx 0.003$! And not surprising, a $k^{-5/3}$-range is observed in the one-dimensional spectra and $\varepsilon \propto u'^3/L$ to an excellent approximation.

So the reason why at least simple shear flows seem to behave according to the Kolmogorov-type turbulence is that in fact $(u'^2/\overline{\varepsilon})\ (1/\overline{\varepsilon})U d\overline{\varepsilon}/dx$ is very small. Thus the local equilibrium hypothesis provides a reasonable approximation to the state in which the turbulence finds itself, even though that state is slowly changing from one spatial location to another. Therefore we observe spectral features very close to those Kolmogorov and others have predicted.

Also we can find in these shear flows the only justification for taking $\overline{\varepsilon} \propto u'^3/L$, since often $P \approx \overline{\varepsilon}$ and $P \sim u'^3/L$. This is most easily seen for a simple two-dimensional mean flow where $P = -\langle uv\rangle dU/dy$. Tennekes and Lumley [7] argue that for simple shear flows vortex the stretching of the turbulence by the mean shear insures that $dU/dy \sim u'/L$ (at least where mean shear energy production dominates). If true, then $P \sim u'^2\ u'/L$ since $-\langle uv\rangle \sim u'2$. But since production and dissipation nearly balance, $\overline{\varepsilon}$ must vary the same way. And for any *finite* value of the kinematic viscosity the turbulence creates the small scales required to perform the necessary dissipation, no matter how small.

By contrast, Figure 3.2 using data from the recent fractal grid experiments of Valente and Vassilicos 2012 [56] shows quite clearly how $(u'^2/\overline{\varepsilon})(1/\overline{\varepsilon})D\overline{\varepsilon}/Dt$ changes downstream of the grid. Very near the grid, production of both energy and dissipation dominate due to the many shear layers created by the grid. And indeed there the turbulence resembles that found in many flows where $D\overline{\varepsilon}/Dt$ is zero. Downstream though as the mean flow becomes more uniform, the ratio approaches the asymptote more typical of decaying turbulence and the turbulence becomes decidedly non-'K41', but consistent with George 1992 [25]).

3.3. *A bit of history explained*

Another mystery can also solved: why did it take so long (from 1941 to 1962) before the first observations of a $k^{-5/3}$ spectral region were made? The answer is that by concentrating on homogeneous time-dependent decaying flows (grid turbulence), researchers were looking in the wrong place. This history is reviewed in Appendix II. It is well-known that by 1961 Kolmogorov was convinced his theory had to be modified since no $k^{-5/3}$-region had been observed, and offered at the 1961 Marseille meeting an alternative (published as [12]) which included internal intermittency of the dissipation fluctuations with a slightly modified power law. But in fact it was at this same meeting that Grant, Stewart and Molliet (published as [40]) offered the first real nearly indisputable confirmation of a $k^{-5/3}$ spectrum from their measurements in a tidal channel off Vancouver Island. Less known, but nearly concurrent with these measurements were the spectral measurements of M.M. Gibson [41] in a high Reynolds number round jet at the Johns Hopkins University, also showing a $k^{-5/3}$ spectral range.

The response of the turbulence community to these two experimental findings was overwhelmingly positive. It became accepted that these and similar results by others removed all further doubt, and validated the 'K41' theory, the problems with the unsteady homogeneous flows notwithstanding (see Appendix II). All subsequent

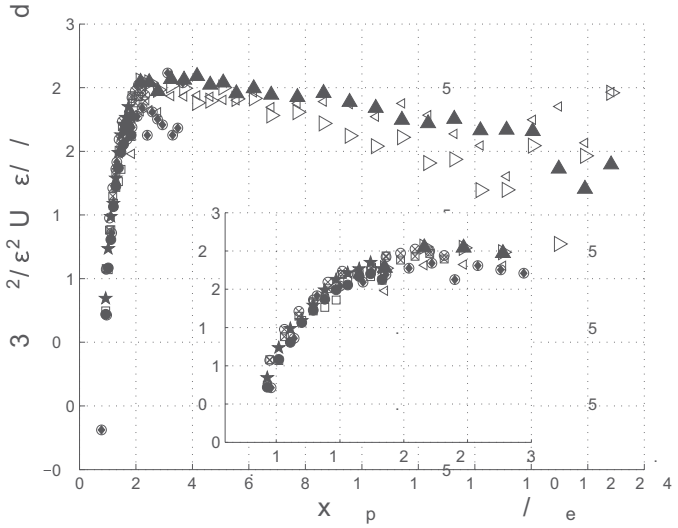


Figure 2. Plot showing evolution of $(u'^2/\bar{\varepsilon})(1/\bar{\varepsilon})D\varepsilon/Dt$ downstream of a fractal grid in wind tunnel as production of energy from shear layers is reduced. Insert shows near grid of rapid increase where production is playing a major role. Note asymptotic behavior as pure decay takes over (from data of Valente and Vassilicos 2012 [56].

failures to observe 'K41'-behavior were attributed to the general categories of either intermittency or of low Reynolds number effects. And (as this paper will prove I suspect, like [25] before it), any attempts to question the generality of 'K41' are still met by great skepticism.

4. Can we recover the $k^{-5/3}$ law even for non-stationary turbulence

As noted earlier, there is considerable experimental evidence for the existence of a $k^{-5/3}$ spectral range in a wide variety of flows. The observations in many shear flows are consistent with the fact that these flows are very close to statistical equilibrium so that $D\bar{\varepsilon}/Dt \approx 0$. But the series of recent experiments by Vasillicos and co-workers (e.g. [54, 56] using fractal grids find well-developed $k^{-5/3}$-range in spectra at high Reynolds numbers; and these are flows far from statistical equilibrium. In fact $\bar{\varepsilon}L/u^3$ is not constant, but varies are R_λ^{-1} with coefficients determined by the upstream conditions. These observations cannot be the same inertial subrange deduced by Obukov [21], since none of the assumptions are satisfied. Clearly there must be another justification.

As noted earlier, the $k^{-5/3}$-law is commonly justified on dimensional grounds by arguing the only $\bar{\varepsilon}$ and ν are the only governing parameters in the inertial subrange. Clearly this argument is specious, and in fact the counter-argument is well-known but not recognized as such. The most commonly used simple spectral model for turbulence just takes $E(k) = \alpha\ \bar{\varepsilon}^{2/3}k^{-5/3}$ with a lower limit of $kL = 1$ and determines L by making the integral equal to $(3/2)u^2$. In other words the very energy we presumed to be unimportant dominates the spectral region we have found. Also no one would ever determine the dissipation by integrating this spectrum.[1] Nor has anyone proposed determining the spectrum by the much more

[1]Note that we avoided this conflict earlier with our insistency on the constancy of the spectral flux, an

logical choice (given that most of the energy lies under it) of using only u^2 and k, since that leads to a k^{-1}-law.

So, as noted earlier, obviously dimensional analysis alone is not enough to justify the choice of only $\bar{\varepsilon}$ and ν as determinative parameters. But let's try it another way by including everything in the dimensional analysis that might be important. For example, restricting to homogeneous turbulence with no mean flow we can write:

$$E(k,t) = f(k;\nu,u^2,\varepsilon,\varepsilon_1,\varepsilon_2,\varepsilon_3,\ldots,P,P_1,P_2,\ldots.) \tag{38}$$

where we have dropped the overlines (since all are ensemble-averaged quantities) and defined:

$$\varepsilon = 2\nu\int_0^\infty k^2 E(k,t)dk \tag{39}$$

$$\varepsilon_1 = (2\nu)^2\int_0^\infty k^4 E(k,t)dk \tag{40}$$

$$\varepsilon_2 = (2\nu)^3\int_0^\infty k^6 E(k,t)dk \tag{41}$$

$$\varepsilon_3 = (2\nu)^4\int_0^\infty k^8 E(k,t)dk \tag{42}$$

$$\cdots \tag{43}$$

and where P is any production of turbulence energy and the P_n are enstrophy-like production terms; i.e.,

$$P_1 = \int_0^\infty k^2 T(k,t)dk \tag{44}$$

$$P_2 = \int_0^\infty k^4 T(k,t)dk \tag{45}$$

$$\cdots \tag{46}$$

These are, of course, in general time-dependent.

Now since we have assumed the flow to be homogeneous:

$$d\varepsilon/dt = P_1 - \varepsilon_1 \tag{47}$$

$$d^2\varepsilon_1/dt = P_2 - \varepsilon_2 \tag{48}$$

$$d^3\varepsilon_2/dt^3 = P_3 - \varepsilon_3 \tag{49}$$

$$\cdots \tag{50}$$

Thus we can reasonably replace the ε_n and P_n by $d\varepsilon/dt, d\varepsilon_1/dt, d\varepsilon_2/dt, \cdots$ so we write instead:

$$E(k,t) = f(k;\nu,u^2,\varepsilon,d\varepsilon/dt,d^2\varepsilon/dt^2,d^3\varepsilon/dt^3,\ldots) \tag{51}$$

argument which is itself valid only if local equilibrium is valid.

While simpler than equation 38, this is still pretty complicated, so clearly some other arguments are necessary to get to the $k^{-5/3}$-law.

There are two obvious length scales, $l_\varepsilon = u^3/\varepsilon$ and $(\nu^3/\varepsilon)^{3/4}$. So we can choose either one and retain their ratio, say $R = l_\varepsilon/\eta_{Kol}$ as a parameter. We've already seen that if there is $k^{-5/3}$-range, it contains most of the energy, so clearly it is the one with energy which we should keep. We can group the rest of the parameters as ratios of time-scales like $\tau_1 = u^2/\varepsilon, \tau_2 = (\varepsilon)/d\varepsilon/dt,\ \tau_3 = (d\varepsilon/dt)/(d^2\varepsilon/dt^2), \cdots$. Hence we can write:

$$E(k,t) = (u^5/\varepsilon)\ f(ku^3/\varepsilon, R; \tau_2/\tau_1, \tau_3/\tau_1, \cdots) \tag{52}$$

or using our definition $l_\varepsilon = u^3/\varepsilon$:

$$E(k,t) = u^2 l_\varepsilon\ f(kl_\varepsilon, R; \tau_2/\tau_1, \tau_3/\tau_1, \cdots) \tag{53}$$

We can quite equivalently also write:

$$E(k,t) = \nu^{1/4}\varepsilon^{1/4}\ f(k\eta_{Kol}, R; \tau_2/\tau_1, \tau_3/\tau_1, \cdots). \tag{54}$$

These look like the low and high wavenumber scaling laws of Tennekes and Lumley [7] (Chapter 8, see also Gamard and George [14], and reduce exactly to them if the time derivatives are identically zero; i.e., if the flow is statistically stationary.

Clearly if $R = l_\varepsilon/\eta_{Kol}$ were the only parameter, we would be able to perform the asymptotic matching as $R \to \infty$ in the manner of [7], or even the large (but finite) R near-asymptotic solution analysis of [14]. **And we still can, but with the additional arguments of $\tau_2/\tau_1,\ \tau_3/\tau_1$, etc.** The result is a power law region in the spectrum which is asymptotic as $R \to \infty$ to $k^{-5/3}$, **but with a coefficient which depends on the time scale ratios**; i.e.,

$$E(k,t) = \alpha\varepsilon^{2/3}k^{-5/3} \tag{55}$$

where $\alpha = \alpha(\tau_2/\tau_1, \tau_3/\tau_1, \cdots)$. Or presuming the first ratio to be the most important we can write as a first approximation: $\alpha = \alpha([u'^2/\varepsilon](1/\varepsilon)d\varepsilon/dt)$.

Clearly α is not a universal constant, but a function of the time-scale ratio. Note that the arguments from which it is derived do **not** depend on the constancy of the spectral flux over the spectral domain in question. Obviously it is the limiting value as $[u'^2/\varepsilon](1/\varepsilon)d\varepsilon/dt \to 0$ that is the counterpart of the traditional Kolmogorov constant. Whether the function, $\alpha(\tau_2/\tau_1)$, is truly universal or not depends on the particular flow and initial conditions, and can remain a matter for debate and experiment.

5. Summary and Conclusions

There are few subjects in post-World War II fluid mechanics which have at one time or another captured the attention of more Nobel prize winners and outstanding mathematicians than the consequences of the Kolmogorov/Batchelor equilibrium range hypothesis. And there are few subjects (in any field) that have been more analyzed with more high-powered mathematics and models, both physical and non-physical. Part of the reason for this is that the equations governing turbulence are

tantalizingly simple. Another is the afore-mentioned 'dissipation anomaly' which has implications and consequences far beyond simple turbulence theory. It is therefore quite surprising that no one seems to have noticed the simple logical flaw in the dimensional/physical analysis at its roots, nor the contradictions it leads to.

There were clues that there might be a problem even in the late '40's with the numerous attempts to reconcile the von Kármán/Howarth similarity analysis with 'K41'. Clearly (as noted in Appendix II) Batchelor himself wrestled with it in a series of papers (even though not saying so directly), before reaching his erroneous conclusion that turbulence could never be described by a single length scale. We now recognize the reasons for his difficulties: As reviewed in Appendix II, the first reason was that the vK/H theory was over-constrained (c.f., George [25]). Now we recognize a second source of Batchelor's 'problem': the decaying turbulence flow he was analyzing was non-stationary, and hence inconsistent with 'K41'.

Recognizing the fallacy of 'local equilibrium' makes turbulence no less difficult. But it does give us a way to sort flows into new categories and distinguish among our ambiguities. So perhaps the field can now move forward with new vigor. As we do so it does seem likely that the important new parameter will be the ratio of time-scales $(u'^2/\overline{\varepsilon})[(1/\overline{\varepsilon})\ D\overline{\varepsilon}/Dt]$. And that a primary focus of our attention should be the dissipation transport equation.

Acknowledgements

While these ideas have been developing for many years I was unable to tie them together until and during the stimulating environment of the Marseille 2011Turbulence Colloquium, which was especially helpful in filling in the historical gaps in my understanding. I am grateful to the organizers, Marie Farge, Keith Moffat and Kai Schneidner for their efforts, and for inviting me. I am especially appreciative of the many helpful discussions, comments and suggestions of my colleagues at Imperial College, especially J. C. Vassilicos, P. Valente and B. Van Wachem. A. Tsinober of Tel Aviv U. and Elaine Oran of the Naval Research Laboratory also contributed useful comments, not all positive. I would be remiss to not acknowledge my own mentors (S. Corrsin, O. M. Phillips, and especially J. L. Lumley and H. Tennekes) who taught me enough about the subtle nuances of K41 to recognize when it was wrong. And finally, I would also like to gratefully acknowledge the support of the Marie Curie Program of the European Community for the past two years.

Appendix I: The classical argument for 'local equilibrium'

The so-called 'K41'-theory of small scale turbulence involves several hypotheses about the nature of small scale turbulence. One of the most thorough summaries is by Monin and Yaglom [9] who state at the outset that:

> "... the mean motion *will* affect the state of small-scale fluctuations, but only indirectly, i.e., through the energy flux associated with the mean motion, which is transferred from the mean flow through the entire hierarchy of disturbances of various orders, and is finally transformed into heat. ... Consequently, the energy dissipation, $\overline{\varepsilon}$, will be the particular characteristic of large-scale motions which will affect the statistical state of the small-scale fluctuations ...." (Monin and Yaglom, vol II, section 21.3)

The phrase *universal equilibrium range* appears to have first been used by Batchelor to describe this 'local equilibrium' of the small scale motions.

The basic justification for this *'universal equilibrium range'* has been quite nicely summarized by Monin and Yaglom as follows[1]:

> "Consider a small range $(k, k + \Delta k)$ along the k-axis. This will correspond to a definite set of turbulent disturbances (total intensity, $E(k)\Delta k$), which will have its own "characteristic length scale" $l_k \sim 1/k$ and also its own "characteristic time scale $T_k = 1/ku'_k$ ...where $u' = \sqrt{\langle u_i u_i \rangle/3}$ will decay with time at the rate $\overline{\varepsilon} = -(3/2)du'^2/dt$. Accordingly, the characteristic time for the turbulence decay will be given by
>
> $$T_o = -u'^2 \ / \ du'^2/dt \ \sim \ u'^2 \ / \ \overline{\varepsilon} \tag{56}$$
>
> It is natural to expect that the "characteristic decay time" will be of the same order as the "characteristic time scale" of the principal energy-containing disturbances which can be identified as corresponding to the maximum $E_{max} = E(k_o)$ of the spectral function $E(k)$. If we suppose that for such disturbancess the characteristic velocity scale u'_{k_o} is of the same order as the root mean square velocity u' determined from the total turbulent kinetic energy, then we obtain
>
> $$-\frac{1}{u'^2}\frac{du'^2}{dt} \sim u' \ k_o, \ i.e., \ \overline{\varepsilon} \equiv -\frac{3}{2}\frac{du'^2}{dt} = A\frac{u'^3}{L} \tag{57}$$
>
> where A is a numerical factor of the order of unity and $L = 1/k_o$ is a length which can be regarded as the "characteristic length scale" of the turbulence as a whole ...."

Monin and Yaglom then cite the measurements of Batchelor and Townsend [10] who suggest that L is proportional to the longitudianl integral length scale and *show the coefficient A to be a slowly varying function of x* (downstream of a grid *sic*) and to vary between from 0.8 to 1.4 with increasing Reynolds number ([4], sec 6.1). Then they continue with (*the itemization has been added for ease of subsequent discussion*):

- (i) "However, it is natural to suppose (and all existing measurements confirm this) that as k increases, the characteristic time scale, $T_k = (ku'_k)^{-1}$ will decrease. In other words, as the spatial scale of the disturbances decrease, there is an increase in the frequency of the corresponding fluctuations. It can then be assumed, however, that under certain conditions (in the first instance, for high enough Reynolds numbers), a definite fraction of the disturbances will be characterized by frequencies such that the turbulence decay can then be regarded as very slow."
- (ii) "These disturbances must naturally rapidly readjust to each other and pass into a state of statistical quasi-equilibrium which is independent of the conditions under which the turbulence is generated."
- (iii) "They subsequently adjust also to the slow variation of the turbulent state, remaining throughout in the same quasi-stationary quasi-equilibrium state, which depends only on certain integral parameters of the turbulence, but does not depend directly on time."

(Monin and Yaglom [9], section 16.5)

The 'certain integral parameters' are of course the 'spatially-averaged' dissipation rate, $\overline{\varepsilon}$ and kinematic viscosity, ν. An additional (and independent) hypothesis

[1] Curiously although many books review Kolmogorov's exact words and hypotheses about the small scale motions, very few actually discuss his even more fundamental assumption of 'local equilbrium'. Instead they simply state it and suggest that experiment has verified the inferred results. Monin and Yaglom [9] at least repeat in more detail Batchelor's [4] arguments for decaying turbulence; hence their inclusion here.

can be added that the small scales are isotropic, even if the large scales are not. This is the so-called *local isotropy*[1]. Later Monin and Yaglom review the prevailing theories (at that time) for internal intermittency, beginning with Kolmogorov's presentation [12] at the antecedent of this Marseille meeting in 1961. Intermittency results in a weak dependence of the small scales on L/η_{Kol} where $\eta_{Kol} = [\nu^3/\varepsilon]^{1/4}$ is the Kolmogorov microscale. While local isotropy and intermittency are of general interest, they will not be considered herein.

The conclusions of the present paper can be summarized as follows. Item (i) is indisputably true, but will be shown to be irrelevant, at least as far as the spectral and two-point correlation equations are concerned. It is also argued that (ii) and (iii) most surely are not true in general, both by showing the flaws in the arguments that they are and by counter-examples. Further it is shown that the assumption of equilibrium is in fact true only for flows which are in strict equilibrium (e.g., forced turbulence). Finally it is argued that 'local equilibrium' can be shown to be approximately true in at least some thin shear flows (e.g., boundary layers, jets, wakes, etc.) where energy production and dissipation are nearly in balance; in fact those flows the measurements in which have led to the erroneous conclusion that Kolmogorov's basic local equilibrium hypothesis was correct and general.

Appendix II: The 'anomalous' unsteady flows

These are the flows that directly contradict 'K41', hence alone should provide enough to disprove its generality. But the problem is the same as with all turbulence experiments: seldom do the experiments speak unequivocally, and always someone somewhere can find a way to re-interpret them to support the conventional wisdom. Therefore we restrict our attention here to those experiments for which an alternative theories have been found which explain them at least as well as the conventional interpretation.

The most important of these anomalous flows is grid turbulence, or more generally homogeneous decaying turbulence, and homogeneous shear flow turbulence. In spite of the eloquence of his 1953 book, it is clear that at least along the way decaying turbulence was problematical even for Batchelor, and remained so. The series of somewhat contradictory papers with Townsend beginning in 1947 and culminating in his book in 1953 show the progression of Batchelor's thinking as he tried to reconcile the 'K41' theory with Townsend's measurements (v.p [42–44]). It appears that Batchelor (and perhaps he alone) understood the full consequences of the dispute over a t^{-1} decay with Corrsin and co-workers which lasted well into the 1960's (e.g., Comte-Bellot and Corrsin [24, 45]), and led Corrsin to actually ship his grids to Cambridge for testing (they never were used to the best of my knowledge). In particular, without $u'^2 \propto t^{-1}$, the constancy of R_λ needed to reconcile the von Karman/Howarth theory with Kolmogorov could not be justified. It is clear it led to Batchelor's final rejection of the single length scale hypothesis, and as well the several attempts of he and his students to prove the Loitskianskii integral to not be invariant (e.g., [46, 47] (v. [9] for useful discussion). The ultimate outcome and his final resolution came in the 1949 paper and his 1953 book in which he argued that no single length scale can collapse turbulence, the view widely held by most today.

My first foray into this mine field began when I was teaching an advanced turbulence class in 1986 (using in fact Monin and Yaglom [9] and Batchelor [4]

[1]Actually this was Kolmogorov's first formal hypothesis, the statistical stationarity of the small scales having already been assumed (v. Tsinober [11]).

as a texts) and a student called to my attention the inconsistency in the von Kármán/Howarth-Batchelor assumption that an appropriate similarity scaling for the non-linear terms should not be simply $T(k,t) = u'^3 g(kL)$ as assumed by all three, but should in fact be determined by the equations themselves (v. [29] for a recent review). When this overconstraint of the problem of isotropic decay was relaxed it was clear that much more general single length scale solutions were possible. Most importantly, the temporal derivative of the spectrum was important at all wavenumbers, and remained so during decay. Morevover the spectra scaled with the turbulence intensity and the Taylor microscale did not depend explicitly on the local Reynolds number, so were valid for any initial conditions, including both high and low Reynolds numbers. Also, these solutions had the interesting properties that the ratio of integral scale to Taylor microscale was constant during decay (i.e., $L/\lambda = constant$) and $T(k,t) \propto u'^3/R_\lambda$, not u'^3 as assumed by others. The decay of the turbulence energy was a power law in time t^{-n}, but not necessarily $n = -1$. And the dissipation was most certainly *not* $\overline{\varepsilon} \propto u^3/L$, but instead $\overline{\varepsilon} \propto \nu u^2/L^2$. Moreover, no case could be made for universality of the results, since a dependence on initial conditions could not be ruled out. These deductions, all from first principles, appeared to explain a number of inconsistencies and were also consistent with a large body of existing data on decaying turbulence (including the Batchelor/Townsend experiments).

These new results were presented at meetings in Minneapolis and Tokyo in 1986 ([48, 49]), but it took many years and many reviews and resubmissions before it was finally published archivally as George [25]. The 1986 Tokyo meeting also gave rise to the paper with Mike Gibson (George and Gibson [50])[1] which applied the same methodology to homogeneous shear flows, and argued on purely theoretical grounds that the Taylor microscale was constant and that the energy grew exponentially. A chance meeting with Zelman Warhaft led to an application to the scalar decay experiments of he and Lumley (Warhaft and Lumley [51], George [52]). Finally a post-doc Honglu Wang and I realized in 1999 that there existed exponentially decaying solutions as well, and this was finally accepted for publication more than a decade later (George and Wang [53]) only after such decay was observed experimentally by Vassilicos and co-workers (Hurst and Vassilicos [26]) at Imperial College in London using a certain class of fractal grids. Subsequently Mazellier and Vassilcos [54] showed how these solutions could be combined into a decay law which began exponentially and ended up as a power law. Over the past five years or so the Imperial College group has published numerous papers showing general agreement with the G92 results, and conclusively showing that this kind of turbulence is definitely not 'K41' (e. g., [55, 56]).

References

[1] A. N. Kolmogorov, *The local structure in incompressible viscous fluids for very large Reynolds number* Dok. Akad. Nauk. S. S. S. R. 30 (1941), pp. 299 – 303.
[2] A. N. Kolmogorov, *Decay of isotropic turbulence in incompressible viscous fluids* Dok. Akad. Nauk. S. S. S. R. 31 (1941), pp. 538 – 541.
[3] A. N. Kolmogorov, *Energy dissipation in locally isotropic turbulence* Dok. Akad. Nauk. S. S. S. R. 32 (1941), pp. 19 – 21.
[4] G. K. Batchelor, *Homogeneous Turbulence* (2nd ed.), Cambridge U. Press, Cambridge, UK,1953.
[5] J. O. Hinze, *Turbulence*, McGraw-Hill, NY, NY, 1959.
[6] A. A. Townsend, *The Structure of Turbulent Shear Flow*, Cambridge U. Press, Cambridge, UK, 1956.
[7] H. Tennekes and J. L. Lumley, *A First Course in Turbulence*, MIT Press, Cambridge, MA, 1972.

[1] This is the aforementioned M. M. Gibson whose jet data were used to justify the $k^{-5/3}$ law in the first place.

[8] U. Frisch *Turbulence*, Cambridge U. Press, Cambridge, UK, 1996.
[9] A. Monin and A. Yaglom, *Statistical Fluid Mechanics*, vol. 2, MIT Press, Cambridge, MA 1972.
[10] G. K. Batchelor and A. A. Townsend *Decay of Isotropic Turbulence in the Initial Period* Proc. Roy. Soc. London Ser. A 193 (1948), pp.539 – 558.
[11] A. Tsinober *An Informal Introduction to Turbulence*, (2nd ed.), Springer, Berlin, DE, 2009.
[12] A. N. Kolmogorov *A refinement of previous hypotheses concerning the local structure of turbulence in a viscous fluid at high Reynolds number*, J. Fluid Mech. 13 (1962), pp 82 –85.
[13] L. Onsager *Statistical hydrodynamics* Nuovo cimento (9), 6, Suppl. 2 (1949), pp. 279 –287.
[14] S. Gamard and W. K. George, *Reynolds Number Dependence of Energy Spectra in the Overlap Region of Isotropic Turbulence.*, J. Flow, Turb. and Comb. 63 (1999), pp. 443–477.
[15] W. Heisenberg *On the theory of statistical and isotropic turbulence* Proc. Roy. Soc. A 195, pp. 402 – 406.
[16] L. S. G. Kovasznay *Spectrum of locally isotropic turbulence* J. Aeronautical Sci. 15 (1948), pp. 745 – 753.
[17] S. Corrsin *Further generalization of Onsager's cascade model for turbulent spectra* Phys. Fluids 7 (1964), pp. 1156 – 1159.
[18] Y. H. Pao *Transfer of turbulent energy and scalar quantities at large wavenumbers* Phys. Fluids 11 (1968), pp. 1371 – 1372.
[19] J. T. Lin *Velocity spectrum of locally isotropic turbulence in the inertial and dissipation ranges* Phys. Fluids 15 (1972), pp. 205 – 207.
[20] R. J. Hill *Models of the scalar spectrum for turbulent advection* J. Fluid Mech. 88 (1978), pp. 541 – 562.
[21] A. M. Obukov *Spectral energy distribution in a turbulent flow* Dokl. Akad. Nauk. S. S. S. R. 32 (1941), pp. 21 – 34.
[22] J. C. R. Hunt and J. C. Vassilicos Kolmogorov's contributions to the physical and geometrical understanding of small-scale turbulence and recent developments. Special edition of Proc. R. Soc. A (Eds. J.C.R. Hunt, O.M. Phillips and D. Williams) 434 (1991), pp. 183–210.
[23] R. H. Kraichnan, *On Kolmogorov's inertial-range theories* J. Fluid Mech. 62 (1974), pp. 305 – 330.
[24] G. Compte-Bellot and S. Corrsin *The use of a contraction to improve the isotropy of grid-generated turbulence* J. Fluid Mech. 25 (1966), pp. 657 –682.
[25] W. K. George *The decay of homogeneous isotropic turbulence*, Phys. Fluids (1992), pp. 1492 –1509.
[26] D. Hurst and J. C. Vassilicos, *Scalings and Decay of Fractal-Generated Turbulence*, Phys. Fluids 19 (2007), p. 035103.
[27] R. Seoud and J. C. Vassilicos, *Dissipation and Decay of Fractal-Generated Turbulence*, Phys. Fluids 19 (2007), p 105108.
[28] P. Valente and J. C. Vassilicos *Dependence of Decaying IsotropicTurbulence on Inflow Conditions* Phys. Lett. A 376 (2011), pp. 510 – 514.
[29] W. K. George *Asymptotic Effect of Initial and Upstream Conditions on Turbulence* J. Fluids Engr. 134 (2012), pp. 061203-1 – 061203-27.
[30] S. Laizet, J. C. Vassilicos and C. Cambon *Interscale energy transfer in decaying turbulence and vorticity-strain rate dynamics in grid-generated turbulence* submitted for publication (2012).
[31] C. Van Atta and W. Y. Chen *Measurements of spectral energy transfer in grid turbulence* J. Fluid Mech. 38 (1969), pp. 743 – 763.
[32] K. N. Helland, C. W. Van Atta, and G. R. Stegun Spectral energy transfer in high Reynolds number turbulence J. Fluid Mech. 79 (1978), pp. 337 – 359.
[33] J. L. Lumley *Similarity and the turbulent energy spectrum* Phys. Fluids 10 (1967), pp. 855 –858.
[34] W. K. George and H. Wang, *The Spectral Transfer in Isotropic Turbulence* in *Proc. IUTAM Symp. on Reynolds Number Scaling in Turbulence*, Princeton NJ, Sept 11 – 13, Kluwer, MA.
[35] 480 L. Mydlarski and Z. Warhaft *On the onset of high-Reynolds-number grid-generated wind tunnel turbulence* J. Fluid Mech. 320 (1996), pp. 331 – 368.
[36] Y. Kaneda, T. Ishihara, M. Yokokawa, K. Itakura, and A. Uno *Energy dissipation rate and energy spectrum in high resolution direct numerical simulations of turbulence in a periodic box* Phys. Fluids 15 (2003), pp L21. Itoh JFM
[37] T. Ishihara, T. Gotoh, and Y. Kaneda *Study High-Reynolds Number Isotropic Turbulence by Direct Numerical Simulation* Ann. Rev. Fluid Mech. 41 (2009), pp. 165 – 180.
[38] B. E. Launder, G. J. Reece and W. Rodi *Progress in the development of a Reynolds -stress turbulence closure model* J. Fluid Mech. 10 (1989) 282 -300.
[39] H. J. Hussein, S. P. Capp, and W. K. George *Velocity measurements in a high-Reynolds-number momentum-conserving, axisymmetric, turbulent jet* J. Fluid Mech. 258 (1994), pp. 31 – 75.
[40] H. L. Grant, R. W. Stewart, and A. Molliet *Turbulence spectra from a tidal channel*, J. Fluid Mech. 2, pp. 263 – 272.
[41] M.M. Gibson *Spectra of turbulence at high Reynolds number* Nature 195 (1962), pp. 1281 – 1283.
[42] G. K. Batchelor and A. A. Townsend *Decay of Vorticity in Isotropic Turbulence* Proc. Roy. Soc. London Ser. A 190 (1947), pp.534 – 550.
[43] G. K. Batchelor *Energy Decay and Self-Preserving Correlation Functions in Isotropic Turbulence* Quart. Appl. Math. 6 (1948), pp. 97 – 116.
[44] G. K. Batchelor and A. A. Townsend *The nature of turbulence motion at large wavenumbers* Proc. Roy. Soc. London Ser. A 199 (1949), pp. 238 – 255.
[45] G. Compte-Bellot and S. Corrsin *Simple Eulerian time correlation of full- and narrow-band velocity signals in grid-generated 'isotropic' turbulence* J. Fluid Mech. 48 (1971), pp. 273 – 337.
[46] I. Proudman and W. H. Reid *On the decay of a normally distributed and homogeneous turbulent velocity field* Phil. Trans. Roy. Soc. A 247 (1954), pp. 163 – 189.
[47] G. K. Batchelor and I. Proudman *The large-scale structure of homogeneous turbulence* Phil. Trans. A 248 (1956), pp. 369 – 405.
[48] W. K. George *The Decay of Isotropic Turbulence* Proc. of 2nd Int. Conf. on Transport Phenomena

in Turbulent Flows, Tokyo (Hirata and Kasaji, eds.) (1987), Hemisphere NY.
[49] W. K. George *The self-preservation of turbulent flows and its relation to initial conditions and coherent structures.* In *Advances in Turbulence* (W. George and R. E. A. Arndt, eds.), Hemisphere, NY George and Arndt (eds.) (1989), pp. 39 –73.
[50] W. K. George and M. M. Gibson *The Self-Preservation of Homogeneous Shear Flow Turbulence* Expts. in Fluids 13, (1992) pp. 229 –238.
[51] Z. Warhaft and J. L. Lumley *An experimental study of the decay of temperature fluctuations in grid-generated turbulence* J. Fluid Mech. 88, (1988) pp. 659 – 684.
[52] W. K. George *Self-preservation of temperature fluctuations in isotropic turbulence* in *Studies in Turbulence* (C. Speziale, T. Gatski and S. Sarkar, eds) (1990), Springer-Verlag, Berlin, pp. 414 – 427.
[53] W. K. George and H. Wang *The Exponential Decay of Homogeneous Turbulence* Phys. Fluids 21 (2009), p. 025108.
[54] N. Mazellier and J. C. Vassilicos *Turbulence without Richardson-Kolmogorov cascade* Phys. Fluids 44 (2010), p. 075101.
[55] R. Gomes-Fernandes, B. Ganapathisubramani and J.C. Vassilicos *PIV of fractal-generated turbulence* J. Fluid Mechanics, 711, (2012), pp 306-336, ISSN:0022-1120.
[56] P. C. Valente and J. C. Vassilicos [56] *Universal dissipation scaling for non-equilibrium turbulence*, Phys. Rev. Lett., 108, (2012), 214503.

REPORT

Final session: New Ideas and Perspectives

Romain Nguyen van yen[a] and Lionel Larchevêque[b]

[a] *Fachbereich Mathematik, Freie Universität Berlin, Germany*;
[b] *IUSTI-CNRS, Aix-Marseille Université, France*

Presidents: Eberhard Bodenschatz, Charles Meneveau and Parviz Moin
Scientific secretaries: Lionel Larchevêque and Romain Nguyen van yen

Introduction by the Session Presidents

Parviz Moin insisted that science should be predictive. He took as example the value of Computational Fluid Dynamics for the Boeing company, showing that the number of wing tests has a plateau between 1995 and 2005 although the computer power has increased a lot. There is no relation between the predictive accuracy of the standard engineering tools and computing power. The plateau is due to the limitations of RANS, whose accuracy does not increase with resolution. There is a strong need to develop LES-type methods which benefit from increased resolution to offer better predictive value for CFD.

Eberhardt Bodenschatz started by quoting Feynman (1963) on the analysis of circulating and turbulent fluids. When are we mathematically satisfied? As questions for the future, he emphasized the development of a Lagrangian theory that takes into account geometry, the measurements of transient turbulent flows, and turbulence in granular matter. He insisted that we should worry about 10% discrepancy, that we should pin things down to the percent level. He then showed a picture of convection which is just after onset, but that we don't understand, and used this to argue that we should go back to understanding the transition in order to tackle coherent structures.

Charles Meneveau made the case that we still need better bridges between the predictive engineering needs and n-th order structure functions. As an example, he pointed out the sub-grid scale stress tensor, that can be written in terms of smaller scale velocity gradients, and given the large scale quantities can be used to predict all the statistics correctly. This cannot be done only from structure functions, but the latter are however interesting because they constrain the statistics. Therefore, it would be very beneficial to predict conditional statistics, for example conditional distribution functions of velocity gradients at certain scales given the other scales. Another thing that has emerged from the discussions, especially at the beginning, was the link between coherent structures and statistics. This has a lot to do with how we plot things : when we look at a field our eyes are immediately drawn to patterns.

Summaries of all the Sessions

Session 1: Homogeneous turbulence and flow structure

by Toshi Gotoh

- Coherent structures are essential for understanding transport of heat, mass and generation of drag and aerodynamic noise.
- Interaction of coherent and incoherent components is non local and nonlinear and it is the critical aspect of turbulence.
- Reconnection constitutes a new alternative scenario for turbulence cascade.
- Lagrangian studies are necessary for understanding of turbulence transport and phenomena and statistics at small scales.

Questions :

(1) What are the dynamical equations of coherent structures for prediction of their evolution?
(2) What is the physical scenario of cascade in turbulence? How does the statistics of turbulence change during cascade?
(3) What is a coherent structure? In DNS we observe a forest of vortices in homogeneous isotropic turbulence and in turbulent boundary layers. The point is that the distribution of strong vortices is important, including their number density, size and mean distance. We have to look at the forest as well as at the leaves.

Session 2: Shear and wake flow turbulence

by Gary Brown

The first order requirement is understanding. That has two components: one of them is qualitative, and the other is quantitative. Qualitative helps you be able to do things because you understand what's going on. Quantitative helps you develop models to make predictions. Why is the Biot-Savart relation so important? Is it kinematic? No, it's dynamic because it's part of the evolution equation for vorticity, which happens to simplify greatly the description for several important problems (example : two point vortices orbiting around each other).

Questions :

(1) Why are there coherent structures? Is it simply stability? Is it rooted in the vorticity distribution that you start with?
(2) If we acknowledge that there are coherent structures, we know that there is a direct cascade, but we know much less about the reverse process. Is there universality in a reverse cascade to the large scales which dominate momentum transport in free shear flows?
(3) If the momentum transport in free shear flows is independent of Re, what is the connection with dissipation as Re goes to infinity?

Session 3: Channel and pipe flow turbulence

by Zhensu She

According to Lumley and Yaglom (2001), we have a crude, practical, working understanding of turbulence but nothing approaching a comprehensive theory. A

new multi-layer similarity theory has been proposed for pipe flows and other flows, based on Lie group analysis.

Questions :

(1) What is the influence of coherent structures on transitional and fully developed turbulent pipe and channel flows?
(2) What is the connection between observed coherent structures and global quantities? How accurate are the data? How well do we understand these features?
(3) Are we near a comprehensive theory for channel/pipe turbulence? How universal is the multi-layer description?

Session 4: Boundary layer turbulence

by Beverley McKeon

From the discussions in Session 4, the following important points emerged.

- What are the elementary structures? What are the fundamental building blocks that we need to think about?
- How are structures in transitional and fully developed turbulent flows related?
- What are the differences between the canonical flows? How do we extend this kind of discussion to non-canonical flows? How do the structures change increasing the Re? Do they survive?
- What is the origin of the large scales? Are the large scale motions accumulations of hairpin packets? What are the pitfalls of Taylor's hypothesis when it is used to measure VLSMs in experiments?
- What is the additional complexity of wall turbulence compared to free-shear flows?
- There is evidence that linear processes are important for wall turbulence, as well as nonlinear stability also. If you remove the linear coupling term wall turbulence will decay. How can we extend linear theory to ideas like control?
- What progress can we expect with dynamical system approaches? How can these be used to describe structures?
- What is the status of our understanding of the near wall cycle? What is driving it? How does scale modulation/amplitude modulation come about? How does the vorticity field structure change throughout the wall layer?
- How should we classify the VLSM motions? Are they inactive close to the wall? The small scales seem to react to sloshing motions.
- How far up in Reynolds number do we need to go when we think about control schemes?
- Are we in a position to write down equations for coherent structures? The previous POD efforts were destined to identify only the large scales, but we should try to include some of the smaller scales.

Questions :

(1) What is the relative importance of linear processes / instabilities in the nonlinear problem of turbulence?
(2) How does collective organization of structures work in wall flows? What are the elemental building blocks?
(3) What do we know / don't know about the large scale outer structures?

Session 5: Turbulent stirring and mixing

by Norbert Peters

The necessity of theoretical insight depends on the level of detail. How deeply do we need to go into anomalous scaling/structure functions in order to predict physics of relevance?

Questions :

(1) Is it time to develop new models beyond the existing Kraichnan type? Should we include models for active scales, true nonlinearity?
(2) Can engineers benefit from fundamental research on mixing?
(3) Can the understanding of critical phenomena help understand anomalous scaling in turbulent mixing? Would renormalization help too?

Session 6: Mathematics for turbulence

by Edriss Titi

The mathematical community works on fluid mechanics in general, and not on turbulence in particular. For example, the recent most fashionable subject is non Newtonian fluids. Concerning turbulence proper, we don't know yet what we can prove.

The solutions of the Navier-Stokes equations in the vanishing viscosity limit converge to something, what does this limit satisfy? We have enough evidence that this is not the Euler equations. We believe that this is the mathematical analogous of the closure problem in turbulence theory. We have shown that the effect of boundary conditions is essential to mathematically treat this problem. As a simple example, consider the equation:

$$\frac{\mathrm{d}}{\mathrm{d}t}u - \nu u_{xx} - (u_x)^4 = 0$$

This equation does not develop singularity in finite time with periodic boundary conditions, but it does with Dirichlet boundary conditions!

The mathematical study of the Navier-Stokes equations relies on the concept of weak solutions. Are they unique or not? This is an open problem for the Navier-Stokes equations, while for the Euler equations we already know that they are not unique. Leray in his seminal work invented the notion of turbulent solutions, because he thought the weak solutions that he had discovered could be non unique. But the physical relevance of this possibility is very dubious. For example, we have the following theorem : as long as the pressure is bounded from below, there is no singularity in the Navier-Stokes equations, and the solution has to remain unique.

Questions :

(1) Should we look for invariant measures and averages, in order to introduce mathematically useful statistical tools for turbulence?
(2) Should we study the stochastically forced Navier-Stokes equations?
(3) Should we work on the deterministic case (issues like finite time singularities, weak limits of solutions)?

Session 7: Geophysical turbulence

by Joel Sommeria

There is a need for focusing the research in geophysical fluid dynamics on well defined benchmark configurations on which everyone could agree. In this meeting,

- the review presentation by Narashima reconciled laboratory convection with moist convection in clouds. He showed that internal heat in clouds due to phase change changes the structure of turbulence and the entrainment rate. He also stressed the importance of unsteadiness.
- Bodenschatz showed how to use laboratory techniques to directly analyse turbulence in clouds and the effect of microphysics.
- Sreenivasan analyzed recent data on solar convection.
- Spiegel proposed an analogy between hot stars and fluidized beds.
- Doering provided rigorous upper bounds on convective fluxes.
- Tatsumi and Cambon advocated the use of two-points closures for turbulence statistics.
- Kevlahan proposed to explain the $k^{-5/3}$ spectrum observed over 11 decades in the interstellar medium in terms of statistics of shocks.

Questions :

(1) Is there a connection between coherent structures observed in the geophysical context, like the Madden-Jullian oscillation, and large scale motions in pipes?
(2) Can we estimate the energy decay in the limit of small Rossby and Froude numbers? How do we solve the problem of missing mixing in the ocean?
(3) Is there a Kolmogorov-type cascade in stratified turbulence?

Session 8: Magneto-hydrodynamic turbulence

by Bérengère Dubrulle

The following themes emerged from the discussions in this meeting.

- Equilibria and their universality: do the spectra depend on initial conditions? What is the role of invariants in defining the equilibria?
- Are mean dynamos or small scale dynamos more important? The importance of modeling correctly the mean Lorentz force, and of taking into account the various invariants, was stressed.
- How do the properties of MHD turbulence depend on the magnetic Prandtl number? Properties of spectra, PDFs, intermittency?
- MHD turbulence is much more non local than hydro turbulence.
- Closure theories: DIA and RDT were discussed.
- Structures in MHD: can they be explained by selective decay/maximum entropy formalisms? Is there a dissipative anomaly in MHD turbulence?

Questions :

(1) Can we deduce from first principles the mean properties of canonical turbulence?
(2) Can we construct a theory to show the possibility of self-consistent MHD dynamo, either laminar or turbulent?
(3) In the limit of zero magnetic diffusivity, does the magnetic dissipation tend to a finite limit?

General discussion

Co-chaired by Parviz Moin, Charles Meneveau, *and* Eberhardt Bodenschatz

Domaradzki: I see coherent structures in many places. I would like to focus on obtaining a quantitative description from this picture of coherent structures. Not just looking at their evolution in movies but getting actual equations with predictive capability for some quantities that are of interest to us (mean flow, root mean square) from this picture. Is it possible at all?

Oberlack: If you go to the history of turbulence modeling, turbulence modelers implemented more and more of the symmetries of the Navier-Stokes equations. Nowadays, the key models do have these symmetries. What we recognized two years ago is that all of the models need additional symmetries, that we call statistical symmetries. Otherwise you will not get, for example, the log-law. Several of these statistical symmetries are already in the present models.

She: Concerning quantification of coherent structures and statistical symmetries, the coherent structures near the wall are related to the scaling of the mixing length in the buffer layer (like $(y^+)^2$). The statistical symmetries may be related to the existence of coherent structures. Can we derive this?

Moin: Do you mean that to link coherent structures with mean flows we need to use symmetries? But what I think is missing is the dynamics of the coherent structures! Perry and Chong, and others, have put the kinematics together to synthesize a coherent flow, but the dynamics is missing.

Wallace: I want to stress the paper of Perry and Chong, who attempted (for the only time to my knowledge) to really explain the statistics in great detail. We know a great deal more about wall flows now that they did then, and we have numerics. Moreover, I find it quite amazing that the statistics of wall flows are so similar to great detail, even the fine scale statistics like dissipation rate, to what they are in a turbulent spot. In the seventies, there were experiments to look at the properties of turbulent spots, and we should come back to that. These spots are like baby turbulence, and they have smooth skins contrary to old turbulence which has bags under its eyes. The continuing debate about whether hairpins exist in fully developed flow is fruitless, because anyway the statistics are the same as for spots where we do see hairpins.

Sreenivasan: It is very clear that something statistical had to be said in order to get the right quantities of interest in turbulence. It has been very clear from the beginning. Of course it is not the standard equilibrium statistical mechanics, nor even the standard chaotic dynamics. We are all trying to look for something like that. There is one interesting dichotomy here: as soon as you speak about statistical descriptions, there are always people studying very closely coherent structures who will look at you with suspicion. But one lesson from the Kraichnan model is that there are certain statistical conservation laws. It simply says that there are certain shape fluctuations, and there are aspects related to them that are preserved as the geometry evolves. It is related to the preservation of certain geometrical properties. If we are clever enough to devise such a law, it will have such connection with coherent structures. One should not think that the statistical view and coherent structures are different from each other, it is just that we do not yet have the tools to relate them.

Moffatt: On the question of dynamical equations for coherent structures, I think that a good starting point are the steady solutions of the Euler equations. Such solutions are going to sit there for a long time. I put forward such a model in a meeting at Cornell. Each blob is locally a solution to the Euler equation, which

is intrinsically unstable.

HUSSEIN: I have always made a distinction between structure and coherent structure: structures are simply there, while coherent structures should, in addition, have a measurable signature on the mean flow. Therefore I think that the latter are inseparable from a statistical approach. We have always tried to look for coherent structures as an object and find an evolution equation as for an individual body. The challenge is to imaginatively decide what is the initial flow. The solution given by the computer of the Navier-Stokes equations is the evolution equation for the structures!

FARGE: As you know we have to be extremely careful about terminology. We have to distinguish what has to do with transition to turbulence (before the mixing transition), and what has to do with fully developed turbulence, after which all the flow is wild but you still see some structures out of highly fluctuating fields. You have zero mean in homogeneous isotropic turbulence but structures are still observed. If I remember well from some talk I heard this week, someone used the word 'turbulent structure'. I propose to use this word when we talk about the fully developed regime (i.e., when, in addition to molecular viscosity, the flow itself generates nonlinear dissipative mechanisms related to those turbulent structures).

BROWN: If you look at the stream-wise vorticity ω_x, you can show that it is uncoupled from the mean velocity profile if the latter is independent of x. This explains why Couette flows can have counter rotating structures that completely fill the gap. Over long times the vorticity accumulates in that flow, although it is not injected at the boundary by the mean flow. Behind these things, there is real physics to be understood in why the large structures emerge the way they do.

KIM: What you all are going to say is so predictable. I know what senior people are going to say, so I would like to ask young scientists, who are going to carry on this research, to speak up.

TITI: I would like to pick up this issue of coherent structures from a different point of view. There is a lot of work at the moment on fast-slow systems. If you have separation of scales, we can proceed by averaging. But in some systems all the components are at the same time fast and slow, for example in molecular dynamics. In that case you have to find equations of motion for measures. I believe that when we talk about coherent structures we see them in Lagrangian coordinates but the equations we are looking for are Eulerian. So I suggest that we should maybe introduce new quantities to describe the coherent structures, we should move from the description that we have for the flows, do some kind of averaging in order to reveal some slow features of the dynamics.

JIMENEZ: I wanted to follow up on the comment by WALLACE, that transitional structures are maybe turbulence. If we have only babies we lose the species because they cannot reproduce. At some point there is something that happens, adolescence, which separates transitional structures from fully developed turbulence, and that difference may be crucial.

BODENSCHATZ: I grew up in pattern formation. The people told me: look at these beautiful cloud streets. Then I came to a meeting in Santa Barbara and we wanted to look at the influence of turbulence on coherent structures. We cannot calculate the wave-number of cloud streets because they are very turbulent but we acknowledge their existence anyway. There is a complicated coupling between the chaotic spatio-temporal pattern of structures and small scales.

MCKEON: There is some value in trying to reconcile the results we get from various approaches because we are all looking at the same flow. One problem that we run into with that is still : what is a coherent structure? How to observe a structure? We know that the criteria that we have are not perfect.

KEVLAHAN: I would like to suggest a way of unifying several of these themes. Compared with a flow having Gaussian statistics, we see that turbulent flows tend to deplete nonlinearity significantly. Moreover if you remove coherent structures from the flow they tend to reemerge quite quickly. So maybe coherent structures deplete nonlinearity locally, but there is something left over. That is what we did with Marie and Kai, when we introduced the split between coherent and incoherent flow components using the wavelet representation. I think that tracking individual particles/structures is going to be very hard, but maybe such a decomposition in a more global sense is possible.

GOTOH: By performing DNS we found structures in turbulent flow (vortex tubes). As the Reynolds number is increased, we are looking at more and more vortices and structures at fine scale. I see some analogy to statistical mechanics: suppose that you have some vortex tubes that interact or reconnect. This could be like interactions among molecules. It is very important to understand these interactions. But when the Reynolds number is high we have a huge amount of structures. Therefore we also need to think of the probability distribution of structures, not only of the individual structures. It is an ensemble of structures we are looking at.

RAY: I would like to respond to the comment of SREENIVASAN about a statistical mechanics of turbulence. In critical theory, people were not afraid to go into dimensions which were no integers. There are special dimensions where the equilibrium solutions are not far away from K41 (for example dimension 4/3). Probably there might be some hope in terms of perturbation theory around these special dimensions. Another comment : the use of higher precision arithmetics may be more useful than going to higher Reynolds number.

GEORGE: I am glad about the question: why are there coherent structures? For most of my career, people have been trying to say that coherent structures are important but they were not able to say what role they play, and we have made a good job computing turbulence without particularly taking them into account. So I think we have maybe wasted too much time talking about them. I found three important things said at this conference:

(1) we should first put the Reynolds number in, and *then* take the limit,
(2) the comment by Keith Moffatt, that we should "tear down those old theories",
(3) Eberhard Bodenschatz this morning saying than a precision of 10% is not good enough.

The reason we accept an error of 10% is that it allows us to reconcile any new result with old theories! So this allows us to keep all the old theories. But we should really go for less than 1% error.

SCHNEIDER: I would like to ask whether it is worthwhile using adaptive methods for turbulence or not? The computational power is going up, maybe it is not worth the trouble. Another comment, in answer to Keith Moffatt: it is very difficult to construct localized eigenfunctions of the curl operator which would be stationary Euler solutions. A third comment: what is the computational resolution which is really required when computing turbulent flows at a given Reynolds number? Those are typically based on the statistical theory only.

BOS: I was interested by a slide of Javier Jimenez actually showing a flow field with streaks, and the streaks were still visible after the phases were scrambled. I think that this shows how much we should really try to separate between the dynamical and kinematic parts of coherent structures.

TATSUMI: Turbulence has randomness and determinism. So far, the randomness of turbulence is represented by statistical averages such as mean velocity and large

structures. But the most proper way of dealing with such random phenomena is non equilibrium statistical mechanics. The probability distribution function of turbulent velocity around such and such mean value should be our main object. We have to use more such notions instead of simply averages. A second point: no one has talked about the future of turbulence research. I am most interested in quantum fluid turbulence, which could lead to deeper understanding of classical turbulence.

Yokoi: For me, as a physicist, structure formation is always related to symmetry breaking. Therefore I agree with Parviz Moin's comments stating that the dynamics of small scale structures is very important to pursue. But it is also important to catch some physical quantities which can represent such structures. In the dynamo problem, cross helicity is very important, and it can be spatially distributed and different across scale even when its global average is zero. Such symmetry breaking often comes from large scale motions.

Titi: Probability distribution functions are very important and are also studied in mathematics. There are even theorems which prove their existence for the Navier-Stokes equations, but the problem is that there are infinitely many of them, and we don't know which one is physical. A little known theorem of Foias states that the mean flows related to all invariant measures which maximize the energy dissipation rate are all the same.

Moin: We haven't discussed as much as we should have the possibility to take advantage of the major development that has taken place in computer hardware. This is one thing that has advanced faster than any instrumentation in physics. The community of weather forecasters, engineers, etc. are all taking advantage of it, and if we don't do the same we are going to be left behind. Using the computers, we can handle the large scale features and then handle the small scales by statistical theories. Given the growth rate that we have, in 7 years we will be able to use 20000 cores as easily as we use 20 cores today.

Taylor: As I said at the beginning I came here to find out what the present situation was in turbulence research. And at the end I see that you are talking in the same terms about the same quantities. There has been evolution but no revolution. At the beginning of the subject someone invented this absurd idealization of homogeneous isotropic turbulence, why has it not been solved yet? Another point: many years ago, in the early days of laboratory plasmas, there were very few diagnostics, but we did have magnetic probes. At a certain point there were loads of records from these probes showing fluctuations. At this point I came across the Hausdorff dimension of these traces, but it got us nowhere. The reason it all failed is that people would say: when you measure this Hausdorff dimension, what on earth does it tell us about the plasma? My suggestion at the time was that there must be some connection between the Hausdorff dimension of the signals and the number of unstable modes of the plasma. The point I want to make is that this work did not have any impact because it did not tell anything about the physics.

1. Closing remarks

Spiegel: Let Keith Moffatt do the Closing Remarks, I want to be part of the discussion. I've been always struck by the fact that over and over I keep seeing the splitting of the equations between mean and fluctuations. I call that the Ptolemy approach. Even as I understand large eddy simulations, that is also a similar decomposition. My way of looking at that was affected strongly by a movie that Leslie Kovaznay showed of a fully developed turbulent flow and what I saw were patches of turbulence with patches of ambient fluid that were flowing right through

them. So I see this as a two fluid model, by analogy with the Landau equations for superfluids. The turbulent fluid is really a fluid made up of excitations, vortex tangles, while the rest is laminar flow which is essentially inviscid. Qualitatively the same effects are there. For me the whole story comes to that kind of models, and I don't see enough of that. I'm still struggling to get the relative densities of the two fluids.

Narashima: Exactly that proposal was made in the 61 meeting by Liepmann, and he called it 'turbular' fluid. He advocated a two fluid theory. However nothing much has happened over that idea in the last 50 years.

Spiegel: Yes, you are right, when I published this I quoted Liepmann. I should have mentioned his contribution here as well. There is also a paper of Crow on that.

She: I wrote this in 1991 in the volume for the 50th anniversary of K41.

Moffatt: I really will make some closing remarks. We've heard a lot about coherent structures, and at least we are a very coherent community, and we make friendship at these meetings that really do endure. I'm sure many of you have similar experiences. We've had this great common endeavor which helps these friendships to endure. In this context I would like to quote to you something that Batchelor said in 1997, in an article called 'Research as a lifestyle': *"Through having common objectives and principles by which new knowledge is assessed and disseminated, scientists concerned with a particular field like fluid mechanics form an international community of great unity and moral strength. I believe that the understanding, trust and goodwill between members of this scientific community transcends geographical and political boundaries and constitutes one of the most important forces for international harmony and friendship in the world today."* From G.K. Batchelor 'Research as a life style', *Appl. Mech. Rev.* **50**, R11-R20 (1997)

Batchelor lived in that conviction, and many of you know that he was a man of wonderful moral force and integrity. Before running off I would like to thank once more Marie and Kai for the organization and the care for detail and for the great stimulus that they've provided to the advance of this subject.

THE END

The `Turbulence Colloquium Marseille TCM2011' was held in the elegant 18th century bastide of the Centre International de Rencontres Mathématiques' (CIRM) on the campus of Aix Marseille University (AMU) in Luminy, just above the famous `Calanques' of Marseille, recognized as UNESCO world heritage.






CIRM belongs to the Société Mathématique de France' (SMF). It can accommodate 80 persons in a charming environment with excellent traditional French cooking. Its auditorium can receive about 100 persons and its library offers an exceptional mathematical collection of about 1000 journals and 30 000 textbooks.









On the evening of the first day there was a `get together aperitif' around a sangria offered in the park under the shade of gorgeous oaks, plane trees and cedars, several hundred years old. A small ceremony was organized to nominate the `Turbulence Control Team' (TCT) made of three tough and courageous mathematicians, namely Claude Bardos, Charles Doering and Edriss Titi. Each one received a black TCT tee-shirt and a water pistol, with the mandate to interrupt any talk or discussion as soon as they detect a mathematical error. Indeed, turbulence being a challenging topic, everyone is welcome to try new hypotheses and theories, as long as they remain compatible with existing mathematical theorems.

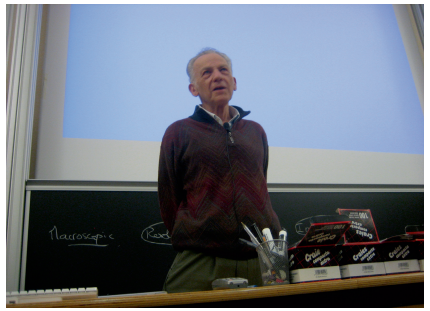


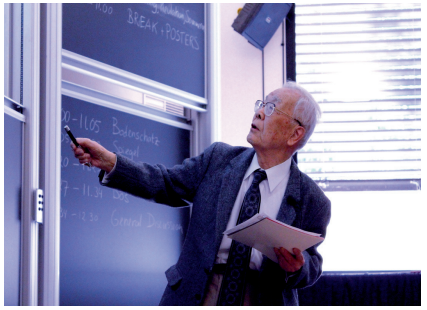
On the evening of Tuesday September 27th we organized a session that commemorated the historical 'Turbulence Marseille Colloquium TCM 1961'. For this we invited the son of Alexandre Favre, who organized TMC 1961. He gave us a moving talk about his father and his dedication to IMST (Institut de Mécanique Statistique de la Turbulence) that he inaugurated on this occasion. Michel Coantic also gave us a vivid recollection of TCM 1961 that he attended as a student, mentioning many amazing stories about Andrei Kolmogorov and the soviet delegation that participated too. On the same session Michael Eckert gave a very interesting talk about the state of turbulence research up to year 1961 and Jean-Paul Dussauge about turbulence research in Marseille.



The conference was held in the auditorium, where wi-fi was disconnected during the lectures, but wine bottles were allowed. Each of the seven sessions were organized on the same pattern, with a one-hour review lecture, followed by a poster presentation and a coffee break, concluded by a one-hour open discussion. On the last day the presidents presented a summary of their session, out of which they drew conclusions and perspectives for further research. This was followed by an open discussion where a list of the most important questions to be addressed emerged.

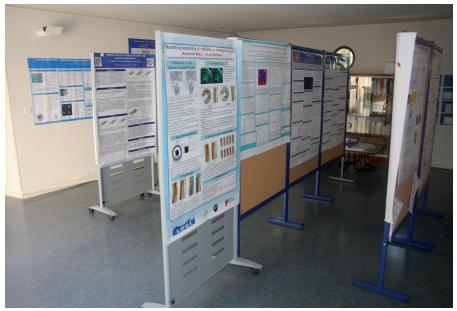


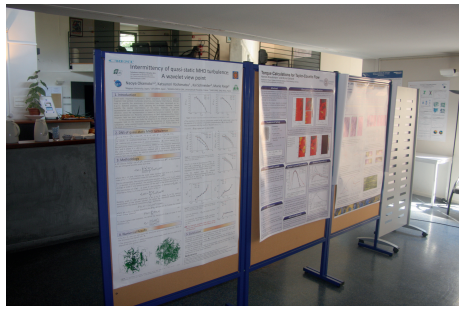


The posters were displayed during the whole conference in a modern building nearby the auditorium. All posters related to a given session were first orally presented, five minutes each. Then, one hour was given to participants to study and discuss posters at their own pace, while coffee, tea and cakes were being served. The organizers were surprised by the very large number of posters that were exhibited and by the lively and fruitful discussions that were thus induced.





On Wednesday September 28th we spent the afternoon on a boat and visited by the sea the stupendous national park of Marseille's `Calanques'. The sun was very bright and CIRM caps were welcomed. We could enjoy the beautiful scenery of Marseille's harbour and `corniche', together with the bright white limestone and the wild marine life of `Calanques'. We also passed by the underwater Cosquer cave, famous for its Paleolithic paintings.








In the evening of Thursday September 29th for the conference banquet the cook of CIRM, Olivier Sylvain, prepared a delicious ‘bouillabaisse’. This is Marseille’s specialty, made out of different local rock fish, shellfish and other seafood. The broth is served with 'rouille', a mayonnaise made of olive oil, saffron and a lot of garlic. It was accompanied by excellent provençal white wine from Bandol, a nearby fisherman harbour famous for its wineries.







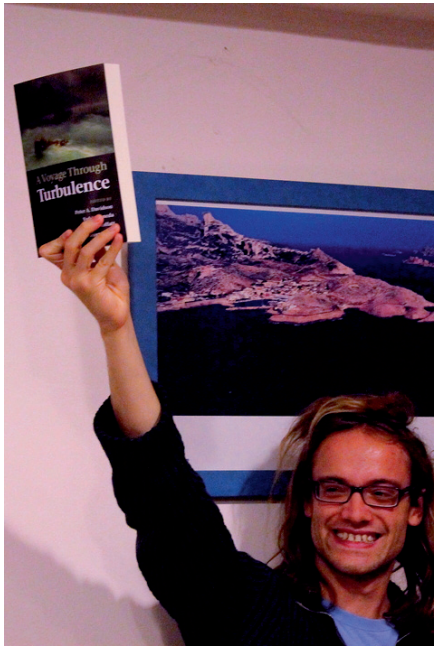




On Wednesday September 28th morning session, participants took a difficult exam that was graded by the TCT mathematicians. The prize ceremony, chaired by Bryan Taylor and Tomomasa Tatsumi, was on the evening of Thursday September 29th. The winners were given a newly published book on the history of turbulence, a Champagne bottle or some kind of tops very popular among Marseilles' kids. A topple over bowl, specially designed for TCM 2011 by a local potter, was also offered to all participants.













Examen final

Name:_____ First Name:_____ Mark:_____

Junior: ☐ Senior: ☐

Exam: Mathematics for Turbulence

Professors C. Bardos, C. Doering and E. Titi

(18 minutes, max 3 lines per answer)

1. What is your understanding of the claim: Turbulent Flows have finite degrees of freedom? What are these degrees of freedom?

2. What is your understanding of an average?

3. Do you think that any notion of solution of Euler or Navier-Stokes should conserve the energy, or satisfy an energy balance? What if a solution does not conserve energy?

4. What is your understanding of dissipation anomaly? Can you formulate the problem as precisely as possible?

5. Do you think that Navier-Stokes or Euler solutions develop a finite time singularity? Is this consistent with the physical observations? If a singularity is proven to be formed, what is the mechanism? How should we modify the models?

6. Do you think the project of searching for singularity computationally makes sense? In which geometry? Do you think that a smooth physical boundary could be the real source of singularity formation? Or should we stick to periodic boundary conditions?

7. Is atmospheric turbulence 3d or 2d? How should we test this matter? What are the right mathematical quantifiers in this case?

8. Is the range of applications of the incompressible Navier-Stokes equations restricted to incompressible fluids?

9. Does triad wavenumber interaction have much to do with fluid motion? What is the equivalent picture in the physical domain?

The exam was graded with a maximum of 90 points by the TCT mathematicians (see page 490), composed of Claude Bardos, Charlie Doering and Edriss Titi. The honorary presidents, Tomomasa Tatsumi and Bryan Taylor, awarded the prices in the senior and junior category, respectively, during the banquet on Thursday September 29th, 2011 (see page 496).

The winners in the senior category were:

1. Bérèngere Dubrulle 85/90
2. Katepalli Sreenivasan 84/90
3. Javier Jimenez 83/90

and in the junior category:

1. Romain Nguyen van yen 84/90
2. Philip Schäfer 80/90
3. Samriddhi Ray / Dmitry Kolomenskiy 70/90

Examen final

List of participants

ANSELMET Fabien
IRPHE - UMR 6594, Ecole Centrale Marseille
49 Rue Joliot Curie - BP 146
13384 Marseille Cedex 13, FRANCE
ansel@irphe.univ-mrs.fr

ANTONIA Robert
University of Newcastle
University drive callaghan nsw
2308 Newcastle, AUSTRALIA
Robert.Antonia@newcastle.edu.au

BAJER Konrad
Univ. of Warszawskiego, Institute of Geophysics
00-681 Warsaw, POLAND
Konrad.Bajer@fuw.edu.pl

BARDOS Claude
Laboratoire Jacques Louis Lions, 31 Avenue Trudaine
75009 Paris, FRANCE
claude.bardos@gmail.com

BODENSCHATZ Eberhard
Max Planck Institute DS, LFPN
Am Fassberg 17
37077 Goettingen, GERMANY
eberhard.bodenschatz@ds.mpg.de

BONTOUX Patrick
M2P2- CNRS, Univ. Paul Cezanne
38 rue Joliot Curie
13451 Marseille cedex, FRANCE
bontoux@l3m.univ-mrs.fr

BOS Wouter
LMFA, Ecole Centrale de Lyon
36, avenue Guy de Collongue ECULLY Cedex, France
69134 Ecully, FRANCE
wouter.bos@ec-lyon.fr

BROWN Garry
Univ. of Princeton, Mechanical and Aerospace Eng.
08540 Princeton, U.S.A.
glb1873@msn.com

CAMBON Claude
LMFA, Ecole Centrale de Lyon
36 avenue Guy de Collongue
69 134 Ecully Cedex, FRANCE
claude.cambon@ec-lyon.fr

CHEN Xi
Univ. of Peking, SKLTCS
100871 Beijing, CHINA
leacher@163.com

CLERCX Herman
Physics Department, CC 2.15 Eindhoven University of Technology PO Box 513
5600 MB Eindhoven, NETHERLANDS (THE)
h.j.h.clercx@tue.nl

COANTIC Michel
Univ. Paul Cezanne IRPHE
49, rue F. Joliot Curie - B.P. 146
13384 Marseille Cedex 13, FRANCE
michel.coantic@wanadoo.fr

DANAILA Luminita
Univ. de Rouen CORIA
Avenue de l'Université
76770 Saint Etienne du Rouvray, FRANCE
danaila@coria.fr

DAVIAUD Francois
CEA Saclay SPEC
91191 Gif sur Yvette cedex, FRANCE
francois.daviaud@cea.fr

DOERING Charles R
University of Michigan, Mathematics, Physics, and Complex Systems
48109-1043 Ann Arbor, MI, U.S.A.
doering@umich.edu

DOMARADZKI Julian
Univ. Southern California,
Aerospace and Mechanical Eng.
854 Downey Way, RRB 203
90089-1191 Los Angeles, U.S.A.
jad@usc.edu

DUBRULLE Bérengère
CEA Saclay, SPEC
91191 Gif sur Yvette, FRANCE
berengere.dubrulle@cea.fr

DUSSAUGE Jean-Paul
Univ. de Provence, IUSTI
5, Rue E. Fermi
13453 Marseille Cedex 13, FRANCE
jean-paul.dussauge@polytech.univ-mrs.fr

ECKERT Michael
Deutsches Museum, Forschungsinstitut
Museumsinsel 1
80538 Munich, GERMANY
m.eckert@deutsches-museum.de

ECKHARDT Bruno
Philipps-Univ. of Marburg, Fachbereich Physik
Renthof 6
35043 Marburg, GERMANY
bruno.eckhardt@physik.uni-marburg.de

ESCANDE Dominique
CNRS-Université de Provence, Equipe Turbulence Plasma/UMR6633
Case 321 Av. Normandie Niemen
13397 Marseille Cedex 20, FRANCE
dominique.escande@univ-provence.fr

FARGE Marie
CNRS, Ecole Normale Supérieure, 24 rue Lhomond,
75231 Paris Cedex 5, FRANCE
farge@lmd.ens.fr

GEORGE Willam K
Imperial College of London, Department of Aeronautics
Exhibition Road, S. Kensington Campus
SW7 2AZ London, UNITED KINGDOM (THE)
georgewilliamk@gmail.com

GODEFERD Fabien
Ecole Centrale de Lyon, LMFA - CNRS
69134 Ecully, FRANCE
fabien.godeferd@ec-lyon.fr

GOTOH Toshiyuki
Nagoya Institute of Technology, Nagare College Gokiso, Showa-ku
466-8555 Nagoya, JAPAN
gotoh.toshiyuki@nitech.ac.jp

HORIUTI Kiyosi
Tokyo Institute of Technology, Dept. Mechano-Aerosp. Eng.
2-12-1 O-okayama, I1-64, Meguro-ku
152-8552 Tokyo, JAPAN
khoriuti@mes.titech.ac.jp

HUSSAIN Fazle
Univ. of Houston, Dept. of Mechanical Engineering
4800 Calhoun Rd
77004 Houston, U.S.A.
fhussain@uh.edu

JIMENEZ Javier
Univ. Politecnica Madrid, Aeronautics
Pl. Cardenal Cisneros 3
28040 Madrid, SPAIN
jimenez@torroja.dmt.upm.es

KAWAHARA Genta
Univ. of Osaka, Graduate School of Engineering Science
560-8531 Osaka, JAPAN
kawahara@me.es.osaka-u.ac.jp

KEVLAHAN Nicholas
Univ. of McMaster, Mathematics and Statistics
L8S 4K1 Hamilton, CANADA
kevlahan@mcmaster.ca

KIDA Shigeo
Univ. of Doshisha, Department of Mechanical Engneering
610-0394 Kyotanabe, JAPAN
shigeokida1947@gmail.com

KIM John
Univ. of California, Mechanical and Aerospace Engineering Department
91302 Los Angeles, U.S.A.
jkim@seas.ucla.edu

KOLOMENSKIY Dmitry
CERFACS
42 Avenue Gaspard Coriolis
31057 Toulouse Cedex 01, FRANCE
dkolom@gmail.com

LARCHEVEQUE Lionel
IUSTI
5, Rue E. Fermi
13453 Marseille Cedex 13, FRANCE
lionel.larcheveque@polytech.univ-mrs.fr

LESCHZINER Michael
South Kensington Campus
Imperial College London
Aeronautics Dept.
SW72AZ London, UNITED KINGDOM (THE)
mike.leschziner@imperial.ac.uk

LUZZATTO-FEGIZ Paolo
Woods Hole Oceanographic Institution
Physical Oceanography
MS #21
02543 Woods Hole, U.S.A.
pluzzattofegiz@whoi.edu

MATTHAEUS William
Univ. of Delaware, Department of Physics and Astronomy
217 Shap Lab
19716 Newark DE, U.S.A.
yswhm@bartol.udel.edu

MCKEON Beverley
California Inst. of Technology, GALCIT
1200 E. California Blvd, MC 301-46
91125 Pasadena, U.S.A.
mckeon@caltech.edu

MENEVEAU Charles
Univ. of Johns Hopkins, ME & CEAFM
3400 N. Charles Street
21218 Baltimore, U.S.A.
meneveau@jhu.edu

MOFFATT Keith
Trinity College, Trinity Street
CB 21 TQ Cambridge, UNITED KINGDOM (THE)
h.k.moffatt@damtp.cam.ac.uk

MOIN Parviz
Univ. of Stanford, Flow Physics and Computational Engineering
488 Escondid Mall, Bldg 500, Rm 500C
94035 Stanford, U.S.A.
moin@stanford.edu

MONTGOMERY David
Physics & Astronomy, Dartmouth,
203 Wilder Physical Laboratory Dartmouth College
Hanover, NH 03755-3528
03755 Hanover, U.S.A.
David.C.Montgomery@dartmouth.edu

NARASIMHA Roddam
JNCASR, Jakkur
560 064 Bangalore, INDIA
roddam@caos.iisc.ernet.in

NGUYEN VAN YEN Romain,
Freie Univ. Berlin, Mathematik und Informatik
Arnimallee 6
14195 Berlin, GERMANY
rnguyen@zedat.fu-berlin.de

OBERLACK Martin
Univ. of Darmstadt,
Chair of Fluid Dynamics Petersenstr. 30
64287 Darmstadt, GERMANY
oberlack@fdy.tu-darmstadt.de

OKAMOTO Naoya
Univ. of Nagoya, Department of Computational Science & Engineering
Furo-cho, Chikusa-ku
464-8603 Nagoya, JAPAN
okamoto@fluid.cse.nagoya-u.ac.jp

PANDIT Rahul
Physics IISc Bangalore, Dept. of Physics Indian Institute of Science
560012 Bangalore, INDIA
rahul@physics.iisc.ernet.in

PETERS Norbert
RWTH Aachen, Institut für Technische Verbrennung
Templergraben 64
52056 Aachen, GERMANY
n.peters@itv.rwth-aachen.de

RAY Samriddhi Sankar
OCA/Nice et IISc/Bangalore, BP 4229,
06304 Nice Cedex 4, FRANCE
samriddhisankarray@gmail.com

REY Claude
M2P2 – UMR 6181 – Tech. Château-Gombert
13451 Marseille, France
crey@l3m.univ-mrs.fr

RICOUX Philippe
TOTAL SA, La Défense 6, 2 place de La Coupole
92078 Paris La Défense cedex, FRANCE
philippe.ricoux@total.com

SCHAEFER Philip
RWTH Aachen, Institut für Technische Verbrennung
Templergraben 64
52056 Aachen, GERMANY
pschaefer@itv.rwth-aachen.de

SCHIESTEL Roland
IRPHE-CNRS (retired) - Chateau-Gombert
13013 MARSEILLE, FRANCE
r.schiest@laposte.net

SCHNEIDER Kai
M2P2 & CMI Univ. Provence, 39 rue Joliot-Curie
13453 Marseille cedex 13, FRANCE
kschneid@cmi.univ-mrs.fr

SHE Zhen-Su
Univ. of Peking, SKLTCS
College of Eng.
100871 Beijing, , CHINA
she@pku.edu.cn

SOMMERIA Joel
Univ. de Grenoble, LEGI
1023 rue de la piscine
38000 Grenoble, FRANCE
joel.sommeria@legi.grenoble-inp.fr

SPIEGEL Ed
Univ. of Columbia, Department of Astronomy
550 West 120th Street
NY 10027 New York, U.S.A.
eas@astro.columbia.edu

SREENIVASAN Katepalli
Univ. of New York, Department of Physics
10012 New York, U.S.A.
katepalli.sreenivasan@nyu.edu

TARDU Sedat
Univ. de Grenoble, LEGI
B.P. 53 X
38041 Grenoble, FRANCE
Sedat.Tardu@hmg.inpg.fr

TATSUMI Tomomasa
Univ. of Kyoto, Department of Fluid Mechanics
007 Kyoto, JAPAN
tatsumi@skyblue.ocn.ne.jp

TAYLOR J Bryan
CCFE (Retired)
OX14 3DB Abingdon, UNITED KINGDOM (THE)
jbt@radwin.freeserve.co.uk

TERPOLILLI Peppino
Total, Direction scientifique
Av Larribeau
64018 Pau cedex, FRANCE
peppino.terpolilli@total.com

TITI Edriss
UC Irvine & Weizmann Institute
Dept. of Mathematics, The University of California
Irvine, CA 92607-3875 USA
92697-3875 Irvine, U.S.A.
etiti@math.uci.edu

VENAILLE Antoine
Univ. de Grenoble, LEGI
1023 rue de la piscine
38000 Grenoble, FRANCE
antoine.venaille@gmail.com

WALLACE James
Univ. of Maryland, Gemstone Program
0100K Ellicot Hall
MD 20742 College Park, U.S.A.
wallace@eng.umd.edu

WESFREID Jose Eduardo
ESPCI, PMMH
10, rue Vauquelin
75005 paris, FRANCE
wesfreid@pmmh.espci.fr

WILCZEK Michael
Univ. Muenster, Institute for Theoretical Physics
Wilhelm-Klemm-Str. 9
48147 Muenster, GERMANY
mwilczek@uni-muenster.de

WILLIAMSON Charles
Univ. of Cornell, Fluid Dynamics Research Labs
144 Upson Hall
14853 Ithaca, U.S.A.
cw26@cornell.edu

YEUNG Pui-kuen
Georgia Inst of Tech, School of Aerospace Engineering
270 Ferst Drive, NW
30332-0150 Atlanta, GA, U.S.A.
pk.yeung@ae.gatech.edu

YOKOI Nobumitsu
Univ. of Tokyo, Institute of Industrial Science 4-6-1.
Komaba, Meguro
153-8505 Tokyo, JAPAN
nobyokoi@iis.u-tokyo.ac.jp